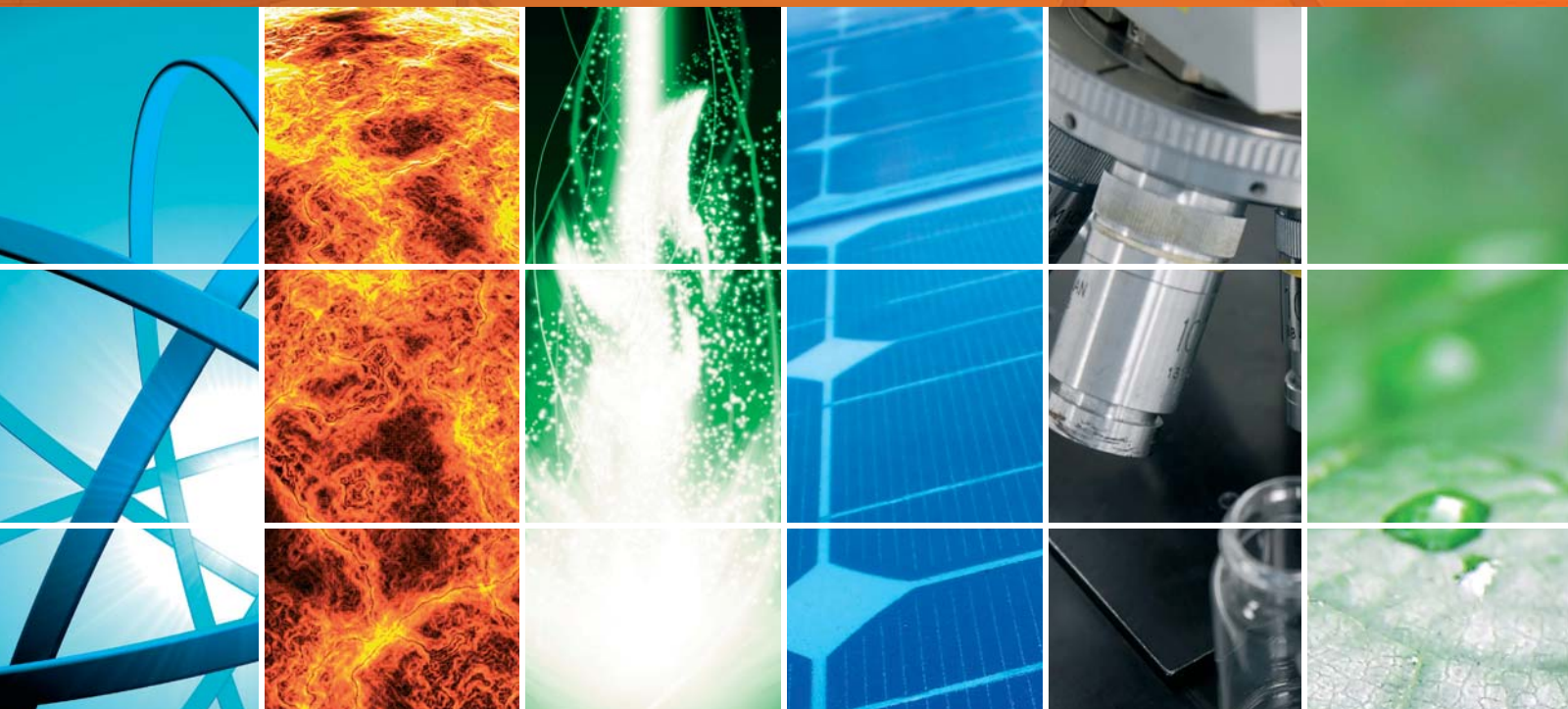


# TiO<sub>2</sub> Photocatalytic Materials

Guest Editors: Jiaguo Yu, Mietek Jaroniec, and Gongxuan Lu





---

# **TiO<sub>2</sub> Photocatalytic Materials**

International Journal of Photoenergy

---

## **TiO<sub>2</sub> Photocatalytic Materials**

Guest Editors: Jiaguo Yu, Mietek Jaroniec, and Gongxuan Lu



---

Copyright © 2012 Hindawi Publishing Corporation. All rights reserved.

This is a special issue published in "International Journal of Photoenergy." All articles are open access articles distributed under the Creative Commons Attribution License, which permits unrestricted use, distribution, and reproduction in any medium, provided the original work is properly cited.

## Editorial Board

M. S. Abdel-Mottaleb, Egypt  
Muhammad Abdul Rauf, UAE  
Nihal Ahmad, USA  
Nicolas Alonso-Vante, France  
Wayne A. Anderson, USA  
Vincenzo Augugliaro, Italy  
Detlef W. Bahnemann, Germany  
Ignazio Renato Bellobono, Italy  
Raghu N. Bhattacharya, USA  
Gion Calzaferri, Switzerland  
Vikram L. Dalal, USA  
Dionysios Dionysiou, USA  
Abderrazek Douhal, Spain  
Samy El-Shall, USA  
Beverley Glass, Australia

Shahed Khan, USA  
Cooper H. Langford, Canada  
Yuexiang Li, China  
Gianluca Li Puma, UK  
Stefan Lis, Poland  
Gilles Mailhot, France  
Ugo Mazzucato, Italy  
Jacek Miller, Poland  
Franca Morazzoni, Italy  
Leonardo Palmisano, Italy  
David Lee Phillips, Hong Kong  
Xie Quan, China  
Tijana Rajh, USA  
Saffa Riffat, UK  
Peter Robertson, UK

J.-L. Scartezzini, Switzerland  
P. J. Sebastian, Mexico  
Panagiotis Smirniotis, USA  
Sam-Shajing Sun, USA  
Masanori Tachiya, Japan  
Gopal N. Tiwari, India  
Veronica Vaida, USA  
Roel van De Krol, The Netherlands  
Mark van Der Auweraer, Belgium  
Johannes Vos, Ireland  
David Worrall, UK  
F. Yakuphanoglu, Turkey  
Jimmy C. Yu, Hong Kong  
Klaas Zachariasse, Germany  
Jincai Zhao, China

## Contents

**TiO<sub>2</sub> Photocatalytic Materials**, Jiaguo Yu, Mietek Jaroniec, and Gongxuan Lu  
Volume 2012, Article ID 206183, 5 pages

**Effect of Al-Cu Bimetallic Components in a TiO<sub>2</sub> Framework for High Hydrogen Production on Methanol/Water Photo-Splitting**, A-Young Kim and Misook Kang  
Volume 2012, Article ID 618642, 9 pages

**TiO<sub>2</sub>-Based Photocatalytic Treatment of Raw and Constructed-Wetland Pretreated Textile Wastewater**, Dunja Mahne, Urška Lavrencic Štangar, Polonca Trebše, and Tjaša Griessler Bulc  
Volume 2012, Article ID 725692, 12 pages

**Preparation of Antibacterial Color-Coated Steel Sheets**, Guoliang Li, Bing Peng, Liyuan Chai, Si Wan, and Lei Jiang  
Volume 2012, Article ID 436963, 7 pages

**Preparation and Photocatalytic Activity of TiO<sub>2</sub>-Deposited Fabrics**, Yang Xu, Wenzheng Xu, Fenglin Huang, and Qufu Wei  
Volume 2012, Article ID 852675, 5 pages

**Photocatalytic Decomposition of Amoxicillin Trihydrate Antibiotic in Aqueous Solutions under UV Irradiation Using Sn/TiO<sub>2</sub> Nanoparticles**, Robab Mohammadi, Bakhshali Massoumi, and Mohammad Rabani  
Volume 2012, Article ID 514856, 11 pages

**Fabrication of Al-Doped TiO<sub>2</sub> Visible-Light Photocatalyst for Low-Concentration Mercury Removal**, Cheng-Yen Tsai, Tien-Ho Kuo, and Hsing-Cheng Hsi  
Volume 2012, Article ID 874509, 8 pages

**Ta/TiO<sub>2</sub>- and Nb/TiO<sub>2</sub>-Mixed Oxides as Efficient Solar Photocatalysts: Preparation, Characterization, and Photocatalytic Activity**, Hussein Znad, Ming H. Ang, and Moses O. Tade  
Volume 2012, Article ID 548158, 9 pages

**Synergistic Effect of Nanophotocatalysis and Nonthermal Plasma on the Removal of Indoor HCHO**, Yuanwei Lu, Dinghui Wang, Yuting Wu, Chongfang Ma, Xingjuan Zhang, and Chunxin Yang  
Volume 2012, Article ID 354032, 8 pages

**TiO<sub>2</sub>:(Fe, S) Thin Films Prepared from Complex Precursors by CVD, Physical Chemical Properties, and Photocatalysis**, V. G. Bessergenev, M. C. Mateus, D. A. Vasconcelos, J. F. M. L. Mariano, A. M. Botelho do Rego, R. Lange, and E. Burkel  
Volume 2012, Article ID 767054, 12 pages

**Photoelectrocatalytic Degradation of Sodium Oxalate by TiO<sub>2</sub>/Ti Thin Film Electrode**, Chen-Yu Chang, Yung-Hsu Hsieh, and Yu-Ying Chen  
Volume 2012, Article ID 576089, 6 pages

**Effects of Homogenization Scheme of TiO<sub>2</sub> Screen-Printing Paste for Dye-Sensitized Solar Cells**, Seigo Ito, Kaoru Takahashi, Shin-ich Yusa, Takahiro Imamura, and Kenji Tanimoto  
Volume 2012, Article ID 405642, 7 pages

**Enhancing Photocatalytic Performance through Tuning the Interfacial Process between TiO<sub>2</sub>-Assembled and Pt-Loaded Microspheres**, Jun Zhang, Liping Li, and Guangshe Li  
Volume 2012, Article ID 913630, 7 pages

**A Review on TiO<sub>2</sub> Nanotube Film Photocatalysts Prepared by Liquid-Phase Deposition**, Jinshu Wang, Qian Cai, Hongyi Li, Yuntao Cui, and Hong Wang  
Volume 2012, Article ID 702940, 11 pages

**Anodization Parameters Influencing the Growth of Titania Nanotubes and Their Photoelectrochemical Response**, Ying-Chin Lim, Zulkarnain Zainal, Wee-Tee Tan, and Mohd Zobir Hussein  
Volume 2012, Article ID 638017, 9 pages

**Hydrothermal Synthesis of Nitrogen-Doped Titanium Dioxide and Evaluation of Its Visible Light Photocatalytic Activity**, Junjie Qian, Guanjun Cui, Mingjun Jing, Yan Wang, Min Zhang, and Jianjun Yang  
Volume 2012, Article ID 198497, 6 pages

**Enhanced Visible Light Photocatalytic Activity of Mesoporous Anatase TiO<sub>2</sub> Codoped with Nitrogen and Chlorine**, Xiuwen Cheng, Xiujuan Yu, Zipeng Xing, and Lisha Yang  
Volume 2012, Article ID 593245, 6 pages

**Enhanced Photocatalytic Activity of TiO<sub>2</sub> Powders (P25) via Calcination Treatment**, Guohong Wang, Lin Xu, Jun Zhang, Tingting Yin, and Deyan Han  
Volume 2012, Article ID 265760, 9 pages

**The Photocatalytic Inactivation Effect of Fe-Doped TiO<sub>2</sub> Nanocomposites on Leukemic HL60 Cells-Based Photodynamic Therapy**, Kangqiang Huang, Li Chen, Meixiang Liao, and Jianwen Xiong  
Volume 2012, Article ID 367072, 8 pages

**Facile Synthesis and Photocatalytic Property of Titania/Carbon Composite Hollow Microspheres with Bimodal Mesoporous Shells**, Guohong Wang, Bei Cheng, Jun Zhang, Lin Xu, and Tingting Yin  
Volume 2012, Article ID 976389, 9 pages

**Removal of a Cationic Dye by Adsorption/Photodegradation Using Electrospun PAN/O-MMT Composite Nanofibrous Membranes Coated with TiO<sub>2</sub>**, Qingqing Wang, Dawei Gao, Chuntao Gao, Qufu Wei, Yibing Cai, Jing Xu, Xiaoya Liu, and Yang Xu  
Volume 2012, Article ID 680419, 8 pages

**Effect of N,C-ITO on Composite N,C-TiO<sub>2</sub>/N,C-ITO/ITO Electrode Used for Photoelectrochemical Degradation of Aqueous Pollutant with Simultaneous Hydrogen Production**, Kee-Rong Wu, Chung-Hsuang Hung, Chung-Wei Yeh, Chien-Chung Wang, and Jiing-Kae Wu  
Volume 2012, Article ID 829327, 10 pages

**Low-Temperature Reverse Microemulsion Synthesis, Characterization, and Photocatalytic Performance of Nanocrystalline Titanium Dioxide**, Zhang Liu, Zicong Jian, Jianzhang Fang, Xiaoxin Xu, Ximiao Zhu, and Shuxing Wu  
Volume 2012, Article ID 702503, 8 pages

**Synthesis of Fe<sub>3</sub>O<sub>4</sub>/C/TiO<sub>2</sub> Magnetic Photocatalyst via Vapor Phase Hydrolysis**, Fuzhi Shi, Yaogang Li, Qinghong Zhang, and Hongzhi Wang  
Volume 2012, Article ID 365401, 8 pages

**Degradation of Gaseous Formaldehyde by Visible Light-Responsive Titania Photocatalyst Filter**, Tun-Ping Teng, Tun-Chien Teng, and Shu-I Pan  
Volume 2012, Article ID 739734, 10 pages

**Investigation on the Photoelectrocatalytic Activity of Well-Aligned TiO<sub>2</sub> Nanotube Arrays**, Xiaomeng Wu, Zhaohui Huang, Yangai Liu, and Minghao Fang  
Volume 2012, Article ID 832516, 7 pages

**Enhancement of Visible-Light Photocatalytic Activity of Mesoporous Au-TiO<sub>2</sub> Nanocomposites by Surface Plasmon Resonance**, Minghua Zhou, Jun Zhang, Bei Cheng, and Huogen Yu  
Volume 2012, Article ID 532843, 10 pages

**Photocatalytic Degradation of NO<sub>x</sub> Using Ni-Containing TiO<sub>2</sub>**, Yao-Hsuan Tseng and Bo-Kai Huang  
Volume 2012, Article ID 832180, 7 pages

**Anatase TiO<sub>2</sub> Nanospindle/Activated Carbon (AC) Composite Photocatalysts with Enhanced Activity in Removal of Organic Contaminant**, Wuyi Zhou, Peng Zhang, and Weian Liu  
Volume 2012, Article ID 325902, 7 pages

**Photocatalytic Oxidation of Triiodide in UVA-Exposed Dye-Sensitized Solar Cells**, Matthew Carnie, Daniel Bryant, Trystan Watson, and David Worsley  
Volume 2012, Article ID 524590, 8 pages

**Preparation and Photocatalytic Property of TiO<sub>2</sub>/Diatomite-Based Porous Ceramics Composite Materials**, Shuilin Zheng, Chunhua Bai, and RuQin Gao  
Volume 2012, Article ID 264186, 4 pages

**Neodymium-Doped TiO<sub>2</sub> with Anatase and Brookite Two Phases: Mechanism for Photocatalytic Activity Enhancement under Visible Light and the Role of Electron**, Douga Nassoko, Yan-Fang Li, Jia-Lin Li, Xi Li, and Ying Yu  
Volume 2012, Article ID 716087, 10 pages

**Photocatalytic Properties of Nitrogen-Doped Bi<sub>12</sub>TiO<sub>20</sub> Synthesized by Urea Addition Sol-Gel Method**, Jiyong Wei, Baibiao Huang, Peng Wang, Zeyan Wang, Xiaoyan Qin, Xiaoyang Zhang, Xiangyang Jing, Haixia Liu, and Jiaoxian Yu  
Volume 2012, Article ID 135132, 8 pages

**Preparation, Photocatalytic Activity, and Recovery of Magnetic Photocatalyst for Decomposition of Benzoic Acid**, Te-Li Su, Chyow-San Chiou, and Hua-Wei Chen  
Volume 2012, Article ID 909678, 8 pages

**The Synthetic Effects of Iron with Sulfur and Fluorine on Photoabsorption and Photocatalytic Performance in Codoped TiO<sub>2</sub>**, Xiaohua Li, Jibao Lu, Ying Dai, Meng Guo, and Baibiao Huang  
Volume 2012, Article ID 203529, 7 pages

**Performance of Ag-TiO<sub>2</sub> Photocatalysts towards the Photocatalytic Disinfection of Water under Interior-Lighting and Solar-Simulated Light Irradiations**, Camilo A. Castro, Adriana Jurado, Diana Sissa, and Sonia A. Giraldo

Volume 2012, Article ID 261045, 10 pages

**Degrading Endocrine Disrupting Chemicals from Wastewater by TiO<sub>2</sub> Photocatalysis: A Review**, Jin-Chung Sin, Sze-Mun Lam, Abdul Rahman Mohamed, and Keat-Teong Lee

Volume 2012, Article ID 185159, 23 pages

**Highly Selective Deethylation of Rhodamine B on TiO<sub>2</sub> Prepared in Supercritical Fluids**, Yuzun Fan, Guoping Chen, Dongmei Li, Yanhong Luo, Nina Lock, Anca Paduraru Jensen, Aref Mamakhel, Jianli Mi, Steen B. Iversen, Qingbo Meng, and Bo B. Iversen

Volume 2012, Article ID 173865, 7 pages

**Effects of Calcination Temperatures on Photocatalytic Activity of Ordered Titanate Nanoribbon/SnO<sub>2</sub> Films Fabricated during an EPD Process**, Li Zhao, Jingrun Ran, Zhan Shu, Guotian Dai, Pengcheng Zhai, and Shimin Wang

Volume 2012, Article ID 472958, 7 pages

**Mechanistic Study of Visible-Light-Induced Photodegradation of 4-Chlorophenol by TiO<sub>2-x</sub>N<sub>x</sub> with Low Nitrogen Concentration**, Guangfeng Shang, Hongbo Fu, Shaogui Yang, and Tongguang Xu

Volume 2012, Article ID 759306, 9 pages

## Editorial

# TiO<sub>2</sub> Photocatalytic Materials

Jiaguo Yu,<sup>1</sup> Mietek Jaroniec,<sup>2</sup> and Gongxuan Lu<sup>3</sup>

<sup>1</sup> State Key Laboratory of Advanced Technology for Material Synthesis and Processing, Wuhan University of Technology, Luoshi Road No. 122, Wuhan 430070, China

<sup>2</sup> Department of Chemistry, Kent State University, Kent, OH 44242, USA

<sup>3</sup> State Key Laboratory for Oxo Synthesis and Selective Oxidation, Lanzhou Institute of Chemical Physics, Chinese Academy of Sciences, Lanzhou 730000, China

Correspondence should be addressed to Jiaguo Yu, jiaguoyu@yahoo.com

Received 24 April 2012; Accepted 24 April 2012

Copyright © 2012 Jiaguo Yu et al. This is an open access article distributed under the Creative Commons Attribution License, which permits unrestricted use, distribution, and reproduction in any medium, provided the original work is properly cited.

Since the discovery of photocatalytic splitting of water on TiO<sub>2</sub> electrodes in 1972 by Honda and Fujishima, a great deal of effort has been devoted in recent years to the development of highly active heterogeneous photocatalysts for environmental applications including air purification, water disinfection, hazardous waste remediation, and water purification, as well as for the energy-related applications, such as, hydrogen production and solar cells. Among the various oxide and nonoxide semiconductor photocatalysts, the photocatalytic performance of titania has been most intensively studied because of its biological and chemical inertness, strong oxidizing power, cost effectiveness, and long-term stability against photocorrosion and chemical corrosion, and especially its energy band edges, which well match the redox potentials of water. However, the photocatalytic performance of TiO<sub>2</sub> must be further enhanced from the practical and commercial viewpoints, mainly due to the high recombination rate of photogenerated conduction band electrons and valence band holes and narrow light-response range resulting from the wide band gap. To resolve these problems, many methods have been proposed to enhance the photocatalytic activity of TiO<sub>2</sub>, including crystal and textural modification, band gap (electronic structure) engineering, interfacial heterostructuring, noble metal loading, metal ion doping, carbon and nitrogen doping, dye sensitization, and also the usage of sacrificial reagents (electron donors or hole scavengers).

This special issue contains thirty nine papers, which mainly deal with environmental purification, hydrogen production, and dye-sensitized solar cells. Among them 30 papers are related to environmental photocatalysis, 4 papers deal with photoelectrocatalysis and photoelectrochemistry, 3

papers are devoted to photocatalytic hydrogen production, and 2 papers focus on dye-sensitized solar cells. Furthermore, this special issue contains two papers related to the photocatalytic degradation of endocrine disrupting chemicals (EDCs) present in wastewater by TiO<sub>2</sub> and to the preparation of film-type TiO<sub>2</sub> nanotube photocatalysts by liquid-phase deposition, respectively. Ten of the aforementioned papers are devoted to the doping or codoping TiO<sub>2</sub> photocatalysts. Eight papers deal with the composite photocatalysts. Two papers are related to the preparation, photocatalytic activity, and recovery of magnetic photocatalysts. Two papers report data on the modification of Degussa-P25 TiO<sub>2</sub> powders. Another two contributions describe the removal of indoor formaldehyde pollutants. Three papers are devoted to bactericidal and antibacterial activity of TiO<sub>2</sub>. One paper deals with photocatalytic selectivity of TiO<sub>2</sub>. Another paper discusses the plasmon photocatalytic selectivity of Au-TiO<sub>2</sub>. Finally, two other papers are related to the low-temperature preparation of TiO<sub>2</sub> and photocatalytic treatment of textile wastewater, respectively. We wish to express our thanks to all the authors for submitting interesting contributions to this special issue. A brief summary of all thirty nine accepted papers is provided below.

In “*Degrading endocrine disrupting chemicals from wastewater by TiO<sub>2</sub> photocatalysis: a review*,” the authors discuss the heterogeneous photocatalysis, the abatement of endocrine-disrupting chemicals (EDCs), phthalates, bisphenol A and chlorophenols in particular, using TiO<sub>2</sub>-based catalysts. Degradation mechanisms, pathways, and intermediate products of various EDCs on TiO<sub>2</sub> photocatalysis are described in detail. The influence of experimental conditions on the photocatalytic degradation of various EDCs on TiO<sub>2</sub> is

covered with a special attention. Finally, the future prospects and challenges for the photocatalytic degradation EDCs on titania are summarized and discussed.

Another contribution "A review on  $\text{TiO}_2$  nanotube film photocatalysts prepared by liquid-phase deposition," provides a concise appraisal of studies on the formation of  $\text{TiO}_2$  nanotube films by liquid-phase deposition based on the template-assisted growth. The formation mechanisms of anodic alumina templates and  $\text{TiO}_2$  nanotube films are discussed. The morphology of  $\text{TiO}_2$  is influenced by the morphology of anodic alumina. This work shows that the proper concentration of deposition solution (0.1 mol/L  $(\text{NH}_4)_2\text{TiF}_6$ ) and proper calcination temperature (400°C) are favorable for the production of  $\text{TiO}_2$  nanotube films.

In "Photocatalytic properties of nitrogen-doped  $\text{Bi}_{12}\text{TiO}_{20}$  synthesized by urea addition sol-gel method," the undoped and nitrogen-doped  $\text{Bi}_{12}\text{TiO}_{20}$  materials were synthesized by sol-gel method in the presence of urea and subjected to annealing at 600°C. The UV-Vis absorption spectra indicate that the absorbance band of N-doped samples is shifted from 420 to 500 nm due to the substitution of oxygen with nitrogen and the formation of Ti-N and N-O bonds. The optimal N-doping amount was determined. The resulting photocatalyst  $\text{Bi}_{12}\text{TiO}_{20-y}\text{N}_y$  ( $y = 0.03$ ) with N/(N+O) mole ratio of about 3% showed better performance than those strongly doped ( $\text{Bi}_{12}\text{TiO}_{20-z}\text{N}_z$ ;  $z = 0.06$ ), undoped ( $\text{Bi}_{12}\text{TiO}_{20}$ ), and slightly doped ( $\text{Bi}_{12}\text{TiO}_{20-x}\text{N}_x$ ;  $x = 0.01$ ).

In "Hydrothermal synthesis of nitrogen-doped titanium dioxide and evaluation of its visible light photocatalytic activity," the N-doped  $\text{TiO}_2$  was synthesized from nanotube titanate precursor via a hydrothermal route in ammonia solution. The N-doped  $\text{TiO}_2$  catalyst showed much higher activity towards degradation of methylene blue and p-chlorophenol under visible light irradiation than Degussa P25. This is due to the enhanced absorption of N-doped  $\text{TiO}_2$  in visible light region associated with the formation of single-electron-trapped oxygen vacancies and the inhibition of recombination of photogenerated electron-hole pair by doped nitrogen.

In "The synthetic effects of iron with sulfur and fluorine on photoabsorption and photocatalytic performance in codoped  $\text{TiO}_2$ ," the structural and electronic properties of iron-fluorine (Fe-F-) and iron-sulfur (Fe-S-) codoped anatase  $\text{TiO}_2$  are investigated by first-principle calculations based on density functional theory. The formation energy of codoped system is lower than that of single-element doping, which indicates the synergic effect of codoping on the stability of the structure. The codopants introduced impurity gap states resulting in the reduction of electron transition energy and thus, the visible light absorption by the samples. It is concluded that Fe-S should be a better codoping pair because it introduces extended impurity states resulting in stronger visible light absorption than those generated by Fe-F codoping compounds. This work explains the recent experiments and guides the selection of the more effective codopants in  $\text{TiO}_2$ .

In "The photocatalytic inactivation effect of Fe-doped  $\text{TiO}_2$  nanocomposites on leukemic HL60 cells-based photodynamic therapy," the photocatalytic inactivation of Fe-doped  $\text{TiO}_2$

on leukemic HL60 cells was investigated using photodynamic therapy (PDT) reaction chamber based on LED light source; the viability of HL60 cells was examined by Cell Counting Kit-8 (CCK-8) assay. The growth of leukemic HL60 cells was significantly inhibited by adding  $\text{TiO}_2$  nanoparticles, and the inactivation efficiency was effectively enhanced by the surface modification of  $\text{TiO}_2$  nanoparticles by Fe doping.

In "Photocatalytic decomposition of amoxicillin trihydrate (AMOX) antibiotic in aqueous solutions under UV irradiation using Sn/ $\text{TiO}_2$  nanoparticles," the effects of Sn-doping on the crystal structure, surface area, adsorption properties, pore size distribution, and optical absorption properties of the catalysts were investigated. The resulting Sn/ $\text{TiO}_2$  nanoparticles exhibited high photocatalytic activity during mineralization of AMOX under UV light due to the increase of generated hydroxyl radicals, band gap energy, specific surface area, and decrease in the crystallite size. The kinetics of AMOX mineralization was explained in terms of the Langmuir-Hinshelwood model.

In "Enhanced visible light photocatalytic activity of mesoporous anatase  $\text{TiO}_2$  codoped with nitrogen and chlorine," anatase mesoporous  $\text{TiO}_2$  photocatalysts codoped with N and Cl (N-Cl- $\text{TiO}_2$ ) were synthesized by one-step sol-gel process in the presence of ammonium chloride. N-Cl- $\text{TiO}_2$  catalyst exhibited higher visible light photocatalytic activity than P25  $\text{TiO}_2$  and N- $\text{TiO}_2$ , which was attributed to the small crystallite size, intense light absorption in visible region, and narrow band gap.

In "Neodymium-doped  $\text{TiO}_2$  with anatase and brookite two phases: mechanism for photocatalytic activity enhancement under visible light and the role of electron," the titania samples doped with neodymium (Nd) were synthesized by a sol-gel method and examined for the photocatalytic degradation of rhodamine-B under visible light. Anatase and brookite phases were detected in these samples. Additionally, Nd as  $\text{Nd}^{3+}$  may enter into the lattice of  $\text{TiO}_2$  and the presence of  $\text{Nd}^{3+}$  substantially enhances the photocatalytic activity of  $\text{TiO}_2$  under visible light. It was found that hydroxyl radicals produced by Nd-doped  $\text{TiO}_2$  under visible light are reactive species for Rh-B degradation and the photogenerated electrons are mainly responsible for the formation of the reactive species.

In "Mechanistic study of visible-light-induced photodegradation of 4-chlorophenol by  $\text{TiO}_{2-x}\text{N}_x$  with low nitrogen concentration," the  $\text{TiO}_{2-x}\text{N}_x$  powders with low N-doping concentrations ( $0.021 < x < 0.049$ ) were prepared by annealing commercial  $\text{TiO}_2$  (P-25) under  $\text{NH}_3$  flow at 550°C. Regardless of UV or visible light, the photoactivities of the samples decreased as  $x$  increased, and  $\text{TiO}_{1.979}\text{N}_{0.021}$  showed the highest activity for the 4-chlorophenol (4-CP) decomposition under visible-light irradiation. The visible-light response for N-doped  $\text{TiO}_2$  could arise from the N-induced midgap level, formed above the valence band (O 2p). Electron spin resonance (ESR) measurements and the radical scavenger methods provided the evidence that the active species ( $\text{OH}^\bullet$  and  $\text{O}_2^{\bullet-}$ ) are responsible for the photodecomposition of 4-CP over  $\text{TiO}_{2-x}\text{N}_x$  under the visible irradiation. A possible photocatalytic mechanism was discussed in detail.

In "*TiO<sub>2</sub>:(Fe, S) thin films prepared from complex precursors by CVD, physical chemical properties, and photocatalysis,*" the TiO<sub>2</sub> thin films were prepared using Ti(dpm)<sub>2</sub>(OPr<sup>i</sup>)<sub>2</sub> and Ti(OPr<sup>i</sup>)<sub>4</sub> (dpm = 2,2,6,6-tetramethylheptane-3,5-dione, Pr<sup>i</sup> = isopropyl) as the precursors. The volatile compounds Fe[(C<sub>2</sub>H<sub>5</sub>)<sub>2</sub>NCS<sub>2</sub>]<sub>3</sub> and [(CH<sub>3</sub>)C]<sub>2</sub>S<sub>2</sub> were used to prepare doped TiO<sub>2</sub> films. The synthesis was done in vacuum or in the presence of Ar and O<sub>2</sub>. Physical, chemical, and photocatalytic properties of the (Fe, S)-doped TiO<sub>2</sub> films were studied. The TiO<sub>2</sub>:(Fe, S) films prepared from the Ti(OPr<sup>i</sup>)<sub>4</sub> precursor showed higher photocatalytic activities, very close to that of Degussa P25 powder in UV region.

In "*fabrication of Al-doped TiO<sub>2</sub> visible-light photocatalyst for low-concentration mercury removal,*" the high-quality Al-doped TiO<sub>2</sub> visible-light photocatalyst was prepared via a single-step direct combination of vaporized Ti, Al, and O<sub>2</sub> using a 6 kW thermal plasma system. The formed Al-doped TiO<sub>2</sub> nanoparticles were a mixture of anatase and rutile phases and had a size between 10 and 105 nm. The absorption spectra of these nanoparticles are shifted towards the visible light region, depending on the Al<sub>2</sub>O<sub>3</sub> addition. Hg<sup>0</sup> breakthrough tests revealed that the nanoparticles showed an appreciable Hg<sup>0</sup> removal capability under visible-light irradiation. Nevertheless, the moisture reduced Hg removal by the nanoparticles, especially when visible-light irradiation was applied, suggesting that the competitive adsorption between H<sub>2</sub>O and Hg species on the active sites of TiO<sub>2</sub> surface occurred.

In "*Effect of Ag-Cu bimetallic components in a TiO<sub>2</sub> framework for high hydrogen production on methanol/water photo-splitting,*" the TiO<sub>2</sub> photocatalysts doped with Ag, Cu, and Cu-Ag were prepared for the production of H<sub>2</sub> from methanol/water photodecomposition. As compared to monometal-incorporated TiO<sub>2</sub>, the H<sub>2</sub> production was markedly enhanced in bimetal-incorporated photocatalyst.

In "*Photoelectrocatalytic degradation of sodium oxalate by TiO<sub>2</sub>/Ti thin film electrode,*" the photocatalytically active TiO<sub>2</sub> thin films were deposited on the titanium substrate plate by chemical vapor deposition (CVD) method, and the photoelectrocatalytic degradation of sodium oxalate was investigated. The additional applied potential in photocatalytic reaction could prohibit recombination of electron/hole pairs, but the photoelectrocatalytic effect was decreased when the applied electric potential was over 0.25 V.

In "*Anodization parameters influencing the growth of titania nanotubes and their photoelectrochemical response,*" the TiO<sub>2</sub> nanotubes (TNTs) were fabricated by electrochemical oxidation of Ti foil in a standard two-electrode cell-containing NH<sub>4</sub>F. The tube length decreased with bath temperature, which can be attributed to the faster chemical dissolution rate at high temperatures. However, nanotubes growth rate was enhanced by ~260% with the addition of EDTA as the complexing agent. Meanwhile, the nanotubes diameter was found to be proportionally dependent on bath temperature but independent of the voltage ramp and addition of EDTA. The photoelectrochemical response under illumination was enhanced by using the calcined TNT.

In "*Effect of N,C-ITO on composite N,C-TiO<sub>2</sub>/N,C-ITO/ITO electrode used for photoelectrochemical degradation*

*of aqueous pollutant with simultaneous hydrogen production,*" the composite Ti/TO electrode was simultaneously used for hydrogen production and degradation of organic pollutants. The N,C-TiO<sub>2</sub> layer in this electrode enhanced not only the photocurrent response at entire applied potentials but also the flat band potential; a shift of about 0.1 V towards cathode was observed, which is beneficial for the PEC process.

In "*Investigation on the photoelectrocatalytic activity of well-aligned TiO<sub>2</sub> nanotube arrays,*" the well-aligned TiO<sub>2</sub> nanotube arrays were fabricated by anodizing Ti foil in viscous F<sup>-</sup> containing organic electrolytes, and their photocatalytic activity was evaluated in the photocatalytic (PC) and photoelectrocatalytic (PEC) degradation of methylene blue (MB) dye in different supporting solutions. The excellent performance of ca. 97% for color removal was reached after 90 min in the PEC process compared to that of PC process which indicates that a certain external potential bias favors the promotion of the electrode reaction rate on the TiO<sub>2</sub> nanotube array when it is under illumination. In addition, it was found that the PEC degradation of MB conducted in supporting solutions was accelerated at low pH and in the presence of Cl<sup>-</sup>.

In "*Photocatalytic oxidation of triiodide in UVA-exposed dye-sensitized solar cells,*" the UVA irradiation of glass mounted dye-sensitized solar cells without UV filtration caused a failure within 400 hours of light exposure. The failure mode was shown to relate to the consumption of I<sub>3</sub><sup>-</sup>, which was directly related to TiO<sub>2</sub> photocatalysis. The device failure was more rapid for the cells under electrical load indicating that the degradation of the electrolyte is related to photogenerated hole production by excitation of TiO<sub>2</sub>. Once depleted by UV exposure, the I<sub>3</sub><sup>-</sup> was regenerated by simple application of a reverse bias, which can restore severely the UV-degraded devices to near original working conditions.

In "*Effects of homogenization scheme of TiO<sub>2</sub> screen-printing paste for dye-sensitized solar cells,*" the TiO<sub>2</sub> screen-printing paste was prepared by two methods to disperse the nanocrystalline TiO<sub>2</sub> powder: a "ball-milling route" and a "mortar-grinding route." The TiO<sub>2</sub> ball-milling (TiO<sub>2</sub>-BM) route gave monodisperse TiO<sub>2</sub> nanoparticles, resulting in high photocurrent density (14.2 mA cm<sup>-2</sup>) and high photoconversion efficiency (8.27%). On the other hand, the TiO<sub>2</sub> mortar-grinding (TiO<sub>2</sub>-MG) route gave large aggregates of TiO<sub>2</sub> nanoparticles, resulting in low photocurrent density (11.5 mA cm<sup>-2</sup>) and low photoconversion efficiency (6.43%).

In "*Enhancing photocatalytic performance through tuning the interfacial process between TiO<sub>2</sub>-assembled and Pt-loaded microspheres,*" the Pt-TiO<sub>2</sub> microspheres were prepared in a solution with subsequent Pt loading through a photoreduction. The Pt loading led to an efficient separation of photogenerated electron-hole pairs. Meanwhile, electrons stored in the "microcapacitor" of TiO<sub>2</sub> microspheres contributed to the enhancement of photocatalytic activity under UV light irradiation.

In "*Facile synthesis and photocatalytic property of titania/carbon composite hollow microspheres with bimodal mesoporous shells,*" the titania/carbon composite hollow microspheres with bimodal mesoporous shells were fabricated

by one-pot procedure involving acidic  $(\text{NH}_4)_2\text{TiF}_6$  aqueous solution in the presence of glucose at  $180^\circ\text{C}$  for 24 h and then calcined at  $450^\circ\text{C}$  for 2–4 h. All  $\text{TiO}_2/\text{C}$  composite hollow spheres generally exhibited bimodal mesopore size distribution with peaks in the range of 2.3–4.5 nm and 5.7–12.7 nm. The  $\text{TiO}_2$ -2 sample showed the highest daylight-induced photocatalytic activity and greatly exceeded that of Degussa P25.

In “*Performance of Ag-TiO<sub>2</sub> photocatalysts towards the photocatalytic disinfection of water under interior-lighting and solar-simulated light irradiations*,” the characterization and photoactivity of Ag-TiO<sub>2</sub> materials was studied using different amounts of silver during the hydrothermal synthesis. The resulting photocatalysts were tested towards photocatalytic disinfection of water using a solar light simulator and an interior-light irradiation setup. The obtained data indicate an increase in the photooxidative effect of TiO<sub>2</sub>, while dark processes show that the partial inactivation is due to the Ag-TiO<sub>2</sub> surface bactericidal effect and possible leached Ag<sup>+</sup>.

In “*Preparation and photocatalytic property of TiO<sub>2</sub>/diatomite-based porous ceramics composite materials*,” the nano-TiO<sub>2</sub>/diatomite-based porous ceramics composite materials were prepared by hydrolysis deposition method using titanium tetrachloride as the precursor of TiO<sub>2</sub> and diatomite as the porous support. After calcination at  $550^\circ\text{C}$ , the thin TiO<sub>2</sub> anatase film was formed on the diatomite with the average grain size of TiO<sub>2</sub> of about 10 nm. The degradation ratio for 5 mg/L malachite green solution reached 86.2% after irradiation for 6 h under ultraviolet.

In “*Anatase TiO<sub>2</sub> nanospindle/activated carbon (AC) composite photocatalysts with enhanced activity in removal of organic contaminant*,” a novel TiO<sub>2</sub>/AC composite photocatalyst was prepared by coating of anatase TiO<sub>2</sub> nanospindles onto the surface of AC particles, which showed better photocatalytic activity than pure TiO<sub>2</sub> due to the synergistic effect between supporting materials and TiO<sub>2</sub> nanospindles. Most importantly, this composite photocatalysts effectively reduced the leaching of TiO<sub>2</sub> from the surface of AC.

In “*Preparation and photocatalytic activity of TiO<sub>2</sub>-deposited fabrics*,” the nanoscale TiO<sub>2</sub> photocatalytic films were formed on the surface of polyester nonwovens by using direct current reactive magnetron sputtering. The test results proved that the grain sizes of the sputtered clusters increased and the coating layer became more compact with increasing film thickness, but the composition of films did not change significantly. The photocatalytic activity of TiO<sub>2</sub>-coated fabrics mostly depended on the film thickness.

In “*Synthesis of Fe<sub>3</sub>O<sub>4</sub>/C/TiO<sub>2</sub> magnetic photocatalyst via vapor phase hydrolysis*,” a core/multishell-structured Fe<sub>3</sub>O<sub>4</sub>/C/TiO<sub>2</sub> magnetic photocatalyst was prepared via vapor phase hydrolysis process. The size and crystallinity of anatase TiO<sub>2</sub> crystallite in the shell could be tuned by temperature and duration of the process. The photocatalytic activity of Fe<sub>3</sub>O<sub>4</sub>/C/TiO<sub>2</sub> was higher than that of the commercial anatase TiO<sub>2</sub> in photocatalytic degradation of methylene blue (MB), and its recycling property was significantly improved. The intermediate carbon layer can effectively eliminate the electron interaction or photodissolution of Fe<sub>3</sub>O<sub>4</sub> occurring at the point of contact.

In “*Preparation, photocatalytic activity, and recovery of magnetic photocatalyst for decomposition of benzoic Acid*,” the optimal experimental parameters of TiO<sub>2</sub> preparation were pH 3, weight ratio of TiO<sub>2</sub>/SiO<sub>2</sub>(Fe<sub>3</sub>O<sub>4</sub>) at 1 and calcination temperature of TiO<sub>2</sub>/SiO<sub>2</sub>/Fe<sub>3</sub>O<sub>4</sub> at  $350^\circ\text{C}$ . Furthermore, the paramagnetic behaviors of the prepared TiO<sub>2</sub>/SiO<sub>2</sub>/Fe<sub>3</sub>O<sub>4</sub> gave rise to the magnetic photocatalyst, which could be separated more easily through the application of a magnetic field.

In “*Enhanced photocatalytic activity of TiO<sub>2</sub> powders (P25) via calcination treatment*,” the authors showed that calcination influenced the microstructures and photocatalytic activity of the P25 TiO<sub>2</sub> powders. An optimal calcination temperature ( $500^\circ\text{C}$ ) was determined, and the photocatalytic activity of TiO<sub>2</sub> powders calcined at  $500^\circ\text{C}$  was nearly twice higher than that of the uncalcined P25 TiO<sub>2</sub>.

In “*Photocatalytic degradation of NO<sub>x</sub> using Ni-containing TiO<sub>2</sub>*,” a nickel-modified titania photocatalyst was prepared by photodeposition method using Degussa-P25 TiO<sub>2</sub> particle and nickel chloride as raw materials. Ni did not enter into the TiO<sub>2</sub> crystal lattice and was uniformly dispersed onto the TiO<sub>2</sub> surface. The modified titanium dioxide with 0.1 mol% of nickel exhibited twice higher the NO<sub>x</sub>-removal activity in comparison to the bare TiO<sub>2</sub> under ultraviolet illumination. The nickel content in this photodeposition process plays an important role in controlling affinity towards NO<sub>x</sub> molecules, recombination rate of electron-hole pair, and the content of active sites on the TiO<sub>2</sub> surface and therefore, affects the optical and photocatalytic properties.

In “*Effects of calcination temperatures on photocatalytic activity of ordered titanate nanoribbon (TNR)/SnO<sub>2</sub> films fabricated during an EPD process*,” the highest photocatalytic activity was obtained for the calcined TNR/SnO<sub>2</sub> film at  $600^\circ\text{C}$  due to the formation of well-crystallized anatase phase, the unique morphology, and the fast charge carrier separation and transfer at the interface of TiO<sub>2</sub> and SnO<sub>2</sub>.

In “*Synergistic effect of nanophotocatalysis and nonthermal plasma on the removal of indoor HCHO*,” the effect of combination of photocatalytic oxidation (PCO) with non-thermal plasma technology (NTP) on the removal of indoor HCHO was investigated. The effects of plasma discharge configuration, the applied voltage, the flow velocity, and the humidity on the HCHO removal were studied. The HCHO removal was shown to be more effective in the line-to-plate electrode discharge reactor; the HCHO reaction rate was enhanced and the amount of air that needs to be cleaned was enlarged. The synergistic effect was observed for the indoor air purification by combining PCO with NTP.

In “*Degradation of gaseous formaldehyde by visible light-responsive titania photocatalyst filter*,” a method is proposed by using electrophoretic deposition (EPD) to fabricate the titania (TiO<sub>2</sub>) photocatalyst filter, which after modification with lithium nitrate (LiNO<sub>3</sub>) became responsive to visible light and effectively degraded gaseous formaldehyde. The best total average degradation performance of this photocatalyst filter was about 9.2% and 16.3% higher than that of the original photocatalyst filter (P-25, Degussa) at the UVA and visible irradiation, respectively, at  $26^\circ\text{C}$ .

In "Preparation of antibacterial color-coated steel sheets," a simple way to manufacture antibacterial color-coated sheet using Ag-loaded TiO<sub>2</sub> is developed. The optimal technical parameters are 2% for silver-loaded titanium dioxide, which is dispersed well as color-coated sheets, reaching the antibacterial efficiency of 99.99%. The efficiency of methyl orange degradation reached 88% in 4 h.

In "Highly selective deethylation of rhodamine B on TiO<sub>2</sub> prepared in supercritical fluids," a pure phase anatase TiO<sub>2</sub> nanoparticles with sizes of 5–8 nm and different crystallinity were synthesized in supercritical isopropanol/water using a continuous flow reactor. Their photodegradation of rhodamine B (RhB) was evaluated under visible light irradiation. The as-prepared TiO<sub>2</sub> nanoparticles showed much higher photodegradation efficiencies than commercial Degussa P25 TiO<sub>2</sub>. Moreover, the photodegradation of RhB on the as-prepared TiO<sub>2</sub> follows a different process than that on P25 TiO<sub>2</sub>, quicker N-deethylation and slower cleavage of conjugated chromophore structure.

In "Enhancement of visible-light photocatalytic activity of mesoporous Au-TiO<sub>2</sub> nanocomposites by surface plasmon resonance," the Au-TiO<sub>2</sub> nanocomposites were prepared by a simple spray hydrolytic method with photoreduction at 90°C. The light absorption, the formation rates of hydroxyl radicals, and photocatalytic decolorization of RhB aqueous solution were significantly enhanced by the embedded Au nanoparticles in the Au-TiO<sub>2</sub> nanocomposites due to the surface plasmon resonance. The composite R<sub>Au</sub>-0.015 sample exhibited the best visible-light photocatalytic activity for decolorization of RhB aqueous solution due to the synergistic effects of the absorption shift into visible and improved efficiency of interfacial charge transfer process.

In "Ta/TiO<sub>2</sub>- and Nb/TiO<sub>2</sub>-mixed oxides as efficient solar photocatalysts: preparation, characterization, and photocatalytic activity," Ta/TiO<sub>2</sub>- and Nb/TiO<sub>2</sub>-mixed oxide photocatalysts were prepared by simple impregnation method using different TiO<sub>2</sub> : Nb mass ratios, followed by calcination at 500°C. Nb/TiO<sub>2</sub>- and Ta/TiO<sub>2</sub>-mixed oxides showed higher activity than the untreated TiO<sub>2</sub> under natural solar light. The maximum activity was observed for Nb/TiO<sub>2</sub> sample (at mass ratio of 1 : 0.1), characterized by the smallest crystalline size (17.79 nm). As compared to the untreated TiO<sub>2</sub>, the solar decolorization and mineralization rates improved by about 140% and 237%, respectively, and the band gap was reduced to 2.80 eV.

In "Removal of a cationic dye by adsorption/photodegradation using electrospun PAN/O-MMT composite nanofibrous membranes coated with TiO<sub>2</sub>," the polyacrylonitrile (PAN)/organic-modified montmorillonite (O-MMT) nanofibrous composite membranes were firstly prepared by electrospinning and then coated with titanium dioxide (TiO<sub>2</sub>) using spin coating technique. With the increase of O-MMT amount, the diameters of the nanofibers decreased, and the adsorption rate of MB was evidently improved. Besides, with the increase of TiO<sub>2</sub> film thickness, the photocatalytic properties were enhanced while the adsorption process was slowed down.

In "Low-temperature reverse microemulsion synthesis, characterization, and photocatalytic performance of nanocrystalline

titanium dioxide," the nanosized TiO<sub>2</sub> nanoparticles were synthesized in n-hexanol/CTAB/water reverse microemulsions. Among all the as-synthesized photocatalysts by aging method, the nanoparticles aged at 65°C for 90 h showed the highest photocatalytic activity, which was higher than that of commercial P25.

In "TiO<sub>2</sub>-based photocatalytic treatment of raw and constructed-wetland pretreated textile wastewater," a combination of photocatalytic and biological degradation of wastewaters generated in textile production (simulation of real textile effluent) is presented.

Jianguo Yu  
Mietek Jaroniec  
Gongxuan Lu

## Research Article

# Effect of Al-Cu Bimetallic Components in a TiO<sub>2</sub> Framework for High Hydrogen Production on Methanol/Water Photo-Splitting

A-Young Kim and Misook Kang

Department of Chemistry, College of Science, Yeungnam University, Gyeongsbuk, Gyeongsan 712-749, Republic of Korea

Correspondence should be addressed to Misook Kang, mskang@ynu.ac.kr

Received 29 August 2011; Revised 3 January 2012; Accepted 3 January 2012

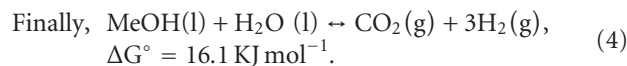
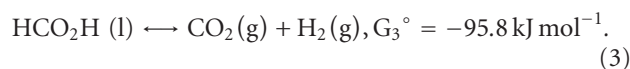
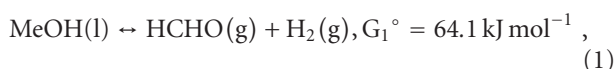
Academic Editor: Gongxuan Lu

Copyright © 2012 A-Y. Kim and M. Kang. This is an open access article distributed under the Creative Commons Attribution License, which permits unrestricted use, distribution, and reproduction in any medium, provided the original work is properly cited.

This study investigated the production of hydrogen over TiO<sub>2</sub>, Cu-TiO<sub>2</sub>, Ag-TiO<sub>2</sub>, and Cu-Ag-TiO<sub>2</sub> photocatalysts incorporated with Cu and Ag ions by a solvothermal method. The Ag metal (200, 220, and 311 plane) peaks at  $2\theta = 44.50, 64.00, \text{ and } 77.60^\circ$  were presented in the Ag-incorporated TiO<sub>2</sub> catalysts. The CuO component (Cu2p<sub>3/2</sub> and Cu2p<sub>1/2</sub> at 930.4 and 949.5 eV) was exhibited in the X-ray photon spectroscopy (XPS) band of the Cu-incorporated TiO<sub>2</sub> photocatalyst. All the absorption plots in the Cu-, Ag-, and Cu-Ag-incorporated catalysts showed excitation characteristics; an asymmetric tail was observed towards a higher wavelength due to scattering. The intensity of the photoluminescence (PL) curves of Cu-Ag-TiO<sub>2</sub>s was smaller, with the smallest case being observed for Cu(0.05)-Ag(0.05)Ti(0.9)O<sub>2</sub> and Cu(0.03)-Ag(0.07)Ti(0.9)O<sub>2</sub>. Based on these optical characteristics, the production of H<sub>2</sub> from methanol/water photodecomposition over the Cu(0.03)-Ag(0.07)Ti(0.9)O<sub>2</sub> photocatalyst at 8,750 mmol after 8 h was greater than that over the other photocatalysts.

## 1. Introduction

The technology for generating hydrogen by the splitting of water using a photocatalyst has attracted much attention. The principle of photocatalytic water decomposition is based on the conversion of light energy into electricity in a semiconductor on exposure to light [1–3]. Semiconductor materials such as MTiO<sub>3</sub> [4, 5] and TiO<sub>x</sub>N<sub>y</sub> [6, 7] have been widely investigated due to their low band gap and high corrosion resistance. However, the photocatalytic decomposition of water on a TiO<sub>2</sub> photocatalyst is ineffective as the amount of hydrogen produced is limited by the rapid recombination of holes and electrons, resulting in the formation of water. Recently, the production of hydrogen has been extended to the photodecomposition of methanol (CH<sub>3</sub>OH), which has a lower splitting energy than water. The following overall methanol decomposition reaction was proposed [8, 9]:



The decomposition energy for methanol is smaller than 0.7 eV, compared to 1.2 eV for water splitting. Most investigations on the production of hydrogen via methanol photodecomposition have focused on M<sub>x</sub>O<sub>y</sub> (M = Cd or Zn) [10, 11] and noble metal (Cu, Ag, Pd, Pt, Au)-doped TiO<sub>2</sub> [12–16], which can be used to activate the photocatalysts using UV light with longer wavelengths. However, the number of known photocatalysts is limited, and their activities remain low. New photocatalysts possessing greater hydrogen-producing activity under visible light irradiation

need to be developed. Moreover, hydrogen-based energy offers the significant advantage of being environmentally friendly. In our previous study [17], a new material, Cu-TiO<sub>2</sub>, where Cu<sub>x</sub>O was substituted into the TiO<sub>2</sub> framework, was investigated as a conducting component to reduce the large band gap of pure TiO<sub>2</sub>. The structural effect of the catalyst on photocatalysis was also evaluated using Cu-incorporated TiO<sub>2</sub> photocatalysts with anatase and rutile structures. The production reached 16,000 μmol after 24 h over Cu-TiO<sub>2</sub> with a rutile structure for water/methanol decomposition. Additionally, in our other paper [18], we reported about the synthesis and characterization of Ag<sub>x</sub>O and found that the hydrogen production from methanol photodecomposition over a mixture of Ag<sub>x</sub>O and TiO<sub>2</sub> was remarkably increased. Moreover, it was further enhanced when Ag<sub>x</sub>O thermally treated at 100°C was added, and the production peaked at 17,000 μmol after 24 h. However, the economic evaluation of this hydrogen production process remained poor, and any Ag and Cu metals remaining after the reaction showed a tendency to precipitate at the bottom of the reactor, where they were rapidly reduced. Subsequently the catalyst was rapidly deactivated.

Therefore, in order to overcome these disadvantages, we prepared a new catalyst in which two metals with different reduction/oxidation abilities were embedded into the TiO<sub>2</sub> framework. We investigated the production of hydrogen from the methanol/water photodecomposition over TiO<sub>2</sub>, Cu(0.1)-Ti(0.9)O<sub>2</sub>, Ag(0.1)-Ti(0.9)O<sub>2</sub>, Cu(0.05)-Ag(0.05)Ti(0.9)O<sub>2</sub>, Cu(0.03)-Ag(0.07)Ti(0.9)O<sub>2</sub>, and Cu(0.07)-Ag(0.03)Ti(0.9)O<sub>2</sub> photocatalysts in which Cu and Ag ions were incorporated into the TiO<sub>2</sub> framework with an anatase structure, prepared using a solvothermal method. To determine the relationship between Cu and Ag species and the catalytic performance for the production of H<sub>2</sub>, these photocatalysts were examined using X-ray diffraction analysis (XRD), X-ray photon spectroscopy (XPS), and UV-visible and photoluminescence (PL) spectroscopy.

## 2. Experimental

**2.1. Preparation of Photocatalysts.** The photocatalysts were prepared using the conventional solvothermal method, as shown in Figure 1. To prepare the sol mixture, titanium tetraisopropoxide (TTIP, 99.95%), copper nitrate (Cu(NO<sub>3</sub>)<sub>2</sub>, 99.9%), and silver nitrate (AgNO<sub>3</sub>, 99.9%), all supplied by Junsei Chemical (Tokyo, Japan), were used as the titanium, copper, and silver precursors, respectively. After 0.9 mol TTIP was added slowly to 250 mL ethanol, Ag and Cu nitrate (totally 10 mol-% per titanium mole) dissolved with ethanol were added into the titanium solution. The mixture was stirred homogeneously for 1 h, and the pH was maintained at 3.0. The final solution was stirred homogeneously and moved to an autoclave for the thermal treatment. TTIP, silver, and copper nitrates were hydrolyzed *via* the OH groups during thermal treatment at 473 K for 8 h under a nitrogen environment at a pressure of approximately 10 atm. The resulting precipitate was washed with distilled water until pH = 7.0 and then dried at 353 K for 24 h.

The six photocatalysts were pure TiO<sub>2</sub>, Cu(0.1)-Ti(0.9)O<sub>2</sub>, Ag(0.1)-Ti(0.9)O<sub>2</sub>, Cu(0.05)-Ag(0.05)Ti(0.9)O<sub>2</sub>, Cu(0.03)-Ag(0.07)Ti(0.9)O<sub>2</sub>, and Cu(0.07)-Ag(0.03)Ti(0.9)O<sub>2</sub>.

**2.2. Characteristics of the Photocatalysts.** The powders for the six synthesized photocatalysts were examined by XRD (MPD, PANalytical, at Yeungnam University Instrumental Analysis Center) with nickel-filtered CuK $\alpha$  radiation (30 kV, 30 mA) at 2 $\theta$  angles ranging from 10 to 80°, a scan speed of 10° min<sup>-1</sup>, and a time constant of 1 s. The sizes and shapes of the particles were measured by transmission electron spectroscopy (TEM; H-7600, Hitachi, at Yeungnam University Instrumental Analysis Center) operated at 120 kV. The UV-visible spectra were obtained using a Cary 500 spectrometer with a reflectance sphere over the special range of 200 to 800 nm. PL spectroscopy was also performed to determine the number of photo-excited electron hole pairs using a PL mapping system (LabRamHR, Jobin Yvon, at Korea Photonics Technology Institute Material Characterization Center). It was also used to examine the number of photo-excited, electron-hole pairs for all samples. Samples of 1.0-mm diameter pellets were measured at room temperature using a He-Cd laser source at 325 nm in the reflection mode. XPS measurements of Cu2p, Ag3d, Ti2p, and O1s were recorded with an ESCA 2000 (VZ MicroTech, Oxford, UK) system, equipped with a nonmonochromatic AlK (1486.6 eV) X-ray source. The powders were pelletized at 1.2 × 10<sup>4</sup> kPa for 1 min, and the 1.0-mm pellets were then maintained overnight in a vacuum (1.0 × 10<sup>-7</sup> Pa) to remove the water molecules from the surface prior to the measurement. The base pressure of the ESCA system was below 1 × 10<sup>-9</sup> Pa. Experiments were recorded with a 200-W source power and an angular acceptance of ±5°. The analyzer axis made an angle of 90° with the specimen surface. Wide scan spectra were measured over a binding energy range of 0 to 1200 eV, with pass energy of 100.0 eV. The Ar<sup>+</sup> bombardment of the photocatalysts was performed with an ion current of 70 to 100 nA, over an area of 10.0 × 10.0 mm, with a total sputter time of 2400 s divided into 60 s intervals. A Shirley function was used to subtract the background in the XPS data analysis. The O1s, Ti2p, Ag3d, and Cu2p XPS signals were fitted using mixed Lorentzian-Gaussian curves.

**2.3. H<sub>2</sub> Production from Methanol/Water Photo Decomposition over Photocatalysts.** The photodecomposition of methanol/water was performed using a liquid photoreactor designed in our laboratory (Figure 2). For methanol/water photodecomposition, 0.5 g of the powdered photocatalysts was added to 2.0 L of a 1.0 : 1.0 methanol/water mixture in a 3.0-L Pyrex reactor. UV-lamps (6 × 3 Wcm<sup>-2</sup> = 18 Wcm<sup>-2</sup>, 30 cm length × 2.0 cm diameter; Shinan, Sunchun, Korea), emitting radiation at 365 nm, were used. The methanol/water decomposition was conducted for 30 h, with stirring, with the hydrogen evolution determined after 1 h. The hydrogen (H<sub>2</sub>) produced during the methanol/water photodecomposition was analyzed using a thermal-conductivity-detector (TCD-) type gas chromatograph (GC, model DS 6200;

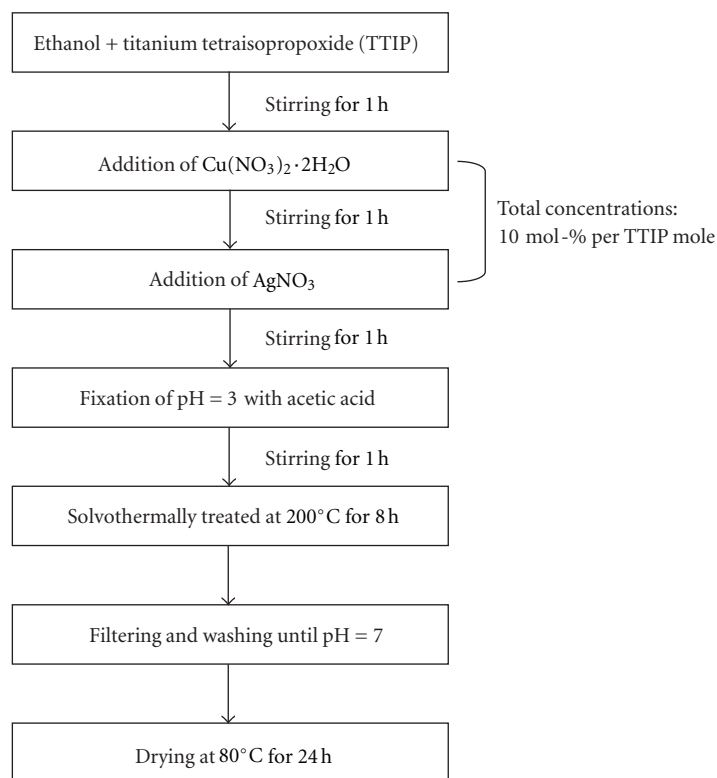


FIGURE 1: The preparation of six photocatalysts, pure  $\text{TiO}_2$ ,  $\text{Cu}(0.1)\text{-Ti}(0.9)\text{O}_2$ ,  $\text{Ag}(0.1)\text{-Ti}(0.9)\text{O}_2$ ,  $\text{Cu}(0.05)\text{-Ag}(0.05)\text{Ti}(0.9)\text{O}_2$ ,  $\text{Cu}(0.03)\text{-Ag}(0.07)\text{Ti}(0.9)\text{O}_2$ , and  $\text{Cu}(0.07)\text{-Ag}(0.03)\text{Ti}(0.9)\text{O}_2$  using a solvothermal method.

Donam Instruments Inc., Gyeonggi-do, Korea). To determine the products and intermediates, the GC was directly connected to the methanol/water decomposition reactor. The GC conditions were as follows: column: Carbosphere (Alltech, Deerfield, IL, USA), injection temp.:  $160^\circ\text{C}$ , initial temp.:  $100^\circ\text{C}$ , final temp.:  $100^\circ\text{C}$ , and detector temp.:  $200^\circ\text{C}$ .

### 3. Results and Discussion

**3.1. Characteristics of the Photocatalysts.** Figure 3 shows the XRD patterns for the six as-synthesized photocatalysts. Generally,  $\text{TiO}_2$  and metal- $\text{TiO}_2$  photocatalysts with an anatase structure are known to perform well in the decomposition of various organic compounds. The diffraction peaks for the anatase and rutile phases are labeled A and R with the corresponding diffraction planes given in parentheses, respectively [19]. Both pure  $\text{TiO}_2$  and metal-incorporated  $\text{TiO}_2$  catalysts showed well-developed anatase structures as synthesized. The Ag metal (200, 220, and 311 plane) peaks at  $2\theta = 44.50$ ,  $64.00$ , and  $77.60^\circ$  were presented in the Ag-incorporated  $\text{TiO}_2$  catalysts [20] and the intensities increased with increasing amount of loaded Ag. These results indicated that the Ag components partially existed on the external surface of  $\text{TiO}_2$  and were unlikely to be incorporated into the framework of the anatase structure. However, the Cu component did not appear in any of the catalysts, which indicated its complete insertion into the  $\text{TiO}_2$  framework. Interestingly, the structural

stability of anatase increased when bimetallic two metals, Cu and Ag, were inserted into the  $\text{TiO}_2$  framework at the same time, compared with when one kind of metal, Cu or Ag, that was inserted. Generally, crystalline domain sizes decrease with increasing line broadening of the peaks. The line broadening of the [101] peak is related to the size of the hexagonal crystalline phase. Scherrer's equation [21],  $t = 0.9\lambda/\beta \cos\theta$ , where  $\lambda$  is the wavelength of the incident X-rays,  $\beta$  is the full width at half maximum height (FWHM) in radians, and  $\theta$  is the diffraction angle, was used to estimate the crystalline domain size. The estimated crystalline domain sizes were 15.04, 13.71, 17.00, 11.80, 15.82, and 15.25 nm for pure  $\text{TiO}_2$ ,  $\text{Cu}(0.1)\text{-Ti}(0.9)\text{O}_2$ ,  $\text{Ag}(0.1)\text{-Ti}(0.9)\text{O}_2$ ,  $\text{Cu}(0.05)\text{-Ag}(0.05)\text{Ti}(0.9)\text{O}_2$ ,  $\text{Cu}(0.03)\text{-Ag}(0.07)\text{Ti}(0.9)\text{O}_2$ , and  $\text{Cu}(0.07)\text{-Ag}(0.03)\text{Ti}(0.9)\text{O}_2$  powders, respectively. The results indicated that the grain growths increased and decreased according to incorporation of Ag and Cu, respectively.

Figure 4 shows TEM images of the particle shapes of the six photocatalysts. A relatively uniform mixture of rhombic and cubic particles was observed with sizes ranging from 10 to 20 nm. The particles were slightly decreased in size when Cu was added but enlarged with Ag addition. The size was the smallest in  $\text{Cu}(0.05)\text{-Ag}(0.05)\text{Ti}(0.9)\text{O}_2$ , which corresponds to the XRD patterns shown in Figure 3.

Table 1 summarizes the atomic composition of the six photocatalysts. The compositions were estimated using energy dispersive X-ray (EDAX) analysis. The ratios of metal

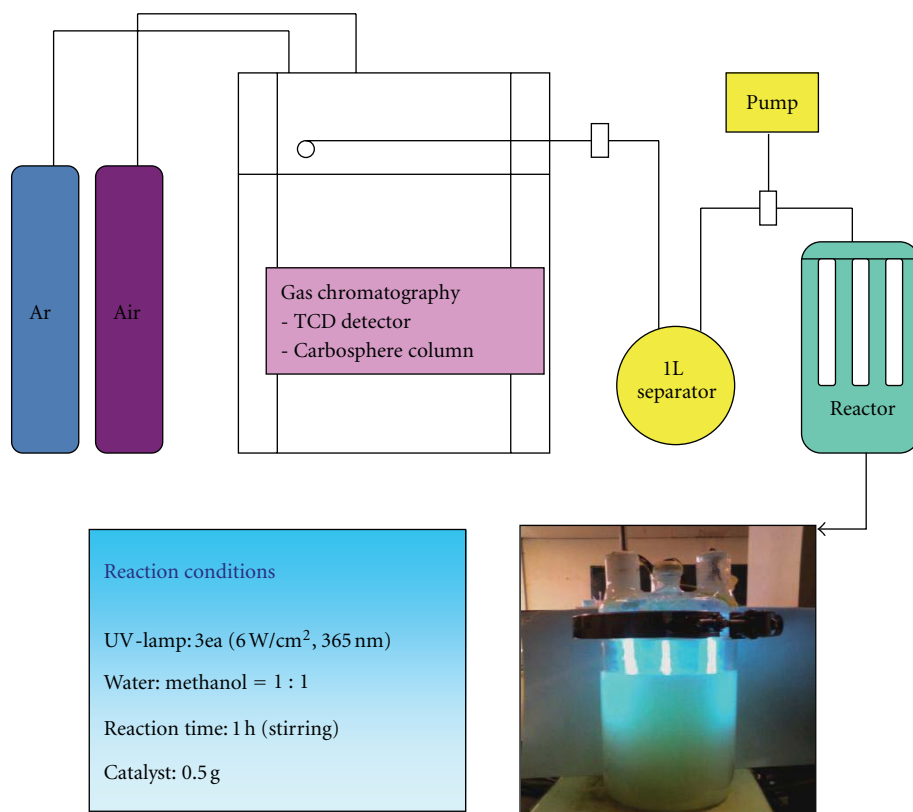


FIGURE 2: The liquid photoreactor used for H<sub>2</sub> production via methanol/water photodecomposition. Reaction conditions: volumetric ratio of CH<sub>3</sub>OH/H<sub>2</sub>O = 1; catalyst weight per 2.0 L solution, 0.5 g; UV intensity at 365 nm, 18 W m<sup>-2</sup>; batch system.

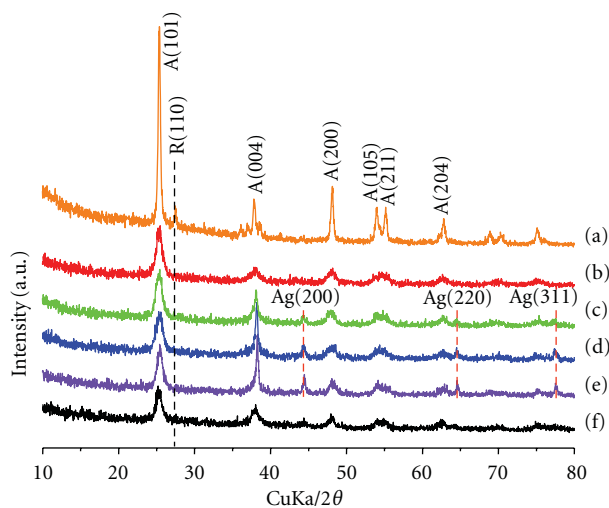


FIGURE 3: The XRD patterns of six photocatalysts as-synthesized. (a) TiO<sub>2</sub>, (b) Cu(0.1)-Ti(0.9)O<sub>2</sub>, (c) Cu(0.07)-Ag(0.03)Ti(0.9)O<sub>2</sub>, (d) Cu(0.05)-Ag(0.05)Ti(0.9)O<sub>2</sub>, (e) Cu(0.03)-Ag(0.07)Ti(0.9)O<sub>2</sub>, and (f) Ag(0.1)-Ti(0.9)O<sub>2</sub>.

(mono or bimetal)/Ti were 0.20, 0.10, 0.16, 0.10, and 0.11 in Cu(0.1)-Ti(0.9)O<sub>2</sub>, Ag(0.1)-Ti(0.9)O<sub>2</sub>, Cu(0.05)-Ag(0.05)Ti(0.9)O<sub>2</sub>, Cu(0.03)-Ag(0.07)Ti(0.9)O<sub>2</sub>, and Cu(0.07)-Ag(0.03)Ti(0.9)O<sub>2</sub> powders, respectively. Similar to the XRD results, the incorporation of Ag component into the TiO<sub>2</sub> framework was more difficult than that of Cu component.

Figure 5 shows the UV-visible spectra of the six photocatalysts. The absorption of the Ti<sup>4+</sup> tetrahedral symmetry normally appears at around 350 nm [22], which is assigned to L-L ( $P \rightarrow \pi$  or  $P \rightarrow \pi^*$ ) transitions localized on the oxygen. In the figure, the absorption bands are around 350 nm for all the photocatalysts, but the intensity of absorption

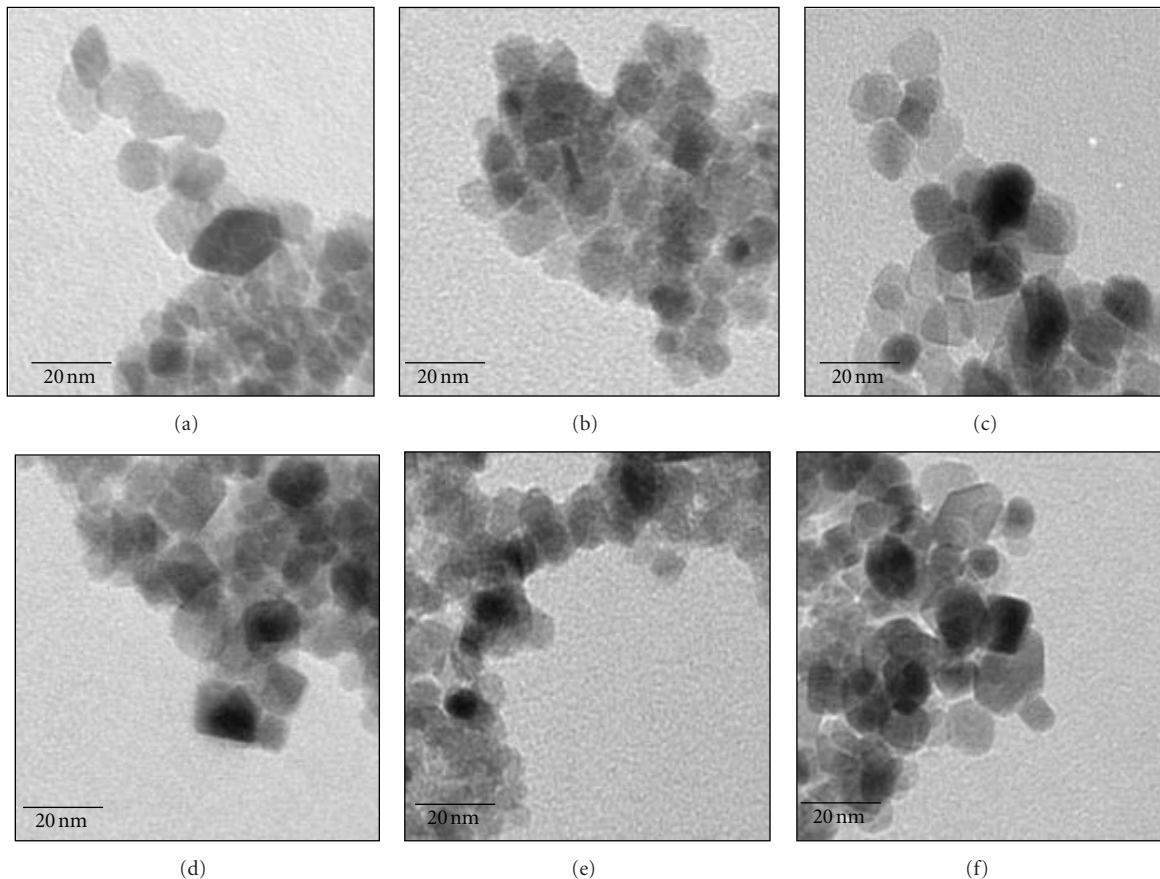


FIGURE 4: The TEM images of six photocatalysts as-synthesized.

TABLE 1: The atomic composition of the six photocatalysts.

Samples	Atomic composition (%)				
	Metal/Ti	O	Ti	Cu	Ag
TiO <sub>2</sub>	—	7.167	28.33	—	—
Cu(0.1)-Ti(0.9)O <sub>2</sub>	0.20	76.99	19.11	3.89	—
Ag(0.1)-Ti(0.9)O <sub>2</sub>	0.10	74.03	23.56	—	2.41
Cu(0.05)-Ag(0.05)Ti(0.9)O <sub>2</sub>	0.11	69.85	27.24	2.11	0.79
Cu(0.03)-Ag(0.07)Ti(0.9)O <sub>2</sub>	0.16	70.78	25.25	2.03	1.94
Cu(0.07)-Ag(0.03)Ti(0.9)O <sub>2</sub>	0.10	71.64	25.27	0.86	1.74

for pure TiO<sub>2</sub> is stronger than for metal-incorporated TiO<sub>2</sub>. The Cu-incorporated materials broadly absorbed at around 650 nm with remarkable intensity, which is allowed by the large spin-orbit coupling constant of the d-d transfer of copper, and the band observed in the visible region can be rationalized in terms of symmetry arguments. Otherwise, the broad band in the Ag-incorporated catalysts at 380 ~ 600 nm was attributed to Ag → O metal-to-ligand charge transfer (MLCT) transitions. The two broad bands observed in the wavelength interval 350–600 nm were therefore assigned to the MLCT and d-d transitions, which indicated that the band gap was narrowed in the Ag- and Cu-inserted TiO<sub>2</sub> catalysts, leading to higher photocatalytic performance.

Figure 6 shows the PL spectra of the six photocatalysts. The PL curve suggests that the electrons in the valence band were transferred to the conduction band, after which the excited electrons were stabilized by photoemission. In general, it is very important that the PL intensity increases with the increasing number of emitted electrons resulting from the recombination between excited electrons and holes, and, consequently, that the photoactivity decreases [23]. In particular, the PL intensity decreases to a greater extent in the presence of a metal that can capture excited electrons or exhibit conductivity, via the relaxation process. The PL curve of pure TiO<sub>2</sub> showed emission at 370–450 nm as a curve type. The band broadening was attributed to the

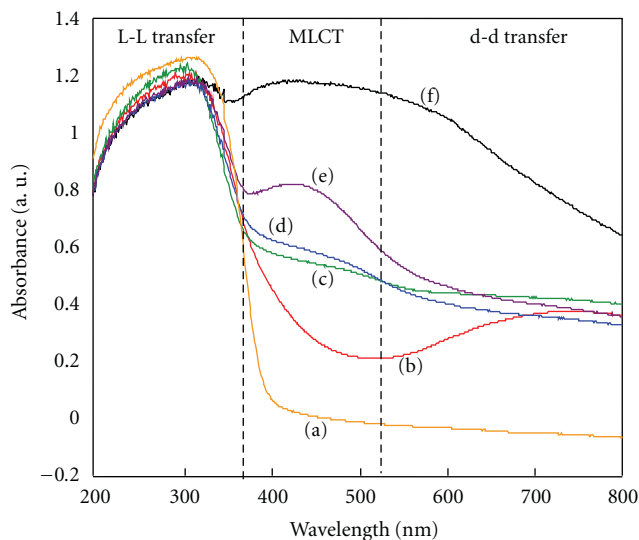


FIGURE 5: The UV-visible spectra of six photocatalysts as-synthesized. (a)  $\text{TiO}_2$ , (b)  $\text{Cu}(0.1)\text{-Ti}(0.9)\text{O}_2$ , (c)  $\text{Cu}(0.07)\text{-Ag}(0.03)\text{Ti}(0.9)\text{O}_2$ , (d)  $\text{Cu}(0.05)\text{-Ag}(0.05)\text{Ti}(0.9)\text{O}_2$ , (e)  $\text{Cu}(0.03)\text{-Ag}(0.07)\text{Ti}(0.9)\text{O}_2$ , and (f)  $\text{Ag}(0.1)\text{-Ti}(0.9)\text{O}_2$ .

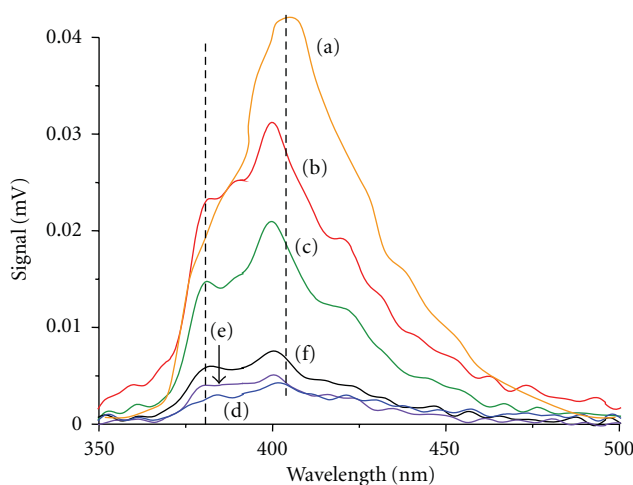


FIGURE 6: The PL spectra of six photocatalysts as-synthesized. (a)  $\text{TiO}_2$ , (b)  $\text{Cu}(0.1)\text{-Ti}(0.9)\text{O}_2$ , (c)  $\text{Cu}(0.07)\text{-Ag}(0.03)\text{Ti}(0.9)\text{O}_2$ , (d)  $\text{Cu}(0.05)\text{-Ag}(0.05)\text{Ti}(0.9)\text{O}_2$ , (e)  $\text{Cu}(0.03)\text{-Ag}(0.07)\text{Ti}(0.9)\text{O}_2$ , and (f)  $\text{Ag}(0.1)\text{-Ti}(0.9)\text{O}_2$ .

overlapped emission from the higher and lower excited states to the ground states. The pattern of the Ag- or Cu-incorporated catalysts showed two curves—at 360 nm and 400 nm—which were attributed to the band gap between the incorporated metals, Ag or Cu, respectively, and that of pure anatase  $\text{TiO}_2$ . Additionally the curves were shifted to a lower wavelength, and the PL intensity decreased significantly with decreasing metal insertion, probably due to the electron-capturing actions of the metal atoms from conduction band of  $\text{TiO}_2$ . Particularly when Ag component was inserted into the  $\text{TiO}_2$  framework, the PL intensity was largely reduced. Consequently, the PL intensity varied according to whether the added metal acted as an electron capturer or not. If the incorporated metals existed on the surface or in the framework of  $\text{TiO}_2$ , they attracted the excited electrons from  $\text{TiO}_2$ , so that the recombination of an electron and a hole was

difficult, thus increasing the number of holes over the valence band and generating more OH radicals.

**3.2.  $\text{H}_2$  Production from Methanol/Water Decomposition over the Six Photocatalysts.** Figure 7 summarizes the evolution of  $\text{H}_2$  from methanol/water decomposition over the six photocatalysts in a batch-type, liquid photosystem. Over pure anatase  $\text{TiO}_2$ , 200 mmol of  $\text{H}_2$  were only collected after methanol/water photodecomposition for 8 h, however the amount of  $\text{H}_2$  gas more increased in the Ag- or Cu-incorporated photocatalysts linearly with increasing time. The  $\text{H}_2$  production was the highest in  $\text{Cu}(0.03)\text{-Ag}(0.07)\text{Ti}(0.9)\text{O}_2$  at 8,750 mmol and finally reached 20,000 mmol after 30 h. therefore, the simultaneously bimetallic addition of Ag and Cu components had a greater influence on the  $\text{H}_2$  production during methanol/water photodecomposition

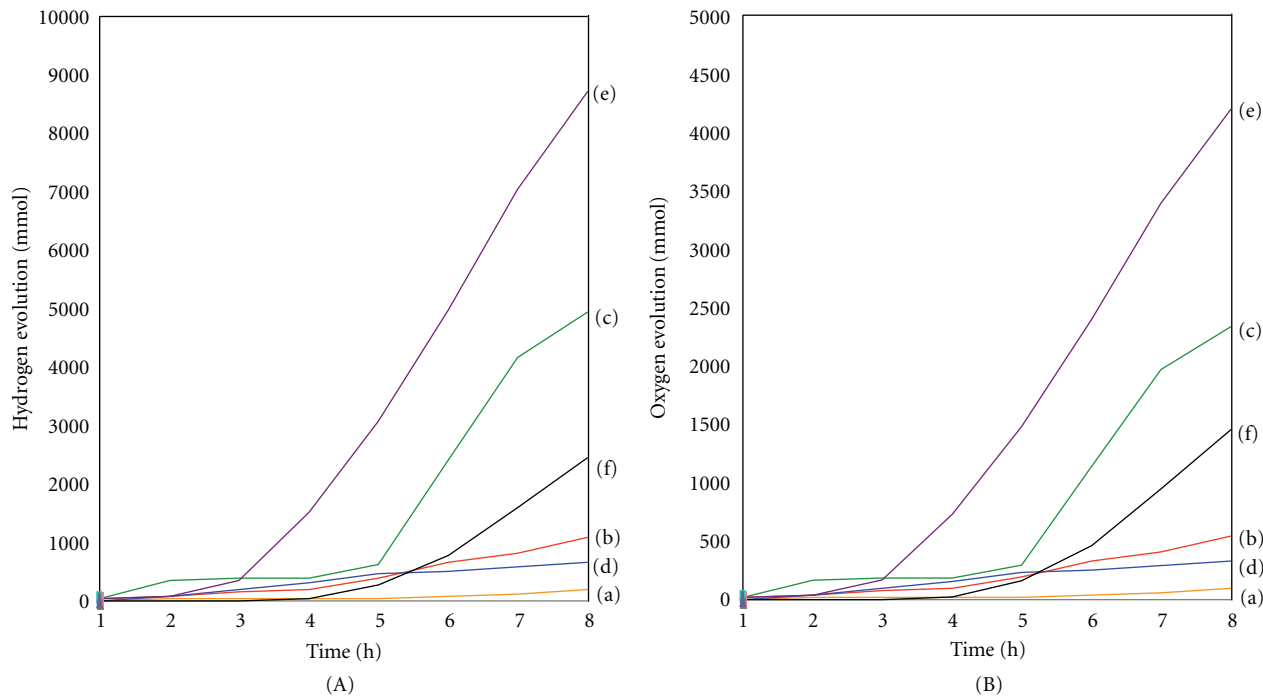


FIGURE 7: The evolution of H<sub>2</sub> from methanol/water decomposition over the six photocatalysts in a batch-type liquid photosystem. (A) accumulated amount of hydrogen gas and (B) accumulated amount of oxygen gas. (a) TiO<sub>2</sub>, (b) Cu(0.1)-Ti(0.9)O<sub>2</sub>, (c) Cu(0.07)-Ag(0.03)Ti(0.9)O<sub>2</sub>, (d) Cu(0.05)-Ag(0.05)Ti(0.9)O<sub>2</sub>, (e) Cu(0.03)-Ag(0.07)Ti(0.9)O<sub>2</sub>, and (f) Ag(0.1)-Ti(0.9)O<sub>2</sub>.

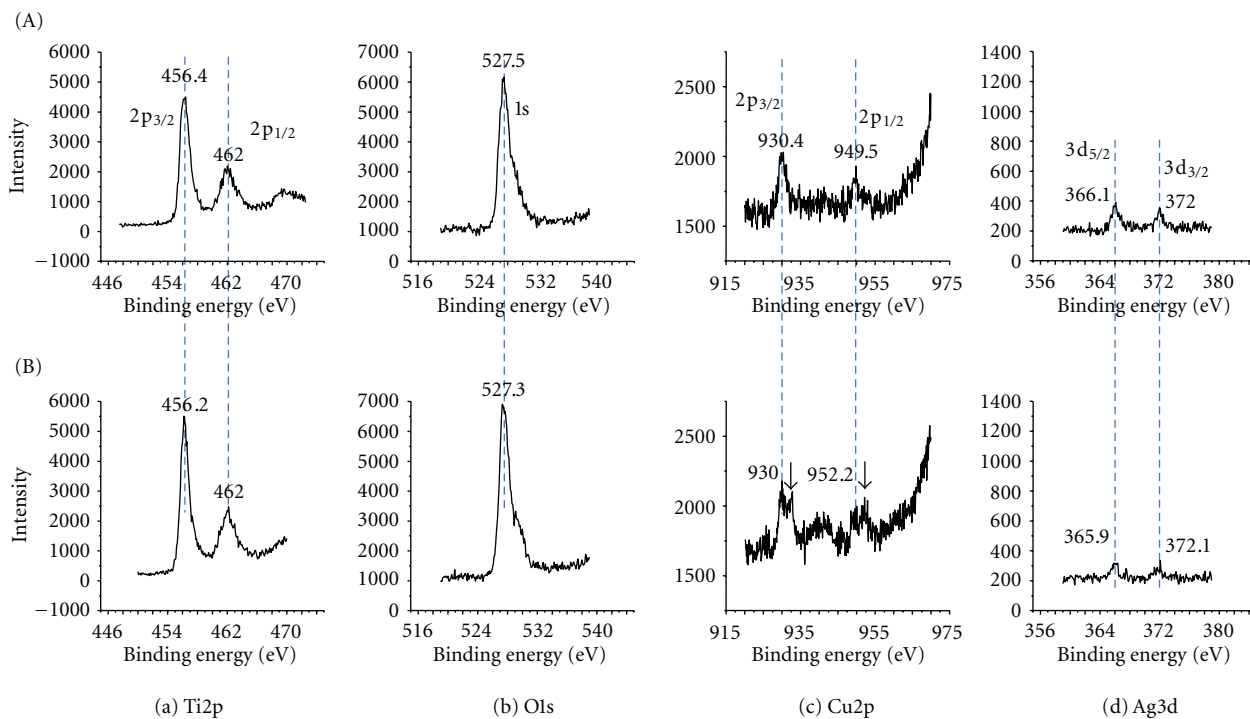


FIGURE 8: The XPS for Cu2p, Ag3d, Ti2p, and O1s of Cu(0.03)-Ag(0.07)Ti(0.9)O<sub>2</sub> before and after the methanol/water photodecomposition reaction: (A) before reaction and (B) after reaction.

than the mono metals, Cu- or Ag-incorporated TiO<sub>2</sub>. Particularly, metal chunks were observed to be deposited in the reactor after the reaction. These results are evidence for the continuing oxidation/reduction actions between Cu and Ag during the reaction.

The Cu(0.03)-Ag(0.07)Ti(0.9)O<sub>2</sub> particles underwent quantitative XPS analyses before and after the reaction, with the typical survey and high-resolution spectra shown in Figure 8. The Ti2p<sub>1/2</sub> and Ti2p<sub>3/2</sub> spin-orbital splitting photoelectrons for anatase TiO<sub>2</sub>s were located at binding energies of 462.0 and 456.4 eV, respectively, and were assigned to the presence of typical Ti<sup>4+</sup> [24]. The measured FWHM of the Ti2p<sub>3/2</sub> peak was larger before reaction than after the reaction. However, there was no subsequent change. In general, a greater FWHM implies a greater amount of less-oxidized metals. The Cu2p<sub>3/2</sub> and Cu2p<sub>1/2</sub> spin-orbital splitting photoelectrons for the anatase Cu(0.03)-Ag(0.07)Ti(0.9)O<sub>2</sub> photocatalyst before the reaction were located at binding energies of 930.4 and 949.5 eV, respectively, and these bands were assigned to CuO. However, these bands were separated into two peaks at binding energies of 932.5 eV of Cu2p<sub>3/2</sub> and 952.5 eV of Cu2p<sub>1/2</sub>, and these bands were assigned to Cu<sub>2</sub>O [24]. On the other hand, the fresh photocatalyst showed Ag3d<sub>5/2</sub> and Ag3d<sub>3/2</sub> spin-orbital splitting photoelectrons at binding energies of 366.1 and 372.0 eV, respectively, which were assigned to AgO, but the peak intensities were dramatically decreased after the reaction. This result indicated that the oxidation state of Cu was reduced and the amount of AgO was decreased during the reaction, which enabled their strong involvement in methanol/water decomposition. The O1s region was decomposed into two contributions: metal (Ti<sup>4+</sup> or Ti<sup>3+</sup>)-O (527.5 eV) in the metal oxide and metal-OH (529.5.0 eV). The ratios of metal-OH/metal-O in the O1s peaks were decreased after the reaction compared to that before the reaction. Additionally, the measured FWHM of the O1s peak was larger after reaction than that before, which was attributed to the exposure of Ag or Cu ions from the surface of TiO<sub>2</sub>.

#### 4. Conclusions

TiO<sub>2</sub> photocatalysts inserted with Ag, Cu, and Cu-Ag were prepared for the production of H<sub>2</sub> gas from methanol/water photodecomposition in a batch-type liquid photosystem. Compared to monometal-incorporated TiO<sub>2</sub>, the H<sub>2</sub> production via methanol/water photodecomposition was markedly enhanced in bimetal-incorporated photocatalyst and reached 8,750 mmol after methanol/water photodecomposition for 8 h over Cu(0.03)-Ag(0.07)Ti(0.9)O<sub>2</sub> photocatalyst. These results confirmed that the simultaneous presence of Cu and Ag components in the framework of the TiO<sub>2</sub> anatase structure improved the H<sub>2</sub> production via methanol/water photodecomposition. Here, we suggested that any Cu or Ag components present in the TiO<sub>2</sub> framework are reduced or decreased by attracting the excited electrons from the valence band of TiO<sub>2</sub>, because of the greater reduction potential of CuO or AgO than that of pure TiO<sub>2</sub>. This hinders the recombination of an electron and a

hole because the CuO or AgO component captures electrons, thereby increasing the number of holes over the valence band and allowing methanol decomposition to continue. The simultaneous insertion of the two ions into the TiO<sub>2</sub> framework induced an increased synergistic effect.

#### Acknowledgments

This research was supported by a Yeungnam University Research Grant, no. 210-A-380-115, and the authors are very grateful for this support.

#### References

- [1] M. Ni, M. K. H. Leung, D. Y. C. Leung, and K. Sumathy, "A review and recent developments in photocatalytic water-splitting using TiO<sub>2</sub> for hydrogen production," *Renewable and Sustainable Energy Reviews*, vol. 11, no. 3, pp. 401–425, 2007.
- [2] R. Dholam, N. Patel, M. Adami, and A. Miotello, "Hydrogen production by photocatalytic water-splitting using Cr- or Fe-doped TiO<sub>2</sub> composite thin films photocatalyst," *International Journal of Hydrogen Energy*, vol. 34, no. 13, pp. 5337–5346, 2009.
- [3] L. S. Yoong, F. K. Chong, and B. K. Dutta, "Development of copper-doped TiO<sub>2</sub> photocatalyst for hydrogen production under visible light," *Energy*, vol. 34, no. 10, pp. 1652–1661, 2009.
- [4] H. Mizoguchi, K. Ueda, M. Orita et al., "Decomposition of water by a CaTiO<sub>3</sub> photocatalyst under UV light irradiation," *Materials Research Bulletin*, vol. 37, no. 15, pp. 2401–2406, 2002.
- [5] T. Ishii, H. Kato, and A. Kudo, "H<sub>2</sub> evolution from an aqueous methanol solution on SrTiO<sub>3</sub> photocatalysts codoped with chromium and tantalum ions under visible light irradiation," *Journal of Photochemistry and Photobiology A*, vol. 163, no. 1–2, pp. 181–186, 2004.
- [6] T. Sreethawong, S. Laehsabee, and S. Chauadej, "Comparative investigation of mesoporous- and non-mesoporous-assembled TiO<sub>2</sub> nanocrystals for photocatalytic H<sub>2</sub> production over N-doped TiO<sub>2</sub> under visible light irradiation," *International Journal of Hydrogen Energy*, vol. 33, no. 21, pp. 5947–5957, 2008.
- [7] J. Yuan, M. Chen, J. Shi, and W. Shangguan, "Preparations and photocatalytic hydrogen evolution of N-doped TiO<sub>2</sub> from urea and titanium tetrachloride," *International Journal of Hydrogen Energy*, vol. 31, no. 10, pp. 1326–1331, 2006.
- [8] R. Gao, J. Stark, D. W. Bahnemann, and J. Rabani, "Quantum yields of hydroxyl radicals in illuminated TiO<sub>2</sub> nanocrystallite layers," *Journal of Photochemistry and Photobiology A*, vol. 148, no. 1–3, pp. 387–391, 2002.
- [9] J. Chen, D. F. Ollis, W. H. Rulkens, and H. Bruning, "Photocatalyzed oxidation of alcohols and organochlorides in the presence of native TiO<sub>2</sub> and metallized TiO<sub>2</sub> suspensions—part (II): photocatalytic mechanisms," *Water Research*, vol. 33, no. 3, pp. 669–676, 1999.
- [10] R. M. Navarro, F. del Valle, and J. L. G. Fierro, "Photocatalytic hydrogen evolution from CdS–ZnO–CdO systems under visible light irradiation: effect of thermal treatment and presence of Pt and Ru cocatalysts," *International Journal of Hydrogen Energy*, vol. 33, no. 16, pp. 4265–4273, 2008.
- [11] G. Guan, T. Kida, T. Harada, M. Isayama, and A. Yoshida, "Photoreduction of carbon dioxide with water over K<sub>2</sub>Ti<sub>6</sub>O<sub>13</sub>

- photocatalyst combined with Cu/ZnO catalyst under concentrated sunlight,” *Applied Catalysis A*, vol. 249, no. 1, pp. 11–18, 2003.
- [12] H. J. Choi and M. Kang, “Hydrogen production from methanol/water decomposition in a liquid photosystem using the anatase structure of Cu loaded TiO<sub>2</sub>,” *International Journal of Hydrogen Energy*, vol. 32, no. 16, pp. 3841–3848, 2007.
- [13] M.-S. Park and M. Kang, “The preparation of the anatase and rutile forms of Ag–TiO<sub>2</sub> and hydrogen production from methanol/water decomposition,” *Materials Letters*, vol. 62, no. 2, pp. 183–187, 2008.
- [14] B. S. Kwak, J. Chae, J. Kim, and M. Kang, “Enhanced hydrogen production from methanol/water photo-splitting in TiO<sub>2</sub> including Pd component,” *Bulletin of the Korean Chemical Society*, vol. 30, no. 5, pp. 1047–1053, 2009.
- [15] J.-J. Zou, H. He, L. Cui, and H.-Y. Du, “Highly efficient Pt/TiO<sub>2</sub> photocatalyst for hydrogen generation prepared by a cold plasma method,” *International Journal of Hydrogen Energy*, vol. 32, no. 12, pp. 1762–1770, 2007.
- [16] O. Rosseler, M. V. Shankar, M. K. L. Du, L. Schmidlin, N. Keller, and V. Keller, “Solar light photocatalytic hydrogen production from water over Pt and Au/TiO<sub>2</sub>(anatase/rutile) photocatalysts: influence of noble metal and porogen promotion,” *Journal of Catalysis*, vol. 269, no. 1, pp. 179–190, 2010.
- [17] S. Xu and D. D. Sun, “Significant improvement of photocatalytic hydrogen generation rate over TiO<sub>2</sub> with deposited CuO,” *International Journal of Hydrogen Energy*, vol. 34, no. 15, pp. 6096–6104, 2009.
- [18] K. Lalitha, J. K. Reddy, M. V. Phanikrishna Sharma, V. D. Kumari, and M. Subrahmanyam, “Continuous hydrogen production activity over finely dispersed Ag<sub>2</sub>O/TiO<sub>2</sub> catalysts from methanol: water mixtures under solar irradiation: a structure-activity correlation,” *International Journal of Hydrogen Energy*, vol. 35, no. 9, pp. 3991–4001, 2010.
- [19] T. Kawahara, T. Ozawa, M. Iwasaki, H. Tada, and S. Ito, “Photocatalytic activity of rutile-anatase coupled TiO<sub>2</sub> particles prepared by a dissolution-reprecipitation method,” *Journal of Colloid and Interface Science*, vol. 267, no. 2, pp. 377–381, 2003.
- [20] J. W. Park and M. Kang, “Synthesis and characterization of Ag<sub>x</sub>O, and hydrogen production from methanol photodecomposition over the mixture of Ag<sub>x</sub>O and TiO<sub>2</sub>,” *International Journal of Hydrogen Energy*, vol. 32, no. 18, pp. 4840–4846, 2007.
- [21] V. Uvarov and I. Popov, “Metrological characterization of X-ray diffraction methods for determination of crystallite size in nano-scale materials,” *Materials Characterization*, vol. 58, no. 10, pp. 883–891, 2007.
- [22] C. Liu, X. Tang, C. Mo, and Z. Qiang, “Characterization and activity of visible-light-driven TiO<sub>2</sub> photocatalyst codoped with nitrogen and cerium,” *Journal of Solid State Chemistry*, vol. 181, no. 4, pp. 913–919, 2008.
- [23] B. Liu, X. Zhao, and L. Wen, “The structural and photoluminescence studies related to the surface of the TiO<sub>2</sub> sol prepared by wet chemical method,” *Materials Science and Engineering B*, vol. 134, no. 1, pp. 27–31, 2006.
- [24] J. F. Mouider, W. F. Stickle, P. E. Soboi, and K. D. Bomben, *Handbook of X-Ray Photoelectron Spectroscopy*, Perkin-Elmer Corporation, Eden Prairie, Minn, USA, 1992.

## Research Article

# TiO<sub>2</sub>-Based Photocatalytic Treatment of Raw and Constructed-Wetland Pretreated Textile Wastewater

Dunja Mahne,<sup>1</sup> Urška Lavrenčič Štangar,<sup>1</sup> Polonca Trebše,<sup>1</sup> and Tjaša Griessler Bulc<sup>2</sup>

<sup>1</sup>Laboratory for Environmental Research, University of Nova Gorica, Vipavska 13, 5001 Nova Gorica, Slovenia

<sup>2</sup>Faculty of Health Sciences, University of Ljubljana, Zdravstvena pot 5, 1000 Ljubljana, Slovenia

Correspondence should be addressed to Urška Lavrenčič Štangar, [urska.lavrencic@ung.si](mailto:urska.lavrencic@ung.si)

Received 20 October 2011; Revised 16 December 2011; Accepted 17 December 2011

Academic Editor: Jiaguo Yu

Copyright © 2012 Dunja Mahne et al. This is an open access article distributed under the Creative Commons Attribution License, which permits unrestricted use, distribution, and reproduction in any medium, provided the original work is properly cited.

Approximately, 15% of the total textile colorant production is estimated to be lost during dyeing and processing of textile fibres. If left untreated, these wastewaters can represent a serious environmental threat. In the present paper a combination of photocatalytic and biological degradation of prepared textile wastewaters (simulation of real textile effluent) is presented. Samples have been monitored through the course of photocatalytic experiments: change in UV-VIS absorbance spectra and complete decolouration were achieved for all three tested dyed wastewaters; however, only partial COD removal was achieved with photocatalytic oxidation (PCOx) and photocatalytic ozonation (PCOz). Toxicity test (*Vibrio fischeri*) of untreated and pretreated (constructed wetland, CW) samples showed a decrease in toxicity values only for the red-dyed wastewater. Comparison of efficiency of PCOx and PCOz for decolouration and mineralization of three structurally different dyes (anthraquinone and two azo dyes) has been done. CW pretreatment caused faster decolouration and substantial COD removal in PCOx (up to 45%). Pretreatment also accelerated decolouration during PCOz, but it accelerated COD removal only in the case of red-dyed wastewater due to short irradiation times applied.

## 1. Introduction

Textile dyes and other industrial dyeing agents represent one of the largest groups of organic molecules. High variety is characteristic for textile dyes' and auxiliary chemicals' composition used in the dyeing and finishing processes. In the world's dye market, azo dyes currently represent 60% share [1]. Due to incomplete dye exhaustion, the spent dye baths and water from washing operations constitute large volumes of dyed wastewaters [2].

Approximately, 15% of the total colorant production is estimated to be lost during dyeing processes [2]. Dyes reduce light penetration into the water, interfere with biological process (photosynthesis), and some exhibit toxic and carcinogenic effects [3]. Due to the complex, recalcitrant, and bioresistant character of textile effluents, a lot of attention has been dedicated to pollution abatement. Traditional physicochemical methods exhibit drawbacks such as secondary waste production (sludge), membrane fouling, and costly adsorbent regeneration [4]. In biological treatment approaches, the anaerobic phase is important for

decolouration by the reductive cleavage of azo bond through which aromatic amines are formed, which are sometimes more toxic than the parent molecule itself [5].

Many new approaches to pollution abatement have been investigated like microbial or enzymatic decomposition and advanced oxidation processes (AOPs) [3, 6]. AOPs exhibit also disinfection action on treated wastewater [7, 8]. TiO<sub>2</sub>-based heterogeneous catalysis' key advantages are absence of mass/phase transfer, possible operation at ambient conditions (under solar irradiation), and, importantly, likelihood of complete mineralization of organic carbon into CO<sub>2</sub>. Efficient decolouration and partial or total mineralization of textile effluents by AOPs has been demonstrated [2–13]. Moreover, ozone introduction into the photocatalytically treated solution considerably increases the amount of highly reactive oxygen-based radicals in consequence increasing the rate of mineralization [14].

Constructed wetlands (CWs) are engineered systems mimicking natural conditions for wastewater treatment. They are considered as an inherently low cost method since

they use natural ability of vegetation, sand media, and its associated microorganisms for pollution removal [15]. The knowledge on effectiveness of CW for pollution removal has increased rapidly in last two decades; mainly, they are applied for municipal wastewaters, but proved to be successful also in storm, agricultural and industrial wastewaters' (acid mine drainage, dairy, and tannery effluent) pollution abatement [16–18].

A variety of pollutants found in the textile wastewaters can be removed by CW such as suspended solids, dyes, organic compounds, and heavy metals [19, 20]. Microbial transformations are prevailing in organic carbon degradation; they provide the majority of total nitrogen removal while plant uptake has a minor role [21]. The decolouration reaction which takes place in extracellular environment is a biological and chemical reaction.

Due to the environmental implications and limitations of each of the above named treatment processes, a lot of research is focused on combining biological and physico-chemical treatment methods. A combination of anaerobic degradation and immobilised  $\text{TiO}_2$  photocatalysis proved as feasible approach to treat dye-containing wastewaters [4, 22]. However, a combination of a CW and  $\text{TiO}_2$ -based photocatalysis was, to our knowledge, only applied for pesticide-polluted wastewaters [23].

The aim of the study was (1) to combine the two promising methods for textile wastewater treatment—CW treatment and  $\text{TiO}_2$  photocatalysis—and to demonstrate advantages/disadvantages and (2) to use a complex matrix of simulated wastewater samples in the pretreatment and photocatalytic irradiation experiments since many studies so far have been performed on pure dye samples and with biodegradation in very low volume reactors.

A 250 L CW model was established (its performance will be published elsewhere) with the aim to obtain partial decolouration of the wastewater and COD removal. The CW pretreated and untreated samples were then subjected to photocatalytic degradation and photocatalytic ozonation in a Carberry-type photoreactor. The aim was to prove the presumption that the CW as the first-stage treatment can considerably shorten the irradiation time needed to meet the discharge limit values.

Simulated wastewaters were prepared according to the wastewater composition from a local textile plant. Three reactive dyes with different structure (monoazo, diazo, and anthraquinone dye) were used in order to establish colouration reduction and treatment efficiency for structurally different dyes. Efficiency in terms of colouration removal, COD reduction, and toxicity assessment was used to evaluate the effect of each treatment combination. The best strategy for a combination of the tested methods is discussed from efficiency point of view.

## 2. Materials and Methods

**2.1. Prepared Wastewater Composition.** Wastewater was synthesized according to the local textile plants' parameters (Tekstina, Ajdovščina) where technological water is mixed with communal wastewater (E! 2983 "TEXTILE WET"

report). The same kind of dyes and textile auxiliaries were added as those used in "Tekstina": Reactive Blue 19, Reactive Red 22 or Reactive Black 5 (Figure 1); meat peptone was added (in experimentally established quantity to meet the BOD of the wastewater) as nutrient [24]. Concentrations of added auxiliaries were calculated from the dye dilution factor. All chemicals were purchased from Bezema Company, Switzerland and used without further purification. Prepared wastewater composition was the following: 100 mg/L dye of Reactive Red, Black or Blue, commercially available as Bezaktiv Blau V-RN SPE2, Bezaktiv Schwartz V-B 150 and Bezaktiv Rot V-BN (Bezema, Switzerland),  $3.3 \mu\text{L/L}$  KOLLASOL DCA (sequestering agent),  $13.2 \mu\text{L/L}$  COLORCONTIN SAN (wetting agent),  $30 \mu\text{L/L}$  EGASOL SF (levelling agent), 250 g/L meat peptone (Fluka, 70174). Due to the fact that wastewater from the dyeing process in "Tekstina" is mixed with water from the rinsing stages and the companies' municipal wastewater, salt (which is normally added to dyeing solutions) was not added to be able to simulate the measured conductivity values.

**2.2. Laboratory Scale CW Model Pretreatment.** An unplanted constructed wetland model was set up to treat prepared wastewater (its performance will be published elsewhere). The model had 2.5 m in length and 0.5 m in width and depth. The media used was washed sand of 8–11 mm particle size at the bottom 10 cm and 2–4 mm particle size in the upper 40 cm. The models' porous volume was 250 L and the hydraulic retention time (HRT) was 24 h with the constant flow of 175 mL/min. The CW model worked under continuous feed operation.

The following parameters were measured *in situ* at 4 measuring points—pH, temperature ( $T$ ), electric conductivity, and dissolved oxygen (DO)—using the WTW MultiLine P4 portable universal pocket-size meter with pH electrode, SenTix 41 temperature probe, Cell Ox 325 dissolved oxygen probe, and TetraCon 325 standard conductivity cell. Samples from the influent and the effluent of the CW model were taken every 24 hours during the operation and directly analyzed. COD was determined photometrically on Nanocolor 500D photometer (Macherey-Nagel, Germany) using standard COD digestion solutions in the range 100–1500 mg/L (ISO 15705, measurement uncertainty =  $\pm 3\%$ ).  $\text{BOD}_5$  was determined after incubation in WTW OxiTop measuring bottles (ISO 5815). Samples were also analysed with LUMISTox toxicity test (Dr. Lange, Germany) bioluminescence inhibition on *Vibrio fischeri* exposed to sample solutions for 30 min at  $15^\circ\text{C}$ . Results were compared to an aqueous control with colour correction (ISO 11348). For qualitative information on colouration reduction the absorbance was measured across the UV and VIS spectra (200–800 nm) in quartz cell with 10 mm optical length, on Hewlett Packard 8453 UV-VIS spectrophotometer (ISO 7887).

**2.3. Photoreactor Setup.** Photocatalytic degradation was carried out in a Carberry-type photoreactor described elsewhere [25]. Duran glass reactor tube used in the experiments has

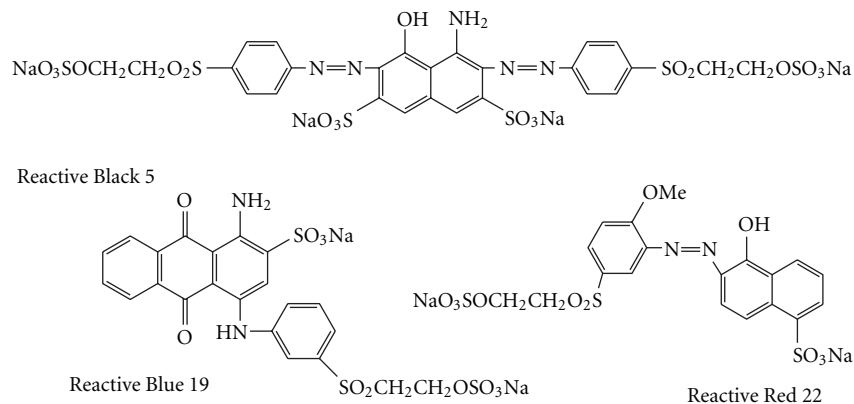


FIGURE 1: Chemical structures of dyes used in the experiments.

a frit with a valve at the lower end to allow the sample to be gas purged (Figure 2(a)). Initial volume of the irradiated sample was 280 mL. 6 low pressure mercury fluorescent lamps (CLEO 20 W, 438 × 26 mm, Philips; broad max at 355 nm) were used as UVA irradiation source.

Photocatalytic paper (Ahlstrom, France) was adjusted to a steel support and radially fastened with 24 thin bars to form a 12 angle star (Figures 2(b) and 2(c), [26]). The photocatalytic paper area was 0.069 m<sup>2</sup> and catalyst mass per unit area (paper + TiO<sub>2</sub>) was 75 g/m<sup>2</sup>, the total mass being 5.18 g. Commercially available paper is impregnated with Millennium PC-500 photocatalytic powder. Prior to fastening the paper onto the support, flowing water was used to rinse off the redundant catalyst.

**2.4. Photocatalytic Degradation.** Oxygen or ozone was bubbled through the lower end frit into the reactor tube. The gas flow was kept constant to keep the solution saturated. In the photocatalytic ozonation experiments the ozone was generated by Pacific Ozone Technology instrument, model LAB 21, fed with pure oxygen (99.5%). Gaseous concentration of ozone was determined by iodometric titration. The flow rate of ozone was calculated to be 0.13 g/h.

**PCO<sub>x</sub> (Photocatalytic Oxidation):** Dyed wastewaters with characteristics presented in the Table 1 were exposed to UVA irradiation under constant oxygen purging for 90 to 210 min, depending on the time needed to achieve decolouration.

**PCO<sub>z</sub> (Photocatalytic Ozonation):** Dye solutions were exposed to UVA irradiation under constant ozone purging for 20 to 30 min, depending on the time needed to achieve decolouration. Argon was introduced into the samples after sampling to prevent further oxidation of the sample.

Samples from both photocatalytic degradation experiments were taken in different time intervals (according to decolouration rate) and analyzed. The absorbance (at respective band wavelengths) was measured; the COD measurements and Lumistox toxicity tests were done to evaluate the toxicity and mineralization (degradation) efficiency.

Due to the very low concentrations of textile auxiliaries added to the prepared textile wastewater (see Section 2.1),

they exhibited a negligible contribution to COD and BOD values of the samples.

### 3. Results and Discussion

**3.1. Changes of Absorbance Spectra after Pretreatment and during Photocatalytic Degradation.** In Figures 3, 4, and 5 time-dependent UV-VIS absorbance spectra measured during PCO<sub>x</sub> experiment of Reactive Blue 19 (RBL19, Figure 3), Reactive Black 5 (RBK5, Figure 4), and Reactive Red 22 (RRD22, Figure 5) containing wastewaters are presented. Absorbance bands of all three dyes decrease with time of irradiation in the UV and VIS region. Measurements at their wavelengths of maximum intensity indicate degradation of dye molecules leading to a complete absence of wastewaters' colouration.

The same starting concentration of three commercial dyes (100 mg/L) exhibited significantly different absorbance at their characteristic absorbance bands (VIS spectra). RBL19 exhibited the lowest absorbance: 0.8, RBK5 the highest absorbance: 3.1, and RRD22: 1.9 on average. This is explained by the different structure of dyes under study, the RBK5 is a diazo dye, the RRD22 is a monoazo dye, and RBL19 is an anthraquinone dye (Figure 1). The goal to use the same concentration of commercial textile dyes (100 mg/L) was followed, even though the initial absorbance of RBK5 reached above 2.5. To verify the absorbance measurements the sample was diluted and calibration curve was done.

When spectra of the pretreated and untreated samples are compared (Figures 3, 4 and 5) it can be observed that the CW model pretreatment had a uniform effect on all dyes—it decreased VIS and increased UV absorbance—a consequence of aromatic amines' formation. This results from the azo bond reduction and chromophore cleavage in anaerobic conditions. The obtained results are in accordance with previous findings [6, 27].

The major difference between both sets of RBL19 degradation spectra (Figures 3(a) and 3(b)) lies in the fact that spectra of the pretreated sample exhibit simultaneous decrease in UV and VIS absorbing components (Figure 3(b)) (band at 592 nm), but in the untreated sample (Figure 3(a)) only minor decrease of UV absorbance is exhibited during

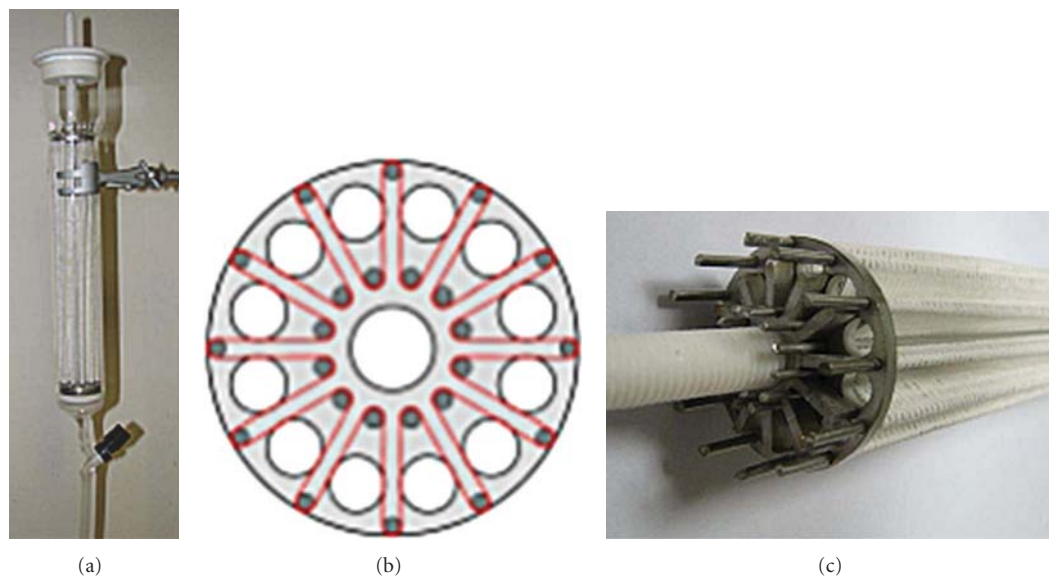


FIGURE 2: (a) Photocatalytic cell with the glass tube. (b) Geometrical shape of the steel paper holder (top view). (c) Photocatalytic paper fixed to the steel holder.

TABLE 1: Characteristics of untreated and pretreated textile wastewater, subjected to photocatalysis.

Parameter	Untreated sample			CW-pretreated sample		
	Blue	Red	Black	Blue	Red	Black
Absorbance at max intensity in Vis	0.88 at 592 nm	1.99 at 520 nm	3.1 at 598 nm	0.55 at 592 nm	0.99 at 520 nm	1.1 at 598 nm
COD [mg/L]	372	351	360	280	215	245
BOD [mg/L]	183	185	187	148	93	100
pH	8.1–8.2	8.1–8.2	8.1–8.2	~7.3	~7.3	~7.3
Toxicity [%]	84	100	100	73	100	100

irradiation. During the pretreatment on average 35% of the dye molecules present in the wastewater is degraded into degradation products which exhibit absorbance in the UV part. These degradation products proved to be more susceptible to photocatalytic degradation compared to the parent compound.

The remaining UV absorbance of the untreated sample after photocatalysis (Figure 3(a)) is attributed to high resistance of anthraquinone dyes to degradation in this spectral range. Aromatic organic intermediates in the sample such as quinones and phenols cause the UV absorbance [28]. According to the references, different degradation products like quinones, phenols and mono- and diacids (maleic, acetic, oxalic) are formed under mild experimental conditions [28, 29].

Absorbance in the UV region is pronounced in both RBK5 (Figures 4(a) and 4(b)) spectra. On contrary to RBL19 (Figure 3), degradation of RBK5 in the untreated (Figure 4(a)) and pretreated (Figure 4(b)) samples is manifested simultaneously in the UV and VIS part of the spectra during irradiation.

In the untreated sample's spectra (Figure 4(a)) a new band is formed after 80 min of irradiation at 260 nm. The pretreated sample (Figure 4(b)) has two distinct bands in the UV, at 335 and 260 nm, the latter one is probably the main

anaerobic degradation product [30]. In a photocatalytic study of the same dye (slurry  $\text{TiO}_2$ ) temporal changes in spectra also showed a newly occurring band in the 260–280 nm region after 90 min of irradiation [31]. The GC-MS analysis revealed formation of aromatic and short chain aliphatic oxygenated hydrocarbon (like butanoic and propanoic acid) compounds [31]. Since the absorbance at 260 nm is present in both sets of spectra (Figures 4(a) and 4(b)) it can be assumed that the same degradation products are formed during anaerobic degradation and after 80 min of untreated sample irradiation.

Both RRD22 wastewater sample's spectra (Figures 5(a) and 5(b)) exhibit characteristic absorbance band at 520 nm. As in the case of RBK5 (Figure 4(b)), the RRD22 dye degradation during CW pretreatment is confirmed by a decrease in VIS and increase in UV absorbance, due to formation of aromatic products (Figure 5(b)). Again as in Figure 4, the RRD22 photocatalytic degradation occurs simultaneously in the UV and VIS part (Figure 5). Absorbance in the UV region at wavelengths between 260 and 300 nm is pronounced in both samples, indicating presence of aromatic compounds (Figures 5(a) and 5(b)). Unfortunately (to our knowledge) no scientific literature data on red dye of the same chemical structure is available, so no degradation products are suggested except those generally characteristic

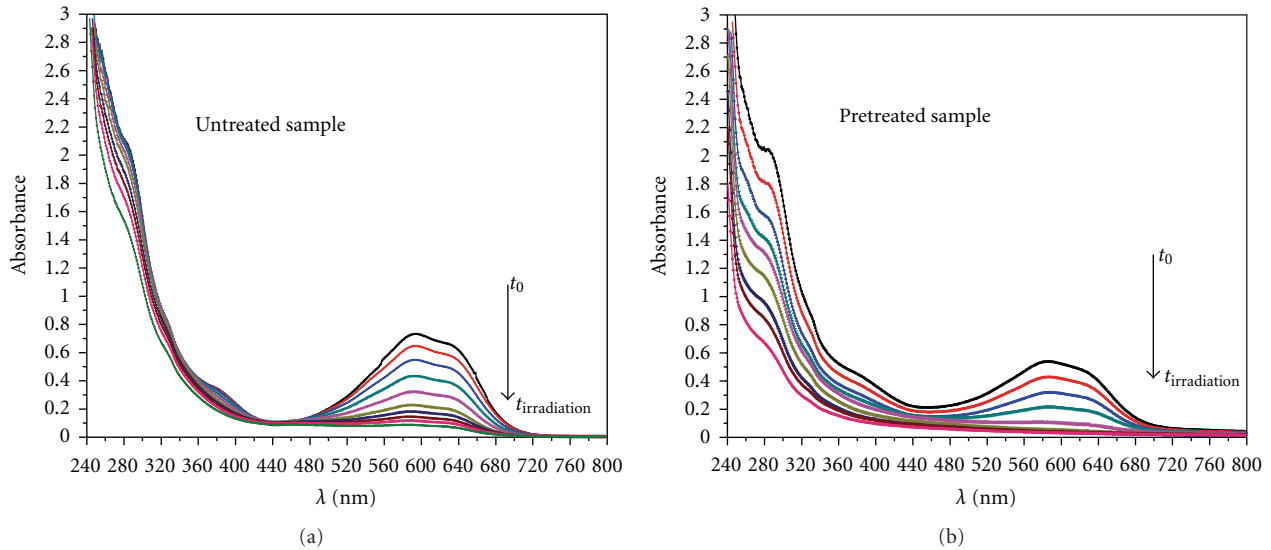


FIGURE 3: UV-Vis spectral changes as function of time of irradiation of untreated (a) and pretreated (b) Reactive Blue 19 textile effluent taken 5 to 15 min intervals, the irradiation time was 90 min.

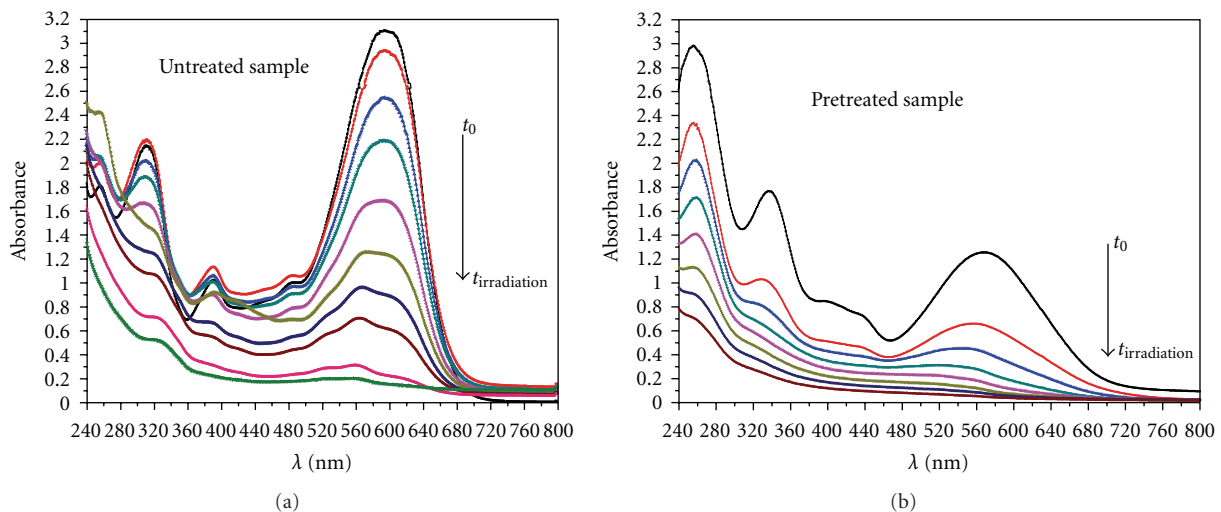


FIGURE 4: Temporal changes in absorption spectra of untreated (a) and pretreated (b) Reactive Black 5 textile effluent taken at 5–15 min intervals, the irradiation time was 210 min.

for textile dye degradation where formic and acetic acid are main degradation products followed by oxalic, glycolic and malonic acids [32].

The absorbance of dyes onto the photocatalytic paper was observed after 2-3 min immersion into the wastewater. By the end of the irradiation as the wastewater decolourised, also the photocatalytic paper discoloured. Since reversible adsorption would result in an unchanged spectrum after irradiation and spectra of all three dyes exhibited completely altered shape, this confirms the oxidative transformation rather than dye adsorption took place.

**3.2. Comparison of Photocatalytic Degradation of Pretreated and Untreated Samples.** In the following Figures 6, 7 and 8 normalised absorbance at the main VIS absorbance band and COD values of samples taken at the same irradiation intervals

are plotted as a function of time of irradiation (average values of 2–6 irradiation experiments). The difference in initial absorbance values between the untreated and pretreated samples is demonstrated. The irradiation time was chosen according to the time needed for each dye to be completely decolourized.

The lowest decrease in absorbance during pretreatment in the CW model was established for the RBL19 (Figure 6). Anthraquinonic dyes have already been reported as more recalcitrant under anaerobic conditions compared to azo dyes [33]. This was confirmed as the average decolouration percent was 35 for RBL19 (Figure 6) and much higher for both azo dyes up to 60% for RBK5 (Figure 7) and over 50% for RRD22 (Figure 8).

When photocatalytic reactions take place on the surface of the catalyst, the pH value of the wastewater is an important

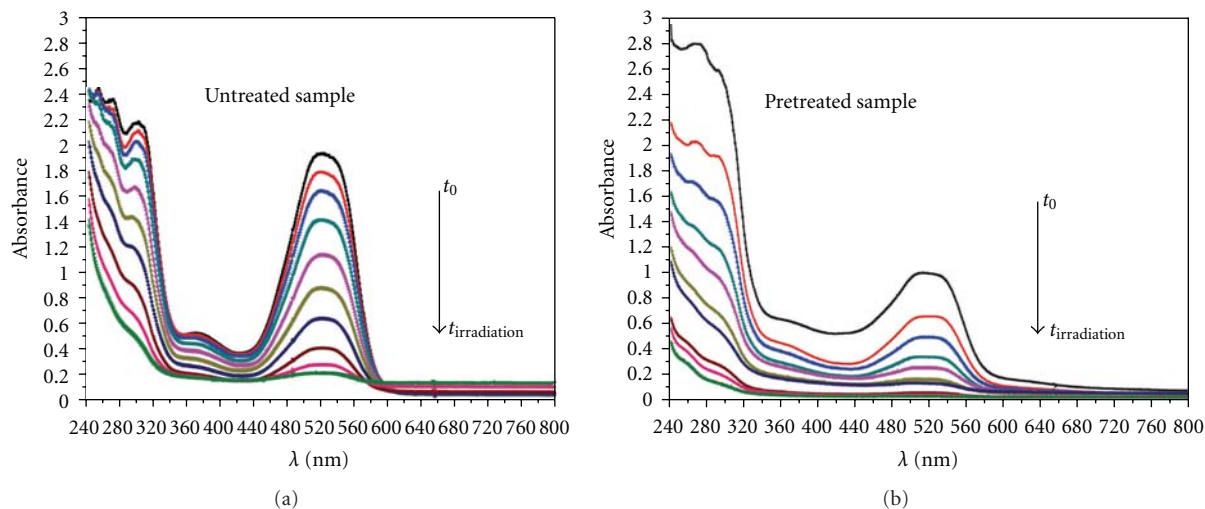


FIGURE 5: Temporal changes in absorption spectra of untreated (a) and pretreated (b) Reactive red 22 textile effluent taken at 5–15 min intervals, the irradiation time was 210 min.

factor since it dictates the surface charge properties of the catalyst. The starting pH of the untreated and pretreated wastewater (Table 1) was higher than the point of zero charge of  $\text{TiO}_2$  and  $\text{SiO}_2$  oxide surfaces (6.2 and 2.5, resp.), which creates electrostatic repulsive effect (ERL) which in turn hinders adsorption of the dye onto the photocatalyst surface. During degradation no significant change of pH was observed (up to 0.2 pH units oscillation), even though the pH values would be expected to decrease due to formation of acidic degradation products [32, 34]. However, it has to be taken into account that prepared wastewater samples beside dyes contained also high amount of organic material (see Section 2.1) which also influenced (buffered) wastewaters' pH values.

Electric conductivity of the pretreated samples was higher than that of the untreated samples, indicating partial organic material mineralization. Increased ion concentration proved to lower the ERL and promote further decolouration and degradation due to cations' negative charge neutralization and dye/catalyst surface interactions promotion. The effect of anions, which compete with the dye for surface adsorption sites is presumed to be less pronounced since negative and neutral sites on the semiconductor surface outnumber the positive ones [35]. Nevertheless, the acidic conditions proved to be more feasible for dye degradation in many studies, so under acidified conditions, the degradation rate would be expected to increase due to no ERL and more efficient electron-transfer process between the positive charged catalyst and negatively charged dye molecule [2, 36]. As in this study the aim was to mimic real conditions of industrial wastewaters' composition, the degradation in acidic media has not been tested.

Catalyst surface area proved to be an important parameter determining degradation rate due to dye/catalyst adsorption dependence [32, 35, 37, 38]. In the case of Degussa P25 aqueous suspension and lower dye concentration (compared to the concentration used in our experiment) PCOx the decolouration was achieved in 15 to 90 min, depending

on the catalyst load [31]. A complete mineralization was reached after 200 min of irradiation of an 85 mg/L RBK5 [39]. Literature data on photocatalytic paper application for dye degradation or mineralization is very scarce. Irradiation in a similar immobilised  $\text{TiO}_2$  reactor with  $\text{H}_2\text{O}_2$  addition reached complete removal of colouration in 30 to 60 min, depending on the concentration of  $\text{H}_2\text{O}_2$  added [40]. A direct comparison is difficult since the reactor setup and the type of  $\text{TiO}_2$  were different.

For RBL19 (Figure 6) the shortest irradiation time, that is, 90 min, was needed to achieve complete decolouration. This is attributed to its lowest initial absorbance indicating the lowest colouration intensity (anthraquinone structure). Nevertheless, 35% difference in initial colouration of the pretreated sample (Figure 6) did not shorten the irradiation time needed to reach complete decolouration and proved the recalcitrance of this anthraquinone dye.

Longer irradiation time (210 min) was needed to decolourise RBK5 (Figure 7) and RRD22 (Figure 8). As resulting from Figures 7 and 8, the PCOx decolouration course exhibits a clear difference in favour of the pretreated samples regarding the required irradiation time for decolouration (about 40% shorter time of irradiation).

Dye molecules colour the wastewater up to a degree which causes screening effect as they absorb UV irradiation, preventing it from reaching the surface of the catalyst and thus reducing reactive radicals formation and reaction efficiency. In Subsection 3.1 the initial absorbance values, which imply to the intensity of colouration, are presented. The substantial difference in initial absorbance and chemical structure (structural formulas in Figure 1) among azo and anthraquinone dyes resulted in almost 60% shorter time needed for RBL19 decolouration. Retardation in light penetration with increasing dye concentration requires higher catalyst surface for the same degradation rate to be achieved [10, 39].

When decolouration curves of untreated samples are compared, it can be ascertained that the RBL19 (Figure 6)

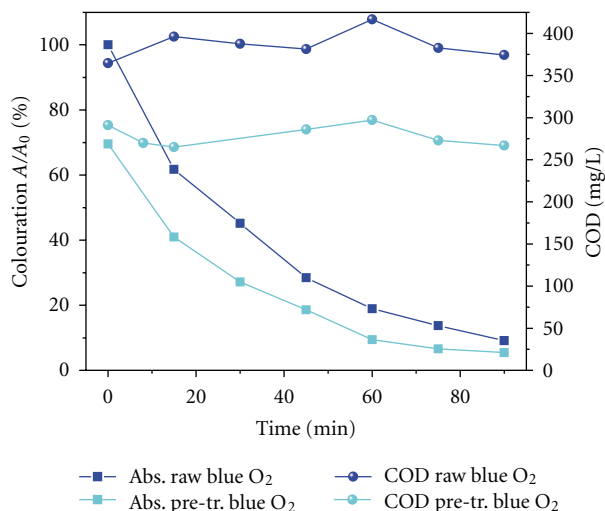


FIGURE 6: Colouration expressed as  $A/A_0$  and COD values of Reactive Blue 19 wastewater samples at different times of PCOx irradiation. Square symbols in all graphs represent absorbance values of untreated and pretreated samples; sphere symbols represent COD values of the same samples.

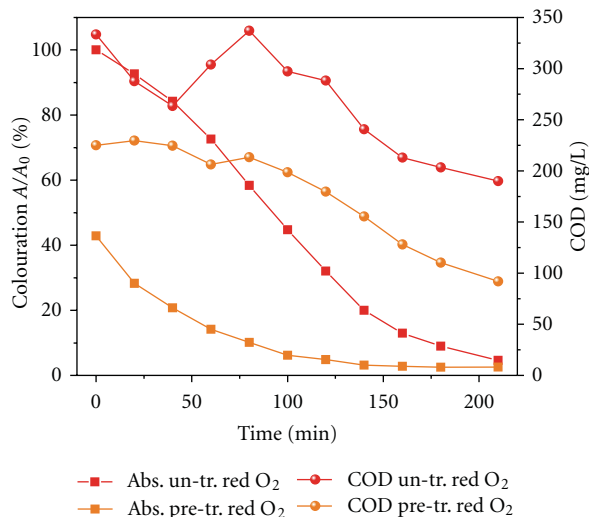


FIGURE 8: Colouration expressed as  $A/A_0$  and COD values of Reactive Red 22 wastewater samples at different times of PCOx irradiation.

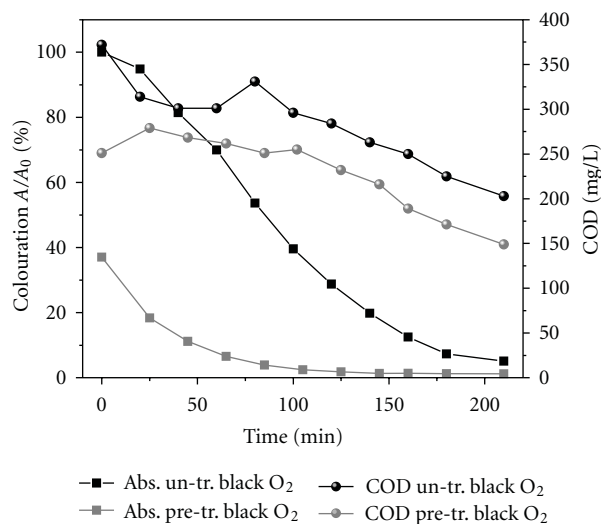


FIGURE 7: Colouration expressed as  $A/A_0$  and COD values of Reactive Black 5 wastewater samples at different times of PCOx irradiation.

curve exhibits first order exponential decay; but RBK5 (Figure 7) and RRD22 (Figure 8) curves exhibit more of a sigmoid shape in the first part of the irradiation experiment. Only after 60 min of irradiation, when initial absorbance decreases for 30%, the curves acquire exponential decay shape. Exhibited characteristic of the curves is attributed to the screening effect of the red and black dye during first part of irradiation due to high initial colouration intensity. When colouration intensity decreases for a certain percent, screening effect is no longer present and further decolouration proceeds exponentially. These findings are in accordance with the published results [34]. Additionally, the screening effect is confirmed by the fact that none of the pretreated samples' decolouration curves has sigmoid shape.

Toxicity of the untreated and pretreated samples towards the *Vibrio fischeri* test organism prior to irradiation was very high (only for the blue-dyed wastewater was lower than 100%) (Table 1). This is attributed to the established textile dyes' toxicity; mother compounds or degradation products are many times found to be carcinogenic or mutagenic [41].

During textile wastewaters' photocatalytic degradation only in the case of pretreated RRD22 a pronounced decrease in toxicity occurred. In all cases the toxicity during the irradiation first increased and later started to decrease. As also the COD values showed sigmoid shape (Figures 6, 7, 8) during irradiation, the toxicity of the samples can be attributed to toxic intermediates formed during first stages of reaction. This confirms the published results by [42]. Prolonged irradiation would be expected to result in further toxicity abatement since COD values started to decrease during the second half of irradiation.

3.3. COD Concentration and Sample Mineralization. From Figures 6, 7, and 8 it can be concluded that decolouration was achieved much faster compared to the mineralization. Since the irradiation time was chosen according to the time needed for disappearance of visible colouration, the obtained mineralization rate is not significant. During dye degradation the intermediate products were formed and partial mineralization as final compound degradation was achieved only at longer irradiation time.

No COD decrease was achieved at RBL19 (Figure 6) untreated wastewater irradiation. This is attributed to the short irradiation time applied. Average COD decrease for untreated wastewaters is similar for black (Figure 7) and red dye (Figure 8), reaching 169 and 143 mg/L, respectively (45 and 43% decrease). These numbers are in agreement with the published data for similar irradiation lengths [43]. Irradiation in a similar immobilised  $TiO_2$  reactor, but with  $H_2O_2$  addition reached 50 mg/L after 240 min of irradiation, in our experiment the COD decrease was higher [40]. After

decolouration of the wastewater is achieved, the COD is reported to decrease sharply [6].

In all untreated water samples an increase in the COD concentration is exhibited in the first 60–80 min of irradiation. After 60 min irradiation of the untreated RBL19 wastewater sample (Figure 6—dark sphere symbol) a peak occurs and no correlation with decolouration can be established. The RBK5 and RRD22 COD curves (Figures 7 and 8—dark sphere symbol) of untreated wastewater samples exhibit an increase in COD concentration, a peak occurring after 80 min which is followed by a decrease. COD curves' sigmoid shape indicates formation of more tolerant intermediate products, which temporarily increase COD of the wastewater [44].

CW pretreatment contributed to COD decrease after photocatalysis of all the wastewater samples ranging from only 24 mg/L (RBL19, Figure 6) to 108 mg/L (RBK5, Figure 7) and 121 mg/L (RRD22, Figure 8). It can be concluded that the pretreatment increases the overall mineralization rate which for real scale textile wastewater treatment plants means shorter irradiation time in order to meet the effluent limits (COD under 120 mg/L) [43]. In the case of pretreated samples, the sigmoid shape of the curve is far less pronounced (Figures 6, 7, 8—light sphere symbol). COD value starts to decrease in the second half of irradiation.

It has to be taken into account that when the wastewater is irradiated, the COD decrease does not depend solely on the dye degradation but is rather influenced by many additional photocatalytic decomposition processes taking place in the irradiated wastewater.

**3.4. Photocatalytic Ozonation.** When ozone molecule is adsorbed onto the surface of the semiconductor an ozonide radical anion is formed, resulting in hydroxyl radical formation. Another pathway of its formation through ozone mediation is the reaction of superoxide anion with the ozone, again leading to hydroxyl radical formation [45, 46]. Furthermore, a synergy effect of TiO<sub>2</sub>-based photocatalysis combined with ozonation has been reported. It results from a series of reactions which are often conditioned by preceding reactions' products [47, 48].

As in PCOx also in PCOz the absorbance spectra of untreated wastewater samples and CW pretreated samples (not shown) indicated a decrease in the absorbance bands in UV and VIS region with time of irradiation and no new absorbance bands occurred. After PCOz the spectra show absence of VIS wavelengths absorbing molecules, while some absorbance in the UV persists and is more pronounced in the untreated samples.

All the untreated and pretreated wastewater samples reached complete decolouration in much shorter time with PCOz compared to PCOx, as following from Figures 9, 10 and 11. The untreated RBK5 (Figure 10) and RRD22 (Figure 11) samples were decolourised in 20 min and RBL19 (Figure 9) in only 10 min. Faster decolouration is attributed to the action of ozone which increases the rate of decolouration [14].

For both RBL19 (Figure 9) wastewater samples the same irradiation time was needed to reduce visible colouration; for

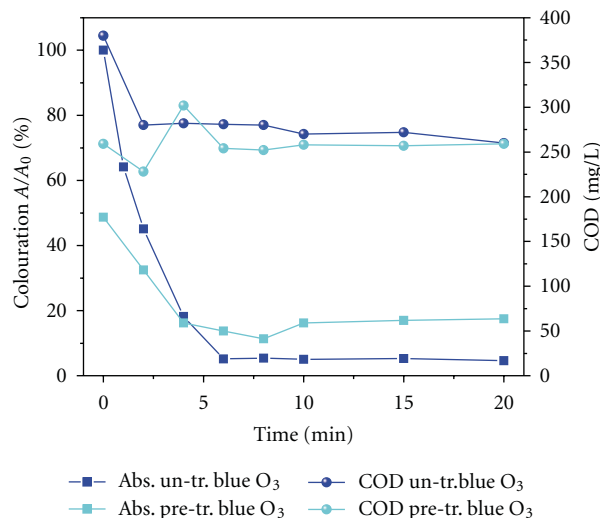


FIGURE 9: Colouration expressed as  $A/A_0$  and COD values of Reactive Blue 19 wastewater samples at different times of PCOz irradiation. Square symbols in all graphs represent absorbance values of untreated and pretreated samples; sphere symbols represent COD values of the same samples.

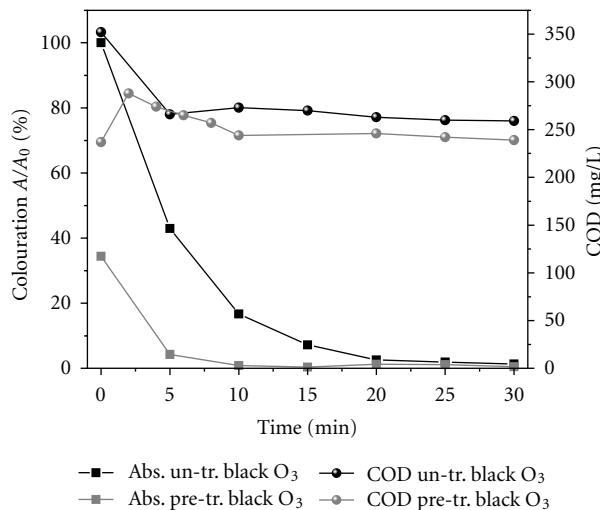


FIGURE 10: Colouration expressed as  $A/A_0$  and COD values of Reactive Black 5 wastewater samples at different times of PCOz irradiation.

RRD22 (Figure 11) the difference between the untreated and pretreated one was only 5 min. Only in the case of RBK5 (Figure 10) the pretreated samples needed considerably shorter (50%) irradiation time.

Since ozone molecule adsorption to the semiconductor surface is an inevitable step for hydroxyl radical formation, the catalyst type, load, and surface area play an important, rate determining role [49, 50]. This was also proven by Wu et al., 2008 [51], where addition of different amounts of TiO<sub>2</sub> did not considerably improve decolouration. To our knowledge, so far there are no publications yet on the dye decolouration with PCOz using Ahlstrom photocatalytic paper as catalyst. The data on PCOz irradiation with

TABLE 2: Irradiation times given in minutes needed to obtain decolouration of different samples and the difference between both methods and between untreated (UN-T.) and pretreated (PRE-T.) samples within each method (PCOx and PCOz).

Colour	Treatment/sample	PCOx (O <sub>2</sub> purging) [min]	PCOz (O <sub>3</sub> purging) [min]	Difference between PCOx and PCOz [%]	Difference between UN-T. and PRE-T. PCOx [%]	Difference between UN-T. and PRE-T. PCOz [%]
Blue, RBL19	Untreated	90	6	93	0	0
	Pretreated	90	6	93		
Red, RRD22	Untreated	210	20	90	43	25
	Pretreated	120	15	88		
Black, RBK5	Untreated	210	20	90	69	50
	Pretreated	65	10	85		

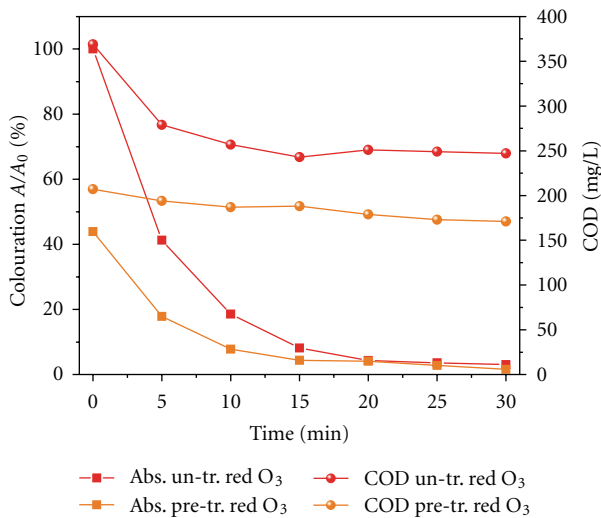


FIGURE 11: Colouration expressed as  $A/A_0$  and COD values of Reactive Red 22 wastewater samples at different times of PCOz irradiation.

P25-Degussa TiO<sub>2</sub> catalyst for monochloroacetic acid and pyridine degradation [46] has proven to be 4 times and 5 times more efficient respectively, compared to the PCOx.

Ozone-mediated dye degradation was established to be the fastest at alkaline pH values since alkaline environment promotes ozone decomposition in favour of hydroxyl radical formation [52, 53]. Thus, the samples' pH values are in favour of radical formation (Table 1). In more alkaline wastewaters degradation rate would be further increased since the difference between pH 2 and 12 was found to be 32% [53].

In Figures 9, 10, and 11 the COD values of the samples obtained during 20 to 30 min irradiation time are also shown (right side scale). For the RBL19 pretreated sample (Figure 9, light sphere symbol) no decrease is exhibited while the untreated sample (Figure 9, dark sphere symbol) exhibits 32% COD decrease. For RBK5 (Figure 10) the COD concentration decrease is evident for untreated samples (26%, 93 mg/L, Figure 10, dark sphere symbol) but was again absent in the pretreated samples (Figure 10, light sphere

symbol). Only in the case of RRD22 wastewater (Figure 11) the PCOz proved to be successful in COD abatement in both sets of samples (33% and 17% for untreated and pretreated samples). Moreover, the more or less pronounced sigmoid COD curves indicate formation of degradation reaction products which can act as ozone scavengers thus decreasing the rate of mineralization. Again it has to be kept in mind that all samples were actually wastewater and not dye solution samples, containing also organic material (see Section 2.1).

Study done by authors in [54] shows that PCOz treatment (P25-Degussa) of textile effluents resulted in almost complete decolouration after 60 min of irradiation and more than 60% decrease in TOC values [54]. This implies to the competition of reaction intermediates with pollutant molecules in O<sub>3</sub> scavenging and only their further degradation to mineralization eventually decreases the overall TOC values. In simulated textile wastewaters prolonged irradiation time would be needed to reach not only decolouration but also higher degree of COD removal.

As in PCOx also in PCOz high toxicity of the samples was exhibited during and after irradiation. Again only toxicity of the untreated RRD22 samples decreased to 82% and of the pretreated RRD22 samples below the toxicity limit (20%).

Large differences are exhibited between the PCOx and PCOz irradiation (decolouration) times (Table 2). The PCOz irradiation time of the RBL19 untreated and pretreated samples was shorter for 93% and of the RRD22 and RBK5 samples between 85 and 90%, compared to PCOx. Again the RBL19 pretreatment did not shorten the decolouration irradiation time but the RRD22 and RBK5 pretreatment shortened it for 25–69%.

For RBL19 was the COD decrease substantial only in untreated samples' PCOz (Table 3); in RRD22 and RBK5 PCOx it accounted for 41–60% and was much lower (or absent) in PCOz. This confirms that the length of irradiation played a crucial role in COD decrease.

## 4. Conclusions

In the paper a comparison between the photocatalytic decolouration and mineralization of untreated and pretreated samples of three prepared textile wastewaters is presented.

TABLE 3: COD removal of samples during irradiation treatment.

Sample/colour	COD removal [%] during irradiation	PCOx irradiation [%]	PCOz irradiation [%]
Blue, RBL19	Untreated	0	32
	Pretreated	8	0
Red, RRD22	Untreated	43	33
	Pretreated	60	17
Black, RBK5	Untreated	45	26
	Pretreated	41	0

During the CW pretreatment of simulated textile wastewater considerable level of decolouration and partial decrease in the COD levels was achieved. It can be concluded that the pretreatment proved to be successful in shortening the decolouration irradiation time for both azo dyes, RRD22 and RBK5 in PCOx and PCOz experiments. This was not the case for RBL19 since the irradiation time is exactly the same regardless of the samples' origin. Overall irradiation time was found to be dependent on the initial colouration intensity due to screening effects at high initial colourations.

Regarding the irradiation time scale, PCOz proved to be more efficient in terms of much shorter decolouration time compared to the PCOx. However, due to shorter irradiation time the COD removal was lower or absent.

To meet the technical water effluents' legislative limits, both experiments would have to be prolonged, due to the insufficient COD removal. Since intermediate products' degradation follows the decolouration step and catalytic decolouration is much faster with ozone purging, photocatalytic ozonation is proposed as a more favourable of the two procedures. But longer ozonation experiments would have to be tested for a COD removal.

A combination of the CW and photocatalytic techniques proved to be a promising approach in increasing cost efficiency in textile wastewater treatment.

## Abbreviations

CW: Constructed wetland  
 PCOx: Photocatalytic oxidation  
 PCOz: Photocatalytic ozonation  
 RBL19: Reactive Blue 19  
 RBK5: Reactive Black 5  
 RRD22: Reactive Red 22.

## Conflict of Interest

There was no conflict of interest present regarding the use of commercial products; all products used in this study were purchased on the market.

## Acknowledgments

This work was supported by the Ministry of Higher Education, Science and Technology of the Republic of Slovenia.

## References

- [1] S. M. D. A. G. U. de Souza, K. A. S. Bonilla, and A. A. U. de Souza, "Removal of COD and color from hydrolyzed textile azo dye by combined ozonation and biological treatment," *Journal of Hazardous Materials*, vol. 179, no. 1–3, pp. 35–42, 2010.
- [2] P. A. Pekakis, N. P. Xekoukoulotakis, and D. Mantzavinos, "Treatment of textile dyehouse wastewater by TiO<sub>2</sub> photocatalysis," *Water Research*, vol. 40, no. 6, pp. 1276–1286, 2006.
- [3] U. G. Akpan and B. H. Hameed, "Parameters affecting the photocatalytic degradation of dyes using TiO<sub>2</sub>-based photocatalysts: a review," *Journal of Hazardous Materials*, vol. 170, no. 2–3, pp. 520–529, 2009.
- [4] F. Harrelkas, A. Paulo, M. M. Alves et al., "Photocatalytic and combined anaerobic-photocatalytic treatment of textile dyes," *Chemosphere*, vol. 72, no. 11, pp. 1816–1822, 2008.
- [5] A. Rachel, M. Subrahmanyam, and P. Boule, "Comparison of photocatalytic efficiencies of TiO<sub>2</sub> in suspended and immobilised form for the photocatalytic degradation of nitrobenzenesulfonic acids," *Applied Catalysis B*, vol. 37, no. 4, pp. 301–308, 2002.
- [6] J. A. Byrne, P. A. Fernandez-Ibañez, P. S.M. Dunlop, D. M.A. Alrousan, and J. W.J. Hamilton, "Photocatalytic enhancement for solar disinfection of water: a review," *International Journal of Photoenergy*, vol. 2011, Article ID 798051, 12 pages, 2011.
- [7] Z. Zhang and J. Gamage, "Applications of photocatalytic disinfection," *International Journal of Photoenergy*, vol. 2010, Article ID 764870, 11 pages, 2010.
- [8] S. Brosillon, H. Djelal, N. Merienne, and A. Amrane, "Innovative integrated process for the treatment of azo dyes: coupling of photocatalysis and biological treatment," *Desalination*, vol. 222, no. 1–3, pp. 331–339, 2008.
- [9] Y. Fan, G. Chen, D. Li et al., "Highly selective deethylation of rhodamine B on TiO<sub>2</sub> prepared in supercritical fluids," *International Journal of Photoenergy*, vol. 2012, Article ID 173865, 6 pages, 2012.
- [10] I. K. Konstantinou and T. A. Albanis, "TiO<sub>2</sub>-assisted photocatalytic degradation of azo dyes in aqueous solution: kinetic and mechanistic investigations: a review," *Applied Catalysis B*, vol. 49, no. 1, pp. 1–14, 2004.
- [11] A. Alinsafi, F. Evenou, E. M. Abdulkarim et al., "Treatment of textile industry wastewater by supported photocatalysis," *Dyes and Pigments*, vol. 74, no. 2, pp. 439–445, 2007.
- [12] J. C. Garcia, J. I. Simionato, A. E. C. D. Silva, J. Nozaki, and N. E. D. Souza, "Solar photocatalytic degradation of real textile effluents by associated titanium dioxide and hydrogen peroxide," *Solar Energy*, vol. 83, no. 3, pp. 316–322, 2009.
- [13] J. G. Yu, H. G. Yu, B. Cheng, X. J. Zhao, J. C. Yu, and W. K. Ho, "The effect of calcination temperature on the surface microstructure and photocatalytic activity of TiO<sub>2</sub> thin films prepared by liquid phase deposition," *Journal of Physical Chemistry B*, vol. 107, no. 50, pp. 13871–13879, 2003.
- [14] T. E. Agustina, H. M. Ang, and V. K. Vareek, "A review of synergistic effect of photocatalysis and ozonation on wastewater treatment," *Journal of Photochemistry and Photobiology C*, vol. 6, no. 4, pp. 264–273, 2005.
- [15] Ü. Mander and W. J. Mitsch, "Pollution control by wetlands," *Ecological Engineering*, vol. 35, no. 2, pp. 153–158, 2009.
- [16] D. P. L. Rousseau, P. A. Vanrolleghem, and N. De Pauw, "Model-based design of horizontal subsurface flow constructed treatment wetlands: a review," *Water Research*, vol. 38, no. 6, pp. 1484–1493, 2004.

- [17] P. A. Mays and G. S. Edwards, "Comparison of heavy metal accumulation in a natural wetland and constructed wetlands receiving acid mine drainage," *Ecological Engineering*, vol. 16, no. 4, pp. 487–500, 2001.
- [18] C. S. C. Calheiros, A. O. S. S. Rangel, and P. M. L. Castro, "Constructed wetland systems vegetated with different plants applied to the treatment of tannery wastewater," *Water Research*, vol. 41, no. 8, pp. 1790–1798, 2007.
- [19] G. L. Baughman and W. S. Perkins, "Treatment of textile effluents in constructed wetlands," *AATCC Magazine*, vol. 1, no. 5, pp. 31–33, 2001.
- [20] T. G. Bulc and A. Ojstršek, "The use of constructed wetland for dye-rich textile wastewater treatment," *Journal of Hazardous Materials*, vol. 155, no. 1-2, pp. 76–82, 2008.
- [21] J. L. Faulwetter, V. Gagnon, C. Sundberg et al., "Microbial processes influencing performance of treatment wetlands: a review," *Ecological Engineering*, vol. 35, no. 6, pp. 987–1004, 2009.
- [22] A. Muhammad, A. Shafeeq, M. A. Butt, Z. H. Rizvi, M. A. Chughtai, and S. Rehman, "Decolorization and removal of COD and BOD from raw and biotreated textile dye bath effluent through advanced oxidation processes (AOPS)," *Brazilian Journal of Chemical Engineering*, vol. 25, no. 3, pp. 453–459, 2008.
- [23] J. Araña, C. Garriga i Cabo, C. Fernández Rodríguez et al., "Combining TiO<sub>2</sub>-photocatalysis and wetland reactors for the efficient treatment of pesticides," *Chemosphere*, vol. 71, no. 4, pp. 788–794, 2008.
- [24] M. Roš and J. Vrtovšek, "The study of nutrient balance in sequencing batch reactor wastewater treatment," *Acta Chimica Slovenica*, vol. 51, no. 4, pp. 779–785, 2004.
- [25] U. Černigoj, U. L. Štangar, and P. Trebše, "Evaluation of a novel Carberry type photoreactor for the degradation of organic pollutants in water," *Journal of Photochemistry and Photobiology A*, vol. 188, no. 2-3, pp. 169–176, 2007.
- [26] M. Kete, "Razvoj pilotnega sistema za čiščenje vode na principu TiO<sub>2</sub> fotokatalize," B.Sc. Thesis, <http://www.p-ng.si/~vanesa/diplome/OKOLJE/slv/31Kete.pdf>.
- [27] F. P. Van Der Zee and S. Villaverde, "Combined anaerobic-aerobic treatment of azo dyes—a short review of bioreactor studies," *Water Research*, vol. 39, no. 8, pp. 1425–1440, 2005.
- [28] S. M. Marques, C. J. Tavares, L. F. Oliveira, and A. M. F. Oliveira-Campos, "Photocatalytic degradation of C.I. Reactive Blue 19 with nitrogen-doped TiO<sub>2</sub> catalysts thin films under UV/visible light," *Journal of Molecular Structure*, vol. 983, no. 1–3, pp. 147–152, 2010.
- [29] M. Saquib and M. Muneer, "Semiconductor mediated photocatalysed degradation of an anthraquinone dye, Remazol Brilliant Blue R under sunlight and artificial light source," *Dyes and Pigments*, vol. 53, no. 3, pp. 237–249, 2002.
- [30] A. Gottlieb, C. Shaw, A. Smith, A. Wheatley, and S. Forsythe, "The toxicity of textile reactive azo dyes after hydrolysis and decolourisation," *Journal of Biotechnology*, vol. 101, no. 1, pp. 49–56, 2003.
- [31] D. E. Kritikos, N. P. Xekoukoulotakis, E. Psillakis, and D. Mantzavinos, "Photocatalytic degradation of reactive black 5 in aqueous solutions: effect of operating conditions and coupling with ultrasound irradiation," *Water Research*, vol. 41, no. 10, pp. 2236–2246, 2007.
- [32] K. Tanaka, K. Padermpole, and T. Hisanaga, "Photocatalytic degradation of commercial azo dyes," *Water Research*, vol. 34, no. 1, pp. 327–333, 2000.
- [33] P. I. M. Firmino, M. E. R. da Silva, F. J. Cervantes, and A. B. dos Santos, "Colour removal of dyes from synthetic and real textile wastewaters in one- and two-stage anaerobic systems," *Bioresource Technology*, vol. 101, no. 20, pp. 7773–7779, 2010.
- [34] M. Styliidi, D. I. Kondarides, and X. E. Verykios, "Pathways of solar light-induced photocatalytic degradation of azo dyes in aqueous TiO<sub>2</sub> suspensions," *Applied Catalysis B*, vol. 40, no. 4, pp. 271–286, 2003.
- [35] A. Aguedach, S. Brosillon, J. Morvan, and E. K. Lhadi, "Influence of ionic strength in the adsorption and during photocatalysis of reactive black 5 azo dye on TiO<sub>2</sub> coated on non woven paper with SiO<sub>2</sub> as a binder," *Journal of Hazardous Materials*, vol. 150, no. 2, pp. 250–256, 2008.
- [36] C. Wang and J. Yao, "Decolorization of methylene blue with TiO<sub>2</sub> sol via UV irradiation photocatalytic degradation," *International Journal of Photoenergy*, vol. 2010, Article ID 643182, 6 pages, 2010.
- [37] Q. Xiang, J. Yu, and M. Jaroniec, "Tunable photocatalytic selectivity of TiO<sub>2</sub> films consisted of flower-like microspheres with exposed {001} facets," *Chemical Communications*, vol. 47, no. 15, pp. 4532–4534, 2011.
- [38] S. Liu, J. Yu, and M. Jaroniec, "Tunable photocatalytic selectivity of hollow TiO<sub>2</sub> microspheres composed of anatase polyhedra with exposed {001} facets," *Journal of the American Chemical Society*, vol. 132, no. 34, pp. 11914–11916, 2010.
- [39] C. Tang and V. Chen, "The photocatalytic degradation of reactive black 5 using TiO<sub>2</sub>/UV in an annular photoreactor," *Water Research*, vol. 38, no. 11, pp. 2775–2781, 2004.
- [40] C. Wang, A. Yediler, D. Lienert, Z. Wang, and A. Kettrup, "Toxicity evaluation of reactive dyestuffs, auxiliaries and selected effluents in textile finishing industry to luminescent bacteria *Vibrio fischeri*," *Chemosphere*, vol. 46, no. 2, pp. 339–344, 2002.
- [41] N. M. Mahmoodi, M. Arami, and N. Y. Limaee, "Photocatalytic degradation of triazinic ring-containing azo dye (Reactive Red 198) by using immobilized TiO<sub>2</sub> photoreactor: bench scale study," *Journal of Hazardous Materials*, vol. 133, no. 1–3, pp. 113–118, 2006.
- [42] C. Lizama, J. Freer, J. Baeza, and H. D. Mansilla, "Optimized photodegradation of reactive blue 19 on TiO<sub>2</sub> and ZnO suspensions," *Catalysis Today*, vol. 76, no. 2–4, pp. 235–246, 2002.
- [43] Official Gazette RS, 45/2007, "Uredba o spremembah in dopolnitvah Uredbe o emisiji snovi in topolote pri dovajanju odpadnih vod v vode in javno kanalizacijo".
- [44] K. Soutsas, V. Karayannis, I. Poullos et al., "Decolorization and degradation of reactive azo dyes via heterogeneous photocatalytic processes," *Desalination*, vol. 250, no. 1, pp. 345–350, 2010.
- [45] A. Alinsafi, F. Evenou, E. M. Abdulkarim et al., "Treatment of textile industry wastewater by supported photocatalysis," *Dyes and Pigments*, vol. 74, no. 2, pp. 439–445, 2007.
- [46] P. Kopf, E. Gilbert, and S. H. Eberle, "TiO<sub>2</sub> photocatalytic oxidation of monochloroacetic acid and pyridine: influence of ozone," *Journal of Photochemistry and Photobiology A*, vol. 136, no. 3, pp. 163–168, 2000.
- [47] M. Addamo, V. Augugliaro, E. García-López, V. Loddo, G. Marci, and L. Palmisano, "Oxidation of oxalate ion in aqueous suspensions of TiO<sub>2</sub> by photocatalysis and ozonation," *Catalysis Today*, vol. 107–108, pp. 612–618, 2005.
- [48] U. Černigoj, U. L. Štangar, and J. Jirkovský, "Effect of dissolved ozone or ferric ions on photodegradation of thiacloprid in presence of different TiO<sub>2</sub> catalysts," *Journal of Hazardous Materials*, vol. 177, no. 1–3, pp. 399–406, 2010.
- [49] U. Černigoj, U. L. Štangar, and P. Trebše, "Degradation of neonicotinoid insecticides by different advanced oxidation

- processes and studying the effect of ozone on TiO<sub>2</sub> photocatalysis," *Applied Catalysis B*, vol. 75, no. 3-4, pp. 229–238, 2007.
- [50] U. Černigoj, U. L. Štangar, P. Trebše, and M. Sarakha, "Determination of catalytic properties of TiO<sub>2</sub> coatings using aqueous solution of coumarin: standardization efforts," *Journal of Photochemistry and Photobiology A*, vol. 201, no. 2-3, pp. 142–150, 2009.
- [51] C. H. Wu, C. Y. Kuo, and C. L. Chang, "Decolorization of C.I. Reactive Red 2 by catalytic ozonation processes," *Journal of Hazardous Materials*, vol. 153, no. 3, pp. 1052–1058, 2008.
- [52] M. F. Sevimli and H. Z. Sarikaya, "Ozone treatment of textile effluents and dyes: effect of applied ozone dose, pH and dye concentration," *Journal of Chemical Technology and Biotechnology*, vol. 77, no. 7, pp. 842–850, 2002.
- [53] A. H. Konsowa, "Decolorization of wastewater containing direct dye by ozonation in a batch bubble column reactor," *Desalination*, vol. 158, no. 1–3, pp. 233–240, 2003.
- [54] S. Gomes De Moraes, R. Sanches Freire, and N. Durán, "Degradation and toxicity reduction of textile effluent by combined photocatalytic and ozonation processes," *Chemosphere*, vol. 40, no. 4, pp. 369–373, 2000.

## Research Article

# Preparation of Antibacterial Color-Coated Steel Sheets

**Guoliang Li, Bing Peng, Liyuan Chai, Si Wan, and Lei Jiang**

*School of Metallurgical Science and Engineering, Central South University, Changsha 410083, China*

Correspondence should be addressed to Bing Peng, pb@mail.csu.edu.cn

Received 15 September 2011; Revised 23 January 2012; Accepted 23 January 2012

Academic Editor: Gongxuan Lu

Copyright © 2012 Guoliang Li et al. This is an open access article distributed under the Creative Commons Attribution License, which permits unrestricted use, distribution, and reproduction in any medium, provided the original work is properly cited.

A simple method to fabricate antibacterial color-coated steel sheet was presented. The Ag-loaded TiO<sub>2</sub> was well dispersed in steel coil coating coupled with some special additives, such as plasticizer, wetting dispersant, and flow agent, and finally became the part of coil coating without any negative influence on the properties of final products. The best process parameters were obtained by substantive trial experiments. Ag-loaded TiO<sub>2</sub> with the addition of 2% (w/w) in steel coil coating not only improved antibacterial efficiency of the antibacterial color-coated sheet by reaching 99.99%, but also greatly increased the degradation percentage of methyl orange to 88% without decreasing physical properties. The antibacterial color-coated sheets are expected to be used as antimicrobial products in the construction industry considering its low cost and high effectiveness in inhibiting the growth of bacteria.

## 1. Introduction

The menace of infection caused awareness around the world by the suddenly globally spreading epidemic disease, such as avian influenza [1], SARS, H1N1, and other unexpected multiplication of germs or other bacteria that pose serious health problems [2, 3]. Great deals of antibacterial products appeared in the cases of antibacterial ceramics [4–7], antibacterial glasses [8–10], antibacterial textiles [11–13], antibacterial plastics [14–16], antibacterial stainless steels [17–20], and so forth. These applications mainly involve the methods of adding antibacterial agents into the overall substrate, modifying the surface of substrate, or directly coating the antibacterial agents. However, the development of antibacterial products in a wide range of areas was still hindered due to the low effective utilization rate of the antibacterial agents, the high cost, and the poor binding force, which existed between antibacterial agents and the substrates restrict. In this paper, the antibacterial agent was firstly poured into the coil coating before being made into the antibacterial color-coated sheet. Sequent research findings demonstrated that antibacterial agents presented a comfortable dispersive distribution on the surface of color-coated sheet, which could remarkably reduce the cost by attributing to the less addition of antibacterial agents and the simple manufacturing technological process. It was also

found that the binding force among the antibacterial agents and substrate got much stronger than ever due to the integration of antibacterial agents into the coil coating.

Served as one category of antibacterial agent, titanium dioxide is the most preferred material to be served as pigment. Unfortunately, the antimicrobial activity of pure TiO<sub>2</sub> is merely valid when it is irradiated under UV light. In addition, the low electron transfer rate to oxygen and high recombination rate of electron-hole employed in UV light impose further limits to the effective photocatalytic sterilization rate of TiO<sub>2</sub> [21–23]. These drawbacks strongly restricted the practical applications of TiO<sub>2</sub> as an effective and promising antimicrobial material. Silver (including Ag ions and Ag nanoparticles) is a well-known and effective inorganic antimicrobial material that has been applied in many fields. However, the high-cost and dark color are two notable obstacles during its applications as large-scale antimicrobial coatings [24–26]. Nevertheless, Ag can act as both an antimicrobial auxiliary agent and a sink for electrons and redox catalyst that may enhance the overall photo-oxidation ability of TiO<sub>2</sub> [27–30]. Thus, it is reasonable and rational to combine Ag with TiO<sub>2</sub> during antimicrobial coatings production.

This study focused on the manufacture of antibacterial color-coated sheet using Ag-loaded TiO<sub>2</sub> as antibacterial agent. The antibacterial agent was firstly poured into steel

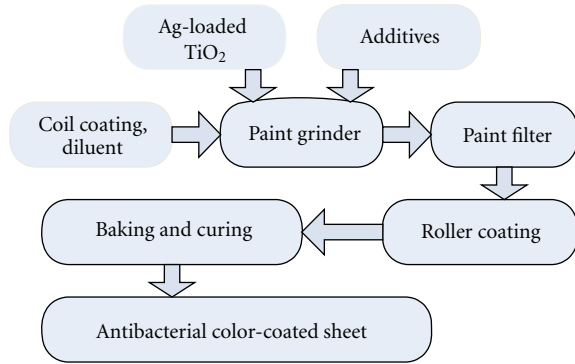


FIGURE 1: Preparation flowsheet of antibacterial color-coated sheet.

coil coating with some additives and made into the antibacterial coil coating. And then, the antibacterial color-coated sheet was manufactured in a normal process. It delivered a technology of less addition of antibacterial agents and simple procedure.

## 2. Experimental

**2.1. Materials.** Ag-loaded  $\text{TiO}_2$  was purchased from Jingui Group (Chenzhou, China). The grain size was 48 nm and the Ag particle size was 10 nm. Coil coatings (including polyester topcoat and epoxy priming paint) and diluents (the main components were ethyl acetate, butyl acetate, benzene, toluene, acetone, ethanol, butanol, etc.) were provided by Center Group (Changshu, China). The additives including plasticizer, wetting dispersant, and flow agents were purchased from Yongyan Ltd. (Shanghai, China).

**2.2. Preparative Method of Antibacterial Color-Coated Sheet.** The preparative process of antibacterial color-coated steel plate is shown in Figure 1. A certain amount of coil coatings, coil coating diluents, silver-loaded titanium dioxide, and some additives including plasticizer, wetting dispersant, and flow agents were added into the paint grinder running in high speed, and then filtered through the paint filter. Finally, the color-coated steel plate was achieved by roll coating, baking and curing.

The Ag-loaded  $\text{TiO}_2$  used in this study was produced by Jingui Group using the technological process developed in our previous studies [31–35].

**2.3. Antibacterial Properties Testing.** Antibacterial properties of products were tested according to “Antibacterial Coating—Antibacterial Performance Test Method, the appendix A of “the People’s Republic of China Chemical Standard HG/T 3950-2007”. In the tests, nutrient agar media (Luria Broth, LB) was prepared in water by mixing tryptone, NaCl, agarose gel powder and yeast extract in the volume percent of 1%, 0.5%, 1.5%, and 0.5% to total of media, respectively. The mixture was put into a conical flask and autoclaved for 45 min at  $120^\circ\text{C}$ . The conical flask was kept in room temperature for 2 h for cooling and then poured into separate

Petri dishes. A  $5\text{ cm} \times 5\text{ cm}$  sample was cut from the antibacterial color-coated sheets for bacterial culture and the surface of all samples was cleaned with absolute ethanol soaked tissue paper before antibacterial test. The samples were placed in separate Petri dishes on top of the pre-deposited LB. A clean soda-lime glass piece was used as a control sample. After placing the antibacterial color-coated sheets samples, a thin layer of LB was further deposited on top. These plates were kept for 1 h for complete gelation of the agar, and after that quantitative solution of *E. coli* was evenly spread over each gel plate in the respective Petri dishes. The plates were incubated for 24 hours to allow the completion of bacterial growth. The bacterial colonies formed in each plate were observed and the bacterial number on each sample was counted with colony counting method. The antibacterial efficiency of the color-coated sheet was calculated in

$$\text{Antibacterial efficiency} = \frac{A_0 - A}{A_0}, \quad (1)$$

where  $A_0$  and  $A$  are the antibacterial number of the control sample and antibacterial color-coated sheet sample, respectively.

**2.4. Photocatalysis Properties.** The methyl orange solution with 3 of pH value was poured into the culture. The photocatalytic activity of the antibacterial color-coated sheet was evaluated on the degradation of methyl orange in an aqueous solution under illumination of UV light (mercury vapor lamp, 40 W, 40 cm long, predominant wavelength 253.7 nm) in a photoreactor system. The degradation of methyl orange was calculated in

$$\text{Degradation} = \frac{B_0 - B}{B_0}, \quad (2)$$

where  $B_0$  and  $B$  are the absorbance of the primal and remaining methyl orange, respectively. The absorbance was measured with UV/vis spectrophotometer (UV-2450, Japan).

**2.5. Duration Properties.** The antibacterial color-coated sheet was made of the white gray coil coating with 2% silver-loaded titanium dioxide, cutting into  $5\text{ cm} \times 5\text{ cm}$  pieces. Forty-five pieces were placed into the  $\varnothing 9\text{ cm}$  culture dish, respectively, with three parallel samples each day. Then each culture dish was poured 30 mL ultra-pure water, and sampled every day. The silver content in the water and the antibacterial properties of the sheets would be tested.

## 3. Results and Discuss

**3.1. Antibacterial Properties.** Addition of antibacterial agent and effective utilization rate are key factors influencing on antibacterial properties of the color-coated sheet. The more antibacterial agents used, the higher antibacterial efficiency obtained, but the cost also increased thereupon. The best dose should satisfy antibacterial requirement and low cost. Ag-loaded  $\text{TiO}_2$  should be highly dispersed under stirring and function of additives to get well compatibility with coil

TABLE 1: Effect of agent amount on antibacterial property of color-coated steel.

The dose of Ag/TiO <sub>2</sub> /wt%	0	1	2	3	4	5
Bacterial count of 1#/cfu	$1.88 \times 10^6$	$2.40 \times 10^5$	172	29	<20	<20
Antibacterial efficiency/%	—	87.23	>99.99	>99.99	>99.99	>99.99
Bacterial count of 2#/cfu	$1.86 \times 10^6$	$2.36 \times 10^5$	166	27	<20	<20
Antibacterial efficiency/%	—	87.31	>99.99	>99.99	>99.99	>99.99
Bacterial count of 3#/cfu	$1.91 \times 10^6$	$2.48 \times 10^5$	180	35	<20	<20
Antibacterial efficiency/%	—	87.02	>99.99	>99.99	>99.99	>99.99
Average antibacterial efficiency/%	—	87.19	>99.99	>99.99	>99.99	>99.99

coating. So, the rotation speed and stirring time are considered.

Table 1 shows the effects of different antibacterial agent dosages on the antibacterial properties of color-coated sheet.

As from Table 1, the antibacterial properties increased with the increase of addition of antibacterial agents. The antibacterial efficiency reached about 87% when 1% (wt) of Ag-loaded TiO<sub>2</sub> was added. Obviously, the antibacterial efficiency reached 99.99% when the antibacterial agents addition was higher than 2%. This could be ascribed to the reactive oxygen antibacterial mechanism. In the presence of water and oxygen, the antibacterial agents containing TiO<sub>2</sub> can adsorb water and oxide, producing HO\* with high oxidative and reactive capacity. HO\* can infiltrate and destruct coenzyme A and also degrade endotoxin, protein lipids and mineralize into CO<sub>2</sub> through particles on the cell surface binding of the hydroxyl groups. Ag<sup>+</sup> in the antibacterial agents can be firmly attached to the bacteria, and further penetrate into the bacterial cell wall when contacting the negatively charged cell membrane. This responds to OH in bacteria and results in bacterial proteins coagulation, cell synthesize enzyme activity destruction, and therefore, loss of reproduce ability and death. Besides, Ag<sup>+</sup> can also destroy bacteria electronic transmission system, respiratory system, and mass transport system for killing bacteria. Silver-loaded titanium dioxide agents have the advantages of both above at high temperature, high security, long-term sterilization, and high antibacterial property even in dark condition. Therefore, the 2% dosage of silver-loaded titanium dioxide in coil coating is determined.

Silver-loaded titanium dioxide was added to the mixture of paint at high speed, and then an original speed. The effects of different rotation speeds on the fineness of the coil coating and gloss of the color-coated steel sheet were investigated.

As seen from Figures 2 and 3, the fineness of the coating decreased and the gloss of color sheet increased gradually with the increase of speed. The fineness of coating is the range of 10–20 μm and the gloss  $35 \pm 5$  according to “evaluation method of dispersion of pigments.” The fineness of coating is about 19 μm and the gloss approximately 32 under speed 4000 r/min, both of which meet the required standards. Antibacterial agents dispersed in the coil coating passes through three processes, namely, wetting, grinding, and dispersion and stability. Wetting is defined as the solvent taking the place of the air and water on the surface of paint. Solvent-based paint is not a problem as the surface tension

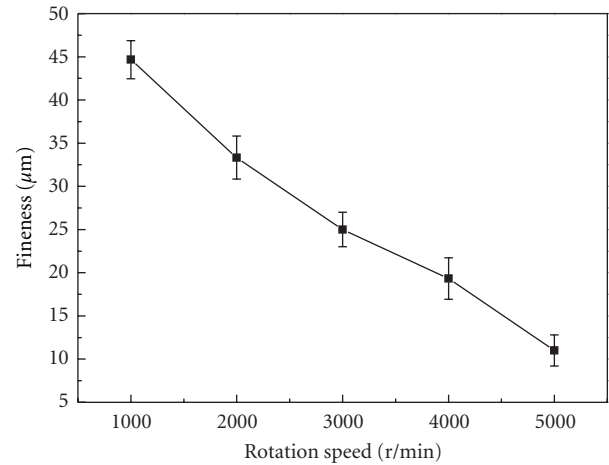


FIGURE 2: Effect of stirring speed on fineness of particles.

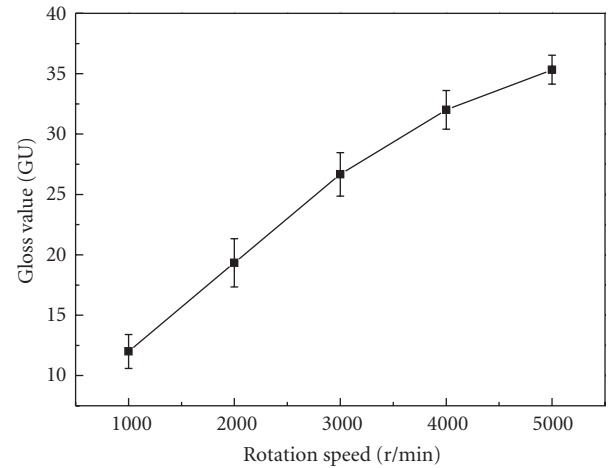


FIGURE 3: Effect of stirring speed on gloss value.

of paint is always lower than that of the general. The silver-loaded titanium dioxide is a nanopowder, but the particles of antibacterial agents would get together due to van der Waals force. Therefore, it is required to redisperse under shearing or impact forces.

When the shear rate ( $D$ ) is constant, the shear force ( $\tau$ ) and viscosity ( $\eta$ ) is proportional as

$$\tau = D\eta. \quad (3)$$

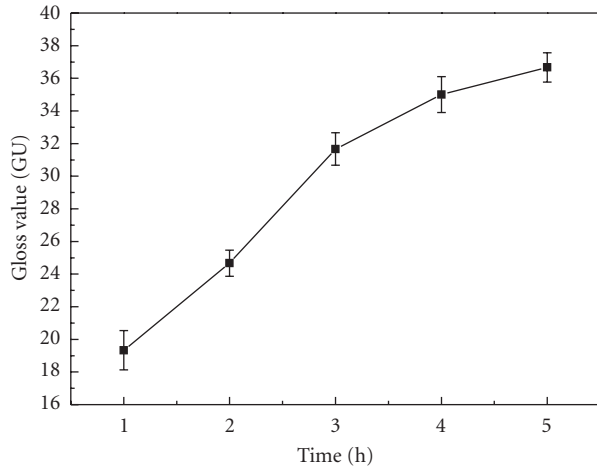


FIGURE 4: Effect of stirring time on fineness of coil coating.

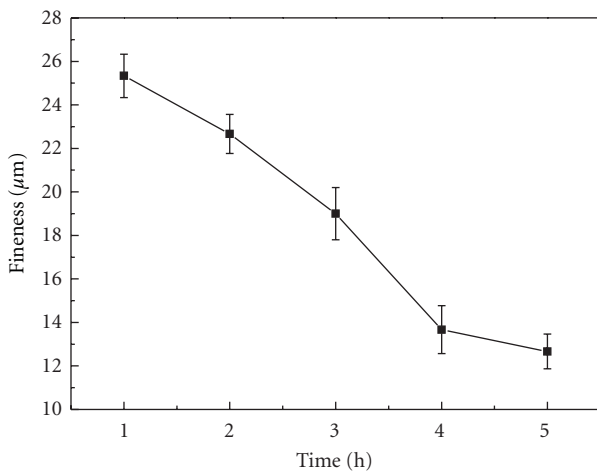


FIGURE 5: Effect of stirring time on gloss of coil coating.

The higher the speed, the greater the shearing force under certain viscosity, which is helpful for the grinding. In summary, silver-loaded titanium dioxide is added to the coil coating under the speed of 4000 r/min.

The effects of stirring time on fineness of the coil coating and gloss of the color-coated sheet were studied under 4000 r/min of rotation speed after adding silver-loaded titanium dioxide to the coil coating.

Figures 4 and 5 show the effects of stirring time on fineness and gloss of coil coating. It is evident that the fineness decreased and the gloss improved with the increase of stirring time. The fineness and the gloss were about 19 μm and 32, respectively, after stirred for 3 h. Both values reached the pigments and the grinding fineness requirements based on “the evaluation method of dispersion of pigments” mentioned above. Consequently, the final choice of grinding time is 3 h.

The surface morphology of color-coated sheet was observed by using SEM in order to detect the effect of antibacterial agent in the coil coating. SEM analysis results of precoated layer of color-coated sheets with and without Ag-loaded TiO<sub>2</sub> are shown in Figure 6. The coated particles after

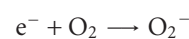
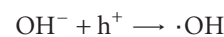
adding antibacterial agents were well distributed except a small part of the reunion, and the particle sizes were about 10 μm, which is quite similar to the ordinary color-coated sheet. The results were in accordance with the measurement results and achieved the required fineness. It was indicated that Ag-loaded TiO<sub>2</sub> almost became the part of coil coating under the function of additives. There was nearly no difference between ordinary color-coated sheet and antibacterial color-coated sheet in appearance and morphology. This was beneficial to the dispersion of antibacterial agents and the improvement of the antibacterial property.

Ag in the antibacterial agent plays an important role in antibacterial property. The most distinguished feature of the ordinary color-coated sheet and antibacterial color-coated sheet lies in the function of silver and titanium dioxide. Although the addition was little, the change of the elements in the ordinary color-coated sheet and antibacterial color-coated sheet should be observed. EDX analysis of color-coated sheet with and without antibacterial agents was undertaken to analyze the change of their elements. The results are showed in Figure 7.

It can be seen from the figures that the elements Ti and Ag in color-coated sheet adding antibacterial agents appeared as compared to those without adding antibacterial agents. However, the dosage of elements was relatively small so that the increase of elements Ti and Ag were not significant. Nonetheless, it also can be indicated that silver-loaded titanium dioxide has been incorporated into the precoated layer of antibacterial color-coated sheet.

**3.2. Photocatalysis Properties.** Figure 8 shows the methyl orange degradation ability of color-loaded sheet. The concentration of methyl orange decreased with time and came to the equilibrium finally. The speed of degradation is not fast with the degradation efficiency of 25% in the first 1 h. However, the degradation efficiency reached about 80% after 2 h. Methyl orange concentration tends to be stable with the degradation efficiency of about 88% at 4th hour. In conclusion, the color-coated sheet synthesized in the present study possesses high degradation of methyl orange. The color-coated sheet adding antibacterial agents has the capability of “self-cleaning.”

Photocatalytic degradation of methyl orange mechanism is as follows: the valence band electrons of silver-loaded titanium dioxide are excited under UV, then they jump across the forbidden band into the conductive band and form the highly reactive negative-charged electron e<sup>-</sup>, while producing a corresponding hole h<sup>+</sup> in the valence band. Then electrons and holes separate and migrate to different positions on the surface of particles and reduction and oxidation happens on the surface of materials. The main reactions are as follows:



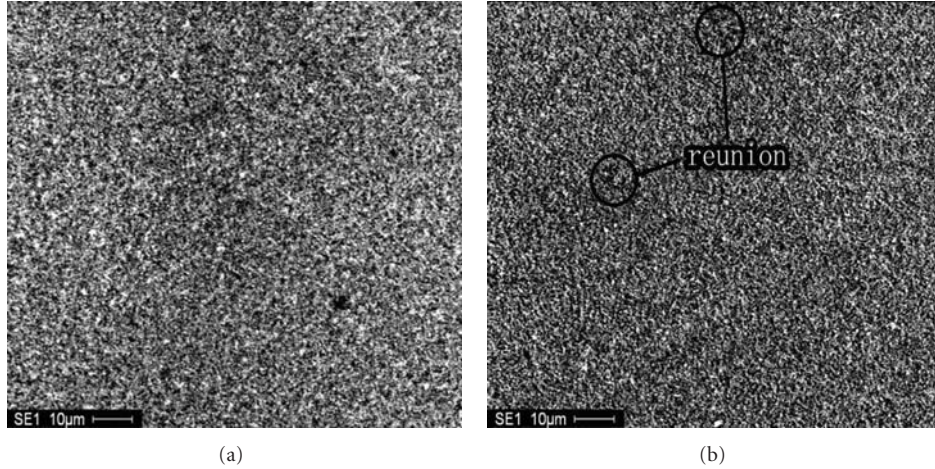


FIGURE 6: SEM of ordinary color-coated sheet (a) and antibacterial color-coated sheet (b).

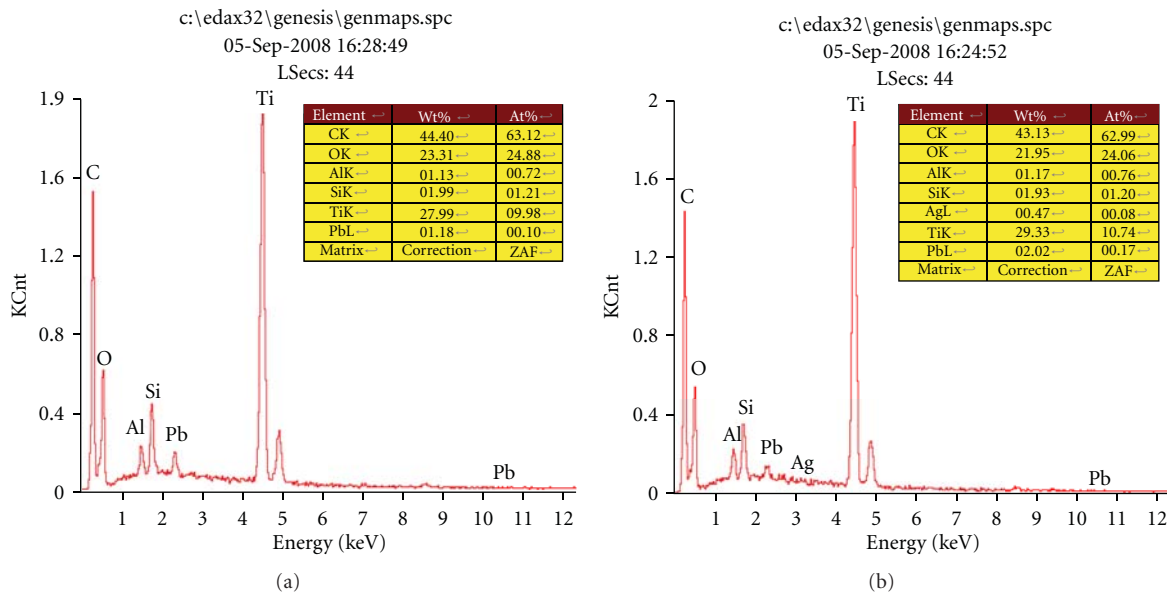
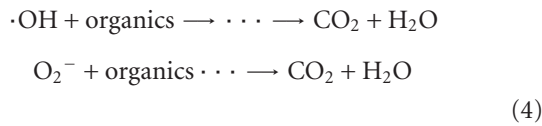


FIGURE 7: EDX of (a) ordinary color-coated sheet and (b) antibacterial color-coated sheet.



3.3. *Stability and Duration Properties.* The stability of antibacterial coil coating was evaluated using the centrifugation settling time and gravity settling time. The settling time of antibacterial agents is equal to the storage period of antibacterial agents in the coil coating under gravity. The time for appearing 10 mm supernatant is the centrifugal settling time  $t_C$ . Gravity settling time  $t_G$  can be calculated by

$$\frac{t_G}{t_C} = \frac{4\pi^2 RN^2}{g}
 \tag{5}$$

TABLE 2: Effect of stability of coil coating under non-modified and modified.

	Non-modified coil coating	Modified coil coating
Time/month	25.1	15.6

As shown in Table 2, the storage period of coil coating is about 2 years without antibacterial agents and 16 months with antibacterial coil coating. The silver-loaded titanium dioxide particles make Brownian motion in the coil coating, which could result in the decline of stability. Flocculation appears under the particles' kinetic energy over the repulsive force when particles contact to each other. Therefore, adding antibacterial agents makes the stability of the coil coating decreased.

TABLE 3: Results of pilot-scale run and practical application (average values).

	Chromatic aberration				Impact/J	MEK/ times	Gloss- iness/(°)	T-bend/T	Film thick- ness/ $\mu\text{m}$	Antibacterial Efficiency
	DL	Da	Db	DE						
Hand sample	0.09	0.06	-0.10	0.21	9	>100	33	3T	14	>99.99%
Bulk sample	0.07	0.03	-0.07	0.10	9	>100	32	2T	14	>99.99%
First batch of commercial product	-0.23	-0.18	0.01	0.28	9	>100	34	3T	14	>99.99%
Second batch of commercial product	-0.09	-0.11	0.06	0.16	9	>100	33	3T	14	>99.99%

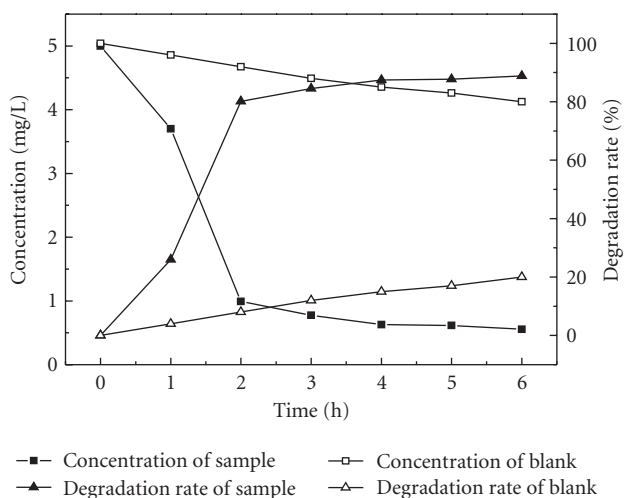


FIGURE 8: Photocatalytic degradation ratio of antibacterial color-coated sheet.

Duration property was characterized by the release of  $\text{Ag}^+$  in the antibacterial color-coated sheet and the antibacterial efficiency after water immersion. The release and antibacterial properties of  $\text{Ag}^+$  in the antibacterial color-coated sheet kept at  $3 \mu\text{g/L}$  and did not change significantly in 15 days. The antibacterial properties of the antibacterial color sheet achieved 99.99%, and  $\text{Ag}^+$  release was not detected when the sheet was immersed in water. Thus, the duration property of antibacterial color-coated sheet is perfect.

**3.4. Pilo-Scalet Run and Practical Application.** The physical properties of antibacterial color-coated sheets conducted "Test methods for prepainted GB/T 13448-2006" and the antibacterial property was finished by "Guangdong Detection Center of Microbiology." Random sampling test was carried out on hand sample, bulk sample, and commercial products. The results in Table 3 indicate that the values of terminal products could meet the first class standard according to "Specification for prepainted steel sheet GB/T 12754-2006."

## 4. Conclusions

A simple way to manufacture antibacterial color-coated sheet using Ag-loaded  $\text{TiO}_2$  is developed. The optimal technical parameters are 2% of silver-loaded titanium dioxide, 4000 r/min of stirring speed, 3 h for stirring time. The silver-loaded titanium dioxide is dispersed well in color-coated sheet and the antibacterial efficiency reaches 99.99%. The efficiency of methyl orange degradation reaches 88% in 4 h. The duration of antibacterial color-coated sheet is long enough. The products of antibacterial color-coated sheet meet the first class standard of prepainted steel sheet and have excellent properties of antibiosis, photocatalysis, and duration.

## Acknowledgments

This study was supported by the National High Technology Research and Development Program of China (2010AA065205), National Science Foundation for Distinguished Young Scholars (50925417), and the Key Project of Science and Technology of Hunan Province (2009FJ1008). All authors would like to give their thanks for the financial support mentioned above.

## References

- [1] A. Mills and S. le Hunte, "An overview of semiconductor photocatalysis," *Journal of Photochemistry and Photobiology A*, vol. 108, no. 1, pp. 1–35, 1997.
- [2] T. Matsunaga, R. Tomoda, T. Nakajima, and H. Wake, "Photoelectrochemical sterilization of microbial cells by semiconductor powders," *FEMS Microbiology Letters*, vol. 29, no. 1-2, pp. 211–214, 1985.
- [3] U. Desselberger, "Emerging and re-emerging infectious diseases," *Journal of Infection*, vol. 40, no. 1, pp. 3–15, 2000.
- [4] M. Korraris, C. C. Trapalis, S. Kossionides et al., "RBS and HIRBS studies of nanostructured  $\text{AgSiO}_2$  sol-gel thin coatings," *Nuclear Instruments and Methods in Physics Research B*, vol. 188, no. 1–4, pp. 67–72, 2002.
- [5] M. Catauro, M. G. Raucci, F. de Gaetano, and A. Marotta, "Antibacterial and bioactive silver-containing  $\text{Na}_2\text{O}\cdot\text{CaO}\cdot 2\text{SiO}_2$  glass prepared by sol-gel method," *Journal of Materials Science*, vol. 15, no. 7, pp. 831–837, 2004.

- [6] G. Fu, P. S. Vary, and C. T. Lin, "Anatase TiO<sub>2</sub> nanocomposites for antimicrobial coatings," *Journal of Physical Chemistry B*, vol. 109, no. 18, pp. 8889–8898, 2005.
- [7] M. Kawashita, S. Tsuneyama, F. Miyaji, T. Kokubo, H. Kozuka, and K. Yamamoto, "Antibacterial silver-containing silica glass prepared by sol-gel method," *Biomaterials*, vol. 21, no. 4, pp. 393–398, 2000.
- [8] A. A. Ahmed, A. A. Ali, D. A. R. Mahmoud, and A. M. El-Fiqi, "Study on the preparation and properties of silver-doped phosphate antibacterial glasses," *Solid State Sciences*, vol. 13, no. 5, pp. 981–992, 2011.
- [9] A. Mukhopadhyay, S. Basak, J. K. Das, S. K. Medda, K. Chattopadhyay, and G. De, "Ag–TiO<sub>2</sub> Nanoparticle codoped SiO<sub>2</sub> films on ZrO<sub>2</sub> barrier-coated glass substrates with antibacterial activity in ambient condition," *Applied Materials & Interfaces*, vol. 9, no. 2, pp. 2540–2546, 2010.
- [10] S. M. Lee, B. S. Lee, T. G. Byun, and K. C. Song, "Preparation and antibacterial activity of silver-doped organic-inorganic hybrid coatings on glass substrates," *Colloids and Surfaces A*, vol. 355, no. 1–3, pp. 167–171, 2010.
- [11] R. Dastjerdi, M. Montazer, and S. Shahsavan, "A novel technique for producing durable multifunctional textiles using nanocomposite coating," *Colloids and Surfaces B*, vol. 81, no. 1, pp. 32–41, 2010.
- [12] R. Dastjerdi and M. Montazer, "A review on the application of inorganic nano-structured materials in the modification of textiles: focus on anti-microbial properties," *Colloids and Surfaces B*, vol. 79, no. 1, pp. 5–18, 2010.
- [13] M. Montazer, E. Pakdel, and A. Behzadnia, "Novel feature of nano-titanium dioxide on textiles: antifelting and antibacterial wool," *Journal of Applied Polymer Science*, vol. 121, no. 6, pp. 3407–3413, 2011.
- [14] J. Payne, "Responding to the consumers' desire for improved hygiene with antibacterial plastics," *Polymers and Polymer Composites*, vol. 12, no. 2, pp. 135–142, 2004.
- [15] M. Marini, S. De Niederhausern, R. Iseppi et al., "Antibacterial activity of plastics coated with silver-doped organic-inorganic hybrid coatings prepared by sol-gel processes," *Biomacromolecules*, vol. 8, no. 4, pp. 1246–1254, 2007.
- [16] H. Z. Zhang, Z. C. He, G. H. Liu, and Y. Z. Qia, "Properties of different chitosan/low-density polyethylene antibacterial plastics," *Journal of Applied Polymer Science*, vol. 113, no. 3, pp. 2018–2021, 2009.
- [17] L. Li-Hsiang, C. Shih-Chung, W. Ching-Zong, H. Jing-Ming, and O. Keng-Lia, "Microstructure and antibacterial properties of microwave plasma nitrided layers on biomedical stainless steels," *Applied Surface Science*, vol. 257, no. 17, pp. 7375–7380, 2011.
- [18] N. F. Atta, A. M. Fekry, and H. M. Hassaneen, "Corrosion inhibition, hydrogen evolution and antibacterial properties of newly synthesized organic inhibitors on 316L stainless steel alloy in acid medium," *International Journal of Hydrogen Energy*, vol. 36, no. 11, pp. 6462–6471, 2011.
- [19] W. Hefeng, T. Bin, L. Xiuyan, and M. Yong, "Antibacterial properties and corrosion resistance of nitrogen-doped TiO<sub>2</sub> coatings on stainless steel," *Journal of Materials Science & Technology*, vol. 27, no. 4, pp. 309–316, 2011.
- [20] L. Ren, L. Nan, and K. Yang, "Study of copper precipitation behavior in a Cu-bearing austenitic antibacterial stainless steel," *Materials and Design*, vol. 32, no. 4, pp. 2374–2379, 2010.
- [21] K. Page, M. Wilson, and I. P. Parkin, "Antimicrobial surfaces and their potential in reducing the role of the inanimate environment in the incidence of hospital-acquired infections," *Journal of Materials Chemistry*, vol. 19, no. 23, pp. 3819–3831, 2009.
- [22] Q. Li, R. C. Xie, Y. W. Li, E. A. Mintz, and J. K. Shang, "Enhanced visible-light-induced photocatalytic disinfection of *E. coli* by carbon-sensitized nitrogen-doped titanium oxide," *Environmental Science and Technology*, vol. 41, no. 14, pp. 5050–5056, 2007.
- [23] F. N. Chen, X. D. Yang, F. F. Xu, Q. Wu, and Y. P. Zhang, "Correlation of photocatalytic bactericidal effect and organic matter degradation of TiO<sub>2</sub> Part I: observation of phenomena," *Environmental Science and Technology*, vol. 43, no. 4, pp. 1180–1184, 2009.
- [24] S. Silver and L. T. Phung, "Bacterial heavy metal resistance: new surprises," *Annual Review of Microbiology*, vol. 50, pp. 753–789, 1996.
- [25] V. Sambhy, M. M. MacBride, B. R. Peterson, and A. Sen, "Silver bromide nanoparticle/polymer composites: dual action tunable antimicrobial materials," *Journal of the American Chemical Society*, vol. 128, no. 30, pp. 9798–9808, 2006.
- [26] H. Y. Lee, H. K. Park, Y. M. Lee, K. Kim, and S. B. Park, "A practical procedure for producing silver nanocoated fabric and its antibacterial evaluation for biomedical applications," *Chemical Communications*, vol. 2007, pp. 2959–2961, 2007.
- [27] M. Es-Souni, H. Fischer-Brandies, and M. Es-Souni, "Versatile nanocomposite coatings with tunable cell adhesion and bactericidal activity," *Advanced Functional Materials*, vol. 18, no. 20, pp. 3179–3188, 2008.
- [28] D. W. Sheel, L. A. Brook, I. B. Ditta et al., "Biocidal silver and silver/titania composite films grown by chemical vapour deposition," *International Journal of Photoenergy*, vol. 2008, Article ID 168185, pp. 1–11, 2008.
- [29] L. Mai, D. Wang, S. Zhang, Y. Xie, C. Huang, and Z. Zhang, "Synthesis and bactericidal ability of Ag/TiO<sub>2</sub> composite films deposited on titanium plate," *Applied Surface Science*, vol. 257, no. 3, pp. 974–978, 2010.
- [30] M. J. Santillán, N. E. Quaranta, and A. R. Boccaccini, "Titania and titania-silver nanocomposite coatings grown by electrophoretic deposition from aqueous suspensions," *Surface and Coatings Technology*, vol. 205, no. 7, pp. 2562–2571, 2010.
- [31] L. Y. Chai, Y. F. Yu, G. Zhang, B. Peng, and S. W. Wei, "Effect of surfactants on preparation of nanometer TiO<sub>2</sub> by pyrohydrolysis," *Transactions of Nonferrous Metals Society of China*, vol. 17, no. 1, pp. 176–180, 2007.
- [32] S. W. WEI, B. PENG, L. Y. CHAI, Y. C. LIU, and Z. Y. LI, "Preparation of doping titania antibacterial powder by ultrasonic spray pyrolysis," *Transactions of Nonferrous Metals Society of China*, vol. 18, no. 5, pp. 1145–1150, 2008.
- [33] L. Y. CHAI, S. W. WEI, B. PENG, and Z. Y. LI, "Adsorption of Ag(I) on H<sub>2</sub>TiO<sub>3</sub> from aqueous solutions," *Transactions of Nonferrous Metals Society of China*, vol. 17, no. 4, pp. 832–835, 2007.
- [34] L. Y. Chai, W. F. Su, B. Peng et al., "Modification of nano-TiO<sub>2</sub> by Al<sub>2</sub>O<sub>3</sub> in-situ coating," *Journal of Central South University of Technology*, vol. 13, no. 1, pp. 17–21, 2006.
- [35] L. Y. Chai, S. W. Wei, B. Peng, and Z. Y. Li, "Effect of thermal treating temperature on characteristics of silver-doped titania," *Transactions of Nonferrous Metals Society of China*, vol. 18, no. 4, pp. 980–985, 2008.

## Research Article

# Preparation and Photocatalytic Activity of TiO<sub>2</sub>-Deposited Fabrics

Yang Xu, Wenzheng Xu, Fenglin Huang, and Qufu Wei

Key Laboratory of Eco-textiles of Ministry of Education, Jiangnan University, Wuxi 214122, China

Correspondence should be addressed to Qufu Wei, qufu.wei@163.com

Received 6 September 2011; Revised 13 December 2011; Accepted 14 January 2012

Academic Editor: Gongxuan Lu

Copyright © 2012 Yang Xu et al. This is an open access article distributed under the Creative Commons Attribution License, which permits unrestricted use, distribution, and reproduction in any medium, provided the original work is properly cited.

Nanoscale titanium dioxide (TiO<sub>2</sub>) photocatalytic films were deposited on the surface of polyester nonwovens by using direct current reactive magnetron sputtering. The effects of coating thickness on the surface structures and properties of TiO<sub>2</sub>-coated fabrics were investigated by X-ray photoelectron spectroscopy (XPS), atomic force microscope (AFM), and scanning electron microscope (SEM). The photocatalytic activity of the functional nonwoven fabrics was evaluated by the degradation of methylene blue. The test results proved that the grain sizes of the sputtered clusters increased and the coating layer became more compact with the increase of film thickness, but the composition of the sputtered films did not have any significant change. At the same time, the photocatalytic activity of TiO<sub>2</sub>-coated fabrics mostly depended on the film thickness which could lead to the optimum thickness for a particular application.

## 1. Introduction

Polyester (PET) nonwoven materials are increasingly used in many industries ranging from wipes to filters due to their unique fibrous structures and relatively low cost [1]. Because of these increasing applications, it is desirable to produce such nonwoven materials with specially designed surface properties, such as surface abrasion, surface adsorption, and surface biocompatibility [2]. However, the surfaces of PET fibers are often not ideal for a particular application. The inert nature of PET fibers has hindered the expanding applications of PET nonwovens.

Nanoscale titanium dioxide (TiO<sub>2</sub>), with excellent properties of photocatalysis [3], has been developed and employed to modify the surface of common nonwovens by various deposition techniques such as chemical vapor deposition, sol-gel deposition, and magnetron sputtering [4–6]. The sol-gel method is one of the most widely used techniques because of its simple process. This kind of method, however, does not adapt to preparing uniform and compact functional films in a large area. The weak adhesive force between the fabric and the function films also cannot satisfy the need for lengthy and repeated usage [7]. In addition, the chemical pollution caused by a wet

process is another serious disadvantage. The magnetron sputtering technique, an environmentally friendly process, has emerged as one of the most promising techniques. It permits large-scale deposition of high-quality films at high deposition rates, and metal target can be used for fabrication of large-scale uniform coatings with a high or low density at a relatively low deposition temperature [8]. It is especially important for thermal sensitive substrates such as PET materials, which cannot endure high temperatures.

It was reported that the structure and properties of TiO<sub>2</sub> films prepared by magnetron sputtering can be modified and controlled by process parameters such as coating thickness, sputtering gas Ar:O<sub>2</sub> ratio, sputtering power, and sputtering pressure [9]. Therefore, the analysis of the coating microstructure with different thickness and its influence on the photocatalytic activity of the TiO<sub>2</sub>-coated fabrics is an interesting subject to study.

In this study, nanoscale TiO<sub>2</sub> films were deposited on the surface of PET nonwovens by using direct current (DC) reactive magnetron sputtering at room temperature. In order to correlate the effect of the thickness on the coating structure and photocatalytic properties, three samples with different thicknesses (20, 60, and 100 nm) were produced. X-ray photoelectron spectroscopy (XPS), atomic

force microscopy (AFM), scanning electron microscope (SEM), and photocatalytic tests were employed to study surface chemical composition, morphology, microstructure, and photocatalytic activity of the materials, respectively.

## 2. Experimental

**2.1. Materials Preparation.** Commercial spunbonded polyester nonwovens ( $100 \text{ g/m}^2$ ) were used as the substrate in this study. It was first washed with ethanol and distilled water before sputter coatings and then dried in an oven at  $40^\circ\text{C}$  for 24 h. The dried samples were further cut into a size of  $6 \times 6 \text{ cm}$  for sputtering.

**2.2. Sputter Coating.** Sputtering coatings of  $\text{TiO}_2$  were performed onto the flexible nonwovens in a magnetron sputter coating system (Shenyang Juzhi Co., Ltd.). A high-purity titanium (Ti) target (diameter: 50 mm; purity: 99.99%) was mounted on the cathode. The target was placed below the substrate holder at a distance of 60 mm. During sputtering, the substrate holder was kept rotating at a speed of 100 rpm to ensure the uniform deposition on the surface of the nonwoven substrate. The sputter chamber was first pumped to a base pressure of  $1.5 \times 10^{-3} \text{ Pa}$  before introducing bombardment gas (argon gas 99.999%) and reacting gas (oxygen gas 99.999%). Based on the previous investigation [10], argon and oxygen gas-flow rates were set at 80 and 12 mL/min, respectively. Coating was performed at pressure of 0.5 Pa with a power of 50 W. The thickness of the deposited layer was examined by a quartal crystal detector FTM-V (Shanghai, China) during the sputtering process.

**2.3. XPS Analysis.** X-ray photoelectron spectroscopy (XPS), a type of Thermo ESCALAB 250 equipment (USA), was used to analyze the elemental composition of the functional fabrics. Measurements were run at a base pressure of  $10^{-6} \text{ Pa}$  using an Al  $K\alpha$  ( $h\nu = 1486.6 \text{ eV}$ ) source and the source was operated at a power of 225 W. All XPS spectra were calibrated with the C 1s peak at 284.6 eV. The spectra were recorded in CAE mode (constant analyzer energy) with analyzer pass energies of 20 eV.

**2.4. Surface Morphology by AFM.** Morphology and distribution of nanoscale  $\text{TiO}_2$  on the fibre surfaces were examined using Benyuan CSPM3300 Atomic Force Microscope (Guangzhou, China). Scanning was carried out in contact mode AFM with a silicon cantilever. All images were obtained at ambient conditions and analyzed by the Imager 4.40 Software equipped with CSPM3300 AFM.

**2.5. SEM Analysis.** A SEM instrument (S-4800, HITACHI, Japan) operated at 5 kV was used to observe the cross-section structure and analyze the growth model of  $\text{TiO}_2$  films. Samples were coated with platinum in order to prevent charge buildup during SEM observations.

**2.6. Photocatalytic Activity.** The photocatalytic activity of the prepared  $\text{TiO}_2$ -coated nonwovens was tested by using

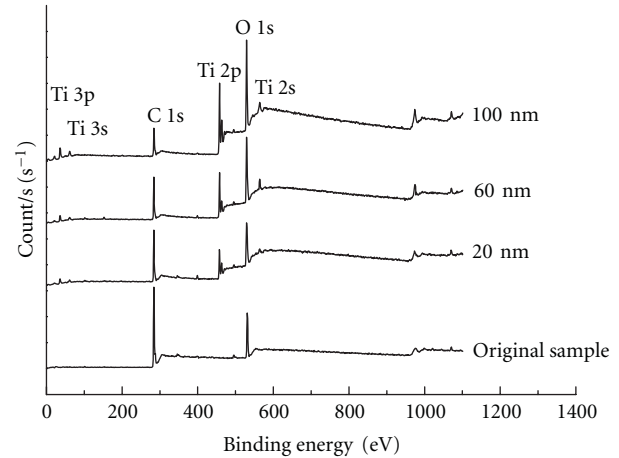


FIGURE 1: XPS survey spectra of samples.

decomposition of methylene blue (MB,  $\text{C}_{16}\text{H}_{18}\text{N}_3\text{S}-\text{Cl}-3\text{H}_2\text{O}$ ) under UV irradiation of ZXC II ultraviolet lamp (245 nm, 30 W, Shanghai, China) [11, 12]. This was done in a lightproof container in order to avoid possible complicating effects of illumination. Test samples with a certain area were dipped into an aqueous MB solution with a concentration of 5 mg/L and pH 6.5. The absorbance of the solution was measured every 30 min by 721 spectrophotometer (Shanghai, China) at a wavelength of 665 nm [13].

The decolorizing ratio  $A_t$  was calculated using the following equation [14]:

$$A_t = \frac{(C_{0t} - C_t)}{C_{0t}} \times 100\%, \quad (1)$$

where  $C_{0t}$  and  $C_t$  represent the absorbency of the MB solution for the uncoated and  $\text{TiO}_2$ -coated samples in  $t$  minutes, respectively. The experiments were repeated for three times; herein, the average values were reported.

## 3. Results and Discussion

**3.1. XPS Analyses.** XPS analysis provides information about film composition and chemical state.

Figure 1 shows the XPS survey spectra of uncoated and coated  $\text{TiO}_2$  PET nonwovens. Photoelectron peaks for C and O are shown in uncoated samples. Presence of peaks, binding energy of C 1s (285.0 eV) and O 1s (531.0 eV), have been related to organic surface of polyester [15]. Ti photoelectron peaks were observed in XPS survey spectra of coated samples, whereas there was no Ti photoelectron peak in uncoated samples. Peak intensity of Ti and O is obviously increased and C is significantly reduced with the increase in coating thickness. Moreover, peak-binding energies for Ti 2p<sub>3/2</sub> and Ti 2p<sub>1/2</sub> peaks of 20 nm, 60 nm, and 100 nm coated films are all about 458.2 eV and 464.0 eV, assigned to  $\text{Ti}^{4+}$  in  $\text{TiO}_2$  with a peak separation of 5.8 eV [16]. It indicates that the increase in coating thickness seems not to have any significant influence on the composition of the sputtered  $\text{TiO}_2$  on the PET nonwoven fabric surface.

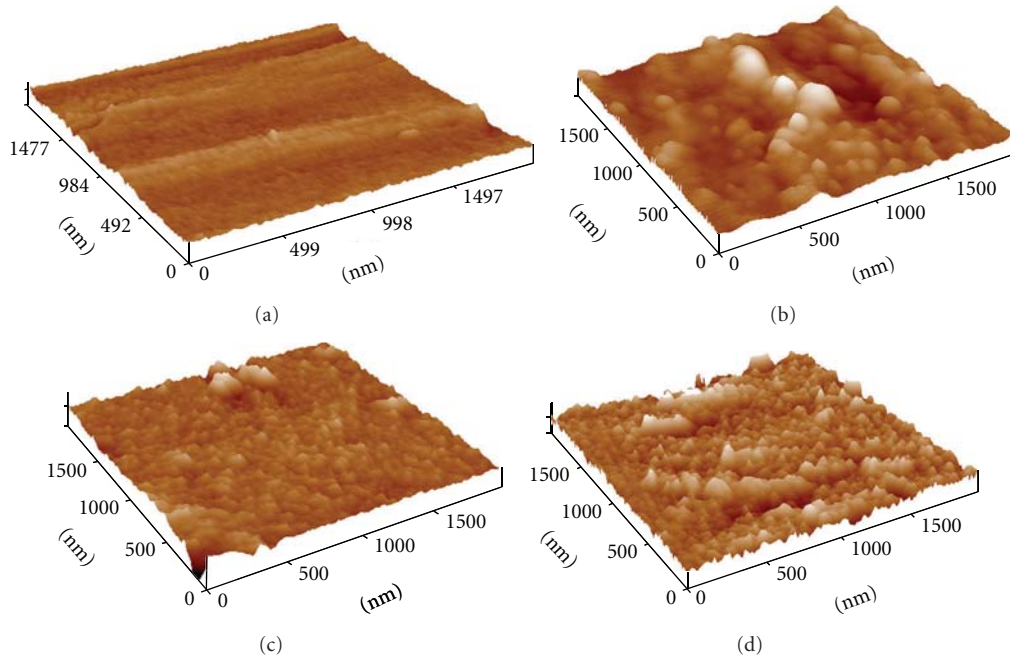


FIGURE 2: AFM images of uncoated and coated PET fiber surface at the scan size of  $2000 \times 2000$  nm (a) uncoated, (b) 20 nm, (c) 60 nm, and (d) 100 nm.

**3.2. Comparison in Surface Morphology.** AFM images reveal the change in the surface microstructure of the polyester fibers after the  $\text{TiO}_2$  coating, as shown in Figure 2.

It is clearly shown that uncoated PET fiber has a relatively smooth surface with some microdefects such as microcracks and point defects on its surface (Figure 2(a)). They might have been formed during the manufacturing process. The sputter coatings of  $\text{TiO}_2$  significantly altered the surface characteristics of the PET fibers (Figures 2(b)–2(d)).  $\text{TiO}_2$  clusters scattered on the PET fiber surface after 20 nm coating, but the clusters have variable sizes from less than 20 nm to over 50 nm (Figure 2(b)). Intrinsic defects on PET surface may be responsible for the rough and loose structure of coating surface, because sputtering particles are preferential nucleation and growth at the defect location of substrate surface in the initial film growth stage [17]. As the coating thickness is increased to 60 nm,  $\text{TiO}_2$  clusters coated on the PET fiber surface have coalesced and looked more even. Average size of the sputtered  $\text{TiO}_2$  cluster is about 31.5 nm and compact coating is formed (Figure 2(c)). AFM image in Figure 2(d) indicates that the increased coating thickness from 60 nm to 100 nm leads to more compact distribution of the  $\text{TiO}_2$  clusters on the fiber surface. The growth of the  $\text{TiO}_2$  clusters is also observed and the size of the sputtered  $\text{TiO}_2$  cluster is increased to 35.1 nm. This is attributed to the collision of the sputtered  $\text{TiO}_2$  grains. The increase in sputter coating thickness leads to the growth of the  $\text{TiO}_2$  clusters and more compact deposition.

**3.3. Microstructure of Film Cross-Section.**  $\text{TiO}_2$ -coated PET nonwoven with 100 nm thickness was broken for the SEM imaging. Broken section image of  $\text{TiO}_2$  films provided

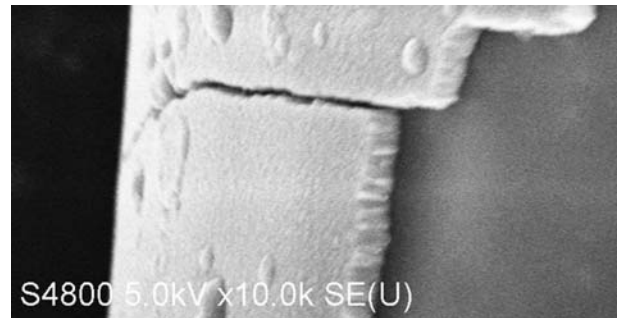


FIGURE 3: Section image of 100 nm thick film.

a more detailed picture of the microstructure and their evolution from the interface to the outer surface, as shown in Figure 3. It clearly reveals that  $\text{TiO}_2$  layers exhibit a columnar microstructure with the columns extending throughout the film thickness. This also implies that the growth of  $\text{TiO}_2$  on PET fiber surface belongs to the island growth mode (Volmer-Weber mode) including nucleation, island growth, impingement and coalescence of islands, and development of a continuous structure as well as film growth [18]. This microstructure might originate from the low adatom mobility of the sputtered particles on the low-temperature substrate surface [19].

**3.4. Photocatalytic Activity.** The photocatalytic activity of  $\text{TiO}_2$ -coated fabrics was evaluated by photocatalytic decomposition of MB in its aqueous solution. Figure 4 shows the absorbency of MB aqueous solutions tested with original and  $\text{TiO}_2$ -coated fabrics under different film thickness. The

TABLE 1: Decolorizing ratios of MB aqueous solutions tested with uncoated and TiO<sub>2</sub>-coated fabrics.

Film thickness	Original sample	20 nm	60 nm	100 nm
Absorbance $C_{240}$	0.340	0.220	0.135	0.130
Decolorizing ratio $A_{240}$ (%)	—	35.29	60.29	61.76

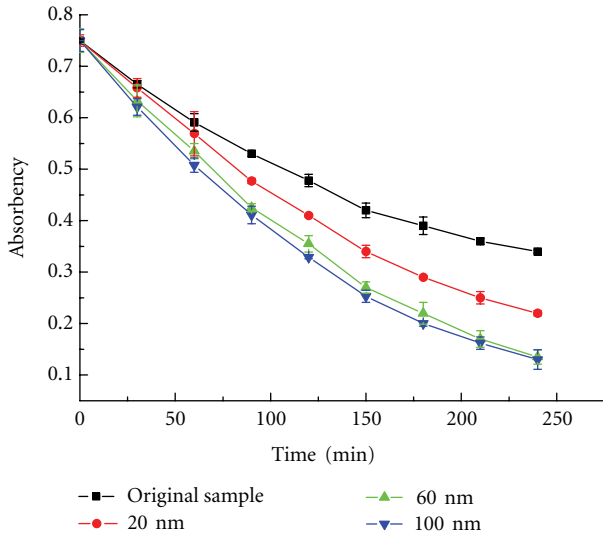


FIGURE 4: Effects of film thickness on the absorbency curve of methylene blue solution.

average results of three absorbency measurements were reproducible with standard deviation typically less than  $\pm 3.0\%$ . The decolorizing ratios calculated from (1) are shown in Table 1.

In photocatalytic tests, it was found that when fabric samples with a certain area were, respectively, immersed into the same quantitative MB aqueous solution, samples would turn into blue due to its adsorption of MB molecules. And with concentration decreasing, the color of MB solution faded and absorbency decreased. The absorbency of MB aqueous solution with the original fabric would tend to stabilize after a period of time because of the surface adsorption/desorption equilibrium [20], but there is a slightly downward trend shown in Figure 4. It may be due to the chemical decomposition of MB induced by UV radiant energy [21]. Under the same test conditions, significant decrease in the absorbency is observed for the 20 nm coated fabric compared to the uncoated fabric. This indicated that the TiO<sub>2</sub> film deposited on the nonwoven surface exhibits decomposition ability of methylene blue. The decolorization ratio  $A_{240\text{min}}$  was 35.29% shown in Table 1. When the coating thickness increased to 60 nm,  $A_{240\text{min}}$  increased to 60.29%, indicating excellent photocatalytic properties. It then increased slowly to 61.76% when the coating thickness is increased to 100 nm. The change of decolorization ratio with different film thicknesses can contribute to the evolution of the film morphology. Photocatalytic processes

are chemical reactions on the surface. Thus, the photocatalytic activity of final TiO<sub>2</sub> film depends strongly on their structures, surface morphology, and total surface area. The increase of surface area should improve the efficiency of the process because it implicates larger contact surfaces exposed to the pollutants [22]. TiO<sub>2</sub> films of 60 nm thickness are more uninterrupted, even than 20 nm films, more even surface structure and smaller particle size contribute to the increase in surface area of the deposited films. This was proved by AFM scans and photocatalytic activity of coated fabrics. When film thickness is increased to 100 nm, the surface roughness and compactness are enhanced, but the surface morphology and particle size only change little, resulting in slight increase in surface area and photocatalytic activity.

Another factor that should have been noted is the thickness of the film. It has effect on both the transmission of UV light in the film and the transportation distance that the electrons and holes produced under UV irradiation need to travel to reach the surface of the film [23]. When the film thickness is relatively thin, the number of photoexcited electron-hole pair grows with the increase of film thickness and photocatalytic activity improved. However, when the film keeps growing thicker, the number of photoexcited electron-hole pair that could move to the photocatalyst surface and participate in the desired photocatalysis reaction remains stable. So, when the film thickness grows to a certain range, the degradation rate would not change evidently with the increase of the film thickness.

#### 4. Conclusions

This study has compared the effect of film thickness on grain growth and microstructure and chemical composition as well as photocatalytic activity of TiO<sub>2</sub> coatings deposited by DC magnetron sputtering at room temperature. The sputter coatings formed nanoscale clusters scattered or covered on the fiber surface subject to the film thickness. Film thickness affected the grain size of the TiO<sub>2</sub> clusters. With increase in film thickness, grain size of the sputtered clusters increased and coating layer became more compact, but the composition of the sputtered films did not have any significant change. The photocatalytic test results proved that film thickness plays an important role in the photocatalytic activity of the TiO<sub>2</sub>-coated fabric. It is believed that there existed a critical thickness related to the photocatalytic activity of TiO<sub>2</sub> thin films. When the film thickness is below the critical thickness, the photocatalytic activity of TiO<sub>2</sub> thin films increases with the thickness increasing. But once the film thickness exceeds the critical thickness, the film thickness has little influence on the photocatalytic activity of the TiO<sub>2</sub> thin films.

## Acknowledgments

This paper was supported by the scientific and technological guidance Project of China National Textile and Apparel Council (CNTAC) (no. 2011014) and the Open Project Program of Key Laboratory of Eco-textiles at Jiangnan University (KLET1013).

## References

- [1] K. Sutherland, "Western European market for woven and nonwoven media," *Filtration and Separation*, vol. 38, no. 9, pp. 26–27, 2001.
- [2] R. Dastjerdi and M. Montazer, "A review on the application of inorganic nano-structured materials in the modification of textiles: focus on anti-microbial properties," *Colloids and Surfaces B*, vol. 79, no. 1, pp. 5–18, 2010.
- [3] F. Akira, T. N. Rao, and D. A. Tryk, "Titanium dioxide photocatalysis," *Journal of Photochemistry and Photobiology C*, vol. 1, no. 1, pp. 1–21, 2000.
- [4] H. Szymanowski, A. Sobczyk, M. Gazicki-Lipman, W. Jakubowski, and L. Klimek, "Plasma enhanced CVD deposition of titanium oxide for biomedical applications," *Surface and Coatings Technology*, vol. 200, no. 1–4, pp. 1036–1040, 2005.
- [5] D. Wu, M. Long, J. Zhou et al., "Synthesis and characterization of self-cleaning cotton fabrics modified by TiO<sub>2</sub> through a facile approach," *Surface and Coatings Technology*, vol. 203, no. 24, pp. 3728–3733, 2009.
- [6] X. Yang, N. Wu, Q. Wei, and L. Chu, "Surface functionalisation of polyester nonwoven fabrics by sputter coating of Titanium Dioxide," *Polymers and Polymer Composites*, vol. 17, no. 6, pp. 347–351, 2009.
- [7] S. Takeda, S. Suzuki, H. Odaka, and H. Hosono, "Photocatalytic TiO<sub>2</sub> thin film deposited onto glass by DC magnetron sputtering," *Thin Solid Films*, vol. 392, no. 2, pp. 338–344, 2001.
- [8] P. Singh and D. Kaur, "Room temperature growth of nanocrystalline anatase TiO<sub>2</sub> thin films by dc magnetron sputtering," *Physica B*, vol. 405, no. 5, pp. 1258–1266, 2010.
- [9] S. K. Zheng, T. M. Wang, G. Xiang, and C. Wang, "Photocatalytic activity of nanostructured TiO<sub>2</sub> thin films prepared by dc magnetron sputtering method," *Vacuum*, vol. 62, no. 4, pp. 361–366, 2001.
- [10] Y. Xu, N. Wu, Q. Wei, and X. Pi, "Preparation and the light transmittance of TiO<sub>2</sub> deposited fabrics," *Journal of Coatings Technology Research*, vol. 6, no. 4, pp. 549–555, 2009.
- [11] X. Yang, L. Xiong, X. Hu, B. He, and G. Chu, "Photocatalytic reaction and degradation of methylene blue on TiO<sub>2</sub> films in vacuum: an X-ray photoelectron spectroscopy study," *Research on Chemical Intermediates*, vol. 38, no. 1, pp. 67–75, 2011.
- [12] E. I. Kapinus, T. A. Khalyavka, V. V. Shimanovskaya, T. I. Viktorova, and V. V. Strelko, "Photocatalytic activity of spectro-pure titanium dioxide: effects of crystalline structure, specific surface area and sorption properties," *International Journal of Photoenergy*, vol. 5, no. 3, pp. 159–166, 2003.
- [13] J. Yao and C. Wang, "Decolorization of methylene blue with TiO<sub>2</sub> sol via UV irradiation photocatalytic degradation," *International Journal of Photoenergy*, vol. 2010, Article ID 643182, 6 pages, 2010.
- [14] C. Ogino, M. F. Dadjour, Y. Iida, and N. Shimizu, "Decolorization of methylene blue in aqueous suspensions of titanium peroxide," *Journal of Hazardous Materials*, vol. 153, no. 1–2, pp. 551–556, 2008.
- [15] H. Krump, I. Hudec, M. Jaššo, E. Dayss, and A. S. Luyt, "Physical-morphological and chemical changes leading to an increase in adhesion between plasma treated polyester fibres and a rubber matrix," *Applied Surface Science*, vol. 252, no. 12, pp. 4264–4278, 2006.
- [16] B. Liu, X. Zhao, Q. Zhao, X. He, and J. Feng, "Effect of heat treatment on the UV-vis-NIR and PL spectra of TiO<sub>2</sub> films," *Journal of Electron Spectroscopy and Related Phenomena*, vol. 148, no. 3, pp. 158–163, 2005.
- [17] Z.-W. Liu, J.-F. Gu, C.-W. Sun, and Q.-Y. Zhang, "Study on nucleation and dynamic scaling of morphological evolution of ZnO film deposition by reactive magnetron sputtering," *Wuli Xuebao/Acta Physica Sinica*, vol. 55, no. 4, pp. 1965–1973, 2006.
- [18] I. Petrov, P. B. Barna, L. Hultman, and J. E. Greene, "Microstructural evolution during film growth," *Journal of Vacuum Science and Technology A*, vol. 21, no. 5, pp. S117–S128, 2003.
- [19] S. Giancaterina, S. Ben Amor, G. Baud et al., "Photoprotective ceramic coatings on poly(ether ether ketone)," *Polymer*, vol. 43, no. 24, pp. 6397–6405, 2002.
- [20] V. Ryabchuk, "Photophysical processes related to photoadsorption and photocatalysis on wide band gap solids: a review," *International Journal of Photoenergy*, vol. 6, no. 3, pp. 95–113, 2004.
- [21] A. Mills and J. Wang, "Photobleaching of methylene blue sensitised by TiO<sub>2</sub>: an ambiguous system?" *Journal of Photochemistry and Photobiology A*, vol. 127, no. 1–3, pp. 123–134, 1999.
- [22] S. C. Jung, S. J. Kim, N. Imaishi, and Y. I. Cho, "Effect of TiO<sub>2</sub> thin film thickness and specific surface area by low-pressure metal-organic chemical vapor deposition on photocatalytic activities," *Applied Catalysis B*, vol. 55, no. 4, pp. 253–257, 2005.
- [23] Z. Yi, C. Guofeng, W. Ma, and W. Wei, "Effect of external bias voltage and coating thickness on the photocatalytic activity of thermal sprayed TiO<sub>2</sub> coating," *Progress in Organic Coatings*, vol. 61, no. 2–4, pp. 321–325, 2008.

## Research Article

# Photocatalytic Decomposition of Amoxicillin Trihydrate Antibiotic in Aqueous Solutions under UV Irradiation Using Sn/TiO<sub>2</sub> Nanoparticles

Robab Mohammadi,<sup>1</sup> Bakhshali Massoumi,<sup>2</sup> and Mohammad Rabani<sup>1</sup>

<sup>1</sup> Department of Chemistry, Islamic Azad University, North-Tehran Branch, P.O. Box 3155636951, Tehran 1477893855, Iran

<sup>2</sup> Department of Chemistry, Payame Noor University, P.O. Box 19395-3697, Tehran 196569-19395/4697, Iran

Correspondence should be addressed to Robab Mohammadi, mohammadi\_rb@yahoo.com

Received 16 December 2011; Accepted 28 December 2011

Academic Editor: Jianguo Yu

Copyright © 2012 Robab Mohammadi et al. This is an open access article distributed under the Creative Commons Attribution License, which permits unrestricted use, distribution, and reproduction in any medium, provided the original work is properly cited.

TiO<sub>2</sub> and Sn/TiO<sub>2</sub> nanoparticles were successfully synthesized by sol-gel method. The resulting nanoparticles were characterized by XRD, TEM, SEM, UV-Vis reflectance spectroscopy, and BET analysis methods. The effects of Sn-doping on the crystal structure, surface area, adsorption properties, pore size distribution, and optical absorption properties of the catalysts were investigated. The effect of different Sn content on the amount of hydroxyl radical was discussed by using salicylic acid as probe molecule. The photocatalytic activity of samples was tested by photocatalytic mineralization of amoxicillin trihydrate (AMOX) as a model pollutant. Sn/TiO<sub>2</sub> nanoparticles exhibited high photocatalytic activity during the mineralization of AMOX under UV light due to increase in the generated hydroxyl radicals, band gap energy, specific surface area, and decrease in the crystallite size. The kinetic of the mineralization of AMOX can be explained in terms of the Langmuir-Hinshelwood model. The values of the adsorption equilibrium constant ( $K_{AMOX}$ ) and the kinetic rate constant of surface reaction ( $k_c$ ) were  $0.56 \text{ (mg L}^{-1}\text{)}^{-1}$  and  $1.86 \text{ mg L}^{-1} \text{ min}^{-1}$ , respectively.

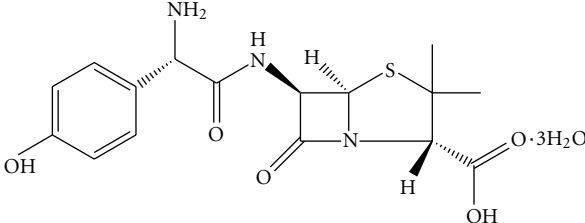
## 1. Introduction

Recently, there has been an increasing concern, particularly in highly developed countries, about penetration of pharmaceuticals into the environment and related risks [1]. A large variety of pharmaceutical compounds have been frequently found in sewage treatment plant effluents and river streams at concentrations up to several  $\mu\text{g L}^{-1}$  [2]. These compounds enter the aquatic environment after their ingestion and subsequent excretion either without modifications or in the form of nonmetabolized parent compounds [3]. Among the various pharmaceutical compounds present in the environment, special emphasis has been given to antibiotics, which are the most often discussed pharmaceuticals because of their potential role in the development of antibiotic-resistant bacteria [4]. The great concern is that waters contaminated with antibiotics can reach waters used for human consumption or municipal water treatment facilities [5]. Due to their antibacterial activity, waters containing antibiotics commonly used in animal and human health

(antibiotics included) are refractory to natural biological degradation or conventional wastewater treatments [6]. Amoxicillin is a semisynthetic  $\beta$ -lactam antibiotic (7-[2-amino-2-(4-hydroxyphenyl)-acetyl] amino-3,3-dimethyl-6-oxo-2-thia-5-azabicyclo [3.2.0] heptane-4-carboxylic acid), used in humans and food-producing animals to treat several diseases. Some authors have found amoxicillin and cloxacillin in wastewater [7].

Several alternatives to destroy these kinds of compounds have been considered in recent studies in the literature. These include reverse osmosis, adsorption on activated carbons, or advanced oxidation technologies, such as Fenton reaction, ozonation, and peroxidation combined with UV light [8]. Heterogeneous photocatalysis using a semiconductor is a new, effective, and rapid technique for the removal of pollutants from water [9]. Among various semiconducting materials, much attention has been given to TiO<sub>2</sub> due to its outstanding stability, inexpensiveness, lack of toxicity, and strong photoactivity [10]. Extensive researches have been focused on synthetic methods of semiconductor

TABLE 1: Chemical structure and characteristics of AMOX.

	Characteristics
IUPAC name	(2 <i>S</i> ,5 <i>R</i> ,6 <i>R</i> )-6-[( <i>R</i> )-(-)-2-amino-2-( <i>p</i> -hydroxyphenyl)acetamido]-3,3-dimethyl-7-oxo-4thia-1-azabicyclo[3.2.0]heptane-2-carboxylic acid trihydrate
Molecular formula	C <sub>16</sub> H <sub>19</sub> N <sub>3</sub> O <sub>5</sub> S <sub>3</sub> H <sub>2</sub> O
Molecular weight	419.45
Appearance	White or almost white powder
Melting point	152–156°C
Structure	

nanoparticles with better crystallinity and photocatalytic performance. Yu et al. [11] prepared CuO/Cu<sub>2</sub>O composite hollow microspheres with controlled diameter and composition and without the addition of templates and additives by hydrothermal synthesis using Cu(CH<sub>3</sub>COO)<sub>2</sub>·H<sub>2</sub>O as a precursor. However, there is still a problem that photocatalytic efficiency is not high because recombination of photogenerated electron-hole pairs influences low photo quantum efficiency [12]. To enhance its photoactivity, TiO<sub>2</sub> is often doped with various metal ions and oxides such as Zn, Pt, Pd, Au, Ag, Cu, WO<sub>3</sub>, and V<sub>2</sub>O<sub>5</sub> [13]. The dopants act as charge separators of photoinduced electron-hole pairs, and it is proposed that, after excitation, the electron migrates to the metal where it becomes trapped and electron-hole recombination is suppressed [14]. Castro et al. [15] presented the performance of Ag-TiO<sub>2</sub> photocatalyst, obtained using the hydrothermal synthesis route, under different light irradiations setups such as solar-simulated and interior-lighting lamps with different irradiation powers, towards the photocatalytic inactivation of *E. coli* in water. A possible way to improve the photocatalytic performance of doped TiO<sub>2</sub> is to explore the cooperative effect by introducing more than one species of foreign elements to the host [16]. Appropriate choice of the codoping pair is the key factor. Li et al. [17] investigated the structural and electronic properties of iron-fluorine (Fe-F) and iron-sulfur- (Fe-S-) codoped anatase TiO<sub>2</sub>. They reported that the photocatalytic performance under visible light of Fe-S-codoped TiO<sub>2</sub> is better than that of Fe-F-codoped one, and Fe-S should be a better codoping pair.

Photocatalytic oxidation of some antibiotics such as Lincomycin, tetracycline, oxolinic acid, and fluoroquinolone has been reported [2, 18–20]. Xekoukoulotakis et al. [4] have reported that the use of UV/TiO<sub>2</sub> was able to achieve 90% TOC reduction after 90 min of reaction with 10 mg L<sup>-1</sup> ERM and 250 mg L<sup>-1</sup> TiO<sub>2</sub>. Abellán et al. [21] have reported 82% of sulfamethoxazole degradation and 23% TOC reduction by UV/TiO<sub>2</sub> in 6 hr. No study on photocatalytic oxidation of amoxicillin·3H<sub>2</sub>O, in aqueous solution using Sn/TiO<sub>2</sub> as a catalyst under UV-C irradiation has been reported.

In this work, preparation and characterization of pure and Sn/TiO<sub>2</sub> nanoparticles is reported. These nanosized catalysts were characterized by the techniques such as XRD, SEM, TEM, DRS, and BET analysis methods. The photocatalytic activity of the prepared nanoparticles has been studied on the mineralization of AMOX, as a prototype molecule. Chemical structure and characteristics of AMOX have been given in Table 1. We investigated in a systematic way the effect of various parameters such as doping content of Sn, the amount of photocatalyst, and AMOX initial concentration on mineralization in model aqueous solutions. A detailed kinetic description of the process was given based on well-known mechanistic/kinetic models, namely, the Langmuir-Hinshelwood (L-H) model whereby the organic reagent was preadsorbed on photocatalyst surface prior to UV illumination. We intentionally decided to investigate sample mineralization rather than substrate decomposition since the rationale of micropollution abatement in aqueous matrices should involve its complete elimination rather than its transformation to other species.

## 2. Experimental

**2.1. Materials.** Titanium n-butoxide (TBOT, Ti(OC<sub>4</sub>H<sub>9</sub>)<sub>4</sub>), ethanol with absolute grade, and tin (IV) chloride were used without any further purification. All chemicals used in this study were analytical grade and purchased from Merck (Germany).

**2.2. Preparation of TiO<sub>2</sub> and Sn/TiO<sub>2</sub> Nanoparticles.** According to [22, 23], for the synthesis of TiO<sub>2</sub> nanoparticles, first titanium n-butoxide was slowly dissolved in ethanol. The prepared solution was sonicated in an ultrasonic bath. The hydrolysis process was then performed by adding of drop by drop H<sub>2</sub>O into a flask containing TBOT/EtOH mixture under reflux and magnetic stirring. The molar ratio of TBOT/EtOH/H<sub>2</sub>O was 1 : 1 : 65. The yellowish transparent sol was yielded after continuously stirring for 3 h. Finally, TiO<sub>2</sub> nanoparticles were gained by calcining the TiO<sub>2</sub> xerogel

at 450°C for 3 h and grinding. The preparation of Sn-doped TiO<sub>2</sub> nanoparticles was the same as that of TiO<sub>2</sub>, except that the water used for the synthesis contained the required amount of tin (IV) chloride.

**2.3. Analytical Methods.** Powder X-ray diffraction (XRD) was used for identification of crystalline phases and estimation of the crystallite size. The X-ray diffraction (XRD) patterns were recorded on a Siemens/D5000 X-ray diffractometer with Cu K $\alpha$  radiation ( $\lambda = 0.15478$  nm). The texture and morphology of the prepared samples were measured by scanning electron microscope (SEM) (Philips XL-30ESM). Transmission electron microscopy (TEM) observation was carried out on Zeiss EM 900–80 keV electron microscopy instrument. The sample for TEM was prepared by dispersing the final powder in ethanol, and the dispersion was then dropped on copper/carbon grid. The nitrogen adsorption and desorption isotherms at 77 K were measured using Bel-sorp mini II. The specific surface area and the pore size distribution (average pore diameter and mean pore volume) were measured from the adsorption isotherm using the Brunauer-Emmett-Teller (BET) method and from the desorption isotherm using the Barret-Joyner-Halender (BJH) method, respectively. Ultraviolet/visible diffuse reflectance spectra (DRS) were taken on Avaspec-2048 TEC spectrometer. Total organic carbon (TOC) was measured with Shimadzu 5000A TOC analyzer equipped with an autosampler (ASI-5000) and platinum-based catalyst. The carrier gas was synthetic air at the rate of 150 mL/min. The samples were acidified to pH < 4 before being sent to TOC analyzer to ensure that inorganic carbon would be released from the solution as CO<sub>2</sub>.

**2.4. Photocatalytic Activity.** Mineralization of AMOX under UV light was used as a model reaction to evaluate the photocatalytic activity of prepared samples. Photocatalytic activity measurements were carried out at atmospheric pressure in a batch quartz reactor [24]. Artificial irradiation was provided by 15 W (UV-C) mercury lamp (Philips, Holland) emitted around 254 nm positioned parallel to the reactor [25]. In each run, desired concentration of AMOX (20 mg L<sup>-1</sup>) and TiO<sub>2</sub> was fed into the quartz tube reactor and it was allowed to equilibrate for 30 min in the darkness. The zero time reading was obtained from blank solution kept in the dark. Aliquots of the mixture were taken at periodic intervals during the irradiation, centrifuged for 10 min at 1000 rpm (Hettich EBA) to remove catalyst particles, and then analyzed for their total organic carbon (TOC) content.

All the concentration profiles can be correlated to irradiation time by the following exponential function with good agreement:

$$\frac{-d\text{TOC}}{dt} = k_{\text{ap}}\text{TOC}. \quad (1)$$

Therefore, the photocatalytic mineralization of AMOX is pseudo-first-order reaction, and its kinetics may also be expressed as

$$\ln\left(\frac{\text{TOC}_0}{\text{TOC}}\right) = k_{\text{ap}}t. \quad (2)$$

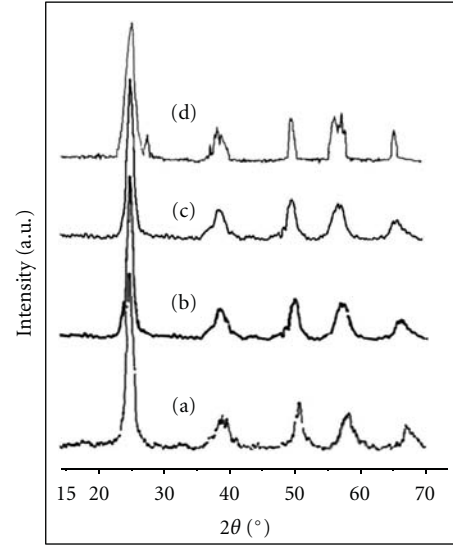


FIGURE 1: XRD patterns of (a) TiO<sub>2</sub>, (b) 1 mol% Sn/TiO<sub>2</sub>, (c) 1.5 mol% Sn/TiO<sub>2</sub>, (d) 3 mol% Sn/TiO<sub>2</sub>.

In this equation, TOC<sub>0</sub> and TOC are the antibiotic concentrations (mg L<sup>-1</sup>) at times 0 and  $t$ , respectively, and  $k_{\text{ap}}$  is the pseudo-first-order rate constant (min<sup>-1</sup>).

### 3. Results and Discussion

#### 3.1. Characterization of Nanoparticles

**3.1.1. X-Ray Diffraction.** Based on the XRD spectra, the crystalline phases could be categorized into two primary components, an anatase (A) and a rutile (R) phase, and represented the intensity of the strongest anatase reflection of (101) plane at  $2\theta = 25.3^\circ \pm 0.1^\circ$ , anatase reflection of (200) plane at  $2\theta = 48.0^\circ \pm 0.1^\circ$ , and the intensity of the strongest rutile reflection of (110) plane at  $2\theta = 27.4^\circ \pm 0.1^\circ$ . Additionally, the anatase phase of TiO<sub>2</sub> crystal is a tetragonal system in lattice geometry [26]. The average crystallite size of the particles was calculated according to following Scherrer's equation [27];

$$D = \frac{k\lambda}{\beta \cos \theta}. \quad (3)$$

In this equation,  $\lambda$  the X-ray wavelength equal to 0.154 nm,  $k$  is a constant taken as 0.89,  $\beta$  is the line width at half maximum height, and  $\theta$  is the diffracting angle. The phase content of a sample can be calculated by following equation [28]:

$$\text{Rutile phase \%} = \frac{100}{1 + 0.08(I_A/I_R)}, \quad (4)$$

where  $I_A$  and  $I_R$  are integrated intensities of the anatase and rutile peaks, respectively. Figure 1 shows the X-ray diffraction patterns of TiO<sub>2</sub> and 1.5 mol% Sn/TiO<sub>2</sub> samples. Intensity of the anatase main peak located in  $2\theta = 25.5^\circ$  indicates a high degree of crystallinity for these nanoparticles. Crystallite

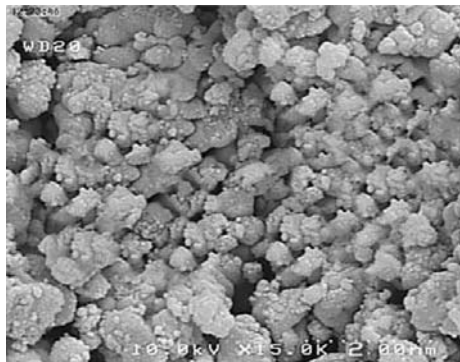


FIGURE 2: SEM image of 1.5 mol% Sn/TiO<sub>2</sub> nanoparticles.

TABLE 2: Phase content and crystallite size of prepared nanoparticles.

Sample	Phase structure	Crystalline size (nm)
TiO <sub>2</sub>	A: 100, R: –	$D_A$ : 10, $D_R$ : –
1 mol% Sn/TiO <sub>2</sub>	A: 100, R: –	$D_A$ : 9.1, $D_R$ : –
1.5 mol% Sn/TiO <sub>2</sub>	A: 100, R: –	$D_A$ : 8.4, $D_R$ : –
3 mol% Sn/TiO <sub>2</sub>	A: 89, R: 11	$D_A$ : 7, $D_R$ : 8.5

size and amount of each phase nanoparticles have been reported in Table 2. The crystallite size of titania decreases with increasing doping concentration. This reduction in crystallite size is proposed due to segregation of the dopant cations at the grain boundary which inhibits the grain growth by restricting direct contact of grains. The phase composition varies with the increasing content of Sn. According to the XRD patterns, the pure TiO<sub>2</sub> sample constituted pure anatase phase. On the other hand, the sample containing Sn shows a multiphase composition as the Sn content increases. The 3 mol% Sn sample is composed of crystallites of both anatase and rutile phase. The formation of crystallites of rutile phase at a low calcination temperature is induced by the presence of Sn, as previously reported [29]. Metal may have been finely dispersed, incorporated in the TiO<sub>2</sub> crystal structure, or crystals are too small for detection due to a relatively low metal doping [30].

**3.1.2. SEM Analysis of Sn/TiO<sub>2</sub> Nanoparticles.** The SEM image of 1.5 mol% Sn/TiO<sub>2</sub> is shown in Figure 2. Since less particle agglomeration occurred, the large surface area conveys high adsorption abilities of the catalysts. This image shows relatively uniform particles which are coherent together.

**3.1.3. TEM Analysis of Sn/TiO<sub>2</sub> Nanoparticles.** Figure 3 shows TEM images of TiO<sub>2</sub> and 1.5 mol% Sn/TiO<sub>2</sub> nanoparticles. It can be seen that the particles exhibit a relatively uniform particle size distribution. The average size of the primary particles estimated from the TEM image is about 7–10 nm, which is in good agreement with that calculated from the XRD pattern using Scherrer equation.

TABLE 3: BET data for TiO<sub>2</sub> and 1.5 mol% Sn/TiO<sub>2</sub>.

Sample	BET surface area (m <sup>2</sup> g <sup>-1</sup> )	Total pore volume (cm <sup>3</sup> g <sup>-1</sup> )	Mean pore diameter (nm)
TiO <sub>2</sub>	47.03	0.112	9.7
1.5 mol% Sn/TiO <sub>2</sub>	80.03	0.178	8.9

**3.1.4. BET Analysis.** Figure 4 shows nitrogen adsorption-desorption isotherms of TiO<sub>2</sub> and 1.5 mol% Sn/TiO<sub>2</sub> samples. Both samples show the isotherm of type IV. At high relative pressure range from 0.4 to 1, the isotherm exhibits a hysteresis loop of type H2 associated with the ink bottle pores, indicating that the powders contain mesopores due to the aggregation of crystallites [31]. The hysteresis loop in the lower relative pressure range ( $0.4 < P/P_0$ ) was related to finer intra-aggregated pores formed between intra-agglomerated primary particles, and that in the higher relative pressure range ( $0.8 < P/P_0 < 1$ ) was associated with larger interaggregated pores produced by interaggregated secondary particles [32]. The porous structure is believed to facilitate the transporting of reactant molecules and products through the interior space due to the interconnected porous networks and favor the harvesting of exciting light due to enlarged surface area and multiple scattering within the porous framework [33].

Figure 5 shows the pore size distribution of 1.5 mol% Sn/TiO<sub>2</sub> as estimated according to the BJH method from the adsorption branch. It can be seen that the diameter range of pores located from 0.97 to 10 nm and the mean diameter of pores is 8.9 nm. With doping of Sn, the average pore size decreases slightly from 9.7 to 8.9 nm (Table 1). There are two possible factors causing the decrease in average pore size. One is that the aggregation of smaller crystallites forms smaller pores. The other is that some ions of doping probably insert into the pore of pure TiO<sub>2</sub>, which also causes pore size to become smaller [34]. The specific surface area determined with the BET method is 80.03 m<sup>2</sup> g<sup>-1</sup> which is higher than 47.03 m<sup>2</sup> g<sup>-1</sup> of TiO<sub>2</sub> sample. The enhanced surface area of 1.5 mol% Sn/TiO<sub>2</sub> compared to nanosized TiO<sub>2</sub> is due to its increase in the mesopore size and mesopore volume [35]. Loganathan et al. [36] have reported that metal doping at a specific concentration can have a favorable effect on the surface area. However, at an excess doping concentration, it could result in the damage of the porous framework, thus negatively affecting the surface area.

The specific surface area, pore volume, and pore size of TiO<sub>2</sub> and 1.5 mol% Sn/TiO<sub>2</sub> nanoparticles are presented in Table 3. The increase of surface area can be useful in the efficiency of the photocatalytic activity as it implies larger contact surfaces exposed to the reagents [37]. It is accepted in heterogeneous photocatalysis process that higher surface area and pore volume can be useful in the formation of photogenerated electron and hole pairs. Hence, heterogeneous photocatalysis is influenced greatly by the surface area and pore structure [38].

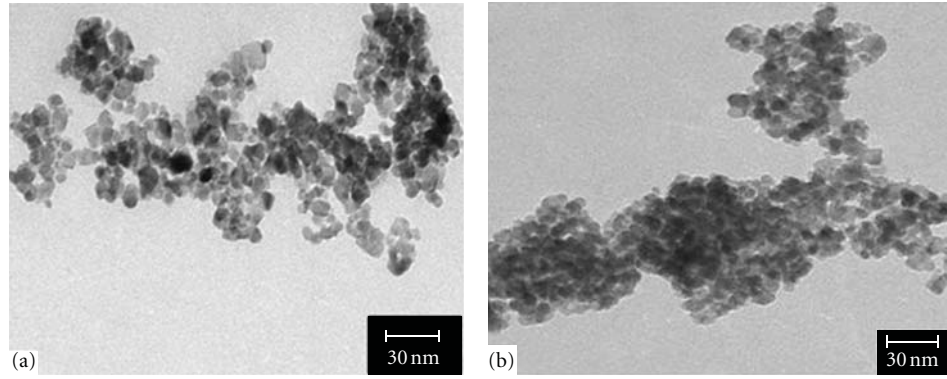


FIGURE 3: TEM images of (a) TiO<sub>2</sub>, (b) 1.5 mol% Sn/TiO<sub>2</sub> nanoparticles.

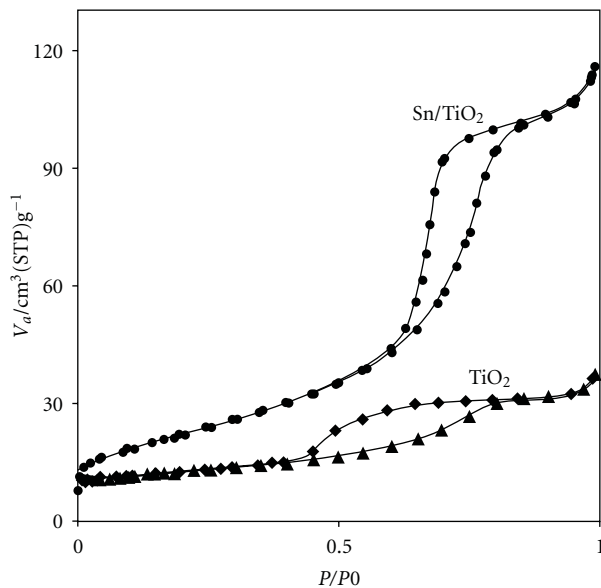


FIGURE 4: Adsorption-desorption isotherms of TiO<sub>2</sub> and 1.5 mol% Sn/TiO<sub>2</sub>.

**3.1.5. DRS Analysis.** To investigate the optical absorption properties of synthesized samples, diffuse reflectance spectra (DRS) were analyzed. Sn-doping obviously affects light absorption characteristics of TiO<sub>2</sub> as shown in Figure 6. The reflectance spectrum of TiO<sub>2</sub> nanoparticles show an absorption threshold at 400 nm, while for Sn/TiO<sub>2</sub> samples the absorption threshold is between 390 and 381 nm. The absorbance of Sn/TiO<sub>2</sub> nanoparticles is shifted toward shorter wavelength than TiO<sub>2</sub> nanoparticles. In general, blue shift of the absorption onset of Sn-doped nanoparticles is associated with the increase of the carrier concentration blocking the lowest states in the conduction band, well known as the Burstein-Moss effect [39, 40]. The theory for band-gap widening for polar semiconductors, proposed by Sernelius et al. [41], in order to describe the experimentally found blue shift in Sn/TiO<sub>2</sub> nanoparticles, considers displacement polarization effects and structural disorder as additional factors that affect the shape of the band tails.

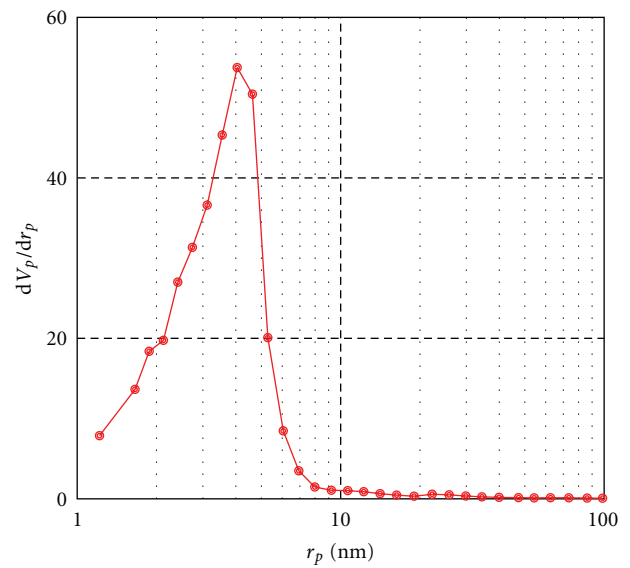


FIGURE 5: Pore diameter distribution of 1.5 mol% Sn/TiO<sub>2</sub>.

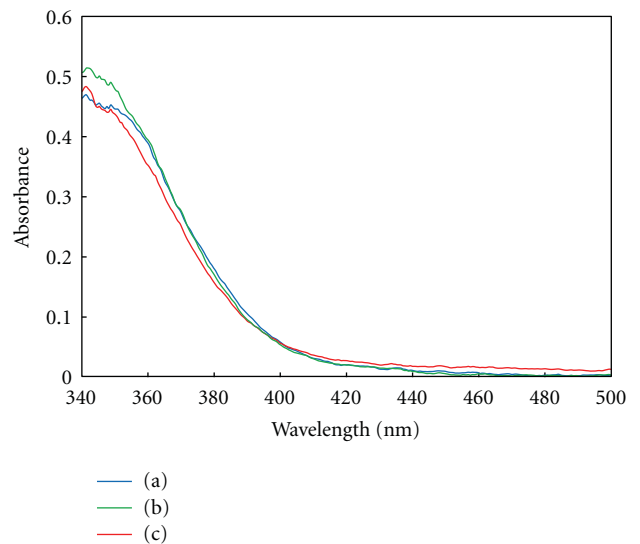


FIGURE 6: UV-Vis absorption spectra of (a) TiO<sub>2</sub>, (b) 1 mol% Sn/TiO<sub>2</sub>, (c) 1.5 mol% Sn/TiO<sub>2</sub>, (d) 3 mol% Sn/TiO<sub>2</sub>.

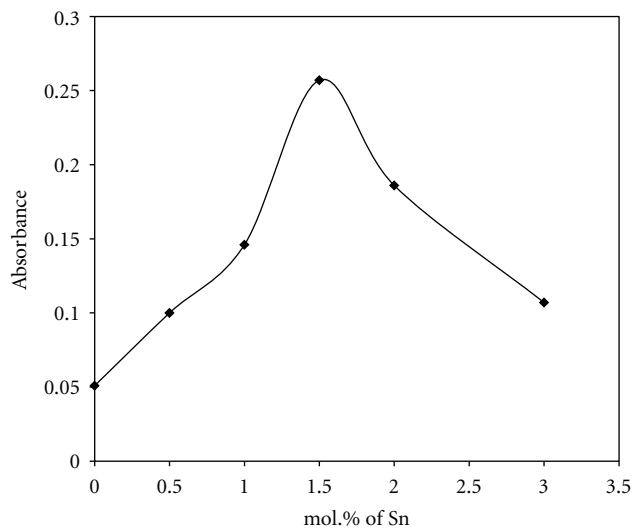


FIGURE 7: Hydroxyl radical amounts on Sn/TiO<sub>2</sub> nanoparticles with different Sn content.

The direct band-gap energy can be estimated from a plot of  $(\alpha h\nu)^2$  versus photon energy ( $h\nu$ ). Sn/TiO<sub>2</sub> nanoparticles show higher band-gap energy than TiO<sub>2</sub> nanoparticles. The band gap energy estimated from DRS analysis for Sn/TiO<sub>2</sub> nanoparticles is between 3.17 and 3.25 eV, which is higher than 3.1 eV for TiO<sub>2</sub>. The band gap plays a critical role in deciding the photocatalytic activity of photocatalysts for the reason that it participates in determining the  $e^-/h^+$  recombination rate. According to Moss-Burstein theory, in heavily doped TiO<sub>2</sub> nanoparticles, the donor electrons occupy states at the bottom of the conduction band. Since the Pauli principal prevents states from being doubly occupied and optical transition is vertical, the valence electrons require extra energy of doped TiO<sub>2</sub> to be boarder than that of pure TiO<sub>2</sub> nanoparticles [42].

**3.1.6. Measurement of Hydroxyl Radical.** It is well understood that hydroxyl radical is generated upon proper photon illumination to photocatalyst. The hydroxyl radical is a powerful oxidizing species, having potential oxidation of approximately 2.8 volt (versus NHE), which may lead to complete mineralization of pollutants. Generally, the greater the formation rate of  $\cdot\text{OH}$  radicals is, the higher separation efficiency of electron-hole pairs is achieved. So, the photocatalytic activity is a positive correlation to the formation rate of  $\cdot\text{OH}$  radicals, namely, a faster formation rate of  $\cdot\text{OH}$  radicals leads to a higher photo-catalytic activity [43]. The effect of different Sn content on the amount of hydroxyl radical was detected using salicylic acid as a probe molecule [44]. The salicylic acid reacted with the hydroxyl radicals to form 2,3-dihydroxybenzoic acid. After reacting 20 min, the amounts of hydroxyl radicals absorbed by the solution at the wavelength of 510 nm were measured. A blank experiment was run before adding the photocatalyst. No change is observed in the absorbance, which indicated that there was no photolysis reaction in salicylic acid under UV irradiation.

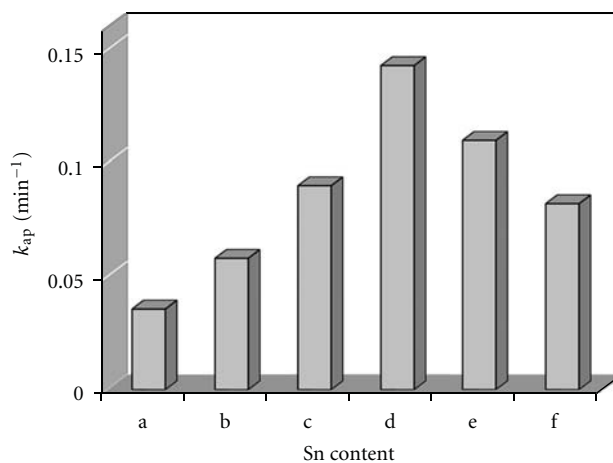


FIGURE 8: Influence of Sn content on the photocatalytic activity of samples under UV irradiation: (a) 0.0% Sn/TiO<sub>2</sub>, (b) 0.5 mol% Sn/TiO<sub>2</sub>, (c) 1 mol% Sn/TiO<sub>2</sub>, (d) 1.5 mol% Sn/TiO<sub>2</sub>, (e) 2 mol% Sn/TiO<sub>2</sub> and (f) 3 mol% Sn/TiO<sub>2</sub>.

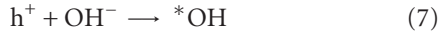
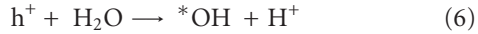
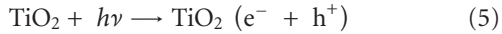
Figure 7 shows the hydroxyl radical with different Sn content. The amount of hydroxyl radicals increases as the Sn content increases. The hydroxyl radical of 1.5 mol% Sn/TiO<sub>2</sub> is very high, indicating that the sample has a high separation rate of photoinduced carriers. However, the amount of hydroxyl radicals can decrease if the Sn content is too high. The reason is that the amount of photoinduced electrons accumulating instantly at the SnO<sub>2</sub> conduction band is too much due to excess SnO<sub>2</sub> so that some photoelectrons can indirectly recombine with holes [45]. Therefore, it can be concluded that the separation rate of photoinduced charge carriers can be improved by doping an appropriate amount of Sn.

### 3.2. Photocatalytic Activity Studies

**3.2.1. Photocatalytic Mineralization of AMOX Using Sn/TiO<sub>2</sub> Nanoparticles.** The results of mineralization of AMOX using Sn/TiO<sub>2</sub> nanoparticles are illustrated in Figure 8. As the irradiation time increased, AMOX degraded into small fragments and subsequently mineralized completely. It could be seen that the photocatalytic activity of Sn/TiO<sub>2</sub> nanoparticles was higher than that of the pure TiO<sub>2</sub>. Further observation showed that photocatalytic activity gradually increased with increasing content of Sn. The slight enhancement of photocatalytic activity of 0.5 mol% Sn/TiO<sub>2</sub> nanoparticles could be assigned to the fact that the excited electrons from the valence band to the conduction band could migrate to Sn nanoparticles and then migrated to O<sub>2</sub> molecules adsorbed on the surface of the Sn. Sn produced an Schottky barrier, which facilitated the electron capture [46]. Especially, when the content of Sn increased to 1.5 mol%, the photocatalytic activity of Sn/TiO<sub>2</sub> nanoparticles significantly increased. The high photo-catalytic activity of 1.5 mol% Sn/TiO<sub>2</sub> sample is due to the following several factors.

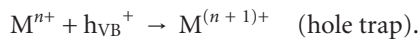
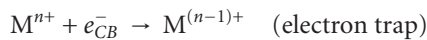
(i) TiO<sub>2</sub> is a photoactive semiconductor that when illuminated with photon energy equal or greater than its

band gap energy, the following reaction took place on the surface of the photo-catalyst:



$\text{SnO}_2$  and  $\text{TiO}_2$  are both wide band gap semiconductors. Although the band gap of  $\text{SnO}_2$  (3.8 eV) is wider than that of  $\text{TiO}_2$  (3.1 V), the Fermi level of  $\text{SnO}_2$  is lower than that of  $\text{TiO}_2$ . It means that the photo-generated electrons may easily transfer from  $\text{TiO}_2$  to  $\text{SnO}_2$ , but not to recombine with the photo-generated holes on the surface of  $\text{TiO}_2$  immediately. Consequently, more and more holes are present on the surface and take part in the reactions of oxidizing  $\text{OH}^-$  and  $\text{H}_2\text{O}$  into hydroxyl radicals. Hydroxyl radicals would be finally responsible for the degradation of pollutants into  $\text{H}_2\text{O}$  and  $\text{CO}_2$  [47, 48]. Furthermore, photo-induced electrons easily transfer from  $\text{TiO}_2$  to  $\text{SnO}_2$  due to their potential difference of conduction band. According to [49], the conduction band (CB) edges of  $\text{TiO}_2$  and  $\text{SnO}_2$  are situated at  $-0.34$  and  $+0.07$  V versus normal hydrogen electrode (NHE) at pH 7. Thus, electron can easily flow into  $\text{SnO}_2$ , which has a more positive conduction band. This results into the decrease in the chance of recombination of photoinduced carriers so that the separation rate of photoinduced electron-hole pairs can improve, that is, the amount of hydroxyl radicals can increase. The amounts of hydroxyl radicals and the efficient charge separation directly influenced the photocatalytic activity [45]. As can be seen in Figure 8, the photocatalytic activity of 1.5 mol%  $\text{Sn}/\text{TiO}_2$  is very high, indicating that the sample has a high separation rate of photoinduced carriers.

(ii) A small amount of metal ions can act as a photo-generated hole and a photo-generated electron trap and inhibit the hole-electron recombination:



The trapped electron may thus be readily transferred to oxygen molecule to form a superoxide radical anion ( $\text{O}_2^{\bullet-}$ ). In addition, the trapped hole can be easily transferred to hydroxyl anion adsorbed on the surface forming hydroxyl radical ( $\text{OH}^\bullet$ ), or it can also be transferred to adsorbed dye molecule to form a dye radical [50].

$\text{Sn}/\text{TiO}_2$  nanoparticles show higher band-gap energy than  $\text{TiO}_2$  nanoparticles, which not only suppressed the electron-hole recombination but also generated more  $\cdot\text{OH}$  radicals [35].

(iii) The superior degradation efficiency of  $\text{Sn}/\text{TiO}_2$  nanoparticles could be attributed to a larger surface area compared to another photocatalyst. A large surface area may be an important factor in certain photocatalytic mineralization reactions, as a large amount of adsorbed organic molecules promotes the reaction rate [51].

(iv) Particle size is another important parameter influencing photocatalytic efficiency, since the electron-hole recombination rate may depend on the particle size. It is well known that in the nanometer-size range, physical and chemical properties of semiconductors are modified (compared with bulk). Small variations in particle diameters lead to great modifications in the surface/bulk ratio, thus influencing the recombination rates of volume and surface electrons and holes [52].

Moreover, a decrease in the activity is expected when the content of Sn becomes too large. The detrimental effect of tin on  $\text{TiO}_2$  photoactivity has several reasons.

(v) The amount of photoinduced electrons accumulating instantly at the  $\text{SnO}_2$  conduction band is too much due to excess  $\text{SnO}_2$  so that some photoelectrons can indirectly recombine with holes [45].

(vi) An excess amount of Sn dopant can produce the recombination center of photoinduced electron and hole pairs. Recombination of  $e^-$ - $h^+$  pairs reduces the rate of photocatalytic mineralization [53].

(vii) Excessive coverage of  $\text{TiO}_2$  catalyst limits the amount of light reaching to the  $\text{TiO}_2$  surface, reducing the number of photogenerated  $e^-$ - $h^+$  pairs and lowering consequently the  $\text{TiO}_2$  photoactivity [54].

(viii) Doped metal may occupy the active sites on the  $\text{TiO}_2$  surface for the desired photocatalytic reactions causing the  $\text{TiO}_2$  to lose its activity [55].

(ix) The probability of the hole capture is increased by the large number of tin particles at high tin dopings, which decrease the probability of holes reacting with adsorbed species at the  $\text{TiO}_2$  surface [56].

Based on the results, the optimum content of Sn-doped  $\text{TiO}_2$  for treatment of AMOX in aqueous solution is 1.5 mol%.

**3.2.2. Effect of the Amount of  $\text{Sn}/\text{TiO}_2$  Nanoparticles.** Photocatalytic mineralization of AMOX may depend on the catalyst amount. In order to investigate the effect of catalyst amount, experiments were carried out by varying the amount of photocatalyst from 100 to 600  $\text{mg L}^{-1}$ , and the mineralization profile is shown in Figure 9. The rate of reaction increases with the increase of photocatalyst up to 400  $\text{mg L}^{-1}$  and a further increase leads to a decrease in the antibiotic mineralization. This observation can be explained in terms of availability of active sites on the catalyst surface and the penetration of UV light into the suspension. The total active surface area increases with increasing catalyst dosage [57]. The reasons for decrease in mineralization rate were aggregation of  $\text{Sn}/\text{TiO}_2$  nanoparticles at high concentration causing a decrease in the number of surface active sites and an increase in the opacity and light scattering of  $\text{Sn}/\text{TiO}_2$  nanoparticles at high concentration. This tends to

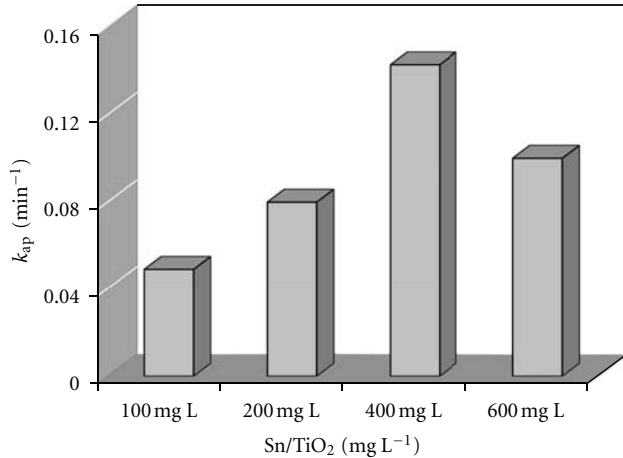


FIGURE 9: Effect of Sn/TiO<sub>2</sub> amount on AMOX mineralization.

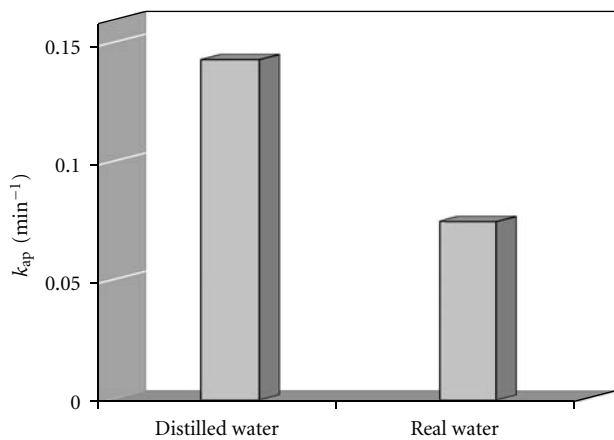


FIGURE 10: Investigation of the efficiency of 1.5 mol% Sn/TiO<sub>2</sub> in mineralization of AMOX from real water.

decrease the passage of irradiation through the sample [58]. The catalyst concentration above which conversion levels off depends on several factors (e.g., reactor geometry, operating conditions, wavelength, and intensity of light source) and corresponds to the point where all catalyst particles, that is, all the surface exposed, are fully illuminated [4]. In this study, the optimum concentration at which all subsequent experiments were conducted was about 400 mg L<sup>-1</sup>.

**3.2.3. Treatment of Real Water Containing AMX.** In order to investigate the efficiency of Sn/TiO<sub>2</sub> nanoparticles in mineralization of AMOX in the real water, 20 mg L<sup>-1</sup> of antibiotic was added into a real water sample (carbonate hardness: 94 mg L<sup>-1</sup> CaCO<sub>3</sub>, sulphate concentration: 175.1 mg L<sup>-1</sup> SO<sub>4</sub><sup>2-</sup>) that was obtained from an irrigation well in Tabriz, Iran. Results in Figure 10 show the effect of presence of common anions such as sulphate, carbonate, and bicarbonate on the mineralization of AMX. It is clear from this figure that, in presence of SO<sub>4</sub><sup>2-</sup>, HCO<sub>3</sub><sup>-</sup>, and CO<sub>3</sub><sup>2-</sup>, the percent of mineralization decreases. This inhibition is

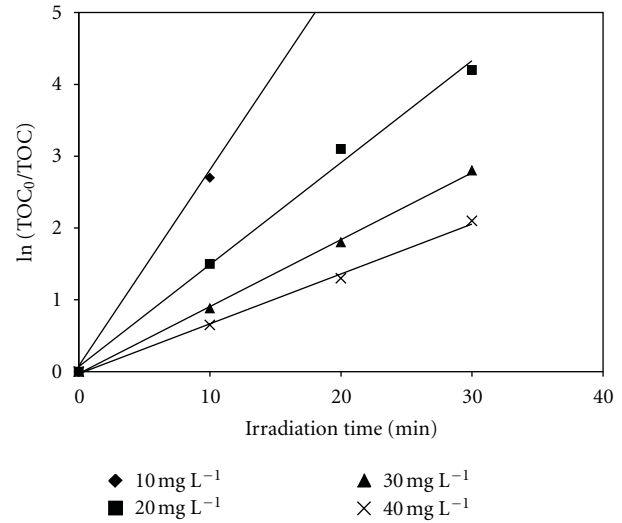
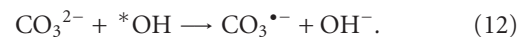
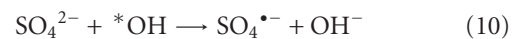


FIGURE 11: Determination of the pseudo-first-order kinetic rate constants,  $k_{ap}$ .

TABLE 4: Pseudo-first-order kinetic rate constants in photocatalytic experiments with different initial concentration of AMOX.

[Sn/TiO <sub>2</sub> ] <sub>0</sub> (mg L <sup>-1</sup> )	[AMOX] <sub>0</sub> (mg L <sup>-1</sup> )	k <sub>ap</sub> (min <sup>-1</sup> )	1/k <sub>ap</sub> (min)	r <sup>2</sup>
400	40	0.068	14.5	0.997
400	30	0.09	11.1	0.999
400	20	0.143	6.95	0.994
400	10	0.25	3.98	0.991

undoubtedly due to their ability to act as hydroxyl radical's scavengers by the following reactions [59]:



These ions may also block the active sites on the Sn/TiO<sub>2</sub> surface thus deactivating the catalysts towards AMOX and intermediate molecules. Although the generated radical anions have been shown to be an oxidant itself, but its oxidation potential is less than that of the hydroxyl radicals.

**3.2.4. Effect of the Initial AMOX Concentration in the Photocatalytic Reaction.** The effect of varying AMOX initial concentration was studied in the range of 10–40 mg L<sup>-1</sup>. Figure 11 shows a plot of ln (TOC<sub>0</sub>/TOC) versus time for all the experiments with different initial concentration of AMOX.

By applying a least square regression analysis, the values of  $k_{ap}$  have been obtained. The results are shown in Figure 12.

Table 4 reports the values of  $k_{ap}$  resulting from plot of ln ([TOC]<sub>0</sub>/[TOC]) versus "Time," which decreases as

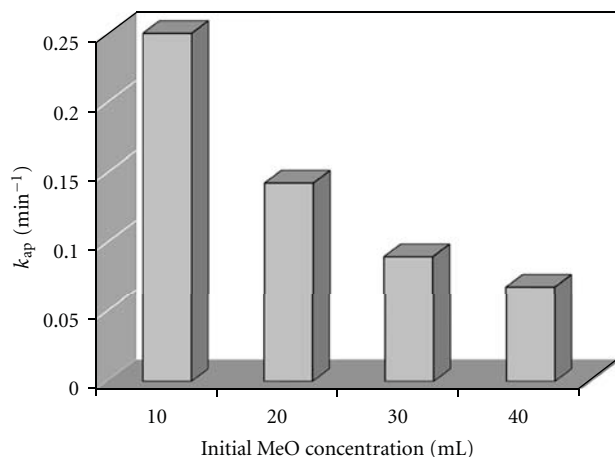


FIGURE 12: Effect of initial AMOX concentration in the photocatalytic reaction.

the initial reactant concentration increases. The presumed reason is that when the initial concentration of antibiotic is increased, more and more antibiotic molecules are adsorbed on the surface of Sn/TiO<sub>2</sub> nanoparticles. The large amount of adsorbed antibiotic is thought to have an inhibitive effect on the reaction of antibiotic molecules with photogenerated holes or hydroxyl radicals, because of the lack of any direct contact between them. This was attributed to the rise of internal optical density, which caused the solution to become impermeable to UV light [60]. Once the concentration of antibiotic is increased, it also causes the antibiotic molecules to absorb light and the photons never reach the photocatalyst surface, and thus the photocatalytic mineralization efficiency decreases [61, 62].

Several reports have established that the heterogeneous photo-oxidation rate fits well to the classic Langmuir-Hinshelwood (L-H) mechanism [63] which in terms of mineralization kinetics can be described as follows:

$$r = \frac{k_c k_{AMOX}(\text{TOC})}{1 + k_{AMOX}(\text{TOC}_0)}, \quad (13)$$

$$\frac{1}{k_{ap}} = \frac{1}{k_c k_{AMOX}} + \frac{\text{TOC}_0}{k_c}, \quad (14)$$

where  $k_{AMOX}$  and  $k_c$  are the Langmuir-Hinshelwood adsorption equilibrium constant and rate constant of surface reaction, respectively. Using the data from photocatalytic experiments with different initial AMOX concentrations, the values of  $k_{AMOX}$  and  $k_c$  can be calculated using the linearized equation by plotting  $1/k_{obs}$  versus  $[\text{TOC}]_0$ . As can be seen in Figure 13, a straight line fitted the experimental data reasonably well (the coefficient of linear regression,  $r$ , was 0.994), thus indicating that photocatalytic mineralization of ERM most probably follows Langmuir-Hinshelwood kinetics. From the slope of the straight line,  $k_c$  was computed equal to  $1.86 \text{ mg L}^{-1} \text{ min}^{-1}$ , while from the intercept,  $k_{AMOX}$  was  $0.56 (\text{mg L}^{-1})^{-1}$ . Yurdakal and his coworkers reported Langmuir-Hinshelwood equation constants for mineralization of Gemfibrozil (GEM) drug in the presence of two

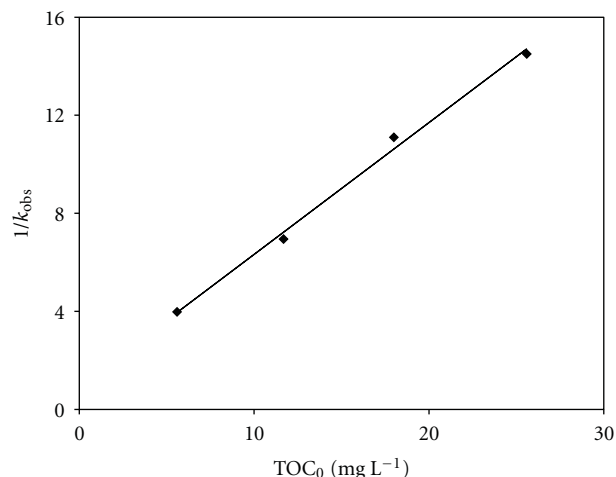


FIGURE 13: Determination of the adsorption equilibrium constant,  $k_{AMOX}$ , and the second order rate constant,  $k_c$ , for the Langmuir-Hinshelwood kinetic model.

commercial polycrystalline TiO<sub>2</sub> powders (Degussa P25 and Merck). The values of  $k_c$  are  $1.91 \times 10^{-8}$  and  $6.78 \times 10^{-9} \text{ mol m}^{-2} \text{ s}^{-1}$  and those of  $K_{GEM}$   $5.11 \times 10^3$  and  $1.07 \times 10^5 \text{ M}^{-1}$  for Degussa P25 and Merck, respectively [3].

#### 4. Conclusions

TiO<sub>2</sub> and Sn/TiO<sub>2</sub> nanoparticles could be prepared by sol-gel method using titanium n-butoxide and tin (IV) chloride as precursors. The XRD results showed that the crystallite size greatly decreased due to Sn-doping but an increase in surface area, pore volume, and band gap energy was observed. Nitrogen adsorption-desorption isotherms showed that the adsorption ability was enhanced owing to Sn-doping. The absorbance of Sn/TiO<sub>2</sub> nanoparticles was shifted toward shorter wavelength than TiO<sub>2</sub> nanoparticles. The effect of Sn dopant on the photoinduced charge property was estimated by measuring hydroxyl radicals using salicylic acid as probe molecule. The photocatalytic efficiency for AMOX decomposition was remarkably enhanced owing to Sn-doping, and 1.5 mol% Sn/TiO<sub>2</sub> sample had the highest photocatalytic activity due to increase in the generated hydroxyl radicals, band gap energy, specific surface area, and decrease in the crystal size. Langmuir-Hinshelwood kinetic model provided a good fit to the photocatalytic mineralization of AMOX, used in this study. This study confirms the potentialities of heterogeneous photocatalysis to decontaminate wastewaters containing organic pollutants.

#### References

- [1] J. Ziemianska, E. Adamek, A. Sobszak, I. Lipska, A. Makowas-ki, and W. Baran, "The study of photocatalytic degradation of sulfonamides applied to municipal wastewater," *Physicochemical Problems of Mineral Processing*, vol. 45, pp. 127–140, 2010.
- [2] A. Paola, M. Addamo, V. Augugliaro et al., "Photodegradation of lincomycin in aqueous solution," *International Journal of Photoenergy*, vol. 2006, Article ID 47418, 6 pages, 2006.

- [3] S. Yurdakal, V. Loddo, V. Augugliaro, H. Berber, G. Palmisano, and L. Palmisano, "Photodegradation of pharmaceutical drugs in aqueous TiO<sub>2</sub> suspensions: mechanism and kinetics," *Catalysis Today*, vol. 129, no. 1-2, pp. 9–15, 2007.
- [4] N. P. Xekoukoulotakis, N. Xinidis, M. Chroni et al., "UV-A/TiO<sub>2</sub> photocatalytic decomposition of erythromycin in water: factors affecting mineralization and antibiotic activity," *Catalysis Today*, vol. 151, no. 1-2, pp. 29–33, 2010.
- [5] D. W. Kolpin, W. E. T. Furlong, M. T. Meyer et al., "Pharmaceuticals, hormones, and other organic wastewater contaminants in U.S. streams, 1999–2000: a national reconnaissance," *Environmental Science and Technology*, vol. 36, no. 6, pp. 1202–1211, 2002.
- [6] R. A. Palominos, A. Mora, M. A. Mondaca, M. Perez-Moya, and H. D. Mansilla, "Oxolinic acid photo-oxidation using immobilized TiO<sub>2</sub>," *Journal of Hazardous Materials*, vol. 158, no. 2-3, pp. 460–464, 2008.
- [7] A. J. Watkinson, E. J. Murby, and S. D. Costanzo, "Removal of antibiotics in conventional and advanced wastewater treatment: implications for environmental discharge and wastewater recycling," *Water Research*, vol. 41, no. 18, pp. 4164–4176, 2007.
- [8] C. Reyes, J. Fernández, J. Freer et al., "Degradation and inactivation of tetracycline by TiO<sub>2</sub> photocatalysis," *Journal of Photochemistry and Photobiology A*, vol. 184, no. 1-2, pp. 141–146, 2006.
- [9] X. Chen and S. S. Mao, "Titanium dioxide nanomaterials: synthesis, properties, modifications and applications," *Chemical Reviews*, vol. 107, no. 7, pp. 2891–2995, 2007.
- [10] Y. Xie and C. Yuan, "Characterization and photocatalysis of Eu<sup>3+</sup>-TiO<sub>2</sub> sol in the hydrosol reaction system," *Materials Research Bulletin*, vol. 39, no. 4-5, pp. 533–543, 2004.
- [11] H. G. Yu, J. G. Yu, S. W. Liu, and S. Mann, "Template-free hydrothermal synthesis of CuO/Cu<sub>2</sub>O composite hollow microspheres," *Chemistry of Materials*, vol. 19, no. 17, pp. 4327–4334, 2007.
- [12] W. Y. Choi, A. Termin, and M. R. Hoffmann, "The role of metal ion dopants in quantum-sized TiO<sub>2</sub>: correlation between photoreactivity and charge carrier recombination dynamics," *Journal of Physical Chemistry*, vol. 98, no. 51, pp. 13669–13679, 1994.
- [13] C. Chen, Z. Wang, S. Ruan, B. Zou, M. Zhao, and F. Wu, "Photocatalytic degradation of C.I. Acid Orange 52 in the presence of Zn-doped TiO<sub>2</sub> prepared by a stearic acid gel method," *Dyes and Pigments*, vol. 77, no. 1, pp. 204–209, 2008.
- [14] G. Sivalingam, K. Nagaveni, M. S. Hegde, and G. Madras, "Photocatalytic degradation of various dyes by combustion synthesized nano anatase TiO<sub>2</sub>," *Applied Catalysis B*, vol. 45, no. 1, pp. 23–38, 2003.
- [15] C. A. Castro, A. Jurado, D. Sissa, and S. A. Giraldo, "Performance of Ag-TiO<sub>2</sub> photocatalysts towards the photocatalytic disinfection of water under interior-lighting and solar-simulated light irradiations," *International Journal of Photoenergy*, vol. 2012, Article ID 261045, 10 pages, 2012.
- [16] L. Jia, C. Wu, Y. Li et al., "Enhanced visible-light photocatalytic activity of anatase TiO<sub>2</sub> through N and S codoping," *Applied Physics Letters*, vol. 98, Article ID 211903, 3 pages, 2011.
- [17] X. Li, J. Lu, Y. Dai, M. Guo, and B. Huang, "The synthetic effects of iron with sulfur and fluorine on photoabsorption and photocatalytic performance in codoped TiO<sub>2</sub>," *International Journal of Photoenergy*, vol. 2012, Article ID 203529, 7 pages, 2012.
- [18] R. A. Palominos, M. A. Mondaca, A. Giraldo, G. Peñuela, M. Pérez-Moya, and H. D. Mansilla, "Photocatalytic oxidation of the antibiotic tetracycline on TiO<sub>2</sub> and ZnO suspensions," *Catalysis Today*, vol. 144, no. 1-2, pp. 100–105, 2009.
- [19] L. K. Ge, J. W. Chen, S. Y. Zhang, X. Y. Cai, Z. Wang, and C. L. Wang, "Photodegradation of fluoroquinolone antibiotic gatifloxacin in aqueous solutions," *Chinese Science Bulletin*, vol. 55, no. 15, pp. 1495–1500, 2010.
- [20] R. A. Palominos, A. Mora, M. A. Mondaca, M. Pérez-Moya, and H. D. Mansilla, "Oxolinic acid photo-oxidation using immobilized TiO<sub>2</sub>," *Journal of Hazardous Materials*, vol. 158, no. 2-3, pp. 460–464, 2008.
- [21] M. N. Abellán, B. Bayarri, J. Gimenez, and J. Costa, "Photocatalytic degradation of sulfamethoxazole in aqueous suspension of TiO<sub>2</sub>," *Applied Catalysis B*, vol. 74, no. 3-4, pp. 233–241, 2007.
- [22] Y. Bessekhouad, D. Robert, and J. V. Weber, "Synthesis of photocatalytic TiO<sub>2</sub> nanoparticles: optimization of the preparation conditions," *Journal of Photochemistry and Photobiology A*, vol. 157, no. 1, pp. 47–53, 2003.
- [23] M. A. Behnajady, H. Eskandarloo, N. Modirshahla, and M. Shokri, "Investigation of the effect of sol-gel synthesis variables on structural and photocatalytic properties of TiO<sub>2</sub> nanoparticles," *Desalination*, vol. 278, no. 1–3, pp. 10–17, 2011.
- [24] N. Modirshahla, A. Hassani, M. A. Behnajady, and R. Rahbarfard, "Effect of operational parameters on decolorization of Acid Yellow 23 from wastewater by UV irradiation using ZnO and ZnO/SnO<sub>2</sub> photocatalysts," *Desalination*, vol. 271, no. 1–3, pp. 187–192, 2011.
- [25] J. Li, J. Xu, W. L. Dai, H. Li, and K. Fan, "Direct hydro-alcohol thermal synthesis of special core-shell structured Fe-doped titania microspheres with extended visible light response and enhanced photoactivity," *Applied Catalysis B*, vol. 85, no. 3-4, pp. 162–170, 2009.
- [26] T. L. Su, C. S. Chiou, and H. W. Chen, "Preparation, photocatalytic activity, and recovery of magnetic photocatalyst for decomposition of benzoic acid," *International Journal of Photoenergy*, vol. 2012, Article ID 909678, 8 pages, 2012.
- [27] M. Hamadani, A. Reisi-Vanani, and A. Majedi, "Sol-gel preparation and characterization of Co/TiO<sub>2</sub> nanoparticles: application to the degradation of methyl orange," *Journal of the Iranian Chemical Society*, vol. 7, supplement 1, pp. S52–S58, 2010.
- [28] R. A. Spurr and H. Myers, "Quantitative analysis of anatase-rutile mixtures with an X-ray diffractometer," *Analytical Chemistry*, vol. 29, no. 5, pp. 760–762, 1957.
- [29] F. Fresno, J. M. Coronado, D. Tudela, and J. Soria, "Influence of the structural characteristics of Ti<sub>1-x</sub>Sn<sub>x</sub>O<sub>2</sub> nanoparticles on their photocatalytic activity for the elimination of methylcyclohexane vapors," *Applied Catalysis B*, vol. 55, no. 3, pp. 159–167, 2005.
- [30] C. R. Estrellan, C. Salim, and H. Hinode, "Photocatalytic decomposition of perfluorooctanoic acid by iron and niobium co-doped titanium dioxide," *Journal of Hazardous Materials*, vol. 179, no. 1–3, pp. 79–83, 2010.
- [31] J. G. Yu, T. T. Ma, and S. W. Liu, "Enhanced photocatalytic activity of mesoporous TiO<sub>2</sub> aggregates by embedding carbon nanotubes as electron-transfer channel," *Physical Chemistry Chemical Physics*, vol. 13, no. 8, pp. 3491–3501, 2011.
- [32] J. G. Yu, S. Liu, and H. Yu, "Microstructures and photoactivity of mesoporous anatase hollow microspheres fabricated by fluoride-mediated self-transformation," *Journal of Catalysis*, vol. 249, no. 1, pp. 59–66, 2007.
- [33] P. Madhusudan, J. Ran, J. Zhang, J. Yu, and G. Liu, "Novel urea assisted hydrothermal synthesis of hierarchical

- BiVO<sub>4</sub>/Bi<sub>2</sub>O<sub>3</sub>CO<sub>3</sub> nanocomposites with enhanced visible-light photocatalytic activity,” *Applied Catalysis B*, vol. 110, pp. 286–295, 2011.
- [34] S. Rahimnejad, S. R. Setayesh, and M. R. Gholami, “A credible role of copper oxide on structure of nanocrystalline mesoporous titanium dioxide,” *Journal of the Iranian Chemical Society*, vol. 5, no. 3, pp. 367–374, 2008.
- [35] L. Kumaresan, M. Mahalakshmi, M. Palanichamy, and V. Murugesan, “Synthesis, characterization, and photocatalytic activity of Sr<sup>2+</sup> doped TiO<sub>2</sub> nanoplates,” *Industrial and Engineering Chemistry Research*, vol. 49, no. 4, pp. 1480–1485, 2010.
- [36] K. Loganathan, P. Bommasamy, P. Muthaiahpillai, and M. Velayutham, “The syntheses, characterizations, and photocatalytic activities of silver, platinum, and gold doped TiO<sub>2</sub> nanoparticles,” *Environmental Engineering Research*, vol. 16, no. 2, pp. 81–90, 2011.
- [37] Y. Kotani, T. Matoda, A. Matsuda, T. Kogure, M. Tatsumisago, and T. Minami, “Anatase nanocrystal-dispersed thin films via sol-gel process with hot water treatment: effects of poly(ethylene glycol) addition on photocatalytic activities of the films,” *Journal of Materials Chemistry*, vol. 11, no. 8, pp. 2045–2048, 2001.
- [38] J. Li, J. Xu, W. L. Dai, H. Li, and K. Fan, “Direct hydro-alcohol thermal synthesis of special core-shell structured Fe-doped titania microspheres with extended visible light response and enhanced photoactivity,” *Applied Catalysis B*, vol. 85, no. 3-4, pp. 162–170, 2009.
- [39] E. Burstein, “Anomalous optical absorption limit in InSb,” *Physical Review*, vol. 93, no. 3, pp. 632–633, 1954.
- [40] T. S. Moss, “The interpretation of the properties of indium antimonide,” *Proceedings of the Physical Society B*, vol. 67, no. 10, pp. 775–782, 1954.
- [41] B. E. Sernelius, K. F. Berggren, Z. Jin, I. Hamberg, and C. G. Granqvist, “Band-gap tailoring of ZnO by means of heavy Al doping,” *Physical Review B*, vol. 37, no. 8, pp. 10244–10248, 1998.
- [42] M. N. Norazia, N. P. Ariyanto, A. A. Khadum, S. Shaari, H. Abdullah, and C. F. Dee, “Structural, morphology and optical properties of Zn<sub>1-x</sub>Sn<sub>x</sub>O (x = 0.0, 0.1 and 0.2) thin films by sol-gel method,” *Solid State Science and Technology*, vol. 18, no. 1, pp. 202–211, 2010.
- [43] J. G. Yu, Q. J. Xiang, and M. H. Zhou, “Preparation, characterization and visible-light-driven photocatalytic activity of Fe-doped titania nanorods and first-principles study for electronic structures,” *Applied Catalysis B*, vol. 90, no. 3-4, pp. 595–602, 2009.
- [44] R. C. Xiong, C. G. Jia, and G. Wei, “Treatment of dyestuffs wastewater with two and three-dimension electrode methods,” *Journal of Beijing University of Chemical Technology*, vol. 29, no. 5, pp. 34–37, 2002.
- [45] X. Li, R. Xiong, and G. Wei, “Preparation and photocatalytic activity of nanoglued Sn-doped TiO<sub>2</sub>,” *Journal of Hazardous Materials*, vol. 164, no. 2-3, pp. 587–591, 2009.
- [46] J. G. Yu, J. F. Xiong, B. Cheng, and S. W. Liu, “Fabrication and characterization of Ag-TiO<sub>2</sub> multiphase nanocomposite thin films with enhanced photocatalytic activity,” *Applied Catalysis B*, vol. 60, no. 3-4, pp. 211–221, 2005.
- [47] B. F. Xin, D. D. Ding, Y. N. Gao, X. G. Jin, H. Fu, and P. Wang, “Preparation of nanocrystalline Sn-TiO<sub>2</sub>-X via a rapid and simple stannous chemical reducing route,” *Applied Surface Science*, vol. 255, no. 11, pp. 5896–5901, 2009.
- [48] Z. Xiufeng, L. Juan, L. Lianghai, and W. Zuoshan, “Preparation of crystalline Sn-doped TiO<sub>2</sub> and its application in visible-light photocatalysis,” *Journal of Nanomaterials*, vol. 2011, Article ID 432947, 5 pages, 2011.
- [49] J. Shang, W. Q. Yao, Y. F. Zhu, and N. Z. Wu, “Structure and photocatalytic performances of glass/SnO<sub>2</sub>/TiO<sub>2</sub> interface composite film,” *Applied Catalysis A*, vol. 257, no. 1, pp. 25–32, 2004.
- [50] M. L. Chen and W. C. Oh, “The improved photocatalytic properties of methylene blue for V<sub>2</sub>O<sub>5</sub>/CNT/TiO<sub>2</sub> composite under visible light,” *International Journal of Photoenergy*, vol. 2010, Article ID 264831, 5 pages, 2011.
- [51] J. G. Yu, X. J. Zhao, J. C. Du, and W. M. Chen, “Preparation, microstructure and photocatalytic activity of the porous TiO<sub>2</sub> anatase coating by sol-gel processing,” *Journal of Sol-Gel Science and Technology*, vol. 17, no. 2, pp. 163–171, 2000.
- [52] M. Zhou, J. Yu, and B. Cheng, “Effects of Fe-doping on the photocatalytic activity of mesoporous TiO<sub>2</sub> powders prepared by an ultrasonic method,” *Journal of Hazardous Materials*, vol. 137, no. 3, pp. 1838–1847, 2006.
- [53] M. A. Behnajady, N. Modirshahla, M. Shokri, and B. Rad, “Enhancement of photocatalytic activity of TiO<sub>2</sub> nanoparticles by silver doping: photodeposition versus liquid impregnation methods,” *Global NEST Journal*, vol. 10, no. 1, pp. 1–7, 2008.
- [54] O. Carp, C. L. Huisman, and A. Reller, “Photoinduced reactivity of titanium dioxide,” *Progress in Solid State Chemistry*, vol. 32, no. 1-2, pp. 33–177, 2004.
- [55] H. M. Coleman, K. Chiang, and R. Amal, “Effects of Ag and Pt on photocatalytic degradation of endocrine disrupting chemicals in water,” *Chemical Engineering Journal*, vol. 113, no. 1, pp. 65–72, 2005.
- [56] N. Sobana, M. Muruganadham, and M. Swaminathan, “Nano-Ag particles doped TiO<sub>2</sub> for efficient photodegradation of Direct azo dyes,” *Journal of Molecular Catalysis A*, vol. 258, no. 1-2, pp. 124–132, 2006.
- [57] M. A. Behnajady, N. Modirshahla, and R. Hamzavi, “Kinetic study on photocatalytic degradation of C.I. Acid Yellow 23 by ZnO photocatalyst,” *Journal of Hazardous Materials*, vol. 133, no. 1–3, pp. 226–232, 2006.
- [58] Z. M. El-Bahy, A. A. Ismail, and R. M. Mohamed, “Enhancement of titania by doping rare earth for photodegradation of organic dye (Direct Blue),” *Journal of Hazardous Materials*, vol. 166, no. 1, pp. 138–143, 2009.
- [59] O. Legrini, E. Oliveros, and A. M. Braun, “Photochemical processes for water treatment,” *Chemical Reviews*, vol. 93, no. 2, pp. 671–698, 1993.
- [60] J. C. Sin, S. M. Lam, A. R. Mohamed, and K. T. Lee, “Degrading endocrine disrupting chemicals from wastewater by TiO<sub>2</sub> photocatalysis: a review,” *International Journal of Photoenergy*, vol. 2012, Article ID 185159, 23 pages, 2012.
- [61] N. Daneshvar, D. Salari, and A. R. Khataee, “Photocatalytic degradation of azo dye acid red 14 in water: investigation of the effect of operational parameters,” *Journal of Photochemistry and Photobiology A*, vol. 157, no. 1, pp. 111–116, 2003.
- [62] A. Mills and S. Morris, “Photomineralization of 4-chlorophenol sensitized by titanium dioxide: a study of the initial kinetics of carbon dioxide photogeneration,” *Journal of Photochemistry and Photobiology A*, vol. 71, no. 1, pp. 75–83, 1993.
- [63] N. Barka, S. Qourzal, A. Assabbane, and Y. Ait-Ichou, “Kinetic modeling of the photocatalytic degradation of methyl orange by supported TiO<sub>2</sub>,” *Journal of Environmental Science and Engineering*, vol. 4, no. 5, pp. 1–5, 2010.

## Research Article

# Fabrication of Al-Doped TiO<sub>2</sub> Visible-Light Photocatalyst for Low-Concentration Mercury Removal

Cheng-Yen Tsai,<sup>1</sup> Tien-Ho Kuo,<sup>2</sup> and Hsing-Cheng Hsi<sup>3</sup>

<sup>1</sup> Graduate Institute of Engineering Science and Technology, National Kaohsiung First University of Science and Technology, No. 2 Jhuoyue Road, Nanzih, Kaohsiung 811, Taiwan

<sup>2</sup> Department of Environmental, Safety, and Health Engineering, Tungnan University, Section 3, 152, Peishen Road, Shenkeng, New Taipei 222, Taiwan

<sup>3</sup> Institute of Environmental Engineering and Management, National Taipei University of Technology, Section 3, No. 1, Chung-Hsiao E. Road, Taipei 106, Taiwan

Correspondence should be addressed to Hsing-Cheng Hsi, hchsi@ntut.edu.tw

Received 13 September 2011; Revised 30 December 2011; Accepted 31 December 2011

Academic Editor: Gongxuan Lu

Copyright © 2012 Cheng-Yen Tsai et al. This is an open access article distributed under the Creative Commons Attribution License, which permits unrestricted use, distribution, and reproduction in any medium, provided the original work is properly cited.

High-quality Al-doped TiO<sub>2</sub> visible-light photocatalyst was prepared via a single-step direct combination of vaporized Ti, Al, and O<sub>2</sub> using a 6 kW thermal plasma system. Results showed that the formed Al-doped TiO<sub>2</sub> nanoparticles were a mixture of anatase and rutile phase and had a size between 10 and 105 nm. The absorption spectra of the nanoparticles shifted towards the visible light regions, depending on the Al<sub>2</sub>O<sub>3</sub> addition. Ti<sup>4+</sup> and Ti<sup>3+</sup> coexisted in the synthesized Al-doped TiO<sub>2</sub>; the Ti<sup>3+</sup> concentration, however, increased with increasing Al<sub>2</sub>O<sub>3</sub> addition due to Al/Ti substitution that caused the occurrence of oxygen vacancy. Hg<sup>0</sup> breakthrough tests revealed that the nanoparticles had an appreciable Hg<sup>0</sup> removal under visible-light irradiation. Nevertheless, moisture reduced Hg removal by the nanoparticles, especially when visible-light irradiation was applied, suggesting that the competitive adsorption between H<sub>2</sub>O and Hg species on the active sites of TiO<sub>2</sub> surface occurred.

## 1. Introduction

Mercury (Hg) releases from nature and anthropogenic sources have been the major focus of environmental studies owing to the toxicity and bioaccumulative behaviors [1]. Hg species in gaseous phase from emission sources in general exist in three main forms: elemental (Hg<sup>0</sup>), oxidized (Hg<sup>2+</sup>), and particle-bound (Hg<sub>p</sub>). Hg<sup>2+</sup> and Hg<sub>p</sub> can be easily removed by air pollution control devices such as wet flue gas desulfurization and electrostatic precipitators. Nevertheless, Hg<sup>0</sup> is highly volatile, insoluble in water, and thus difficult to remove from a gas stream.

Using titanium dioxide (TiO<sub>2</sub>) photocatalysts as adsorbents and catalysts has been advised as a novel technique to effectively remove Hg<sup>0</sup> [2–11]. Wu et al. [2] used in situ produced TiO<sub>2</sub> particles to remove Hg under UV irradiation. Upon irradiation with UV light, active sites become available on the TiO<sub>2</sub> particle surface and effectively adsorbed Hg to

form a complex with TiO<sub>2</sub>. The manufacturing procedures strongly influence the purity and surface characteristics of resulting TiO<sub>2</sub> nanoparticles, which afterward affect the photocatalytic properties. Sol-gel method has been widely used in the bench-scale TiO<sub>2</sub> nanoparticles fabrication due to its simplicity to perform [12–15]. Nevertheless, the processing temperature of sol-gel method syntheses is relatively low. A multistep fabrication procedure, that is, sample synthesis and subsequent calcination, was thus needed to transform the obtained TiO<sub>2</sub> into anatase or rutile. Thermal plasma has been shown to possess advantages to develop nanoparticles with clean surface and narrow particle size distribution. Using thermal plasma as a heating source may directly vaporize Ti metal having a high melting point at 1941 K and induce the high-purity TiO<sub>2</sub> formation in a single step.

A decisive obstruction in the successful application of TiO<sub>2</sub> is the band gap energy of 3.2 eV causing the TiO<sub>2</sub> only being activated by UV irradiation. Visible-light (VL) TiO<sub>2</sub>

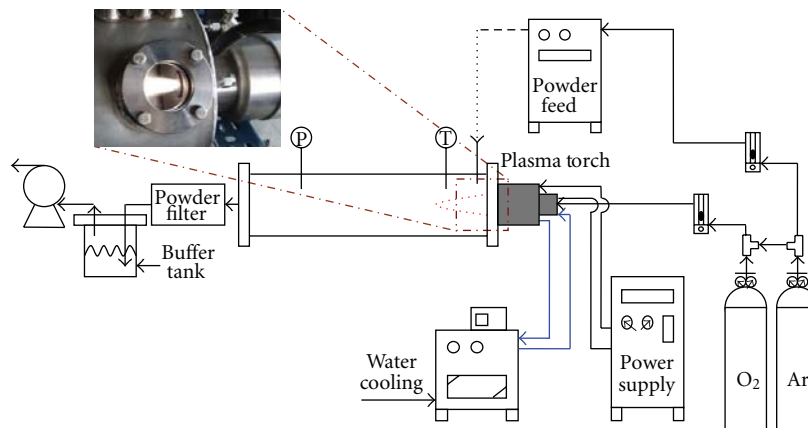


FIGURE 1: Schematic diagram of non-transferred DC plasma torch system for synthesis Al-doped TiO<sub>2</sub> photocatalysts.

photocatalysts have therefore obtained great attention in recent years. Several studies have indicated that an improved TiO<sub>2</sub> photocatalyst excited by VL sources can be prepared by substitutional doping with metal atoms, such as Fe [16, 17], Er [18], and Al [19–23]. Because the ionic radii for Al and Ti are similar (0.053 nm for Al<sup>3+</sup> and 0.061 nm for Ti<sup>4+</sup>), Al can easily fill into a regular cation position and form a substitutional solid solution. Numerous studies have shown that Al-doped TiO<sub>2</sub> nanoparticles can be manufactured via vapor-phase. Lee et al. [19] prepared Al-doped TiO<sub>2</sub> with thermal plasma using TiCl<sub>4</sub> and AlCl<sub>3</sub> as precursors. The absorption band of synthesized Al-doped TiO<sub>2</sub> nanoparticles shifted from the UV region to the VL region. Choi et al. [23] prepared Al-doped TiO<sub>2</sub> nanoparticles using a citrate-nitrate autocombustion system with Ti solution and Al(NO<sub>3</sub>)<sub>3</sub> solution as precursors. The authors also demonstrated that Al-doped TiO<sub>2</sub> gas sensor was more selective and sensitive to CO and O<sub>2</sub> under 600°C.

In our previous study, high-purity TiO<sub>2</sub> nanoparticles using Ti metal as a precursor were successfully manufactured with a transferred plasma torch [24]. Nevertheless, using transferred DC plasma torch as the heating source has defects on low nanoparticles yield. Another plasma system was established in our earlier study using a nontransferred DC plasma torch as the heating source [25]. Our preliminary test has shown that Al-doped TiO<sub>2</sub> nanoparticles can be successfully formed in a single step via this non-transferred DC thermal plasma system. However, the anatase/rutile ratio of the formed Al-doped TiO<sub>2</sub> was below 58.2 wt%, which may be due to the higher plasma power (i.e., 8 kW). In this study, Al-doped TiO<sub>2</sub> photocatalyst with a broad absorption spectrum was developed under a lower plasma power (i.e., 6 kW). The photocatalyst fabricated from this innovative single-step procedure was tested for Hg<sup>0</sup> capture under both UV and VL irradiation. We expected that a reducing plasma power can increase the anatase ratio of the formed Al-doped TiO<sub>2</sub> crystal. The greater content of anatase phase in TiO<sub>2</sub> may enhance the transformation of Hg<sup>0</sup> into Hg<sup>2+</sup>, which could subsequently enhance the removal effectiveness of TiO<sub>2</sub>. The Hg<sup>0</sup> removal effectiveness of Al-doped TiO<sub>2</sub> in the presence of O<sub>2</sub>, H<sub>2</sub>O, and light irradiation was

further discussed. Notably, few studies have examined the VL photocatalytic effects of Al-doped TiO<sub>2</sub> on removal of Hg<sup>0</sup> at an extreme low concentration, namely, μg Nm<sup>-3</sup> level.

## 2. Experimental Details

**2.1. Synthesis of Al-Doped TiO<sub>2</sub> Nanoparticles.** The DC plasma torch apparatus used for preparing TiO<sub>2</sub> nanoparticles is illustrated in Figure 1. The system comprised a non-transferred plasma torch connected to a DC power supply (Model PHS-15C, Taiwan Plasma Corp., Taiwan), a stainless steel reaction chamber (i.d. = 30 cm; length = 100 cm), a stainless steel powder feeder, a powder filter, a buffer tank, and a vacuum pump (GVD-050A, ULVAC) for shifting the particles floating in the exhaust gas. The plasma torch consisted of a water-cooled copper alloy electrode. The system was performed at 30 A and 200 V. Titanium powder (99.8% purity), Al<sub>2</sub>O<sub>3</sub> powder (99.9% purity), and ultrahigh-purity (UHP) O<sub>2</sub> were used as precursors. A mixture of UHP Ar and O<sub>2</sub> was used as the plasma gas. The flow rate was 60 L min<sup>-1</sup> at Ar : O<sub>2</sub> = 3 : 1 by volume. UHP Ar with a flow rate of 2 L min<sup>-1</sup> was also used as the carrier gas of the Ti and Al<sub>2</sub>O<sub>3</sub> powder feedstock. The Al<sub>2</sub>O<sub>3</sub>/Ti mass ratio was controlled at 0, 0.1, 0.3, and 0.5. The powder feeding rate was fixed at 0.2 g min<sup>-1</sup>. The gas stream containing the formed TiO<sub>2</sub> nanoparticles was passed through the stainless steel powder filter and a buffer tank induced by the vacuum pump.

**2.2. Al-Doped TiO<sub>2</sub> Nanoparticle Characterization.** The particle size and morphology of TiO<sub>2</sub> nanoparticles were examined with a transmission electron microscope (TEM, Philips CM-200). Powder X-ray diffraction (XRD, Rigaku Rinet 200) with Cu Kα radiation (λ = 1.5405 Å) was used for crystal structure identification. The JCPDS database was used for powder crystalline phase identification. The mass fractions of anatase to rutile in formed TiO<sub>2</sub> nanoparticles were calculated by [26],

$$f_A = \frac{1}{1 + 1.26I_R/I_A}, \quad (1)$$

where  $f_A$  is the mass fraction of anatase,  $I_A$  is the intensity of (101) reflection of anatase, and  $I_R$  is the intensity of (110) reflection of rutile. The diffuse reflectance UV-visible spectra (UV-Vis) of TiO<sub>2</sub> nanoparticles were measured from 300 to 800 nm using a spectrophotometer (Hitachi U-3010). X-ray photoelectron spectroscopy (XPS, ULVAC-PHI 1600) was used for Ti, O, Al, and Cu bonding patterns identification. The obtained XPS spectra were deconvoluted with the XPSPEAK software.

**2.3. Hg Removal Experiments.** Al-doped TiO<sub>2</sub> synthesized at the Al<sub>2</sub>O<sub>3</sub>/Ti mass ratio of 0.5 was evaluated for the removal effectiveness of low-concentration gaseous Hg<sup>0</sup>. Gaseous Hg<sup>0</sup> was generated with a certificated Hg<sup>0</sup> permeation tube (VICI Metronics) which heated at  $70 \pm 0.1^\circ\text{C}$  to ensure a constant Hg<sup>0</sup> diffusion rate. Gaseous Hg<sup>0</sup> with a known concentration was mixed with N<sub>2</sub>, O<sub>2</sub>, and water vapor which was generated by streaming N<sub>2</sub> passed through a water bubbler. All gas mixing and Hg<sup>0</sup> injection occurred within a temperature-controlled chamber and heated tubes/lines to prevent water condensation. The generated Hg<sup>0</sup>-containing gas with a concentration of  $10\text{--}15\ \mu\text{g Hg}^0\ \text{Nm}^{-3}$  and a flow rate of  $1.5\ \text{L min}^{-1}$  flowed through the photochemical reactor with 30 mg Al-doped TiO<sub>2</sub> were irradiated with UV or VL light. The photochemical reactor was a cylindrical quartz tube with an i.d. = 25 mm and a length = 150 mm. The nanoparticles were uniformly coated onto a glass slide, which was placed horizontally in the tube. The UV and VL light sets was located 1 cm above the tube. The photochemical tube reactor was operated at  $25^\circ\text{C}$  and atmospheric pressure. The effluent gas from the photochemical reactor flowed through a moisture trap (i.e., a neffion tube) to remove H<sub>2</sub>O from the gas stream and thus to minimize the interference in Hg detection. The tail gas then flowed through a gold amalgamation column held by a heating coil (Brooks Rand model AC-01) where the Hg<sup>0</sup> in the gas was adsorbed. The Hg<sup>0</sup> that was concentrated on the gold was then thermally desorbed and sent as a concentrated Hg stream to a cold-vapor atomic fluorescence spectrophotometer (Model III, Brooks Rand Lab) for analysis. Six minutes were needed to complete a test run; ten runs were performed for each test condition. Finally, the exhaust was passed through a carbon trap before it was effluent into the fume hood.

### 3. Results and Discussion

Figure 2 illustrates the TEM images of the nanoparticles produced at various Al<sub>2</sub>O<sub>3</sub>/Ti mass ratios. TEM results indicated that the synthesized Al-doped TiO<sub>2</sub> was homogeneous, without significant phase separation or coating on the surface. It was also noticed that the synthesized nanoparticles was in hexagonal or spherical shapes; adding Al<sub>2</sub>O<sub>3</sub> powder had insignificant effects on the shape of the formed nanoparticles. The darker areas in the TEM micrographs showed the agglomeration of Al-doped TiO<sub>2</sub> nanoparticles. The powder size of the feedstock Ti and Al<sub>2</sub>O<sub>3</sub> powder were about  $5\text{--}15\ \mu\text{m}$ . However, nanoparticles formed at Al<sub>2</sub>O<sub>3</sub>/Ti mass ratios of 0 to 0.5 were approximately between 10 and

TABLE 1: Crystal phases of Al-doped TiO<sub>2</sub> synthesized at various Al<sub>2</sub>O<sub>3</sub>/Ti mass ratio.

Al <sub>2</sub> O <sub>3</sub> /Ti mass ratio	$f_A$ (wt.%)	Phase detected
0	64.31	Anatase, rutile
0.1	62.67	Anatase, rutile
0.3	59.67	Anatase, rutile
0.5	53.77	Anatase, rutile, Al <sub>2</sub> O <sub>3</sub>

105 nm. These observation results indicate that the injected Ti and Al<sub>2</sub>O<sub>3</sub> powders successfully vaporized at the high flame temperature and subsequently synthesized Al-doped TiO<sub>2</sub> nanoparticles via the recombination of vaporized Ti, O and Al atoms in the thermal plasma environment.

XRD powder patterns for the nanoparticles fabricated at various Al<sub>2</sub>O<sub>3</sub>/Ti mass ratios are presented in Figure 3. All the peak intensity of powder diffraction was normalized by anatase (101). The experimental results suggested that most of the diffraction peaks could be designated as the presence of anatase and rutile phases. However, the diffraction peaks standing for Al<sub>2</sub>O<sub>3</sub> appeared as Al<sub>2</sub>O<sub>3</sub>/Ti = 0.5, based on  $2\theta = 35.15^\circ, 43.35^\circ, 52.5^\circ, \text{ and } 57.5^\circ$  that are indexed to the Al<sub>2</sub>O<sub>3</sub> diffraction pattern. These observations are consistent with our previous work [25] and suggest that at Al<sub>2</sub>O<sub>3</sub>/Ti = 0.5 loading, the thermal plasma was less effective to vaporize the Al<sub>2</sub>O<sub>3</sub> powders and to induce the interactions between Ti, O, and Al atoms. Moreover, the relative content of anatase, depicted with the  $f_A$  value (Table 1), noticeably reduced with increasing Al<sub>2</sub>O<sub>3</sub>/Ti due to consequent transformation into rutile at an elevating temperature [27]. Notably, the TiO<sub>2</sub> was fabricated at a fixed plasma power of 6 kW. The plasma temperature change at various Al<sub>2</sub>O<sub>3</sub>/Ti ratios should be small and may not markedly influence the transformation of anatase into rutile. The enhancement in transformation of anatase into rutile may also attribute to the increase in Al doping [19, 21, 22, 28].

Figure 4 demonstrates the UV-visible spectra of the Al-doped TiO<sub>2</sub> nanoparticles synthesized at various Al<sub>2</sub>O<sub>3</sub>/Ti mass ratios over the wavelength range of 300–800 nm. The commercial Degussa P-25 photocatalyst was also tested for comparison. The experimental results showed that the absorption edge was at  $\sim 390\ \text{nm}$  for P-25 photocatalyst. The TiO<sub>2</sub> nanoparticles synthesized in thermal plasma at the Al<sub>2</sub>O<sub>3</sub>/Ti mass ratio of 0 to 0.3 possessed an absorption edge at  $\sim 400\ \text{nm}$ . The absorption spectra of Al-doped TiO<sub>2</sub> slightly shifted from UV to VL region with reference to an increase in Al<sub>2</sub>O<sub>3</sub>/Ti mass ration can be assigned to the band gap narrowing relation to the interstitial Al species in the TiO<sub>2</sub> crystal [19, 29, 30]. Especially, TiO<sub>2</sub> synthesized at Al<sub>2</sub>O<sub>3</sub>/Ti = 0 also had band gap absorption at  $\sim 400\ \text{nm}$ , which was comparable to that of Al-doped TiO<sub>2</sub> formed at Al<sub>2</sub>O<sub>3</sub>/Ti = 0.1. The extent of red shift and band broadening may be attributed to the presence of oxygen vacancies in TiO<sub>2</sub> crystal formed in the high-temperature plasma flame. Numerous studies have shown the appearance of the visible-light activity was attributed to the newly formed oxygen vacancy state in the TiO<sub>2</sub> band structure [24, 31]. Further

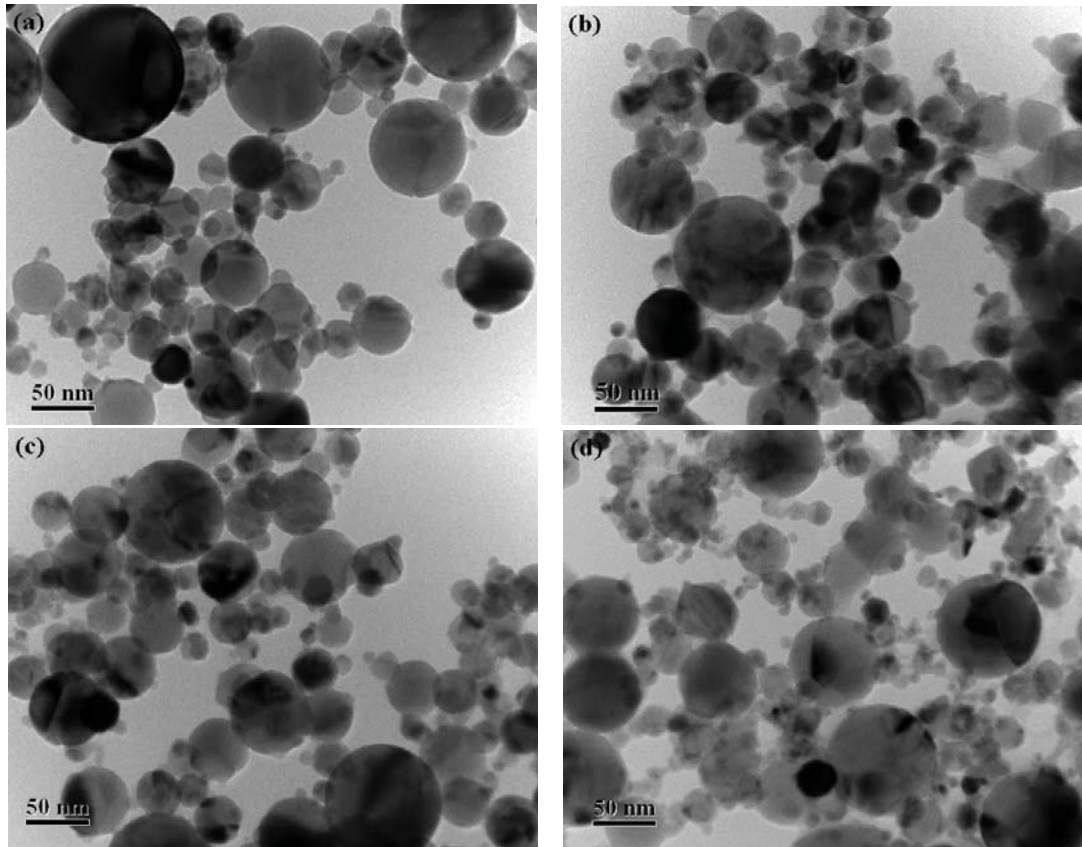


FIGURE 2: TEM images of  $\text{TiO}_2$  nanoparticles synthesized at  $\text{Al}_2\text{O}_3/\text{Ti}$  mass ratio of (a) 0, (b) 0.1, (c) 0.3, and (d) 0.5.

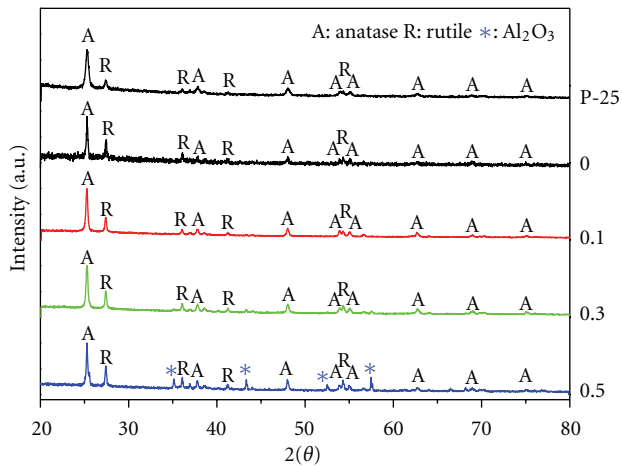


FIGURE 3: XRD patterns of  $\text{TiO}_2$  nanoparticles synthesized at  $\text{Al}_2\text{O}_3/\text{Ti} = 0$  to 0.5 and Degussa P-25.

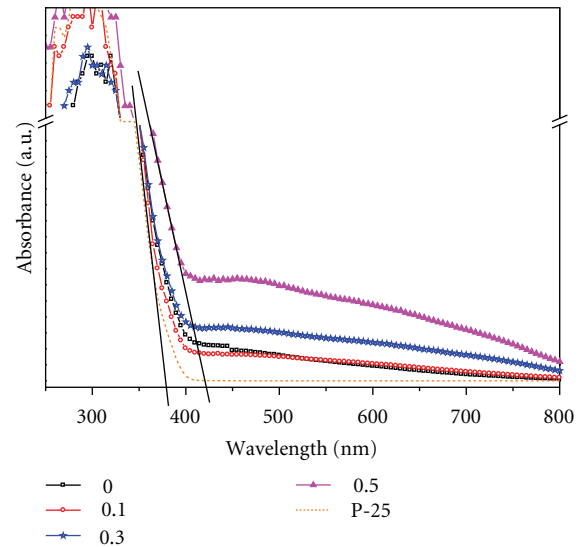


FIGURE 4: Optical absorption spectra of synthesized Al-doped  $\text{TiO}_2$  and commercial P-25 photocatalyst.

evidences and explanation are presented based on XPS analysis. In contrast, the Al-doped  $\text{TiO}_2$  synthesized at  $\text{Al}_2\text{O}_3/\text{Ti} = 0.5$  showed strong absorption in the VL range, suggesting that the extent of red shift and broadening was greatly dependent on  $\text{Al}_2\text{O}_3$  concentrations in the plasma environment.

The XPS spectra of  $\text{Ti}_{2p}$  for the synthesized  $\text{TiO}_2$  nanoparticles are shown in Figure 5. The  $\text{Al}_{2p}$  spectra for the

synthesized  $\text{TiO}_2$  nanoparticles at a  $\text{Al}_2\text{O}_3/\text{Ti}$  mass ratio of 0.1, 0.3, and 0.5 are shown in Figure 6. The  $\text{Ti}_{2p}$  XPS spectra acquired from  $\text{TiO}_2$  fabricated at various  $\text{Al}_2\text{O}_3/\text{Ti}$  mass ratios were deconvoluted into four peaks within 456.4–464.5 eV, including  $\text{Ti}_{2p_{1/2}}^{4+}$ ,  $\text{Ti}_{2p_{1/2}}^{3+}$ ,  $\text{Ti}_{2p_{3/2}}^{4+}$ , and  $\text{Ti}_{2p_{3/2}}^{3+}$ . These

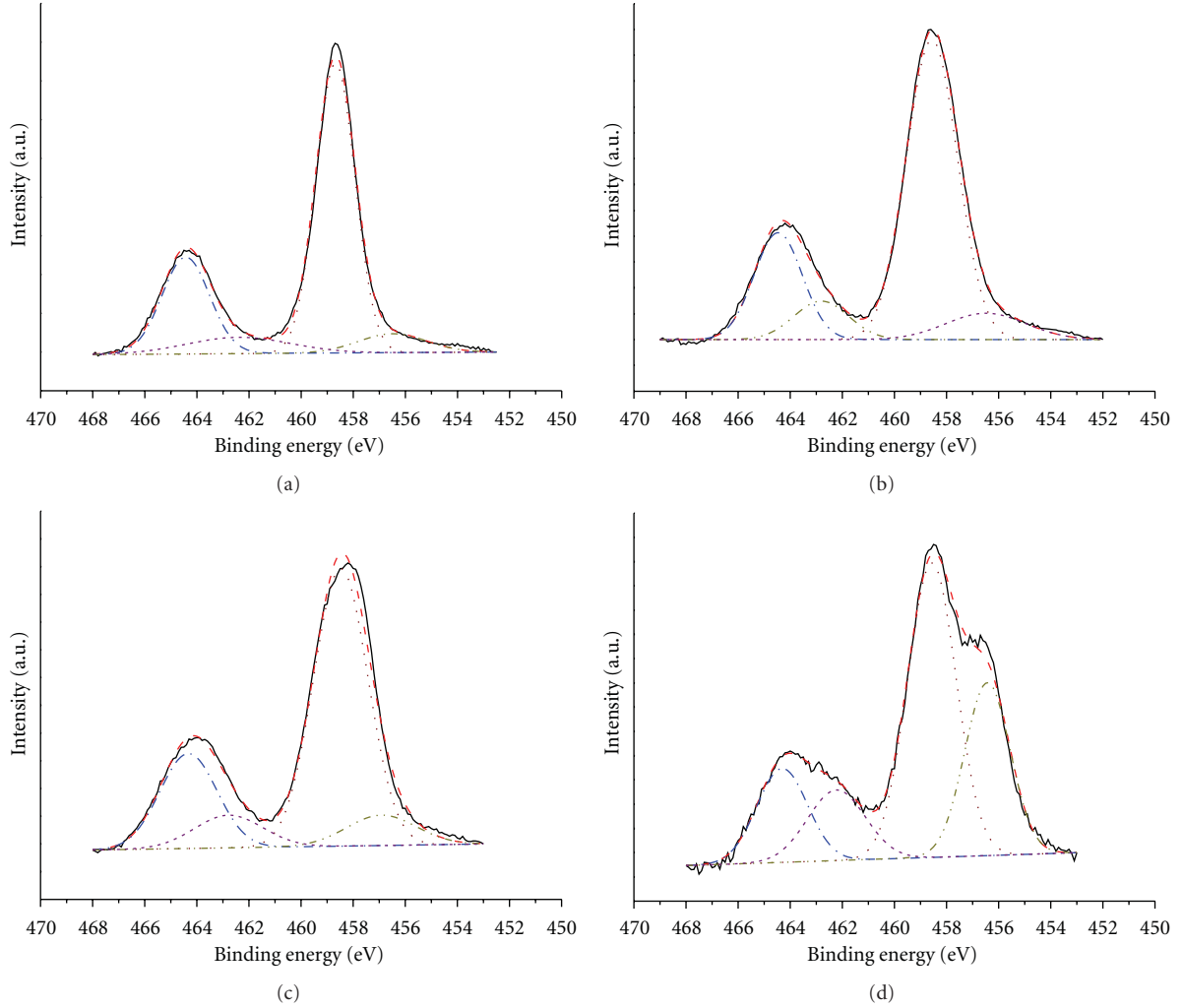


FIGURE 5:  $Ti_{2p}$  XPS spectra of  $TiO_2$  synthesized at  $Al_2O_3/Ti$  mass ratio of (a) 0, (b) 0.1, (c) 0.3, and (d) 0.5.

peaks are indications to the presence of  $TiO_2$  ( $Ti_{2p_{1/2}}^{4+}$  and  $Ti_{2p_{3/2}}^{4+}$ ) and  $Ti_2O_3$  ( $Ti_{2p_{1/2}}^{3+}$  and  $Ti_{2p_{3/2}}^{3+}$ ), respectively [32]. For the Al-doped  $TiO_2$ , the  $Al_{2p}$  peaks at a binding energy of 75.5 eV can be attributed to the presence of  $Al^{3+}$ . The results suggested that the  $Al^{3+}$  content enhanced with an increase in  $Al_2O_3$  addition. The calculated  $Ti^{3+}/(Ti^{3+} + Ti^{4+})$  ratios for Al-doped  $TiO_2$  at  $Al_2O_3/Ti = 0, 0.1, 0.3,$  and  $0.5$  were 3.1, 17.1, 17.5, and 33.2%, respectively, based on the deconvoluted peak area. These data indicated that  $Ti^{3+}$  concentration greatly enhanced with increasing  $Al_2O_3$  addition owing to the transformation of  $TiO_2$  into  $Ti_2O_3$ . We suspected that  $Ti^{4+}/Al^{3+}$  ionic substitution may take place during the Al doping. If this assumption held, when  $Ti^{4+}$  (ionic radius = 0.061 nm) is substituted by  $Al^{3+}$  (ionic radius = 0.053 nm) from  $TiO_2$  crystal, the lattice mismatch occurs as a result of that the ionic radius of  $Ti^{4+}$  is larger than that of  $Al^{3+}$ . To atone for the smaller ionic radius of  $Al^{3+}$ , a Ti species having an ionic radius larger than  $Ti^{4+}$  is needed. Consequently,  $Ti^{4+}$  is reduced to  $Ti^{3+}$  (ionic radius = 0.067 nm). The observed  $Ti^{3+}$  peaks in the present study are consistent with Steveson et al. [33] and our previous work [25]. In addition,

TABLE 2: Atomic percentage of synthesized  $TiO_2$  nanoparticles based on XPS examinations.

$Al_2O_3/Ti$ mass ratio	Composition (at.%)			
	O	Al	Ti	Cu
0	74.17	0	23.25	2.57
0.1	65.95	6.77	25.33	1.95
0.3	62.96	10.45	23.13	3.46
0.5	57.83	22.09	15.44	4.63

the formal charge generated by the substitution of  $Ti^{4+}$  with  $Al^{3+}$  can also be compensated via the formation of  $O^-$  from  $O^{2-}$ , which resulted in the oxygen vacancies found in Al-doped  $TiO_2$  [21, 33, 34].

Notably, about 1.95–4.62 at.% Cu was found in the formed Al-doped  $TiO_2$  based on the XPS analysis (Table 2). The Cu impurity was from the vaporization of plasma torch made of Cu alloy under the high-temperature plasma environment. Associated with the results from the UV-visible

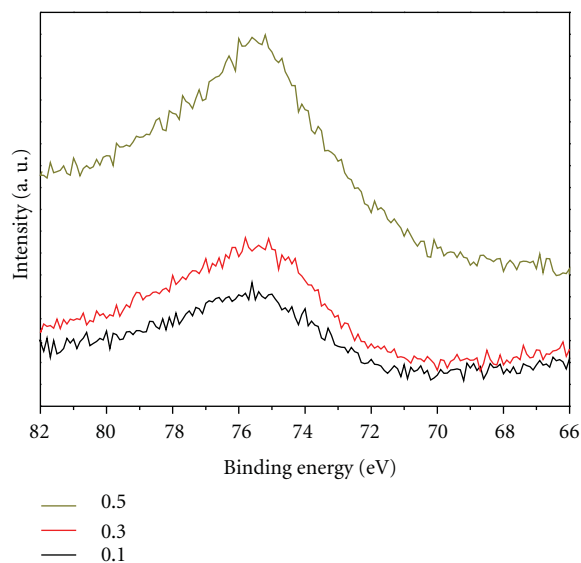


FIGURE 6:  $\text{Al}_{2p}$  XPS spectra of  $\text{TiO}_2$  produced at  $\text{Al}_2\text{O}_3/\text{Ti}$  mass ratio of 0.1, 0.3, and 0.5.

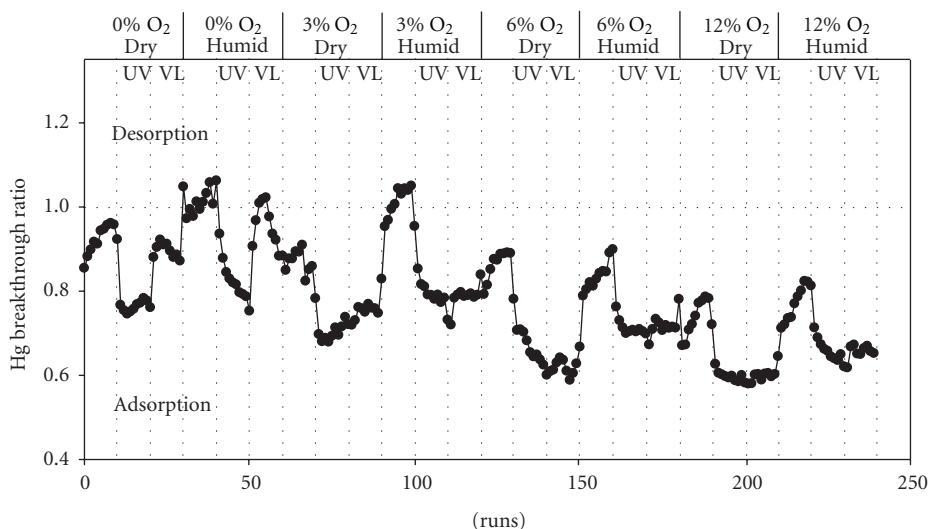


FIGURE 7: Hg breakthrough ratio of Al-doped  $\text{TiO}_2$  in the continuous adsorption experiment under various test conditions.

analysis, the doped Cu and the oxygen vacancy may synergistically contribute to the observed red shift in the UV-visible absorption spectrum for the non-Al-doped  $\text{TiO}_2$  (i.e.,  $\text{Al}_2\text{O}_3/\text{Ti} = 0$ ). Nevertheless, Zhang et al. suggested that Cu content  $< 38$  at.% in  $\text{TiO}_2$  had negligible effects on the  $\text{Ti}_{2p}$  binding energy of XPS examinations [35]. Therefore, isomorphous substitution due to Al doping into  $\text{TiO}_2$  crystal should be the major contribution of the increasing  $\text{Ti}^{3+}$ . The red shift in the absorption spectra of  $\text{TiO}_2$  nanoparticles thus primarily was attributed to the Al doping and generated oxygen vacancy (Figure 4).

The  $\text{Hg}^0$  adsorption breakthrough results for Al-doped  $\text{TiO}_2$  nanoparticles synthesized at  $\text{Al}_2\text{O}_3/\text{Ti} = 0.5$  are shown in Figure 7. The experimental parameters included  $\text{O}_2$  concentration, humidity, and the type of light sources. These parameters were tested alternately by gradually increasing the

$\text{O}_2$  concentration from 0% to 12% combined with introducing  $\text{H}_2\text{O}$  (20% relative humidity) and UV/VL irradiation to the photocatalytic reactor. The experimental results showed that  $\text{Hg}^0$  capture was very small with rapid breakthrough at the 0%  $\text{O}_2$ , dry ( $\text{H}_2\text{O} < 0.1$  vol%), and dark condition (runs 0–10 in Figure 7), manifesting that the synthesized Al-doped  $\text{TiO}_2$  ( $\text{Al}_2\text{O}_3/\text{Ti} = 0.5$ ) was less effective in removal of  $\text{Hg}^0$  under the test condition. This result was anticipated because  $\text{Hg}^0$  appeared to the main Hg species at the 0%  $\text{O}_2$ , dry, and dark condition and was not easy to form a strong binding with the surface of  $\text{TiO}_2$ . However, an increase in the  $\text{Hg}^0$  capture to 25% was apparently observed when UV irradiation was applied (breakthrough down to approximately 0.75; runs 11–20). The significant enhancement in  $\text{Hg}^0$  removal for Al-doped  $\text{TiO}_2$  nanoparticles under UV irradiation is a strong indication that this sample had

a good photocatalytic potential to transform  $\text{Hg}^0$  into  $\text{Hg}^{2+}$  that enhanced the adsorption onto Al-doped  $\text{TiO}_2$ . It is also noteworthy that without the presence of  $\text{O}_2$ , VL was less effective in photocatalytic oxidation than UV (runs 21–30). In addition, a significant decrease in  $\text{Hg}^0$  capture was observed at the humid condition (runs 31–60). This result suggests that  $\text{H}_2\text{O}$  competitively adsorbs onto the  $\text{TiO}_2$  active sites, causing the reemission of adsorbed Hg species, which can be  $\text{Hg}^0$  or  $\text{Hg}^{2+}$  needed to be further examined. The experimental results presented here are in agreement with those found in earlier studies [6, 7, 24, 36]. Li and Wu reported that the physically adsorbed  $\text{Hg}^0$  can be desorbed from the surface of a  $\text{SiO}_2$ - $\text{TiO}_2$  composite by water vapor at high concentration, which suggested that  $\text{Hg}^0$  is only weakly adsorbed on the sorbent surface [6]. Dissimilar to  $\text{H}_2\text{O}$ ,  $\text{O}_2$  notably improved the adsorption of  $\text{Hg}^0$ ; increasing  $\text{O}_2$  concentration strongly enhanced the  $\text{Hg}^0$  capture of Al-doped  $\text{TiO}_2$  up to 40% (equivalent to breakthrough of 0.6; Figure 7). It is noteworthy that when  $\text{O}_2$  was > 6%,  $\text{Hg}^0$  capture was similar for Al-doped  $\text{TiO}_2$  under either UV or VL irradiation (runs 131–150 and 221–240). These data not only revealed the importance of  $\text{O}_2$  in enhancing  $\text{Hg}^0$  capture, but also verified the visible-light activity of the synthesized Al-doped  $\text{TiO}_2$  nanoparticles on  $\text{Hg}^0$  oxidation/adsorption.

#### 4. Conclusion

Al-doped  $\text{TiO}_2$  nanoparticles were successfully synthesized in a single step using Ti powders,  $\text{Al}_2\text{O}_3$  powders, and  $\text{O}_2$  by a nontransferred plasma torch system.  $\text{TiO}_2$  nanoparticles formed at  $\text{Al}_2\text{O}_3/\text{Ti}$  mass ratios 0 to 0.5 were approximately between 10 and 105 nm. The crystal phases of the formed  $\text{TiO}_2$  nanoparticles were mainly in anatase and rutile forms. However, increasing the  $\text{Al}_2\text{O}_3$  addition caused the ratio of anatase to rutile decreased. The presence of oxygen vacancy and the substitution of  $\text{Ti}^{4+}$  with  $\text{Al}^{3+}$  were suspected to cause the slight red shift in the absorption edge to lower energy due to band gap narrowing. Al doping and oxygen vacancy in the  $\text{TiO}_2$  crystal may also result in the phase transformation from  $\text{TiO}_2$  to  $\text{Ti}_2\text{O}_3$ . Hg breakthrough results showed that the  $\text{Hg}^0$  removal with formed Al-doped  $\text{TiO}_2$  in a dry condition was greater than that in a humid condition when light irradiation was applied. Hg capture was also found to be markedly enhanced by increasing  $\text{O}_2$  concentration. Nevertheless,  $\text{H}_2\text{O}$  showed deteriorating effects on the adsorption of Hg through competition for active sites on the Al-doped  $\text{TiO}_2$  surface. Results presented here suggest that  $\text{Hg}^0$  removal using synthesized Al-doped  $\text{TiO}_2$  nanoparticles may be greatly affected by the extent of catalytic transformation of  $\text{Hg}^0$  into  $\text{Hg}^{2+}$  and amphoteric (hydrophilic-hydrophobic) surface properties of Al-doped  $\text{TiO}_2$ .

We envision that the photocatalyst can be successfully used to capture Hg from coal-derived flue gas. Nevertheless, it is imperative to note that this study employed gas streams consisting of  $\text{Hg}^0$  in a moisture-oxygen-nitrogen mix. Coal-derived flue gas is a complex mixture also containing fly ash particles, moisture, CO, and many acid gases. For example, a typical untreated flue gas derived from the combustion of

a US low sulfur eastern bituminous coal can contain 5–7%  $\text{H}_2\text{O}$ , 3–4%  $\text{O}_2$ , 15–16%  $\text{CO}_2$ , 1 ppbv total Hg, 20 ppm CO, 10 ppm hydrocarbons, 100 ppm HCl, 800 ppm  $\text{SO}_2$ , 10 ppm  $\text{SO}_3$ , 500 ppm  $\text{NO}_x$ , and balance  $\text{N}_2$  [9–11]. The influences of the flue gas components on Hg removal using  $\text{TiO}_2$  photocatalysts are thus highly needed to be further investigated.

#### Acknowledgments

This paper was supported by National Science Council of Taiwan (NSC95-2622-E-327-002-CC3) and Taiwan Plasma Corp., Kaohsiung, Taiwan. The authors acknowledge Mr. Chin-Cheng Ho, Taiwan Plasma Corp. and Dr. Hsunling Bai, National Chiao Tung University, Taiwan, for their technical assistance. The authors also thank the two anonymous reviewers for their valuable comments and suggestions to improve the quality of the paper.

#### References

- [1] E. G. Pacyna, J. M. Pacyna, K. Sundseth et al., “Global emission of mercury to the atmosphere from anthropogenic sources in 2005 and projections to 2020,” *Atmospheric Environment*, vol. 44, no. 20, pp. 2487–2499, 2010.
- [2] C. Y. Wu, T. G. Lee, G. Tyree, E. Arar, and P. Biswas, “Capture of mercury in combustion systems by in situ-generated titania particles with UV irradiation,” *Environmental Engineering Science*, vol. 15, no. 2, pp. 137–148, 1998.
- [3] E. Pitoniak, C. Y. Wu, D. Londeree et al., “Nanostructured silica-gel doped with  $\text{TiO}_2$  for mercury vapor control,” *Journal of Nanoparticle Research*, vol. 5, no. 3–4, pp. 281–292, 2003.
- [4] P. Biswas and C. Y. Wu, “Nanoparticles and the environment,” *Journal of the Air and Waste Management Association*, vol. 55, no. 6, pp. 708–746, 2005.
- [5] E. Pitoniak, C. Y. Wu, D. W. Mazyck, K. W. Powers, and W. Sigmund, “Adsorption enhancement mechanisms of silica-titania nanocomposites for elemental mercury vapor removal,” *Environmental Science and Technology*, vol. 39, no. 5, pp. 1269–1274, 2005.
- [6] Y. Li and C. Y. Wu, “Role of moisture in adsorption, photocatalytic oxidation, and reemission of elemental mercury on a  $\text{SiO}_2$ - $\text{TiO}_2$  nanocomposite,” *Environmental Science and Technology*, vol. 40, no. 20, pp. 6444–6448, 2006.
- [7] Y. Li and C. Y. Wu, “Kinetic study for photocatalytic oxidation of elemental mercury on a  $\text{SiO}_2$ - $\text{TiO}_2$  nanocomposite,” *Environmental Engineering Science*, vol. 24, no. 1, pp. 3–12, 2007.
- [8] E. J. Granite, W. P. King, D. C. Stanko, and H. W. Pennline, “Implications of mercury interactions with band-gap semiconductor oxides,” *Main Group Chemistry*, vol. 7, no. 3, pp. 227–237, 2008.
- [9] E. J. Granite, H. W. Pennline, and J. S. Hoffman, “Effects of photochemical formation of mercuric oxide,” *Industrial and Engineering Chemistry Research*, vol. 38, no. 12, pp. 5034–5037, 1999.
- [10] E. J. Granite and H. W. Pennline, “Photochemical removal of mercury from flue gas,” *Industrial and Engineering Chemistry Research*, vol. 41, no. 22, pp. 5470–5476, 2002.
- [11] E. J. Granite, M. C. Freeman, R. A. Hargis, W. J. O’Dowd, and H. W. Pennline, “The thief process for mercury removal from flue gas,” *Journal of Environmental Management*, vol. 84, no. 4, pp. 628–634, 2007.

- [12] H. Yamashita, M. Harada, J. Misaka, M. Takeuchi, K. Ikeue, and M. Anpo, "Degradation of propanol diluted in water under visible light irradiation using metal ion-implanted titanium dioxide photocatalysts," *Journal of Photochemistry and Photobiology A*, vol. 148, no. 1–3, pp. 257–261, 2002.
- [13] C. Di Valentin, G. Pacchioni, A. Selloni, S. Livraghi, and E. Giamello, "Characterization of paramagnetic species in N-doped TiO<sub>2</sub> powders by EPR spectroscopy and DFT calculations," *Journal of Physical Chemistry B*, vol. 109, no. 23, pp. 11414–11419, 2005.
- [14] S. P. Qiu and S. J. Kalita, "Synthesis, processing and characterization of nanocrystalline titanium dioxide," *Materials Science and Engineering A*, vol. 435–436, pp. 327–332, 2006.
- [15] M. Kanna and S. Wongnawa, "Mixed amorphous and nanocrystalline TiO<sub>2</sub> powders prepared by sol-gel method: characterization and photocatalytic study," *Materials Chemistry and Physics*, vol. 110, no. 1, pp. 166–175, 2008.
- [16] S. M. Oh, S. S. Kim, J. E. Lee, T. Ishigaki, and D. W. Park, "Effect of additives on photocatalytic activity of titanium dioxide powders synthesized by thermal plasma," *Thin Solid Films*, vol. 435, no. 1–2, pp. 252–258, 2003.
- [17] X. H. Wang, J. G. Li, H. Kamiyama, and T. Ishigaki, "Fe-doped TiO<sub>2</sub> nanopowders by oxidative pyrolysis of organometallic precursors in induction thermal plasma: synthesis and structural characterization," *Thin Solid Films*, vol. 506–507, pp. 278–282, 2006.
- [18] J. G. Li, X. H. Wang, H. Kamiyama, T. Ishigaki, and T. Sekiguchi, "RF plasma processing of Er-doped TiO<sub>2</sub> luminescent nanoparticles," *Thin Solid Films*, vol. 506–507, pp. 292–296, 2006.
- [19] J. E. Lee, S. M. Oh, and D. W. Park, "Synthesis of nano-sized Al doped TiO<sub>2</sub> powders using thermal plasma," *Thin Solid Films*, vol. 457, no. 1, pp. 230–234, 2004.
- [20] X. W. Zhang, M. H. Zhou, and L. C. Lei, "Preparation of anatase TiO<sub>2</sub> supported on alumina by different metal organic chemical vapor deposition methods," *Applied Catalysis A*, vol. 282, no. 1–2, pp. 285–293, 2005.
- [21] C. Z. Li, L. Y. Shi, D. M. Xie, and H. Du, "Morphology and crystal structure of Al-doped TiO<sub>2</sub> nanoparticles synthesized by vapor phase oxidation of titanium tetrachloride," *Journal of Non-Crystalline Solids*, vol. 352, no. 38–39, pp. 4128–4135, 2006.
- [22] M. Q. Wang, B. Gong, X. Yao, Y. Wang, and R. N. Lamb, "Preparation and microstructure properties of Al-doped TiO<sub>2</sub>-SiO<sub>2</sub> gel-glass film," *Thin Solid Films*, vol. 515, no. 4, pp. 2055–2058, 2006.
- [23] Y. J. Choi, Z. Seeley, A. Bandyopadhyay, S. Bose, and S. A. Akbar, "Aluminum-doped TiO<sub>2</sub> nano-powders for gas sensors," *Sensors and Actuators B*, vol. 124, no. 1, pp. 111–117, 2007.
- [24] C. Y. Tsai, H. C. Hsi, H. Bai, K. S. Fan, and C. Chen, "TiO<sub>2-x</sub> nanoparticles synthesized using He/Ar thermal plasma and their effectiveness on low-concentration mercury vapor removal," *Journal of Nanoparticle Research*, vol. 13, no. 10, pp. 4739–4748, 2011.
- [25] C. Y. Tsai, H. C. Hsi, H. Bai, K. S. Fan, and H. D. Sun, "Novel synthesis of Al-doped TiO<sub>2</sub> nanoparticles by direct combination of aluminum, titanium and oxygen using thermal plasma torch," *Japan Journal of Applied Physics*, vol. 51, p. 01AL01-1-6, 2012.
- [26] R. A. Spurr, "Quantitative analysis of anatase-rutile mixtures with an X-ray diffractometer," *Analytical Chemistry*, vol. 29, no. 5, pp. 760–762, 1957.
- [27] S. Karvinen, "The effects of trace elements on the crystal properties of TiO<sub>2</sub>," *Solid State Sciences*, vol. 5, no. 5, pp. 811–819, 2003.
- [28] M. L. Taylor, G. E. Morris, and R. S. Smart, "Influence of aluminum doping on titania pigment structural and dispersion properties," *Journal of Colloid and Interface Science*, vol. 262, no. 1, pp. 81–88, 2003.
- [29] B. Y. Lee, S. H. Park, M. S. Kang, S. C. Lee, and S. J. Choung, "Preparation of Al/TiO<sub>2</sub> nanometer photo-catalyst film and the effect of H<sub>2</sub>O addition on photo-catalytic performance for benzene removal," *Applied Catalysis A*, vol. 253, no. 2, pp. 371–380, 2003.
- [30] H. K. Shon, D. L. Cho, S. H. Na, J. B. Kim, H. J. Park, and J. H. Kim, "Development of a novel method to prepare Fe- and Al-doped TiO<sub>2</sub> from wastewater," *Journal of Industrial and Engineering Chemistry*, vol. 15, no. 4, pp. 476–482, 2009.
- [31] I. Nakamura, N. Negishi, S. Kutsuna, T. Ihara, S. Sugihara, and K. Takeuchi, "Role of oxygen vacancy in the plasma-treated TiO<sub>2</sub> photocatalyst with visible light activity for NO removal," *Journal of Molecular Catalysis A*, vol. 161, no. 1–2, pp. 205–212, 2000.
- [32] C. T. Wang and S. H. Ro, "Nanoparticle iron-titanium oxide aerogels," *Materials Chemistry and Physics*, vol. 101, no. 1, pp. 41–48, 2007.
- [33] M. Steveson, T. Bredow, and A. R. Gerson, "MSINDO quantum chemical modelling study of the structure of aluminium-doped anatase and rutile titanium dioxide," *Physical Chemistry Chemical Physics*, vol. 4, no. 2, pp. 358–365, 2002.
- [34] U. Gesenhues and T. Rentschler, "Crystal growth and defect structure of Al<sup>3+</sup>-doped rutile," *Journal of Solid State Chemistry*, vol. 143, no. 2, pp. 210–218, 1999.
- [35] W. J. Zhang, Y. Li, S. L. Zhu, and F. H. Wang, "Copper doping in titanium oxide catalyst film prepared by dc reactive magnetron sputtering," *Catalysis Today*, vol. 93–95, pp. 589–594, 2004.
- [36] Y. Li, P. Murphy, and C. Y. Wu, "Removal of elemental mercury from simulated coal-combustion flue gas using a SiO<sub>2</sub>-TiO<sub>2</sub> nanocomposite," *Fuel Processing Technology*, vol. 89, no. 6, pp. 567–573, 2008.

## Research Article

# Ta/TiO<sub>2</sub>- and Nb/TiO<sub>2</sub>-Mixed Oxides as Efficient Solar Photocatalysts: Preparation, Characterization, and Photocatalytic Activity

Hussein Znad, Ming H. Ang, and Moses O. Tade

Chemical Engineering Department, Curtin University, GPO Box U 1987, Perth, WA 6845, Australia

Correspondence should be addressed to Hussein Znad, h.znad@curtin.edu.au

Received 7 December 2011; Accepted 15 December 2011

Academic Editor: Jiaguo Yu

Copyright © 2012 Hussein Znad et al. This is an open access article distributed under the Creative Commons Attribution License, which permits unrestricted use, distribution, and reproduction in any medium, provided the original work is properly cited.

Ta/TiO<sub>2</sub>- and Nb/TiO<sub>2</sub>-mixed oxides photocatalysts were prepared by simple impregnation method at different TiO<sub>2</sub> : Nb or Ta mass ratios of 1 : 0.1, 1 : 0.5, and 1 : 1, followed by calcination at 500°C. The prepared powders have been characterized by XRD, XPS, UV-Vis spectra, and SEM. The photocatalytic activity was evaluated under natural solar light for decolorization and mineralization of azo dye Orange II solution. The results showed that Nb/TiO<sub>2</sub>- and Ta/TiO<sub>2</sub>-mixed oxides have higher activity than the untreated TiO<sub>2</sub> under natural solar light. The maximum activity was observed for Nb/TiO<sub>2</sub> sample (at mass ratio of 1 : 0.1), which is characterized by the smallest crystalline size (17.79 nm). Comparing with the untreated TiO<sub>2</sub>, the solar decolorization and mineralization rates improved by about 140% and 237%, respectively, and the band gap reduced to 2.80 eV. The results suggest that the crystal lattices of TiO<sub>2</sub> powder are locally distorted by incorporating Nb<sup>5+</sup> species into TiO<sub>2</sub>, forming a new band energy structure, which is responsible for the absorption in the visible region. Unlike Ta/TiO<sub>2</sub>, the Nb/TiO<sub>2</sub>-mixed oxides can prevent the grain size growth of the treated TiO<sub>2</sub>, which is important to achieve high solar photoactivity.

## 1. Introduction

Titanium dioxide (TiO<sub>2</sub>) is nontoxic, efficient photo-catalyst, chemically stable, and relatively inexpensive. Although TiO<sub>2</sub> is the most popular photocatalytic material, it has not been applied widely in the field of environmental pollution control under solar light. The band gap ( $E_g$ ) of TiO<sub>2</sub> anatase is ~3.2 eV and lies in the UV range so that only 5–8% of sunlight photons have the required energy to activate the catalyst [1, 2]. This relatively large band gap has significantly limited its application, particularly under solar and/or visible light. An effective way to improve the TiO<sub>2</sub> photocatalytic activity is to introduce foreign metal ions as dopants into its lattice. Depending on the dopant type and concentration, the band gap of TiO<sub>2</sub> can be tailored to extend the photoresponsiveness into the visible light region. Usually, the UV activity of undoped TiO<sub>2</sub> is much greater than the visible light activity of the doped material. Therefore, for solar applications, the photocatalysts should be tested under simulated solar irradiation or under real sun conditions [3].

TiO<sub>2</sub> doped with Tantalum (Ta) and niobium (Nb) by sol-gel method has been widely used in gas sensing film application [4–6]. Generally those metal dopants (Ta and Nb) are used in sensor applications to inhibit the TiO<sub>2</sub> phase transformation from anatase to rutile and to hinder grain growth during heating. Niobium oxide and, in particular, its most stable form, Nb<sub>2</sub>O<sub>5</sub>, is an interesting semiconductor with a band gap of about 3.9 eV (decreasing to about 3.5 eV in the amorphous state), with a high dielectric constant and high index of refraction, which has found important applications in electronics and optical applications, including thin films (antireflective coatings, solar control, etc.) [7].

Atashbar et al. [8] prepared thin films of TiO<sub>2</sub> doped with niobium oxide, for use in oxygen sensing applications. Thick film gas sensors made by Nb- or Ta-doped TiO<sub>2</sub> have also been prepared and investigated for atmospheric pollutant monitoring [5]. Vanadium and tantalum-doped titanium oxide (TiTaV) as a novel material for gas sensing has been prepared by Carotta et al. [4]. Furubayashi et al. [9] pointed out that Nb-doped anatase TiO<sub>2</sub> film has excellent electrical conductivity and transparency.

TABLE 1: Composition of prepared samples.

Sample reference	TiO <sub>2</sub> : Nb (mass ratio)	Nb molar %	Sample reference	TiO <sub>2</sub> : Ta (mass ratio)	Ta molar %
Pure TiO <sub>2</sub>	1 : 0	0	Pure TiO <sub>2</sub>	1 : 0	0
TNb1	1 : 0.1	2.9	TTa1	1 : 0.1	1.8
TNb2	1 : 0.5	13	TTa2	1 : 0.5	8.3
TNb3	1 : 1	23	TTa3	1 : 1	15.3

Technological interest in Nb-doped TiO<sub>2</sub> derives from the fact that Nb doping leads to enhanced photocatalytic activity in the destruction of organochloride pollutants such as dichlorobenzene [10]. Some investigators [11–13] reported that photocatalytic activity of Nb-doped TiO<sub>2</sub> was much better than that of pure TiO<sub>2</sub>. Castro et al. [11] prepared Nb-doped TiO<sub>2</sub> by a simple, lowcost, and low-temperature hydrothermal technique. The Nb-doped TiO<sub>2</sub> was more active than undoped TiO<sub>2</sub> for diquat degradation under UV light irradiation. Yang et al. [14] prepared micrometer-sized Nb-doped TiO<sub>2</sub> porous spheres by ultrasonic spray pyrolysis method. Comparing with pure TiO<sub>2</sub>, the prepared Nb-doped TiO<sub>2</sub> enhanced photocatalytic activity for the photodegradation of aqueous methylene blue solution under both visible and solar light irradiation. The enhanced photocatalytic activities of Ta codoped TiO<sub>2</sub> thin films under visible light have also been reported by Obata et al. [15].

However, to our knowledge, the photocatalytic activity of Nb/TiO<sub>2</sub>- and Ta/TiO<sub>2</sub>-mixed oxides for wastewater treatment under natural solar light, has not yet been reported. Furthermore, modifying the commercial TiO<sub>2</sub> (Degussa P25), which is relatively cheap and commercially available, to improve its solar photoactivity are an interesting subject.

Very limited attempts were found recently in the literature to improve the Degussa P25 photoactivity [16, 17]; in both cases, the photocatalyst activity was tested only under UV light. For photocatalytic hydrogen production, Yu et al. successfully improved the commercial P25 TiO<sub>2</sub> by impregnation with copper nitrate followed by calcinations at 350°C [18], and by a simple precipitation method using Ni (OH)<sub>2</sub> clusters [19]. Zhao et al. [20] fabricated ordered titanate nanoribbon (TNR)/SnO<sub>2</sub> films by electrophoretic deposition (EPD) using hydrothermally prepared titanate (P25 Degussa) as a precursor. The photocatalytic activity was evaluated by decolorization of RhB aqueous solution under UV irradiation. Shang et al. [21] prepared N-doped TiO<sub>2</sub> powder by annealing commercial TiO<sub>2</sub> (P25) under an NH<sub>3</sub> flow at 550°C. 4-chlorophenol decomposition was used to evaluate the photocatalytic activity under the visible light irradiation. Qi et al. [22] and Yu et al. [23] used the commercial P25 to prepare Pt/TiO<sub>2</sub> catalysts and CdS-sensitized Pt/P25 for photocatalytic hydrogen production. Recently, Znad and Kawase [1] successfully doped the commercial TiO<sub>2</sub> (Degussa P25) with a nonmetal dopant (sulfur) and improved its solar photo-catalytic activity for decolourizing polluted wastewater.

In the present work, with the aim of developing more efficient and cost-effective solar photocatalyst and to investigate the metal ions (such as Nb and Ta) influence, the Ta/TiO<sub>2</sub>- and Nb/TiO<sub>2</sub>-mixed oxides photocatalysts have been

prepared by simple impregnation method using the well-known TiO<sub>2</sub> (Degussa P25) as a Ti precursor and, respectively, niobium oxide (Nb<sub>2</sub>O<sub>5</sub>) and tantalum oxide (Ta<sub>2</sub>O<sub>5</sub>) as a metal oxides. Nb and Ta ions were chosen since these elements have ionic radii similar to that of Ti, so that they could replace it in a substitutional solution with negligible distortion of the lattice. Concentrations higher than the solubility limits have been chosen to study the possible segregation of a mixed oxide.

This work was mainly devoted to find out whether the metal ions (Nb and Ta) can improve the photocatalytic activity (or properties) of TiO<sub>2</sub> under natural solar light, beside its well-known activity in film sensing application.

## 2. Experimental

*2.1. Preparation of Ta/TiO<sub>2</sub>- and Nb/TiO<sub>2</sub>-Mixed Oxides Photocatalyst.* The Ta/TiO<sub>2</sub>- and Nb/TiO<sub>2</sub>-mixed oxides photocatalysts were prepared by a simple impregnation method. The mass ratios for the different samples are shown in Table 1. For comparison, untreated Degussa P25 TiO<sub>2</sub> (pure TiO<sub>2</sub>) was used in this work. Degussa P25 is a mixture of anatase and rutile (80 : 20) with a BET surface area of about 52.4 m<sup>2</sup>/g and average primary particle size of about 20 nm.

In a typical preparation (described for sample TTa2 = 1 : 0.5 as representative of the series), Tantalum oxide Ta<sub>2</sub>O<sub>5</sub> (0.5 g, 1.13 mmol) was suspended in 30 mL ethanol under stirring. 1 g (12.52 mmol) of Degussa P25 TiO<sub>2</sub> powder was suspended in 30 mL ethanol and the suspension then sonicated for 1 h at room temperature. The two suspensions of TiO<sub>2</sub> and Nb<sub>2</sub>O<sub>5</sub> or Ta<sub>2</sub>O<sub>5</sub> were mixed under vigorous stirring for 4 hours at room temperature and then dried under vacuum to obtain a powder which was further dried in oven for 8 h at 80°C. The obtained powder, was ground and then calcinated at 500°C for 3 h in the presence of air with a ramp rate of 2°C/min.

*2.2. Characterization.* The crystalline structure of the prepared Ta/TiO<sub>2</sub>- and Nb/TiO<sub>2</sub>-mixed oxides photocatalysts was characterized by X-ray powder diffraction (XRD) analysis (RINT Ultima III, Rigaku co., Japan) using Cu Ka radiation at a scan rate of 4 degree/min. The acceleration voltage and the applied current were 40 kV and 40 mA, respectively. The mean size of crystallite ( $D$ , nm) was calculated from full-width at half maxima (FWHM) of corresponding X-ray diffraction peaks using Scherrer's formula  $D = 0.89\lambda/\beta \cos \phi$ , where  $\lambda$  is the wavelength of the X-ray radiation ( $\lambda = 1.54056$  nm Cu Ka),  $\beta$  is the full-width at half maximum (rad), and  $\phi$  is the reflect angle. The content of anatase

$w_A$  (%) was determined according to the following equation [24]:  $w_A$  (%) =  $\{I_A/(I_A + 1.265I_R)\} \times 100$ , where  $I_R$  and  $I_A$  are the intensities of the diffraction peaks of rutile (110) and anatase (101), respectively, obtained from XRD patterns. X-ray photoelectron spectra (XPS) of the powders were measured using Shimadzu ESCA 750 photoelectron spectrometer with an MgK $\alpha$  1253.6 eV; the shift of binding energy due to relative surface charging was corrected using the C1s level at 285 eV as an internal standard. The diffuse reflectance UV-Vis spectra were measured with an Ocean Optics high-resolution HR4000 USB spectrometer (HR4000 Ocean Optics Inc.) with an extended wavelength range from 190 to 1100 nm. The microstructures of the samples were observed by a scanning electron microscope, SEM (JSM-5310LV, Jeol Co., Japan).

**2.3. Photocatalytic Activity Measurement.** Solar photocatalytic decolorization and mineralization of Orange II dye was carried out in 300 mL Pyrex glass beaker. All the reactions were carried out according to the following procedure: 0.4 g of photocatalyst (modified or unmodified TiO<sub>2</sub>) was added to 250 mL of aqueous dye (Orange II) solution (20 mg/L). The dyes solution was mixed with a magnetic stirrer during the course of the experiment. At the beginning, the solution mixture was stirred for 30 min in the dark to ensure establishment of the dye's equilibrium adsorption/desorption. Then sun light was allowed to irradiate the reaction mixture, and at regular time intervals, samples were taken from the suspension and the change of Orange-II concentration was measured using UV-Vis spectrophotometer (TU-1900 UV spectrometer) at fixed wavelength of 486 nm. For this purpose, the photocatalyst was immediately removed from the sample by filtration, using a 0.4  $\mu$ m syringe filter. Solar experiments were carried out from 10:00 AM to 5:00 PM during May in Saitama, Japan. During the solar experiments, the UV and the visible ranges (illuminance) of the solar light intensity were measured by the UV radiometer (UVR-2, TOPCON, with UD-36 (310–400 nm/average 365 nm) detector, Tokyo, Japan) and illuminance meter (T-10, Konica Minolta), respectively. The accumulated solar energy was calculated by [25]

$$Q_n = Q_{n-1} + \Delta t I \left( \frac{A}{V} \right), \quad \Delta t = t_n - t_{n-1}. \quad (1)$$

$Q_n$  accumulated solar energy per unit of slurry volume (KJL<sup>-1</sup>),  $\Delta t$  is the time difference between radiation measurements ( $h$ ),  $I$  is the solar light intensity per unit of irradiation surface area measured during time interval  $\Delta t$  (Wm<sup>-2</sup>),  $A$  is the irradiated surface area of the photoreactor (m<sup>2</sup>), and  $V$  is the photoreactor volume (m<sup>3</sup>).

### 3. Results and Discussion

**3.1. Characterization of the Prepared Photocatalysts.** Figures 1(a) and 1(b) show the XRD patterns of Ta/TiO<sub>2</sub>- and Nb/TiO<sub>2</sub>-mixed oxides photocatalysts beside the unmodified TiO<sub>2</sub> samples. The anatase (101) peak was used to determine the grain size by Scherer's formula. It is evident that the Nb

and Ta contents significantly influenced the particle size (FWHM) and crystallinity (anatase and rutile phases) of the modified samples. It was observed that the XRD patterns of TTa1 and TNb1 samples showed no signals originating the presence of Ta<sub>2</sub>O<sub>5</sub> and Nb<sub>2</sub>O<sub>5</sub> metal oxides, respectively. Actually at these low concentrations (2.9 mol% Ta and 1.8 mol% Nb), Ta and Nb ions are randomly dispersed in the crystallographic sites of anatase structure. Furthermore, the absence of metal peaks could come from their ultra fine dispersion on TiO<sub>2</sub> particles as very small clusters or due to very low metal content.

Figure 1(a) shows the X-ray diffraction patterns for the Ta/TiO<sub>2</sub>-mixed oxides samples, at high concentrations of 8.3% Ta and 15.3% Ta (TTa2 and TTa3 samples), the results clearly show the presence of peaks corresponding to orthorhombic Ta<sub>2</sub>O<sub>5</sub> (JCPDS 79–1375) [26]. The intensities of those peaks significantly increased with increasing the Ta<sub>2</sub>O<sub>5</sub> concentration mainly due to segregation. Furthermore, increasing the Ta<sub>2</sub>O<sub>5</sub> concentration could not prevent the grain growth, the average crystalline size of unmodified TiO<sub>2</sub> (TTa0) increased from 19.50 nm to 21.80 nm for TTa3 (see SEM results). In contrary the results of the grain size analysis of Nb/TiO<sub>2</sub>-mixed oxide photocatalyst (Figure 1(b)) showed that the grain growth of the unmodified TiO<sub>2</sub> (TNb0) have been retarded due to the addition of niobium ion. The crystalline size of TNb1 and TNb3 was 17.79 nm and 18 nm, respectively.

Moreover, increasing the Nb<sub>2</sub>O<sub>5</sub> concentration has stabilized the anatase phase, the anatase content for TNb1, TNb2, and TNb3 samples was about 86%. Our results are consistent with the results of Arbiol et al. [27] who studied the effect of Nb doping in samples synthesized by induced laser pyrolysis. They found that the presence of Nb substitutional ions in the anatase structure hindered the particles growth and transformation from anatase to rutile in TiO<sub>2</sub> nanoparticles.

The above trend of XRD results is in agreement with the SEM analysis that indicates a decrease of the TNb particle size, as the Nb ion prevents the grain growth [28]. SEM analysis was used to attain morphological structure of the investigated photocatalysts.

The SEM images of the Ta/TiO<sub>2</sub>- and Nb/TiO<sub>2</sub>-mixed oxides samples besides the unmodified TiO<sub>2</sub> sample (TNb1, TTa1, and unmodified TiO<sub>2</sub>) are shown in Figure 2. The SEM image of unmodified TiO<sub>2</sub> (Figure 2(a)) reveals that the powder consists of large micron-scale spherical agglomerates, which consist of tightly packed nanoparticles. For TTa1 sample (Figure 2(b)), some large particles obviously appear. It can be deduced that the appearing large particles may be due to the agglomeration of nanoparticles during the heat treatment. However, TNb1 sample (Figure 2(c)) seems to be relatively homogenous and to contain no large particles. The powder that possesses a sponge-like structure was found to be fine and slightly agglomerate. This structure is beneficial to enhancing the adsorption of reactants [29].

XPS spectra of the unmodified TiO<sub>2</sub>-, Nb/TiO<sub>2</sub>- and Ta/TiO<sub>2</sub>-mixed oxides powders are shown in Figure 3(a) for Ti 2p, Figure 3(b) for Nb 3d, and Figure 3(c) for Ta 4f. Figure 3(a) shows that the peak position of Ti 2p<sub>3/2</sub> corresponds to that of the Ti<sup>4+</sup> oxidation state [1]. It appears that

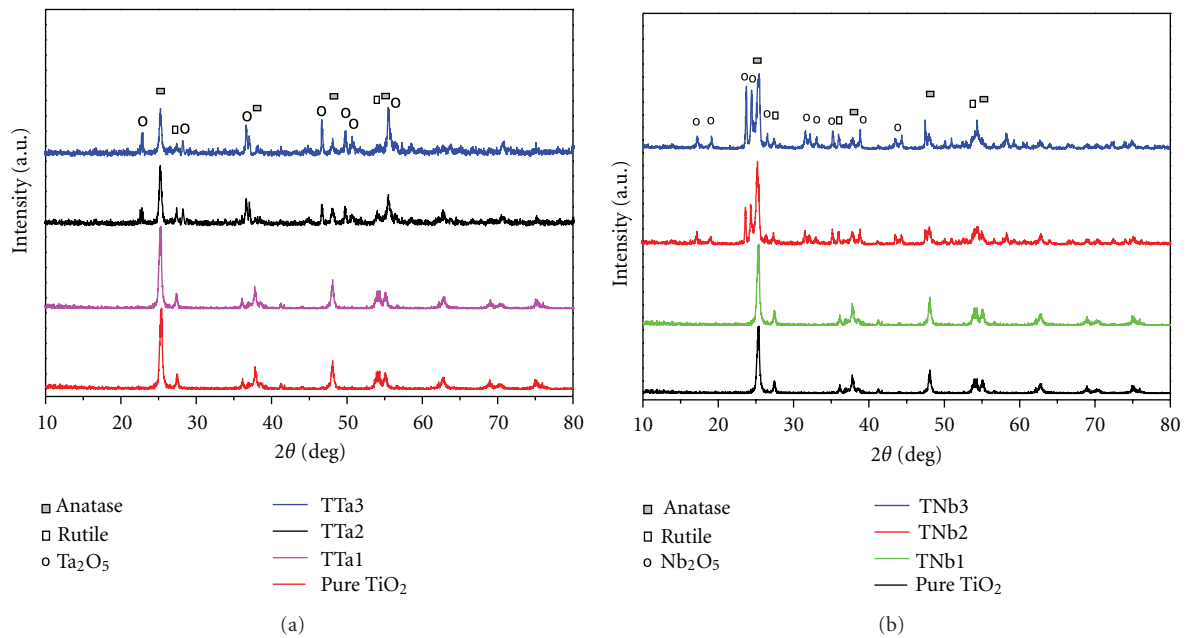


FIGURE 1: (a) XRD results for untreated (pure  $\text{TiO}_2$ ) and Ta/ $\text{TiO}_2$ -mixed oxides at different  $\text{TiO}_2$  : Ta ratios and  $500^\circ\text{C}$  calcination temperature for 3 hours. (b) XRD results for untreated (pure  $\text{TiO}_2$ ) and Nb/ $\text{TiO}_2$ -mixed oxides at different  $\text{TiO}_2$  : Nb ratios and  $500^\circ\text{C}$  calcination temperature for 3 hours.

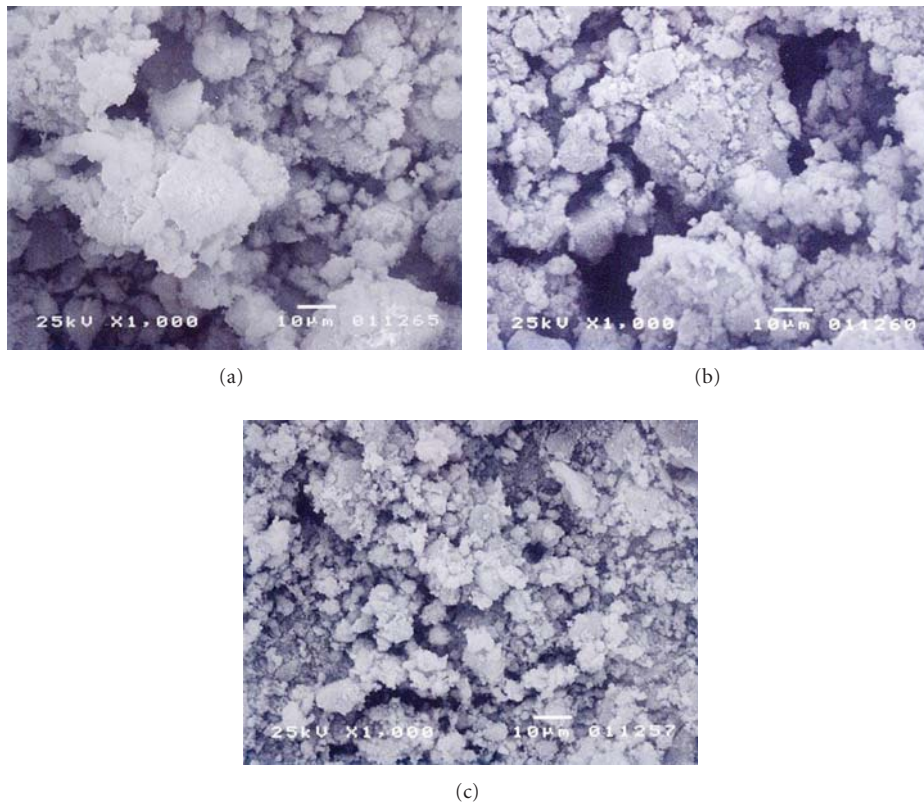


FIGURE 2: SEM photographs showing the untreated  $\text{TiO}_2$  (Degussa P25) (a) and treated samples after calcinations at  $500^\circ\text{C}$  for 4 hours (b) Ta/ $\text{TiO}_2$ -mixed oxides (TTa1), (c) Nb/ $\text{TiO}_2$ -mixed oxides (TNb1).

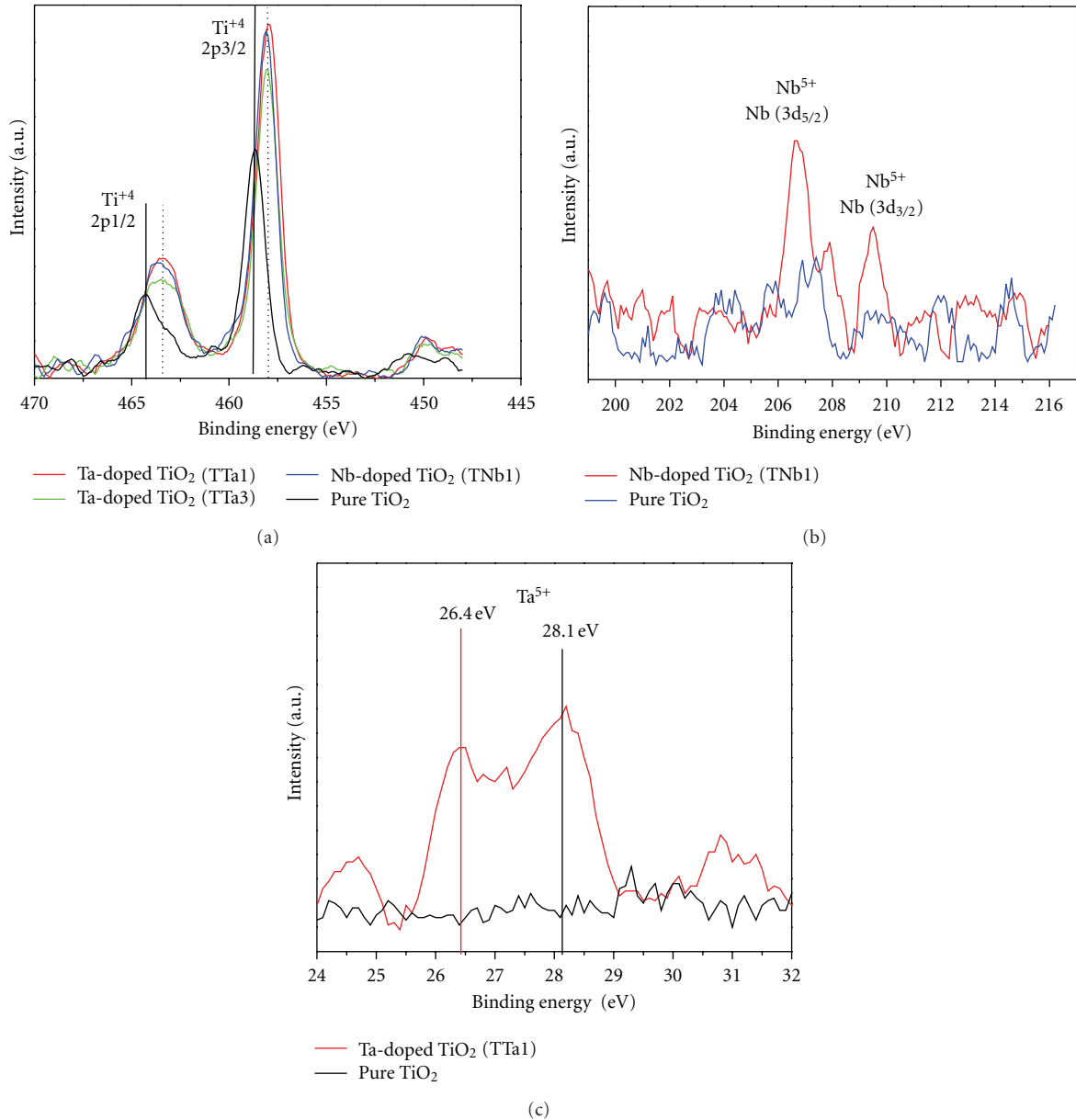


FIGURE 3: (a) XPS profiles of Ti2p spectra for the untreated TiO<sub>2</sub> (Degussa P25) and treated TiO<sub>2</sub> photocatalyst after calcination at 500°C for 3 hours in air. (b) Typical Nb 3d spectrum for Nb/TiO<sub>2</sub> mixed oxides. (c) Typical Ta 4f spectrum for Ta/TiO<sub>2</sub> mixed oxides.

the TiO<sub>2</sub> phase has been changed due to Nb and Ta species, since the full width at half-maximum (FWHM) for Ti 2p<sub>3/2</sub> for the treated and untreated TiO<sub>2</sub> samples is not the same. This is in contrast to Atashbar et al. [8] who found no change in TiO<sub>2</sub> phase due to Nb species as the FWHM for both the Nb-treated and untreated TiO<sub>2</sub> was the same, which could be attributed to the low amount of Nb used in their work (1% wt). Concerning the Nb 3d spectra for Nb/TiO<sub>2</sub>-mixed oxide (TNb1) shown in Figure 3(b), two peaks are observed at 206.7 and 209.8 eV, the peaks represent the 3d<sub>5/2</sub> and 3d<sub>3/2</sub> components, respectively. The center of the Nb 3d<sub>3/2</sub> peak corresponds to that of Nb<sup>5+</sup> oxidation state [8, 30]. Nb<sup>5+</sup> species, substituting for Ti<sup>4+</sup> in the crystalline lattice, could be a reason for anatase stabilization. Figure 3(c) shows the XPS

results for Ta 4f spectra for Ta/TiO<sub>2</sub>-mixed oxide (TTa1). The peaks at 26.4 eV and 28.1 eV were assigned to Ta<sup>5+</sup> [15]. No impurities, such as Ta<sub>2</sub>O<sub>5</sub>, were observed for the sample at 1.8 mol% Ta (TTa1), indicating that the Ta ion was substituted at Ti sites. Therefore, it can be concluded that the oxidation state of both tantalum and niobium ions in titania (anatase) is +5. Several authors [31, 32] have illustrated that both Nb<sup>5+</sup> and Ta<sup>5+</sup> ions substitute for Ti<sup>4+</sup> ions in normal lattice sites. In order to maintain the equilibrium of charges, the extrapositive charge due to Nb<sup>5+</sup> or Ta<sup>5+</sup> may be compensated by the creation of an equivalent amount of Ti<sup>3+</sup> ions [33] or by the presence of vacancies in the cation sites [34]. Oxygen vacancies facilitate visible light absorption by generating discrete states about 0.75 eV and 1.18 eV below

TABLE 2: Characterization of the prepared samples.

Sample	Crystalline size, $D$ (nm)	Anatase content (%)	Band gap (eV)	Decolorization rate, $K_{ap}$ ( $\text{min}^{-1}$ )
Pure $\text{TiO}_2$	19.50	80.02	3.10	0.0152
<b>Nb/TiO<sub>2</sub> (TNb1)</b>	<b>17.79</b>	<b>86.03</b>	<b>2.80</b>	<b>0.0364</b>
Nb/TiO <sub>2</sub> (TNb3)	18.00	85.70	2.93	0.0216
Ta/TiO <sub>2</sub> (TTa1)	20.74	75.50	3.01	0.0212
Ta/TiO <sub>2</sub> (TTa3)	21.80	82.01	2.98	0.0192

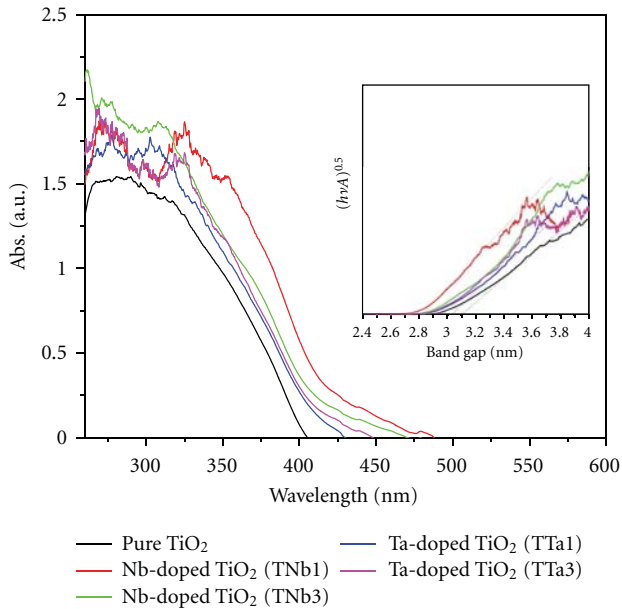


FIGURE 4: UV-vis diffuse reflectance spectra of the Ta/TiO<sub>2</sub>, Nb/TiO<sub>2</sub>, and untreated TiO<sub>2</sub> at different ratios. The insert Figure shows the band gap estimation.

the conduction band of titanium dioxide [35]. Oxygen vacancies are active electron traps. Since the oxygen defect states lie close to the conduction band of titania, the electrons captured by oxygen defects can be promoted to the surface by visible light absorption.

Figure 4 shows the UV-Vis absorbance spectra of the untreated TiO<sub>2</sub> (pure TiO<sub>2</sub>), Ta/TiO<sub>2</sub>-mixed oxides (TTa1 and TTa3), and Nb/Ti-mixed oxides (TNb1 and TNb3). Noticeable shifts of the optical absorption shoulders toward the visible light regions of the solar spectrum were observed for all modified photocatalysts. Notably, this shift towards the longer wavelength originates from the band gap narrowing of TiO<sub>2</sub> by Ta and Nb ions; this feature was more evident for (TNb1). The results clearly indicate that visible light absorption of the TiO<sub>2</sub> (P25 Degussa) is enhanced by introducing the Ta and Nb ions.

Estimations of the bandgap energies were obtained from the diffuse reflectance spectra of the prepared powders. The relationship between the absorption coefficient ( $\alpha$ ) and incident photon energy ( $h\nu$ ) can be written as  $\alpha = B_d(h\nu - E_g)^{0.5}/\lambda$ , where  $B_d$  is the absorption constant for direct transition [36]. A plot of  $(A h\nu)^{0.5}$  versus  $h\nu$  from the spectral data

is shown in the insert to Figure 4. Extrapolating the linear part of the curve for the photocatalysts gives the band gap values. The linear part of the curve for the untreated TiO<sub>2</sub> gives a band gap value of 3.10 eV, which is very close to the commercial Degussa TiO<sub>2</sub> (3–3.2 eV) [37, 38]. The estimated band gap energies of the samples from Figure 4 are summarized in Table 2. The maximum band gap reduction was 0.30 eV for TNb1. It has been acknowledged that solar wavelength shows maximum irradiance at the wavelength region of 450–480 nm [39]. Since TNb1 band gap corresponds to this region, it can absorb relatively higher photon flux compared to untreated TiO<sub>2</sub>. Probably the distortion of the local lattice of TiO<sub>2</sub> by Nb<sup>5+</sup> and Ta<sup>5+</sup> is responsible for the absorption in the visible region and to the shift of the onset of their absorption edge near 400 nm. Previous results (Figure 3) clearly showed that the crystal lattices of the TiO<sub>2</sub> powders are locally distorted by incorporating Nb<sup>5+</sup> and Ta<sup>5+</sup> species into TiO<sub>2</sub>. These would imply that the Nb and Ta ions can form a new band above the valence band and relatively narrow the band-gap of the photocatalyst, giving rise to the absorption edge in the visible light region (Figure 4). It was found that the solar photocatalytic activity for TNb1 is better than TNb3 (Table 2). Too much of new-generated band-gap structures due to higher Nb or Ta ions concentration could act as recombination centers for electron-hole pairs and consequently reduce the photoactivity of the catalyst.

**3.2. Solar Photocatalyst Activity.** To evaluate the photocatalytic activity of the prepared photocatalysts (TTa1, TTa3, TNb1, and TNb3), under natural solar light irradiation, tests were carried out to decolorize and mineralize Orange II dye in an aqueous suspension at an initial Orange II concentration of 20 mg/L. Figure 5 demonstrates the solar photodecolorization and mineralization observed for Orange II in the presence of treated and untreated TiO<sub>2</sub> powders. It worth mentioned here that in the dark experiments there is not a definite correlation between the adsorption properties and the activity of the samples, that is, the sponge-like structure sample (TNb1) does not mean the higher the decomposition rate of Orange II dye in the dark. Xie et al. [29] got the same conclusion when comparing the photocatalytic and adsorption properties of their prepared samples.

During the course of the solar experiments, the total accumulated UV light (350–400 nm) and the total accumulated visible light (400–750 nm) were 0.457 KJ/L and 51.94 KJ/L, respectively.

A plot of  $\ln(C/C_0)$  versus  $t$  represents approximate linear straight lines, showing the case of the first-order reaction.

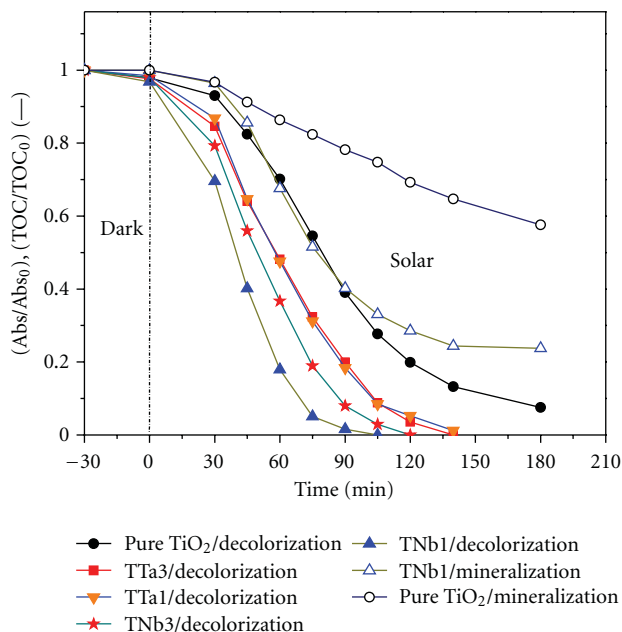


FIGURE 5: Solar photocatalytic decolorization of Orange II applying treated and untreated  $\text{TiO}_2$ . (Orange II conc. = 10 mg/L, catalyst conc. = 1.8 g/L).

The slope of the line equals the apparent first-order rate constant ( $K_{ap}$ ), the estimated  $K_{ap}$  values are summarized in Table 2.

The activity of the samples was found to be dependent on the metal ions (Nb or Ta) and its amount (1 : 0.1 or 1 : 1 mass ratios). Compared with the untreated  $\text{TiO}_2$ , both Ta/Ti- and Nb/ $\text{TiO}_2$ -mixed oxides photocatalysts exhibit better photocatalytic activity, and obviously Nb/ $\text{TiO}_2$  sample can more readily photodegrade and mineralized Orange II dye than Ta/ $\text{TiO}_2$  sample (Table 2). The untreated- $\text{TiO}_2$  photocatalytic activity under solar light increased about 140% by treating with Nb at mass ratio of 1 : 0.1 (TNb1); however, it was only about 40% by treating with Ta at mass ratio of 1 : 0.1 (TTa1). Mineralization of the Orange II dye also has been tested under natural solar light (Figure 5). The TNb1 sample significantly enhanced the mineralization rate of Orange II dye (by about 237%). The stability of the catalysts has been tested by using the photocatalysts repeatedly three times (results are not shown). No visible change of the photoactivity has been observed throughout these three runs. One may raise the doubt of whether it is the photocatalyst that plays the key role in decomposing Orange II dye because the dye can absorb visible light itself. If the decomposition of Orange II dye is due to the light absorbance itself, then the efficiency of the decomposition using a different photocatalysts may not vary so much as shown in Figure 5. Orange II dye was not a subject of photolysis, and any change in Orange II dye concentration can be attributed only to the heterogeneous photocatalysis [40].

It seems that Nb ions introduce some shallow donor levels below the conduction band edge, which can act as electron traps to retard electron-hole recombination as indicated by band gap reduction in Figure 4. Therefore, the life-

time of photogenerated electrons and holes can be increased, which is beneficial to enhancing the photocatalytic efficiency [14]. It was found that the solar photocatalytic activity for TNb1 is better than TNb3 (Table 2). Higher Nb or Ta ions concentration could act as recombination centers for electron-hole pairs and consequently reduce the photoactivity of the catalyst. The excess loading of metal particles may cover active sites on the  $\text{TiO}_2$  surface thereby reducing photodegradation efficiency [40]. Yu et al. [41] and Zhou et al. [42] pointed out that the photocatalytic activity of the metal dopants ( $\text{Fe}^{3+}$  ions) is strongly dependent on the dopant concentration since the metal ion ( $\text{Fe}^{3+}$ ) can serve not only as a mediator of interfacial charge transfer but also as a recombination center. Also the morphology and surface structure (Figure 2) as well as the electronic structure of  $\text{TiO}_2$  product modified by Nb and Ta ions should play important roles in enhancing photoactivity [43]. An efficient way to enhance the performance of the photocatalyst is to create the hierarchically porous structures in photocatalytic materials [44]. The solar photoactivities of Nb/ $\text{TiO}_2$  mixed oxide powder (TNb1) are predominantly attributed to an improvement in anatase crystallinity, sponge-like surface structure, low band gap, and low particle size.

#### 4. Conclusions

The commercially available  $\text{TiO}_2$  photocatalyst (Degussa P25) has been treated with niobium (Nb) and tantalum (Ta) ions, employing simple impregnation method at room temperature. The prepared Nb/ $\text{TiO}_2$ - and Ta/ $\text{TiO}_2$ -mixed oxide powders showed higher activity than the untreated  $\text{TiO}_2$  under natural solar light. The maximum activity was observed for Nb/ $\text{TiO}_2$  sample at mass ratio of 1 : 0.1 (TNb1). Comparing with the untreated  $\text{TiO}_2$ , the solar decolorization and mineralization rates improved by 140% and 237%, respectively, and the band gap reduced to 2.80 eV and with a stabilized anatase phase (86% anatase content). XPS results showed that the oxidation state of Ta and Nb ions in titania is +5 and leads to the substitution of  $\text{Ti}^{4+}$  by  $\text{Nb}^{5+}$  and  $\text{Ta}^{5+}$  in Nb/ $\text{TiO}_2$  and Ta/ $\text{TiO}_2$  samples, respectively. The results suggest that the crystal lattices of Nb/ $\text{TiO}_2$  powder are locally distorted by incorporating  $\text{Nb}^{5+}$  species into  $\text{TiO}_2$ , forming a new band energy structure, which is responsible for the absorption in the visible region. The Nb/ $\text{TiO}_2$  sample (TNb1) that is characterized by the smallest crystalline size (17.79 nm), not only stabilizes the anatase phase but also prevents the grain growth to some extent, which is important to achieve high solar photoactivity, while Ta/ $\text{TiO}_2$  sample did not. Therefore, Nb/ $\text{TiO}_2$ -mixed oxide is more suitable than Ta/ $\text{TiO}_2$  one. The metal ions (Nb or Ta) segregation become significant in the treated samples of higher than 1.8% Ta and 2.9% Nb. The solar photoactivities of Nb/ $\text{TiO}_2$  powder are predominantly attributed to an improvement in anatase crystallinity, low band gap, and low particle size.

#### Acknowledgment

This research was supported by Japan Society for the Promotion of Science (JSPS) grant in aid.

## References

- [1] H. Znad and Y. Kawase, "Synthesis and characterization of S-doped Degussa P25 with application in decolorization of Orange II dye as a model substrate," *Journal of Molecular Catalysis A: Chemical*, vol. 314, no. 1-2, pp. 55–62, 2009.
- [2] C. Adán, A. Bahamonde, A. Martínez-Arias, M. Fernández-García, L. A. Pérez-Estrada, and S. Malato, "Solar light assisted photodegradation of ethidium bromide over titania-based catalysts," *Catalysis Today*, vol. 129, no. 1-2, pp. 79–85, 2007.
- [3] B. J. Anthony, P. A. Fernandez-Ibañez, P. S. M. Dunlop, D. M. A. Alrousan, and J. W. J. Hamilton, "Photocatalytic enhancement for solar disinfection of water: a review," *International Journal of Photoenergy*, vol. 2011, Article ID 798051, 2011.
- [4] M. C. Carotta, V. Guidi, C. Malagù et al., "Vanadium and tantalum-doped titanium oxide (TiTaV): a novel material for gas sensing," *Sensors and Actuators, B*, vol. 108, no. 1-2, pp. 89–96, 2005.
- [5] E. Traversa, M. L. Vona, S. Licoccia et al., "Sol-gel processed TiO<sub>2</sub>-based nano-sized powders for use in thick-film gas sensors for atmospheric pollutant monitoring," *Journal of Sol-Gel Science and Technology*, vol. 22, no. 1-2, pp. 167–179, 2001.
- [6] E. Comini, M. Ferroni, V. Guidi et al., "Effects of Ta/Nb-doping on titania-based thin films for gas-sensing," *Sensors and Actuators, B*, vol. 108, no. 1-2, pp. 21–28, 2005.
- [7] A. Mattsson, M. Leideborg, K. Larsson, G. Westing, and L. Österlund, "Adsorption and solar light decomposition of acetone on anatase TiO<sub>2</sub> and niobium doped TiO<sub>2</sub> thin films," *Journal of Physical Chemistry B*, vol. 110, no. 3, pp. 1210–1220, 2006.
- [8] M. Z. Atashbar, H. T. Sun, B. Gong, W. Wlodarski, and R. Lamb, "XPS study of Nb-doped oxygen sensing TiO<sub>2</sub> thin films prepared by sol-gel method," *Thin Solid Films*, vol. 326, no. 1-2, pp. 238–244, 1998.
- [9] Y. Furubayashi, T. Hitosugi, Y. Yamamoto et al., "A transparent metal: Nb-doped anatase TiO<sub>2</sub>," *Applied Physics Letters*, vol. 86, no. 25, Article ID 252101, 3 pages, 2005.
- [10] H. Cui, K. Dwight, S. Soled, and A. Wold, "Surface acidity and photocatalytic activity of Nb<sub>2</sub>O<sub>5</sub>/TiO<sub>2</sub> photocatalysts," *Journal of Solid State Chemistry*, vol. 115, no. 1, pp. 187–191, 1995.
- [11] A. L. Castro, M. R. Nunes, M. D. Carvalho et al., "Doped titanium dioxide nanocrystalline powders with high photocatalytic activity," *Journal of Solid State Chemistry*, vol. 182, no. 7, pp. 1838–1845, 2009.
- [12] H. C. Yao, M. C. Chiu, D. C. Tsai, and C. J. Huang, "Effect of annealing on the Nb-doped TiO<sub>2</sub> films prepared by DC/RF cosputtering," *Journal of the Electrochemical Society*, vol. 155, no. 9, pp. G173–G179, 2008.
- [13] A. Kubacka, M. F. García, and G. Colón, "Nanostructured Ti-M mixed-metal oxides: toward a visible light-driven photocatalyst," *Journal of Catalysis*, vol. 254, no. 2, pp. 272–284, 2008.
- [14] J. Yang, X. Zhang, C. Wang et al., "Solar photocatalytic activities of porous Nb-doped TiO<sub>2</sub> microspheres prepared by ultrasonic spray pyrolysis," *Solid State Sciences*, vol. 14, no. 1, pp. 139–144, 2012.
- [15] K. Obata, H. Irie, and K. Hashimoto, "Enhanced photocatalytic activities of Ta, N co-doped TiO<sub>2</sub> thin films under visible light," *Chemical Physics*, vol. 339, no. 1–3, pp. 124–132, 2007.
- [16] M. Janus and A. W. Morawski, "New method of improving photocatalytic activity of commercial Degussa P25 for azo dyes decomposition," *Applied Catalysis B: Environmental*, vol. 75, no. 1-2, pp. 118–123, 2007.
- [17] N. Bowering, D. Croston, P. G. Harrison, and G. S. Walker, "Silver modified degussa P25 for the photocatalytic removal of nitric oxide," *International Journal of Photoenergy*, vol. 2007, Article ID 90752, 8 pages, 2007.
- [18] J. Yu, Y. Hai, and M. Jaroniec, "Photocatalytic hydrogen production over CuO-modified titania," *Journal of Colloid and Interface Science*, vol. 357, no. 1, pp. 223–228, 2011.
- [19] J. Yu, Y. Hai, and B. Cheng, "Enhanced photocatalytic H<sub>2</sub>-production activity of TiO<sub>2</sub> by Ni(OH)<sub>2</sub> cluster modification," *Journal of Physical Chemistry C*, vol. 115, no. 11, pp. 4953–4958, 2011.
- [20] L. Zhao, J. Ran, Z. Shu, G. Dai, P. Zhai, and S. Wang, "Effects of calcination temperatures on photocatalytic activity of ordered titanate nanoribbon/SnO<sub>2</sub> films fabricated during an EPD process," *International Journal of Photoenergy*, vol. 2012, Article ID 472958, 2012.
- [21] G. Shang, H. Fu, S. Yang, and T. Xu, "Mechanistic study of visible-light-induced photodegradation of 4-chlorophenol by TiO<sub>2-x</sub>N<sub>x</sub> with low nitrogen concentration," *International Journal of Photoenergy*, vol. 2012, Article ID 759306, 2012.
- [22] L. Qi, J. Yu, and M. Jaroniec, "Preparation and enhanced visible-light photocatalytic H<sub>2</sub> production activity of CdS-sensitized Pt/TiO<sub>2</sub> nanosheets with exposed (001) facets," *Physical Chemistry Chemical Physics*, vol. 13, no. 19, pp. 8915–8923, 2011.
- [23] J. Yu, L. Qi, and M. Jaroniec, "Hydrogen production by photocatalytic water splitting over Pt/TiO<sub>2</sub> nanosheets with exposed (001) facets," *Journal of Physical Chemistry C*, vol. 114, no. 30, pp. 13118–13125, 2010.
- [24] T. Ohno, M. Akiyoshi, T. Umebayashi, K. Asai, T. Mitsui, and M. Matsumura, "Preparation of S-doped TiO<sub>2</sub> photocatalysts and their photocatalytic activities under visible light," *Applied Catalysis A: General*, vol. 265, no. 1, pp. 115–121, 2004.
- [25] M. Tokumura, H. T. Znad, and Y. Kawase, "Decolorization of dark brown colored coffee effluent by solar photo-Fenton reaction: effect of solar light dose on decolorization kinetics," *Water Research*, vol. 42, no. 18, pp. 4665–4673, 2008.
- [26] K. V. Baiju, P. Shajesh, W. Wunderlich, P. Mukundan, S. R. Kumar, and K. G. K. Warriar, "Effect of tantalum addition on anatase phase stability and photoactivity of aqueous sol-gel derived mesoporous titania," *Journal of Molecular Catalysis A: Chemical*, vol. 276, no. 1-2, pp. 41–46, 2007.
- [27] J. Arbiol, J. Cerdà, G. Dezanneau et al., "Effects of Nb doping on the TiO<sub>2</sub> anatase-to-rutile phase transition," *Journal of Applied Physics*, vol. 92, no. 2, p. 853, 2002.
- [28] M. D. Koninck, P. Manseau, and B. Marsan, "Preparation and characterization of Nb-doped TiO<sub>2</sub> nanoparticles used as a conductive support for bifunctional CuCo<sub>2</sub>O<sub>4</sub> electrocatalyst," *Journal of Electroanalytical Chemistry*, vol. 611, no. 1-2, pp. 67–79, 2007.
- [29] Y. Xie, Y. Li, and X. Zhao, "Low-temperature preparation and visible-light-induced catalytic activity of anatase F-N-codoped TiO<sub>2</sub>," *Journal of Molecular Catalysis A: Chemical*, vol. 277, no. 1-2, pp. 119–126, 2007.
- [30] J. F. Moulder, W. F. Stickle, P. E. Sool, and K. D. Bomben, *Handbook of X-Ray Photoelectron Spectroscopy*, Perkin-Elmer Corporation, Eden Prairie, Minn, USA, 1999.
- [31] A. H. Meitzler, "Structural transformations occasioned by crystallographic shear in PLZT and TiO<sub>2</sub> ceramics," *Ferroelectrics*, vol. 11, no. 3-4, pp. 503–510, 1975.
- [32] M. Nazrullah and H. U. Anderson, "Compensation modes in counter-doped Rutile," *Journal of Solid State Chemistry*, vol. 90, pp. 373–376, 1991.
- [33] M. Valigi, D. Cordischi, G. Minelli, P. Natale, and P. Porta, "A structural, thermogravimetric, magnetic, electron spin resonance, and optical reflectance study of the NbO<sub>x</sub>TiO<sub>2</sub>

- system,” *Journal of Solid State Chemistry*, vol. 77, no. 2, pp. 255–263, 1988.
- [34] M. Sacerdoti, M. C. Dalconi, M. C. Carotta et al., “XAS investigation of tantalum and niobium in nanostructured TiO<sub>2</sub> anatase,” *Journal of Solid State Chemistry*, vol. 177, no. 6, pp. 1781–1788, 2004.
- [35] S. Y. Dhupal, T. L. Daulton, J. Jiang, B. Khomami, and P. Biswas, “Synthesis of visible light-active nanostructured TiO<sub>x</sub> ( $x < 2$ ) photocatalysts in a flame aerosol reactor,” *Applied Catalysis B: Environmental*, vol. 86, no. 3-4, pp. 145–151, 2009.
- [36] X. H. Wang, J. G. Li, H. Kamiyama et al., “Pyrogenic iron(III)-doped TiO<sub>2</sub> nanopowders synthesized in RF thermal plasma: phase formation, defect structure, band gap, and magnetic properties,” *Journal of the American Chemical Society*, vol. 127, no. 31, pp. 10982–10990, 2005.
- [37] J. Zhao and X. Yang, “Photocatalytic oxidation for indoor air purification: a literature review,” *Building and Environment*, vol. 38, no. 5, pp. 645–654, 2003.
- [38] S. Perathoner, R. Passalacqua, G. Centi, D. S. Su, and G. Weinberg, “Photoactive titania nanostructured thin films: synthesis and characteristics of ordered helical nanocoil array,” *Catalysis Today*, vol. 122, no. 1-2, pp. 3–13, 2007.
- [39] K. Nagaveni, G. Sivalingam, M. S. Hegde, and G. Madras, “Solar photocatalytic degradation of dyes: high activity of combustion synthesized nano TiO<sub>2</sub>,” *Applied Catalysis B*, vol. 48, no. 2, pp. 83–93, 2004.
- [40] V. Štengl and D. Králová, “TiO<sub>2</sub>/ZnS/CdS nanocomposite for hydrogen evolution and orange II dye degradation,” *International Journal of Photoenergy*, vol. 2011, Article ID 532578, 2011.
- [41] J. Yu, Q. Xiang, and M. Zhou, “Preparation, characterization and visible-light-driven photocatalytic activity of Fe-doped titania nanorods and first-principles study for electronic structures,” *Applied Catalysis B: Environmental*, vol. 90, no. 3-4, pp. 595–602, 2009.
- [42] M. Zhou, J. Yu, and B. Cheng, “Effects of Fe-doping on the photocatalytic activity of mesoporous TiO<sub>2</sub> powders prepared by an ultrasonic method,” *Journal of Hazardous Materials B*, vol. 137, no. 3, pp. 1838–1847, 2006.
- [43] J. Yu, S. Liu, and H. Yu, “Microstructures and photoactivity of mesoporous anatase hollow microspheres fabricated by fluoride-mediated self-transformation,” *Journal of Catalysis*, vol. 249, no. 1, pp. 59–66, 2007.
- [44] J. Yu and L. Qi, “Template-free fabrication of hierarchically flower-like tungsten trioxide assemblies with enhanced visible-light-driven photocatalytic activity,” *Journal of Hazardous Materials*, vol. 169, no. 1–3, pp. 221–227, 2009.

## Research Article

# Synergistic Effect of Nanophotocatalysis and Nonthermal Plasma on the Removal of Indoor HCHO

Yuanwei Lu,<sup>1</sup> Dinghui Wang,<sup>2</sup> Yuting Wu,<sup>1</sup> Chongfang Ma,<sup>1</sup>  
Xingjuan Zhang,<sup>3</sup> and Chunxin Yang<sup>3</sup>

<sup>1</sup>Key Laboratory of Enhanced Heat Transfer and Energy Conservation of Ministry of Education,  
College of Environmental and Energy Engineering, Beijing University of Technology, Beijing 100022, China

<sup>2</sup>Research Institute Guodian United Power Technology Co, Ltd, Beijing 100039, China

<sup>3</sup>School of Aeronautic Science and Engineering, Beijing University of Aeronautics and Astronautics, Beijing 100191, China

Correspondence should be addressed to Yuanwei Lu, luyuanwei910@hotmail.com

Received 28 October 2011; Revised 20 December 2011; Accepted 20 December 2011

Academic Editor: Jiaguo Yu

Copyright © 2012 Yuanwei Lu et al. This is an open access article distributed under the Creative Commons Attribution License, which permits unrestricted use, distribution, and reproduction in any medium, provided the original work is properly cited.

Photocatalysis is an effective method of air purification at the condition of a higher pollutant concentration. However, its wide application in indoor air cleaning is limited due to the low level of indoor air contaminants. Immobilizing the nanosized TiO<sub>2</sub> particles on the surface of activated carbon filter (TiO<sub>2</sub>/AC film) could increase the photocatalytic reaction rate as a local high pollutant concentration can be formed on the surface of TiO<sub>2</sub> by the adsorption of AC. However, the pollutant removal still decreased quickly with the increase in flow velocity, which results in a decrease in air treatment capacity. In order to improve the air treatment capacity by the photocatalytic oxidation (PCO) method, this paper used formaldehyde (HCHO) as a contaminant to study the effect of combination of PCO with nonthermal plasma technology (NTP) on the removal of HCHO. The experimental results show that HCHO removal is more effective with line-to-plate electrode discharge reactor; the HCHO removal and the reaction rate can be enhanced and the amount of air that needs to be cleaned can be improved. Meanwhile, the results show that there is the synergistic effect on the indoor air purification by the combination of PCO with NTP.

## 1. Introduction

Indoor air quality has become an important issue in recent years. Research shows that the level of indoor contaminants is 2–10 times higher than that in outdoor. In general, indoor volatile organic compounds (VOCs) coming from office products, insulating materials, synthetic furniture, press wood, and so forth have the relations to adverse health effects such as allergic reactions, headache, eye, nose, and throat irritation, and even cancer. The traditional method of cleaning indoor contaminants is physical adsorption, but the adsorbent has the properties of adsorption saturation and needs to be alternated periodically.

Photocatalysis is a promising technology for indoor air purification, which has been used in many fields since the research of photocatalytic water split on TiO<sub>2</sub> electrodes was reported in 1972 [1–10]. This photocatalytic method is effective in the case of a higher pollutant concentration, but its wide application is limited due to the low level of in-

door air contaminants. In order to improve the removal of pollutant in indoor air, many researches have investigated the photodegradation of indoor air pollutants by loading TiO<sub>2</sub> catalysts on activated carbon filter (TiO<sub>2</sub>/AC film) to increase the local concentration of pollutants on the surface of catalyst [11–20]. However, the contaminants removal still decreased sharply with the rise in flow velocity, especially at the low level of indoor pollutant concentration. Therefore, it is needed to improve the reaction rate at higher flow velocity for the flow velocity will directly affect the amount of air to be cleaned, which is important to the practical application of this method.

Nonthermal plasma (NTP) technology has been widely studied for VOCs oxidation. It has been reported as a most hopeful air cleaning technology to remove toxic volatile contaminants in air. The NTP approach is energy-efficient and is capable of removing various indoor pollutants simultaneously. Atmospheric plasma discharges generate high-energy electrons, while the background gas remains close to

room temperature [21, 22]. The energetic electrons excite, dissociate, and ionize gas molecules producing chemically active species (atomic oxygen, hydroxyl radicals, ozone, etc.). These species are capable of oxidizing volatile organic compounds. Recently, activated carbon, catalyst, and nonthermal plasma are combined together as a new treatment method to solve the problem of environmental pollution [23]. Studies [24] have proved that the atmospheric electric discharges emit radiation with wavelength between 290 and 400 nm. This UV emission range lies within the absorption spectrum range of  $\text{TiO}_2$ . Therefore, placing photocatalytic material, such as semiconductor  $\text{TiO}_2$ , into the plasma zone can improve the photocatalytic efficiency of air purification because the photocatalytic reaction can be triggered by both the high-energy plasma species and the UV emission during the plasma discharge. At the same time, the directional migration of electrons in the high voltage electric field can decrease the recombination of the electron-hole pairs in the process of photocatalysis. However, the effects of the plasma discharge configuration, flow velocity and humidity on the removal of contaminants by the combination of NTP with PCO are still scarce.

The objective of this study is to investigate the effect of combination of PCO with NTP on the removal of indoor HCHO. The effects of plasma discharge configuration, the applied voltage, the flow velocity and the humidity on the HCHO removal were studied. The reaction rate and HCHO removal were used as two parameters to evaluate HCHO removal efficiency.

## 2. Experiment

**2.1. Reagents and Catalyst Preparation.** The reactant gas HCHO was acquired from an HCHO penetration equipment. The detailed experimental setup has been described elsewhere [12].

$\text{TiO}_2$  (Degussa p-25) was used as the photocatalyst. Water suspension with 5 wt% of  $\text{TiO}_2$  was coated on a piece of honeycomb activated carbon (AC) filter by the dipping method and then was calcined at  $180^\circ\text{C}$  for 1 h with a ramp of  $3^\circ\text{C}/\text{min}$  to form the  $\text{TiO}_2$ -coated film (i.e.,  $\text{TiO}_2/\text{AC}$  film). The area of the netlike AC film was  $75\text{ mm} \times 25\text{ mm}$ . The amount of  $\text{TiO}_2$  loaded was determined by the weight difference before and after the coating procedure. The weight of  $\text{TiO}_2$  loaded was about 0.12 g. Figure 1 shows the  $\text{TiO}_2$  films coated on the honeycomb AC filter.

**2.2. Electrode Configuration of Plasma Discharge System.** Because the indoor HCHO concentration is low relative to that coming from industry, the indoor contaminants removal method should have properties such as low energy consumption, no undesired intermediate products, safe use, simple configuration and being used at room temperature and atmospheric pressure. Comparing the characteristics of different plasma methods, the direct current (DC) streamer discharge mode can satisfy the above properties. Pine-to-plate and wire-to-plate electrode configuration were designed for producing plasma, as shown in Figures 2 and 3. The

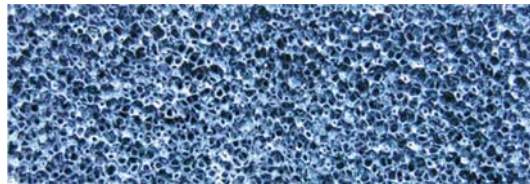


FIGURE 1:  $\text{TiO}_2/\text{AC}$  film.



FIGURE 2: Pine-to-plate electrode configuration.

two-electrode configuration adopted anode discharge to produce plasmas. The anode pine (or wire) was connected with the positive side of the high-voltage DC power and the cathode plate was connected with negative (ground) electrode. When the DC high-voltage power was turned on, the NTP will be produced between anode needle (or wire) and cathode plate.

**2.3. Plasma and  $\text{TiO}_2/\text{AC}$  Hybrid Configuration.** Figure 4 shows the hybrid configuration of plasma and catalyst film. The  $\text{TiO}_2/\text{AC}$  film was placed between the wire and the plate electrode. Using such a combination of PCO with NTP, HCHO can be fully degraded for the HCHO and its secondary products can be adsorbed on the surface of  $\text{TiO}_2$  by the adsorption of active carbon until it was completely oxidized into carbon dioxide and water. Also, the local higher HCHO concentration generated by the adsorption of active carbon on the  $\text{TiO}_2$  surface can improve the removal of HCHO.

**2.4. Experimental Section.** The schematic experimental system is detailed [12], and the configuration of the experimental section is illustrated in Figure 5. The reactant gas with a constant concentration, humidity, and reaction flow velocity can be formed in the experimental system [12]. The reactant gas flowed through the reactor and was decomposed in it. The reactor in the experimental section was made of stainless steel with a volume of 195 mL ( $3\text{H} \times 13\text{L} \times 5\text{W cm}$ ).

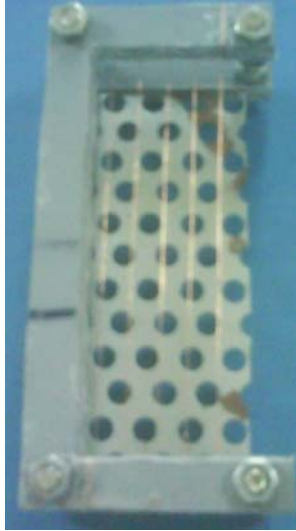


FIGURE 3: Wire-to-plate electrode configuration.

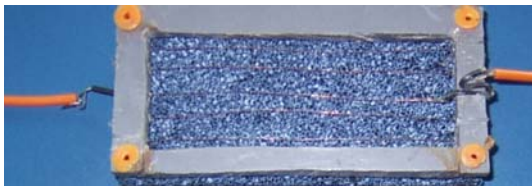


FIGURE 4: The hybrid configuration and catalyst film.

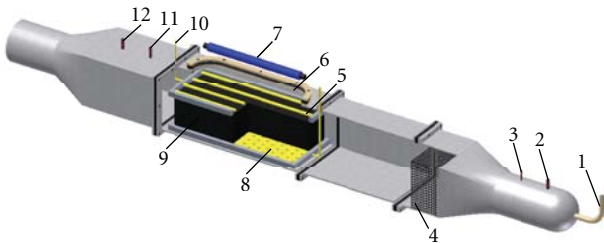


FIGURE 5: Experimental section. (1) Reactant stream inlet. (2) Zero air inlet (3) Humidified air inlet. (4) Mixer. (5) Electrode wire (6) Quartz glass window. (7) UV lamp (8) Electrode plate. (9) TiO<sub>2</sub> film. (10) Lead thread. (11) Sampling port. (12) Humidity and temperature sampling port.

The upper wall of the reactor is made of quartz for light entrance. Illumination was provided by an 8 W UV lamp, which emits light at a primary wavelength of 365 nm and was horizontally placed on the upper of the quartz window of the reactor. The UV light intensity of  $1180 \mu\text{W}/\text{cm}^2$  was determined by a UV meter (UV-A) in all of the experiments. The TiO<sub>2</sub> film was inserted between the plasma electrodes to take advantage of the UV emission coming from the plasma discharge. The one-pass removal efficiency of HCHO in plasma discharge system with and without TiO<sub>2</sub> film was studied. There is a fully developed region before the

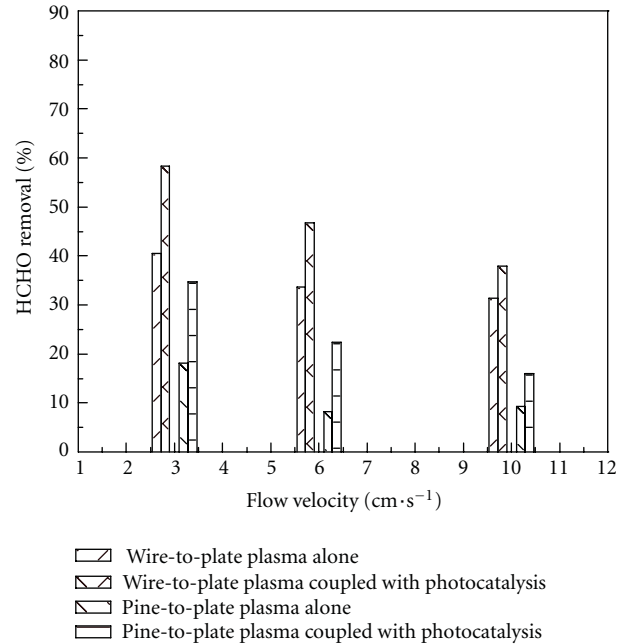


FIGURE 6: The removal of HCHO varies with flow velocity by different corona discharge.

reactor to form a stable air stream, and a mixer was placed inside it to mix the reactant gas well. The sampling port was set at the end of reactor. After the inlet concentration equaled to the outlet concentration, that is to say, the experimental system reached equilibrium (about 1 to 2 h), the HCHO concentration, temperature, and humidity in experimental system were recorded as an initial data. Then the UV lamp and the DC high-voltage power were turned on and the HCHO removal reaction was initiated. After HCHO concentration at the reactor outlet did not change with time, the concentration, temperature, and humidity were recorded again. Then the degradation of HCHO was ended and the reaction product mixture was collected. The experiments were carried out at room temperature, and under atmospheric pressure. The HCHO concentration was measured with the HCHO analyzer 4160 type (measure accuracy of  $\pm 2.0\%$  of reading), which was produced by the American Interscan Corporation. The temperature and humidity were measured by a Vaisala HUMICAP indicator HMI41 and probe type sensor HMP46 (at 20°C, measure accuracy of  $\pm 1.0\%$  RH at the humidity range of 0~90% RH and of  $\pm 1.0\%$  RH at the humidity range of 90~100% RH).

### 3. Results and Discussions

*3.1. Optimal Electrode Configuration of NTP Discharge.* Figure 6 shows the HCHO removal by pine-to-plate and wire-to-plate corona discharge with or without TiO<sub>2</sub> photocatalyst at different flow velocity with initial HCHO concentration  $1.19 \text{ mg}/\text{m}^3$ . The HCHO removal is defined as

$$\text{HCHO removal (\%)} = \frac{100(C_{\text{in}} - C_{\text{out}})}{C_{\text{in}}}, \quad (1)$$

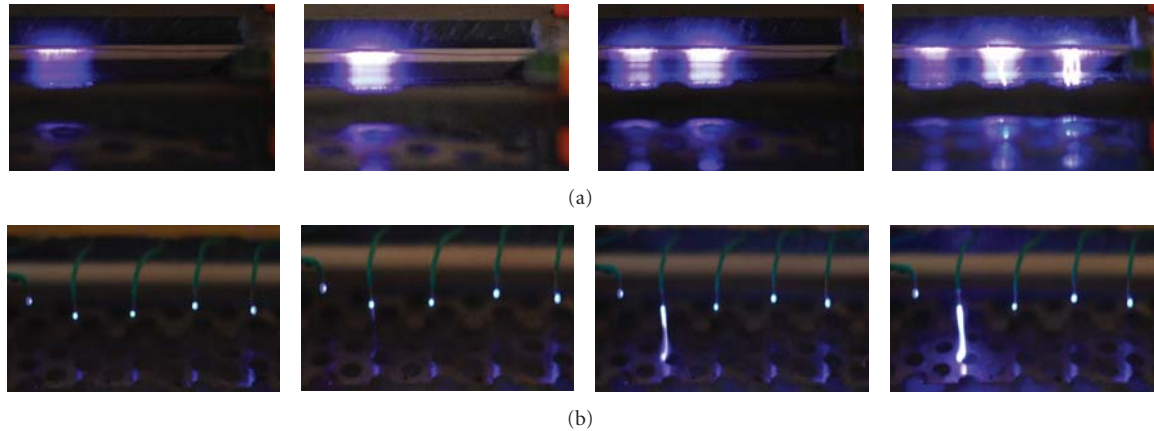


FIGURE 7: Corona discharge variation with the increase of applied voltage for the different electrode system. (a) Corona discharge variation with the increase in applied voltage for the line-to-plate electrode system. (b) Corona discharge variation with the increase in applied voltage for the pine-to-plate electrode system.

where  $C_{in}$  and  $C_{out}$  are the initial concentration and the steady outlet concentration ( $\text{mg}/\text{m}^3$ ), respectively. It can be seen that the HCHO removal with wire-to-plate electrode discharge configuration was higher than that with pine-to-plate configuration. For example, the removal of HCHO was only 18.2% by the pine-to-plate plasma discharge configuration but nearly 41% by the wire-to-plate discharge at flow velocity of 3 cm/s. However, when the plasma discharge coupled with  $\text{TiO}_2$  film the HCHO removal can be enhanced significantly. As shown in Figure 6, the HCHO removal reached nearly 60% when wire-to-plate plasma discharge coupled with photocatalysis and about 35% by combination of pine-to-plate plasma discharge with photocatalysis at the same flow velocity. Apparently, the wire-to-plate discharge configuration has a higher HCHO removal. The reason can be explained obviously by the streamer discharge photos of different electrode configuration, as shown in Figure 7. The photos from left to right in Figure 7 show the electrode discharge intensity varying with the increase in applied voltage. It can be seen that the streamer discharge propagated from the wire (or the tip of pine) electrode to plate electrode and its length and luminescence intensity increased with the increase in applied voltage. These streamers bridge the gap with flamelike discharge pattern and cover the surface of the catalyst. The wire-to-plate corona discharge has higher luminescence intensity than that of the pine-to-plate discharge when the discharge voltage increased from the lower to the breakdown voltage. So the wire-to-plate discharge system has higher removal of HCHO than that in the pine-to-plate discharge system. Also the in situ oxidative species ( $\cdot\text{HO}$ ) can be produced during the NTP production, which can decompose the low-concentration organic compounds. At same time, some physical effects, such as strong fields and streamer (including ultraviolet (UV) light), can also enhance the photocatalytic removal of HCHO during corona discharge process. Therefore, the removal of HCHO can be improved by the combination of plasma with  $\text{TiO}_2$  photocatalysis.

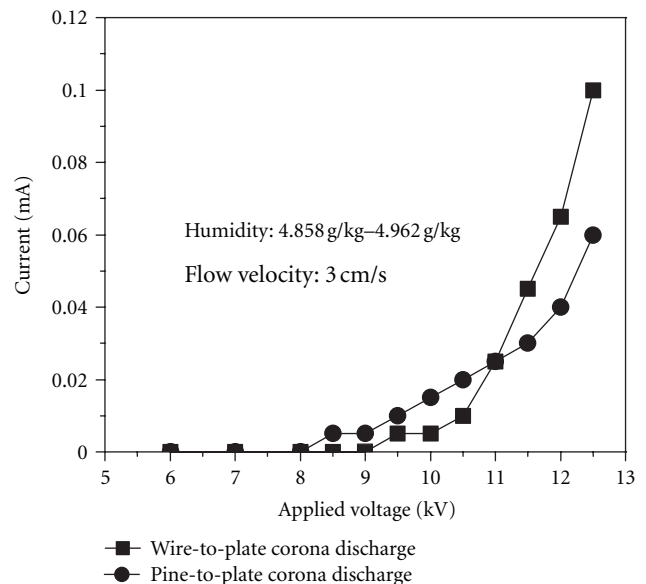


FIGURE 8: Corona current as a function of applied voltage.

The higher performance of the wire-to-plate electrode structure can also be explained by the time-average current-applied voltage characteristics, as shown in Figure 8. It can be seen that corona current was very small when applied voltage is less than 8 kV. At first, corona current generated by pine-to-plate discharge was greater than that generated by the wire-to-plate discharge with the increase in applied voltage. With the further increase in applied voltage, the corona current from wire-to-plate discharge increased sharply, and exceeded the corona current from the pine-to-plate discharge. The corona current was 0.1 mA in wire-to-plate discharge system at the applied voltage of 12.5 kV and only 0.06 mA in the needle-to-plate discharge system. From the above analysis, one can conclude that the wire-to-plate electrode system is effective for the removal of HCHO.

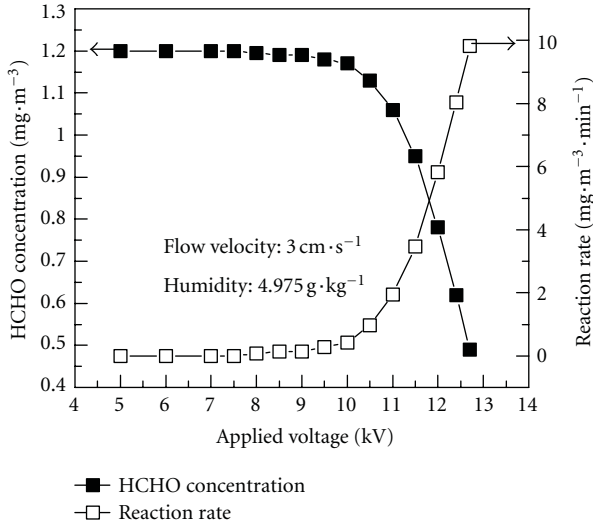


FIGURE 9: The removal of HCHO varies with the applied voltage.

Based on the above optimization results, the following study used the wire-to-pine discharge system to investigate the effect of applied voltage, flow velocity, and humidity on the removal of HCHO.

**3.2. Effect of Applied Voltage on the HCHO Removal.** Figure 9 shows that the HCHO concentration and reaction rate vary with the applied voltage in the wire-to-plate electrode discharge system. In this paper, the reaction rate ( $\text{mg}/(\text{m}^3 \cdot \text{min})$ ) is defined as [10]

$$r = \frac{(C_{\text{in}} - C_{\text{out}})Q}{V}, \quad (2)$$

where  $Q$  is the flow rate of air stream ( $\text{mL}/\text{min}$ ) and  $V$  is the volume of photoreactor ( $\text{mL}$ ).

One can see that the HCHO concentration remained constant and the reaction rate of HCHO was zero when the applied voltage was small, which shows that there was not any NTP produced at small applied voltage. With the increase in applied voltage, the reaction rate of HCHO increased and the concentration of HCHO began to decrease. When the applied voltage reached breakdown voltage, the concentration of HCHO and reaction rate changed irregularly. Figure 9 only shows the result at the applied voltage that was less than breakdown voltage. It can be seen that the corona discharge was excited between wire and plate electrode when the applied voltage was larger than the exciting voltage, and corona discharge intensity enlarged when the applied voltage increased. As a result, a large amount of higher-energy plasmas produced, which collided with HCHO molecule and decomposed it. So the HCHO concentration decreased and the reaction rate increased with the increase in applied voltage. However, the applied voltage should not exceed the breakdown voltage to maintain high HCHO removal.

**3.3. Effect of Flow Velocity on the HCHO Removal.** Figure 10 shows the effect of flow velocity on the HCHO removal

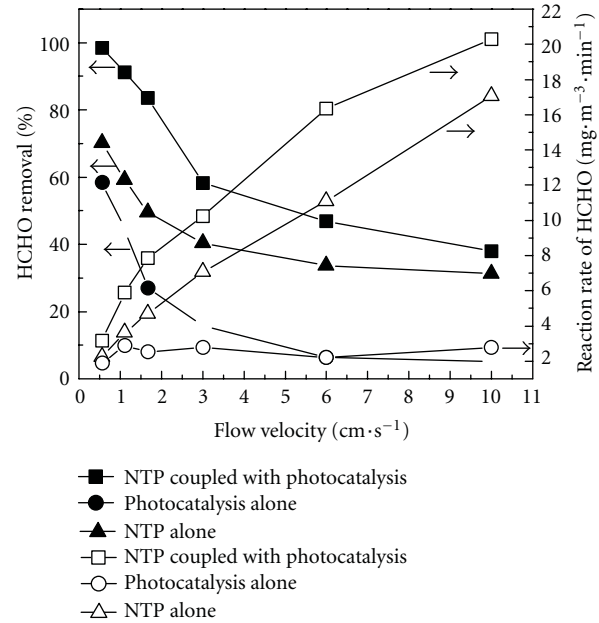


FIGURE 10: The effect of flow velocity on the HCHO removal and reaction rate by different method.

and reaction rate by the different method with HCHO initial concentration of  $1.18\text{--}1.24 \text{ mg}/\text{m}^3$  at humidity level of  $2.1 \text{ g}/\text{kg}$  (relative humidity, 18.8%) and applied voltage of  $11.5 \text{ kV}$ . From Figure 10, we can see that HCHO removal decreased (but the reaction rate increased) with the increase in flow velocity. The HCHO removal and reaction rate were higher by the NTP method than those by the PCO. The reason is that the high-energy active species (atomic oxygen, hydroxyl radicals, ozone, etc.) generated in the NTP discharge process have stronger reactivity than the  $\cdot\text{HO}$  radical generated during the PCO process. So the HCHO was strongly oxidized by the NTP method. As a result, the combination of NTP with PCO enhanced the HCHO removal and reaction rate significantly.

In fact, for the photocatalytic removal of HCHO, our study has found that the photocatalytic reaction rate first increased and then changed little with the increase in flow velocity, while the removal of HCHO decreased with it. The reason is that photocatalytic reaction took place from the diffusion control process to the photocatalytic reaction control process with the rise in flow velocity [12]. The same results marked by hollow and solid circles in Figure 10 were found again. However, for the removal of HCHO by the NTP method, the increase in flow velocity improved the reaction rate continuously with the applied voltage of  $11.5 \text{ kV}$ . It means that the number of NTPs is far greater than the HCHO molecules that collided with it. Therefore, the increase of flow velocity enhanced the diffusion of HCHO and resulted in the increase in reaction rate, which was consistent with reaction kinetics. So the reaction rate of HCHO by the NTP method was controlled by diffusion transfer. However, the removal of HCHO decreased with the increase in flow velocity for the predominant influence of residence time

TABLE 1: The synergistic effect of NTP and PCO.

Velocity/(cm/s)		0.56	1.11	1.67	3.0	6	10
Removal (%)	PCO	58.4	44.4	27.0	15.8	6.3	5.2
	NTP	70.2	59.2	45.6	40.5	33.6	31.4
	Both	98.4	91.3	83.6	58.3	46.8	37.9
Reaction rate (mg/m <sup>3</sup> · s)	PCO	1.87	2.87	2.54	2.77	2.21	2.77
	NTP	2.23	3.64	4.69	7.06	11.1	17.1
	Both	3.15	5.89	7.84	10.2	16.3	20.3

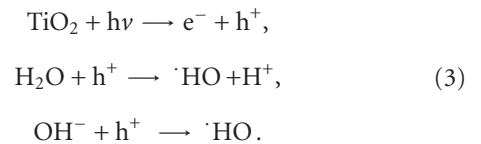
reduced. The less residence time means that the collision probability of active species with HCHO gas from inlet to the outlet of the reactor decreased, while the amount of HCHO gas per unit time that collided with the plasma increased with the rise in flow velocity, which was coincident with the effect of flow velocity on the reaction rate. Comparing with the rise in reaction rate, the amount of pollutant needed to be cleaned increased quickly with the increase in flow velocity, so the removal of HCHO was higher at the lower flow velocity than that at the higher flow velocity due to the predominant influence of residence time.

Because the high energy plasma and the UV light emission from the association of the NTP can excite the TiO<sub>2</sub> photocatalyst to produce the ·HO radical, which not only can enhance the oxidative ability of NTP but also can improve the photocatalytic ability of PCO, the combination of PCO with NTP shows the synergistic effect of both. As shows in Table 1, which is the same data as that in Figure 10, the HCHO removal (or reaction rate) by the combination of NTP with PCO was larger than its sum by PCO and by NTP with the rise in flow velocity. For example, HCHO removal was 37.4% at the flow velocity of 10 cm/s, which was larger than the sum of 5.2% by PCO and 31.4% by NTP. Also, the reaction rate of 20.3 mg/(m<sup>3</sup> · min) by combination of NTP and PCO was larger than the sum of 2.77 mg/(m<sup>3</sup> · min) by PCO and 17.1 mg/(m<sup>3</sup> · min) by NTP. Therefore, the synergistic effects of PCO and NTP can obviously enhance the degradation of indoor pollutant. It can be seen that the synergistic effect mainly exists in the process that is controlled by photocatalytic reaction (as flow velocity is larger than 1.1 cm/s). It implies that the TiO<sub>2</sub> photocatalyst activity was not fully excited by the UV light lamp in this paper during the process predominated by photocatalytic reaction when the flow velocity was larger than 1.1 cm/s. The combination of PCO with NTP excited the photocatalyst activity and resulted in the synergistic effect. When flow velocity was less than 1.1 cm/s, the photocatalytic reaction was controlled by diffusion process, during which the number of ·HO radical generated by PCO far outweighed the HCHO molecule that touched it, so the synergistic effect was not manifested.

The above results proved again that the HCHO removal is controlled by the resident time of HCHO in the reactor, while the reaction rate is controlled by the diffusion of HCHO. At the lower flow velocity, the resident time of HCHO in the reactor is higher, so the collision probability of HCHO with the active species is higher when the unit

volume HCHO gas flows from the inlet to the outlet of the reactor. While the collision probability per unit time reduced at the lower flow velocity as the diffusion of HCHO was weak, this resulted in the decrease in reaction rate. At the higher flow velocity, the resident time was lower, while the collision probability per unit time was enhanced, so the HCHO removal decreased, but the reaction rate increased. For the practical indoor air purification, higher flow velocity and higher reaction rate can increase air treatment capacity and decrease air treatment time, which is very important for the practical application of air purification technology. It can be seen that the combination of PCO with NTP can improve the HCHO removal in higher flow velocity, which may be a route to purify the indoor pollutants.

*3.4. Effect of Humidity on the HCHO Removal.* For the photocatalytic oxidation of HCHO, the bound molecular water on the surface of TiO<sub>2</sub> will directly affect the production of the hydroxyl radical (·HO). The ·HO is one of the most important oxidative species in the decomposing of HCHO for its higher oxidation potential (2.8 eV). The primary reactions are given as follows:



So, a certain amount of water vapor benefits the removal of HCHO. However, the heavy or light water vapor on the catalyst surface will lead to the decrease in reaction rate. In the absence of water vapor, the production of the ·HO is limited, while excessive water vapor on the surface of TiO<sub>2</sub> will occupy the active sites of reactants on the surface, which results in the competitive adsorption of water vapor and reactant on the TiO<sub>2</sub> surface.

For the nonthermal plasma discharge, it has been observed that air humidity affects to a great extent the behaviors of coronas [24]. When a high voltage is applied to the anode (thin wire), electrons presented in the air move towards the anode and are ionized by collision, forming avalanches within the ionization zone around the anode. The ionization process in the gap is dependent on the field strength as well as the water vapor content in air. So the water vapor content controls the ionization process, which in turn controls the growth of the second generation of avalanches. The lower content of water vapor in air accelerates the collision of

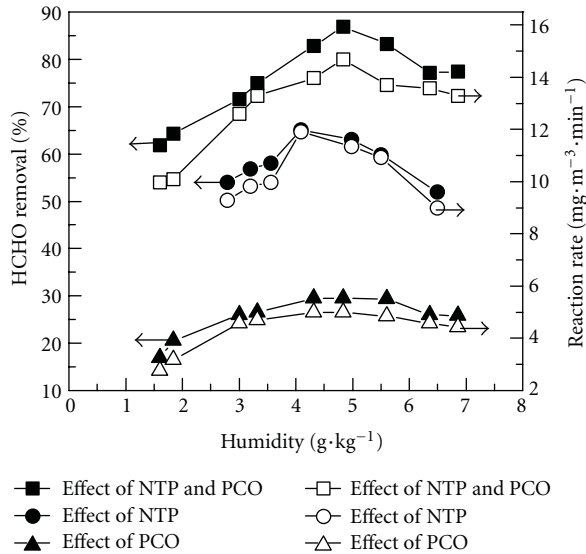


FIGURE 11: The effect of humidity on the removal and reaction rate of HCHO by different methods.

electron with water. As a result, the hydroxyl radical produces, which can oxidize the HCHO molecule touched with it. As the relative humidity increased, the thin water film formed on the surface of wire anode, which baffled the emission of photons from the primary avalanche. Therefore, the number of activated plasma decreased and the removal of HCHO reduced. Therefore, there exists the optimal humidity for the removal of HCHO by NTP discharge.

From the above analysis, it can be concluded that the effect of humidity on HCHO removal by combination of PCO with NTP should have the similar results. Figure 11 shows the effect of humidity on the HCHO removal and reaction rate by different methods with flow velocity of 3 cm/s at the applied voltage of 11.5 kV. The similar results were obtained. The effect of humidity on HCHO removal and reaction rate had optimal value. The optimal humidity was about 4.1 g/kg (relative humidity, 37.2%) by NTP discharge, but 4.3 g/kg (relative humidity 39.1%) by PCO method, and about 4.8 g/kg (relative humidity 43.4%) by the combination of PCO with NTP. Because water vapor is the main substance for generating the active species during the degradation of HCHO by PCO (or by NTP), more water vapor is needed for HCHO removal by the combination of PCO with NTP. To the photocatalytic degradation of HCHO, the effect of humidity on the reaction rate was not obvious after humidity was greater than the optimal value, which has been proved by our research group years ago [25], but it is clear by NTP discharge method. Therefore, for the HCHO removal by the combination of PCO with NTP, the reaction rate increased quickly with the rise in humidity and reached the maximum at optimal humidity and decreased hereinafter. When the humidity was far above the optimal value, the effect of humidity on the HCHO removal was unobvious. The reason is that the excessive water can form competitive adsorption with HCHO on the TiO<sub>2</sub> surface, but its influence

is relatively small, so the photocatalytic reaction became the control process for HCHO removal when humidity was larger than the optimal value. From Figure 11, one can see that the HCHO removal was nearly 87% and the reaction rate was 14.7 mg/(m<sup>3</sup> · min) at optimal humidity of 4.8 g/kg by the combination of PCO with NTP. However, the optimal humidity is still lower than that that in common ambient conditions. Therefore, as a future method of indoor air purification application, it is needed to improve the HCHO removal at higher humidity conditions.

## 4. Conclusions

- (1) The wire-to-plate configuration electrode system for producing NTP can be used in pollutant degradation for indoor air purification.
- (2) The combination of PCO with NTP shows the synergistic effect for HCHO removal. When the photocatalytic reaction changed from the diffusion control process to the photocatalytic reaction control process with the increase in flow velocity, the synergistic effect became more and more obvious. So the combination of PCO and NTP might be a valid pathway to purify indoor air.
- (3) The effects of humidity on the removal of HCHO by PCO, NTP discharge, or the combination of the both had an optimal humidity range. But the optimal humidity was lower than that in the common ambient conditions. Therefore, it is needed to try to redesign the reactor so as the combination of NTP with PCO can work effectively in a higher humidity range.

## Acknowledgments

This project was supported by the National Natural Science Foundation (50476036), National Basic Research Program of China (2012CB720106), and the Open Foundation of the Key Laboratory of Heat Transfer and Energy Conversion, Beijing Municipality, Beijing University of Technology.

## References

- [1] A. Fujishima and K. Honda, "Electrochemical photolysis of water at a semiconductor electrode," *Nature*, vol. 238, no. 5358, pp. 37–38, 1972.
- [2] S. B. Kim and S. C. Hong, "Kinetic study for photocatalytic degradation of volatile organic compounds in air using thin film TiO<sub>2</sub> photocatalyst," *Applied Catalysis B*, vol. 35, no. 4, pp. 305–315, 2002.
- [3] S. B. Kim, H. T. Hwang, and S. C. Hong, "Photocatalytic degradation of volatile organic compounds at the gas-solid interface of a TiO<sub>2</sub> photocatalyst," *Chemosphere*, vol. 48, no. 4, pp. 437–444, 2002.
- [4] L. Zhao, J. Ran, Z. Shu et al., "Effects of calcination temperatures on photocatalytic activity of ordered titanate nanoribbon/SnO<sub>2</sub> films fabricated during an EPD process," *International Journal of Photoenergy*, vol. 2012, Article ID 472958, 7 pages, 2012.

- [5] J. Yu, J. C. Yu, M. K. P. Leung et al., "Effects of acidic and basic hydrolysis catalysts on the photocatalytic activity and microstructures of bimodal mesoporous titania," *Journal of Catalysis*, vol. 217, no. 1, pp. 69–78, 2003.
- [6] J. Gamage and Z. Zhang, "Applications of photocatalytic disinfection," *International Journal of Photoenergy*, vol. 2010, Article ID 764870, 11 pages, 2010.
- [7] J. Yu, S. Liu, and H. Yu, "Microstructures and photoactivity of mesoporous anatase hollow microspheres fabricated by fluoride-mediated self-transformation," *Journal of Catalysis*, vol. 249, no. 1, pp. 59–66, 2007.
- [8] J. A. Byrne, P. A. Fernandez-Ibañez, P. S. M. Dunlop, D. M. A. Alrousan, and J. W. J. Hamilton, "Photocatalytic enhancement for solar disinfection of water: a review," *International Journal of Photoenergy*, vol. 2011, Article ID 798051, 2008.
- [9] J. Yu, G. Wang, B. Cheng, and M. Zhou, "Effects of hydrothermal temperature and time on the photocatalytic activity and microstructures of bimodal mesoporous TiO<sub>2</sub> powders," *Applied Catalysis B*, vol. 69, no. 3-4, pp. 171–180, 2007.
- [10] J. G. Yu, T. T. Ma, and S. W. Liu, "Enhanced photocatalytic activity of mesoporous TiO<sub>2</sub> aggregates by embedding carbon nanotubes as electron-transfer channel," *Physical Chemistry Chemical Physics*, vol. 13, no. 8, pp. 3491–3501, 2011.
- [11] C. H. Ao and S. C. Lee, "Indoor air purification by photocatalyst TiO<sub>2</sub> immobilized on an activated carbon filter installed in an air cleaner," *Chemical Engineering Science*, vol. 60, no. 1, pp. 103–109, 2005.
- [12] Y. Lu, D. Wang, and C. Ma, "The effect of activated carbon adsorption on the photocatalytic removal of formaldehyde," *Building and Environment*, vol. 45, no. 3, pp. 615–621, 2010.
- [13] P. Chin, L. P. Yang, and D. F. Ollis, "Formaldehyde removal from air via a rotating adsorbent combined with a photocatalyst reactor: kinetic modeling," *Journal of Catalysis*, vol. 237, no. 1, pp. 29–37, 2006.
- [14] C. H. Ao and S. C. Lee, "Enhancement effect of TiO<sub>2</sub> immobilized on activated carbon filter for the photodegradation of pollutants at typical indoor air level," *Applied Catalysis B*, vol. 44, no. 3, pp. 191–205, 2003.
- [15] C. H. Ao and S. C. Lee, "Combination effect of activated carbon with TiO<sub>2</sub> for the photodegradation of binary pollutants at typical indoor air level," *Journal of Photochemistry and Photobiology A*, vol. 161, no. 2-3, pp. 131–140, 2004.
- [16] C. H. Ao, S. C. Lee, J. Z. Yu, and J. H. Xu, "Photodegradation of formaldehyde by photocatalyst TiO<sub>2</sub>: effects on the presences of NO, SO<sub>2</sub> and VOCs," *Applied Catalysis B*, vol. 54, no. 1, pp. 41–50, 2004.
- [17] C. H. Ao and S. C. Lee, "Indoor air purification by photocatalyst TiO<sub>2</sub> immobilized on an activated carbon filter installed in an air cleaner," *Chemical Engineering Science*, vol. 60, no. 1, pp. 103–109, 2005.
- [18] C. H. Ao, S. C. Lee, C. L. Mak, and L. Y. Chan, "Photodegradation of volatile organic compounds (VOCs) and NO for indoor air purification using TiO<sub>2</sub>: promotion versus inhibition effect of NO," *Applied Catalysis B*, vol. 42, no. 2, pp. 119–129, 2003.
- [19] L. U. Yuanwei, L. I. Wencai, W. Wang, and C. Ma, "Combination of activated carbon with TiO<sub>2</sub> for the photodegradation of indoor formaldehyde(I)," *Acta Energetica Solaris Sinica*, vol. 29, no. 1, pp. 114–118, 2008 (Chinese).
- [20] L. U. Yuanwei, L. I. Wencai, W. Wang, and C. Ma, "Combination of activated carbon with TiO<sub>2</sub> for the photodegradation of indoor formaldehyde(II)," *Acta Energetica Solaris Sinica*, vol. 29, no. 5, pp. 550–554, 2008 (Chinese).
- [21] C. Subrahmanyam, M. Magureanu, A. Renken, and L. Kiwi-Minsker, "Catalytic abatement of volatile organic compounds assisted by non-thermal plasma—part 1: a novel dielectric barrier discharge reactor containing catalytic electrode," *Applied Catalysis B*, vol. 65, no. 1-2, pp. 150–156, 2006.
- [22] T. Yamamoto, K. Mizuao, I. Tamori et al., "Catalysis-assisted plasma technology for carbon tetrachloride destruction," *IEEE Transactions on Industry Applications*, vol. 32, no. 1, pp. 100–105, 1996.
- [23] J. Van Durme, J. Dewulf, W. Sysmans, C. Leys, and H. Van Langenhove, "Efficient toluene abatement in indoor air by a plasma catalytic hybrid system," *Applied Catalysis B*, vol. 74, no. 1-2, pp. 161–169, 2007.
- [24] L. Fouad and S. Elhazek, "Effect of humidity on positive corona discharge in a three electrode system," *Journal of Electrostatics*, vol. 35, no. 1, pp. 21–30, 1995.
- [25] M. Chang, *The study of the performance evaluation for photocatalytic indoor air purification*, M.S. thesis, University of Technology, Beijing, China, 2005.

## Research Article

# TiO<sub>2</sub>:(Fe, S) Thin Films Prepared from Complex Precursors by CVD, Physical Chemical Properties, and Photocatalysis

V. G. Bessergenev,<sup>1</sup> M. C. Mateus,<sup>1</sup> D. A. Vasconcelos,<sup>1</sup> J. F. M. L. Mariano,<sup>1</sup>  
A. M. Botelho do Rego,<sup>2</sup> R. Lange,<sup>3</sup> and E. Burkel<sup>4</sup>

<sup>1</sup>FCT, Universidade do Algarve, Campus de Gambelas, 8005-117 Faro, Portugal

<sup>2</sup>CQFM and IN, IST, Universidade Técnica de Lisboa, 1049-001 Lisboa, Portugal

<sup>3</sup>Informatics and Electrotechnics, University of Rostock, 18055 Rostock, Germany

<sup>4</sup>Institute of Physics, University of Rostock, 18055 Rostock, Germany

Correspondence should be addressed to V. G. Bessergenev, vbess@ualg.pt

Received 17 October 2011; Accepted 30 November 2011

Academic Editor: Jiaguo Yu

Copyright © 2012 V. G. Bessergenev et al. This is an open access article distributed under the Creative Commons Attribution License, which permits unrestricted use, distribution, and reproduction in any medium, provided the original work is properly cited.

The TiO<sub>2</sub> thin films were prepared using Ti(dpm)<sub>2</sub>(OPr<sup>i</sup>)<sub>2</sub> and Ti(OPr<sup>i</sup>)<sub>4</sub> (dpm = 2,2,6,6-tetramethylheptane-3,5-dione, Pr<sup>i</sup> = isopropyl) as the precursors. The volatile compounds Fe[(C<sub>2</sub>H<sub>5</sub>)<sub>2</sub>NCS<sub>2</sub>]<sub>3</sub> and [(CH<sub>3</sub>)C]<sub>2</sub>S<sub>2</sub> were used to prepare doped TiO<sub>2</sub> films. The synthesis was done in vacuum or in the presence of Ar and O<sub>2</sub>. The pressure in the CVD chamber was varied between 1.2 × 10<sup>-4</sup> mbar and 0.1 mbar, with the system working either in the molecular beam or gas flow regime. Physical, chemical, and photocatalytic properties of the (Fe, S)-doped TiO<sub>2</sub> films were studied. Those TiO<sub>2</sub>:(Fe, S) films prepared from the Ti(OPr<sup>i</sup>)<sub>4</sub> precursor show increased photocatalytic activities, very close to those of Degussa P25 powder in UV region.

## 1. Introduction

Drinking water pollution due to agrochemical compounds is the problem for which urgent remedial measures need to be found. As it was shown, among the various semiconductors used in photocatalysis, TiO<sub>2</sub> is essentially the best material for environmental purification. The only drawback of TiO<sub>2</sub> is that its band gap is at 3.2 eV for the anatase and at 3.0 eV for the rutile structure lying in the near-UV region of the electromagnetic spectrum: 385 nm and 410 nm, respectively. As UV light constitutes only 5% of the solar spectrum [1], 95% of the solar photons are unusable for TiO<sub>2</sub> photocatalysis. Therefore, extensive efforts have been made in the development of TiO<sub>2</sub>-doped photocatalysts that can utilize solar light more efficiently.

It is generally accepted that the theoretical model of photocatalysis consists of different consecutive steps where each one is essential for the activity and efficiency of the photocatalyst. The initial step of the photocatalytic process consists in the generation of electron-hole pairs upon irradiation of the material with photons whose energies are

at least equal to that of the band gap. In this step, parameters like the relation between adsorption/reflection coefficients and the quantum efficiency of electron-hole generation are very important. In the second step, the formed electron-hole pairs can either recombine in the bulk or travel up to the surface, where they can participate in chemical reactions. In this step, the lifetime and the velocity of the electron-hole recombination are of extreme importance. The next step is the creation of H\* and OH\* radicals as a result of the electron-hole interaction with water, and finally a probable multiple-step reaction of organic compounds with active radicals. In this step, hydrophilic properties of the photocatalytic surfaces are crucial. However so far, the influence of the different stages of this model on the final efficiency of the photocatalysts was not well determined.

Therefore, it is evident that any modification of the TiO<sub>2</sub>-based photocatalysts resulting in an improving of the efficiency of the above-described steps will represent a breakthrough in the field. For this purpose, many scientific works have appeared during recent years. A thorough analysis of the different approaches is beyond the scope of this paper,

and only some selected reports will be summarized below. (i) One class of the reports is on the doping of TiO<sub>2</sub> with various transition metals (V, Cr, Mn, Fe, Co, Ni, Au, Ag, Pt, Nb, Cu, W, etc.) to lower the band-gap energy. It was shown by ab initio band calculations based on the density functional theory that an electron-occupied level occurs and electrons are localized around each dopant [2]. As the atomic number of the dopant increases, the localized level shifts to lower energy; thus, for Co the energy level is sufficiently low to be at the top of the valence band, while other metals produce midgap states [2]. In some experimental studies, it was shown that doping with metal ions such as V<sup>5+</sup>, Cu<sup>2+</sup>, Fe<sup>3+</sup>, and W<sup>6+</sup> leads to an enhanced photoactivity [3, 4] whereas in other studies it was shown to lead to a reduction of the photoactivity [5, 6]. (ii) Another class of reports is on the TiO<sub>2</sub> doping with nonmetals such as N [1, 7–9], S [10–16], F [17], C [8, 18, 19], Br, or Cl [20]. The main idea of nonmetals doping is to create electron-hole trapping centres or charge separating surfaces [21] as well as to shift the optical absorption into the visible region. (iii) A third class of reports is dealing with the increase of the adsorption of pollutants by increasing the hydrophilicity under UV-light illumination [22, 23]. One can suppose that for TiO<sub>2</sub>:Fe thin films both of these mechanisms can be activated.

So far, the main obstacle in application of TiO<sub>2</sub> thin films prepared by different techniques is that its photocatalytic activity is much lower than that of the Degussa P25 TiO<sub>2</sub> reference powder. Recently, some new techniques have been developed to prepare pure [24–27] and doped TiO<sub>2</sub> thin films [28–30] to enhance the photocatalytic activities.

Different techniques have been used to prepare doped TiO<sub>2</sub> thin films where Ti or O atoms were partly substituted, namely, pulsed laser deposition (TiO<sub>2-x</sub>N<sub>x</sub> [23]), ion implantation (TiO<sub>2</sub>:Fe [28, 31], TiO<sub>2</sub>:Sn [29]), cosputtering (TiO<sub>2</sub>:Co [30]), deep coating (Fe modified nanotube arrays [32]), or sol-gel methods (TiO<sub>2</sub>:Fe [23], TiO<sub>2</sub>:Cr [33]).

By the studies of charge separation efficiency, it was recently shown that in the anatase form of TiO<sub>2</sub>-oriented thin films, the photo-generated holes can be transported towards the surface once the photon energy irradiation reaches its optical bandgap [34]. By this fact, one can partly explain the enhanced photocatalytic activity of the anatase form in comparison with the rutile form. Recently, a photocatalytic activity of a set of TiO<sub>2</sub> samples with different anatase/rutile ratios, prepared by calcinations at different temperatures from commercial photocatalyst Degussa P25, was studied [35]. Results indicate that samples with higher anatase/rutile ratios presented higher intrinsic activity (intrinsic activity is activity calculated per unit area). Photocatalytic activity was studied for the photodegradation of propane/isobutene/butane (40/35/25%) gas mixture [35]. Photocatalytic activity for aqueous solutions of polluting organic matters of immobilized TiO<sub>2</sub> photocatalysts, such as thin films, can be compared with the activity of Degussa P25 powder (anatase/rutile = 80/20), immobilized on the surface of the substrate.

There are some other important factors that can have strong influence on the photocatalytic activity, namely, the roughness of the photocatalyst surface that determines the

active surface, the adhesion of the pollutant molecules to the surface of the photocatalyst, the surface contamination of the photocatalyst, and so on. Therefore, a common standard is needed to compare the photocatalytic activity of TiO<sub>2</sub> photocatalysts prepared by different methods [36].

In this paper, the TiO<sub>2</sub> thin films were prepared using Ti(dpm)<sub>2</sub>(OPr<sup>i</sup>)<sub>2</sub> (dpm = 2,2,6,6-tetramethylheptane-3,5-dione, Pr<sup>i</sup> = isopropyl) and Ti(OPr<sup>i</sup>)<sub>4</sub> (TTIP) as precursors. The volatile compounds Fe[(C<sub>2</sub>H<sub>5</sub>)<sub>2</sub>NCS<sub>2</sub>]<sub>3</sub> (FeDtc) and [(CH<sub>3</sub>)C]<sub>2</sub>S<sub>2</sub> (di-*tert*-butyldisulphide—TBDS) were used to prepare TiO<sub>2</sub>:(Fe, S)-doped films. The P25 Degussa powder was used as standard to compare the photocatalytic activities of the thin films.

## 2. Methods

**2.1. TiO<sub>2</sub> Thin Films Preparation.** The TiO<sub>2</sub> films were obtained in a standard vacuum apparatus with a turbomolecular pump (ALCATEL TMP 5400 CP) producing vacuum down to 5 × 10<sup>-7</sup> mbar. During the deposition, the pressure of the volatile precursor decomposition products determined the available lower pressure limit. The vaporisation was conducted from an open surface evaporator. The temperature of the vapour source varied in the range of 90°C to 210°C, and the substrate temperature was stabilised around 400°C to 600°C.

Different types of rectangular or round glass and fused silica plates up to 78.5 cm<sup>2</sup> were used as substrates. All substrates were cleaned carefully right before loading using the following procedure. The substrates were cleaned in water using a detergent and then rinsed in distilled water. Afterwards, the substrates were immersed in sulphuric acid (~95%) for about 24 hours, then rinsed by distilled water, washed with acetone, and finally dried by a flux of filtered air.

The film thicknesses, ranging from 30 nm to 2000 nm, were measured by weight. The growth rate was varied from several nanometers to several tens of nanometers per minute.

For the preparation of the doped TiO<sub>2</sub> films, the CVD apparatus was modified by additional gas supply lines allowing to let inert gases (Ar, He) and O<sub>2</sub> into the chamber. The pressure in the CVD chamber was varied between 1.2 × 10<sup>-4</sup> mbar and 0.1 mbar, with the system working either in the molecular vapour stream or gas flow regime. The [(CH<sub>3</sub>)C]<sub>2</sub>S<sub>2</sub> (TBDS) was used to dope TiO<sub>2</sub> thin films with sulphur, presumably by substituting some oxygen sites of the TiO<sub>2</sub> crystal structure with sulphur. The TBDS is liquid with a vapour pressure of about 1 mbar at 25°C. The TBDS was placed in an ampoule, heated by a furnace, outside the vacuum chamber, and then connected with the Ar/O<sub>2</sub> gas supply line.

For the preparation of the iron-doped TiO<sub>2</sub> thin films, the Fe[(C<sub>2</sub>H<sub>5</sub>)<sub>2</sub>NCS<sub>2</sub>]<sub>3</sub> complex compound was used. The temperatures of the evaporating points of TTIP and Fe[(C<sub>2</sub>H<sub>5</sub>)<sub>2</sub>NCS<sub>2</sub>]<sub>3</sub> are different. Thus, to dope only the surface layers of TiO<sub>2</sub> thin film, a small amount of Fe[(C<sub>2</sub>H<sub>5</sub>)<sub>2</sub>NCS<sub>2</sub>]<sub>3</sub> was placed into the same evaporator

TABLE 1: Typical conditions of TiO<sub>2</sub> thin film synthesis.

Sample	Precursor	Substrate	Thickness, nm	$T_{\text{sub}}$ , °C	$P_{\text{max}}$ , mbar	$R$ , MOhm	Flux, % Ar/O <sub>2</sub> *
1		Glass	250	540	$1.2 \cdot 10^{-4}$		Vacuum
2		Quartz	250	450	$1.4 \cdot 10^{-4}$		Vacuum
3		Quartz	150	500	$2.4 \cdot 10^{-5}$		Vacuum
4	Ti(dpm) <sub>2</sub> (Opr) <sup>i</sup> <sub>2</sub>	Quartz	295	550	$1.6 \cdot 10^{-4}$		Vacuum
5		Quartz	300	600	$4.0 \cdot 10^{-4}$		Vacuum
9		Glass	150	450	$1.4 \cdot 10^{-1}$	>200	50/100
10		Glass	215	450	$1.4 \cdot 10^{-1}$	>200	50/100
18		Ceramic	165	465	$1.1 \cdot 10^{-4}$		Vacuum
23		Quartz	55	450	$2.1 \cdot 10^{-1}$	>200	100/0
24		Quartz	485	450	$6.4 \cdot 10^{-5}$	>200	Vacuum
26	TTIP	Glass	250	400	$1.2 \cdot 10^{-4}$		Vacuum
30		Glass	1745	400	$2.1 \cdot 10^{-1}$	>200	50/100
31		Glass	970	450	$3.7 \cdot 10^{-1}$	>200	50/100
65		Glass	970	450	$1.5 \cdot 10^{-1}$	>200	50/100
66		Glass	970	400	$1.5 \cdot 10^{-1}$		50/100
72	TTIP + FeDtc (0.008 g)	Glass	890	400	$1.1 \cdot 10^{-1}$		50/100
73	TTIP + FeDtc (0.008 g)	Quartz	800	400	$1.1 \cdot 10^{-1}$		50/100
74	TTIP + FeDtc (0.016 g)	Glass	803	400	$1.0 \cdot 10^{-1}$		50/100
75	TTIP + FeDtc (0.016 g)	Quartz	918	400	$1.0 \cdot 10^{-1}$		50/100
76	TTIP + FeDtc (0.032 g)	Glass	516	400	$1.1 \cdot 10^{-1}$		50/100
77	TTIP + FeDtc (0.032 g)	Quartz	593	400	$1.1 \cdot 10^{-1}$		50/100
79	TTIP + FeDtc (0.008 g)	Quartz	1045	400	$1.0 \cdot 10^{-1}$		50/100
80	TTIP + FeDtc (0.016 g)	Glass	560	400	$1.0 \cdot 10^{-1}$		50/100
81	TTIP + FeDtc (0.016 g)	Quartz	580	400	$1.0 \cdot 10^{-1}$		50/100
83	TTIP + FeDtc (0.032 g)	Quartz	760	400	$1.0 \cdot 10^{-1}$		50/100
85	TTIP + FeDtc (0.064 g)	Quartz	480	400	$1.1 \cdot 10^{-1}$		50/100
86	TTIP + FeDtc (0.3 g)	Glass	147	400	$1.1 \cdot 10^{-1}$		50/100
87	TTIP + FeDtc (0.3 g)	Quartz	145	400	$1.1 \cdot 10^{-1}$		50/100

\* 100% Flux of Ar and oxygen correspond to 20 mL/min at normal pressure.

used for the TTIP evaporation. These two complex compounds were separated in order to avoid a chemical interaction. To prepare uniformly doped TiO<sub>2</sub> thin films, the Fe[(C<sub>2</sub>H<sub>5</sub>)<sub>2</sub>NCS<sub>2</sub>]<sub>3</sub> was placed into the evaporator inside the vacuum chamber and the TTIP into the evaporator outside the vacuum chamber. The vapours of TTIP were admitted into the vacuum chamber by an Ar/O<sub>2</sub> flux. By the use of Fe[(C<sub>2</sub>H<sub>5</sub>)<sub>2</sub>NCS<sub>2</sub>]<sub>3</sub>, some Ti sites in the TiO<sub>2</sub> crystal structure are presumably substituted by Fe. However, since each molecule of Fe[(C<sub>2</sub>H<sub>5</sub>)<sub>2</sub>NCS<sub>2</sub>]<sub>3</sub> contains Fe-S bonds, this substitution may be complex which could mean, that not only Ti sites will be substituted by Fe atoms, but also that oxygen sites are being substituted by sulphur. As shown, the FeS<sub>x</sub> films resulting from the decomposition of Fe[(C<sub>2</sub>H<sub>5</sub>)<sub>2</sub>NCS<sub>2</sub>]<sub>3</sub> in vacuum can be easily transformed into FeO<sub>x</sub> films depending on the oxygen pressure [37]. So, the concentration of sulphur can be tuned by the changes in the Ar/O<sub>2</sub> ratio independently of Fe concentration. Some of the film preparation conditions are summarised in Table 1.

**2.2. Characterization Methods.** Structural information on as-prepared TiO<sub>2</sub> thin films was obtained from synchrotron radiation experiments. High-resolution grazing-incidence

X-ray diffraction (GIXRD) as well as  $\theta$ - $2\theta$  experiments were performed at the high-resolution powder diffractometer at the DESY/HASYLAB synchrotron radiation laboratory, using synchrotron radiation wavelength equal to  $\lambda = 0.0709494$  nm. Thin films deposited on either glass or fused silica substrates were analysed.

The trace analysis of the TiO<sub>2</sub> films was performed by laser ionization mass spectrometry (LIMS). A double-focusing mass spectrometer with Mattauch-Herzog geometry and laser plasma ion source (EMAL-2) was used. The energy output of Nd-YAG laser (wavelength of 1064 nm); pulse duration; repetition rate; diameter of laser spot on sample surface were adjusted to evaporate and ionize of the deposited films only. The glass substrates are transparent for Nd-YAG laser radiation and were not destroyed. At the chosen radiation power density ( $\sim 1 \times 10^9$  W/cm<sup>2</sup>), the measured concentration of Si (main component of the substrate) was not exceeding 10<sup>-2</sup>% wt. Step motors provided the scanning of the samples in two directions ( $X$ - $Y$ ). The area of the analyzed surface was about 0.5 cm<sup>2</sup>. The concentrations of the impurities were evaluated with respect to the Ti (matrix element of deposited layer) as the internal standard.

Scanning electron microscopy (SEM) was used to perform surface imaging and bulk compositional analysis of doped  $\text{TiO}_2$ :(Fe, S) samples. The Zeiss Supra 25 field emission SEM (FESEM) microscope with currently highest resolution ( $\sim 2$  nm), equipped with a liquid nitrogen-free, Peltier cooled (cooling time  $< 30$  s) EDX detector X-Flash 3001 with Quantax (Bruker AXS, Berlin, Germany) was used.

The  $\text{TiO}_2$  films were analysed by X-ray photoelectron spectroscopy (XPS) using XSAM800 (KRATOS) X-ray spectrometer operated in the fixed analyser transmission (FAT) mode. A  $\text{Mg K}\alpha$  (1253.7 eV) X-ray source was used. The analyser was operated at 20 eV pass energy both for detail and survey spectra. All the binding energies were referenced to the C 1s peak at 285.0 eV or O 1s peak at 529.9 eV.

Atomic force microscopy measurements were performed on a Solver PRO Scanning Probe Microscope at room temperature and atmospheric pressure in a contact mode with feedback control switched on.

The transmission coefficient of the  $\text{TiO}_2$  films prepared on the quartz substrates was measured using a ‘‘Cintra-40’’ UV-Vis spectrophotometer. The absorbance onset at 390 nm corresponds to the  $\text{TiO}_2$  semiconductor gap width.

Conversion electron Mossbauer spectroscopy (CEMS) was performed at room temperature on a Wissel constant acceleration spectrometer, using a Rikon-5 detector and a  $^{57}\text{Co}/\text{Rh}$  source. The resulting spectra were calibrated with alpha-Fe foil and fitted using an integrated least-squares computer program to determine the hyperfine parameters.

The layout of the photoreactor apparatus is described in detail in [38]. Briefly, the volume of irradiated solution was of 7.9 mL at 1 mm optical thickness. A 200 W Xenon lamp was used as a UV light source, and a water filter with fused silica windows was used in order to avoid an excessive heating of the solution. The photocatalytic process in water requires the presence of  $\text{O}_2$  as electron acceptor; thus, a continuous flow of air was injected by means of an air pump. Fenarimol (Riedel, 99.7%) 5 mg/L solutions were prepared in bidistilled water. The Fenarimol solution was left in contact with the reactor cell about 12 h in the dark before irradiation in order to achieve the adsorption equilibrium of the pesticide between the solution and the cell surfaces. During irradiation, 100  $\mu\text{L}$  samples were taken every 0.5 h or 1 h and immediately analysed on an HPLC system (Merck-Hitachi 655A-11 system with 655A-22 UV detector) under the following experimental conditions: LichroCART 125-4 column: Lichrospher 100 RP-18, 5  $\mu\text{m}$ ; eluent: acetonitrile (Merck Lichrosolv) 65%, bidistilled water 35%; 1,1 mL/min flow; UV detection at 220 nm. The total irradiation time was between 3 and 5 hours for each sample. To compare the reaction rates obtained for the thin films, commercial  $\text{TiO}_2$  P25 powder (Degussa) with identical amount by weight (7 mg) was deposited on fused silica substrates by evaporation from a  $\text{TiO}_2$  aqueous suspension and tested under identical experimental conditions as the CVD films.

### 3. Results and Discussion

XRD studies of crystal structure for samples prepared with the precursor  $\text{Ti}(\text{dpm})_2(\text{OPr}^i)_2$  as well as thermal de-

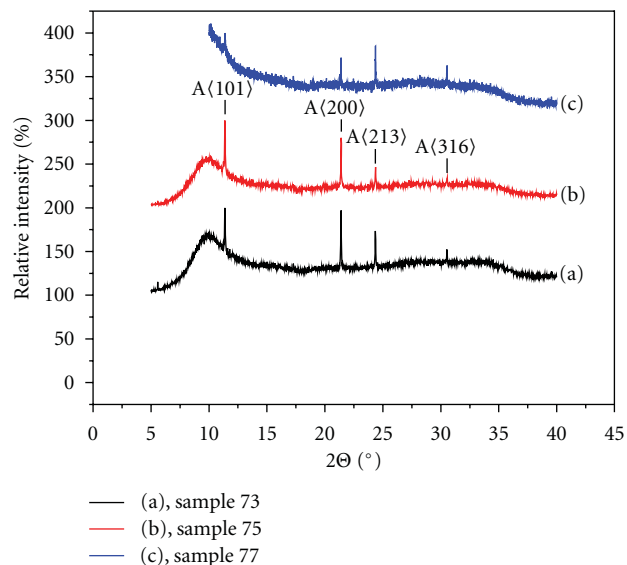


FIGURE 1: X-ray diffraction patterns for anatase  $\text{TiO}_2$ :(Fe, S) thin films obtained from the internal evaporator in a controlled  $\text{Ar}/\text{O}_2$  atmosphere.

composition mass spectrometry studies for the precursor  $\text{Ti}(\text{dpm})_2(\text{OPr}^i)_2$  in vacuum and in the presence of oxygen were reported in detail earlier [38, 39]. In the present work, thin films prepared from precursors  $\text{Ti}(\text{dpm})_2(\text{OPr}^i)_2$ , TTIP, and doped  $\text{TiO}_2$ :(Fe, S) were studied using  $\theta$ - $2\theta$  configuration of XRD. The most significant difference between films deposited from precursors  $\text{Ti}(\text{dpm})_2(\text{OPr}^c)_2$  and TTIP is that for precursor  $\text{Ti}(\text{dpm})_2(\text{OPr}^i)_2$ , polycrystalline rutile films were obtained, while for TTIP the films consist of polycrystalline anatase. It is important to emphasize that the synthesis conditions for films derived from both precursors were very similar (see Table 1), and the resulting crystal structure was independent of the substrate (glass, fused silica or Si-wafer). Thus, the choice of the precursor can be used to control the form of the titanium dioxide produced. It was noted that there is a difference in the thin film crystal orientation, when  $\text{TiO}_2$  films have been prepared with TTIP precursor placed into the evaporator inside or outside the vacuum chamber. We suppose that the difference in the microcrystal orientation is due to differences in the vapour content of the TTIP precursor evaporated at different conditions. According to the XRD results, the presence of Fe and S in the crystal structure of  $\text{TiO}_2$  thin films does not change the type of crystal modification, and it remains the anatase structure. Typical XRD patterns are shown in Figures 1 and 2. No additional peaks belonging to separate iron oxides are observed.

Average concentration of impurities in the  $\text{TiO}_2$  films was obtained by laser ionization mass spectrometry. The results of the LIMS analysis are shown at Table 2.

All the analyzed samples were synthesized on fused silica substrates, so that the presence of Na and Ca is relatively small and the presence of these elements should be related to the heated parts used in the construction of the substrate heater. Large sample to sample contamination variability

TABLE 2: The results of mass-spectrometry analysis; the values are shown in %. n/d: not detected; the detectability threshold is given in brackets.

Impurity	Sample 1	Sample 2	Sample 3	Sample 4	Sample 5
C	$\approx 5 \cdot 10^{-1}$				
N	$\leq 2 \cdot 10^{-2}$	$\leq 2 \cdot 10^{-2}$	$\leq 2 \cdot 10^{-2}$	$\leq 4 \cdot 10^{-2}$	$\leq 4 \cdot 10^{-2}$
Na	$< 2 \cdot 10^{-1}$				
Mg	$< 1 \cdot 10^{-2}$				
Al	$5 \cdot 10^{-3}$	$3 \cdot 10^{-2}$	$7 \cdot 10^{-3}$	$4 \cdot 10^{-3}$	$1 \cdot 10^{-2}$
P	$3 \cdot 10^{-3}$	$3 \cdot 10^{-3}$	$3 \cdot 10^{-3}$	$1 \cdot 10^{-3}$	$2 \cdot 10^{-3}$
Cl	$1 \cdot 10^{-2}$	$5 \cdot 10^{-2}$	$1 \cdot 10^{-2}$	$7 \cdot 10^{-3}$	$4 \cdot 10^{-2}$
K	$2 \cdot 10^{-1}$	$4 \cdot 10^{-2}$	$2 \cdot 10^{-2}$	$1 \cdot 10^{-2}$	$2 \cdot 10^{-2}$
Ca	$7 \cdot 10^{-2}$	$1 \cdot 10^{-1}$	$3 \cdot 10^{-2}$	$8 \cdot 10^{-2}$	$8 \cdot 10^{-2}$
Cr	$1 \cdot 10^{-3}$	$7 \cdot 10^{-4}$	$5 \cdot 10^{-4}$	$1 \cdot 10^{-3}$	$5 \cdot 10^{-3}$
Mn	$6 \cdot 10^{-4}$	$1 \cdot 10^{-3}$	$9 \cdot 10^{-4}$	$3 \cdot 10^{-4}$	$1 \cdot 10^{-3}$
Fe	$1 \cdot 10^{-2}$	$3 \cdot 10^{-1}$	$2 \cdot 10^{-1}$	$1 \cdot 10^{-1}$	$1 \cdot 10^{-1}$
Co	n/d ( $6 \cdot 10^{-4}$ )				
Ni	$2 \cdot 10^{-3}$	$8 \cdot 10^{-4}$	n/d ( $6 \cdot 10^{-4}$ )	n/d ( $6 \cdot 10^{-4}$ )	$5 \cdot 10^{-3}$
Cu	$3 \cdot 10^{-3}$	$4 \cdot 10^{-1}$	$2 \cdot 10^{-1}$	$1 \cdot 10^{-1}$	$1 \cdot 10^{-1}$
Zn	$3 \cdot 10^{-2}$	$4 \cdot 10^{-2}$	$1 \cdot 10^{-1}$	$2 \cdot 10^{-2}$	$5 \cdot 10^{-2}$

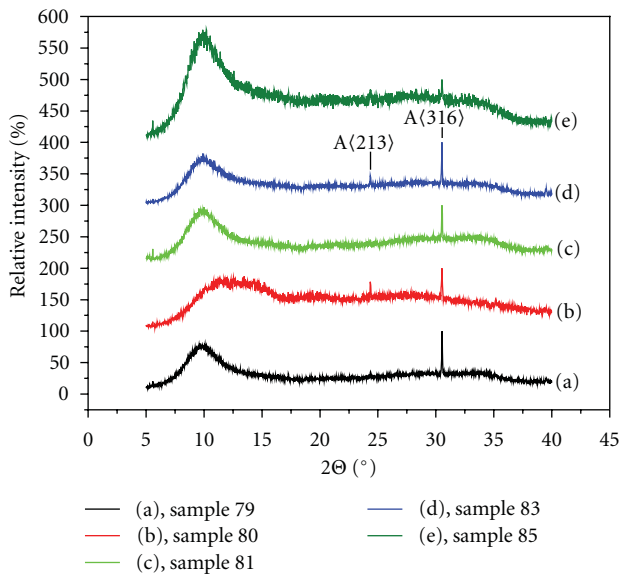


FIGURE 2: X-ray diffraction patterns for anatase  $\text{TiO}_2:(\text{Fe}, \text{S})$  thin films obtained from the external evaporator in a controlled  $\text{Ar}/\text{O}_2$  atmosphere.

is observed for Fe, Cu, K, and Zn. The origin of the Zn contamination for sample 3 and the K contamination for sample 1 is not yet clear. The Fe and Cu impurities probably originate from the interaction of the precursor vapors with the metallic parts of the CVD apparatus. The presence of C at  $5 \cdot 10^{-1}\%$  wt can be attributed to the residual carbon deposited during the process of the precursor decomposition.

Some typical images of the surfaces of  $\text{TiO}_2:(\text{Fe}, \text{S})$  samples obtained by SEM are shown in Figures 3(a) and 3(b). Elemental analysis obtained by EDX (e.g., sample 72) is shown in Figure 4 and Table 3. EDX spectra were taken

at the sample angles of  $30^\circ$  and  $60^\circ$  to examine influence of the substrate. Analysis shows that there are not significant differences in the spectra between these both positions of the sample.

XPS spectra were taken at the angle of  $0^\circ$  and  $60^\circ$  relative to the normal to the surface of the sample in order to document the changes in composition of the film in dependence of the depth near the surface. The relative contents of the elements are given in Table 4. The XPS results demonstrated that samples 30 and 31 are slightly contaminated with sodium and zinc, respectively. The origin of this contamination is unclear. These samples were analysed by XPS after their photocatalytic activity studies were performed. Therefore, these contaminations may originate from the aqueous solutions that have been in contact with the sample surface. Comparing the mass spectrometry data with those of the XPS analysis, we note that a larger concentration of carbon is found on the surface compared to the bulk, indicating the redistribution of carbon during thin-film growth. Several process parameters affect the surface contamination by carbon, including the synthesis temperature, the oxygen concentration in the vapour phase during film growth, and the type of precursor.

The total carbon content decreases with increasing process temperature for samples synthesized from  $\text{Ti}(\text{dpm})_2(\text{OPr}^i)_2$  in vacuum. The carbon content is also lower for samples prepared in the presence of oxygen under otherwise identical conditions, which may be explained in at least two different ways. Firstly, as it was shown by mass spectrometric analysis of the  $\text{Ti}(\text{dpm})_2(\text{OPr}^i)_2$  decomposition products that the thermolysis mechanism is different in vacuum and in presence of oxygen [39].

Secondly, the decomposition products will form gaseous CO and  $\text{CO}_2$  much more easily in the presence of oxygen than in vacuum. The total carbon content of the samples prepared from TTIP in the presence of oxygen is even lower

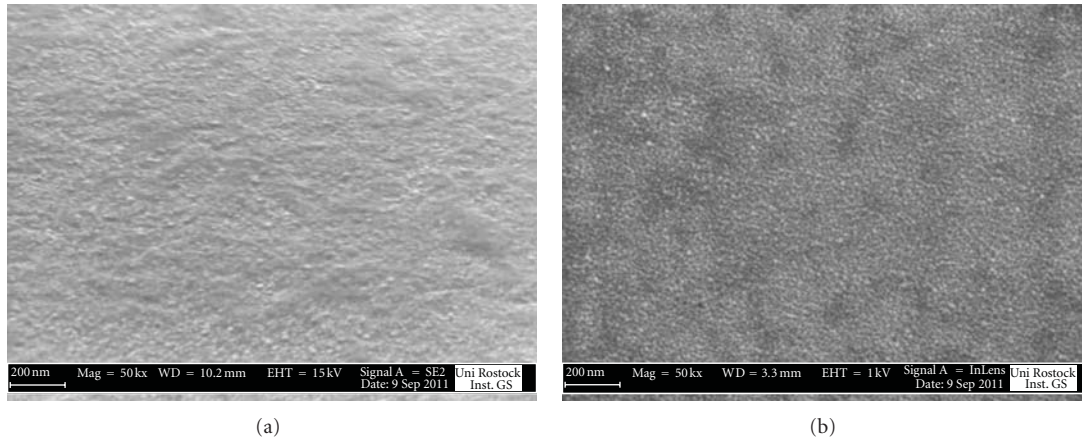


FIGURE 3: (a) SEM image of the  $\text{TiO}_2:(\text{Fe}, \text{S})$  sample 72. (b) SEM image of the  $\text{TiO}_2:(\text{Fe}, \text{S})$  sample 74.

TABLE 3: Quantitative results of the EDX analysis of  $\text{TiO}_2:(\text{Fe}, \text{S})$ , sample 72.

Element	OZ	Series	Netto	C, wt% normalized	C, at%
C	6	K-series	3957	0.96	1.60
Na	11	K-series	79956	9.62	8.43
Mg	12	K-series	23091	2.42	2.01
Al	13	K-series	7444	0.73	0.55
Si	14	K-series	285189	28.55	20.47
S	16	K-series	922	0.11	0.07
K	19	K-series	3966	0.66	0.34
Ca	20	K-series	20759	4.29	2.15
Ti	22	K-series	6252	1.94	0.82
Fe	26	K-series	457	0.29	0.10
O	8	K-series	201328	50.43	63.46

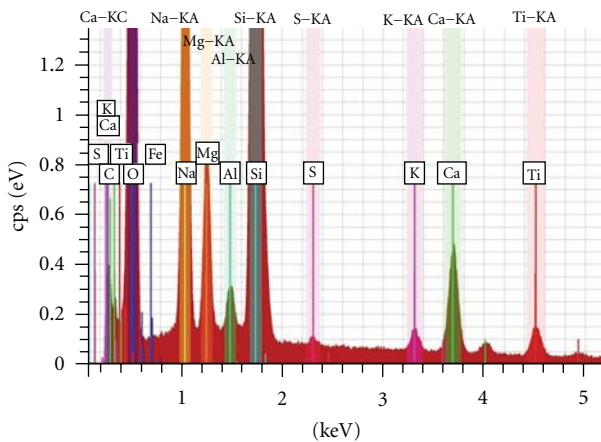


FIGURE 4: EDX spectrum of the  $\text{TiO}_2:(\text{Fe}, \text{S})$ , Sample 72.

and increases with increasing processing temperature, which is probably related to a different kinetic mechanism of thin-film growth. The latter hypothesis is supported by the fact that the crystal structures of the films prepared from the two precursors are different.

Comparing the results of LIMS, EDX, and XPS tests, Tables 2, 3, and 4, it can be concluded that the initial presence of Fe, without doping, is at a concentration of about 0.1%, and S is not found by LIMS. When a small amount of the precursor  $\text{FeDtc}$  (of 0.008 g and 0.016 g) had evaporated, a small concentration of Fe and S was detected by EDX in the volume of the films. However, as the analysis of XPS Fe and S does not register them in the surface layers, this means that the concentration of Fe and S in these layers is less than the detection limit by the XPS (around 0.1%).

The surface morphology of the  $\text{TiO}_2:\text{Fe}$  thin films was investigated as a function of various parameters, such as thickness, the type of substrate, percentage of doping element, and the mode of deposition, meaning deposition from the interior or exterior sources of the precursor vapours. The AFM results demonstrated that the  $\text{TiO}_2$  film samples have a porous polycrystalline structure with a typical crystallite size of about 100 nm. The results of the AFM studies are shown in Figures 5(a)–5(d) and 6(a)–6(d) and in Table 5. As it can be seen, the surface roughness does not depend on the type of substrate (Figures 5(a) and 5(b)). However, the surface roughness depends on the thin film thickness, the mode of the film preparation, and on the doping element concentration. Average crystallite size data was determined from AFM

TABLE 4: Composition (atom percentage, %) of TiO<sub>2</sub> films according to XPS analyses (The composition is shown for XPS spectra taken at 0°).

Attribution		Sample 1	Sample 30	Sample 31	Sample 65	Sample 66	Sample 75	Sample 77	Sample 85
Ti, 2p	Ti	12.9	20.9	20.7	21.7	22.0	18.34	16.93	11.2
Oxygen, 1s	O	40.7	63.2	59.0	61.24	59.4	52.72	51.84	43.65
Carbon total	C	39.0	14.8	20.3	17.1	22.0	23.21	27.1	33.0
Fluorine, 1s	F	—	—	—	—	—	5.2	2.34	8.04
Sodium, 1s	Na	—	—	—	—	—	—	—	3.0
Iron, 2p	Fe	—	—	—	—	—	—	1.02	0.47
Sulphur, 2p	S	—	—	—	—	—	0.53	0.77	0.57
Stoichiometry		TiO <sub>2.4</sub>	TiO <sub>2.48</sub>	TiO <sub>2.47</sub>	TiO <sub>2.25</sub>	TiO <sub>2.25</sub>	TiO <sub>2.22</sub>	TiO <sub>2.3</sub>	TiO <sub>2.2</sub>

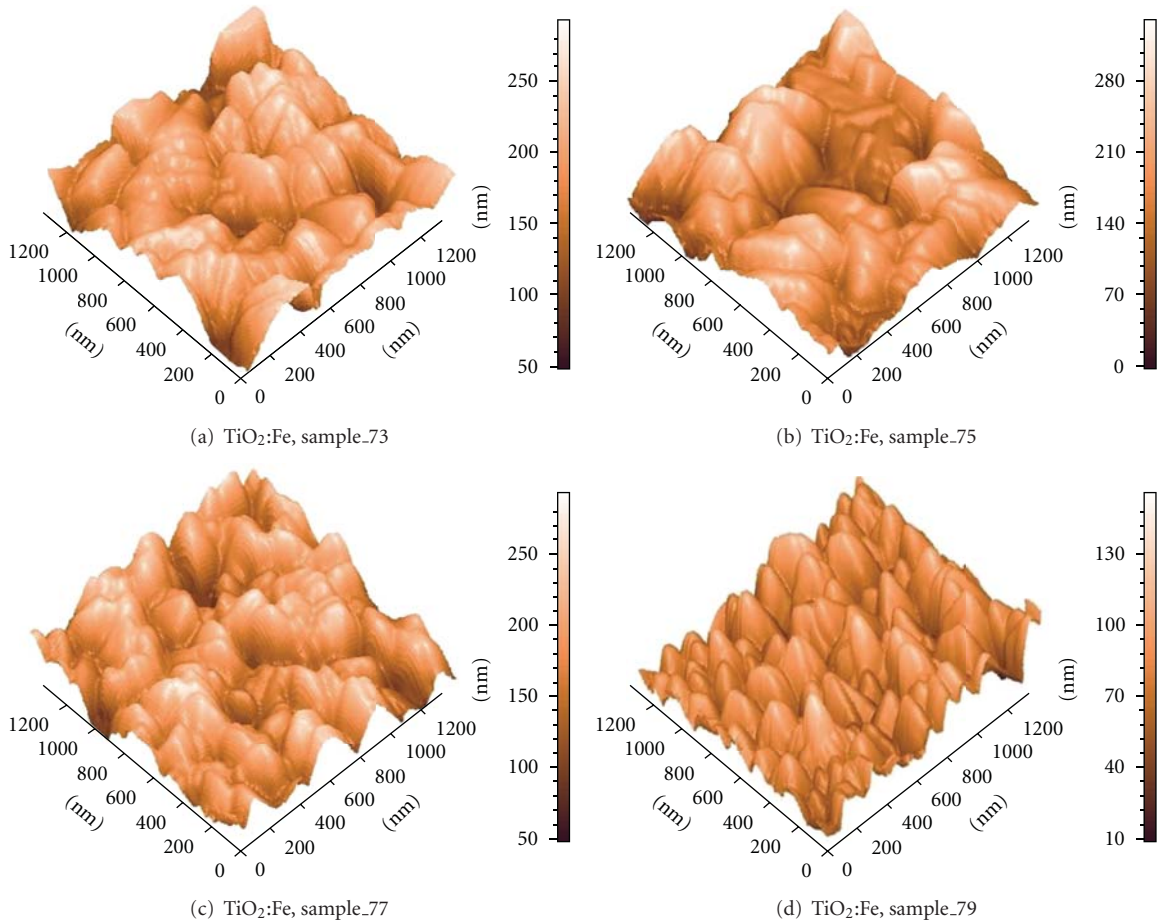


FIGURE 5: The AFM image of the samples with the thin film thickness 600–1000 nm (the field size is 1.2  $\mu\text{m}$  by 1.2  $\mu\text{m}$ ; the shades of grey correspond to the vertical scale of the recording of 0 to 250 nm). Samples 73–77 (internal evaporator), sample 79, (external evaporator).

analysis. This analysis was found to give data whose values are coincident with those obtained by X-ray line broadening using Warren-Averbach analysis [40]. The average crystallite sizes in dependence on the thin films thicknesses are shown in Figure 7. It is important to note that when the concentration of Fe was increased, the average crystallite size was found to be decreased. It can be noted that the usage of the internal evaporator also leads to much bigger crystallite sizes.

Figure 8 shows the UV-Vis transmittance spectra of the prepared samples. The absorption threshold of all the

samples TiO<sub>2</sub>:Fe (1–5%) is about 370 nm to –385 nm, which corresponds to the band-gap energy of anatase (3.2 eV). The film thickness of the samples 73 and 75 is about 1  $\mu\text{m}$ ; therefore, the transmittance in the visible range of the light spectrum is not high (about 50%), and it is not connected with the photon adsorption due to the presence of the Fe impurities. The transmittance spectra of the heavy doped Sample 87 is different because of the mixing of TiO<sub>2</sub> and Fe<sub>3</sub>O<sub>4</sub> phases. With the increasing content of Fe, the prepared samples acquired a reddish tinge, while sample 87 turned pale red.

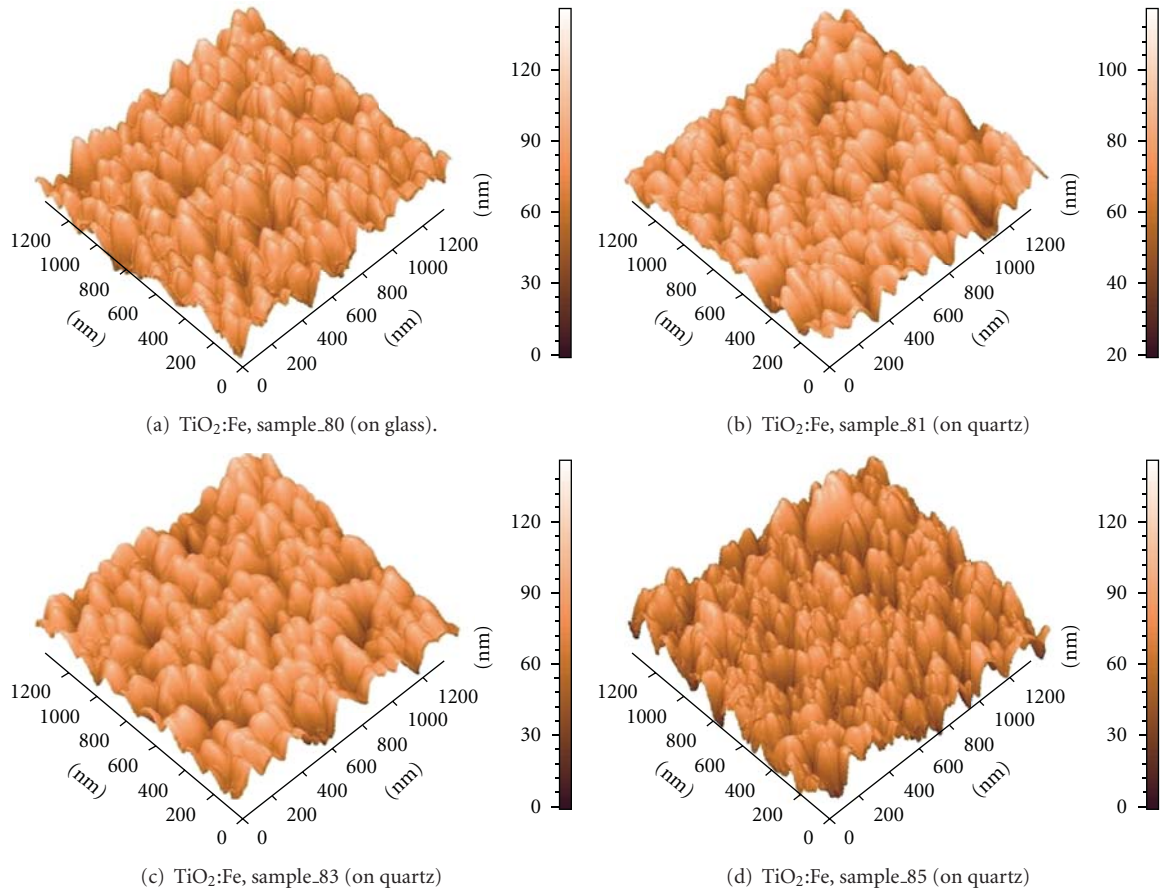


FIGURE 6: The AFM image of the sample with the thin film thickness  $\sim 500$  nm (the field size is  $1.2 \mu\text{m}$  by  $1.2 \mu\text{m}$ ; the shades of grey correspond to the vertical scale of the recording of 0 to 250 nm). External evaporator.

TABLE 5: Surface morphology data of the samples TiO<sub>2</sub>:Fe obtained by AFM.

Sample	Film thickness (nm)	Quantity of FeDtc in the evaporator (g)	Evaporation mode	Maximum size, $h$ (nm)	Medium size $\langle h \rangle$ (nm)	Medium irregularity $S_{\Delta h}$ (nm)
73	800	0.008	Internal	381	203	51.8
75	918	0.016	Internal	370	208	51.2
77	593	0.032	Internal	338	228	36.1
79	1045	0.008	External	215	104	22.8
80	560	0.016	External	142	72	13.3
81	580	0.016	External	134	84	15.1
83	760	0.032	External	183	114	18.2
85	480	0.064	External	120	67	11.8
87	145	0.300	External	79	39	10.1

The conversion electron Mössbauer spectra (CEMS) recorded from sample 87 are shown in Figure 9. It consists of a single sextet, which suggests magnetic ordering of the Fe<sup>3+</sup> ions. As shown recently [41], at <sup>57</sup>Fe concentrations of about 0.1% to  $-1\%$ , CEMS spectra exhibit the doublet lines of the hyperfine splitting. The effects of magnetic correlations were explained by the existence of the bound magnetic polaron (BMP) mechanism [41]. CEMS spectra obtained in this study were obtained for the samples with the concentration

of Fe that is much higher, because of a small concentration of isotope <sup>57</sup>Fe in FeDtc precursor. The ordering type of magnetite (Fe<sub>3</sub>O<sub>4</sub>) was observed.

The kinetics of the Fenarimol decay and the kinetics of its intermediate photoproduct ( $m/z$  328) formation for different thin films are shown in Figures 10(a) and 10(b), respectively. Abundances of Fenarimol and the intermediate photoproduct are expressed here by the respective chromatographic peak areas, which for the same experimental conditions are

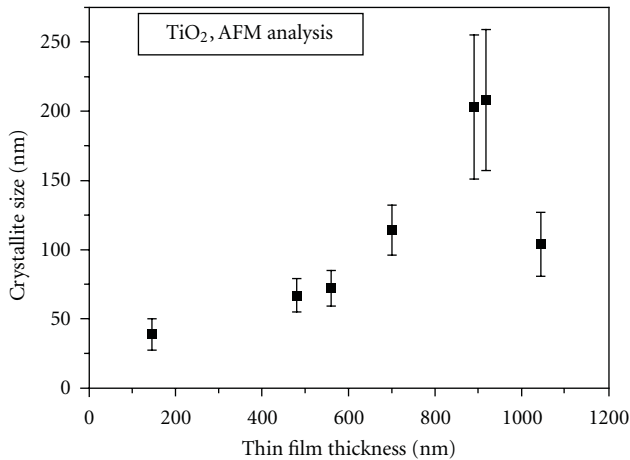


FIGURE 7: Results of AFM analysis of average particle sizes in anatase  $\text{TiO}_2$  thin films in dependence on thin film thickness.

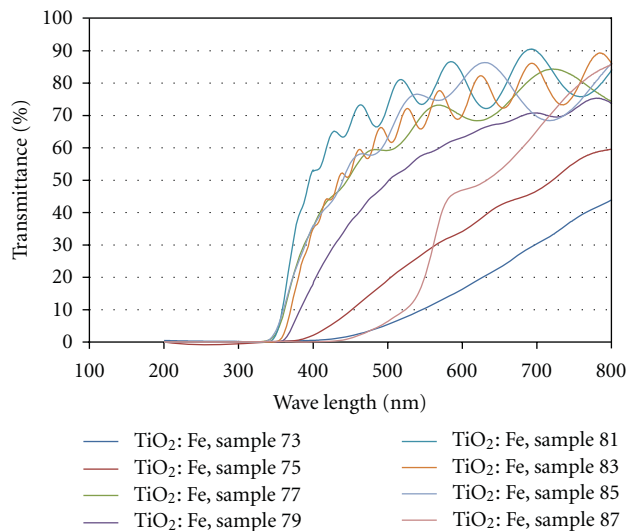


FIGURE 8: Transmittance UV-Vis spectra of iron doped  $\text{TiO}_2$  thin films. Samples 73–77 were prepared from the internal, and Samples 79–87 from the external precursors vapor source.

proportional to the chemical concentration for each instant of analysis time.

Of all the films tested, the  $\text{TiO}_2$  films prepared from TTIP were the only samples to exhibit photocatalytic activity. As one can see, only for these samples the concentration of intermediate photoproducts starts to decrease after about 1.5 hours of irradiation. The photocatalytic performance of the same weight of the Degussa P25 powder deposited on glass is still better than that of the CVD films (Figure 10). However, one should take the difference in the specific area of the CVD thin films and that of the Degussa powder film into account. The CVD films grown for this study had a good transparency to the eye. AFM images revealed the film crystallites of about 100 nm in diameter. Therefore, following [24], we may presume the electrode-specific surface area was not very different from the geometric area ( $\sim 0.00785 \text{ m}^2$ ). In the case where 7 mg, the typical mass of a CVD film, of the Degussa

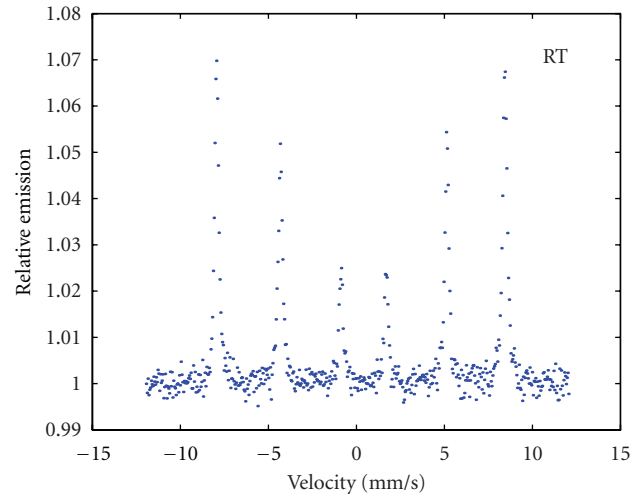


FIGURE 9: Mössbauer spectra of the  $\text{TiO}_2\text{:Fe}$ , Sample 87 at room temperature (RT).

P25 powder was dissolved in water, the specific area would be about  $0.35 \text{ m}^2$  supposing well-separated microcrystals (about  $50 \text{ m}^2/\text{g}$  [22]). However, it is clear that powder deposited on the glass substrate does not have such a big specific surface area. As follows from Figure 10(a), samples 65 and 66 were the most active photocatalytic thin films. Samples 65 and 66 were prepared from TTIP + FeDtc (0.008 g) and 66 from TTIP + TBDS (Vapours), respectively (see Table 1), so that the first sample is supposed to be doped with Fe and with S, and the second sample only with S. However, the XPS analysis did not show the presence of Fe or S on the surface layer of these samples. The relative concentration of other elements (Ti, O, and C) revealed by XPS is typical for the samples prepared from TTIP (see Table 4). Further increase of the amount of FeDtc precursor during the synthesis (samples 75, 77 and 85) resulted in the preparation of the  $\text{TiO}_2\text{:}(\text{Fe}, \text{S})$ -doped thin films as it was shown by XPS. However, the photocatalytic activity of these samples is lower than that of 65 and 66 samples. It was also found that samples 75, 77, and 85 are contaminated with fluorine, the source of such contamination and its influence on photocatalytic activity is not established yet.

After analysis of the obtained results, the following can be stated: (1) the  $\text{TiO}_2\text{:}(\text{Fe}, \text{S})$  thin films, prepared from TTIP by CVD, are in the anatase form, which is most effective for photocatalysis. (2) The most effective surface was observed for the films with the thickness of about  $1 \mu\text{m}$ . Just this kind of films was used in the studies of photocatalytic efficiency. (3) There is no presence of crystalline iron oxide phases in  $\text{TiO}_2\text{:}(\text{Fe}, \text{S})$  thin films revealed by XRD. (4) When the concentration of Fe is low, the transmittance spectra are similar to those of nondoped thin films. For this reason, the UV part of the radiation spectrum was used to compare the photocatalytic activity of  $\text{TiO}_2\text{:}(\text{Fe}, \text{S})$  thin films with that of Degussa P25 powder. (5) According to theoretical results, the doping of  $\text{TiO}_2$  with transitional metals, such as Fe, leads to the appearance of electronic states inside the band-gap of  $\text{TiO}_2$  and, thus, to an increase of the photocatalytic efficiency.

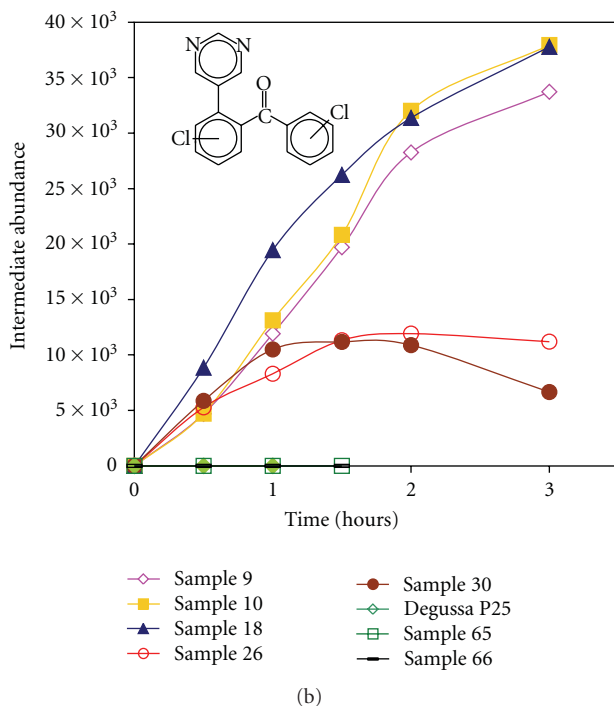
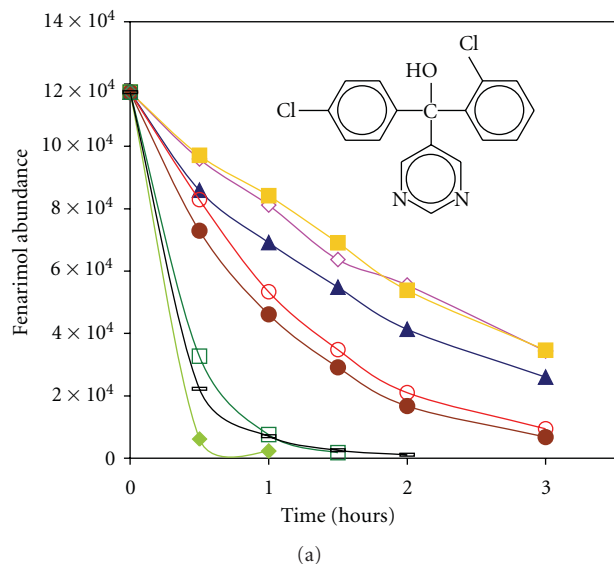


FIGURE 10: Contents of Fenarimol solution (a) and intermediate photoproduct (b) in dependence on time, under UV illumination, when in contact with several different  $\text{TiO}_2$  thin films.

Therefore, the increased photocatalytic activity of optimally prepared  $\text{TiO}_2:(\text{Fe}, \text{S})$  thin films in the UV region can be expected in comparison with non-doped Degussa P25 powder. It can be seen, that in the experiments on Fenarimol photocatalytic decay, the photocatalytic activity (PhAc) of  $\text{TiO}_2:(\text{Fe}, \text{S})$  (PhAc( $\text{TiO}:\text{Fe}$ )) is comparable with that of Degussa P25 (PhAc(P25)), but PhAc( $\text{TiO}:\text{Fe}$ ) is still lower than PhAc(P25).

There is a contradiction with the theoretical model. It can be pointed out that the hydrophilicity of  $\text{TiO}_2:\text{Fe}$  is anomalously high under UV light irradiation [24, 25]. This means

the presence of anchoring water splitting centres and, as a result, the more effective creation of  $\text{H}^+$  and  $\text{OH}^-$  radicals. This effect is supposed to be favourable for PhAc( $\text{TiO}:\text{Fe}$ ). In practice, this does not lead to greater PhAc( $\text{TiO}:\text{Fe}$ ) in the UV region as compared to PhAc(P25). It can be assumed that the generation of electron-hole pairs at the Fe impurity gives a small contribution to the PhAc( $\text{TiO}:\text{Fe}$ ). It was shown earlier (see, e.g., [42]) that PhAc(doped  $\text{TiO}_2$ ) is higher than PhAc(non-doped  $\text{TiO}_2$  and P25) in the visible light region. In the UV region the PhAc(doped  $\text{TiO}_2$ ) is still lower than the PhAc(P25). This only means that the excitation mechanisms of electron-hole pair through the  $\text{TiO}_2$  bandgap by incident photons with energy lower than band-gap energy is switched off in the main mechanism of photocatalysis. Powder P25 also has some PhAc(P25) in visible light region, possibly due to lattice defects and impurities.

#### 4. Conclusions

The physical and photocatalytic properties of thin films  $\text{TiO}_2:\text{Fe}$  and  $\text{TiO}_2:\text{S}$  prepared by CVD using complex compound precursors,  $\text{Ti}(\text{dpm})_2(\text{OPr}^i)_2$ ,  $\text{Ti}(\text{OPr}^i)_4$ , and  $\text{Fe}[(\text{C}_2\text{H}_5)_2\text{NCS}_2]_3$ ,  $[(\text{CH}_3)_2\text{C}]_2\text{S}_2(\text{TBDS})$  were discussed. Two different crystalline forms, rutile and anatase, could be prepared using these precursors, as demonstrated by XRD. LIMS and XPS analysis revealed that the surface composition is different from that of the film, basically because of carbon presence. From the results of LIMS, EDX, and XPS tests for low-doped samples, it can be concluded that small concentrations of Fe and S of both elements are present in the films. As it is shown from the Mössbauer spectra, Fe ions are magnetically ordered in the heavy-doped  $\text{TiO}_2$  thin films. By this fact, the lowering of the photocatalytic activity due to existence of the additional channel of the photon energy relaxation can be explained. The structure of  $\text{TiO}_2$  thin film photocatalyst has a dominating effect on the photodegradation rate of the Fenarimol test compound, namely only the anatase form of pure and doped  $\text{TiO}_2$  thin films shows photocatalytic activity. It was shown that an increased photocatalytic activity of (Fe, S)-doped  $\text{TiO}_2$  thin-films is, actually, very close to Degussa P25 powder activity. However, to answer the question of what exactly happened with this kind of substitution of Ti or O sites by Fe and S in  $\text{TiO}_2$ , further studies by XPS and nuclear resonant methods using synchrotron radiation are needed.

#### Acknowledgments

The authors are grateful to Fundação para a Ciência e Tecnologia for the financial support given in the framework of the Projects POCTI/43520/FIS/2000 and CONC-REEQ/700/2001. The steady support of HASYLAB is highly appreciated. The authors thank R. Lange for the technical assistance with SEM and EDX. The collaboration with M. Stir and R. C. Nicula in the initial phase of this work is gratefully acknowledged.

## References

- [1] S. Yin, Q. Zhang, F. Saito, and T. Sato, "Preparation of visible light-activated titania photocatalyst by mechanochemical method," *Chemistry Letters*, vol. 32, no. 4, pp. 358–359, 2003.
- [2] T. Umabayashi, T. Yamaki, H. Itoh, and K. Asai, "Analysis of electronic structures of 3d transition metal-doped TiO<sub>2</sub> based on band calculations," *Journal of Physics and Chemistry of Solids*, vol. 63, no. 10, pp. 1909–1920, 2002.
- [3] J. Zhu, W. Zheng, B. He, J. Zhang, and M. Anpo, "Characterization of Fe-TiO<sub>2</sub> photocatalysts synthesized by hydrothermal method and their photocatalytic reactivity for photodegradation of XRG dye diluted in water," *Journal of Molecular Catalysis A*, vol. 216, no. 1, pp. 35–43, 2004.
- [4] A. Di Paola, G. Marci, L. Palmisano et al., "Preparation of polycrystalline TiO<sub>2</sub> photocatalysts impregnated with various transition metal ions: characterization and photocatalytic activity for the degradation of 4-nitrophenol," *Journal of Physical Chemistry B*, vol. 106, no. 3, pp. 637–645, 2002.
- [5] D. W. Bahnemann, S. N. Kholuiskaya, R. Dillert, A. I. Kulak, and A. I. Kokorin, "Photodestruction of dichloroacetic acid catalyzed by nano-sized TiO<sub>2</sub> particles," *Applied Catalysis B*, vol. 36, no. 2, pp. 161–169, 2002.
- [6] K. Nagaveni, M. S. Hegde, and G. Madras, "Structure and photocatalytic activity of Ti<sub>1-x</sub>M<sub>x</sub>O<sub>2±δ</sub> (M = W, V, Ce, Zr, Fe, and Cu) synthesized by solution combustion method," *Journal of Physical Chemistry B*, vol. 108, no. 52, pp. 20204–20212, 2004.
- [7] R. Asahi, T. Morikawa, T. Ohwaki, K. Aoki, and Y. Taga, "Visible-light photocatalysis in nitrogen-doped titanium oxides," *Science*, vol. 293, no. 5528, pp. 269–271, 2001.
- [8] I. N. Martyanov, S. Uma, S. Rodrigues, and K. J. Klabunde, "Structural defects cause TiO<sub>2</sub>-based photocatalysts to be active in visible light," *Chemical Communications*, vol. 10, no. 21, pp. 2476–2477, 2004.
- [9] G. Shang, H. Fu, S. Yang, and T. Xu, "Mechanistic study of visible-light-induced photodegradation of 4-chlorophenol by TiO<sub>2-x</sub>N<sub>x</sub> 0.021 < x < 0.049 with low nitrogen concentration," *International Journal of Photoenergy*, vol. 2012, Article ID 759306, 2012.
- [10] T. Umabayashi, T. Yamaki, H. Itoh, and K. Asai, "Band gap narrowing of titanium dioxide by sulfur doping," *Applied Physics Letters*, vol. 81, no. 3, p. 454, 2002.
- [11] T. Ma, M. Akiyama, E. Abe, and I. Imai, "High-efficiency dye-sensitized solar cell based on a nitrogen-doped nanostructured titania electrode," *Nano Letters*, vol. 5, no. 12, pp. 2543–2547, 2005.
- [12] C. Di Valentin, G. Pacchioni, A. Selloni, S. Livraghi, and E. Giamello, "Characterization of paramagnetic species in N-doped TiO<sub>2</sub> powders by EPR spectroscopy and DFT calculations," *Journal of Physical Chemistry B*, vol. 109, no. 23, pp. 11414–11419, 2005.
- [13] S. Livraghi, A. Votta, M. C. Paganini, and E. Giamello, "The nature of paramagnetic species in nitrogen doped TiO<sub>2</sub> active in visible light photocatalysis," *Chemical Communications*, no. 4, pp. 498–500, 2005.
- [14] S. Livraghi, M. C. Paganini, E. Giamello, A. Selloni, C. Di Valentin, and G. Pacchioni, "Origin of photoactivity of nitrogen-doped titanium dioxide under visible light," *Journal of the American Chemical Society*, vol. 128, no. 49, pp. 15666–15671, 2006.
- [15] A. Ghicov, J. M. Macak, H. Tsuchiya et al., "Ion implantation and annealing for an efficient N-doping of TiO<sub>2</sub> nanotubes," *Nano Letters*, vol. 6, no. 5, pp. 1080–1082, 2006.
- [16] M. Batzill, E. H. Morales, and U. Diebold, "Influence of nitrogen doping on the defect formation and surface properties of TiO<sub>2</sub> rutile and anatase," *Physical Review Letters*, vol. 96, no. 2, Article ID 026103, 2006.
- [17] T. Yamaki, T. Umabayashi, T. Sumita et al., "Fluorine-doping in titanium dioxide by ion implantation technique," *Nuclear Instruments and Methods in Physics Research B*, vol. 206, pp. 254–258, 2003.
- [18] Y. Choi, T. Umabayashi, S. Yamamoto, and S. Tanaka, "Fabrication of TiO<sub>2</sub> photocatalysts by oxidative annealing of TiC," *Journal of Materials Science Letters*, vol. 22, no. 17, pp. 1209–1211, 2003.
- [19] X. Hong, Z. Wang, W. Cai et al., "Visible-light-activated nanoparticle photocatalyst of iodine-doped titanium dioxide," *Chemistry of Materials*, vol. 17, no. 6, pp. 1548–1552, 2005.
- [20] H. Luo, T. Takata, Y. Lee, J. Zhao, K. Domen, and Y. Yan, "Photocatalytic activity enhancing for titanium dioxide by co-doping with bromine and chlorine," *Chemistry of Materials*, vol. 16, no. 5, pp. 846–849, 2004.
- [21] L. Zhao, J. Ran, Z. Shu, G. Dai, P. Zhai, and S. Wang, "Effects of calcination temperatures on photocatalytic activity of ordered titanate nanoribbon/SnO<sub>2</sub> films fabricated during an EPD process," *International Journal of Photoenergy*, vol. 2012, Article ID 472958, 2012.
- [22] A. Mills, N. Elliott, I. P. Parkin, S. A. O'Neill, and R. J. Clark, "Novel TiO<sub>2</sub> CVD films for semiconductor photocatalysis," *Journal of Photochemistry and Photobiology A*, vol. 151, no. 1–3, pp. 171–179, 2002.
- [23] H. Jiang and L. Gao, "Enhancing the UV inducing hydrophilicity of TiO<sub>2</sub> thin film by doping Fe ions," *Materials Chemistry and Physics*, vol. 77, no. 3, pp. 878–881, 2002.
- [24] M. L. Hitchman and F. Tian, "Studies of TiO<sub>2</sub> thin films prepared by chemical vapour deposition for photocatalytic and photoelectrocatalytic degradation of 4-chlorophenol," *Journal of Electroanalytical Chemistry*, vol. 538–539, pp. 165–172, 2002.
- [25] Y. Suda, H. Kawasaki, T. Ueda, and T. Ohshima, "Preparation of high quality nitrogen doped TiO<sub>2</sub> thin film as a photocatalyst using a pulsed laser deposition method," *Thin Solid Films*, vol. 453–454, pp. 162–166, 2004.
- [26] J. G. Yu, H. G. Yu, B. Cheng, X. J. Zhao, J. C. Yu, and W. K. Ho, "The effect of calcination temperature on the surface microstructure and photocatalytic activity of TiO<sub>2</sub> thin films prepared by liquid phase deposition," *Journal of Physical Chemistry B*, vol. 107, no. 50, pp. 13871–13879, 2003.
- [27] Q. Xiang, J. Yu, and M. Jaroniec, "Tunable photocatalytic selectivity of TiO<sub>2</sub> films consisted of flower-like microspheres with exposed 001 facets," *Chemical Communications*, vol. 47, no. 15, pp. 4532–4534, 2011.
- [28] S. K. Zheng, T. M. Wang, C. Wang, and G. Xiang, "Photocatalytic activity study of TiO<sub>2</sub> thin films with and without Fe ion implantation," *Nuclear Instruments and Methods in Physics Research B*, vol. 187, no. 4, pp. 479–484, 2002.
- [29] S. K. Zheng, T. M. Wang, W. C. Hao, and R. Shen, "Improvement of photocatalytic activity of TiO<sub>2</sub> thin film by Sn ion implantation," *Vacuum*, vol. 65, no. 2, pp. 155–159, 2002.
- [30] B. Z. Rameev, F. Yildiz, L. R. Tagirov, B. Aktaş, W. K. Park, and J. S. Moodera, "ESR study of Co-doped TiO<sub>2</sub> thin films," *Journal of Magnetism and Magnetic Materials*, vol. 258–259, pp. 361–364, 2003.
- [31] J. Yu, Q. Xiang, and M. Zhou, "Preparation, characterization and visible-light-driven photocatalytic activity of Fe-doped titania nanorods and first-principles study for electronic structures," *Applied Catalysis B*, vol. 90, no. 3–4, pp. 595–602, 2009.

- [32] Z. Xu and J. Yu, "Visible-light-induced photoelectrochemical behaviors of Fe-modified TiO<sub>2</sub> nanotube arrays," *Nanoscale*, vol. 3, no. 8, pp. 3138–3144, 2011.
- [33] Y. Li, W. Wlodarski, K. Galatsis et al., "Gas sensing properties of p-type semiconducting Cr-doped TiO<sub>2</sub> thin films," *Sensors and Actuators B*, vol. 83, no. 1–3, pp. 160–163, 2002.
- [34] T. Sumita, T. Yamaki, S. Yamamoto, and A. Miyashita, "Photo-induced surface charge separation of highly oriented TiO<sub>2</sub> anatase and rutile thin films," *Applied Surface Science*, vol. 200, no. 1–4, pp. 21–26, 2002.
- [35] V. Collins-Martínez, A. L. Ortiz, and A. A. Elguézabal, "Influence of the anatase/rutile ratio on the TiO<sub>2</sub> photocatalytic activity for the photodegradation of light hydrocarbons," *International Journal of Chemical Reactor Engineering*, vol. 5, article A92, 2007.
- [36] J. Ryu and W. Choi, "Substrate-specific photocatalytic activities of TiO<sub>2</sub> and multiactivity test for water treatment application," *Environmental Science and Technology*, vol. 42, no. 1, pp. 294–300, 2008.
- [37] V. G. Bessergenev, R. J. F. Pereira, and A. M. Botelho do Rego, "Thin film sulphides and oxides of 3d metals prepared from complex precursors by CVD," *Surface and Coatings Technology*, vol. 201, no. 22-23, pp. 9141–9145, 2007.
- [38] V. G. Besserguenev, R. J. F. Pereira, M. C. Mateus, I. V. Khmelinskii, R. C. Nicula, and E. Burkel, "TiO<sub>2</sub> thin film synthesis from complex precursors by CVD, its physical and photocatalytic properties," *International Journal of Photoenergy*, vol. 5, no. 2, pp. 99–105, 2003.
- [39] V. G. Bessergenev, I. V. Khmelinskii, R. J. F. Pereira, V. V. Krisuk, A. E. Turgambaeva, and I. K. Igumenov, "Preparation of TiO<sub>2</sub> films by CVD method and its electrical, structural and optical properties," *Vacuum*, vol. 64, no. 3-4, pp. 275–279, 2002.
- [40] A. A. Gribb and J. F. Banfield, "Particle size effects on transformation kinetics and phase stability in nanocrystalline TiO<sub>2</sub>," *American Mineralogist*, vol. 82, no. 7-8, pp. 717–728, 1997.
- [41] M. N. Grecu, S. Constantinescu, D. Tărăbășanu-Mihăilă, D. Ghica, and I. Bibicu, "Spin dynamics in <sup>57</sup>Fe-doped TiO<sub>2</sub> anatase nanoparticles," *Physica Status Solidi B*, vol. 248, no. 12, pp. 2927–2931, 2011.
- [42] X. Yang, F. Ma, K. Li et al., "Mixed phase titania nanocomposite codoped with metallic silver and vanadium oxide: new efficient photocatalyst for dye degradation," *Journal of Hazardous Materials*, vol. 175, no. 1–3, pp. 429–438, 2010.

## Research Article

# Photoelectrocatalytic Degradation of Sodium Oxalate by TiO<sub>2</sub>/Ti Thin Film Electrode

Chen-Yu Chang,<sup>1</sup> Yung-Hsu Hsieh,<sup>2</sup> and Yu-Ying Chen<sup>2</sup>

<sup>1</sup> Center of General Education, National Taitung College, 889 Jhengci N. Rd., Taitung 95045, Taiwan

<sup>2</sup> Department of Environmental Engineering, National Chung Hsing University, 250 Kuo-Kung Road, Taichung 40227, Taiwan

Correspondence should be addressed to Chen-Yu Chang, cyc1136@ntc.edu.tw

Received 19 October 2011; Revised 18 December 2011; Accepted 19 December 2011

Academic Editor: Jiaguo Yu

Copyright © 2012 Chen-Yu Chang et al. This is an open access article distributed under the Creative Commons Attribution License, which permits unrestricted use, distribution, and reproduction in any medium, provided the original work is properly cited.

The photocatalytically active TiO<sub>2</sub> thin film was deposited on the titanium substrate plate by chemical vapor deposition (CVD) method, and the photoelectrocatalytic degradation of sodium oxalate was investigated by TiO<sub>2</sub> thin film reactor prepared in this study with additional electric potential at 365 nm irradiation. The batch system was chosen in this experiment, and the controlled parameters were pH, different supporting electrolytes, applied additional potential, and different electrolyte solutions that were examined and discussed. The experimental results revealed that the additional applied potential in photocatalytic reaction could prohibit recombination of electron/hole pairs, but the photoelectrocatalytic effect was decreased when the applied electric potential was over 0.25 V. Among the electrolyte solutions added, sodium sulfate improved the photoelectrocatalytic effect most significantly. At last, the better photoelectrocatalytic degradation of sodium oxalate occurred at pH 3 when comparing the pH influence.

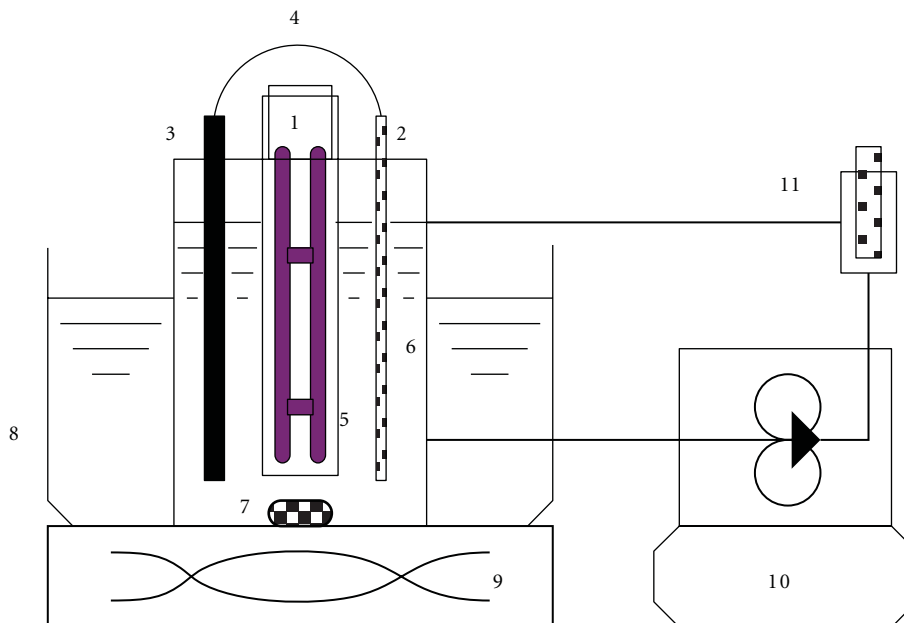
## 1. Introduction

Oxalic acid is frequently used in leather bleaching, chemical synthesis, printing and dye industries, rust removal, metal decontamination, and household bathroom cleaning. Therefore, cases of accidental oxalic acid poisoning are common. In addition, oxalic acid and its soluble salts can cause poisoning through the stomach and intestines, respiratory tract, skin, and eye contact with LD<sub>50</sub> between 375 and 475 mg Kg<sup>-1</sup>. Oxalate itself is also toxic to the kidney. In recent years, advanced oxidation processes have been extensively used in decomposing harmful or decomposition-resistant pollutants in the environment. Among them, the photocatalysis reaction using UV together with semiconductor is thought to be a treatment technology with high potential. Compared to other semiconductor metal oxides, titanium dioxide (TiO<sub>2</sub>) is the most frequently used photocatalyst for photochemical reaction due to the cheap cost, stable properties, and high photocatalytic effect. However, the recombination of electron-hole pairs occurs during the photocatalytic reaction process, resulting in the reduction of decomposition efficiency. In order to resolve such a problem for the increase of quantum efficiency, the following

approaches are frequently adopted: (1) application of a positive electric potential on the TiO<sub>2</sub> electrode to use the electric field force to drive away electrons in order to prevent further recombination; (2) combination of 2 semiconductors (such as TiO<sub>2</sub>/SnO<sub>2</sub>) at comparable energy levels to allow one (like SnO<sub>2</sub>) to absorb electrons during photoexcitation in order to improve decomposition efficiency; (3) addition of precious metal ions such as Ag or Pt in the reaction solution for the absorption for electrons [1–5]. This study used UV light of high energy to excite the photocatalyst to form hydroxyl radicals with high oxidizing ability to efficiently decompose organic pollutants in water in order to attain the goals of removal and mineralization [6–19].

## 2. Experimental Details

**2.1. Preparation of TiO<sub>2</sub> Photoreactor.** The modified chemical vapor deposition (CVD) [20] was used for the catalyst preparation used in the present study. The procedure is described as follows: The tetraisopropyl orthotitanate (Ti(OC<sub>3</sub>H<sub>7</sub>)<sub>4</sub>) (TTIP >98%, Merck Co.) solution and deionized water were placed in two aeration bottles separately. In the 60°C water bath, the aeration bottles were flushed with



(1) UV lamp, (2) anode ( $\text{TiO}_2/\text{Ti}$  plates), (3) cathode (graphite), (4) external loop, (5) annular quartz tube, (6) reactor (pyrex), (7) magnetic stone, (8) water bath, (9) magnetic stirrer/hot plate, (10) circulating pump, and (11) pH meter.

FIGURE 1: Photoelectrocatalytic apparatus.

high-purity nitrogen gas to take out the airflow containing  $\text{TiO}_2$  and water vapor. Teflon tubing was used on the other end into the reactor. The tubing was wrapped with heating tapes to approximately  $95 \pm 5^\circ\text{C}$  to avoid condensation. The substrate to be coated with the catalyst was placed in the tubular high-temperature oven to maintain the reaction temperature at  $400^\circ\text{C}$ . During the preparation, the formation of white smoke inside the reactor was observed with the naked eye, indicating that the  $\text{TiO}_2$  crystal nucleus has started to grow on the wall of the tubing. The reactor was rotated to alter the position of the  $\text{TiO}_2$  coating to allow it to coat evenly on the entire titanium substrate. Finally, the reactor was calcined at  $500^\circ\text{C}$  for 24 hours to eliminate impurities and purify  $\text{TiO}_2$  to achieve the anatase as the major crystal form.

**2.2. Photoelectrocatalytic Procedure.** The liquid-phase photoelectrocatalytic system consisted of a UV lamp of 13 W and 365 nm, an annular reactor, a completely mixing chamber, a magnetic stirrer, a voltage supplier, and a circulating water bath. The apparatus is illustrated in Figure 1. In this study, the experiments were conducted in batches at constant temperature and sample volume. Other parameters including pH values, additional applied electric potentials, and the type of electrolytes were under control in the experiments (Table 1). 1 N  $\text{HClO}_4$  and 4 N  $\text{NaOH}$  were used to adjust the pH value of aqueous samples. Besides, a peristaltic pump was used to draw sample into the reactor for the continuous refluxing batch experiments for 4 hours.

TABLE 1: Reaction conditions.

Conditions	Range
Water bath temperature	$20 \pm 1^\circ\text{C}$
The initial concentration of sodium oxalate	2 mM
Sample volume	350 mL
Flow rate	$300 \text{ mL min}^{-1}$
Refluxing time	4 hours
UV wavelength	365 nm
Irradiation intensity	$3 \text{ mW cm}^{-2}$
pH	3~7
Additional applied electric potentials	0, 0.25, 0.5, 1 V
Electrolyte solution (2 mM)	$\text{NaCl}$ , $\text{NaNO}_3$ , $\text{Na}_2\text{SO}_4$ , $\text{Na}_2\text{CO}_3$

**2.3. Quantitation of Species.** The relationships between the residual rates of sodium oxalate and the various controlled parameters were investigated in order to obtain the effect of  $\text{TiO}_2/\text{Ti}$  thin film electrode. Ion chromatograph (IC; JASCO, Japan, Model PU-1580i) equipped with the Shodex IC SI-90-4E column and total organic carbon instruments (TOC; Shimadzu, Japan, Model TOC-VCSN) were employed for the analysis of the experiment to investigate the variations of the residual rates and the mineralization rates under parameters described above.

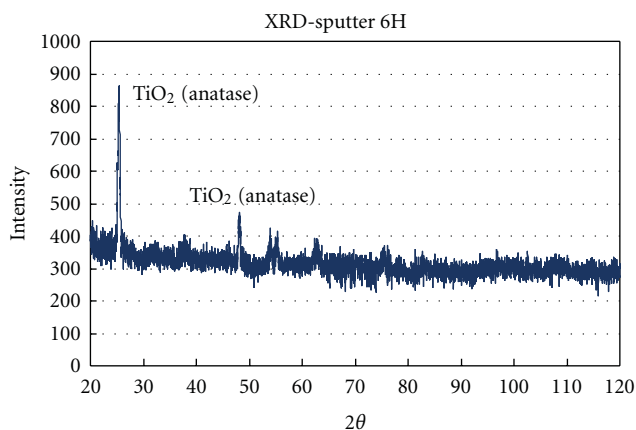


FIGURE 2: XRD spectrum of  $\text{TiO}_2$  prepared by CVD method.

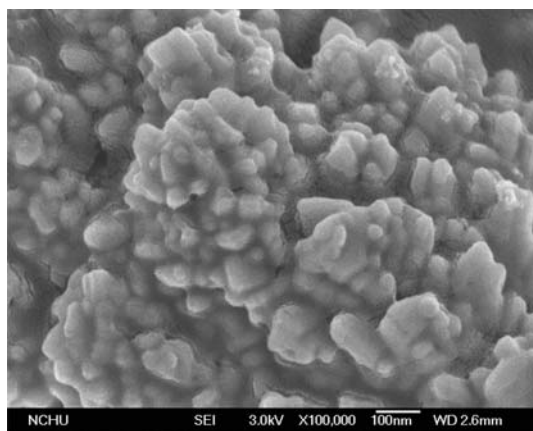


FIGURE 3: SEM image of  $\text{TiO}_2$  prepared by CVD method.

### 3. Results and Discussion

**3.1. Photocatalyst Properties.** The photocatalyst prepared by the modified CVD method under the optimal conditions described above was analyzed by the X-ray diffractometer (XRD) to examine the crystals form. As illustrated in Figure 2, the three major diffraction peaks of the anatase crystal structure appear at the  $2\theta$  values of 25.4 and 48.2; Compared with the JCPDS database (nos. 21-1276 and 21-1272), the crystal structure of the photocatalyst prepared in the experiment was mostly in the anatase form. The SEM image of the catalyst at magnification of 100,000 times illustrated in Figure 3, the structures of  $\text{TiO}_2$  particles were not rather uniform, with the appearance of clustered ball shape and the crystal surface of porous structure.

**3.2. Photoelectrocatalytic Tests.** Figure 4 shows the residuals of sodium oxalate in the  $\text{TiO}_2$  photocatalytic reaction alone, direct electrolysis alone, and photoelectrocatalytic process. It was clearly observed in the experimental data that at  $20^\circ\text{C}$ , pH 4, a volume flow rate of  $300\text{ mL min}^{-1}$ , and sodium oxalate of  $2\text{ mM}$  in the batch completely mixing reactor with the additional applied electric potential of  $1\text{ V}$  and the UV

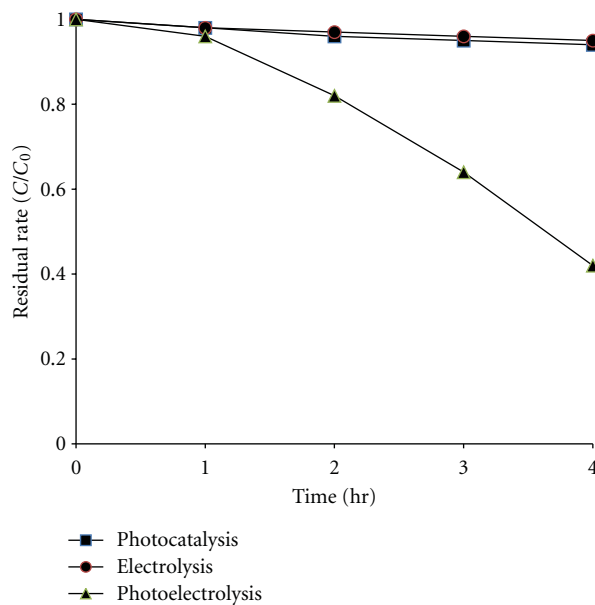


FIGURE 4: Residual rates of sodium oxalate under the different reactions at pH 4.

irradiation of  $365\text{ nm}$  for 4 hours for the photoelectrocatalytic degradation reaction experiment was able to increase the removal and mineralization rates of sodium oxalate from 6% to approximately 57%. According to Waldner's study, it was proposed that when  $\text{TiO}_2$  generated electron-hole pairs under UV irradiation, the additional applied electric potential inhibited the recombination of electron-hole pairs. The holes interacted with the water molecules or hydroxide ion ( $\text{OH}^-$ ) absorbed on the surface of  $\text{TiO}_2$  to form hydroxyl radical ( $\cdot\text{OH}$ ), thus enhancing the oxidation reaction effect of holes [18, 19]. Moreover, according to the experimental results in Figure 5, it was observed that the mineralization rates of sodium oxalate had mostly comparable trends as the removal rate. It was suggested that the structure of sodium oxalate was rather simple, thus it was less likely to form intermediates. As a result, the degraded ones could be almost mineralized.

**3.3. pH Effect.** In general, as the pH of aqueous solution increases, the yield of hydroxyl radical in the photocatalytic reaction also increases. However, different pH values will directly affect the species distribution ratio of reactants in the solution. Moreover, pH values could also alter the surface electric property of photocatalyst, thus affecting the adsorption and desorption properties and abilities of reactants by the photocatalyst. Therefore, for different pollutants, the pH value controlled in the reaction could show a dramatic effect on the overall removal rate.

Figure 6 illustrated the residual rates of sodium oxalate at pH 3~7. The result indicated that sodium oxalate at  $2\text{ mM}$ , applied voltage of  $1\text{ V}$ , light intensity of  $3\text{ mW cm}^{-2}$ , volume flow rate of  $300\text{ mL min}^{-1}$ , temperature at  $20 \pm 1^\circ\text{C}$ , and UV light irradiation at  $365\text{ nm}$  on the titanium substrate plate coated with  $\text{TiO}_2$  in the reactor for 4 hours to undergo

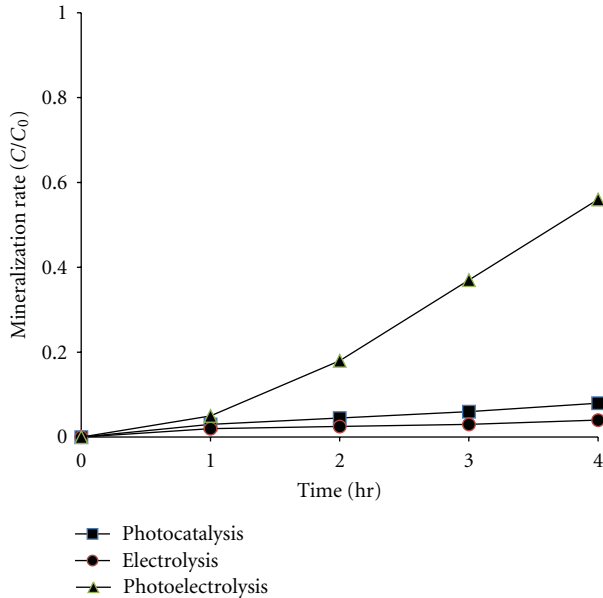


FIGURE 5: Mineralization rates of sodium oxalate under the different reactions at pH 4.

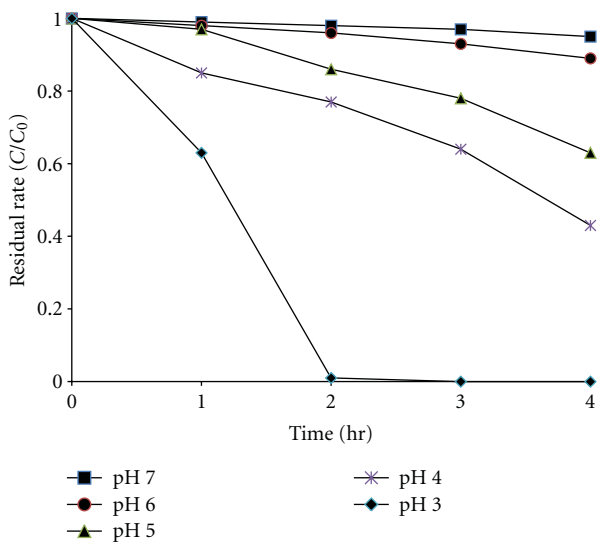


FIGURE 6: Residual rates of sodium oxalate under the photoelectrocatalytic reaction at different pH.

the photoelectrocatalytic reaction gave the most favorable treatment effect at pH 3. After a reaction for 150 minutes, the removal rate reached almost 100%. However, as pH values increased, the removal rate of sodium oxalate in the aqueous solution decreased. The cause of this phenomenon was probably that oxalate at the first ionization state ( $pK_{a1} = 1.2$ ,  $pK_{a2} = 4.2$ ) showed a more favorable reaction rate with  $\bullet\text{OH}$ . Furthermore, in the solid-liquid interface reaction, a low pH value was favorable for the adsorption of oxalate on the  $\text{TiO}_2$  surface, allowing the holes excited by UV/ $\text{TiO}_2$  to undergo the direct or indirect oxidation reaction in order to achieve the goal of sodium oxalate degradation [19]. The

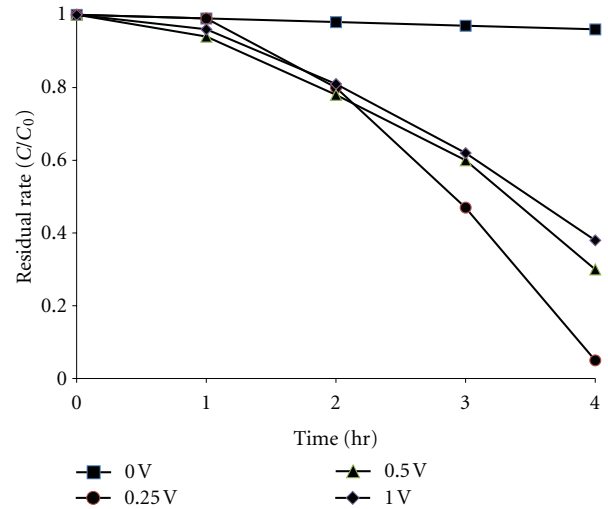


FIGURE 7: Residual rates of sodium oxalate under photoelectrocatalytic reactions with different additional applied electric potentials.

reason for the higher adsorption at lower pH was that the  $pH_{zpc}$  of  $\text{TiO}_2$  between 6.3~7.6 and the  $pK_a$  values of oxalic acid were approximately 1.2 and 4.2. As a result, when the pH value of the solution was higher than the  $pK_a$  of sodium oxalate but lower than the  $pH_{zpc}$  of  $\text{TiO}_2$ , sodium oxalate ionized a  $\text{Na}^+$  cation and formed  $\text{NaC}_2\text{O}_4^-$  with a negative charge. Meanwhile, the  $\text{TiO}_2$  surface carried a positive charge and a more favorable adsorption quantity was afforded due to the electrostatic attraction interaction between  $\text{TiO}_2$  and oxalic acid.

**3.4. Additional Applied Electric Potential Effect.** Figure 7 illustrates the results of the different additional applied electric potentials of 0.25 V, 0.5 V, and 1 V to the photoelectrocatalytic experiment of sodium oxalate. From the result shown, it was evident that the sodium oxalate removal effect was quite limited in the absence of the additional applied electric potential for the photocatalytic reactions. It was proposed that the electron-hole pairs excited by UV/ $\text{TiO}_2$  underwent the recombination reaction easily, leading to the consequence that the holes could not directly or indirectly oxidize organic substances. Consequently, the overall photocatalytic effect was reduced. However, the results of this experiment demonstrate that the additional applied electric potentials (0.25 V, 0.5 V, and 1 V) on the working electrode significantly improved the overall photoelectrocatalytic reactions. As the additional applied electric potentials varied, the degradation of sodium oxalate also varied to different degrees. Among them, the voltage of 0.25 V afforded a more favorable photoelectrocatalytic reaction. After 4 hours of the photoelectrocatalytic reaction, approximately 95% of sodium oxalate in the aqueous solution was removed. Nevertheless, when the additional applied electric potential was increased to 0.5 V, the sodium oxalate removal effect was lowered. Moreover, when it was increased to 1 V, the sodium oxalate removal rate was merely 57%. Therefore, the experimental results revealed that the applied voltage

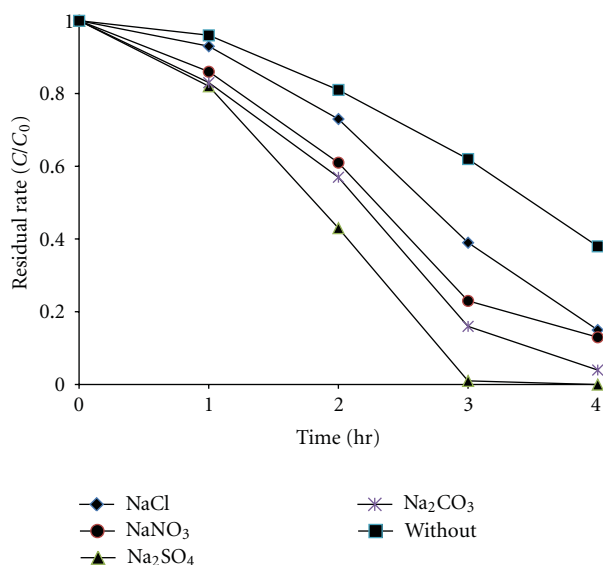


FIGURE 8: Residual rates of sodium oxalate under photoelectrocatalytic reactions with different electrolytes.

could reduce the recombination of electron-hole pairs, thus improving the overall removal effect. But, when an excess voltage was applied, the photoelectrocatalytic effect was worsened owing to the recombination reaction of the electrons of the additional applied electric potential itself and the holes carried on  $\text{TiO}_2$ .

**3.5. Electrolyte Solution Effect.** This experiment used sodium oxalate solution at an initial concentration of 2 mM followed by adding 0.2 mM of NaCl,  $\text{NaNO}_3$ ,  $\text{Na}_2\text{SO}_4$ , and  $\text{Na}_2\text{CO}_3$  electrolyte solution individually. The UV light at 365 nm was used to irradiate on the titanium substrate coated with  $\text{TiO}_2$  and the extra applied potential of 1 V was applied. The pH of the aqueous solution was controlled at  $4 \pm 0.1$  and the temperature at  $20 \pm 1^\circ\text{C}$  for the photoelectrocatalytic reaction in the complete mixing chamber for 4 hours to examine the effect of each electrolyte solution on the degradation of sodium oxalate. The results of this experiment are shown in Figure 8. The sodium oxalate degradation reaction the added electrolyte solution ( $\text{NaCl}$ ,  $\text{NaNO}_3$ ,  $\text{Na}_2\text{SO}_4$ , and  $\text{Na}_2\text{CO}_3$ ) was better than the one without the added electrolyte solution, indicating each electrolyte solution added was able to improve the photoelectrocatalytic reaction. Among them, adding  $\text{Na}_2\text{SO}_4$  showed the most favorable effect, with the sodium oxalate degradation rate reaching over 99% after 3 hours of operation time. The effects in the improvement of photoelectrocatalysis by different electrolyte solutions were found to vary in the order of  $\text{Na}_2\text{SO}_4 > \text{Na}_2\text{CO}_3 > \text{NaNO}_3 > \text{NaCl}$ . According to the study by Jorge, it was pointed out after adding different electrolyte solutions ( $\text{Na}_2\text{SO}_4$ ,  $\text{KNO}_3$ , and  $\text{NaCl}$ ) that  $\text{Na}_2\text{SO}_4$  was able to enhance the photoelectrocatalytic reaction to a greater extent, followed by  $\text{KNO}_3 > \text{NaCl}$ . This was because more photoelectric current was generated after adding  $\text{Na}_2\text{SO}_4$  to the system. The difference in the enhanced photoelectrocatalytic effects

from adding  $\text{Na}_2\text{SO}_4$  versus  $\text{NaCl}$  was found to be about over 10% [17]. This result was consistent with the conclusion of the present study.

## 4. Conclusions

The CVD method was used to prepare the  $\text{TiO}_2/\text{Ti}$  photocatalysis thin film reactor with the oxidation temperature controlled at  $400^\circ\text{C}$  and the calcination temperature at  $550^\circ\text{C}$  in this study. Not only the  $\text{TiO}_2$  purity was improved, but also the crystal structure was maintained at the anatase crystal form. Under the controlled parameters, the optimal experimental conditions were pH 3, 0.25 additional applied electric potential, and adding  $\text{Na}_2\text{SO}_4$  electrolyte in this study. The experimental results also showed that the effect of the photoelectrocatalytic process on the sodium oxalate removal efficiency was superior to that of the photocatalytic reaction alone. Moreover, it should be mentioned that the additional applied electric potential, in most cases, could enhance the overall degradation efficiency. However, the excessively high bias voltage could reduce the photocatalytic effect owing to the recombination of the electrons of the voltage itself and the holes carried on  $\text{TiO}_2$ . The search for the so-called “threshold dose” in the future study should be an attractive research subject.

## References

- [1] J. Yu, Y. Hai, and B. Cheng, “Enhanced photocatalytic  $\text{H}_2$ -production activity of  $\text{TiO}_2$  by  $\text{Ni}(\text{OH})_2$  cluster modification,” *The Journal of Physical Chemistry C*, vol. 115, no. 11, pp. 4953–4958, 2010.
- [2] W. C. Oh and M. L. Chen, “The improved photocatalytic properties of methylene blue for  $\text{V}_2\text{O}_3/\text{CNT}/\text{TiO}_2$  composite under visible light,” *International Journal of Photoenergy*, vol. 2010, Article ID 264831, 5 pages, 2010.
- [3] J. Yu, J. Xiong, B. Cheng, and S. Liu, “Fabrication and characterization of  $\text{Ag-TiO}_2$  multiphase nanocomposite thin films with enhanced photocatalytic activity,” *Applied Catalysis B*, vol. 60, no. 3-4, pp. 211–221, 2005.
- [4] J. Zhou, Y. Cheng, and J. G. Yu, “-light-driven plasmonic photocatalyst  $\text{Ag}/\text{AgCl}/\text{TiO}_2$  nanocomposite thin films,” *Journal of Photochemistry and Photobiology A*, vol. 223, no. 1-3, pp. 82–87, 2005.
- [5] Y. Li, G. Lu, and S. Li, “Photocatalytic transformation of rhodamine B and its effect on hydrogen evolution over  $\text{Pt}/\text{TiO}_2$  in the presence of electron donors,” *Journal of Photochemistry and Photobiology A*, vol. 152, no. 1-3, pp. 219–228, 2002.
- [6] C. Y. Chang, Y. H. Hsieh, L. L. Hsieh, K. S. Yao, and T. C. Cheng, “Establishment of activity indicator of  $\text{TiO}_2$  photocatalytic reaction-Hydroxyl radical trapping method,” *Journal of Hazardous Materials*, vol. 166, no. 2-3, pp. 897–903, 2009.
- [7] G. Shang, H. Fu, S. Yang, and T. Xu, “Mechanistic study of visible-light-induced photodegradation of 4-chlorophenol by  $\text{TiO}_{2-x}\text{N}_x$  with low nitrogen concentration,” *International Journal of Photoenergy*, vol. 2012, Article ID 759306, 9 pages, 2012.
- [8] Z. Zhang and J. Gamage, “Applications of photocatalytic disinfection,” *International Journal of Photoenergy*, vol. 2010, Article ID 764870, 11 pages, 2010.
- [9] J. A. Byrne, P. A. Fernandez-Ibañez, P. S. M. Dunlop, D. M. A. Alrousan, and J. W. J. Hamilton, “Photocatalytic enhancement

- for solar disinfection of water: a review," *International Journal of Photoenergy*, vol. 2011, Article ID 798051, 12 pages, 2011.
- [10] J. Yu and B. Wang, "Effect of calcination temperature on morphology and photoelectrochemical properties of anodized titanium dioxide nanotube arrays," *Applied Catalysis B*, vol. 94, no. 3-4, pp. 295-302, 2010.
- [11] J. Yu, G. Dai, and B. Cheng, "Effect of crystallization methods on morphology and photocatalytic activity of anodized TiO<sub>2</sub> nanotube array films," *The Journal of Physical Chemistry C*, vol. 114, no. 45, pp. 19378-19385, 2010.
- [12] K. S. Yao, T. C. Cheng, S. J. Li et al., "Comparison of photocatalytic activities of various dye-modified TiO<sub>2</sub> thin films under visible light," *Surface and Coatings Technology*, vol. 203, no. 5-7, pp. 922-924, 2008.
- [13] L. Zhao, J. Ran, Z. Shu, G. Dai, P. Zhai, and S. Wang, "Effects of calcination temperatures on photocatalytic activity of ordered titanate nanoribbon/SnO<sub>2</sub> films fabricated during an EPD process," *International Journal of Photoenergy*, vol. 2012, Article ID 472958, 7 pages, 2012.
- [14] M. Zhou, J. Yu, S. Liu, P. Zhai, and L. Jiang, "Effects of calcination temperatures on photocatalytic activity of SnO<sub>2</sub>/TiO<sub>2</sub> composite films prepared by an EPD method," *Journal of Hazardous Materials*, vol. 154, no. 1-3, pp. 1141-1148, 2008.
- [15] M. Y. Chang, Y. H. Hsieh, T. C. Cheng, K. S. Yao, T. C. Cheng, and C. T. Ho, "Photocatalytic degradation of 2,4-dichlorophenol wastewater using porphyrin/TiO<sub>2</sub> complexes activated by visible light," *Thin Solid Films*, vol. 517, no. 14, pp. 3888-3891, 2009.
- [16] G. Dai, J. Yu, and G. Liu, "Synthesis and enhanced visible-light photoelectrocatalytic activity of p-N junction BiOI/TiO<sub>2</sub> nanotube arrays," *The Journal of Physical Chemistry C*, vol. 115, no. 15, pp. 7339-7346, 2011.
- [17] S. M. Alves Jorge, J. J. de Sene, and A. de Oliveira Florentino, "Photoelectrocatalytic treatment of p-nitrophenol using Ti/TiO<sub>2</sub> thin-film electrode," *Journal of Photochemistry and Photobiology A*, vol. 174, no. 1, pp. 71-75, 2005.
- [18] G. Waldner, M. Pourmodjib, R. Bauer, and M. Neumann-Spallart, "Photoelectrocatalytic degradation of 4-chlorophenol and oxalic acid on titanium dioxide electrodes," *Chemosphere*, vol. 50, no. 8, pp. 989-998, 2003.
- [19] G. Waldner, R. Gómez, and M. Neumann-Spallart, "Using photoelectrochemical measurements for distinguishing between direct and indirect hole transfer processes on anatase: case of oxalic acid," *Electrochimica Acta*, vol. 52, no. 7, pp. 2634-2639, 2007.
- [20] T. C. Cheng, K. S. Yao, Y. H. Hsieh, L. L. Hsieh, and C. Y. Chang, "Optimizing preparation of the TiO<sub>2</sub> thin film reactor using the Taguchi method," *Materials and Design*, vol. 31, no. 4, pp. 1749-1751, 2010.

## Research Article

# Effects of Homogenization Scheme of TiO<sub>2</sub> Screen-Printing Paste for Dye-Sensitized Solar Cells

Seigo Ito,<sup>1</sup> Kaoru Takahashi,<sup>1</sup> Shin-ich Yusa,<sup>2</sup> Takahiro Imamura,<sup>2</sup> and Kenji Tanimoto<sup>3</sup>

<sup>1</sup>Department of Electric Engineering and Computer Sciences, Graduate School of Engineering, University of Hyogo, 2167 Shosha, Himeji, Hyogo 671-2280, Japan

<sup>2</sup>Department of Materials Science and Chemistry, Graduate School of Engineering, University of Hyogo, 2167 Shosha, Himeji, Hyogo 671-2280, Japan

<sup>3</sup>Specialty Materials Research Laboratory, Nissan Chemical Industries, Ltd., 11-1 Kitasode, Sodegaurashi, Chiba 299-0266, Japan

Correspondence should be addressed to Seigo Ito, itou@eng.u-hyogo.ac.jp

Received 15 October 2011; Revised 2 December 2011; Accepted 2 December 2011

Academic Editor: Jianguo Yu

Copyright © 2012 Seigo Ito et al. This is an open access article distributed under the Creative Commons Attribution License, which permits unrestricted use, distribution, and reproduction in any medium, provided the original work is properly cited.

TiO<sub>2</sub> porous electrodes have been fabricated for photoelectrodes in dye-sensitized solar cells (DSCs) using TiO<sub>2</sub> screen-printing paste from nanocrystalline TiO<sub>2</sub> powder dried from the synthesized sol. We prepared the TiO<sub>2</sub> screen-printing paste by two different methods to disperse the nanocrystalline TiO<sub>2</sub> powder: a “ball-milling route” and a “mortal-grinding route.” The TiO<sub>2</sub> ball-milling (TiO<sub>2</sub>-BM) route gave monodisperse TiO<sub>2</sub> nanoparticles, resulting in high photocurrent density (14.2 mA cm<sup>-2</sup>) and high photoconversion efficiency (8.27%). On the other hand, the TiO<sub>2</sub> mortal-grinding (TiO<sub>2</sub>-MG) route gave large aggregate of TiO<sub>2</sub> nanoparticles, resulting in low photocurrent density (11.5 mA cm<sup>-2</sup>) and low photoconversion efficiency (6.43%). To analyze the photovoltaic characteristics, we measured the incident photon-to-current efficiency, light absorption spectroscopy, and electrical impedance spectroscopy of DSCs.

## 1. Introduction

Dye-sensitized solar cells (DSCs) have been researched in the pursuit of a cost-effective solar generation system [1–3]. DSCs are composed of nanocrystalline-TiO<sub>2</sub> electrodes, sensitizing dyes, and electrolytes sandwiched between conducting substrates. The purpose of this work is to optimize the industrial fabrication methods of TiO<sub>2</sub>-coating paste for nanocrystalline-TiO<sub>2</sub> electrodes. TiO<sub>2</sub> colloidal sol has produced DSCs with over 10% conversion efficiency [4]. DSCs fabricated using nanocrystalline-TiO<sub>2</sub> powders (P25, Degussa, by TiCl<sub>4</sub> fumed method) have over 9% conversion efficiency [5]. Thus, the TiO<sub>2</sub> sol methods have been investigated to produce DSCs with higher conversion efficiency [6, 7]. However, TiO<sub>2</sub> sol can aggregate and easily form precipitates, resulting in difficulties with long-term preservation. Alternatively, DSCs fabricated by using the TiO<sub>2</sub> powder method have lower conversion efficiency, but the powder without liquid improves long-term preservation and is suitable for transportation due to its light weight. Hence,

it is important to find an industrial fabrication method to disperse nanocrystalline TiO<sub>2</sub> powder homogeneously. The purpose of this paper is to compare the characteristics and photovoltaic effects of DSCs using two TiO<sub>2</sub> homogenizing methods (ball milling and mortal grinding, named as TiO<sub>2</sub>-BM and TiO<sub>2</sub>-MG, resp.). The nanocrystalline TiO<sub>2</sub> powder was synthesized by sol gel method. As a result, an appropriate method for the industrial manufacture of nanocrystalline-TiO<sub>2</sub> electrodes has been identified.

## 2. Experimental

The methods used to fabricate TiO<sub>2</sub> paste from a TiO<sub>2</sub> particle source are shown in Figure 1. At first, TiO<sub>2</sub> nanoparticle was synthesized by peptization of titanium alkoxide, adjustment of pH, and hydrothermal reaction. The resulting TiO<sub>2</sub> nanoparticle was deionized, dried at 110°C, and heated at 380°C, resulting in anatase ( $d = 21$  nm, by BET).

For the TiO<sub>2</sub> ball-milling paste (Figure 1, left side, named as “TiO<sub>2</sub>-BM”), acetic acid and water were added to the

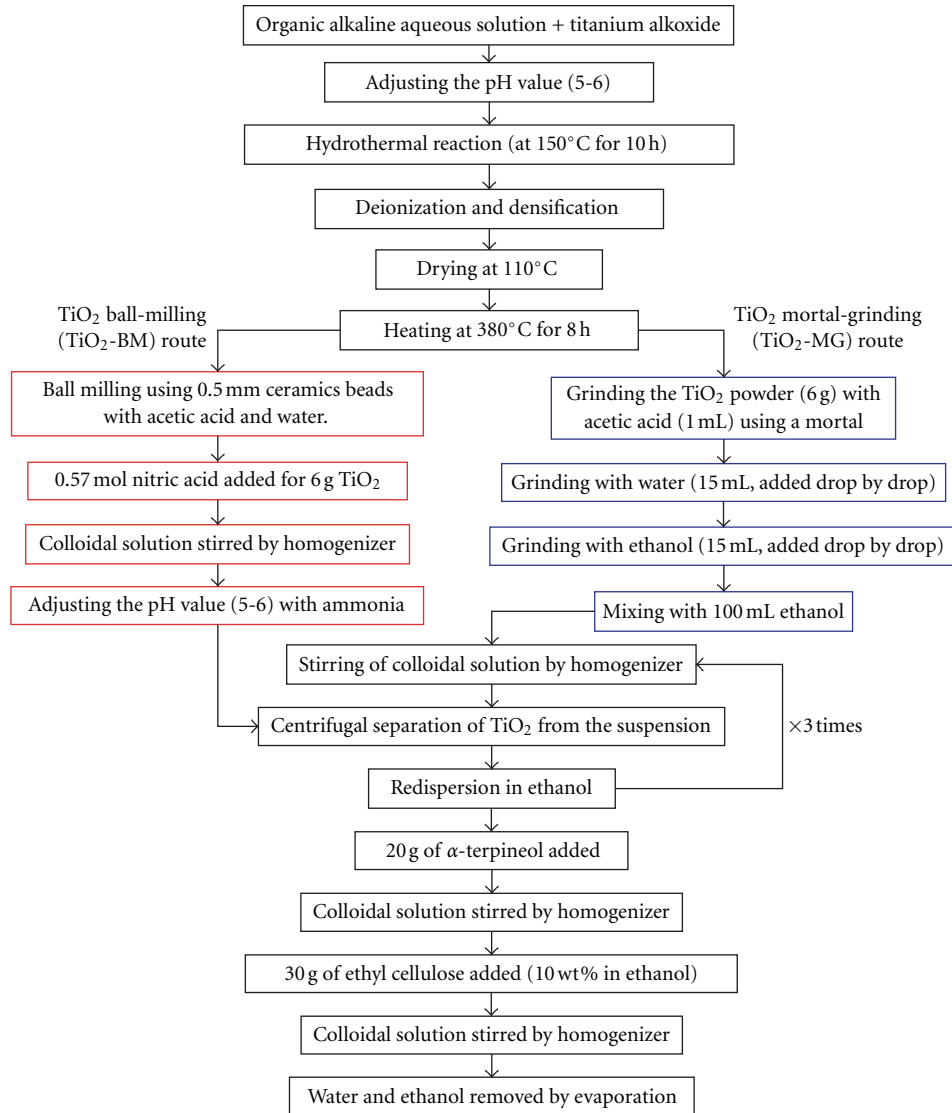


FIGURE 1: Fabrication methods of TiO<sub>2</sub> pastes.

nanocrystalline TiO<sub>2</sub> powder and mixed using ball milling with 0.5 mm ceramics balls. And then, nitric acid (0.57 mol for 6 g TiO<sub>2</sub>) was added to the TiO<sub>2</sub> dispersion, and the pH value was adjusted to 5.7 using ammonium water. The resulting precipitation was centrifuged and washed with ethanol three times to remove nitric acid and water. After centrifugation, 20 g of  $\alpha$ -terpineol (Tokyo Chemical Industries, Co. Ltd.) and 30 g of a mixture of two ethyl celluloses in ethanol (5 wt% of ethyl cellulose no. 46080 and 5 wt% of ethyl cellulose no. 86480, Tokyo Chemical Industries, Co. Ltd.) were added. The mixture was stirred by a magnet tip and sonicated using an ultrasonic horn (VC505, 500 W, Sonics & Materials Inc.). The contents in the dispersion were concentrated by using an evaporator at 35°C to remove ethanol and water.

For the TiO<sub>2</sub> mortar-grinding paste (Figure 1, right side, named as TiO<sub>2</sub>-MG), the heated TiO<sub>2</sub> powder (6 g), acetic acid (1 mL), water (5 mL), and ethanol (15 mL) were mixed

drop by drop in a mortar and grinded. The resulting mixture was transferred to a beaker and rinsed with 100 mL ethanol. The subsequent procedures were the same as those for TiO<sub>2</sub>-BM paste.

To prepare the DSC working electrodes, F-doped tin oxide (FTO, Nippon Sheet Glass Co. Ltd., Japan) glass plates were first cleaned in a detergent solution using an ultrasonic bath for 15 min and then rinsed with tap water, pure water, and ethanol. After treatment in a UV-O<sub>3</sub> system for 18 min, the FTO glass plates were immersed into a 40 mM aqueous TiCl<sub>4</sub> aq. solution at 70°C for 30 min and washed with pure water and ethanol before drying. The plates were then repeatedly coated with the TiO<sub>2</sub> pastes (TiO<sub>2</sub>-BM or TiO<sub>2</sub>-MG) by screen printing and drying at 125°C, to a thickness of 17  $\mu$ m. After drying at 125°C, a TiO<sub>2</sub> paste for a light-scattering TiO<sub>2</sub> film containing 400 nm anatase particles (PST-400C, CCIC-JGC, Japan) was deposited by screen printing to a thickness of 4-5  $\mu$ m. The

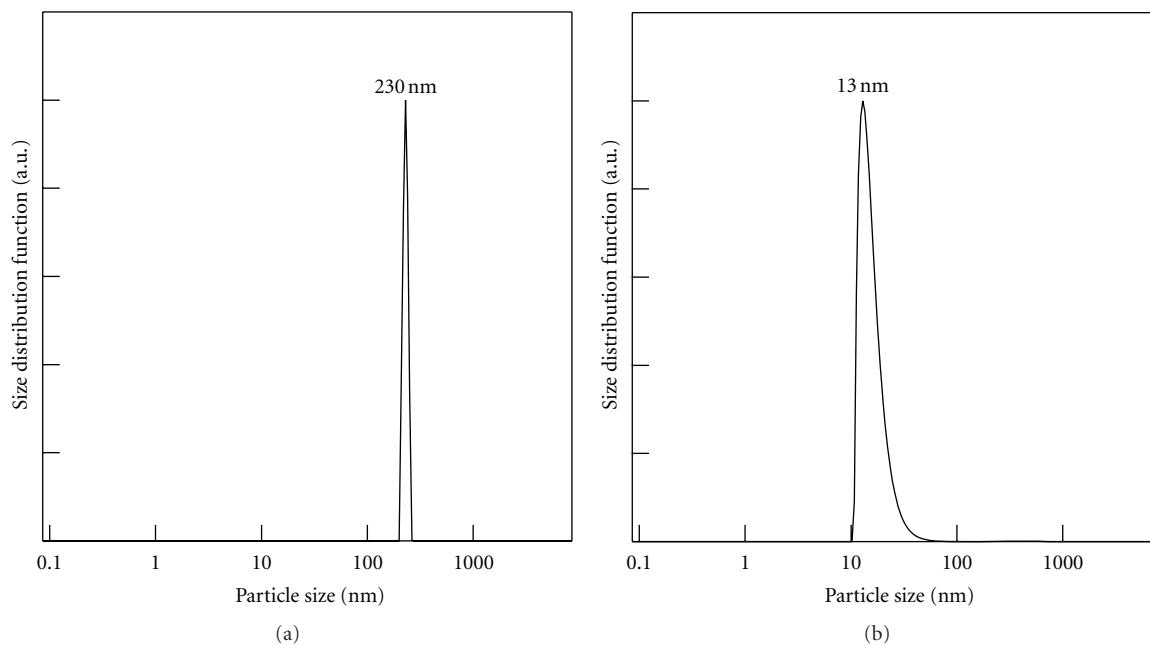


FIGURE 2: DLS measurements of  $\text{TiO}_2$ -MG (a) and  $\text{TiO}_2$ -BM (b) dispersions.

electrodes coated with the  $\text{TiO}_2$  pastes were gradually heated under an air flow at  $325^\circ\text{C}$  for 5 min,  $375^\circ\text{C}$  for 5 min,  $450^\circ\text{C}$  for 15 min, and  $500^\circ\text{C}$  for 15 min. The sintered  $\text{TiO}_2$  film was treated again with 40 mM  $\text{TiCl}_4$  solution, as described above, rinsed with pure water and ethanol, and sintered again at  $500^\circ\text{C}$  for 30 min. After cooling to  $80^\circ\text{C}$ , the  $\text{TiO}_2$  electrode was immersed into a 0.5 mM N-719 dye (Solaronix SA, Switzerland) solution in a mixture of acetonitrile and *tert*-butyl alcohol (volume ratio: 1 : 1) and kept at room temperature for 20–24 h to ensure complete sensitizer uptake.

To prepare the counter electrode, a hole was drilled in a FTO glass plate. The perforated sheet was washed with  $\text{H}_2\text{O}$  and a solution of 0.1 M HCl in ethanol and cleaned by ultrasound in an acetone bath for 10 min. After removing residual organic contaminants by heating in air for 15 min at  $400^\circ\text{C}$ , the Pt catalyst was deposited on the FTO glass by coating with a drop of  $\text{H}_2\text{PtCl}_6$  solution (2 mg Pt in 1 mL ethanol), and heat treatment was carried out again at  $400^\circ\text{C}$  for 15 min. The additional Pt electrode content on FTO did not influence conversion efficiency. The Pt fabricated from  $\text{H}_2\text{PtCl}_6$  was better than sputtered Pt films and metal Pt plates.

The dye-covered  $\text{TiO}_2$  electrode and Pt-counter electrode were assembled into a sandwich-type cell and sealed with a hot-melt gasket of  $25\ \mu\text{m}$  thickness made of the ionomer Surlin 1702 (DuPont) on a heating stage. The hole in the back of the counter electrode was covered with a hot-melt ionomer film (Bynel 4164,  $35\ \mu\text{m}$  thickness, DuPont) by using a hot soldering iron covered with fluorine-polymer film. A needle was used to make a hole in the hot-melt ionomer film. A drop of the electrolyte, a solution of 0.60 M 1-methyl-3-propylimidazolium iodide, 0.03 M  $\text{I}_2$ , 0.10 M guanidinium thiocyanate, and 0.50 M 4-*tert*-butylpyridine

in a mixture of acetonitrile and valeronitrile (volume ratio: 85 : 15) was placed into the hole. The cell was put into a small vacuum chamber for a few seconds to remove internal air. Exposing the electrolyte to ambient pressure again caused the electrolyte to be driven into the cell, a method known as vacuum-back filling. Finally, the hole was covered with additional hot-melt ionomer film and a cover glass (0.1 mm thickness) and sealed using a hot soldering iron. The edge of the FTO plate outside of the cell was scraped slightly with sandpaper or a file for good electrical contact with the photovoltaic measurement setup. A solder (Cerasolza, Asahi Glass) was applied on each side of the FTO electrodes by an ultrasonic-soldering system.

Photovoltaic measurements were conducted with an AM 1.5 solar simulator ( $100\ \text{mW cm}^{-2}$ , Yamashita Denso Co. Ltd., Japan). The power of the simulated light was calibrated by using a reference Si photodiode equipped with an IR-cutoff filter (BS520, Bunko Keiki Co. Ltd., Japan) in order to reduce the mismatch in the region of 350–750 nm between the simulated light and AM 1.5 to less than 2% [8, 9]. I-V curves were obtained by applying an external bias to the cell and measuring the generated photocurrent with a digital source meter. Reflecting absorbance, incident photon-to-current efficiency (IPCE), and electrical impedance were measured on Lamda 750 (Perkin Elmer), CEP-2000 (Bunkou Keiki Co. Ltd., Japan), and SP-150 (Bio-Logic) apparatuses, respectively.

### 3. Results and Discussion

Dynamic light scattering (DLS) measurements of each paste diluted in ethanol are shown in Figure 2. It was clear that the  $\text{TiO}_2$ -MG paste contained large  $\text{TiO}_2$  aggregates, but the  $\text{TiO}_2$ -BM paste contained monodispersed  $\text{TiO}_2$  particles.

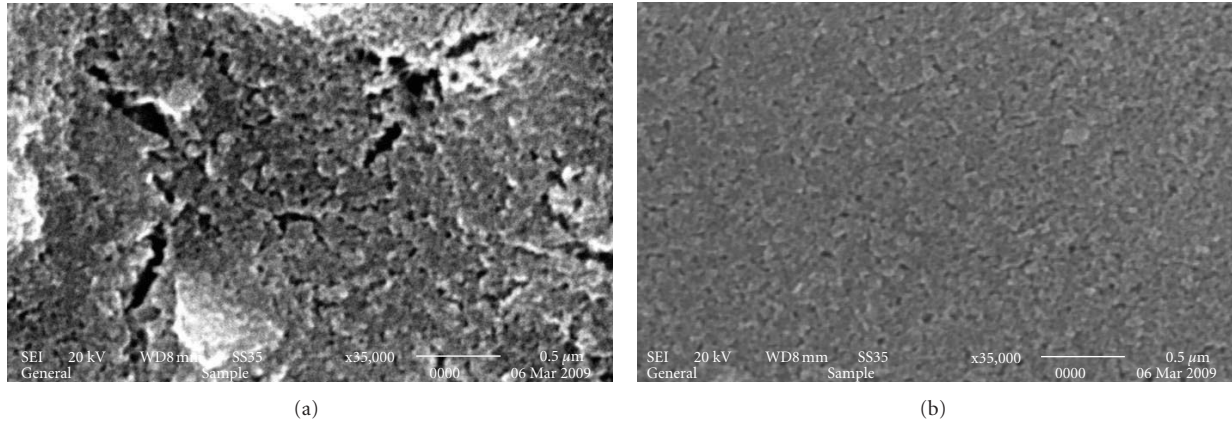


FIGURE 3: Surface structures of nanocrystalline-TiO<sub>2</sub> layer made using the TiO<sub>2</sub>-MG paste (a) and the TiO<sub>2</sub>-BM paste (b). Magnification is  $\times 35,000$ . Each scale bar is 500 nm.

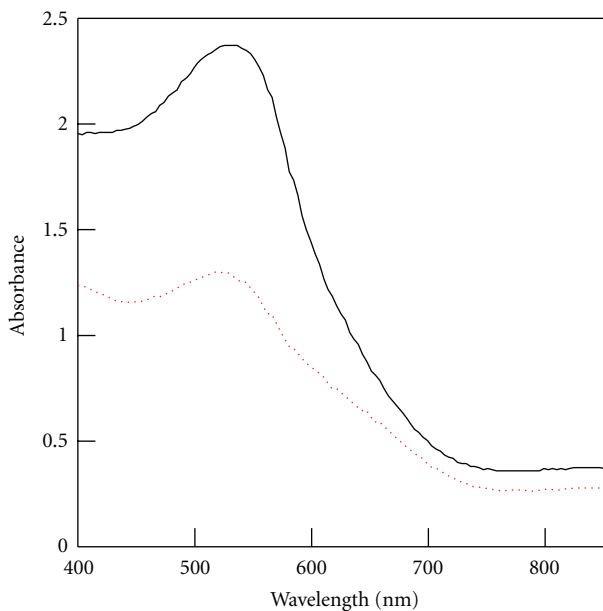


FIGURE 4: Absorbance spectra of nanocrystalline-TiO<sub>2</sub> electrodes with a sensitizing dye (N719): TiO<sub>2</sub>-BM paste (solid line) and TiO<sub>2</sub>-MG paste (dotted line).

Although the resulting size of a TiO<sub>2</sub> particle (Figure 2(b)) was smaller than that obtained by BET measurement (21 nm), the results were reliable enough to investigate the manner of dispersion.

The surface morphology of each screen-printed TiO<sub>2</sub> paste (Figure 3) showed that the TiO<sub>2</sub>-MG paste contained large TiO<sub>2</sub> aggregates and cracks, but the TiO<sub>2</sub>-BM paste gave a smooth surface. Hence, the morphology was projected the evaluation by using DLS measurements (Figure 2).

Figure 4 shows the reflectance-absorption spectra of dye-adsorbed nanocrystalline-TiO<sub>2</sub> electrodes from TiO<sub>2</sub>-BM and TiO<sub>2</sub>-MG pastes. The electrodes prepared from TiO<sub>2</sub>-BM paste absorbed the incident light more effectively than

those obtained from TiO<sub>2</sub>-MG paste. Since the surface morphology was smooth and flat (Figure 3(b)), the electrodes from TiO<sub>2</sub>-BM paste were transparent and the incident light was introduced deeply into the nanocrystalline-TiO<sub>2</sub> electrodes and largely absorbed. On the other hand, the large aggregates and cracks in nanocrystalline-TiO<sub>2</sub> electrodes from TiO<sub>2</sub>-MG paste (Figure 3(a)) scattered the incident light and reflected it without absorption. Aggregates that formed during the drying process from the dispersion of TiO<sub>2</sub> could not be redispersed using the mortar grinding and ultrasonic homogenization.

The amount of adsorbed dye was confirmed by desorption from the nanocrystalline-TiO<sub>2</sub> electrodes using a 0.01 M NaOH *aq.* solution. The nanocrystalline-TiO<sub>2</sub> electrodes (17  $\mu\text{m}$  thickness) from TiO<sub>2</sub>-BM and TiO<sub>2</sub>-MG pastes adsorbed  $1.5 \times 10^{-7} \text{ mol cm}^{-2}$  and  $6.5 \times 10^{-8} \text{ mol cm}^{-2}$ , respectively. Hence, it was confirmed that the nanocrystalline-TiO<sub>2</sub> electrodes from TiO<sub>2</sub>-BM paste adsorbed double the amount of dye compared with those from TiO<sub>2</sub>-MG paste, due to the high dispersion of TiO<sub>2</sub> nanoparticles in the TiO<sub>2</sub>-BM paste.

In order to confirm the effect by human eyes, the photographs of DSCs were shown in Figure 5. It was very clear that TiO<sub>2</sub>-BM was very dark purple color, on the other hand, TiO<sub>2</sub>-MG was very light pink color, which means that DSC with TiO<sub>2</sub>-BM absorbs light effectively, but TiO<sub>2</sub>-MG cannot absorb light so much.

The IPCE spectra and photo I-V curves of DSCs using nanocrystalline-TiO<sub>2</sub> electrodes are shown in Figures 6 and 7, respectively. Projecting the results of Figures 4 and 5, the IPCE and photocurrent density of DSCs from TiO<sub>2</sub>-BM paste were greater than those from TiO<sub>2</sub>-MG paste. The photovoltaic results are summarized in Table 1. The photoconversion efficiency using the TiO<sub>2</sub>-BM paste was higher by 29% compared with the TiO<sub>2</sub>-MG paste. However, considering the large difference of light-absorbing effect (Figures 4 and 5), it was surprising that the difference of IPCE value and photocurrent was not so much. Hence, it was considered that the light diffusion and trapping effect in

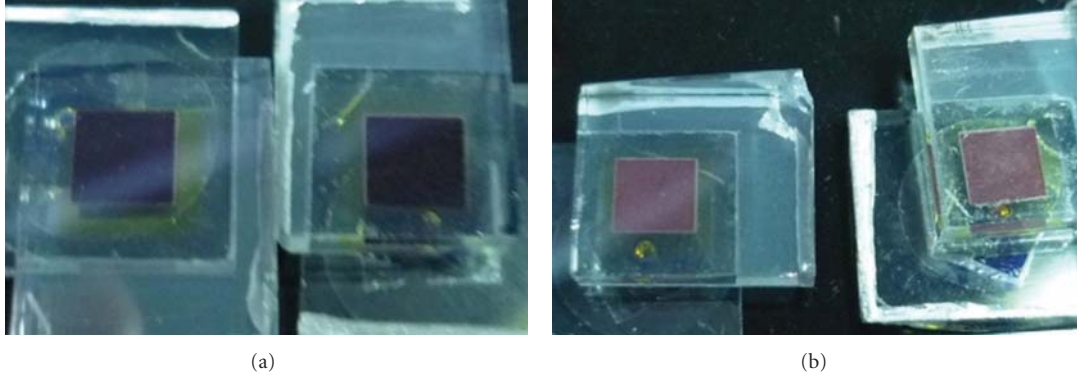


FIGURE 5: Photographs of DSCs using TiO<sub>2</sub>-BM (a) and TiO<sub>2</sub>-MG (b).

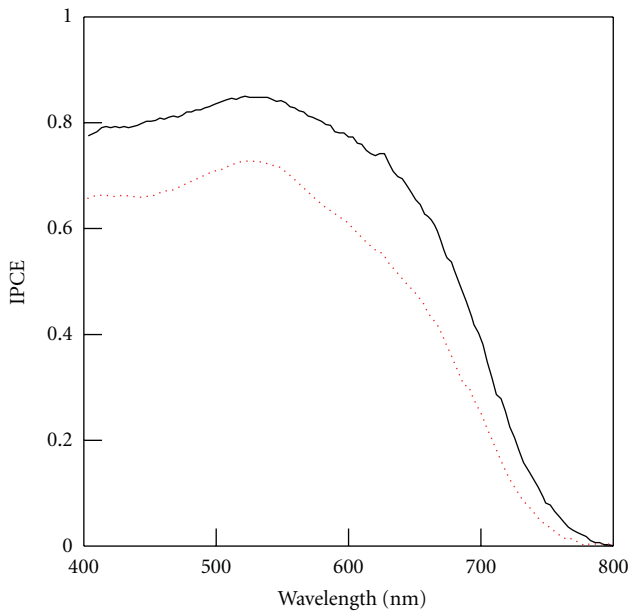


FIGURE 6: Incident photon-to-current conversion efficiency (IPCE) spectra of DSCs: TiO<sub>2</sub>-BM paste (solid line), TiO<sub>2</sub>-MG paste (dotted line).

TiO<sub>2</sub>-MG electrode would be significant to improve the photovoltaic effects. These phenomena might be projected the variation of mesoporous structures in the nanocrystalline-TiO<sub>2</sub> electrodes, which can be confirmed using the measurements results of the specific surface area and pore-size distributions [10, 11].

Figure 8 shows the electrical impedance spectra of DSCs. The center semicircles indicating the impedance of the interface between dyed TiO<sub>2</sub> and the electrolyte [12] were analyzed using an equivalent circuit (Figure 9) [3]. The results are summarized in Table 2. Although the series resistances ( $R_s$ ) were the same, the constant phase element (CPE, showing the capacitance) of TiO<sub>2</sub>-BM paste was greater by 20% than that of TiO<sub>2</sub>-MG paste, and the parallel resistance ( $R_p$ ) of TiO<sub>2</sub>-MG paste was twice that of TiO<sub>2</sub>-BM paste. The large CPE of the TiO<sub>2</sub> electrodes prepared from TiO<sub>2</sub>-BM paste suggested a larger surface area than

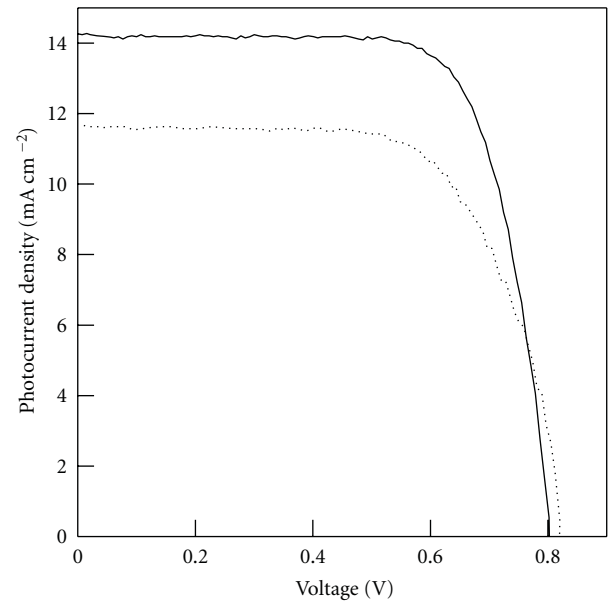


FIGURE 7: Photo I-V curve of DSCs under 100 mA cm<sup>-2</sup> (AM 1.5): TiO<sub>2</sub>-BM paste (solid line), TiO<sub>2</sub>-MG paste (dotted line). The active areas of DSCs were 5 × 5 mm<sup>2</sup>.

TABLE 1: Photoelectric characteristics of DSCs fabricated using TiO<sub>2</sub>-MG paste and TiO<sub>2</sub>-BM paste. Each data was the average of three DSCs.

	TiO <sub>2</sub> -MG	TiO <sub>2</sub> -BM
$J_{sc}$ [mA cm <sup>-2</sup> ]	11.5 ± 0.1	14.2 ± 0.01
$V_{oc}$ [V]	0.821 ± 0.006	0.798 ± 0.001
$FF$	0.682 ± 0.03	0.731 ± 0.04
$\eta$ [%]	6.43 ± 0.1	8.27 ± 0.08

that obtained from TiO<sub>2</sub>-MG paste, which resulted in greater dye adsorption and larger photocurrent density. Due to the large  $R_p$  of TiO<sub>2</sub>-MG paste, the charge lifetime in DSCs ( $\tau = R_p \times CPE$ ) from TiO<sub>2</sub>-MG paste was greater than that from TiO<sub>2</sub>-BM paste, thus suggesting a higher open-circuit photovoltage (20 mV).

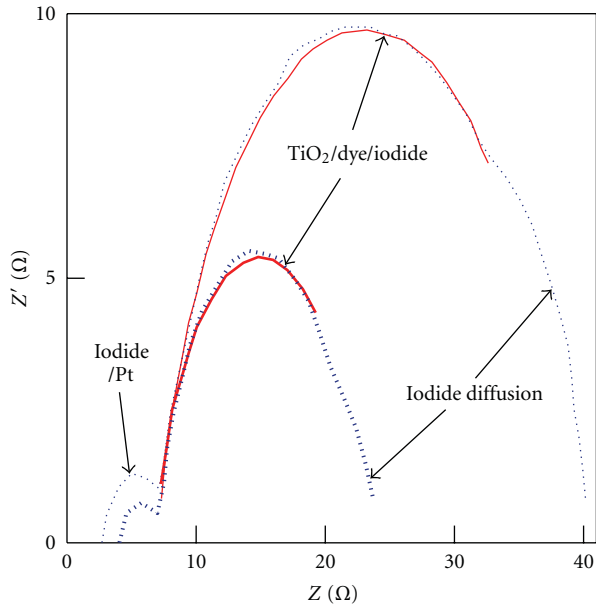


FIGURE 8: Electrical impedance spectra of DSCs under irradiation ( $100 \text{ mW cm}^{-2}$ , AM 1.5):  $\text{TiO}_2$ -BM paste (thick-dotted line),  $\text{TiO}_2$ -MG paste (thin-dotted line). Each solid curve shows the fitting results.

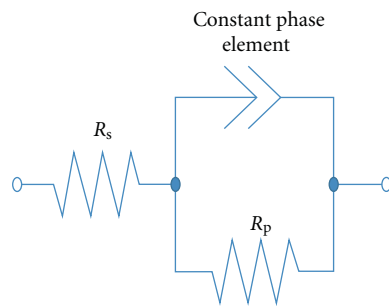


FIGURE 9: An equivalent circuit for analysis of  $\text{TiO}_2$  electrodes in DSCs.

TABLE 2: Electrochemical impedance components from Figure 8.

	$R_s$ [ $\Omega$ ]	CPE [F]	$R_p$ [ $\Omega$ ]
$\text{TiO}_2$ -MG paste	12.60	$1.205 \times 10^{-3}$	26.12
$\text{TiO}_2$ -BM paste	12.79	$1.435 \times 10^{-3}$	12.77

#### 4. Conclusion

This work demonstrated a comparison of different dispersion methods of fabricating coating paste for nanocrystalline- $\text{TiO}_2$  electrodes in DSCs. By using the same source of nanocrystalline  $\text{TiO}_2$  powder, it was confirmed that the paste using mortar grinding ( $\text{TiO}_2$ -MG) produced a lower photocurrent and lower photoconversion efficiency compared using ball milling ( $\text{TiO}_2$ -BM). Large  $\text{TiO}_2$  aggregates were produced during the drying process which caused a deterioration of dye adsorption and light penetration and resulted in a significant reduction in photocurrent density. Aggregates resulting from mortar grinding could not be

redispersed by using an ultrasonic homogenizer with acid and polymer. Since powder materials can give the benefit for the manufacture of DSCs about transportation and preservation of nanocrystalline  $\text{TiO}_2$ , this ball milling method of dispersing  $\text{TiO}_2$  nanoparticles from the dried powder is significant progress toward a cost-effective photovoltaic system. We hope that the results of this paper contribute to the industrial application of DSCs.

#### Conflict of Interest

The authors declare no conflict of interest.

#### Acknowledgments

The FTO glass plates and the glue films (Surlyn and Byne) were provided by Nippon Sheet Glass Co. Ltd. and Tamapoly Co. Ltd., respectively. The IPCE spectra were measured on a system at Osaka University (Professor S. Yanagida and Dr. K. Manseki).

#### References

- [1] B. O'Regan and M. Grätzel, "A low-cost, high-efficiency solar cell based on dye-sensitized colloidal  $\text{TiO}_2$  films," *Nature*, vol. 353, no. 6346, pp. 737–740, 1991.
- [2] M. Grätzel, "Photoelectrochemical cells," *Nature*, vol. 414, no. 6861, pp. 338–344, 2001.
- [3] S. Ito, S. M. Zakeeruddin, P. Comte, P. Liska, D. Kuang, and M. Grätzel, "Bifacial dye-sensitized solar cells based on an ionic liquid electrolyte," *Nature Photonics*, vol. 2, no. 11, pp. 693–698, 2008.
- [4] S. Ito, T. N. Murakami, P. Comte et al., "Fabrication of thin film dye sensitized solar cells with solar to electric power conversion efficiency over 10%," *Thin Solid Films*, vol. 516, no. 14, pp. 4613–4619, 2008.
- [5] S. Ito, P. Chen, P. Comte et al., "Fabrication of screen-printing pastes from  $\text{TiO}_2$  powders for dye-sensitized solar cells," *Progress in Photovoltaics*, vol. 15, no. 7, pp. 603–612, 2007.
- [6] A. Islam, S. Prakash Singh, and L. Han, "Synthesis and application of new ruthenium complexes containing  $\beta$ -diketonato ligands as sensitizers for nanocrystalline  $\text{TiO}_2$  solar cells," *International Journal of Photoenergy*, vol. 2011, Article ID 204639, 8 pages, 2011.
- [7] J. Yu, Q. Li, J. Fan, and B. Cheng, "Fabrication and photovoltaic performance of hierarchically titanate tubular structures self-assembled by nanotubes and nanosheets," *Chemical Communications*, vol. 47, no. 32, pp. 9161–9163, 2011.
- [8] M. K. Nazeeruddin, P. Péchy, T. Renouard et al., "Engineering of efficient panchromatic sensitizers for nanocrystalline  $\text{TiO}_2$ -based solar cells," *Journal of the American Chemical Society*, vol. 123, no. 8, pp. 1613–1624, 2001.
- [9] S. Ito, H. Matsui, K. I. Okada et al., "Calibration of solar simulator for evaluation of dye-sensitized solar cells," *Solar Energy Materials and Solar Cells*, vol. 82, no. 3, pp. 421–429, 2004.
- [10] J. Yu, J. Fan, and K. Lv, "Anatase  $\text{TiO}_2$  nanosheets with exposed (001) facets: improved photoelectric conversion efficiency in dye-sensitized solar cells," *Nanoscale*, vol. 2, no. 10, pp. 2144–2149, 2010.

- [11] J. Yu, J. Fan, and L. Zhao, "Dye-sensitized solar cells based on hollow anatase TiO<sub>2</sub> spheres prepared by self-transformation method," *Electrochimica Acta*, vol. 55, no. 3, pp. 597–602, 2010.
- [12] L. Han, N. Koide, Y. Chiba, and T. Mitate, "Modeling of an equivalent circuit for dye-sensitized solar cells," *Applied Physics Letters*, vol. 84, no. 13, pp. 2433–2435, 2004.

## Research Article

# Enhancing Photocatalytic Performance through Tuning the Interfacial Process between TiO<sub>2</sub>-Assembled and Pt-Loaded Microspheres

Jun Zhang,<sup>1,2</sup> Liping Li,<sup>3</sup> and Guangshe Li<sup>2</sup>

<sup>1</sup> School of Chemistry and Chemical Engineering, Inner Mongolia University, Hohhot 010021, China

<sup>2</sup> State Key Lab of Structural Chemistry, Fujian Institute of Research on the Structure of Matter, Chinese Academy of Sciences, Fuzhou 350002, China

<sup>3</sup> Key Lab of Optoelectronic Materials Chemistry and Physics, Fujian Institute of Research on the Structure of Matter, Chinese Academy of Sciences, Fuzhou 350002, China

Correspondence should be addressed to Guangshe Li, [guangshe@fjirm.ac.cn](mailto:guangshe@fjirm.ac.cn)

Received 10 November 2011; Accepted 2 December 2011

Academic Editor: Jiaguo Yu

Copyright © 2012 Jun Zhang et al. This is an open access article distributed under the Creative Commons Attribution License, which permits unrestricted use, distribution, and reproduction in any medium, provided the original work is properly cited.

This work reports on a simple two-step approach to rutile TiO<sub>2</sub>-assembled microspheres loaded by Pt with an aim to tune semiconductor-metal interfacial processes for enhancing the photocatalytic performance. Systematic sample characterizations and structural analysis indicate that Pt loading did not produce any significant influences on the lattice structure of TiO<sub>2</sub>-assembled microspheres. Instead, upon Pt loading, Schottky barrier was formed in the interfaces between microspheres and Pt nanoparticles, which inhibited efficiently the recombination of photo-generated electron-hole pairs essential for the photocatalytic activities. In addition, TiO<sub>2</sub> microspheres also showed a capacity of electrons storage and releasing as represented by a high dielectric constant, which increased the utility rate of photogenerated electrons. All these structural advantages contribute to the excellent photocatalytic activity under ultraviolet light irradiation. The interfacial process between microspheres and Pt nanoparticles was further tuned through adjusting the loading Pt content of metal Pt. As a consequence, the best photocatalytic activity on TiO<sub>2</sub> was obtained at 0.85 wt% Pt loading, above or below which photocatalytic activity was apparently decreased.

## 1. Introduction

Degradation of organic pollutants by photocatalytic technology has attracted increasing attention [1, 2]. In all kinds of photocatalysts, simple oxide semiconductors (e.g., TiO<sub>2</sub>, ZnO, and SnO<sub>2</sub>) have been extensively studied [3–6], among which TiO<sub>2</sub> nanomaterials characterized by the advantages of nontoxicity, stability, cheapness, and high activity have become the basis of promising photocatalysts [7, 8]. However, due to the wide bandgap and low quantum efficiency, the practical applications are always restricted [9–11]. Therefore, some endeavors (like doping foreign elements [12, 13] and coupled semiconductors or composites [5]) have been implemented, and some gains are obtained. Even so, efficient methods in enhancing photocatalytic activity are still challenging, since the elements introduced into the semiconductors often act as the recombination of

photogenerated electrons and holes that would decrease the quantum efficiency.

One has to execute some other routes such as imprinting external fields or depositing some noble metals. For example, when H<sub>2</sub> [14] and magnetic field [15] are involved into the systems, the photocatalytic activities can be significantly improved, while the reaction systems became complicated, seemingly not favorable for comprehension of photocatalytic process. In addition, loading noble metal (e.g., Au, Ag, Pt, Pd) onto semiconductors has been observed to greatly improve the photocatalytic activity [9, 16–18], in which the efficient utility of photogenerated electrons in the photo-degradation process is critical but often ignored.

In this work, we synthesized TiO<sub>2</sub>-assembled microspheres with different Pt loading content through microsphere formation with a subsequent photoreduction deposition of Pt nanoparticles. With tuning the loading quantity of

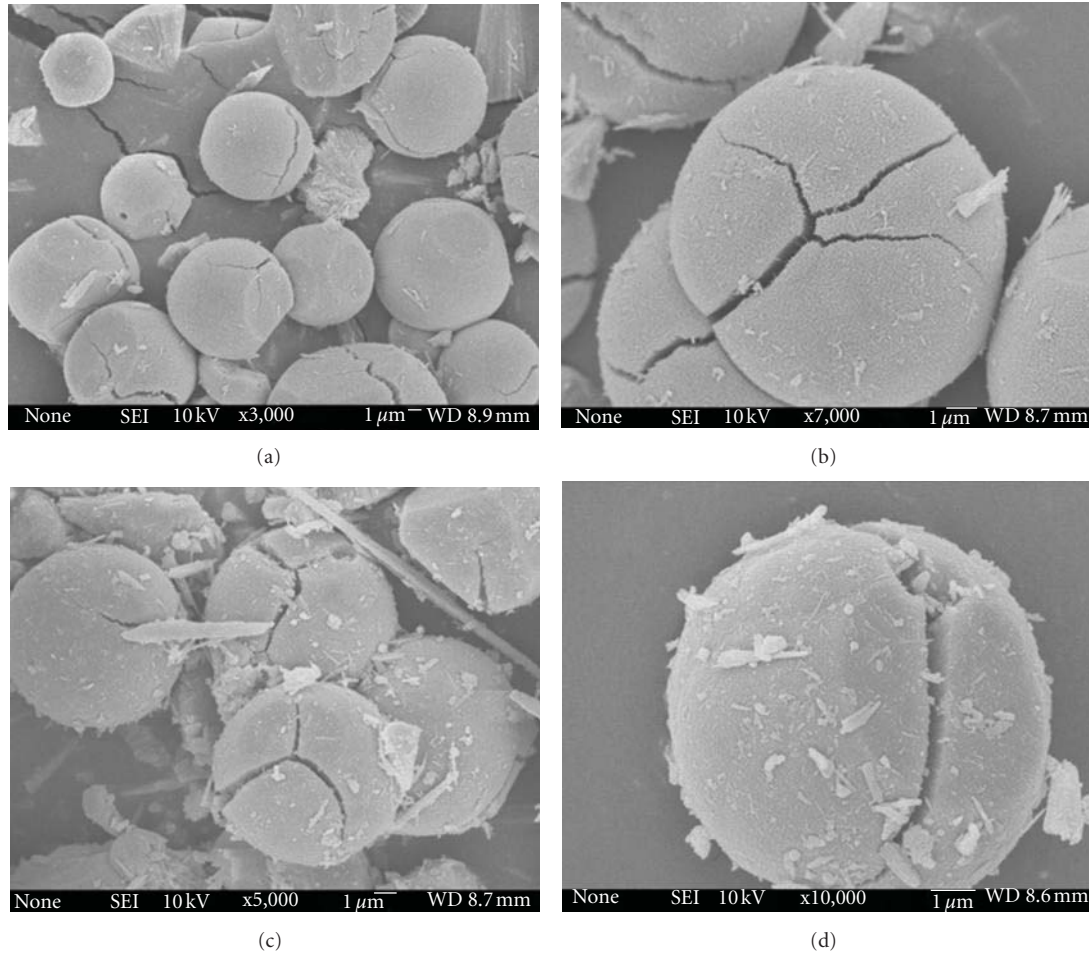


FIGURE 1: SEM images of the samples: (a, b) PureTiO<sub>2</sub> and (c, d) 1.0-Pt-TiO<sub>2</sub>.

metal Pt, an optimum photocatalytic activity was achieved at a loading of 0.85 wt% Pt. Further, the impacts of Pt loading content were investigated as a measure for the interfacial process between microspheres and Pt nanoparticles responsible for the enhanced photocatalytic activities.

## 2. Experimental Section

**2.1. Sample Preparation.** All reagents employed in the experiments were analytical grade and used without further purification. TiO<sub>2</sub> microspheres were fabricated according to the solution chemistry described in our previous work [19]. Briefly, 20.5 mL TiCl<sub>4</sub> (Alpha, 99%) was added dropwise into 60 mL distilled water at 0°C in an ice-water bath under vigorously magnetic stirring to form a given concentration aqueous solution. After stirring for about 1 h, the solution was transferred to a Teflon-lined stainless steel autoclave (100 mL). After reaction at 160°C for 2 h, the autoclave was allowed to cool to room temperature naturally, and the final product was washed carefully with distilled water to remove Cl<sup>-</sup> in the residue solution. The resulting product was dried at 80°C for 4 h in air.

Pt-deposited TiO<sub>2</sub> microspheres were prepared via a photoreduction process. Generally, 0.5 g of the as-prepared

TiO<sub>2</sub> microspheres was immersed into 100 mL solution of H<sub>2</sub>PtCl<sub>4</sub> (Sino-Platinum Co., Ltd.) in distilled water. 0.1 M acetic acid (Sinopharm Chemical Reagent Co., Ltd.) was used to adjust the pH of suspension to about 3. Then, high-purity nitrogen passes through the suspension for 15 min to remove the oxygen in suspension. After stirring for 3 h, the mixture solution was irradiated for 3.5 h by a 300 W high-pressure xenon lamp while stirring. Finally, the specimen was centrifuged and washed with distilled water until no Cl<sup>-</sup> was detected in the rinsing water. The quantity of H<sub>2</sub>PtCl<sub>4</sub> needed was set according to the mass ratio of metal Pt to TiO<sub>2</sub> as 0.1 wt%, 0.5 wt%, 1.0 wt%, and 3 wt%, and the corresponding samples were named as 0.1-Pt-TiO<sub>2</sub>, 0.5-Pt-TiO<sub>2</sub>, 1.0-Pt-TiO<sub>2</sub>, and 3.0-Pt-TiO<sub>2</sub>. After being dried in vacuum at 80°C, the resulting products were obtained.

**2.2. Sample Characterization.** Powder X-ray diffraction (XRD) patterns of the samples were collected on Rigaku MinFlex benchtop X-ray diffractometer with Cu K<sub>α</sub> irradiation. The crystallite sizes for the samples were calculated according to Scherrer formula,  $D = 0.89\lambda/\beta \cos \theta$ , where  $\lambda$  is the X-ray wavelength employed,  $\theta$  is the diffraction angle matches along with diffraction peak (110), and  $\beta$  is defined as

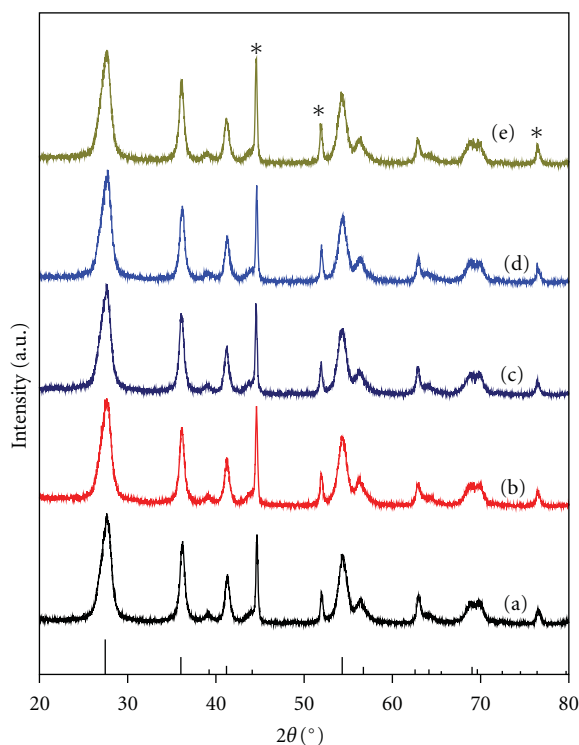


FIGURE 2: XRD patterns of the samples: (a) PureTiO<sub>2</sub>, (b) 0.1-Pt-TiO<sub>2</sub>, (c) 0.5-Pt-TiO<sub>2</sub>, (d) 1.0-Pt-TiO<sub>2</sub>, and (e) 3.0-Pt-TiO<sub>2</sub>. Vertical bars represent the standard diffraction data for bulk rutile TiO<sub>2</sub>. \*represents the diffraction lines of internal standard nickel.

the peak width at half height after the instrumental broadening is subtracted. The lattice parameters of the samples were calculated by a least-squares method using Rietica Rietveld software. Ni powder serves as an internal standard for peak position determination. Morphologies of the samples were observed by field emission scanning electron microscopy (FE-SEM) (JEOL JSM-6700). The specific loading contents of Pt for all samples were measured by Inductively Coupled Plasma OES spectrometer (ICP) (Ultima2). UV-vis diffuse reflectance spectra of the samples were obtained using a Varian Cary 500 UV-vis-NIR spectrometer. Infrared spectra of the samples were measured on a Perkin-Elmer IR spectrophotometer at a resolution of  $4\text{ cm}^{-1}$  using the KBr pellet technique.

**2.3. Photocatalytic Activity Evaluation.** Photocatalytic activities test of samples was implemented on a UV light photoreactor, which was constructed by a quartz tube (4.6 cm in inner diameter and 17 cm in length) surrounded by four UV lamps ( $\lambda = 254\text{ nm}$ , 4 W). Methyl orange (MO) was taken as a probe molecule for evaluating the photocatalytic activity. All experiments were performed at room temperature. Namely, 100 mg of the sample was dispersed in 100 mL MO (10 mg/L) solution and magnetically stirred for 5 h to establish adsorption/desorption equilibrium of MO solution on the sample surfaces before illumination. Then, the suspension solution was irradiated by light and

collected at a regular time interval. Finally, the collected solution was centrifuged at a rate of 8500 rpm to remove the solid power and UV-vis absorption spectra of the supernatant were measured with a Perkin-Elmer UV lambda 35 spectrophotometer.

### 3. Results and Discussion

Figure 1 shows the SEM images of pure TiO<sub>2</sub> and 1.0-Pt-TiO<sub>2</sub> samples. It is explicit to found that pure TiO<sub>2</sub> sample exhibits a microsize spherical morphology as constructed by bundles of nanowires, in which nanowires grew from the center of microsphere to the outward surface along with the direction [001], exposing the outer surface (110) of nanowire and tip (001) of nanowire while keeping a roughly parallel configuration [19]. Upon photoreduction deposition, very small Pt particles are dispersed uniformly onto the microspheres, since there are no obvious changes in the microsphere morphology. Further, Pt deposited onto the microspheres is in metallic state as indicated by XPS and TEM [20].

The exact loading contents of metal Pt for all samples were determined by ICP. For sample 0.1-Pt-TiO<sub>2</sub>, the Pt content measured was 0.1 wt%, which is close to the initial one. With increasing the initial Pt content, the corresponding measured Pt increased, such as from 0.43 wt% for 0.5-Pt-TiO<sub>2</sub> to 0.85 wt% for 1.0-Pt-TiO<sub>2</sub> and further to 1.46 wt% for 3.0-Pt-TiO<sub>2</sub>.

XRD patterns for TiO<sub>2</sub> microspheres with and without Pt deposition were shown in Figure 2. Without Pt deposition, TiO<sub>2</sub> microspheres were highly crystallized, as indicated by strong diffraction peaks. All diffraction peaks matched well with the standard diffraction data for rutile phase (JCPDS, No. 21-1276), which demonstrated the formation of a pure rutile phase for TiO<sub>2</sub> microspheres. After Pt deposition, no significant changes were seen in XRD patterns. Based on the Scherrer formula' calculation, the primary particle sizes for TiO<sub>2</sub> samples with and without Pt modification were all about 6.2 nm. Therefore, Pt modification has no apparent influence on the particle size of TiO<sub>2</sub> microspheres. Besides this, no traces of metal Pt were detected from the XRD patterns in the Pt-TiO<sub>2</sub> series samples, regardless of Pt content. One of the primary reasons for this phenomenon is that Pt content in Pt-TiO<sub>2</sub> samples is too low to be detected.

Further, Pt deposition has no apparent effects on the lattice structure of rutile TiO<sub>2</sub>. As indicated by structural refinements, the lattice parameters of all samples almost kept the same within the experimental errors. For instance, the lattice parameters for 3.0-Pt-TiO<sub>2</sub> were  $a = 0.46143 (\pm 0.00009)\text{ nm}$  and  $c = 0.29582 (\pm 0.00006)$ , respectively, which are closer to that of  $a = 0.46160 (\pm 0.0005)$ ,  $c = 0.29622 (\pm 0.0004)$  of pure TiO<sub>2</sub>. Combining the analytic results of SEM and XRD, it can be concluded that the structure of rutile TiO<sub>2</sub> microspheres remained unchanged after Pt loading.

It is well known that the premise of photocatalytic reaction is the adsorption of incidence light by catalysts. Therefore, UV-visible diffuse spectrum measurements appear to

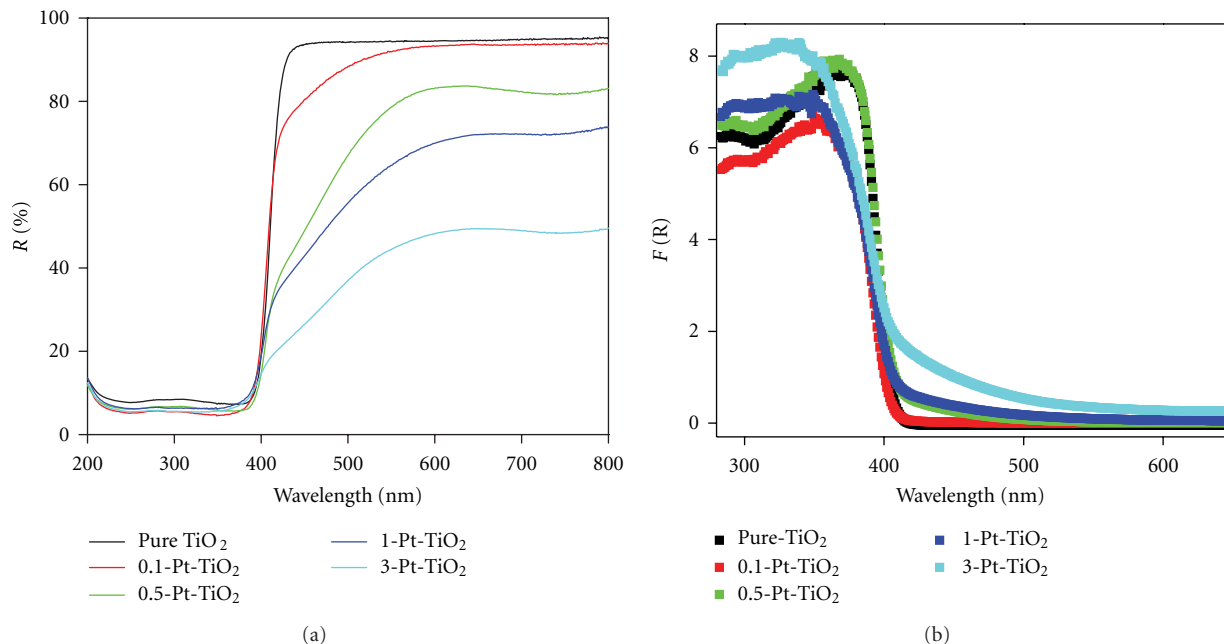


FIGURE 3: UV-visible diffusion reflectance spectra of  $\text{TiO}_2$  microspheres with Pt loaded.

be particularly important. Figure 3 shows the UV-visible diffuse reflectance spectrum (UV-Vis DRS) of all samples prepared. Pure  $\text{TiO}_2$  microspheres reflect above 90% visible light and all samples showed intense absorbance in the UV region ( $200 < \lambda < 400 \text{ nm}$ ). Differently, as the content of Pt loading increases, strong plasma response was observed in the visible region. Pt deposition is thus playing a critical role in the visible light adsorption because highly dispersed Pt nanoparticles can absorb nearly all the incident light [21]. It is worth emphasizing that this absorbance of visible light does not contribute a lot to the UV-light activity likely because visible light with a low energy does not allow an efficient light excitation.

Degradation of MO molecules is employed for the photocatalytic property evaluation of the samples. Specific degradation rate of MO molecule in the solution is monitored by examining the intensity variation of characteristic absorption peak of MO at 464 nm. As shown in Figure 4, all Pt-loaded microspheres exhibited a fast degradation of MO molecules. Particularly in the starting 30 min, all Pt-loaded microspheres showed a high removal of MO molecule beyond 67%, while less than 27% MO molecules were degraded by the pure  $\text{TiO}_2$  microspheres in this period of irradiation (Figure 4(c)). Moreover, the photocatalytic performance of 1.0-Pt- $\text{TiO}_2$  sample is comparable with that of P25. Further, with increasing the Pt loading content, the photocatalytic activities became better, as indicated by the observation that the complete degradation time of MO became shortened from 80 min to 40 min as the loading quantity increased from 0.1 wt% to 0.85 wt%. Loading content to 0.85 wt% led to an optimum photocatalytic activity as indicated by a fast degradation of MO molecule in 40 min. However, higher Pt loading does not always mean high

photocatalytic efficiency. For instance, the photocatalytic efficiency of 3.0-Pt- $\text{TiO}_2$  was only half of that for 1.0-Pt- $\text{TiO}_2$  in the whole photocatalytic process.

The optimized photocatalytic activities with Pt loading described above might be interpreted as follows. Firstly, loading metal Pt onto surfaces of  $\text{TiO}_2$  microspheres is beneficial for electronic transfer that decreases the recombination of photoinduced electrons and holes and thereby can greatly enhance the photoquantum efficiency. Nevertheless, too much metal Pt loadings may hinder the direct interaction between the incident light and microspheres, which leads to an incomplete excitement of photocatalysts. On the other hand, Pt nanoparticles loaded may attract holes to serve as recombination centers through recombining with electrons, which leads to a decrease in quantum efficiency [22]. As proposed in Scheme 1, metal Pt loaded was mainly deposited onto the face (110) and photogenerated electrons migrated predominantly along the direction [110] to metal Pt [20]. However, too much Pt loading led to the covering of the external surface of  $\text{TiO}_2$  microsphere with Pt nanoparticles (Scheme 1(b)), which contribute negatively to the photocatalytic activity because of the not enough direct interaction between incident light and semiconductor. Consequently, overfull Pt loading does not help to increase the photocatalytic activity. Also, the above phenomenon indicates that metal Pt loading only favored to the transfer of electrons and does not possess photocatalytic activity inherently or the activity is far less than  $\text{TiO}_2$  sample prepared in this work.

FT-IR spectra of Pure  $\text{TiO}_2$  and 1.0-Pt- $\text{TiO}_2$  samples after MO degradation were given in Figure 5. For comparison, the FT-IR spectrum for Pure  $\text{TiO}_2$  microspheres was also shown. The surface chemistry of the microspheres is characterized

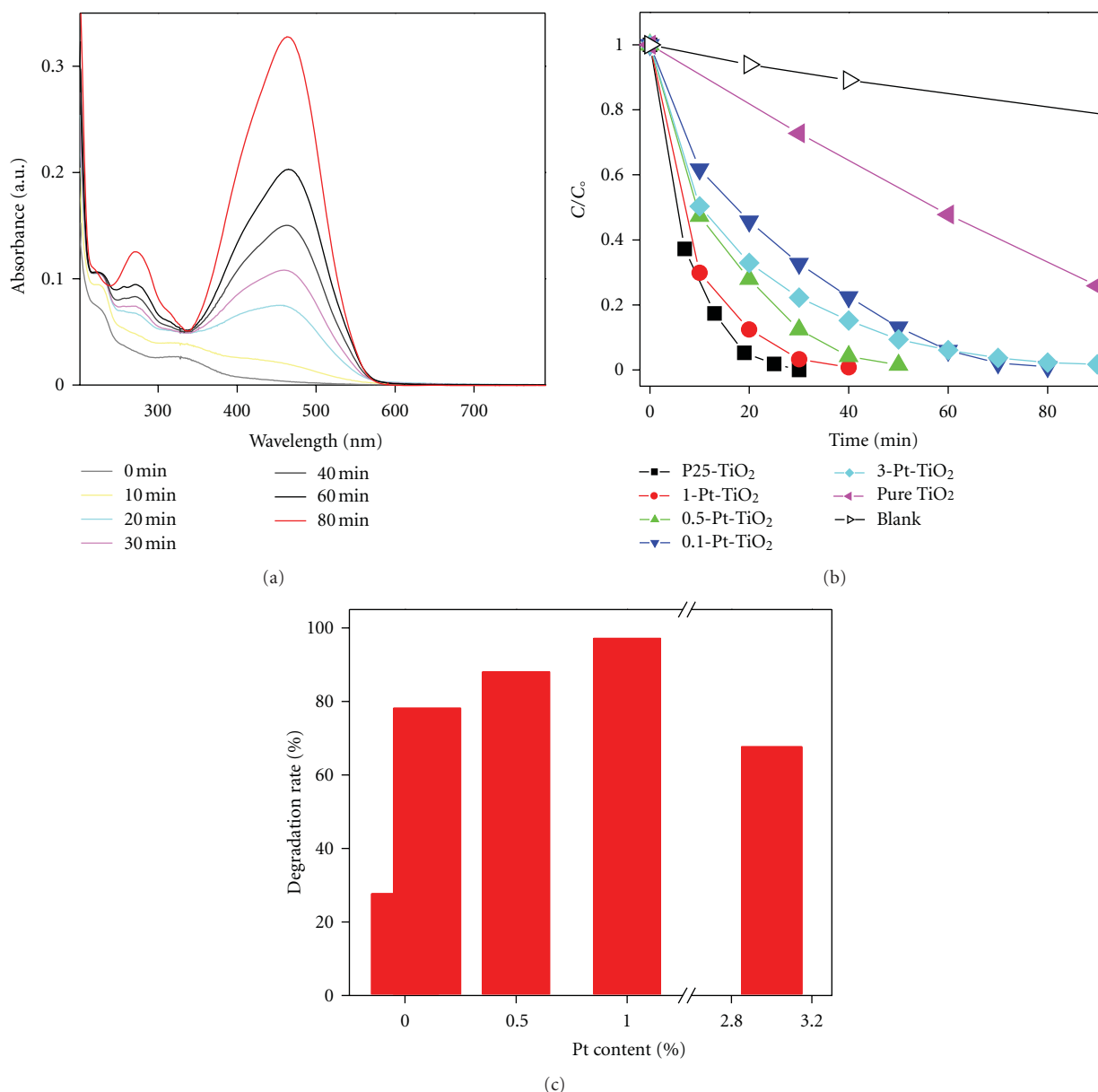
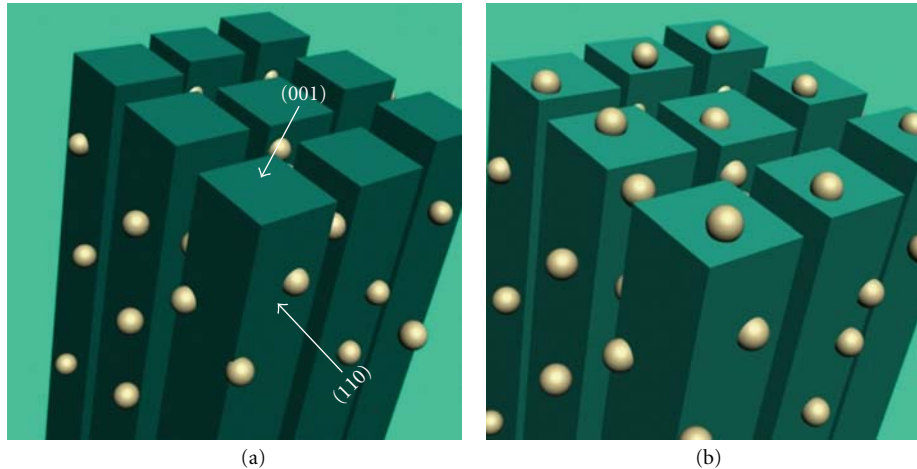


FIGURE 4: (a) Typical time-dependent absorption spectra of MO solution in the presence of 3.0-Pt-TiO<sub>2</sub> under ultraviolet light irradiation; (b)  $C/C_0$  as a function of irradiating time of MO solution for different samples in 90 min under UV light irradiation; (c) degradation rate for different Pt loading content of TiO<sub>2</sub> after irradiation for 30 min under UV light with a wavelength of 254 nm irradiation. The photocatalytic performances of PureTiO<sub>2</sub> and commercial P25-TiO<sub>2</sub> were measured in the same conditions for comparison.

by a band observed around  $1625\text{ cm}^{-1}$  for the H–O flexural vibration [23] and the bands centered at  $1250$  and  $1155\text{ cm}^{-1}$  for the vibrations of –C–O– bonds. The lattice nature for the microspheres is represented by the bands observed between  $700$  and  $500\text{ cm}^{-1}$  for the stretching bending vibrations of TiO<sub>2</sub>, the band around  $500\text{ cm}^{-1}$  for the stretching vibration of Ti–O–Ti, and that around  $600\text{ cm}^{-1}$  for bending vibration band of Ti–O and O–Ti–O. It is striking that some new weak bands appeared at  $1250$  and  $1155\text{ cm}^{-1}$  for both PureTiO<sub>2</sub> and 1.0-Pt-TiO<sub>2</sub> after photocatalytic reaction, which are not observed before the photocatalytic reaction as for PureTiO<sub>2</sub>. These new bands are probably due to the residual segments

of the organic molecules degraded. Moreover, the vibration signals of these new bands for PureTiO<sub>2</sub> sample are stronger than those for 1.0-Pt-TiO<sub>2</sub> sample, which indicates that the adsorbed residual organic pieces after MO degradation by PureTiO<sub>2</sub> are much more. Therefore, Pt loading is in favor of the complete degradation of organic molecules.

Based on the previous experimental results, one can see that loading metal Pt onto TiO<sub>2</sub> microspheres greatly improved the photocatalytic efficiency. This finding can be explained in terms of the special assembly structure of TiO<sub>2</sub> microspheres and the interfacial interactions between metal Pt and microspheres. As shown in Scheme 2, excitement of



SCHEME 1: Pictures illustrating the loading of Pt onto TiO<sub>2</sub> microspheres: (a) <0.85 wt% Pt and (b) >0.85 wt% Pt.

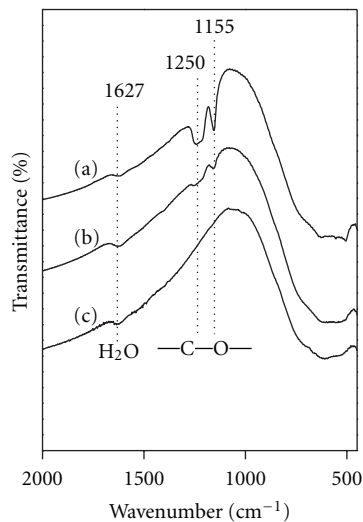
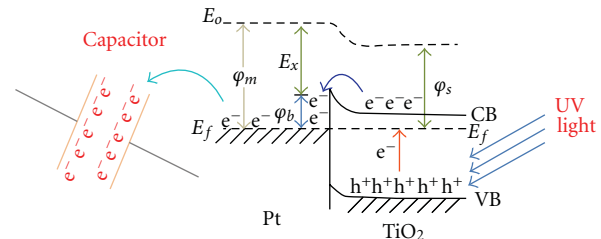


FIGURE 5: FT-IR spectra for given samples: (a) PureTiO<sub>2</sub> sample after photocatalytic reaction; (b) 1.0-Pt-TiO<sub>2</sub> sample after photocatalytic reaction; (c) PureTiO<sub>2</sub> sample before photocatalytic reaction.

microspheres by ultraviolet light leads to the separation of photogenerated electron-hole pairs. Since the work function of metal Pt is  $\varphi_m = 5.36$  eV, larger than that of 4.2 eV for the face (110) of TiO<sub>2</sub> [24], the Fermi energy level for microspheres locates above that of metal Pt. Therefore, electrons can easily transfer from the conduction band of TiO<sub>2</sub> to metal Pt. Continuous transfer of electrons leads to the formation of Schottky barriers at the interfaces between Pt and TiO<sub>2</sub> microspheres. Due to the existence of Schottky barriers [7], reverse process for electrons migration from metal Pt to TiO<sub>2</sub> is hard to occur. Therefore, recombination of photogenerated electrons and holes can be efficiently inhibited and photoquantum efficiency increased spontaneously.



SCHEME 2: Reaction mechanism proposed for the photocatalytic removal of MO molecules.

It is well known that the separation of light-induced electron-hole pairs is critical in the photocatalytic reaction. However, some photochemical processes except for the enhancement of photoquantum efficiency are hardly discussed. For example, the highly efficient utility of photo-generated electrons and holes in photo-degradation process plays an important role in enhancing the photocatalytic efficiency. In our recent work, self-assembled TiO<sub>2</sub> microspheres sample has been found to exhibit a giant dielectric property [25], which is closely related to the cavities structure in between the parallel adjacent nanowires within the microspheres that can be taken as microcapacitors. These microcapacitors possess a giant dielectric constant and therefore might provide a superior electronic storage capacity. Because the production of light-induced electrons is faster than the degradation of MO molecule in photocatalytic reaction, compensating the time difference of photogenerated electrons and degradation reaction participated by electrons is pretty necessary. Due to the existences of microcapacitors, the accumulation and releasing of electrons can enhance the utility of electrons, while avoiding the recombination of electrons and holes. Therefore, dual roles from Pt deposition and special structure of TiO<sub>2</sub> microspheres contribute to the efficient separation of light-induced electrons and holes that greatly enhances the utility of electrons in favor of the optimum photocatalytic activities.

## 4. Conclusions

We have fabricated the Pt-TiO<sub>2</sub> microspheres by a solution chemistry with a subsequent Pt loading through a photoreduction. Pt loading led to an efficient separation of photogenerated electron-hole pairs. Meanwhile, electrons stored in the “microcapacitor” of TiO<sub>2</sub> microspheres contributed to the enhancement of photocatalytic activity under UV light irradiation. Varying the Pt loading content gives rise to an optimum catalytic efficiency. By monitoring the surface chemistry of Pt-TiO<sub>2</sub> microspheres before and after photocatalytic reactions, we found that the degradation of MO molecules was more complete in the presence of Pt loading.

## Acknowledgments

This work was financially supported by NSFC (no. 20773132, 20771101), National Basic Research Program of China (2007CB613306), and Directional program CAS (KJJCXZ–YWM05). The authors declare no conflict of interest.

## References

- [1] M. L. Chen and W. C. Oh, “The improved photocatalytic properties of methylene blue for V<sub>2</sub>O<sub>3</sub>/CNT/TiO<sub>2</sub> composite under visible light,” *International Journal of Photoenergy*, vol. 2010, Article ID 264831, pp. 1–5, 2010.
- [2] L. Zhao, J. Ran, Z. Shu, S. Wang, G. Dai, and P. Zhai, “Effects of calcination temperatures on photocatalytic activity of ordered titanate nanoribbon/SnO<sub>2</sub> films fabricated during an EPD process,” *International Journal of Photoenergy*, vol. 2012, 2012.
- [3] N. A. Jamalluddin and A. Z. Abdullah, “Reactive dye degradation by combined Fe(III)/TiO<sub>2</sub> catalyst and ultrasonic irradiation: effect of Fe(III) loading and calcination temperature,” *Ultrasonics Sonochemistry*, vol. 18, no. 2, pp. 669–678, 2011.
- [4] Y. Zhang, J. Xu, P. Xu, Y. Zhu, X. Chen, and W. Yu, “Decoration of ZnO nanowires with Pt nanoparticles and their improved gas sensing and photocatalytic performance,” *Nanotechnology*, vol. 21, no. 28, Article ID 285501, pp. 1–7, 2010.
- [5] J. Pan, S.-M. Hühne, H. Shen et al., “SnO<sub>2</sub>-TiO<sub>2</sub> Core-shell nanowire structures: investigations on solid state reactivity and photocatalytic behavior,” *Journal of Physical Chemistry C*, vol. 115, no. 35, pp. 17265–17269, 2011.
- [6] S. J. Kim, N. H. Lee, H. J. Oh, S. C. Jung, W. J. Lee, and D. H. Kim, “Photocatalytic properties of nanotubular-shaped TiO<sub>2</sub> powders with anatase phase obtained from titanate nanotube powder through various thermal treatments,” *International Journal of Photoenergy*, vol. 2011, pp. 1–7, 2011.
- [7] A. L. Linsebigler, G. Lu, and J. T. Yates, “Photocatalysis on TiO<sub>2</sub> surfaces: principles, mechanisms, and selected results,” *Chemical Reviews*, vol. 95, no. 3, pp. 735–758, 1995.
- [8] C. Chen, W. Ma, and J. Zhao, “Semiconductor-mediated photodegradation of pollutants under visible-light irradiation,” *Chemical Society Reviews*, vol. 39, no. 11, pp. 4206–4219, 2010.
- [9] C. Wang, L. Yin, L. Zhang, N. Liu, N. Lun, and Y. Qi, “Platinum-nanoparticle-modified TiO<sub>2</sub> nanowires with enhanced photocatalytic property,” *ACS Applied Materials and Interfaces*, vol. 2, no. 11, pp. 3373–3377, 2010.
- [10] J. A. Byrne, P. A. Fernandez-Ibañez, P. S. M. Dunlop, D. M. A. Alrousan, and J. W. J. Hamilton, “Photocatalytic enhancement for solar disinfection of water: a review,” *International Journal of Photoenergy*, vol. 2011, pp. 1–12, 2011.
- [11] Z. Zhang and J. Gamage, “Applications of photocatalytic disinfection,” *International Journal of Photoenergy*, vol. 2010, Article ID 764870, pp. 1–11, 2010.
- [12] Z. Yao, F. Jia, S. Tian, C. Li, Z. Jiang, and X. Bai, “Microporous Ni-Doped TiO<sub>2</sub> film photocatalyst by plasma electrolytic oxidation,” *ACS Applied Materials and Interfaces*, vol. 2, no. 9, pp. 2617–2622, 2010.
- [13] S. Tojo, T. Tachikawa, M. Fujitsuka, and T. Majima, “Iodine-doped TiO<sub>2</sub> photocatalysts: correlation between band structure and mechanism,” *Journal of Physical Chemistry C*, vol. 112, no. 38, pp. 14948–14954, 2008.
- [14] Y. Chen, D. Li, X. Wang, L. Wu, X. Wang, and X. Fu, “Promoting effects of H<sub>2</sub> on photooxidation of volatile organic pollutants over Pt/TiO<sub>2</sub>,” *New Journal of Chemistry*, vol. 29, no. 12, pp. 1514–1519, 2005.
- [15] W. Zhang, X. Wang, and X. Fu, “Magnetic field effect on photocatalytic degradation of benzene over Pt/TiO<sub>2</sub>,” *Chemical Communications*, vol. 9, no. 17, pp. 2196–2197, 2003.
- [16] V. Iliev, D. Tomova, S. Rakovsky, A. Eliyas, and G. L. Puma, “Enhancement of photocatalytic oxidation of oxalic acid by gold modified WO<sub>3</sub>/TiO<sub>2</sub> photocatalysts under UV and visible light irradiation,” *Journal of Molecular Catalysis A: Chemical*, vol. 327, no. 1–2, pp. 51–57, 2010.
- [17] H. Y. Chuang and D. H. Chen, “Fabrication and photocatalytic activities in visible and UV light regions of Ag@TiO<sub>2</sub> and NiAg@TiO<sub>2</sub> nanoparticles,” *Nanotechnology*, vol. 20, no. 10, Article ID 105704, 2009.
- [18] H. Bahruji, M. Bowker, P. R. Davies, and F. Pedrono, “New insights into the mechanism of photocatalytic reforming on Pd/TiO<sub>2</sub>,” *Applied Catalysis B: Environmental*, vol. 107, no. 1–2, pp. 205–209, 2011.
- [19] W. Hu, L. Li, W. Tong, and G. Li, “Supersaturated spontaneous nucleation to TiO<sub>2</sub> microspheres: synthesis and giant dielectric performance,” *Chemical Communications*, vol. 46, no. 18, pp. 3113–3115, 2010.
- [20] J. Zhang, L. Li, T. Yan, and G. Li, “Selective Pt deposition onto the face (110) of TiO<sub>2</sub> assembled microspheres that substantially enhances the photocatalytic properties,” *Journal of Physical Chemistry C*, vol. 115, no. 28, pp. 13820–13828, 2011.
- [21] A. V. Vorontsov, E. N. Savinov, and J. Zhensheng, “Influence of the form of photodeposited platinum on titania upon its photocatalytic activity in CO and acetone oxidation,” *Journal of Photochemistry and Photobiology A: Chemistry*, vol. 125, no. 1–3, pp. 113–117, 1999.
- [22] W. Mu, J. M. Herrmann, and P. Pichat, “Room temperature photocatalytic oxidation of liquid cyclohexane into cyclohexanone over neat and modified TiO<sub>2</sub>,” *Catalysis Letters*, vol. 3, no. 1, pp. 73–84, 1989.
- [23] M. Hamadani, A. Reisi-Vanani, and A. Majedi, “Synthesis, characterization and effect of calcination temperature on phase transformation and photocatalytic activity of Cu,S-codoped TiO<sub>2</sub> nanoparticles,” *Applied Surface Science*, vol. 256, no. 6, pp. 1837–1844, 2010.
- [24] C. W. Oatley, “The adsorption of oxygen and hydrogen on platinum and the removal of these gases by positive-ion bombardment,” *Proceedings of the Physical Society*, vol. 51, no. 2, article 309, pp. 318–328, 1939.
- [25] W. Hu, L. Li, W. Tong, and G. Li, “Water-titanate intercalated nanotubes: fabrication, polarization, and giant dielectric property,” *Physical Chemistry Chemical Physics*, vol. 12, no. 39, pp. 12638–12646, 2010.

## Review Article

# A Review on TiO<sub>2</sub> Nanotube Film Photocatalysts Prepared by Liquid-Phase Deposition

Jinshu Wang, Qian Cai, Hongyi Li, Yuntao Cui, and Hong Wang

*School of Materials Science and Engineering, Beijing University of Technology, Beijing 100124, China*

Correspondence should be addressed to Jinshu Wang, wangjinshu2002@hotmail.com

Received 15 September 2011; Revised 18 November 2011; Accepted 18 November 2011

Academic Editor: Jiaguo Yu

Copyright © 2012 Jinshu Wang et al. This is an open access article distributed under the Creative Commons Attribution License, which permits unrestricted use, distribution, and reproduction in any medium, provided the original work is properly cited.

TiO<sub>2</sub> nanotube film is a promising photocatalyst associated with its unique physical and chemical properties such as optic, electronic, high specific surface area. Liquid-phase decomposition provides a feasible way for the preparation of functional thin film. This paper reviews and analyzes the formation mechanism of TiO<sub>2</sub> nanotube film by liquid phase deposition. The effect of preparation parameters, such as the kinds of electrolyte solution for the preparation of anodic alumina template, volume fraction of Al<sub>2</sub>O<sub>3</sub> on the template, the concentration of the deposition solution, and heat treatment, on the formation of TiO<sub>2</sub> nanotube film has been analyzed. The effects of doping of metallic and nonmetallic elements on the photocatalytic activity of TiO<sub>2</sub> nanotube have been discussed.

## 1. Introduction

Nowadays, humans are more and more concerned about environmental issues. Large amounts of organic pollutants are being released into the ecosystem over the past few decades and they cause a serious threat to the environment [1]. Researchers all over the world have been working on various approaches to address the issue. In the past decades, the traditional physical techniques, such as adsorption, biological treatment, coagulation, ultrafiltration, and ion exchange on synthetic resins, have been adopted for the removal of organic pollutants from wastewaters [2]. However, these methods might cause secondary pollution, and degradation of organic pollutants is usually incomplete and selective.

Since the discovery of photocatalytic splitting of water on TiO<sub>2</sub> electrodes by Fujishima and Honda in 1972 [3], heterogeneous photocatalysis has attracted much attention as a new purification technique for air and water [4–6]. Titania nanostructures have been widely investigated for applications in optical devices [7], gas sensors [8], and dye-sensitized solar cells [9]. Titania semiconductor photocatalysts have demonstrated advantages such as transparency [10], wide bandgap [11], biological and chemical inertness [12, 13], strong oxidizing capability, and nontoxicity [14]. So titania exhibits good performance on the degradation of organic pollutants under ultraviolet radiation. Many other

photocatalysts such as CdS, WO<sub>3</sub>, and SrTiO<sub>3</sub> also exhibit a certain photocatalytic activity [15–17].

Crystalline titania has many morphologies such as nanofibers, nanoparticles, nanorods, nanospheres, nanotubes, and nanowires [18–20]. Titania nanotubes are highly efficient in photocatalysis since titania nanotubes have a relatively higher interfacial charge transfer rate and surface area compared with the spherical TiO<sub>2</sub> particles [21]. Many approaches have been developed for the preparation of TiO<sub>2</sub> nanotubes, that is, chemical vapor deposition (CVD), anodic oxidation, seeded growth, the wet chemical (hydrothermal method and the sol-gel method) [22–24], and liquid-phase deposition of templates. Among these methods, liquid-phase deposition (LPD) of template method is one of the simplest and most practical one to fabricate TiO<sub>2</sub> nanotubes, since it has so many advantages such as low cost, mild reaction condition, simple equipment requirement and allows TiO<sub>2</sub> films to be deposited over large areas.

## 2. Liquid-Phase Deposition of Template Method: Formation of Titania Nanotubes

A variety of oxide nanohole sheets have been prepared by a liquid-phase deposition method. The liquid-phase deposition can be applied readily to the preparation of thin films

on various types of substrates with large surface areas and a variety of morphologies, since the LPD is performed in an aqueous solution. In the LPD process, using anodic alumina template as a scavenger and starting materials, the metal oxide films can be fabricated by only one-step reaction. The liquid-phase deposition of template method consists of two major steps: (a) preparation of anodic aluminum oxide templates; (b) liquid-phase deposition.

Anodic alumina oxide (AAO) has been used as template for the fabrication of several kinds of functional devices with nanometer dimensions due to its unique structure, such as controllable pore diameter, extremely narrow pore size distribution, and ideally cylindrical pore shape [25–30]. Since the diameter of the cylindrical pores of the templates can be varied between 10 and 200 nm by altering the preparation conditions, the templating method has a number of interesting and useful features for the production of microscopically tailored materials [31]. The AAO films with an ordered array of holes [32–36] can be used as templates for the preparation of nanotubes, nanowires [37–42], nanodots, and nanopillars [43–45] as well as micro-electromechanical systems (MEMS) devices [46]. The AAO films with pore diameter ranging from 4 to 250 nm, density as high as  $10^{11}$  pores/cm<sup>-1</sup>, and film thickness varying from 0.1 to 300  $\mu$ m, have been realized [37, 38]. The anodic aluminum oxide template has been widely applied in the preparation of various nanomaterials. Highly ordered polycrystalline Si nanowire arrays were synthesized with porous anodic aluminum oxide templates by chemical vapor deposition [47].

We made the highlighted changes according to the list to references. Please check.

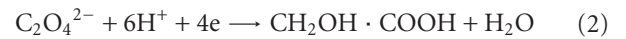
Yamanaka et al. have prepared titania nanotubes successfully with anodic aluminum oxide (AAO) templates as precursor by liquid-phase deposition method [48] and the morphology of the AAO templates and titania nanotubes formed is shown in Figure 1. The AAO templates have many pores and their mean sizes are approximately 200 nm (Figure 1(a)), and titania nanotubes formed keep the morphology of AAO with nearly the same size (Figure 1(b)). The titania nanotubes array which consist of many grains with approximately 20 nm in diameter have the thickness as high as about 50  $\mu$ m, as shown in Figures 1(c) and 1(d). In the past, AAO templates had to be stripped from the aluminum substrates and removed the barrier layers. However, the AAO templates made in this way are brittle, so it is limited to fabricate large area nanotube array. Jiang et al. prepared titania nanotubes in a large scale by LPD method using AAO templates without stripping from the Al substrates [49], which provided a simple and feasible way for the preparation of the TiO<sub>2</sub> films in a large scale.

### 3. Liquid-Phase Deposition of Template Method: Formation Mechanism of Titania Nanotubes

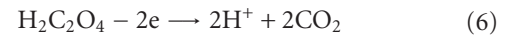
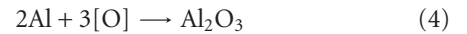
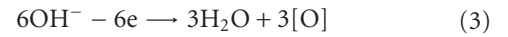
*3.1. Formation Mechanism of AAO Template.* The titania nanotubes are synthesized in situ on the anodic aluminum

oxide templates. So the morphology of the titania nanotubes is correlated with the morphology of AAO templates. There are two types of aluminum oxide films prepared by anodizing the aluminum: barrier type and porous type [50]. The barrier-type AAO template is formed by anodizing Al foil in the electrolyte solution such as citric acid, boric acid, and glycolic acid in which Al has very low solubility. However, the porous-type AAO template can be formed by anodizing in the electrolyte solution such as sulfuric acid, oxalic acid, and phosphoric acid in which Al has better solubility. Taking oxalic acid as an example, the reaction equations can be written as below [51].

Cathode Reaction:

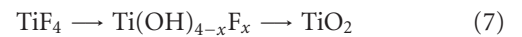


Anode Reaction:



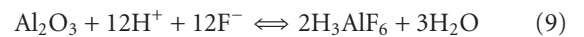
At the beginning of the anodizing process, the amorphous oxide is formed. Oxide is dissolved with the electric field enhancement, leading to the formation of porous oxide.

*3.2. Formation Mechanism of Titania Nanotubes.* Imai et al. first reported that crystalline titania films could be deposited from aqueous solutions of TiF<sub>4</sub> at PH1-3 and the hydrolysis of TiF<sub>4</sub> in solution occurred in a stepwise manner to produce titania [31]:



Titania forms on the inner walls of the nanochannels of the alumina template through heterogeneous nucleation and then grows into nanotubes which keep the porous morphology of alumina.

Using anodic alumina films as the templates, the following chemical reactions might take place:



Therefore, TiO<sub>2</sub> can be formed by the hydrous reaction of TiF<sub>6</sub><sup>2-</sup> accompanied by an F<sup>-</sup> consuming reaction, where Al<sub>2</sub>O<sub>3</sub> is taken as scavenger for F<sup>-</sup>. The equilibrium reaction (8) is shifted to the right side by the reaction of Al<sub>2</sub>O<sub>3</sub>, H<sup>+</sup> and F<sup>-</sup>, since Al<sub>2</sub>O<sub>3</sub> reacts readily with F<sup>-</sup> ions to give the more stable AlF<sub>6</sub><sup>3-</sup>. The product TiO<sub>2</sub> · nH<sub>2</sub>O deposits in situ on anodic alumina template. We present an illustration for the formation of titanium hydrous oxide nanotubes array films [52], as shown in Figure 2. When the AAO templates are immersed into (NH<sub>4</sub>)<sub>2</sub>TiF<sub>6</sub> solution,

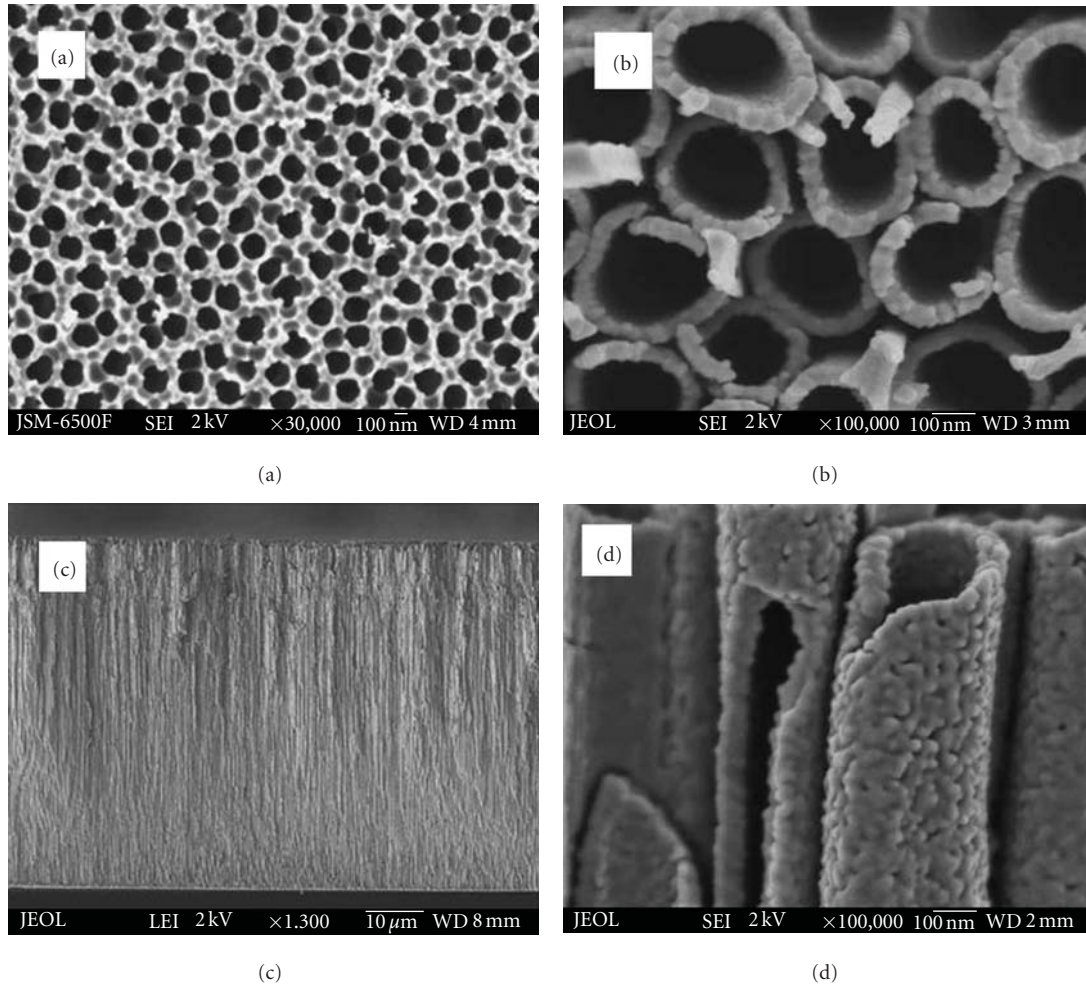


FIGURE 1: FE-SEM photographs of the titania nanohole arrays: (a) surface morphology of anodic alumina as starting material, (b) surface morphology of titania nanohole array, (c) cross-section of titania nanohole array, and (d) cross-section detailing (c) [48].

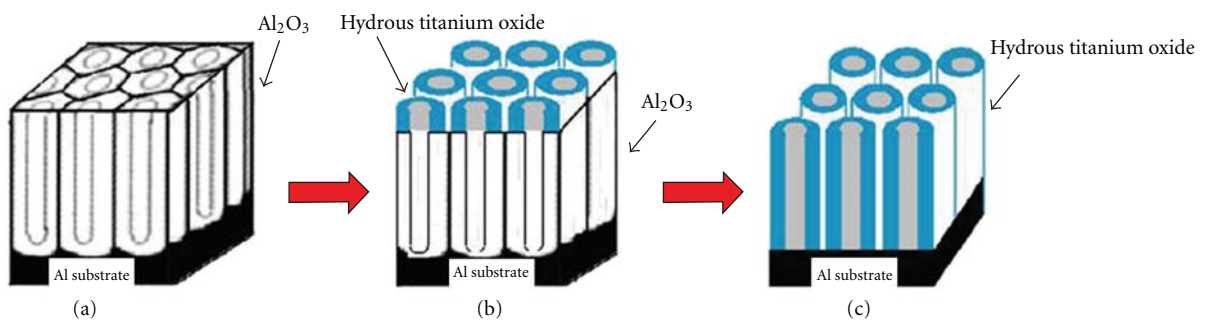
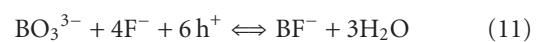
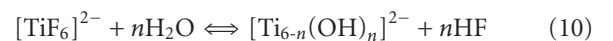


FIGURE 2: Schematic diagram of the formation of the titania nanohole array: (a) before deposition, (b) during deposition, and (c) after deposition [52].

the hydrolysis of reaction of  $[\text{TiF}_6]^{2-}$  takes place at the surface. Hydrous titanium oxide deposits in situ on the AAO templates, accompanied with the consumption of AAO templates, as shown in Figure 2(b). Hydrous titanium oxide is formed from the surface to the inner part of AAO template with the prolonging of the reaction time (Figure 2(c)). After calcinations,  $\text{TiO}_2$  nanotubes can be formed.

Kanawori et al. described the formation mechanism by the addition of boric acid [43] which is used as scavenger for  $\text{F}^-$  ion. The reactions are shown below.



Boric acid promotes reaction (10) to the right side by consuming  $F^-$ , leading to the formation of hydrous titanium oxide.

#### 4. Factors Influencing the Formation and Photocatalytic Activity of Titania Nanotube Film

There are several factors which affect the formation of titania nanotubes: (a) the electrolyte solution used to prepare AAO templates (such as phosphoric acid, oxalic acid, and sulfuric acid), (b) oxidation temperature, (c) anodizing voltage, (d) oxidation time, (e) the concentration of the deposition solution, (f) deposition temperature, (g) deposition time, and (h) the temperature of heat treatment. These factors can be summarized as (1) the preparation parameters of AAO template, (2) liquid-phase deposition parameters, (3) Heat treatment. The characteristics and morphology of titania nanotubes such as specific surface area, film thickness, crystal structure and others are dependent on the selected above-mentioned conditions.

*4.1. Effect of Preparation Parameters of AAO Template on the Morphology of TiO<sub>2</sub> Nanoarrays.* The AAO templates are prepared with a modified two-step anodization process. The pore size, pore density, and the thickness of the AAO template are approximately proportional to the anodization voltage, but the quality of the ordering in the AAO structure also highly depends on the first anodization time [34]. Zhang et al. anodized aluminum in a 0.3 M oxalic acid solution with outer voltage of 40 V at 0°C for different time. After removing the preliminary oxidization layer, the second anodization was carried out at 0°C for about 1 h under the same conditions as the first anodization step. Afterward, the AAO template was immersed into a 5 wt% phosphoric acid solution to widen the nanochannels. The outer diameter of the AAO pore is 180 nm, and the wall thickness of the AAO pore is 55 nm [53]. Jiang et al. used 10% phosphoric acid instead of oxalic acid to oxidize aluminum with outer voltage of 120 V at room temperature for 1 h. Then the aluminum was immersed in the 1.8% H<sub>2</sub>CrO<sub>4</sub> : 6% H<sub>3</sub>PO<sub>4</sub> = 1 : 1 (volume ratio) mixed solution to remove preliminary oxidization layer. The second anodization step was the same as the first anodization step but for 4 h [49]. After widening the nanochannels, the AAO templates were obtained with larger aperture than the AAO templates made in oxalic acid. We also find in our work that the anodic alumina templates prepared in oxalic acid have relatively small pore diameter, as shown in Figure 3(a). The mean outside diameter and inside diameter of that prepared in oxalic acid are about 100 nm and 25 nm, respectively. On the other hand, the templates prepared in phosphoric acid have large pore diameter, as shown in Figure 3(b), that is, the mean outside diameter of the tubule and inside diameter are about 250 nm and 150 nm, respectively. The pores in all the templates are uniform and arranged regularly. The pore size formed in the membrane is related to the anodizing voltage applied in the electrolyte. It is reported that the maximum anodizing voltage applied in the electrolyte is in the order phosphoric acid > oxalic

acid. The anodizing process will be blocked when a voltage higher than  $V_{max}$  is employed. To obtain the template with large pores, high anodizing voltage should be applied in the electrolyte; therefore, anodic alumina template prepared with phosphoric acid has the larger pore size.

We have studied the relationship between volume fraction of Al<sub>2</sub>O<sub>3</sub> in the template and the morphology of TiO<sub>2</sub> nanoarray [54]. When the volume fraction of Al<sub>2</sub>O<sub>3</sub> in the template is more than 0.71, such as the template prepared in oxalic acid, the ordered aligned titania nanorods can be obtained (Figure 3(c)) whereas the ordered aligned titania nanotubes can be synthesized when the volume fraction of Al<sub>2</sub>O<sub>3</sub> in the template (e.g., the template prepared in phosphoric acid) is less than 0.71, as shown in Figure 3(d). Therefore, the morphology of TiO<sub>2</sub> nanoarray depends on the volume fraction of Al<sub>2</sub>O<sub>3</sub> in the template which can be controlled by the preparation parameters of AAO templates.

*4.2. Effect of Concentration of the Deposition Solution.* The concentration of the deposition solution should be controlled in an appropriate value. In our study, it is found that 0.1 mol/L (NH<sub>4</sub>)<sub>2</sub>TiF<sub>6</sub> is suitable for the deposition, and the morphology of TiO<sub>2</sub> nanotube is shown in Figure 4(b). If the concentration of the deposition solution is too low, only a small number of TiO<sub>2</sub> nanotubes can be produced with a large amount of alumina remained, as shown in Figure 4(a). If the concentration of the deposition solution is too high, the reaction is so severe that parts of TiO<sub>2</sub> nanotubes will be destroyed (Figure 4(c)).

*4.3. Effect of Heat Treatment.* TiO<sub>2</sub> prepared by LPD method exhibits as amorphous phase [57]. It is well known that it shows poor photocatalytic activity since amorphous TiO<sub>2</sub> has defects in its crystal structure. To prepare anatase TiO<sub>2</sub> with a high surface area and good crystallization is essential to improve the photocatalytic activity. Calcination is a simple way for the crystallization of TiO<sub>2</sub>. When annealing at 400°C for 2 h, the amorphous TiO<sub>2</sub> films change to anatase phase [52, 58]. With increasing calcination temperature, the photocatalytic activity increases due to the formation of anatase TiO<sub>2</sub> and the improvement of crystallization [59]. With further increase in the calcination temperature from 600 to 800°C, the photocatalytic activity rapidly decreased due to the vanishing of anatase phase, collapse of nanotube structures, and decrease of surface areas [60]. TiO<sub>2</sub> has three types of crystal structures: anatase, rutile, and brookite. Among them, the anatase films show best photocatalytic property. It is also found that a mixed phase of anatase and rutile or brookite shows excellent photocatalytic ability [61] due to the reduction of the combination probability of the hole-electron pairs.

Recently, vapor-thermal treatment can be applied to the crystallization of TiO<sub>2</sub>. In vapor-thermal treatment, the as-prepared TiO<sub>2</sub> nanotube array film was placed on the support to avoid direct contact with the water, which was then placed into a 100-mL stainless steel autoclave with a 100 mL Teflon liner. Two mL distilled water was added into the liner. This method is different from hydrothermal method,

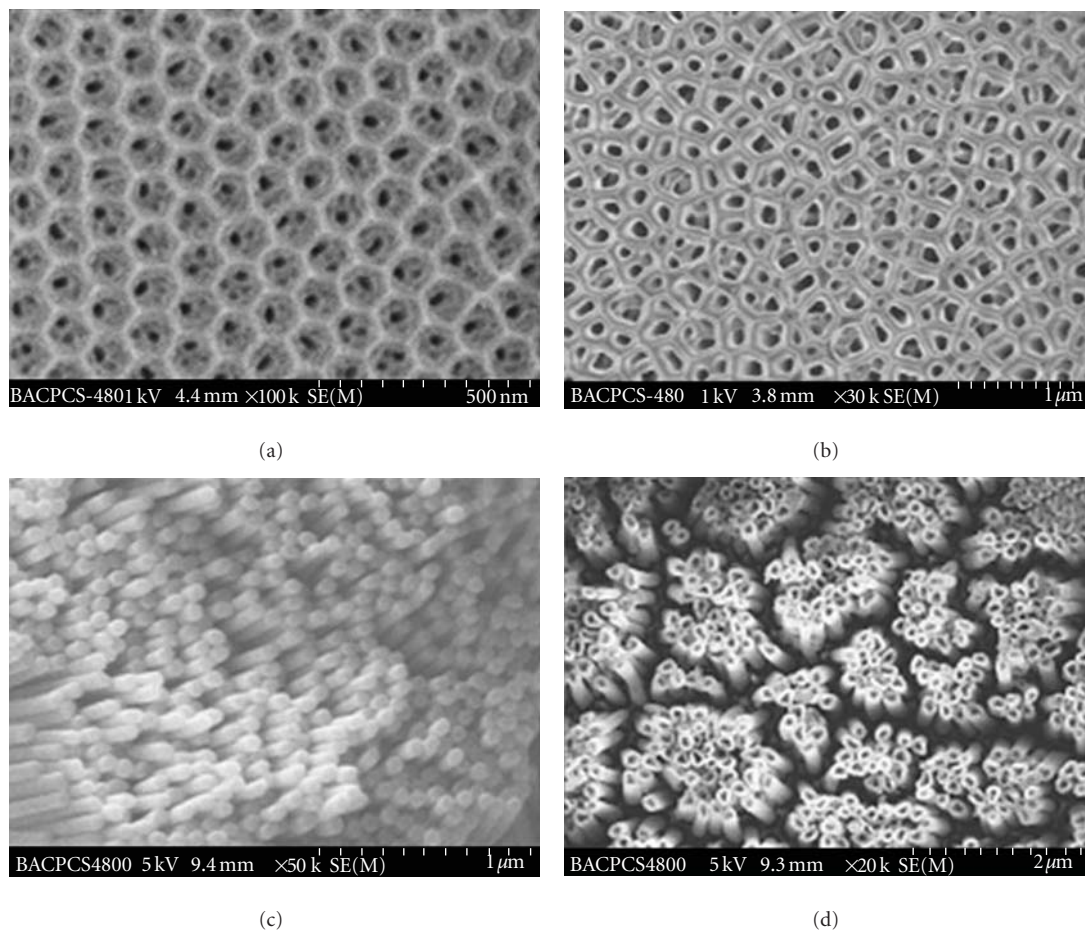


FIGURE 3: FE-SEM of titanium oxide nanotubes array films: (a) AAO membrane (oxalic acid), (b) AAO membrane (phosphoric acid), (c) surface morphology of titanium oxide nanotubes array films (oxalic acid), and (d) surface morphology of titanium oxide nanotubes array films (phosphoric acid) [54].

in which the  $\text{TiO}_2$  nanotube array film was put into Teflon-lined autoclave, which was then filled with water up to 80% of the total volume. The vapor-thermal-treated films have better crystallization than the calcined films and remained tubular structures compared with the hydrothermal-treated samples. So the vapor-thermal treatment exhibits better photocatalytic activity than the calcined and hydrothermal treated films (Figure 5) [55].

## 5. Modification of Titania Nanotube Photocatalysts

In order to improve the photocatalytic activity, various approaches, such as nonmetal anions doping, surface improvement with noble metal, transition metal cation doping, and semiconductor composite, have been attempted to hamper the recombination of the photogenerated hole-electron pairs in the photocatalysis [62].

Nonmetal dopants, such as N, S, C, and P have been applied in the photocatalysis to broaden the utilization of solar energy in visible region [63–65]. Asahi et al. [66] found that the substitutional doping of N was the most effective for its contribution to the bandgap narrowing by mixing its

p states with O 2p states. Although doping with S shows a similar band-gap narrowing, it is difficult to incorporate it into the  $\text{TiO}_2$  lattice. The states introduced by C and P are too deep in the gap to overlap sufficiently with the band states of  $\text{TiO}_2$  to transfer photoexcited carriers to reactive sites at the catalyst surface within their lifetime. However, sulfur doping has been reported to have better photoabsorption as compared to nitrogen doping [63]. Compared with the single-element doping, the codoped  $\text{TiO}_2$  can provide better photocatalytic performance. Synergistic effect of doped S and N forms a new band above the valence band and narrows the band-gap of the photocatalyst, leading to photo-absorption and catalytic activity in the visible light region [67].

Some researchers fabricated metal-doped  $\text{TiO}_2$  films. Zhao et al. successfully prepared Zn-doped titania nanotubes, which was about 20 nm red shift in the spectrum of UV-vis absorption compared with  $\text{TiO}_2$  nanotubes [68]. Fe-doped titania nanotubes improve the photocatalytic ability of titania by hindering the recombination of photogenerated hole electron and a stronger absorption in the 410–650 nm range [69, 70]. The photocatalytic performance of a series of Pt/RE/ $\text{TiO}_2$  photocatalysts has been investigated. The activities of all rare-earth-doped  $\text{TiO}_2$  samples have been

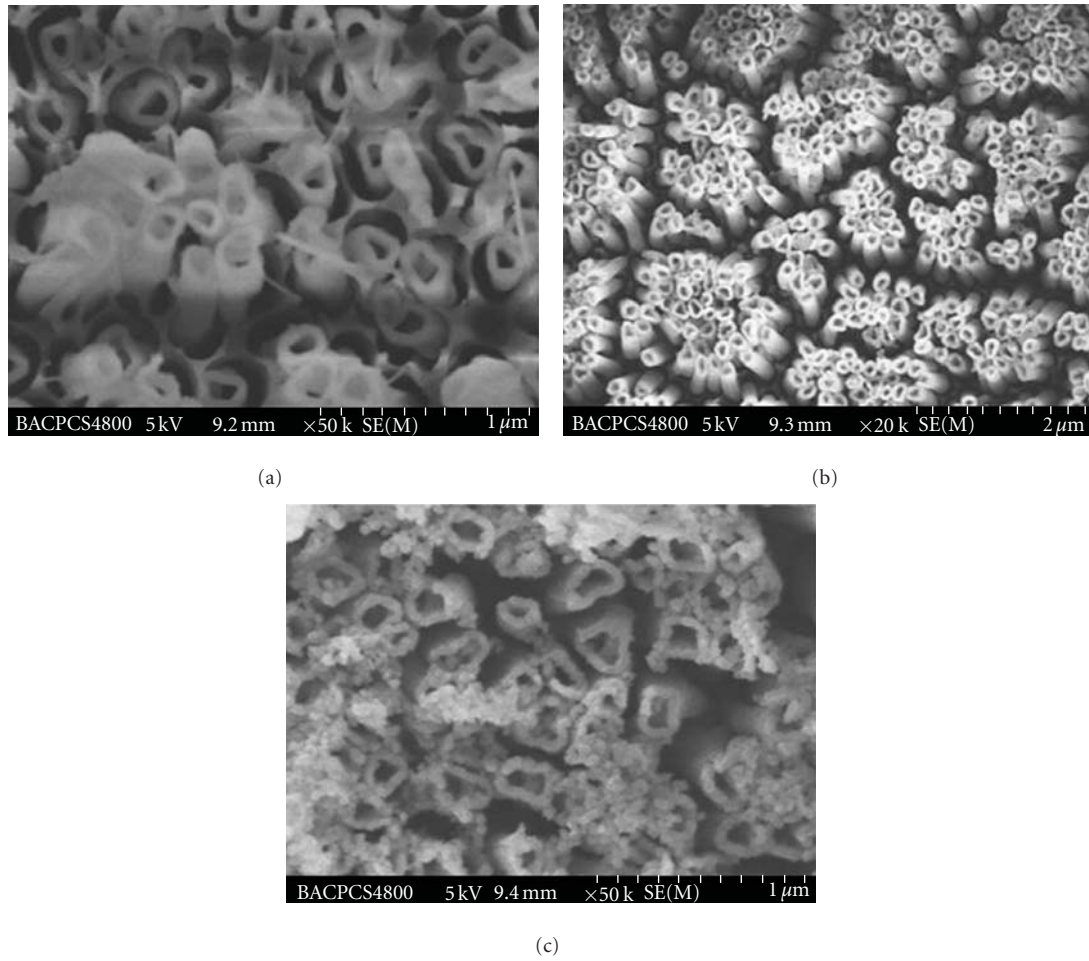


FIGURE 4: SEM micrographs of TiO<sub>2</sub> nano tubes prepared with different concentration of deposition solution ((NH<sub>4</sub>)<sub>2</sub>TiF<sub>6</sub>): (a) 0.05 mol/L, (b) 0.1 mol/L, (c) 0.3 mol/L.

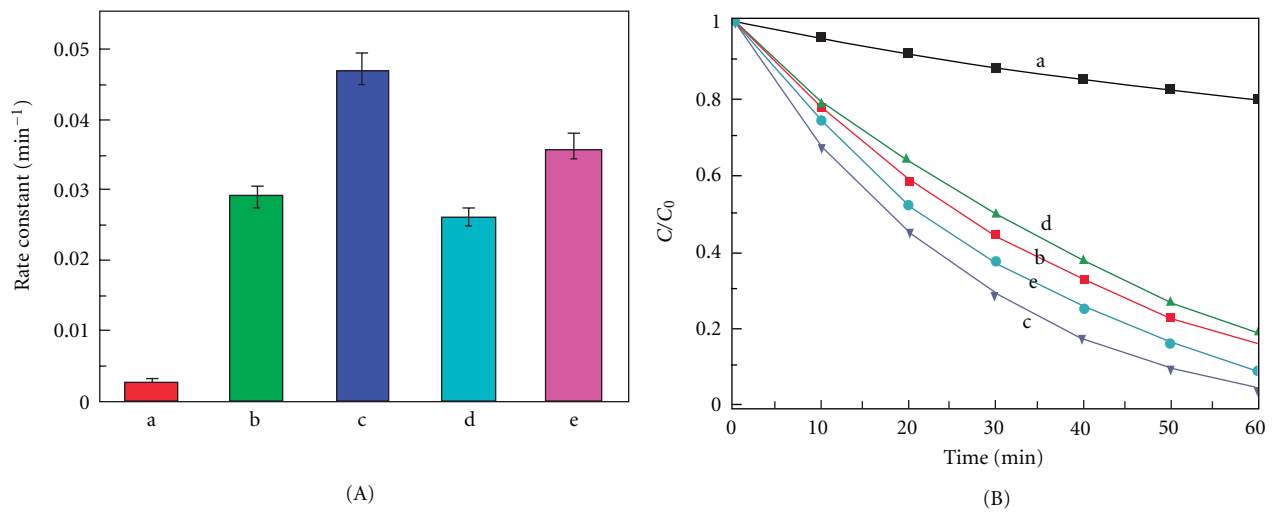


FIGURE 5: Comparison of photocatalytic activity of the TNs samples before and after treatment for the photocatalytic decomposition of MO in water: (a) untreated, (b) calcination, (c) vapor thermal, and (d) hydrothermal. (A) Apparent rate constants. (B)  $C/C_0-t$  curve. C and  $C_0$  denote the reaction and initial concentration of MO in the system, respectively [55].

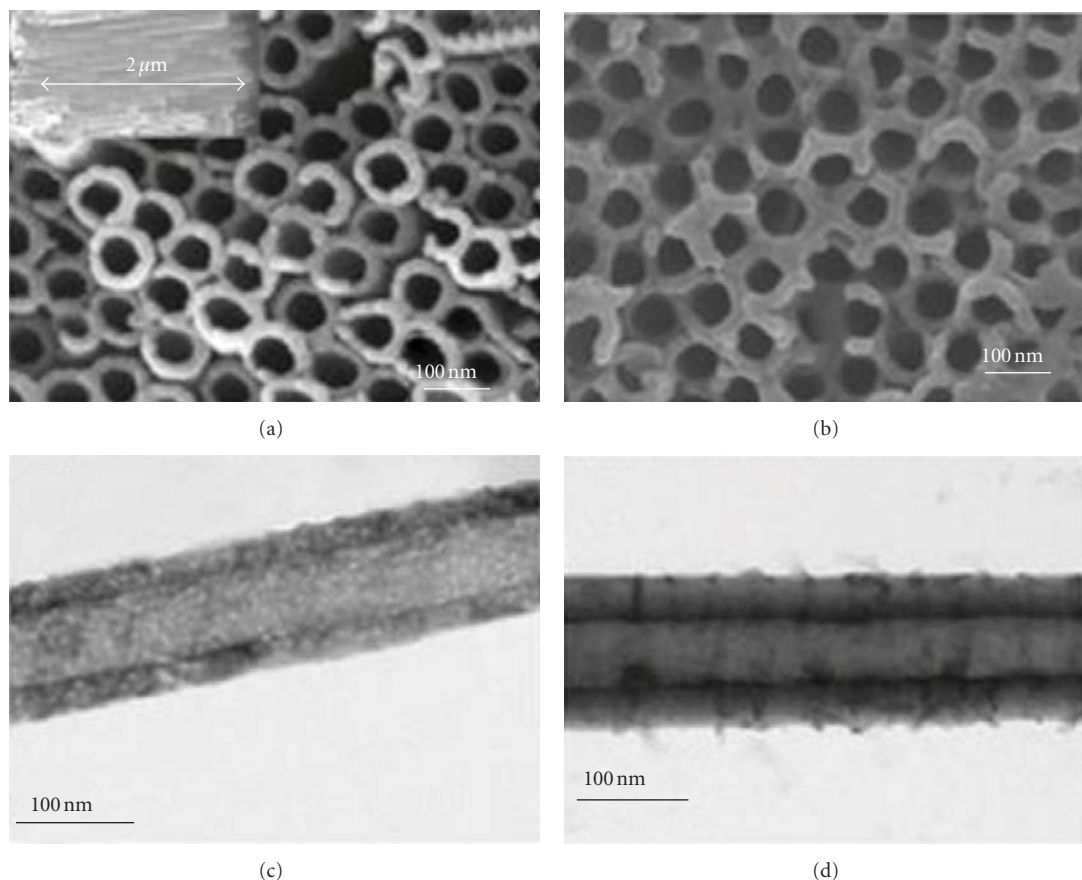


FIGURE 6: SEM (a, b) and TEM (c, d) images of self-organized  $\text{TiO}_2$  NTs (a, c) and  $\text{BiOI/TiO}_2$  NTs (b, d). (a) Top and side (inset) view SEM images of the unmodified  $\text{TiO}_2$  NTs. (b) Top SEM image of  $\text{BiOI/TiO}_2$  NTs. (c) TEM images of the unmodified  $\text{TiO}_2$  NTs. (d) TEM images of  $\text{BiOI/TiO}_2$  NTs [56].

increased compared to those of pure  $\text{TiO}_2$  in the order:  $\text{La/TiO}_2 > \text{Sm/TiO}_2 > \text{Eu/TiO}_2 > \text{Dy/TiO}_2 > \text{Er/TiO}_2$ . It is shown that the transformation from anatase to rutile has been prevented, which can enhance the activities of the photocatalysts. The data of lattice distortion implies that  $\text{Ti}^{4+}$  can enter (antidope) into rare earth oxide that exists on the surface of titanium dioxide. The flat-band potential of conduction of  $\text{RE/TiO}_2$  has been shifted negatively since the lattice distortion raises the Fermi level, which causes flat-band potential of the conduction of  $\text{TiO}_2$ . As a result, the photoinduced electrons of the conduction band have stronger reduction capability and thus the photocatalytic activity is improved [71].

Chen et al. studied the doping effect of eight transition metal ion dopants on the crystal phase and the photoreactivity of  $\text{TiO}_2$  nanoparticles [72]. Among all the eight doping metal ions of  $\text{Zn}^{2+}$ ,  $\text{Fe}^{3+}$ ,  $\text{Cu}^{2+}$ ,  $\text{Co}^{2+}$ ,  $\text{Ni}^{2+}$ ,  $\text{Cr}^{3+}$ ,  $\text{V}^{5+}$ , and  $\text{Mn}^{2+}$ ,  $\text{Fe}^{3+}$  and  $\text{Ni}^{2+}$  ions doping can improve the photocatalytic activity of  $\text{TiO}_2$  effectively. In general, red shift occurs to Ni-doped  $\text{TiO}_2$  nanoparticles. Among the ions investigated, Ni-doped  $\text{TiO}_2$  nanoparticles have shown highest photoreactivity at the concentration of 0.002 at.%, about 1.9 times that of the pure  $\text{TiO}_2$ . Ion doping is shown to reduce the diameter and influence the fraction of anatase.

Data also indicates that the combination of anatase diameter and ion radius might play an important role in the photoreactivity of  $\text{TiO}_2$  nanoparticles. Apart from the transition metal ions shown above, the noble metal nanoparticles such as silver can also improve the photocatalytic activity of  $\text{TiO}_2$  [73].

Coupling  $\text{TiO}_2$  films with other semiconductors is considered as a good way because coupling two semiconductors with different redox energy levels can increase the charge separation for their corresponding conduction and valence bands [74, 75].  $\text{WO}_3$  is an appropriate material to couple with  $\text{TiO}_2$  because  $\text{WO}_3$  has a suitable conduction band potential to allow the transfer of photogenerated electrons from  $\text{TiO}_2$  facilitating effective charge separation [76]. However, coupled  $\text{WO}_3$  did not shift the optical absorption to the visible region. The improvement of photocatalytic activity is attributed to the increased surface acidity, better separation between photoinduced carriers, and higher content of anatase [77].  $\text{BiOI}$  is an attractive p-type semiconductor with a narrow bandgap of 1.94 eV, which is introduced to prepare p-n junction  $\text{BiOI/TiO}_2$  nanotube arrays. After being coated with  $\text{BiOI}$ , the space between individual nanotube of  $\text{TiO}_2$  has been filled and the wall thickness of  $\text{TiO}_2$  nanotubes increases by ca. 8 nm (Figure 6). Meanwhile, the Fermi level

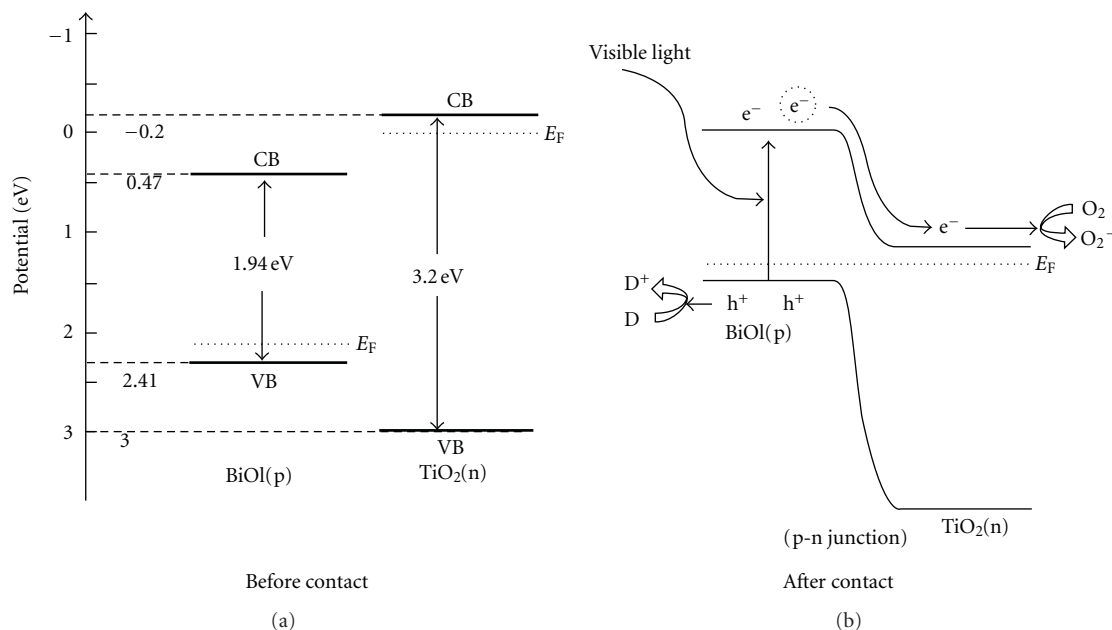


FIGURE 7: Schematic diagrams for (a) energy bands of p-BiOI and *n*-TiO<sub>2</sub> before contact and (b) the formation of a p-n junction and its energy band diagram at equilibrium and transfer of photoinduced electrons from p-BiOI to *n*-TiO<sub>2</sub> under visible-light irradiation [56].

of BiOI is moved up, while the Fermi level of TiO<sub>2</sub> is moved down until an equilibrium state is formed (Figure 7). Thus, the photogenerated electron-hole pairs will be separated effectively by the p-n junction formed in the p-BiOI/*n*-TiO<sub>2</sub> interface, and the recombination of electron-hole pairs can be reduced. So the p-n junction BiOI/TiO<sub>2</sub> nanotube arrays can display much greater photoelectrocatalytic activity under visible-light irradiation [56]. We prepared TiO<sub>2</sub>/SiO<sub>2</sub> composite nanotube photocatalysts by the anodic aluminum oxide (AAO) liquid-phase deposition method [78]. The Ti-O-Si bonds are formed on the surface and the surface hydroxyl concentration is increased, resulting in enhanced photocatalytic activity, being about 20% higher than pure TiO<sub>2</sub> films. Moreover, the TiO<sub>2</sub>/SiO<sub>2</sub> composite exhibits a wider conduction band which would effectively prohibit recombination of photogenerated electrons and holes.

## 6. Conclusions

This paper reviews a serial study of TiO<sub>2</sub> nanotube films prepared by liquid-phase deposition based on the template-based growth. The formation mechanisms of anodic alumina template and TiO<sub>2</sub> nanotube film have been discussed. The morphology of TiO<sub>2</sub> is affected by the morphology of anodic alumina. High anodizing voltage and phosphoric acid are favorable for the formation of large pore alumina template. The volume of alumina in the template affects the morphology of TiO<sub>2</sub> nanotube films. Using the template with a certain volume fraction of Al<sub>2</sub>O<sub>3</sub> (less than 0.71), the ordered aligned titania nanotubes can be obtained. Proper concentration of deposition solution (0.1 mol/L (NH<sub>4</sub>)<sub>2</sub>TiF<sub>6</sub>) and proper calcinations temperature (400°C) are favorable for the production of TiO<sub>2</sub> nanotube films.

Doping of metal and nonmetal elements can improve the photocatalytic activity.

## Acknowledgments

This work is financially supported by Beijing Municipal Commission of Education Key Foundation (KZ201010005-0001); Beijing Innovation Talent Project (PHR201006101); Beijing New Century Hundred, Thousand and Ten Thousand Talent Project, State key Laboratory of Electronic Thin Films and Integrated Devices (UESTC: KFJJ201001) and Guangxi Natural Science Foundation (2010GXNSFB013-009).

## References

- [1] N. M. Mahmoodi and M. Arami, "Degradation and toxicity reduction of textile wastewater using immobilized titania nanophotocatalysis," *Journal of Photochemistry and Photobiology B*, vol. 94, no. 1, pp. 20–24, 2009.
- [2] F. Sayilkan, S. Erdemoğlu, M. Asiltürk et al., "Photocatalytic performance of pure anatase nanocrystallite TiO<sub>2</sub> synthesized under low temperature hydrothermal conditions," *Materials Research Bulletin*, vol. 41, no. 12, pp. 2276–2285, 2006.
- [3] A. Fujishima and K. Honda, "Electrochemical photolysis of water at a semiconductor electrode," *Nature*, vol. 238, no. 5358, pp. 37–38, 1972.
- [4] J. G. Yu, H. G. Yu, B. Cheng, and C. Trapalis, "Effects of calcination temperature on the microstructures and photocatalytic activity of titanate nanotubes," *Journal of Molecular Catalysis A*, vol. 249, no. 1-2, pp. 135–142, 2006.
- [5] J. G. Yu, G. H. Wang, B. Cheng, and M. H. Zhou, "Effects of hydrothermal temperature and time on the photocatalytic activity and microstructures of bimodal mesoporous TiO<sub>2</sub>

- powders," *Applied Catalysis B*, vol. 69, no. 3-4, pp. 171-180, 2007.
- [6] J. A. Byrne, P. A. Fernandez-Ibanez, P. S. M. Dunlop, D. M. A. Alrousan, and J. W. J. Hamilton, "Photocatalytic enhancement for solar disinfection of water: a review," *International Journal of Photoenergy*, vol. 2011, Article ID 798051, 12 pages, 2011.
- [7] C. C. Chang and W. C. Chen, "High-refractive-index thin films prepared from aminoalkoxysilane-capped pyromellitic dianhydride-titania hybrid materials," *Journal of Polymer Science A*, vol. 39, no. 19, pp. 3419-3427, 2001.
- [8] S. K. Hazra and S. Basu, "High sensitivity and fast response hydrogen sensors based on electrochemically etched porous titania thin films," *Sensors and Actuators B*, vol. 115, no. 1, pp. 403-411, 2006.
- [9] S. Q. Fan, C. J. Li, G. J. Yang, L. Z. Zhang, J. C. Gao, and Y. X. Xi, "Fabrication of nano-TiO<sub>2</sub> coating for dye-sensitized solar cell by vacuum cold spraying at room temperature," *Journal of Thermal Spray Technology*, vol. 16, no. 5-6, pp. 893-897, 2007.
- [10] V. E. Nawin, S. Noriaki, C. Tawatchai, K. Takeyuki, and T. Wiwut, "A step towards length control of titanate nanotubes using hydrothermal reaction with sonication pretreatment," *Nanotechnology*, vol. 19, no. 3, pp. 1-6, 2008.
- [11] R. R. Djenadic, L. M. Nikolic, K. P. Giannakopoulos, B. Stojanovic, and V. V. Srdic, "One-dimensional titanate nanostructures: synthesis and characterization," *Journal of the European Ceramic Society*, vol. 27, no. 13-15, pp. 4339-4343, 2007.
- [12] C. K. Lee, C. C. Wang, M. D. Lyu, L. C. Juang, S. S. Liu, and S. H. Hung, "Effects of sodium content and calcination temperature on the morphology, structure and photocatalytic activity of nanotubular titanates," *Journal of Colloid and Interface Science*, vol. 316, no. 2, pp. 562-569, 2007.
- [13] J. H. Zhang, X. Xiao, and J. M. Nan, "Hydrothermal-hydrolysis synthesis and photocatalytic properties of nano-TiO<sub>2</sub> with an adjustable crystalline structure," *Journal of Hazardous Materials*, vol. 176, no. 1-3, pp. 617-622, 2010.
- [14] M. C. Neves, J. M. F. Nogueira, T. Trindade, M. H. Mendonça, M. I. Pereira, and O. C. Monteiro, "Photosensitization of TiO<sub>2</sub> by Ag<sub>2</sub>S and its catalytic activity on phenol photodegradation," *Journal of Photochemistry and Photobiology A*, vol. 204, no. 2-3, pp. 168-173, 2009.
- [15] Y. C. Yu, Y. X. Ding, S. L. Zuo, and J. J. Liu, "Photocatalytic activity of nanosized cadmium sulfides synthesized by complex compound thermolysis," *International Journal of Photoenergy*, vol. 2011, Article ID 762929, 5 pages, 2011.
- [16] R. Azimirad, P. K. Hosravi, A. Z. Moshfegh et al., "Synthesis of W(17)O(47) nanothick plates with preferred orientation and their photocatalytic activity," *Surface and Interface Analysis*, vol. 43, no. 11, pp. 1397-1402, 2011.
- [17] J. S. Wang, S. Yin, and T. Sato, "Synthesis and characterization of fibrous SrTiO<sub>3</sub> particles," *Materials Science and Engineering B*, vol. 131, no. 1-3, pp. 248-251, 2006.
- [18] L. L. Costa and A. G. S. Prado, "TiO<sub>2</sub> nanotubes as recyclable catalyst for efficient photocatalytic degradation of indigo carmine dye," *Journal of Photochemistry and Photobiology A*, vol. 201, no. 1, pp. 45-49, 2009.
- [19] M. H. Seo, M. Yuasa, T. Kida, J. S. Huh, K. Shimano, and N. Yamazoe, "Gas sensing characteristics and porosity control of nanostructured films composed of TiO<sub>2</sub> nanotubes," *Sensors and Actuators B*, vol. 137, no. 2, pp. 513-520, 2009.
- [20] F. M. Wang, Z. S. Shi, F. Gong, J. T. Jiu, and M. Adachi, "Morphology control of anatase TiO<sub>2</sub> by surfactant-assisted hydrothermal method\*\* supported by the natural science foundation of tianjin (No.06YFJMJC05000)," *Chinese Journal of Chemical Engineering*, vol. 15, no. 5, pp. 754-759, 2007.
- [21] C. Colmenares, R. Luque, J. M. Campelo, F. Colmenares, Z. Karpiński, and A. A. Romero, "Nanostructured photocatalysts and their applications in the photocatalytic transformation of lignocellulosic biomass: an overview," *Materials*, vol. 2, no. 4, pp. 2228-2258, 2009.
- [22] Y. P. Guo, N. H. Lee, H. J. Oh et al., "Preparation of titanate nanotube thin film using hydrothermal method," *Thin Solid Films*, vol. 516, no. 23, pp. 8363-8371, 2008.
- [23] D. L. Morgan, H. Y. Zhu, R. L. Forst, and E. R. Waclawik, "Determination of a morphological phase diagram of titania/titanate nanostructures from alkaline hydrothermal treatment of Degussa P25," *Chemistry of Materials*, vol. 20, no. 12, pp. 3800-3802, 2008.
- [24] N. H. Lee, H. J. Oh, S. C. Jung, W. J. Lee, D. H. Kim, and S. J. Kim, "Photocatalytic properties of nanotubular-shaped TiO<sub>2</sub> powders with anatase phase obtained from titanate nanotube powder through various thermal treatments," *International Journal of Photoenergy*, vol. 2011, Article ID 327821, 7 pages, 2011.
- [25] G. Che, B. B. Lakshmi, E. R. Fisher, and C. R. Martin, "Carbon nanotubule membranes for electrochemical energy storage and production," *Nature*, vol. 393, no. 6683, pp. 346-349, 1998.
- [26] H. Masuda, K. Nishio, and N. Baba, "Fabrication of porous TiO<sub>2</sub> films using two-step replication of microstructure of anodic alumina," *Japanese Journal of Applied Physics*, vol. 31, no. 12, part 1, pp. L1775-L1777, 1992.
- [27] B. B. Lakshmi, C. J. Patrissi, and C. R. Martin, "Sol-Gel Template Synthesis of Semiconductor Oxide Micro- and Nanostructures," *Chemistry of Materials*, vol. 9, no. 11, pp. 2544-2550, 1997.
- [28] J. P. Tu, L. P. Zhu, K. Hou, and S. Y. Guo, "Synthesis and frictional properties of array film of amorphous carbon nanofibers on anodic aluminum oxide," *Carbon*, vol. 41, no. 6, pp. 1257-1263, 2003.
- [29] Y. Yang, Z. Hu, Q. Wu, Y. N. Lü, X. Z. Wang, and Y. Chen, "Template-confined growth and structural characterization of amorphous carbon nanotubes," *Chemical Physics Letters*, vol. 373, no. 5-6, pp. 580-585, 2003.
- [30] S. Z. Chu, K. Wada, S. Inoue, and S. Todoroki, "Fabrication of oxide nanostructures on glass by aluminum anodization and sol-gel process," *Surface and Coatings Technology*, vol. 169-170, no. 2, pp. 190-194, 2003.
- [31] H. Imai, Y. Takei, K. Shimizu, M. Matsuda, and H. Hirashima, "Direct preparation of anatase TiO<sub>2</sub> nanotubes in porous alumina membranes," *Journal of Materials Chemistry*, vol. 9, no. 12, pp. 2971-2972, 1999.
- [32] H. Masuda and K. Fukuda, "Ordered metal nanohole arrays made by a two-step replication of honeycomb structures of anodic alumina," *Science*, vol. 268, no. 5216, pp. 1466-1468, 1995.
- [33] H. Masuda and M. Satoh, "Fabrication of gold nanodot array using anodic porous alumina as an evaporation mask," *Japanese Journal of Applied Physics*, vol. 35, no. 1, pp. L126-L129, 1996.
- [34] A. P. Li, F. Muller, A. Birner, K. Nielsch, and U. Gösele, "Polycrystalline nanopore arrays with hexagonal ordering on aluminum," *Journal of Vacuum Science and Technology A*, vol. 17, no. 4, pp. 1428-1431, 1999.
- [35] H. Asoh, K. Nishio, M. Nakao, A. Yokoo, T. Tamamura, and H. Masuda, "Fabrication of ideally ordered anodic porous

- alumina with 63 nm hole periodicity using sulfuric acid," *Journal of Vacuum Science and Technology B*, vol. 19, no. 2, pp. 569–572, 2001.
- [36] P. P. Mardilovich, A. N. Govyadinov, N. I. Mukhurov, A. M. Rzhvskii, and R. Paterson, "New and modified anodic alumina membranes. Part I. Thermotreatment of anodic alumina membranes," *Journal of Membrane Science*, vol. 98, no. 1-2, pp. 131–142, 1995.
- [37] T. Xu, G. Zangari, and R. M. Metzger, "Periodic holes with 10 nm diameter produced by grazing Ar<sup>+</sup> milling of the barrier layer in hexagonally ordered nanoporous alumina," *Nano Letters*, vol. 2, no. 1, pp. 37–41, 2002.
- [38] T. Kyotani, L. Tsai, A. Tomita et al., "Preparation of ultrafine carbon tubes in nanochannels of an anodic aluminum oxide film," *Chemistry of Materials*, vol. 8, no. 8, pp. 2109–2113, 1996.
- [39] G. Che, B. B. Lakshmi, C. R. Martin, E. R. Fisher, and R. S. Ruoff, "Chemical vapor deposition based synthesis of carbon nanotubes and nanofibers using a template method," *Chemistry of Materials*, vol. 10, no. 1, pp. 260–267, 1998.
- [40] J. Li, C. Papadopoulos, J. M. Xu, and M. Moskovits, "Highly-ordered carbon nanotube arrays for electronics applications," *Applied Physics Letters*, vol. 75, no. 3, pp. 367–369, 1999.
- [41] K. B. Shelimov and M. Moskovits, "Composite nanostructures based on template-grown boron nitride nanotubules," *Chemistry of Materials*, vol. 12, no. 1, pp. 250–254, 2000.
- [42] G. Sauer, G. Brehm, S. Schneider et al., "Highly ordered monocrystalline silver nanowire arrays," *Journal of Applied Physics*, vol. 91, no. 5, pp. 3243–3247, 2002.
- [43] Y. Kanamori, K. Hane, H. Sai, and H. Yugami, "100 nm period silicon antireflection structures fabricated using a porous alumina membrane mask," *Applied Physics Letters*, vol. 78, no. 2, pp. 142–143, 2001.
- [44] S. Shingubara, O. Okino, Y. Murakami, H. Sakaue, and T. Takahagi, "Fabrication of nanohole array on Si using self-organized porous alumina mask," *Journal of Vacuum Science and Technology B*, vol. 19, no. 5, pp. 1901–1904, 2001.
- [45] D. Crouse, Y. H. Lo, A. E. Miller, and M. Crouse, "Self-ordered pore structure of anodized aluminum on silicon and pattern transfer," *Applied Physics Letters*, vol. 76, no. 1, pp. 49–51, 2000.
- [46] J. Y. Liang, H. Chik, A. J. Yin, and J. Xu, "Two-dimensional lateral superlattices of nanostructures: nonlithographic formation by anodic membrane template," *Journal of Applied Physics*, vol. 91, no. 4, p. 2544, 2002.
- [47] M. K. Li, C. W. Wang, and H. L. Li, "Synthesis of ordered Si nanowire arrays in porous anodic aluminum oxide templates," *Chinese Science Bulletin*, vol. 46, no. 21, pp. 1793–1796, 2001.
- [48] S. Yamanaka, T. Hamaguchi, H. Muta, K. Kurosaki, and M. Uno, "Fabrication of oxide nanohole arrays by a liquid phase deposition method," *Journal of Alloys and Compounds*, vol. 373, no. 1-2, pp. 312–315, 2004.
- [49] W. F. Jiang, Y. H. Ling, X. D. Bai, H. Y. Li, and D. Q. Cang, "In-situ template synthesis of TiO<sub>2</sub> array films on Al substrates," *Rare Metal Materials and Engineering*, vol. 36, no. 7, pp. 1178–1180, 2007.
- [50] Y. C. Zhao, M. Chen, T. Xu, W. M. Liu, and X. Liu, "Preparation of porous anodic oxide film on aluminum and its application in synthesis of 1-dimensional nanomaterials," *Chinese Journal of Chemical Physics*, vol. 17, no. 4, pp. 369–374, 2004.
- [51] Z. Y. Liu, J. X. Chen, D. Z. Zhangm, and G. Q. Sun, "Investigation on nanostructural porous alumina with two dimension ordered arrangements," *Journal of Sichuan University*, vol. 38, no. 3, p. 374, 2001.
- [52] Y. T. Cui, J. S. Wang, H. Y. Li, and Z. Z. Wang, "Study on synthesis in situ and photocatalytic activity of TiO<sub>2</sub> nanotubes array films," *Journal of Inorganic Materials*, vol. 23, no. 6, pp. 1259–1262, 2008.
- [53] J. Zhang, J. E. Kielbasa, and D. L. Carroll, "Controllable fabrication of porous alumina templates for nanostructures synthesis," *Materials Chemistry and Physics*, vol. 122, no. 1, pp. 295–300, 2010.
- [54] Y. T. Cui, J. S. Wang, H. Y. Li, and Z. Z. Wang, "Effects of AAO template on the surface microstructure of TiO<sub>2</sub> nanoarray films fabricated by liquid phase deposition," *Chinese Journal of Inorganic Chemistry*, vol. 25, no. 7, pp. 1274–1278, 2009.
- [55] J. G. Yu, G. P. Dai, and B. Cheng, "Effect of crystallization methods on morphology and photocatalytic activity of anodized TiO<sub>2</sub> nanotube array films," *Journal of Physical Chemistry C*, vol. 114, no. 45, pp. 19378–19385, 2010.
- [56] G. P. Dai, J. G. Yu, and G. Liu, "Synthesis and enhanced visible-light photoelectrocatalytic activity of p-n junction BiOI/TiO<sub>2</sub> nanotube arrays," *The Journal of Physical Chemistry C*, vol. 115, no. 15, pp. 7339–7346, 2011.
- [57] L. Zhao, J. R. Ran, Z. Shu, G. T. Dai, P. C. Zhai, and S. M. Wang, "Effects of calcination temperatures on photocatalytic activity of ordered titanate nanoribbon/SnO<sub>2</sub> films fabricated during an EPD process," *International Journal of Photoenergy*, vol. 2012, Article ID 472958, 7 pages, 2012.
- [58] W. F. Jiang, D. Q. Cang, S. J. Hao, Y. H. Ling, X. D. Bai, and Y. B. Zong, "Fabrication of TiO<sub>2</sub> nanorod array film on Al plate by liquid phase deposition method," *Materials Science and Engineering*, vol. 24, no. 6, pp. 805–807, 2006.
- [59] J. G. Yu, H. G. Yu, B. Cheng, X. J. Zhao, J. C. Yu, and W. K. Ho, "The effect of calcination temperature on the surface microstructure and photocatalytic activity of TiO<sub>2</sub> thin films prepared by liquid phase deposition," *Journal of Physical Chemistry B*, vol. 107, no. 50, pp. 13871–13879, 2003.
- [60] J. G. Yu and B. Wang, "Effect of calcination temperature on morphology and photoelectrochemical properties of anodized titanium dioxide nanotube arrays," *Applied Catalysis B*, vol. 94, no. 3-4, pp. 295–302, 2010.
- [61] P. F. Xing, J. S. Wang, J. X. Jin, Z. Q. Zhang, and Z. H. Wang, "Preparation of S-N Co-doped TiO<sub>2</sub> visible light photocatalysts by mechan-chemical method and its photocatalytic activity," *Journal of Nanoscience and Nanotechnology*, vol. 4, no. 2, pp. 29–33, 2007.
- [62] L. Sun, J. Li, C. L. Wang et al., "Ultrasound aided photochemical synthesis of Ag loaded TiO<sub>2</sub> nanotube arrays to enhance photocatalytic activity," *Journal of Hazardous Materials*, vol. 171, no. 1–3, pp. 1045–1050, 2009.
- [63] Y. Okour, H. K. Shon, I. J. El Saliby, R. Naidu, J. B. Kim, and J. H. Kim, "Preparation and characterization of titanium dioxide (TiO<sub>2</sub>) and thiourea-doped titanate nanotubes prepared from wastewater flocculated sludge," *Bioresource Technology*, vol. 101, no. 5, pp. 1453–1458, 2009.
- [64] J. J. Xu, Y. H. Ao, M. D. Chen, and D. G. Fu, "Low-temperature preparation of Boron-doped titania by hydrothermal method and its photocatalytic activity," *Journal of Alloys and Compounds*, vol. 484, no. 1-2, pp. 73–79, 2009.
- [65] G. F. Shang, H. B. Fu, S. G. Yang, and T. G. Xu, "Mechanistic study of visible-light-induced photodegradation of 4-chlorophenol by TiO<sub>2-x</sub>N<sub>x</sub> ((0.021 < x < 0.049)) with Low Nitrogen Concentration," *International Journal of Photoenergy*, vol. 2012, Article ID 759306, 9 pages, 2012.

- [66] R. Asahi, T. Morikawa, T. Ohwaki, K. Aoki, and Y. Taga, "Visible-light photocatalysis in nitrogen-doped titanium oxides," *Science*, vol. 293, no. 5528, pp. 269–271, 2001.
- [67] A. Y. Bai, W. Liang, G. L. Zheng, and X. G. Zhao, "Photocatalytic properties under visible light of S and N Co-doped titanium oxide films," *Journal of Taiyuan University of Technology*, vol. 42, no. 1, pp. 74–77, 2011.
- [68] H. M. Zhao, Y. Chen, X. Quan, and X. L. Ruan, "Preparation of Zn-doped TiO<sub>2</sub> nanotubes electrode and its application in pentachlorophenol photoelectrocatalytic degradation," *Chinese Science Bulletin*, vol. 52, no. 11, pp. 1456–1461, 2007.
- [69] J. Li, H. Yun, and C. J. Lin, "The Fe-doped TiO<sub>2</sub> nanotube arrays as a photoanode for cathodic protection of stainless steel," *Acta Physico*, vol. 23, no. 12, pp. 1886–1892, 2007.
- [70] Z. H. Xu and J. G. Yu, "Visible-light-induced photoelectrochemical behaviors of Fe-modified TiO<sub>2</sub> nanotube arrays," *Nanoscale*, vol. 3, no. 8, pp. 3138–3144, 2011.
- [71] T. H. Wang, Y. X. Li, S. Q. Peng, G. X. Lü, and S. B. Li, "Activity of rare earth doped TiO<sub>2</sub> deposited with Pt for photocatalytic hydrogen generation," *Acta Chimica Sinica*, vol. 63, no. 9, pp. 797–801, 2005.
- [72] J. Chen, M. Yao, and X. Wang, "Investigation of transition metal ion doping behaviors on TiO<sub>2</sub> nanoparticles," *Journal of Nanoparticle Research*, vol. 10, no. 1, pp. 163–171, 2008.
- [73] J. G. Yu, G. P. Dai, and B. B. Huang, "Fabrication and characterization of visible-light-driven plasmonic photocatalyst Ag/AgCl/TiO<sub>2</sub> nanotube arrays," *Journal of Physical Chemistry C*, vol. 113, no. 37, pp. 16394–16401, 2009.
- [74] L. Wu, J. C. Yu, and X. Z. Fu, "Characterization and photocatalytic mechanism of nanosized CdS coupled TiO<sub>2</sub> nanocrystals under visible light irradiation," *Journal of Molecular Catalysis A*, vol. 244, no. 1-2, pp. 25–32, 2006.
- [75] D. R. Catal, "Photosensitization of TiO<sub>2</sub> by MxOy and MxSy nanoparticles for heterogeneous photocatalysis applications," *Catalysis Today*, vol. 122, no. 1-2, pp. 20–26, 2007.
- [76] K. K. Akurati, A. Vital, J. P. Dellemann et al., "Flame-made WO<sub>3</sub>/TiO<sub>2</sub> nanoparticles: relation between surface acidity, structure and photocatalytic activity," *Applied Catalysis B*, vol. 79, no. 1-2, pp. 53–62, 2008.
- [77] J. He, Q. Luo, Q. Z. Cai, X. W. Li, and D. Q. Zhang, "Microstructure and photocatalytic properties of WO<sub>3</sub>/TiO<sub>2</sub> composite films by plasma electrolytic oxidation," *Materials Chemistry and Physics*, vol. 129, no. 1-2, pp. 242–248, 2011.
- [78] Z. Z. Wang, J. S. Wang, H. Y. Li, G. S. Sun, and K. L. Huang, "Fabrication and photocatalytic activity of TiO<sub>2</sub>/SiO<sub>2</sub> composite nanotubes," *Chemical Intermediate*, vol. 37, no. 2, pp. 541–549, 2011.

## Research Article

# Anodization Parameters Influencing the Growth of Titania Nanotubes and Their Photoelectrochemical Response

Ying-Chin Lim,<sup>1</sup> Zulkarnain Zainal,<sup>1,2</sup> Wee-Tee Tan,<sup>3</sup> and Mohd Zobir Hussein<sup>1,2</sup>

<sup>1</sup> Centre of Excellence for Catalysis Science and Technology and Department of Chemistry, Faculty of Science, Universiti Putra Malaysia, Selangor Darul Ehsan, 43400 Serdang, Malaysia

<sup>2</sup> Advanced Materials and Nanotechnology Laboratory, Institute of Advanced Technology (ITMA), Universiti Putra Malaysia, Selangor Darul Ehsan, 43400 Serdang, Malaysia

<sup>3</sup> Department of Chemistry, Faculty of Science, Universiti Putra Malaysia, Selangor Darul Ehsan, 43400 Serdang, Malaysia

Correspondence should be addressed to Zulkarnain Zainal, zulkar@science.upm.edu.my

Received 14 September 2011; Revised 19 November 2011; Accepted 19 November 2011

Academic Editor: Jianguo Yu

Copyright © 2012 Ying-Chin Lim et al. This is an open access article distributed under the Creative Commons Attribution License, which permits unrestricted use, distribution, and reproduction in any medium, provided the original work is properly cited.

TiO<sub>2</sub> nanotubes (TNTs) were fabricated by electrochemical oxidation of Ti foil in a standard two-electrode cell-containing NH<sub>4</sub>F. The effects of bath temperature, voltage ramp prior to constant voltage held during anodization and present of complexing agent on the crystalline phase, nanotube growth, and dimensional change of TNT were investigated using XRD and FESEM. The results show that tube length decreases with bath temperature attributed to faster chemical dissolution rate at high temperature. However, nanotubes growth rate was enhanced by ~260% with the addition of EDTA as the complexing agent. Meanwhile, the nanotubes diameter was found to be proportionally dependent on bath temperature but independent of the voltage ramp and addition of EDTA. Photoelectrochemical response under illumination was enhanced by using the calcined TNT and is strongly affected by its dimensional changes. Thus, desired properties of TNT can be obtained by tuning the electrochemical condition for a wide-range application.

## 1. Introduction

Over the past decades, titania has gained much attention compared to other oxide semiconductor due to its remarkable properties including strong oxidizing power, non-toxicity, chemical and biological inertness, and long-term photostability. Thus, it has found enormous application in photocatalysis [1–9], photoelectrochemical water splitting [10, 11], self-cleaning application [12], sensing [13, 14], and photovoltaic cells [15, 16]. In addition, high level biocompatibility nature of titania facilitates its application in biomedical field where TiO<sub>2</sub> layers on Ti or Ti alloys are in direct contact with biological tissue in dental implants and orthopedic applications [17, 18]. Compared with conventional TiO<sub>2</sub> nanoparticles, TiO<sub>2</sub> nanotubes (TNTs) offer some peculiar advantages such as high specific surface area resulting from the hollow channel structure, high mechanical stability, and unique nanoarchitecture with fewer interfacial grain boundaries, which promote charge transport and enhanced electron-hole separation [16].

Thus, considerable studies have been focused on fabricating TNT including sol-gel [19], hydrothermal processes [20, 21], template-assisted synthesis [22], seeded growth [23], and electrochemical anodization [24]. Among the synthetic methodology, electrochemical anodization of Ti in electrolytes containing fluoride provides a relatively simple and effective way of synthesizing nanotubular or porous structures. The synthesized nanotubes are highly ordered, well-defined with high aspect ratios, and are vertically oriented to the substrate. Most importantly, the dimensions of nanotubes could be controlled precisely and modified easily by choosing the suitable electrochemical conditions. Zwilling et al. [25] in 1999 were the first to report on successful anodization of Ti and its alloy (Ti-6Al-4V) which was carried out in chromic acid with and without the addition of hydrofluoric acid. In 2001, Grimes and coworkers [26] have successfully synthesized well-aligned and highly ordered TNT through potentiostatic anodization of Ti in aqueous electrolyte containing hydrofluoric acid. Following this work, TNT with various diameters (22–600 nm), tube

lengths (0.2–1000  $\mu\text{m}$ ), and wall thicknesses (7–34 nm) has been obtained by controlling the electrochemical conditions. Nanoarchitecturing processes of this material and its unique properties could be obtained from a variety of reports in the literature [27–33], thus making it of considerable interest in scientific community and practical importance.

To date, the mechanistic model for nanotubes formation is believed to be the formation of pits by  $\text{F}^-$  which later develops into pores and transform into cylindrical nanotubular structures. Also, the nanotubes growth inward the Ti occurs at the bottom of nanotubes (tube tip) followed by oxidation at that region. Both the oxidation and dissolution rate of the tube tip are affected by several anodization conditions including bath temperature, electric field across the oxide layer, and the amount of  $\text{F}^-$  present. However, few studies have been carried out to study the effect of this important anodization conditions (e.g., bath temperature) on the morphology, nanotube growth, and photoelectrochemical properties of TNT [34, 35].

In this work, we accomplished the systematic study of the anodization conditions by expanding our investigation on the effect of bath temperature, voltage sweeping rate and addition of complexing agent on the formation and growth of TNT using previously optimized conditions [36]. Even though Banerjee et al. [37] has investigated the use of complexing agent on the growth of TNT, however, organic electrolyte with  $\text{pH} \approx 6.4$  was being used in their work. To the best of our knowledge, this is the first report on the effect of complexing agent in aqueous electrolyte on the dimensional change of the TNT. As the photo-induced processes are strongly dependent on the morphology, microstructures, and anodization conditions, study on the photoelectrochemical properties of TNT synthesized under different experimental conditions was investigated and discussed.

## 2. Experimental

**2.1. Preparation of  $\text{TiO}_2$  Nanotubes.** Sheets of Ti foil (0.127 mm, 99.7%, Sigma Aldrich) were first cut into small rectangular size of 10 mm  $\times$  25 mm. Prior to anodization, they were degreased by sonicating in acetone, isopropanol, and deionized (DI) water, followed by chemically etched in 6 M  $\text{HNO}_3$  for 10 minutes. Then, they were rinsed with excess DI water and dried in air. Electrochemical anodization of Ti was carried out in a homemade designed two-electrode cell with clean Ti foil as the working electrode and a high density graphite electrode as the counter electrode. All anodization experiments were conducted at room temperature ( $\sim 27^\circ\text{C}$  except when studying the effect of bath temperature) in 0.15 M  $\text{NH}_4\text{F}$  adjusted to pH 4 using  $\text{H}_2\text{SO}_4$ . Anodization was carried out by applying a constant voltage with no ramp (except when studying the effect of voltage ramp) using a DC power supply (Consort Mini, Cleaver Scientific Ltd). To investigate the effect of EDTA in the formation of TNT, 0.2 M ( $\text{Na}_2[\text{H}_2\text{EDTA}]$ ) and  $\text{NH}_4\text{F}$  were mixed together at pH 4.5. The resultant TNT is hereinafter designated as TNT/EDTA. To facilitate comparison, another TNT sample was also synthesized without the addition of

EDTA under similar experimental condition (pH 4.5). From our previous work [34], it is known that anodization of less than 10 V resulted in ring-like structure while highly-ordered and well-defined nanotubes were obtained at a voltage of 10 V and above. Employing higher voltage yielded a nanoporous at 30 V and nodule-like structure at 40 V. Hence, in this study, applied voltage was limited to 20 V to synthesize all the TNT films. The anodized samples were immediately rinsed with deionized water and subsequently dried in air. Calcination of films was carried out in a Thermolyne 21100 furnace at  $500^\circ\text{C}$  in open air atmosphere with a heating rate of  $2^\circ\text{C}/\text{min}$  for 2 h.

**2.2. Characterization of As-Anodized and Calcined  $\text{TiO}_2$  Nanotubes.** The crystallinity of the as-anodized and calcined TNT films was determined by X-ray diffraction (XRD@Shimadzu D6000) using a diffractometer with  $\text{Cu K}\alpha$  radiation ( $\lambda = 1.5406 \text{ \AA}$ ). The surface morphology of the films was acquired by a field-emission scanning electron microscope, FESEM (Zeiss SUPRA 40 VP, Germany) operating at electron beam voltage of 5 kV. Quantitative measurements of the geometrical features of TNT were done using image analysis software; Image J. About 100 measurements of tube diameter and wall thickness were taken per sample from three different locations to ensure the measurements were representative. In order to obtain the thickness of the nanotube layer, direct cross-sectional micrographs were taken from mechanically bent samples. At least five measurements of the cross section were taken from different areas on each sample to ensure the measurements reflected the actual tube length. Photoelectrochemical current response measurements were performed in a conventional three-electrode cell equipped with a flat quartz window. It consisted of a synthesized TNT working electrode, a platinum wire counter electrode, and an  $\text{Ag}/\text{AgCl}$  reference electrode. The photocurrent was measured with a scanning potentiostat ( $\mu$ -III AUTOLAB) under chopped irradiation from 120 V 300 W halogen lamp during a potential sweep from +2.0 to  $-0.2$  V with a sweep rate of 20 mV/s. The TNT films were irradiated from the front side through the quartz window in a 10 ppm methyl orange solution with 0.1 M KCl as the supporting electrolyte.

## 3. Results and Discussion

**3.1. Effect of Bath Temperature.** Figure 1 depicts the XRD patterns of as-anodized (at  $35^\circ\text{C}$ ) and calcined TNT. It is obvious that TNT synthesized at  $35^\circ\text{C}$  (Figure 1(a)) exhibits amorphous structure as only diffraction peaks of Ti substrate (JCPDS no. 44-1294) are visible, which is similar to TNT fabricated at room temperature ( $\sim 27^\circ\text{C}$ ) [36]. Although Xiao et al. observed formation of crystalline TNT in dimethyl sulfoxide at electrolyte temperature of  $50$ – $60^\circ\text{C}$  [38], however, bath temperature higher than  $35^\circ\text{C}$  is not being used in our study as this lead to the formation of different surface morphology other than nanotubes as will be discussed later. Nevertheless, TNT crystallizes to form a mixture of anatase (101) at  $25.4^\circ$  (JCPDS no. 21-1272)

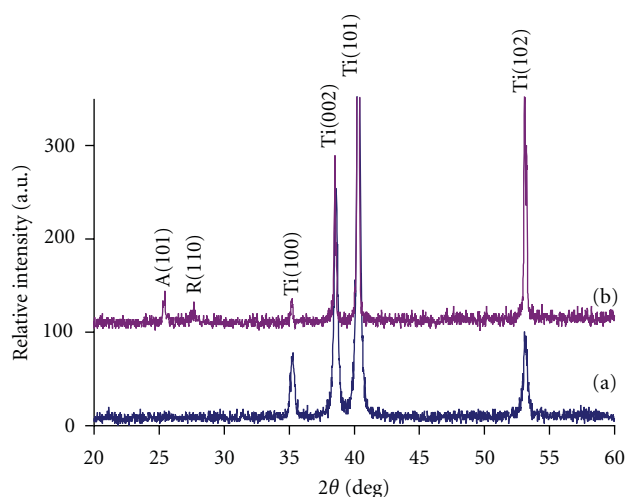


FIGURE 1: XRD patterns of (a) as-anodized TNT synthesized at 35°C and (b) calcined TNT. A, R, and Ti represent anatase, rutile, and titanium, respectively.

and rutile (110) (JCPDS no. 21-1276) phase at 27.6° after calcination at 500°C as shown in Figure 1(b).

TNT was synthesized at 20 V in five different electrolyte bath temperatures: 10, 18, 27, 35, and 40°C. Figure 2 shows the FESEM micrographs of the top morphology of TNT fabricated in different bath temperatures. It can be clearly seen that TNT fabricated at low bath temperature was covered with lots of surface debris whereas clean TNT could be obtained when much higher anodization temperature was used (18°C and above) as shown in Figures 2(a)–2(c). In addition, tube length changes by a factor of two, corresponding to a decrease in length with increasing anodization temperature from  $430 \pm 16$  nm at 10°C to  $240 \pm 13$  nm at 35°C. For tube wall thickness, only slight decrease from  $21 \pm 3$  nm to  $15 \pm 3$  nm could be observed.

For electrochemical oxidation of Ti in fluorinated electrolyte, it is well known that there are three processes, namely, field-assisted oxidation of Ti, field-assisted dissolution of Ti metal ions, and chemical etching of Ti and TiO<sub>2</sub> by fluoride ions that control the formation of TNT. As both chemical etching process and solubility of product ions are greatly affected by temperature change, with etching rates typically being exponential functions of the temperature. Therefore, at lower anodization temperature, thicker wall and longer tube obtained could be ascribed to weaker chemical dissolution at the pore bottom as well as slower oxide etching rate by fluoride ions at the tube top [39]. On the contrary, chemical dissolution by F<sup>-</sup> and dissolution of oxide layer occurs at a faster rate at higher temperature. Chemical dissolution at the tube bottom will reduce the thickness of the oxide layer, and hence field-assisted dissolution will reoccur at the tube bottom. By this process, pores will penetrate the Ti substrate resulting in longer nanotube. However, shorter tube observed at high temperature in this study might be due to that chemical dissolution rate at the tube top occurs faster than that at the tube bottom. Nevertheless, it is worth mentioning that tube diameter increases with increasing

anodization temperature being  $58 \pm 7$  nm at 10°C and  $81 \pm 11$  nm at 35°C. This observation, however, is in contrast with the finding reported by Mor et al. [39] who found no discernible change in tube diameter fabricated at different electrolyte temperatures. As reported elsewhere, change in tube diameter is generally influenced by applied voltage with larger tube diameter associated with the use of higher applied voltage [40, 41].

Larger tube diameter observed at high anodization temperature may be ascribed to increase in horizontal dissolution as the earlier formed parts of the tube wall (tube mouth) at the top are subjected to longer exposure in fluoride etching environment and thus decelerating dissolution in vertical direction [42]. As a result, tube growth at the tube bottom will be relatively slower. In contrast, the tube mouth will experience relatively faster dissolution leading to larger tube diameter.

Nanotubular structure completely disappeared (Figure 2(d)) when anodization of Ti is carried out at 40°C, suggesting a temperature limit above which nanotubular structure will diminish. It is known that soon after oxide layer is formed, dissolution occurs from many directions and, with increasing anodization temperature, velocity of F<sup>-</sup> drift also increases. This led to faster chemical dissolution of oxide layer at multiple directions before formation of nanotubular structure. Moreover, it is believed that magnetic agitation during anodization enhanced the severity of chemical dissolution which in return results in the formation of nodule-like structure observed at 40°C.

**3.2. Effect of Voltage Ramp prior to Constant Potential.** It was also noticed that the length of TNT could be controlled by voltage ramp prior to constant voltage at 20 V during anodization. By employing a voltage ramp, a desired pH gradient could be established between the tube bottom and the tube mouth. Thus this will create a preference environment conducive for the growth of longer tube [43].

Figures 3(a) and 3(b) show the polarization curves for voltage ramp rate between 10 mV/s and 350 mV/s and current transients at 20 V once the voltage ramp has ended, respectively. It is apparent from Figure 3(a) that the current density increases at the beginning of anodization, followed by a sudden drop indicating the formation of thin barrier oxide layer.

However, it is observed that the exact position for the current density rise strongly depends on the voltage ramp rate (see corresponding solid arrow in Figure 3(a)), consistent with different electric fields driving ion transport during voltage ramping [35]. Current fluctuations during voltage ramping could be observed after the initial sudden drop is ascribed to the field-assisted oxidation which increased the resistance of the oxide layer and field-assisted dissolution promoted by F<sup>-</sup> (pore formation).

Once the voltage ramp was terminated, the current becomes relatively constant as shown in Figure 3(b), indicating an equilibrium between pore growth rate at the bottom of the pores and chemical etching rate of the oxide film at the oxide/electrolyte interface is achieved leading to tube

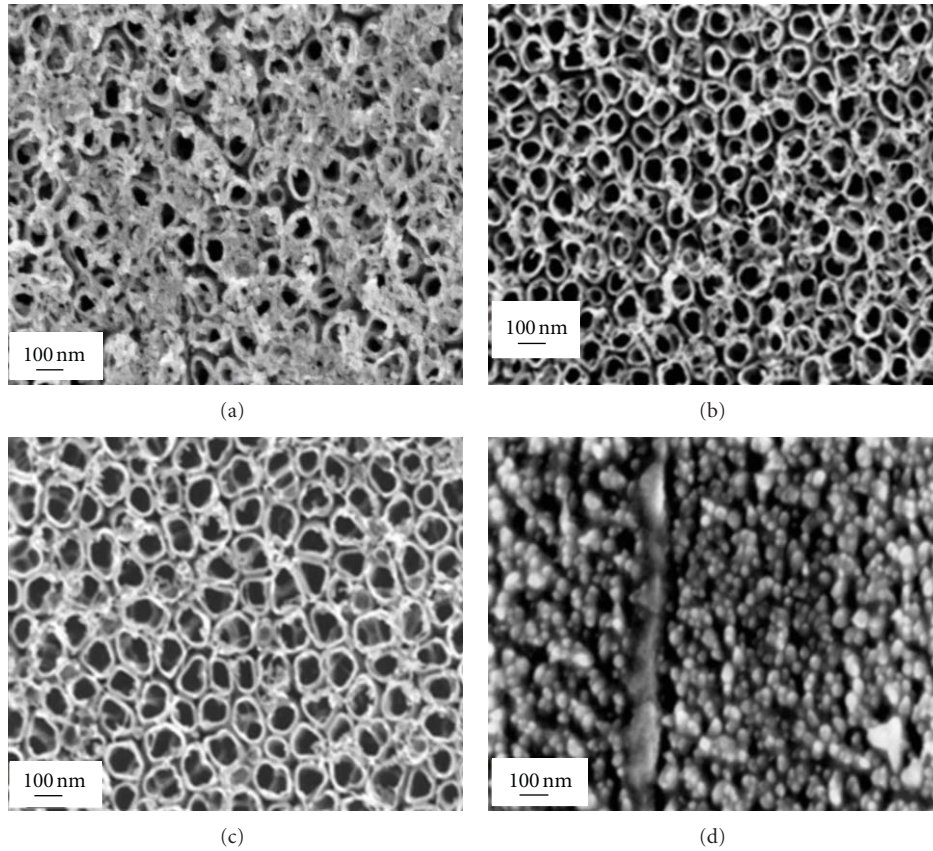


FIGURE 2: FESEM images of TNT synthesized at (a) 10°C, (b) 18°C, (c) 35°C, and (d) 40°C for 1 h.

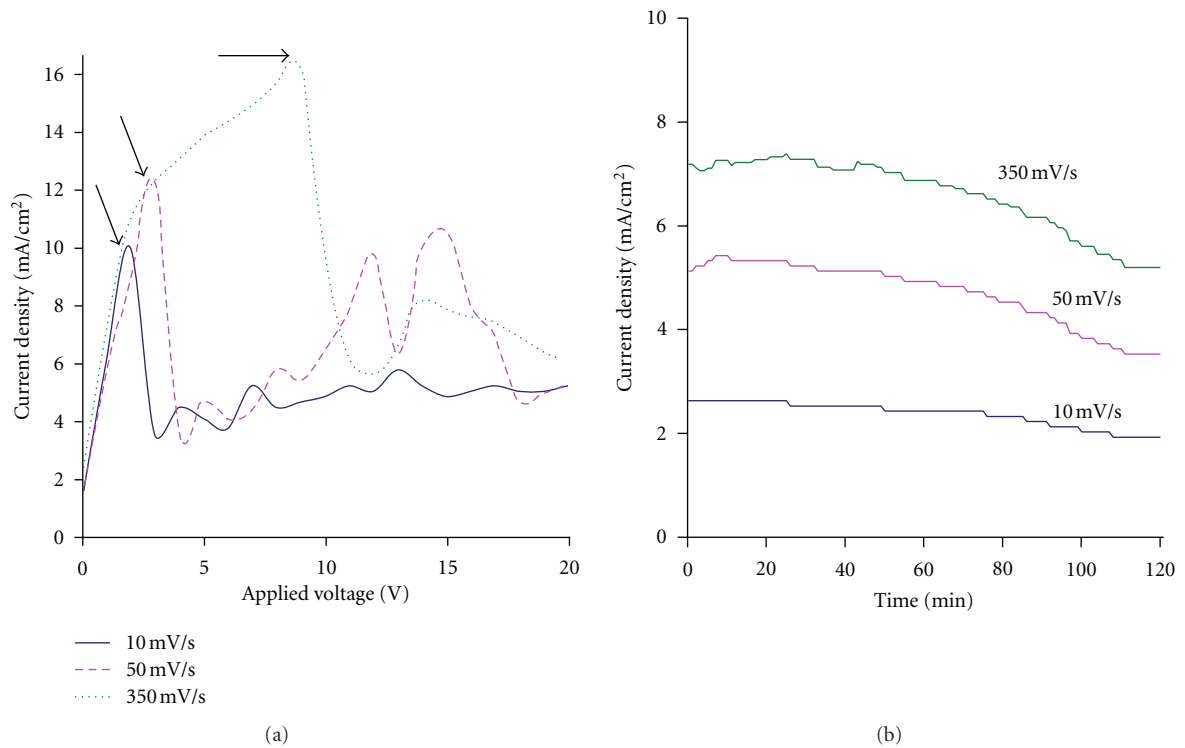


FIGURE 3: (a) Polarization curves at different voltage ramps prior to constant voltage at 20 V and (b) current transients at 20 V after the voltage ramp has completed.

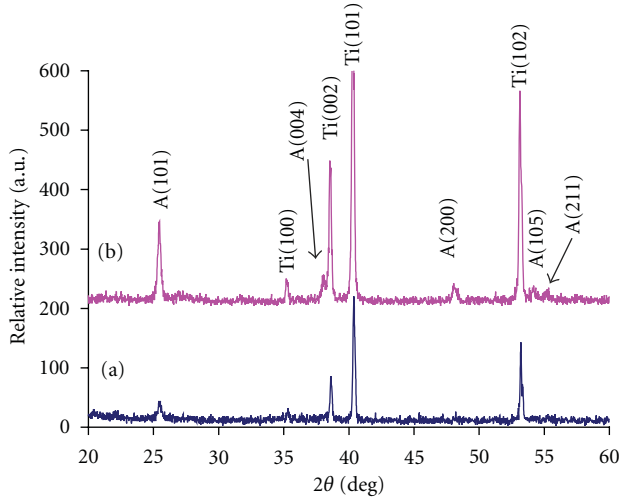


FIGURE 4: XRD patterns of (a) TNT and (b) TNT/EDTA calcined at 500°C. A and Ti represent anatase and titanium, respectively.

TABLE 1: Dimensional data of TNT produced at different voltage ramps prior to constant voltage of 20 V.

Voltage ramp (mV/s)	Tube diameter (nm)	Wall thickness (nm)	Tube length (nm)
10	67 ± 9	15 ± 3	444 ± 11
50	70 ± 8	17 ± 3	607 ± 18
350	70 ± 6	16 ± 3	388 ± 9
No ramp	75 ± 9	17 ± 4	393 ± 17

formation [44]. TNT produced without applying voltage ramp prior to constant voltage has a length of about 390 nm which is similar to that synthesized using voltage ramp of 350 mV/s as shown in Table 1. No significant structural difference was observed for TNT formed with a difference voltage ramp.

Nevertheless, it is noted that lowering the ramp to 50 mV/s did increase the tube length to about 600 nm, suggesting that pore formation occurs while the oxide layer is relatively thin. Further decreasing the ramp to 10 mV/s does not increase in the layer thickness. Therefore, employing 50 mV/s prior constant voltage could be regarded as the optimized voltage ramp as thickest oxide layers are obtained. It is also observed that the tube diameter is independent of voltage ramp, which is mainly affected by anodization voltage [34].

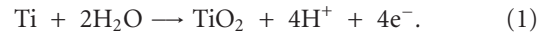
**3.3. Effect of Addition of Complexing Agent.** Figure 4 shows the XRD pattern of TNT and TNT/EDTA anodized at 20 V for 1 h in pH 4.5 electrolyte. Even though no significant difference in crystal phase was observed for both samples, however, relative intensity of anatase peak at 25.4° (101) increases for TNT/EDTA sample. In addition, TNT/EDTA sample also possessed additional anatase peaks at 38.1° (004), 48.1° (200), 54.0° (105), and 55.1° (211), respectively. Therefore, it is reasonable to infer that the tube length

(thickness of oxide layer) of the TNT/EDTA sample had increased compared to TNT sample.

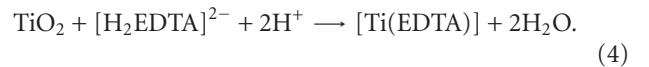
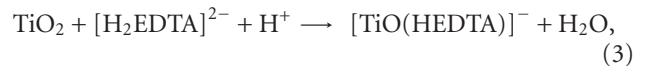
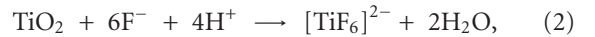
Figures 5(a) and 5(b) show the representative FESEM images of TNT and TNT/EDTA samples and it is obvious that no morphology changes for both samples. From the inset in Figure 5, highly ordered nanotubes with open mouth were formed, and the average inner diameter was measured to be 63 ± 8 nm and the outer diameter was of 92 ± 11 nm, with a wall thickness of 15 ± 4 nm. However, the cross-sectional view of TNT/EDTA (Figure 5(b)) clearly reveals that addition of EDTA has played a very vital role in increasing the tube length by 2.6 times from 300 ± 19 to 770 ± 58 nm within 1 h of anodization with a growth rate of approximately 13 nm/min.

As shown in Figure 6, an initial current drop during anodization for both TNT and TNT/EDTA samples was observed due to the formation of an oxide layer. However, two different current behaviors could be observed depending on the presence of complexing agent. In the absence of EDTA, a gradual increase in current density is observed ascribed to the thinning of the oxide layer (promoted by F<sup>-</sup>) until it reaches a steady state. At this stage, nanotube formation takes place and no thickness change exists in the barrier oxide layer. With the presence of EDTA, current density decreases smoothly after the initial current decay without a local minimum.

EDTA is widely recognized as an efficient chelating agent. In aqueous acidic electrolyte, it is believed that Ti metal oxidizes to form a thin oxide layer on the Ti metal at the solid-liquid interface under applied voltage according to.



Even though TiO<sub>2</sub> is thermodynamically stable in both acidic and alkaline medium, however, with the presence of F<sup>-</sup> and [H<sub>2</sub>EDTA]<sup>2-</sup>, substantial chemical dissolution occurs according to the following [37, 44, 45]:



Therefore, oxide layer becomes thinner with time at a faster rate.

As mentioned earlier, there are three processes control the formation of TNT, namely, field-assisted oxidation of Ti, field-assisted dissolution of Ti metal ions, and chemical dissolution of TiO<sub>2</sub>. As thickness reduces, field-assisted dissolution will reoccur and pore will penetrate inside Ti and tubes become longer [40]. Therefore, substantial dissolution in the presence of EDTA could enhance the growth rate of nanotubes as both the field-assisted and chemical etching occur at a faster rate.

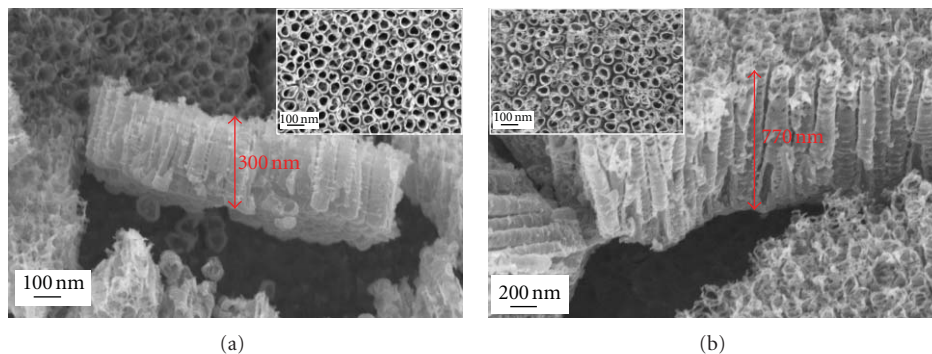


FIGURE 5: FESEM cross-sectional view images of (a) TNT and (b) TNT/EDTA; the insets show the top view images of the corresponding samples.

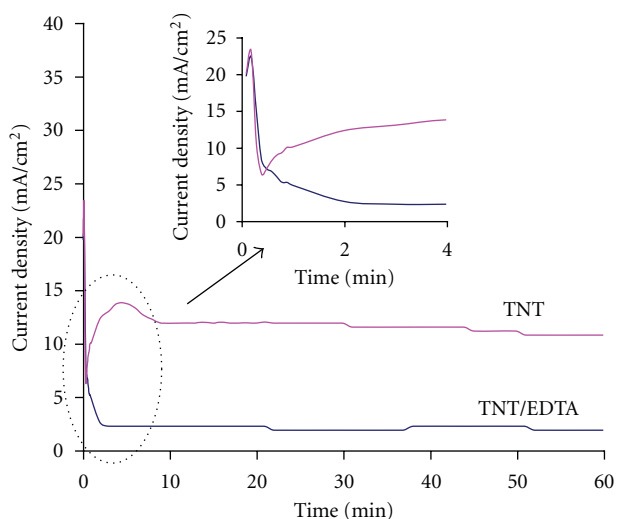


FIGURE 6: Current density transient recorded during anodization with and without the presence of complexing agent. Inset is the magnifying view of the initial anodization stage.

However, it was observed that nanotube length increases with elevating anodization duration from 30 to 60 min after which it drops to about  $690 \pm 36$  nm after 120 min of anodization. It was also found that for TNT/EDTA sample, tube diameter remained constant with increasing anodization time, indicating that anodization duration mainly influences the depth of the nanotubes. The result is in good agreement with the literature data [46].

**3.4. Photoelectrochemical Response of TNT.** In order to evaluate the effect of different dimensions and crystallization of TNT on its photoelectrochemical response, the as-anodized and calcined TNTs synthesized at different electrolyte temperatures, voltage ramps and presence of EDTA were used as photoanode in the photoelectrochemical cell. The photocurrent was recorded by intermittently irradiating the electrodes from halogen lamp using linear sweep photovoltammetry. Figure 7 illustrates the corresponding experimental results of as-anodized and calcined TNTs prepared at various bath temperatures and voltage ramps.

Apparently, all the as-anodized TNTs show a negligible photocurrent density (as low as  $2 \mu\text{A}/\text{cm}^2$ ) and substantial enhancement of photoresponse after calcination at  $500^\circ\text{C}$ . This result is expected as the as-anodized TNT exhibited amorphous structure as revealed by the XRD study (Figures 1(a) and 4(a)). Usually, amorphous TNT contains more defect sites than the crystallized one, which causes the recombination of photogenerated charge carriers. Therefore, photogenerated electrons have difficulty to conduct charge transfer on amorphous TNT under external bias condition to generate photocurrent [7]. This kind of TNT photoanode will be expected to exhibit very low photocatalytic or photoelectrocatalytic reactivity. On the contrary, significant increases in photocurrent for calcined samples is likely attributed to the higher photogenerated electron-hole pairs caused by the higher amount of anatase and rutile content. This result also indicates the necessity to form crystalline phase for the application of this material as photoanode.

For calcined TNT prepared at various bath temperatures, photoresponse increases with decreasing bath temperature except for TNT fabricated at  $10^\circ\text{C}$ . Higher photocurrent means that photogenerated electrons have been transferred from TNT photoanode to counter electrode more effectively via external circuit under illumination. Interestingly, it is found that even though TNT length produced at room temperature, about  $27^\circ\text{C}$  (tube length  $\sim 290$  nm), is relatively shorter, the photocurrent response is yet comparable to that synthesized at  $10^\circ\text{C}$  (tube length  $\sim 430$  nm). Two reasons may account for such observation. Firstly, as shown in Figure 2(a), debris covering the surface of nanotubes could be observed for TNT synthesized at  $10^\circ\text{C}$ . This unwanted debris will reduce the surface area and thus limit the light absorption ability of the sample. Therefore, for TNT synthesized at  $27^\circ\text{C}$ , its photoresponse is still comparable even though it has a relatively shorter tube length. Secondly, wall thickness and tube diameters are critical in influencing the photoresponse. In this respect, TNT with thinner wall (15 nm) in our study demonstrated relatively higher photocurrent response than that of thicker wall (21 nm). It is known that when  $\text{TiO}_2$  is irradiated, electrons and holes are generated. Unless they could be separated by either being trapped or migrating to the semiconductor surface, otherwise they always recombine immediately once photogenerated [30, 47]. With thinner

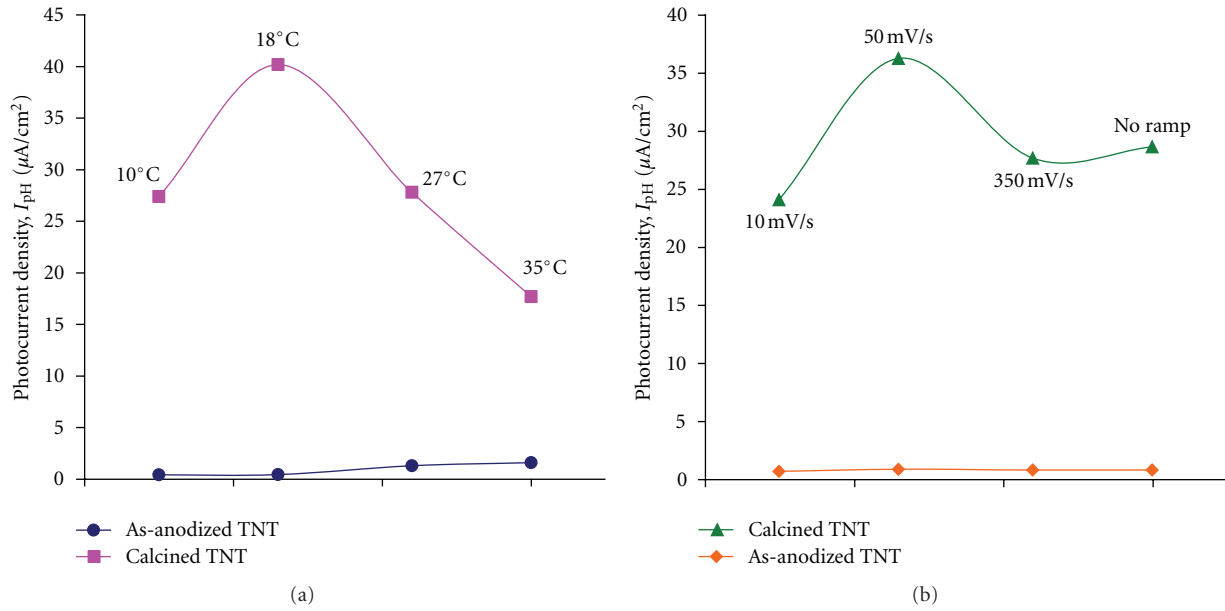


FIGURE 7: Comparison of photocurrent density at 1.0 V (versus Ag/AgCl) of as-anodized and calcined TNTs prepared in pH 4 electrolytes (a) at different electrolyte temperatures and (b) using different voltage ramps prior to constant voltage of 20 V. All the photocurrent measurements were obtained using 10 ppm methyl orange solution from 300 W halogen lamp at scan rate of 20 mV/s.

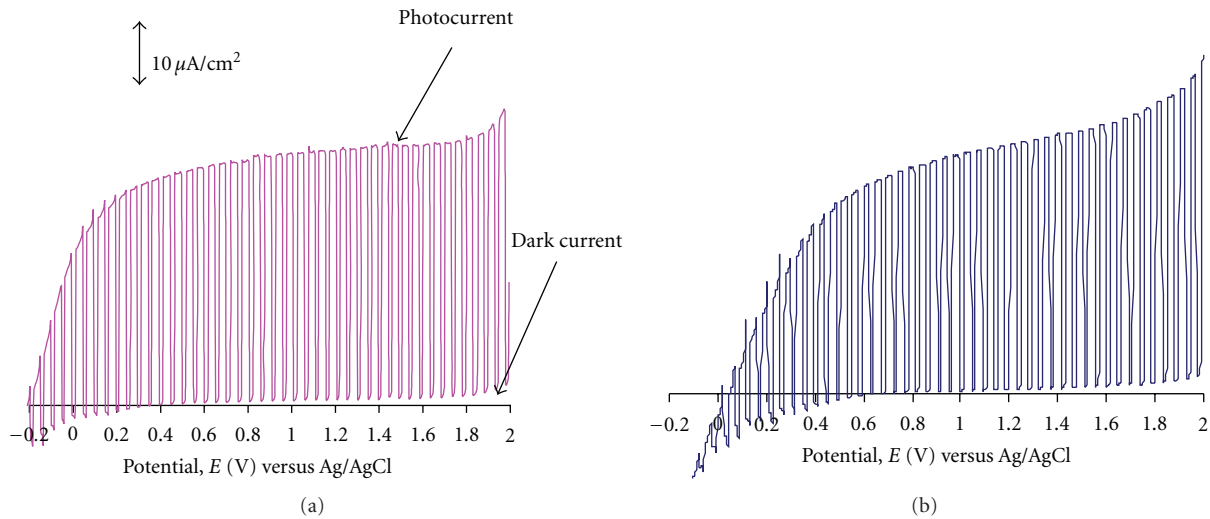


FIGURE 8: Photoresponse of (a) TNT/EDTA and (b) TNT prepared at 20 V for 1 h at pH 4.5. All the photocurrent measurement were obtained using 10 ppm methyl orange with 0.1 M KCl as supporting electrolyte from 300 W halogen lamp at scan rate of 20 mV/s.

wall, photogenerated hole could reach the oxidizable species in the electrolyte easily and reducing the recombination. Moreover, surface states increase rapidly as the wall thickness reduced, and thus resulting in low surface recombination [48]. On the other hand, TNT synthesized at  $18^\circ\text{C}$  demonstrated the highest photocurrent density, and its value is about twice the value of that fabricated at  $35^\circ\text{C}$ . Apart from short tube length obtained at  $35^\circ\text{C}$  which in return resulted in low incident photon absorption, low photoelectrochemical current density observed may reflect the quick recombination of photogenerated charge carriers

and low transfer efficiency of photogenerated electron to counter electrode via external circuit.

Generally, TNT obtained with voltage ramp prior to 2 h constant voltage has comparable or longer nanotube length than without ramp. Longest tube was obtained by applying a voltage ramp of 50 mV/s prior to constant voltage. Considering similar tube diameter and wall thickness obtained at different voltage ramps, availability of large active surface area increases linearly with increasing tube length. Thus, higher photocurrent density for TNT synthesized at 50 mV/s voltage ramping was mostly ascribed to the higher active

surface area which improves the light-harvesting capability and better photon absorption of this photoanode.

Figures 8(a) and 8(b) show the variation of photocurrent density with potential for calcined TNT/EDTA and TNT prepared at pH 4.5, respectively. Both curves exhibited the typical of n-type semiconductor. Both samples exhibited almost negligible dark current, indicating inactive photoreaction of TNT under dark condition (without illumination). However, the responsive photoresponse for both samples increased drastically under light illumination implying good transfer and recombination of photo-induced charge carriers [49]. In comparison, TNT/EDTA sample exhibited higher photocurrent than TNT sample due to longer tubes obtained than the latter. Moreover, enhancement of photocurrent density could be observed over entire potential range of +1.5 to -0.2 V, implying higher photoelectrochemical reactivity of TNT/EDTA photoanode. The curve slope is also steeper for TNT/EDTA in comparison to that of TNT. Therefore, one could expect that TNT fabricated with the addition of EDTA may demonstrate high photoresponse and act as promising material as photoanode in photoelectrochemical cells.

#### 4. Conclusions

In summary, we have successfully synthesized self-organized TNT using electrochemical method in  $\text{NH}_4\text{F}$  containing electrolyte. The influence of electrolyte temperature, voltage ramp prior to constant voltage, and the addition of EDTA on the dimensions of TNT has been investigated. It was found that TNT can still be fabricated at  $35^\circ\text{C}$ ; however, the tube length decreases whereas tube diameter increases with elevated temperature from 10 to  $35^\circ\text{C}$ . On the other hand, applying voltage ramp prior to constant voltage at 20 V during anodization has no influence on the tube diameter and wall thickness. Nevertheless, optimized voltage ramp at 50 mV/s resulted in thickest oxide layers. In addition, nanotube growth rate can be enhanced dramatically with the addition of EDTA. Based on the photoelectrochemical measurement, it can be concluded that structure of TNT including tube length and wall thickness is important factor influencing the photoresponse. Therefore, electrochemical parameters can be manipulated to obtain desired dimensions for various applications such as solar cells and photoelectrocatalysis.

#### Acknowledgment

This work was supported by an FRGS grant (no. 01-04-10-859FR) from the Ministry of Higher Education, Malaysia.

#### References

- [1] M. R. Hoffmann, S. T. Martin, W. Choi, and D. W. Bahnemann, "Environmental applications of semiconductor photocatalysis," *Chemical Reviews*, vol. 95, no. 1, pp. 69–96, 1995.
- [2] J. Yu, L. Zhang, B. Cheng, and Y. Su, "Hydrothermal preparation and photocatalytic activity of hierarchically sponge-like macro-/mesoporous Titania," *Journal of Physical Chemistry C*, vol. 111, no. 28, pp. 10582–10589, 2007.
- [3] F. Han, V. S. R. Kambala, M. Srinivasan, D. Rajarathnam, and R. Naidu, "Tailored titanium dioxide photocatalysts for the degradation of organic dyes in wastewater treatment: a review," *Applied Catalysis A: General*, vol. 359, no. 1-2, pp. 25–40, 2009.
- [4] J. A. Byrne, P. A. Fernandez-Ibañez, P. S.M. Dunlop, D. M.A. Alrousan, and J. W.J. Hamilton, "Photocatalytic enhancement for solar disinfection of water: a review," *International Journal of Photoenergy*, vol. 2011, Article ID 798051, 2011.
- [5] J. Yu, W. Wang, B. Cheng, and B. L. Su, "Enhancement of photocatalytic activity of Mesoporous  $\text{TiO}_2$  powders by hydrothermal surface fluorination treatment," *Journal of Physical Chemistry C*, vol. 113, no. 16, pp. 6743–6750, 2009.
- [6] H. J. Oh, J. H. Lee, Y. J. Kim, S. J. Suh, J. H. Lee, and C. S. Chi, "Synthesis of effective titania nanotubes for wastewater purification," *Applied Catalysis B: Environmental*, vol. 84, no. 1-2, pp. 142–147, 2008.
- [7] J. Yu, G. Dai, and B. Cheng, "Effect of crystallization methods on morphology and photocatalytic activity of anodized  $\text{TiO}_2$  nanotube array films," *Journal of Physical Chemistry C*, vol. 114, no. 45, pp. 19378–19385, 2010.
- [8] G. Dai, J. Yu, and G. Liu, "Synthesis and enhanced visible-light photoelectrocatalytic activity of p-N junction  $\text{BiOI}/\text{TiO}_2$  nanotube arrays," *Journal of Physical Chemistry C*, vol. 115, no. 15, pp. 7339–7346, 2011.
- [9] S. Wang, L. Zhao, J. Ran, Z. Shu, G. Dai, and P. Zhai, "Effects of calcination temperatures on photocatalytic activity of ordered titanate nanoribbon/ $\text{SnO}_2$  films fabricated during an EPD process," *International Journal of Photoenergy*, vol. 2012, Article ID 472958, 2012.
- [10] N. K. Allam, K. Shankar, and C. A. Grimes, "Photoelectrochemical and water photoelectrolysis properties of ordered  $\text{TiO}_2$  nanotubes fabricated by Ti anodization in fluoride-free HCl electrolytes," *Journal of Materials Chemistry*, vol. 18, no. 20, pp. 2341–2348, 2008.
- [11] K. Shankar, J. I. Basham, N. K. Allam et al., "Recent advances in the use of  $\text{TiO}_2$  nanotube and nanowire arrays for oxidative photoelectrochemistry," *Journal of Physical Chemistry C*, vol. 113, no. 16, pp. 6327–6359, 2009.
- [12] G. K. Mor, M. A. Carvalho, O. K. Varghese, M. V. Pishko, and C. A. Grimes, "A room-temperature  $\text{TiO}_2$ -nanotube hydrogen sensor able to self-clean photoactively from environmental contamination," *Journal of Materials Research*, vol. 19, no. 2, pp. 628–634, 2004.
- [13] S. Liu and A. Chen, "Coadsorption of horseradish peroxidase with thionine on  $\text{TiO}_2$  nanotubes for biosensing," *Langmuir*, vol. 21, no. 18, pp. 8409–8413, 2005.
- [14] Z. Xu and J. Yu, "A novel solid-state electrochemiluminescence sensor based on  $\text{Ru}(\text{bpy})_3^{2+}$  immobilization on  $\text{TiO}_2$  nanotube arrays and its application for detection of amines in water," *Nanotechnology*, vol. 21, no. 24, Article ID 245501, 2010.
- [15] J. R. Jennings, A. Ghicov, L. M. Peter, P. Schmuki, and A. B. Walker, "Dye-sensitized solar cells based on oriented  $\text{TiO}_2$  nanotube arrays: transport, trapping, and transfer of electrons," *Journal of the American Chemical Society*, vol. 130, no. 40, pp. 13364–13372, 2008.
- [16] J. Yu, J. Fan, and K. Lv, "Anatase  $\text{TiO}_2$  nanosheets with exposed (001) facets: improved photoelectric conversion efficiency in dye-sensitized solar cells," *Nanoscale*, vol. 2, no. 10, pp. 2144–2149, 2010.
- [17] A. Kar, K. S. Raja, and M. Misra, "Electrodeposition of hydroxyapatite onto nanotubular  $\text{TiO}_2$  for implant applications," *Surface and Coatings Technology*, vol. 201, no. 6, pp. 3723–3731, 2006.

- [18] K. C. Papat, L. Leoni, C. A. Grimes, and T. A. Desai, "Influence of engineered titania nanotubular surfaces on bone cells," *Biomaterials*, vol. 28, no. 21, pp. 3188–3197, 2007.
- [19] Z. Miao, D. Xu, J. Ouyang, G. Guo, X. Zhao, and Y. Tang, "Electrochemically induced sol-gel preparation of single-crystalline TiO<sub>2</sub> nanowires," *Nano Letters*, vol. 2, no. 7, pp. 717–720, 2002.
- [20] S.-J. Kim, N.-H. Lee, H.-J. Oh, S.-C. Jung, W.-J. Lee, and D.-H. Kim, "Photocatalytic properties of nanotubular-shaped TiO<sub>2</sub> powders with anatase phase obtained from titanate nanotube powder through various thermal treatments," *International Journal of Photoenergy*, vol. 2011, Article ID 327821, 2011.
- [21] T. Kasuga, M. Hiramatsu, A. Hoson, T. Sekino, and K. Niihara, "Formation of titanium oxide nanotube," *Langmuir*, vol. 14, no. 12, pp. 3160–3163, 1998.
- [22] M. S. Sander, M. J. Côté, W. Gu, B. M. Kile, and C. P. Tripp, "Template-assisted fabrication of dense, aligned arrays of titania nanotubes with well-controlled dimensions on substrates," *Advanced Materials*, vol. 16, no. 22, pp. 2052–2057, 2004.
- [23] Z. R. Tian, J. A. Voigt, J. Liu, B. McKenzie, and H. Xu, "Large oriented arrays and continuous films of TiO<sub>2</sub>-based nanotubes," *Journal of the American Chemical Society*, vol. 125, no. 41, pp. 12384–12385, 2003.
- [24] J. M. Macak, H. Tsuchiya, A. Ghicov et al., "TiO<sub>2</sub> nanotubes: self-organized electrochemical formation, properties and applications," *Current Opinion in Solid State and Materials Science*, vol. 11, no. 1-2, pp. 3–18, 2007.
- [25] V. Zwillig, E. Darque-Ceretti, A. Boutry-Forveille, D. David, M. Y. Perrin, and M. Aucouturier, "Structure and physico-chemistry of anodic oxide films on titanium and TA6V alloy," *Surface and Interface Analysis*, vol. 27, no. 7, pp. 629–637, 1999.
- [26] C. A. Grimes, D. Gong, O. K. Varghese et al., "Titanium oxide nanotube arrays prepared by anodic oxidation," *Journal of Materials Research*, vol. 16, no. 12, pp. 3331–3334, 2001.
- [27] M. Zhou, J. Yu, B. Cheng, and H. Yu, "Preparation and photocatalytic activity of Fe-doped mesoporous titanium dioxide nanocrystalline photocatalysts," *Materials Chemistry and Physics*, vol. 93, no. 1, pp. 159–163, 2005.
- [28] J. Yu, G. Dai, and B. Huang, "Fabrication and characterization of visible-light-driven plasmonic photocatalyst Ag/AgCl/TiO<sub>2</sub> nanotube arrays," *Journal of Physical Chemistry C*, vol. 113, no. 37, pp. 16394–16401, 2009.
- [29] Z. Xu and J. Yu, "Visible-light-induced photoelectrochemical behaviors of Fe-modified TiO<sub>2</sub> nanotube arrays," *Nanoscale*, vol. 3, no. 8, pp. 3138–3144, 2011.
- [30] J. Yu and B. Wang, "Effect of calcination temperature on morphology and photoelectrochemical properties of anodized titanium dioxide nanotube arrays," *Applied Catalysis B: Environmental*, vol. 94, no. 3-4, pp. 295–302, 2010.
- [31] J. M. Macak and P. Schmuki, "Anodic growth of self-organized anodic TiO<sub>2</sub> nanotubes in viscous electrolytes," *Electrochimica Acta*, vol. 52, no. 3, pp. 1258–1264, 2006.
- [32] S. Yoriya and C. A. Grimes, "Self-Assembled TiO<sub>2</sub> nanotube arrays by anodization of titanium in diethylene glycol: approach to extended pore widening," *Langmuir*, vol. 26, no. 1, pp. 417–420, 2010.
- [33] K. Zhu, N. R. Neale, A. Miedaner, and A. J. Frank, "Enhanced charge-collection efficiencies and light scattering in dye-sensitized solar cells using oriented TiO<sub>2</sub> nanotubes arrays," *Nano Letters*, vol. 7, no. 1, pp. 69–74, 2007.
- [34] J. M. Macak, H. Hildebrand, U. Marten-Jahns, and P. Schmuki, "Mechanistic aspects and growth of large diameter self-organized TiO<sub>2</sub> nanotubes," *Journal of Electroanalytical Chemistry*, vol. 621, no. 2, pp. 254–266, 2008.
- [35] V. M. Prida, E. Manova, V. Vega et al., "Temperature influence on the anodic growth of self-aligned Titanium dioxide nanotube arrays," *Journal of Magnetism and Magnetic Materials*, vol. 316, no. 2, pp. 110–113, 2007.
- [36] L. Y. Chin, Z. Zainal, M. Z. Hussein, and T. W. Tee, "Fabrication of highly ordered TiO<sub>2</sub> nanotubes from fluoride containing aqueous electrolyte by anodic oxidation and their photoelectrochemical response," *Journal of Nanoscience and Nanotechnology*, vol. 11, no. 6, pp. 4900–4909, 2011.
- [37] S. Banerjee, M. Misra, S. K. Mohapatra, C. Howard, S. K. Mohapatra, and S. K. Kamilla, "Formation of chelating agent driven anodized TiO<sub>2</sub> nanotubular membrane and its photo-voltaic application," *Nanotechnology*, vol. 21, no. 14, Article ID 145201, pp. 1–9, 2010.
- [38] X. Xiao, K. Ouyang, R. Liu, and J. Liang, "Anatase type titania nanotube arrays direct fabricated by anodization without annealing," *Applied Surface Science*, vol. 255, no. 6, pp. 3659–3663, 2009.
- [39] G. K. Mor, K. Shankar, M. Paulose, O. K. Varghese, and C. A. Grimes, "Enhanced photocleavage of water using titania nanotube arrays," *Nano Letters*, vol. 5, no. 1, pp. 191–195, 2005.
- [40] Z. Lockman, S. Sreekantan, S. Ismail, L. Schmidt-Mende, and J. L. MacManus-Driscoll, "Influence of anodisation voltage on the dimension of titania nanotubes," *Journal of Alloys and Compounds*, vol. 503, no. 2, pp. 359–364, 2010.
- [41] Y. Lai, H. Zhuang, L. Sun, Z. Chen, and C. Lin, "Self-organized TiO<sub>2</sub> nanotubes in mixed organic-inorganic electrolytes and their photoelectrochemical performance," *Electrochimica Acta*, vol. 54, no. 26, pp. 6536–6542, 2009.
- [42] H. Yin, H. Liu, and W. Z. Shen, "The large diameter and fast growth of self-organized TiO<sub>2</sub> nanotube arrays achieved via electrochemical anodization," *Nanotechnology*, vol. 21, no. 3, Article ID 035601, 2010.
- [43] J. M. Macák, H. Tsuchiya, and P. Schmuki, "High-aspect-ratio TiO<sub>2</sub> nanotubes by anodization of titanium," *Angewandte Chemie—International Edition*, vol. 44, no. 14, pp. 2100–2102, 2005.
- [44] M. Paulose, K. Shankar, S. Yoriya et al., "Anodic growth of highly ordered TiO<sub>2</sub> nanotube arrays to 134 μm in length," *Journal of Physical Chemistry B*, vol. 110, no. 33, pp. 16179–16184, 2006.
- [45] B. Karadakov and P. Nenova, "Spectrophotometric study of the reaction of titanium(IV) and ethylenediaminetetraacetic acid (EDTA)," *Journal of Inorganic and Nuclear Chemistry*, vol. 33, no. 8, pp. 2541–2545, 1971.
- [46] E. Y. Kim, J. H. Park, and G. Y. Han, "Design of TiO<sub>2</sub> nanotube array-based water-splitting reactor for hydrogen generation," *Journal of Power Sources*, vol. 184, no. 1, pp. 284–287, 2008.
- [47] A. Hagfeldt, H. Lindström, S. Södergren, and S. E. Lindquist, "Photoelectrochemical studies of colloidal TiO<sub>2</sub> films: the effect of oxygen studied by photocurrent transients," *Journal of Electroanalytical Chemistry*, vol. 381, no. 1-2, pp. 39–46, 1995.
- [48] H. C. Liang and X. Z. Li, "Effects of structure of anodic TiO<sub>2</sub> nanotube arrays on photocatalytic activity for the degradation of 2,3-dichlorophenol in aqueous solution," *Journal of Hazardous Materials*, vol. 162, no. 2-3, pp. 1415–1422, 2009.
- [49] Y. Xie, L. M. Zhou, and H. Huang, "Enhanced photoelectrochemical current response of titania nanotube array," *Materials Letters*, vol. 60, no. 29-30, pp. 3558–3560, 2006.

## Research Article

# Hydrothermal Synthesis of Nitrogen-Doped Titanium Dioxide and Evaluation of Its Visible Light Photocatalytic Activity

Junjie Qian, Guanjun Cui, Mingjun Jing, Yan Wang, Min Zhang, and Jianjun Yang

Key Laboratory for Special Functional Materials, Henan University, Kaifeng 475004, China

Correspondence should be addressed to Jianjun Yang, hndxyjj@sina.com

Received 14 September 2011; Revised 6 November 2011; Accepted 8 December 2011

Academic Editor: Mietek Jaroniec

Copyright © 2012 Junjie Qian et al. This is an open access article distributed under the Creative Commons Attribution License, which permits unrestricted use, distribution, and reproduction in any medium, provided the original work is properly cited.

Nitrogen-doped titanium dioxide (N-doped TiO<sub>2</sub>) photocatalyst was synthesized from nanotube titanic acid (denoted as NTA; molecular formula H<sub>2</sub>Ti<sub>2</sub>O<sub>5</sub> · H<sub>2</sub>O) precursor *via* a hydrothermal route in ammonia solution. As-synthesized N-doped TiO<sub>2</sub> catalysts were characterized by means of X-ray diffraction, transmission electron microscopy, diffuse reflectance spectrometry, X-ray photoelectron spectroscopy, electron spin resonance spectrometry and Fourier transform infrared spectrometry. It was found that nanotube ammonium titanate (NAT) was produced as an intermediate during the preparation of N-doped TiO<sub>2</sub> from NTA, as evidenced by the N1s X-ray photoelectron spectroscopic peak of NH<sub>4</sub><sup>+</sup> at 401.7 eV. The catalyst showed much higher activities to the degradation of methylene blue and p-chlorophenol under visible light irradiation than Degussa P25. This could be attributed to the enhanced absorption of N-doped TiO<sub>2</sub> in visible light region associated with the formation of single-electron-trapped oxygen vacancies and the inhibition of recombination of photo-generated electron-hole pair by doped nitrogen.

## 1. Introduction

Titania, as a currently known most effective photocatalyst, have been widely applied in purifying air and water, deodorization, and many other environmentally related fields [1]. However, TiO<sub>2</sub> can only be induced by ultraviolet (UV), due to its large bandgap of ca. 3 eV [2]. As a result, TiO<sub>2</sub> in practical application can only utilize a small fraction (~5%) of solar energy [3]. To increase the efficiency for solar energy transformation and utilization, many researchers have attempted to extend the absorption range of TiO<sub>2</sub> from UV region to visible light (Vis in short) region by doping various cations [4–6] and anions [7, 8]. It has been found that N doping induces considerable visible light response of anatase TiO<sub>2</sub>; the mechanisms for the visible light response of N-doped TiO<sub>2</sub>, however, still remain disputable. About one decade ago, Asahi et al. reported a visible light active TiO<sub>2-x</sub>N<sub>x</sub> film by sputtering a TiO<sub>2</sub> target in the mixture of N<sub>2</sub> and Ar (volume ratio 40%:60%); and they suggested that the incorporation of dopant N atom into the crystal lattice of TiO<sub>2</sub> via substituting Ti atom was indispensable for band-gap narrowing and photocatalytic activity generation [9]. In 2003, Irie et al. reported a TiO<sub>2-x</sub>N<sub>x</sub> powder prepared

by annealing anatase TiO<sub>2</sub> under an ammonia flow; and they supposed that the isolated narrow band formed above the valence band of TiO<sub>2</sub> was responsible for the visible light response of N-doped TiO<sub>2</sub> [10]. Ihara et al. also prepared a visible light responsive photocatalyst by treating the hydrolysis product of Ti(SO<sub>4</sub>)<sub>2</sub> in ammonia (a precursor for N doping); and they deduced that oxygen-deficient sites formed in grain boundaries gave rise to visible light activity of as-prepared N-doped product, while doped N at oxygen-deficient sites played a key role as a blocker for reoxidation [11]. Zhang et al. observed that the visible-light absorption of vacuum-dehydrated product of NTA was proportional to the intensity of electron spin resonance (ESR) signal [12]. We supposed in our previous researches that the visible light sensitization of N-doped TiO<sub>2</sub> was due to the formation of single-electron-trapped oxygen vacancies (SETOVs), and doped-N played a role in preventing photogenerated electrons and holes from recombination [12, 13].

In the present research, we make use of a hydrothermal method to prepare N-doped TiO<sub>2</sub> by selecting NTA as a precursor, hoping to harvest TiO<sub>2</sub>-based photocatalyst with high visible light activity while heat-treatment temperature is considerably lowered as compared with that for calcination

of NTA in flowing ammonia [12]. This article reports the preparation and characterization of N-doped TiO<sub>2</sub> photocatalyst, as well as its photocatalytic activity for the degradation of methylene blue (MB) and p-chlorophenol (4-CP) under visible light irradiation.

## 2. Experimental Section

**2.1. Preparation of Samples.** NTA was prepared using the method reported in literature [14]. N-doped TiO<sub>2</sub> powders were prepared using a two-step protocol. Firstly, 1 g of NTA and 50 mL of ammonia solution (mass fraction 25% ~ 28%) was added into a Teflon-lined stainless steel autoclave (75 mL) and airproofed and heated at 130, 160 and 210°C for 3 h in an oven. Then, the autoclave was cooled in air down to room temperature after the reaction was completed, followed by filtration, drying at 60°C in vacuum (-0.1 MPa) overnight, and grinding to yield samples denoted as N-NTA-130, N-NTA-160, and N-NTA-210, respectively. Sample H-NTA-210 for a comparative study was also prepared in the same manners except that distilled water was used to replace ammonia solution.

**2.2. Characterization.** X-ray diffraction (XRD) patterns were measured with a Philips X'Pert Pro X-ray diffractometer (Cu K $\alpha$  radiation, 2 $\theta$  range 7~90°, scan step size 0.04°, scanning interval 0.5 s, generator voltage 40 kV, tube current 40 mA). A JEM-100CX transmission electron microscope (TEM; JEOL Ltd., Japan) was performed at an accelerating voltage of 100 kV to observe the morphology and microstructure of various as-prepared photocatalysts. Diffuse reflection spectra (DRS) were obtained with a UV-Vis spectrophotometer (UV-3010; Shimadzu, Japan; reference: BaSO<sub>4</sub>). An Axis Ultra X-ray photoelectron spectroscope (XPS; Kratos, England) equipped with a multichannel detector was performed to analyze the chemical states of various photocatalysts, where Al K $\alpha$  radiation ( $h\nu = 1486.6$  eV) was used as the excitation source. All the binding energies were referenced to the C1s peak at 284.8 eV of surface adventitious carbon. Electron spin resonance (ESR) spectra were collected with a Bruker ESP 300E apparatus (reference: diphenyl-picryl hydrazide (DPPH),  $g = 2.0036$ ). Fourier transform infrared (FTIR) spectra were recorded with a Nicolet 360 spectrometer (Nicolet Company, USA).

**2.3. Evaluation of Visible Light Photocatalytic Activity.** The photocatalytic activities of various photocatalysts were evaluated by monitoring the degradation of MB and 4-CP under the irradiation of a 500 W xenon lamp as the light source ( $I_{420} = 2.1$  mW/cm<sup>2</sup>) with which a filter and a water cell were attached to eliminate UV ( $\lambda < 420$  nm) and infrared light. Into a quartz reactor (140 mL) charged with 100 mL of the aqueous solution of MB (10 mg/L) or 4-CP (0.15 mM) was added 100 mg of to-be-tested photocatalyst powder. The adsorption equilibrium of aqueous MB or 4-CP on the photocatalyst was reached in the reactor prior to irradiation. The concentration of MB was monitored with a visible light spectrometer (722, Shanghai Jingke Instrument Plant, China) at 664 nm, and that of 4-CP was measured with

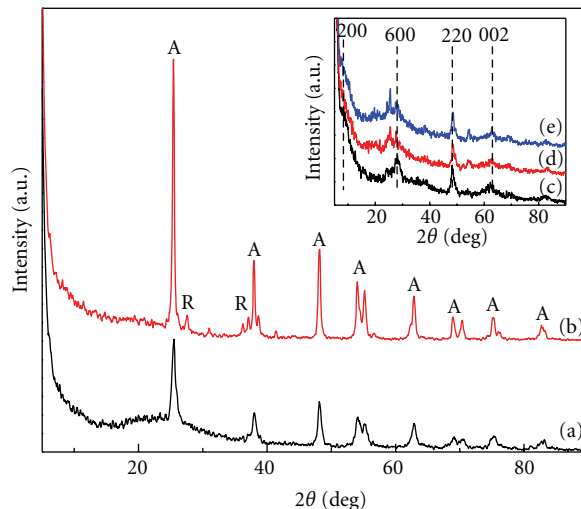


FIGURE 1: XRD patterns of (a) H-NTA-210 and (b) N-NTA-210. The inset shows the XRD patterns of orthorhombic systems of (c) NTA, (d) N-NTA-130, and (e) N-NTA-160.

an UV-Vis spectrometer (752, Shanghai Oppler Instrument Plant, China) at 225 nm.

## 3. Results and Discussion

The XRD patterns of undoped TiO<sub>2</sub> and three N-doped TiO<sub>2</sub> samples are compared in Figure 1. Samples N-NTA-130 and N-NTA-160 still retain the orthorhombic form (inset in Figure 1) and nanotubular morphology of precursor NTA (Figure 2). This differs from our previous finding in that the tubular shape of orthorhombic NTA is destroyed in association with conversion into anatase TiO<sub>2</sub> when NTA is heated in distilled water at 130°C or 160°C [15]. However, sample N-NTA-210 shows strong diffraction peaks of anatase TiO<sub>2</sub> as well as additional diffraction peaks of rutile phase (27.4, 36.1, 39.2, 41.2, 44.1, and 56.6°), which indicates that hydrothermal treatment of orthorhombic NTA in ammonia solution at an elevated temperature of 210°C also facilitates its transformation to TiO<sub>2</sub>. In the meantime, all the XRD peaks of sample H-NTA-210 can be well indexed as anatase TiO<sub>2</sub> (25.4, 37.9, 48.2, 54.1, and 55.2°); and both H-NTA-210 and N-NTA-210 have diamond shapes, but the size of the former is a little bit smaller than that of the latter (Figure 2). We assume that nanotube ammonium titanate (NAT) is formed as an intermediate through a simple acid-base reaction (1) when NTA is hydrothermally treated in ammonia at 130°C or 160°C, but it is transformed to TiO<sub>2</sub> at 210°C (reaction (2)). This supposition is supported by corresponding FTIR data shown in Figure 3. Namely, both N-NTA-130 and N-NTA-160 show a broad band at 3400 cm<sup>-1</sup> and a sharp peak at 1630 cm<sup>-1</sup> attributed to the stretching vibration and flexural vibration of hydroxyl groups [16] as well as a broad band within 750~400 cm<sup>-1</sup> corresponding to the flexural vibration of Ti-O and Ti-O-Ti groups. Particularly, they also show the stretching and flexural vibration bands of N-H at 3140 cm<sup>-1</sup> and

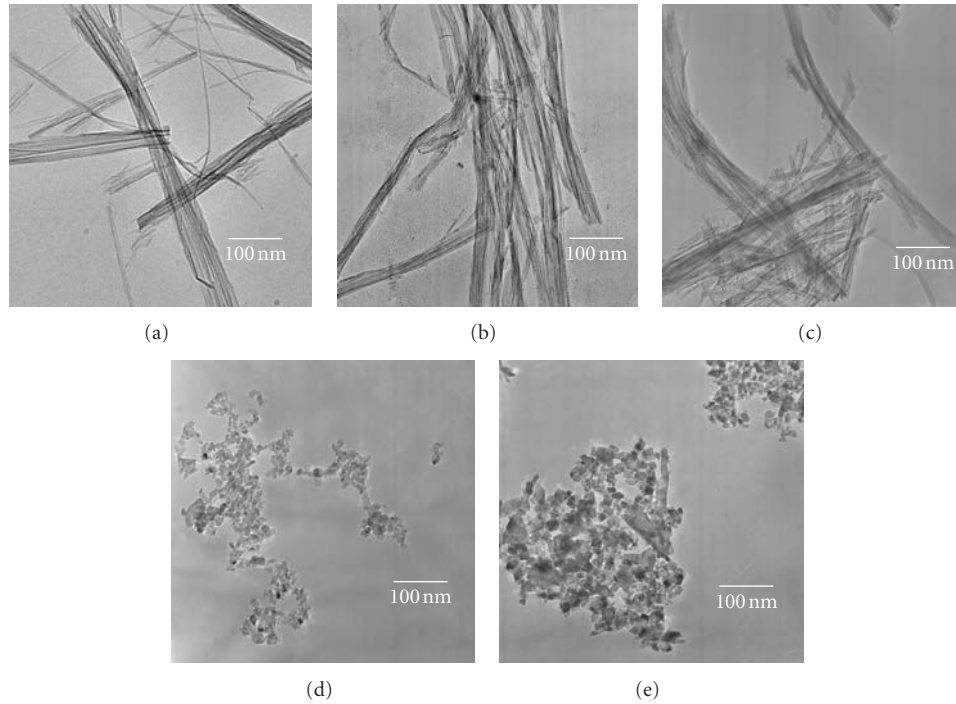
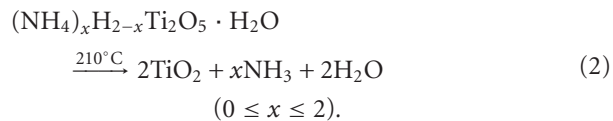
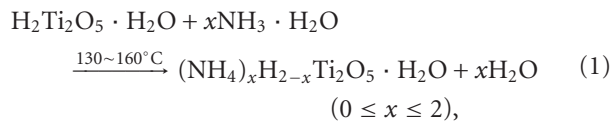


FIGURE 2: TEM images of (a) NTA, (b) N-NTA-130, (c) N-NTA-160, (d) H-NTA-210, and (e) N-NTA-210.

$1400\text{ cm}^{-1}$  [17], which confirms that intermediate NAT is indeed generated during hydrothermal treatment of NTA in ammonia at  $130^\circ\text{C}$  or  $160^\circ\text{C}$ . However, no stretching and flexural vibration bands of N-H are observed for N-NTA-210, which is due to the decomposition of intermediate NAT at an elevated temperature of  $210^\circ\text{C}$ :



XPS spectra of NTA and various N-doped  $\text{TiO}_2$  samples were measured to further elucidate the chemical states of N. As shown in Figure 4, precursor NTA shows no N1s XPS signal; but samples N-NTA-130, N-NTA-160, and N-NTA-210 show N1s XPS peaks at 400.0 eV and 401.7 eV. It is usually recognized that N1s XPS peak of N-doped  $\text{TiO}_2$  at 397.0 eV is assigned to atomic Ti-N [12, 18–20]; but the assignment of the N1s XPS peaks at 400.0 eV and 401.7 eV are still under argument. Asahi et al. assigned them as molecularly chemisorbed  $\gamma\text{-N}_2$ , but Sato et al. argued that molecular  $\text{N}_2$  could not be adsorbed on metal oxide like  $\text{TiO}_2$  at room temperature and suggested that the N1s core level of N-doped  $\text{TiO}_2$  at 400.0 eV was attributed to N–O bonding (i.e., Ti–O–N), possibly at interstitial site [20]. Irie et al. assigned the N1s XPS peak of N-doped  $\text{TiO}_2$  at 400.0 eV as NO [10]. In the present research, the N1s XPS peak at ca.

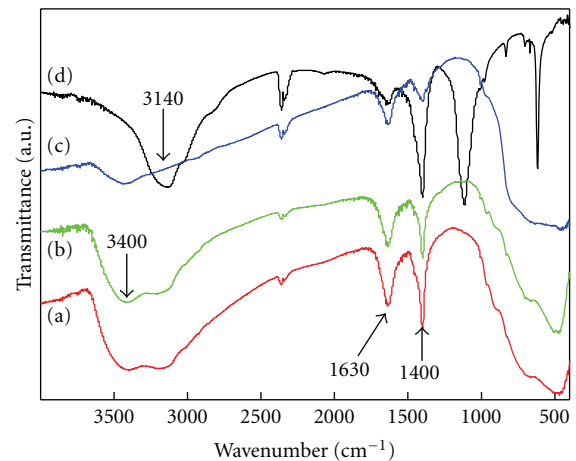


FIGURE 3: FTIR spectra of (a) N-NTA-130, (b) N-NTA-160, (c) N-NTA-210, and (d) reference  $(\text{NH}_4)_2\text{SO}_4$ .

401.7 eV confirms the presence of N in a third chemical state. Since this N1s XPS peak is only observed for N-NTA-130 and N-NTA-160 but not for N-NTA-210, we tentatively assign it as  $\text{NH}_4^+$  of intermediate NAT, as evidenced by relevant FTIR analyses.

Photocatalytic tests indicate that samples NTA, N-NTA-130, and N-NTA-160 have no photocatalytic activity for the discoloration of MB; but sample N-NTA-210 is able to effectively catalyze the discoloration reaction of MB, following the first-order reaction kinetics model (the kinetic constants are ranked as  $k(\text{N-NTA-210}) > k(\text{H-NTA-210}) > k(\text{P25})$ ,

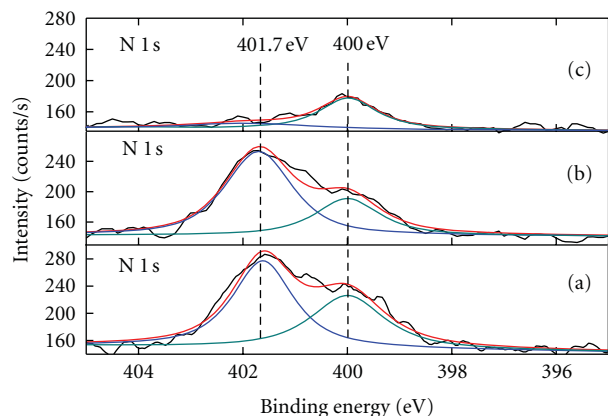


FIGURE 4: XPS spectra of (a) N-NTA-130, (b) N-NTA-160, and (c) N-NTA-210.

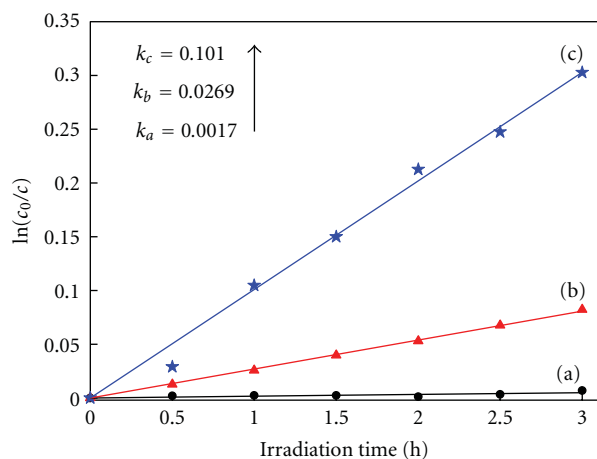


FIGURE 5: Kinetics of the photocatalytic decomposition of MB on different  $\text{TiO}_2$  powders under visible light irradiation: (a) P25, (b) H-NTA-210, and (c) N-NTA-210.

see Figure 5. In the meantime, NTA, N-NTA-130, and N-NTA-160 are inert to the degradation of colorless organic pollutant 4-CP under visible light irradiation; but H-NTA-210 and N-NTA-210 can well accelerate the degradation of 4-CP under the same conditions, and N-NTA-210 possesses better photocatalytic activity than H-NTA-210 (Figure 6).

It is well known that photocatalytic activity is dependent on light absorption efficiency and separation efficiency of photogenerated electrons and holes. Figure 7 shows the UV-Vis spectra of various photocatalysts. Precursor NTA does not show any absorption in visible light region, but samples H-NTA-210 and N-NTA-210 both show broadened absorptions at  $\lambda > 400$  nm, which corresponds to their enhanced ESR signals at  $g = 2.003$  (Figure 8) and accounts for better visible photocatalytic activity of N-NTA-210 as compared with Degussa P25. Besides, the present research once again provides evidence to the supposition that SETOV density in  $\text{TiO}_2$  lattice is proportional to the absorption intensity of the photocatalyst in visible light region (Figure 9) [12, 21–23].

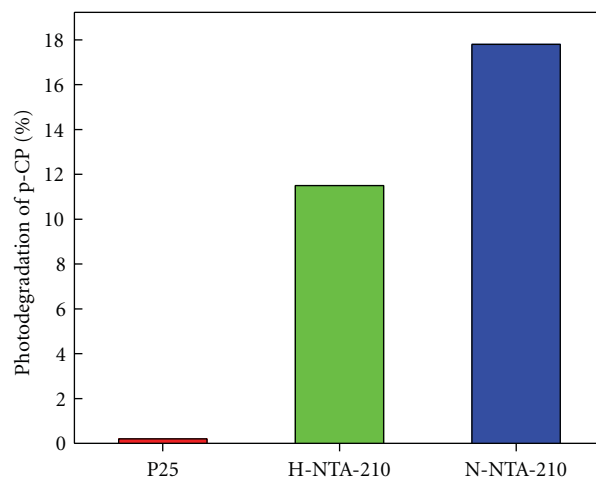


FIGURE 6: Photocatalytic degradation of p-chlorophenol on P25, H-NTA-210, and N-NTA-210.

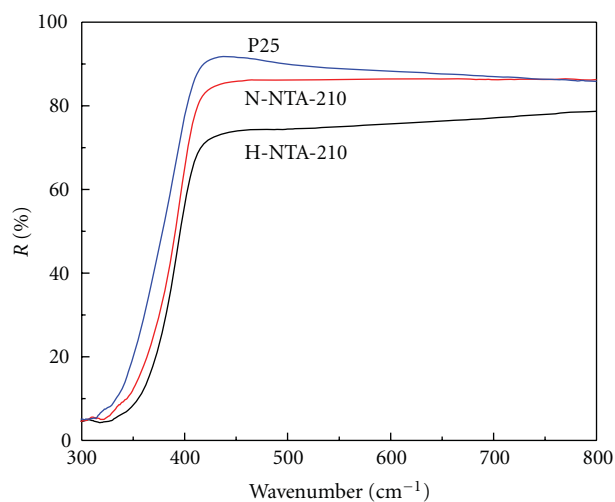


FIGURE 7: DRS of H-NTA-210, N-NTA-210 and P25.

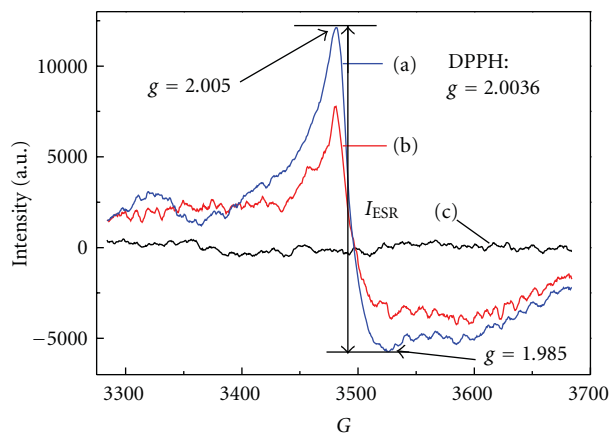


FIGURE 8: ESR spectra of (a) H-NTA-210, (b) N-NTA-210, and (c) P25 (reference compound: diphenyl picryl hydrazyl (DPPH),  $g = 2.0036$ ).

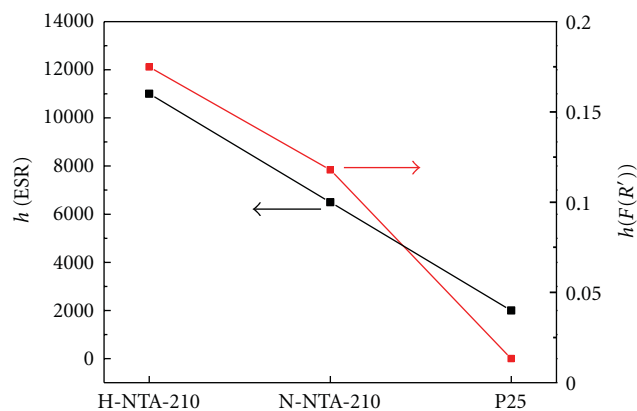


FIGURE 9: The relation between intensity of  $g$  value signal and visible light absorption of three  $\text{TiO}_2$  samples;  $h(\text{ESR})$  refers to the signal intensity at  $g = 2.003$ ,  $h(F(R'))$  refers to the absorption intensity at 450 nm,  $F(R') = (1 - R_\infty)^2 / (2R_\infty)$ ,  $F(R')$  and  $R_\infty$  refer to absorptivity and reflectance at  $\lambda = 450$  nm.

Aside from the light absorption efficiency, the separation efficiency of electrons and holes is another important factor to influence the activity of photocatalysts. Ordinarily, photoinduced electrons and holes can be generated in photocatalysts under light excitation; and the photoinduced electrons and holes can be separated on the surface of photocatalysts to take part in chemical reactions or recombine. Some researchers have reported that the mixed crystal effect and high crystallinity in a semiconductor is in favor of retarding the recombination of photogenerated electrons and holes [24, 25], resulting in enhanced photocatalytic activity. This, however, does not seem to be dominant in the present research. Namely, although H-NTA-210 has a stronger SETOV intensity and broader visible light absorption than N-NTA-210, the former possesses poorer photocatalytic activity than the latter. The enhanced photocatalytic activity of N-NTA-210 as compared with that of H-NTA-210, that we suppose, may be attributed to N doping which retards the recombination of photoinduced electrons and holes in  $\text{TiO}_2$  matrix. This can be described using equations (3)–(5) [13]. Briefly, photoinduced electrons in  $\text{TiO}_2$  matrix arrive at the intraband contributed by SETOV ((3);  $V_o^\cdot$  refers to SETOV), but they tend to jump back and recombine with holes. When nitrogen atoms are doped into  $\text{TiO}_2$  lattices, the back-jumping routes are forbidden and the recombination is reduced greatly, allowing more photoinduced electrons to take part in the chemical reactions. In the meantime, N atoms in Ti–O–N bond occupy interstitial sites and allow their electron clouds to transfer towards O atom with a higher electronegativity. As a result, dopant N in N-doped  $\text{TiO}_2$  possesses a higher chemical valence than the N in  $\text{NH}_4^+$  and is able to entrap another electron from  $V_o^{\cdot\cdot}$  ((4);  $V_o^{\cdot\cdot}$  refers to double-electron-trapped oxygen vacancy). Nevertheless, interstitial N atom with an excessive electron is unstable and allows its electron could to transfer towards  $\text{O}_2$  molecule in gas or solution medium (5). Although Ti–O–N bond also exists in samples N-NTA-130 and N-NTA-160 as in

N-NTA-210, N-NTA-130 and N-NTA-160 without SETOV do not possess visible light photocatalytic activity:



#### 4. Summary

A simple and mild hydrothermal method has been established to prepare nanoscale N-doped  $\text{TiO}_2$  photocatalyst with good visible light catalytic activity, where heat treatment of precursor NTA in ammonia solution at 210°C for 3 h facilitates structural transformation from orthorhombic NTA to N-doped  $\text{TiO}_2$ . Heat treatment of the same precursor at lowered temperature of 130°C and 160°C gives rise to intermediate NAT deserving further research, a potential precursor for fabricating novel N-doped  $\text{TiO}_2$ . As-prepared N-NTA-210 possesses better photocatalytic performance than Degussa P25 for the degradation of MB and 4-CP under visible light irradiation, which is attributed to the formation of a large number of SETOV on the surface of N-doped  $\text{TiO}_2$  and the occupation of interstitial sites in the crystal lattice of  $\text{TiO}_2$  by dopant N as Ti–O–N.

#### Acknowledgments

The authors thank the National Natural Science Foundation of China (no. 20973054) for financial support.

#### References

- [1] M. R. Hoffmann, S. T. Martin, W. Choi, and D. W. Bahnemann, "Environmental applications of semiconductor photocatalysis," *Chemical Reviews*, vol. 95, no. 1, pp. 69–96, 1995.
- [2] S. P. Kowalczyk, F. R. McFeely, L. Ley, V. T. Gritsyna, and D. A. Shirley, "The electronic structure of  $\text{SrTiO}_3$  and some simple related oxides ( $\text{MgO}$ ,  $\text{Al}_2\text{O}_3$ ,  $\text{SrO}$ ,  $\text{TiO}_2$ )," *Solid State Communications*, vol. 23, no. 3, pp. 161–169, 1977.
- [3] U. Siemon, D. Bahnemann, J. J. Testa, D. Rodríguez, M. I. Litter, and N. Bruno, "Heterogeneous photocatalytic reactions comparing  $\text{TiO}_2$  and  $\text{Pt/TiO}_2$ ," *Journal of Photochemistry and Photobiology A*, vol. 148, no. 1–3, pp. 247–255, 2002.
- [4] M. Mrowetz, W. Balcerski, A. J. Colussi, and M. R. Hoffmann, "Oxidative power of nitrogen-doped  $\text{TiO}_2$  photocatalysts under visible illumination," *Journal of Physical Chemistry B*, vol. 108, no. 45, pp. 17269–17273, 2004.
- [5] W. Choi, A. Termin, and M. R. Hoffmann, "The role of metal ion dopants in quantum-sized  $\text{TiO}_2$ : correlation between photoreactivity and charge carrier recombination dynamics," *Journal of Physical Chemistry*, vol. 98, no. 51, pp. 13669–13679, 1994.
- [6] M. Takeuchi, H. Yamashita, M. Matsuoka et al., "Photocatalytic decomposition of NO under visible light irradiation on the Cr-ion-implanted  $\text{TiO}_2$  thin film photocatalyst," *Catalysis Letters*, vol. 67, no. 2–4, pp. 135–137, 2000.
- [7] J. L. Gole, J. D. Stout, C. Burda, Y. Lou, and X. Chen, "Highly efficient formation of visible light tunable  $\text{TiO}_{2-x}\text{N}_x$  photocatalysts and their transformation at the nanoscale,"

- Journal of Physical Chemistry B*, vol. 108, no. 4, pp. 1230–1240, 2004.
- [8] H. Irie, Y. Watanabe, and K. Hashimoto, “Carbon-doped anatase TiO<sub>2</sub> powders as a visible-light sensitive photocatalyst,” *Chemistry Letters*, vol. 32, no. 8, pp. 772–773, 2003.
- [9] R. Asahi, T. Morikawa, T. Ohwaki, K. Aoki, and Y. Taga, “Visible-light photocatalysis in nitrogen-doped titanium oxides,” *Science*, vol. 293, no. 5528, pp. 269–271, 2001.
- [10] H. Irie, Y. Watanabe, and K. Hashimoto, “Nitrogen-concentration dependence on photocatalytic activity of TiO<sub>2-x</sub>N<sub>x</sub> powders,” *Journal of Physical Chemistry B*, vol. 107, no. 23, pp. 5483–5486, 2003.
- [11] T. Ihara, M. Miyoshi, Y. Iriyama, O. Matsumoto, and S. Sugihara, “Visible-light-active titanium oxide photocatalyst realized by an oxygen-deficient structure and by nitrogen doping,” *Applied Catalysis B*, vol. 42, no. 4, pp. 403–409, 2003.
- [12] S. Zhang, W. Li, Z. Jin et al., “Study on ESR and inter-related properties of vacuum-dehydrated nanotubed titanate acid,” *Journal of Solid State Chemistry*, vol. 177, no. 4-5, pp. 1365–1371, 2004.
- [13] Y. Wang, C. Feng, M. Zhang, J. Yang, and Z. Zhang, “Visible light active N-doped TiO<sub>2</sub> prepared from different precursors: origin of the visible light absorption and photoactivity,” *Applied Catalysis B*, vol. 104, no. 3-4, pp. 268–274, 2011.
- [14] J. Yang, Z. Jin, X. Wang et al., “Study on composition, structure and formation process of nanotube Na<sub>2</sub>Ti<sub>2</sub>O<sub>4</sub>(OH)<sub>2</sub>,” *Journal of the Chemical Society. Dalton Transactions*, no. 20, pp. 3898–3901, 2003.
- [15] G. Cui, Z. Xu, Y. Wang, M. Zhang, and J. Yang, “A new method to prepare the novel anatase TiO<sub>2</sub>,” *Surface Review and Letters*, vol. 15, no. 4, pp. 509–513, 2008.
- [16] P. M. Kumar, S. Badrinarayanan, and M. Sastry, “Nanocrystalline TiO<sub>2</sub> studied by optical, FTIR and X-ray photoelectron spectroscopy: correlation to presence of surface states,” *Thin Solid Films*, vol. 358, no. 1, pp. 122–130, 2000.
- [17] B. Erdem, R. A. Hunsicker, G. W. Simmons, E. David Sudol, V. L. Dimonie, and M. S. El-Aasser, “XPS and FTIR surface characterization of TiO<sub>2</sub> particles used in polymer encapsulation,” *Langmuir*, vol. 17, no. 9, pp. 2664–2669, 2001.
- [18] N. C. Saha and H. G. Tompkins, “Titanium nitride oxidation chemistry: an x-ray photoelectron spectroscopy study,” *Journal of Applied Physics*, vol. 72, no. 7, pp. 3072–3079, 1992.
- [19] S. K. Joung, T. Amemiya, M. Murabayashi, and K. Itoh, “Mechanistic studies of the photocatalytic oxidation of trichloroethylene with visible-light-driven N-doped TiO<sub>2</sub> photocatalysts,” *Chemistry*, vol. 12, no. 21, pp. 5526–5534, 2006.
- [20] S. Sato, R. Nakamura, and S. Abe, “Visible-light sensitization of TiO<sub>2</sub> photocatalysts by wet-method N doping,” *Applied Catalysis A*, vol. 284, no. 1-2, pp. 131–137, 2005.
- [21] C. Burda, Y. Lou, X. Chen, A. C. S. Samia, J. Stout, and J. L. Gole, “Enhanced nitrogen doping in TiO<sub>2</sub> nanoparticles,” *Nano Letters*, vol. 3, no. 8, pp. 1049–1051, 2003.
- [22] K. Yamada, H. Yamane, S. Matsushima et al., “Effect of thermal treatment on photocatalytic activity of N-doped TiO<sub>2</sub> particles under visible light,” *Thin Solid Films*, vol. 516, no. 21, pp. 7482–7487, 2008.
- [23] Z. Lin, A. Orlov, R. M. Lambert, and M. C. Payne, “New insights into the origin of visible light photocatalytic activity of nitrogen-doped and oxygen-deficient anatase TiO<sub>2</sub>,” *Journal of Physical Chemistry B*, vol. 109, no. 44, pp. 20948–20952, 2005.
- [24] S. Liu, J. Yu, and S. Mann, “Synergetic codoping in fluorinated Ti<sub>1-x</sub>Zr<sub>x</sub>O<sub>2</sub> hollow microspheres,” *Journal of Physical Chemistry C*, vol. 113, no. 24, pp. 10712–10717, 2009.
- [25] I. Shiyonovskaya and M. Hepel, “Decrease of recombination losses in bicomponent WO<sub>3</sub>/TiO<sub>2</sub> films photosensitized with cresyl violet and thionine,” *Journal of the Electrochemical Society*, vol. 145, no. 11, pp. 3981–3985, 1998.

## Research Article

# Enhanced Visible Light Photocatalytic Activity of Mesoporous Anatase TiO<sub>2</sub> Codoped with Nitrogen and Chlorine

Xiuwen Cheng,<sup>1,2,3</sup> Xiujuan Yu,<sup>1,2</sup> Zipeng Xing,<sup>1,2</sup> and Lisha Yang<sup>1,2</sup>

<sup>1</sup>Department of Environmental Science and Engineering, Heilongjiang University, Xuefu Road 74, Nangang District, Harbin 150080, China

<sup>2</sup>Key Laboratory of Chemical Engineering Process & Technology for High-Efficiency Conversion, College of Heilongjiang Province, Harbin 150080, China

<sup>3</sup>State Key Laboratory of Urban Water Resources and Environment (SKLUWRE), Department of Environmental Science and Engineering, Harbin Institute of Technology, Huanghe Road 73, Nangang District, Harbin 150090, China

Correspondence should be addressed to Xiujuan Yu, yuxjuan@hit.edu.cn

Received 26 November 2011; Revised 10 December 2011; Accepted 10 December 2011

Academic Editor: Jiaguo Yu

Copyright © 2012 Xiuwen Cheng et al. This is an open access article distributed under the Creative Commons Attribution License, which permits unrestricted use, distribution, and reproduction in any medium, provided the original work is properly cited.

Anatase mesoporous titanium dioxide codoped with nitrogen and chlorine (N-Cl-TiO<sub>2</sub>) photocatalysts were synthesized through simple one-step sol-gel reactions in the presence of ammonium chloride. The resulting materials were characterized by X-ray diffraction (XRD), transmission electron microscope (TEM), X-ray photoelectron spectroscopy (XPS), and ultraviolet-visible diffuse reflection spectrum (UV-vis DRS). XRD results indicated that codoping with nitrogen and chlorine could effectively retard the phase transformation of TiO<sub>2</sub> from anatase to rutile and the growth of the crystallite sizes. XPS revealed that nitrogen and chlorine elements were incorporated into the lattice of TiO<sub>2</sub> through substituting the lattice oxygen atoms. DRS exhibited that the light absorption of N-Cl-TiO<sub>2</sub> in visible region was greatly improved. As a result, the band gap of TiO<sub>2</sub> was reduced to 2.12 eV. The photocatalytic activity of the as-synthesized TiO<sub>2</sub> was evaluated for the degradation of RhB and phenol under visible light irradiation. It was found that N-Cl-TiO<sub>2</sub> catalyst exhibited higher visible light photocatalytic activity than that of P25 TiO<sub>2</sub> and N-TiO<sub>2</sub>, which was attributed to the small crystallite size, intense light absorption in visible region, and narrow band gap.

## 1. Introduction

Titanium dioxide (TiO<sub>2</sub>) is known as a semiconductor with various kinds of application in solar energy conversion, gas sensors, air purification, and waste water treatment due to its cheapness, nontoxicity, and strong oxidation power [1–6]. However, anatase TiO<sub>2</sub> can only be excited by UV light with wavelengths less than 388 nm, which only accounts for a small part of the solar spectrum [7]. In order to effectively extend the light absorption to visible region and enhance the photocatalytic activity, many attempts have been made, such as dye sensitization, noble metal deposition, coupling of TiO<sub>2</sub> with a narrow semiconductor and doping of TiO<sub>2</sub> with foreign ions. Among these, doping of TiO<sub>2</sub> with foreign ions has been an effective and feasible approach to improve the visible light response and photocatalytic activity [8–13]. Recently, many researches indicate that TiO<sub>2</sub> doping

with two different species into the lattice could further enhance the visible light photocatalytic activity. Sun et al. [14] synthesized C-S-codoped TiO<sub>2</sub> by the hydrolysis of tetrabutyl titanate in a mixed aqueous solution containing thiourea and urea. Lv et al. [15] prepared C-N-codoped TiO<sub>2</sub> nanoparticles with visible light photocatalytic activity. Xu and Zhang [16] reported an enhanced photocatalytic activity of the C-Cl-codoped TiO<sub>2</sub> powders towards the degradation of RhB under visible light irradiation. Although such reports demonstrated successful fabrication of relative high photocatalytic activity, they still suffered from some deficiencies due to the discharge of poisonous gases, troublesome procedure during the reaction process.

In this study, N-Cl-codoped TiO<sub>2</sub> photocatalyst (N-Cl-TiO<sub>2</sub>) has been synthesized through simple one-step sol-gel reactions in the presence of ammonium chloride. N and Cl elements were incorporated into the lattice of TiO<sub>2</sub> through

substituting the lattice oxygen atoms. As expected, the N-Cl-codoped TiO<sub>2</sub> catalyst exhibited higher visible light response and photocatalytic activity than that of P25 TiO<sub>2</sub> and N-TiO<sub>2</sub>. Further, the activity-enhanced mechanism was also discussed in detail.

## 2. Experimental

**2.1. Synthesis of Materials.** Typically, a solution consisting of 10 mL absolute EtOH, 12 mL dilute HNO<sub>3</sub> (1 : 5, volume ratio between HNO<sub>3</sub> and DI water), and the desired amount of ammonium chloride was added dropwise into a solution containing 40 mL absolute EtOH and 10 mL Ti(OBu)<sub>4</sub> within 120 min under vigorous stirring. After being aged for 6 h at room temperature, the TiO<sub>2</sub> precursor was received by drying the wet gel in an oven for 36 h. Finally, the N-Cl-codoped TiO<sub>2</sub> sample was obtained by calcining the precursor at 623 K for 4 h with a heating rate of 3 K·min<sup>-1</sup>. For comparison, pure TiO<sub>2</sub> and N-TiO<sub>2</sub> catalysts were synthesized as the reference according to the previous work of our groups [17].

**2.2. Characterization of Materials.** X-ray diffraction (XRD) patterns were collected on Model D/MAX-IIIIB diffractometer equipped with Cu K $\alpha$  radiation source ( $\lambda = 0.15406$  nm). An accelerating voltage of 40 kV and an emission current of 30 mA with a scanning rate of 5°·min<sup>-1</sup> were employed, respectively. Transmission electron microscopy (TEM) was taken on a JEOL JEM-2010 EX instrument operated at an accelerating voltage of 200 kV. High-resolution transmission electron micrograph (HRTEM) was obtained by employing a FEI TECNAI G2 S-TWIN with a 200 kV accelerating voltage. X-ray photoelectron spectroscopy (XPS) was performed on a Model PHI-5700 ESCA apparatus with Al K $\alpha$  X-ray source. All the binding energies (BE) were referenced with the adventitious carbon (binding energy = 284.6 eV). The ultraviolet-visible diffuse reflectance spectroscopy (UV-vis DRS) of the as-synthesized TiO<sub>2</sub> samples was recorded with a Model Shimadzu UV-2550 spectrophotometer.

**2.3. Evaluation of Photocatalytic Activity.** The experiments were carried out in a 100 mL quartz photochemical reactor and the visible light source was provided from a side of the reactor, by a 350 W Xe-arc lamp equipped with a UV-cutoff filter ( $\lambda > 420$  nm). In each run, 20 mg TiO<sub>2</sub> catalyst was added into 20 mL RhB solution of 10 mg·L<sup>-1</sup>. Prior to photoreaction, the solution was magnetically stirred in the dark for 30 min to establish the equilibrium of adsorption-desorption. At given time intervals, the samples after filtration and centrifugation were analyzed by a T6 UV-vis spectrometer. In addition, the photodegradation of uncolored phenol was similar to that of RhB, and the concentration was determined by the colorimetric method of 4-aminoantipyrine at the wavelength of 510 nm.

## 3. Results and Discussion

**3.1. XRD and TEM Analysis.** Figure 1 showed the XRD patterns of the pure and N-Cl-codoped TiO<sub>2</sub> samples. It can

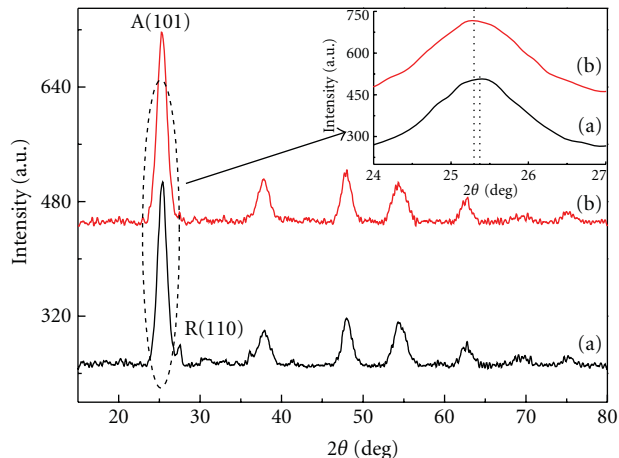


FIGURE 1: XRD patterns of pure (a) and N-Cl-doped (b) TiO<sub>2</sub> photocatalysts.

be seen that pure TiO<sub>2</sub> contained anatase (JCPDS. No 21–1272) and trace of rutile (JCPDS. No 21–1276). However, N-Cl-TiO<sub>2</sub> consisted of anatase as a unique phase (JCPDS. No 21–1272), indicating that codoping with nitrogen and chlorine could effectively retard the formation of rutile. In addition, no XRD peaks relate to the dopants were detected. One reason was that the concentration of the dopants was so low that it cannot be detected by XRD. The other was that the dopants were incorporated into the lattice of TiO<sub>2</sub> through substituting oxygen atoms or located in the interstitial sites. Further, as seen from the inset of Figure 1, the diffraction peak position of N-Cl-codoped TiO<sub>2</sub> shifted to lower angle in comparison with the pure TiO<sub>2</sub>, suggesting that oxygen atoms in the lattice of anatase in codoped TiO<sub>2</sub> sample may be substituted by the dopants. Further, the average crystallite sizes of the as-synthesized samples can be calculated by applying the Debye-Scherrer formula [18] on the anatase (101) diffraction peaks:

$$d = \frac{K\lambda}{\beta \cos \theta}, \quad (1)$$

where  $d$  is the crystallite size,  $\lambda$  is the wavelength of X-ray radiation (in our test,  $\lambda = 0.15418$  nm),  $K$  is a constant ( $K = 0.89$ ),  $\beta$  is the full width at half-maximum, and  $\theta$  is the diffraction angle. The calculated  $d$  values were 10 and 5 nm for pure and N-Cl-codoped TiO<sub>2</sub>, respectively. Thus, we can conclude that codoping with N and Cl elements could effectively retard the phase transformation of TiO<sub>2</sub> from anatase to rutile and growth of the crystallite size.

The crystal structure and grain size of N-Cl-codoped TiO<sub>2</sub> sample were also evaluated with TEM and HRTEM. Figure 2 showed the TEM and HRTEM images of mesoporous N-Cl-TiO<sub>2</sub> photocatalyst. As shown in Figure 2(a), many spherical aggregates of nanoparticles were observed with the nanoparticles at about 5~10 nm in crystallite sizes. However, an obvious agglomerative phenomenon was observed. As shown in Figure 2(b), the lattice fringes of nanocrystals revealed the lattice spacing of 0.352 nm, which

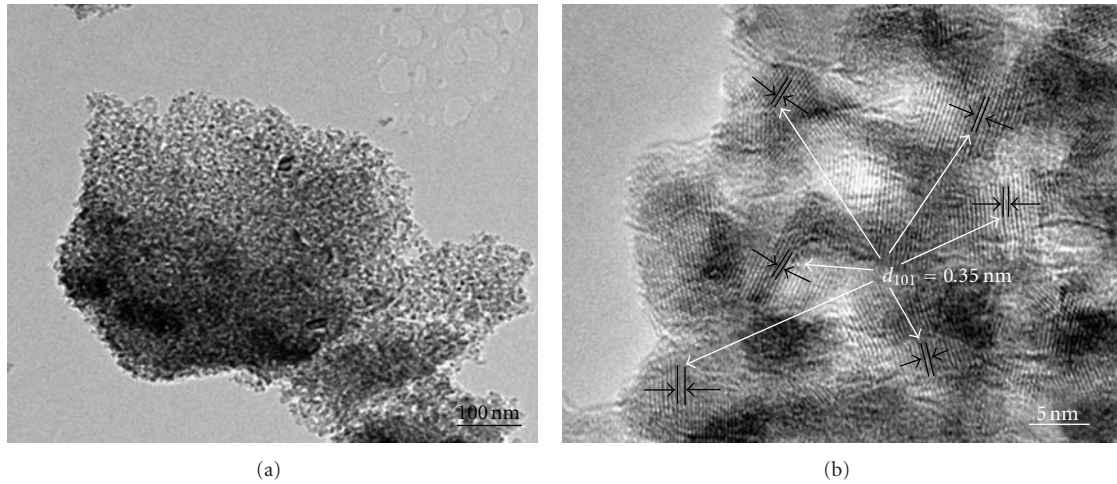


FIGURE 2: TEM (a) and HRTEM (b) images of N-Cl-codoped  $\text{TiO}_2$  photocatalyst.

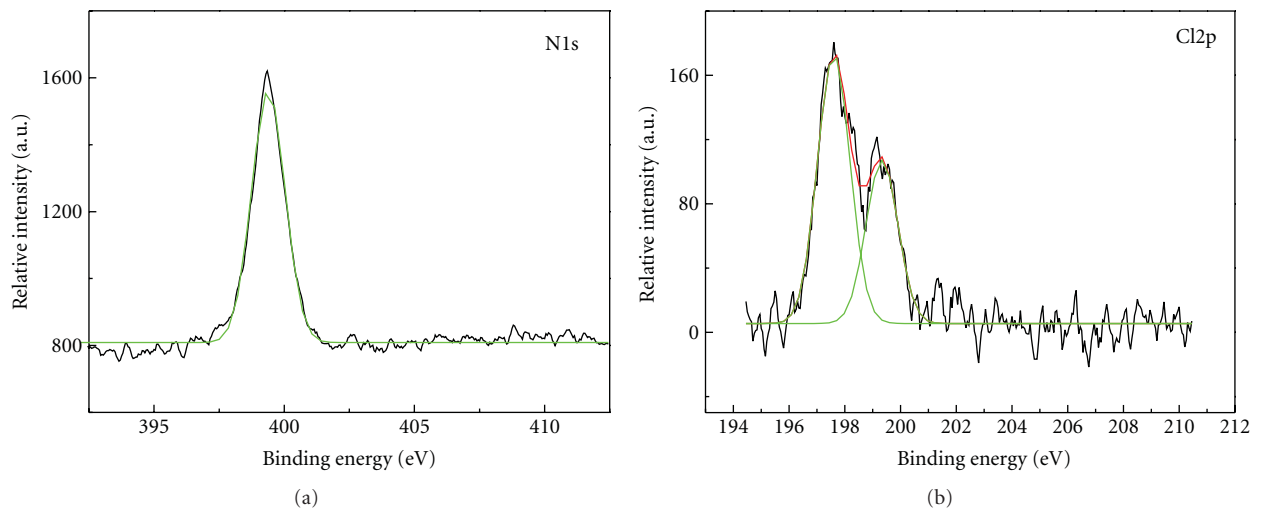


FIGURE 3: High-resolution XPS spectra of N1s (a) and Cl2p (b) for N-Cl-codoped  $\text{TiO}_2$  photocatalyst.

was in good accordance with the anatase (101) lattice fringes of 0.352 nm [19].

**3.2. XPS Analysis.** In order to investigate the chemical states of the N-Cl-codoped  $\text{TiO}_2$  sample, XPS was conducted and shown in Figure 3. As seen from Figure 3(a), a single peak at binding energy of 399.6 eV was observed, which was attributed to the presence of substitutional N in O-Ti-N bond [20, 21], indicating that some lattice oxygen were substituted by nitrogen atoms, which correlated with the visible light photocatalytic activity of doped  $\text{TiO}_2$ . As shown in Figure 3(b), two peaks at 197.7 and 199.3 eV seen from the Cl2p core-level XPS spectrum were observed. The strong peak at 197.7 eV was assigned to  $\text{Cl}^-$  ions physically adsorbed on the surface of codoped  $\text{TiO}_2$  [22], while the minor peak located at 199.3 eV might be assigned to the Cl incorporated into the lattice of  $\text{TiO}_2$  [16], indicating that nitrogen and chlorine were incorporated into the lattice of  $\text{TiO}_2$  through substituting the lattice oxygen atoms.

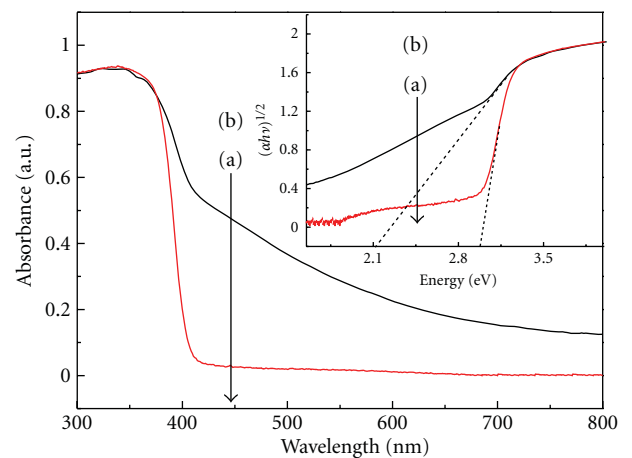


FIGURE 4: UV-vis DRS of the pure (a) and N-Cl-codoped (b)  $\text{TiO}_2$  photocatalysts.

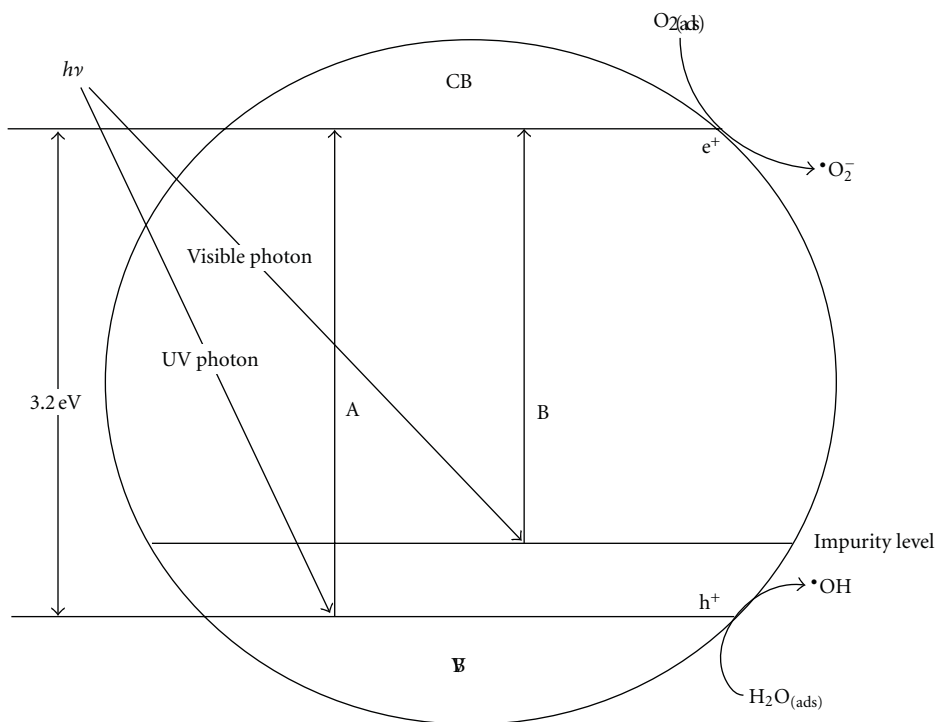


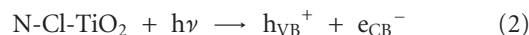
FIGURE 5: Scheme of photocatalytic mechanism of N-Cl-codoped-TiO<sub>2</sub> photocatalyst.

**3.3. DRS Analysis.** Generally speaking, narrower band gap of a semiconductor corresponds to a higher photocatalytic activity. In order to investigate the optical absorbance property of pure and N-Cl-codoped TiO<sub>2</sub> samples, ultraviolet-visible diffuse reflection spectra were conducted and shown in Figure 4. In addition, band gap energies were also calculated according to the Kubelka-Munk function [23], which was shown in the insert in Figure 4. Noticeably, both as-synthesized TiO<sub>2</sub> samples showed a typical absorbance spectrum with an intense transition in the UV region of the spectra, corresponding to the band gap energy of 3.2 eV from the intrinsic band gap of pure anatase. However, the light absorption edge of N-Cl-codoped TiO<sub>2</sub> sample was greatly red-shifted to the visible light region, demonstrating a decrease in the band gap energy, which was responsible for the impurity level (formed from hybridization of N2p and Cl2p levels) in the band gap of TiO<sub>2</sub>. After calculating, the band gap energy of N-Cl-codoped TiO<sub>2</sub> was 2.12 eV. As a result, the N-Cl-codoped TiO<sub>2</sub> should most probably possess excellent visible light photocatalytic activity for organic degradation.

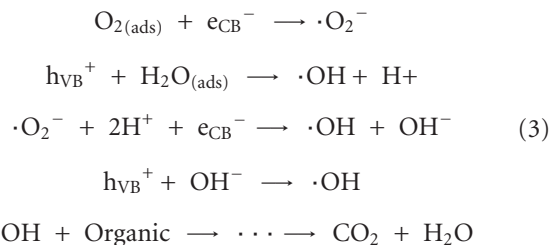
**3.4. Mechanism Analysis.** Based on the above analysis, a possible photocatalytic mechanism was proposed and shown in Figure 5. Nitrogen and chlorine were incorporated into the lattice of TiO<sub>2</sub> through substituting lattice oxygen atoms. Thus, a new impurity level was formed from the hybridization of N2p and Cl2p levels between the valence band and conduction band of TiO<sub>2</sub>. As shown in Figure 5, pure TiO<sub>2</sub> exhibited a relatively low visible photocatalytic activity for the degradation of pollutants due to its wide

band gap (3.2 eV, process A). After codoping with nitrogen and chlorine elements, electrons can be promoted from the impurity level to the conduction band of TiO<sub>2</sub> (process B), thereby enhancing the separation efficiency of photoinduced charge carriers. As a result, more departed photoinduced electrons and holes can participate in the photocatalytic reactions. Further, the process of visible light photocatalytic oxidation of phenol can be described as followed

Firstly, electrons and holes were generated under visible irradiation.



Then, the departed electrons and holes can react with the absorbed O<sub>2</sub> and H<sub>2</sub>O molecules, respectively, forming the main active species (such as ·O<sub>2</sub><sup>-</sup> and ·OH) responsible for the degradation of organic pollutants, such as RhB and phenol in our case. Eventually, organic pollutants were mineralized into small molecules, such as CO<sub>2</sub> and H<sub>2</sub>O



**3.5. Photocatalytic Activity.** The photocatalytic activities of the TiO<sub>2</sub> samples were evaluated by photocatalytic degradation of RhB and phenol under visible light irradiation.

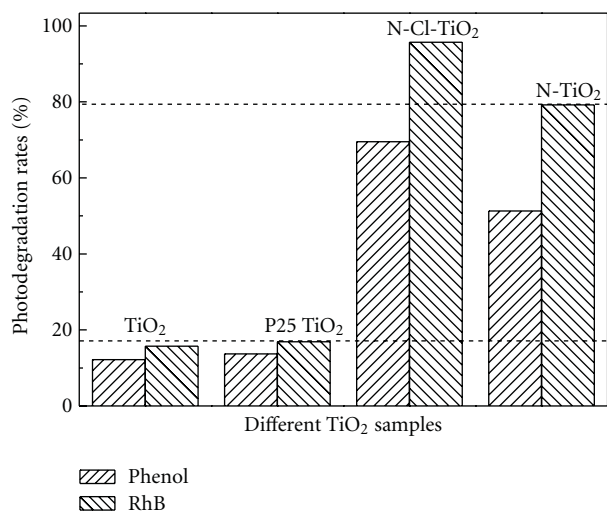


FIGURE 6: Photocatalytic degradation rates of RhB and phenol on different TiO<sub>2</sub> samples.

Figure 6 showed the photocatalytic degradation rates of RhB and phenol on different TiO<sub>2</sub> samples. As a comparison, the photocatalytic activity of P25 TiO<sub>2</sub> and N-TiO<sub>2</sub> was also measured and shown in Figure 6. As seen from Figure 6, N-Cl-codoped TiO<sub>2</sub> sample exhibited higher photocatalytic activities than that of P25 TiO<sub>2</sub> and N-TiO<sub>2</sub> catalysts, suggesting that the visible-induced photocatalytic reactions can contribute to the degradation of the colored RhB and uncolored phenol. Under the visible light irradiation for 120 min, 95.7% and 82% degradation rates could be achieved for colored RhB and uncolored phenol, respectively. The enhanced photocatalytic activity of N-Cl-codoped TiO<sub>2</sub> was attributed to the small crystallite size, intense light absorption in visible region, and narrow band gap energy.

#### 4. Conclusions

Based on the above analysis, the following conclusions can be drawn: (1) N-Cl-codoped TiO<sub>2</sub> catalyst with high visible light photocatalytic activity has been successfully synthesized through simple one-step sol-gel reactions in the presence of ammonium chloride. (2) TiO<sub>2</sub> codoping with N and Cl could effectively retard the phase transformation of TiO<sub>2</sub> from anatase to rutile and growth of crystallite size. (3) N and Cl elements were incorporated into the lattice of TiO<sub>2</sub> through substituting some oxygen atoms, which could form a new impurity level between the valence band and conduction band of TiO<sub>2</sub>. (4) Codoping with N and Cl could greatly improve the photoresponse of TiO<sub>2</sub>, thereby reducing the band gap. (5) The enhanced activity of N-Cl-codoped TiO<sub>2</sub> was mainly attributed to the small crystallize size, intense light absorption in visible region, and narrow band gap.

#### Acknowledgments

The authors wish to gratefully acknowledge the financial support by National Natural Science Foundation of China for

Youth (21106035) and Youth Scholar Backbone Supporting Plan Project for general colleges and universities of Heilongjiang province (1151G034).

#### References

- [1] J. Gamage and Z. Zhang, "Applications of photocatalytic disinfection," *International Journal of Photoenergy*, vol. 2010, Article ID 764870, 11 pages, 2010.
- [2] M. Grätzel, "Photoelectrochemical cells," *Nature*, vol. 414, no. 6861, pp. 338–344, 2001.
- [3] M. Andersson, L. Österlund, S. Ljungström, and A. Palmqvist, "Preparation of nanosize anatase and rutile TiO<sub>2</sub> by hydrothermal treatment of microemulsions and their activity for photocatalytic wet oxidation of phenol," *Journal of Physical Chemistry B*, vol. 106, no. 41, pp. 10674–10679, 2002.
- [4] J. Yu, L. Qi, and M. Jaroniec, "Hydrogen production by photocatalytic water splitting over Pt/TiO<sub>2</sub> nanosheets with exposed (001) facets," *Journal of Physical Chemistry C*, vol. 114, no. 30, pp. 13118–13125, 2010.
- [5] J. Anthony, P. A. Fernandez-Ibañez, P. S. M. Dunlop, D. M. A. Alrousan, and J. W. J. Hamilton, "Photocatalytic enhancement for solar disinfection of water: a review," *International Journal of Photoenergy*, vol. 2011, Article ID 798051, 12 pages, 2011.
- [6] Y. Zhu, J. Shi, Z. Zhang, C. Zhang, and X. Zhang, "Development of a gas sensor utilizing chemiluminescence on nanosized titanium dioxide," *Analytical Chemistry*, vol. 74, no. 1, pp. 120–124, 2002.
- [7] S.-K. Joung, T. Amemiya, M. Murabayashi, and K. Itoh, "Relation between photocatalytic activity and preparation conditions for nitrogen-doped visible light-driven TiO<sub>2</sub> photocatalysts," *Chemistry*, vol. 12, pp. 5526–5534, 2006.
- [8] A. Solbrand, A. Henningsson, S. Södergren, H. Lindström, A. Hagfeldt, and S. E. Lindquist, "Charge transport properties in dye-sensitized nanostructured TiO<sub>2</sub> thin film electrodes studied by photoinduced current transients," *Journal of Physical Chemistry B*, vol. 103, no. 7, pp. 1078–1083, 1999.
- [9] M. Zhou, J. Yu, and B. Cheng, "Effects of Fe-doping on the photocatalytic activity of mesoporous TiO<sub>2</sub> powders prepared by an ultrasonic method," *Journal of Hazardous Materials*, vol. 137, no. 3, pp. 1838–1847, 2006.
- [10] R. Asahi, T. Morikawa, T. Ohwaki, K. Aoki, and Y. Taga, "Visible-light photocatalysis in nitrogen-doped titanium oxides," *Science*, vol. 293, no. 5528, pp. 269–271, 2001.
- [11] M. Bowker, P. Stone, R. Bennett, and N. Perkins, "Formic acid adsorption and decomposition on TiO<sub>2</sub>(1 1 0) and on Pd/TiO<sub>2</sub>(1 1 0) model catalysts," *Surface Science*, vol. 511, no. 1-3, pp. 435–448, 2002.
- [12] J. Yu, Q. Xiang, and M. Zhou, "Preparation, characterization and visible-light-driven photocatalytic activity of Fe-doped titania nanorods and first-principles study for electronic structures," *Applied Catalysis B*, vol. 90, no. 3-4, pp. 595–602, 2009.
- [13] S. Kohtani, A. Kudo, and T. Sakata, "Spectral sensitization of a TiO<sub>2</sub> semiconductor electrode by CdS microcrystals and its photoelectrochemical properties," *Chemical Physics Letters*, vol. 206, no. 1-4, pp. 166–170, 1993.
- [14] H. Sun, Y. Bai, Y. Cheng, W. Jin, and N. Xu, "Preparation and characterization of visible-light-driven carbon—sulfur-codoped TiO<sub>2</sub> photocatalysts," *Industrial and Engineering Chemistry Research*, vol. 45, no. 14, pp. 4971–4976, 2006.

- [15] K. Lv, H. Zuo, J. Sun et al., "(Bi, C and N) codoped TiO<sub>2</sub> nanoparticles," *Journal of Hazardous Materials*, vol. 161, no. 1, pp. 396–401, 2009.
- [16] H. Xu and L. Zhang, "Controllable one-pot synthesis and enhanced visible light photocatalytic activity of tunable C-Cl-Codoped TiO<sub>2</sub> nanocrystals with high surface area," *Journal of Physical Chemistry C*, vol. 114, no. 2, pp. 940–946, 2010.
- [17] Y. Q. Wang, X. J. Yu, and D. Z. Sun, "Synthesis, characterization, and photocatalytic activity of TiO<sub>2</sub>-xNx nanocatalyst," *Journal of Hazardous Materials*, vol. 144, no. 1-2, pp. 328–333, 2007.
- [18] Q. Zhang, L. Gao, and J. Guo, "Effects of calcination on the photocatalytic properties of nanosized TiO<sub>2</sub> powders prepared by TiCl<sub>4</sub> hydrolysis," *Applied Catalysis B*, vol. 26, no. 3, pp. 207–215, 2000.
- [19] W. Zhou, F. Sun, K. Pan et al., "Well-ordered large-pore mesoporous anatase TiO<sub>2</sub> with remarkably high thermal stability and improved crystallinity: preparation, characterization, and photocatalytic performance," *Advanced Functional Materials*, vol. 21, no. 10, pp. 1922–1930, 2011.
- [20] J. H. Xu, J. Li, W. L. Dai, Y. Cao, H. Li, and K. Fan, "Simple fabrication of twist-like helix N,S-codoped titania photocatalyst with visible-light response," *Applied Catalysis B*, vol. 79, no. 1, pp. 72–80, 2008.
- [21] Y. Cong, J. Zhang, F. Chen, and M. Anpo, "Synthesis and characterization of nitrogen-doped TiO<sub>2</sub> nanophotocatalyst with high visible light activity," *Journal of Physical Chemistry C*, vol. 111, no. 19, pp. 6976–6982, 2007.
- [22] H. Xu and L. Zhang, "Selective nonaqueous synthesis of C-Cl-codoped TiO<sub>2</sub> with visible-light photocatalytic activity," *Journal of Physical Chemistry C*, vol. 114, no. 26, pp. 11534–11541, 2010.
- [23] F. Spadavecchia, G. Cappelletti, S. Ardizzone et al., "Solar photoactivity of nano-N-TiO<sub>2</sub> from tertiary amine: role of defects and paramagnetic species," *Applied Catalysis B*, vol. 96, no. 3-4, pp. 314–322, 2010.

## Research Article

# Enhanced Photocatalytic Activity of TiO<sub>2</sub> Powders (P25) via Calcination Treatment

Guohong Wang,<sup>1</sup> Lin Xu,<sup>1</sup> Jun Zhang,<sup>2</sup> Tingting Yin,<sup>1</sup> and Deyan Han<sup>1</sup>

<sup>1</sup> College of Chemistry and Environmental Engineering, Hubei Normal University, Huangshi, Hubei 435002, China

<sup>2</sup> State Key Laboratory of Advanced Technology for Material Synthesis and Processing, Wuhan University of Technology, Luoshi Road 122, Wuhan 430070, China

Correspondence should be addressed to Guohong Wang, wanggh2003@163.com

Received 14 September 2011; Revised 7 November 2011; Accepted 8 November 2011

Academic Editor: Jiaguo Yu

Copyright © 2012 Guohong Wang et al. This is an open access article distributed under the Creative Commons Attribution License, which permits unrestricted use, distribution, and reproduction in any medium, provided the original work is properly cited.

P25 TiO<sub>2</sub> powders were calcined at different temperatures in a muffle furnace in air. The P25 powders before and after calcination treatment were characterized with XRD FTIR, UV-visible diffuse reflectance spectra, SEM, TEM, HRTEM, and N<sub>2</sub> adsorption-desorption measurements. The photocatalytic activity was evaluated by the photocatalytic oxidation of methyl orange aqueous solution under UV light irradiation in air. The results showed that calcination treatment obviously influenced the microstructures and photocatalytic activity of the P25 TiO<sub>2</sub> powders. The synergistic effect of the phase structure, BET surface area, and crystallinity on the photocatalytic of TiO<sub>2</sub> powders (P25) after calcination was investigated. An optimal calcination temperature (500°C) was determined. The photocatalytic activity of TiO<sub>2</sub> powders calcined at 500°C was nearly 2 times higher than that of the uncalcined P25 TiO<sub>2</sub>. The highest photocatalytic activities of the calcined samples at 500°C for 4 h might be ascribed to the enhancement of anatase crystallization and the optimal mass ratio (ca. 1 : 2) of rutile to anatase.

## 1. Introduction

A number of investigations have focused on the semiconductor photocatalyst for its applications in solar energy conversion and environmental purification since Fujishima and Honda discovered the photocatalytic splitting of water on the TiO<sub>2</sub> electrodes in 1972 [1, 2]. Among various oxide semiconductor photocatalysts, titania has been proven to be the most suitable for widespread environmental applications for its biological and chemical inertness, strong oxidizing power, cost effectiveness, and long-term stability against photo- and chemical corrosion [3–6]. However, the practical applications of TiO<sub>2</sub> are greatly limited due to the wide band-gap (anatase ca. 3.2 eV, rutile ca. 3.0 eV) and the resultant low utilization of solar energy and fast recombination of photogenerated electrons and holes [7–9]. Therefore, the photocatalytic activity of titania must be further enhanced from the point of view of practical use and commerce. Many methods have been developed for enhancing the efficiency of the TiO<sub>2</sub> powders. These include doping with metal and nonmetal elements [10–13], dye sensitization [14, 15], and semiconductor coupling [16, 17], and so forth.

It is wellknown that the photocatalytic activity of TiO<sub>2</sub> system mainly depends on its intrinsic properties, such as phase structures, specific surface area, crystallinity, and preparing methods [18]. For example, many studies have confirmed that the anatase phase of titania is a good photocatalytic material due to its low recombination rate of photogenerated electrons and holes [19, 20]. In our previous observations, it was found that the composite of two phases of titania was more beneficial for suppressing the recombination of photogenerated electrons and holes and thus enhanced the photocatalytic activity [21]. In addition, a posttreatment condition is also another important factor that influences the photocatalytic activity of TiO<sub>2</sub> powders. Usually, two principle posttreatment methods have been used to control the physicochemical properties of the TiO<sub>2</sub> powders. One is hydrothermal treatment. Yu et al. [22] demonstrated an obvious increase of photocatalytic activity after hydrothermal treatment of TiO<sub>2</sub> (P25) and thought that the increase in photoactivity can be attributed to the formation of more hydroxyl groups in the surface of TiO<sub>2</sub>. Another method is calcination after treatment. By changing the calcination conditions, such as calcination temperatures,

calcination time, and heating rate crystalline products with different compositions, structures, and morphologies have been obtained. Yu et al. suggested that thermal treatment could allow more oxygen molecules to be adsorbed on the surface of TiO<sub>2</sub> [23]. Sato et al. and Zhang et al. thought that an enhancement in photocatalytic activity was ascribed to the fact that the calcination released lattice oxygen from TiO<sub>2</sub> [24, 25]. However, to the best of our knowledge, few studies have been carried out on the synergistic effect of the phase structure, BET surface area, and crystallinity on the photocatalytic of TiO<sub>2</sub> powders (P25) after calcination. In the present work, we prepared highly active TiO<sub>2</sub> powder photocatalyst via calcination after treatment of Degussa P25. The photocatalytic activity of the as-prepared TiO<sub>2</sub> powders was evaluated by the photocatalytic oxidation of methyl orange aqueous solution under UV light irradiation in air. The reasons for the enhanced photocatalytic activity of the calcinations-treated TiO<sub>2</sub> samples were discussed.

## 2. Experimental Section

**2.1. Sample Preparation.** Commercial Degussa P25 TiO<sub>2</sub> was used as supplied. In a typical calcination process, 1.0 g of P25 powder was transferred into a 30 mL crucible, followed by calcination at 400–800°C in a muffle furnace for 4 h. After the thermal treatment, the crucible containing catalysts was cooled to room temperature to obtain the as-synthesized TiO<sub>2</sub> powders. The calcined P25 and untreated Degussa P25 samples were characterized for evaluating the changes in properties.

**2.2. Characterization.** The X-ray diffraction (XRD) patterns obtained on an X-ray diffractometer (type D8 ADVANCE) using Cu-K $\alpha$  irradiation at a scan rate ( $2\theta$ ) of 0.02° s<sup>-1</sup> were used to determine the identity of any phase present and their crystallite size. The accelerating voltage and the applied current were 15 kV and 20 mA, respectively. If the sample contains anatase and rutile phases, the phase content of titania can be calculated from the integrated intensities of anatase (101) and rutile (110) peaks, according to the following equation [22]:

$$f_R = \frac{1.26 I_R}{I_A + 1.26 I_R}, \quad (1)$$

where  $I_A$  and  $I_R$  represent the integrated intensity of the anatase (101) and rutile (110) peaks, respectively. With (1), the phase contents of anatase and rutile in TiO<sub>2</sub> samples can be calculated. The average crystallite sizes of anatase and rutile were determined according to the Scherrer equation. Crystallite sizes and shapes were observed using transmission electron microscopy (TEM) and high-resolution transmission electron microscopy (HRTEM) (JEOL-2010F at 200 kV). The samples for TEM observation were prepared by dispersing the TiO<sub>2</sub> powders in an absolute ethanol solution under ultrasonic irradiation; the dispersion was then dropped on carbon-copper grids. The Brunauer-Emmett-Teller surface area ( $S_{\text{BET}}$ ) of the powders was analyzed by nitrogen adsorption in a Micromeritics ASAP 2020 nitrogen

adsorption apparatus (USA). All the samples were degassed at 180°C prior to nitrogen adsorption measurements. The BET surface area was determined by multipoint BET method using the adsorption data in the relative pressure ( $P/P_0$ ) range of 0.05–0.3. Desorption isotherm was used to determine the pore-size distribution via the Barret-Joyner-Halender (BJH) method, assuming a cylindrical pore modal [26–28]. The nitrogen adsorption volume at the relative pressure ( $P/P_0$ ) of 0.994 was used to determine the pore volume and average pore size. The morphologies of TiO<sub>2</sub> powders were observed using scanning electron microscopy (SEM) (type JSM-7001F, Japan) with an acceleration voltage of 20 kV. The UV-Vis spectra were obtained by an UV-Vis spectrophotometer (UV-2550, Shimadzu, Japan). Infrared (IR) spectra on pellets of the samples mixed with KBr were recorded on a Nicolet 5700 FTIR spectrometer at a resolution of 0.09 cm<sup>-1</sup>. The concentration of the samples was kept at about 0.25–0.3%.

**2.3. Measurement of Photocatalytic Activity.** The photocatalytic activity evaluation of TiO<sub>2</sub> powders for the photocatalytic decolorization of methyl orange aqueous solution was performed at ambient temperature. The detailed experimental process can be found in our previous studies [5]. The photocatalytic decolorization of methyl orange aqueous solution is a pseudo-first-order reaction and its kinetics may be expressed as  $\ln(c_0/c) = kt$ , where  $k$  is the apparent rate constant, and  $c_0$  and  $c$  are the adsorption-desorption equilibrium and reaction concentrations of aqueous methyl orange, respectively.

## 3. Results and Discussion

**3.1. Phase Structure.** The effect of calcination temperature on phase structures was studied using XRD. Figure 1 shows the XRD patterns of P25 powders before and after calcination at different temperatures for 4 h. It can be seen that all the samples were composed of both rutile and anatase phases. Further observation shows that with increasing calcination temperature from 400 to 500°C, the intensity of both anatase and rutile peaks gradually increases, indicating an enhancement of crystallization. With further increasing temperature from 600 to 800°C, the intensities of anatase diffraction peaks decreased gradually and ultimately disappeared, and meanwhile the intensities of rutile diffraction peaks steadily became stronger. Therefore, the calcination temperature obviously influences the crystallization and phase composition of the P25 powders. The effects of calcination temperatures on physical properties of P25 TiO<sub>2</sub> powders are shown in Table 1. It can be seen that the mass fraction of rutile phase slightly increases with increasing calcination temperature. Before calcination, the mass fraction of rutile was ca. 27.3%. At 700°C, the content of rutile reached ca. 90.8%. No anatase phase was detected at 800°C, which is in good agreement with results in the literature [29]. Therefore, it is reasonable to suggest that high calcination temperature results in the phase transformation from anatase to rutile. Usually, phase transformation is accompanied with crystal growth.

TABLE 1: Effect of temperature on physicochemical properties of TiO<sub>2</sub> samples.

Temperature (°C)	<sup>a</sup> Phase content (%)	<sup>b</sup> Crystalline size (nm)	<sup>c</sup> S <sub>BET</sub> (m <sup>2</sup> /g)	<sup>d</sup> Pore volume (cm <sup>3</sup> /g)	Average pore size (nm)	<sup>e</sup> Porosity (%)
P25	A: 72.7; R: 27.3	29.5	45.7	0.177	7.57	41.5
400	A: 72.7; R: 27.3	31.7	25.9	0.0929	8.24	27.1
500	A: 66.4; R: 33.6	33.8	22.7	0.0597	10.7	19.4
600	A: 55.2; R: 44.8	48.6	18.7	0.0503	10.5	17.0
700	A: 9.8; R: 90.2	63.2	8.59	0.0177	14.4	7.00
800	R: 100	99.0	4.39	0.00831	15.5	3.45

Calcination time: 4 h

<sup>a</sup>A and R denote anatase and rutile, respectively. <sup>b</sup>Average crystalline size of TiO<sub>2</sub> was determined by XRD using Scherrer equation. <sup>c</sup>The BET surface area was determined by multipoint BET method using the adsorption data in  $P/P_0$  range from 0.05 to 0.3. <sup>d</sup>Pore volume and average pore size were determined by nitrogen adsorption volume at  $P/P_0 = 0.994$ . <sup>e</sup>The porosity is estimated from the pore volume determined using the desorption data at  $P/P_0 = 0.994$ .

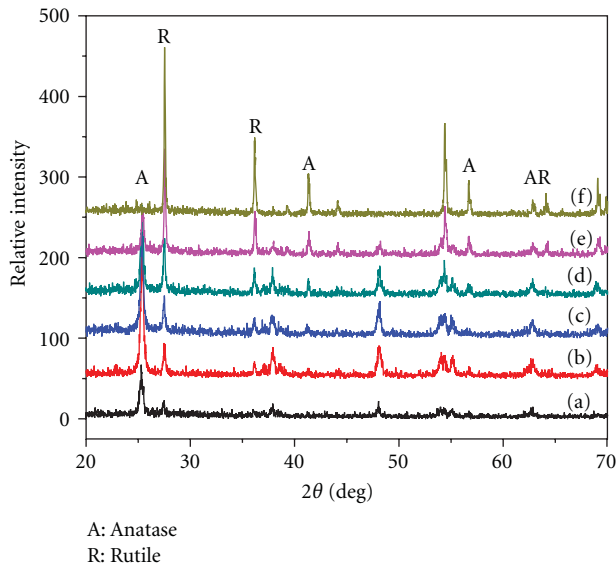


FIGURE 1: XRD patterns of P25 samples before (a) and after calcination at 400 (b), 500 (c), 600 (d), 700 (e), and 800°C (f) for 4 h.

As the calcination temperature is raised, XRD reflections corresponding to both the anatase and rutile phase become narrower, which indicates the increase of crystallite size. The average crystallite size was shown in Table 1. The average crystallite size of samples treated at lower temperature (below 500°C) increased slightly from about 29.5 to 33.8 nm (see Table 1). However, higher temperature caused rapid increase of crystallite size up to about 63.2 and 99 nm for samples calcined at 700 and 800°C, respectively. The similar results were observed by Górska et al. [30] for five different samples of TiO<sub>2</sub> calcinated at 400–750°C.

3.2. FT-IR. The preparation methods and conditions could affect the hydroxylation state of titania powders. The FT-IR spectroscopy of the P25 before and after calcination

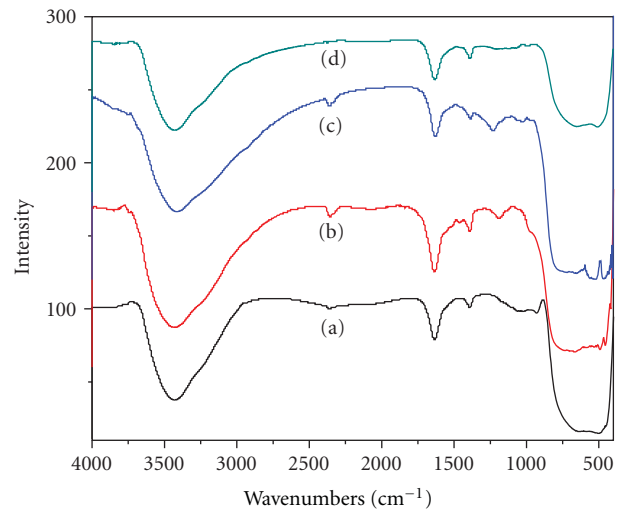


FIGURE 2: FT-IR spectra of the P25 powders before (a) and after calcination at 400 (b), 500 (c), and 600°C (d) for 4 h.

treatment of 4 h is shown in Figure 2. It is believed that the broad peak at 3400 and the peak at 1650 cm<sup>-1</sup> correspond to the surface-adsorbed water and hydroxyl groups, respectively. The main peak at 400–700 cm<sup>-1</sup> was attributed to Ti-O stretching and Ti-O-Ti bridging stretching modes [31]. Notably, with increasing temperature, the surface-adsorbed water and hydroxyl groups decreased slightly. This was due to the decrease of specific surface areas and pore volume (as shown in Table 1), which caused the reduction of the adsorbed water [32]. According to our previous study, the hydroxyl groups on the surface of samples contribute to enhancement of the photocatalytic activity [33], because they can interact with photogenerated holes, which gives better charge transfer and inhibits the recombination of electron-hole pairs [34, 35].

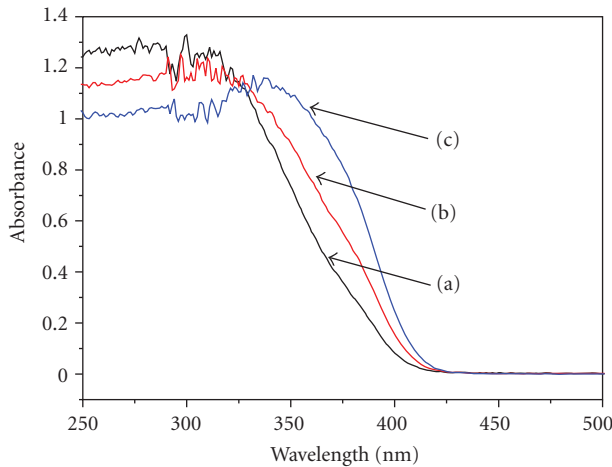


FIGURE 3: UV-Vis absorption spectra of P25 powders before (a) and after calcination at 500 (b), and 700°C (c) for 4 h.

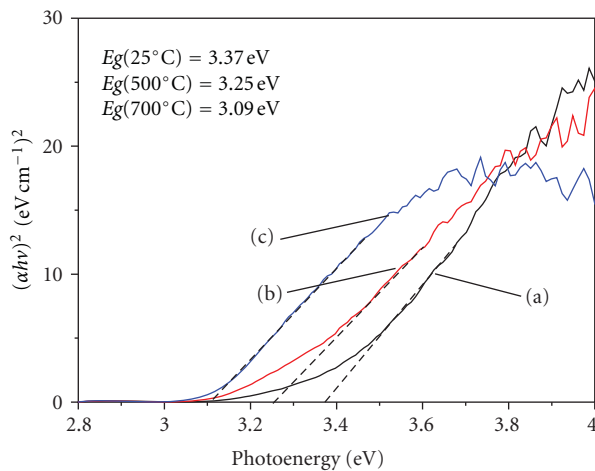


FIGURE 4: Plots of  $(h\nu\alpha)^2$  versus photon energy for the P25 powders before (a) and after calcination at 500 (b), and 700°C (c) for 4 h.

**3.3. UV-Vis Spectra.** Usually, calcination temperature obviously affects light absorption characteristics of  $\text{TiO}_2$  [36–38]. The influences of temperature on the light absorption characteristics of  $\text{TiO}_2$  powders are shown in Figure 3. A significant increase at wavelengths shorter than 420 nm could be attributed to absorption of light caused by the excitation of electrons from the valence band to the conduction band of  $\text{TiO}_2$ . A red shift of the absorbance spectra of  $\text{TiO}_2$  powders calcined at 500 and 700°C in the band gap transition was observed as compared with the uncalcined P25 powders. The differences in adsorption were attributed to the change of crystallite size and phase structure (see Table 1).

The adsorption edges shifted toward longer wavelengths for the powders after calcination at 500 and 700°C. This clearly indicated a decrease in the band gap energy of  $\text{TiO}_2$ . To further explore the effect of calcination temperature on the absorption edge, the band gap energy can be estimated from a plot of  $(h\nu\alpha)^{1/2}$  versus photon energy ( $h\nu$ ). The intercept of the tangent to the plot will give a good approximation of the indirect band gap energy for  $\text{TiO}_2$ . The relation

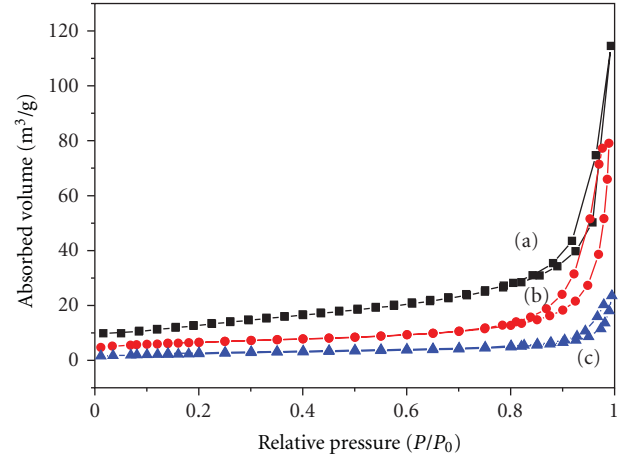


FIGURE 5: Nitrogen adsorption-desorption isotherms of the P25 powders before (a) and after calcination at 500 (b) and 700°C (c) for 4 h.

between the absorption coefficient ( $\alpha$ ) and incident photon energy ( $h\nu$ ) can be written as  $\alpha = B_i(h\nu - E_g)^{1/2}/h\nu$ , where  $B_i$  is absorption constants for indirect transitions [39–41]. Since absorbance ( $A$ ) is proportional to absorption coefficient ( $\alpha$ ), we use absorbance ( $A$ ) to substitute absorption coefficient ( $\alpha$ ) [40].

Plots of  $(h\nu\alpha)^2$  versus photon energy ( $h\nu$ ) for  $\text{TiO}_2$  powders are shown in Figure 4. The band gap energies estimated from the intercept of the tangents of the plots are 3.37, 3.25, and 3.10 eV for the P25 powders before and after calcination at 500 and 700°C for 4 h, respectively. This showed that the band gap of  $\text{TiO}_2$  samples monotonically became narrower with increasing calcinations temperatures. This may be due to the following factors: (1) an increase in the crystallite size resulted in the decrease of band gap energy, which was in accordance with previous results reported by Xiao et al. [42]; (2) lower value of band gap for samples after calcination at 500 and 700°C may be a result of phase transformation from anatase to rutile [30].

**3.4. BET Surface Areas and Pore Distribution.** Figure 5 shows nitrogen adsorption-desorption isotherms of the P25 powders before and after calcination at 500 and 700°C. It can be seen that all the samples show a type H3 hysteresis according to BDDT classification [26], indicating the presence of mesopores (2–50 nm). Moreover, the observed hysteresis approaches to  $P/P_0 = 1$ , suggesting the presence of large pores (>50 nm) [43, 44]. Further observation indicates that with increasing calcination temperature, the hysteresis loops shift to higher relative pressure range and the areas of the hysteresis loops decrease. This indicated that the average pore size increased and the volume of pore decreased with increasing calcination temperatures [45]. When the calcination temperature is higher than 700°C, the hysteresis loops of the obtained samples are difficult to be observed (not shown in Figure 5), indicating that some pores collapse during the calcination. The pore size distribution calculated from the desorption branch of the isotherm is presented

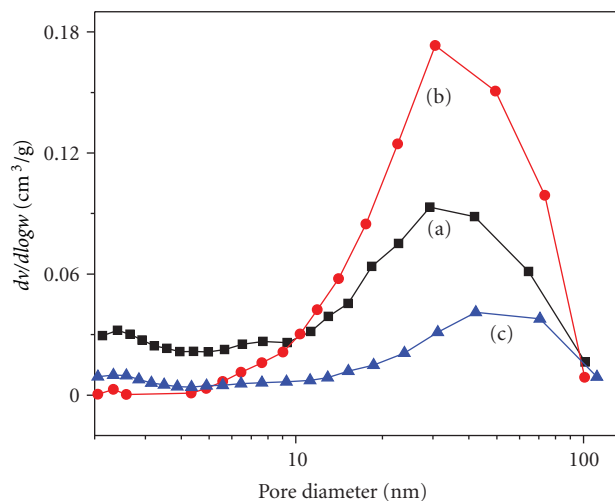


FIGURE 6: Pore diameter distribution curves of the P25 powders before (a) and after calcination at 500 (b) and 700°C (c) for 4 h.

in Figure 6. It can be seen that calcination temperature significantly influences the pore size distribution of the TiO<sub>2</sub> powders. Before calcination, the P25 TiO<sub>2</sub> has a wide pore size distribution from mesopore to macropore. With increasing calcination temperatures, the curves of the pore size distribution shift to the macropore region and the pore volumes decrease slowly. At 700°C, the pore size distribution becomes even, indicating the disappearance of pores [6]. Usually, the average pore size is connected with the TiO<sub>2</sub> crystallite size and the average pore size increased with an increase in the crystallite size of TiO<sub>2</sub> powders [21, 22, 46, 47]. Accordingly, the decrease of pore volume located at 2–10 nm for the calcined P25 powders indicated the decrease of smaller TiO<sub>2</sub> crystallites (<10 nm). This is in good agreement with the XRD analysis in which smaller anatase crystallites were transformed into rutile phase. Table 1 shows the physical properties of the P25 powders before and after calcination treatment at different temperatures for 4 h. Before calcination treatment, P25 TiO<sub>2</sub> shows a large BET-specific surface area, and its value reaches 45.7 m<sup>2</sup>/g. After calcination treatment above 400°C, the BET-specific surface areas of the P25 samples clearly decrease. Further observation shows that with increasing calcination temperatures, the BET-specific surface areas, pore volumes, and porosity steadily decrease; meantime, the average pore size increases.

**3.5. SEM and TEM.** The calcination process also affects the morphologies of the resulting P25 TiO<sub>2</sub> powders. Figure 7 shows SEM images of the P25 TiO<sub>2</sub> powders before and after calcination treatment at 400, 500, and 700°C for 4 h. It can be seen from Figure 7(a) that before calcination treatment, the powders are smaller aggregated particles, resulting in a high porous volume due to aggregation among tiny TiO<sub>2</sub> particles (see Figure 6). Conversely, after calcination treatment, the powders are composed of larger agglomerated particles. This may be caused by the phase transformation from anatase to rutile, resulting in the decrease in the pore volume (as shown

in Table 1). It is interesting to observe from Figure 7 that with increasing calcination temperature from 400 to 700°C, the particle sizes of the aggregates gradually increase. This may be ascribed to the fact that the interaction of smaller particles results in their aggregation into many spherical particles with bigger sizes. The morphology and microstructures of P25 TiO<sub>2</sub> powders are further investigated by TEM and HRTEM analysis. Figure 8(a) shows a typical TEM image of the TiO<sub>2</sub> powders after calcination at 500°C for 4 h. It can be seen that the particles exhibit a relatively uniform particle size distribution. The average size of the primary particles estimated from the TEM image is about 35 nm, which is in good agreement with that calculated from the XRD pattern using Scherrer equation (33.8 nm). Further observation indicates that a large number of mesopores come from the aggregation of primary particles or crystallites. Figure 8(b) presents a typical HRTEM lattice image of the TiO<sub>2</sub> nanoparticles after calcination at 500°C for 4 h. The selected area electron diffraction (SAED) patterns (inset in Figure 8(b)) reveal the polycrystalline nature of the anatase and rutile phases for the P25 TiO<sub>2</sub> powders. By measuring the lattice fringes, the resolved interplanar distances are ca. 0.35 and 0.33 nm, corresponding to the (101) planes of anatase and the (110) planes of rutile, respectively. This further confirms the mixed biphasic structures of the sample after calcination at 500°C for 4 h.

**3.6. Photocatalytic Activity.** The photocatalytic activity of the P25 TiO<sub>2</sub> before and after calcination at various temperatures was evaluated by photocatalytic oxidation of methyl orange (MO) aqueous solution under UV light irradiation in air. Figure 9 shows the relationship between the apparent rate constants (*k*) of MO degradation and calcination temperatures. Prior to calcination, the P25 TiO<sub>2</sub> showed high photocatalytic activity with a rate constant of  $6.02 \times 10^{-3}$ , which is a well known and recognized as an excellent photocatalyst. It has been reported that the P25 TiO<sub>2</sub> photocatalyst consists of an amorphous state together with a mixture of anatase and rutile [48]. Further observation indicates that the calcined sample at 400°C for 4 h shows a higher photocatalytic activity with a rate constant of  $10.2 \times 10^{-3}$ . This may be due to the fact calcination treatment enhanced the phase transformation of the P25 TiO<sub>2</sub> powders from amorphous to anatase. The rate constants increase with increasing calcination temperatures. The enhancement of photocatalytic activity at elevated calcination temperatures can be ascribed to an obvious improvement in anatase crystallinity (as shown in Figure 1). At 500°C, the *k* reaches the highest value of  $12.1 \times 10^{-3}$ . With further increasing the calcination temperature, the *k* decreases slightly. This is due to the decrease in specific surface areas and the content of anatase (as shown in Table 1). The highest photocatalytic activities of the calcined samples at 500°C might be explained by the optimal mass ratio of rutile to anatase.

Generally, photocatalytic activity of mesoporous TiO<sub>2</sub> is strongly dependent on its phase structure, crystallite size, surface areas, and pore structure. Larger specific surface area allows more organic reactants to be absorbed onto the surface of the photocatalyst, while higher pore volume results

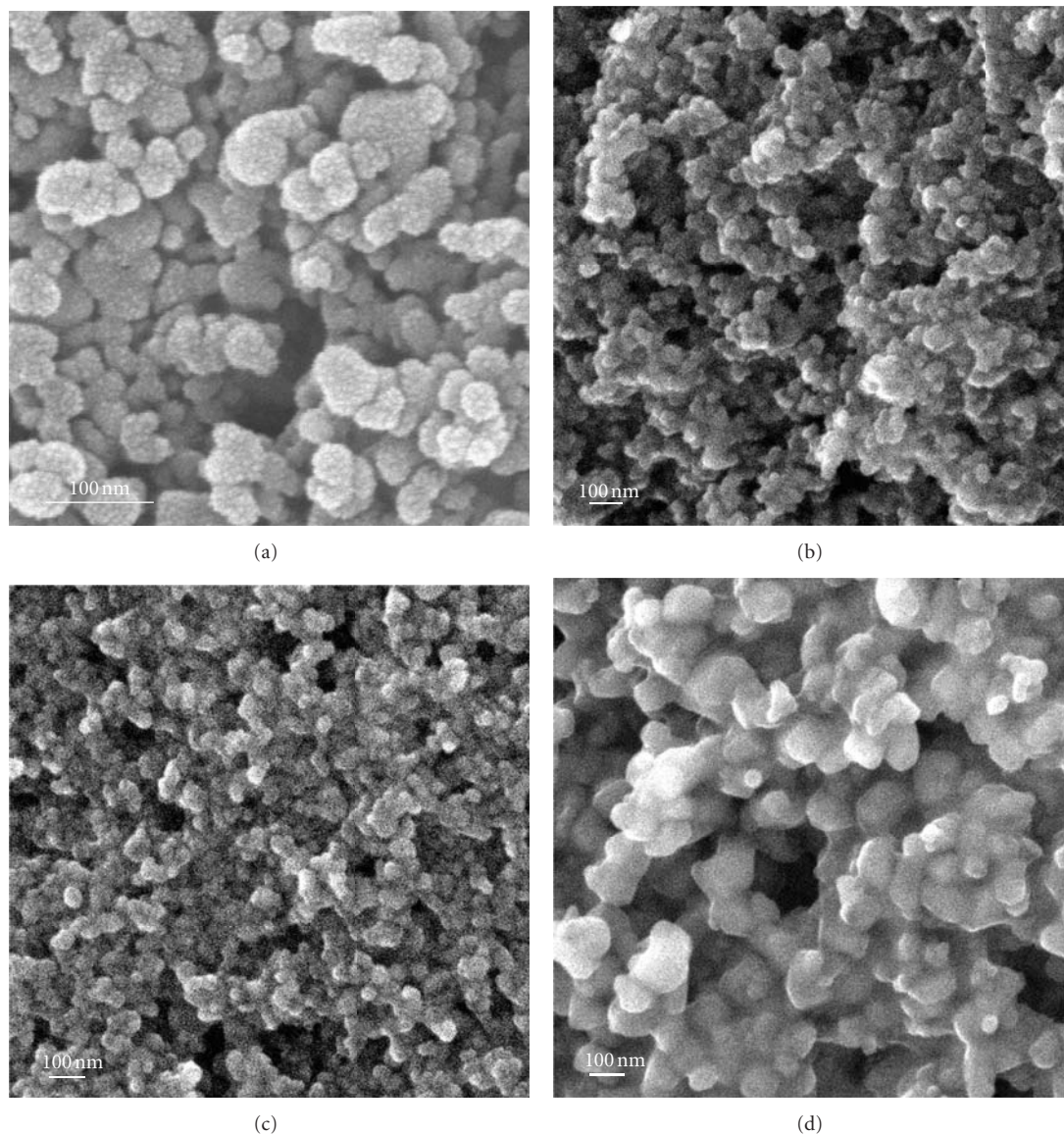


FIGURE 7: SEM images of the P25 powders before (a) and after calcined at 400 (b), 500 (c), and 700°C (d) for 4 h.

in a rapider diffusion of various inorganic products during the photocatalytic reaction. Therefore, it is expected that the uncalcined sample exhibits a relative high photocatalytic activity due to its large specific surface areas and pore volume. However, the powders with a large surface area are usually associated with large amounts of crystalline defects or weak crystallization, which favor the recombination of photogenerated electrons and holes, leading to a poor photoactivity. Therefore, the large surface area is a requirement, but not a decisive factor. It is well known that the mixture of anatase and rutile  $\text{TiO}_2$  has higher degradation efficiency than pure anatase for the oxidation of various organic compounds [48–50]. Moreover, the content of rutile has played important role in photocatalytic reaction. For example, Bacsa et al. found that the catalyst with 30% rutile content showed a maximum catalytic activity for the

photocatalyzed degradation of *p*-coumaric acid [51]. It was reported the  $\text{TiO}_2$  powders containing 77% anatase and 23% rutile had highest photocatalytic activity in degradation of 4-chlorophenol [52]. Thus, the mass ratio of rutile to anatase is another important factor that influences the photocatalytic efficiency [53, 54]. In our present work, the uncalcined P25 powders possess a large specific surface area of  $45.7 \text{ m}^2/\text{g}$ . After calcination at 500°C, the specific surface areas decrease to  $22.7 \text{ m}^2/\text{g}$ . Such a large decrease in specific surface area should lead to a decrease in the photocatalytic activity. However, the 500°C sample shows the highest photocatalytic activity. The increase of photocatalytic activity at 500°C might be due to the enhancement of anatase crystallization and increase of rutile content in photocatalysts (as shown in Figure 1 and Table 1). The former is beneficial to reduce the recombination rate of the photogenerated electrons and

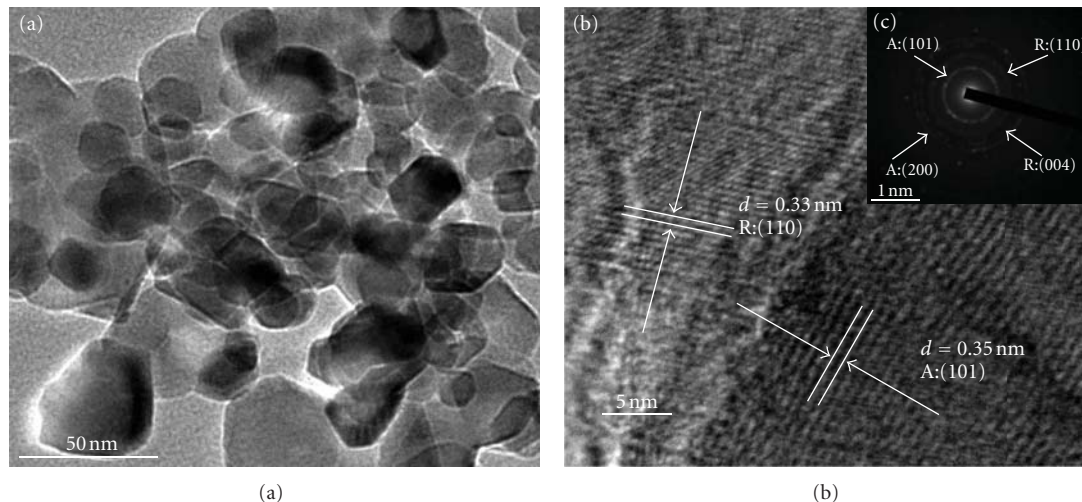


FIGURE 8: TEM (a) and HRTEM (b) images and SAED pattern (inset in (b)) of the  $\text{TiO}_2$  samples calcined at  $500^\circ\text{C}$  for 4 h.

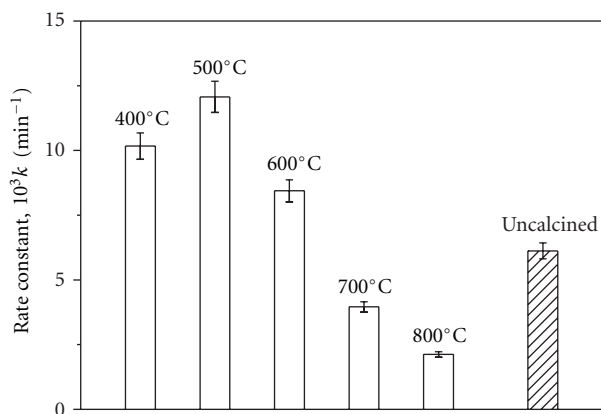


FIGURE 9: Effects of calcination temperatures on the apparent rate constants of the P25 powders.

holes due to the decrease in number of the defects. The latter can enhance the transfer and separation of photogenerated electrons and holes, implying that the mass ratio of rutile to anatase also obviously influences photocatalytic activity and an optimal rutile-to-anatase mass ratio is probably ca. 1 : 2 according to our results. According to the aforementioned deduction, it is not difficult to explain that the 700 and 800°C samples show a lower photocatalytic activity than the 500°C sample due to the increase of rutile content in photocatalysts.

#### 4. Conclusion

Calcination treatment exhibits a marked influence on the microstructures and photocatalytic activity of the P25  $\text{TiO}_2$  powders. With increasing calcination temperature, the average crystallite size, average pore size, and rutile content increase. In contrast, the BET-specific surface areas, pore volumes, and porosity steadily decrease. The synergistic effect of the phase structure, BET surface area, and crystallinity on the

photocatalytic of  $\text{TiO}_2$  powders (P25) after calcination was investigated. An optimal calcination temperature ( $500^\circ\text{C}$ ) was determined. The photocatalytic activity of  $\text{TiO}_2$  powders at an optimal calcination temperature was nearly 2 times higher than that of the uncalcined P25  $\text{TiO}_2$ . The highest photocatalytic activities of the calcined samples at  $500^\circ\text{C}$  for 4 h might be ascribed to the enhancement of anatase crystallization and the optimal mass ratio (ca. 1 : 2) of rutile to anatase.

#### Acknowledgments

This work was partially supported by NSFC (21075030, 51072154, and 51102190) and the Mid-young Scholars' Science and Technology Programs, Hubei Provincial Department of Education (Q20082202).

#### References

- [1] A. Fujishima and K. Honda, "Electrochemical photolysis of water at a semiconductor electrode," *Nature*, vol. 238, no. 5358, pp. 37–38, 1972.
- [2] S. W. Liu, J. G. Yu, and M. Jaroniec, "Anatase  $\text{TiO}_2$  with dominant high-energy {001} facets: synthesis, properties, and applications," *Chemistry of Materials*, vol. 23, no. 18, pp. 4085–4093, 2011.
- [3] A. Yu, G. Q. M. Lu, J. Drennan, and I. R. Gentle, "Tubular titania nanostructures via layer-by-layer self-assembly," *Advanced Functional Materials*, vol. 17, no. 14, pp. 2600–2605, 2007.
- [4] Q. J. Xiang, J. G. Yu, and P. K. Wong, "Quantitative characterization of hydroxyl radicals produced by various photocatalysts," *Journal of Colloid and Interface Science*, vol. 357, no. 1, pp. 163–167, 2011.
- [5] J. G. Yu, H. G. Yu, B. Cheng, X. J. Zhao, J. C. Yu, and W. K. Ho, "The effect of calcination temperature on the surface microstructure and photocatalytic activity of  $\text{TiO}_2$  thin films prepared by liquid phase deposition," *Journal of Physical Chemistry B*, vol. 107, no. 50, pp. 13871–13879, 2003.
- [6] J. G. Yu, J. F. Xiong, B. Cheng, and S. W. Liu, "Fabrication and characterization of Ag- $\text{TiO}_2$  multiphase nanocomposite thin

- films with enhanced photocatalytic activity," *Applied Catalysis B: Environmental*, vol. 60, no. 3-4, pp. 211–221, 2005.
- [7] Y. Z. Fan, G. P. Chen, D. M. Li et al., "Highly selective dehydrochlorination of Rhodamine B on TiO<sub>2</sub> prepared in supercritical fluids," *International Journal of Photoenergy*, vol. 2012, Article ID 173865, 7 pages, 2012.
- [8] N. H. Lee, H. J. Oh, S. C. Jung, W. J. Lee, D. H. Kim, and S. J. Kim, "Photocatalytic properties of nanotubular-shaped TiO<sub>2</sub> powders with anatase phase obtained from titanate nanotube powder through various thermal treatments," *International Journal of Photoenergy*, vol. 2011, Article ID 327821, 7 pages, 2011.
- [9] J. A. Byrne, P. A. Fernandez, P. S. M. Dunlop, D. M. A. Alrousan, and J. W. J. Hamilton, "Photocatalytic enhancement for solar disinfection of water: a review," *International Journal of Photoenergy*, vol. 2011, Article ID 798051, 12 pages, 2011.
- [10] L. C. Kong, G. T. Duan, G. M. Zuo, W. Cai, and Z. Cheng, "Rattle-type Au@TiO<sub>2</sub> hollow microspheres with multiple nanocores and porous shells and their structurally enhanced catalysis," *Materials Chemistry and Physics*, vol. 123, no. 2-3, pp. 421–426, 2010.
- [11] V. Rodríguez-González, S. O. Alfaro, L. M. Torres-Martínez, S. H. Cho, and S. W. Lee, "Silver-TiO<sub>2</sub> nanocomposites: synthesis and harmful algae bloom UV-photoelimination," *Applied Catalysis B: Environmental*, vol. 98, no. 3-4, pp. 229–234, 2010.
- [12] L. Ravichandran, K. Selvam, and M. Swaminathan, "Highly efficient activated carbon loaded TiO<sub>2</sub> for photo defluoridation of pentafluorobenzoic acid," *Journal of Molecular Catalysis A: Chemical*, vol. 317, no. 1-2, pp. 89–96, 2010.
- [13] J. G. Yu, T. T. Ma, and S. W. Liu, "Enhanced photocatalytic activity of mesoporous TiO<sub>2</sub> aggregates by embedding carbon nanotubes as electron-transfer channel," *Physical Chemistry Chemical Physics*, vol. 13, no. 8, pp. 3491–3501, 2011.
- [14] S. Pavasupree, Y. Suzuki, S. Yoshikawa, and R. Kawahata, "Synthesis of titanate, TiO<sub>2</sub> (B), and anatase TiO<sub>2</sub> nanofibers from natural rutile sand," *Journal of Solid State Chemistry*, vol. 178, no. 10, pp. 3110–3116, 2005.
- [15] Y. Q. Gai, J. B. Li, S. S. Li, J. B. Xia, and S. H. Wei, "Design of narrow-gap TiO<sub>2</sub>: a passivated codoping approach for enhanced photoelectrochemical activity," *Physical Review Letters*, vol. 102, no. 3, Article ID 036402, 4 pages, 2009.
- [16] M. L. Chen and W. C. Oh, "The improved photocatalytic properties of methylene blue for V<sub>2</sub>O<sub>3</sub>/CNT/TiO<sub>2</sub> composite under visible light," *International Journal of Photoenergy*, vol. 2010, Article ID 264831, 5 pages, 2010.
- [17] L. Zhao, J. R. Ran, Z. Shu, G. Dai, P. C. Zhai, and S. M. Wang, "Effects of calcination temperatures on photocatalytic activity of ordered titanate nanoribbon/SnO<sub>2</sub> films fabricated during an EPD process," *International Journal of Photoenergy*, vol. 2012, Article ID 472958, 7 pages, 2012.
- [18] X. Qin, L. Q. Jing, G. H. Tian, Y. Qu, and Y. Feng, "Enhanced photocatalytic activity for degrading Rhodamine B solution of commercial Degussa P25 TiO<sub>2</sub> and its mechanisms," *Journal of Hazardous Materials*, vol. 172, no. 2-3, pp. 1168–1174, 2009.
- [19] C. Deiana, E. Fois, S. Coluccia, and G. Martra, "Surface structure of TiO<sub>2</sub> P25 nanoparticles: infrared study of hydroxy groups on coordinative defect sites," *Journal of Physical Chemistry C*, vol. 114, no. 49, pp. 21531–21538, 2010.
- [20] A. I. Kontos, I. M. Arabatzis, D. S. Tsoukleris et al., "Efficient photocatalysts by hydrothermal treatment of TiO<sub>2</sub>," *Catalysis Today*, vol. 101, no. 3-4, pp. 275–281, 2005.
- [21] J. G. Yu and G. H. Wang, "Hydrothermal synthesis and photocatalytic activity of mesoporous titania hollow microspheres," *Journal of Physics and Chemistry of Solids*, vol. 69, no. 5-6, pp. 1147–1151, 2008.
- [22] J. G. Yu, H. G. Yu, B. Cheng, M. Zhou, and X. Zhao, "Enhanced photocatalytic activity of TiO<sub>2</sub> powder (P25) by hydrothermal treatment," *Journal of Molecular Catalysis A: Chemical*, vol. 253, no. 1-2, pp. 112–118, 2006.
- [23] J. C. Yu, J. Lin, D. Lo, and S. K. Lam, "Influence of thermal treatment on the adsorption of oxygen and photocatalytic activity of TiO<sub>2</sub>," *Langmuir*, vol. 16, no. 18, pp. 7304–7308, 2000.
- [24] S. Sato, T. Kadowaki, and K. Yamaguti, "Photocatalytic oxygen isotopic exchange between oxygen molecule and the lattice oxygen of TiO<sub>2</sub> prepared from titanium hydroxide," *Journal of Physical Chemistry*, vol. 88, no. 14, pp. 2930–2931, 1984.
- [25] M. Zhang, Q. Wang, C. C. Chen, L. Zang, W. Ma, and J. Zhao, "Oxygen atom transfer in the photocatalytic oxidation of alcohols by TiO<sub>2</sub>: oxygen isotope studies," *Angewandte Chemie—International Edition*, vol. 48, no. 33, pp. 6081–6084, 2009.
- [26] K. S. W. Sing, D. H. Everett, R. A. W. Haul et al., "Reporting physisorption data for gas/solid systems with special reference to the determination of surface area and porosity," *Pure and Applied Chemistry*, vol. 57, no. 4, pp. 603–619, 1985.
- [27] J. G. Yu, T. T. Ma, G. Liu, and B. Cheng, "Enhanced photocatalytic activity of bimodal mesoporous titania powders by C<sub>60</sub> modification," *Dalton Transactions*, vol. 40, no. 25, pp. 6635–6644, 2011.
- [28] P. Madhusudan, J. R. Ran, J. Zhang, J. Yu, and G. Liu, "Novel urea assisted hydrothermal synthesis of hierarchical BiVO<sub>4</sub>/Bi<sub>2</sub>O<sub>3</sub>CO<sub>3</sub> nanocomposites with enhanced visible-light photocatalytic activity," *Applied Catalysis B: Environmental*, vol. 110, pp. 286–295, 2011.
- [29] J. G. Yu, Y. R. Su, and B. Cheng, "Template-free fabrication and enhanced photocatalytic activity of hierarchical macro-/mesoporous titania," *Advanced Functional Materials*, vol. 17, no. 12, pp. 1984–1990, 2007.
- [30] P. Górska, A. Zaleska, E. Kowalska et al., "TiO<sub>2</sub> photoactivity in vis and UV light: the influence of calcination temperature and surface properties," *Applied Catalysis B: Environmental*, vol. 84, no. 3-4, pp. 440–447, 2008.
- [31] J. G. Yu, Y. R. Su, B. Cheng, and M. Zhou, "Effects of pH on the microstructures and photocatalytic activity of mesoporous nanocrystalline titania powders prepared via hydrothermal method," *Journal of Molecular Catalysis A: Chemical*, vol. 258, no. 1-2, pp. 104–112, 2006.
- [32] J. G. Yu and H. G. Yu, "Facile synthesis and characterization of novel nanocomposites of titanate nanotubes and rutile nanocrystals," *Materials Chemistry and Physics*, vol. 100, no. 2-3, pp. 507–512, 2006.
- [33] J. G. Yu, G. H. Wang, B. Cheng, and M. Zhou, "Effects of hydrothermal temperature and time on the photocatalytic activity and microstructures of bimodal mesoporous TiO<sub>2</sub> powders," *Applied Catalysis B: Environmental*, vol. 69, no. 3-4, pp. 171–180, 2007.
- [34] P. Du, A. Bueno-López, M. Verbaas et al., "The effect of surface OH-population on the photocatalytic activity of rare earth-doped P25-TiO<sub>2</sub> in methylene blue degradation," *Journal of Catalysis*, vol. 260, no. 1, pp. 75–80, 2008.
- [35] Y. H. Ao, J. J. Xu, and D. G. Fu, "Study on the effect of different acids on the structure and photocatalytic activity of mesoporous titania," *Applied Surface Science*, vol. 256, no. 1, pp. 239–245, 2009.

- [36] J. G. Yu, M. H. Zhou, B. Cheng, and X. Zhao, "Preparation, characterization and photocatalytic activity of in situ N, S-codoped TiO<sub>2</sub> powders," *Journal of Molecular Catalysis A: Chemical*, vol. 246, no. 1-2, pp. 176–184, 2006.
- [37] M. H. Zhou, J. G. Yu, S. W. Liu, P. C. Zhai, and L. Jiang, "Effects of calcination temperatures on photocatalytic activity of SnO<sub>2</sub>/TiO<sub>2</sub> composite films prepared by an EPD method," *Journal of Hazardous Materials*, vol. 154, no. 1–3, pp. 1141–1148, 2008.
- [38] J. W. Shi, S. H. Chen, S. M. Wang, Z. L. Ye, P. Wu, and B. Xu, "Favorable recycling photocatalyst TiO<sub>2</sub>/CFA: effects of calcination temperature on the structural property and photocatalytic activity," *Journal of Molecular Catalysis A: Chemical*, vol. 330, no. 1-2, pp. 41–48, 2010.
- [39] K. N. P. Kumar, J. Kumar, and K. Keizer, "Effect of peptization on densification and phase-transformation behavior of sol-gel-derived nanostructured titania," *Journal of the American Ceramic Society*, vol. 77, no. 5, pp. 1396–1400, 1994.
- [40] N. Serpone, D. Lawless, and R. Khairutdinov, "Size effects on the photophysical properties of colloidal anatase TiO<sub>2</sub> particles: size quantization versus direct transitions in this indirect semiconductor?" *Journal of Physical Chemistry*, vol. 99, no. 45, pp. 16646–16654, 1995.
- [41] H. G. Yu, J. G. Yu, B. Cheng, and M. Zhou, "Effects of hydrothermal post-treatment on microstructures and morphology of titanate nanoribbons," *Journal of Solid State Chemistry*, vol. 179, no. 2, pp. 349–354, 2006.
- [42] Q. Xiao and L. L. Ouyang, "Photocatalytic activity and hydroxyl radical formation of carbon-doped TiO<sub>2</sub> nanocrystalline: effect of calcination temperature," *Chemical Engineering Journal*, vol. 148, no. 2-3, pp. 248–253, 2009.
- [43] J. G. Yu and J. G. Ran, "Facile preparation and enhanced photocatalytic H<sub>2</sub>-production activity of Cu(OH)<sub>2</sub> cluster modified TiO<sub>2</sub>," *Energy & Environmental Science*, vol. 4, no. 4, pp. 1364–1371, 2011.
- [44] C. C. Tsai and H. Teng, "Regulation of the physical characteristics of titania nanotube aggregates synthesized from hydrothermal treatment," *Chemistry of Materials*, vol. 16, no. 22, pp. 4352–4358, 2004.
- [45] J. G. Yu, J. C. Yu, M. K. P. Leung et al., "Effects of acidic and basic hydrolysis catalysts on the photocatalytic activity and microstructures of bimodal mesoporous titania," *Journal of Catalysis*, vol. 217, no. 1, pp. 69–78, 2003.
- [46] Q. J. Xiang, K. L. Lv, and J. G. Yu, "Pivotal role of fluorine in enhanced photocatalytic activity of anatase TiO<sub>2</sub> nanosheets with dominant (001) facets for the photocatalytic degradation of acetone in air," *Applied Catalysis B: Environmental*, vol. 96, no. 3-4, pp. 557–564, 2010.
- [47] S. W. Liu, J. G. Yu, and M. Jaroniec, "Tunable photocatalytic selectivity of hollow TiO<sub>2</sub> microspheres composed of anatase polyhedra with exposed {001} facets," *Journal of the American Chemical Society*, vol. 132, no. 34, pp. 11914–11916, 2010.
- [48] D. C. Hurum, A. G. Agrios, K. A. Gray, T. Rajh, and M. C. Thurnauer, "Explaining the enhanced photocatalytic activity of Degussa P25 mixed-phase TiO<sub>2</sub> using EPR," *Journal of Physical Chemistry B*, vol. 107, no. 19, pp. 4545–4549, 2003.
- [49] J. G. Yu, L. J. Zhang, B. Cheng, and Y. Su, "Hydrothermal preparation and photocatalytic activity of hierarchically sponge-like macro-/mesoporous titania," *Journal of Physical Chemistry C*, vol. 111, no. 28, pp. 10582–10589, 2007.
- [50] N. R. C. Fernandes Machado and V. S. Santana, "Influence of thermal treatment on the structure and photocatalytic activity of TiO<sub>2</sub> P25," *Catalysis Today*, vol. 107-108, pp. 595–601, 2005.
- [51] R. R. Bacsa and J. Kiwi, "Effect of rutile phase on the photocatalytic properties of nanocrystalline titania during the degradation of p-coumaric acid," *Applied Catalysis B: Environmental*, vol. 16, no. 1, pp. 19–29, 1998.
- [52] S. Bakardjieva, J. Šubrt, V. Štengl, M. J. Dianez, and M. J. Sayagues, "Photoactivity of anatase-rutile TiO<sub>2</sub> nanocrystalline mixtures obtained by heat treatment of homogeneously precipitated anatase," *Applied Catalysis B: Environmental*, vol. 58, no. 3-4, pp. 193–202, 2005.
- [53] J. G. Yu and B. Wang, "Effect of calcination temperature on morphology and photoelectrochemical properties of anodized titanium dioxide nanotube arrays," *Applied Catalysis B: Environmental*, vol. 94, no. 3-4, pp. 295–302, 2010.
- [54] K. L. Lv, Q. J. Xiang, and J. G. Yu, "Effect of calcination temperature on morphology and photocatalytic activity of anatase TiO<sub>2</sub> nanosheets with exposed {001} facets," *Applied Catalysis B: Environmental*, vol. 104, no. 3-4, pp. 275–281, 2011.

## Research Article

# The Photocatalytic Inactivation Effect of Fe-Doped TiO<sub>2</sub> Nanocomposites on Leukemic HL60 Cells-Based Photodynamic Therapy

Kangqiang Huang,<sup>1</sup> Li Chen,<sup>2</sup> Meixiang Liao,<sup>3</sup> and Jianwen Xiong<sup>1</sup>

<sup>1</sup>Laboratory of Quantum Information Technology, School of Physics and Telecommunication Engineering, South China Normal University, Guangzhou 510006, China

<sup>2</sup>Department of Physics and Optoelectronic Engineering, Guangdong University of Technology, Guangzhou 510006, China

<sup>3</sup>School of Physics and Engineering, Sun Yat-sen University, Guangzhou 510275, China

Correspondence should be addressed to Jianwen Xiong, jwxiong@scnu.edu.cn

Received 7 October 2011; Revised 6 December 2011; Accepted 6 December 2011

Academic Editor: Jiaguo Yu

Copyright © 2012 Kangqiang Huang et al. This is an open access article distributed under the Creative Commons Attribution License, which permits unrestricted use, distribution, and reproduction in any medium, provided the original work is properly cited.

The Fe-doped TiO<sub>2</sub> nanocomposites synthesized by a deposition-precipitation method were characterized by X-ray diffraction (XRD), transmission electron microscope (TEM), X-ray photoelectron spectroscopy (XPS), and UV-vis adsorption spectra and then were taken as a new “photosensitizer” for photodynamic therapy (PDT). The photocatalytic inactivation of Fe-doped TiO<sub>2</sub> on Leukemic HL60 cells was investigated using PDT reaction chamber based on LED light source, and the viability of HL60 cells was examined by Cell Counting Kit-8 (CCK-8) assay. The experimental results showed that the growth of leukemic HL60 cells was significantly inhibited by adding TiO<sub>2</sub> nanoparticles, and the inactivation efficiency could be effectively enhanced by the surface modification of TiO<sub>2</sub> nanoparticles with Fe doping. Furthermore, the optimized conditions were achieved at 5 wt% Fe/TiO<sub>2</sub> at a final concentration of 200 μg/mL, in which up to 82.5% PDT efficiency for the HL60 cells can be obtained under the irradiation of 403 nm light (the power density is 5 mW/cm<sup>2</sup>) within 60 minutes.

## 1. Introduction

Photodynamic therapy (PDT) is a new technique for cancer treatment. It takes advantage of the selective accumulation of photosensitizers, which accumulate in tumor tissues and produce singlet oxygen to inactivate the tumor cells through series of the photochemical reactions or photobiological reactions at a specific light wavelength within the absorption spectra of the photosensitizer, to achieve local treatment purposes [1]. In PDT, light, oxygen, and photosensitizer are combined to produce a selective therapeutic effect in the target tissue [2, 3]. Among these three agents, photosensitizer, as the energy carrier and the interaction bridge, is playing an important role in tumor treatment [1, 4]. However, tumors in human body with varying degrees of depth the application of traditional photosensitizers is restricted because of their inherent properties. Therefore, seeking

for a high-performance photosensitizer and improving the existing properties of photosensitizer have become the main focus of PDT study.

Compared to other semiconductor oxides, TiO<sub>2</sub> has been widely used and proved to be an important potential photosensitizer because of their unique physical and biological properties [5–7], such as photostable, inexpensive, nontoxic properties, and it has high oxidative power, no secondary pollution. Moreover, with the rapidly development of nanotechnology, nanoparticles have shown a wide range of potential applications in biological and biomedical fields [8–11]. TiO<sub>2</sub> nanoparticles as an anticancer drug or used for energy transfer material to improve the traditional photodynamic effect have been noticed [12–15]. Nevertheless, the electron-hole pairs of TiO<sub>2</sub> can be formed only under ultraviolet light. Additionally, the photogenerated holes are easy to recombine with the photoinduced electrons, which

greatly reduce the photocatalytic inactivation efficiency of TiO<sub>2</sub> nanoparticles and hinder its practical applications [16–19]. Fortunately, it has been demonstrated that the photocatalytic efficiency and the visible light absorption of TiO<sub>2</sub> can be effectively improved by the method of transition metal doping [20–23].

In this paper, nanoparticles of TiO<sub>2</sub> and Fe-doped TiO<sub>2</sub> were used as a photosensitizer to kill cancer cells. Up to our knowledge, there still no previous report on the study of photocatalytic inactivation effects of Fe/TiO<sub>2</sub> on HL60 cells. Our experimental results show that the photocatalytic inactivation efficiency on human HL60 cancer cells could be greatly enhanced by the Fe modification of TiO<sub>2</sub> nanoparticles, which have not only significantly improved the selective inactivation of tumor cells *in vitro* and accurate PDT dosimetry, but also have potential clinical applications when TiO<sub>2</sub> nanoparticles are used as a photosensitizer or energy transferor in photodynamic therapy.

## 2. Materials and Methods

**2.1. Chemicals and Apparatus.** HL60 cells were kindly provided by the Department of Medicine of Sun Yat-sen University in China. The TiO<sub>2</sub> nanoparticles, Fe/TiO<sub>2</sub> (2%) and Fe/TiO<sub>2</sub> (5%) nanocomposites, 5-aminolevulinic acid (ALA) and phosphate buffered saline (PBS) were purchased from Sigma (USA). The Cell Counting Kit-8 (CCK-8) was purchased from Dojindo (Japan). RPMI medium 1640 and foetal calf serum (FCS) were obtained from Gibco BRL (USA). All chemicals used were of the highest purity commercially available. The stock solutions of the compounds were prepared in serum-free medium immediately before using in experiments.

These apparatus, including D8 Focus X-ray diffraction (XRD) (Bruker, Germany), AXIS Ultra X-ray photoelectron spectroscopy (XPS) (Kratos, UK), U-3010 UV-visible spectrophotometer (Hitachi, Japan), JEM-2100HR transmission electron microscope (TEM, Japan), HH.CP-TW80 CO<sub>2</sub> incubator, DG5031 ELISA reader, XDS-1A inverted microscope, PDT reaction chamber, 96-well plates, cell count board, and so on were used in this research.

**2.2. Light Source.** To reach a high efficiency of PDT, An in-house built lamp with many high-power light-emitting diodes (LEDs), emitting light in the visible-light region 400–410 nm and with a peak at 403 nm, was taken as light sources in the experiments. The fluence rate at the position of the sample was 5 mW/cm<sup>2</sup> as measured with a photodiode. As shown in Figure 1, the blue LEDs can better meet the needs of PDT experiments.

**2.3. Preparation of TiO<sub>2</sub> Nanoparticles and Fe-Doped TiO<sub>2</sub> Nanocomposites Solutions.** The pure TiO<sub>2</sub> nanoparticles, 2 wt% Fe/TiO<sub>2</sub> and 5 wt% Fe/TiO<sub>2</sub> nanocomposites, were synthesized using the deposition-precipitation method. Firstly, Ti(SO<sub>4</sub>)<sub>2</sub> (6 g), neopelex (DBS, 0.18 g), CO(NH<sub>2</sub>)<sub>2</sub> (32 g), definite volumes of doubly distilled water (250 mL), absolute ethyl alcohol (0.25 mL), and 98% H<sub>2</sub>SO<sub>4</sub> were

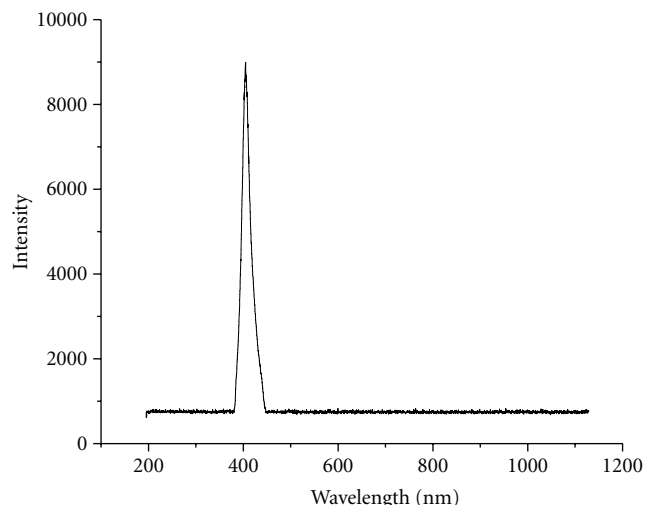


FIGURE 1: The emission spectra of the blue LEDs.

mixed with appropriate amount of Fe<sub>2</sub>(SO<sub>4</sub>)<sub>3</sub> (0 g, 0.1 g, 0.5 g resp.) to make up the reaction liquid, which then would be treated in water bath at 80°C under vigorous stirring for 2 to 3 hours at pH 8. Afterwards, the reactant was transferred from the water bath to be deposited for 24 h. The third process was the washing and filtering, SO<sub>4</sub><sup>2-</sup> and DBS were removed by washing with deionized water. BaCl<sub>2</sub> solution was employed to check whether SO<sub>4</sub><sup>2-</sup> exists. The formatting of BaSO<sub>4</sub> white sediment indicated more washing was needed. The resulting precipitates were washed again with ethyl before dehydration, drying in the dry-box for 3 h. Finally, The Fe-doped TiO<sub>2</sub> was obtained after calcined at 400°C for 30 min and grinded for 15 min.

The prepared nanoparticles were encapsulated in three bottles, respectively. Subsequently, they were placed in YX-280B-type pressure steam sterilizer with a high temperature and high pressure (120°C, 1.5 atm) to sterilize for 30 minutes. Finally, an appropriate amount of culture medium was added to fully dissolve the nanoparticles. All solutions were filtered through a 0.22 μm membrane filter and stored in the dark at 4°C before taken into the experiments.

**2.4. Cell Culture.** Human leukemia HL60 cells were cultured in RPMI 1640 medium supplemented with 10% fetal bovine serum (FBS) in a humidified incubator with 5% CO<sub>2</sub> at 37°C until confluent. All experiments were performed using cells during the logarithmic growth phase. The cell concentration was measured using a cell count board and the cell density was adjusted to the required final concentration.

**2.5. Cell Viability Assay.** There are many ways to check the cell viability. The method of CCK-8 (Cell Counting Kit-8), which is much simpler, more sensitive, and reproducible than the traditional method of MTT [24], was used to detect the activation of cell during the experiment. CCK-8 assay based on the ability of a mitochondrial dehydrogenase enzyme from viable cells contains WST-8, which can be reduced to

a highly water-soluble yellow-colored formazan dye by dehydrogenase in the presence of an electron carrier (1-methoxy PMS). The number of surviving cells is directly proportional to the level of the formazan product created. The amount of formazan dye can be reflected by the absorbance at 450 nm. Therefore, the characteristic of CCK-8 can be used directly for cell proliferation and toxicity analysis.

**2.6. Experimental Design.** Firstly, 96-well plates were divided into several parts according to experimental needs (including the control groups and zero groups). Three repeated wells were set under the same experimental conditions. Secondly, HL60 cells in logarithmic growth phase were seeded in 96-well plates, afterwards the prepared solutions of TiO<sub>2</sub>, Fe/TiO<sub>2</sub> (2%), Fe/TiO<sub>2</sub> (5%) at various concentrations were added in the appropriate samples respectively, and each well was infused with an appropriate volume of cell culture medium to ensure that the final volume was 200 μL, while the zero pores contain only 200 μL of culture medium. Thirdly, light exposure was carried out immediately after 4 h incubation (The average fluence rate used was 5 mW/cm<sup>2</sup>, the irradiation dose was 18 J/cm<sup>2</sup>). After that, 20 μL of solution was added to each well and incubated for other 4 hours. Finally, the OD values of the samples were detected by the ELISA reader based on dual-wavelength method (the test wavelength at 450 nm and reference wavelength at 630 nm). Three parallel tests were performed for each sample to ensure accuracy.

**2.7. Statistical Analysis.** Data are presented as means ± S.D. (standard deviation) from at least three independent experiments. Statistical analysis was then performed using the statistical software SPSS11.5, Values of  $P < 0.05$  were considered statistically significant.

### 3. Results and Discussion

#### 3.1. Characterization of Fe-TiO<sub>2</sub> Nanocomposites

**3.1.1. X-Ray Diffraction.** The crystallite size is calculated by the Scherrer formula [25]:

$$D = \frac{K\lambda}{\beta \cos \theta}, \quad (1)$$

where  $D$  is the crystalline size,  $\lambda$  is the X-ray wavelength (0.1541 nm),  $K$  is the constant usually taken as 0.89,  $\theta$  is the Bragg's angle  $2\theta = 25.3^\circ$  for anatase phase titania, and  $\beta$  is the pure full width of the diffraction line at half of the maximum intensity. According to the above formula, it is estimated that the average particle sizes are 20.2 nm, 19.8 nm, 17.2 nm for pure TiO<sub>2</sub>, 2 wt% Fe-doped TiO<sub>2</sub>, and 5 wt% Fe-doped TiO<sub>2</sub>, respectively. Apparently, the incorporation of Fe into TiO<sub>2</sub> could effectively inhibit the crystal grain growth of TiO<sub>2</sub>, leading to smaller particle.

XRD was also used to further examine the average crystalline properties of the Fe-doped TiO<sub>2</sub>. As shown in Figure 2, the XRD diffraction peaks of the synthesized Fe-doped samples around  $2\theta$  of 25.26°, 37.73°, 48.28°, 54.36°,

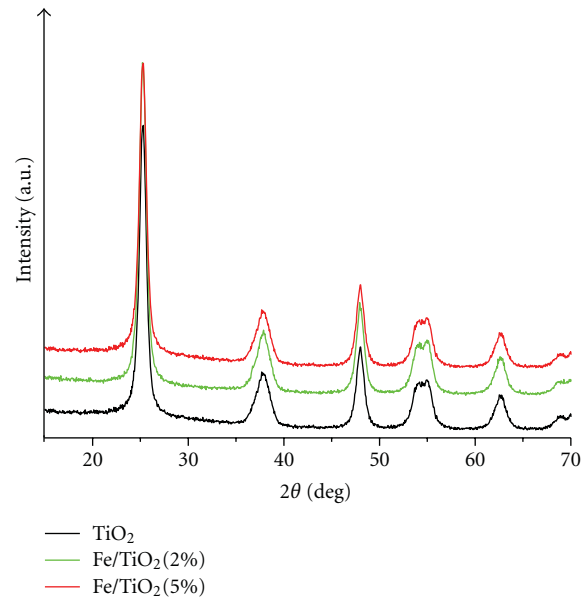


FIGURE 2: The XRD patterns of TiO<sub>2</sub> nanoparticles and Fe-doped TiO<sub>2</sub> nanocomposites calcined at 400°C.

56.43°, 62.17°, which could be indexed to the characteristic peaks (1 0 1), (0 0 4), (2 0 0), (1 0 5), (2 1 1), and (2 0 4) of anatase TiO<sub>2</sub>. Thus, the Fe-doped TiO<sub>2</sub> nanocomposites obtained by the deposition-precipitation method have primarily the anatase phase. Furthermore, it is demonstrated that the diffraction peaks of Fe-doped TiO<sub>2</sub> gradually shift towards smaller angle with the increase of Fe-doping concentration compared with that of pure TiO<sub>2</sub>, indicating that the lattices of TiO<sub>2</sub> have been expanded by the Fe-doping, which make it possible for Fe<sup>3+</sup> to diffuse into the TiO<sub>2</sub> lattices to replace Ti<sup>4+</sup>. Additionally, there is no indication of a peak corresponding to iron oxide (Fe<sub>2</sub>O<sub>3</sub>) observed, further indicating that Fe<sup>3+</sup> exists by replacing part of Ti<sup>4+</sup> in the crystal lattices of TiO<sub>2</sub>, which is mainly contributed to the ionic radius of Fe<sup>3+</sup> (0.064 nm) to be almost equal to that of Ti<sup>4+</sup> (0.068 nm).

**3.1.2. TEM Studies.** The morphology and size of the Fe-doped TiO<sub>2</sub> nanocomposites were studied with a JEM-2100HR transmission electron microscope. As can be seen in Figure 3, TiO<sub>2</sub> particles are spherical or square-shaped with a primary particle size of approximately 18 nm. The measurements are basically consistent with the XRD results.

**3.1.3. XPS Analysis.** In order to determine whether the successful implementation of the Fe doping, the surface of Fe/TiO<sub>2</sub> (5%) nanocomposites calcined at 400°C has been investigated using XPS analysis. As can be observed from Figure 4, the characteristic peak corresponding to Fe<sub>2p</sub> is located at 710 eV, which reveals that Fe in the doped samples exists mainly in the form of Fe<sup>3+</sup> [26]. The result is consistent with the results obtained by X-ray diffraction. Additionally, according to the XPS measurements, the concentration of

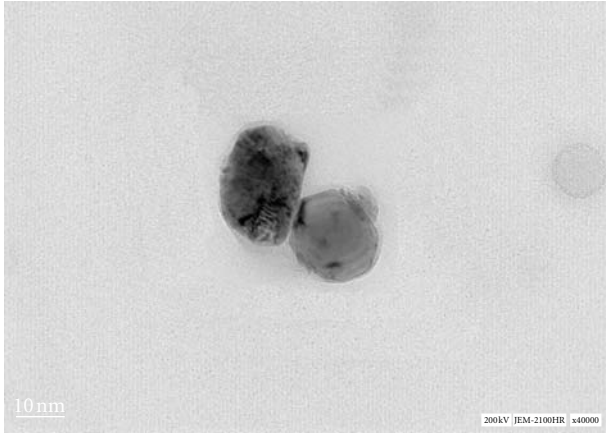


FIGURE 3: The TEM images of 5 wt% Fe/TiO<sub>2</sub> nanocomposites prepared by deposition-precipitation method.

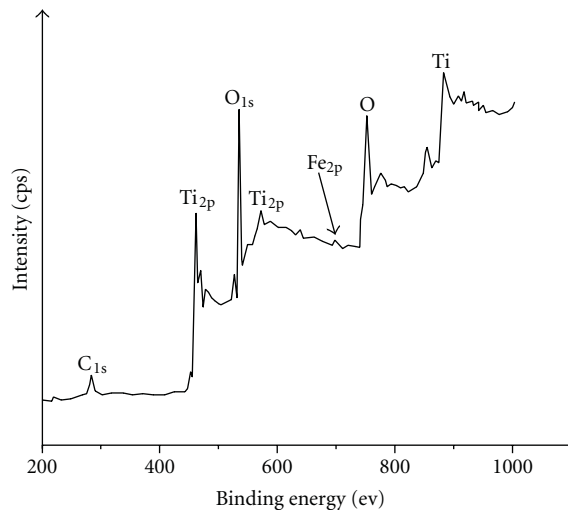


FIGURE 4: The XPS spectra of Fe/TiO<sub>2</sub> (5%) calcined at 400°C.

Fe over the surface of TiO<sub>2</sub> is 4.68 wt%, which is basically consistent with the theoretical expectation.

**3.1.4. UV-Vis Spectroscopy.** The UV-visible absorption spectra of TiO<sub>2</sub> nanoparticles doped with different amounts of Fe in the visible light region were measured using U-3010 UV-visible spectrometer, as shown in Figure 5.

The UV-Vis absorption spectra show that the absorption edges of Fe-doped TiO<sub>2</sub> nanoparticles are slightly shifted to longer wavelengths “red-shift” with increasing amount of Fe, and the absorption for the doped TiO<sub>2</sub> in the visible light region is significantly enhanced compared with that of pure TiO<sub>2</sub>. Additionally, as shown in Figure 5, the starting point of absorption edge of updoped TiO<sub>2</sub> is 393 nm while that for Fe/TiO<sub>2</sub> (2%) is 407 nm and Fe/TiO<sub>2</sub> (5%) is 425 nm, indicating that the visible light absorption of TiO<sub>2</sub> nanoparticles has been effectively enhanced by the surface modification with Fe.

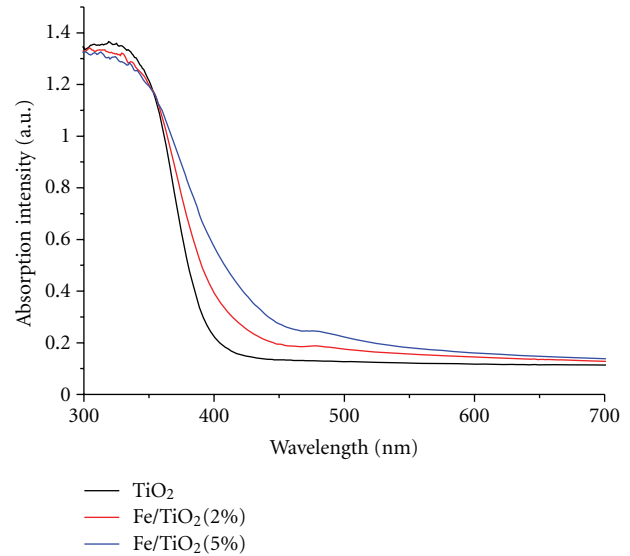


FIGURE 5: The UV-Vis absorption spectra of TiO<sub>2</sub> with different amounts of Fe doping.

**3.2. Effects of Photoexcited TiO<sub>2</sub> with or without Fe Doping on Proliferation of HL60 Cells.** HL60 cells in the logarithmic phase at a density of  $1 \times 10^5$  cells/mL were seeded into 96-well culture plates which had been divided into 4 groups, namely: the control group, the TiO<sub>2</sub> group, the Fe/TiO<sub>2</sub> (2%) group, the Fe/TiO<sub>2</sub> (5%) group, respectively. The final concentration of the groups with nanoparticles was 200  $\mu$ g/mL. Besides, some culture media were added, respectively, so as to the total volume is 200  $\mu$ L per well. The optical density values (OD values) of the samples were measured by DG5031 ELISA reader for 6 consecutive days without adding nutrients. The experimental data are presented in Figure 6.

As can be seen from Figure 6, all the HL60 cells showed a low growth rate on the first day indicating they were in the adaptation period. The growth rate for the HL60 cells increased rapidly in the logarithmic phase during the next three days. In this paper, the cells during this period were used in all experiments. On the fifth day, due to nutrient depletion, metabolite accumulation, and environmental changes, the growth rate of cells becomes more and more slow and stabilized downgradually. With the continuous depletion of nutrients and the accumulation of toxic metabolites, the number of viable cells started to decrease from the sixth day.

Figure 6 also demonstrates that the OD values of the experimental groups in the presence of nanoparticles are much lower and with a shorter growth phase than that of the control group under the same conditions. Apparently, TiO<sub>2</sub> nanoparticles or Fe/TiO<sub>2</sub> nanocomposites have a certain degree of inhibitory or toxic effects on the proliferation of HL60 cells. Moreover, the inhibition effects on HL60 cells become more and more obvious with the increasing Fe-doping concentration.

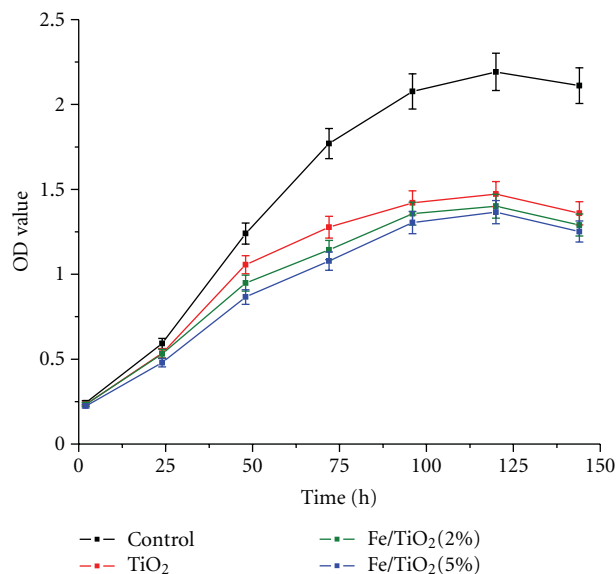


FIGURE 6: The influence of different nanoparticles on the proliferation of HL60 cells. Data represent the means  $\pm$  S.D. (standard deviation) from five independent experiments. \* $P < 0.05$  as compared to control (untreated) cells.

**3.3. Influence of Nanoparticles Concentrations on the Relative Survival of HL60 Cells.** It is required for the photosensitive antitumor drugs used in PDT not only to have high photocatalytic inactivation capability under light irradiation, but also to have no toxicity in the dark. Therefore, it is very important to investigate the self-generated toxicity of  $\text{TiO}_2$  nanoparticles or  $\text{Fe/TiO}_2$  nanocomposites. The toxicity of  $\text{TiO}_2$  or  $\text{Fe/TiO}_2$  was measured by exposing HL60 cells in the medium containing various concentrations of  $\text{TiO}_2$  or  $\text{Fe/TiO}_2$  (0  $\mu\text{g/mL}$ , 50  $\mu\text{g/mL}$ , 100  $\mu\text{g/mL}$ , 150  $\mu\text{g/mL}$ , 200  $\mu\text{g/mL}$ , 250  $\mu\text{g/mL}$ , 500  $\mu\text{g/mL}$ , 1000  $\mu\text{g/mL}$ ) for 48 hours in dark, respectively. The OD values of HL60 cells at different concentrations of nanoparticles were normalized by the OD values of control group (the final concentration of nanoparticles was 0  $\mu\text{g/mL}$ ). The relative survival rates of HL60 cells are shown in Figure 7.

As can be seen from Figure 7, with the increasing concentration of nanoparticles solution, the viability of HL60 cells decreased gradually. At a concentration of 1000  $\mu\text{g/mL}$ , the three survival rates were 77%, 73%, 65.3%, respectively. In comparison, when the concentration reduced the range of 0~250  $\mu\text{g/mL}$ , the survival rates of HL60 cells were all above 90%. In this case, the  $\text{TiO}_2$  nanoparticles and  $\text{Fe/TiO}_2$  nanocomposites could be considered as basically nontoxic materials for cancer cells in the dark, which is in agreement with the suggestions reported in references [27, 28] that  $\text{TiO}_2$  is nontoxic for animals.

**3.4. Influence of Nanocomposites-Based PDT on the Viability of HL60 Cells.** The HL60 cells were inoculated into two 96-well plates marked with A or B. The cell suspensions of A plate were exposed to light after incubating for 24 hours and then preincubated for another 24 hours in the dark. The

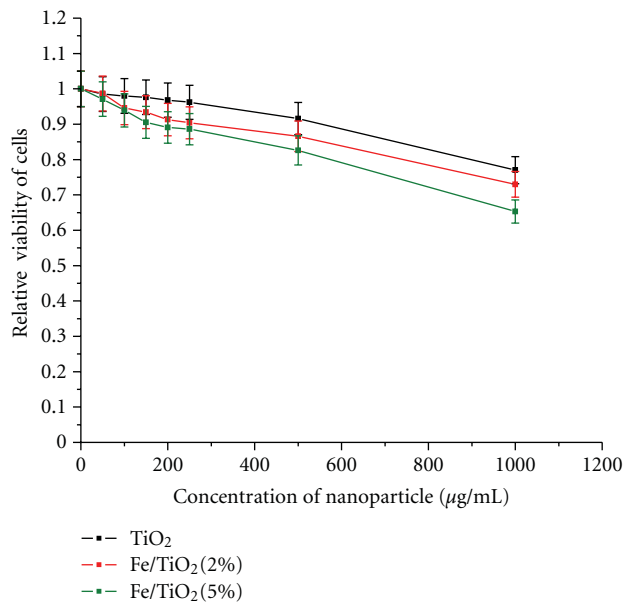


FIGURE 7: The influence of nanomaterial concentration on the relative viability of HL60 cells. Data are presented as the means  $\pm$  S.D. from five independent measurements. \* $P$  values are less than 0.05 as compared with untreated control cells.

HL60 cells in plate B were incubated for 48 hours in the incubator without light treatment. The final concentration of nanoparticles  $\text{TiO}_2$  nanoparticles or  $\text{Fe/TiO}_2$  nanocomposites was 200  $\mu\text{g/mL}$  and each experiment was repeated three times in order to reduce the error. The OD values of experimental groups were then measured by DG5031 ELISA reader, as shown in Table 1.

These measured OD values of cells after light irradiation were normalized by the OD values of cells without light treatment. The relative survival of HL60 and PDT efficiency under different nanoparticles were calculated by the following equations: relative viability =  $\text{OD}_{\text{Light}}/\text{OD}_{\text{Dark}}$ , and PDT efficiency =  $1 - \text{relative viability}$ . The results are presented in Figure 8.

According to the measurements shown in Table 1, the OD values of HL60 cells exposed to light are significantly lower than that of the control group without light treatment, for both in the absence and in the presence of nanoparticles. Illumination causes a decline survival rate of tumor cells without  $\text{TiO}_2$  nanocomposites which is mainly due to the near-ultraviolet light (403 nm) which itself has a certain degree of killing effect on tumor cells. PDT is designed to "selectively kill tumor cells while not harming normal cells as possible." If light irradiation have a greater killing effect on tumor cell in the absence of photosensitive drugs, it will also inevitably lead to a greater damage to normal cells. Therefore, more attention should be paid to light elements of PDT, to minimize light damage on normal cells. Our previous experiments have demonstrated that the light density of 5  $\text{mW/cm}^2$  and the light irradiation dose of 18  $\text{J/cm}^2$  are the best inactivation parameters of tumor HL60 cells-based photodynamic therapy, which are

TABLE 1: The influence of light irradiation on OD values of HL60 cells with different nanoparticles. Data and the points are presented as the means  $\pm$  S.D from three independent measurements. Statistical analysis was then performed and showed that the differences to be significant ( $*P < 0.05$ ).

	Control	TiO <sub>2</sub>	Fe/TiO <sub>2</sub> (2%)	Fe/TiO <sub>2</sub> (5%)
Light treatment	1.073	0.946	0.937	0.875
	1.092	0.957	0.916	0.881
	$\pm 0.031$	$\pm 0.032$	$\pm 0.021$	$\pm 0.006$
Without light treatment	1.136	0.921	0.881	0.889
	1.067	1.004	0.930	0.879
	$\pm 0.031$	$\pm 0.015$	$\pm 0.041$	$\pm 0.011$
Light treatment	0.440	0.283	0.291	0.231
	0.869	0.283	0.168	0.154
	$\pm 0.007$	$\pm 0.015$	$\pm 0.041$	$\pm 0.011$
Without light treatment	0.434	0.301	0.287	0.254
	0.452	0.265	0.202	0.256

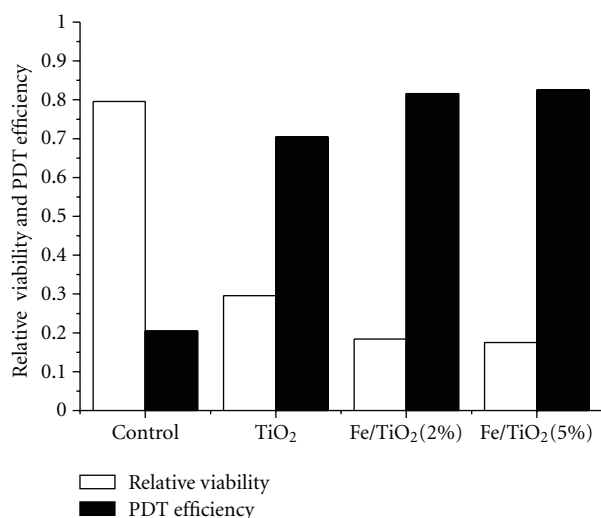
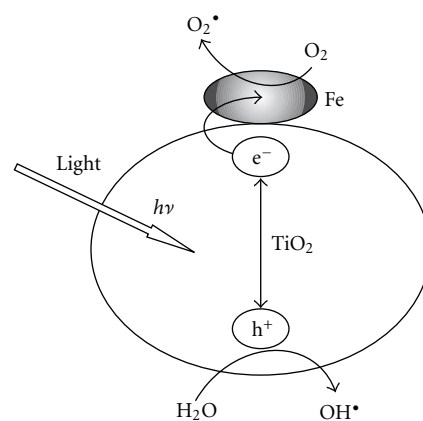


FIGURE 8: The relative viability of HL60 cells and PDT efficiency of different nanoparticles.

consistent with the literature reports [29, 30]. Therefore, a more effective approach to solve the problem is to enhance the visible light absorption of TiO<sub>2</sub>. Furthermore, the OD values of HL60 cells exposed to light with nanoparticles are significantly lower than these without nanoparticles, which is in agreement with our previous result that nanoparticles have a certain degree of inhibition/toxicity on the growth of cells.

As shown in Figure 8, the relative survival rate of HL60 cells in the presence of nanoparticles is significantly lower than that without nanoparticles. It means that PDT efficiency of HL60 cells with nanoparticles is higher than that of HL60 cells without nanoparticles. In addition, Fe/TiO<sub>2</sub> nanocomposites present much higher efficiency in photokilling HL60 cancer cells than TiO<sub>2</sub> nanoparticles. These results reveal that the modification of Fe on the surface of TiO<sub>2</sub> nanoparticles can greatly enhance the photocatalytic inactivation effect of TiO<sub>2</sub> on HL60 cells. Additionally, Fe/TiO<sub>2</sub> (5%) group displays a little higher inactivation efficiency compared



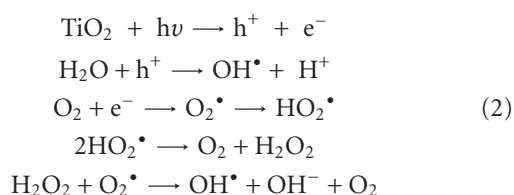
SCHEME 1: The possible mechanism of ROS production by Fe-doped TiO<sub>2</sub> nanocomposites under light irradiation.

with Fe/TiO<sub>2</sub> (2%) group, when 200  $\mu$ g/mL Fe/TiO<sub>2</sub> (5%) nanocomposites were added, the inactivation efficiency of HL60 cells can up to 82.5% after a 60-minute irradiation. Although a higher concentration of Fe/TiO<sub>2</sub> nanocomposites or TiO<sub>2</sub> nanoparticles could achieve a higher-photocatalytic killing effect, but it is not preferable to use a very high concentration of photocatalyst for practical consideration as it might block the blood vessels. On the other hand, at high dopant concentrations, due to the decrease of the distance between trapping sites, the recombination rate of the photoinduced electrons and holes increases, resulting in lower photocatalytic activity. Therefore, the doping concentration of Fe should not be too high.

It has been demonstrated that the cell damage mechanism based on light-excited Fe/TiO<sub>2</sub> nanocomposites is accomplished through a series of chain reactions by means of reactive oxygen species- (ROS-) induced cell death [31–33].

The generation mechanism of reactive oxygen species (ROS) on Fe-doped TiO<sub>2</sub> nanocomposites under UV irradiation is displayed in Scheme 1. When illuminated by ultraviolet light, photoinduced electrons and holes could be created, which can transfer to the surface of Fe nanoparticles and reduce the dissolved O<sub>2</sub> to produce the superoxide anion

$O^{\bullet-}$ . At the same time, the photogenerated holes on the  $TiO_2$  surface can further react with water to generate powerful hydroxyl radicals ( $OH^{\bullet}$ ) and other oxidative radicals ( $HO_2^{\bullet}$ ), which are capable of destroying the membrane and component of tumor cells. The recombination rate of the photoproducted electrons and holes can be effectively inhibited by the above process, so the photocatalytic activity of  $TiO_2$  nanoparticles is significantly enhanced by the modification of Fe. Additionally, the enhanced photocatalytic activity of Fe-doped  $TiO_2$  nanocomposites can also be explained by a new energy level produced in the bandgap of  $TiO_2$  due to the dispersion of Fe nanoparticles, as suggested in the literature [30–37]. Regardless of complexity, it is apparent that there are several key photosensitive that have been involved which could be also explained as follows:



#### 4. Conclusion

In this paper, the prepared Fe/ $TiO_2$  characterized by X-ray diffraction (XRD), transmission electron microscope (TEM), X-ray photoelectron spectroscopy (XPS), and UV-Vis adsorption spectra, respectively, was successfully applied as a photosensitizer-based photodynamic therapy to kill human HL60 cancer cells *in vitro*. The experimental results show that the absorption of  $TiO_2$  nanoparticles in the visible light region could be enhanced effectively by the method of Fe doping, and both pure  $TiO_2$  and Fe/ $TiO_2$  nanocomposites at high concentrations can have a significant inhibition/toxicity on the growth of HL60 cells. It is also found that the photocatalytic inactivation effect on HL60 cells with nanoparticles is obviously higher than that without nanoparticles under the same conditions. Furthermore, Fe/ $TiO_2$  nanocomposites presented much higher PDT efficiency in photokilling HL60 cancer cells than  $TiO_2$  nanoparticles. These indicate that the photocatalytic inactivation effects of  $TiO_2$  on HL60 cells could be greatly improved by the modification of Fe on the surface of  $TiO_2$  nanoparticles. The PDT efficiency of Fe/ $TiO_2$  (5%) nanocomposites on HL60 cells can reach 82.5% at a concentration of 200  $\mu\text{g}/\text{mL}$  after a 60-minute light treatment. The high photocatalytic inactivation effects of Fe/ $TiO_2$  nanocomposites on human HL60 cancer cells suggests that it may be an important potential photosensitizer-based photodynamic therapy for cancer treatment [38–40].

#### Acknowledgments

This work has been financially supported by National Natural Science Foundation of China (61072029), Natural Science Foundation of Guangdong Province (10151063101000025), and Science and Technology Planning Project of Guangzhou city (2010Y1-C111).

#### References

- [1] J. C. Kennedy, R. H. Pottier, and D. C. Pross, "Photodynamic therapy with endogenous protoporphyrin. IX: basic principles and present clinical experience," *Journal of Photochemistry and Photobiology B*, vol. 6, no. 1-2, pp. 143–148, 1990.
- [2] A. Lesar, J. Ferguson, and H. Moseley, "An investigation of the fluorescence induced by topical application of 5-aminolaevulinic acid and methyl aminolaevulinate at different body sites on normal human skin," *Photodiagnosis and Photodynamic Therapy*, vol. 8, no. 1, pp. 20–28, 2011.
- [3] D. Grebeňová, H. Cajthamlová, J. Bartošová et al., "Selective destruction of leukaemic cells by photo-activation of 5-aminolaevulinic acid-induced protoporphyrin-IX," *Journal of Photochemistry and Photobiology B*, vol. 47, no. 1, pp. 74–81, 1998.
- [4] H. S. de Bruijn, W. Sluiter, A. van der Ploeg-van den Heuvel, H. J. C. M. Sterenborg, and D. J. Robinson, "Evidence for a bystander role of neutrophils in the response to systemic 5-aminolevulinic acid-based photodynamic therapy," *Photodermatology Photoimmunology and Photomedicine*, vol. 22, no. 5, pp. 238–246, 2006.
- [5] Y. Kubota, T. Shuin, C. Kawasaki et al., "Photokilling of T-24 human bladder cancer cells with titanium dioxide," *British Journal of Cancer*, vol. 70, no. 6, pp. 1107–1111, 1994.
- [6] P. Edyta, E. Carsten, O. S. Mathias et al., "Nanodrug applications in photodynamic therapy," *Photodiagnosis and Photodynamic Therapy*, vol. 8, no. 1, pp. 14–29, 2011.
- [7] M. Zhou, J. Yu, and B. Cheng, "Effects of Fe-doping on the photocatalytic activity of mesoporous  $TiO_2$  powders prepared by an ultrasonic method," *Journal of Hazardous Materials*, vol. 137, no. 3, pp. 1838–1847, 2006.
- [8] P. Juzenas, W. Chen, Y. P. Sun et al., "Quantum dots and nanoparticles for photodynamic and radiation therapies of cancer," *Advanced Drug Delivery Reviews*, vol. 60, no. 15, pp. 1600–1614, 2008.
- [9] H. Sakai, R. Baba, K. Hashimoto, Y. Kubota, and A. Fujishima, "Selective killing of a single cancerous cell T24 with  $TiO_2$  semiconducting microelectrode under irradiation," *Chemistry Letters*, vol. 24, no. 3, pp. 185–186, 1995.
- [10] J. Gamage and Z. Zhang, "Applications of photocatalytic disinfection," *International Journal of Photoenergy*, vol. 2010, Article ID 764870, 11 pages, 2010.
- [11] J. A. Byrne, P. A. Fernandez-Ibañez, P. S. M. Dunlop, D. M. A. Alrousan, and J. W. J. Hamilton, "Photocatalytic enhancement for solar disinfection of water: a review," *International Journal of Photoenergy*, vol. 2011, Article ID 798051, 12 pages, 2011.
- [12] N. Lagopati, P. V. Kitsiou, A. I. Kontos et al., "Photo-induced treatment of breast epithelial cancer cells using nanostructured titanium dioxide solution," *Journal of Photochemistry and Photobiology A*, vol. 214, no. 2-3, pp. 215–223, 2010.
- [13] Y. Xiong, X. Fei, J. Xiong, and Z. Zhang, "Study on preparation of visible light-activated nitrogen-doped  $TiO_2$  and its photodesdrucing effect on Leukemic HL60 cells *in vitro*," *Rare Metal Materials and Engineering*, vol. 35, no. 11, pp. 1735–1739, 2006.
- [14] L. Tessa, O. Em, A. Mayra et al., "Study of the stabilization of zinc phthalocyanine in sol-gel  $TiO_2$  for photodynamic therapy applications," *Nanomedicine*, vol. 6, no. 6, pp. 777–785, 2010.
- [15] L. Chen, J.-W. Xiong, G.-X. Liu, and Z.-X. Zhang, "An experimental study on effects of nanoparticle  $TiO_{2-x}N_x$  on inactivation of leukemic HL60 cells *in vitro* based on ALA-PDT," *Journal of Optoelectronics Laser*, vol. 18, no. 10, pp. 1265–1268, 2007.

- [16] A. Di Paola, S. Ikeda, G. Marci, B. Ohtani, and L. Palmisano, "Transition metal doped TiO<sub>2</sub>: physical properties and photocatalytic behaviour," *International Journal of Photoenergy*, vol. 3, no. 4, pp. 171–176, 2001.
- [17] M. Jakob, H. Levanon, and P. V. Kamat, "Charge distribution between UV-irradiated TiO<sub>2</sub> and gold nanoparticles: determination of shift in the Fermi level," *Nano Letters*, vol. 3, no. 3, pp. 353–358, 2003.
- [18] N. Serpone, A. Salinaro, S. Horikoshi, and H. Hidaka, "Beneficial effects of photo-inactive titanium dioxide specimens on plasmid DNA, human cells and yeast cells exposed to UVA/UVB simulated sunlight," *Journal of Photochemistry and Photobiology A*, vol. 179, no. 1-2, pp. 200–212, 2006.
- [19] J. Yu, Q. Xiang, and M. Zhou, "Preparation, characterization and visible-light-driven photocatalytic activity of Fe-doped titania nanorods and first-principles study for electronic structures," *Applied Catalysis B*, vol. 90, no. 3-4, pp. 595–602, 2009.
- [20] L. Liu, P. Miao, Y. Xu, Z. Tian, Z. Zou, and G. Li, "Study of Pt/TiO<sub>2</sub> nanocomposite for cancer-cell treatment," *Journal of Photochemistry and Photobiology B*, vol. 98, no. 3, pp. 207–210, 2010.
- [21] H. Li, Z. Bian, J. Zhu, Y. Huo, H. Li, and Y. Lu, "Mesoporous Au/TiO<sub>2</sub> nanocomposites with enhanced photocatalytic activity," *Journal of the American Chemical Society*, vol. 129, no. 15, pp. 4538–4539, 2007.
- [22] C. Karunakaran, G. Abiramasundari, P. Gomathisankar, G. Manikandan, and V. Anandi, "Cu-doped TiO<sub>2</sub> nanoparticles for photocatalytic disinfection of bacteria under visible light," *Journal of Colloid and Interface Science*, vol. 352, no. 1, pp. 68–74, 2010.
- [23] Y.-S. Li, F.-L. Jiang, Q. Xiao et al., "Enhanced photocatalytic activities of TiO<sub>2</sub> nanocomposites doped with water-soluble mercapto-capped CdTe quantum dots," *Applied Catalysis B*, vol. 101, no. 1-2, pp. 118–129, 2010.
- [24] J. W. Xiong, H. XIAO, L. Chen, J. M. Wu, and Z. X. Zhang, "Research on different detection conditions between MTT and CCK-8," *Acta Laser Biology Sinica*, vol. 16, no. 5, pp. 526–531, 2007.
- [25] C. Lettmann, K. Hildenbrand, H. Kisch, W. Macyk, and W. F. Maier, "Visible light photodegradation of 4-chlorophenol with a coke-containing titanium dioxide photocatalyst," *Applied Catalysis B*, vol. 32, no. 4, pp. 215–227, 2001.
- [26] Y. Cong, J. Zhang, F. Chen, M. Anpo, and D. He, "Preparation, photocatalytic activity, and mechanism of Nano-TiO<sub>2</sub> Co doped with nitrogen and Iron (III)," *The Journal of Physical Chemistry C*, vol. 111, no. 28, pp. 10618–10623, 2007.
- [27] A. L. Linsebigler, G. Lu, and J. T. Yates, "Photocatalysis on TiO<sub>2</sub> surfaces: principles, mechanisms, and selected results," *Chemical Reviews*, vol. 95, no. 3, pp. 735–758, 1995.
- [28] W. G. Wamer, J. J. Yin, and R. R. Wei, "Oxidative damage to nucleic acids photosensitized by titanium dioxide," *Free Radical Biology and Medicine*, vol. 23, no. 6, pp. 851–858, 1997.
- [29] Z. X. Zhang, S. J. Zhang, B. Q. Zhang, and M. L. Chen, "Leukemic cells killed by photodynamic therapy with 5 aminolevulinic acid: an experimental study," *Chinese Journal of Laser Medicine & Surgery*, vol. 14, no. 4, pp. 249–252, 2005.
- [30] H. Xiao, J. W. Xiong, J. M. Wu, and Z. X. Zhang, "Research of parameters on ALA-PDT destruction of leukaemia cell," *Acta Laser Biology Sinica*, vol. 13, no. 5, pp. 353–357, 2004.
- [31] A. Kathiravan and R. Renganathan, "Photoinduced interactions between colloidal TiO<sub>2</sub> nanoparticles and calf thymus-DNA," *Free Radical Biology & Medicine*, vol. 28, no. 7, pp. 1374–1378, 2009.
- [32] J. Xu, Y. Sun, J. Huang et al., "Photokilling cancer cells using highly cell-specific antibody-TiO<sub>2</sub> bioconjugates and electroporation," *Bioelectrochemistry*, vol. 71, no. 2, pp. 217–222, 2007.
- [33] F. R. James, J. D. Simon, J. F. D. Nicholas, and N. J. Awadhesh, "Hydroxyl radicals (radical dotOH) are associated with titanium dioxide (TiO<sub>2</sub>) nanoparticle-induced cytotoxicity and oxidative DNA damage in fish cells," *Mutation Research*, vol. 640, no. 1-2, pp. 113–122, 2008.
- [34] J. Xu, Y. Sun, Y. Zhao, J. Huang, C. Chen, and Z. Jiang, "Photocatalytic inactivation effect of gold-doped TiO<sub>2</sub> (Au/TiO<sub>2</sub>) nanocomposites on human colon carcinoma LoVo cells," *International Journal of Photoenergy*, vol. 2007, Article ID 97308, 7 pages, 2007.
- [35] T. G. Bajnóczy, N. Balázs, K. Mogyorósi et al., "The influence of the local structure of Fe(III) on the photocatalytic activity of doped TiO<sub>2</sub> photocatalysts—an EXAFS, XPS and Mössbauer spectroscopic study," *Applied Catalysis B*, vol. 103, no. 1-2, pp. 232–239, 2011.
- [36] Q. Li, C. Zhang, and J. Li, "Photocatalytic and microwave absorbing properties of polypyrrole/Fe-doped TiO<sub>2</sub> composite by in situ polymerization method," *Journal of Alloys and Compounds*, vol. 509, no. 5, pp. 1953–1957, 2011.
- [37] H. Fu, G. Shang, S. Yang, and T. Xu, "Mechanistic study of visible-light-induced photodegradation of 4-chlorophenol by TiO<sub>2-x</sub>N<sub>x</sub> (0.021 < x < 0.049 ) with low nitrogen concentration," *International Journal of Photoenergy*, vol. 2012, Article ID 759306, 9 pages, 2012.
- [38] K. Naeem and F. Ouyang, "Fe<sup>3+</sup>-doped TiO<sub>2</sub> nanoparticles and its photocatalytic activity under UV light," *Physica B*, vol. 405, no. 1, pp. 221–226, 2010.
- [39] W. H. Suh, K. S. Suslick, G. D. Stucky, and Y. H. Suh, "Nanotechnology, nanotoxicology, and neuroscience," *Progress in Neurobiology*, vol. 87, no. 3, pp. 133–170, 2009.
- [40] Y. Yalçın, M. Kiliç, and Z. Çinar, "Fe<sup>3+</sup>-doped TiO<sub>2</sub>: a combined experimental and computational approach to the evaluation of visible light activity," *Applied Catalysis B*, vol. 99, no. 3-4, pp. 469–477, 2010.

## Research Article

# Facile Synthesis and Photocatalytic Property of Titania/Carbon Composite Hollow Microspheres with Bimodal Mesoporous Shells

Guohong Wang,<sup>1,2</sup> Bei Cheng,<sup>2</sup> Jun Zhang,<sup>2</sup> Lin Xu,<sup>1</sup> and Tingting Yin<sup>1</sup>

<sup>1</sup> College of Chemistry and Environmental Engineering, Hubei Normal University, Huangshi, Hubei, 435002, China

<sup>2</sup> State Key Laboratory of Advanced Technology for Material Synthesis and Processing, Wuhan University of Technology, Luoshi Road No. 122, Wuhan 430070, China

Correspondence should be addressed to Guohong Wang, wanggh2003@163.com

Received 14 September 2011; Accepted 14 November 2011

Academic Editor: Gongxuan Lu

Copyright © 2012 Guohong Wang et al. This is an open access article distributed under the Creative Commons Attribution License, which permits unrestricted use, distribution, and reproduction in any medium, provided the original work is properly cited.

Titania/carbon composite hollow microspheres with bimodal mesoporous shells are one-pot fabricated by hydrothermal treatment of the acidic  $(\text{NH}_4)_2\text{TiF}_6$  aqueous solution in the presence of glucose at  $180^\circ\text{C}$  for 24 h and then calcined at  $450^\circ\text{C}$ . The as-prepared samples were characterized by XRD, SEM, TEM, HRTEM, UV-visible spectroscopy, and nitrogen adsorption-desorption isotherms. The photocatalytic activity of the as-prepared samples was evaluated by daylight-induced photocatalytic decolorization of methyl orange aqueous solution at ambient temperature. The effects of calcination time on the morphology, phase structure, crystallite size, specific surface area, pore structures, and photocatalytic activity of the microspheres were investigated. The results indicated that the as-obtained  $\text{TiO}_2/\text{C}$  composite hollow spheres generally exhibit bimodal mesopore size distribution with their peak intra-aggregated mesopore size in the range of 2.3–4.5 nm and peak interaggregated mesopore size in the range of 5.7–12.7 nm, depending on specific calcination time. The daylight-induced photoactivity of as-obtained hollow  $\text{TiO}_2/\text{C}$  microspheres generally exceeds that of Degussa P25. The influences of calcination time on the photoactivity are discussed in terms of carbon content, phase structures, and pore structures.

## 1. Introduction

Photocatalytic degradation of organic compounds for the purpose of purifying water or wastewater from industries and households has attracted great attention in the past decade [1–7]. Among various oxide semiconductor photocatalysts, titania is a very important photocatalyst due to its biological and chemical inertness, strong oxidizing power, nontoxicity, and long-term stability against photo and chemical corrosion. In order to commercialize this treatment technique, it is of great importance to improve the preparative methods of titania, because the morphology, microstructures, and photocatalytic activity of  $\text{TiO}_2$  are significantly influenced by the preparative conditions and methods [8–11].

The fabrication of  $\text{TiO}_2$  hollow structures attracts special attention due to their low density, high surface area, good surface permeability and larger light-harvesting capacities [9]. Especially, micro- or nanometer scale  $\text{TiO}_2$  hollow spheres with controllable structure, composition, and properties have shown a promising perspective in many fields such as catalysts, adsorbents, sensors, light fillers, and chemical reactors [12–16]. While hollow  $\text{TiO}_2$  structures have been synthesized without the assistance of templates by the spray-drying technique and via Ostwald ripening and chemically induced self-transformation [17–20], the templating method has been most frequently applied for the synthesis of hollow  $\text{TiO}_2$  structures with tailored properties. For example, Hard templates (e.g., polymer latex, carbon, and anodic aluminium oxide templates) and soft

templates (e.g., supermolecules, ionic liquids, surfactant, and organogel) have been extensively employed to produce TiO<sub>2</sub> hollow structures either by controlled surface precipitation of inorganic molecule precursors or by direct surface reactions utilizing specific functional groups [21–27]. Very recently, a general method for the synthesis of metal oxide hollow spheres has been developed using carbonaceous polysaccharide microspheres prepared from saccharide solution as templates by Sun and coworkers and Titirici and coworkers [28, 29].

Carbon materials (e.g., amorphous carbon, activated carbon, and graphite) have attracted considerable attention due to their widespread applications as absorbents, catalyst supports, and nanocomposites [30]. Carbon is chemically inert at low temperature and a suitable support for titanium dioxide photocatalysts. Various studies have demonstrated that titanium/carbon composite photocatalysts can result in a synergistic effect of both adsorption and photocatalysis and can dramatically improve the daylight-induced photocatalytic activity of titania for different modal organic components [30–37].

However, preparation of well-crystallized titanium/carbon composite hollow microspheres with high daylight-induced photocatalytic activity keeps still a great challenge. In this study, titanium/carbon composite hollow microspheres with bimodal mesoporous shell are one-pot fabricated according to the method reported by Titirici and coworkers [29] and their visible light photocatalytic activity is investigated.

## 2. Experimental Section

**2.1. Sample Preparation.** All chemicals used in this study were reagentgrade without further purification. Distilled water was used in all experiment. (NH<sub>4</sub>)<sub>2</sub>TiF<sub>6</sub> was used as a titanium source. In a typical synthesis, 15 g (75.5 mmol) of glucose and 3.0 g (15.1 mmol) of (NH<sub>4</sub>)<sub>2</sub>TiF<sub>6</sub> were dissolved in 80 and 40 mL of distilled water under stirring, respectively. The above two solutions were mixed and the pH of the mixed solutions was adjusted to ca. 3 using 1 M HCl or NaOH aqueous solutions. Then the reaction solution was transferred into a 200 mL Teflon-lined stainless steel autoclave, followed by hydrothermal treatment of the mixture at 180°C for 24 h. After hydrothermal reaction, the black or puce precipitates were centrifuged and then washed with distilled water and absolute alcohol for 5 times. The washed precipitates were dried in a vacuum oven at 60°C for 8 h. Finally, the dried mixtures were calcined in air at 450°C for 0.5–4.0 h, the TiO<sub>2</sub>/C composites, with the color from black to grey when the calcined time was increased, were obtained. The abbreviations of TiO<sub>2</sub>/C composites with different calcined time are shown in Tables 1 and 2.

**2.2. Characterization.** The carbon content of the composite catalysts was monitored using a DTA-TG instrument (Netzsch STA 449C) in airflow of 100 mL min<sup>-1</sup> at a heating rate of 10°C min<sup>-1</sup> from room temperature to 900°C. The X-ray diffraction (XRD) patterns obtained on an X-ray

diffractometer (type HZG41B-PC) using Cu K $\alpha$  irradiation at a scan rate of 0.05° 2 $\theta$  s<sup>-1</sup> were used to determine the identity of any phase present and their crystallite size. The accelerating voltage and the applied current were 15 kV and 20 mA, respectively. The phase composition of TiO<sub>2</sub> can be calculated from the integrated intensities of anatase (101), rutile (110), and brookite (121) peaks. If a sample contained anatase and rutile two phases, the mass fraction of rutile could be calculated according to the following equation (1) [38].

$$W_R = \frac{A_R}{0.886A_A + A_R}, \quad (1)$$

where  $A_A$  and  $A_R$  represent the integrated intensity of the anatase (101) and rutile (110) peaks, respectively. The average crystallite sizes of anatase and rutilites were determined according to the Scherrer equation using the FWHM data of each phase after correcting the instrumental broadening [38]. Morphology observation was performed on a JSM-5610LV scanning electron microscope (SEM, JEOL, Japan). Crystallite sizes and shapes were observed using transmission electron microscopy (TEM) and high-resolution transmission electron microscopy (HRTEM) (JEOL-2010F at 200 kV). The samples for TEM observation were prepared by dispersing the TiO<sub>2</sub> powders in an absolute ethanol solution under ultrasonic irradiation; the dispersion was then dropped on carbon-copper grids. The Brunauer-Emmett-Teller (BET) surface area ( $S_{\text{BET}}$ ) of the powders was analyzed by nitrogen adsorption in a Micromeritics ASAP 2020 nitrogen adsorption apparatus (USA). All the samples were degassed at 180°C prior to nitrogen adsorption measurements. The BET surface area was determined by multipoint BET method using the adsorption data in the relative pressure ( $P/P_0$ ) range 0.05 ~ 0.3. Desorption isotherm was used to determine the pore size distribution via the Barret-Joyner-Halender (BJH) method, assuming a cylindrical pore modal [39–41]. The nitrogen adsorption volume at the relative pressure ( $P/P_0$ ) of 0.994 was used to determine the pore volume and average pore size. UV-visible diffuse reflectance spectra of as-prepared TiO<sub>2</sub> powders were obtained for the dry-pressed disk samples using a UV-visible spectrophotometer (UV2550, Shimadzu, Japan). BaSO<sub>4</sub> was used as a reflectance standard in the UV-visible diffuse reflectance experiment. The morphologies of TiO<sub>2</sub> powders were observed using scanning electron microscopy (SEM) (type JSM-5610LV, Japan) with an acceleration voltage of 20 kV.

**2.3. Measurement of Photocatalytic Activity.** The evaluation of photocatalytic activity of the prepared samples for the photocatalytic decolorization of methyl orange aqueous solution was performed at ambient temperature, as reported in our previous studies [42]. Experiments were as follows: 0.04 g of the prepared powders were dispersed in a 20 mL of methyl orange aqueous solution with a concentration of  $3.1 \times 10^{-5}$  mol L<sup>-1</sup> in a dish (with a diameter of ca. 7.0 cm). The solution was allowed to reach an adsorption-desorption equilibrium among the photocatalyst, methyl orange, and

TABLE 1: Effects of calcination time on phase structure, phase content, and average crystallite sizes of TiO<sub>2</sub>/C composite microspheres at 450°C.

Time (h)	Material abbreviations	Carbon mass ratio in composites <sup>a</sup> (wt.%)	Anatase		Rutile	
			Crystalline Size <sup>b</sup> (nm)	Content <sup>c</sup> (%)	Crystalline Size <sup>b</sup> (nm)	Content <sup>c</sup> (%)
0.5	TiO <sub>2</sub> -0.5	32.9	11 (1.0)	86.2	36	13.2
1	TiO <sub>2</sub> -1	8.2	17 (1.27)	83.5	41	16.5
2	TiO <sub>2</sub> -2	5.0	18 (1.39)	82.5	58	17.5
4	TiO <sub>2</sub> -4	1.9	21 (1.47)	80.6	68	18.4

<sup>a</sup>Estimated from the data of TGA-DSC measurement. <sup>b</sup>Average crystalline size of TiO<sub>2</sub> was determined by XRD using Scherrer equation. Relative anatase crystallinity: the relative intensity of the diffraction peak from the anatase (101) plane (indicated in parentheses, reference = sample calcined at 450°C for 0.5 h). <sup>c</sup>Determined by XRD method.

TABLE 2: Effects of calcination time on surface areas and pore parameters of TiO<sub>2</sub>/C composite microspheres at 450°C.

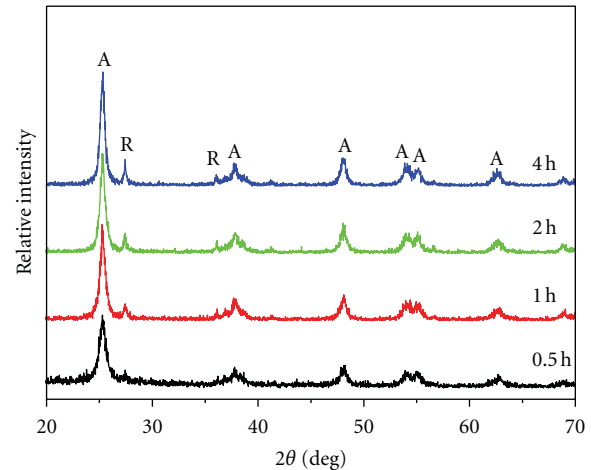
Time (h)	Material abbreviations	S <sub>BET</sub> <sup>a</sup> (m <sup>2</sup> /g)	Pore volume <sup>b</sup> (cm <sup>3</sup> /g)	Average pore Size <sup>b</sup> (nm)	Porosity <sup>c</sup> (%)
0.5	TiO <sub>2</sub> /C-0.5	210.5	0.129	2.4	33.5
1	TiO <sub>2</sub> /C-1	55.3	0.076	5.5	22.8
2	TiO <sub>2</sub> /C-2	46.4	0.073	6.3	22.2
4	TiO <sub>2</sub> /C-4	20.8	0.044	8.5	14.6

<sup>a</sup>The BET surface area was determined by multipoint BET method using the adsorption data in  $P/P_0$  range from 0.05 to 0.3. <sup>b</sup>Pore volume and average pore size were determined by nitrogen adsorption volume at  $P/P_0 = 0.994$ . <sup>c</sup>The porosity is estimated from the pore volume determined using the desorption data at  $P/P_0 = 0.994$ .

water before daylight irradiation. An 18-W daylight lamp (3 cm above the dish) was used as a light source. The integrated daylight intensity was  $0.46 \pm 0.01$  mW/cm<sup>2</sup>, as measured by a UV radiometer (made in the photoelectric instrument factory of Beijing Normal University) with the peak intensity of 420 nm. After visible-light irradiation for 60 min, the reaction solution was filtrated, and the concentration of methyl orange aqueous solution was determined by a UV-visible spectrophotometer (UV-2550, SHIMADZU, Japan). As for the methyl orange aqueous solution with low concentration, its photocatalytic decolorization is a pseudo-first-order reaction and its kinetics may be expressed as  $\ln(c_0/c) = kt$ , where  $k$  is the apparent rate constant, and  $c_0$  and  $c$  are the adsorption-desorption equilibrium and reaction concentrations of methyl orange, respectively. Each set of photocatalytic measurements were repeated for three times, and the experimental error was found to be within  $\pm 5\%$ .

### 3. Results and Discussion

**3.1. Crystal Structure.** Figure 1 shows the XRD pattern of the composites catalysts prepared at 450°C for different calcined time. The phase content, crystal size, and relative anatase crystallinity of TiO<sub>2</sub>/C samples are shown in Table 1. At 450°C for 0.5 h, anatase and rutile phases appear, and their mass percentages are 86.2% and 13.8%, respectively. With increasing calcined time, crystallite size, relative anatase crystallinity, and rutile content increases gradually. This may be ascribed to the fact that the longer calcined time enhance grain growth and favor the phase transformation of anatase to rutile. On the other hand, with increasing calcined time

FIGURE 1: XRD patterns of TiO<sub>2</sub>/C composite hollow spheres after calcination at 450°C for 0.5 (a), 1 (b), 2 (c), and 4 h (d).

from 0.5 to 4 h, the carbon content of TiO<sub>2</sub>/C samples changes from 32.9 to 1.9%. The presence of carbon layer may suppress the phase transformation of anatase to rutile to a certain extent. Similar results were reported by Shanmugam et al. and Tsumurae al. [33, 43]. The carbon layers are acting as barriers for phase transformation of anatase to rutile.

**3.2. SEM and TEM Studies.** SEM and TEM were used to characterize the morphology and crystal structure of the as-prepared samples. Calcination of the TiO<sub>2</sub>/C composites in air resulted in the formation of hollow TiO<sub>2</sub>/C

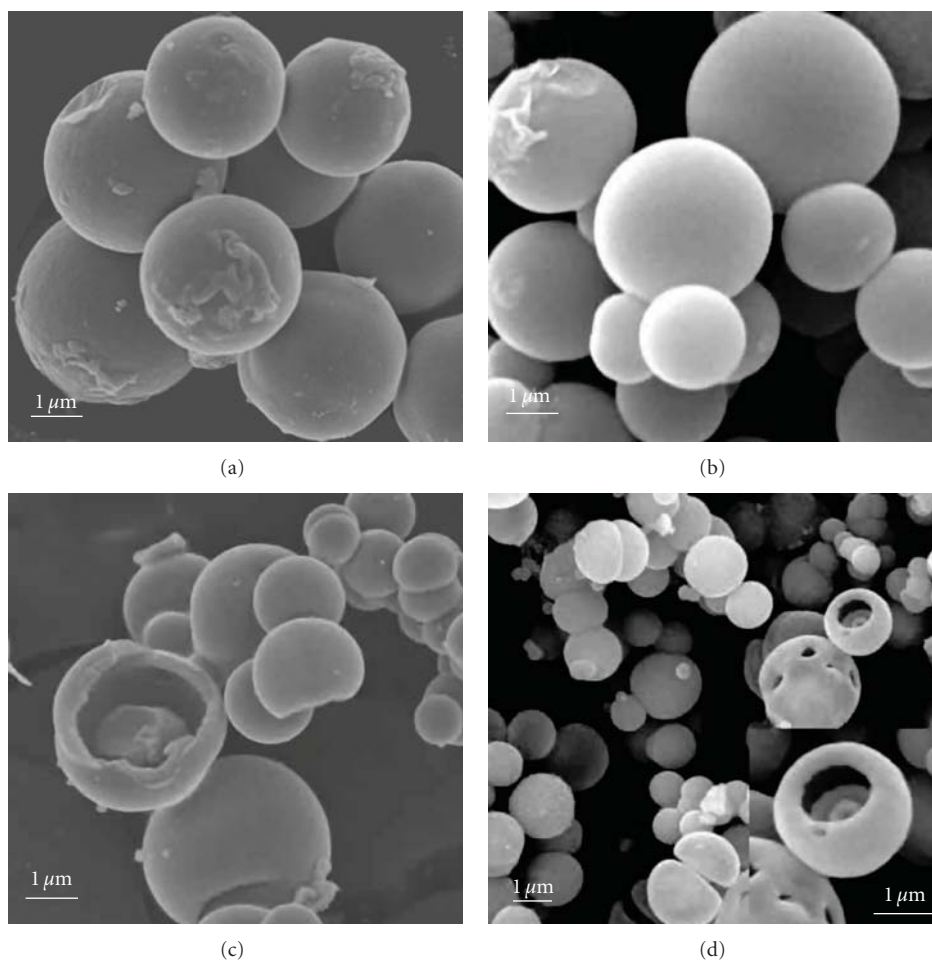


FIGURE 2: SEM image of the  $\text{TiO}_2/\text{C}$  composite hollow spheres calcined at  $450^\circ\text{C}$  for 0.5 (a), 1 (b), 2 (c), and 4 h (d).

microspheres. Figure 2 displays the SEM images of hollow  $\text{TiO}_2/\text{C}$  microspheres obtained after hydrothermal reaction and calcination in air at  $450^\circ\text{C}$  for different time. It can be seen from Figure 2(a) that after calcination for 0.5 h, the microspheres with surface wrinkles have a uniform diameter of ca.  $4\ \mu\text{m}$ . It is interesting to note that with increasing calcination time, the diameter of microspheres decrease drastically probably due to a large amount of carbon removed during calcination, resulting in drastic shrinkage of corresponding hollow spheres. At  $400^\circ\text{C}$  for above 2 h, the samples are composed of hollow spheres with a diameter range from 0.5 to  $2.0\ \mu\text{m}$  and cavities are occasionally found in some broken microspheres with a shell thickness  $\sim 400\ \text{nm}$  (Figure 2(c) and inset in Figure 2(d)).

The morphology and microstructures of  $\text{TiO}_2/\text{C}$  hollow spheres are further investigated by TEM analysis. Figure 3(a) shows a typical TEM image of the samples calcined at  $450^\circ\text{C}$  for 2 h. There is a strong contrast difference observed for all microspheres with dark edge and bright center, clearly confirming their hollow structures. Further observation indicates that the prepared hollow microspheres appear unique sphere-in-sphere superstructures. Li and coworkers

reported the similar sphere-in-sphere superstructures prepared solvothermally in glycerol, alcohol, and ethyl ether, which allow multireflections of electromagnetic waves, such as ultraviolet and visible light, within their interior cavities, endowing these spheres with greatly enhanced properties [44]. Figure 3(b) presents a typical HRTEM lattice image of the  $\text{TiO}_2$  nanoparticles in the shell of  $\text{TiO}_2/\text{C}$  hollow microspheres. The selected area electron diffraction (SAED) patterns (inset in Figure 3(b)) reveal the polycrystalline nature of the anatase and rutile phases for the  $\text{TiO}_2/\text{C}$  hollow microspheres. By measuring the lattice fringes, the resolved interplanar distances are ca. 0.35 and 0.33 nm, corresponding to the (101) planes of anatase and the (110) planes of rutile, respectively. This further confirms the mixed biphasic structures of hollow microspheres.

**3.3. Pore Structure and BET Surface Areas.** Figure 4 shows the nitrogen adsorption-desorption isotherms of the  $\text{TiO}_2/\text{C}$  composite hollow spheres calcined at  $450^\circ\text{C}$  for 0.5–4 h. It can be seen that all the samples show a type IV isotherm with two hysteresis loops. The shapes of two hysteresis loops are different from each other. At low relative pressures between

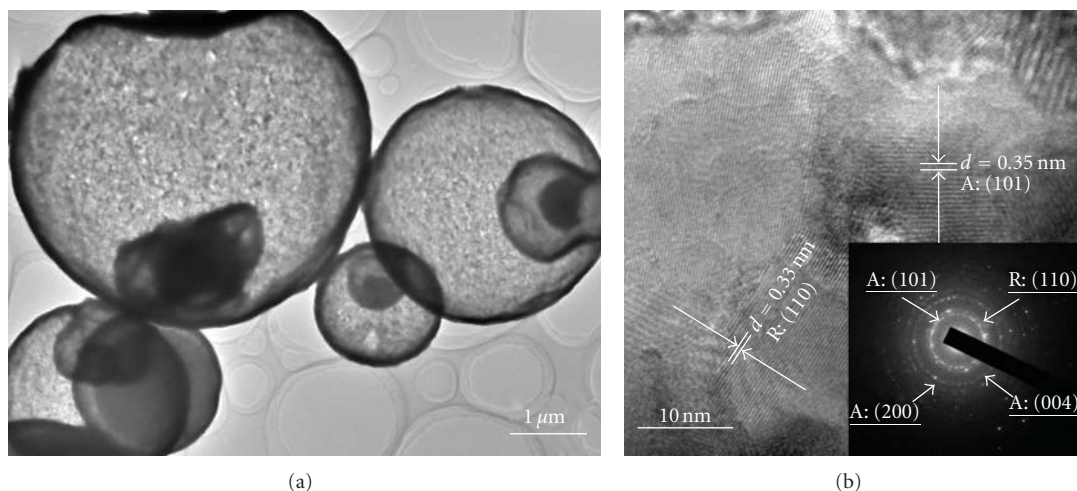


FIGURE 3: TEM (a) and corresponding HRTEM (b) images of the  $\text{TiO}_2/\text{C}$  composite hollow spheres calcined at  $450^\circ\text{C}$  for 2 h.

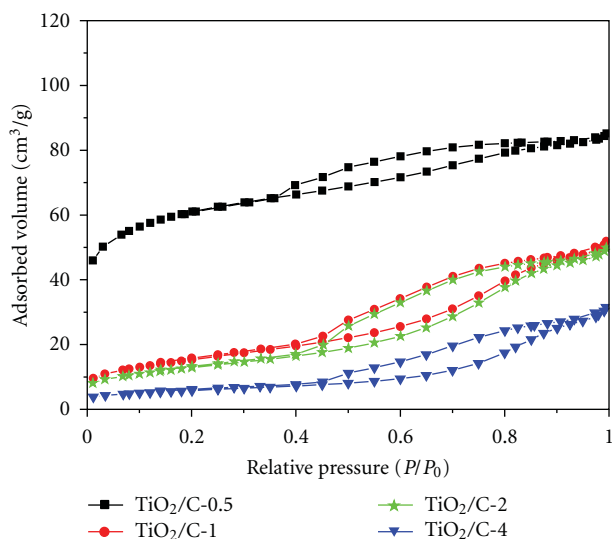


FIGURE 4: Nitrogen adsorption-desorption isotherms of the  $\text{TiO}_2/\text{C}$  hollow spheres calcined at  $450^\circ\text{C}$  for 0.5–4 h.

0.4 and 0.8, the hysteresis loops are of type H2, which can be observed in the pores with narrow necks and wider bodies (ink-bottle pores) [45, 46]. However, at high relative pressures between 0.8 and 1.0, the shape of the hysteresis loop is of a type H3, associated with plate-like particles giving rise to narrow slit-shaped pores [39, 46]. Further observation indicates that with increasing calcination time, the hysteresis loops shifted to a higher relative pressure region. The isotherms of the  $\text{TiO}_2/\text{C}$  composites prepared at  $450^\circ\text{C}$  for 0.4–4 h having two hysteresis loops indicate bimodal pore-size distributions in the mesoporous regions existed in the shells.

Figure 5 shows the corresponding pore-size distributions of the  $\text{TiO}_2/\text{C}$  composite hollow spheres calcined at  $450^\circ\text{C}$

for 0.5–4 h. All samples show bimodal pore-size distributions, consisting of finer intra-aggregated pores and larger interaggregated pores. For example, the sample calcined at  $450^\circ\text{C}$  for 0.5 h has small mesopores (peak pore: ca. 2.3 nm) and larger mesopores (peak pore: ca. 5.8 nm), which are related to finer aggregated pore formed between small anatase crystallites 11 nm in size, and larger aggregated pore produced by large rutile crystallites 36 nm in size (see Table 1), respectively. Further observation indicates that with increasing calcination time, the corresponding maximum peaks shift to the right, indicating the increase of pore size. There are two possible factors resulting in the increase of pore size. One is that the aggregation of greater crystallites forms bigger pores. The other is that the content of carbon in the shells decreases, which probably inserts into the pore of  $\text{TiO}_2$  to cause the decrease in pore size. The effects of calcination time on physical properties of  $\text{TiO}_2/\text{C}$  hollow microspheres are shown in Table 2. With increasing calcination time, the BET-specific surface areas, pore volumes, and porosity steadily decrease. However, the average pore size increases. This is ascribed to the fact that increase of calcination time resulted in decrease of the carbon content in the  $\text{TiO}_2/\text{C}$  composites.

**3.4. UV-Vis Spectrum.** Usually, the carbon content obviously influences light absorption characteristics of  $\text{TiO}_2/\text{C}$  composites [32–35]. Figure 6 shows the UV-visible absorption spectra of the  $\text{TiO}_2/\text{C}$  composite hollow spheres calcined at  $450^\circ\text{C}$  for 0.5–4 h. A significant increase in the absorption at wavelengths shorter than 400 nm can be assigned to the intrinsic band gap absorption of  $\text{TiO}_2$  [3]. It is noticeable that there is an obvious correlation between the calcination time and the UV-vis spectrum change. With increasing calcination time, the absorption in the near UV and visible-light region gradually decreases and the absorption edge of the samples shows an obvious blue shift. The differences in adsorption are attributed to the change of carbon content in the  $\text{TiO}_2/\text{C}$  composites. This clearly indicates an increase in the band gap

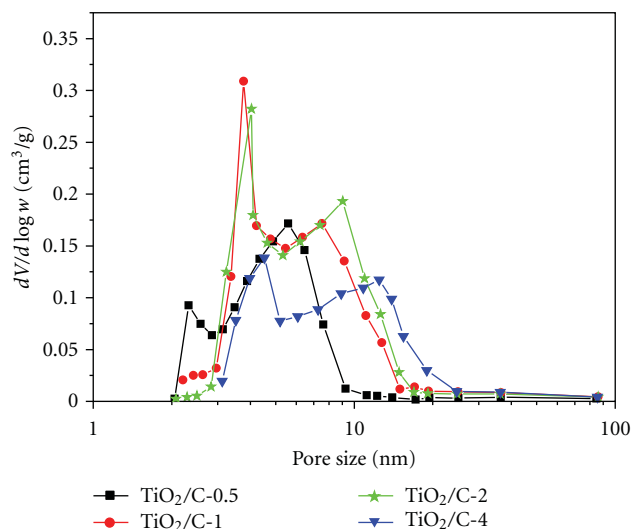


FIGURE 5: Pore-size distribution curves of the  $\text{TiO}_2/\text{C}$  hollow spheres calcined at  $450^\circ\text{C}$  for 0.5–4 h.

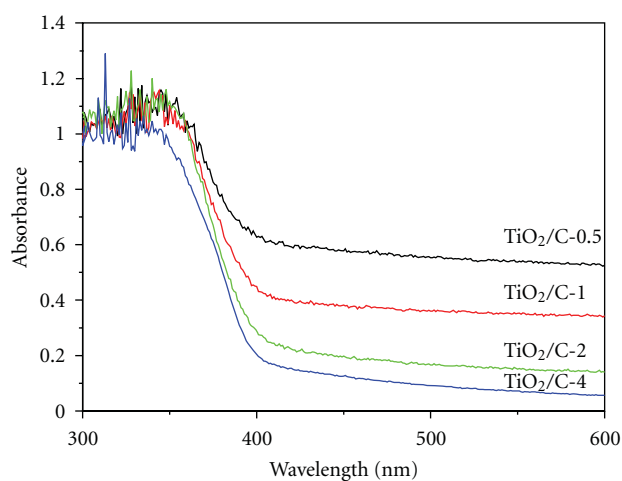


FIGURE 6: UV-vis spectra of  $\text{TiO}_2$  hollow spheres calcined at  $450^\circ\text{C}$  for 0.5–4 h.

energy of  $\text{TiO}_2$ . Band gap energy could be estimated from Figure 6. The intercept of the tangent to the plot would give an approximation of the band gap energy for indirect band gap materials such as  $\text{TiO}_2$  [47, 48]. The band gap energies were estimated to be about 3.05, 3.09, 3.15, and 3.20 eV for the  $\text{TiO}_2/\text{C}$  hollow spheres calcined at  $450^\circ\text{C}$  for 0.5, 1.0, 2.0, and 4 h, respectively. Obviously, the longer calcination time is, the bigger value of the band energies. This is due to the difference in carbon content of  $\text{TiO}_2/\text{C}$  composites [34, 49].

**3.5. Photocatalytic Activity.** The photocatalytic activity of the as-prepared  $\text{TiO}_2/\text{C}$  composite hollow spheres was evaluated by the daylight-induced photocatalytic decolorization of methyl orange aqueous solution at ambient temperature. For comparison, the daylight-induced photocatalytic activities of the commercial  $\text{TiO}_2$  powder Degussa P25 (P25) were also

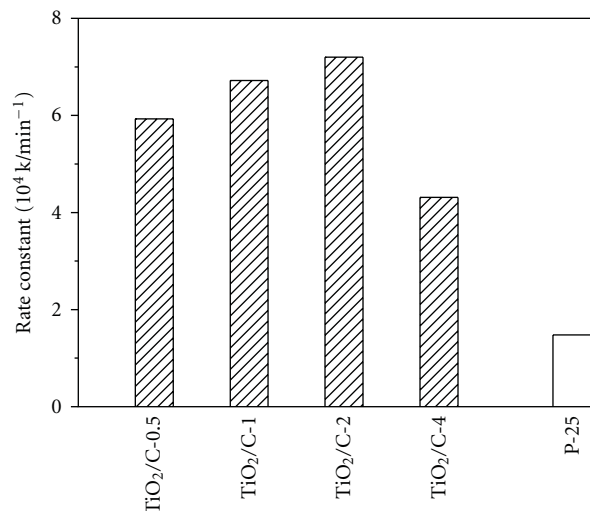


FIGURE 7: Effects of calcination temperatures on the apparent rate constants of the  $\text{TiO}_2/\text{C}$  composite hollow microspheres.

tested. Figure 7 shows the comparisons of the apparent rate constants of P25 and the  $\text{TiO}_2/\text{C}$  composite hollow spheres at various calcination time. It can be seen that the  $\text{TiO}_2/\text{C}$ -0.5 sample has a high daylight-induced photocatalytic activity. This is due to the fact that the  $\text{TiO}_2/\text{C}$ -0.5 sample has the large carbon content of about 32.9% and surface area of  $210.5\text{ m}^2/\text{g}$  (see Table 1). With increasing calcination time, the daylight-induced photocatalytic increases. At  $450^\circ\text{C}$  for 2 h, the photocatalytic activity of the  $\text{TiO}_2/\text{C}$ -2 sample reaches a maximum value, and its activity exceeds that of Degussa P25, which is recognized as an excellent photocatalyst [3, 43–45]. On the one hand, this is attributed to the former having bimodal mesoporous structures, which is more beneficial in enhancing the adsorption and desorption of reactants and products, respectively [45]. On the other hand, the high photocatalytic activity of the  $\text{TiO}_2/\text{C}$ -2 sample is due to its large surface area and high adsorption ability in the near UV and visible-light region. With further increasing calcination time, the photocatalytic activity of the powders decreases. The highest daylight-induced photocatalytic activity of the  $\text{TiO}_2$ -2 sample is due to the following factors.

Usually,  $\text{TiO}_2/\text{C}$  composite photocatalysts can result in a synergistic effect of both  $\text{TiO}_2$  and carbon on the photocatalytic degradation of different modal organic components. Carbon can dramatically improve the photocatalytic activity of titania as coadsorbent due to its very high surface area. Therefore, the carbon content in the  $\text{TiO}_2/\text{C}$  composite catalysts plays an important role in its visible-light photocatalytic activity. It can be seen from Figure 7 that the  $\text{TiO}_2/\text{C}$ -2 sample with higher carbon content shows the superior photocatalytic activity compared with the  $\text{TiO}_2/\text{C}$ -4 sample. This may be ascribed to the fact that higher carbon content results in a intense increase in absorption in the near UV and visible-light region and a red shift in the absorption edge of the  $\text{TiO}_2$ -2 sample (as shown in Figure 6), implying that the  $\text{TiO}_2$ -2 sample can be easier activated by visible

light and more photo-generated electrons and holes can be generated and participate in the photocatalytic reactions. However, adsorption of carbon is not only factor for the enhancement of the photocatalytic activity of  $\text{TiO}_2$ . For example, compared with the  $\text{TiO}_2$ -2 sample, the two  $\text{TiO}_2/\text{C}$ -0.5 and  $\text{TiO}_2/\text{C}$ -1 samples with the larger carbon content have lower daylight-induced photocatalytic activity. This result can be interpreted in two aspects. On one hand, the surplus carbon of the two  $\text{TiO}_2/\text{C}$ -0.5 and  $\text{TiO}_2/\text{C}$ -1 samples can scatter the photons in the photoreaction system [35]. On the other hand, the lower carbon content of the  $\text{TiO}_2/\text{C}$ -2 sample enables the methyl orange aqueous solution to get the active site easier and faster [33]. Therefore, the  $\text{TiO}_2/\text{C}$ -2 sample with an optimum carbon content of about 5.0% has the highest daylight-induced photocatalytic activity.

Apart from the above carbon content, another possible understanding is that the  $\text{TiO}_2$ -1 sample possesses a relative large surface area and good anatase crystallinity (as shown in Tables 1 and 2). Usually, a large specific surface area may enhance the rate of photocatalytic degradation reactions, as a large amount of adsorbed organic molecules promote the photocatalytic reaction [50, 51]. However, the specific surface areas and crystallinity usually appear to be two conflicting intrinsic properties for  $\text{TiO}_2$  nanoparticles [52]. The powders with a large surface area are usually associated with large amounts of crystalline defects or weak crystallization, which favor the recombination of photo-generated electrons and holes, leading to a poor photoactivity [53–55]. For example, with increasing calcination time from 0.5 to 2 h, the surface area decreases greatly, but the photocatalytic activity increases. This may be due to the increase of the relative anatase crystallinity (as shown in Table 1). So a balance between specific surface area and crystallinity is a very important factor in determining the photocatalytic activity of  $\text{TiO}_2$  powders. According to the above results and discussion, the  $\text{TiO}_2/\text{C}$ -2 sample possesses a relative large surface area and good anatase crystallinity (as shown in Tables 1 and 2), resulting in a highest daylight-induced photocatalytic activity.

#### 4. Conclusions

Titania/carbon composite hollow microspheres with bimodal mesoporous shells are one-pot fabricated by hydrothermal treatment of the acidic  $(\text{NH}_4)_2\text{TiF}_6$  aqueous solution in the presence of glucose at  $180^\circ\text{C}$  for 24 h and then calcined at  $450^\circ\text{C}$  for 2–4 h. Calcination time obviously influenced on the morphology, phase structure, crystallite size, specific surface area, pore structures, and daylight-induced photocatalytic activity of the as-obtained hollow microspheres. All  $\text{TiO}_2/\text{C}$  composite hollow spheres generally exhibit bimodal mesopore size distribution with their peak intra-aggregated mesopore size in the range of 2.3–4.5 nm and peak interaggregated mesopore size in the range of 5.7–12.7 nm. The  $\text{TiO}_2$ -2 sample showed the highest daylight-induced photocatalytic activity and greatly exceeded that of Degussa P25.

#### Acknowledgments

This work was partially supported by NSFC (21075030, 51072154 and 51102190) and the Mid-young Scholars' Science and Technology Programs, Hubei Provincial Department of Education (Q20082202).

#### References

- [1] M. R. Hoffmann, S. T. Martin, W. Choi, and D. W. Bahnemann, "Environmental applications of semiconductor photocatalysis," *Chemical Reviews*, vol. 95, no. 1, pp. 69–96, 1995.
- [2] J. Yu, T. Ma, G. Liu, and B. Cheng, "Enhanced photocatalytic activity of bimodal mesoporous titania powders by  $\text{C}_{60}$  modification," *Dalton Transactions*, vol. 40, no. 25, pp. 6635–6644, 2011.
- [3] J. G. Yu, H. G. Yu, B. Cheng, X. J. Zhao, J. C. Yu, and W. K. Ho, "The effect of calcination temperature on the surface microstructure and photocatalytic activity of  $\text{TiO}_2$  thin films prepared by liquid phase deposition," *Journal of Physical Chemistry B*, vol. 107, no. 50, pp. 13871–13879, 2003.
- [4] P. Madhusudan, J. Ran, J. Zhang, J. Yu, and G. Liu, "Novel urea assisted hydrothermal synthesis of hierarchical  $\text{BiVO}_4/\text{Bi}_2\text{O}_3\text{CO}_3$  nanocomposites with enhanced visible-light photocatalytic activity," *Applied Catalysis B*, vol. 110, pp. 286–295, 2011.
- [5] A. Yu, G. Q. M. Lu, J. Drennan, and I. R. Gentle, "Tubular titania nanostructures via layer-by-layer self-assembly," *Advanced Functional Materials*, vol. 17, no. 14, pp. 2600–2605, 2007.
- [6] M. Andersson, L. Österlund, S. Ljungström, and A. Palmqvist, "Preparation of nanosize anatase and rutile  $\text{TiO}_2$  by hydrothermal treatment of microemulsions and their activity for photocatalytic wet oxidation of phenol," *Journal of Physical Chemistry B*, vol. 106, no. 41, pp. 10674–10679, 2002.
- [7] H. Yu, J. Yu, B. Cheng, and S. Liu, "Novel preparation and photocatalytic activity of one-dimensional  $\text{TiO}_2$  hollow structures," *Nanotechnology*, vol. 18, Article ID 65604, 8 pages, 2007.
- [8] J. Yu and H. Tang, "Solvochemical synthesis of novel flower-like manganese sulfide particles," *Journal of Physics and Chemistry of Solids*, vol. 69, no. 5–6, pp. 1342–1345, 2008.
- [9] J. Yu, S. Liu, and H. Yu, "Microstructures and photoactivity of mesoporous anatase hollow microspheres fabricated by fluoride-mediated self-transformation," *Journal of Catalysis*, vol. 249, no. 1, pp. 59–66, 2007.
- [10] J. Yu, G. Wang, B. Cheng, and M. Zhou, "Effects of hydrothermal temperature and time on the photocatalytic activity and microstructures of bimodal mesoporous  $\text{TiO}_2$  powders," *Applied Catalysis B*, vol. 69, no. 3–4, pp. 171–180, 2007.
- [11] G. Wang, "Hydrothermal synthesis and photocatalytic activity of nanocrystalline  $\text{TiO}_2$  powders in ethanol-water mixed solutions," *Journal of Molecular Catalysis A*, vol. 274, no. 1–2, pp. 185–191, 2007.
- [12] Z. Zhong, Y. Yin, B. Gates, and Y. Xia, "Preparation of mesoscale hollow spheres of  $\text{TiO}_2$  and  $\text{SnO}_2$  by templating against crystalline arrays of polystyrene beads," *Advanced Materials*, vol. 12, no. 3, pp. 206–209, 2000.
- [13] Y. Z. Zhu, Y. L. Cao, Z. H. Li, J. Ding, J. S. Liu, and Y. B. Chi, "Synthesis and photonic band calculations of NCP face-centered cubic photonic crystals of  $\text{TiO}_2$  hollow spheres,"

- Journal of Colloid and Interface Science*, vol. 306, no. 1, pp. 133–136, 2007.
- [14] D. Wang, C. Song, Y. Lin, and Z. Hu, “Preparation and characterization of TiO<sub>2</sub> hollow spheres,” *Materials Letters*, vol. 60, no. 1, pp. 77–80, 2006.
- [15] J. Yu and J. Zhang, “A simple template-free approach to TiO<sub>2</sub> hollow spheres with enhanced photocatalytic activity,” *Dalton Transactions*, vol. 39, no. 25, pp. 5860–5867, 2010.
- [16] V. Jokanović, B. Jokanović, J. Nedeljković, and O. Milošević, “Modeling of nanostructured TiO<sub>2</sub> spheres obtained by ultrasonic spray pyrolysis,” *Colloids and Surfaces A*, vol. 249, no. 1–3, pp. 111–113, 2004.
- [17] S. Liu, J. Yu, and M. Jaroniec, “Tunable photocatalytic selectivity of hollow TiO<sub>2</sub> microspheres composed of anatase polyhedra with exposed 001 facets,” *Journal of the American Chemical Society*, vol. 132, no. 34, pp. 11914–11916, 2010.
- [18] J. Yu, Q. Xiang, J. Ran, and S. Mann, “One-step hydrothermal fabrication and photocatalytic activity of surface-fluorinated TiO<sub>2</sub> hollow microspheres and tabular anatase single microcrystals with high-energy facets,” *Crystal Engineering communication*, vol. 12, no. 3, pp. 872–879, 2010.
- [19] J. Li and C. Z. Hua, “Size tuning, functionalization, and reactivation of Au in TiO<sub>2</sub> nanoreactors,” *Angewandte Chemie*, vol. 44, no. 28, pp. 4342–4345, 2005.
- [20] J. Yu, H. Guo, S. A. Davis, and S. Mann, “Fabrication of hollow inorganic microspheres by chemically induced self-transformation,” *Advanced Functional Materials*, vol. 16, no. 15, pp. 2035–2041, 2006.
- [21] T. Peng, A. Hasegawa, J. Qiu, and K. Hirao, “Fabrication of titania tubules with high surface area and well-developed mesostructural walls by surfactant-mediated templating method,” *Chemistry of Materials*, vol. 15, no. 10, pp. 2011–2016, 2003.
- [22] Q. Peng, S. Xu, Z. Zhuang, X. Wang, and Y. Li, “A general chemical conversion method to various semiconductor hollow structures,” *Small*, vol. 1, no. 2, pp. 216–221, 2005.
- [23] S. Kobayashi, K. Hanabusa, N. Hamasaki, M. Kimura, H. Shirai, and S. Shinkai, “Preparation of TiO<sub>2</sub> hollow-fibers using supramolecular assemblies,” *Chemistry of Materials*, vol. 12, no. 6, pp. 1523–1525, 2000.
- [24] T. Nakashima and N. Kimizuka, “Interfacial synthesis of hollow TiO<sub>2</sub> microspheres in ionic liquids,” *Journal of the American Chemical Society*, vol. 125, no. 21, pp. 6386–6387, 2003.
- [25] T. Z. Ren, Z. Y. Yuan, and B. L. Su, “Surfactant-assisted preparation of hollow microspheres of mesoporous TiO<sub>2</sub>,” *Chemical Physics Letters*, vol. 374, no. 1–2, pp. 170–175, 2003.
- [26] J. H. Jung, H. Kobayashi, K. J. C. Van Bommel, S. Shinkai, and T. Shimizu, “Creation of novel helical ribbon and double-layered nanotube TiO<sub>2</sub> structures using an organogel template,” *Chemistry of Materials*, vol. 14, no. 4, pp. 1445–1447, 2002.
- [27] S. M. Liu, L. M. Gan, L. H. Liu, W. D. Zhang, and H. C. Zeng, “Synthesis of single-crystalline TiO<sub>2</sub> nanotubes,” *Chemistry of Materials*, vol. 14, no. 3, pp. 1391–1397, 2002.
- [28] X. Sun, J. Liu, and Y. Li, “Use of carbonaceous polysaccharide microspheres as templates for fabricating metal oxide hollow spheres,” *Chemistry*, vol. 12, no. 7, pp. 2039–2047, 2006.
- [29] M. M. Titirici, M. Antonietti, and A. Thomas, “A generalized synthesis of metal oxide hollow spheres using a hydrothermal approach,” *Chemistry of Materials*, vol. 18, no. 16, pp. 3808–3812, 2006.
- [30] D. Zhang, D. Yang, H. Zhang, C. Lu, and L. Qi, “Synthesis and photocatalytic properties of hollow microparticles of titania and titania/carbon composites templated by sephadex G-100,” *Chemistry of Materials*, vol. 18, no. 15, pp. 3477–3485, 2006.
- [31] Y. Tao, S. Schwartz, C. Y. Wu, and D. W. Mazyck, “Development of a TiO<sub>2</sub>/AC composite photocatalyst by dry impregnation for the treatment of methanol in humid airstreams,” *Industrial and Engineering Chemistry Research*, vol. 44, no. 19, pp. 7366–7372, 2005.
- [32] W.-C. Oh and M.-L. Chen, “The improved photocatalytic properties of methylene blue for V<sub>2</sub>O<sub>5</sub>/CNT/TiO<sub>2</sub> composite under visible light,” *International Journal of Photoenergy*, vol. 2010, Article ID 264831, 12 pages, 2010.
- [33] S. Shanmugam, A. Gabashvili, D. S. Jacob, J. C. Yu, and A. Gedanken, “Synthesis and characterization of TiO<sub>2</sub>@C core-shell composite nanoparticles and evaluation of their photocatalytic activities,” *Chemistry of Materials*, vol. 18, no. 9, pp. 2275–2282, 2006.
- [34] J. Yu, T. Ma, and S. Liu, “Enhanced photocatalytic activity of mesoporous TiO<sub>2</sub> aggregates by embedding carbon nanotubes as electron-transfer channel,” *Physical Chemistry Chemical Physics*, vol. 13, no. 8, pp. 3491–3501, 2011.
- [35] W. Wang, P. Serp, P. Kalck, and J. L. Faria, “Visible light photodegradation of phenol on MWNT-TiO<sub>2</sub> composite catalysts prepared by a modified sol-gel method,” *Journal of Molecular Catalysis A*, vol. 235, no. 1–2, pp. 194–199, 2005.
- [36] Q. Xiang, J. Yu, and M. Jaroniec, “Enhanced photocatalytic H<sub>2</sub>-production activity of graphene-modified titania nanosheets,” *Nanoscale*, vol. 3, no. 9, pp. 3670–3678, 2011.
- [37] Y. Tao, C. Y. Wu, and D. W. Mazyck, “Microwave-assisted preparation of TiO<sub>2</sub>/activated carbon composite photocatalyst for removal of methanol in humid air streams,” *Industrial and Engineering Chemistry Research*, vol. 45, no. 14, pp. 5110–5116, 2006.
- [38] J. Yu, J. C. Yu, M. K. P. Leung et al., “Effects of acidic and basic hydrolysis catalysts on the photocatalytic activity and microstructures of bimodal mesoporous titania,” *Journal of Catalysis*, vol. 217, no. 1, pp. 69–78, 2003.
- [39] K. S. W. Sing, D. H. Everett, and R. A. W. Haul, “Reporting physisorption data for gas/solid systems with special reference to the determination of surface area and porosity,” *Pure and Applied Chemistry*, vol. 57, no. 4, pp. 603–619, 1985.
- [40] S. J. Gregg and K. S. W. Sing, *Adsorption, Surface Area and Porosity*, Academic Press, London, UK, 1982.
- [41] E. P. Barrett, L. G. Joyner, and P. P. Halenda, “The determination of pore volume and area distributions in porous substances. I. Computations from nitrogen isotherms,” *Journal of the American Chemical Society*, vol. 73, no. 1, pp. 373–380, 1951.
- [42] H. Yu, J. Yu, S. Liu, and S. Mann, “Template-free hydrothermal synthesis of CuO/Cu<sub>2</sub>O composite hollow microspheres,” *Chemistry of Materials*, vol. 19, no. 17, pp. 4327–4334, 2007.
- [43] T. Tsumura, N. Kojitani, I. Izumi, N. Iwashita, M. Toyoda, and M. Inagaki, “Carbon coating of anatase-type TiO<sub>2</sub> and photoactivity,” *Journal of Materials Chemistry*, vol. 12, no. 5, pp. 1391–1396, 2002.
- [44] H. Li, Z. Bian, J. Zhu et al., “Mesoporous titania spheres with tunable chamber structure and enhanced photocatalytic activity,” *Journal of the American Chemical Society*, vol. 129, no. 27, pp. 8406–8407, 2007.

- [45] J. Yu, J. C. Yu, W. Ho et al., "Effects of alcohol content and calcination temperature on the textural properties of bimodally mesoporous titania," *Applied Catalysis A*, vol. 255, no. 2, pp. 309–320, 2003.
- [46] J. G. Yu, J. C. Yu, B. Cheng, S. K. Hark, and K. Iu, "The effect of F<sup>-</sup> doping and temperature on the structural and textural evolution of mesoporous TiO<sub>2</sub> powders," *Journal of Solid State Chemistry*, vol. 174, no. 2, pp. 372–380, 2003.
- [47] K. N. P. Kumar, J. Kumar, and K. Keizer, "Effect of peptization on densification and phase-transformation behavior of sol-gel-derived nanostructured titania," *Journal of the American Ceramic Society*, vol. 77, no. 5, pp. 1396–1400, 1994.
- [48] N. Serpone, D. Lawless, and R. Khairutdinov, "Size effects on the photophysical properties of colloidal anatase TiO<sub>2</sub> particles: size quantization or direct transitions in this indirect semiconductor?" *Journal of Physical Chemistry*, vol. 99, no. 45, pp. 16646–16654, 1995.
- [49] J. Yu, M. Zhou, B. Cheng, and X. Zhao, "Preparation, characterization and photocatalytic activity of in situ N,S-codoped TiO<sub>2</sub> powders," *Journal of Molecular Catalysis A*, vol. 246, no. 1-2, pp. 176–184, 2006.
- [50] J. Yu, M. Zhou, B. Cheng, H. Yu, and X. Zhao, "Ultrasonic preparation of mesoporous titanium dioxide nanocrystalline photocatalysts and evaluation of photocatalytic activity," *Journal of Molecular Catalysis A*, vol. 227, no. 1-2, pp. 75–80, 2005.
- [51] M. Zhou, J. Yu, B. Cheng, and H. Yu, "Preparation and photocatalytic activity of Fe-doped mesoporous titanium dioxide nanocrystalline photocatalysts," *Materials Chemistry and Physics*, vol. 93, no. 1, pp. 159–163, 2005.
- [52] G. Liu, Z. Chen, C. Dong et al., "Visible light photocatalyst: iodine-doped mesoporous titania with a bicrystalline framework," *Journal of Physical Chemistry B*, vol. 110, no. 42, pp. 20823–20828, 2006.
- [53] O. Carp, C. L. Huisman, and A. Reller, "Photoinduced reactivity of titanium dioxide," *Progress in Solid State Chemistry*, vol. 32, no. 1-2, pp. 33–177, 2004.
- [54] K. Tanaka, M. F. V. Capule, and T. Hisanaga, "Effect of crystallinity of TiO<sub>2</sub> on its photocatalytic action," *Chemical Physics Letters*, vol. 187, no. 1-2, pp. 73–76, 1991.
- [55] B. Ohtani, Y. Ogawa, and S. I. Nishimoto, "Photocatalytic activity of amorphous-anatase mixture of titanium(IV) oxide particles suspended in aqueous solutions," *Journal of Physical Chemistry B*, vol. 101, no. 19, pp. 3746–3752, 1997.

## Research Article

# Removal of a Cationic Dye by Adsorption/Photodegradation Using Electrospun PAN/O-MMT Composite Nanofibrous Membranes Coated with TiO<sub>2</sub>

Qingqing Wang,<sup>1</sup> Dawei Gao,<sup>1</sup> Chuntao Gao,<sup>1</sup> Qufu Wei,<sup>1</sup>  
Yibing Cai,<sup>1</sup> Jing Xu,<sup>2</sup> Xiaoya Liu,<sup>2</sup> and Yang Xu<sup>1</sup>

<sup>1</sup> Key Laboratory of Eco-Textiles, Ministry of Education, Jiangnan University, Wuxi 214122, China

<sup>2</sup> School of Chemical and Material Engineering, Jiangnan University, Wuxi 214122, China

Correspondence should be addressed to Qufu Wei, qufu.wei@163.com

Received 8 September 2011; Revised 5 November 2011; Accepted 14 November 2011

Academic Editor: Mietek Jaroniec

Copyright © 2012 Qingqing Wang et al. This is an open access article distributed under the Creative Commons Attribution License, which permits unrestricted use, distribution, and reproduction in any medium, provided the original work is properly cited.

Polyacrylonitrile (PAN)/organic-modified montmorillonite (O-MMT) composite nanofibrous membranes were firstly prepared by electrospinning and then coated with titanium dioxide (TiO<sub>2</sub>) using spin coating technique. The structural morphology of the nanofibrous membranes with different mass ratio of O-MMT before and after spin coating was investigated by scanning electron microscope (SEM) and transmission electron microscope (TEM). The chemical property of adsorbed methylene blue (MB) was analyzed by infrared spectroscopy (IR). The adsorption and photodegradation capability of the TiO<sub>2</sub>-coated PAN/O-MMT composite nanofibrous membranes were evaluated by adsorption rate of MB and K/S values of the membranes before and after UV irradiation. The experimental results indicated that with the increase of O-MMT amount, the diameters of the nanofibers decreased and the adsorption rate of MB was evidently improved. Besides, with the increase of TiO<sub>2</sub> film layers, the photocatalytic properties were enhanced while the adsorption process was slowed down.

## 1. Introduction

Industrial dyes have been recognized as one of the largest sources of water contamination. Some of the dyes and their metabolites are toxic and carcinogenic and reported to have connections with different respiratory disorders worldwide [1]. Many efforts have been devoted in recent years to remove dyes from wastewaters, such as carbon adsorption, filtration, chemical precipitation, photodegradation, biodegradation, electrolytic chemical treatment, and membrane technology [2]. Adsorption removal is an effective and simple method for dye treatment but usually produces large amount of sludge [3], which may cause secondary pollution. As is known, no individual treatment technique is ideal enough to efficiently remove dyes from wastewaters with no secondary contaminants generated. So combining two or more treatment techniques together seems quite necessary.

So far, activated carbon is the most widely used adsorbent for organic substances, including dyes, due to its

high adsorption capacity, high specific surface area, and low selectivity [4]. However, it is too expensive. Hence, lots of studies have investigated alternative adsorbents with high efficiency for dye removal at a reasonable cost [5–7]. Electrospun nanofibrous membrane is a good choice for it possesses a number of interesting characteristics such as high porosity, large surface area per unit mass, high gas permeability, and small interfibrous porous size [8]. The introduction of specific functional groups onto the electrospun nanofibers [9, 10] or addition of inorganic nanoparticles like montmorillonite (MMT) [11] into polymer matrix was reported for the removal or adsorption of specific materials from aqueous solutions. Some recent studies [12, 13] indicated that MMT clay has been accepted as one of the low-cost adsorbents for cationic dye adsorption because there are plenty of negative charges on MMT clays and it has large cation-exchange capacity (CEC). However, to the best of our knowledge, there is no literature focusing on the adsorption capacity of cationic dye onto the electrospun nanofibers based on

polymers and MMT clays. PAN is easily to be electrospun into nanofibers and it is stable in the environment. So in this work, we studied the adsorption properties of methylene blue (MB) onto the electrospun PAN/MMT composite nanofibers.

As we have mentioned herein before, adsorption process would result in secondary pollution, so  $\text{TiO}_2$  was introduced onto the composite nanofibrous membrane by spin coating. Due to its chemical stability, nontoxicity, and high photocatalytic reactivity,  $\text{TiO}_2$  has been recognized as the best candidate for photocatalytic applications [14, 15]. A low temperature process is adopted because it is beneficial for the use of low thermally resistant materials such as plastics, wood, or paper as substrates [16].

In this paper, low-temperature  $\text{TiO}_2$  was synthesized and spin coated onto the surface of electrospun PAN/O-MMT composite nanofibrous membrane. The adsorption and photocatalysis processes were investigated, and the effects of O-MMT concentration and spin coating layers on adsorption capacity and photocatalytic efficiency of the composite membranes were evaluated through the adsorption and degradation of MB from aqueous solution.

## 2. Experimental

**2.1. Materials.** The montmorillonite (MMT, cation exchange capacity, 97 meq/100 g of clay) organically modified by cetyltrimethyl ammonium bromide (CTAB) was a kind gift from Zhejiang Fenghong Clay Chemicals Co., Ltd. The average thickness of the O-MMT was less than 25 nm, and the ratio of diameter to thickness was about 200. The polyacrylonitrile (PAN, Mw = 79,100) powder was obtained from Aldrich. The 99.5% N, N-dimethyl formamide (DMF), tetrabutyl titanate ( $\text{Ti}(\text{OC}_4\text{H}_9)_4$ , CP), ethanol (EtOH, AR) and hydrochloric acid (HCl, AR) were all used as received.

**2.2. Preparation of Electrospun Composite Nanofibers.** 3 g PAN powder was dissolved in 27 mL DMF by magnetically stirring for 24 hrs at room temperature. Then the polymer solution was centrifuged at the speed of 4000 rpm for 10 min to remove the impurities. After the purification process, certain quantity of O-MMT powders was added into the polymer solution and stirred another 6 h to prepare electrospinning solutions with 0, 1, 3, 5 wt.% O-MMT, respectively.

The polymer solutions were electrospun at a positive voltage of 12 kv with a working distance of 15 cm, and the flowrate was set as 0.5 mL/h.

**2.3. Synthesis of Low-Temperature  $\text{TiO}_2$ .** The low-temperature  $\text{TiO}_2$  sol was prepared by firstly dissolving 10 mL  $\text{Ti}(\text{OC}_4\text{H}_9)_4$  in 5 mL absolute ethanol. After magnetically stirring for a certain time at room temperature until it was completely homogeneous, the solution was added dropwise into the blended solution of deionized water and HCl. The mixtures were placed at room temperature for 5 days to obtain transparent  $\text{TiO}_2$  sol.

**2.4. Spin Coating Technique.** The PAN and PAN/O-MMT composite nanofibrous membranes were cut into 7 cm\*7 cm

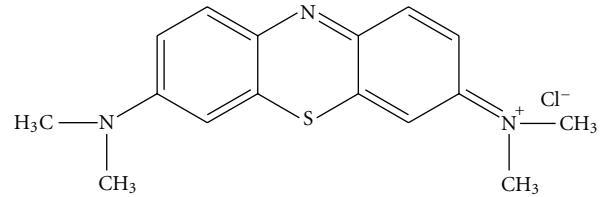


FIGURE 1: The chemical structure of methylene blue.

squares. The aluminum foil side was pasted on the disc. An amount of 0.1 mL  $\text{TiO}_2$  sol was spin coated on the surface of the nanofibrous membranes at the speed of 4000 rpm. The membranes coated with  $\text{TiO}_2$  were dried at 60°C in vacuum oven for 10 min.

**2.5. Adsorption and Photocatalytic Degradation of MB.** The adsorption performance of the PAN and PAN/O-MMT composite nanofiber membranes coated with  $\text{TiO}_2$  was evaluated through the decreased UV absorbency of MB solution. The chemical structure of MB is shown in Figure 1. The concentration of MB was 0.02 g/L. The samples weighed 0.05 g were placed in beakers containing 40 mL MB solution, and the absorbency of the MB solution at the wavelength of 664 nm was measured every 10 min by a UV-vis spectrophotometer (UV-2100, China). The adsorption rate of MB can be calculated using the following formula:

$$\text{Adsorption rate} = \frac{A_0 - A}{A_0}, \quad (1)$$

where  $A_0$  and  $A$  are the absorbency of the initial and remaining MB, respectively.

The photocatalytic performance of the membranes was evaluated by an Xrite-8400 spectrophotometer under illuminant D65 using the 10° standard observer [17]. The relative color strength and staining on the white nanofibrous membrane were determined with the Kubelka-Munk equations. The color strength was signified by the  $K/S$  value,

$$\frac{K}{S} = \frac{1 - R^2}{2R}, \quad (2)$$

where  $K$  is the absorption coefficient,  $S$  is the scattering coefficient, and  $R$  is the fraction reflectance (value from 0 to 1) of the dyed substrate at the wavelength of minimum reflectance. The  $K/S$  values are proportional to the dyeing color [18].

After adsorption process, the nanofibrous membranes were dried and the  $K/S$  value was measured. Then the membranes were placed in beakers with 40 mL deionized water under 100 w ultraviolet (UV) light at a wavelength of 254 nm. After 48 hour's irradiation, the membranes were taken out and dried for measuring the  $K/S$  value.

**2.6. Characterization.** Scanning electron microscope (SEM, Quanta 200, Holland FEI Company) was used to investigate the surface morphology of the PAN and PAN/O-MMT composite nanofibers before and after spin coating. The samples were coated with a thin layer of gold by sputtering before the SEM imaging. Diameters of the electrospun nanofibers

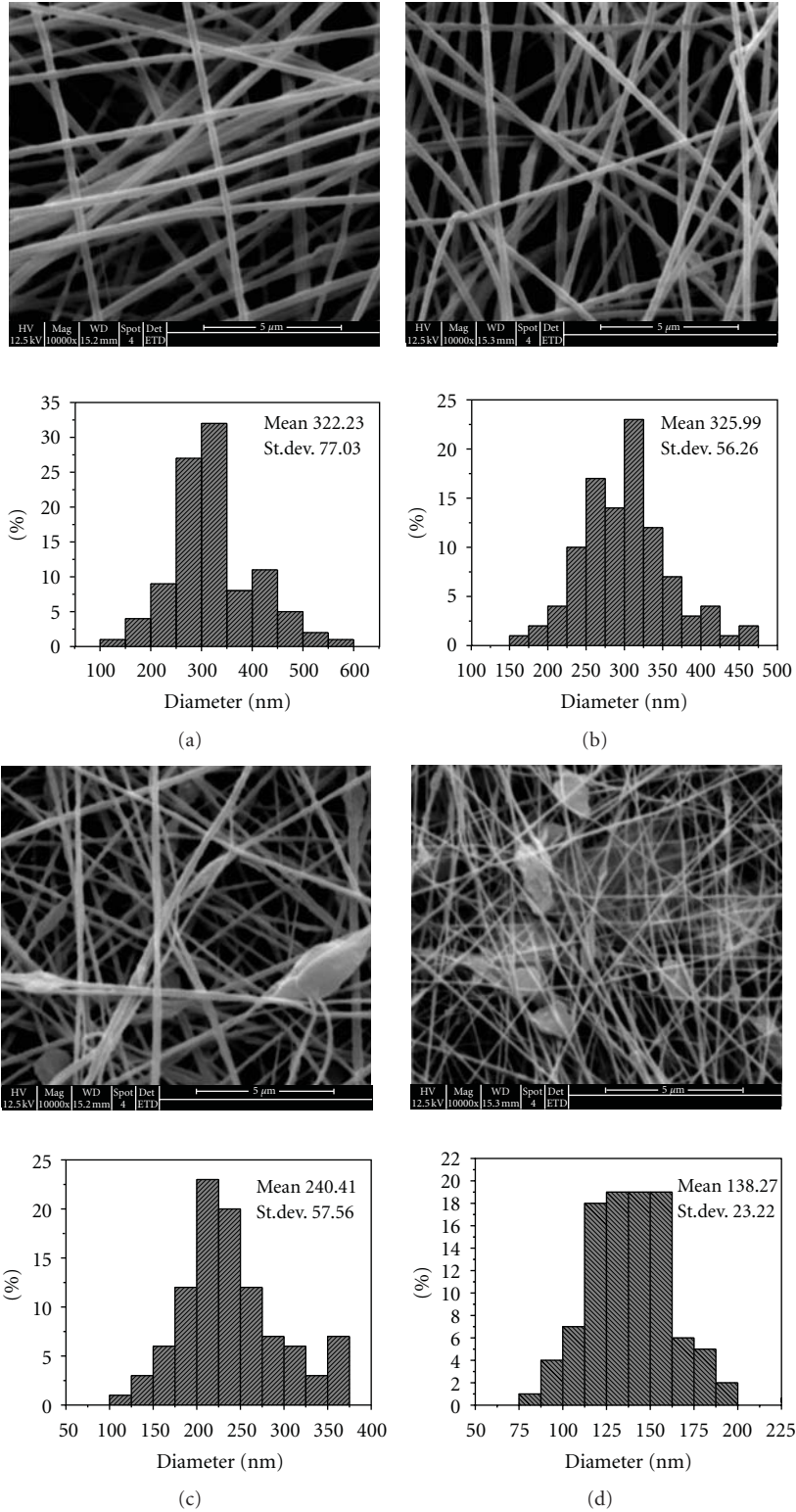


FIGURE 2: SEM images and diameter histogram distribution chart of PAN and PAN/O-MMT composite nanofibers: (a) 0 wt.% O-MMT; (b) 1 wt.% O-MMT; (c) 3 wt.% O-MMT; (d) 5 wt.% O-MMT.

were measured by Adobe Acrobat 7.0 professional from the SEM images, and 100 fibers were analyzed for each sample to obtain an average fiber diameter. In detail, after the SEM images were opened by Adobe Acrobat professional, the

distance measurement was clicked to measure the diameter of the nanofibers. The zoom factor was set according to the scale plate in the SEM images before measuring. Every time the diameters were measured, a serial number was given to

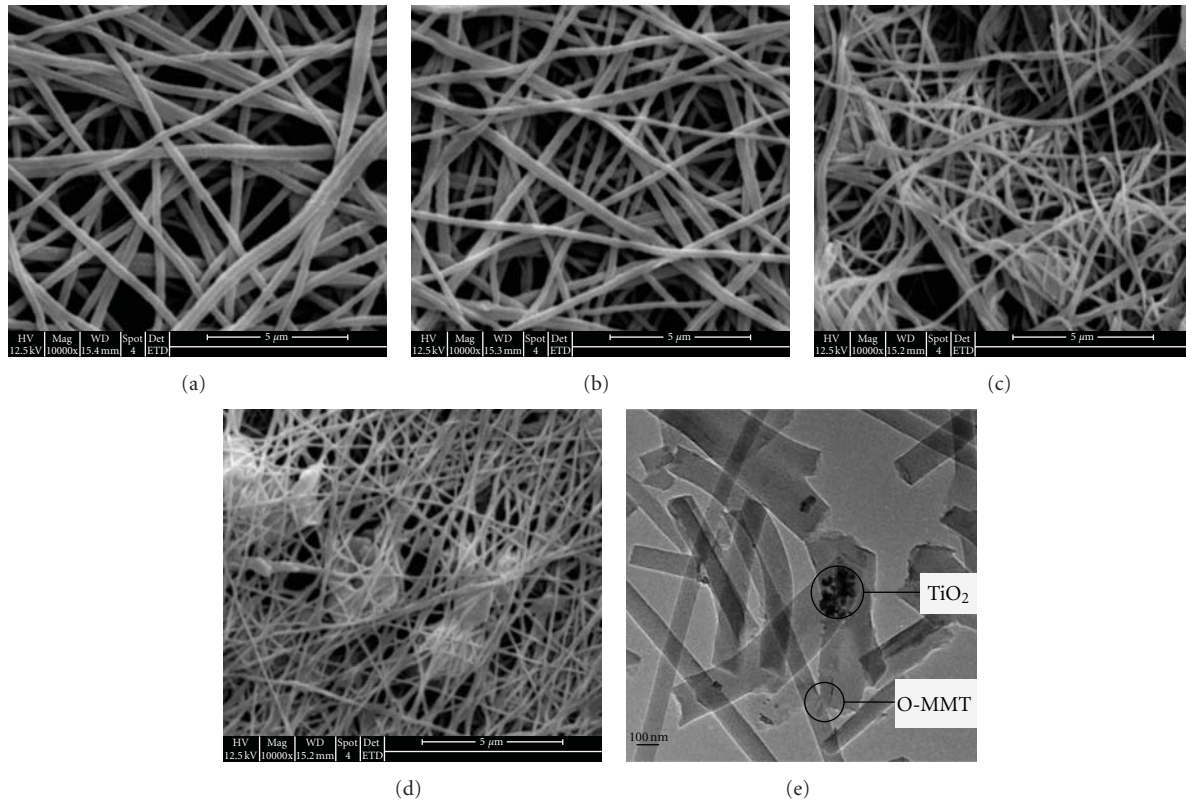


FIGURE 3: SEM (a–d) and TEM (e) images of PAN and PAN/O-MMT spin coated with  $\text{TiO}_2$ : (a) 0 wt.% O-MMT; (b) 1 wt.% O-MMT; (c) 3 wt.% O-MMT; (d) 5 wt.% O-MMT; (e) TEM of c.

the data obtained. Finally, the data were exported to origin professional 7.0 to analyze the diameter distribution.

Transmission electron microscope (TEM, JEOL2010, Philips) was employed to analyze the intercalation structure of the PAN/O-MMT composite nanofibers and the existence of  $\text{TiO}_2$  particles. The nanofibrous membranes after spin coating were pestled into powders and then dissolved in blend solution of deionized water and ethanol, using ultrasonic vibration to fully disperse the nanofibrous powders, and then dripped onto a 200-mesh Cu grid.

The intercalation structures of the MB in O-MMT layers after adsorption process were investigated by Fourier Transform Infrared Spectroscopy (FTIR, Nicolet Nexus, Thermo Electron Corporation) in the range  $4000\text{--}400\text{ cm}^{-1}$ , using KBr-pressed method. The spectra were recorded with 32 scans with a resolution of  $4\text{ cm}^{-1}$ .

### 3. Results and Discussion

**3.1. Structural Morphology of the As-Spun PAN and PAN/O-MMT Composite Nanofibers.** Morphologies of the electrospun nanofibers with different content of O-MMT were investigated by SEM, as shown in Figure 2. As can be seen from this figure, the morphology and average diameter of the electrospun PAN/O-MMT composite nanofibers are significantly affected by the amount of O-MMT added. With the increase of O-MMT loading, the average diameters of the composite nanofibers are decreased and some beaded structures are formed, as indicated in Figures 2(c) and

2(d). For pure PAN nanofibers, grooves can be seen on the surface of the most nanofibers, which might be caused by the solvent volatilization. The diameters of pure PAN nanofibers were ranged from 250 to 550 nm, mostly distributed in 350–375 nm, while the average diameter of the electrospun PAN composite nanofibers with 1 wt.% O-MMT was approximately 325 nm, just slightly decreased compared to pure PAN nanofibers, and no sign of beaded formation, as indicated in Figure 2(b). When the amount of O-MMT increased to 3 wt.% and 5 wt.%, the average diameters of the composite nanofibers were further decreased to 240 nm and 138 nm, respectively. The beaded structures of the nanofibers were also formed, which could be attributed to the aggregation (multilayer stacks) of the O-MMT [19], as shown in Figures 2(c) and 2(d). The loading O-MMT containing a quaternary ammonium ion as an organic modifier and  $\text{Na}^+$  and  $\text{Zn}^{2+}$  ions located between MMT layers improved the conductivity of PAN/O-MMT solutions. During the electrospinning process, the charged density in ejected jets was increased, and thus stronger elongation forces were imposed to the jets because of the self-repulsion of the excess charges under the electrical field, resulting in smaller diameters of the electrospun nanofibers [20].

**3.2. Surface Morphology of the Electrospun Nanofibers Coated with  $\text{TiO}_2$ .** The surface morphology after spin coating was investigated by SEM, and TEM was employed to investigate the dispersion of O-MMT and  $\text{TiO}_2$ .

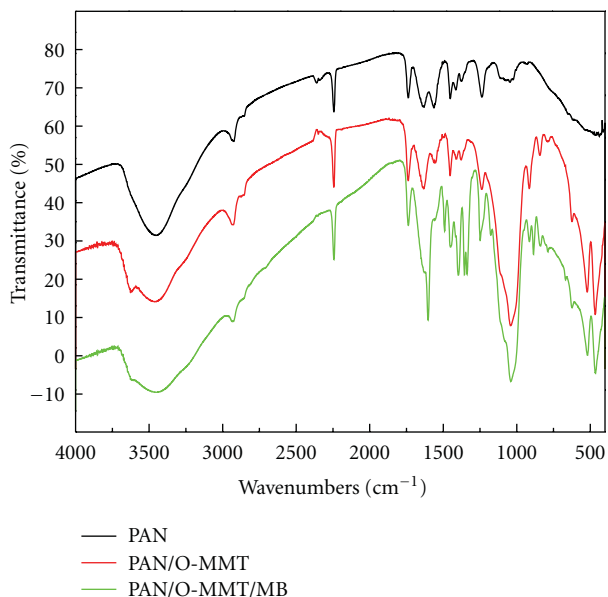


FIGURE 4: FTIR spectra of PAN, PAN/O-MMT nanofibers, and PAN/O-MMT nanofibers adsorbed with MB.

After spin coating, all fibers kept their fibrous shape, but became more densely packed and relaxed, as shown in Figures 3(a)–3(d). The nanofibers with smaller diameters tend to stick together. And so the pores generated by the nanofibers intertwining together became smaller. This is in accordance with the experimental phenomenon. After spin coating, the membranes shrank and became stiffer.

Figure 3(e) shows the TEM micrograph of the PAN/O-MMT composite nanofibers coated with  $\text{TiO}_2$  sol, in which the brighter fibers represent the PAN matrix and the dark narrow stripes as well as the particles stand for the O-MMT and  $\text{TiO}_2$ , respectively. The O-MMT lamellas exfoliated and oriented along the fibers axis direction. This alignment might be attributed to the traction force generated by the electric field. Besides, the coated  $\text{TiO}_2$  sol clustered on the surface of the nanofibers but not uniformly distributed.

**3.3. FTIR Analysis.** The FTIR spectra of PAN, PAN/O-MMT nanofibers, and PAN/O-MMT nanofibers adsorbed with MB are presented in Figure 4. It can be seen from the PAN curve that the peak at  $2242\text{ cm}^{-1}$  can be assigned to nitrile groups, while those at  $2940$  and  $1452\text{ cm}^{-1}$  are, respectively, ascribed to the C–H stretching vibration and bending vibration. Compared with the spectra of PAN nanofibers, PAN/O-MMT showed the development of additional bands at  $3618$ ,  $1037$ ,  $838$ ,  $518$ , and  $464\text{ cm}^{-1}$ , corresponding to Al–O stretching vibration, Si–O stretching vibration, Si–O–H stretching vibration, Si–O–Al stretching vibration, and Si–O–Si bending vibration of MMT, respectively. After MB adsorption process, some additional bands can also be seen from Figure 4. The bands at  $2805$  and  $2709\text{ cm}^{-1}$  are assigned to symmetric and asymmetric stretching vibrations of methyl and methylene groups, whereas the characteristic peaks at  $1604$  and  $1335\text{ cm}^{-1}$  are stretching vibrations of C=C in aromatic rings and C–N stretching vibrations of tertiary

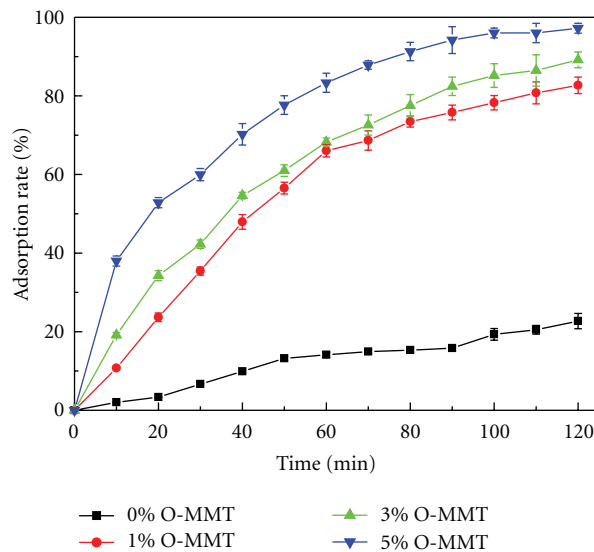


FIGURE 5: Effect of the amounts of O-MMT on adsorption capacity of the membranes for MB.

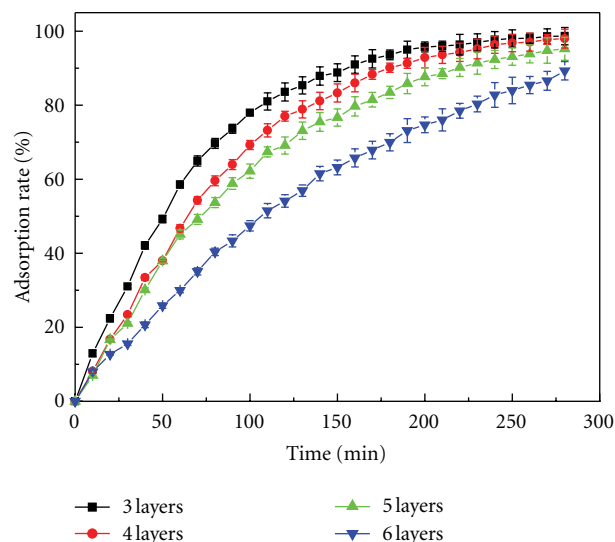


FIGURE 6: Effect of the  $\text{TiO}_2$  film layers on adsorption capacity of the membranes for MB: the substrate is PAN composite nanofibrous membranes with 3 wt.% O-MMT.

amines of MB, respectively. A new IR band at  $912\text{ cm}^{-1}$  is shown, which might be attributed to  $\text{Si-O}^{\delta-}\cdots\delta^+-\text{MB}^+$  from the polarized Si–O bond, that is, MB combined with  $\text{SiO}_2$  in MMT. This confirms the intercalation of MB onto the MMT component of PAN/O-MMT composite nanofibers.

**3.4. Adsorption Properties of the Membranes.** The effects of different concentrations of O-MMT on adsorption capacity of PAN and PAN/O-MMT composite nanofibers for MB are shown in Figure 5. The error bars represent the standard deviation of three separate replicates of each experiment. It is clear that O-MMT content is an important factor affecting adsorption capacity of the membranes. As can be seen from Figure 5, the adsorption rates at 120 min of the four samples

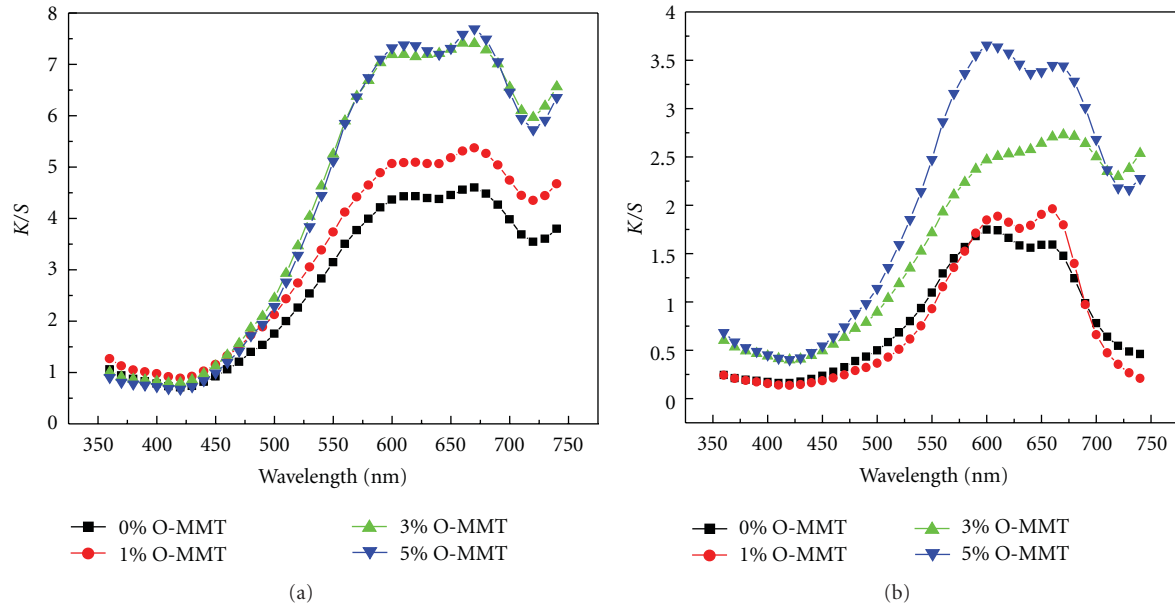


FIGURE 7: K/S curves of the PAN composite nanofibers with different mass ratios of O-MMT before (a) and after (b) photocatalytic process: the substrate is PAN/O-MMT composite nanofibrous membranes coated with three layers of  $\text{TiO}_2$ .

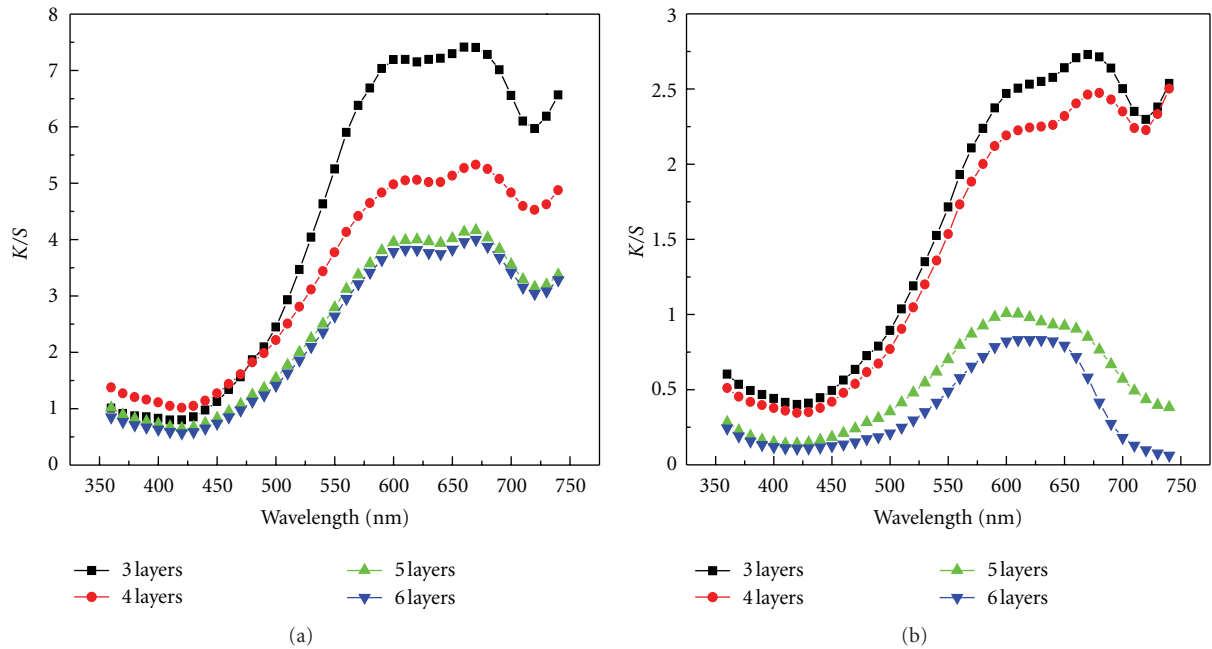


FIGURE 8: K/S curves of the membranes coated with different layers before (a) and after (b) photocatalytic process: the substrate is PAN composite nanofibrous membranes with 3% O-MMT.

with 0, 1, 3, and 5 wt.% O-MMT were 22.69%, 82.69%, 89.18%, and 97.21%, respectively. According to the SEM analysis, the addition of O-MMT decreased the nanofibers diameter, so the specific surface area was increased, resulting in higher MB adsorption rate. Besides, the introduced MMT generated a loose and porous surface [21]. This surface is convenient for the penetration of dye molecules into the composite nanofibers' surface and then may be of benefit to adsorption capacities of the membranes [22].

The effect of  $\text{TiO}_2$  film layers on adsorption capacities of PAN composite nanofibers with 3 wt.% O-MMT for MB was also investigated, the results are shown in Figure 6, and the error bars represent the standard deviation of three separate replicates of each experiment. At the end of this experiment, the adsorption rates for the four samples coated with 3, 4, 5, and 6 layers of  $\text{TiO}_2$  film were 98.66%, 97.98%, 95.23%, and 89.30%, respectively. So the  $\text{TiO}_2$  coating layers have no significant effect on the adsorption capacities, but

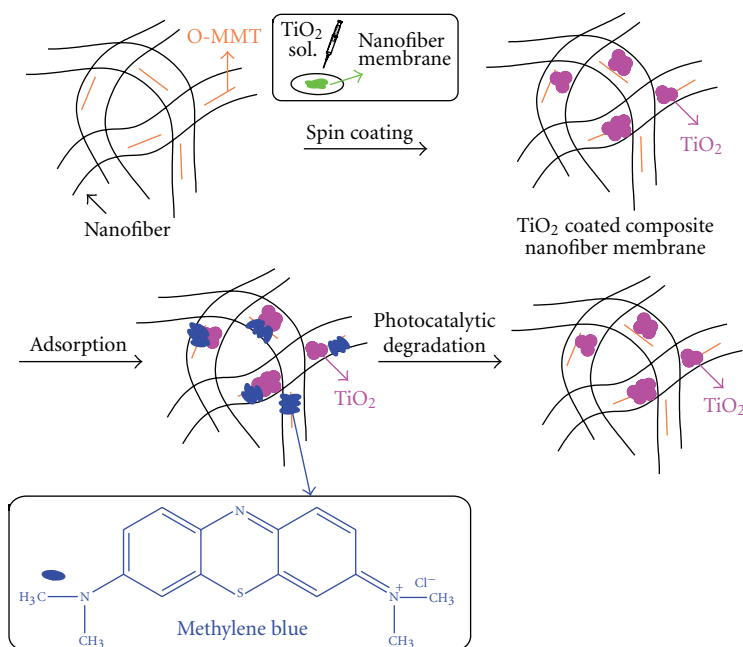


FIGURE 9: The flow chart of the formation of the composite membranes and the process of adsorption and photocatalytic degradation.

the adsorption process was slowed down. According to the SEM analysis, the nanofibers stick together and the pores among the nanofibers were narrowed or blocked after the spin coating process. Hence, the coating layers might hinder MB from contacting with O-MMT; thus it takes longer time to adsorb the same amount of MB than the uncoated membranes.

**3.5. Photocatalytic Activity of the Composite Membranes.** After adsorption process, the nanofiber membranes became blue with different degree of dye depth. K/S value is usually used to evaluate the depth of dyeing, so it was employed here to measure the degree of MB adsorption and photocatalytic degradation.

Before photocatalytic process, the membranes coated with three layers of  $\text{TiO}_2$  were immersed in MB solutions for 36 hrs to reach adsorption equilibrium. Then the membranes were taken out and dried for K/S measurement; the corresponding K/S curves were shown in Figure 7(a). It can be seen that the K/S values for PAN composite nanofibers with 0, 1, 3 and 5 wt.% O-MMT were 4.5995, 5.3702, 7.4117, and 7.6924, respectively. The results indicated that the addition of O-MMT increased markedly the dye depth of nanofiber membranes.

After 48 hrs UV irradiation, the membranes became light blue. And the K/S values of the four samples decreased to 1.5913, 1.9621, 2.7069, and 3.4409, respectively, as shown in Figure 7(b). It could be inferred that the O-MMT concentration only has effect on the adsorption capacity of O-MMT; however, the degradation rate of MB was not affected by the O-MMT content. Therefore, it can be concluded that the effect of O-MMT content on the photocatalytic degradation of MB adsorbed by the composite membranes could be neglected.

The number of  $\text{TiO}_2$  film layers has impact on the MB adsorption rate, as explained hereinbefore. However, the film layers may change the photocatalytic capacities evidently. So the effect of film layers on MB photodegradation is also investigated, as shown in Figure 8.

After adsorption process, the K/S values for the four membranes spin coated with 3, 4, 5, and 6 layers of  $\text{TiO}_2$  films were 7.4117, 5.3248, 4.1635, and 4.0003, respectively. As shown in Figure 8(a), membranes coated with 3 layers  $\text{TiO}_2$  films exhibited higher dye uptake rate. This phenomenon may be caused by  $\text{TiO}_2$  films' hindrance for the MB molecules to reach the ionic sites in MMT sheets.

Then, after 48 hrs UV irradiation, the K/S values for the four samples became 2.7069, 2.4031, 0.9042, and 0.7183, respectively. The photocatalytic activity of the film was improved with the increased number of layers. When the  $\text{TiO}_2$  film grew thicker, the film contained more  $\text{TiO}_2$  catalyst. Therefore, the  $\text{TiO}_2$  particles continuously hydrolyzed and produced more oxidative groups such as  $\cdot\text{OH}$ ,  $\cdot\text{O}^{2-}$ , and  $\cdot\text{OOH}$ , and so catalytic activity of  $\text{TiO}_2$  thin film was accelerated.

**3.6. Mechanisms of Adsorption and Photocatalytic Degradation.** The preparation of the composite membrane spin coated by  $\text{TiO}_2$  and its use in MB adsorption and degradation are illustrated in Figure 9. As is seen, the as-spun PAN/O-MMT nanofibers with intercalated structure were fabricated by electrospinning, and the O-MMT was oriented along the fiber axis direction. After spin coating, the  $\text{TiO}_2$  particles were randomly distributed on the surface of nanofibers. Then during the process of adsorption, part of the MB molecules was entrapped in the pores of the nanofibrous network, and some of the MB molecules were intercalated into interlayers of the MMT sheets, lying parallel to

the aluminosilicate layers [23]. When the membranes were exposed to UV irradiation, the TiO<sub>2</sub> particles were continuously hydrolyzed and produced large quantities of oxidative groups such as ·OH, ·O<sup>2-</sup>, and ·OOH, which accelerated the photodegradation of MB molecules. And so the membranes could be recycled and no secondary pollution was generated.

#### 4. Conclusion

The PAN and PAN/O-MMT composite nanofibrous membranes coated with TiO<sub>2</sub> films were prepared and used for MB adsorption and photodegradation. The effects of O-MMT amount concentration and TiO<sub>2</sub> spin coating layers on the structural morphology, adsorption, and photocatalytic properties of nanofiber membranes were investigated. The results revealed that with the increase of O-MMT concentration, the membranes showed better adsorption of O-MMT and have no effect on the photocatalytic degradation. Besides, when the number of film layers increased, the adsorption process of MB was slowed down, but the photocatalytic ability was greatly improved. And this kind of materials have potential prospect in water treatment polluted by cationic dye.

#### Acknowledgments

This work was supported by the Specialized Research Fund for the Innovation Project of Jiangsu Graduate Education (no. CXZZ11\_0471), the Doctoral Program of higher education (no. 20090093110004), the Natural Science Foundation of Jiangsu Province (no. BK2010140), and the scientific and technological guidance project of China National Textile and Apparel Council (no. 2011014).

#### References

- [1] T. P. S. Sumanjit and W. K. Ravneet, "Removal of health hazards causing acidic dyes from aqueous solutions by the process of adsorption," *Online Journal of Health and Allied Sciences*, vol. 6, no. 3, article 3, 2007.
- [2] A. Latif, S. Noor, Q. M. Sharif, and M. Najeebullah, "Different techniques recently used for the treatment of textile dyeing effluents: a review," *Journal of the Chemical Society of Pakistan*, vol. 32, no. 1, pp. 115–124, 2010.
- [3] M. X. Zhu, L. Lee, H. H. Wang, and Z. Wang, "Removal of an anionic dye by adsorption/precipitation processes using alkaline white mud," *Journal of Hazardous Materials*, vol. 149, no. 3, pp. 735–741, 2007.
- [4] P. Pengthamkeerati, T. Satapanajaru, N. Chatsatapattayakul, P. Chairattananamokorn, and N. Sananwai, "Alkaline treatment of biomass fly ash for reactive dye removal from aqueous solution," *Desalination*, vol. 261, no. 1-2, pp. 34–40, 2010.
- [5] P. Janoš, H. Buchtová, and M. Rýznarová, "Sorption of dyes from aqueous solutions onto fly ash," *Water Research*, vol. 37, no. 20, pp. 4938–4944, 2003.
- [6] M. Özacar and I. A. Şengil, "Adsorption of reactive dyes on calcined alunite from aqueous solutions," *Journal of Hazardous Materials*, vol. 98, no. 1–3, pp. 211–224, 2003.
- [7] S. Wang and Z. H. Zhu, "Sonochemical treatment of fly ash for dye removal from waste water," *Journal of Hazardous Materials*, vol. 126, pp. 91–95, 2005.
- [8] K. Saeed, S. Haider, T. J. Oh, and S. Y. Park, "Preparation of amidoxime-modified polyacrylonitrile (PAN-oxime) nanofibers and their applications to metal ions adsorption," *Journal of Membrane Science*, vol. 322, no. 2, pp. 400–405, 2008.
- [9] Z. Ma, K. Masaya, and S. Ramakrishna, "Immobilization of Cibacron blue F3GA on electrospun polysulphone ultra-fine fiber surfaces towards developing an affinity membrane for albumin adsorption," *Journal of Membrane Science*, vol. 282, no. 1-2, pp. 237–244, 2006.
- [10] Z. Ma, M. Kotaki, and S. Ramakrishna, "Electrospun cellulose nanofiber as affinity membrane," *Journal of Membrane Science*, vol. 265, no. 1-2, pp. 115–123, 2005.
- [11] R. Y. Lin, B. S. Chen, G. L. Chen, J. Y. Wu, H. C. Chiu, and S. Y. Suen, "Preparation of porous PMMA/Na<sup>+</sup>-montmorillonite cation-exchange membranes for cationic dye adsorption," *Journal of Membrane Science*, vol. 326, no. 1, pp. 117–129, 2009.
- [12] A. H. Gemeay, A. S. El-Sherbiny, and A. B. Zaki, "Adsorption and kinetic studies of the intercalation of some organic compounds onto Na<sup>+</sup>-montmorillonite," *Journal of Colloid and Interface Science*, vol. 245, no. 1, pp. 116–125, 2002.
- [13] C. C. Wang, L. C. Juang, T. C. Hsu, C. K. Lee, J. F. Lee, and F. C. Huang, "Adsorption of basic dyes onto montmorillonite," *Journal of Colloid and Interface Science*, vol. 273, no. 1, pp. 80–86, 2004.
- [14] H. Ichinose, M. Terasaki, and H. Katsuki, "Properties of peroxotitanium acid solution and peroxy-modified anatase sol derived from peroxotitanium hydrate," *Journal of Sol-Gel Science and Technology*, vol. 22, no. 1-2, pp. 33–40, 2001.
- [15] W. Y. Gan, H. Zhao, and R. Amal, "Photoelectrocatalytic activity of mesoporous TiO<sub>2</sub> thin film electrodes," *Applied Catalysis A*, vol. 354, no. 1-2, pp. 8–16, 2009.
- [16] Z. Liuxue, L. Peng, and S. Zhixing, "Photocatalysis anatase thin film coated PAN fibers prepared at low temperature," *Materials Chemistry and Physics*, vol. 98, no. 1, pp. 111–115, 2006.
- [17] B. Mahltig and T. Textor, "Combination of silica sol and dyes on textiles," *Journal of Sol-Gel Science and Technology*, vol. 39, no. 2, pp. 111–118, 2006.
- [18] D. Juan, Z. Li, and C. Shuilin, "Wash fastness of dyed fabric treated by the sol-gel process," *Coloration Technology*, vol. 121, no. 1, pp. 29–36, 2005.
- [19] H. Qiao, Y. Cai, F. Chen et al., "Influences of organic-modified Fe-montmorillonite on structure, morphology and properties of polyacrylonitrile nanocomposite fibers," *Fibers and Polymers*, vol. 10, no. 6, pp. 750–755, 2010.
- [20] Y. Cai, Q. Li, Q. Wei, Y. Wu, L. Song, and Y. Hu, "Structures, thermal stability, and crystalline properties of polyamide6/organic-modified Fe-montmorillonite composite nanofibers by electrospinning," *Journal of Materials Science*, vol. 43, no. 18, pp. 6132–6138, 2008.
- [21] J. P. Zhang, L. Wang, and A. Q. Wang, "Preparation and properties of Chitosan-g-poly(acrylic acid)/montmorillonite superadsorbent nanocomposite via in situ intercalative polymerization," *Industrial and Engineering Chemistry Research*, vol. 46, pp. 2497–2502, 2007.
- [22] L. Wang, J. Zhang, and A. Wang, "Removal of methylene blue from aqueous solution using chitosan-g-poly(acrylic acid)/montmorillonite superadsorbent nanocomposite," *Colloids and Surfaces A*, vol. 322, no. 1–3, pp. 47–53, 2008.
- [23] G. Akçay and M. K. Yurdakoç, "Nonyl- and dodecylamines intercalated bentonite and illite from Turkey," *Turkish Journal of Chemistry*, vol. 23, no. 1, pp. 105–113, 1999.

## Research Article

# Effect of N,C-ITO on Composite N,C-TiO<sub>2</sub>/N,C-ITO/ITO Electrode Used for Photoelectrochemical Degradation of Aqueous Pollutant with Simultaneous Hydrogen Production

Kee-Rong Wu,<sup>1</sup> Chung-Hsuang Hung,<sup>2</sup> Chung-Wei Yeh,<sup>3</sup> Chien-Chung Wang,<sup>1</sup>  
and Jiing-Kae Wu<sup>1</sup>

<sup>1</sup>Department of Marine Engineering, National Kaohsiung Marine University, Kaohsiung 811, Taiwan

<sup>2</sup>Department of Safety, Health and Environmental Engineering, National Kaohsiung First University of Science and Technology, Kaohsiung 811, Taiwan

<sup>3</sup>Department of Information System, Kao Yuan University, Kaohsiung 811, Taiwan

Correspondence should be addressed to Kee-Rong Wu, krwu@mail.nkmu.edu.tw

Received 15 September 2011; Revised 11 November 2011; Accepted 11 November 2011

Academic Editor: Jiaguo Yu

Copyright © 2012 Kee-Rong Wu et al. This is an open access article distributed under the Creative Commons Attribution License, which permits unrestricted use, distribution, and reproduction in any medium, provided the original work is properly cited.

This study reports the effect of N,C-ITO (indium tin oxide) layer on composite N,C-TiO<sub>2</sub>/N,C-ITO/ITO (Ti/TO) electrode used for efficient photoelectrocatalytic (PEC) degradation of aqueous pollutant with simultaneous hydrogen production. The structural properties of the composite Ti/TO electrode that determined by X-ray diffraction and Raman scattering, show primarily the crystallized anatase TiO<sub>2</sub> phase and distinct diffraction patterns of polycrystalline In<sub>2</sub>O<sub>3</sub> phase. Under solar light illumination, the composite Ti/TO electrode yields simultaneously a hydrogen production rate of 12.0 μmol cm<sup>-2</sup> h<sup>-1</sup> and degradation rate constant of 12.6 × 10<sup>-3</sup> cm<sup>-2</sup> h<sup>-1</sup> in organic pollutant. It implies that the overlaid N,C-TiO<sub>2</sub> layer enhances not only the photocurrent response of the composite Ti/TO electrode at entire applied potentials, but also the flat band potential; a shift of about 0.1 V toward cathode, which is desperately beneficial in the PEC process. In light of the X-ray photoelectron spectroscopy findings, these results are attributable partly to the synergetic effect of N,C-codoping into the TiO<sub>2</sub> and ITO lattices on their band gap narrowing and photosensitizing as well. Thus, the Ti/TO electrode can potentially serve an efficient PEC electrode for simultaneous pollutant degradation and hydrogen production.

## 1. Introduction

The photoelectrocatalytic (PEC) splitting of water using solar energy has attracted substantial attention as a means of producing hydrogen as a clean and renewable resource [1–3]. Researchers have sought suitable photocatalysts of the splitting of water since a pioneering work of Fujishima and Honda by employing titanium dioxide (TiO<sub>2</sub>) semiconductor as photoanode in 1972 [4]. As an anatase TiO<sub>2</sub> photoanode is excited by incident light with wavelengths shorter than 387 nm, electrons and holes can be generated. In short, the photogenerated holes oxidize and decompose water, even some organic or inorganic substances in aqueous solution, at the photoanode while the electrons can interact with hydrogen ions into hydrogen at the counter platinum

(Pt) electrode. It has been shown that hydrogen production can be enhanced by irradiating Pt/TiO<sub>2</sub> suspensions with simultaneous degradation of azo dyes [5]. Moreover, photoelectrolytic cleavage of biomass wastes, such as urine, ethanol and glycerol, in water is much more efficient for electricity generation [6] and hydrogen production [7–9].

For efficient PEC splitting of water, the n-type photoanode is required to have narrow band gap around 2.0 eV, suitable negative flat band potential, good stability and high quantum efficiency [10]. Among various semiconductor photocatalysts, TiO<sub>2</sub> is one of the most popular catalysts because it is environmentally friendly and chemically stable in electrolyte solution with high quantum efficiency. However, the use of TiO<sub>2</sub> is limited by its wide band gap (~3.2 eV). Alternatively, semiconductors with smaller

band gaps, such as CdS (2.4 eV), Fe<sub>2</sub>O<sub>3</sub> (2.3 eV), and Cu<sub>2</sub>O (2.2 eV), commonly suffer from photocorrosion in electrolyte solution and fast recombination of the photo-generated carriers [10–13]. It is well known that metal or semiconductor with a high work function coupled with other semiconductor can significantly enhance the oxidation ability of photogenerated holes in the semiconductor, due to efficient carrier separation. A heterostructured film, such as TiO<sub>2</sub>/ITO (indium tin oxide), TiO<sub>2</sub>/WO<sub>3</sub>, CdS/TiO<sub>2</sub> or TiO<sub>2</sub>/SnO<sub>2</sub>, has been proposed for providing a potential driving force for photogenerated charge carrier separation [14–18]. Dai et al. have demonstrated that the superior photocatalytic reactions of the TiO<sub>2</sub>/ITO film are mostly associated with the photogenerated holes because ITO has a higher work function (~4.7 eV) [19] than TiO<sub>2</sub> and a Schottky barrier can form at the TiO<sub>2</sub>/ITO interface, where the ITO thin film accepts electrons [16]. One should note that both the proximity of their conduction band to conduction band [20] and the proper redox positions of heterostructure play significant roles on charge carrier transfer and thus photocatalysis in the heterostructured film.

Photocatalysis is well known to be a very useful technique in various environmental applications for degrading a wide range of contaminants in air or water. TiO<sub>2</sub> is one of the most suitable semiconductors for several environmental applications, including air purification, water disinfection and hazardous waste remediation [21–23]. TiO<sub>2</sub> codoped with anionic species, such as carbon (C) and nitrogen (N), appears to have very promising visible-light photocatalytic properties in NO oxidation, methylene blue (MB) degradation, and *Escherichia coli* disinfection [24–27]. Yin et al. have shown that substitution of the O sites by N and C is responsible for visible-light photocatalytic activities [27]. It has been found that the N,C-TiO<sub>2</sub> films prepared at low doping concentrations of N (1.3%) and C (1.8%) have exhibited superior photocatalytic degradation of MB solution [28]. Moreover, TiO<sub>2-x</sub>N<sub>x</sub> catalyst with a low doping concentration ( $x = 0.021$ ) has shown the highest activity for the 4-chlorophenol decomposition under the visible-light irradiation [29, 30]. On the other hand, both N-doped In<sub>2</sub>O<sub>3</sub> [31] and ITO (N-ITO) [32] and C-doped In<sub>2</sub>O<sub>3</sub> [33] electrodes were demonstrated to be promising photocatalysts with favorable PEC properties, especially under visible light ( $\lambda > 378$  nm). However, both ITO and N-ITO films exhibit no photocatalytic activity in degradation of MB solution [32], though photocatalytic degradation of azo dyes has been reported active [34]. We previously found that an applied potential could serve as a highly efficient way to suppress hole-electron recombination of the N-ITO electrode, where the generated photocurrent density sharply increased with its applied potential. This was ascribed mostly to better electrical conductivity [31] and proper positions of the flat band potentials [35] as a result of suppression of InN and SnO<sub>2</sub> phases in the domain-structured N-ITO electrode which was prepared at a low N-doping content [32]. However, the origin of visible-light ability of the N-ITO films has not been exploited yet. To enhance the visible-light PEC response, the heterostructured TiO<sub>2</sub>/ITO electrodes were codoped with N and C ions grown on ITO glass

substrate, as a layered composite N,C-TiO<sub>2</sub>/N,C-ITO/ITO electrode (Ti/TO), for better durability and charge carriers transfer and thus PEC capability [36].

Dimethyl sulfoxide (DMSO) is one of the most common phenol-free organic solvents applied in semiconductor manufacturing industries due to its superior solvent property and water miscibility. However, DMSO is unable to be removed effectively by most typical biological wastewater treatment units [37]. The biodegradation of DMSO might cause the formation of some volatile and noxious compounds such as dimethylsulfide, methylmercaptan and hydrogen sulfide, causing another pollution problem [38]. Since that DMSO is also an effective radical scavenger for hydroxyl radicals ( $\bullet$ OH), the wastewater treatment processes that can produce high-concentration  $\bullet$ OH radicals will be candidate processes for DMSO removal. Accordingly, some advanced oxidation processes (AOPs) such as H<sub>2</sub>O<sub>2</sub>/UV [39], O<sub>3</sub>/UV [40], corona discharge [41], or UV/TiO<sub>2</sub>-based photocatalysts [42] are being developed for the particular purpose of reducing the DMSO concentration in the wastewater. In this study, we aim at the characterization of N,C-TiO<sub>2</sub>/ITO electrode with emphasis on the role of the intercalated N,C-ITO layer for PEC degradation of DMSO aqueous pollutant with simultaneous hydrogen production.

## 2. Experimental Procedure

An in-house closed-field unbalanced magnetron sputtering system (MIRDC, Taiwan) was used to prepare the samples. This system has four vertical magnetron targets each of dimensions 300 × 110 × 10 mm. TiO<sub>2</sub>/ITO film electrodes were codoped with N and C ions on as-received ITO (17 Ω/sq. and 100 ± 10 nm thick) glass substrates. In short, a N,C-ITO film was initially deposited onto an unheated rotating substrate using ITO and graphite targets, on one side of the chamber. After the intercalated N,C-ITO film was completed, the substrate holder was rotated toward a pair of titanium targets (99.5% purity) without opening the chamber for the successive deposition of N,C-TiO<sub>2</sub> layer. This heterostructured composite N,C-TiO<sub>2</sub>/N,C-ITO/ITO electrode was denoted as Ti/TO. Meanwhile, two other types of N,C-TiO<sub>2</sub>/ITO and N,C-ITO/ITO film electrodes, denoted as N,C-TiO<sub>2</sub> and N,C-ITO, respectively, were prepared for comparison. All other sputtering parameters were held constant where the O<sub>2</sub> and N<sub>2</sub> gas proportion was kept at a low rate of 9% in an Ar/O<sub>2</sub>/N<sub>2</sub> gas mixture, which had a total flow rate of 55 sccm. Details of the N,C-TiO<sub>2</sub> films, which were prepared at low doping concentrations of N and C were presented elsewhere [28, 32]. An as-received ITO electrode with a thickness of 300 nm was used for comparison. Table 1 presents the physical, morphological, and microstructural properties of the samples.

The crystal structures of the samples were analyzed using a high-resolution X-ray diffractometer (XRD, Rigaku ATX-E) and Micro-PL/Raman spectroscopy (Jobin-Yvon T64000). The surface topography of each sample was analyzed using an atomic force microscope (AFM, SPI 3800N, Seiko) with a scan resolution of 512 × 512 pixels. The microstructure and

TABLE 1: Physical and microstructural properties of samples along with their H<sub>2</sub> yield rates in 4.0 N Na<sub>2</sub>CO<sub>3</sub> solution under irradiation of AM 1.0 simulated solar light and 1.5 V applied bias.

Sample	Thickness of TiO <sub>2</sub> : ITO, nm	XRD intensity ratio		RMS, nm	H <sub>2</sub> yield rate, μmol cm <sup>-2</sup> h <sup>-1</sup>
		(400)/(222)	(440)/(222)		
N,C-ITO	— : 1.4	12.15	4.51	16.3	24.6
N,C-TiO <sub>2</sub>	2.1 : —	0.97	0.77	18.5	25.0
Ti/TO	0.4 : 1.4	38.53	5.93	33.6	28.8
ITO	— : 0.3	0.99	0.65	<2.0	—

thickness of the films were investigated by a scanning electron microscope (SEM, JEOL JSM-6700F). The X-ray photoelectron spectroscopy (XPS) analysis was carried out with a high-resolution X-ray photoelectron spectrometer (ULVAC-PHI Quantera SXM/Auger AES 650). Optical absorption of the samples was measured with respect to air using a UV spectrophotometer (Hitachi UV-2900).

PEC oxidation tests were performed using a standard PEC three-cell system that included a sample anode, a saturated calomel electrode (SCE) as a reference electrode and a Pt wire counter electrode 2.0 M Na<sub>2</sub>CO<sub>3</sub> solution, (pH ~ 11). The initial concentration of DMSO was 0.03 M. The DMSO residual concentration was monitored by a gas chromatography (GC, HP4890) with flame ionization detection (FID) as its detector. The analytic conditions of the GC/FID for DMSO quantification were capillary separation column (60-m long × 0.53 mm, 5 μm, VOCOL, Supelco Co.), temperature ramping from 100°C up to 220°C, and detector temperature was set at 250°C. The system was controlled by a potentiostat (CHI 610C). The samples were illuminated by artificial sunlight (Newport 96000 150 W solar simulator) with a light intensity of Air Mass (AM) 1.0 (75 mW cm<sup>-2</sup>).

### 3. Results and Discussion

**3.1. Microstructural, Morphological, and Optical Properties.** Figure 1 presents the XRD patterns of all three samples along with ITO substrate, which shows distinct diffraction patterns of polycrystalline In<sub>2</sub>O<sub>3</sub> phase [36]. All ITO preferred planes revealed in the N,C-TiO<sub>2</sub> are about the same characteristics as in the ITO electrode. However, N,C-ITO and Ti/TO samples exhibit a significantly different pattern against the ITO substrate; the former two exhibit relatively large intensity ratios of (400)/(222) and (440)/(222) planes, as listed in Table 1, which are associated with the increase in resistivity of the host ITO. The increase in resistance of conducting ITO substrate has been correlated to the decrease in fill factor of dye-sensitized TiO<sub>2</sub> solar cells [43]. The intensity ratio that is mostly ascribed to the N dopant increases with its concentration in the ITO lattice [32]. This implies that the intensity ratio, namely, resistivity, can be suppressed by doping fewer amount of N with C ions into the host ITO. In addition, a phase separation of small SnO<sub>2</sub> particles in the host crystalline ITO lattice may occur, since tin is liable to be segregated close to the surface of the lattice or along its grain boundaries under elevated deposition or posttreatment

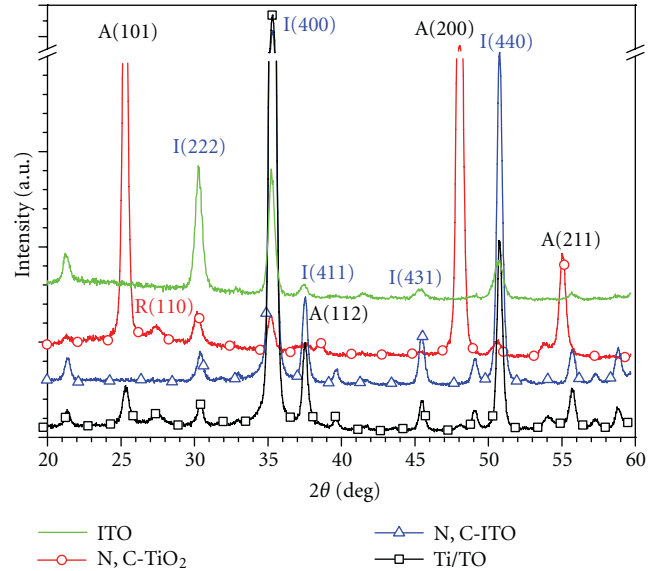


FIGURE 1: XRD patterns of the composite Ti/TO electrode along with N,C-TiO<sub>2</sub>, N,C-ITO, and ITO film electrodes, where A, R, and I stand for anatase, rutile, and ITO phase, respectively.

conditions [44, 45]. This can cause the increase in resistivity of the N,C-ITO films. The segregation of SnO<sub>2</sub> particles can be further examined by Raman scattering spectra in the following section.

Raman spectra are known to be very sensitive to local crystallinity and microstructures near the film surface. The Raman spectra shown in Figure 2 reveal a typical pattern of the anatase TiO<sub>2</sub> phase for both N,C-TiO<sub>2</sub> and Ti/TO samples [36]. The most intense Raman peaks of the two samples are in the range of  $144 \pm 0.5$  cm<sup>-1</sup>, which implies well-crystallized nature of the anatase TiO<sub>2</sub> phase [46]. A broad peak around 235 cm<sup>-1</sup> of SnO<sub>2</sub> phase is observed in sample N,C-ITO. The same broad peak with very weak intensity is also observed in Ti/TO sample, as shown in the inset of Figure 2. This confirms the finding that a little SnO<sub>2</sub> phase is segregated from the host ITO lattice, as discussed in the XRD patterns in Figure 1.

Figure 3 displays representative SEM surface morphologies of the N,C-ITO, Ti/TO and N,C-TiO<sub>2</sub> along with ITO substrate. The N,C-ITO film reveals various shapes and sizes of prismatic grains (50–200 nm) with few small

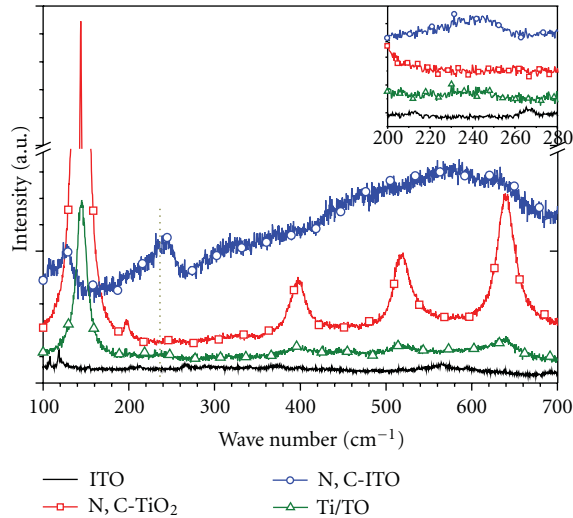


FIGURE 2: Raman spectra of the composite Ti/TO electrode along with N,C-TiO<sub>2</sub>, N,C-ITO, and ITO film electrodes.

subgrains oriented in the same direction on the surface of the film, as shown in Figure 3(a). This grain-subgrain structure is commonly found in typical DC-sputtered ITO film in Figure 3(b) [44] and on N-ITO films prepared at an optimal N content [32]. This implies that the N,C-ITO film still preserves a relatively low resistance. As presented in Figure 3(c), the columnar film morphology observed on the Ti/TO is more distinct in comparison with that on the N,C-TiO<sub>2</sub> in Figure 3(d). The AFM measurements also indicate that the N,C-ITO has the RMS roughness of 16.3 nm, where the N,C-TiO<sub>2</sub> has the value of 18.5 nm. The composite Ti/TO electrode is of the highest RMS of 33.6 nm, as shown in Table 1. One can expect that a significant increase in surface morphology renders more reactive surface area of the sample.

Figure 4 shows the absorption spectra of four samples. Both the UV light absorbing absorption and absorption edge are enhanced for the Ti/TO as a result of the synergetic effect of two film components, as compared to that of the N,C-ITO or N,C-TiO<sub>2</sub> alone. The band gap energy of the Ti/TO electrode is estimated to be about 2.75 eV while the ITO substrate is reportedly of a large band gap energy of ~3.8 eV. Notably, the N,C-ITO and N,C-TiO<sub>2</sub> have barely the same value of 2.98 eV, but the UV absorption of the former is stronger than that of the latter. This implies that the Ti/TO electrode benefits an enhanced absorbing capability in the UV regions from being supported on the N,C-ITO instead of pure ITO substrate.

**3.2. XPS Spectra Analysis.** After *in situ* Ar<sup>+</sup> etching for a depth of 5 nm, the C1s, In3d, Sn3d, N1s, and O1s core levels on the ITO and N,C-ITO film electrode were measured by high-resolution XPS (step size = 0.01 eV) in order to examine the effect of carbon and nitrogen dopants on the Ti/TO electrode. The binding energies were calibrated using the C1s energy of 284.6 eV. As shown in Figure 5(a), an

intensive C1s peak is observed in the N,C-ITO, but a very weak peak is noticed in the ITO. The former is mostly attributed to free graphitic nature (C–C) and is regarded as a photosensitizer [47], whereas the latter is the result of Ar<sup>+</sup> etching off the adventitious carbon on the air-exposed ITO surface. No other noticeable XPS peak can be found in the N,C-ITO within the narrow scan range (i.e., 280–292 eV). This implies that the sputtered carbons did not substitute the lattice oxygen atoms to form the In–C or Sn–C bond. This is because a relatively low carbon concentration is used during the film deposition. Moreover, the O1s XPS spectra of the ITO film in Figure 5(b) were resolved into two peaks; one, at 530.6 eV, is probably due to oxygen in hydroxyl (OH) groups; the other, at 529.8 eV, is assigned to the In–O and Sn–O bonds in crystalline In<sub>2</sub>O<sub>3</sub> and SnO<sub>2</sub>, respectively [31]. The N,C-ITO shows a shift to lower binding energy (529.65 eV) for the O1s peak of the crystalline In<sub>2</sub>O<sub>3</sub> and SnO<sub>2</sub>. This shift is in good agreement with the results found for substitutional N-doped TiO<sub>2</sub> and In<sub>2</sub>O<sub>3</sub> and C-doped In<sub>2</sub>O<sub>3</sub> [31, 33].

The N1s XPS spectra show only a weakened peak at around 396 eV in the N,C-ITO and no such peak is found in the ITO film (see Figure 5(c)). The best fitting of the N1s XPS spectra was obtained at a binding energy of 395.9 eV. No such peaks at 398 eV and 400 eV were found due to a relatively low nitrogen concentration used the electrode deposition [48]. Thus, the N1s XPS peak at 395.9 eV that results from the substitution of the oxygen sites by nitrogen ions is highly responsible for the visible-light photocatalytic activity [49], whereas the C1s peak at 284.6 eV of the graphite source is regarded as a photosensitizer.

As seen in Figure 5(d), the core level of In3d of the N,C-ITO sample shows a small shift to a lower binding energy, as compared with that of the ITO film. After curve fitting using Gaussian distribution functions, the In3d XPS peak appears only at 444.1 eV with a full width at half maximum (FWHM) of 1.4 eV, which is very close to a value of 444.4 eV of the ITO sample and the reported value of 444.2 eV of crystalline In<sub>2</sub>O<sub>3</sub> in the literature [50]. The formation of InN phase can be ruled out since no other In3d XPS peak at 442.4 eV can be rationally deconvoluted from the spectra of the N,C-ITO. A little lower binding energy shift suggests that N-substitution could hardly modify the electronic interaction of indium with the oxygen anions under our sputtering conditions.

Alternatively, two peaks, 8.5 eV apart, due to Sn3d<sub>3/2</sub> and Sn3d<sub>5/2</sub> XPS peaks, are observed in Figure 5(e). The best fitting for the ITO sample was achieved with two components at binding energies of 486.1 and 487.1 eV (figure not shown). The first peak is assigned to SnO and the second to SnO<sub>2</sub> [50]. However, these two components shifted to lower binding energies of 485.8 and 486.7 eV for the N,C-ITO. A shift to a lower binding energy implies that the creation of SnN (486.2 eV) may not occur in the N,C-ITO [51]. Thus, the formation of SnN phase can be ruled out. Instead, this binding energy shift suggests a reduction of the Sn cation valence state due to a substitutional cationic doping. When N replaces O, the valence state of Sn<sup>4+</sup> is reduced to Sn<sup>2+</sup>, causing the binding energy of the Sn3d<sub>5/2</sub>

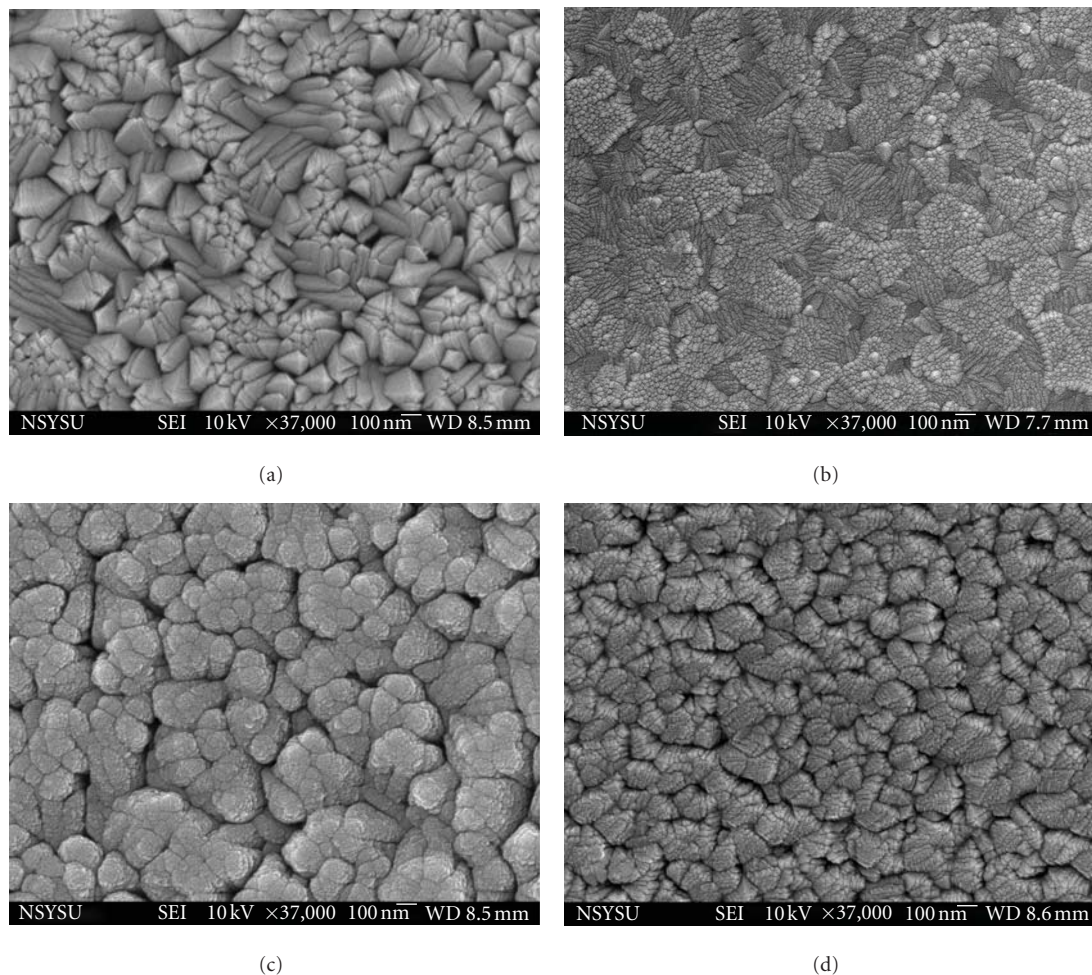


FIGURE 3: Plain view of SEM images of: (a) N,C-ITO, (b) ITO, (c) Ti/TO, and (d) N,C-TiO<sub>2</sub> films.

peak to shift to lower energy. Meanwhile, the atomic ratio of SnO<sub>2</sub>/SnO phase of the N,C-ITO is higher than that of the ITO indicating the formation of an SnO<sub>2</sub>-rich surface which confirms the results revealed by the XRD and Raman measurements. One can conclude that the observed red shifts in absorption and the band gap narrowing can be mostly attributed to the N-doping, but be a little to the C-doping of the N,C-ITO layer.

**3.3. Photoelectrochemical Properties.** Figure 6 shows a set of current-voltage (*I-V*) characteristics recorded on the composite Ti/TO electrode along with N,C-TiO<sub>2</sub>, N,C-ITO, and ITO film electrodes in Na<sub>2</sub>CO<sub>3</sub> solution under illumination of AM 1.0 simulated solar light. The illuminated photocurrent increases sharply as the applied potential reaches 0.5 V and 0.3 V versus SCE on the Ti/TO and N,C-ITO, respectively. Note that there is no saturation of photocurrent observed in both two samples, which indicates efficient charge separation under illumination, while the saturation of photocurrent can be seen on the N,C-TiO<sub>2</sub> electrode at a typical applied potential of 0.3 V versus SCE. Under illumination, however, the ITO substrate exhibits no

gain of photocurrent with a breakdown point at about 0.9 V versus SCE. This indicates that the N and C dopants can enhance the PEC properties of pristine ITO film. That is, a shift of the flat band (onset) potential from  $-0.7$  to  $-0.82$  V versus SCE is achieved by using the intercalated N,C-ITO layer, which can be estimated from the *I-V* measurements in the PEC test [52]. Under solar light illumination, a relatively high photoactive response of the Ti/TO electrode is attributable to, at least in part, the synergetic effect of N,C-codoping on band gap narrowing [25] and photosensitizing [47]. Moreover, the N,C-TiO<sub>2</sub> layer (400 nm thick) enhances not only the photocurrent response of the layered Ti/TO electrode at the entire applied potentials, but also the flat band (onset) potential from  $-0.82$  to  $-0.91$  V versus SCE; a shift of negative flat band potential is desired for facilitating the PEC process [10, 52].

Under irradiation of AM 1.0 simulated solar light and 1.5 V applied bias, the layered Ti/TO film electrode has the highest photocurrent density of  $0.47 \text{ mA cm}^{-2}$ , that is, a gain of  $0.42 \text{ mA cm}^{-2}$ , and a hydrogen yield rate of  $28.8 \mu\text{mol cm}^{-2} \text{ h}^{-1}$  in 4.0 N Na<sub>2</sub>CO<sub>3</sub> solution (pH  $\sim 11$ ), as shown in Figure 6 and Table 1. Comparatively, the N,C-ITO electrode has a photocurrent density of  $0.46 \text{ mA cm}^{-2}$ ,

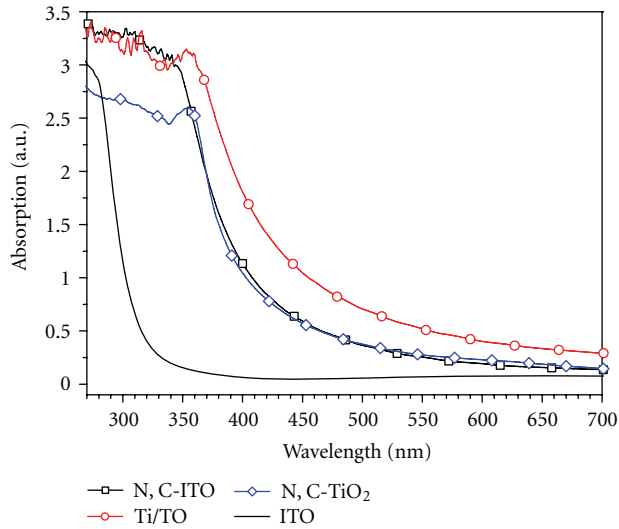


FIGURE 4: Absorption spectra of the composite Ti/TO electrode along with N,C-TiO<sub>2</sub>, N,C-ITO and ITO film electrodes.

TABLE 2: Hydrogen yield rates and degradation rate constants of the Ti/TO and N,C-TiO<sub>2</sub> electrodes under illumination of AM 1.0 stimulated solar light.

sample	H <sub>2</sub> yield rate, $\mu\text{mol cm}^{-2} \text{h}^{-1}$		DMSO rate constant, $\text{cm}^{-2} \text{h}^{-1}$	
	0.5 V	1.5 V	0.5 V	1.5 V
N,C-TiO <sub>2</sub>	10.2	11.8	$12.5 \times 10^{-3}$	$12.8 \times 10^{-3}$
Ti/TO	0.3	12.0	$10.8 \times 10^{-3}$	$12.6 \times 10^{-3}$

that is, a gain of only  $0.35 \text{ mA cm}^{-2}$ , and a hydrogen yield rate of  $24.6 \mu\text{mol cm}^{-2} \text{h}^{-1}$ , respectively. However, the N,C-TiO<sub>2</sub> electrode exhibits a photocurrent density of  $0.09 \text{ mA cm}^{-2}$  and a relatively high hydrogen yield rate of  $25.0 \mu\text{mol cm}^{-2} \text{h}^{-1}$ , respectively.

The PEC activity of the Ti/TO and N,C-TiO<sub>2</sub> electrodes was further evaluated by degrading DMSO pollutant mixed in Na<sub>2</sub>CO<sub>3</sub> aqueous solution with simultaneous hydrogen production under irradiation of AM 1.0 simulated solar light. As shown in Figure 7 and Table 2, the hydrogen yield rate obtained at 1.5 V is  $12.0 \mu\text{mol cm}^{-2} \text{h}^{-1}$ , about 40 times higher than that ( $0.3 \mu\text{mol cm}^{-2} \text{h}^{-1}$ ) at 0.5 V versus SCE, which is correlated well with a sharp increase in a photocurrent density of  $0.65 \text{ mA cm}^{-2}$ , that is, a gain of  $0.61 \text{ mA cm}^{-2}$ , at 1.5 V versus SCE. Under illumination of AM 1.0 simulated solar light, the degrading rate constant of DMSO is equal to  $10.8 \times 10^{-3} \text{ cm}^{-2} \text{h}^{-1}$  and  $12.6 \times 10^{-3} \text{ cm}^{-2} \text{h}^{-1}$  at an applied bias of 0.5 V and 1.5 V versus SCE, respectively. In other words, only a 17% increase in degradation rate constant is gained as the applied bias was raised from 0.5 V to 1.5 V, but a 50% increase in degradation rate constant was obtained from photocatalytic ( $7.2 \times 10^{-3} \text{ cm}^{-2} \text{h}^{-1}$ ) to PEC reaction at 0.5 V. The N,C-TiO<sub>2</sub> electrode yields about the same hydrogen evolution of  $11.8 \mu\text{mol cm}^{-2} \text{h}^{-1}$  at 1.5 V versus SCE as the Ti/TO, whereas it evolves a hydrogen yield rate of  $10.2 \mu\text{mol cm}^{-2} \text{h}^{-1}$  at 0.5 V versus SCE which is much

greater—34 times—than the Ti/TO. This is in accordance with the photocurrent density of the N,C-TiO<sub>2</sub> electrode displayed in Figure 7. These imply that the Ti/TO electrode is preferably suitable for PEC applications with a higher applied bias and the N,C-TiO<sub>2</sub> electrode is generally applicable to a wide range of applied bias.

It is known that an applied bias is used to facilitate the electron transport across the TiO<sub>2</sub>/ITO interface and the external circuit [53]. When the applied bias is sufficiently high to pull all of the excited electrons, the concentration of photogenerated holes can be the rate-determining step at the catalyst/electrolyte interface. The saturated photocurrent depends not only upon the types of catalysts and their morphology, crystal phase, and crystallinity, but also upon the types of electrolyte, organic compound, and their concentrations [53–56]. For instance, the TiO<sub>2</sub> nanopore arrays that revealed a saturated photocurrent of 5.8 times as high as that for coated TiO<sub>2</sub> nanofilm electrode has had 2 times as high as the coated TiO<sub>2</sub> nanofilm electrode at an applied bias of 0.5 V versus SCE in PEC process for degradation of aqueous tetracycline solution [56]. This indicates that upon an applied bias on the high photocurrent-saturated electrode, the separation and transport efficiency of photogenerated electron/hole pairs is much higher than that for the conventional coated TiO<sub>2</sub> electrode. This implies that the higher the saturated photocurrent is, the greater the photocatalytic oxidation and the better the efficiency can be rationally expected [54]. However, the reasons for this unexpected low increase in the DMSO rate constant of the Ti/TO electrode are not clear yet and further investigation is being undertaken in our lab.

## 4. Conclusion

The Ti/TO film electrode that combines a versatile layer of N,C-TiO<sub>2</sub> and a novel intercalated layer of N,C-ITO reveals a synergetic photocatalytic capability for simultaneous DMSO degradation and hydrogen production. The structural properties of the sample electrodes, determined by X-ray diffraction (XRD) and Raman scattering, show that the overlaid N,C-TiO<sub>2</sub> film exhibits primarily the crystallized anatase TiO<sub>2</sub> phase and the intercalated N,C-ITO film shows distinct diffraction patterns of polycrystalline In<sub>2</sub>O<sub>3</sub> phase. Under AM 1.0 simulated solar light irradiation and 1.5 V applied potential, the photocurrent density of the Ti/TO film electrode is 20% and 4.7 times higher than that of the N,C-ITO and N,C-TiO<sub>2</sub> electrodes, respectively. Moreover, the Ti/TO electrode yields simultaneously a hydrogen production rate of  $12.0 \mu\text{mol cm}^{-2} \text{h}^{-1}$  and degradation rate constant of  $12.6 \times 10^{-3} \text{ cm}^{-2} \text{h}^{-1}$ , whereas the N,C-ITO electrode shows no pollutant oxidation. In view of the synergetic effect of N,C-codoping on the composite Ti/TO electrode, not only the N,C-TiO<sub>2</sub> layer enhances the photocurrent response and a cathode shift of the flat band potential, but also the intercalated N,C-ITO layer can significantly increase photocurrent response at a high applied potential. These are desperately beneficial in the PEC process of pollutant degradation and hydrogen production as well.

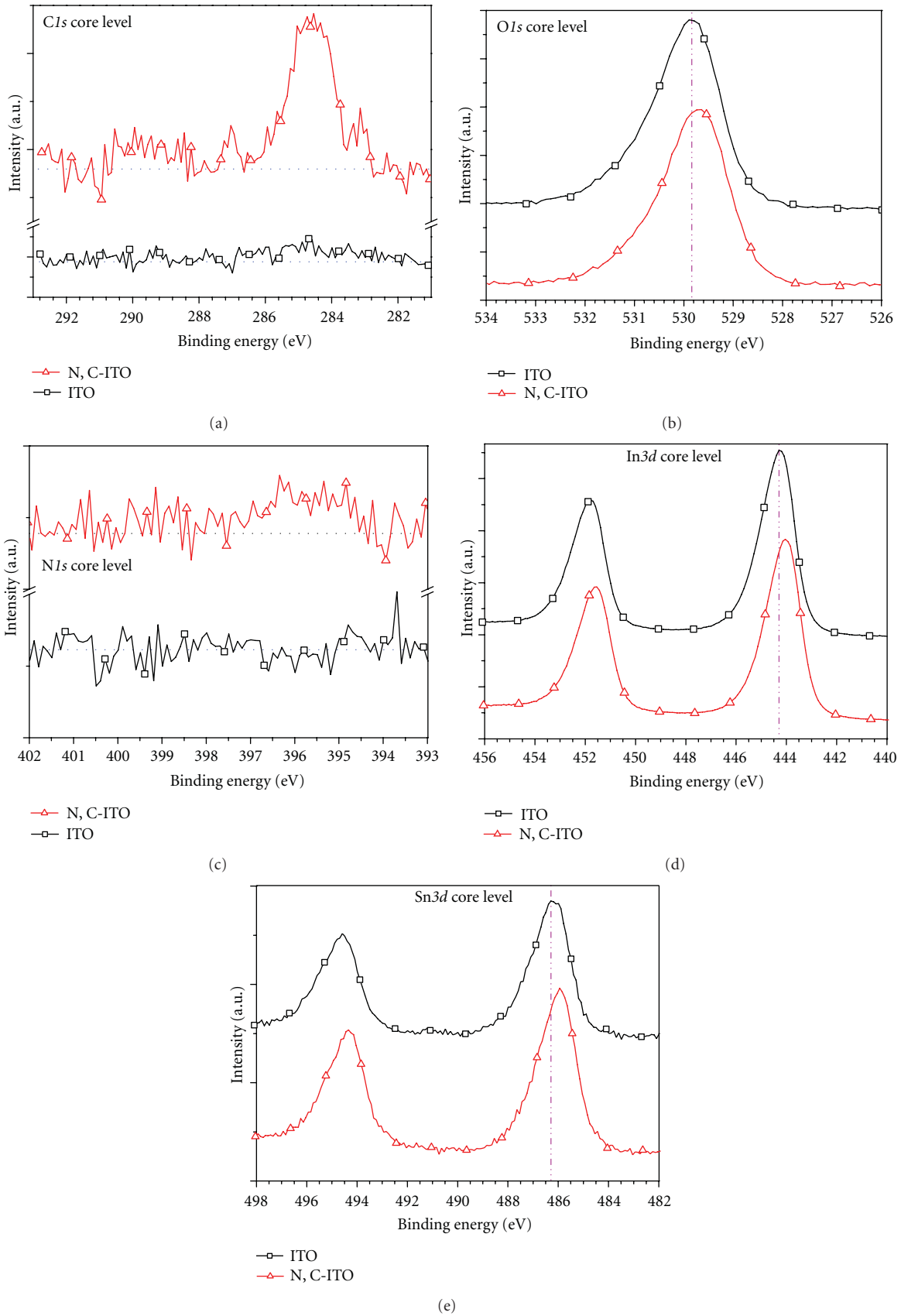


FIGURE 5: XPS high-resolution spectra of: (a) C1s, (b) O1s, (c) N1s, (d) In3d, and (e) Sn3d core levels for the N,C-ITO and ITO film electrodes.

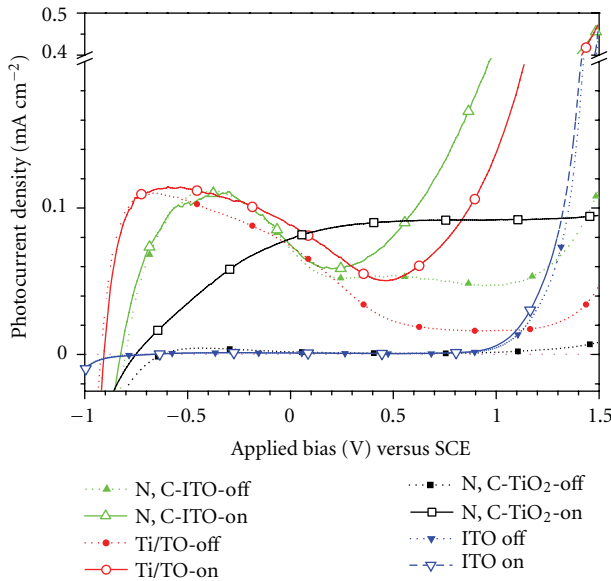


FIGURE 6: Photocurrent response of the Ti/TO and N,C-TiO<sub>2</sub> electrodes along with N,C-ITO and ITO substrates in Na<sub>2</sub>CO<sub>3</sub> solution.

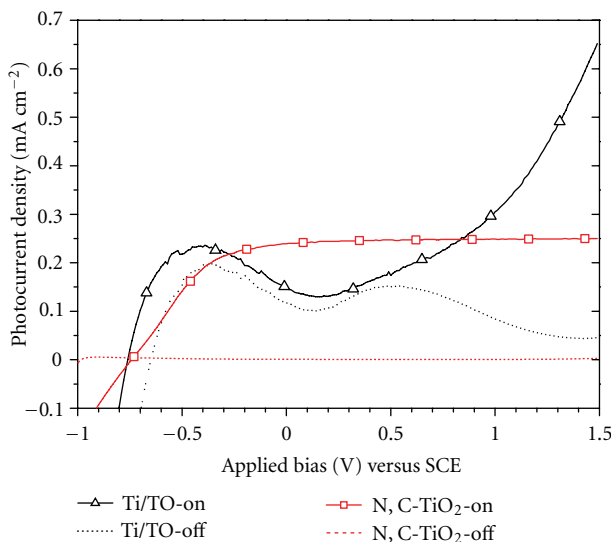


FIGURE 7: Photocurrent response of the Ti/TO and N,C-TiO<sub>2</sub> electrodes in Na<sub>2</sub>CO<sub>3</sub> mixed with DMSO aqueous solution.

## Acknowledgment

The authors would like to thank the National Science Council of Taiwan, for financially supporting this research under Contract no. NSC 98-2221-E-022-004-MY2.

## References

[1] T. Bak, J. Nowotny, M. Rekas, and C. C. Sorrell, "Photoelectrochemical hydrogen generation from water using solar energy. Materials-related aspects," *International Journal of Hydrogen Energy*, vol. 27, no. 10, pp. 991–1022, 2002.

[2] B. Marsen, E. L. Miller, D. Paluselli, and R. E. Rocheleau, "Progress in sputtered tungsten trioxide for photoelectrode applications," *International Journal of Hydrogen Energy*, vol. 32, no. 15, pp. 3110–3115, 2007.

[3] J. Yu and J. Ran, "Facile preparation and enhanced photocatalytic H<sub>2</sub>-production activity of Cu(OH)<sub>2</sub> cluster modified TiO<sub>2</sub>," *Energy and Environmental Science*, vol. 4, no. 4, pp. 1364–1371, 2011.

[4] A. Fujishima and K. Honda, "Electrochemical photolysis of water at a semiconductor electrode," *Nature*, vol. 238, no. 5358, pp. 37–38, 1972.

[5] A. Patsoura, D. I. Kondarides, and X. E. Verykios, "Enhancement of photoinduced hydrogen production from irradiated Pt/TiO<sub>2</sub> suspensions with simultaneous degradation of azo-dyes," *Applied Catalysis B*, vol. 64, no. 3-4, pp. 171–179, 2006.

[6] M. Kaneko, H. Ueno, K. Ohnuki, M. Horikawa, R. Saito, and J. Nemoto, "Direct electrical power generation from urine, wastes and biomass with simultaneous photodecomposition and cleaning," *Biosensors and Bioelectronics*, vol. 23, no. 1, pp. 140–143, 2007.

[7] D. I. Kondarides, V. M. Daskalaki, A. Patsoura, and X. E. Verykios, "Hydrogen production by photo-induced reforming of biomass components and derivatives at ambient conditions," *Catalysis Letters*, vol. 122, no. 1-2, pp. 26–32, 2008.

[8] M. Antoniadou, P. Bouras, N. Strataki, and P. Lianos, "Hydrogen and electricity generation by photoelectrochemical decomposition of ethanol over nanocrystalline titania," *International Journal of Hydrogen Energy*, vol. 33, no. 19, pp. 5045–5051, 2008.

[9] H. Park, A. Bak, Y. Y. Ahn, J. Choi, and M. R. Hoffmann, "Photoelectrochemical performance of multi-layered BiO<sub>x</sub>-TiO<sub>2</sub>/Ti electrodes for degradation of phenol and production of molecular hydrogen in water," *Journal of Hazardous Materials*. In press.

[10] J. Nowotny, T. Bak, M. K. Nowotny, and L. R. Sheppard, "Titanium dioxide for solar-hydrogen I. Functional properties," *International Journal of Hydrogen Energy*, vol. 32, no. 14, pp. 2609–2629, 2007.

[11] X. Yong and M. A. A. Schoonen, "The absolute energy positions of conduction and valence bands of selected semiconducting minerals," *American Mineralogist*, vol. 85, no. 3-4, pp. 543–556, 2000.

[12] E. L. Miller, D. Paluselli, B. Marsen, and R. E. Rocheleau, "Development of reactively sputtered metal oxide films for hydrogen-producing hybrid multijunction photoelectrodes," *Solar Energy Materials and Solar Cells*, vol. 88, no. 2, pp. 131–144, 2005.

[13] Z. Xu and J. Yu, "Visible-light-induced photoelectrochemical behaviors of Fe-modified TiO<sub>2</sub> nanotube arrays," *Nanoscale*, vol. 3, no. 8, pp. 3138–3144, 2011.

[14] Y. Ma, J. B. Qiu, Y. A. Cao, Z. S. Guan, and J. N. Yao, "Photocatalytic activity of TiO<sub>2</sub> films grown on different substrates," *Chemosphere*, vol. 44, no. 5, pp. 1087–1092, 2001.

[15] H. Irie, H. Mori, and K. Hashimoto, "Interfacial structure dependence of layered TiO<sub>2</sub>/WO<sub>3</sub> thin films on the photoinduced hydrophilic property," *Vacuum*, vol. 74, no. 3-4, pp. 625–629, 2004.

[16] W. Dai, X. Wang, P. Liu, Y. Xu, G. Li, and X. Fu, "Effects of electron transfer between TiO<sub>2</sub> films and conducting substrates on the photocatalytic oxidation of organic pollutants," *Journal of Physical Chemistry B*, vol. 110, no. 27, pp. 13470–13476, 2006.

[17] H. Chen, S. Chen, X. Quan, H. Yu, H. Zhao, and Y. Zhang, "Fabrication of TiO<sub>2</sub>-Pt coaxial nanotube array Schottky structures for enhanced photocatalytic degradation of phenol

- in aqueous solution,” *Journal of Physical Chemistry C*, vol. 112, no. 25, pp. 9285–9290, 2008.
- [18] J. Bai, J. Li, Y. Liu, B. Zhou, and W. Cai, “A new glass substrate photoelectrocatalytic electrode for efficient visible-light hydrogen production: CdS sensitized TiO<sub>2</sub> nanotube arrays,” *Applied Catalysis B*, vol. 95, no. 3–4, pp. 408–413, 2010.
- [19] J. R. Sheats, H. Antoniadis, M. Hueschen et al., “Organic electroluminescent devices,” *Science*, vol. 273, no. 5277, pp. 884–888, 1996.
- [20] A. J. Nozik and R. Memming, “Physical chemistry of semiconductor-liquid interfaces,” *Journal of Physical Chemistry*, vol. 100, no. 31, pp. 13061–13078, 1996.
- [21] A. Fujishima, T. N. Rao, and D. A. Tryk, “Titanium dioxide photocatalysis,” *Journal of Photochemistry and Photobiology C*, vol. 1, no. 1, pp. 1–21, 2000.
- [22] J. Gamage and Z. Zhang, “Applications of photocatalytic disinfection,” *International Journal of Photoenergy*, vol. 2010, Article ID 764870, 11 pages, 2010.
- [23] J. A. Byrne, P. A. Fernandez-Ibañez, P. S.M. Dunlop, D. M.A. Alrousan, and J. W.J. Hamilton, “Photocatalytic enhancement for solar disinfection of water: a review,” *International Journal of Photoenergy*, vol. 2011, Article ID 798051, 12 pages, 2011.
- [24] T. Sano, N. Negishi, K. Koike, K. Takeuchi, and S. Matsuzawa, “Preparation of a visible light-responsive photocatalyst from a complex of Ti<sup>4+</sup> with a nitrogen-containing ligand,” *Journal of Materials Chemistry*, vol. 14, no. 3, pp. 380–384, 2004.
- [25] D. Noguchi, Y. Kawamata, and T. Nagatomo, “The response of TiO<sub>2</sub> photocatalysts codoped with nitrogen and carbon to visible light,” *Journal of the Electrochemical Society*, vol. 152, no. 9, pp. D124–D129, 2005.
- [26] Q. Li, R. Xie, W. L. Yin, E. A. Mintz, and K. S. Jian, “Enhanced visible-light-induced photocatalytic disinfection of E. coli by carbon-sensitized nitrogen-doped titanium oxide,” *Environmental Science and Technology*, vol. 41, no. 14, pp. 5050–5056, 2007.
- [27] S. Yin, M. Komatsu, Q. Zhang, F. Saito, and T. Sato, “Synthesis of visible-light responsive nitrogen/carbon doped titania photocatalyst by mechanochemical doping,” *Journal of Materials Science*, vol. 42, no. 7, pp. 2399–2404, 2007.
- [28] K. R. Wu and C. H. Hung, “Characterization of N,C-codoped TiO<sub>2</sub> films prepared by reactive DC magnetron sputtering,” *Applied Surface Science*, vol. 256, no. 5, pp. 1595–1603, 2009.
- [29] Q. Xiang, J. Yu, W. Wang, and M. Jaroniec, “Nitrogen self-doped nanosized TiO<sub>2</sub> sheets with exposed 001 facets for enhanced visible-light photocatalytic activity,” *Chemical Communications*, vol. 47, no. 24, pp. 6906–6908, 2011.
- [30] H. Fu, G. Shang, S. Yang, and T. Xu, “Mechanistic study of visible-light-induced photodegradation of 4-chlorophenol by TiO<sub>2-x</sub>N<sub>x</sub> with low nitrogen concentration,” *International Journal of Photoenergy*, vol. 2012, Article ID 759306, 9 pages, 2012.
- [31] K. R. Reyes-Gil, E. A. Reyes-García, and D. Raftery, “Nitrogen-doped in<sub>2</sub>O<sub>3</sub> thin film electrodes for photocatalytic water splitting,” *Journal of Physical Chemistry C*, vol. 111, no. 39, pp. 14579–14588, 2007.
- [32] K. R. Wu, C. W. Yeh, C. H. Hung, L. H. Cheng, and C. Y. Chung, “Photoelectrochemical properties of nitrogen-doped indium tin oxide thin films prepared by reactive DC magnetron sputtering,” *Thin Solid Films*, vol. 518, no. 5, pp. 1581–1584, 2009.
- [33] Y. Sun, C. J. Murphy, K. R. Reyes-Gil, E. A. Reyes-García, J. P. Lilly, and D. Raftery, “Carbon-doped in<sub>2</sub>O<sub>3</sub> films for photoelectrochemical hydrogen production,” *International Journal of Hydrogen Energy*, vol. 33, no. 21, pp. 5967–5974, 2008.
- [34] M. H. Habibi and N. Talebian, “Photocatalytic degradation of an azo dye X6G in water: a comparative study using nanostructured indium tin oxide and titanium oxide thin films,” *Dyes and Pigments*, vol. 73, no. 2, pp. 186–194, 2007.
- [35] Y. Bessekhouad, D. Robert, and J. V. Weber, “Bi<sub>2</sub>S<sub>3</sub>/TiO<sub>2</sub> and CdS/TiO<sub>2</sub> heterojunctions as an available configuration for photocatalytic degradation of organic pollutant,” *Journal of Photochemistry and Photobiology A*, vol. 163, no. 3, pp. 569–580, 2004.
- [36] K. R. Wu, C. H. Hung, C. W. Yeh, C. C. Wang, and T. P. Cho, *The TechConnect World*, Paper No. 545, Anaheim, Calif, USA, 2010.
- [37] S. Matsui, Y. Okawa, and R. Ota, “Experience of 16 years’ operation and maintenance of the Fukushima industrial wastewater treatment plant of the Kashima petrochemical complex—II. Biodegradability of 37 organic substances and 28 process wastewaters,” *Water Science and Technology*, vol. 20, no. 10, pp. 201–210, 1988.
- [38] S.-J. Park, T.-I. Yoon, J.-H. Bae, H.-J. Seo, and H.-J. Park, “Biological treatment of wastewater containing dimethyl sulphoxide from the semi-conductor industry,” *Process Biochemistry*, vol. 36, no. 6, pp. 579–589, 2001.
- [39] Y. Lee, C. Lee, and J. Yoon, “Kinetics and mechanisms of DMSO (dimethylsulfoxide) degradation by UV/H<sub>2</sub>O<sub>2</sub> process,” *Water Research*, vol. 38, no. 10, pp. 2579–2588, 2004.
- [40] J. J. Wu, M. Muruganandham, and S. H. Chen, “Degradation of DMSO by ozone-based advanced oxidation processes,” *Journal of Hazardous Materials*, vol. 149, no. 1, pp. 218–225, 2007.
- [41] C. Lee, Y. Lee, and J. Yoon, “Oxidative degradation of dimethylsulfoxide by locally concentrated hydroxyl radicals in streamer corona discharge process,” *Chemosphere*, vol. 65, no. 7, pp. 1163–1170, 2006.
- [42] M. N. Abellán, R. Dillert, J. Giménez, and D. Bahnemann, “Evaluation of two types of TiO<sub>2</sub>-based catalysts by photodegradation of DMSO in aqueous suspension,” *Journal of Photochemistry and Photobiology A*, vol. 202, no. 2–3, pp. 164–171, 2009.
- [43] S. Ngamsinlapasathian, T. Sreethawong, Y. Suzuki, and S. Yoshikawa, “Doubled layered ITO/SnO<sub>2</sub> conducting glass for substrate of dye-sensitized solar cells,” *Solar Energy Materials and Solar Cells*, vol. 90, no. 14, pp. 2129–2140, 2006.
- [44] M. Kamei, Y. Shigesato, and S. Takaki, “Origin of characteristic grain-subgrain structure of tin-doped indium oxide films,” *Thin Solid Films*, vol. 259, no. 1, pp. 38–45, 1995.
- [45] N. Nadaud, N. Lequeux, M. Nanot, J. Jové, and T. Roisnel, “Structural studies of tin-doped indium oxide (ITO) and In<sub>4</sub>Sn<sub>3</sub>O<sub>12</sub>,” *Journal of Solid State Chemistry*, vol. 135, no. 1, pp. 140–148, 1998.
- [46] V. Swamy, A. Kuznetsov, L. S. Dubrovinsky, R. A. Caruso, D. G. Shchukin, and B. C. Muddle, “Finite-size and pressure effects on the Raman spectrum of nanocrystalline anatase TiO<sub>2</sub>,” *Physical Review B*, vol. 71, no. 18, Article ID 184302, 2005.
- [47] S. W. Hsu, T. S. Yang, T. K. Chen, and M. S. Wong, “Ion-assisted electron-beam evaporation of carbon-doped titanium oxide films as visible-light photocatalyst,” *Thin Solid Films*, vol. 515, no. 7–8, pp. 3521–3526, 2007.
- [48] R. Asahi and T. Morikawa, “Nitrogen complex species and its chemical nature in TiO<sub>2</sub> for visible-light sensitized photocatalysis,” *Chemical Physics*, vol. 339, no. 1–3, pp. 57–63, 2007.
- [49] S. Yin, M. Komatsu, Q. Zhang, F. Saito, and T. Sato, “Synthesis of visible-light responsive nitrogen/carbon doped titania photocatalyst by mechanochemical doping,” *Journal of Materials Science*, vol. 42, no. 7, pp. 2399–2404, 2007.

- [50] C. Nunes De Carvalho, A. M. Botelho Do Rego, A. Amaral, P. Brogueira, and G. Lavareda, "Effect of substrate temperature on the surface structure, composition and morphology of indium-tin oxide films," *Surface and Coatings Technology*, vol. 124, no. 1, pp. 70–75, 2000.
- [51] Y. Inoue, M. Nomiya, and O. Takai, "Physical properties of reactive sputtered tin-nitride thin films," *Vacuum*, vol. 51, no. 4, pp. 673–676, 1998.
- [52] M. Radecka, M. Rekas, A. Trenczek-Zajac, and K. Zakrzewska, "Importance of the band gap energy and flat band potential for application of modified TiO<sub>2</sub> photoanodes in water photolysis," *Journal of Power Sources*, vol. 181, no. 1, pp. 46–55, 2008.
- [53] D. Jiang, H. Zhao, S. Zhang, and R. John, "Comparison of photocatalytic degradation kinetic characteristics of different organic compounds at anatase TiO<sub>2</sub> nanoporous film electrodes," *Journal of Photochemistry and Photobiology A*, vol. 177, no. 2-3, pp. 253–260, 2006.
- [54] M. Park, A. Heo, E. Shim, J. Yoon, H. Kim, and H. Joo, "Effect of length of anodized TiO<sub>2</sub> tubes on photoreactivity: photocurrent, Cr(VI) reduction and H<sub>2</sub> evolution," *Journal of Power Sources*, vol. 195, no. 15, pp. 5144–5149, 2010.
- [55] Y. Liu, B. Zhou, J. Li, X. Gan, J. Bai, and W. Cai, "Preparation of short, robust and highly ordered TiO<sub>2</sub> nanotube arrays and their applications as electrode," *Applied Catalysis B*, vol. 92, no. 3-4, pp. 326–332, 2009.
- [56] Y. Liu, X. Gan, B. Zhou et al., "Photoelectrocatalytic degradation of tetracycline by highly effective TiO<sub>2</sub> nanopore arrays electrode," *Journal of Hazardous Materials*, vol. 171, no. 1–3, pp. 678–683, 2009.

## Research Article

# Low-Temperature Reverse Microemulsion Synthesis, Characterization, and Photocatalytic Performance of Nanocrystalline Titanium Dioxide

Zhang Liu,<sup>1</sup> Zicong Jian,<sup>2</sup> Jianzhang Fang,<sup>1</sup> Xiaoxin Xu,<sup>1</sup> Ximiao Zhu,<sup>1</sup> and Shuxing Wu<sup>1</sup>

<sup>1</sup> School of Chemistry and Environment, South China Normal University, Guangzhou 510006, China

<sup>2</sup> School of Environment, South China University of Technology, Guangzhou 510640, China

Correspondence should be addressed to Jianzhang Fang, fangjzh@scnu.edu.cn

Received 30 October 2011; Revised 24 November 2011; Accepted 24 November 2011

Academic Editor: Jiaguo Yu

Copyright © 2012 Zhang Liu et al. This is an open access article distributed under the Creative Commons Attribution License, which permits unrestricted use, distribution, and reproduction in any medium, provided the original work is properly cited.

Nanocrystalline titanium dioxide (TiO<sub>2</sub>) was synthesized in microemulsions by using cetyltrimethylammonium bromide (CTAB) as surfactant. In order to investigate the crystal transformation and photoactivity at low temperature, the as-prepared precipitates were aged at 65°C or calcined at various temperatures. Analyses using powder X-ray diffraction (XRD) and Fourier transform infrared microscopy (FT-IR) showed that precursors without aging or calcination were noncrystal and adsorbed by surfactant. After aging for 6 h, the amorphous TiO<sub>2</sub> began to change into anatase. The obtained catalysts, which were synthesized in microemulsions with weight ratios of n-hexanol/CTAB/water as 6 : 3 : 1 and calcined at 500°C, presented the highest photocatalytic degradation rate on methyl orange (MO), while the catalysts, which were aged at 65°C for 90 h, also exhibited an outstanding photocatalytic performance and a little higher than that of the commercial titania photocatalyst Degussa P25.

## 1. Introduction

TiO<sub>2</sub> is well-known for its applications in oxide semiconductors, oxygen sensors, photovoltaics, photocatalysis, and pigments [1–4]. Extensive researches have been focus on synthetic methods of semiconductor nanoparticles with better crystallinity and photocatalytic performance [5, 6]. Among various approaches explored, the reverse microemulsion process seems an efficient way to obtain nanosized TiO<sub>2</sub> [7]. Many scholars [8, 9] suggested that the main advantages of the microemulsion method were the low reaction temperature, the short processing time, and the attractive effect of preventing agglomeration in the formed nanoparticles. The property of microemulsion is mainly determined by the characteristics of the forming surfactant. Therefore, a proper surfactant may simplify producing the desired nanosized TiO<sub>2</sub>. One of the goals of this article is showing the application of microemulsions which acted as nanoparticles reactors.

In a typical procedure for TiO<sub>2</sub> preparation, samples usually need to be treated under several hundred degrees centi-

grade [10–12]. Some researches, however, have sought the possibility of synthesizing TiO<sub>2</sub> in low temperatures, and obtained certain progress. Qi et al. [13] synthesized TiO<sub>2</sub> at 100°C and discussed the heterogeneous nucleation mechanism. Liu et al. [14] obtained TiO<sub>2</sub> with small crystalline size and large specific surface area around 100°C. Although TiO<sub>2</sub> obtained under low temperatures has been studied, the microemulsion-resulted products which underwent different aging time and related photocatalytic activities were seldom discussed.

In the present study, the phase behavior of cetyltrimethylammonium bromide (CTAB) in n-hexanol/water system was studied through the electrical conductivity and the phase diagrams. Nanosized TiO<sub>2</sub> particles were synthesized in n-hexanol/CTAB/water reverse microemulsion under low aging temperature or high calcination temperature, and the powders were characterized by X-ray diffraction (XRD), Fourier transform infrared spectroscopy (FT-IR), and transmission electron microscopy (TEM) techniques. A simulated organic pollutant, methyl orange (MO), was decomposed on TiO<sub>2</sub> suspensions under UV irradiation.

## 2. Materials and Methods

**2.1. Analysis of Microemulsions.** The electrical conductivity of ternary system was measured using a DDS-307 conductivity meter (Leici Instruments, Shang Hai, China). Deionized water was added dropwise to the mixture of n-hexanol and CTAB at room temperature until the system became turbid. The weight ratio of n-hexanol to CTAB was fixed at 2, while the water concentration was represented by quality percentage.

Depending on the preparation procedure of microemulsions, phase diagrams were constructed using a conventional titration technique and the homogeneous phase regions were obtained at different temperatures (25, 65, 80°C). Stock solutions of CTAB and n-hexanol at the certain weight ratio were prepared at room temperature. Deionized water was added dropwise to glass vials containing n-hexanol/CTAB mixtures, which were maintained at various temperatures in water bath. The as-prepared microemulsions were sealed and shaken by a magnetic stirrer. The mass of added water was determined by weighting the glass vial before and after adding to the mixture.

**2.2. Preparation of TiO<sub>2</sub> Nanoparticles.** In a typical procedure, microemulsion of n-hexanol:CTAB:water with weight ratio of 6:3:1, was firstly prepared by mixing three component through a magnetic stirrer and stirred for 60 min until the systems became clear and equality. Maintaining that the molar ratio of water to Ti(OBu)<sub>4</sub> is 15, a specific weight of Ti(OBu)<sub>4</sub> was added dropwise into the microemulsion system and further stirred for 120 min.

To obtain samples treated by high temperature, the solid precipitates were centrifuged from the microemulsion system and washed with ethanol and deionized water for five times. The precursors were dried at 105°C for 12 h. Then the sample was calcined for 3 h at 300, 400, 500, 600, and 700°C.

To obtain samples treated by low temperature, after Ti(OBu)<sub>4</sub> was added into the microemulsion and stirred for 120 min, the whole mixtures were kept in water bath (65°C) with different aging time. The final products were obtained after centrifugation, washing, and drying processes as above.

**2.3. Photocatalytic Activity Measurement.** The photocatalytic reaction was conducted in a 200 mL cylindrical glass vessel fixed in the XPA photochemical reactor (Nanjing Xujiang Machine-electronic Plant, China). The reactor consisted of magnetic stirrer, quartz cool trap, and condenser that can keep the reaction temperature steady and prevent the evaporation of water. A 300 W Hg lamp with center wavelength of 365 nm was used as the UV light source. Methyl orange (MO) was used as a target pollutant, with an initial concentration of 10 mg L<sup>-1</sup>.

100 mg photocatalyst powder was dispersed in 200 mL MO solution sufficiently for 30 min to achieve adsorption/desorption equilibration. Subsequently, the Hg lamp was turn on. At regular intervals (10 min), about 5 mL of the suspension was sampled and filtered through a 0.45 μm

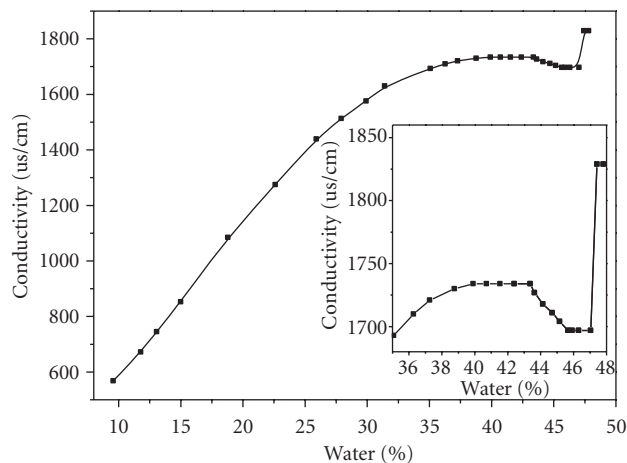


FIGURE 1: Relationship between the electrical conductivity and the water concentration with the weight ratio of n-hexanol to CTAB is 1.5.

membrane filter. The concentration of the remaining pollutant was measured by its absorbance ( $A$ ) at 464 nm with a Hitachi UV-3010 spectrophotometer (Tokyo, Japan). The degradation ratio ( $X$ ) of the reactant was calculated by  $X(\%) = 100(A_0 - A_t)/A_0$ , where  $A_0$  and  $A_t$  are the absorbencies at time zero and at time  $t$ .

**2.4. Characterization of TiO<sub>2</sub> Nanoparticles.** XRD patterns were recorded on a Dandong Aolong/Y-2000 X-ray diffractometer (Dan dong, China) with Cu  $K\alpha$  radiation ( $\lambda = 0.15406$  nm). The average particle size was calculated according to the Scherrer equation  $d = k\lambda/\beta \cos \theta$ , where  $k$  is a constant,  $\lambda$  is the wavelength of the X-rays,  $\theta$  is the angle at the maximum peak, and  $\beta$  is the full width of the peak at half height. FT-IR spectra were recorded using a Shimadzu IRPrestige-21 Fourier transform spectrometer (Japan) by blending the sample into a KBr pellet. The particle size and morphology were observed on a JEOL JEM-2010 (HR) transmission electron microscope (Japan) (working voltage at 100 kv). The thermogravimetric analysis of precursors was measured using a STA449c/1/41G thermal analyzer (Netzsch, Germany).

## 3. Results and Discussion

**3.1. Analysis of Microemulsions.** In the ternary system, the electric conductivity is determined by the movement of counter-ions in water phase, and the oil phase was not conducting, which was confirmed by the conductivity measurement of n-hexanol ( $0.04 \mu\text{s cm}^{-1}$ ). Bromine anions dissociated from the surfactant into the water phase while adding water, and this improved the conductive capacity when the anions pass through the membranes between reverse micelles during collision. Therefore, the diameter and the collision frequency of droplets are the main determinants for electrical conductivity. Figure 1 shows the conductivity of the n-hexanol/CTAB system related to water concentration.

As it can be seen, conductivity increased rapidly when water concentration was raised from 10% to 35%, and the mixture kept transparent. This was a solubilization process of reverse micelles. Water molecules gathered around the hydrophilic groups and formed water droplets. Adding water not only caused an increased amount of droplets, but also enlarged volumes of droplets, both of them resulted in the increase of collision frequency. According to the theory of sticky droplet collisions [15], many narrow water channels were formed in continuous phase when droplets collided. Hence, ions in water phase were able to pass through the oil phase via such channels and led to the increase of electrical conductivity. Moreover, adding water caused the ionization of CTAB, and this led to sharply increased amount of bromine anions. In a word, the conductivity presented nearly a straight increase with the adding water.

As water concentration rising from 35% to 43%, conductivity increased slowly and reached a maximum; meanwhile, the mixture became viscous and exhibited a characteristic refraction which was an indicative of formation of liquid crystal. In this process, the volumes of water droplets were enlarged. Because the ionization of the surfactant molecules tended to be equilibrium [16], the amount of dissociative ions slowly increased to a maximum. In addition, the bigger droplets the lower migration rate, and this also reduced the conductivity. Once the liquid crystal formed, the interfacial film became rigid and the formation of conductance chains stopped. Thus, the electrical conductivity maintained at a certain value after a slow increase.

After the maximum stage, the conductivity reduced gradually to a minimum value as water concentration rise from 43% to 47%. The system became ropier and appeared as opalescence. The numbers of dissociating ions kept unchanged as adding water, while the volume of droplets were enlarged so much that reduced their mobility. Moreover, when the system reaches the utmost of water content with lower migration, the interface arranged in no regulation. Hence, the viscosity collision replaced the elastic collision. The lower migration rate of water droplets would certainly result in the reduced electrical conductivity.

With the continuous addition of water, the electrical conductivity increased abruptly and the whole solution became opaque and turbid, and the system became multiphase. Such turbidity is called demulsification. Before demulsification, the mixture maintained monophasic.

The water concentrations at the points of demulsification within certain weight ratios of n-hexanol to surfactant were recorded as the maximum concentration, while the ones at the points of mutual soluble of these three contents were recorded as the minimum concentration. The relation between water concentration and the weight ratios of n-hexanol to surfactant under different temperatures was shown in Figure 2.

As shown in Figure 2, solid lines represent the maximum concentration of water, while dashed lines represents the minimum, and the region between two lines is the monophasic region of the n-hexanol/CTAB/water system. The maximum water concentration increased sharply and reached a high value as the ratio increased to 1.6, and fell back

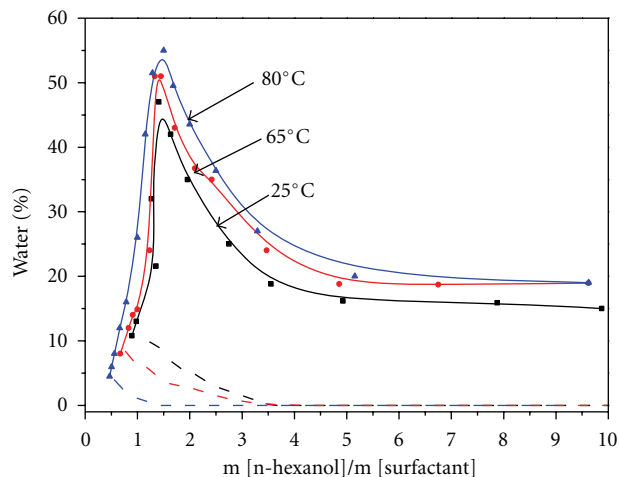


FIGURE 2: Relationship between water solubilization and mass ratio of n-hexanol to CTAB.

to a stable value. This phenomenon of self-emulsification was due to that n-hexanol reacted as a cosurfactant and the oil phase at the same time. When the surfactant was more than n-hexanol, n-hexanol performed as the cosurfactant that stabilized the interface layer and increased the water solubilization. When the weight ratio tended to 1.6, numbers of n-hexanol molecular in the interface layer were near saturation, and the excess n-hexanol existed as an oil phase which prevented the solubilization of water. Hence, the maximum water concentration was no longer determined only by n-hexanol but also by the property of CTAB.

The area of the monophasic region is affected obviously by temperature, which can be explained as follows high temperature can improve the hydrophilicity of surfactant, raise the number of water molecules that were controlled by each surfactant molecule, and enlarge the volume of droplets.

**3.2. Characterization of Photocatalyst.** In this work, the precursor was prepared in a reverse microemulsion of n-hexanol, CTAB, and water with weight ratio of 6:3:1 under 120 min vigorous stirring, and the final products were obtained by further treatment of precursors by calcination and aging methods.

TG-DSC curve for precursor was shown in Figure 3. TG graph revealed that from 50 to 100°C, the sample lost weight slowly, which was attributed to the volatilization of physically absorbed water. From 100 to 280°C, the precursor had a gradual weight loss, which was caused by the evaporation of n-hexanol (boiling point at 156°C). As the temperature increased from 280 to 320°C, the precursor had a sharp weight loss, which corresponded to the burning of residual surfactant. Such burning also caused a weak exothermic peak in DSC curve around 300°C. After 320°C, the curve was obtained as flat, indicating that the weight of precursor had little change.

DSC curve of precursor showed one endothermic peak at 120°C due to the evaporation of n-hexanol. In the subsequent process, one main exothermic peak and two weak

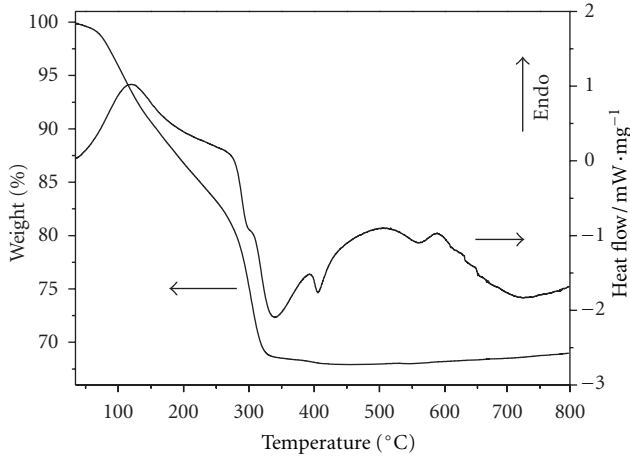
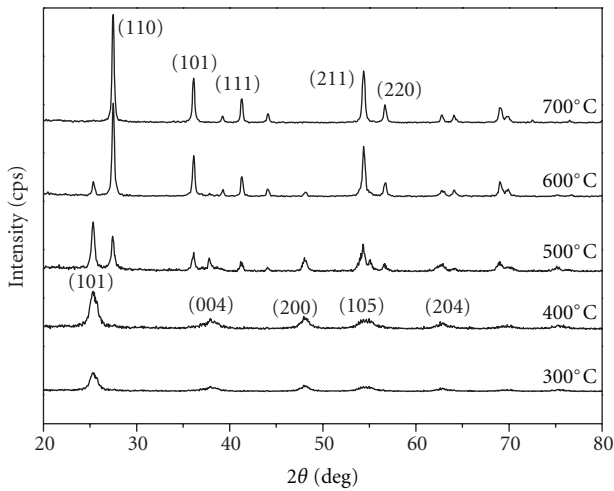


FIGURE 3: TG-DSC curves of a precursor.

FIGURE 4: XRD patterns of TiO<sub>2</sub> precursor calcined at different temperatures.

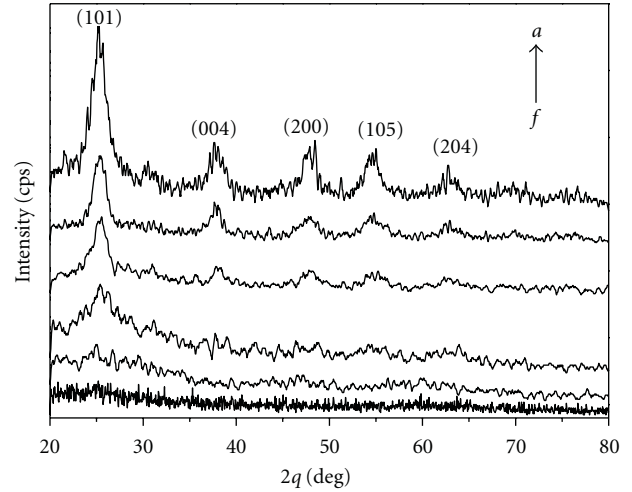
exothermic peaks were obtained. The first one around 300–320°C was caused by the burning surfactant which has been discussed above, the one at 400°C corresponded to the crystallization of anatase, and the third one at 500–600°C was the crystallization of rutile. These transitions of crystal phase could be confirmed by XRD pattern.

Figure 4 shows the XRD pattern of TiO<sub>2</sub> calcined at different temperatures. At 400°C the XRD pattern showed a weak peak at  $2\theta = 25.30^\circ$ , implying that TiO<sub>2</sub> was crystallized purely as anatase phase. The XRD patterns of samples calcined at 500 and 600°C showed peaks at  $2\theta = 25.30^\circ$  and  $2\theta = 27.50^\circ$ , indicating that both anatase and rutile existed. No anatase peak was found in the XRD pattern of the sample calcined at 700°C. Moreover, as the calcination temperature increased, all peaks became stronger and sharper, implying that the crystallinity became higher. Altogether, the XRD patterns presented the process of transition from anatase to rutile.

TABLE 1: Crystallite structure and size of TiO<sub>2</sub> calcined at different temperature.

Temperature (°C)	Structure	Crystallite size (nm)
300	100% A	19 A
400	100% A	20 A
500	61% A + 39% R	25A + 21 R
600	12% A + 88% R	29A + 27 R
700	3% A + 97% R	33 R

R: rutile; A: anatase.

FIGURE 5: XRD patterns of TiO<sub>2</sub> precursor aged at 65°C for (a) 0 h, (b) 6 h, (c) 12 h, (d) 48 h, (e) 90 h, (f) 135 h.

The average particle size, according to the Scherrer equation  $d = k\lambda/\beta \cos \theta$ , was shown in Table 1. As the temperature raise, the average particle size rises from 19 to 33 nm.

Figure 5 presents the XRD patterns of TiO<sub>2</sub> aged at 65°C from 0 h to 135 h. The precursor, that is, the sample aged for 0 h, displayed amorphous phase with no peak in the XRD pattern. The sample represented a very weak peak at  $2\theta = 25.30^\circ$  after aging for 6 h, indicating TiO<sub>2</sub> began to show the symptom of crystallization. As the aging proceeded, characteristic peaks grew slowly, and all these peaks indicated that the samples were crystallized as pure anatase. The crystallinity became better and better as the aging time became longer; however, the patterns showed little difference between samples aged for 48 h, 90 h, or 135 h. It was obviously that all the peaks were wide, which means the diameters of TiO<sub>2</sub> crystal domain were small.

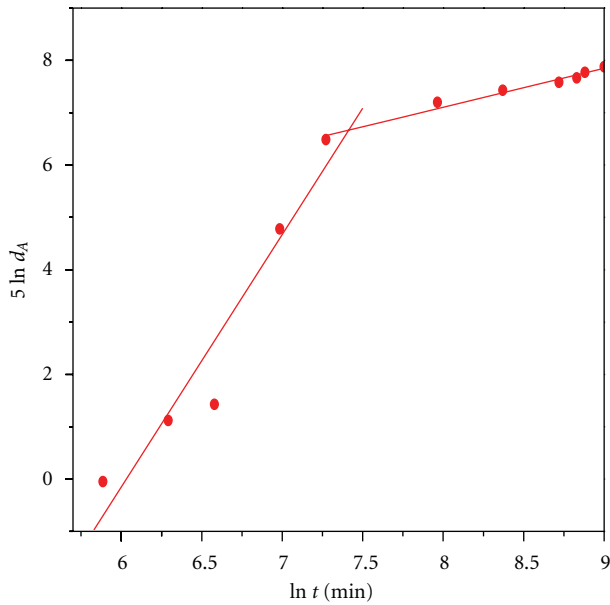
The diameters of the particles, according to the Scherrer equation, were shown in Table 2. As the aging time prolong, the average crystallite size rise from 0 to 4.8 nm. Samples aged longer than 48 h were almost unchanged in crystallite size.

The mechanism of TiO<sub>2</sub> crystal growth is considered as a process of diffusion controlled, and according to the phase transition theory of crystallization [17], relation between crystallite size of anatase and aging time could be fitted as

$$d_A^5 - d_{A0}^5 = kt^f, \quad (1)$$

TABLE 2: Crystallite structure and size of TiO<sub>2</sub> at different aging time.

Ageing time (h)	Structure	Crystallite size (nm)
0	Unformed	—
6	Unformed	0.99
12	Anatase	1.33
24	Anatase	3.66
48	Anatase	4.22
72	Anatase	4.42
102	Anatase	4.55
114	Anatase	4.63
120	Anatase	4.73
135	Anatase	4.83

FIGURE 6: Fitting curves of  $5 \ln d_A$  and  $\ln t$ .

where  $d_{A0}$  (nm) is the initial diameter;  $d_A$  (nm) is the diameter when aging time is  $t$  (min);  $f$  is the series of aging time to diameter grow;  $k$  is the rate of crystal growth. Considering  $d_A^5 \gg d_{A0}^5$ , the natural logarithm of (1) is simplified as

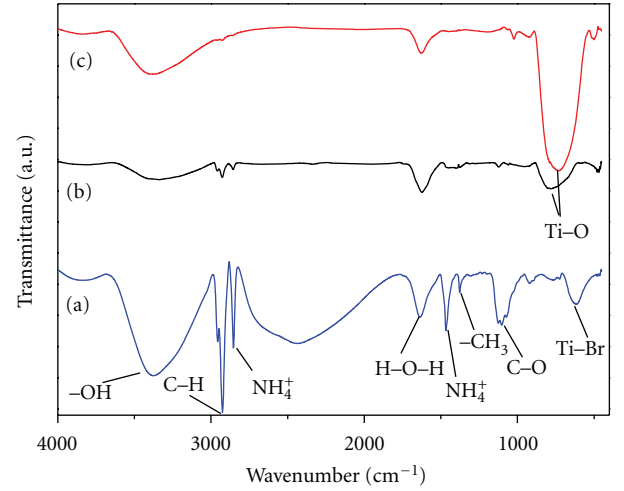
$$5 \ln d_A = f \ln t + \ln k. \quad (2)$$

Equation (2) is the relation between aging time ( $t$ /min) and crystallite size ( $d_A$ /nm). Took  $\ln t$  as transverse axis and  $5 \ln d_A$  as vertical axis, and constructed their linearity, the relation are shown in Figure 6. Fitting curves were obtained by subsection simulation. Table 3 showed the series of aging time to diameter grow  $f$  and the rate of crystal growth  $k$ .

Fitting curves showed that, at the beginning of aging process, crystallite grew quickly with an extreme low rate of crystal growth. Such phenomenon might be explained by the phase transition from amorphous to anatase. During this stage, system formed plenty of crystal nucleuses. After being aged for 26 h, the growth of crystal was not obvious, and

TABLE 3: Rate constant of crystal growth and chronological series.

Stage	$f$	$\ln k$	$k$
1	4.83169	-29.15146	$2.19 \times 10^{-13}$
2	0.74674	1.13029	3.10
$t_a$	1588/min (26/h)		

FIGURE 7: FT-IR spectra of (a) TiO<sub>2</sub> precursor, (b) TiO<sub>2</sub> precursor aging at 65°C for 120 h, (c) TiO<sub>2</sub> precursor calcined at 500°C.

the diameter was effected slightly by aging time ( $f = 0.75$ ). This might be the process that crystal grew from imperfect to perfect. The work showed that anatase could be obtained at low temperature.

Figure 7 shows the FT-IR spectra of TiO<sub>2</sub> precursor treated by calcination and aging process. The band at about 3400 cm<sup>-1</sup> was indexed to the stretching vibration of the O-H bond and free water and the band at about 1631 cm<sup>-1</sup> was attributed to the O-H bending vibration of chemically adsorbed water [18]. Bands at 2700 and 1462 cm<sup>-1</sup> were considered as the characteristic peaks of ammonium; 2850 cm<sup>-1</sup> was the stretching vibration band of C-H bond in methylene, while 1050 cm<sup>-1</sup> was the vibration of C-O bond [19]. These bands showed that precursor adsorbed a large number of organic compounds, provided by n-hexanol and CTAB. Calcination or aging were able to remove these organic compounds. The stretching vibration of Ti-Br bond caused a wide band around 600 cm<sup>-1</sup>, while band around 800 cm<sup>-1</sup> was the characteristic peak of Ti-O bond [18, 19]. These bands showed that, precursors must be heated to form Ti-O bond.

Figure 8 shows the typical TEM images of TiO<sub>2</sub> aged at 65°C for 120 h. TiO<sub>2</sub> synthesized by aging method in low temperature was regular and spherical, to a certain extent. The particle size distribution was wide, ranging from 6 nm to 19 nm. The average particle size was roughly estimated as 12 nm from the obtained images. These images suggested that synthesis of TiO<sub>2</sub> in our microemulsion system with aging process at low temperature can bring about nanoparticles with relatively small and uniform sizes.

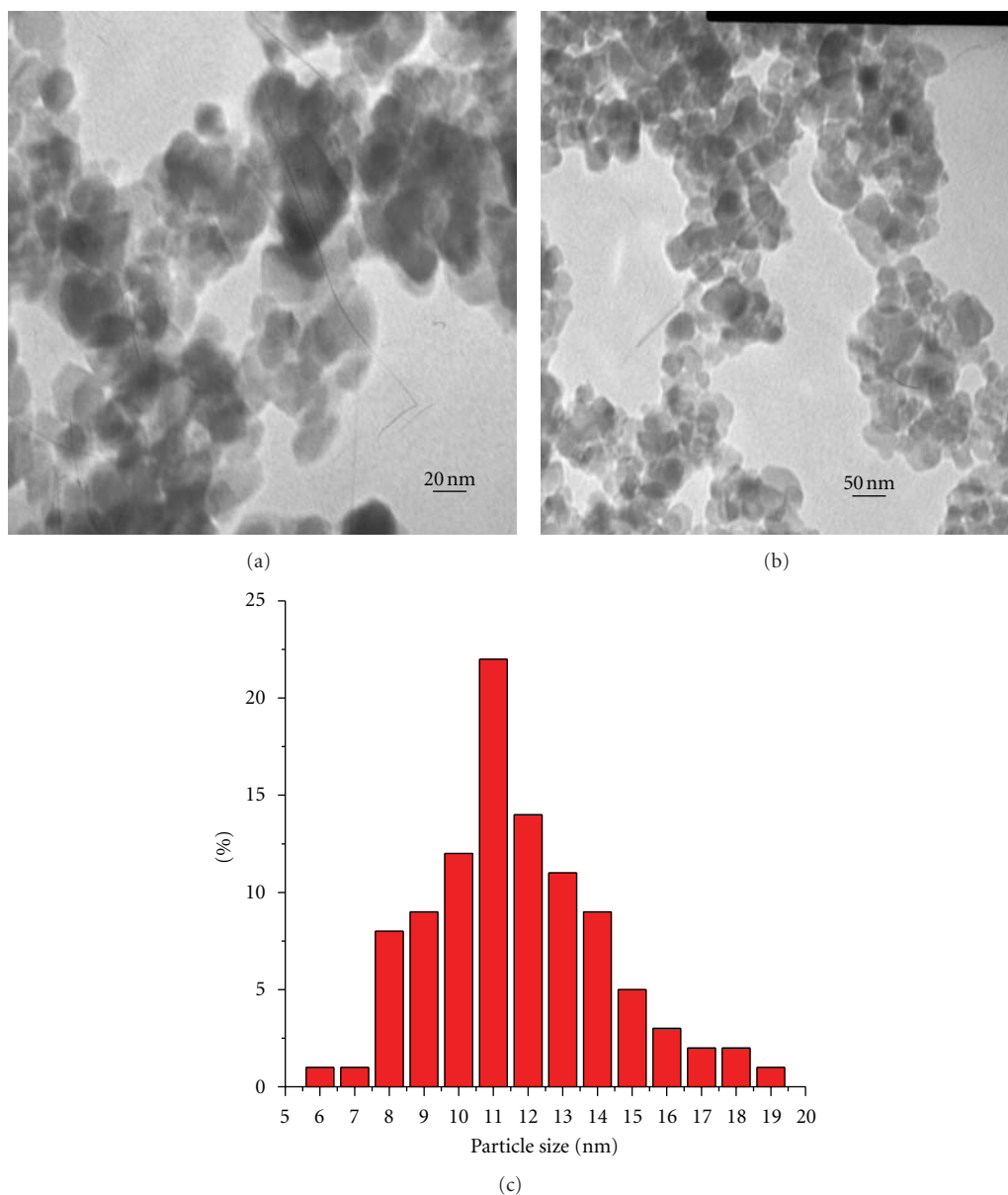


FIGURE 8: TEM and particle-size distribution graphs of TiO<sub>2</sub> aging at 65°C for 120 h.

**3.3. Photocatalytic Activity.** The degradation process of methyl orange (MO) was obtained by measuring the solution every 10 min during UV irradiation, and results were shown in Figure 9 as UV-Vis spectra curves. The photocatalytic reaction was under catalysis of TiO<sub>2</sub> calcined at 500°C for 3 h. There were two absorption peaks in the curves, the one at 464 nm was caused by the azo bond and the other one at 265 nm was caused by benzene ring [20]. During the decomposition process, both azo bond and benzene ring were degraded. In this research, the concentration of MO was roughly represented by the absorption at the maximum wavelength, which appeared at 464 nm as shown in Figure 9.

In order to compare the photocatalytic performance of as-obtained products synthesized in different conditions, various samples involving TiO<sub>2</sub> calcined at 500°C for 3 h,

TiO<sub>2</sub> aged at 65°C for 72, 90, 120 h, and P25 were conducted in UV-irradiated MO solutions, and degradation rates of MO were showed in Figure 10. It was demonstrated that the sample of TiO<sub>2</sub> calcined at 500°C for 3 h had the best photoactivity which degraded 98% after 60 min (Figure 10 (a)). Sample of TiO<sub>2</sub> aged at 65°C for 90 h also presented a high photoactivity which degraded over 74% after 60 min (Figure 10 (b)). These two samples had better photoactivity than commercial P25, which degraded 71% after 60 min (Figure 10 (c)). The relatively high photocatalytic activity of TiO<sub>2</sub> aged at 65°C for 90 h was suggested to be responsible for the exhibited crystallinity and the enhanced adsorption ability caused by presence of amorphous titania. The results also showed that aging time affected photocatalytic activities of TiO<sub>2</sub> obviously (Figure 10 (b), (d), and (e)). The efficiency

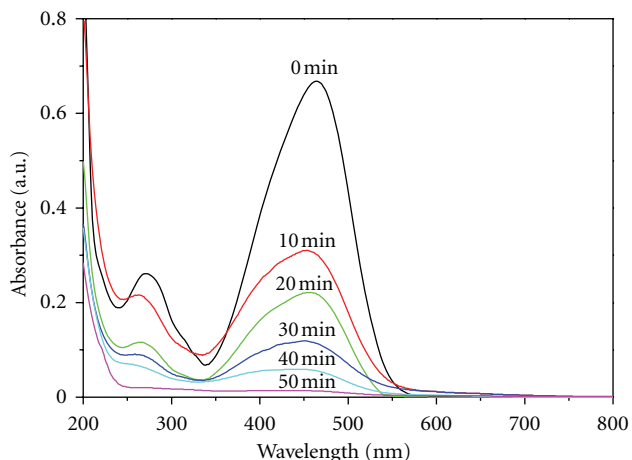


FIGURE 9: Degradation process of MO by aged TiO<sub>2</sub> under ultraviolet light irradiation, analyzed by UV-Vis absorption spectra for solutions separated from the TiO<sub>2</sub> suspensions irradiated for different periods.

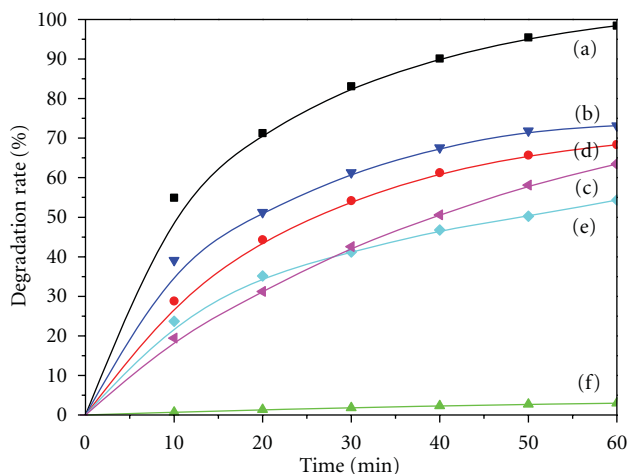


FIGURE 10: Degradation ratio of MO under ultraviolet light irradiation over catalysts as: (a) TiO<sub>2</sub> calcined at 500°C, (b) TiO<sub>2</sub> aged at 65°C for 90 h, (c) TiO<sub>2</sub> aged at 65°C for 120 h, (d) commercial P25, (e) TiO<sub>2</sub> aged at 65°C for 72 h, (f) blank.

of UV photocatalysis toward MO was low (Figure 10 (f)). TiO<sub>2</sub> aged for 90 h represented the best photoactivity among samples prepared by aging process.

#### 4. Conclusions

Nanosized TiO<sub>2</sub> nanoparticles were synthesized in n-hexanol/CTAB/water reverse microemulsions. The precursors were treated at 500°C calcination or 65°C aging in water bath, and investigated by XRD, FT-IR, and TEM. The results show precursor is amorphous as Ti-Br compounds; aging at low temperature is capable to form anatase TiO<sub>2</sub> with reasonable photocatalytic performance. Among all the as-synthesized photocatalysts by aging method, the nanoparticles aged at 65°C for 90 h showed the highest photocatalytic

activity, and at the same time higher than that of commercial P25.

#### Acknowledgment

The authors would like to gratefully acknowledge the South China Normal University for financing this paper.

#### References

- [1] J. A. Byrne, P. A. Fernandez-Ibañez, P. S. M. Dunlop, D. M. A. Alrousan, and J. W. J. Hamilton, "Photocatalytic enhancement for solar disinfection of water: a review," *International Journal of Photoenergy*, vol. 2011, Article ID 798051, 12 pages, 2011.
- [2] J. Yu, J. C. Yu, M. K. P. Leung et al., "Effects of acidic and basic hydrolysis catalysts on the photocatalytic activity and microstructures of bimodal mesoporous titania," *Journal of Catalysis*, vol. 217, no. 1, pp. 69–78, 2003.
- [3] Y. Fan, G. Chen, D. Li et al., "Highly selective deethylation of rhodamine B on TiO<sub>2</sub> prepared in supercritical fluids," *International Journal of Photoenergy*, vol. 2012, Article ID 173865, 7 pages, 2012.
- [4] P. Calandra, G. Calogero, A. Sinopoli, and P. G. Gucciardi, "Metal nanoparticles and carbon-based nanostructures as advanced materials for cathode application in dye-sensitized solar cells," *International Journal of Photoenergy*, vol. 2010, Article ID 109495, 15 pages, 2010.
- [5] J. Yu, S. Liu, and H. Yu, "Microstructures and photoactivity of mesoporous anatase hollow microspheres fabricated by fluoride-mediated self-transformation," *Journal of Catalysis*, vol. 249, no. 1, pp. 59–66, 2007.
- [6] H. Yu, J. Yu, S. Liu, and S. Mann, "Template-free hydrothermal synthesis of CuO/Cu<sub>2</sub>O composite hollow microspheres," *Chemistry of Materials*, vol. 19, no. 17, pp. 4327–4334, 2007.
- [7] Y. Lai, Y. Chen, H. Zhuang, and C. Lin, "A facile method for synthesis of Ag/TiO<sub>2</sub> nanostructures," *Materials Letters*, vol. 62, no. 21–22, pp. 3688–3690, 2008.
- [8] C. H. Lu, W. H. Wu, and R. B. Kale, "Microemulsion-mediated hydrothermal synthesis of photocatalytic TiO<sub>2</sub> powders," *Journal of Hazardous Materials*, vol. 154, no. 1–3, pp. 649–654, 2008.
- [9] W. Liu and R. Guo, "The photostabilization of hemoglobin in triton X-100 aqueous solution and triton X-100/n-C<sub>5</sub>H<sub>11</sub>OH/H<sub>2</sub>O microemulsion," *Photochemistry and Photobiology*, vol. 86, no. 4, pp. 835–843, 2010.
- [10] C. Hu, S. Duo, T. Liu, J. Xiang, and M. Li, "Comparison of photocatalytic performance of anatase TiO<sub>2</sub> prepared by low and high temperature route," *Applied Surface Science*, vol. 257, no. 8, pp. 3697–3701, 2011.
- [11] L. Zhao, J. Ran, Z. Shu, G. Dai, P. Zhai, and S. Wang, "Effects of calcination temperatures on photocatalytic activity of ordered titanate nanoribbon/SnO<sub>2</sub> films fabricated during an EPD process," *International Journal of Photoenergy*, vol. 2012, Article ID 472958, 7 pages, 2012.
- [12] N.-H. Lee, H.-J. Oh, S.-C. Jung, W.-J. Lee, D.-H. Kim, and S.-J. Kim, "Photocatalytic properties of nanotubular-shaped TiO<sub>2</sub> powders with anatase phase obtained from titanate nanotube powder through various thermal treatments," *International Journal of Photoenergy*, vol. 2011, Article ID 327821, 7 pages, 2011.
- [13] B. Qi, L. Wu, Y. Zhang, Q. Zeng, and J. Zhi, "Low-temperature and one-step synthesis of rutile TiO<sub>2</sub> aqueous sol

- by heterogeneous nucleation method," *Journal of Colloid and Interface Science*, vol. 345, no. 2, pp. 181–186, 2010.
- [14] A. R. Liu, S. M. Wang, Y. R. Zhao, and Z. Zheng, "Low-temperature preparation of nanocrystalline TiO<sub>2</sub> photocatalyst with a very large specific surface area," *Materials Chemistry and Physics*, vol. 99, no. 1, pp. 131–134, 2006.
- [15] A. Jada, J. Lang, and R. Zana, "Relation between electrical percolation and rate constant for exchange of material between droplets in water in oil microemulsions," *The Journal of Physical Chemistry*, vol. 93, no. 1, pp. 10–12, 1989.
- [16] R. Duro, C. Souto, J. L. Gómez-Amoza, R. Martínez-Pacheco, and A. Concheiro, "Interfacial adsorption of polymers and surfactants: implications for the properties of disperse systems of pharmaceutical interest," *Drug Development and Industrial Pharmacy*, vol. 25, no. 7, pp. 817–829, 1999.
- [17] D. Shechtman, I. Blech, D. Gratias, and J. W. Cahn, "Metallic phase with long-range orientational order and no translational symmetry," *Physical Review Letters*, vol. 53, no. 20, pp. 1951–1953, 1984.
- [18] K. Lv, H. Zuo, J. Sun et al., "(Bi, C and N) codoped TiO<sub>2</sub> nanoparticles," *Journal of Hazardous Materials*, vol. 161, no. 1, pp. 396–401, 2009.
- [19] J. Fang, F. Wang, K. Qian, H. Bao, Z. Jiang, and W. Huang, "Bi-functional N-doped mesoporous TiO<sub>2</sub> photocatalysts," *The Journal of Physical Chemistry C*, vol. 112, no. 46, pp. 18150–18156, 2008.
- [20] S. Al-Qaradawi and S. R. Salman, "Photocatalytic degradation of methyl orange as a model compound," *Journal of Photochemistry and Photobiology A*, vol. 148, no. 1–3, pp. 161–168, 2002.

## Research Article

# Synthesis of $\text{Fe}_3\text{O}_4/\text{C}/\text{TiO}_2$ Magnetic Photocatalyst via Vapor Phase Hydrolysis

Fuzhi Shi,<sup>1</sup> Yaogang Li,<sup>2</sup> Qinghong Zhang,<sup>2</sup> and Hongzhi Wang<sup>1</sup>

<sup>1</sup> State Key Laboratory for Modification of Chemical Fibers and Polymer Materials, Donghua University, Shanghai 201620, China

<sup>2</sup> Engineering Research Center of Advanced Glasses Manufacturing Technology, MOE, Donghua University, Shanghai 201620, China

Correspondence should be addressed to Qinghong Zhang, zhangqh@dhu.edu.cn and Hongzhi Wang, wanghz@dhu.edu.cn

Received 14 September 2011; Revised 15 November 2011; Accepted 15 November 2011

Academic Editor: Jiaguo Yu

Copyright © 2012 Fuzhi Shi et al. This is an open access article distributed under the Creative Commons Attribution License, which permits unrestricted use, distribution, and reproduction in any medium, provided the original work is properly cited.

A core/multi-shell-structured  $\text{Fe}_3\text{O}_4/\text{C}/\text{TiO}_2$  magnetic photocatalyst is prepared via vapor phase hydrolysis process. The as-synthesized core/multi-shell-structured composite is characterized by X-ray diffraction (XRD), field emission scanning electron microscopy (FE-SEM), transmission electron microscopy (TEM), high-resolution electron microscopy (HRTEM),  $\text{N}_2$  adsorption-desorption isotherm analyses, vibrating sample magnetometer (VSM), and ultraviolet-visible (UV-Vis) absorption spectroscopy. TEM and HRTEM show that well-crystallized anatase  $\text{TiO}_2$  nanocrystals are immobilized on the surface of as-prepared  $\text{Fe}_3\text{O}_4/\text{C}$  microspheres with dimensions around 200 nm.  $\text{N}_2$  adsorption-desorption isotherm analysis shows that the obtained photocatalyst exists disorderedly mesoporous structure. The photocatalytic efficiency of the catalyst in degradation of methylene blue is evaluated, and the  $\text{Fe}_3\text{O}_4/\text{C}/\text{TiO}_2$  photocatalyst with low  $\text{TiO}_2$  content (37%) has a relatively higher activity than commercial anatase  $\text{TiO}_2$ . The intermediate carbon layer avoids the photodissolution of  $\text{Fe}_3\text{O}_4$  effectively, and the recycling property is largely improved due to the existence of magnetic  $\text{Fe}_3\text{O}_4$  core.

## 1. Introduction

Titanium dioxide ( $\text{TiO}_2$ ) nanoparticles have inspired scientists for their potential application in treatment of environmental pollutants in wastewater [1–9]. However, there have been two obvious deficiencies in their practical application. One is the wide bandgap of  $\text{TiO}_2$  ( $\approx 3.2$  eV), so only a small ultraviolet fraction of solar light can be used. The other is the separation of nanosized photocatalyst from wastewater, which is too difficult and energy consumptive [10]. Both deficiencies result in the low treatment efficiency and increase the loss of photocatalyst. Doping  $\text{TiO}_2$  with foreign element [11, 12] and mixing  $\text{TiO}_2$  with sensitizer [13, 14] are two most important ways to enhance the utilizing of sunlight. And the related researches on catalyst immobilization have also attracted wide attention in order to solve the separation and recycle of the suspended  $\text{TiO}_2$  nanoparticles [15, 16]. Some researchers have coated  $\text{TiO}_2$  over glass, zeolite, and other substrates to avoid the catalyst-recovering step [17–19].

Recently, magnetic photocatalysts have been addressed to resolve the separation of  $\text{TiO}_2$  nanoparticles [20–23]. Cheng

et al. [22] obtained a core/shell-structured bactericidal photocatalyst with  $\text{Fe}_3\text{O}_4$  core and  $\text{TiO}_2$  shell for bactericidal application. Xuan et al. [23] fabricated  $\text{Fe}_3\text{O}_4/\text{TiO}_2$  hollow spheres through poly(styrene-acrylic acid) (PSA) template method and carried out the photodegradation of RhB as a model reaction to investigate the photocatalytic activity of the hollow photocatalyst. Nevertheless, Beydoun et al. [24] indicated that the photodissolution of  $\text{Fe}_3\text{O}_4$  would occur during the light irradiation. So the barrier layer between magnetic  $\text{Fe}_3\text{O}_4$  and  $\text{TiO}_2$  was prepared to reduce the negative effects [25–28]. Song and Gao [8] synthesized the bi-functional titania/silica-coated magnetic spheres and used MB to evaluate their photocatalytic properties. Ye et al. [28] obtained the core/shell-structured  $\text{Fe}_3\text{O}_4/\text{SiO}_2/\text{TiO}_2$  magnetic nanocomposites with enhanced photocatalytic activity by combining sol-gel process with calcinations. Presence of silica coating is essential to reduce the negative effect to magnetite during the photocatalytic process [8, 28]. However, Wang et al. [29] indicated that the carbon shell coated on  $\text{Fe}_3\text{O}_4$  microspheres was more compact than others, so the direct contact can be avoided effectively. Its benefit to protect

the magnetic carriers enhance the photocatalytic activity and extend the lifetime of magnetic photocatalyst.

Herein, we develop a novel and controllable strategy to prepare the unique  $\text{Fe}_3\text{O}_4/\text{C}/\text{TiO}_2$  core/multi-shell-structured photocatalyst via vapor phase hydrolysis (VPH) process. It is crucial that  $\text{TiO}_2$  in the shell is perfectly crystallized without calcination. In VPH method, the water molecules are gently contacting with alkoxide in vapor phase with the advantage of hydrothermal treatment to obtain highly crystallized  $\text{TiO}_2$ . The size and crystallinity of anatase  $\text{TiO}_2$  crystallite in the shell could be tuned by reaction temperature, duration, and the thickness of anatase shell could also be tuned by varying tetrabutyl titanate (TBOT) content. Finally, the photocatalytic degradation of MB was selected as a model reaction to demonstrate the unique advantage in their photocatalytic activity and recycle facet.

## 2. Experimental Procedure

**2.1. Materials.** Commercial anatase  $\text{TiO}_2$ ,  $\text{FeCl}_3 \cdot 6\text{H}_2\text{O}$ , ethylene glycol (EG), sodium acetate (NaAc), polyethylene glycol (PEG), oleic acid, cetyltrimethylammonium bromide (CTAB), glucose, TBOT, and absolute ethanol were analytical grade and purchased from Shanghai Chemical Reagent Co., China. All chemicals were used as received without any purification. The distilled water for all processes was purified by ion exchange and then followed by distillation. The specific surface area of commercial anatase  $\text{TiO}_2$  is  $19 \text{ m}^2/\text{g}$  and the crystallite size is about 80 nm.

**2.2. Synthesis of  $\text{Fe}_3\text{O}_4$  Microspheres.** The ferrite core was first fabricated by solvothermal method, as described by others [30–32]. Typically, 1.35 g  $\text{FeCl}_3 \cdot 6\text{H}_2\text{O}$  was dissolved in 50 mL EG to form a clear solution, followed by addition of 3.6 g NaAc and 1.0 g PEG. The mixture was stirred vigorously for 30 min at room temperature and then sealed in a 70 mL Teflon-lined autoclave. The autoclave was heated to  $200^\circ\text{C}$  for 12 h. After it was cooled to room temperature, the black products were collected by magnet and rinsed with distilled water and ethanol. The final product was dried under vacuum at  $60^\circ\text{C}$  for 8 h.

**2.3. Fabrication of  $\text{Fe}_3\text{O}_4/\text{C}$  Nanocomposites.** The magnetic  $\text{Fe}_3\text{O}_4/\text{C}$  nanocomposite was fabricated according to the route of Wang et al. [29]. The reactant mixtures were prepared by dissolving glucose in the aqueous solution containing oleic-acid-stabilized  $\text{Fe}_3\text{O}_4$  nanoparticles. Typically, 4 g glucose was dissolved in 40 mL oleic-acid-stabilized  $\text{Fe}_3\text{O}_4$  suspension (2.5 g/L). After that, the mixture was sealed in a 50 mL Teflon-sealed autoclave and heated to  $170^\circ\text{C}$  for 3 h. Finally, the product isolated from the mixture by external magnetic field was rinsed with distilled water and ethanol. The final product was dried under vacuum at  $60^\circ\text{C}$  for 8 h.

**2.4. Preparation of Magnetic  $\text{Fe}_3\text{O}_4/\text{C}/\text{TiO}_2$  Microspheres.** 0.1 g  $\text{Fe}_3\text{O}_4/\text{C}$  powders and TBOT were added into 8 mL ethanolic solution and stirred for 2 min to obtain a colloidal

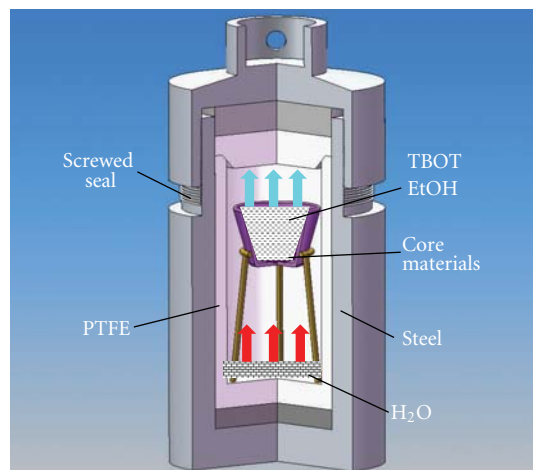


FIGURE 1: The setup of the vapor phase hydrolysis device.

solution which was then transferred into the vapor phase hydrolysis device (VPHD, as shown in Figure 1) quickly. 3 mL deionized water was located at the bottom of VPHD as liquid phase to produce vapor at elevated temperature, thus the liquid water did not contact with TBOT directly and the fierce hydrolysis was avoided. The sealed VPHD was heated to different temperature for varying duration. The TBOT content, the reaction temperature, and duration were varied as shown in Table 1. The as-synthesized powder was collected by magnet, rinsed with distilled water and ethanol for several times, and subsequently dried under vacuum at  $60^\circ\text{C}$  for 8 h.

**2.5. Characterizations.** The powder phase composition was identified by X-ray diffraction (XRD) equipment (D/max 2550 PC, Rigaku Co., Japan), using  $\text{Cu K}\alpha$  radiation at 40 kV and 200 mA. The crystallite sizes of  $\text{Fe}_3\text{O}_4$  and anatase are estimated from the corresponding XRD peak at  $2\theta = 35.4^\circ$  and  $2\theta = 25.3^\circ$  by Scherrer formula ( $D = k\lambda/\beta \cos \theta$ ), where  $D$  is the crystallite size,  $\lambda$  is the wavelength of the X-ray radiation ( $\text{Cu K}\alpha = 0.15406 \text{ nm}$ ),  $k$  is usually taken as 0.89,  $\beta$  is the line width at half-maximum height of the (311) peak of  $\text{Fe}_3\text{O}_4$  and the (101) peak of anatase after subtracting the instrumental line broadening, and  $\theta$  is the diffraction angle. The morphology and size of the particles were observed by transmission electron microscope (JEM-2100F, JEOL, Japan) equipped with an energy-dispersive X-ray and field emission scanning electron microscope (S-4800, Hatachi, Japan). The nitrogen adsorption-desorption isotherm was obtained at 77 K using an Autosorb-1 MP (Quantachrome, USA) utilizing Barrett-Emmett-Teller (BET) calculations of specific surface area and Barrett-Joyner-Halenda (BJH) calculations of pore volume and pore size (diameter) distributions from the desorption branch of the isotherm. Magnetic characterization was conducted on vibrating sample magnetometer (6000, PPMS, USA). The carbon content in the  $\text{Fe}_3\text{O}_4/\text{C}$  nanocomposites and Sample B is quantitatively measured by Elementar Analyzer (Vario EL III, Elementar, Germany).

TABLE 1: Summary of the preparative parameters and the specific surface areas.

Sample	Fe <sub>3</sub> O <sub>4</sub> /C powder (g)	Anatase calculated from TBOT (g)	Temperature (°C)	Time (h)	S <sub>BET</sub> (m <sup>2</sup> /g)
A	0.1	0.125	150	10	57
B	0.1	0.25	150	10	61
C	0.1	0.5	150	10	72
D	0.1	0.25	150	5	58
E	0.1	0.25	150	20	53
F	0.1	0.25	100	10	155
G	0.1	0.25	200	10	39
H	0.1	—	150	10	38

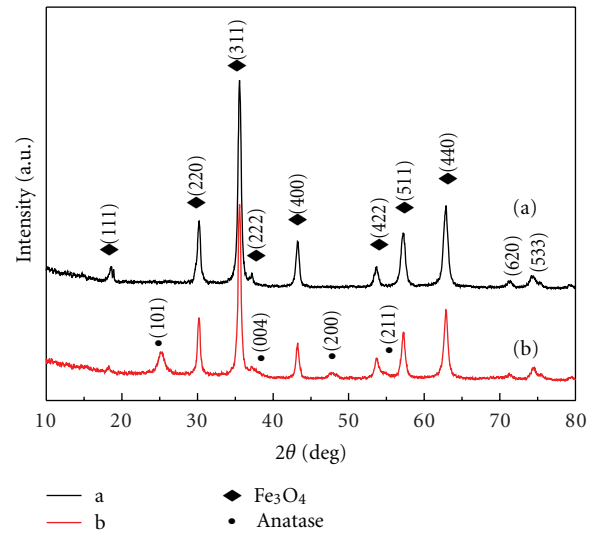
**2.6. Photocatalytic Reaction .** Ultraviolet (UV) light photocatalytic reactions were carried out to characterize the degradation rate of methylene blue (MB). The suspension was irradiated with a 300 W medium-pressure mercury lamp. First, 0.4 g catalyst (Sample B or commercial anatase TiO<sub>2</sub>) was suspended in 500 mL 5.35 × 10<sup>-5</sup> M methylene blue (MB) solution. Oxygen was also bubbled into suspension at a flow rate of 100 mL/min during the whole experiment. Prior to photobleaching, the MB-solution-containing catalyst was stirred and stored in dark for 30 min to obtain the saturated absorption of MB. The MB concentration was determined in the sequence of 15, 30, 60, 90, 120, and 180 min using Lambda 35 UV-Vis spectrophotometer (Perkin-Elmer, Waltham, USA) by collecting the absorbance of MB at wavelength of 665 nm.

In order to investigate the recycle property and long-term photocatalytic activity, Sample B was used to degrade MB solutions five times. After ultraviolet light irradiation for 3 h, the magnetic photocatalyst was recycled by external magnetic field, washed three times with deionized water and dried at 105°C for 5 h, the recovered photocatalyst was subsequently used to degrade fresh MB solution under the same irradiation conditions for 3 h. Then 3-cycle, 4-cycle and 5-cycle were also carried out in the same process.

The degradation rate ( $H$ ) of MB was calculated using  $H = C/C_0 \times 100\%$ , where  $C$  and  $C_0$  are the concentration of remaining MB at different intervals and primal MB solution.

### 3. Results and Discussion

**3.1. X-Ray Diffraction Analysis.** The crystallinity and structure of as-prepared Fe<sub>3</sub>O<sub>4</sub> particle and Fe<sub>3</sub>O<sub>4</sub>/C/TiO<sub>2</sub> nanocomposite are confirmed by XRD. As showed in Figure 2, the peak position and relative intensity of Fe<sub>3</sub>O<sub>4</sub> (curve a) match well with standard powder diffraction date (JCPDS No. 74-2402), indicating phase purity of Fe<sub>3</sub>O<sub>4</sub>. Well-resolved diffraction peaks reveal good crystallinity of Fe<sub>3</sub>O<sub>4</sub>. The average crystallite size of as-prepared ferrite powder estimated by Scherrer formula is around 14 nm, which is in agreement with the result of Zhang et al. [31]. There is no diffraction peaks of carbon appears in curve b due to its amorphous nature and low content compared with Fe<sub>3</sub>O<sub>4</sub> and anatase TiO<sub>2</sub>. In addition to all diffraction peaks of Fe<sub>3</sub>O<sub>4</sub>, there are other four diffraction peaks appear at  $2\theta = 25.3^\circ, 37.8^\circ, 48.1^\circ$ , and  $55.1^\circ$  which correspond to (101), (004), (200), and (211)

FIGURE 2: XRD pattern of (a) Fe<sub>3</sub>O<sub>4</sub> and (b) Sample B.

planes of anatase TiO<sub>2</sub> (JCPDS No. 21-1272), respectively. The crystallite size of anatase TiO<sub>2</sub> calculated by Scherrer formula is to be ca. 11.2 nm. And the intensity of XRD peaks of Fe<sub>3</sub>O<sub>4</sub> has been decreased because there is some carbon and anatase TiO<sub>2</sub> coated on it. XRD results demonstrate that the crystalline anatase TiO<sub>2</sub> and Fe<sub>3</sub>O<sub>4</sub> coexist in Sample B.

**3.2. Morphology and EDS Analysis.** The morphologies of the selected samples are revealed by TEM (Figure 3) and SEM (Figure 4). The Fe<sub>3</sub>O<sub>4</sub> crystallites are ultrafine as observed in Figure 3(a) and connect tightly to one another to form spheres. And the diameter of the aggregated particles is around 200 nm (Figure 4(a)). Figure 3(b) shows that amorphous carbon and well-crystallized anatase TiO<sub>2</sub> formed on the surface of Fe<sub>3</sub>O<sub>4</sub> microspheres, and the amorphous carbon shell is compact while polycrystalline titania shell is around the carbon shell. The carbon content in the Fe<sub>3</sub>O<sub>4</sub>/C nanocomposites and Sample B is measured to be 4.4 wt.% and 2.8 wt.%. The crystallite sizes of Fe<sub>3</sub>O<sub>4</sub> and anatase TiO<sub>2</sub> are around 15 and 12 nm, which is in agreement with the calculation of XRD. The distances marked in the pattern (Figure 3(c)) between (101) plane of anatase and (311) plane of Fe<sub>3</sub>O<sub>4</sub> are 0.35 nm and 0.25 nm, respectively. A well-defined core/multishell structure with Fe<sub>3</sub>O<sub>4</sub> as core, carbon

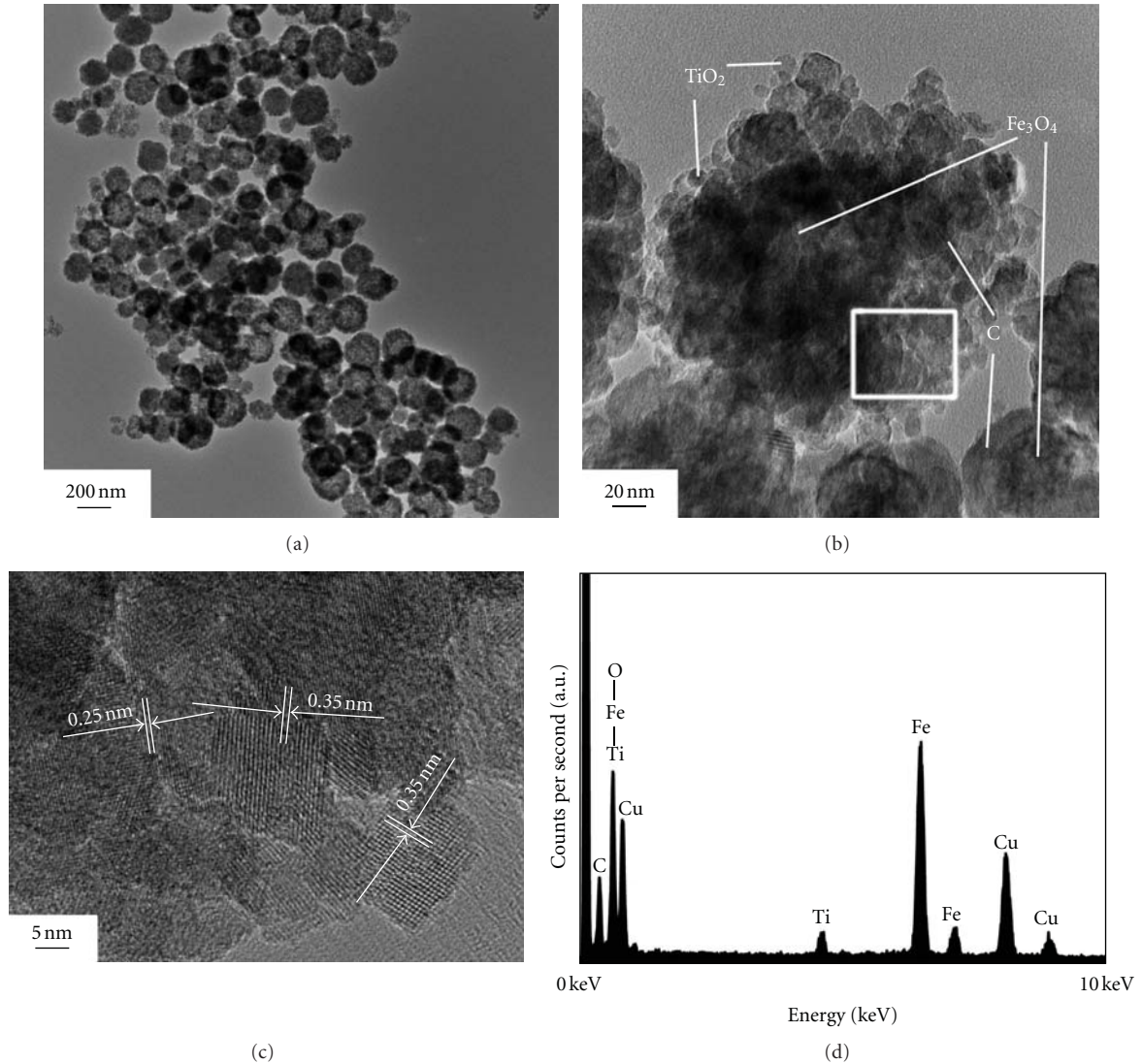


FIGURE 3: TEM images of (a)  $\text{Fe}_3\text{O}_4$ , (b) Sample B, HRTEM image (c), and EDS result (d) of the selected area in image (b).

as intermediate shell, and anatase as outer shell is indeed formed by the evidence of TEM images (Figures 3(b) and 3(c)). The direct contact between  $\text{Fe}_3\text{O}_4$  and  $\text{TiO}_2$  was inhibited. The EDS results of the selected area in Figure 3(b) are given in Figure 3(d). Ti, Fe, and some C elements come from Sample B; Cu and C come from copper grid and carbon film for TEM analysis. Figure 4 gives the SEM images of the selected samples. It provides more structural information about the three-dimensional morphology of the product. A large quantity of as-prepared  $\text{Fe}_3\text{O}_4$ , carbon-coated  $\text{Fe}_3\text{O}_4$ , and core/multi-shell-structured  $\text{Fe}_3\text{O}_4/\text{C}/\text{TiO}_2$  with narrow distributions has been synthesized. As shown in Figure 4(b), the greater crosslinking degrees and slickness of the  $\text{Fe}_3\text{O}_4/\text{C}$  surface can be seen compared with Figure 4(a) due to the amorphous carbon. Because the small anatase  $\text{TiO}_2$  crystallite is coated on the surface of  $\text{Fe}_3\text{O}_4/\text{C}$  particles, the result that the surface of Sample B becomes rough can be obtained from Figure 4(c). Up to now, the core/multishell-structured

$\text{Fe}_3\text{O}_4/\text{C}/\text{TiO}_2$  composite is confirmed by the evidence of SEM and TEM analysis.

**3.3. Magnetic Study.** The magnetic property of as-prepared  $\text{Fe}_3\text{O}_4$ ,  $\text{Fe}_3\text{O}_4/\text{C}$  and  $\text{Fe}_3\text{O}_4/\text{C}/\text{TiO}_2$  is investigated with vibrating sample magnetometer at room temperature. Figure 5 gives the magnetization-hysteresis loops of samples with different composition. It shows that the magnetic saturation value of samples is closely related with the thickness of nonmagnetic shells in given external magnetic field [8]. The magnetic saturation values are 75.1 emu/g for  $\text{Fe}_3\text{O}_4$  [30], 65.1 emu/g for  $\text{Fe}_3\text{O}_4/\text{C}$ , and 56.1 emu/g for  $\text{Fe}_3\text{O}_4/\text{C}/\text{TiO}_2$  particles. The decrease of saturation magnetization is most likely attributed to the existence of nonmagnetic C and  $\text{TiO}_2$  shells on the surface of  $\text{Fe}_3\text{O}_4$  as shown in curves b and c. Because of the magnetic core, it is notable that these magnetic photocatalysts could be easily recycled from solution

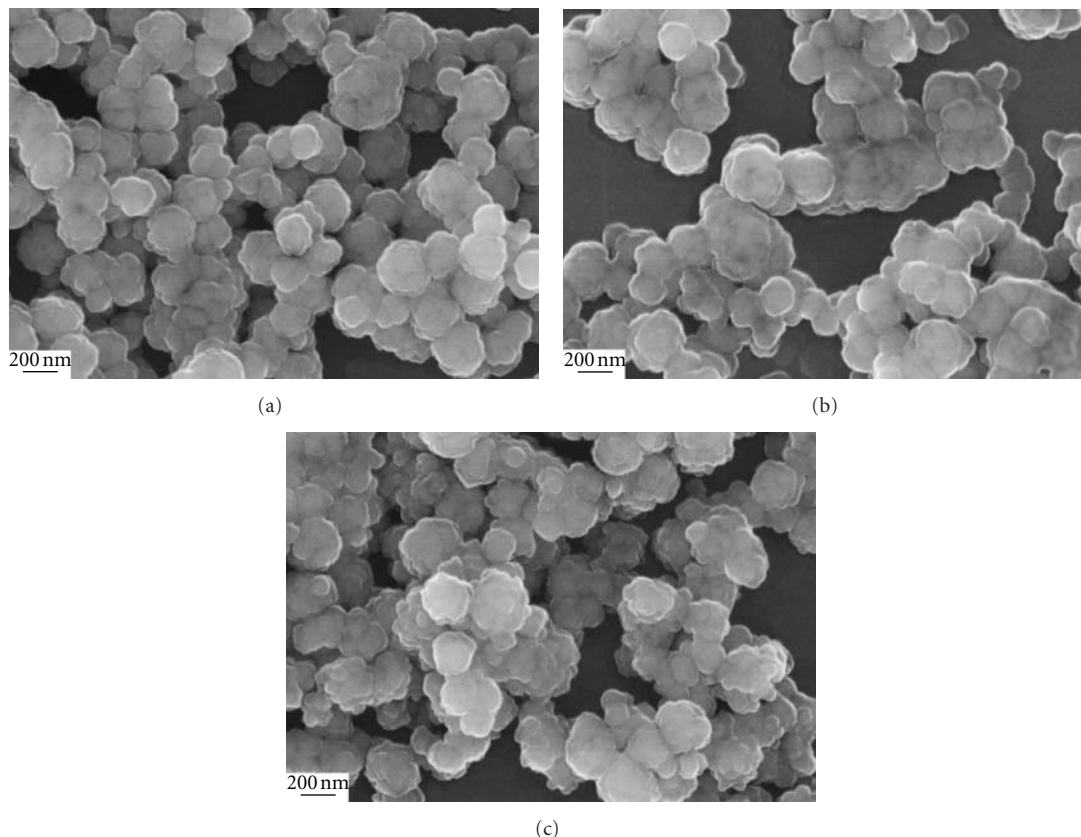


FIGURE 4: SEM images of (a) Fe<sub>3</sub>O<sub>4</sub>, (b) carbon-coated Fe<sub>3</sub>O<sub>4</sub> microspheres and (c) Sample B.

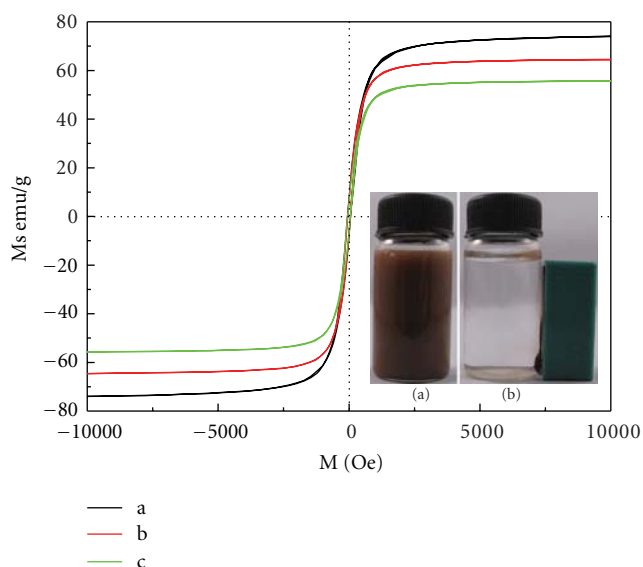


FIGURE 5: Room-temperature magnetization curves of a: Fe<sub>3</sub>O<sub>4</sub>; b: Fe<sub>3</sub>O<sub>4</sub>/C; c: Sample B; Sample B separated from aqueous solution by an external magnetic field (inset).

after treatment by external magnetic field. The inset is the image of Sample B separated from aqueous solution by an external magnetic field (inset). The magnetic photocatalyst (Sample B) is recycled by attracting towards the magnet

located in right-hand side of sample vials over a short period, demonstrating the high magnetic sensitivity of as-synthesized magnetic photocatalyst.

**3.4. Nitrogen Adsorption-Desorption Analysis.** The N<sub>2</sub> adsorption-desorption isotherm (Figure 6(a)) of all four samples presents type-IV-like curve with an H3 hysteresis loop, characteristic of mesopores in the spherical cores and shells. Comparing with Sample H, the hysteresis loop of Sample F is shifted to low  $P/P_0$  direction relatively because small crystallite stacking small intraparticles pores on the surface of Fe<sub>3</sub>O<sub>4</sub>/C spheres. The hysteresis loops of Sample B, G are also shifted to low  $P/P_0$  direction, but it is not obvious in the Figure 6(a). The hysteresis loop of Samples F, B, and G illustrates the fact that the larger crystallite stacking larger intraparticles pores at elevated temperature. The pore size of Sample F is smaller than that of Sample B. It can be explained that the anatase crystallite prepared under 100°C is ultrafine and cumulates small pores. Figure 6(b) gives the pore-size distribution curves of different samples, confirming a preferred porous structure with pore volumes ( $V_p$ ) 0.36, 0.32, 0.40, and 0.42 cm<sup>3</sup>/g and average pore diameters 68.1, 4.7, 9.5, and 81.5 nm corresponding to Samples H, F, B and G, respectively. The high specific surface area of Sample F (155 m<sup>2</sup>/g) is the result of fine anatase crystalline prepared under this temperature. Such a porous structure can promote more adsorption of pollutants.

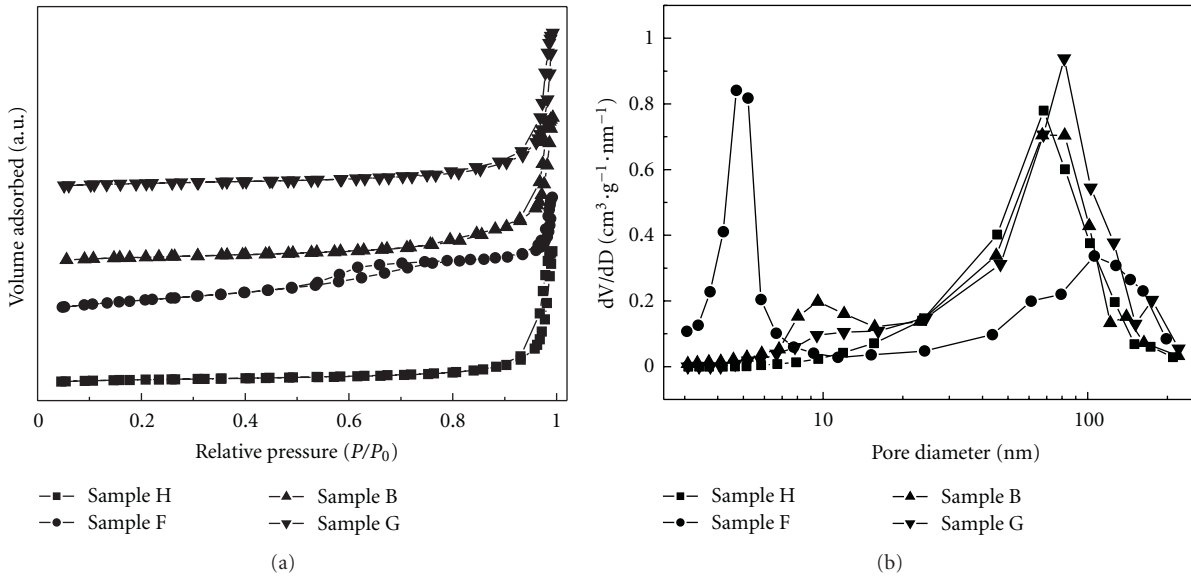


FIGURE 6: N<sub>2</sub> adsorption-desorption isotherm (a) of different samples at 77 K with corresponding pore size distributions (b) calculated by Barrett-Joyner-Halenda (BJH) method from desorption branch. All adsorption-desorption isotherm curves in (a) are added some units along the volume adsorbed axis (Y axis) in order to observe clearly. (■) Sample H, (●) Sample F, (▲) Sample B, and (▼) Sample G.

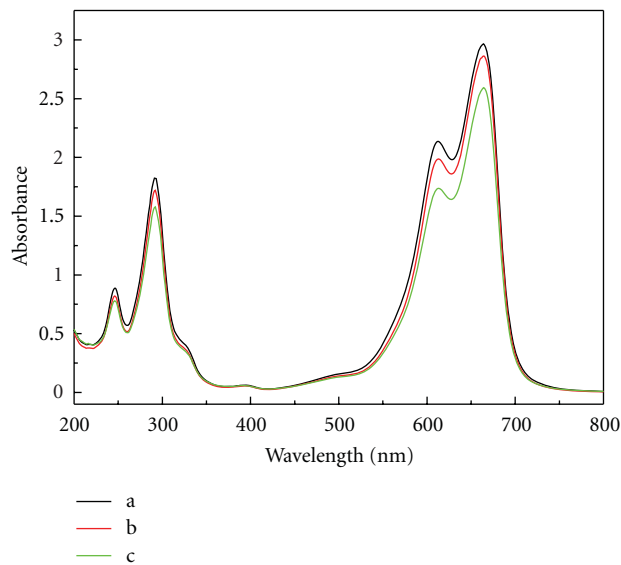


FIGURE 7: The UV-Vis of MB solution after suspending catalysts in dark for 30 min, a: no catalyst; b: commercial TiO<sub>2</sub> and c: Sample B.

**3.5. Photocatalytic Activity.** Different catalysts are suspended into the MB solution for 30 min in the dark as the adsorption experiment. Figure 7 indicates that the concentration of MB solution is almost no any change (3.33%) in commercial TiO<sub>2</sub> suspension. In contrast, the adsorption of Sample B reaches 12.5%. This adsorption property could increase the local concentration of MB near the titania layer and enhance the photocatalysis efficiency [33]. Figure 8(a) shows the photocatalytic activities of Sample B and commercial anatase TiO<sub>2</sub> in photocatalytic decomposition of MB under ultraviolet light irradiation. As shown in Figure 8(a), the decolorization ratio of MB (control) was less than 20% [34]

after 180 min irradiation due to the photodecomposition. Because of the anatase TiO<sub>2</sub> located on the outsurface of Fe<sub>3</sub>O<sub>4</sub>/C/TiO<sub>2</sub> microspheres, it can utilize the light effectively than solid TiO<sub>2</sub> sphere. The TiO<sub>2</sub> content in Sample B is 37%, so the photocatalytic activity of Sample B is relatively higher than that of commercial anatase TiO<sub>2</sub>. If the iron oxide directly contacts with a crystalline titanium dioxide phase, electronic interactions between the titanium dioxide coating and the iron oxide core, when the photogenerated electrons in the titanium dioxide phase are transferred into the lower lying conduction band of the iron oxide phase. It is these injected electrons which lead to the reduction of the iron oxide

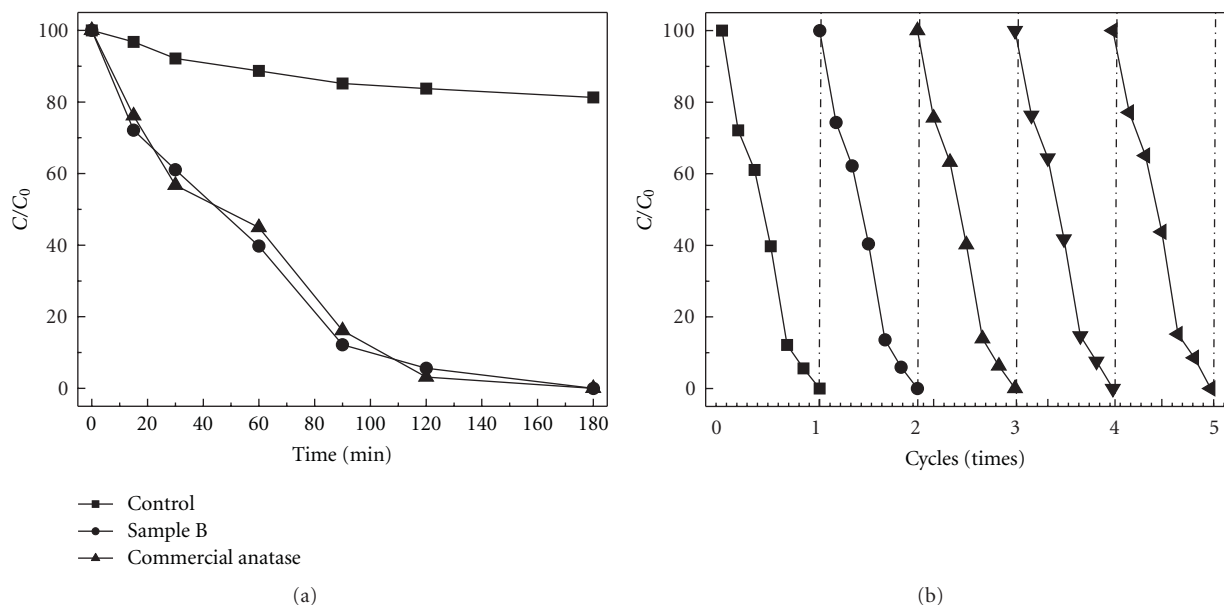


FIGURE 8: Photocatalytic efficiency of commercial anatase  $\text{TiO}_2$  and Sample B to methylene blue (MB); (b) the long-term photocatalytic activity of Sample B.

core, with Fe ions are being formed and migrating to the solution through the porous titanium dioxide coating [24, 33]. So the protection role of intermediate carbon layer is to avoid the direct contact between  $\text{Fe}_3\text{O}_4$  and titania. Due to the compacted coating with intermediate carbon layer, it can be avoided the electron interaction or photodissolution of  $\text{Fe}_3\text{O}_4$  probably occurrence of at the point of contact. The long-term photocatalytic activity of Sample B is showed in Figure 8(b). MB is removed completely from the solution in every cycle and photocatalytic degradation efficiency is not varied. Owing to the regenerative property of magnetic photocatalyst and relatively high photocatalytic activity, the  $\text{Fe}_3\text{O}_4/\text{C}/\text{TiO}_2$  hybrid spheres are well likely to be promising catalyst in the near future.

#### 4. Conclusions

In summary, the core/multi-shell-structured  $\text{Fe}_3\text{O}_4/\text{C}/\text{TiO}_2$  magnetic photocatalyst has been prepared via a vapor phase hydrolysis process, and the thickness of  $\text{TiO}_2$  shell can be tuned from monolayer to several hundred nanometers by varying the TBOT content. The size and crystallinity of anatase  $\text{TiO}_2$  crystallite in the shell could be tuned by temperature and duration. The photocatalytic activity of  $\text{Fe}_3\text{O}_4/\text{C}/\text{TiO}_2$  photocatalyst has relatively higher activity than commercial anatase  $\text{TiO}_2$  in photocatalytic degradation of methylene blue (MB) but its recycling property is improved largely. The intermediate carbon layer can avoid the electron interaction or photodissolution of  $\text{Fe}_3\text{O}_4$  probably occurring at the point of contact effectively.

#### Acknowledgments

This research was supported by the Opening Project of State Key Laboratory of High Performance Ceramics and

Superfine Microstructure (no. SKL201002SIC), the National Natural Science Foundation of China (no. 50772127 and no. 50925312), Shanghai Leading Academic Discipline Project (B603), and the Program of Introducing Talents of Discipline to Universities (no.111-2-04).

#### References

- [1] C. Wang and J. Yao, "Decolorization of methylene blue with  $\text{TiO}_2$  sol via UV irradiation photocatalytic degradation," *International Journal of Photoenergy*, vol. 2010, Article ID 643182, 6 pages, 2010.
- [2] S.-J. Kim, N.-H. Lee, H.-J. Oh, S.-C. Jung, W.-J. Lee, and D.-H. Kim, "Photocatalytic properties of nanotubular-shaped  $\text{TiO}_2$  powders with anatase phase obtained from titanate nanotube powder through various thermal treatments," *International Journal of Photoenergy*, vol. 2011, Article ID 327821, 7 pages, 2011.
- [3] G. Dagan and M. Tomkiewicz, " $\text{TiO}_2$  aerogels for photocatalytic decontamination of aquatic environments," *Journal of Physical Chemistry*, vol. 97, no. 49, pp. 12651–12655, 1993.
- [4] J. Wang, X. Han, W. Zhang et al., "Controlled growth of monocryalline rutile nanoshuttles in anatase  $\text{TiO}_2$  particles under mild conditions," *CrystEngComm*, vol. 11, no. 4, pp. 564–566, 2009.
- [5] J. A. Byrne, P. A. Fernandez-Ibañez, P. S.M. Dunlop, D. M.A. Alrousan, and J. W.J. Hamilton, "Photocatalytic enhancement for solar disinfection of water: a review," *International Journal of Photoenergy*, vol. 2011, Article ID 798051, 12 pages, 2011.
- [6] Z. Zhang and J. Gamage, "Applications of photocatalytic disinfection," *International Journal of Photoenergy*, vol. 2010, Article ID 764870, 11 pages, 2010.
- [7] X. Song and L. Gao, "Fabrication of hollow hybrid microspheres coated with silica/titania via sol-gel process and enhanced photocatalytic activities," *Journal of Physical Chemistry C*, vol. 111, no. 23, pp. 8180–8187, 2007.

- [8] X. Song and L. Gao, "Fabrication of bifunctional titania/silica-coated magnetic spheres and their photocatalytic activities," *Journal of the American Ceramic Society*, vol. 90, no. 12, pp. 4015–4019, 2007.
- [9] W.-C. Oh and M.-L. Chen, "The improved photocatalytic properties of methylene blue for  $V_2O_3/CNT/TiO_2$  composite under visible light," *International Journal of Photoenergy*, vol. 2010, Article ID 264831, 5 pages, 2010.
- [10] G. Cao, Y. Li, Q. Zhang, and H. Wang, "Hierarchical porous, self-supporting La- and F-codoped  $TiO_2$  with high durability for continuous-flow visible light photocatalysis," *Journal of the American Ceramic Society*, vol. 93, no. 5, pp. 1252–1255, 2010.
- [11] Y. Lv, L. Yu, H. Huang, H. Liu, and Y. Feng, "Preparation, characterization of P-doped  $TiO_2$  nanoparticles and their excellent photocatalytic properties under the solar light irradiation," *Journal of Alloys and Compounds*, vol. 488, no. 1, pp. 314–319, 2009.
- [12] Y. Lv, Y. Ding, J. Zhou, W. Xiao, and Y. Feng, "Preparation, characterization, and photocatalytic activity of N, S-Codoped  $TiO_2$  nanoparticles," *Journal of the American Ceramic Society*, vol. 92, no. 4, pp. 938–941, 2009.
- [13] M. Ruimin, P. Guo, L. Yang et al., "Theoretical screening of  $-NH_2$ -,  $-OH$ -,  $-CH_3$ -,  $-F$ - and  $-SH$ -Substituted porphyrins as sensitizer candidates for dye-sensitized solar cells," *Journal of Physical Chemistry A*, vol. 114, no. 4, pp. 1973–1979, 2010.
- [14] W. J. Youngblood, S. H. Anna Lee, K. Maeda, and T. E. Mallouk, "Visible light water splitting using dye-sensitized oxide semiconductors," *Accounts of Chemical Research*, vol. 42, no. 12, pp. 1966–1973, 2009.
- [15] Q. Zhang, W. Fan, and L. Gao, "Anatase  $TiO_2$  nanoparticles immobilized on ZnO tetrapods as a highly efficient and easily recyclable photocatalyst," *Applied Catalysis B: Environmental*, vol. 76, no. 1-2, pp. 168–173, 2007.
- [16] Z. Ding, X. Hu, G. Q. Lu, P. L. Yue, and P. F. Greenfield, "Novel silica gel supported  $TiO_2$  photocatalyst synthesized by CVD method," *Langmuir*, vol. 16, no. 15, pp. 6216–6222, 2000.
- [17] L. K. Tan, M. K. Kumar, W. W. An, and H. Gao, "Transparent, well-aligned  $TiO_2$  nanotube arrays with controllable dimensions on glass substrates for photocatalytic applications," *ACS applied materials & interfaces*, vol. 2, no. 2, pp. 498–503, 2010.
- [18] D. I. Petkowicz, R. Brambilla, C. Radtke et al., "Photodegradation of methylene blue by in situ generated titania supported on a NaA zeolite," *Applied Catalysis A*, vol. 357, no. 2, pp. 125–134, 2009.
- [19] T. Kemmitt, N. I. Al-Salim, M. Waterland, V. J. Kennedy, and A. Markwitz, "Photocatalytic titania coatings," *Current Applied Physics*, vol. 4, no. 2–4, pp. 189–192, 2004.
- [20] K. F. Ya, Z. Peng, Z. H. Liao, and J. J. Chen, "Preparation and photocatalytic property of  $TiO_2-Fe_3O_4$  core-shell nanoparticles," *Journal of Nanoscience and Nanotechnology*, vol. 9, no. 2, pp. 1458–1461, 2009.
- [21] D. G. Shchukin, A. I. Kulak, and D. V. Sviridov, "Magnetic photocatalysts of the core-shell type," *Photochemical and Photobiological Sciences*, vol. 1, no. 10, pp. 742–744, 2002.
- [22] T. C. Cheng, K. S. Yao, N. Yeh et al., "Visible light activated bactericidal effect of  $TiO_2/Fe_3O_4$  magnetic particles on fish pathogens," *Surface and Coatings Technology*, vol. 204, no. 6-7, pp. 1141–1144, 2009.
- [23] S. Xuan, W. Jiang, X. Gong, Y. Hu, and Z. Chen, "Magnetically separable  $Fe_3O_4/TiO_2$  hollow spheres: fabrication and photocatalytic activity," *Journal of Physical Chemistry C*, vol. 113, no. 2, pp. 553–558, 2009.
- [24] D. Beydoun, R. Amal, G. K. C. Low, and S. McEvoy, "Novel photocatalyst: titania-coated magnetite. activity and photodissolution," *Journal of Physical Chemistry B*, vol. 104, no. 18, pp. 4387–4396, 2000.
- [25] F. Chen, Y. Xie, J. Zhao, and G. Lu, "Photocatalytic degradation of dyes on a magnetically separated photocatalyst under visible and UV irradiation," *Chemosphere*, vol. 44, no. 5, pp. 1159–1168, 2001.
- [26] Z. H. Liao, J. J. Chen, K. F. Yao, F. H. Zhao, and R. X. Li, "Preparation and characterization of nanometer-sized magnetic photocatalyst," *Wuji Cailiao Xuebao/Journal of Inorganic Materials*, vol. 19, no. 4, pp. 749–754, 2004.
- [27] T. A. Gad-Allah, S. Kato, S. Satokawa, and T. Kojima, "Role of core diameter and silica content in photocatalytic activity of  $TiO_2/SiO_2/Fe_3O_4$  composite," *Solid State Sciences*, vol. 9, no. 8, pp. 737–743, 2007.
- [28] M. M. Ye, Q. A. Zhang, Y. X. Hu et al., "Magnetically recoverable core-shell nanocomposites with enhanced photocatalytic activity," *Chemistry—A European Journal*, vol. 16, no. 21, pp. 6243–6250, 2010.
- [29] Z. Wang, H. Guo, Y. Yu, and N. He, "Synthesis and characterization of a novel magnetic carrier with its composition of  $Fe_3O_4$ /carbon using hydrothermal reaction," *Journal of Magnetism and Magnetic Materials*, vol. 302, no. 2, pp. 397–404, 2006.
- [30] H. Deng, X. Li, Q. Peng, X. Wang, J. Chen, and Y. Li, "Monodisperse magnetic single-crystal ferrite microspheres," *Angewandte Chemie-International Edition*, vol. 44, no. 18, pp. 2782–2785, 2005.
- [31] Q. Zhang, M. Zhu, Q. Zhang, Y. Li, and H. Wang, "Fabrication and magnetic property analysis of monodisperse manganese-zinc ferrite nanospheres," *Journal of Magnetism and Magnetic Materials*, vol. 321, no. 19, pp. 3203–3206, 2009.
- [32] C. Hou, H. Yu, Q. Zhang, Y. Li, and H. Wang, "Preparation and magnetic property analysis of monodisperse Co-Zn ferrite nanospheres," *Journal of Alloys and Compounds*, vol. 491, no. 1-2, pp. 431–435, 2010.
- [33] X. Yu, S. Liu, and J. Yu, "Superparamagnetic  $\gamma-Fe_2O_3@SiO_2@TiO_2$  composite microspheres with superior photocatalytic properties," *Applied Catalysis B*, vol. 104, no. 1-2, pp. 12–20, 2011.
- [34] Z. Wang, L. Mao, and J. Lin, "Preparation of  $TiO_2$  nanocrystallites by hydrolyzing with gaseous water and their photocatalytic activity," *Journal of Photochemistry and Photobiology A*, vol. 177, no. 2-3, pp. 261–268, 2006.

## Research Article

# Degradation of Gaseous Formaldehyde by Visible Light-Responsive Titania Photocatalyst Filter

Tun-Ping Teng,<sup>1</sup> Tun-Chien Teng,<sup>2</sup> and Shu-I Pan<sup>1</sup>

<sup>1</sup>Department of Industrial Education, National Taiwan Normal University, No. 162, Section 1, He-Ping E. Road, Da-an District, Taipei City 10610, Taiwan

<sup>2</sup>Department of Mechatronic Technology, National Taiwan Normal University, No. 162, Section 1, He-Ping E. Road, Da-an District, Taipei City 10610, Taiwan

Correspondence should be addressed to Tun-Chien Teng, walter.teng@ntnu.edu.tw

Received 2 September 2011; Revised 13 November 2011; Accepted 13 November 2011

Academic Editor: Jiaguo Yu

Copyright © 2012 Tun-Ping Teng et al. This is an open access article distributed under the Creative Commons Attribution License, which permits unrestricted use, distribution, and reproduction in any medium, provided the original work is properly cited.

A method is proposed that uses electrophoretic deposition (EPD) to fabricate the titania (TiO<sub>2</sub>) photocatalyst filter and then successfully modifies it by lithium nitrate (LiNO<sub>3</sub>) to be visible light responsive such that the modified photocatalyst filter effectively degrades gaseous formaldehyde. The performance of degrading gaseous formaldehyde is evaluated in the photocatalytic circulation reactor for different temperature and light sources. The results show that the modified TiO<sub>2</sub> photocatalyst filter has much better degradation performance for gaseous formaldehyde than the original TiO<sub>2</sub> photocatalyst filter regardless of light source, and the performance is better at the higher ambient temperature. The best total average degradation performance of the modified photocatalyst filter is about 9.2% and 16.3% higher than the original photocatalyst filter (P-25, Degussa) for the UVA and visible irradiation, respectively, at 26°C.

## 1. Introduction

With the growth of the global economy, the kinds of the material used in interior decorating are gradually diversified. The woods and paints widely used in interior decorating usually contain organic solvent such as formaldehyde, and the solvent gradually volatilizes into the air to degrade the quality of the indoor air. When people require higher quality of the indoor air, how to eliminate the volatile organic gaseous pollution becomes an important research topic in the recent year. With the development of nanotechnology, utilizing degradation reaction by photocatalyst to eliminate the organic pollution is a hot topic [1–3]. The research topic on eliminating the organic pollution by the photocatalyst includes how to coat the photocatalyst material and how to excite photocatalytic reaction by visible lights. To coat the photocatalyst material firmly on the substrate is the first step to apply the photocatalyst material in HVAC (heating, ventilation, and air conditioning) system and air cleaning [4, 5]. The coated material must not peel off to result in the second pollution for the long time use and even can be

reusable after wash. Further, if the material can be modified to be responsive to visible light (visible light responsive) instead of being only responsive to ultraviolet light (UV light responsive), the material can be used as photocatalyst indoors with no need of the extra UV or even artificial light source and thus can be more widely and practically used.

Photocatalytic film can be fabricated in many ways, but the most popular methods are sputtering [6], chemical vapor deposition (CVD) [7], sol-gel [8], spin coating [9], and electrophoretic deposition (EPD). The EPD method is low cost and can easily form thin films with different materials on irregular-shaped objects just by a simple setup [10–14]. Many researchers use organic solvent suspensions, such as acetylacetone and isopropanol as the working fluids in the EPD process [15–18]. Using organic solvents can prevent bubble formation during water electrolysis and suppress the Joule heating effect and electrochemical attacks on the electrode [19]. Due to the recent awareness of environment protection, some other studies report that aqueous suspensions are used as electrophoretic working fluids. In recent years, several researchers have already proposed some

practical techniques to solve the above problems of water electrolysis. These studies also report the successful fabrication of TiO<sub>2</sub> nanophotocatalytic films [20, 21] and other materials coating [22, 23]. Although aqueous suspensions in EPD process have some disadvantages including cracks, unevenness, and holes in the deposited film, the EPD has advantages of low cost and relatively less pollution. The poor quality of the film caused by bubbling during the EPD process can be improved by adding surfactants or dispersants [24, 25].

As the main excitation light source for TiO<sub>2</sub> photocatalyst is UV light, and the UV and visible light share 4% and 43%, respectively, in the solar spectrum, it results in decline in the practicality of TiO<sub>2</sub> photocatalyst [26]. Therefore, it is an important research direction to modify the TiO<sub>2</sub> photocatalyst to be excited under the visible light irradiation. The main two ways to modify TiO<sub>2</sub> photocatalyst to be visible light responsive are as follows: first, add metal ion to modify the TiO<sub>2</sub> photocatalyst, which can effectively degrade the phenol, 2,4-dinitroaniline, Malachite green oxalate, 4-hydroxybenzoic acid, benzamide, rhodamine B (RhB), and formaldehyde under the visible light irradiation [26–30]. Second, add nonmetallic materials to modify TiO<sub>2</sub> photocatalyst, which can effectively degrade the nitrogen monoxide (NO), acetone, and formaldehyde and be used for water treatment under visible light [30–35]. Except for the kinds of the adding material, concentration, shape, and structure of TiO<sub>2</sub> also have effects on the degradation of pollutants [27–29, 36]. Furthermore, the spectra of the exciting light source also affect photocatalytic degradation of pollutants [31].

The gaseous formaldehyde is the most common indoor pollutants. Regarding decomposition of the TiO<sub>2</sub> photocatalyst for gaseous formaldehyde, the main kinds of the related research are described as follows: first, increase the specific surface area and porosity of TiO<sub>2</sub> to promote the utilization of light irradiation and adsorption to enhance the effect of TiO<sub>2</sub> on decomposing gaseous formaldehyde. The related methods include mixing TiO<sub>2</sub> with the porous material, activated carbon [37] or zeolite [38], to enhance the effects on adsorbing and decomposing gaseous formaldehyde. Moreover, the chemical precipitation-peptization method was used to produce TiO<sub>2</sub> hydrosols with an anatase crystal structure which had smaller particle sizes, higher surface areas, larger porosity, and higher transparency to enhance the effect on decomposing gaseous formaldehyde [39]. Second, produce Pt/TiO<sub>2</sub>/Al<sub>2</sub>O<sub>3</sub> photocatalyst on an anodic alumite plate by the electrodeposition technology to increase adsorption of oxygen which is activated and quickly formed into O : Pt<sub>surface</sub> species at ambient temperature for further photocatalytic decomposition of formaldehyde [40]. Third, dope other materials to lower the energy gap and make the TiO<sub>2</sub> photocatalyst to be visible light responsive in order to increase utilization of the light spectrum and performance of decomposing gaseous formaldehyde. The doped materials include Cr ion to form Cr/TiO<sub>2</sub> [30]; N, and S to form N, S codoped TiO<sub>2</sub> [32]; C, N and S to form C, N, S tridoped TiO<sub>2</sub> powders [33]; N and F to form N-F-TiO<sub>2</sub> [41]. All the above doped material can greatly aid decomposing gaseous formaldehyde.

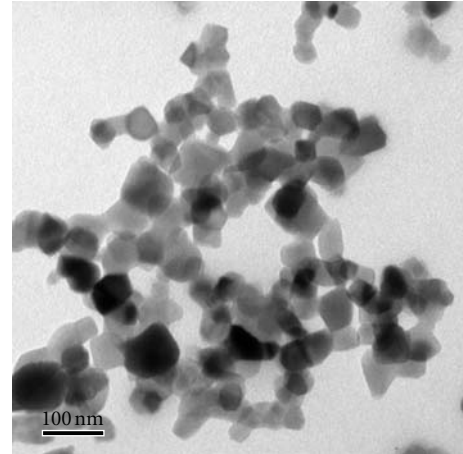


FIGURE 1: TEM images of TiO<sub>2</sub> nanoparticles.

From the above literatures and discussion, one can find that the TiO<sub>2</sub> photocatalyst has excellent degradation performance for many pollutants, and several techniques can modify TiO<sub>2</sub> photocatalyst that is originally UV light responsive to be visible light responsive. In this study, the photocatalyst was coated on a stainless steel plate with holes to form the photocatalyst filter by EPD. The working fluid of EPD was TiO<sub>2</sub>/water nanofluid prepared by two-step synthesis method. Alginate was added as an anionic dispersant to change the zeta potential of TiO<sub>2</sub> particles, and thus the TiO<sub>2</sub> nanoparticles that originally deposited on the cathode would change to deposit on the anode, which could effectively reduce the bubble problem in water electrolysis leading to a poor film deposition. The photocatalyst filter was modified by LiNO<sub>3</sub> and evaluated for the performance of degrading gaseous formaldehyde in the photocatalytic circulation reactor under different temperature and light sources.

## 2. Experimental

**2.1. Materials.** The phase of the TiO<sub>2</sub> nanoparticles (P-25, Degussa) consists of 70% anatase and 30% rutile. Figure 1 shows transmission electron microscope (TEM, H-7100, Hitachi) image of the particles with an average particle size of about 20~40 nm. In order to confirm the material of the sample used in this study again, X-ray diffraction (XRD, D8 Advance, Bruker) using CuK<sub>α</sub> ( $\lambda = 0.15418$  nm) radiation at 295 K was used for this purpose. All peaks were measured by XRD and assigned in comparison with those of the joint committee on powder diffraction standards data (PCPDFWIN 2.4) [42]. Figure 2 confirms that the major material used in this study was anatase TiO<sub>2</sub>.

**2.2. Preparation of Working Fluid for EPD.** The TiO<sub>2</sub>/water nanofluid was fabricated by the two-step synthesis method in this study. First of all, we prepared a bulk liquid by adding 0.2, 0.4, and 0.6 wt.% of anionic dispersant (alginate, Alfa Aesar) to distilled water. This anionic dispersant reinforced the dispersion of TiO<sub>2</sub> nanoparticles and changed the

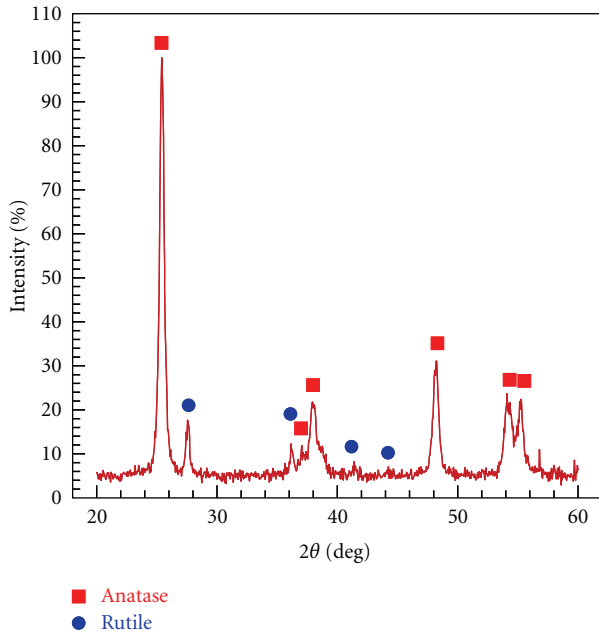


FIGURE 2: XRD patterns of TiO<sub>2</sub> nanoparticles.

deposition direction of TiO<sub>2</sub> nanoparticles [25]. The TiO<sub>2</sub> nanoparticles were then measured by a precise electronic balance (XT-620 M, Precisa) and were added to the bulk liquid by several times to form the TiO<sub>2</sub>/water nanofluid with a concentration of 1.0 wt.%. In this nanofluid synthesis process, an electromagnetic stirrer, homogenizer, and ultrasonic vibrator were used to reinforce the dispersion and suspension effects. After preparation, the nanofluid was kept still for 24 hours. If no obvious deposition was observed, the fluid was used as the EPD process working fluid. The surface charge of the TiO<sub>2</sub> nanoparticles was measured by a zeta potential analyzer (SZ-100, Horiba) to examine the effect of the added anionic dispersant on depositing on the anode. As shown in Figure 3, the measured zeta potential of the TiO<sub>2</sub> nanoparticles without the anionic dispersant was about 28 mV, while that with the anionic dispersant was about -58~66 mV. These results indicate that the zeta potential of the TiO<sub>2</sub> nanoparticles changes from positive to negative after adding the anionic dispersant to the TiO<sub>2</sub>/water nanofluid, which effectively deposits the TiO<sub>2</sub> nanoparticles on the anode.

**2.3. EPD Process.** Figure 4 shows the EPD setup adopted in this study. To fix the electrophoretic electrode distance (20 mm), a 304 stainless steel EPD electrode was vertically fixed on a polypropylene (PP) holder. The stand was then placed in a glass beaker to form an EPD setup. The size of the flat electrodes 304 stainless steel plates was all 60 mm × 10 mm × 0.3 mm. The length of the electrode actually immersed in the working fluid was 45 mm. The EPD process in this study adopted various constant current power supply (EV243, Consort) levels (3, 5, 7, and 9 mA) and various process durations (3, 5, and 7 min.) for TiO<sub>2</sub>/water nanofluid for each concentration of alginate.

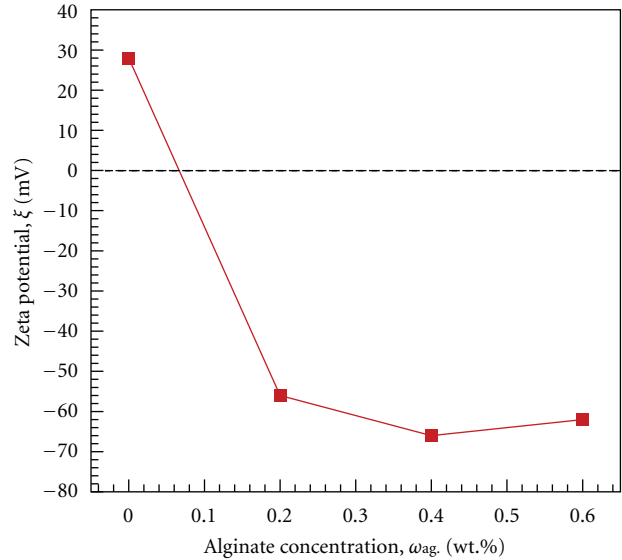


FIGURE 3: The zeta potential for the 1.0 wt.% TiO<sub>2</sub> nanoparticles suspended in base liquid.

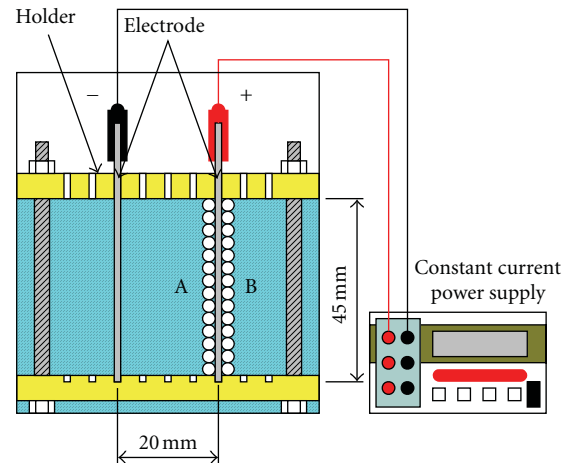


FIGURE 4: Experimental setup for EPD process.

**2.4. Analysis and Modification of TiO<sub>2</sub>-Deposited Film.** A film thickness meter (MiniTest 730, ElektroPhysik) with accuracy of ±0.75% was used to measure the average thickness of the film made by EPD at 5 points of each sample for different experimental parameters on side A and side B of electrode plates. In order to keep the photocatalyst filter from peeling off to result in pollution in application, so we checked the samples and selected the process condition for producing the smoothest and cracks-free deposited film as the optimal EPD parameter by an optical microscope (BH2-UMA, Olympus). Moreover, the surface of deposited film on the sample made at the optimal process parameter was checked again in higher magnification through a scanning electron microscope (SEM, JSM-6360, JEOL). The samples of the optimal photocatalyst deposition parameter were sintered by 300~700°C/2 hr in a high-temperature furnace, and then their crystalline state was, respectively, analyzed by

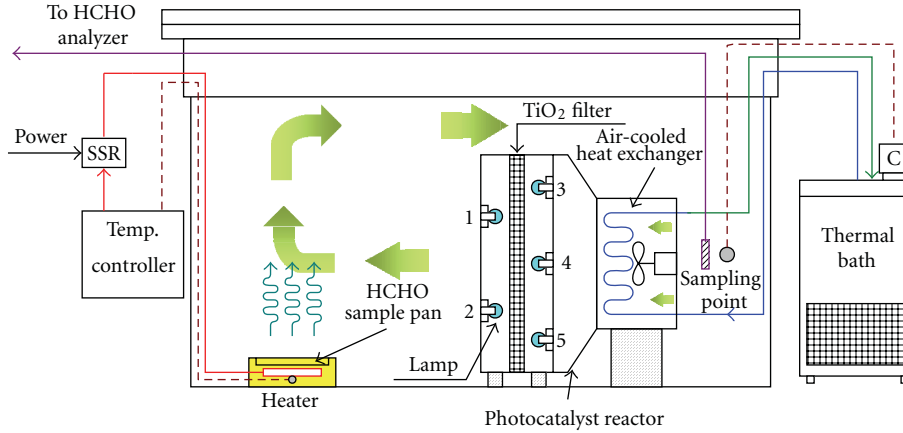


FIGURE 5: The installation of photocatalytic circulation reactor.

XRD in order to determine the optimal sintered temperature for manufacturing the photocatalyst filter. Next, the photocatalytic material was coated on a stainless steel plate (#304, 80 mm × 73 mm × 0.3 mm) with holes ( $\phi = 5$  mm) by EPD to produce the photocatalyst filter at the optimal photocatalyst deposition parameters. Further, the photocatalyst filter was immersed in 0.1 M lithium nitrate ( $\text{LiNO}_3$ ) aqueous solution for 20 seconds and through the drying process at 50°C in order to modify the original  $\text{TiO}_2$  photocatalyst filter to be visible light responsive [28, 29]. Because the photocatalyst film deposited by EPD had porous structure, it easily adsorbed the dopant when it was immersed in  $\text{LiNO}_3$  aqueous solution. The main reason for using  $\text{LiNO}_3$  to modify the photocatalyst is that Li ion can reduce the energy gap of the  $\text{TiO}_2$  and thus make  $\text{TiO}_2$  responsive to the lights of longer wavelength. Further,  $\text{LiNO}_3$  is not a toxic chemical, so it is very suitable to be adopted in modifying photocatalyst for indoor air quality improvement.

**2.5. Assess Degradation Performance for Gaseous Formaldehyde.** The installation of photocatalytic circulation reactor is shown as Figure 5. The photocatalyst reactor consisted of the six photocatalyst filters (each dimension of photocatalyst filter was 80 mm × 73 mm × 0.3 mm) on the holder and five lamps. Types of the five lamps were T5/8W of UVA lamps (F8T5/BL, GOODLY) or fluorescent lamps (TL8W/840, Philips) for different condition. Among the five lamps, three lamps were put toward the A-side of photocatalyst filter and the other two lamps toward the B-side. The gaseous formaldehyde was obtained by heating 0.5  $\mu\text{L}$  of 35 wt.% formaldehyde aqueous solution to evaporate at 40°C. In order to maintain steady circulation of the gaseous formaldehyde in the photocatalytic circulation reactor, the air-cooled heat exchanger with a fan was installed in front of the reactor to maintain a constant wind speed and ambient temperature. Ambient temperature was set, respectively, at 26 and 22°C according to ASHRAE standard summer and winter [43]. The concentration of gaseous formaldehyde was measured by gaseous formaldehyde analyzer (YES plus, Critical Environment Technologies) for every 20 minutes. The formaldehyde

analyzer measured the gaseous formaldehyde in the range of 0 to 10 ppm with an accuracy of 0.05 ppm. The measurement for formaldehyde gas started at 10 minutes after instillation of formaldehyde aqueous solution and turned on the light source at 40 minutes after the measurement started in order to ensure that the measurement for the concentration change of the fully evaporated formaldehyde is mainly due to photocatalytic degradation.

In order to accurately determine the actual performance of the photocatalyst filter for degrading gaseous formaldehyde, the background absorption test is necessary. As the equipments also adsorb gaseous formaldehyde, one must measure the trend of the concentration of the gaseous formaldehyde as the experimental background value for the different photocatalyst filters with the light source being turned off. The test of background value for the original photocatalyst (nonmodified) filter is named “background 1”, and the test for the modified photocatalyst filter is named “background 2” for the different light sources. The actual performance of the photocatalyst filter for degrading gaseous formaldehyde is evaluated by comparing the experimental measured value to the corresponding background value. All experimental parameters of this study are summarized in Table 1.

**2.6. Data Analysis.** In this study, for easy comparison of the actual performance of the photocatalyst filter for degrading gaseous formaldehyde, the “total average degradation performance ( $\eta_d$ )” is introduced. The background values are used as baseline ( $D_{b,avg}$ ), and all the experimental data obtained for the different experimental parameters are compared with the corresponding baseline values. Moreover, the concentration of gaseous formaldehyde ( $D_{d,k}$ ) in the reactor is measured for every 20 minutes after the light is turned on. The  $\eta_d$  is defined as

$$\eta_d = \left[ 1 - \frac{[\sum_{k=1}^n D_{d,k}]/n}{[\sum_{k=1}^n D_{b,k}]/n} \right] \times 100\%. \quad (1)$$

TABLE 1: List of the experimental parameters.

Fabrication of TiO <sub>2</sub> -deposited film by EPD	
Concentration of TiO <sub>2</sub> (wt.%)	1.0
Concentration of alginate (wt.%)	0.2, 0.4 and 0.6
Working current (mA)	3, 5, 7 and 9
Sintered temperature (°C)	300, 400, 500, 600 and 700
Concentration of LiNO <sub>3</sub> for modification (M)	0.1
Photocatalytic degradation for gaseous formaldehyde	
Light source/power (W)	UVA and visible light (fluorescent lamps) × 5/8 Original TiO <sub>2</sub> filter (P-25) × 6 (background 1)
Filter type	Modified TiO <sub>2</sub> filter (P-25 + LiNO <sub>3</sub> ) × 6 (background 2)
Ambient temperature (°C)	22 and 26
Volume of test pollutant (μL)	0.5 (35% formaldehyde aqueous solution)
Heating temperature for test pollutant (°C)	40

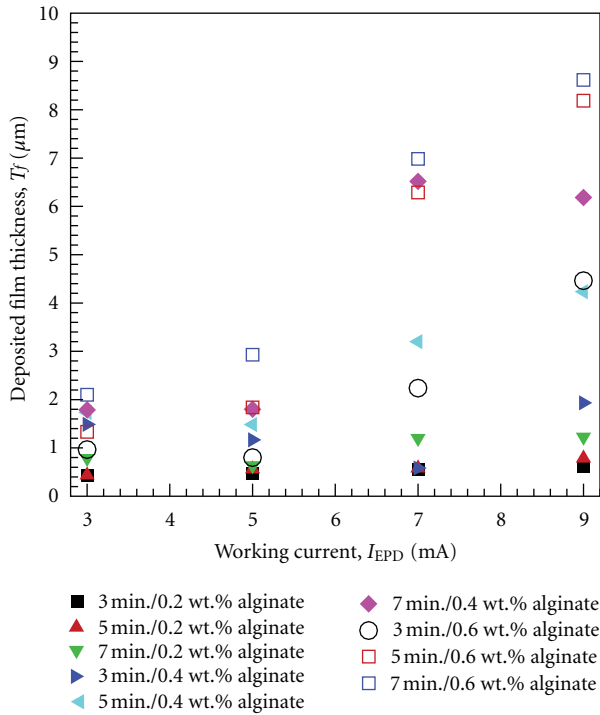


FIGURE 6: Deposited film thickness on side A varies with the working currents dispersant for different concentration and durations.

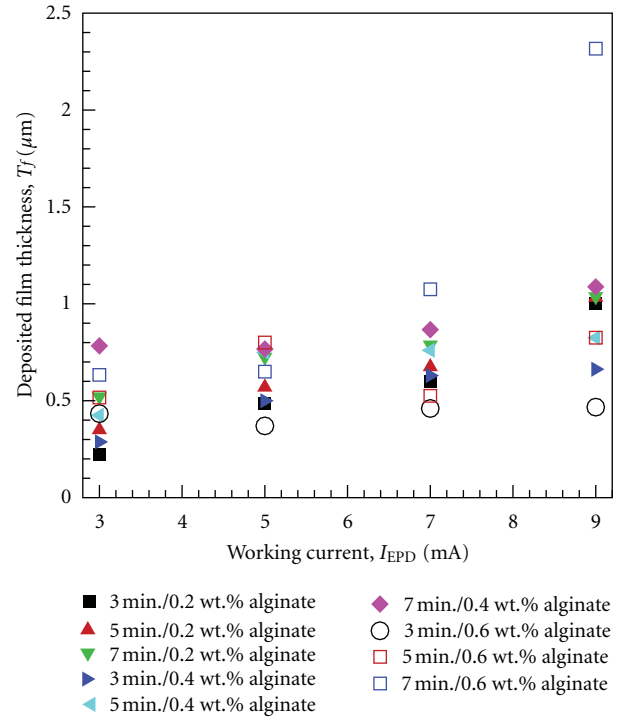


FIGURE 7: Deposited film thickness on side B varies with the working currents dispersant for different concentration and durations.

### 3. Results and Discussion

**3.1. Characterization of the TiO<sub>2</sub>-Deposited Film Fabricated by EPD.** Figures 6 and 7 show the variation of the thickness of deposited film on side A and side B, respectively, for different working currents, dispersant concentration, and working durations. Both the figures show the film thickness generally trends up with increase in the working current, dispersant concentration, and working duration. However, in Figure 6, the deposited film thickness in some case is not proportional to the working current for the working

duration of 3 minutes. This phenomenon is mainly because the deposited film on the sample is prone to peel off due to its poor adhesion when the deposition time is short. As the dispersant (alginate) increases the electric conductivity of the work fluid and thus increases the deposition rate, the film thickness is still roughly proportional to the working current even for the short working duration. Further, the longer working duration also increases the deposited film thickness and strengthens the deposited film. The above-mentioned problems can be resolved when the dispersant concentration

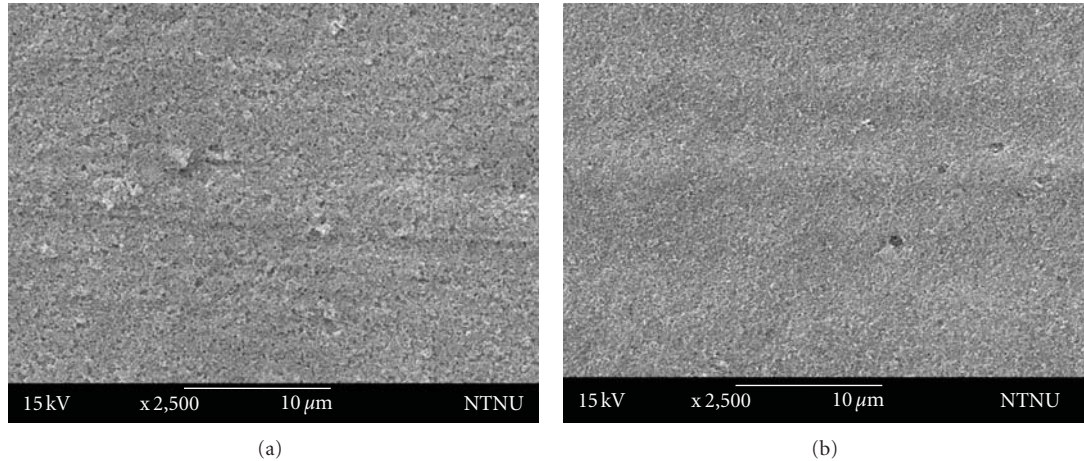


FIGURE 8: SEM photograph of the  $\text{TiO}_2$ -deposited film at the optimal parameter of EPD, (a) side A, (b) side B.

and working duration are raised up to 0.4 wt.% and five minutes, respectively. Furthermore, for the same experimental parameters, the thickness of the film on side A is greater than side B. As the working current increases, the difference becomes more obvious. This phenomenon is mainly because the electric field is stronger as the current increases and thus the nanoparticles in the suspension more easily deposit on side A through the shorter path. Therefore, thickness of the deposited film on side A is thicker than side B for the same parameters of EPD.

The optimal EPD parameters for manufacturing the photocatalyst filter are determined by checking the smoothness, uniformity, and crack of the deposited film through an optical microscope. The optimal process parameters of EPD in this study are as follows: 1.0 wt.%  $\text{TiO}_2$ , 0.4 wt.% alginate, 9 mA, and 5 minutes. With checking the samples through the optical microscope, one can find that the surface of deposited film is bumped and uneven when the deposition rate is too low, and the cracks appear when the deposition rate is too high. The SEM images of the deposited film made at the optimal EPD process parameters are shown in Figure 8. In Figure 8, one can find that either surface of side A or B is smooth and crack-free. Moreover, the surface roughness of side B is less than side A due to the lower deposition rate on side B.

In order to increase the strength and adhesion of the deposited film, the samples made at the optimal parameters were sintered by  $300^\circ\text{C}\sim 700^\circ\text{C}$  for 2 hours. Figure 9 shows the XRD patterns of the deposited film made at the optimal parameters for different sintered temperatures. In Figure 9, one can find that the crystalline state of rutile (hkl = 110) has no significant growth when the sintered temperature is less than  $600^\circ\text{C}$ , but has significantly grown when the sintered temperature reaches  $700^\circ\text{C}$ . Regarding the surface condition, the cracks appear when the sintered temperature is above  $500^\circ\text{C}$ . With considering the effect of photocatalyst and strength of the deposited film, the sintered temperature and duration for the deposited film of the photocatalyst in this study were set at  $400^\circ\text{C}$  for 2 hours.

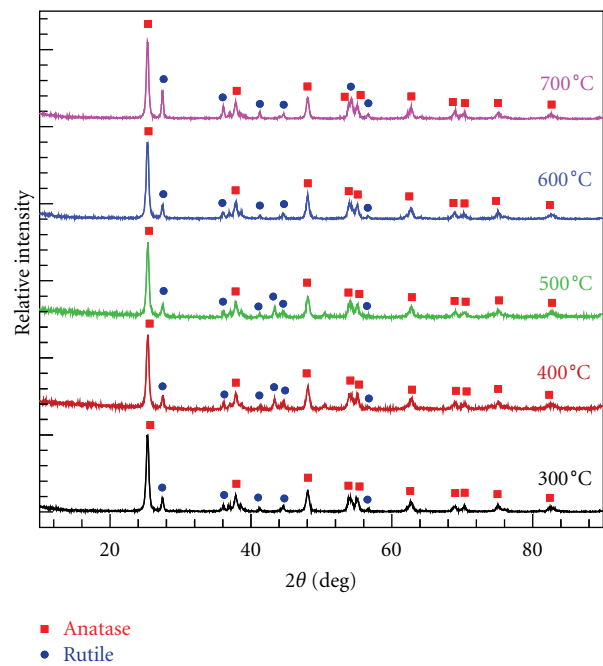


FIGURE 9: XRD patterns of the  $\text{TiO}_2$ -deposited film sintered at different temperatures.

### 3.2. Effect of Various Parameters on Photocatalytic Degradation for Gaseous Formaldehyde

**3.2.1. UVA Light Irradiation.** Figures 10 and 11 illustrate the degradation for gaseous formaldehyde in the cases with different temperature and types of photocatalyst filter under UVA light irradiation. In those figures, one can find that the highest concentration of the gaseous formaldehyde appears at 100 to 120 minutes after the circulation reactor starts. It is mainly because the drops of formaldehyde aqueous solution have been completely vaporized at that moment to reach the peak concentration. In addition, the UVA lights are turned on at 40 minutes after the circulation reactor starts and thus

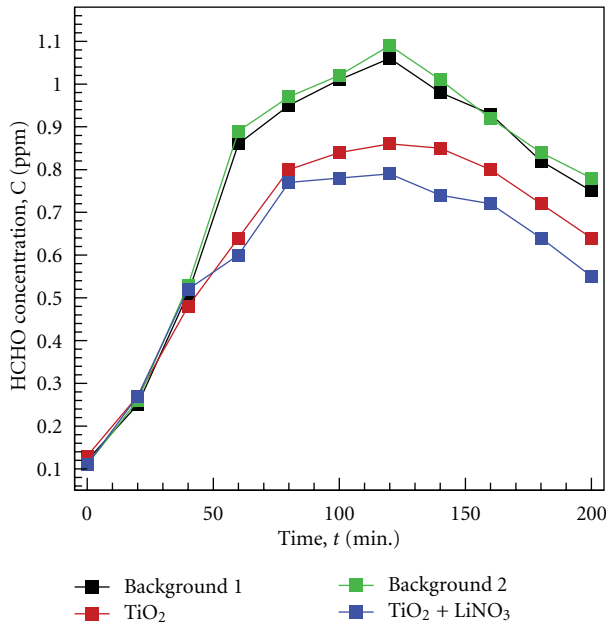


FIGURE 10: The degradation performance for gaseous formaldehyde under irradiation of UVA lamps at 26°C.

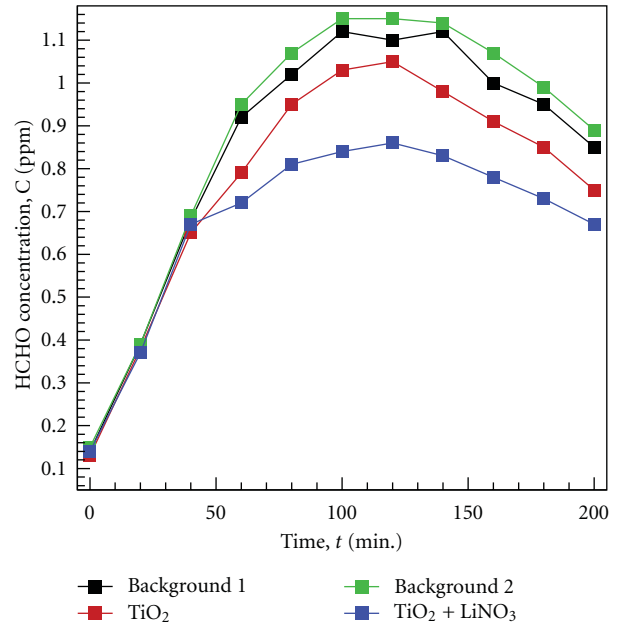


FIGURE 12: The degradation performance for gaseous formaldehyde under irradiation of visible light lamps at 26°C.

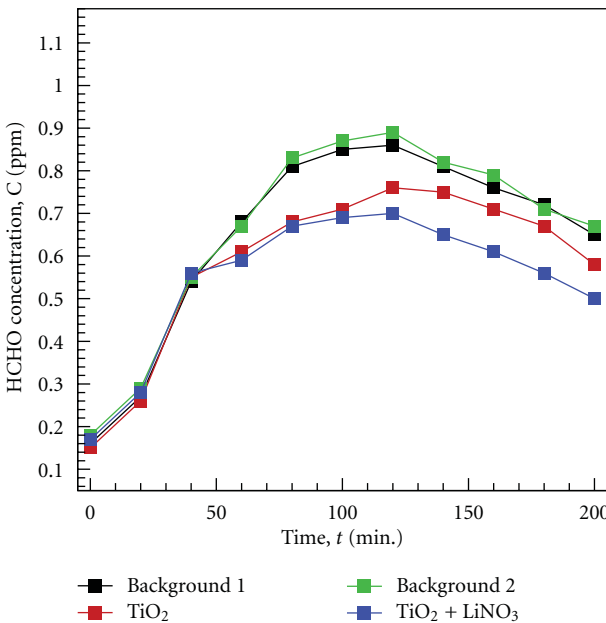


FIGURE 11: The degradation performance for gaseous formaldehyde under irradiation of UVA lamps at 22°C.

the reduced concentration is compared with the background test. Therefore, the photocatalyst filter is proved to effectively degrade the gaseous formaldehyde through photocatalytic reaction. By the way, the concentration in the background test for the modified photocatalyst filter (background 2) is higher than that for the original photocatalyst filter (background 1). This phenomenon is mainly because the surface of the photocatalyst filter modified by immersing in LiNO<sub>3</sub> aqueous solution is finer and smoother such that

the capacity of adsorbing gaseous formaldehyde is lower. Further, the background concentration at higher ambient temperature is higher because the gaseous molecules more easily vaporize and more dramatically move to lead hardly condensing on the wall of the equipment at higher temperature. From the experimental results, one can find that the higher ambient temperature can enhance the degradation of the photocatalyst filter for the gaseous formaldehyde, and the modified photocatalyst filter has better degradation performance than the original photocatalyst filter for the same test parameters under UVA light irradiation.

3.2.2. *Visible Light Irradiation.* Figures 12 and 13 illustrate the degradation for gaseous formaldehyde in the cases with different temperature and types of photocatalyst filter under visible light (fluorescent lamps) irradiation. The overall trends of the results in Figures 12 and 13 are substantially consistent with those in Figures 10 and 11, respectively. However, one can find that the degradation of original photocatalyst filter for gaseous formaldehyde is significantly lower than the modified photocatalyst filter under the visible light irradiation. Similarly, the degradation for gaseous formaldehyde is better at the higher ambient temperature under the visible light irradiation. Moreover, the background concentration for the visible light is slightly higher than the UVA light. As the background test is slightly executed in an enclosed space without lights, the background concentration has nothing to do with the illumination wavelength. This phenomenon might be due to the difference in surface adsorption of the lamps. In this study, the performance of degrading gaseous formaldehyde is evaluated as compared with the background test for the same photocatalyst filters

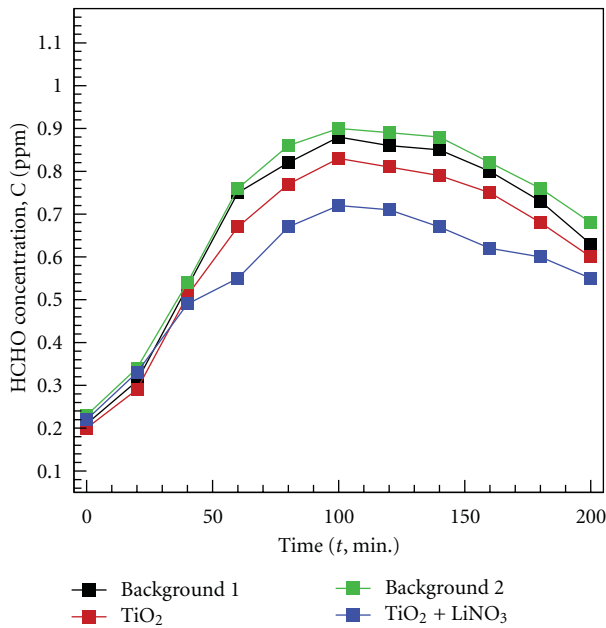


FIGURE 13: The degradation performance for gaseous formaldehyde under irradiation of visible light lamps at 22°C.

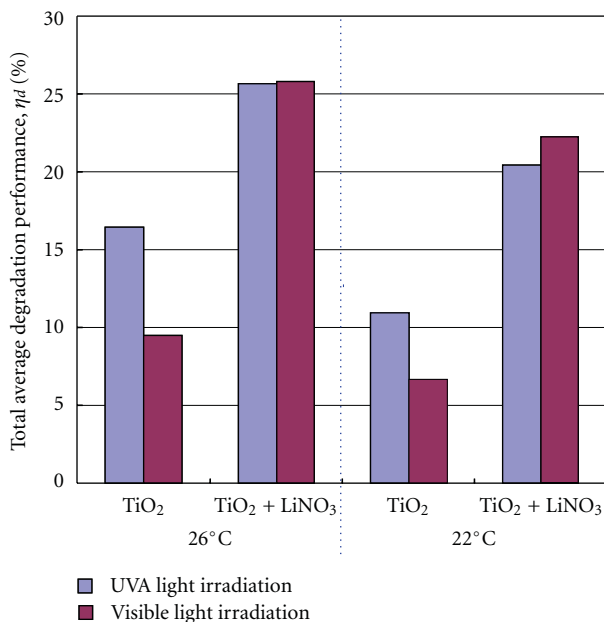


FIGURE 14: The total average degradation performance for gaseous formaldehyde.

and ambient temperature, so the difference in the background value has no effect on evaluating performance.

**3.2.3. Comparison of Degradation Performance.** All the experiment results in Figures 10 to 13 are summarized in Figure 14. In Figure 14, one can find that the modified photocatalyst filter has much better total average degradation performance for gaseous formaldehyde than the original

photocatalyst filter in all the cases. The total average degradation performance of the original photocatalyst filter under visible irradiation is much lower than that under the UVA irradiation. By contrast, the total average degradation performance of the modified photocatalyst filter has little difference between the two light sources. The modified photocatalyst filter has the best performance at 26°C, and the performance is 9.2% and 16.3% higher than that of the original photocatalyst filter for UVA and visible irradiation, respectively. The relevant experimental results confirm that the method proposed in this study to use EPD to fabricate the photocatalyst filter and then modify it by LiNO<sub>3</sub> can successfully produce the visible light responsive photocatalyst filter with better performance to effectively degrade gaseous formaldehyde.

## 4. Conclusions

The method to fabricate the photocatalyst filter by EPD and modify it by LiNO<sub>3</sub> to be visible light responsive is proposed in this study, which can provide the modified photocatalyst filter with higher degradation performance for gaseous formaldehyde than the original photocatalyst filter in a low-cost and practical way. Through the related tests on the degradation performance for gaseous formaldehyde in all the cases with different ambient temperature, types of filter, and light sources, one can find that the degradation performance of the modified photocatalyst filter for gaseous formaldehyde is much higher than the original photocatalyst filter in all the cases. The best total average degradation performance of the modified photocatalyst filter for gaseous formaldehyde is about 9.2% and 16.3% higher than the original photocatalyst filter for UVA and visible irradiation, respectively, at 26°C. Finally, the related achievements can be also applied to design the photocatalytic air cleaner with visible light responsive function to make the related products be used more efficiently, conveniently, and widely.

## Acknowledgment

This project is funded by National Taiwan Normal University of Taiwan (Contract nos. 98091009 and 98091011).

## References

- [1] Y. Zhang, R. Yang, and R. Zhao, "A model for analyzing the performance of photocatalytic air cleaner in removing volatile organic compounds," *Atmospheric Environment*, vol. 37, no. 24, pp. 3395–3399, 2003.
- [2] C. H. Ao and S. C. Lee, "Indoor air purification by photocatalyst TiO<sub>2</sub> immobilized on an activated carbon filter installed in an air cleaner," *Chemical Engineering Science*, vol. 60, no. 1, pp. 103–109, 2005.
- [3] J. P. Mo, Y. P. Zhang, Q. Xu, J. J. Lamson, and R. Zhao, "Photocatalytic purification of volatile organic compounds in indoor air: a literature review," *Atmospheric Environment*, vol. 43, no. 14, pp. 2229–2246, 2009.
- [4] C. H. Ao and S. C. Lee, "Enhancement effect of TiO<sub>2</sub> immobilized on activated carbon filter for the photodegradation of

- pollutants at typical indoor air level," *Applied Catalysis B*, vol. 44, no. 3, pp. 191–205, 2003.
- [5] J. M. Peralta-Hernández, J. Manríquez, Y. Meas-Vong et al., "Photocatalytic properties of nano-structured TiO<sub>2</sub> films obtained by means of electrophoretic deposition," *Journal of Hazardous Materials*, vol. 147, no. 1-2, pp. 588–593, 2007.
- [6] C. C. Chen, W. J. Yang, and C. Y. Hsu, "Investigation into the effects of deposition parameters on TiO<sub>2</sub> photocatalyst thin films by rf magnetron sputtering," *Superlattices and Microstructures*, vol. 46, no. 3, pp. 461–468, 2009.
- [7] P. Evans and D. W. Sheel, "Photoactive and antibacterial TiO<sub>2</sub> thin films on stainless steel," *Surface and Coatings Technology*, vol. 201, no. 22-23, pp. 9319–9324, 2007.
- [8] S. H. Zhang, B. F. Hu, B. Xie, S. Y. Zhang, and F. Y. Li, "Preparation of titania film by pyrolysis of chelated tetrabutyl titanate," *Key Engineering Materials*, vol. 368-372, pp. 1468–1470, 2008.
- [9] J. Yu and X. Zhao, "Effect of substrates on the photocatalytic activity of nanometer TiO<sub>2</sub> thin films," *Materials Research Bulletin*, vol. 35, no. 8, pp. 1293–1301, 2000.
- [10] J. Van Tassel and C. A. Randall, "Electrophoretic deposition and sintering of thin/thick PZT films," *Journal of the European Ceramic Society*, vol. 19, no. 6-7, pp. 955–958, 1999.
- [11] C. Kaya, F. Kaya, A. R. Boccaccini, and K. K. Chawla, "Fabrication and characterisation of Ni-coated carbon fibre-reinforced alumina ceramic matrix composites using electrophoretic deposition," *Acta Materialia*, vol. 49, no. 7, pp. 1189–1197, 2001.
- [12] C. Du, D. Heldbrant, and N. Pan, "Preparation and preliminary property study of carbon nanotubes films by electrophoretic deposition," *Materials Letters*, vol. 57, no. 2, pp. 434–438, 2002.
- [13] O. van der Biest, S. Put, G. Anné, and J. Vleugels, "Electrophoretic deposition for coatings and free standing objects," *Journal of Materials Science*, vol. 39, no. 3, pp. 779–785, 2004.
- [14] L. Besra and M. Liu, "A review on fundamentals and applications of electrophoretic deposition (EPD)," *Progress in Materials Science*, vol. 52, no. 1, pp. 1–61, 2007.
- [15] S. Yanagida, A. Nakajima, Y. Kameshima, N. Yoshida, T. Watanabe, and K. Okada, "Preparation of a crack-free rough titania coating on stainless steel mesh by electrophoretic deposition," *Materials Research Bulletin*, vol. 40, no. 8, pp. 1335–1344, 2005.
- [16] M. J. Santillán, F. Membrives, N. Quaranta, and A. R. Boccaccini, "Characterization of TiO<sub>2</sub> nanoparticle suspensions for electrophoretic deposition," *Journal of Nanoparticle Research*, vol. 10, no. 5, pp. 787–793, 2008.
- [17] S. Dor, S. Ruhle, A. Ofir, M. Adler, L. Grinis, and A. Zaban, "The influence of suspension composition and deposition mode on the electrophoretic deposition of TiO<sub>2</sub> nanoparticle agglomerates," *Colloids and Surfaces A*, vol. 342, no. 1–3, pp. 70–75, 2009.
- [18] S. Bonnas, H. J. Ritzhaupt-Kleissl, and J. Hauselt, "Electrophoretic deposition for fabrication of ceramic microparts," *Journal of the European Ceramic Society*, vol. 30, no. 5, pp. 1159–1162, 2010.
- [19] B. Ferrari, J. C. Fariñas, and R. Moreno, "Determination and control of metallic impurities in alumina deposits obtained by aqueous electrophoretic deposition," *Journal of the American Ceramic Society*, vol. 84, no. 4, pp. 733–739, 2001.
- [20] F. Q. Tang, T. Uchikoshi, K. Ozawa, and Y. Sakka, "Effect of polyethylenimine on the dispersion and electrophoretic deposition of nano-sized titania aqueous suspensions," *Journal of the European Ceramic Society*, vol. 26, no. 9, pp. 1555–1560, 2006.
- [21] S. Lebrette, C. Pagnoux, and P. Abelard, "Fabrication of titania dense layers by electrophoretic deposition in aqueous media," *Journal of the European Ceramic Society*, vol. 26, no. 13, pp. 2727–2734, 2006.
- [22] L. Besra, T. Uchikoshi, T. S. Suzuki, and Y. Sakka, "Application of constant current pulse to suppress bubble incorporation and control deposit morphology during aqueous electrophoretic deposition (EPD)," *Journal of the European Ceramic Society*, vol. 29, no. 10, pp. 1837–1845, 2009.
- [23] B. Raissi, E. Marzbanrad, and A. R. Gardeshzadeh, "Particle size separation by alternating electrophoretic deposition," *Journal of the European Ceramic Society*, vol. 29, no. 15, pp. 3289–3291, 2009.
- [24] F. Q. Tang, Y. Sakka, and T. Uchikoshi, "Electrophoretic deposition of aqueous nano-sized zinc oxide suspensions on a zinc electrode," *Materials Research Bulletin*, vol. 38, no. 2, pp. 207–212, 2003.
- [25] D. Zhitomirsky, J. A. Roether, A. R. Boccaccini, and I. Zhitomirsky, "Electrophoretic deposition of bioactive glass/polymer composite coatings with and without HA nanoparticle inclusions for biomedical applications," *Journal of Materials Processing Technology*, vol. 209, no. 4, pp. 1853–1860, 2009.
- [26] W. Yin, W. Wang, L. Zhou, S. Sun, and L. Zhang, "CTAB-assisted synthesis of monoclinic BiVO<sub>4</sub> photocatalyst and its highly efficient degradation of organic dye under visible-light irradiation," *Journal of Hazardous Materials*, vol. 173, no. 1–3, pp. 194–199, 2010.
- [27] V. Brezová, A. Blažková, Ľ. Karpinský et al., "Phenol decomposition using M<sup>III</sup>/TiO<sub>2</sub> photocatalysts supported by the sol-gel technique on glass fibres," *Journal of Photochemistry and Photobiology A*, vol. 109, no. 2, pp. 177–183, 1997.
- [28] T. López, J. Hernandez-Ventura, R. Gómez et al., "Photodecomposition of 2, 4-dinitroaniline on Li/TiO<sub>2</sub> and Rb/TiO<sub>2</sub> nanocrystallite sol-gel derived catalysts," *Journal of Molecular Catalysis A*, vol. 167, no. 1-2, pp. 101–107, 2001.
- [29] Y. Bessekhouad, D. Robert, J. V. Weber, and N. Chaoui, "Effect of alkaline-doped TiO<sub>2</sub> on photocatalytic efficiency," *Journal of Photochemistry and Photobiology A*, vol. 167, no. 1, pp. 49–57, 2004.
- [30] R. C. W. Lam, M. K. H. Leung, D. Y. C. Leung, L. L. P. Vrijmoed, W. C. Yam, and S. P. Ng, "Visible-light-assisted photocatalytic degradation of gaseous formaldehyde by parallel-plate reactor coated with Cr ion-implanted TiO<sub>2</sub> thin film," *Solar Energy Materials and Solar Cells*, vol. 91, no. 1, pp. 54–61, 2007.
- [31] S. Yin, P. Zhnag, B. Liu et al., "Microwave-assisted hydrothermal synthesis of monoclinic nitrogen-doped titania photocatalyst and its DeNO<sub>x</sub> ability under visible LED light irradiation," *Research on Chemical Intermediates*, vol. 36, no. 1, pp. 69–75, 2010.
- [32] J. Yu, M. Zhou, B. Cheng, and X. Zhao, "Preparation, characterization and photocatalytic activity of in situ N,S-codoped TiO<sub>2</sub> powders," *Journal of Molecular Catalysis A*, vol. 246, no. 1-2, pp. 176–184, 2006.
- [33] M. Zhou and J. Yu, "Preparation and enhanced daylight-induced photocatalytic activity of C,N,S-tridoped titanium dioxide powders," *Journal of Hazardous Materials*, vol. 152, no. 3, pp. 1229–1236, 2008.
- [34] J. A. Byrne, P. A. Fernandez-Ibañez, P. S. M. Dunlop, D. M. A. Alrousan, and J. W. J. Hamilton, "Photocatalytic enhancement for solar disinfection of water: a review," *International Journal of Photoenergy*, vol. 2011, Article ID 798051, 12 pages, 2011.

- [35] T. Ochiai, K. Nakata, T. Murakami et al., "Development of solar-driven electrochemical and photocatalytic water treatment system using a boron-doped diamond electrode and TiO<sub>2</sub> photocatalyst," *Water Research*, vol. 44, no. 3, pp. 904–910, 2010.
- [36] G. Dai, J. Yu, and G. Liu, "Synthesis and enhanced visible-light photoelectrocatalytic activity of p-n junction BiOI/TiO<sub>2</sub> nanotube arrays," *The Journal of Physical Chemistry C*, vol. 115, pp. 7339–7346, 2011.
- [37] B. Huang and S. Saka, "Photocatalytic activity of TiO<sub>2</sub> crystallite-activated carbon composites prepared in supercritical isopropanol for the decomposition of formaldehyde," *Journal of Wood Science*, vol. 49, no. 1, pp. 79–85, 2003.
- [38] H. Ichiura, T. Kitaoka, and H. Tanaka, "Removal of indoor pollutants under UV irradiation by a composite TiO<sub>2</sub>-zeolite sheet prepared using a papermaking technique," *Chemosphere*, vol. 50, no. 1, pp. 79–83, 2003.
- [39] T. Liu, F. Li, and X. Li, "TiO<sub>2</sub> hydrosols with high activity for photocatalytic degradation of formaldehyde in a gaseous phase," *Journal of Hazardous Materials*, vol. 152, no. 1, pp. 347–355, 2008.
- [40] L. Wang, M. Sakurai, and H. Kameyama, "Study of catalytic decomposition of formaldehyde on Pt/TiO<sub>2</sub> alumite catalyst at ambient temperature," *Journal of Hazardous Materials*, vol. 167, no. 1–3, pp. 399–405, 2009.
- [41] Y. Li, Y. Jiang, S. Peng, and F. Jiang, "Nitrogen-doped TiO<sub>2</sub> modified with NH<sub>4</sub>F for efficient photocatalytic degradation of formaldehyde under blue light-emitting diodes," *Journal of Hazardous Materials*, vol. 182, no. 1–3, pp. 90–96, 2010.
- [42] JCPDS-ICDD, "The International Centre for Diffraction Data," *PCPDFWIN 2.4*, 2003.
- [43] ASHRAE, *ASHRAE Handbook—HVAC Systems and Equipment (SI)*, American Society of Heating, Refrigerating and Air-Conditioning Engineers, Atlanta, Ga, USA, 2008.

## Research Article

# Investigation on the Photoelectrocatalytic Activity of Well-Aligned TiO<sub>2</sub> Nanotube Arrays

Xiaomeng Wu,<sup>1,2</sup> Zhaohui Huang,<sup>1</sup> Yangai Liu,<sup>1</sup> and Minghao Fang<sup>1</sup>

<sup>1</sup> School of Materials Science and Technology, China University of Geosciences-Beijing, Beijing 100083, China

<sup>2</sup> School of Materials Science and Engineering, Beijing University of Aeronautics and Astronautics, Beijing 100191, China

Correspondence should be addressed to Zhaohui Huang, huang118@cugb.edu.cn

Received 29 August 2011; Revised 5 November 2011; Accepted 5 November 2011

Academic Editor: Jiaguo Yu

Copyright © 2012 Xiaomeng Wu et al. This is an open access article distributed under the Creative Commons Attribution License, which permits unrestricted use, distribution, and reproduction in any medium, provided the original work is properly cited.

Well-aligned TiO<sub>2</sub> nanotube arrays were fabricated by anodizing Ti foil in viscous F<sup>-</sup> containing organic electrolytes, and the crystal structure and morphology of the TiO<sub>2</sub> nanotube array were characterized and analyzed by XRD, SEM, and TEM, respectively. The photocatalytic activity of the TiO<sub>2</sub> nanotube arrays was evaluated in the photocatalytic (PC) and photoelectrocatalytic (PEC) degradation of methylene blue (MB) dye in different supporting solutions. The excellent performance of ca. 97% for color removal was reached after 90 min in the PEC process compared to that of PC process which indicates that a certain external potential bias favors the promotion of the electrode reaction rate on TiO<sub>2</sub> nanotube array when it is under illumination. In addition, it is found that PEC process conducted in supporting solutions with low pH and containing Cl<sup>-</sup> is also beneficial to accelerate the degradation rate of MB.

## 1. Introduction

Photocatalysis of the TiO<sub>2</sub> semiconductor has received increasing attention for the application of degrading a great variety of organic contaminants in water, and the interest lies in the simplicity and low cost of the photocatalytic system which is mainly composed of an ultraviolet or a visible light source and the TiO<sub>2</sub> [1–9]. Up to now, improving the photocatalytic efficiency of TiO<sub>2</sub> thin-film photoreactors remains a major task in achieving maximum potential in commercial applications. Fortunately, this task can be fulfilled to a great extent by (1) using nanoporous TiO<sub>2</sub> films to increase the active surface area for photoreactions; (2) applying a positive potential bias on TiO<sub>2</sub> photocatalysts to suppress markedly the recombination rate of photogenerated electrons and holes. Under potential bias conditions, the photocatalytic reactions on TiO<sub>2</sub> surface may be considered as special electrode reactions involving electron-hole (e-h) pairs on TiO<sub>2</sub> photoelectrode/liquid interface. Inspired by the concept of achieving charge separation in a semiconductor system with an electrochemical bias introduced by Fujishima and Honda [10], an externally applied anodic bias is induced to the field

of photocatalysis to improve the degradation efficiency and received satisfying results [11–14].

A new form of photocatalyst, TiO<sub>2</sub> nanotube arrays possessing higher quantum efficiency, less grain boundaries, and more excellent adsorption ability derives from its specific structure than compact or nanoporous films comprised of randomly oriented nanoparticles, has demonstrated its potential in environmental applications and exhibited a remarkably improved photocatalytic activity as compared to traditional films [15–22]. However, few studies have been intentionally reported dealing with the possibility to use in situ photoelectrogenerated active chlorine to improve pollutants degradation rate [23, 24]. Therefore, in this study, we have examined the effects of applied potentials, electrolyte, and pH value on the photoelectrocatalytic (PEC) degradation of MB over TiO<sub>2</sub> nanotube array, and the effect of in situ generated active chlorine during the PEC degradation of MB was also evaluated. The motivation of this work is to gain an insight into the photoelectrocatalytic degradation characteristics of organic matters by TiO<sub>2</sub> nanotube arrays, and to offer fundamental information for the practical application of PEC in wastewater treatment.

## 2. Experimental

**2.1. Synthesis of TiO<sub>2</sub> Nanotube Arrays.** TiO<sub>2</sub> nanotube arrays were synthesized by anodic oxidation of titanium foil (0.1 mm thick, 99.6% purity). The titanium foil surface was treated before oxidation as follows: degrease in acetone, etch in mixed acid of HF and HNO<sub>3</sub> (concentrated solution, volume ratio 1 : 9), and rinsed with deionized water followed by drying in a cold air stream. The anodic oxidation was carried out in a two-electrode cell, with a platinum plate as the counter electrode. The electrochemical treatment consisted of potential ramping from the open-circuit potential to the target potential and then being held for a specified time period. The electrolyte was NH<sub>4</sub>F (0.5 wt %) in mixed solvent of glycol and deionized water with a volume ratio of 9 : 1; the oxidation potential and period were 50 V and 0.5 h. After anodic oxidation, the samples were rinsed in deionized water and dried in a cold air stream. A subsequent thermal annealing of the oxide layer was carried out at 500°C in N<sub>2</sub> for 1 h using a heating rate of 10°C/min and cooling naturally in order to convert the amorphous oxide into anatase phase.

**2.2. Characterization of Photocatalysts.** X-ray diffraction (XRD, Bruker D8 Advance) was used to examine the crystal structure of the nanocomposites. The morphologies of the samples were examined by field emission scanning electron microscopy (FESEM, Hitachi S-4800), and transmission electron microscope (TEM, JEOL 2010F) was used for investigating the microstructure of the samples. Photoelectrochemical measurements were performed with an IM6ex Potentiostat.

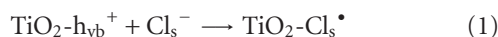
**2.3. Photoelectrocatalytic Activity Tests.** All the electrochemical measurements were carried out with a universal electrochemical interface and an impedance spectrum analyzer Zahner IM6e. The instrument was connected with a conventional three-electrode system (TiO<sub>2</sub> nanotube array with effective electrode area of 1 cm<sup>2</sup>, a saturated calomel electrode (SCE) and a Pt foil served as the working electrode, reference electrode, and counter electrode, resp.) which was established on a quartz beaker containing 600 mL test solution. For the experiments of PC and PEC oxidation, the TiO<sub>2</sub> nanotube array electrode (4 cm<sup>2</sup>) were used as the photoanode, while a Pt electrode and a saturated calomel electrode (SCE) were used as counter and reference electrodes, respectively. All voltages reported are versus SCE unless otherwise noted. About 100 mL of 10 mg L<sup>-1</sup> aqueous MB solution was served as target pollutant, in which 0.1 M NaCl and 0.1 M Na<sub>2</sub>SO<sub>4</sub> was added as supporting electrolyte, respectively. The solution pH value was adjusted by adding a small quantity of HCl, H<sub>2</sub>SO<sub>4</sub>, or NaOH. Both the PC and PEC oxidation reactions were carried out in a certain photoreactor system, and 250 W metal-halogen lamp (CMH-2500) with intensity of 100 mW/cm<sup>2</sup> was used as simulated solar light and the visible wavelength was controlled through a 400 nm cut filter. The MB concentrations were measured using UV-2100 spectrophotometer (SHIMADZU, Japan).

## 3. Results and Discussion

**3.1. Characterization of TiO<sub>2</sub> Nanotube Array.** Figure 1 shows FESEM images of TiO<sub>2</sub> nanotube arrays formed by anodization. It is clear that TiO<sub>2</sub> layer consists of nanotube arrays with a uniform tube diameter of 100 nm, a wall thickness of 25 nm, and the thickness of the layer is approximately 2.6 μm. It is also apparent that pore mouths are open on the top of the layer while on the bottom of the structure the tubes are closed. As shown in Figure 1(c), the magnified top-view image of the TiO<sub>2</sub> nanotube array after annealing indicates the TiO<sub>2</sub> layer retained its structural integrity. Figure 2 shows XRD patterns of the TiO<sub>2</sub> nanotube array before and after annealing in N<sub>2</sub> at 500°C for 1 h. It is apparent that as-anodized TiO<sub>2</sub> shows only the peaks from a Ti substrate, while the annealed sample shows clearly the crystalline signature of anatase, in other words the as-anodized TiO<sub>2</sub> exhibits an amorphous structure.

**3.2. Photoelectrochemical Characterization of TiO<sub>2</sub> Nanotube Array.** The photoelectrochemical current density reflects the generation, separation, and transfer efficiency of photoexcited electrons from the valence to the conduction band of TiO<sub>2</sub>. Photocurrent-potential curves under dark conditions (curve I) and under illumination, both in 0.1 mol L<sup>-1</sup> Na<sub>2</sub>SO<sub>4</sub> (curve II) and NaCl (curve III) are compared to each other in Figure 3. According to the literature [25], by illuminating the semiconductor with light energy greater than that of the band gap, electron-hole pairs are generated at the electrode surface. A bias potential positive to the flat-band potential produces a bending of the conduction band causing a more effective charge separation and increases the photocurrent (*i<sub>ph</sub>*) that begins to flow and likely promotes a better oxidative degradation process. As expected, Figure 4 shows that, under illumination, TiO<sub>2</sub> photoelectrode gives rise to a photocurrent in Na<sub>2</sub>SO<sub>4</sub> at -0.20 V, but in NaCl media the onset potential shifts to a less positive potential of -0.38 V, both at pH = 6.0. In addition to this shift in potential, photocurrent in NaCl media was also higher than in Na<sub>2</sub>SO<sub>4</sub> electrolyte.

In comparing curves II and III in Figure 3, one can notice that the nature of the electrolyte could affect the photocurrent intensity. The photocurrent intensity obtained for sulphate solutions corresponds simply to the contribution from the injection of electrons in the conduction band and hole transfer rate scavenged by OH<sup>-</sup>. On the other hand, it is assumed that chloride ions might be oxidized at a less positive potential under photoelectrocatalytic conditions compared to that of electrochemical conditions as denoted by the following [24, 26]:



The dependence of photocurrent and dye discoloration rate on chloride concentration may be attributed to the

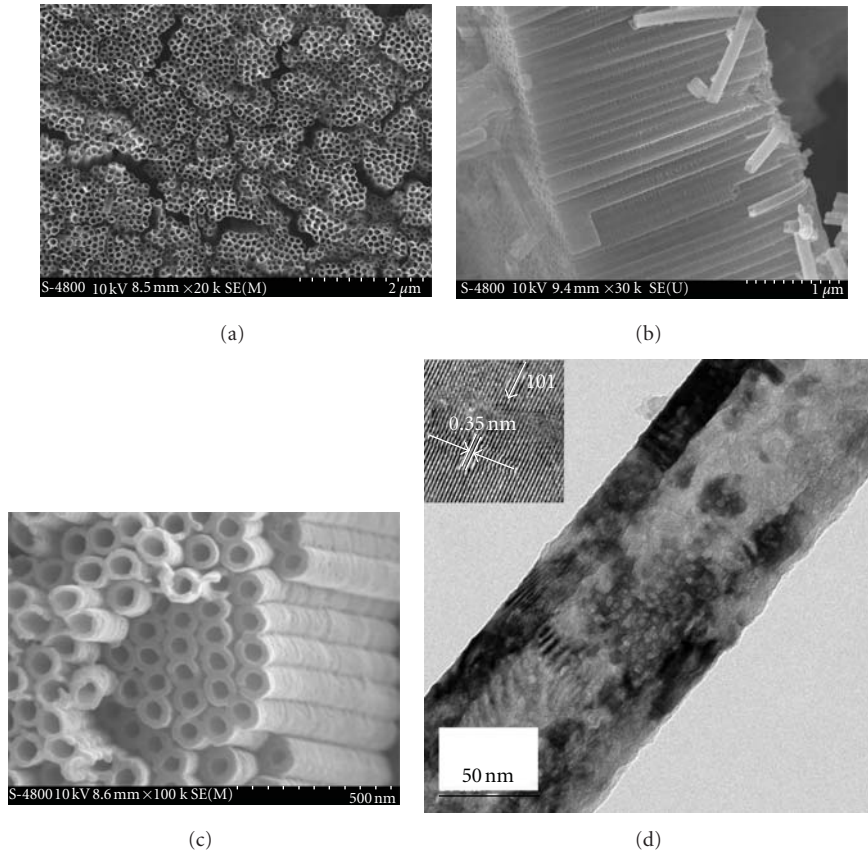


FIGURE 1: FESEM top-view images (a) and cross-section (b) of  $\text{TiO}_2$  nanotube arrays and the magnified image of the  $\text{TiO}_2$  nanotube arrays after annealing (c). TEM images of a typical annealed single  $\text{TiO}_2$  nanotube (d) and high magnification image showing a lattice spacing of 0.35 nm, corresponding to anatase phase (inset).

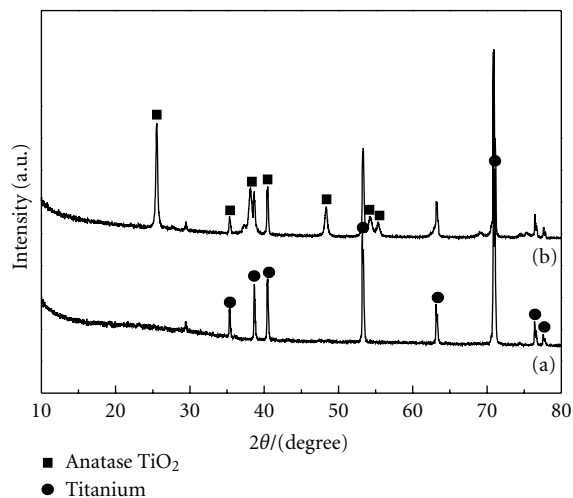


FIGURE 2: XRD patterns of as-prepared  $\text{TiO}_2$  nanotube arrays before and after annealing in  $\text{N}_2$  stream at  $500^\circ\text{C}$  for 1 h.

improvement of  $\text{Cl}^-$  adsorption on the electrode surface under conditions of high concentrations of chloride [19]. At higher adsorption conditions, electron/holes generated at a steady rate or  $\text{OH}^\bullet$  radicals are more easily transferred to

the  $\text{Cl}^-$  ions improving the photocatalysis process due to the minimization of charge recombination.

Besides, the small visible light response, as shown in the inset of Figure 3, may indicate a slight modification of  $\text{TiO}_2$  bandgap derived from carbon incorporation in our experiment. Considering the  $\text{TiO}_2$  nanotube array was prepared in organic electrolytes, it is assumed that organic residue (glycol) might provide carbon source to react with the  $\text{TiO}_2$  matrix to form  $\text{TiO}_{2-x}\text{C}_x$  at high temperature under inert atmosphere [27], and the EDX analysis demonstrated that the sample which contained a small fraction of carbon remains (2.79 wt%) after annealing. The bandgap reduction extends the utilization of solar energy to visible light region while the intragap band introduction allows the absorption of visible photons of even lower energy and the carbon-doping enables the  $\text{TiO}_2$  nanotubes to absorb longer wavelength light which is further verified by UV-Vis spectra shown in Figure 4. The strength of photoresponse depends on the density of states in the bands, and the increase of carbon-doping density in the  $\text{TiO}_2$  thin films increases the density of states of the valence band edge and the intragap band, thereby enhancing the photoresponse of  $\text{TiO}_2$  nanotubes [28]. However, the reactivity of the holes generated in the intragap band toward oxidation of MB is assumed to be low because the density of states in the

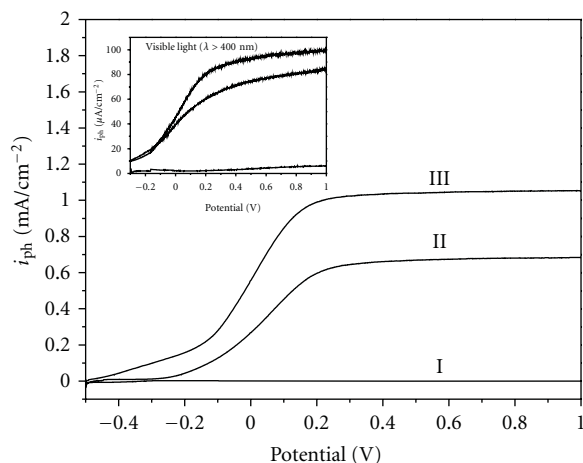


FIGURE 3: Photocurrent-potential curves obtained for TiO<sub>2</sub> nanotube arrays electrode under dark conditions (curve I) and for 0.1 mol L<sup>-1</sup> Na<sub>2</sub>SO<sub>4</sub> (curve II) and 0.1 mol L<sup>-1</sup> NaCl (curve III) under illumination (complete solar spectrum). The inset shows the corresponding visible light response of the electrode ( $\lambda > 400$  nm). Scan rate = 10 mV s<sup>-1</sup>, pH = 6.0.

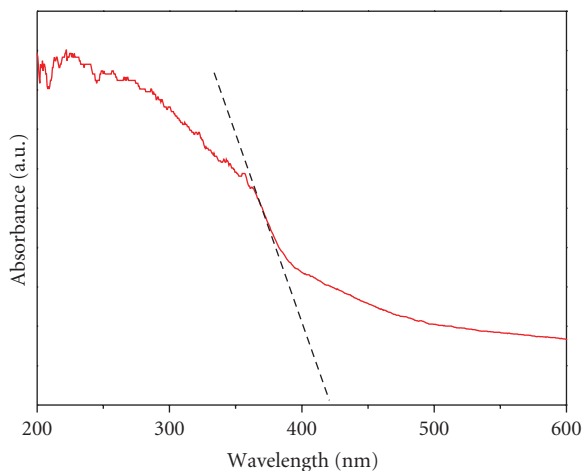


FIGURE 4: UV-Vis diffuse reflectance spectrum (DRS) for TiO<sub>2</sub> nanotube array.

intragap band is much smaller than that in the valence and conduction bands [29].

The evaluation of the stability of the above TiO<sub>2</sub> nanotube arrays is carried out by potentiostatic (current versus time,  $I-t$ ) measurements. Figure 5 shows the  $I-t$  curve obtained from the PEC cell containing Pt as the cathode and TiO<sub>2</sub> (4 cm<sup>2</sup>) as a photoanode. It shows about 1.0 mA/cm<sup>2</sup> current density when an external bias of +0.6 V electrode is applied to the TiO<sub>2</sub> nanotubes electrode. The photocurrent value goes down to zero as soon as the illumination of light on the photoanode is stopped, and the cell is run intermittently for 25 min without sacrificing the photocurrent. This result suggests that the photogenerated charge carriers transfer effectively from the working electrode to the counter electrode and the great activity of TiO<sub>2</sub> nanotube array in the photocatalysis process.

**3.3. Comparison of Rate Constants for PC or PEC Processes.** The UV spectra of MB in the PEC process (biased at +0.6 V) at various reaction intervals are presented in Figure 6. The reduction in absorbance is likely due to the degradation of the MB chromophore, and the peak shift is due to demethylation occurring both at the catalyst surface and bulk solution [30]. It is well documented that the MB degradation meets the first-order photoelectrocatalytic reaction rate and its kinetics can also be expressed as  $\ln(C/C_0) = kt$ , where  $k$  is the apparent rate constant,  $t$  is the illumination time, and  $C$  and  $C_0$  are the actual reaction and initial concentration of MB solution, respectively. Figure 7 shows the degradation kinetic curves as a function of time recorded for the TiO<sub>2</sub> nanotube array by PC and PEC, respectively. In the case of PEC, applied potentials ranged between 0 and +0.6 V and absorbance decay at 664 nm was monitored over 15 min of the experiment, an almost completed degradation (96.74%) was observed around 90 min at a low bias level of +0.6 V, while the MB degradation ratio for PC process only achieves to 26.32% and reaction rate constant is 0.00297 min<sup>-1</sup>. It is evident that the degradation efficiency of PEC is considerably higher than that of PC at the same time and it increases with the applied potential bias; the corresponding reaction rate constants are 0.00933 min<sup>-1</sup>, 0.02298 min<sup>-1</sup>, 0.03501 min<sup>-1</sup>, 0.04747 min<sup>-1</sup> for external bias potential at 0 V, 0.2 V, 0.4 V, and 0.6 V, respectively. These results clearly demonstrate that the degradation rate increases as a function of applied potential up to  $E = +0.6$  V. It was reported that further increases in potential lead to a slight reduction in degradation. The reason should be attributed mainly to the evolution of the oxygen bubbles at the surface of the TiO<sub>2</sub> nanotubes which hinders electrode reaction.

As calculated from onset potential measurements (Figure 3), the flat-band potential for TiO<sub>2</sub> at pH = 6.0 in 0.1 mol L<sup>-1</sup> NaCl media is about 0.38 V. All of the applied potentials employed in this study are positive of this flat-band potential. Therefore, there is always a potential gradient over the TiO<sub>2</sub> film, resulting in an electric field, which keeps photogenerated charges apart. Since the magnitude of the limiting current is a measure of the overall photoelectrocatalytic performance of an electrode, theoretically, the degradation rate of PEC should reach its maximum when the photocurrent is in saturation; however, the overall MB degradation efficiency still maintains an increasing trend despite the photocurrent being almost constant when the bias potential is higher than +0.2 V, as seen in Figure 3, and the plausible explanation of the phenomenon may be ascribed to that more positive potential bias favors the specific adsorption of Cl<sup>-</sup> on the surface of TiO<sub>2</sub> nanotube array electrode; therefore in situ photoelectrochemically generated active chlorine that can diffuse into bulk solution to react with MB, differing from OH<sup>•</sup> radicals that usually only survive in the region of interface is responsible for the further enhancement of degradation rate of MB with increasing positive bias potential.

**3.4. Effect of Supporting Electrolyte.** The supporting electrolyte also plays an important role in a photoelectrocatalytic process, and the effect of the supporting electrolyte on the

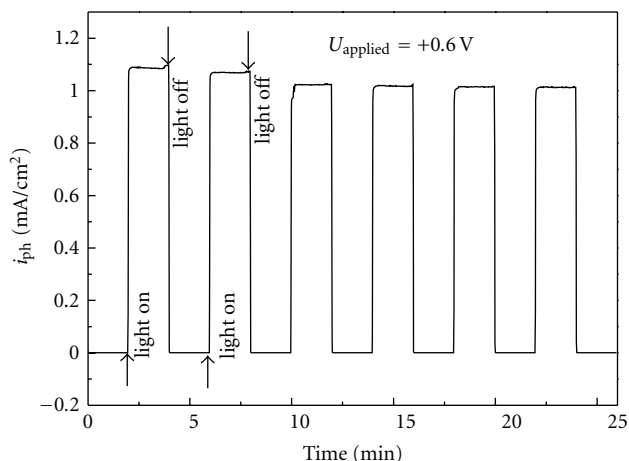


FIGURE 5: Photocurrent densities versus time of TiO<sub>2</sub> nanotubes array being applied with 0.6 V bias potential (versus SCE) under simulated solar light illumination. A 0.1 M NaCl solution was used as the electrolyte.

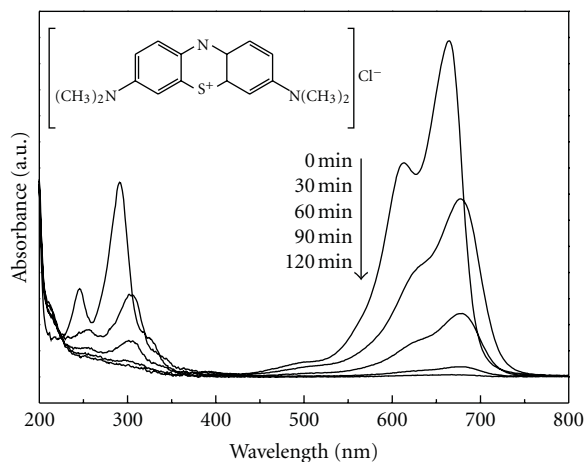
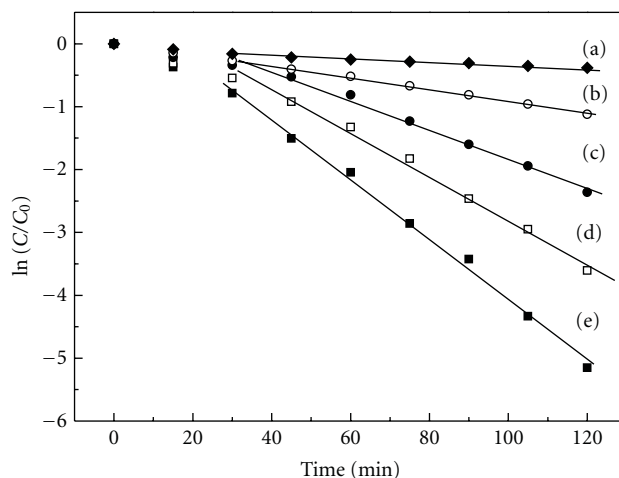


FIGURE 6: Change of UV-Vis spectra of methylene blue at various reaction intervals for PEC process in the presence of +0.6 V versus SCE anodic bias. Inset is the chemical structure of MB.

performance of TiO<sub>2</sub> nanotubular arrays was tested monitoring the degradation of 10 mg L<sup>-1</sup> of MB in 0.1 mol L<sup>-1</sup> of Na<sub>2</sub>SO<sub>4</sub> and NaCl. Figure 8 shows the influence of the type of electrolyte on the removal of color investigated through experiments conducted with 10 mg L<sup>-1</sup> MB in 0.1 mol/L NaCl and 0.1 mol/L Na<sub>2</sub>SO<sub>4</sub>, respectively. The higher degradation rate is observed in chloride media, indicating that the mechanism of MB degradation in NaCl solution is different than that operating in the other non-chloride containing supporting electrolytes. Obviously, the result is in line with the photocurrent difference between curves II and III in Figure 3; one can notice that the nature of the electrolyte affects the photocurrent response. It seems that the photocurrent intensity obtained for sulphate solutions corresponds simply to the contribution from the injection of electrons in the conduction band and hole transfer rate scavenged by OH<sup>-</sup> [31]. Nevertheless, it is



◆ Open-circuit,  $|k| = 0.00297 \text{ min}^{-1}$  ○ 0 V,  $|k| = 0.00933 \text{ min}^{-1}$   
● 0.2 V,  $|k| = 0.02298 \text{ min}^{-1}$  □ 0.4 V,  $|k| = 0.03501 \text{ min}^{-1}$   
■ 0.6 V,  $|k| = 0.04747 \text{ min}^{-1}$

FIGURE 7: MB degradation kinetic curves of TiO<sub>2</sub> nanotube array under various conditions.

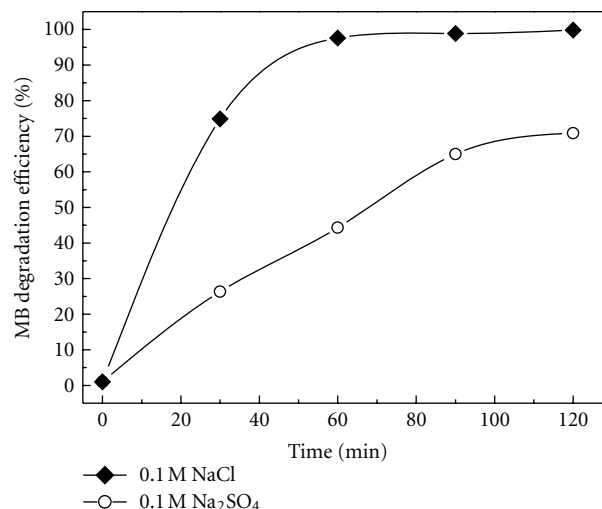


FIGURE 8: The comparison of degradation efficiency via PEC route in 0.1 M NaCl and Na<sub>2</sub>SO<sub>4</sub>, bias at 0.6 V.

known that chloride ions are commonly electrochemically oxidized to chlorine at potentials over +1 V, and as stated above, chloride ions could be oxidized to form some active chloride species at a less positive potential under photoelectrocatalytic conditions which was confirmed by the more detailed studies of Hepel and Hazelton [32]. Therefore, the comparing experiment illustrates that the selection of suitable supporting electrolyte also favors the improvement of degradation efficiency in photoelectrocatalytic system.

**3.5. Effect of Solution pH Value.** The influence of pH on the discoloration rate of MB is presented in Figure 9. Initial degradation rates are plotted as function of different pH values ( $C_0 = 10 \text{ mg L}^{-1}$ ,  $E = +0.6 \text{ V}$ , and  $0.1 \text{ mol L}^{-1}$  NaCl).

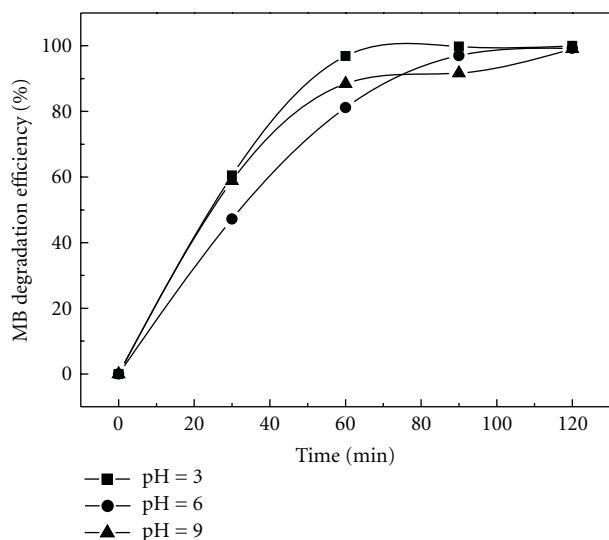


FIGURE 9: Effect of solution pH on photoelectrocatalytic degradation of MB.

It can be seen that the degradation rate is highest over the pH range 4~6 and decreases noticeably at higher pH. These results show that color removal is to a great extent faster at acidic medium but mineralization could be preponderant at  $\text{pH} \geq 6$ . In all further investigations  $\text{pH} = 6.0$  was selected as the optimum pH to investigate the dye degradation using chlorine medium, where mineralization and color removal are favorable. Since  $\text{TiO}_2$  usually has an isoelectric point at a  $\text{pH} 5.7$ , it would seem that at pH values higher than the isoelectric point, negative ions (e.g.,  $\text{Cl}^-$ ) are repelled from the  $\text{TiO}_2$  surface leading to lower degradation efficiencies. As a consequence, both the percentage of chlorine generation and the adsorption of the dye are diminished in conditions where the pH of the solution is higher than the pH of isoelectric point [33]. In alkaline solutions, the formation of  $\text{OH}^\bullet$  radicals is predominant over  $\text{Cl}^\bullet$  radicals and  $\text{Cl}_2$  but the kinetics of MB degradation is still slower than in acidic media. In addition, it should be noted that the noticeable change of the degradation efficiency at  $\text{pH} = 9$  during the PEC process is considered to be due to the constantly decreased concentrations of the  $\text{OH}^-$ , which is responsible for hydroxyl radical generation and the degradation of the MB during the photocatalytic oxidation process [34].

#### 4. Conclusion

The photocatalytic degradation efficiency of methylene blue (MB) in aqueous solutions showed a remarkable increase by means of illumination with electroassisted way in the presence of  $\text{TiO}_2$  nanotube array electrode. The rate constant of photoelectrocatalytic degradation was greater than that of photocatalytic processes either in isolation or as a sum of individual processes, indicating an obviously synergistic effect among photo- and electroprocesses. In addition, low pH and high concentration of  $\text{Cl}^-$  solutions are beneficial to the degradation rate of MB. In situ photoelectrocatalytic generated active chlorine that can diffuse into the bulk

solution should be responsible for the enhancement of degradation rate of MB. Hence, the photoelectrocatalytic process with in situ generated active chlorine will be an attractive method in the treatment of wastewater.

#### Acknowledgments

The authors gratefully acknowledge the financial support to this work from the National Natural Science Foundation of China (no. 51032007) and the New Star Technology Plan of Beijing (no. 2007A080).

#### References

- [1] M. Grandcolas, A. Louvet, N. Keller, and V. Keller, "Layer-by-layer deposited titanate-based nanotubes for solar photocatalytic removal of chemical warfare agents from textiles," *Angewandte Chemie - International Edition*, vol. 48, no. 1, pp. 161–164, 2009.
- [2] T. L. Thompson and J. T. Yates, "Surface science studies of the photoactivation of  $\text{TiO}_2$ —new photochemical processes," *Chemical Reviews*, vol. 106, no. 10, pp. 4428–4453, 2006.
- [3] M. Radecka, M. Rekas, E. Kusior et al., " $\text{TiO}_2$ -based nanopowders and thin films for photocatalytic applications," *Journal of Nanoscience and Nanotechnology*, vol. 10, no. 2, pp. 1032–1042, 2010.
- [4] R. Asahi, T. Morikawa, T. Ohwaki, K. Aoki, and Y. Taga, "Visible-light photocatalysis in nitrogen-doped titanium oxides," *Science*, vol. 293, no. 5528, pp. 269–271, 2001.
- [5] D. V. Bavykin, J. M. Friedrich, and F. C. Walsh, "Protonated titanates and  $\text{TiO}_2$  nanostructured materials: synthesis, properties, and applications," *Advanced Materials*, vol. 18, no. 21, pp. 2807–2824, 2006.
- [6] Y. Z. Fan, G. P. Chen, D. M. Li et al., "Highly selective deethylation of rhodamine B on  $\text{TiO}_2$  prepared in supercritical fluids," *International Journal of Photoenergy*, vol. 2012, Article ID 173865, 7 pages, 2012.
- [7] S. Wang, L. Zhao, J. Ran, Z. Shu, G. Dai, and P. Zhai, "Effects of calcination temperatures on photocatalytic activity of ordered titanate nanoribbon/ $\text{SnO}_2$  films fabricated during an EPD process," *International Journal of Photoenergy*, vol. 2012, Article ID 472958, 7 pages, 2012.
- [8] S.-J. Kim, N.-H. Lee, H.-J. Oh, S.-C. Jung, W.-J. Lee, and D.-H. Kim, "Photocatalytic properties of nanotubular-shaped  $\text{TiO}_2$  powders with anatase phase obtained from titanate nanotube powder through various thermal treatments," *International Journal of Photoenergy*, vol. 2011, Article ID 327821, 7 pages, 2011.
- [9] J. A. Byrne, P. A. Fernandez-Ibañez, P. S.M. Dunlop, D. M.A. Alrousan, and J. W.J. Hamilton, "Photocatalytic enhancement for solar disinfection of water: a review," *International Journal of Photoenergy*, vol. 2011, Article ID 798051, 12 pages, 2011.
- [10] A. Fujishima and K. Honda, "Electrochemical photolysis of water at a semiconductor electrode," *Nature*, vol. 238, no. 5358, pp. 37–38, 1972.
- [11] N. Chandrasekharan and P. Y. Kamat, "Improving the photoelectrochemical performance of nanostructured  $\text{TiO}_2$  films by adsorption of gold nanoparticles," *Journal of Physical Chemistry B*, vol. 104, no. 46, pp. 10851–10857, 2000.
- [12] X. Z. Li, H. L. Liu, P. T. Yue, and Y. P. Sun, "Photoelectrocatalytic oxidation of rose Bengal in aqueous solution

- using a Ti/TiO<sub>2</sub> mesh electrode,” *Environmental Science and Technology*, vol. 34, no. 20, pp. 4401–4406, 2000.
- [13] M. C. Li and J. N. Shen, “Photoelectrochemical oxidation behavior of organic substances on TiO<sub>2</sub> thin-film electrodes,” *Journal of Solid State Electrochemistry*, vol. 10, no. 12, pp. 980–986, 2006.
- [14] J. Li, L. Zheng, L. Li, Y. Xian, and L. Jin, “Fabrication of TiO<sub>2</sub>/Ti electrode by laser-assisted anodic oxidation and its application on photoelectrocatalytic degradation of methylene blue,” *Journal of Hazardous Materials*, vol. 139, no. 1, pp. 72–78, 2007.
- [15] Y. Lai, L. Sun, Y. Chen, H. Zhuang, C. Lin, and J. W. Chin, “Effects of the structure of TiO<sub>2</sub> nanotube array on Ti substrate on its photocatalytic activity,” *Journal of the Electrochemical Society*, vol. 153, no. 7, pp. D123–D127, 2006.
- [16] Y. Lai, H. Zhuang, L. Sun, Z. Chen, and C. Lin, “Self-organized TiO<sub>2</sub> nanotubes in mixed organic-inorganic electrolytes and their photoelectrochemical performance,” *Electrochimica Acta*, vol. 54, no. 26, pp. 6536–6542, 2009.
- [17] D. Wang, T. Hu, L. Hu et al., “Microstructured arrays of TiO<sub>2</sub> nanotubes for improved photo-electrocatalysis and mechanical stability,” *Advanced Functional Materials*, vol. 19, no. 12, pp. 1930–1938, 2009.
- [18] S. P. Albu, A. Ghicov, J. M. Macak, R. Hahn, and P. Schmuki, “Self-organized, free-standing TiO<sub>2</sub> nanotube membrane for flow-through photocatalytic applications,” *Nano Letters*, vol. 7, no. 5, pp. 1286–1289, 2007.
- [19] G. Zhang, H. Huang, Y. Zhang, H. L. W. Chan, and L. Zhou, “Highly ordered nanoporous TiO<sub>2</sub> and its photocatalytic properties,” *Electrochemistry Communications*, vol. 9, no. 12, pp. 2854–2858, 2007.
- [20] Z. Xu and J. Yu, “Visible-light-induced photoelectrochemical behaviors of Fe-modified TiO<sub>2</sub> nanotube arrays,” *Nanoscale*, vol. 3, no. 8, pp. 3138–3144, 2011.
- [21] J. Yu and B. Wang, “Effect of calcination temperature on morphology and photoelectrochemical properties of anodized titanium dioxide nanotube arrays,” *Applied Catalysis B*, vol. 94, no. 3–4, pp. 295–302, 2010.
- [22] J. Yu, G. Dai, and B. Cheng, “Effect of crystallization methods on morphology and photocatalytic activity of anodized TiO<sub>2</sub> nanotube array films,” *Journal of Physical Chemistry C*, vol. 114, no. 45, pp. 19378–19385, 2010.
- [23] J. S. Do and W. C. Yeh, “In situ degradation of formaldehyde with electrogenerated hypochlorite ion,” *Journal of Applied Electrochemistry*, vol. 25, no. 5, pp. 483–489, 1995.
- [24] M. V. B. Zanoni, J. J. Sene, and M. A. Anderson, “Photoelectrocatalytic degradation of Remazol Brilliant Orange 3R on titanium dioxide thin-film electrodes,” *Journal of Photochemistry and Photobiology A*, vol. 157, no. 1, pp. 55–63, 2003.
- [25] M. Radecka, M. Rekas, A. Trenczek-Zajac, and K. Zakrzewska, “Importance of the band gap energy and flat band potential for application of modified TiO<sub>2</sub> photoanodes in water photolysis,” *Journal of Power Sources*, vol. 181, no. 1, pp. 46–55, 2008.
- [26] X. F. Cheng, W. H. Leng, O. Y. Pi, Z. Zhang, J. Q. Zhang, and C. N. Cao, “Enhancement of photocatalytic activity of TiO<sub>2</sub> film electrode by in situ photoelectro-generating active chlorine,” *Transactions of Nonferrous Metals Society of China (English Edition)*, vol. 17, no. 5, pp. 1087–1092, 2007.
- [27] S. Liu, L. Yang, S. Xu, S. Luo, and Q. Cai, “Photocatalytic activities of C-N-doped TiO<sub>2</sub> nanotube array/carbon nanorod composite,” *Electrochemistry Communications*, vol. 11, no. 9, pp. 1748–1751, 2009.
- [28] W. H. Leng, Z. Zhang, J. Q. Zhang, and C. N. Cao, “Investigation of the kinetics of a TiO<sub>2</sub> photoelectrocatalytic reaction involving charge transfer and recombination through surface states by electrochemical impedance spectroscopy,” *Journal of Physical Chemistry B*, vol. 109, no. 31, pp. 15008–15023, 2005.
- [29] C. Xu and S. U. M. Khan, “Photoresponse of visible light active carbon-modified -n-TiO<sub>2</sub> thin films,” *Electrochemical and Solid-State Letters*, vol. 10, no. 3, pp. B56–B59, 2007.
- [30] L. Rizzo, J. Koch, V. Belgiorno, and M. A. Anderson, “Removal of methylene blue in a photocatalytic reactor using polymethylmethacrylate supported TiO<sub>2</sub> nanofilm,” *Desalination*, vol. 211, no. 1–3, pp. 1–9, 2007.
- [31] M. F. Brugnera, K. Rajeshwar, J. C. Cardoso, and M. V. B. Zanoni, “Bisphenol A removal from wastewater using self-organized TiO<sub>2</sub> nanotubular array electrodes,” *Chemosphere*, vol. 78, no. 5, pp. 569–575, 2010.
- [32] M. Hepel and S. Hazelton, “Photoelectrocatalytic degradation of diazo dyes on nanostructured WO<sub>3</sub> electrodes,” *Electrochimica Acta*, vol. 50, no. 25–26, pp. 5278–5291, 2005.
- [33] J. Luo and M. Hepel, “Photoelectrochemical degradation of naphthol blue black diazo dye on WO<sub>3</sub> film electrode,” *Electrochimica Acta*, vol. 46, no. 19, pp. 2913–2922, 2001.
- [34] M. Hepel and J. Luo, “Photoelectrochemical mineralization of textile diazo dye pollutants using nanocrystalline WO<sub>3</sub> electrodes,” *Electrochimica Acta*, vol. 47, no. 5, pp. 729–740, 2001.

## Research Article

# Enhancement of Visible-Light Photocatalytic Activity of Mesoporous Au-TiO<sub>2</sub> Nanocomposites by Surface Plasmon Resonance

Minghua Zhou,<sup>1,2</sup> Jun Zhang,<sup>2</sup> Bei Cheng,<sup>2</sup> and Huogen Yu<sup>2</sup>

<sup>1</sup>Laboratory of Medical Chemistry, Hubei University of Chinese Medicine, Shiyan, Hubei 442000, China

<sup>2</sup>State Key Laboratory of Advanced Technology for Material Synthesis and Processing, Materials College, Wuhan University of Technology, 122 Luoshi Road, Wuhan 430070, China

Correspondence should be addressed to Bei Cheng, chengbei2003@yahoo.com.cn and Huogen Yu, yuhuogen@yahoo.cn

Received 30 October 2011; Accepted 2 November 2011

Academic Editor: Jiaguo Yu

Copyright © 2012 Minghua Zhou et al. This is an open access article distributed under the Creative Commons Attribution License, which permits unrestricted use, distribution, and reproduction in any medium, provided the original work is properly cited.

Mesoporous Au-TiO<sub>2</sub> nanocomposite plasmonic photocatalyst with visible-light photoactivity was prepared by a simple spray hydrolytic method using photoreduction technique at 90°C. The prepared samples were characterized by X-ray diffraction, scanning electron microscopy, transmission electron microscopy, and N<sub>2</sub> adsorption-desorption isotherms. The formation of hydroxyl radicals ( $\bullet$ OH) on the surface of visible-light illuminated Au-TiO<sub>2</sub> nanocomposites was detected by the luminescence technique using terephthalic acid as probe molecules. The photocatalytic activity was evaluated by photocatalytic decolorization of Rhodamine-B (RhB) aqueous solution under visible-light irradiation ( $\lambda > 420$  nm). The results revealed that the TiO<sub>2</sub> could be crystallized *via* spray hydrolysis method, and the photoreduction technique was facilitated to prepare Au nanoparticles in the mesoporous TiO<sub>2</sub> at 90°C. The light absorption, the formation rate of hydroxyl radicals, and photocatalytic decolorization of Rhodamine-B aqueous solution were significantly enhanced by those embedded Au nanoparticles in the Au-TiO<sub>2</sub> nanocomposites. The prepared Au-TiO<sub>2</sub> nanocomposites exhibit a highly visible-light photocatalytic activity for photocatalytic degradation of RhB in water, and their photocatalytic activity is higher than that of the pristine TiO<sub>2</sub> nanoparticles due to the surface plasmon resonance.

## 1. Introduction

Since the discovery of photocatalytic water splitting on TiO<sub>2</sub> single-crystal electrodes by Fujishima and Honda in 1972 [1], nanosized TiO<sub>2</sub> semiconductor has been always regarded as one of the most promising photocatalysts in practical applications, especially water cleaning and removal of volatile organic compounds (VOCs) in air, due to its high photocatalytic activity, chemical stability, low cost, and nontoxicity [2–12]. Recently, highly dispersed noble metal nanoparticles with desirable morphologies have attracted great attention due to their unusual catalytic, electric, optical properties and surface plasmon absorption, and their widespread potential usefulness in diverse fields such as biomedicine, photocatalysis, energy conversion, and storage and nanodevices [13–19]. Some investigations have indicated that noble metal Au nanoparticles deposited on TiO<sub>2</sub> surface

can obviously enhance the photocatalytic performance *via* suppressing the recombination of electron-hole pairs, and also extending the light response in the visible region [14, 20, 21]. However, the practical applicability of such a composite structure is limited owing to exposing both the Au nanoparticles to reactants and the surrounding, while the corrosion or dissolution of the Au nanoparticles during the photocatalytic reaction is likely to limit the usage of Au, especially for long-term working [13]. To overcome this shortcoming, the Au nanoparticles embedded or wrapped by the TiO<sub>2</sub> aggregates have attracted considerable attention, and significant advances have been made in recent years. The TiO<sub>2</sub> aggregates offer protection for Au nanoparticles against dissolution, photocorrosion, and chemical corrosion under extreme conditions, as well as being used for decomposition of dye wastewater. Among the various phases of TiO<sub>2</sub>, anatase has proven to be the most suitable one due to its

two distinctive performances. One is that the photogenerated electrons of anatase can rapidly reduce Au ions at interface [22]. The other is that the conduction band of anatase can transfer the photogenerated electrons of the excited Au to adsorbed  $O_2$  and then to form active superoxide radical anions [23–25].

Several techniques, such as sol-gel method, chemical vapor deposition, laser vaporization, modified impregnation, precipitation-reduction, and photoreduction, have been developed to design and modulate the Au-TiO<sub>2</sub> composite nanoparticles. The preferred and versatile method is the sol-gel process, which has many advantages, such as simple equipment required, flexible control of pore structures, and the concentration of Au [26–30]. Usually, the TiO<sub>2</sub> aggregates obtained by this method are amorphous in nature and calcination temperatures higher than 400°C are required to realize the phase transformation from amorphous to anatase. However, such high calcination temperatures will not only lead to the increase of crystallite size and the decrease of specific surface areas and pore volume, but also induce the heat-aggregation of Au nanoparticles. Generally, the Au particles have exhibited highly catalytic activity only with smaller nanoscale size [31–34]. So, in order to obtain crystallized Au-TiO<sub>2</sub> composite nanoparticles with higher specific surface areas and pore volume, the temperature of phase transformation from amorphous to anatase must be lowered.

In this paper, a novel and simple method, a low-temperature spray hydrolysis assisted with photoreduction technique, was proposed for the synthesis of Au-TiO<sub>2</sub> nanocomposites. The Au nanoparticles (Au colloids) were prepared by photoreduction technique using a 350 W xenon lamp as a light source. Au-TiO<sub>2</sub> nanocomposites were prepared by spraying the mixed solution of  $Ti(OC_4H_9)_4$  and EtOH into hot distilled water in the presence of Au nanoparticles (ca. 90°C). The formation of hydroxyl radicals ( $\bullet OH$ ) on the surface of visible-light illuminated Au-TiO<sub>2</sub> composite samples was detected by the photoluminescence technique using terephthalic acid as probe molecules. The photocatalytic activity of the Au-TiO<sub>2</sub> composite samples was evaluated by photocatalytic decolorization of RhB aqueous solution under visible-light irradiation ( $\lambda > 420$  nm).

## 2. Experimental

**2.1. Preparation of Au Nanoparticles.** All the involved chemicals in this study were purchased from Shanghai Chemical Reagent Co., Ltd, and used without further purification. Typically, 10 mL aqueous solution of sodium citrate (38.8 mM) was added into 100 mL aqueous solution of  $HAuCl_4 \cdot 4H_2O$  (1 mM) under vigorous stirring. A 350 W xenon lamp was used a light source to irradiate the mixed solution during the reduction process. The color of the solution was gradually changed from light-yellow to fuchsia. After irradiation for another 30 mins, it was cooled to room temperature.

**2.2. Preparation of Au-TiO<sub>2</sub> Composite Nanoparticles.** In a typical synthesis [35], 10 mL of mixed solution of Tetrabutyl

titanate (TBOT) and ethanol (volume ratio of TBOT to ethanol, 1 : 4) was sprayed into a 250 mL beaker containing 200 mL hot distilled water (90°C), in which the added above Au nanoparticles was used as Au source. The corresponding nominal atomic ratio of Au to Ti, which hereafter was designated as  $R_{Au}$ , was 0.003, 0.006, 0.015, 0.030, and 0.060 nominal atomic % (at. %). After further stirring for 2 h at 90°C, the resultant mixed solution was aged for 2 h at 90°C. The aged wet precipitates were filtrated, rinsed with distilled water and absolute alcohol for two times. Then the precipitates were dried in a vacuum oven at 80°C for 10 h and finally ground to obtain Au-TiO<sub>2</sub> composite samples. As a control experiment, the pristine TiO<sub>2</sub> product was also prepared under the same condition but without adding Au nanoparticles.

**2.3. Characterization.** X-ray diffraction (XRD) patterns obtained on a D/Max-RB X-ray diffractometer (Rigaku, Japan) using  $Cu K\alpha$  irradiation at a scan rate ( $2\theta$ ) of  $0.05^\circ s^{-1}$  were used to determine the phase structure of the obtained samples. The average crystallite sizes of anatase were determined according to the Scherrer equation using the full width at half maximum (FWHM) data of anatase phase after correcting the instrumental broadening. Morphology observation was performed on a S-4800 field emission scanning electron microscope (FESEM, Hitachi, Japan). Transmission electron microscopy (TEM) and high-resolution transmission electron microscopy (HRTEM) observation were conducted using a JEM 2100F microscope at an accelerating voltage of 200 kV. The Brunauer-Emmett-Teller surface areas ( $S_{BET}$ ) of the samples were analyzed by nitrogen adsorption in a Micromeritics ASAP 2020 nitrogen adsorption apparatus (USA). All the samples were degassed at 80°C prior to nitrogen adsorption measurements. The BET surface area was determined by a multipoint BET method using the adsorption data in the relative pressure ( $P/P_0$ ) range of 0.05 to 0.30. Desorption isotherm was used to determine the pore size distribution via the Barret-Joyner-Halender (BJH) method, assuming a cylindrical pore modal [36]. The nitrogen adsorption volume at the relative pressure ( $P/P_0$ ) of 0.994 was used to determine the pore volume and average pore size. UV-visible absorbance spectra of Au-TiO<sub>2</sub> composite nanoparticles were obtained for the dry-pressed disk samples with a UV-visible spectrophotometer (UV-2550, Shimadzu, Japan).  $BaSO_4$  was used as a absorption standard in the UV-visible absorbance experiment. X-ray photoelectron spectroscopy (XPS) measurements were performed on a Kratos XSAM800 XPS system with  $Cu K\alpha$  source. During the experiments the pressure in the chambers was about  $10^{-7}$  Pa. All the binding energies were referenced to the C1s peak at 284.8 eV of the surface adventitious carbon.

**2.4. Analysis of Hydroxyl Radical ( $\bullet OH$ ).** The formation of hydroxyl radical ( $\bullet OH$ ) on the surface of photoirradiated Au-TiO<sub>2</sub> is detected by photoluminescence (PL) technique using terephthalic acid as a probe molecule. Terephthalic acid readily reacts with  $\bullet OH$  to produce highly fluorescent product, 2-hydroxyterephthalic acid [37, 38]. This technique has

been widely used in radiation chemistry, sonochemistry, and biochemistry [37–39] for the detection of  $\bullet\text{OH}$  generated in water. The intensity of the PL peak of 2-hydroxyterephthalic acid is in proportional to the amount of  $\bullet\text{OH}$  radicals produced in water [37–39]. The optimal concentration of terephthalic acid solution was about  $5 \times 10^{-4}$  M in a diluted NaOH aqueous solution ( $2 \times 10^{-3}$  M). This method relies on the PL signal at 425 nm of the hydroxylation of terephthalic acid with  $\bullet\text{OH}$  generated at the water/ $\text{TiO}_2$  interface. The method is rapid, sensitive, and specific, only needs a simple standard PL instrumentation.

In order to measure the concentration of hydroxyl radical ( $\bullet\text{OH}$ ) of the prepared samples, the typical experimental procedures are as follows Au- $\text{TiO}_2$  composite samples were weighed and then uniformly dispersed into 20 mL distilled water under 10 min ultrasonic shaking to form  $\text{TiO}_2$  suspension. The photocatalyst was prepared by coating the above aqueous suspension of  $\text{TiO}_2$  samples onto one dish with a diameter of about 9.0 cm. The weight of catalysts used for each experiment was kept 0.10 g. The dishes containing composite powders were dried in an oven at  $80^\circ\text{C}$  for about 2 h to evaporate the water and then cooled to room temperature before being used. A 20 mL of the  $5 \times 10^{-4}$  M terephthalic acid aqueous solution with a concentration of  $2 \times 10^{-3}$  M NaOH was added into the coated dish, which was then irradiated with a 15 W daylight lamp. In order to ensure only the visible light irradiation, each dish was covered with an ultraviolet cutoff filter ( $\lambda > 420$  nm). PL spectra of generated 2-hydroxyterephthalic acid were measured on a fluorescence spectrophotometer (F-7000, Hitachi, Japan) using a 315 nm excitation wavelength at a scan speed of  $1200 \text{ nm min}^{-1}$  with the PMT voltage of 700 V. The width of excitation slit and emission slit were 1.0 nm.

**2.5. Photocatalytic Activity.** The visible-light photocatalytic activity of the Au- $\text{TiO}_2$  composite samples was evaluated by photocatalytic decolorization of RhB aqueous solution. The detailed procedure was similar to our previous works [40]. Here, the weight of the photocatalyst used was kept at about 0.1 g. A 15 W daylight lamp (6 cm above the dishes, just mentioned above) was used as a light source and each dish was covered with an ultraviolet cutoff filter. The absorbance of RhB was determined by a UV-visible spectrophotometer (UV2550, Shimadzu, Japan). The concentration of RhB ( $c$ ) was in proportion to the light absorbance ( $A$ ) at 550 nm according to Beer-Lambert law. As for the Rhodamine-B aqueous with a concentration of  $1 \times 10^{-5}$  M, its photocatalytic decolorization is a pseudofirst-order reaction and its kinetics may be expressed as [41, 42]:

$$\ln \frac{A_0}{A_t} = kt, \quad (1)$$

where  $k$  is the apparent rate constant, and  $A_0$  and  $A_t$  are the initial and reaction absorbance of RhB aqueous, respectively.

### 3. Results and Discussion

**3.1. Phase Structures.** XRD was used to investigate the changes of phase structure of the as-prepared Au- $\text{TiO}_2$  nano-

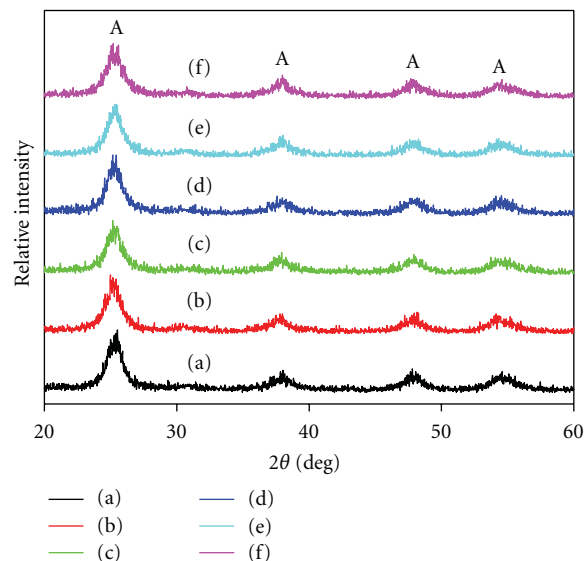


FIGURE 1: XRD patterns of the Au- $\text{TiO}_2$  composite powders prepared with different  $R_{\text{Au}}$ : (a) 0, (b) 0.003, (c) 0.006, (d) 0.015, (e) 0.030, and (f) 0.060.

composites and pure  $\text{TiO}_2$ . Figure 1 shows the effects of  $R_{\text{Au}}$  on phase structures of the Au- $\text{TiO}_2$  composite powders. It can be seen that the diffraction peaks of all samples were indexed with the anatase phase of  $\text{TiO}_2$ , which was consistent with our previous work [35]. With increasing the  $R_{\text{Au}}$ , the intensities of anatase peaks steadily become weaker and the width of the diffraction peaks ( $2\theta = 25.3^\circ$ ) of anatase slightly became wider. This was probably due to the fact that Au nanoparticles suppress the crystallization of  $\text{TiO}_2$  xerogel powders. However, the XRD diffraction peaks of Au could not be seen in the Figure 1, which was attributed to the fact that the content of Au was so low that it could not be detected by XRD diffractometer.

The microstructure of the Au- $\text{TiO}_2$  composite powder was further studied by TEM and HRTEM. Figure 2(a) shows the TEM image of the  $R_{\text{Au}}=0.060$  composite sample. It can be observed from Figure 2(a) that the nanocrystallite appears as an agglomerated status, and mesoporous structures without a long-range order. The size of the primary particles estimated from the TEM image was about  $6 \pm 1$  nm, which was in accord with the value of crystallize size (6.0 nm) calculated from XRD pattern using the Scherrer equation (as shown in Table 1). Figure 2(b) shows the corresponding HRTEM image of the  $R_{\text{Au}}=0.060$  composite powder. Further observation shows that all the particles are crystallized as evidence from the well-resolved Au (111) (0.25 nm) and  $\text{TiO}_2$  (101) (0.35 nm) crystalline lattices as shown in the inset of Figure 2(b) [42–44].

Effects of the  $R_{\text{Au}}$  on the surface morphology of the prepared Au- $\text{TiO}_2$  composite powders were characterized by FESEM. Figure 3 illustrates FESEM images of all the Au- $\text{TiO}_2$  composite powders, indicating their nonuniform growth and particle size distribution in spherical morphology, which changed slightly with the different Au modification. This agglomeration process was attributed to Van der Waals

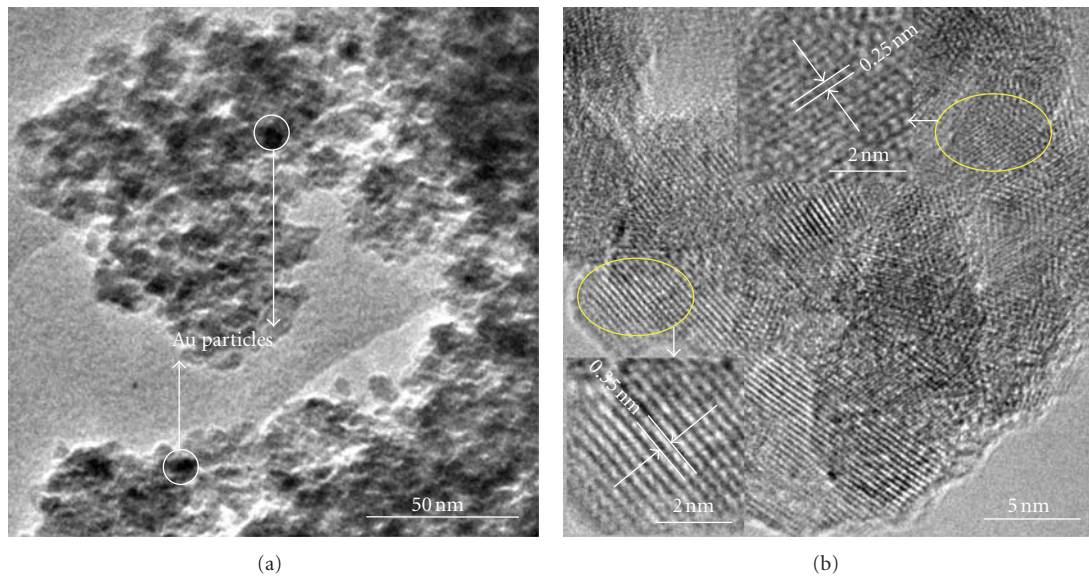


FIGURE 2: TEM (a) and HRTEM (b) images of the  $R_{Au}$ -0.060 composite powder.

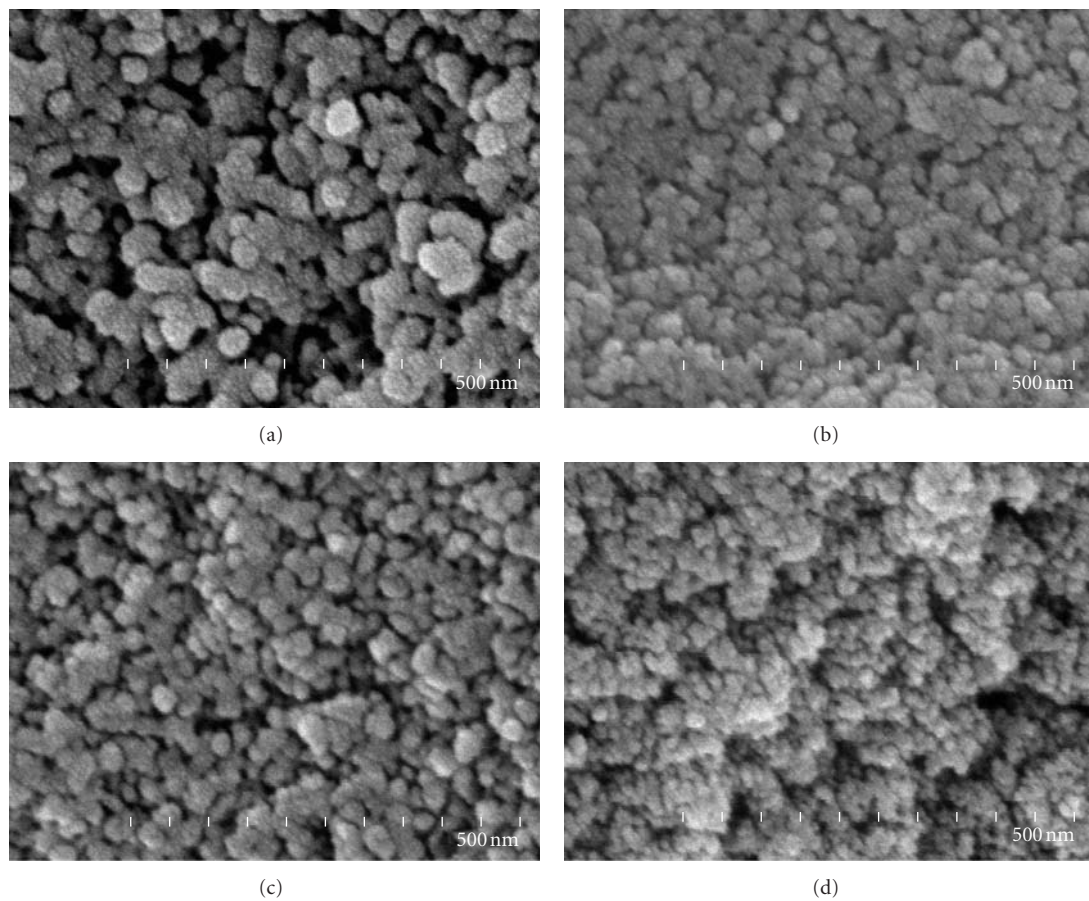


FIGURE 3: FESEM images of the Au-TiO<sub>2</sub> composite powders prepared with different  $R_{Au}$ : (a) 0, (b) 0.003, (c) 0.015, and (d) 0.060.

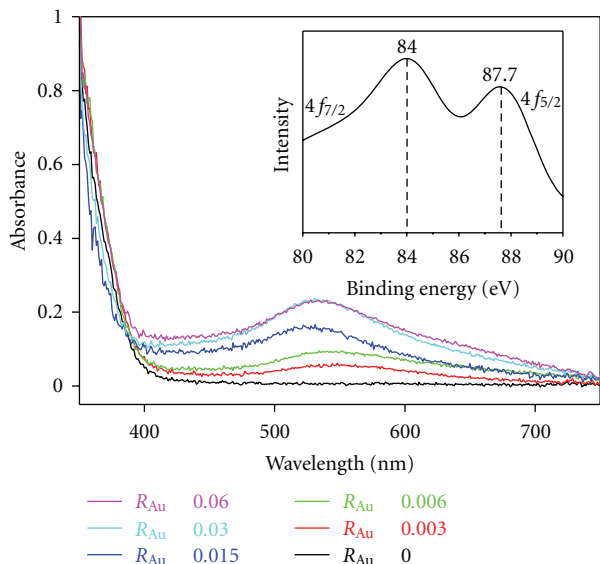


FIGURE 4: UV-Vis absorbance spectra of the Au-TiO<sub>2</sub> composite powders prepared with different  $R_{Au}$  and (inset) high-resolution XPS spectrum of Au 4f of the  $R_{Au}$ -0.060 sample.

forces. In order to reduce the surface energy, the primary particles have a tendency to form an agglomerate, by forming nearly spherical or equiaxed agglomerates, in a minimum surface-to-volume ratio and hence minimum surface free energy can be achieved. All the Au-TiO<sub>2</sub> composite powders are composed of such nanoscale particles, indicating that the composite powders prepared by this low-temperature spray method possess large specific surface area and the high volume fraction of atoms located both on the surface and at the grain boundaries. Therefore, this Au-TiO<sub>2</sub> composite nanocrystalline can provide more active sites for catalysis. Furthermore, all the Au-TiO<sub>2</sub> composite powders have roughness surface accompanied with many mesopores. In general, such nanoscale particles with such diameter will be more promising because light harvesting can be further enhanced. In this respect, nanocrystalline Au-TiO<sub>2</sub> composite particles with this special morphology can enhance the absorbance of the light resulting in the enhancement of photocatalytic activity. Further observations indicated that the powders without Au nanoparticles modification (pristine TiO<sub>2</sub>) have large particles. With increasing the  $R_{Au}$ , the average size of aggregated particles decreases.

**3.2. UV-Visible Absorbance Spectra.** Figure 4 shows UV-Vis absorbance spectra for the composite Au-TiO<sub>2</sub> samples. A significant increase at wavelengths longer than 400 nm could be attributed to the plasmon resonance absorbance of the Au nanoparticles [22, 44]. The Au-TiO<sub>2</sub> composite powders compared with the pristine TiO<sub>2</sub> powders have a slight red shift in the band gap transition. Moreover, a characteristic absorbance signal at 530 nm give the valid evidence that the Au phase existed in the products, though direct observation by XRD failed [24, 33, 45–47]. Further observation indicates that the intensity of the surface plasmon absorbance increase

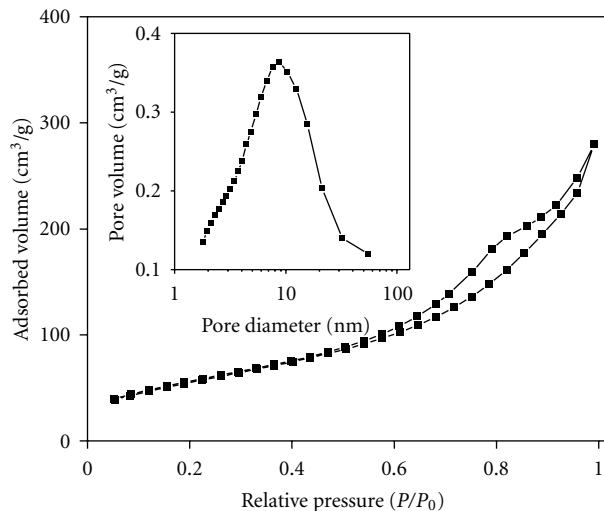
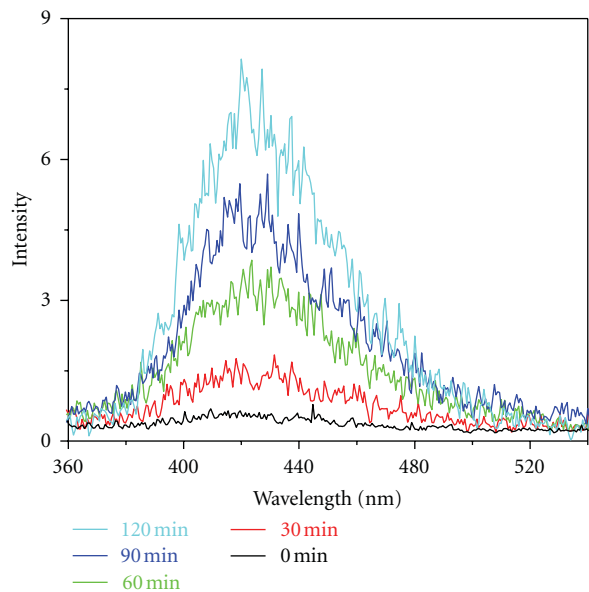


FIGURE 5: N<sub>2</sub> adsorption-desorption isotherm and pore size distribution curve (inset) of the  $R_{Au}$ -0.015 composite powder.

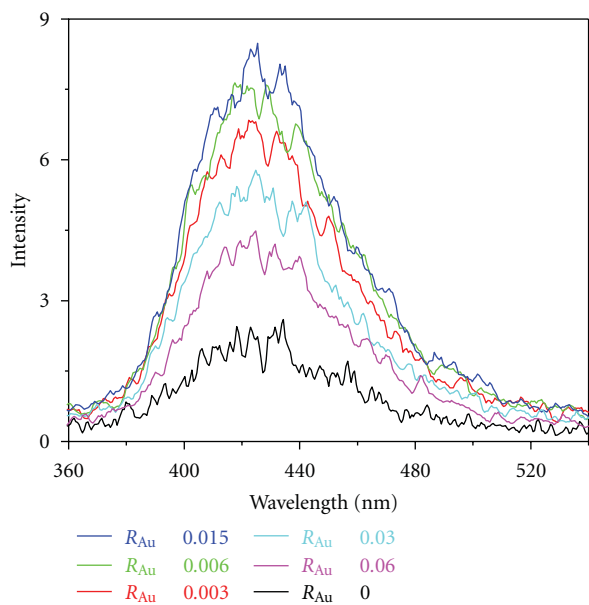
with increasing  $R_{Au}$ , which is probably due to the more Au nanoparticles embedded in TiO<sub>2</sub> aggregates. The enhanced light absorption in the visible light region can therefore increase the quantities of photogenerated electrons and holes that participate in photocatalytic reactions. In order to verify the chemical state of Au element in the Au-TiO<sub>2</sub> composite powders, the  $R_{Au}$ -0.060 sample was also characterized with XPS. High-resolution XPS spectrum (inset in Figure 4) shows binding energy of Au<sub>4f<sub>7/2</sub></sub> at 84.0 and Au<sub>4f<sub>5/2</sub></sub> at 87.7 eV, which are significantly different from Au<sub>4f<sub>7/2</sub></sub><sup>+</sup> (84.6 eV) and Au<sub>4f<sub>7/2</sub></sub><sup>3+</sup> (87.0 eV). The result suggests that the Au species is in the metallic state [25, 44, 48, 49].

**3.3. BET Specific Surface Areas and Pore Structure.** All the prepared Au-TiO<sub>2</sub> composite powders have similar nitrogen adsorption-desorption isotherms and pore size distribution curves. Therefore, Figure 5 only presents the nitrogen adsorption-desorption isotherm and pore size distribution (inset) of the  $R_{Au}$ -0.015 sample. It can be seen that isotherm was of types IV [36]. At high relative pressure range from 0.5 to 1.0, the isotherm exhibits a hysteresis loop of type H2 associated with the ink bottle pores, indicating that the powders contain mesopores due to the aggregation of crystallites [4–6]. The corresponding pore size distribution curve of the  $R_{Au}$ -0.015 sample is also shown in inset of Figure 5. It can be seen that the  $R_{Au}$ -0.015 sample exhibits a narrow pore size distribution with the average pore diameters about 5.7 nm.

Table 1 shows the effects of  $R_{Au}$  on the physical properties of the Au-TiO<sub>2</sub> composite powders. It can be seen that all the prepared samples possess large specific surface area ( $S_{BET} > 200$  m<sup>2</sup>/g) and big pore volume ( $V_p > 0.30$  cm<sup>3</sup>/g). With increasing  $R_{Au}$ , the average pore sizes decrease from 8.1 to 5.4 nm while the specific surface area and pore volume change slightly. Generally, the heterogeneous photocatalysis is a surface-based process, and therefore a large surface area has positive effects on such a process. A larger surface



(a)



(b)

FIGURE 6: (a) Fluorescence spectral changes with irradiation time on  $R_{Au}$ -0.015 sample and (b) the dependence of the fluorescence intensity on  $R_{Au}$  at a fixed 120 min under visible-light irradiation.

area provides more surface active sites for the adsorption of reactant molecules, which thus make the photocatalytic process more efficient [50–53]. Moreover, the porous structure is believed to facilitate the transporting of reactant molecules and products through the interior space due to the interconnected porous networks, and it favors the harvesting of exciting light due to enlarged surface area and multiple scattering within the porous framework [54–56].

**3.4. Hydroxyl Radical Analysis.** The PL emission spectrum excited at 315 nm of terephthalic acid solution was measured

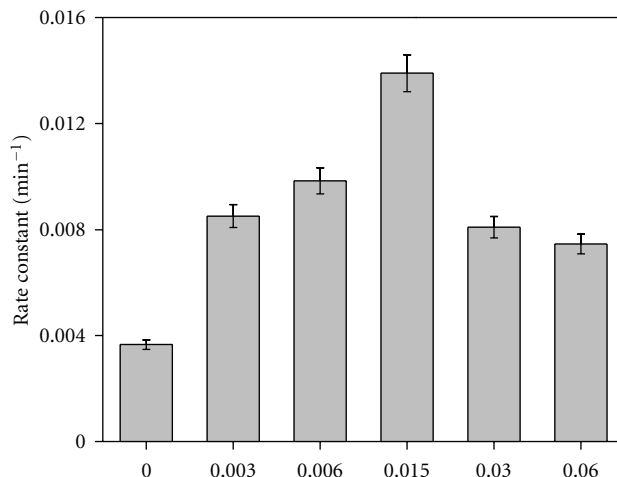


FIGURE 7: Dependence of apparent rate constants ( $k$ ) of the Au-TiO<sub>2</sub> composite samples on the  $R_{Au}$ .

every 30 min under visible-light irradiation. Figure 6(a) shows the changes of PL spectra of terephthalic acid solution with irradiation time. It can be seen that a gradual increase in PL intensity at wavelength range of 360–540 nm is observed with increasing irradiation time. Moreover, the generated spectra have the identical shape and peak position (at 425 nm). However, no PL increase is observed in the absence of visible-light or TiO<sub>2</sub> samples. This suggests that the signal of PL is only caused by the reaction of terephthalic acid with •OH formed on the interface of the Au-TiO<sub>2</sub>/water during visible-light irradiation [37, 38].

Generally, the greater the formation rate of •OH radicals is, the higher separation efficiency of electron-hole pairs is achieved. So, the photocatalytic activity is in positive correlation to the formation rate of •OH radicals, namely, a faster formation rate of •OH radicals leads to a higher photocatalytic activity [38]. Figure 6(b) shows the dependence of PL intensity against irradiation time. It can be easily seen that at a fixed time (120 min), the formation rate of •OH radicals on the Au-TiO<sub>2</sub> composite powders is larger than that of the pristine TiO<sub>2</sub>. This implies that the Au-TiO<sub>2</sub> composite powders have higher photocatalytic activity than the pristine TiO<sub>2</sub>. Further observation shows that the order of the formation rate of •OH radicals formed on the surface of as-prepared samples is as follows:  $R_{Au}$ -0.015 >  $R_{Au}$ -0.006 >  $R_{Au}$ -0.003 >  $R_{Au}$ -0.030 >  $R_{Au}$ -0.060 >  $R_{Au}$ -0 (pristine TiO<sub>2</sub>), which suggests that the  $R_{Au}$  influences the formation rate of •OH radicals and there is an optimum ratio of Au to TiO<sub>2</sub>.

**3.5. Photocatalytic Activity of the Au-TiO<sub>2</sub> Composite Powders.** The photocatalytic activity of the Au-TiO<sub>2</sub> composite powders was evaluated by photocatalytic decolorization of Rhodamine-B aqueous solution under visible-light irradiation ( $\lambda > 420$  nm) at room temperature. Figure 7 shows the relationship between the apparent rate constants ( $k$ ) and  $R_{Au}$ . It can be seen that the  $R_{Au}$  has a great effect on the photocatalytic activity of the composite samples. Without

TABLE 1: Effects of  $R_{Au}$  on physical properties of the Au-TiO<sub>2</sub> composite powders.

Sample ( $R_{Au}$ )	Phase content	<sup>a</sup> Crystalline size/nm	<sup>b</sup> $S_{BET}$ m <sup>2</sup> /g	<sup>c</sup> $V_p$ cm <sup>3</sup> /g	<sup>c</sup> Porosity (%)	<sup>c</sup> Average pore size/nm
0	Anatase	6.7	235.5	0.57	69.0	8.1
0.003	Anatase	6.7	208.4	0.46	64.2	7.5
0.006	Anatase	6.5	211.7	0.34	57.0	7.1
0.015	Anatase	6.5	205.0	0.43	62.6	5.7
0.030	Anatase	6.3	215.9	0.38	59.7	5.8
0.060	Anatase	6.0	212.4	0.34	57.0	5.4

<sup>a</sup>: Average crystalline size of TiO<sub>2</sub> was determined on the basis of the broadening of the anatase {101} diffraction peak using the Scherrer equation.

<sup>b</sup>: The BET surface area was determined by multipoint BET method using the adsorption data in the relative pressure ( $P/P_0$ ) range of 0.05–0.2.

<sup>c</sup>: Pore volume, porosity, and average pore size were determined by nitrogen adsorption volume at the relative pressure of 0.994.

Au modification, the prepared pristine TiO<sub>2</sub> powders have the poor visible-light photocatalytic activity presumably due to the self-sensitization of RhB molecules, which extends the absorption of titania into the visible-light region [57]. Importantly, the photocatalytic activity of all Au-TiO<sub>2</sub> samples is higher than that of pristine TiO<sub>2</sub>. Further observation shows the reaction rate increases with the increasing of Au content when the value of  $R_{Au}$  is below 0.015, and the  $R_{Au}$ -0.015 sample has the best photocatalytic activity among these samples. Therefore, the appropriate modification of the gold nanoparticles can enhance the photocatalytic activity of TiO<sub>2</sub> remarkably, which is ascribed to the synergetic effect of the dye-photosensitized and the surface plasmon resonance of Au nanoparticles in the Au-TiO<sub>2</sub> nanocomposites.

The possible photocatalytic enhanced mechanism of the Au-TiO<sub>2</sub> nanocomposite powders can be explained according to the recently reported mechanism [4, 15, 22, 47]. The noble metal nanoparticles can be photoexcited by the visible light due to their plasmon resonance. Under visible-light irradiation, the electrons and holes can be formed on the surface of the Au nanoparticles, and then they are immediately separated via the following processes. The electrons transfer to the adsorbed oxygen molecules via the conduction band of TiO<sub>2</sub> and then are trapped through formation of superoxide radical anions. The superoxide radicals and the trapped electrons can combine to produce H<sub>2</sub>O<sub>2</sub>, finally forming hydroxyl radicals. Both hydroxyl radical and superoxide radical anions are strong oxidants which can oxidize the organic molecules (RhB) on the surface of the composite powders, resulting in the formation of intermediate organic species and subsequently complete oxidation of these species to water and carbon dioxide. These improvements would be beneficial to the photooxidation of RhB using the Au modified TiO<sub>2</sub> under visible-light irradiation. When the  $R_{Au}$  reaches 0.030, the Au-TiO<sub>2</sub> composite powders show relatively lower photocatalytic activity, which is probably due to the fact that more Au nanoparticles may act as the centers of electron-hole recombination and reduce quantum efficiency [44].

Figure 8 shows the change of absorption spectra of RhB aqueous solution during its visible-light photocatalytic decolorization using the  $R_{Au}$ -0.015 sample as the photocatalyst. It can be seen that the absorption peak at  $\lambda = 550$  nm drops gradually with increasing visible-light irradiation time. After visible-light irradiation for ca. 180 minutes, the absorp-

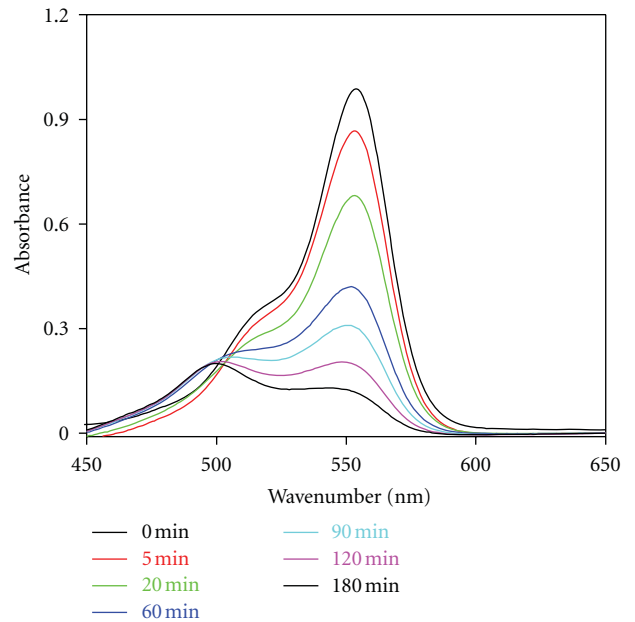


FIGURE 8: The dependence of absorbance ( $A$ ) of RhB aqueous solution on the visible-light irradiation time.

tion peak of RhB aqueous solution is very weak and the color of the RhB aqueous solution changes from orange to near no color, indicating that the Au-TiO<sub>2</sub> composite powders can completely decolorize RhB aqueous solution under visible-light irradiation. Usually, the complete decolorization of RhB requires a long time due to the fact that its decolorization goes through two different stages: the ring cleavage in the initial photocatalytic degradation stage and subsequent oxidation of the fragments in the latter stage [40, 58]. Therefore, these composite powders prepared by this method could be useful for environmental applications such as air purification, water disinfection and purification, and hazardous waste remediation due to their cheap preparation process, controllable structure, large specific surface area, and high visible-light photocatalytic activity.

#### 4. Conclusions

Au-TiO<sub>2</sub> nanocomposites can be facily prepared by a simple spray hydrolytic method and assisted with photoreduction technique at 90°C. The light absorption, the

formation rates of hydroxyl radicals, and photocatalytic decolorization of RhB aqueous solution were significantly enhanced by those embedded Au nanoparticles in the Au-TiO<sub>2</sub> nanocomposites due to surface plasmon resonance of Au nanoparticles. The composite  $R_{Au}$ -0.015 sample exhibited the best visible-light photocatalytic activity for photocatalytic decolorization of RhB aqueous solution due to the synergistic effects of the absorption shift into visible and improved efficiency of interfacial charge transfer process.

## Acknowledgments

This paper was partially supported by the National Natural Science Foundation of China (51072154 and 51102190), Natural Science Foundation of Hubei Province (2010CDA078), National Basic Research Program of China (2009CB939704), and Self-determined and Innovative Research Funds of SKLWUT. This paper was also supported by the Key Science Research Project of the Hubei Provincial Department of Education (D20112107) and the Science Research Project of Hubei University of Medicine (2009QDJ25).

## References

- [1] A. Fujishima and K. Honda, "Electrochemical photolysis of water at a semiconductor electrode," *Nature*, vol. 238, no. 5358, pp. 37–38, 1972.
- [2] M. A. Fox and M. T. Dulay, "Heterogeneous photocatalysis," *Chemical Reviews*, vol. 93, no. 1, pp. 341–357, 1993.
- [3] M. R. Hoffmann, S. T. Martin, W. Choi, and D. W. Bahnemann, "Environmental applications of semiconductor photocatalysis," *Chemical Reviews*, vol. 95, no. 1, pp. 69–96, 1995.
- [4] J. Zhou, Y. Cheng, and J. Yu, "Preparation and characterization of visible-light-driven plasmonic photocatalyst Ag/AgCl/TiO<sub>2</sub> nanocomposite thin films," *Journal of Photochemistry and Photobiology A*, vol. 223, no. 2-3, pp. 82–87, 2011.
- [5] J. Yu, T. Ma, and S. Liu, "Enhanced photocatalytic activity of mesoporous TiO<sub>2</sub> aggregates by embedding carbon nanotubes as electron-transfer channel," *Physical Chemistry Chemical Physics*, vol. 13, no. 8, pp. 3491–3501, 2011.
- [6] J. Yu, Y. Su, and B. Cheng, "Template-free fabrication and enhanced photocatalytic activity of hierarchical macro-/mesoporous titania," *Advanced Functional Materials*, vol. 17, no. 12, pp. 1984–1990, 2007.
- [7] S. Wang, L. Zhao, J. Ran, Z. Shu, G. Dai, and P. Zhai, "Effects of calcination temperatures on photocatalytic activity of ordered titanate nanoribbon/SnO<sub>2</sub> films fabricated during an EPD process," *International Journal of Photoenergy*, vol. 2012, Article ID 472958, 7 pages, 2012.
- [8] H. Fu, G. Shang, S. Yang, and T. Xu, "Mechanistic study of visible-light-induced photodegradation of 4-chlorophenol by TiO<sub>2-x</sub>N<sub>x</sub> (0.021 <  $x$  < 0.049) with low nitrogen concentration," *International Journal of Photoenergy*, vol. 2012, Article ID 759306, 9 pages, 2012.
- [9] S.-J. Kim, N.-H. Lee, H.-J. Oh, S.-C. Jung, W.-J. Lee, and D.-H. Kim, "Photocatalytic properties of nanotubular-shaped TiO<sub>2</sub> powders with anatase phase obtained from titanate nanotube powder through various thermal treatments," *International Journal of Photoenergy*, vol. 2011, Article ID 327821, 7 pages, 2011.
- [10] J. A. Byrne, P. A. Fernandez-Ibañez, P. S. M. Dunlop, D. M. A. Alrousan, and J. W. J. Hamilton, "Photocatalytic enhancement for solar disinfection of water: a review," *International Journal of Photoenergy*, vol. 2011, Article ID 798051, 12 pages, 2011.
- [11] W.-C. Oh and M.-L. Chen, "The improved photocatalytic properties of methylene blue for V<sub>2</sub>O<sub>5</sub>/CNT/TiO<sub>2</sub> composite under visible light," *International Journal of Photoenergy*, vol. 2010, Article ID 264831, 5 pages, 2010.
- [12] Z. Zhang and J. Gamage, "Applications of photocatalytic disinfection," *International Journal of Photoenergy*, vol. 2010, Article ID 764870, 11 pages, 2010.
- [13] T. Hirakawa and P. V. Kamat, "Charge separation and catalytic activity of Ag@TiO<sub>2</sub> core-shell composite clusters under UV-irradiation," *Journal of the American Chemical Society*, vol. 127, no. 11, pp. 3928–3934, 2005.
- [14] P. Mulvaney, "Surface plasmon spectroscopy of nanosized metal particles," *Langmuir*, vol. 12, no. 3, pp. 788–800, 1996.
- [15] Q. Xiang, J. Yu, B. Cheng, and H. C. Ong, "Microwave-hydrothermal preparation and visible-light photoactivity of plasmonic photocatalyst Ag-TiO<sub>2</sub> nanocomposite hollow spheres," *Chemistry—An Asian Journal*, vol. 5, no. 6, pp. 1466–1474, 2010.
- [16] B. Cheng, Y. Le, and J. Yu, "Preparation and enhanced photocatalytic activity of Ag@TiO<sub>2</sub> core-shell nanocomposite nanowires," *Journal of Hazardous Materials*, vol. 177, no. 1–3, pp. 971–977, 2010.
- [17] J. J. Mock, M. Barbic, D. R. Smith, D. A. Schultz, and S. Schultz, "Shape effects in plasmon resonance of individual colloidal silver nanoparticles," *Journal of Chemical Physics*, vol. 116, no. 15, pp. 6755–6759, 2002.
- [18] R. Jin, Y. C. Cao, E. Hao, G. S. Métraux, G. C. Schatz, and C. A. Mirkin, "Controlling anisotropic nanoparticle growth through plasmon excitation," *Nature*, vol. 425, no. 6957, pp. 487–490, 2003.
- [19] F. Kim, J. H. Song, and P. Yang, "Photochemical synthesis of gold nanorods," *Journal of the American Chemical Society*, vol. 124, no. 48, pp. 14316–14317, 2002.
- [20] M. Jakob, H. Levanon, and P. V. Kamat, "Charge distribution between UV-irradiated TiO<sub>2</sub> and gold nanoparticles: determination of shift in the Fermi level," *Nano Letters*, vol. 3, no. 3, pp. 353–358, 2003.
- [21] V. Subramanian, E. E. Wolf, and P. V. Kamat, "Catalysis with TiO<sub>2</sub>/gold nanocomposites. Effect of metal particle size on the fermi level equilibration," *Journal of the American Chemical Society*, vol. 126, no. 15, pp. 4943–4950, 2004.
- [22] Y. Tian and T. Tatsuma, "Mechanisms and applications of plasmon-induced charge separation at TiO<sub>2</sub> films loaded with gold nanoparticles," *Journal of the American Chemical Society*, vol. 127, no. 20, pp. 7632–7637, 2005.
- [23] L. Xiao, J. Zhang, Y. Cong, B. Tian, F. Chen, and M. Anpo, "Synergistic effects of doped Fe(3+) and deposited Au on improving the photocatalytic activity of TiO<sub>2</sub>," *Catalysis Letters*, vol. 111, no. 3-4, pp. 207–211, 2006.
- [24] R. S. Sonawane and M. K. Dongare, "Sol-gel synthesis of Au/TiO<sub>2</sub> thin films for photocatalytic degradation of phenol in sunlight," *Journal of Molecular Catalysis A*, vol. 243, no. 1, pp. 68–76, 2006.
- [25] V. Iliev, D. Tomova, L. Bilyarska, and G. Tyuliev, "Influence of the size of gold nanoparticles deposited on TiO<sub>2</sub> upon the photocatalytic destruction of oxalic acid," *Journal of Molecular Catalysis A*, vol. 263, no. 1-2, pp. 32–38, 2007.
- [26] F. B. Li, X. Z. Li, and M. F. Hou, "Photocatalytic degradation of 2-mercaptobenzothiazole in aqueous La<sup>3+</sup>-TiO<sub>2</sub> suspension

- for odor control,” *Applied Catalysis B*, vol. 48, no. 3, pp. 185–194, 2004.
- [27] D. I. Enache, J. K. Edwards, P. Landon et al., “Solvent-free oxidation of primary alcohols to aldehydes using Au-Pd/TiO<sub>2</sub> catalyst,” *Science*, vol. 311, no. 5759, pp. 362–365, 2006.
- [28] F. Boccuzzi, A. Chiorino, M. Manzoli et al., “Au/TiO<sub>2</sub> nanosized samples: a catalytic, TEM, and FTIR study of the effect of calcination temperature on the CO oxidation,” *Journal of Catalysis*, vol. 202, no. 2, pp. 256–267, 2001.
- [29] M. Daté and M. Haruta, “Moisture effect on CO oxidation over Au/TiO<sub>2</sub> catalyst,” *Journal of Catalysis*, vol. 201, no. 2, pp. 221–224, 2001.
- [30] X. Z. Li and F. B. Li, “Study of Au/Au<sup>3+</sup>-TiO<sub>2</sub> photocatalysts toward visible photooxidation for water and wastewater treatment,” *Environmental Science and Technology*, vol. 35, no. 11, pp. 2381–2387, 2001.
- [31] N. Lopez, J. K. Nørskov, T. V. W. Janssens et al., “The adhesion and shape of nanosized Au particles in a Au/TiO<sub>2</sub> catalyst,” *Journal of Catalysis*, vol. 225, no. 1, pp. 86–94, 2004.
- [32] I. M. Arabatzis, T. Stergiopoulos, D. Andreeva, S. Kitova, S. G. Neophytides, and P. Falaras, “Characterization and photocatalytic activity of Au/TiO<sub>2</sub> thin films for azo-dye degradation,” *Journal of Catalysis*, vol. 220, no. 1, pp. 127–135, 2003.
- [33] V. Subramanian, E. E. Wolf, and P. V. Kamat, “Influence of metal/metal ion concentration on the photocatalytic activity of TiO<sub>2</sub>—Au composite nanoparticles,” *Langmuir*, vol. 19, no. 2, pp. 469–474, 2003.
- [34] M. Epifani, C. Giannini, L. Tapfer, and L. Vasanelli, “Sol-gel synthesis and characterization of Ag and Au nanoparticles in SiO<sub>2</sub>, TiO<sub>2</sub>, and ZrO<sub>2</sub> thin films,” *Journal of the American Ceramic Society*, vol. 83, no. 10, pp. 2385–2393, 2000.
- [35] M. Zhou, J. Yu, S. Liu, P. Zhai, and B. Huang, “Spray-hydrolytic synthesis of highly photoactive mesoporous anatase nanospheres for the photocatalytic degradation of toluene in air,” *Applied Catalysis B*, vol. 89, no. 1–2, pp. 160–166, 2009.
- [36] K. S. Sing, D. H. Everett, R. A. W. Haul et al., “Reporting physisorption data for gas/solid systems,” *Pure and Applied Chemistry*, vol. 57, no. 4, pp. 603–619.
- [37] J. Yu, W. Wang, B. Cheng, and B. L. Su, “Enhancement of photocatalytic activity of Mesoporous TiO<sub>2</sub> powders by hydrothermal surface fluorination treatment,” *Journal of Physical Chemistry C*, vol. 113, no. 16, pp. 6743–6750, 2009.
- [38] J. Yu, Q. Xiang, and M. Zhou, “Preparation, characterization and visible-light-driven photocatalytic activity of Fe-doped titania nanorods and first-principles study for electronic structures,” *Applied Catalysis B*, vol. 90, no. 3–4, pp. 595–602, 2009.
- [39] K. I. Ishibashi, A. Fujishima, T. Watanabe, and K. Hashimoto, “Detection of active oxidative species in TiO<sub>2</sub> photocatalysis using the fluorescence technique,” *Electrochemistry Communications*, vol. 2, no. 3, pp. 207–210, 2000.
- [40] J. Yu and X. Yu, “Hydrothermal synthesis and photocatalytic activity of zinc oxide hollow spheres,” *Environmental Science and Technology*, vol. 42, no. 13, pp. 4902–4907, 2008.
- [41] M. Zhou, J. Yu, S. Liu, P. Zhai, and L. Jiang, “Effects of calcination temperatures on photocatalytic activity of SnO<sub>2</sub>/TiO<sub>2</sub> composite films prepared by an EPD method,” *Journal of Hazardous Materials*, vol. 154, no. 1–3, pp. 1141–1148, 2008.
- [42] H. Takahashi, I. Harrowfield, C. MacRae, N. Wilson, and K. Tsutsumi, “Analytical TEM study on the dispersion of Au nanoparticles in Au/TiO<sub>2</sub> catalyst prepared under various temperatures,” *Surface and Interface Analysis*, vol. 31, no. 2, pp. 73–78, 2001.
- [43] T. Akita, K. Tanaka, S. Tsubota, and M. Haruta, “Analytical high-resolution TEM study of supported gold catalysts: orientation relationship between Au particles and TiO<sub>2</sub> supports,” *Journal of Electron Microscopy*, vol. 49, no. 5, pp. 657–662, 2000.
- [44] J. Yu, L. Yue, S. Liu, B. Huang, and X. Zhang, “Hydrothermal preparation and photocatalytic activity of mesoporous Au-TiO<sub>2</sub> nanocomposite microspheres,” *Journal of Colloid and Interface Science*, vol. 334, no. 1, pp. 58–64, 2009.
- [45] J. Yu, J. Xiong, B. Cheng, and S. Liu, “Fabrication and characterization of Ag-TiO<sub>2</sub> multiphase nanocomposite thin films with enhanced photocatalytic activity,” *Applied Catalysis B*, vol. 60, no. 3–4, pp. 211–221, 2005.
- [46] J. Yu, H. Tao, and B. Cheng, “In situ monitoring of heterogeneous catalytic reactions,” *ChemPhysChem*, vol. 11, no. 8, pp. 1617–1618, 2010.
- [47] J. Yu, G. Dai, and B. Huang, “Fabrication and characterization of visible-light-driven plasmonic photocatalyst Ag/AgCl/TiO<sub>2</sub> nanotube arrays,” *Journal of Physical Chemistry C*, vol. 113, no. 37, pp. 16394–16401, 2009.
- [48] T. Diemant, Z. Zhao, H. Rauscher, J. Bansmann, and R. J. Behm, “Interaction of CO with planar Au/TiO<sub>2</sub> model catalysts at elevated pressures,” *Topics in Catalysis*, vol. 44, no. 1–2, pp. 83–93, 2007.
- [49] A. Zwijnenburg, A. Goossens, W. G. Sloof et al., “XPS and Mössbauer characterization of Au/TiO<sub>2</sub> propene epoxidation catalysts,” *Journal of Physical Chemistry B*, vol. 106, no. 38, pp. 9853–9862, 2002.
- [50] Y. Zhang, G. Li, Y. Wu, Y. Luo, and L. Zhang, “The formation of mesoporous TiO<sub>2</sub> spheres via a facile chemical process,” *Journal of Physical Chemistry B*, vol. 109, no. 12, pp. 5478–5481, 2005.
- [51] Z. Liu, D. D. Sun, P. Guo, and J. O. Leckie, “One-step fabrication and high photocatalytic activity of porous TiO<sub>2</sub> hollow aggregates by using a low-temperature hydrothermal method without templates,” *Chemistry*, vol. 13, no. 6, pp. 1851–1855, 2007.
- [52] Q. Li, B. Guo, J. Yu et al., “Highly efficient visible-light-driven photocatalytic hydrogen production of CdS-cluster-decorated graphene nanosheets,” *Journal of the American Chemical Society*, vol. 133, no. 28, pp. 10878–10884, 2011.
- [53] Q. Xiang, J. Yu, and M. Jaroniec, “Enhanced photocatalytic H<sub>2</sub>-production activity of graphene-modified titania nanosheets,” *Nanoscale*, vol. 3, no. 9, pp. 3670–3678, 2011.
- [54] R. K. Rana, Y. Mastai, and A. Gedanken, “Acoustic cavitation leading to the morphosynthesis of mesoporous silica vesicles,” *Advanced Materials*, vol. 14, no. 19, pp. 1414–1418, 2002.
- [55] P. Madhusudan, J. Ran, J. Zhang, J. Yu, and G. Liu, “Novel urea assisted hydrothermal synthesis of hierarchical BiVO<sub>4</sub>/Bi<sub>2</sub>O<sub>3</sub>CO<sub>3</sub> nanocomposites with enhanced visible-light photocatalytic activity,” *Applied Catalysis B*, vol. 110, pp. 286–295, 2011.
- [56] J. Yu, L. Zhang, B. Cheng, and Y. Su, “Hydrothermal preparation and photocatalytic activity of hierarchically sponge-like macro-/mesoporous Titania,” *Journal of Physical Chemistry C*, vol. 111, no. 28, pp. 10582–10589, 2007.
- [57] Q. Xiang, J. Yu, and M. Jaroniec, “Nitrogen and sulfur codoped TiO<sub>2</sub> nanosheets with exposed 001 facets: synthesis, characterization and visible-light photocatalytic activity,” *Physical Chemistry Chemical Physics*, vol. 13, no. 11, pp. 4853–4861, 2011.

- [58] H. Fu, C. Pan, W. Yao, and Y. Zhu, "Visible-light-induced degradation of rhodamine B by nanosized  $\text{Bi}_2\text{WO}_6$ ," *Journal of Physical Chemistry B*, vol. 109, no. 47, pp. 22432–22439, 2005.

## Research Article

# Photocatalytic Degradation of NO<sub>x</sub> Using Ni-Containing TiO<sub>2</sub>

Yao-Hsuan Tseng and Bo-Kai Huang

*Department of Chemical Engineering, National Taiwan University of Science and Technology, Taipei 106, Taiwan*

Correspondence should be addressed to Yao-Hsuan Tseng, tyh@mail.ntust.edu.tw

Received 15 August 2011; Revised 28 October 2011; Accepted 28 October 2011

Academic Editor: Jiaguo Yu

Copyright © 2012 Y.-H. Tseng and B.-K. Huang. This is an open access article distributed under the Creative Commons Attribution License, which permits unrestricted use, distribution, and reproduction in any medium, provided the original work is properly cited.

The nickel-containing titania was synthesized and employed in the photomineralization of NO<sub>x</sub>. A nickel-modified titania photocatalyst was prepared by photodeposition method with using Degussa-P25 TiO<sub>2</sub> particle and nickel chloride as raw materials, respectively. The physical analyses were carried out using X-ray photoelectron spectroscopy (XPS), X-ray diffraction (XRD), transmittance electron microscope (TEM), and photoluminescence spectroscopy (PL), to observe changes in particles following nickel modification. The results showed that Ni does not enter into the TiO<sub>2</sub> crystal lattice and is dispersed onto the TiO<sub>2</sub> surface uniformly. Ni improved the intensity of PL spectra with an appropriate Ni content on the TiO<sub>2</sub> surface. The modified titanium dioxide with 0.1 mol% of nickel exhibited two times the NO<sub>x</sub>-removal activity of bare TiO<sub>2</sub> under ultraviolet illumination. The nickel content in this photodeposition process plays an important role in affinity to NO<sub>x</sub> molecules, recombination rate of electron-hole pair, and content of active site on the TiO<sub>2</sub> surface and therefore affects the optical and photocatalytic properties.

## 1. Introduction

Since the discovery of the photoelectrochemical splitting of water using titanium dioxide electrodes [1–3], researchers have extensively studied semiconductor-based photocatalysis. Today, titanium dioxide is a representative photocatalyst material, due to its powerful redox properties and wide range of applications, such as air purification, water purification, deodorization, self-cleaning surfaces, antibacterial coating, and so forth [1, 4–7].

The photocatalytic capacity of TiO<sub>2</sub> powder heavily depends on its microstructure and physical properties, which are in turn determined by the preparation conditions [8–10]. Several attempts have been made to increase the photodegradation efficiency of TiO<sub>2</sub>, by either noble metal deposition or ion doping [11–14]. For example, Pt-doped, N-doped, C-doped, and S-doped TiO<sub>2</sub> are applied as visible-light-responsive photocatalysts [1, 12–14], and cocatalysts and co-adsorbents, such as Ag, Au, activated carbon, and carbon nanotubes (CNTs) [10, 15–17], are used for the improvement of photocatalytic activity under UV illumination. However, in developing their widespread use for any practical application, the cost and stability of the material must be considered first. The anion and noble metal dopants do not have much practicability due to their insufficient

stability, complicated preparation process, and expensive raw material. In contrast, transition metal cations have been found to be applied dopants and cocatalysts for the improvement of photocatalytic activity [18–24]. Some researchers report that the Ni<sup>2+</sup> ion dopant improves the photocatalytic activity of certain semiconductor photocatalyst because the existence of Ni<sup>2+</sup> suppresses recombination of electron-hole pair on the TiO<sub>2</sub> surface [18–20]. However, the raw material and processes of these previous works, such as organic precursors, sol-gel, and ion-implantation methods [18–22], are not inexpensive enough for mass production. Herein, we present a facile and cost-effective method for the preparation of highly active nickel-containing TiO<sub>2</sub> developed using TiO<sub>2</sub> particle and nickel chloride.

## 2. Experimental Details

**2.1. Preparation of Ni-TiO<sub>2</sub> Particle.** The nickel-containing, nanostructured TiO<sub>2</sub> particles were prepared by the photoreduction process by using nickel chloride and Degussa P25 as a nickel precursor and a pristine photocatalyst, respectively. Ni-TiO<sub>2</sub> was prepared by mixing 3 g of nonporous TiO<sub>2</sub> (Degussa P25), 50 mL of ethanol, and certain amount of NiCl<sub>2</sub>·6H<sub>2</sub>O in 200 mL of double-distilled water. The

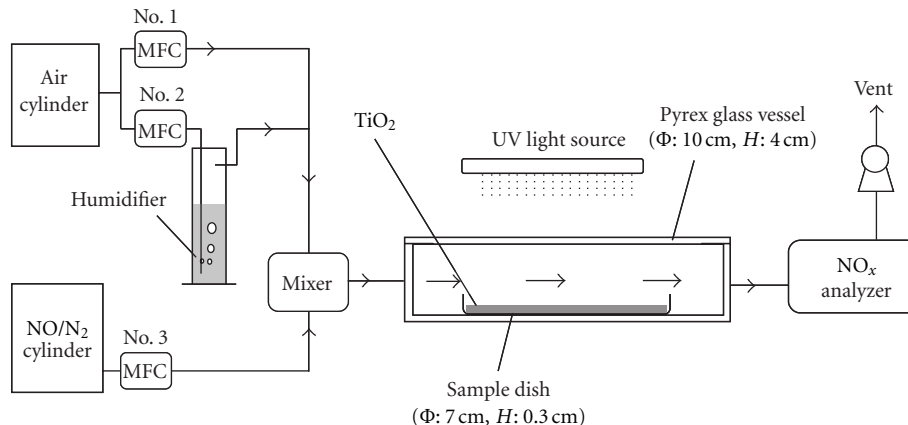


FIGURE 1: Schematic continuous flow reaction system for photocatalytic degradation of NO.

solution was well mixed by ultrasonic treatment for 1 h. The initial pH value was adjusted to 8 with 0.1 M of NaOH solution [23]. A nitrogen stream at the rate of 30 mL/min was continuously introduced into the reaction chamber to remove oxygen in the solution. The solution was then irradiated with four UVC lamps (Philips TUV 10 W/G10 T8) with an intensity of  $2 \text{ mW/cm}^2$  for 3 h. Ni ions were reduced to nickel metallic nanoparticles by the photo-generated electrons of  $\text{TiO}_2$ , then deposited on the surface of  $\text{TiO}_2$ . The Ni- $\text{TiO}_2$  particles were obtained by centrifugation at 10000 rpm, washing with DI water, and drying at 373 K for 12 h. Sample nomenclature was defined as follows:  $x\%$  Ni/ $\text{TiO}_2$  photocatalyst prepared by the photodeposition process with nickel content  $x$  mol%. The Ni/ $\text{TiO}_2$  molar ratios were controlled at 0, 0.05, 0.1, 0.2, 0.5, 1, 2, and 4%.

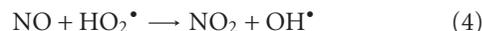
**2.2. Characterization.** The photocatalyst crystal phase was identified using X-ray diffraction with  $\text{Cu K}\alpha$  ( $\lambda = 0.154 \text{ nm}$ ) radiation (Shimadzu Rigaku D/Max RCXRD 6000). Average particle size and morphology was obtained by transmission electron microscopy (TEM, Hitachi S600-100 KV). The photoluminescence spectroscopy (PL) data were obtained on a luminescence spectrometer (Jasco FP-6500LE) under excitation with 325 nm irradiation. Material compositions were determined by X-ray photoelectron spectroscopy (Perkin Elmer SSI-M probe XPS system and S4800) and energy dispersion spectroscopy (Horiba, EX-210).

**2.3. Photocatalytic Activity.** Figure 1 depicted the continuous flow system used for  $\text{NO}_x$  degradation over  $\text{TiO}_2$ . A round-shaped Pyrex glass vessel ( $\phi \times H$ , 10 cm  $\times$  4 cm) was used as the photoreactor to conduct the degradation of  $\text{NO}_x$ , and a sample dish ( $\phi$ , 7 cm) was located inside the vessel containing the  $\text{TiO}_2$  powder. A black lamp provided a UV light source with an intensity of  $1 \text{ mW/cm}^2$  (Sankyo Denki FL 20SBLB, main peak located at 352 nm). The  $\text{NO}_x$  degradation was carried out at room temperature using an air stream containing 1.0 ppm NO as feedstock. Two mass flow controllers (MFCs) (Brooks 5850E) manipulated relative humidity (RH = 50%) in the feeding stream. The

reaction gas in the feeding stream passed through the vessel containing  $\text{TiO}_2$  powder (0.2 g) at a flow rate of 1 L/min. An on-line chemiluminescent  $\text{NO}_x$  analyzer (Eco Physics, CLD 700 AL) continuously monitored NO and  $\text{NO}_2$  concentrations for gas analysis in the outlet.

### 3. Results and Discussion

**3.1. Photocatalytic  $\text{NO}_x$  Degradation over Ni- $\text{TiO}_2$ .** Many researchers use NO oxidation to determine photocatalytic reactivity in various  $\text{TiO}_2$  photocatalytic applications [11–13, 15, 25]. The electron-hole pair ( $e^-$ - $h^+$ ) generated upon light excitation is trapped at the  $\text{TiO}_2$  surface as spatially separated redox-active sites. The general mechanism of  $\text{NO}_x$  oxidation by photocatalyst is as follows. Hydrogen ions and hydroxide ions are dissociated from water. The active oxygen species are produced on the  $\text{TiO}_2$  surface. The nitric monoxide is oxidized to nitric acid or nitrous acid by active oxygen species. Based on the gas-phase chemistry of  $\text{NO}_x$  [25, 26], NO is converted to  $\text{HNO}_3$  as a consecutive photooxidation via a  $\text{NO}_2$  intermediate:



Finally, the nitric acid forms on the catalyst. Photocatalyst activity will lessen as acid accumulates. To illustrate the reaction behavior of NO photocatalytic oxidation, 0.2 g of 0.1% Ni- $\text{TiO}_2$  and  $1 \text{ mW/cm}^2$  of light intensity were used to conduct the experiment. At first, a 1 ppm NO gas stream was introduced into the photoreactor under dark conditions. As shown in the Figure 2, in the beginning, the NO concentration in the gas phase dropped rapidly without

TABLE 1: The apparent quantum yields and selectivities of  $\text{NO}_2$  of various catalysts: catalyst loading: 0.2 g, intensity of irradiation:  $1 \text{ mW/cm}^2$ , inlet concentration of NO, 1 ppm, inlet flow rate, 1 L/min, relative humidity: 55%, reaction temperature,  $26^\circ \text{C}$ .

Catalyst	P25	0.05% Ni	0.1% Ni	0.2% Ni	0.5% Ni	1% Ni	4% Ni
$\Phi$ (%)	2.13	2.63	2.85	2.58	2.07	1.80	1.30
$\text{Sel.}_{\text{NO}_2}$ (%)	62.8	30.7	24.4	29.5	36.9	48.5	56.0

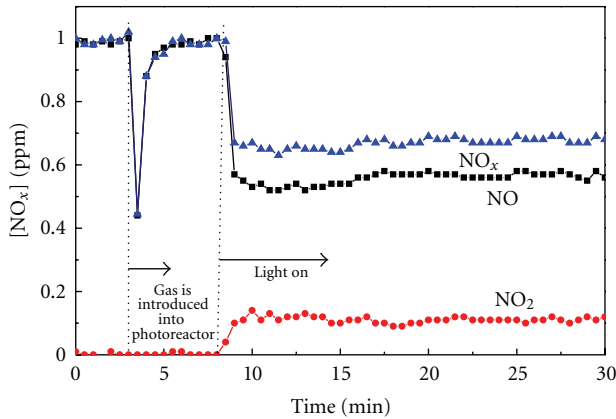


FIGURE 2: Time-course of the changes in concentration of NO,  $\text{NO}_2$ , and  $\text{NO}_x$  in the presence of 0.1% Ni-TiO<sub>2</sub> under UV light, reaction conditions as given in Table 1.

generation of  $\text{NO}_2$  due to NO adsorption on the  $\text{TiO}_2$ . A few minutes later (2–4 min), the NO was saturated on the  $\text{TiO}_2$  and in the photoreactor, and the NO concentration was thus returned to 1 ppm. The UV lamps were turned on to start this photocatalytic reaction. The steady state of this photocatalytic reaction was achieved as soon as the photocatalyst was illuminated. The NO concentration decreased from 1 to 0.57 ppm, and the  $\text{NO}_2$  concentration increased to 0.1 ppm. The  $\text{NO}_x$  concentration, which represents the accumulated mixture of NO and  $\text{NO}_2$ , was maintained at 0.67 ppm under UV illumination. The activities of these  $\text{TiO}_2$  samples do not obviously decrease during 30 mins of operation, due to the short reaction time.

Figure 3 shows the  $\text{NO}_x$  removal and  $\text{NO}_2$  generation rates obtained using various Ni-containing  $\text{TiO}_2$  particles under UV irradiation. The  $\text{NO}_x$  removal activity for these samples with different Ni content decreased in the order: 0.1% Ni-TiO<sub>2</sub> > 0.2% Ni-TiO<sub>2</sub> > 0.05% Ni-TiO<sub>2</sub> > 0.5% Ni-TiO<sub>2</sub> > 1% Ni-TiO<sub>2</sub> > P25 > 4% Ni-TiO<sub>2</sub>, indicating the optimal Ni content is 0.1 mol%. The 0.1% Ni-TiO<sub>2</sub> has two times the  $\text{NO}_x$ -removal activity of P25 particle. Under UV illumination, these Ni-containing photocatalysts exhibit better activities in  $\text{NO}_x$  mineralization than pristine  $\text{TiO}_2$ , except for 4% Ni-TiO<sub>2</sub>. The apparent quantum efficiency ( $\Phi$ ) and selectivity of  $\text{NO}_2$  ( $\text{Sel.}_{\text{NO}_2}$ ) further computed based on the following equations [12, 13, 27] are listed in Table 1:

$$\varphi = \frac{\text{mole of (NO + NO}_2\text{) degraded}}{\text{Einstein of incident photons}} \quad (7)$$

$$\text{Sel.}_{\text{NO}_2} = \frac{[\text{NO}_2]_{\text{generated}}}{[\text{NO}]_{\text{converted}}} \quad (8)$$

The order of apparent quantum efficiency (0.1% Ni-TiO<sub>2</sub> > 0.05% Ni-TiO<sub>2</sub> > 0.2% Ni-TiO<sub>2</sub> > P25 > 0.5% Ni-TiO<sub>2</sub> > 1% Ni-TiO<sub>2</sub> > 4% Ni-TiO<sub>2</sub>) is not consistent with the  $\text{NO}_x$  removal activity. It indicates that the nickel content over 0.5% is excess to reduce the active area of  $\text{TiO}_2$ , resulting in the small quantum efficiency. When comparing the reaction behaviours over P25 and 0.05–0.2% Ni-TiO<sub>2</sub> samples, no significant difference in the NO conversion was observed, and the  $\text{NO}_2$  generation rates over these Ni-TiO<sub>2</sub> samples were much less than that over P25, resulting in the better photocatalytic activity of the Ni-TiO<sub>2</sub>. The selectivity of  $\text{NO}_2$  of the photocatalyst has a great effect on the  $\text{NO}_x$ -removal activity, as shown in Table 1 and Figure 3. For example, the  $\text{NO}_x$  removal activity of 1% Ni-TiO<sub>2</sub> is better than P25 even if the quantum efficiency of P25 is larger than 1% Ni-TiO<sub>2</sub>. It might be the Ni particle has a good affinity to  $\text{NO}_2$ . The platinum-modified  $\text{TiO}_2$  also has this property [16], and Ni is much cheaper than Pt. It is a worthy property for NO removal photocatalysis because  $\text{NO}_2$  is an undesired intermediate in the consecutive oxidation of NO, where the threshold concentrations of  $\text{NO}_2$  and NO are 3 and 25 ppm, respectively, [12].

According to the reaction scheme of the photooxidation of NO, the photocatalyst would be deactivated after long-term operation due to the coverage of active sites by adsorbed  $\text{NO}_3^-$  ions at the catalyst surface. However, the adsorbed  $\text{NO}_3^-$  ions could be easily rinsed out with DI water, enabling regeneration of the catalyst. Figure 3 also indicates the removal rates of  $\text{NO}_x$  over 1st-, 3rd-, and 5th-regenerated 0.1% Ni-TiO<sub>2</sub> samples. The experimental results indicate the photocatalytic activity will be gradually decreased with the increase in operation and regeneration times. The photocatalytic activity of 0.1% Ni-TiO<sub>2</sub> sample becomes stable after four reaction and regeneration cycles. It showed that over 93% of the photocatalytic activity could be recovered after multi-reaction-regeneration cycles. The reason for the slight decrease of photocatalytic activity is that the unstable nickel particles peel off from the  $\text{TiO}_2$  surface in the regeneration procedure. It can be confirmed by checking the nickel contents with using energy dispersive X-ray analysis after the regeneration procedure. It indicates most nickel particles on the  $\text{TiO}_2$  surface are quite stable. This means that the prepared Ni-TiO<sub>2</sub> could provide very good stability for  $\text{NO}_x$  degradation. As a result, good stability, easy regeneration, and high reactivity will provide a great opportunity for the application in air purification with using nickel-modified photocatalysts.

3.2. *Characterization of Ni-TiO<sub>2</sub>*. Figure 4 illustrates the X-ray diffraction patterns of the samples before and after

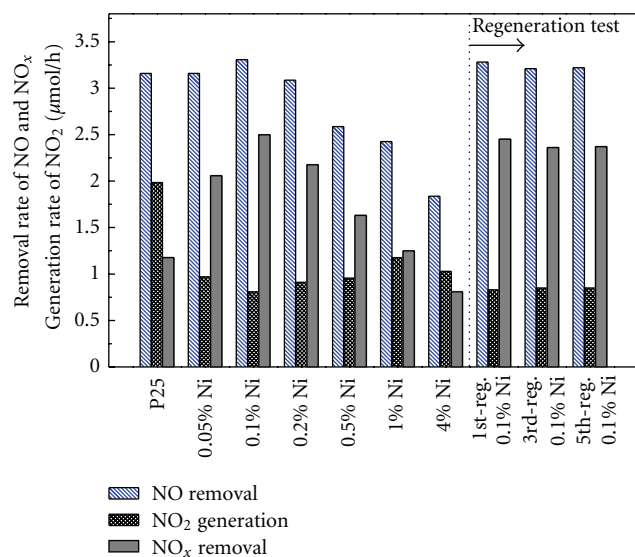


FIGURE 3: Effect of Ni content and regeneration time on the removal rate of NO<sub>x</sub>.

photodeposition treatment. The XRD pattern of the prepared TiO<sub>2</sub> powder in Figure 4 reveals the peaks of anatase (101) and rutile (110) at  $2\theta = 25.4^\circ$  and  $27.5^\circ$ , respectively, indicating that the bulk P25 TiO<sub>2</sub> composition is a mixture of rutile and anatase. Since all samples were dried at the relatively low temperature of 373 K and only a small amount of Ni salt was added, there were no significant differences between the samples. No peaks corresponding to crystalline phase of Ni metal and NiO were found due to small crystallite size and low nickel content. According to Scherrer's equation, by using the full width at half maximum height of the main peaks at  $2\theta = 25.4^\circ$  and  $27.5^\circ$ , respectively, for anatase and rutile phases, the TiO<sub>2</sub> anatase and rutile grain sizes of all prepared samples were around 21 and 15 nm. The results indicate that the addition of Ni salt produced insignificant changes in the primary TiO<sub>2</sub> particle size.

Figure 5 shows the morphology of the Ni-deposited titanium oxide as captured by TEM. The deposited Ni particles measuring approximately 1–3 nm were dispersed on the surface of the P25. The pH value of the slurry influences the morphology of deposited metal particles on the TiO<sub>2</sub> surface [28]. This study finds that the reduction rate increases as the pH value increases. However, Ni particles cannot adhere well on TiO<sub>2</sub> when the pH value is higher than 10. The optimal pH value for the photodeposition of Ni in our study was found to be 8 [23]. The stability of Ni-TiO<sub>2</sub> was confirmed by checking their TEM images after the photocatalytic reaction and regeneration procedure.

Element composition and chemical states on the surface of prepared samples were determined by XPS high-resolution scans over the Ti 2p and Ni 2p spectra regions. Figure 6(a) shows the Ni 2p spectra of Ni-TiO<sub>2</sub> samples. For 0.1–1% Ni-TiO<sub>2</sub> samples, their spectra exhibit broad peaks due to the small amount of Ni, and indicate the existence of Ni(II) and Ni(III) in these TiO<sub>2</sub> particles. However, the plenty amount of Ni(0) is found on the surface of 4% Ni-TiO<sub>2</sub> particle. In the preparation of Ni-TiO<sub>2</sub> via the

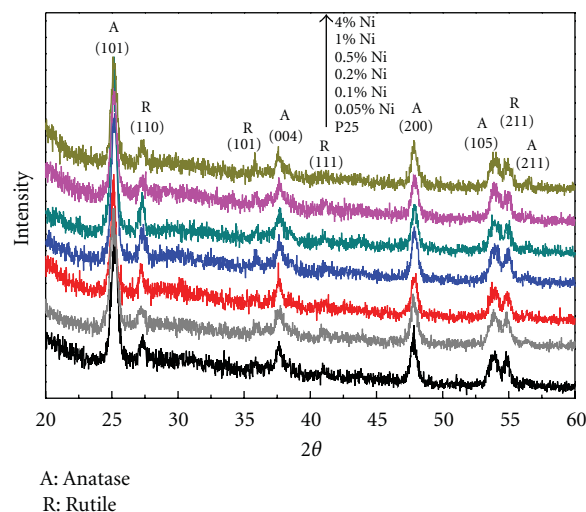


FIGURE 4: XRD patterns of prepared TiO<sub>2</sub> samples.

photodeposition process, the valence state of nickel on the TiO<sub>2</sub> surface should be zero because nickel ions are reduced by the photo-produced electrons from the TiO<sub>2</sub>. The Ni 2p<sub>3/2</sub> peaks of the samples assigned for Ni(0), Ni(II), and Ni(III) of binding energy are 852.9, 854.3, and 855.9 eV, respectively, [18–20, 23]. The compounds regarding Ni(II) and Ni(III) are major in the forms of NiO and Ni<sub>2</sub>O<sub>3</sub> because the existence of Cl on the TiO<sub>2</sub> surface is not observed. The metal oxides could be resulted from the oxidation of small nickel particles by heating in air [23, 29]. The Ni content of 4% Ni-TiO<sub>2</sub> should be much more than those of other samples, and therefore partial nickel on the 4% Ni-TiO<sub>2</sub> are not oxidized. The relatively atomic ratios of Ni(0), Ni(II), and Ni(III) species on the 4% Ni-TiO<sub>2</sub> are 55:26:19, as estimated from XPS results. In Figure 6(b), Ti (2p<sub>3/2,1/2</sub>) core level spectra confirm that the Ti(IV) is indeed present in the pristine TiO<sub>2</sub> sample. However, the Ti 2p<sub>3/2</sub> peak becomes broad and asymmetric with increasing Ni content. We interpreted the Ti 2p<sub>3/2</sub> peak for the Ni-TiO<sub>2</sub> sample as a combination of the Ti(IV) (peak at 458.7 eV) and a Ti(III) (peak at 457.2 eV). The appearance of Ti(III) is probably due to the loss of oxygen atoms from TiO<sub>2</sub> during the oxidation of metallic nickel particles. Moreover, following the Ar<sup>+</sup> ion etching process of 4% Ni-TiO<sub>2</sub>, the peak intensities associated with the Ti(III) species decreased; after 90 s of etching (etching depth = 5 nm), the Ti(III) species could not be observed on the TiO<sub>2</sub>. This shows that the Ti(III) species exists predominantly on the surface, as shown in Figure 6(b). It indicates the partial Ti(IV) species on the surface is reduced to Ti(III) as the metallic nickel is oxidized to nickel oxide.

The photoluminescence emission spectra were detected for various photocatalysts, as presented in Figure 7, to elucidate the fate of e<sup>-</sup>/h<sup>+</sup> pairs in the semiconductor particles (TiO<sub>2</sub>). As anticipated, the pristine TiO<sub>2</sub> photocatalyst (P25) shows a broad PL emission band, which is similar to the results of the literature [30]. The P25 and Ni-TiO<sub>2</sub> samples exhibit similar excitonic PL emission band, demonstrating that the nickel species does not cause the new PL phenomena.

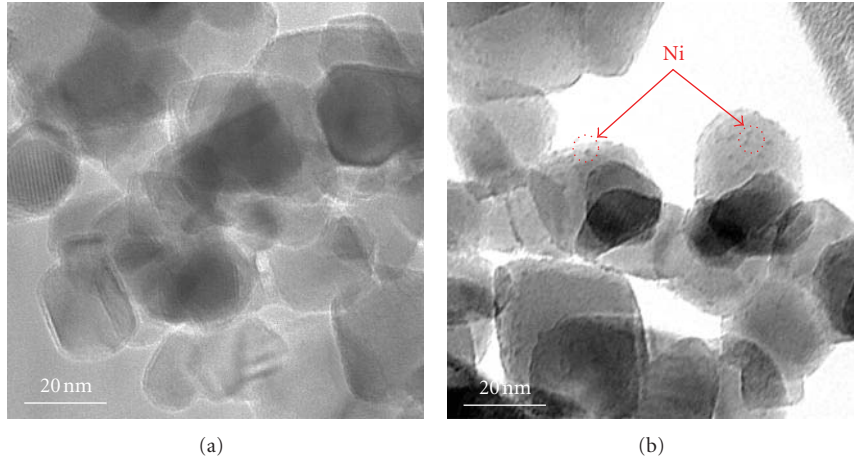
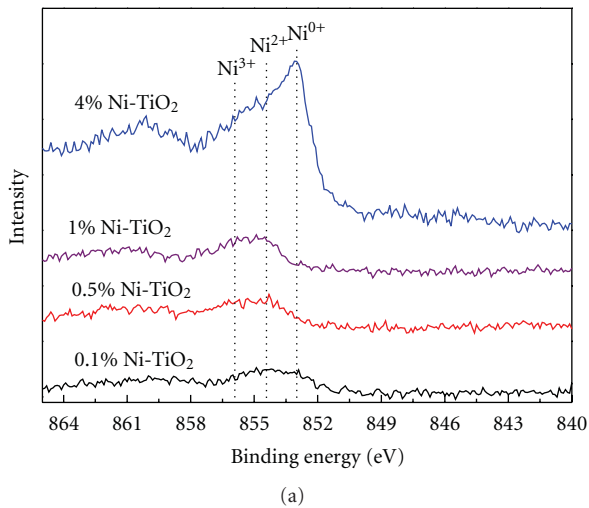
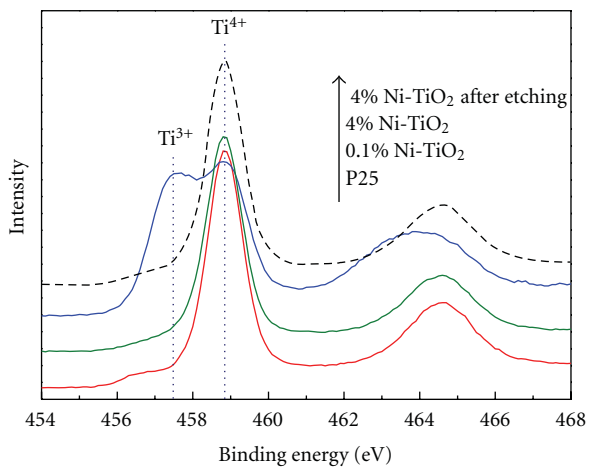


FIGURE 5: TEM morphology of (a) P25 and (b) 1% Ni-TiO<sub>2</sub>.



(a)



(b)

FIGURE 6: (a) XPS spectra over Ni 2p (b) Ti 2p of prepared samples.

The spectrum exhibits a broad emission region from 350 to 450 nm wavelengths with an excitation wavelength of 325 nm. The PL intensities of Ni-TiO<sub>2</sub> particles lessen with

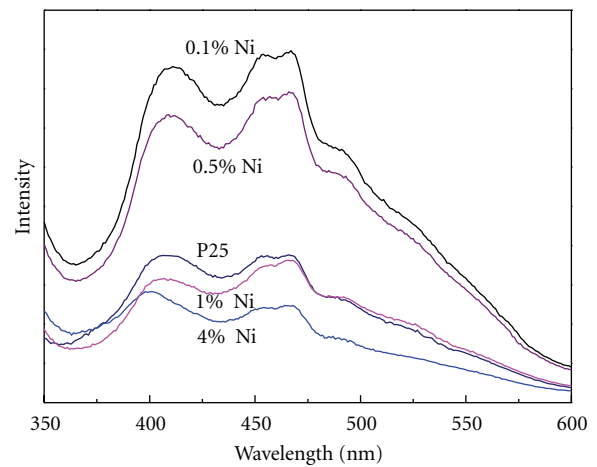


FIGURE 7: Photoluminescence spectra of prepared TiO<sub>2</sub> samples.

the increase in the Ni content. A small amount of Ni gives a higher PL intensity of the Ni-TiO<sub>2</sub> particle than P25, but the PL intensity of the Ni-TiO<sub>2</sub> is smaller than that of pristine TiO<sub>2</sub> as the Ni content is more than 1%. It indicates that Ni species in the higher concentration condition do not act as a trapping site to capture photogenerated electron from TiO<sub>2</sub> conduction band, but it becomes the recombination centre of electron-hole as its concentration is less than 0.5%. The excitonic PL intensity of TiO<sub>2</sub> decreases as the increase in particle size, which is ascribed to the decrease in the content of surface oxygen vacancy and defect with increasing particle size [11, 30]. In this work, the TiO<sub>2</sub> size effect on PL intensity should be not significant here due to the small difference in crystallite size between these samples (see Figure 4). Therefore, the loss in PL intensities of 4% and 1% Ni-TiO<sub>2</sub> results from the active sites on the TiO<sub>2</sub> surface are covered by the Ni species. The metal particles on the TiO<sub>2</sub> surface, such as Ag, Au, Pt, act as trapping sites to capture photogenerated electron from TiO<sub>2</sub> conduction band, separating the photogenerated electron-hole pairs [14, 16]. The Ni species on the as-synthesized Ni-TiO<sub>2</sub> particles seems to be the recombination sites of the photogenerated

electron-hole pairs. It is probably as the metallic Ni and Ni ions could capture photogenerated holes and electrons, respectively. Thus, the recombination rate of photogenerated electrons and holes increased, leading to an increase in the PL signal. Some literatures report that the Ni dopant suppresses recombination of electron-hole pair on the TiO<sub>2</sub> surface [18–20]. The different phenomena observed in the former reports and this work are reasonably due to the different preparation process and Ni content. The Ni content used in the former works is 2–10 mol%, so the PL intensity of TiO<sub>2</sub> decreased obviously in the existence of large Ni content [18, 19]. For the above reasons, the results indicate the 0.1% Ni-TiO<sub>2</sub> should exhibit the smallest photocatalytic activity. However, the 0.1% Ni-TiO<sub>2</sub> exhibits the highest removal rate of NO under UV illumination than other samples. It reveals there should be another factors influencing its activity. The light absorbance is not the reason for good photoactivity of Ni-TiO<sub>2</sub> because the UV-vis diffuse reflectance spectra of P25 and 0.1% Ni-TiO<sub>2</sub> are the same (not shown here). Thus, the nickel species exhibits a good affinity to NO and NO<sub>2</sub> molecules, so the photogenerated active oxygen species on TiO<sub>2</sub> particles could contact NO<sub>x</sub> molecules rapidly, resulting in the enhancement of PL intensity and NO<sub>x</sub> removal rate on the 0.1% Ni-TiO<sub>2</sub>.

#### 4. Conclusions

In this study, the Ni-containing TiO<sub>2</sub> particle was successfully prepared via a photodeposition process. Characterization results revealed that the particle size, crystal structure, and light absorption were unchanged after modification with Ni salt. PL spectra identified that the small amount of Ni on TiO<sub>2</sub> enhances the recombination of photogenerated electrons and holes. The nickel species exhibits a good affinity to NO<sub>x</sub> molecules, resulting in the increase in NO<sub>x</sub> removal rate and the decrease in selectivity of NO<sub>2</sub> over the TiO<sub>2</sub>. The excess Ni content on TiO<sub>2</sub> hinders reaction rate, due to coverage effect of nickel species on the active site on TiO<sub>2</sub> surface. Thus, 0.1 mol% Ni content is the proper content to prepare the highly photocatalytic material for removal of NO<sub>x</sub>. In conclusion, this simple and energy-saving process for the production of Ni-containing photocatalysts can be applied practically for removal of NO<sub>x</sub>.

#### Acknowledgment

The authors would like to thank the National Science Council of Taiwan, for financial support of this research under contracts NSC-99-2221-E-011-082.

#### References

- [1] A. Fujishima, T. N. Rao, and D. A. Tryk, "Titanium dioxide photocatalysis," *Journal of Photochemistry and Photobiology C*, vol. 1, no. 1, pp. 1–21, 2000.
- [2] J. Yu and J. Ran, "Facile preparation and enhanced photocatalytic H<sub>2</sub>-production activity of Cu(OH)<sub>2</sub> cluster modified TiO<sub>2</sub>," *Energy and Environmental Science*, vol. 4, no. 4, pp. 1364–1371, 2011.
- [3] J. Yu, Y. Hai, and M. Jaroniec, "Photocatalytic hydrogen production over CuO-modified titania," *Journal of Colloid and Interface Science*, vol. 357, no. 1, pp. 223–228, 2011.
- [4] Y. Fan, G. Chen, D. Li et al., "Highly selective deethylation of rhodamine B on TiO<sub>2</sub> prepared in supercritical fluids," *International Journal of Photoenergy*, vol. 2012, Article ID 173865, 2012.
- [5] H. Fu, G. Shang, S. Yang, and T. Xu, "Mechanistic study of visible-light-induced photodegradation of 4-chlorophenol by TiO<sub>2-x</sub>N<sub>x</sub> (0.021 < x < 0.049) with low nitrogen concentration," *International Journal of Photoenergy*, vol. 2012, Article ID 759306, 2012.
- [6] J. A. Byrne, P. A. Fernandez-Ibañez, P. S. M. Dunlop, D. M. A. Alrousan, and J. W. J. Hamilton, "Photocatalytic enhancement for solar disinfection of water: a review," *International Journal of Photoenergy*, vol. 2011, Article ID 798051, 2011.
- [7] M. L. Chen and W. C. Oh, "The improved photocatalytic properties of methylene blue for V<sub>2</sub>O<sub>3</sub>/CNT/TiO<sub>2</sub> composite under visible light," *International Journal of Photoenergy*, vol. 2010, Article ID 264831, 2010.
- [8] R. J. Tan, Y. H. Tseng, and C. H. Kuo, "Crystal size control of TiO<sub>2</sub> using experimental strategies in sol-gel process," *Micro and Nano Letters*, vol. 5, no. 6, pp. 361–364, 2010.
- [9] S. Wang, L. Zhao, J. Ran, Z. Shu, G. Dai, and P. Zhai, "Effects of calcination temperatures on photocatalytic activity of ordered titanate nanoribbon/SnO<sub>2</sub> films fabricated during an EPD process," *International Journal of Photoenergy*, vol. 2012, Article ID 472958, 2012.
- [10] S. J. Kim, N. H. Lee, H. J. Oh, S. C. Jung, W. J. Lee, and D. H. Kim, "Photocatalytic properties of nanotubular-shaped TiO<sub>2</sub> powders with anatase phase obtained from titanate nanotube powder through various thermal treatments," *International Journal of Photoenergy*, vol. 2011, Article ID 327821, 2011.
- [11] Y. C. Hsiao and Y. H. Tseng, "Preparation of Pd-containing TiO<sub>2</sub> film and its photocatalytic properties," *Micro and Nano Letters*, vol. 5, no. 5, pp. 317–320, 2010.
- [12] Y. H. Tseng, C. S. Kuo, C. H. Huang, and Y. Y. Li, "Preparation of visible-light-responsive nitrogen-carbon co-doped titania by chemical vapor deposition," *Zeitschrift für Physikalische Chemie*, vol. 224, no. 6, pp. 843–856, 2010.
- [13] Y. H. Tseng and C. H. Kuo, "Photocatalytic degradation of dye and NO<sub>x</sub> using visible-light-responsive carbon-containing TiO<sub>2</sub>," *Catalysis Today*, vol. 174, no. 1, pp. 114–120, 2011.
- [14] H. W. Chen, Y. Ku, and Y. L. Kuo, "Effect of Pt/TiO<sub>2</sub> characteristics on temporal behavior of *o*-cresol decomposition by visible light-induced photocatalysis," *Water Research*, vol. 41, no. 10, pp. 2069–2078, 2007.
- [15] Y. H. Tseng, C. Y. Yen, M. Y. Yen, and C. C. M. Ma, "Effects of the acid pretreated multi-walled carbon nanotubes on the photocatalytic capacity of TiO<sub>2</sub>/multi-walled carbon nanotubes nanocomposites," *Micro and Nano Letters*, vol. 5, no. 1, pp. 1–6, 2010.
- [16] C. H. Huang, I. K. Wang, Y. M. Lin, Y. H. Tseng, and C. M. Lu, "Visible light photocatalytic degradation of nitric oxides on PtO<sub>x</sub>-modified TiO<sub>2</sub> via sol-gel and impregnation method," *Journal of Molecular Catalysis A*, vol. 316, no. 1-2, pp. 163–170, 2009.
- [17] Y. H. Tseng, Y. L. Huang, S. L. Liu, Y. M. Lin, and J. H. Huang, "Photocatalytic composite material, method for producing the same and application thereof," Chinese Patent no. I324948, 2010.
- [18] S. H. Woo, W. W. Kim, S. J. Kim, and C. K. Rhee, "Photocatalytic behaviors of transition metal ion doped TiO<sub>2</sub>

- powder synthesized by mechanical alloying,” *Materials Science and Engineering A*, vol. 448–451, pp. 1151–1154, 2007.
- [19] D. H. Kim, D. K. Choi, S. J. Kim, and K. S. Lee, “The effect of phase type on photocatalytic activity in transition metal doped TiO<sub>2</sub> nanoparticles,” *Catalysis Communications*, vol. 9, no. 5, pp. 654–657, 2008.
- [20] M. Dhayal, S. D. Sharma, C. Kant, K. K. Saini, and S. C. Jain, “Role of Ni doping in surface carbon removal and photocatalytic activity of nano-structured TiO<sub>2</sub> film,” *Surface Science*, vol. 602, no. 6, pp. 1149–1154, 2008.
- [21] J. Wang, S. Uma, and K. J. Klabunde, “Visible light photocatalysis in transition metal incorporated titania-silica aerogels,” *Applied Catalysis B*, vol. 48, no. 2, pp. 151–154, 2004.
- [22] D. Y. Wang, H. C. Lin, and C. C. Yen, “Influence of metal plasma ion implantation on photo-sensitivity of anatase TiO<sub>2</sub> thin films,” *Thin Solid Films*, vol. 515, no. 3, pp. 1047–1052, 2006.
- [23] C. S. Kuo, Y. H. Tseng, H. Y. Lin et al., “Synthesis of a CNT-grafted TiO<sub>2</sub> nanocatalyst and its activity triggered by a DC voltage,” *Nanotechnology*, vol. 18, no. 46, Article ID 465607, 2007.
- [24] J. Yu, Y. Hai, and B. Cheng, “Enhanced photocatalytic H<sub>2</sub>-production activity of TiO<sub>2</sub> by Ni(OH)<sub>2</sub> cluster modification,” *Journal of Physical Chemistry C*, vol. 115, no. 11, pp. 4953–4958, 2011.
- [25] Y. H. Tseng, C. S. Kuo, C. H. Huang et al., “Visible-light-responsive nano-TiO<sub>2</sub> with mixed crystal lattice and its photocatalytic activity,” *Nanotechnology*, vol. 17, no. 10, pp. 2490–2497, 2006.
- [26] R. Atkinson, D. L. Baulch, R. A. Cox, R. F. Hampson Jr., J. A. Kerr, and A. Troe, “Evaluated kinetic and photochemical data for atmospheric chemistry: supplement III,” *International Journal of Chemical Kinetics*, vol. 21, no. 2, pp. 115–150, 1989.
- [27] S. Y. Treschev, P. W. Chou, Y. H. Tseng, J. B. Wang, E. V. Perevedentseva, and C. L. Cheng, “Photoactivities of the visible-light-activated mixed-phase carbon-containing titanium dioxide: the effect of carbon incorporation,” *Applied Catalysis B*, vol. 79, no. 1, pp. 8–16, 2008.
- [28] F. Zhang, J. Chen, X. Zhang et al., “Synthesis of titania-supported platinum catalyst: the effect of pH on morphology control and valence state during photodeposition,” *Langmuir*, vol. 20, no. 21, pp. 9329–9334, 2004.
- [29] H. Y. Lin, Y. F. Chen, and Y. W. Chen, “Water splitting reaction on NiO/InVO<sub>4</sub> under visible light irradiation,” *International Journal of Hydrogen Energy*, vol. 32, no. 1, pp. 86–92, 2007.
- [30] J. Liqiang, Q. Yichun, W. Baiqi et al., “Review of photoluminescence performance of nano-sized semiconductor materials and its relationships with photocatalytic activity,” *Solar Energy Materials and Solar Cells*, vol. 90, no. 12, pp. 1773–1787, 2006.

## Research Article

# Anatase TiO<sub>2</sub> Nanospindle/Activated Carbon (AC) Composite Photocatalysts with Enhanced Activity in Removal of Organic Contaminant

Wuyi Zhou, Peng Zhang, and Weian Liu

*Institute of Biomaterials, South China Agricultural University, Guangzhou 510642, China*

Correspondence should be addressed to Wuyi Zhou, zhouwuyi@scau.edu.cn

Received 23 July 2011; Revised 17 October 2011; Accepted 1 November 2011

Academic Editor: Jiaguo Yu

Copyright © 2012 Wuyi Zhou et al. This is an open access article distributed under the Creative Commons Attribution License, which permits unrestricted use, distribution, and reproduction in any medium, provided the original work is properly cited.

This paper embarks upon the three levels of analysis ranging from nanoscale materials synthesis to combination and functionality. Firstly, we have prepared anatase TiO<sub>2</sub> nanospindles with an even length of about 200 nm and a central width of about 25 nm by hydrothermal synthesis method at 100°C for 6 h. Secondly, we have dispersed TiO<sub>2</sub> nanospindles on the surface of activated carbon (AC) and fabricated TiO<sub>2</sub>/AC composite *via* a dip-coating method. Thirdly, the TiO<sub>2</sub>/AC composite has been studied as the photocatalyst to remove the organic contaminants in the waste water and exhibits excellent degradation rate in comparison with pure anatase TiO<sub>2</sub> nanospindles.

## 1. Introduction

Up to date, titanium dioxide (TiO<sub>2</sub>) has attracted much attention as heterogeneous photocatalyst and has been widely applied in the environment science owing to its significant advantages such as nontoxicity, low cost, chemical stability, and superior photoactivity over other semiconductors that have been investigated [1–5]. People have fabricated a variety of geometric structures of TiO<sub>2</sub> nanoparticles that comprises zero dimensional (0D) structure such as spheric nanoparticle [6, 7] and one-dimensional (1D) structure as nanowire [8, 9], nanorod [10], nanobelt [11, 12], or nanotubes [13, 14]. The later is particularly useful in dealing with waste water owing to the large surface to volume ratio which further improves the photocatalytic activity comparing to spheric particles under the irradiation of visible light. So far, numerous efforts have been developed to the fabrication of TiO<sub>2</sub> nanoscale materials with special morphologies by some traditional methods such as, sol-gel, micelle, and hydrothermal or solvothermal methods [15]. However, few studies reported the synthesis of anatase TiO<sub>2</sub> nanospindles by these methods [16, 17]. Qiu et al. [18] had fabricated anatase TiO<sub>2</sub> nanospindles by a hydrothermal treatment method and found they provided a good solution to the problems

of poor electron transport and severe aggregation of TiO<sub>2</sub> nanoparticles.

In general, one main drawback of the TiO<sub>2</sub> nanostructures, when used in the practical application, comes from their easy loss during the process of water treatment, resulting in low utilization rate and high cost, which limits their widespread use. Some attempts have been employed to improve the reuse efficiency of TiO<sub>2</sub>, for example, the immobilization of TiO<sub>2</sub> nanoparticles onto some supports such as carbon nanotube [19, 20], glass [21], ceramic [22], and activated carbon [23–27]. However, the current immobilization techniques are still not stable enough to improve the reaction efficiency for the reducing of TiO<sub>2</sub> dispersion and introducing transfer limit of the mass. It has also been observed that the lixiviation of TiO<sub>2</sub> particles from the supports occurs after running a period. However, among these supports, the activated carbon (AC) particles were chosen broadly as the support to increase remarkably the photoactivity of TiO<sub>2</sub> because of the high adsorption capability of the AC [25, 28–30], which was expected to solve above-mentioned problem.

In the present work, we are planning to report a novel TiO<sub>2</sub>/AC composite photocatalyst by the coating of anatase TiO<sub>2</sub> nanospindles onto the surface of columniform AC particles, which showed a promising photocatalytic activity than

pure TiO<sub>2</sub> due to the synergistic effect between supporting materials and TiO<sub>2</sub> nanospindles. Most importantly, this composite photocatalysts effectively reduced the lixiviation of TiO<sub>2</sub> from the surface of AC.

## 2. Experimental Procedure

**2.1. Preparation of Anatase TiO<sub>2</sub> Nanospindles.** Firstly, TiOSO<sub>4</sub> powders (93 wt%, Liaoning Dandong Chemical Company) with a weight of 3.00 g were dissolved into 350 mL deionized water by a vigorous stirring for 0.5 h, and then aqueous solution of NH<sub>3</sub>·H<sub>2</sub>O (28%, Nanjing Chemical Company) with a concentration of 10 wt% was added dropwise into the above solution to adjust the pH value to 6.5. After a continuous stirring of 0.5 h, the white precipitation was obtained by a centrifugal separation. Secondly, the obtained precipitation was mixed with 250 mL deionized water with a vigorous stirring again. After that, a mixture solution involving 2 g of sodium oxalate and 150 mL deionized water was added slowly into the above solution. After a vigorous stirring for 0.5 h, the precipitation was separated by a centrifuge. Finally, the mixture including 4 g of H<sub>2</sub>O<sub>2</sub> (30%, Guangdong Zhongcheng Chemical Ltd.) and 250 mL deionized water was used as the react reagent, which was reacted with the obtained products from step 2 for 12 h until a brown transparent solution was produced finally, and then it was kept heating at 100°C for 6 h. The large scale of TiO<sub>2</sub> nanospindles was formed and uniformly distributed in the water.

**2.2. Preparation of TiO<sub>2</sub>/AC Composite Photocatalyst.** In a typical procedure, 1 g of commercial granular AC particles with an average diameter of 4 mm (Guangzhou Wuhuan Activated Carbon Company, China) was suspended in the above TiO<sub>2</sub> suspension by continuous slow stirring for 1 h and then kept at room temperature for 10 h. Thereafter, the AC granular particles with the TiO<sub>2</sub> coating were obtained after a simple vacuum filtration process and then dried at 70°C for 12 h. Finally, the prepared *x*TiO<sub>2</sub>/AC composite photocatalysts with various content of TiO<sub>2</sub> were formed by repeating above experimental procedure, where *x* is 0, 0.5, 1, 1.5, and 2, representing the wt% of TiO<sub>2</sub>.

**2.3. Characterization.** The obtained TiO<sub>2</sub> nanospindles were characterized by XRD on a D/MAX-RC diffractometer operated at 30 kV and 100 mA with CuK<sub>α</sub> radiation. The anatase crystallite size was obtained from the line broadening of the 200 diffraction peak and calculated by the Scherrer equation,  $D = K\lambda/\beta \cos \theta$ , where  $\theta$  is a shape factor ( $K = 0.9$  in this work),  $\lambda$  is the wavelength of the incident X-rays, and  $\beta$  is the broadening of the peak at half the maximum height (full width at half-maximum) measured in radians. The surface morphology and particle size of TiO<sub>2</sub> nanospindles were examined by means of transmission electronic microscopy (TEM) on an FEI-XL30 transmission. The morphology of the TiO<sub>2</sub>/AC composite was observed by a scanning electronic microscope (SEM, Hitachi S-2300) equipped with an energy dispersive spectroscopy using an accelerating voltage

of 200 kV. To obtain the cross section of the samples, we broke the sample after being frozen in liquid nitrogen for 10 minutes. FTIR measurement of the sample was performed on an Avatar FTIR equipment. The contact angle between water and the external surface of AC was measured to evaluate the hydrophilicity property using a contact angle meter (Motic Images plus 2.0). The specific surface area of the samples obtained was measured in a Gemini VII 2390 Series Surface Area Analyzer (from Micromeritics) with the BET method.

**2.4. Evaluation of Photocatalytic Activity.** The photocatalytic degradation experiments were carried out using a cylindrical batch reactor opened at the air with 250 mL of capacity. A 175 W 365 nm commercial halogen lamp was used as the visible irradiation source. The total UV intensity was 2.1–2.2 mW/cm<sup>2</sup> by turning on all the UV light. The UV emission of the lamp was filtered to close to sunlight while avoiding its variation with time and cloudiness [25]. Methylene blue (MB) purchased from Aldrich was chosen as a model molecule for the photocatalytic test. Each catalyst of 50 mg/L was suspended in MB aqueous solution (0.05 mol·L<sup>-1</sup>) followed by sonication for 15 minutes. Before the irradiation, the suspension was maintained in the dark for 1 h to reach complete equilibrium adsorption. After being irradiated under the visible light, 2 mL of suspension was withdrawn periodically and immediately centrifuged at 5000 rpm for five times, and its absorbance at 664 nm was measured by UV-Vis spectroscopy (1501, Shimadzu).

## 3. Results and Discussion

**3.1. Morphology and Structure of TiO<sub>2</sub> Nanospindles.** In general, TiO<sub>2</sub> nanospindle was prepared by hydrothermal treatment of Ti source precursor with NaOH solution or water/alcohol mixture at a higher temperature (160°C) [24]. However, herein we fabricated successfully the TiO<sub>2</sub> nanospindle particles after a desirable heating treatment at 100°C. TEM images (Figures 1(a) and 1(b)) clearly indicated the unique morphologies of the synthesized TiO<sub>2</sub> nanospindles, which have an even length of about 200 nm and a central width of about 25 nm. XRD pattern in Figure 1(c) shows clearly that the TiO<sub>2</sub> nanospindle particles are anatase crystal structure (JCPDS card no. 21-1272), and their crystal size of TiO<sub>2</sub> is about 6.5 nm, which is calculated according to the Sherrer equation. This revealed that anatase TiO<sub>2</sub> nanospindles were directly produced after the continuous heating treatment processing. It is suggested that the heating temperature of the solution at 100°C is feasible enough for the nucleation of anatase from the amorphous crystal. In general, to obtain anatase TiO<sub>2</sub> nanospindle prepared by hydrothermal method, the temperature is higher than 160°C [28]. Therefore, it is more practical to fabricate large-scale anatase TiO<sub>2</sub> nanospindles in the current work for the easily synthetic process and lower cost. FTIR spectra of nanospindle of TiO<sub>2</sub> are shown in Figure 1(d). The main absorption peaks were located at 3420.7, 1622.3, and 520.1 cm<sup>-1</sup>. The band at 3420.7 cm<sup>-1</sup> was assigned to –OH stretching of surface hydroxyl group and at 1622.3 cm<sup>-1</sup> to –OH vibration of

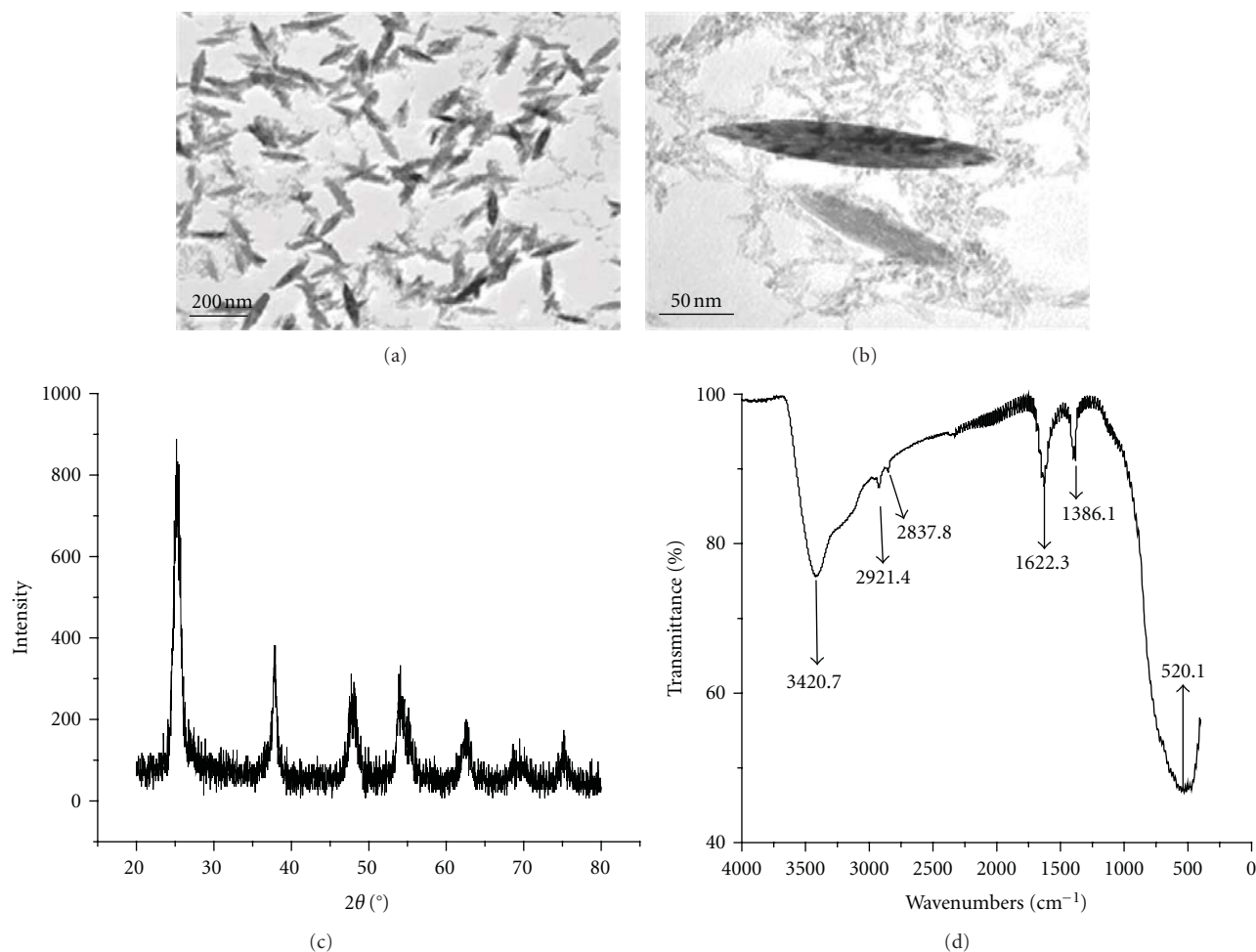


FIGURE 1: TEM images of the as-prepared large  $\text{TiO}_2$  nanospindles (a, b). XRD diffraction of as-prepared  $\text{TiO}_2$  nanospindles (c). FT-IR spectrum of as-prepared  $\text{TiO}_2$  nanospindles (d).

physically adsorbed water. The band at  $520.1\text{ cm}^{-1}$  was ascribed to the Ti–O stretching vibration [31]. Weak bands at  $2837.8$  to  $2921.4\text{ cm}^{-1}$  can be assigned to the O–H stretching of  $\text{H}_2\text{O}_2$  at the  $\text{TiO}_2$  surface.

**3.2. Physical Properties of Nanospindles  $\text{TiO}_2/\text{AC}$  Composite Photocatalyst.** The surface morphologies of  $\text{TiO}_2/\text{AC}$  composite catalysts were characterized by SEM with the result shown in Figure 2. It is clearly found in Figure 2(a) that the pure AC without  $\text{TiO}_2$  coating has a very rough surface structure with plenty of small pores. The average size of the pores was as large as approximately  $3.5\text{ }\mu\text{m}$ , which has enough space to accommodate  $\text{TiO}_2$  nanoparticles. With the increasing content of  $\text{TiO}_2$  coating (see Figures 2(b) and 2(c)), the surface of AC became more and more smooth and expressly the sample with 1 wt%  $\text{TiO}_2$  coating indicated a flattest surface structure. This indicated that this concentration of  $\text{TiO}_2$  nanospindles coating on the surface of AC produced an optimal layer. Most of  $\text{TiO}_2$  nanospindles were entirely filled into the pores of AC, resulting in the formation of glossy surfaces. However, it was discovered that there were still a few pores on the surface which was

able to absorb some organic compounds. Further increase of  $\text{TiO}_2$  coating such as 2 wt%  $\text{TiO}_2$  content, most of  $\text{TiO}_2$  nanospindles were scattered on the top layer of AC resulting in the formation of incompact and rougher external structure on the surface. The result of increasing size of  $\text{TiO}_2$  was from the interaction between  $\text{TiO}_2$  and AC. It could be found in Figure 2(e) that plenty of  $\text{TiO}_2$  nanospindles laid on the surface of AC and produced a tight surface morphology as the further increase of  $\text{TiO}_2$ . Moreover, the BET surface area of 1.5 wt%  $\text{TiO}_2/\text{AC}$ , 2.0 wt%  $\text{TiO}_2/\text{AC}$  composite, and pure AC particles were  $299.22$ ,  $250.01$  and  $372.02\text{ m}^2\text{ g}^{-1}$ , respectively. The pore volumes of them were  $0.15$ ,  $0.10$ , and  $0.20\text{ cm}^3/\text{g}$ , respectively, which indicated that the surface area of  $\text{TiO}_2/\text{AC}$  was less than that of pure AC due to that the coated  $\text{TiO}_2$  particles occupied the pores of granular AC. Moreover, with the increasing of  $\text{TiO}_2$  nanospindles, the surface area and pore volume of the catalysts decreased gradually. This suggested that most of  $\text{TiO}_2$  nanospindles were entirely filled into the AC pore as with the increasing content of  $\text{TiO}_2$  coating and decreased the surface area. The EDS analysis confirmed that the Ti elements with a concentration of 19.74% were existed on the surface of AC,

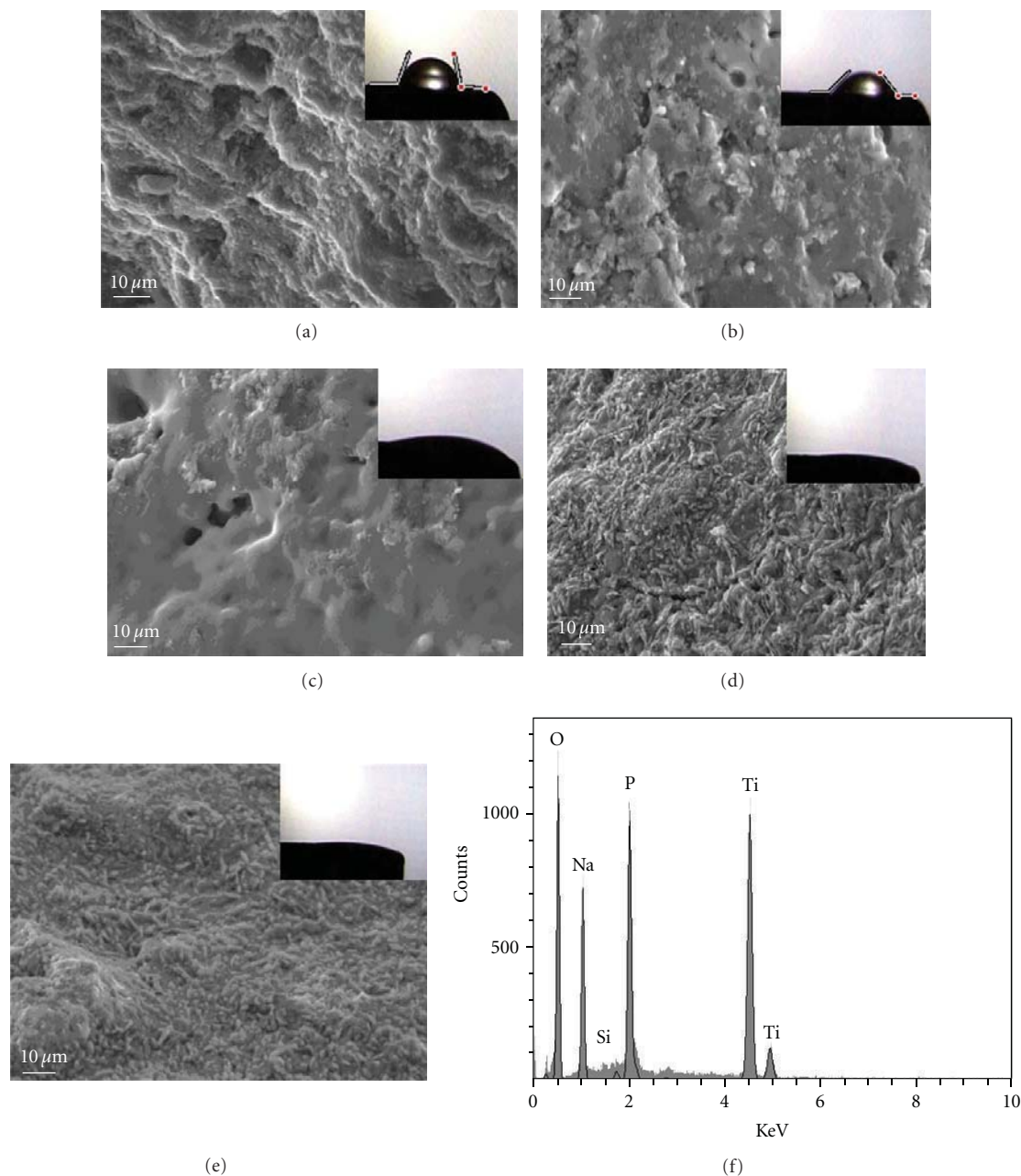


FIGURE 2: SEM image of AC without coating (a), with 0.5 wt% TiO<sub>2</sub> coating (b), with 1 wt% TiO<sub>2</sub> coating (c), with 1.5 wt% TiO<sub>2</sub> coating (d), with 2 wt% TiO<sub>2</sub> coating (e), and EDS analysis of the sample with 1.5 wt% TiO<sub>2</sub> coating (f).

but carbon element is almost not detected. This result further revealed that the top layer on the surface of AC has been occupied completely by TiO<sub>2</sub>. The contact angle data of TiO<sub>2</sub>/AC composite catalyst is shown in the inset image of Figure 2. The naked AC showed a high water contact angle of  $115 \pm 2.5^\circ$ , which indicated that the pure AC had a superior hydrophobicity. However, the contact angle of the surface of the TiO<sub>2</sub>/AC composite catalyst was enormously decreased compared to the naked AC. It was almost tiled when the water droplet was contacted with the surface of the sample with 1.5 wt% of TiO<sub>2</sub> coating, suggesting that the TiO<sub>2</sub> nanoparticles changed significantly the polarity

of AC surface from hydrophobicity to hydrophilicity. The images in Figure 3 exhibit the cross-sectional structures of TiO<sub>2</sub>/AC composites photocatalysts. It was clearly observed that the sample with 1.5 wt% of TiO<sub>2</sub> was covered by a thin layer of TiO<sub>2</sub> coating with the thickness of about 5 μm when compared to the naked AC.

The surface hydrophilicity of activated carbon plays an essential role in degradation process of organic compounds. In general, the higher hydrophilicity of surface is able to induce stronger capability in absorbing more aqueous organic molecules. This will be beneficial for the degradation process of organic contaminants.

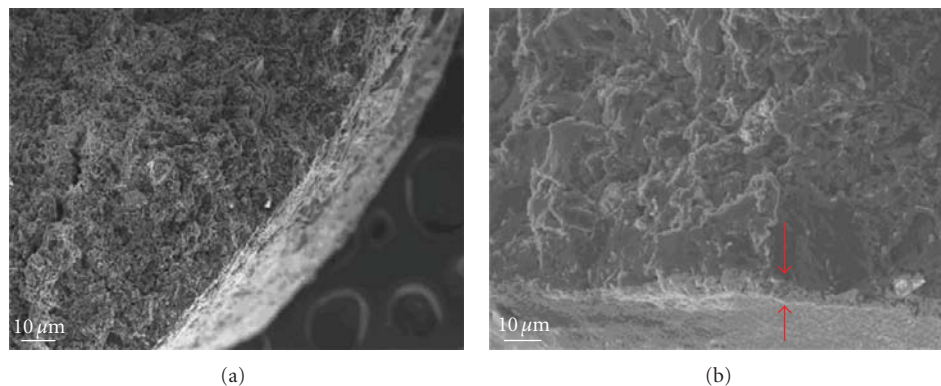


FIGURE 3: SEM image of cross-sectional area of the samples ((a), naked AC; (b), 1.5wt% TiO<sub>2</sub>/AC).

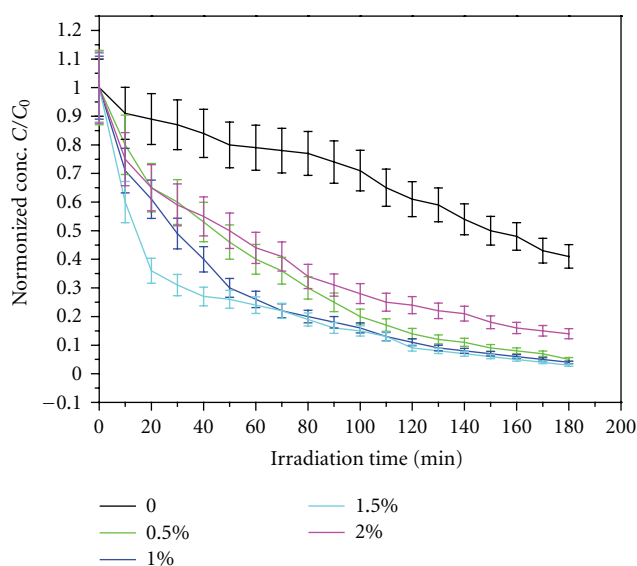


FIGURE 4: Photocatalytic degradation of methylene blue over TiO<sub>2</sub> and  $x$ TiO<sub>2</sub>/AC ([MB] = 0.05 mol L<sup>-1</sup>; reaction time  $t$  = 180 min).

**3.3. Photocatalytic Activity.** To assess the photocatalytic activity of the TiO<sub>2</sub>/AC samples, methylene blue (MB) was used as a model organic substrate in the suspended TiO<sub>2</sub>/AC reaction system under visible light irradiation as probe reaction. As we know, the MB (initial absorbance 0.8–1.0) owns two special absorption peaks separately located at 290 nm and 665 nm. The results of degradation experiment displayed in Figure 4 show that the MB solution with 1.5% TiO<sub>2</sub>/AC catalysts changed colour from blueness to almost colorlessness within 180 minutes of irradiation. The UV-Vis absorption spectra curves of MB studied at different times of irradiation are detailedly showed in Figure 5, where the photocatalytic degradation rate of MB on naked TiO<sub>2</sub> in this work was obviously lower than  $x$ TiO<sub>2</sub>/AC composite. However, for these composite catalysts with various content of TiO<sub>2</sub>, they showed the sharp reduce of degradation rate in the initial 30 minutes which mainly resulted from the adsorption of AC. However, after 30 minutes of irradiation, these samples displayed gradual tendency of decreasing rate

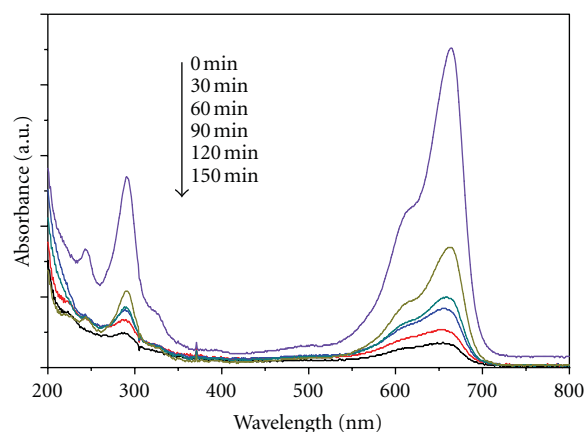


FIGURE 5: UV spectra of 1.5 wt% TiO<sub>2</sub>/AC sample suspended in methylene blue solution ([MB] = 0.05 mol L<sup>-1</sup>).

which mainly caused by the photocatalytic degradation of TiO<sub>2</sub> catalysts. It is widely accepted that AC is able to adsorb a wide range of synthetic organic compounds due to its high porosity. Therefore, the harmful organic compounds in the waster water will be moved easily to the surface of the catalysts. The TiO<sub>2</sub> nanospindle coating on the surface of AC indicated excellent capability in photocatalytic degrading organic compounds. These TiO<sub>2</sub> nanospindles are capable of prolonging the separation lifetime of photogenerated e<sup>-</sup>/h<sup>+</sup>, resulting in the increasing rate of •OH radical generation by the photocatalyst. Therefore, the synergistic effect between AC and TiO<sub>2</sub> nanospindles indicates greater degradation rate than pure TiO<sub>2</sub> nanospindles. Considering the immobilization of TiO<sub>2</sub> onto support, it is necessary to characterize the reuse efficiency of these composite catalysts. The results of the repetitive test on this sample with 1.5 wt% TiO<sub>2</sub> showed that degradation rate on MB is still greater than 90% after the reuse of 15 times.

## 4. Summary

In this work, anatase TiO<sub>2</sub> nanospindles with an even length of about 200 nm and a central width of about 25 nm were

fabricated by a simple hydrothermal treatment method. This method is more available to produce large-scale anatase TiO<sub>2</sub> nanospindles for the easy process and lower cost. We also prepared TiO<sub>2</sub>/AC composite catalysts by the dip coating technique, where all the samples with TiO<sub>2</sub> coating indicated much better photocatalytic activity than naked AC. The photocatalytic activity experiments discovered that the sample with 1.5% TiO<sub>2</sub> coating exhibited the highest photocatalytic activity for the synergistic effect between AC and TiO<sub>2</sub> nanospindles.

## Acknowledgments

The work was supported by the National Natural Science Funding (China, no. 31101854) and Guangdong Province Scientific and Technology Funding, China.

## References

- [1] M. A. Fox and M. T. Dulay, "Heterogeneous photocatalysis," *Chemical Reviews*, vol. 93, no. 1, pp. 341–357, 1993.
- [2] M. Inagaki, Y. Nakazawa, M. Hirano, Y. Kobayashi, and M. Toyoda, "Preparation of stable anatase-type TiO<sub>2</sub> and its photocatalytic performance," *International Journal of Inorganic Materials*, vol. 3, no. 7, pp. 809–811, 2001.
- [3] M. R. Hoffmann, S. T. Martin, and W. Choi, "Environmental applications of semiconductor photocatalysis," *Chemical Reviews*, vol. 95, no. 1, pp. 69–96, 1995.
- [4] Q. J. Xiang, J. G. Yu, and M. Jaroniec, "Enhanced photocatalytic H<sub>2</sub>-production activity of graphene-modified titania nanosheets," *Nanoscale*, no. 3, pp. 3670–3678, 2011.
- [5] J. A. Byrne, P. A. Fernandez-Ibañez, P. Dunlop, D. Alrousan, and J. Hamilton, "Photocatalytic enhancement for solar disinfection of water: a review," *International Journal of Photoenergy*, vol. 2011, article 798051, pp. 1–12, 2011.
- [6] W. Y. Zhou, S. Q. Tang, L. Wan, K. Wei, and D. Y. Li, "Preparation of nano-TiO<sub>2</sub> photocatalyst by hydrolyzation-precipitation method with metatitanic acid as the precursor," *Journal of Materials Science*, vol. 39, no. 3, pp. 1139–1141, 2004.
- [7] S. O. Baumann, M. J. Elser, M. Auer, J. Bernardi, N. Hüsing, and O. Diwald, "Solid-solid interface formation in TiO<sub>2</sub> nanoparticle networks," *Langmuir*, vol. 27, no. 5, pp. 1946–1953, 2011.
- [8] J. Jitputti, Y. Suzuki, and S. Yoshikawa, "Synthesis of TiO<sub>2</sub> nanowires and their photocatalytic activity for hydrogen evolution," *Catalysis Communications*, vol. 9, no. 6, pp. 1265–1271, 1995.
- [9] J.-S. Lee, Y.-I. Lee, H. Song, D.-H. Jang, and Y.-H. Choa, "Synthesis and characterization of TiO<sub>2</sub> nanowires with controlled porosity and microstructure using electrospinning method," *Current Applied Physics*, vol. 11, no. 1, pp. S210–S214, 2011.
- [10] X. Feng, J. Zhai, and L. Jiang, "The fabrication and switchable superhydrophobicity of TiO<sub>2</sub> nanorod films," *Angewandte Chemie*, vol. 117, no. 32, pp. 5245–5248, 2005.
- [11] Y. Wang, G. Du, H. Liu et al., "A photocatalytic reduction method for the preparation of TiO<sub>2</sub> nanobelt supported noble metals (Ag, Au)," *Journal of Nanoscience and Nanotechnology*, vol. 9, no. 3, pp. 2119–2123, 2009.
- [12] L. Zhao, J. R. Ran, Z. Shu, G. T. Dai, P. C. Zhai, and S. M. Wang, "Effects of calcination temperatures on photocatalytic activity of ordered titanate nanoribbon/SnO<sub>2</sub> films fabricated during an EPD process," *International Journal of Photoenergy*, vol. 2012, pp. 1–7, 2012.
- [13] S. M. Liu, L. M. Gan, L. H. Liu, W. D. Zhang, and H. C. Zeng, "Synthesis of single-crystalline TiO<sub>2</sub> nanotubes," *Chemistry of Materials*, vol. 14, no. 3, pp. 1391–1397, 2002.
- [14] N. H. Lee, H. J. Oh, S. C. Jung et al., "Photocatalytic properties of nanotubular-shaped TiO<sub>2</sub> powders with anatase phase obtained from titanate nanotube powder through various thermal treatments," *International Journal of Photoenergy*, vol. 2011, pp. 1–7, 2011.
- [15] X. B. Chen and S. S. Mao, "Titanium dioxide nanomaterials: synthesis, properties, modifications and applications," *Chemical Reviews*, vol. 107, no. 7, pp. 2891–2959, 2007.
- [16] R. H. Chu, J. C. Yan, S. Y. Lian, Y. H. Wang, F. C. Yan, and D. W. Chen, "Shape-controlled synthesis of nanocrystalline titania at low temperature," *Solid State Communications*, vol. 130, no. 12, pp. 789–792, 2004.
- [17] Y. C. Qiu, W. Chen, and S. H. Yang, "Double-layered photoanodes from variable-size anatase TiO<sub>2</sub> nanospindles: a candidate for high-efficiency dye-sensitized solar cells," *Angewandte Chemie*, vol. 122, no. 21, pp. 3757–3761, 2010.
- [18] Y. C. Qiu, K. Y. Yan, S. H. Yang, L. M. Jin, H. Deng, and W. S. Li, "Synthesis of size-tunable anatase TiO<sub>2</sub> nanospindles and their assembly into anatase/titanium oxynitride/titanium nitride/graphene nanocomposites for rechargeable lithium ion batteries with high cycling performance," *ACS Nano*, vol. 4, no. 11, pp. 6515–6526, 2010.
- [19] S. W. Lee and W. M. Sigmund, "Formation of anatase TiO<sub>2</sub> nanoparticles on carbon nanotubes," *Chemical Communications*, vol. 9, no. 6, pp. 780–781, 2003.
- [20] J. G. Yu, T. T. Ma, and S. W. Liu, "Enhanced photocatalytic activity of mesoporous TiO<sub>2</sub> aggregates by embedding carbon nanotubes as electron-transfer channel," *Physical Chemistry Chemical Physics*, vol. 13, no. 8, pp. 3491–3501, 2011.
- [21] Y. X. Chen, W. M. Liu, C. F. Ye, L. G. Yu, and S. K. Qi, "Preparation and characterization of self-assembled alkanephosphate monolayers on glass substrate coated with nano-TiO<sub>2</sub> thin film," *Materials Research Bulletin*, vol. 36, no. 15, pp. 2605–2612, 2001.
- [22] T. Yazawa, F. Machida, K. Oki, A. Mineshige, and M. Kobune, "Novel porous TiO<sub>2</sub> glass-ceramics with highly photocatalytic ability," *Ceramics International*, vol. 35, no. 4, pp. 1693–1697, 2009.
- [23] S. X. Liu, X. Y. Chen, and X. Chen, "A TiO<sub>2</sub>/AC composite photocatalyst with high activity and easy separation prepared by a hydrothermal method," *Journal of Hazardous Materials*, vol. 143, no. 1-2, pp. 257–263, 2007.
- [24] T.-T. Lim, P.-S. Yap, M. Srinivasan, and A. Fane, "TiO<sub>2</sub>/AC composites for synergistic adsorption-photocatalysis processes: present challenges and further developments for water treatment and reclamation," *Critical Reviews in Environmental Science and Technology*, vol. 41, no. 13, pp. 1173–1230, 2011.
- [25] H. Slimen, A. Houas, and J. P. Nogier, "Elaboration of stable anatase TiO<sub>2</sub> through activated carbon addition with high photocatalytic activity under visible light," *Journal of Photochemistry and Photobiology A: Chemistry*, vol. 221, no. 10, pp. 13–21, 2011.
- [26] S. M. Lam, J. C. Sin, and A. R. Mohamed, "Parameter effect on photocatalytic degradation of phenol using TiO<sub>2</sub>-P25/activated carbon (AC)," *Korean Journal of Chemical Engineering*, vol. 27, no. 4, pp. 1109–1116, 2010.
- [27] J. C. Sin, S. M. Lam, and A. R. Mohamed, "Optimizing photocatalytic degradation of phenol by TiO<sub>2</sub>/GAC using response

- surface methodology,” *Korean Journal of Chemical Engineering*, vol. 28, no. 1, pp. 84–92, 2011.
- [28] T. Cordero, C. Duchamp, J. M. Chovelon, C. Ferronato, and J. Matos, “Influence of L-type activated carbons on photocatalytic activity of TiO<sub>2</sub> in 4-chlorophenol photodegradation,” *Journal of Photochemistry and Photobiology A: Chemistry*, vol. 191, no. 2-3, pp. 122–131, 2007.
- [29] J. Matos, J. Laine, J. M. Herrmann et al., “Influence of activated carbon upon titania on aqueous photocatalytic consecutive runs of phenol photomineralization,” *Applied Catalysis B: Environmental*, vol. 70, no. 1–4, pp. 461–469, 2007.
- [30] M. Hirano and K. Date, “Scandium-doped anatase (TiO<sub>2</sub>) nanoparticles directly formed by hydrothermal crystallization,” *Journal of the American Ceramic Society*, vol. 88, no. 9, pp. 2604–2607, 2005.
- [31] C. H. Ao and S. C. Lee, “Enhancement effect of TiO<sub>2</sub> immobilized on activated carbon filter for the photodegradation of pollutants at typical indoor air level,” *Applied Catalysis B: Environmental*, vol. 44, no. 3, pp. 191–205, 2003.

## Research Article

# Photocatalytic Oxidation of Triiodide in UVA-Exposed Dye-Sensitized Solar Cells

Matthew Carnie, Daniel Bryant, Trystan Watson, and David Worsley

*SPECIFIC, College of Engineering, Swansea University, Baglan Bay Innovation Centre, Central Avenue, Baglan Energy Park, Baglan, Port Talbot SA12 7AZ, UK*

Correspondence should be addressed to David Worsley, d.a.worsley@swansea.ac.uk

Received 14 September 2011; Accepted 27 October 2011

Academic Editor: Jiaguo Yu

Copyright © 2012 Matthew Carnie et al. This is an open access article distributed under the Creative Commons Attribution License, which permits unrestricted use, distribution, and reproduction in any medium, provided the original work is properly cited.

UVA irradiation of glass mounted dye-sensitized solar cells without UV filtration causes failure within 400 hours of light exposure. The failure mode is shown to relate to consumption of  $I_3^-$ , which is directly related to  $TiO_2$  photo-catalysis. The onset of failure is easily determined from electrochemical impedance data where the recombination resistance of the  $TiO_2$ /electrolyte back reaction drops markedly prior to the onset of degradation. At the point of complete cell failure this impedance value then dramatically increases as there is no longer an interfacial reaction possible between the  $TiO_2$  and the  $I_3^-$  depleted electrolyte. Device failure is most rapid for cells under electrical load indicating that the degradation of the electrolyte is related to photogenerated hole production by excitation of the  $TiO_2$ . Once depleted by UV exposure, the  $I_3^-$  can be regenerated by simple application of a reverse bias which can restore severely UV degraded devices to near original working conditions.

## 1. Introduction

As an alternative to conventional silicon solar cells, dye-sensitized solar cells (DSCs) have been studied for some 20 years [1–3]. The photoelectrode most often used in DSCs is a nanoporous layer of  $TiO_2$  sintered onto a conductive glass or metal substrate. The photocatalytic properties of  $TiO_2$  are well documented [4–6], and photocatalytic reactions may proceed via several steps [7], the most important of which is the production of electron-hole pairs by direct excitation of the  $TiO_2$  with UV light. This results in a redox process, creating radicals which can ultimately result in degradative attack on organic molecules in the vicinity of the  $TiO_2$  [8]. Since both the DSC dye and the electrolyte have organic components, both are potentially susceptible to photocatalytic attack. It has been shown, however, that modification of the crystal structure and polarity of the  $TiO_2$  surface can impart photocatalytic selectivity leading to the possibility that one component could be degraded more favourably over the other [9, 10].

Some notable works have been published on DSC stability [11–19] as well as a comprehensive review published

in 2010 [20]. The degradation of cells exposed to UV irradiation has been noted many times, as has a corresponding depletion in  $I_3^-$  from the electrolyte. Depletion of  $I_3^-$  has been observed in DSC cells subjected to outdoor testing as evidenced by an increase in the Nernst diffusion impedance and changes to the cell's Raman spectra [16], and it has been shown that in extreme cases decreased  $I_3^-$  concentration can cause a reduction in  $J_{SC}$  by diffusion limitation [21]. The mechanism of  $I_3^-$  depletion has been suggested as either the sublimation of iodine [11] or perhaps the formation of iodate by reactions with water or other impurities in the electrolyte [22]. It appears, however, that  $I_3^-$  depletion could be as a result of a photoreactions as Sommeling et al. demonstrated that electrolyte bleaching occurred rapidly in illuminated cells held at 85° but did not occur in cells held at 85° and kept in the dark [13]. In DSCs, the photogenerated hole in the  $TiO_2$  valence band is said to be quenched by the iodide ion in the electrolyte [14]. However, DSC modules can degrade quickly under UV illumination [23], and the fact that filtering at  $\lambda < 384$  nm improves the stability of a DSC cell [24] suggests that the photocatalytic properties of

the  $\text{TiO}_2$  contribute at least in part to the degradation of the DSC.

A number of trends have been reported during long-term and accelerated tests. These include an increase in  $J_{\text{SC}}$  and a decrease in  $V_{\text{OC}}$  [18]. Electrochemical impedance spectroscopy (EIS) has also been used to monitor degradation, and it has been shown that the modelled resistance of the  $\text{TiO}_2$ /electrolyte back reaction decreases concurrently with the decrease in  $V_{\text{OC}}$  and that the drop in  $V_{\text{OC}}$  is due to a positive shift in the  $\text{TiO}_2$  conduction band [25]. This can also explain the increase in  $J_{\text{SC}}$ , as a positive shift of the conduction band should increase electron injection efficiency [24]. The Nernst diffusion impedance of  $\text{I}_3^-$  has been shown to increase as a result of the change of the components of the electrolyte during long-term outdoor testing [16]. It was our primary aim with this work to examine the electrochemical and cell efficiency changes that occur in the early stages of DSCs exposed to UV light in order to determine whether failure was related to electrolyte or dye degradation and whether this resulted from photocatalysis. A key secondary goal was to determine if irradiation of cells under load or at open circuit had an effect since, in many cases, longevity testing is conducted in the latter condition. In order to achieve these aims, we have developed some rapid testing methods building on the electrochemical methods proposed by others [13, 14, 18, 25] and using a spectrophotometric method to determine degradation rates of dye and electrolyte in situ without the need for destruction of the cells. We have then used these systems to examine the effectiveness of some UV filtration and in terms of a potential method to revive cells that have been partially photodegraded.

## 2. Experimental

**2.1. Cell Preparation.** The photoanode was prepared by the doctor blading of a commercial  $\text{TiO}_2$  paste (DSL 18NRT (Dyesol)) onto Solaronix TCO22-15 fluorine-doped  $\text{SnO}_2$  glass followed by sintering at  $500^\circ\text{C}$  for 30 minutes giving a  $7\ \mu\text{m}$  dry film thickness. The counter electrodes were prepared by the deposition of 5 mM chloroplatinic acid and heat-treated at  $400^\circ\text{C}$  for 30 minutes. N719 dye was prepared at 0.3 mM in a 1 : 1 acetonitrile/T-butanol solution. Adsorption of the dye to the  $\text{TiO}_2$  was achieved by immersion of the electrode in the dye solution over a period of 16–20 hours.  $50\ \mu\text{m}$  Surlyn gaskets were used to separate the electrodes and an electrolyte solution (0.8 M 1-propyl-3-methylimidazolium iodide (PMII), 0.3 M benzimidazole, 0.1 M  $\text{I}_2$ , and 0.05 M guanidinium thiocyanate dissolved in N-methoxy propionitrile) was then introduced to the cell by vacuum injection. All test cells were made with a working electrode area of  $1\ \text{cm}^2$  except those cells used for UV-Vis measurements which had a working electrode area of  $6.25\ \text{cm}^2$ , and the larger cells were needed in order to completely cover the sample aperture of the spectrophotometer.

**2.2. Measurements.** Photovoltaic characterisation was carried out using an Oriel Sol3A (94023A) utilizing a xenon arc

lamp, an AM 1.5 filter, and a Keithley 2400 source meter. A reference measurement was provided using a monocrystalline silicon reference cell traceable to the National Renewable Energy Laboratory (NREL) that enabled adjustment of the solar simulator to the standard light intensity of one sun that is,  $100\ \text{mW}/\text{cm}^2$ .

Impedance spectroscopy measurements were carried out on a Solartron SI 1280 Electrochemical Measurement Unit using ZPlot software. Cells were measured in a two-electrode setup in the dark. All cell measurements in this study were conducted with a bias potential of  $-0.68\ \text{V}$ , and the corresponding resistance values were averaged for the cell sets in question. AC amplitude was  $\pm 10\ \text{mV}$  with a frequency range of 20 kHz to 0.1 Hz.

UV exposure was conducted using a custom-made bank of  $6 \times 8\ \text{W}$  UVA lamps held 5 cm above the test cells. Measured intensity of the UV lamps was  $0.64\ \text{Wm}^{-2}$  at a  $\lambda_{\text{max}}$  of 354 nm. This is of comparable UV intensity to ASTM G173–03 (2008) which is given as  $0.61\ \text{Wm}^{-2}$  at 354 nm [26].

## 3. Results and Discussion

**3.1. Effect of UV Exposure upon Cell Efficiency.** Exposure of unprotected DSCs to UV light induces failure which is illustrated in Figure 1 for identical cells forward illuminated and kept in the dark. After around 400 hours of exposure, the efficiency of the UV-exposed cells falls off dramatically whilst, in the dark, it is relatively constant. The change in efficiency, however, follows on from measurable electrochemical changes in the cell that occur well before the failure of the device as determined by its overall cell efficiency.

**3.2. IV Measurements at 120-Hour Exposure.** Figure 2 shows the typical  $I$ - $V$  curves of a cell at 0-hour and 120-hour UV exposures for the cells illustrated in Figure 1. After just 120-hour exposure, well before detectable changes in efficiency, it can be seen that  $V_{\text{OC}}$  decreases whilst  $J_{\text{SC}}$  increases. The change in  $V_{\text{OC}}$  has been attributed to UV exposure causing a positive shift in the  $\text{TiO}_2$  conduction band. This would explain the drop in  $V_{\text{OC}}$  as this is given by the energy difference of the  $\text{TiO}_2$  quasi-Fermi level and that of the redox potential of the electrolyte [27]. The increase in  $J_{\text{SC}}$  due to UV illumination has been reported previously and has also been attributed to the positive shift in the conduction band [28].

**3.3. EIS Measurements at 120-Hour Exposure.** Figure 3 shows illustrative EIS Nyquist and Bode phase angle plots of the same cell type, again at 0-hour and 120-hour exposures. The larger semicircle of the Nyquist plot (Figure 3(a)) represents the impedance of the  $\text{TiO}_2$ /electrolyte back reaction ( $R_{\text{BR}}$ ). It is clear from the Nyquist plot that the cell experiences a large decrease in  $R_{\text{BR}}$  whilst the decrease in the phase angle at lower frequencies shown in the Bode phase plot (Figure 3(b)) suggests that electron lifetimes in the  $\text{TiO}_2$  are reduced. Both of these results can be explained by an increase in the rate of the back reaction (1) [25]. This could arise from an initial exposure of the  $\text{TiO}_2$  surface, possibly by detachment of dye

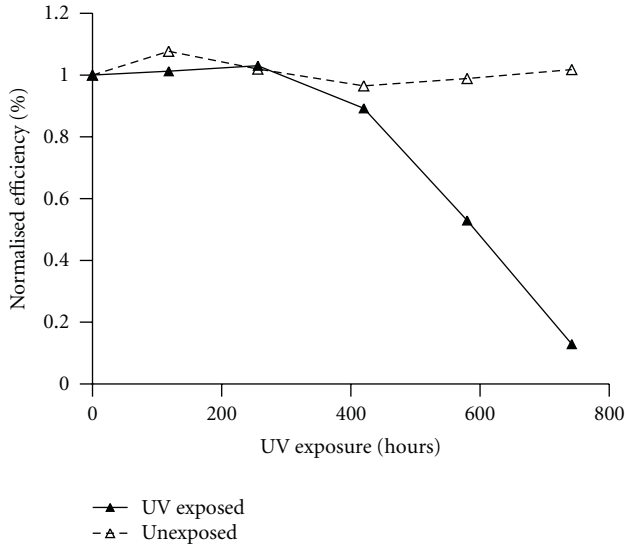


FIGURE 1: The effect of UV exposure on the  $\% \eta$  of DSC test cells compared to that of cells kept in the dark (unexposed).

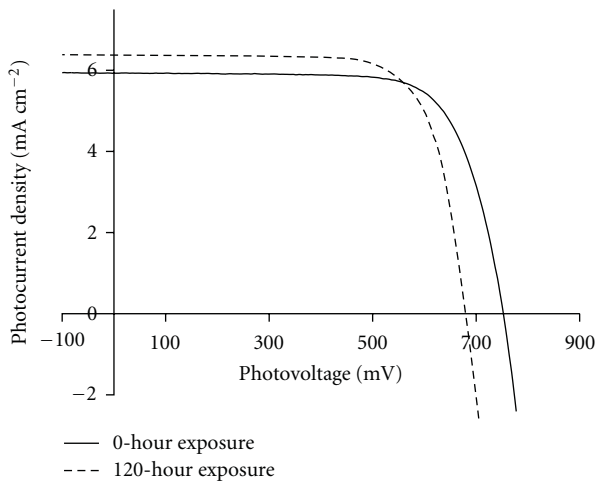
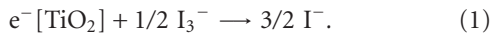


FIGURE 2:  $I$ - $V$  curves of a typical cell at 0-hour and 120-hour UV exposures. It can be seen that  $V_{OC}$  has decreased, whilst  $J_{SC}$  has increased; however, as can be seen in Figure 1, there is no observable significant changes to cell efficiency.

ligands or by the initial removal of adsorbed organic species from the electrolyte



**3.4. Longer-Term Testing of Cells Irradiated in Reverse and under Load.** Following these initial tests on forward illuminated cells, a more systematic study was performed on a wider range of conditions. Batches of 4 cells were irradiated from the WE (Forward) side, and, from the CE (Reverse) side, in addition, some were irradiated under a load provided by 100  $\Omega$  resistor. These are compared to cells that were kept in the dark at 40°C as this was the measured temperature under the UV lamps. Figure 4 shows the mean efficiencies and the  $V_{OC}$  of the cells subjected to UV irradiation over

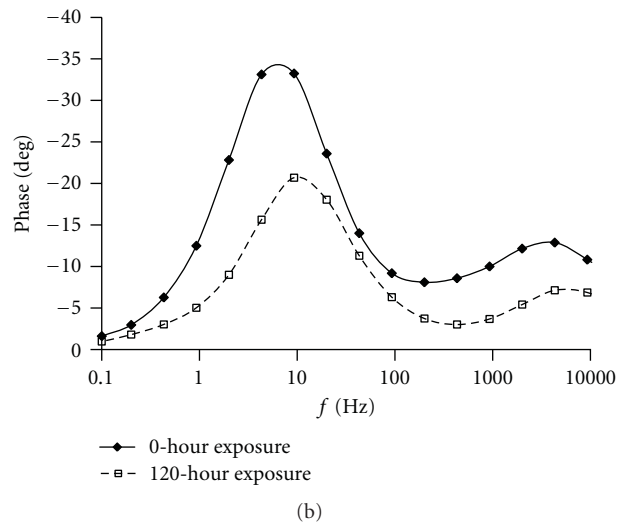
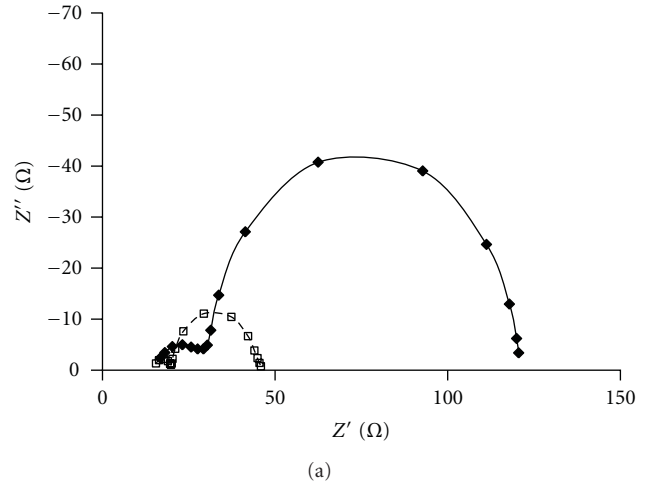


FIGURE 3: Nyquist plot (a) and Bode phase diagram (b) of the same cell as in Figure 2. These results are typical of all the cells exposed during this experiment.

the time period shown. In Figure 4, it is clear that there is a pattern in the relative rates of degradation of the cells tested. First to fail are the cells irradiated under load followed by cells irradiated from the WE side and then cells irradiated from the CE side. Cells kept in the dark at 40°C show comparatively little sign of degradation, despite a gradual decline in efficiency. This pattern is repeated when looking at the drop in  $V_{OC}$  values but, in this case, the drop in  $V_{OC}$  manifests itself much more quickly than the decline in efficiency. This data illustrates some important points. Firstly, the reverse illumination where photons travel through the electrolyte reduces photodegradation considerably as the electrolyte is acting as a filter. It does not, however, reduce the rate to zero. Secondly, the cells under load fail more quickly which suggests that the photogenerated electrons from the dye activation have a role to play in reducing the rate of failure when the cells are at open circuit.

Figure 5 shows the change in  $J_{SC}$  and the change in  $R_{BR}$  over the exposure period. The value of  $R_{BR}$  falls off

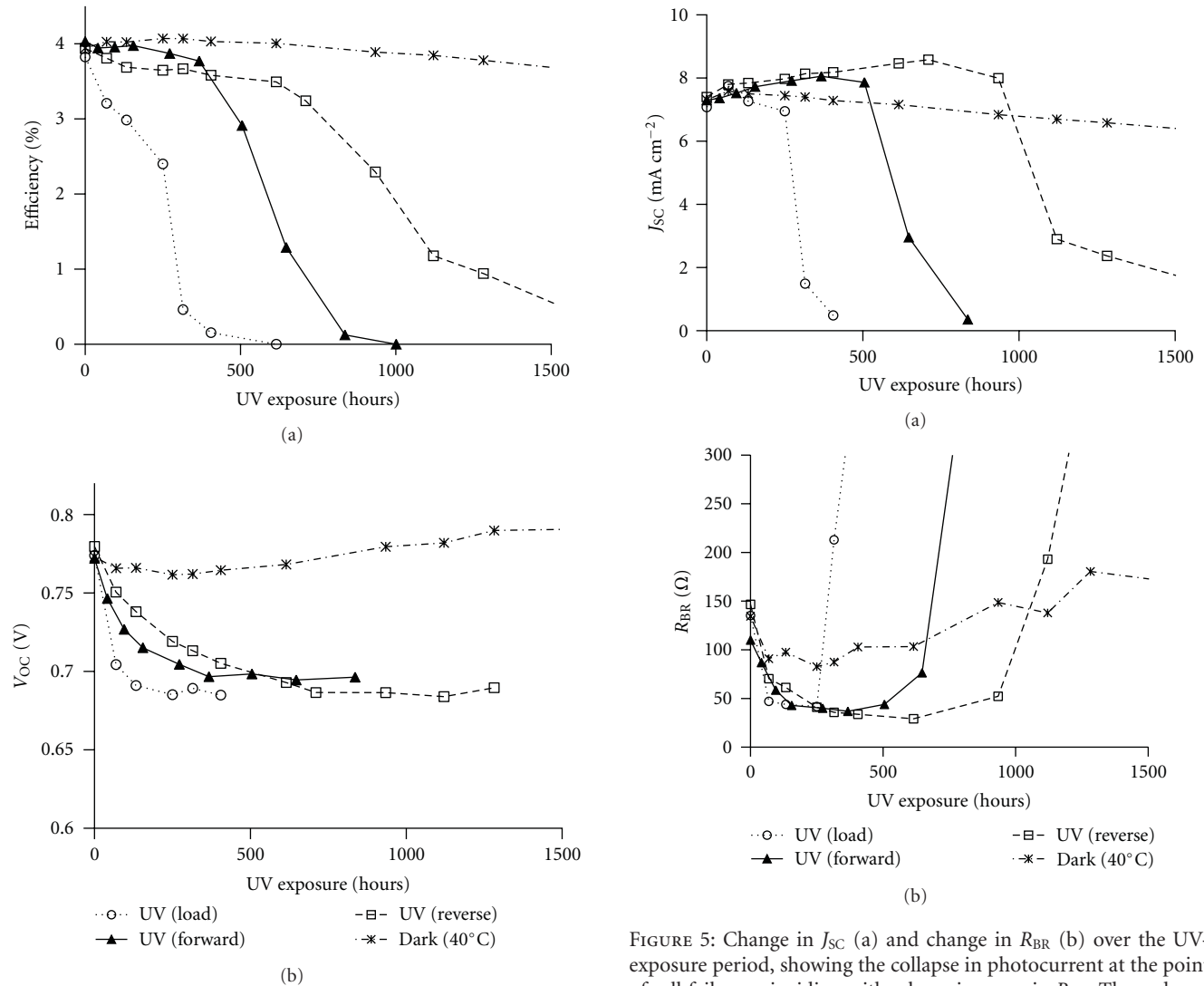


FIGURE 4: Change in (a)  $\eta$  and in (b)  $V_{OC}$  over the UV-exposure period. There is a clear order of cell degradation whereby cells under load and illuminated from the WE side fail before those under opencircuit (also illuminated from the WE side) which fail faster than those under opencircuit and illuminated from the CE side. Data is also shown for cells under opencircuit and kept in the dark for the exposure period.

quite quickly for all the cells suggesting that there is an increasing area of  $TiO_2$  in contact with the electrolyte after the initial UV exposure. Cells that are continually exposed to UV irradiation suffer a collapse in photocurrent and simultaneously a large increase in  $R_{BR}$ . The onset of photodegradation also coincides with a loss of colour from the electrolyte which is measured by UV-Vis and is noticeable to the eye at the point of failure. This along with the collapse in  $J_{SC}$  and the large increase in  $R_{BR}$  strongly suggests that the cell degradation reaches a point where the  $I_3^-$  has been consumed until there are not enough charge carriers available to give the cell a viable photocurrent.

FIGURE 5: Change in  $J_{SC}$  (a) and change in  $R_{BR}$  (b) over the UV-exposure period, showing the collapse in photocurrent at the point of cell failure coinciding with a large increase in  $R_{BR}$ . The order of cell failure is the same as in Figure 4.

**3.5. Triiodide Depletion Measured with UV-Vis.** UV-Vis spectroscopy is a useful method for analysing which of the components in the DSC is failing since both the dye and the electrolyte have absorbances which can be analysed simultaneously and in situ without taking the cells apart. The changing UV visible absorbance spectra for the forward illuminated cells are shown in Figure 6. It can be seen that the absorbance related to the adsorbed N719 dye (at ca 530 nm) remains relatively constant and the main colour shift is at much lower wavelengths where the electrolyte is absorbing. This adds weight to the suggestion that it is the failure of the electrolyte that is responsible for the failure of the cells, despite the fact that it is the dye that is adsorbed on the  $TiO_2$ .

This is more clearly illustrated in Figure 7 where the absorbance of the cell at 531 nm (the  $\lambda_{max}$  of the dye) and 450 nm (a representation of the electrolyte absorbance) is plotted as a function of time. 450 nm was chosen to represent dye colouration as the  $\lambda_{max}$  of the  $I^-/I_3^-$  redox couple is hidden by the large absorbance of the  $TiO_2$ . Figure 7 shows

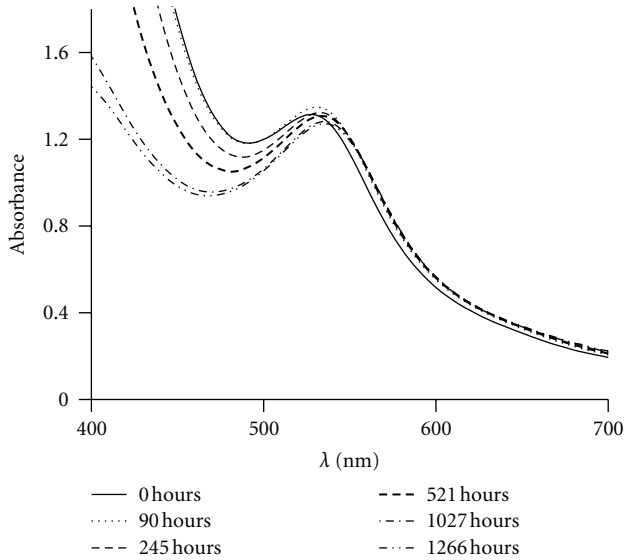


FIGURE 6: UV-Vis spectra of a typical cell over the exposure period shown.

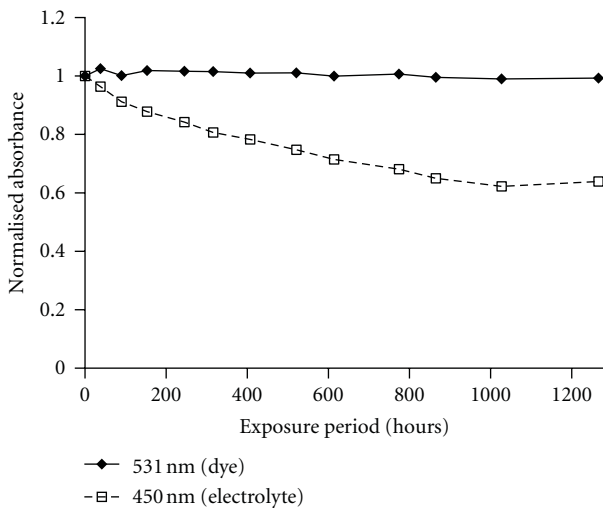


FIGURE 7: The changing absorbance of the cell at 531 nm (representing dye colouration) and at 450 nm (representing electrolyte colouration) of cells over the exposure period.

that the electrolyte is clearly being degraded whilst dye absorbance remains constant.

Having observed that the electrolyte was being degraded it was desirable to work out the origin of the failure. It could be that the electrolyte is directly attacked or that it is related to  $\text{TiO}_2$  photoreactions. Figure 8 illustrates the changes in electrolyte absorbance at 450 nm as a function of UV exposure time for two model cells. The first model cell was assembled from two counter electrodes (to examine whether UV alone caused the failure). The second cell type was essentially a full DSC assembly but without any dyeing step.

It can be seen from the data in Figure 8 below that the UV exposure alone does not cause failure but that having a

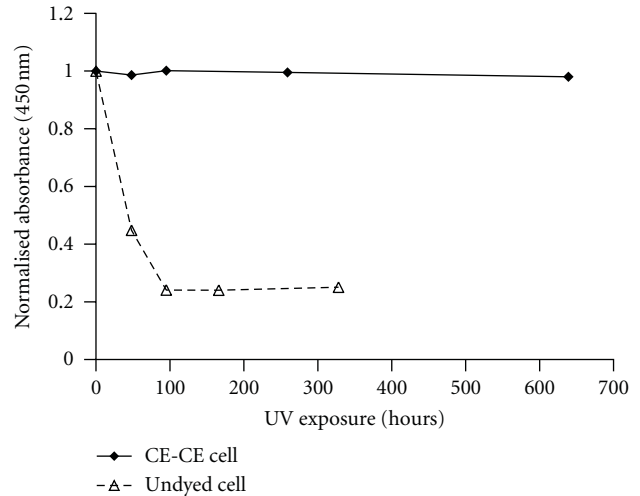


FIGURE 8: Change in absorbance of model cells. The undyed cell is essentially a complete DSC. The CE-CE cell consists of two counter electrodes and the electrolyte. This clearly shows that  $\text{TiO}_2$  is required for electrolyte degradation under UV illumination.

$\text{TiO}_2$  electrode causes very rapid failure. There is almost no colour change in the CE-CE cell, and it could be argued that the Pt is absorbing some of the UV light. Whilst this is true, it has been shown in Figure 5 that cells exposed via the CE side still degrade meaning that there is enough UV light reaching the  $\text{TiO}_2$  to initiate consumption of the  $\text{I}_3^-$ . If  $\text{TiO}_2$  was not involved in  $\text{I}_3^-$  consumption, then it would be expected that there might be a colour change in the CE-CE cell despite the UV absorbing properties of the Pt layer.

Comparing the data in Figure 8 with that from Figure 7 where the dye is included on the  $\text{TiO}_2$ , the presence of the dye dramatically slows the rate of cell failure. We believe this is for two reasons. Firstly, the dye will have taken up sites on the  $\text{TiO}_2$ , and, secondly, it seems that at open circuit the dye is able to inject electrons into the  $\text{TiO}_2$  (as evidenced by the accelerated failure under load). Hence, it appears that it is the  $\text{TiO}_2$  and photooxidation by photogenerated holes that are the primary reason for attack on the electrolyte. Since it appears that photocatalytic oxidation could be responsible for the discoloration, the question remains what is the oxidised iodine containing species. At this stage, we have not been able to establish via chemical testing. One possibility for oxidation would be the reverse of (1), but this would of course give rise to a darker electrolyte. Since discoloration is observed, it therefore seems likely that the oxidation yields iodate as suggested in previous work [22]. Further work is in progress to assess; it is potentially the case that by drying and removing oxygen this pathway could be reduced although the  $\text{TiO}_2$  surface will still have a large quantity of surface bound hydroxyl groups that could lead to this.

**3.6. UV Filtering.** To investigate this further, a series of cells was irradiated with UV in the presence and absence of filters with certain wavelength cutoffs. The data shown earlier shows that  $V_{OC}$  changes are an early indicator of the

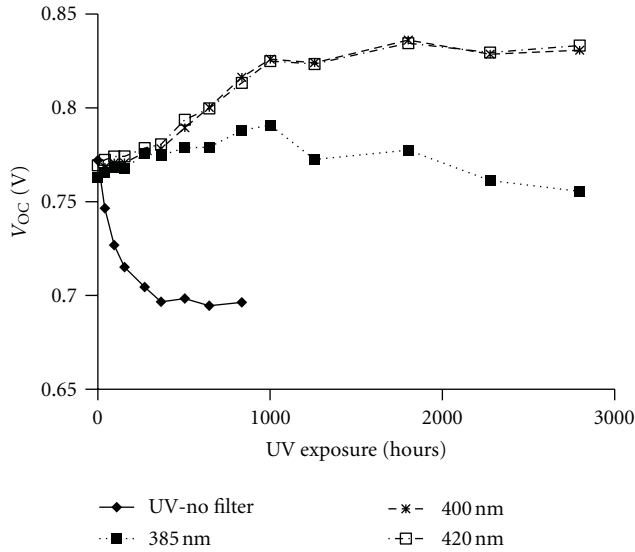


FIGURE 9:  $V_{OC}$  data for cells filtered at 385 nm, 400 nm, and 420 nm over the exposure period compared to cells exposed without a UV filter.

onset of cell degradation; for this reason, the change in  $V_{OC}$  was chosen as an indicator of the effectiveness of UV filters.  $V_{OC}$  data for these cells is shown in Figure 9. The initial increase in the  $V_{OC}$  of all the filtered cells is typical of cells kept in the dark. It can be seen that the introduction of a 385 nm filter causes an initial increase in  $V_{OC}$ , but, after some time, the  $V_{OC}$  begins to decline indicating, albeit delayed, the onset of photodegradation. Using higher wavelength cut-off filters of 400 and 420 nm appears to stop this photooxidation completely (within our exposure times at least). This data again points to the potential for  $TiO_2$  photocatalysis to contribute to degradation since the  $TiO_2$  bandgap for direct excitation is in the range 360–380 nm. The removal of this range of photons clearly prevents cell failure occurring rapidly.

**3.7. Triiodide Regeneration by Application of a Reverse Bias.** During the course of these investigations, it was found that UV-degraded and therefore  $I_3^-$  depleted cells can be regenerated by application of a reverse bias of around +1.3 V. Figure 10 shows the IV curves of the same cell before UV exposure, after UV exposure, and after electrolyte regeneration treatment. It can be seen that the cell, having undergone regeneration treatment, after a period of UV exposure, shows no significant recovery in  $V_{OC}$  but a partial recovery in  $J_{SC}$ , with increase being attributed to the regeneration of  $I_3^-$  charge carriers in the electrolyte. The production of  $I_3^-$  via application of reverse bias has been noted before by Hauch and Georg [21], but it is not believed to have been reported in connection with the regeneration of UV-degraded DSCs. It was also found during these investigations that the less severely UV degraded the cell, the more effective the regeneration treatment is at recovering the cell to its original properties. It may be possible that by refining this treatment (in terms of the polarisation time, magnitude, and

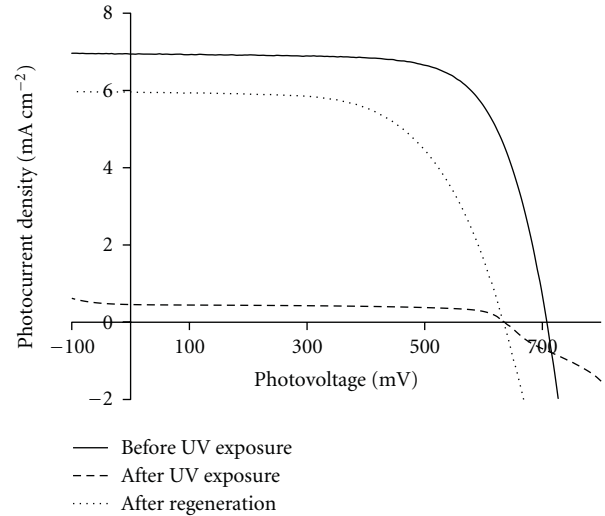


FIGURE 10:  $I$ - $V$  curves of a typical photodegraded DSC cell before UV exposure, after UV exposure, and after electrolyte regeneration treatment.

its frequency of application) the regeneration of the devices could be more effectively controlled. This is an attractive solution to restoring device performance since it could be periodically applied (e.g., at night) to maintain cell longevity.

#### 4. Conclusion

Photocatalytic reactions instigated by UV irradiation are detrimental to dye-sensitized solar cell performance, and this study shows there are subtle changes that occur within a few days of exposure that manifest themselves before changes in cell efficiency are detected. The open circuit voltage, short circuit current, and back reaction resistance ( $V_{OC}$ ,  $J_{SC}$ , and  $R_{BR}$ ) all change relatively rapidly, and these are therefore potentially important indicators of cell degradation which can be to quickly evaluate UV protection measures, such as spectral cut-off filters. In addition, spectrophotometry is an important and simple tool for evaluating which component of the cell (dye or electrolyte) is under attack and enable kinetics of the processes to be simultaneously evaluated.

The focus for degradation in cell performance in our tests seems to be through  $TiO_2$  photocatalysed attack on the electrolyte leading to consumption of the triiodide in the electrolyte. This seems to come from an initial exposure of  $TiO_2$  surfaces which is evidenced by a reduction in  $R_{BR}$ . The fall in  $R_{BR}$  coincides with the onset of discolouration of the electrolyte and is far more rapid in cells under load. This indicates that, at open circuit, electrons injected into the  $TiO_2$  by the dye are able to quench photogenerated holes as there is no external transport mechanism. When an external circuit is present, fewer  $TiO_2$  electron-hole pair recombinations occur, leading to an increase in hole concentration and an increase in the rate of  $I_3^-$  consumption and therefore cell degradation. In addition, removal of bandgap photons in the range <400 nm stops the degradation of the electrolyte from occurring. One reaction that could occur from the oxidative

hole is the conversion of  $I^-$  to  $I_3^-$  resulting in increased triiodide production and therefore an increase absorbance at 450 nm. Since this is not the case, then it could be possible that the triiodide is oxidised to iodate. Work is continuing in order to determine whether or not this is the case and to establish if iodate is the reaction product and the nature of the oxygen source (water or oxygen in the electrolyte or directly from OH moieties on the  $TiO_2$  surface).

It seems that in the timescale of our irradiations, at least the dye is not subject to degradation. Since it is the  $TiO_2$  photocatalysed oxidation that dominates, DSC stability can be improved as would be expected by including appropriate filters into the device to remove photons in the range of the bandgap of the  $TiO_2$ . In addition, application of a reverse bias appears to regenerate depleted triiodide and restore cell performance of UV-photodegraded DSCs. Work is also continuing to establish whether a periodically applied reverse bias to DSCs under UV and visible light soaking conditions is an effective means of maintaining cell performance.

## Acknowledgment

The authors would like to acknowledge support from the Engineering Physical Science Research Council (EP/E035205), the ERDF, through the Low Carbon Research Institute, Tata Steel Europe, PV Accelerator, Shotton Works, Deeside, and SPECIFIC at the College of Engineering, Swansea University.

## References

- [1] M. Grätzel, "The advent of mesoscopic injection solar cells," *Progress in Photovoltaics*, vol. 14, no. 5, pp. 429–442, 2006.
- [2] M. Grätzel and B. O'Regan, "A low-cost, high-efficiency solar cell based on dye-sensitized colloidal  $TiO_2$  films," *Nature*, vol. 353, no. 6346, pp. 737–740, 1991.
- [3] M. K. Nazeeruddin, A. Kay, I. Rodicio et al., "Conversion of light to electricity by cis-X2bis(2,2'-bipyridyl-4,4'-dicarboxylate)ruthenium(II) charge-transfer sensitizers (X = Cl-, Br-, I-, CN-, and SCN-) on nanocrystalline  $TiO_2$  electrodes," *Journal of the American Chemical Society*, vol. 115, no. 14, pp. 6382–6390, 1993.
- [4] J. Li, L. M. Peter, and R. Potter, "Photoelectrochemical response of  $TiO_2$  pigmented membranes," *Journal of Applied Electrochemistry*, vol. 14, no. 4, pp. 495–504, 1984.
- [5] A. Mills, R. H. Davies, and D. Worsley, "Water purification by semiconductor photocatalysis," *Chemical Society Reviews*, vol. 22, no. 6, pp. 417–425, 1993.
- [6] A. Wold, "Photocatalytic properties of titanium dioxide ( $TiO_2$ )," *Chemistry of Materials*, vol. 5, no. 3, pp. 280–283, 1993.
- [7] D. F. Ollis, E. Pelizzetti, and N. Serpone, *Photocatalysis: Fundamentals and Applications*, John Wiley and Sons, New York, NY, USA, 1989.
- [8] A. J. Robinson, J. R. Searle, and D. A. Worsley, "Novel flat panel reactor for monitoring photodegradation," *Materials Science and Technology*, vol. 20, no. 8, pp. 1041–1048, 2004.
- [9] S. Liu, J. Yu, and M. Jaroniec, "Tunable photocatalytic selectivity of hollow  $TiO_2$  microspheres composed of anatase polyhedra with exposed 001 facets," *Journal of the American Chemical Society*, vol. 132, no. 34, pp. 11914–11916, 2010.
- [10] Q. Xiang, J. Yu, and M. Jaroniec, "Tunable photocatalytic selectivity of  $TiO_2$  films consisted of flower-like microspheres with exposed 001 facets," *Chemical Communications*, vol. 47, no. 15, pp. 4532–4534, 2011.
- [11] H. Matsui, K. Okada, T. Kitamura, and N. Tanabe, "Thermal stability of dye-sensitized solar cells with current collecting grid," *Solar Energy Materials and Solar Cells*, vol. 93, no. 6-7, pp. 1110–1115, 2009.
- [12] M. Grätzel, "Photovoltaic performance and long-term stability of dye-sensitized mesoscopic solar cells," *Comptes Rendus Chimie*, vol. 9, no. 5-6, pp. 578–583, 2006.
- [13] P. M. Sommeling, M. Späth, H. J. P. Smit, N. J. Bakker, and J. M. Kroon, "Long-term stability testing of dye-sensitized solar cells," *Journal of Photochemistry and Photobiology A*, vol. 164, no. 1–3, pp. 137–144, 2004.
- [14] A. Hinsch, J. M. Kroon, R. Kern et al., "Long-term stability of dye-sensitized solar cells," *Progress in Photovoltaics*, vol. 9, no. 6, pp. 425–438, 2001.
- [15] R. Harikisun and H. Desilvestro, "Long-term stability of dye solar cells," *Solar Energy*, vol. 85, no. 6, pp. 1179–1188, 2011.
- [16] N. Kato, K. Higuchi, H. Tanaka, J. Nakajima, T. Sano, and T. Toyoda, "Improvement in long-term stability of dye-sensitized solar cell for outdoor use," *Solar Energy Materials and Solar Cells*, vol. 95, no. 1, pp. 301–305, 2011.
- [17] H. Tributsch, A. Barkschat, T. Moehl, and B. MacHt, "The function of  $TiO_2$  with respect to sensitizer stability in nanocrystalline dye solar cells," *International Journal of Photoenergy*, vol. 2008, Article ID 814951, 13 pages, 2008.
- [18] N. Kato, Y. Takeda, K. Higuchi et al., "Degradation analysis of dye-sensitized solar cell module after long-term stability test under outdoor working condition," *Solar Energy Materials and Solar Cells*, vol. 93, no. 6-7, pp. 893–897, 2009.
- [19] M. Toivola, J. Halme, L. Peltokorpi, and P. Lund, "Investigation of temperature and aging effects in nanostructured dye solar cells studied by electrochemical impedance spectroscopy," *International Journal of Photoenergy*, vol. 2009, Article ID 786429, 15 pages, 2009.
- [20] M. I. Asghar, K. Miettunen, J. Halme et al., "Review of stability for advanced dye solar cells," *Energy and Environmental Science*, vol. 3, no. 4, pp. 418–426, 2010.
- [21] A. Hauch and A. Georg, "Diffusion in the electrolyte and charge-transfer reaction at the platinum electrode in dye-sensitized solar cells," *Electrochimica Acta*, vol. 46, no. 22, pp. 3457–3466, 2001.
- [22] B. Macht, M. Turrión, A. Barkschat, P. Salvador, K. Ellmer, and H. Tributsch, "Patterns of efficiency and degradation in dye sensitization solar cells measured with imaging techniques," *Solar Energy Materials and Solar Cells*, vol. 73, no. 2, pp. 163–173, 2002.
- [23] H. Pettersson and T. Gruszecki, "Long-term stability of low-power dye-sensitized solar cells prepared by industrial methods," *Solar Energy Materials and Solar Cells*, vol. 70, no. 2, pp. 203–212, 2001.
- [24] K. Tennakone, G. R. R. A. Kumara, I. R. M. Kottegoda, K. G. U. Wijayantha, and V. P. S. Perera, "A solid-state photovoltaic cell sensitized with a ruthenium bipyridyl complex," *Journal of Physics D*, vol. 31, no. 12, pp. 1492–1496, 1998.
- [25] H. Desilvestro, M. Bertoz, S. Tulloch, and G. Tulloch, "Packaging, scale-up and commercialization of dye solar cells," in *Dye-Sensitized Solar Cells*, K. Kalyanasundaram, Ed., EPFL Press, Lausanne, Switzerland, 2010.
- [26] ASTM International ASTM G173-03. Standard Tables for Reference Solar Spectral Irradiances: Direct Normal and Hemispherical on 37° Tilted Surface, 2008.

- [27] M. Grätzel, "Perspectives for dye-sensitized nanocrystalline solar cells," *Progress in Photovoltaics*, vol. 8, no. 1, pp. 171–185, 2000.
- [28] S. Ferrere and B. A. Gregg, "Large increases in photocurrents and solar conversion efficiencies by UV illumination of dye sensitized solar cells," *Journal of Physical Chemistry B*, vol. 105, no. 32, pp. 7602–7605, 2001.

## Research Article

# Preparation and Photocatalytic Property of TiO<sub>2</sub>/Diatomite-Based Porous Ceramics Composite Materials

Shuilin Zheng,<sup>1</sup> Chunhua Bai,<sup>1</sup> and RuQin Gao<sup>2</sup>

<sup>1</sup> School of Chemical and Environmental Engineering, China University of Mining and Technology, Beijing 100083, China

<sup>2</sup> Institute of Environmental Engineering, North China Institute of Water Conservancy and Hydroelectric Power, Zhengzhou 450011, China

Correspondence should be addressed to Chunhua Bai, baichunhua1978@163.com

Received 13 July 2011; Revised 11 September 2011; Accepted 16 October 2011

Academic Editor: Jiaguo Yu

Copyright © 2012 Shuilin Zheng et al. This is an open access article distributed under the Creative Commons Attribution License, which permits unrestricted use, distribution, and reproduction in any medium, provided the original work is properly cited.

The diatomite-based porous ceramics was made by low-temperature sintering. Then the nano-TiO<sub>2</sub>/diatomite-based porous ceramics composite materials were prepared by hydrolysis deposition method with titanium tetrachloride as the precursor of TiO<sub>2</sub> and diatomite-based porous as the supporting body of the nano-TiO<sub>2</sub>. The structure and microscopic appearance of nano-TiO<sub>2</sub>/diatomite-based porous ceramics composite materials was characterized by XRD and SEM. The photocatalytic property of the composite was investigated by the degradation of malachite green. Results showed that, after calcination at 550°C, TiO<sub>2</sub> thin film loaded on the diatomite-based porous ceramics is anatase TiO<sub>2</sub> and average grain size of TiO<sub>2</sub> is about 10 nm. The degradation ratio of the composite for 5 mg/L malachite green solution reached 86.2% after irradiation for 6 h under ultraviolet.

## 1. Introduction

Among various oxide semiconductor photocatalysts, titania appears to be a promising and important prospect for using in environment purification due to its strong oxidizing power, photoinduced hydrophilicity, nontoxicity, considering cost, and chemical and photochemical stability [1–3]. And its photocatalytic performance may be further improved, through surface modification, or made into special shape like nanotubular [4, 5]. But nano-TiO<sub>2</sub> is not convenient to use and hard to recycle after using, so it has been an important research direction for nano-TiO<sub>2</sub>-photo catalysis that the nano-TiO<sub>2</sub> is made to load on some porous material, such as charcoal, silica, hierarchical flower-like boehmite superstructures (HFBS), hierarchical flower-like  $\beta$ -Ni(OH)<sub>2</sub> superstructures, montmorillonite, and diatomite [6–10].

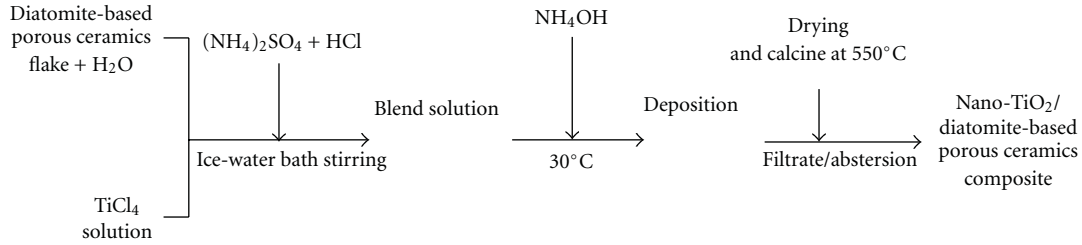
The diatomite is a natural mineral materials with amorphous silica as main composition, which is low in bulk density, stable in chemical property, and large in specific area. Many researchers have reported on the photocatalytic material with diatomite as substrate. However, few were about the loaded nano-TiO<sub>2</sub> on the surface of diatomite-based porous ceramics. In this paper, taking diatomite as base and adding

an amount of ultrafine tourmaline and sintering additive, we prepared the diatomite-based porous ceramics by low-temperature sintering and analyzed its characterization, and then the nano-TiO<sub>2</sub>/diatomite-based porous ceramics composite was made by hydrolysis deposition method with titanium tetrachloride as the precursor of TiO<sub>2</sub> and diatomite-based porous as the supporting body of the nano-TiO<sub>2</sub>. The photocatalysis property of the composite for the degradation of malachite green was tested.

## 2. Experimental Section

The diatomite is from Linjiang Meston Powder Material Co., Ltd., whose main composition is SiO<sub>2</sub> 80.39%, Al<sub>2</sub>O<sub>3</sub> 4.07%, and Fe<sub>2</sub>O<sub>3</sub> 1.87%. Its median particle size is 7.8  $\mu$ m, specific surface area 20.88 m<sup>2</sup>/g. Other materials are ultra-fine tourmaline (median particle size 2.80  $\mu$ m), sintering assistant, cementing agent, and dispersing agent.

Titanium tetrachloride, ammonium sulfate, is from Beijing Yili Fine Chemical Co., Ltd. Malachite-green is from Beijing Beihua Chemical Co., Ltd. First, the diatomite, tourmaline, sintering assistant with water, some dispersing agent,



SCHEME 1

and cementing agent were mixed and milled to 1.2  $\mu\text{m}$  average particle size in the sand mill Mini-Zeta and then dried in oven at 105°C and formed under 40 MPa, sintered at 960°C. The preparation route of the composite of nano-TiO<sub>2</sub> supported on diatomite-based porous ceramic is as in Scheme 1.

The phase composition of the carrier and titanium dioxide thin membrane has been confirmed by Dutch X-ray diffraction (tube voltage 40 kV, tube electric current 40 mA, Cu target, length of stride  $A = 1.5406\lambda$ , the rate of march 5°/min, collects diffraction data scope 20°~80°). The microstructure of porous ceramics composite was observed with scanning electronic microscope (SEM, ST-2000).

Photocatalytic activity experiments of the nano-TiO<sub>2</sub>/diatomite-based porous ceramics composites was carried out in a photo-catalytic test equipment shown in Figure 1, taking 5 mg/L, 10 mg/L, and 20 mg/L malachite green solution as initial density. First, the composites were soaked 24 h in the malachite green solution then dried and put on the support in the beaker (1 g sample for 100 g malachite green solution). The position of the composites is 5 mm under the liquid level, and the distance between the liquid level and ultraviolet tube is 50 mm. The 5 mL reaction suspension sample was taken in space for 30 min. The absorbency of suspension in irradiated photo-catalytic degradation processing (in the lens hood) was tested with a spectrophotometer (UV-2000, Shanghai) at solution characteristic wavelength (malachite green  $\lambda_{\text{max}} = 618 \text{ nm}$ ). Photo-catalytic activity of the nano-TiO<sub>2</sub>/diatomite-based porous ceramics composites was characterized by malachite green solution degeneration rate or decoloration rate. According to Langmuir law, there is a linear relation between the absorbency and the density at the characteristic wavelength. The decoloration rate calculates as follows:

$$\eta = \frac{(A_0 - A_t)}{A_0} \times 100\%. \quad (1)$$

Herein,  $\eta$  stands for the malachite green solution decoloration rate,  $A_0$  stands for the absorbency of malachite green solution, and  $A_t$  stands for the absorbency after illumination  $t$  time.

### 3. Results and Discussion

Figure 2 shows the SEM photograph of diatomite-based porous ceramics (Figure 2(a)) and the nano-TiO<sub>2</sub>/diatomite-based porous ceramics composite (Figure 2(b)). As in Figure 2(a), plentiful diatomaceous primitive hole and the

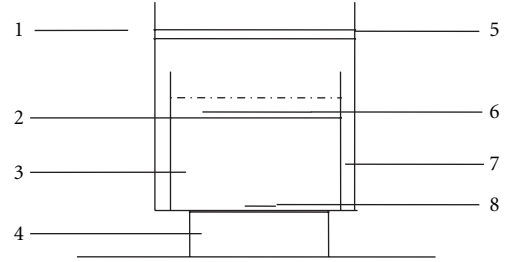


FIGURE 1: The instrument of degradation on malachite-green 1-Lens hood; 2-support; 3-malachite green solution; 4-magnetic force stirrer; 5-high-pressure mercury lamp; 6-diatomite-based porous ceramics loaded titanium dioxide; 7-cooling water; 8-roter.

crevice formed by the pellet stack in the diatomite-based porous ceramics can be observed, the aperture of which is tiny. As in Figure 2(b), on the diatomite-based porous ceramics surface and the opening wall, the size of grain that is dispersed evenly in the diatomite-based porous ceramics surface and the passageway is about 10 nm. This kind of microstructure is important to increase the active sites of the photochemical catalysis and improve the photochemical catalysis efficiency. And the BET surface area of composite is 28.9 m<sup>2</sup>/g.

The XRD patterns of samples of diatomite-based porous ceramics and nano-TiO<sub>2</sub>/diatomite-based porous ceramics composites are shown in Figure 3. The peaks at  $2\theta = 26.8^\circ$ ,  $36.8^\circ$  are characteristic peaks of silica, which show that silica is the primarily composition of diatomite-based porous ceramics. For the nano-TiO<sub>2</sub>/diatomite-based porous ceramics composite, the characteristic peaks of anatase crystal TiO<sub>2</sub> have been shown at  $2\theta = 25.2^\circ$  (101),  $37.7^\circ$  (004),  $48.0^\circ$  (200), and so on, which explains that the tiny grain deposited on surface of the diatomite-based porous ceramics was anatase.

By diffraction peak width  $B$  at half intension of Figure 3(2), the average grain size of TiO<sub>2</sub> calculated by Scherrer's formula is 10.6 nm, which is consistent with Figure 2(b) observed.

Figure 4 is EDS spectra of diatomite porous ceramics and nano-TiO<sub>2</sub>/diatomite-based porous ceramics composites. As in Figure 4(a), diatomite-based porous ceramics is mainly composed of Si, O, Al, K, Fe, Si, and so forth, and the Si, O element content is outstanding, which is consistent with its X-diffraction pattern of diatomite-based porous ceramics. For the nano-TiO<sub>2</sub>/diatomite-based porous ceramics composite, the Ti element peaks may be seen from Figure 4(b).

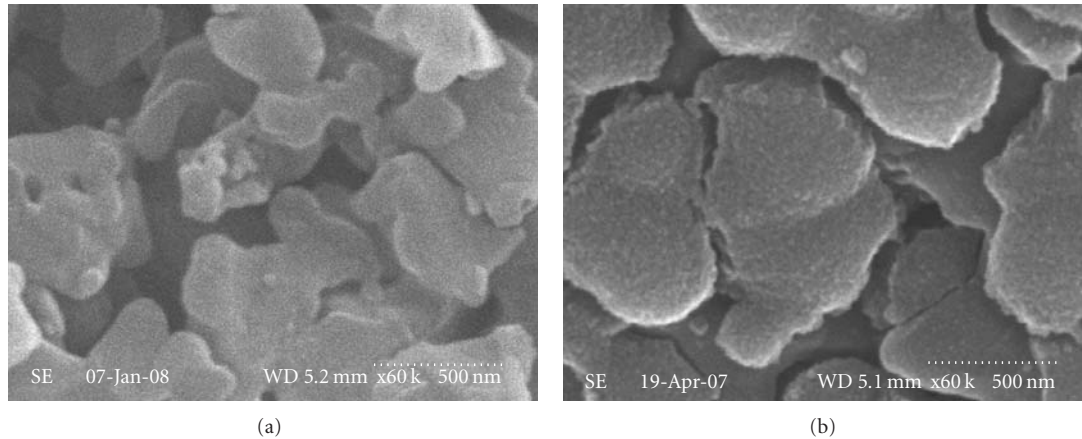


FIGURE 2: SEM photograph of diatomite-based porous ceramics (a) and nano-TiO<sub>2</sub>/diatomite-based porous ceramics composite (b).

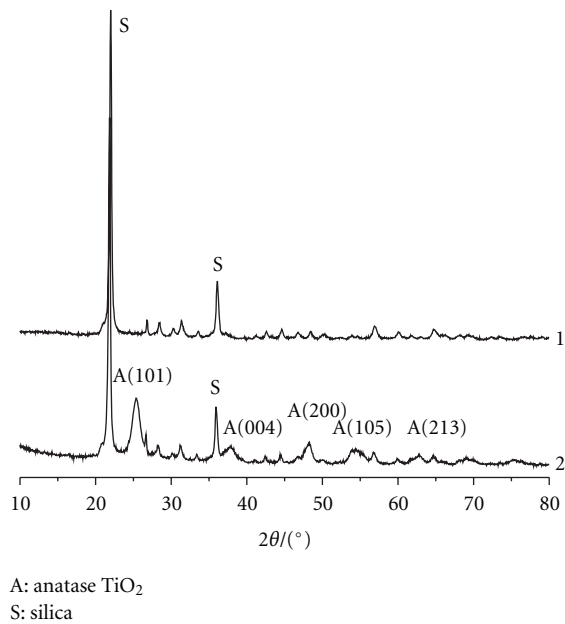


FIGURE 3: XRD patterns of samples. 1: diatomite-based porous ceramics. 2: nano-TiO<sub>2</sub>/diatomite-based porous ceramics composite.

Because of Ti element in surface layer of the diatomite-based porous ceramics, Si, Al, and other elements peaks intensity is obviously dropped. And the TiO<sub>2</sub> concentration of the composite obtained through EDS spectra is about 10.11%.

Figure 5 is the degradation rate curve of different initial densities of malachite green solution with the illumination time. The results indicate that degeneration rate rises gradually with the illumination time. At first, the degradation speed is quick, which slows down after 3 h. With illumination time increases, the intermediary products increase, accumulate on the TiO<sub>2</sub> film, and then reduce the active sites participating in the response, which decrease the photocatalytic activity. The higher the initial density is, the lower is the photocatalysis degradation rate. With the malachite green density thickens, the solution light-admitting quality drops as well as the ultraviolet light intensity which irradiates

to the film surface to stimulate photochemical catalysis reduces. When initial density of the malachite green solution is 5 mg/L, the degradation rate of it is at its maximum, which reaches 82.4% and is higher than pure TiO<sub>2</sub> (74.5%) in 6 h.

Nano-TiO<sub>2</sub>/diatomite-based porous ceramics composites can improve the photocatalysis effect for malachite green solution, which is related to the properties of support material. Firstly, the porous ceramics surface and the opening wall are quite rough, the specific surface area is high, and the physical adsorption force between ceramics and the TiO<sub>2</sub> particles is strong. Once they contact, opposite electric charges will accumulate in the contact surface for electron transporting, which attract mutually, and strengthen the adsorption of TiO<sub>2</sub> thin film to carrier. Secondly, the pore structures of the diatomite-based porous ceramics provide more surface activity sites and increase illumination area of TiO<sub>2</sub> thin film and the number of the catalyst granule, which is advantageous to improve the photocatalysis efficiency. The primary cause of low nano-TiO<sub>2</sub> photocatalysis quantum efficiency is when the valence band electrons jump to conduction band after absorbed proper photon, lots of electrons in conduction band will return and recombine with holes in valence band. Electrons and holes will be excited, when nano-TiO<sub>2</sub> loaded on diatomite-based porous ceramics contact with light. Although the photocatalyst of the inner pore cannot obtain illumination, which is advantageous to the electron transporting. It will reduce the recombination probability of surface layer holes and electrons and improve the photocatalysis activity.

Moreover, the ultrafine tourmaline introduced in the diatomite-based porous ceramics will increase the photocatalytic activity of the material. The tourmaline itself in the diatomite-based porous ceramics has permanent electrode, and strong electric field (superficial field intensity achieves 10<sup>7</sup> V/cm<sup>3</sup>) existing on the surface will affect nano-TiO<sub>2</sub> under ultraviolet illumination. The conduction band electrons stimulated by high-energy photon are shifted to other mediums or the tourmaline-positive electrode in the tourmaline electric field, which reduces the compound probability of the holes and the electrons and raises the photoproduction hole applying factor.

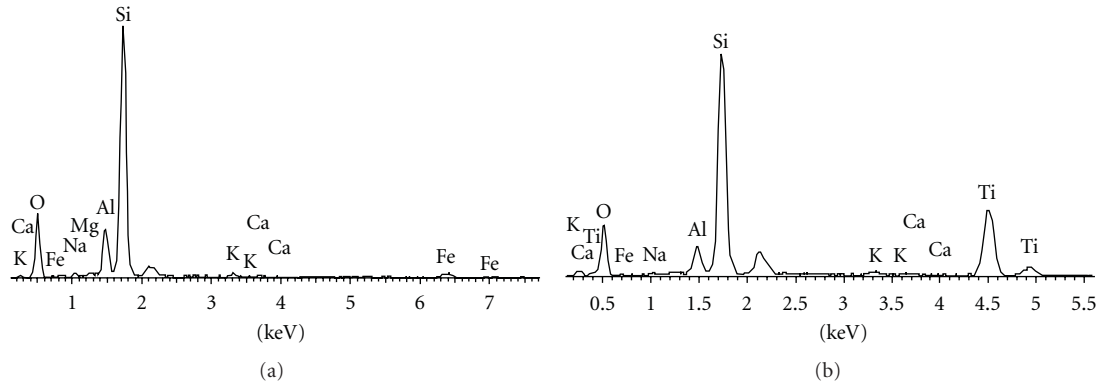


FIGURE 4: EDS spectra of diatomite-based porous ceramics (a) and Nano-TiO<sub>2</sub>/diatomite-based porous ceramics composite (b).

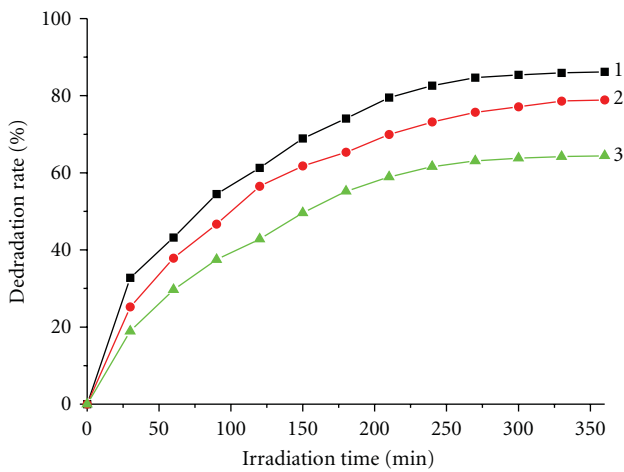


FIGURE 5: Photocatalysis degeneration curves of malachite green. 1: 5 mg/L; 2: 10 mg/L; 3: 20 mg/L.

#### 4. Conclusions

Taking diatomite as the main material with same ultrafine tourmaline powders and sintering additive added, the porous ceramics with tiny apertures has been made by sintering at low temperature.

Nano-TiO<sub>2</sub> diatomite-based porous ceramics composites with titanium tetrachloride as the precursor has been made by hydrolysis deposition. TiO<sub>2</sub> thin film loaded on the surface of diatomite-based porous ceramics is anatase TiO<sub>2</sub> crystal, and the average grain size of TiO<sub>2</sub> is about 10 nm.

Using the nano-TiO<sub>2</sub> diatomite-based porous ceramics composites to catalyze the malachite green, the degradation ratio of the malachite green reached 86.2% after irradiation 6 h under ultraviolet with initial density of malachite green solution 5 mg/L.

#### References

[1] J. A. Byrne, P. A. Fernandez-Ibañez, P. S.M. Dunlop, D. M.A. Alrousan, and J. W.J. Hamilton, "Photocatalytic enhancement

for solar disinfection of water: a review," *International Journal of Photoenergy*, vol. 2011, Article ID 798051, 12 pages, 2011.

- [2] G. F. Shang, H. B. Fu, S. G. Yang, and T. G. Xu, "Mechanistic study of visible-light-induced photodegradation of 4-chlorophenol by TiO<sub>2-x</sub>N<sub>x</sub> with Low Nitrogen Concentration," *International Journal of Photoenergy*, vol. 2012, Article ID 759306, 9 pages, 2012.
- [3] J. Yu, J. F. Xiong, B. Cheng, and S. Liu, "Fabrication and characterization of Ag-TiO<sub>2</sub> multiphase nanocomposite thin films with enhanced photocatalytic activity," *Applied Catalysis B*, vol. 60, no. 3-4, pp. 211–221, 2005.
- [4] W. C. Oh and M. L. Chen, "The improved photocatalytic properties of methylene blue for V<sub>2</sub>O<sub>3</sub>/CNT/TiO<sub>2</sub> composite under visible light," *International Journal of Photoenergy*, vol. 2010, Article ID 264831, 5 pages, 2010.
- [5] N. H. Lee, H. J. Oh, S. C. Jung, W. J. Lee, D. H. Kim, and S. J. Kim, "Photocatalytic properties of nanotubular-shaped TiO<sub>2</sub> powders with anatase phase obtained from titanate nanotube powder through various thermal treatments," *International Journal of Photoenergy*, vol. 2011, Article ID 327821, 7 pages, 2011.
- [6] P. Pucher, M. Benmami, R. Azouani et al., "Nano-TiO<sub>2</sub> sols immobilized on porous silica as new efficient photocatalyst," *Applied Catalysis A*, vol. 332, no. 2, pp. 297–303, 2007.
- [7] X. X. Yu, J. Yu, B. Cheng, and M. Jaroniec, "Synthesis of hierarchical flower-like AlOOH and TiO<sub>2</sub>/AlOOH superstructures and their enhanced photocatalytic properties," *Journal of Physical Chemistry C*, vol. 113, no. 40, pp. 17527–17535, 2009.
- [8] G. K. Zhang, X. M. Ding, F. S. He et al., "Low-temperature synthesis and photocatalytic activity of TiO<sub>2</sub> pillared montmorillonite," *Langmuir*, vol. 24, no. 3, pp. 1026–1030, 2008.
- [9] J. Yu, W. Wang, and B. Cheng, "Synthesis and enhanced photocatalytic activity of a hierarchical porous flowerlike *p-n* junction NiO/TiO<sub>2</sub> photocatalyst," *Chemistry*, vol. 5, no. 12, pp. 2499–2506, 2010.
- [10] Y. Jia, W. Han, G. Xiong, and W. Yang, "Layer-by-layer assembly of TiO<sub>2</sub> colloids onto diatomite to build hierarchical porous materials," *Journal of Colloid and Interface Science*, vol. 323, no. 2, pp. 326–331, 2008.

## Research Article

# Neodymium-Doped TiO<sub>2</sub> with Anatase and Brookite Two Phases: Mechanism for Photocatalytic Activity Enhancement under Visible Light and the Role of Electron

Douga Nassoko,<sup>1</sup> Yan-Fang Li,<sup>1</sup> Jia-Lin Li,<sup>1</sup> Xi Li,<sup>2,3</sup> and Ying Yu<sup>1</sup>

<sup>1</sup> Institute of Nanoscience and Nanotechnology, Central China Normal University, Wuhan 430079, China

<sup>2</sup> Jiangsu Huannengtong Environment Protection Co. Ltd, Zhenjiang 212006, China

<sup>3</sup> Zhenjiang King Lithium Cell Co. Ltd, Zhenjiang 212006, China

Correspondence should be addressed to Ying Yu, yuying@phy.ccnu.edu.cn

Received 14 August 2011; Accepted 30 September 2011

Academic Editor: Jiaguo Yu

Copyright © 2012 Douga Nassoko et al. This is an open access article distributed under the Creative Commons Attribution License, which permits unrestricted use, distribution, and reproduction in any medium, provided the original work is properly cited.

Titanium dioxide (TiO<sub>2</sub>) doped with neodymium (Nd), one rare earth element, has been synthesized by a sol-gel method for the photocatalytic degradation of rhodamine-B under visible light. The prepared samples are characterized by X-ray diffractometer, Raman spectroscopy, UV-Vis diffuse reflectance spectroscopy, X-ray photoelectron spectroscopy, and Brunauer-Emmett-Teller measurement. The results indicate that the prepared samples have anatase and brookite phases. Additionally, Nd as Nd<sup>3+</sup> may enter into the lattice of TiO<sub>2</sub> and the presence of Nd<sup>3+</sup> substantially enhances the photocatalytic activity of TiO<sub>2</sub> under visible light. In order to further explore the mechanism of photocatalytic degradation of organic pollutant, photoluminescence spectrometer and scavenger addition method have been employed. It is found that hydroxide radicals produced by Nd-doped TiO<sub>2</sub> under visible light are one of reactive species for Rh-B degradation and photogenerated electrons are mainly responsible for the formation of the reactive species.

## 1. Introduction

Dye wastewater discharged into nature mainly by dyestuff, textile industry, and some artificial way causes severe ecological problems. These compounds are highly colored and can heavily contaminate water source. Chemical oxidation method for dye wastewater treatment is too costly and physical adsorption method often results in secondary pollution [1]. Many attempts have been carried out to develop efficient biological methods to decolorize these effluents but they have not been very successful. Semiconductor TiO<sub>2</sub> as a photocatalyst has been deeply investigated and can successfully degrade various organic pollutants [2–6]. However, the overall efficiency achieved so far with TiO<sub>2</sub>-based systems is not sufficiently high to enable practical applications. This low efficiency is mainly due to the fast recombination of charge carriers produced by irradiated TiO<sub>2</sub> and thus the low quantum yield in the generation of

reactive species for organic degradation [7, 8]. Moreover, due to its large bandgap (~3.2 eV), all photo-driven applications of TiO<sub>2</sub> require ultraviolet light excitation. As a consequence, TiO<sub>2</sub> shows photocatalytic activities under only a small fraction (<5%) of solar irradiation [9], limiting its practical applications. Therefore, the modification of TiO<sub>2</sub> to enhance light absorption and photocatalytic activities under visible light has been the subject of recent research [10].

Many factors that influence the photodegradation efficiency of organic pollutants over TiO<sub>2</sub> have been reported during the past 30 years. The main focus is the physical properties of TiO<sub>2</sub>, including crystal phases, crystal facets, crystallinity, particle size, surface area, porosity, and morphology. It is not easy to make a reliable correlation between the structure and photoactivity of TiO<sub>2</sub> because the solid physical properties often affect one another. In general, anatase is considered to be much more active than rutile, while a mixture of anatase and rutile, like Degussa

P25, is claimed to be more active than anatase. So far, TiO<sub>2</sub> with anatase and brookite phases as a photocatalyst has been rarely studied because brookite TiO<sub>2</sub> has no activity for organic pollutant degradation and it needs higher temperature to prepare. Moreover, there has been little report about brookite TiO<sub>2</sub> preparation at low temperature.

The investigations about introducing foreign species are in progress for improving the photocatalytic activity of TiO<sub>2</sub> and broadening its absorption to solar spectrum. Among them, titania doped with metals or metallic cations such as transition metallic cations, rare metal cations, and noble metal have been widely explored [11, 12]. On one hand, these doped metallic cations tend to serve as recombination centers. As a result, in most cases, photoexcited charges are recombined by the sites of doping metallic cations [13]. On the other hand, it has been reported that suitable amount of metallic cation doping can promote the separation of photogenerated electrons for the improvement of photocatalytic activity [14, 15]. It is obvious that there is conflict. So, although there are quite a few publications about metal-doped TiO<sub>2</sub>, the mechanism for the improvement of photocatalytic activity has not been clear so far. It needs explore in detail.

In this paper, to explore the mechanism of photodegradation of organic pollutant by rare earth element-doped TiO<sub>2</sub>, neodymium (Nd) ion was selected as a TiO<sub>2</sub> dopant due to its stability to form complexes with various Lewis bases in the interaction of these functional groups with f-orbitals of neodymium metal [16]. Thus, incorporation of Nd ion into a TiO<sub>2</sub> matrix could provide an effective method to concentrate the organic pollutant at semiconductor surface. Here, Nd-doped TiO<sub>2</sub> samples were prepared by sol-gel method together with pure TiO<sub>2</sub> for comparison. The characteristics and properties of these photocatalyst were studied. The photocatalytic activity was evaluated by measuring photodegradation efficiency of rhodamine-B (Rh-B) under visible light. The photocatalytic mechanism of Nd-doped TiO<sub>2</sub> was also investigated in detail by photoluminescence spectrometer (PL) [17] and scavenger addition method [18].

## 2. Experimental Section

**2.1. Materials.** The chemicals used in this experiment except P25 were all analytical reagent and purchased from Shanghai Guoyao Chemical Co. Pure TiO<sub>2</sub>, P25, was commercial product from Germany. The used water throughout the whole research was double-distilled water.

**2.2. Experimental Procedure.** Neodymium-doped TiO<sub>2</sub> samples (Nd-doped TiO<sub>2</sub>) were prepared by sol-gel method. First, 5 mL of TiCl<sub>4</sub> was dissolved and hydrolyzed with 200 mL distilled frozen water (0°C). Second, Nd<sub>2</sub>O<sub>3</sub> with certain amount required for doping was suspended into a small amount of ethanol and then added to the above solution to produce transparent Nd<sup>3+</sup> aqueous solution under vigorous stirring. Third, 10 M NaOH aqueous solution was added dropwisely into the transparent TiCl<sub>4</sub> aqueous solution with

Nd<sup>3+</sup> to obtain a grey precipitate with an ultimate suspension of pH = 10.

In order to remove residual Na<sup>+</sup> and Cl<sup>-</sup> ions, the precipitate was adequately washed with deionized water till the pH value of filtrated water was below 7. Then, the amorphous Nd-doped TiO<sub>2</sub> was well dispersed into 400 mL of water, and chloride acid (20%) was added with corresponding amount. The above suspension was adjusted to pH 1.5, stirred for 4 hours at room temperature, and then had been aged at 70°C for 24 h in airproof condition. Finally, Nd<sup>3+</sup>-modified TiO<sub>2</sub> sol was formed with uniform, stable, and semitransparent characteristics. The obtained sol can maintain homogenous distribution for a long time without sedimentation and delamination. Powder sample was prepared by aging, gelation, and vacuum-drying treatment of the above sol at 70°C for 8 hours. TiO<sub>2</sub> sample was also prepared by the same procedure without the addition of the neodymium oxide suspension. The pure TiO<sub>2</sub> and Nd-doped TiO<sub>2</sub> samples were annealed in air at 400°C for 3 hours and ground to fine particles for different analysis.

**2.3. Characterization of Photocatalysts.** The crystalline phases of the synthesized TiO<sub>2</sub> and Nd-doped TiO<sub>2</sub> catalyst were analyzed by a Y-2000 diffractometer (*D/max* 30 kV) using graphite monochromatic copper radiation (Cu K $\alpha$ ) ( $\lambda$  = 0.154178 nm) at a scan rate of 0.06° 2 $\theta$ ·s<sup>-1</sup> at 40 kV, 40 mA over the diffraction angle range of 10 ~ 60°. Raman spectroscopy measurements were performed by using a Jobin Yvon Lab RAM HR 800UV micro-Raman system under an Ar<sup>+</sup> (514.5 nm) laser excitation. UV-Vis diffuse reflectance spectra (DRS) were recorded with a PerkinElmer Lambda 35 Spectrophotometer. X-ray photoelectron spectra (XPS) measurements were performed in a PHI Quantum 2000 XPS system with a monochromatic Al K $\alpha$  source and charge neutralizer to analyze surface chemicals and evaluate the amount and states of Nd atoms in the prepared samples. Nitrogen adsorption/desorption isotherms and Brunauer-Emmett-Teller (BET) specific surface area (*S*<sub>BET</sub>) were recorded on a Micrometrics ASAP 2010 analyzer (accelerated surface area and porosimetry system). All the samples were treated at 100°C prior to BET measurements. Barret-Joyner-Halender (BJH) method was used to determine pore size distribution. The formation of hydroxyl radicals (\*OH) on the surface of prepared samples under visible light was detected by a terephthalic acid (TA) probe method [17]. The PL spectra of generated 2-hydroxyterephthalic acid (TAOH) were measured by using a PerkinElmer Lambda 55 fluorescence spectrophotometer.

**2.4. Photocatalytic Activity Measurement.** The photocatalytic activities of the prepared samples were examined by the degradation of Rh-B under visible light. A 350 W Xenon lamp (Lap Pu, XQ) was used as a light source with a 420 nm cutoff filter right above the reactor to provide visible-light irradiation. The experiments were performed in self-constructed beaker-like glassware reactor with double walls for cooling system. 0.1 g of prepared sample was dispersed in 100 mL Rh-B solution with concentration of 10  $\mu$ M. Prior to

irradiation, the solution was stirred in dark for 30 minutes to reach an adsorption/desorption equilibrium. Then, the solution was exposed to light while stirring. 1 mL suspension was collected every 30 minutes and was centrifuged for solid-liquid separation. Rh-B residue concentration was determined by measuring characteristic absorption intensity of Rh-B absorption spectrum over a Shimadzu UV-1700 UV-vis spectrophotometer.

Scavenger addition method [18] was used to explore the mechanism of photodegradation of Rh-B over Nd-doped TiO<sub>2</sub>. The whole process was almost the same as that of the above photocatalytic activity measurement except with the presence of different scavengers: sodium oxalate (Na<sub>2</sub>Cr<sub>2</sub>O<sub>4</sub>) as hole scavenger, KI as hole, and •OH scavenger and K<sub>2</sub>Cr<sub>2</sub>O<sub>6</sub> (Cr (VI)) as electron scavenger.

### 3. Results and Discussion

**3.1. Characterization of TiO<sub>2</sub> and Nd-Doped TiO<sub>2</sub> Photocatalysts.** The degree of crystallinity and crystal structure of the prepared TiO<sub>2</sub> and Nd-doped TiO<sub>2</sub> samples were examined by XRD. The diffractograms recorded are shown in Figure 1. It reveals that the samples had anatase and brookite phases, a mixture of crystal structure. The phase content for the prepared samples is displayed in Table 1. With the increase in Nd doping amount, brookite phase content increased. In this study, the addition of NaOH to reaction solution increased pH value, leading to the increase of OH<sup>-</sup> concentration. This might promote the formation of brookite phase because its complex consumed the amount of OH<sup>-</sup> twice as much as rutile's one. However, too much NaOH could result in the formation of amorphous TiO<sub>2</sub> which contained much more OH<sup>-</sup> than brookite complex [19–22]. The grain sizes of the prepared TiO<sub>2</sub> and Nd-doped TiO<sub>2</sub> powders were calculated using Scherrer equation:

$$D = \frac{K\lambda}{\beta \cos \theta}, \quad (1)$$

where  $D$  is crystalline size,  $\lambda$  the wavelength of X-ray radiation (0.1541 nm),  $K$  the constant usually taken as 0.89, and  $\beta$  the peak width at half-maximum height and  $\theta$  diffraction angle. The obtained crystalline sizes are shown in Table 1. There was almost no change for crystallite size when Nd was incorporated (20.32 nm for pure TiO<sub>2</sub> and 20.35 nm for Nd-doped TiO<sub>2</sub> with Ti : Nd = 11 : 1). The phase content of TiO<sub>2</sub> can be calculated from the integrated intensities of anatase (101), rutile (101), and brookite (121) peaks with the following formulas [23]:

$$\begin{aligned} W_A &= \frac{k_A A_A}{k_A A_A + A_R + k_B A_B}, \\ W_R &= \frac{A_R}{k_A A_A + A_R + k_B A_B}, \\ W_B &= \frac{k_B A_B}{k_A A_A + A_R + k_B A_B}, \end{aligned} \quad (2)$$

where  $W_A$ ,  $W_R$ ,  $W_B$  represent the weight fractions of anatase, rutile, and brookite, respectively. The other symbols  $A_A$ ,  $A_R$ ,

and  $A_B$  are the integrated intensities of anatase (101), rutile (110), and brookite (121) peaks, respectively. The variables  $k_A$  and  $k_B$  are two coefficients and their values are 0.886 and 2.721, respectively. The calculated data are shown in Table 1.

Substantially, the enlarged peaks at (101) (JCPDS number: 21-1272) and (121) plane for the three samples (Figures 1(B) and 1(C)) showed a slight shift to smaller angles with Nd incorporation. It indicates that Nd ion could enter into TiO<sub>2</sub> lattice or interstitial site. We know that the difference in ionic radius between neodymium ion (Nd<sup>3+</sup> = 0.11 nm) and titanium ion (Ti<sup>4+</sup> = 0.064 nm) is large. Without calcination treatment in high temperature, neodymium ions introduced by the coprecipitation-peptization method would unlikely enter into TiO<sub>2</sub> crystal structure. Actually, during TiCl<sub>4</sub> hydrolysis and peptization reaction, neodymium and oxygen ions could form Nd-O oxide on the superficial layer of TiO<sub>2</sub> [19, 20] particle by chemical bonding process and Nd<sup>3+</sup> ions mainly existed as Nd–O–Ti in Nd-doped TiO<sub>2</sub> mixture [25]. So, the conversion from amorphous to well-crystalline structure usually requires high annealing temperature of at least 400°C.

The XRD studies revealed the anatase and brookite structure of the prepared samples. The formation of the structure was further confirmed by Raman spectroscopy. In Figure 2(A), Raman spectra of pure TiO<sub>2</sub> and Nd-doped TiO<sub>2</sub> are shown. It can be seen that the peaks observed at around 144.86, 398.17, 515.33, and 637.86 cm<sup>-1</sup> were attributed to anatase TiO<sub>2</sub>. The strongest Eg mode at 144.86 cm<sup>-1</sup> arising from the external vibration of the anatase structure was well resolved, which indicates that anatase phase was formed in the as-prepared nanocrystals [24]. Its amplified figure is shown in Figure 2(B). It can be found that there was a distinct shift to high wave number after Nd doping, which is also an evidence to verify that Nd may be introduced into the lattice or interstitial site of titania. Additionally, there were three weak peaks at 240.22, 317.01, and 360.44 cm<sup>-1</sup> attributed to vibration modes for brookite phase of TiO<sub>2</sub> in Figure 2(A). The absence of the characteristic vibration modes of Nd or Nd<sub>2</sub>O<sub>3</sub> in the Raman spectra suggests that there was no Nd<sub>2</sub>O<sub>3</sub> segregation into TiO<sub>2</sub>.

The UV-Vis diffuse reflectance spectra (DRS) for the doped and the undoped TiO<sub>2</sub> nanoparticles samples are presented in Figure 3. Modification of TiO<sub>2</sub> with Nd significantly affected the light absorption property of the photocatalysts. A red shift of the absorption edge toward the visible region was observed for Nd-doped TiO<sub>2</sub> compared with pure TiO<sub>2</sub>. From XRD and Raman data, we can see that Nd doping led to a little change of TiO<sub>2</sub> crystal structure and there was a little shift for the main peaks. The change of TiO<sub>2</sub> crystal structure may be due to the incorporation of Nd ion into TiO<sub>2</sub> lattice. It can result in new energy level in the bandgap and charge transfer between TiO<sub>2</sub> valence band and Nd ion doping level [21]. As a result, the Nd-doped TiO<sub>2</sub> had lower bandgap and the presence of Nd in the doped photocatalyst facilitated visible-light absorption. By plotting  $(\alpha E)^{1/2}$  versus  $E$  with  $\alpha$  the absorption coefficient, the bandgap was calculated to be 3.11 eV for pure TiO<sub>2</sub>, 2.57 eV for Nd-doped TiO<sub>2</sub> with Ti : Nd = 23 : 1 and 2.33 eV

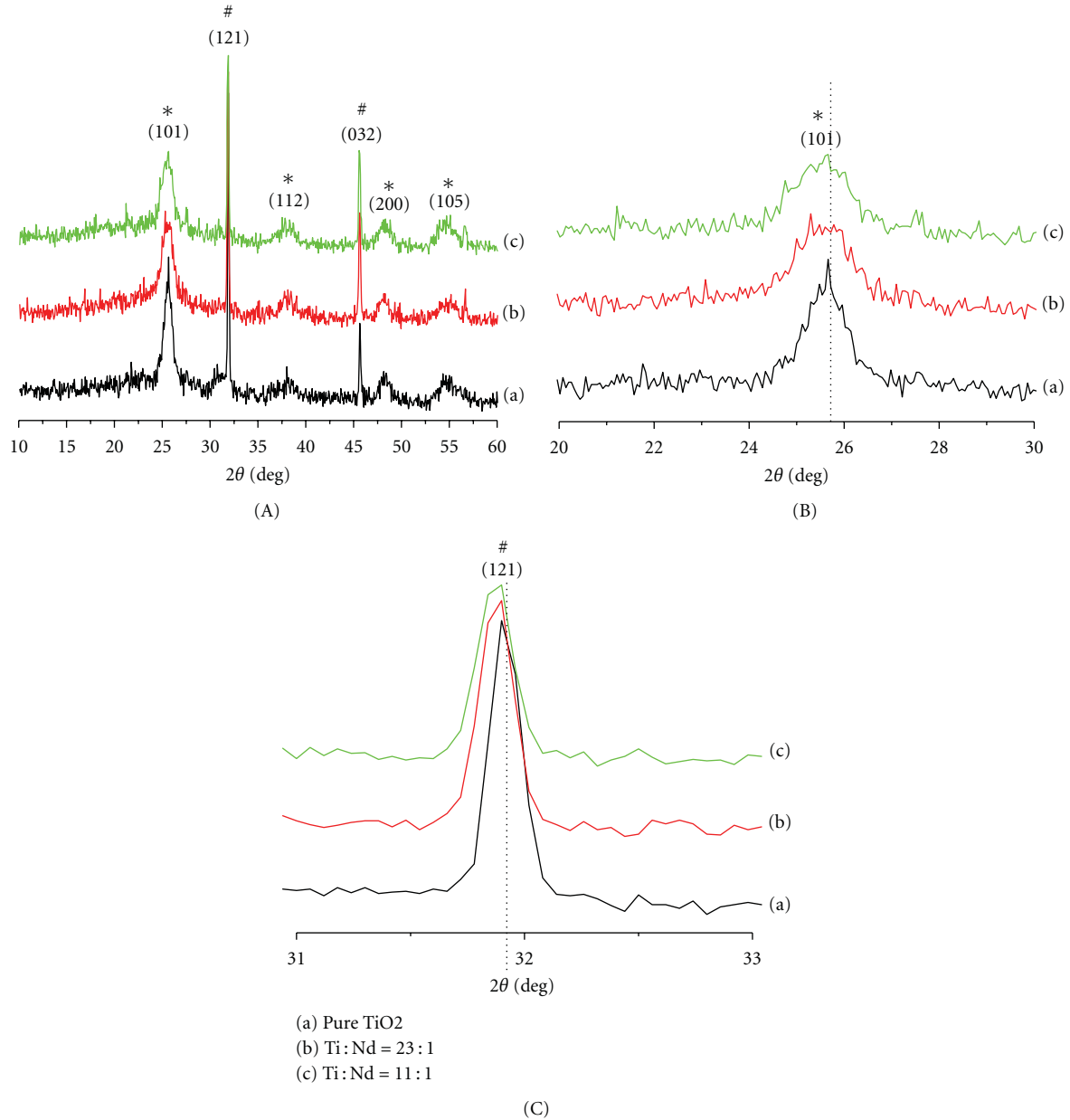


FIGURE 1: (A) XRD patterns of pure TiO<sub>2</sub> (a), Nd-doped TiO<sub>2</sub> with Ti:Nd = 23:1 (b), and Nd-doped TiO<sub>2</sub> with Ti:Nd = 11:1 (c). \*anatase, #brookite. (B) The enlarged peak at (101) plane and (C) enlarged peak at (121) plane.

TABLE 1: Summary of the physicochemical properties of TiO<sub>2</sub> and Nd-doped TiO<sub>2</sub> composites.

Sample	Average size crystalline size (nm) <sup>a</sup>	Phase content <sup>b</sup> (%)		BET surface area (m <sup>2</sup> ·g <sup>-1</sup> )	Pore size (nm) <sup>c</sup>	Total volume pore (cm <sup>3</sup> ·g <sup>-1</sup> )	Bandgap (eV)
		Anatase	Brookite				
Pure TiO <sub>2</sub>	20.32	13.97	86.02	72.46	3.54	0.172	3.11
Nd-doped TiO <sub>2</sub> (Ti:Nd = 23:1)	20.32	9.500	90.49	67.18	2.40	0.0830	2.57
Nd-doped TiO <sub>2</sub> (Ti:Nd = 11:1)	20.35	7.660	92.35	59.54	2.76	0.0831	2.33

<sup>a</sup>Determined by XRD using Scherrer equation based on (121) peak.

<sup>b</sup>Calculated using the formula in [24].

<sup>c</sup>Calculated from  $S_{BET}$ .

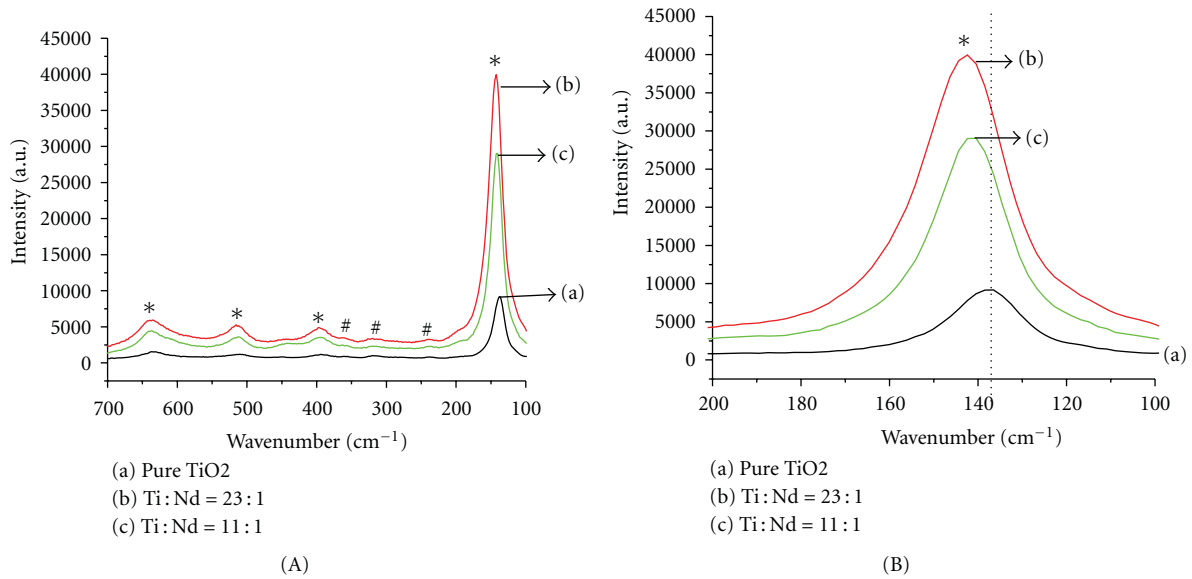


FIGURE 2: (A) Raman spectra of pure  $\text{TiO}_2$  (a), Nd-doped  $\text{TiO}_2$  with Ti:Nd = 23:1 (b), and Nd-doped  $\text{TiO}_2$  with Ti:Nd = 11:1 (c). (B) The enlarged peak at  $144.86 \text{ cm}^{-1}$ .

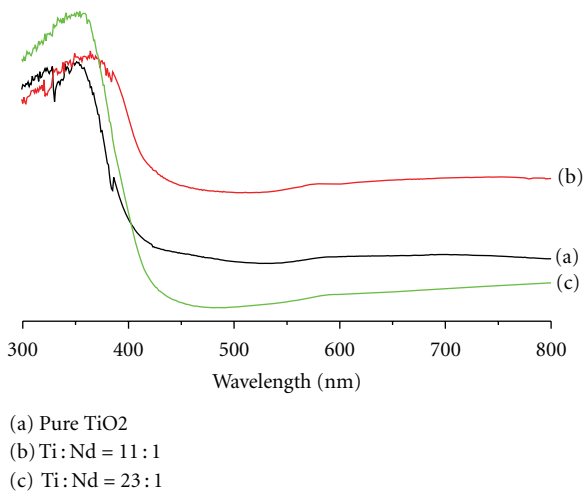


FIGURE 3: UV-Vis diffuse reflectance spectra of pure  $\text{TiO}_2$  (a), Nd-doped  $\text{TiO}_2$  with Ti:Nd = 23:1 (b), and Nd-doped  $\text{TiO}_2$  with Ti:Nd = 11:1 (c).

for that with Ti:Nd = 11:1. So, with the presence of Nd ion in  $\text{TiO}_2$  lattice, the bandgap of the materials decreased distinctly. Additionally, with the increase of Nd doping amount, the bandgap decreased gradually. It indicates that the Nd-doped  $\text{TiO}_2$  samples may have the higher ability to absorb visible light.

XPS technique is used to investigate chemical component at the surface of a sample. Figure 4 shows high-resolution XPS spectrum for Nd in the doped  $\text{TiO}_2$  sample. Although the peak for Nd was not so distinct, it can be confirmed that Nd was present in the doped sample. Figure 5 shows the high-resolution XPS spectrum for Ti 2p in pure  $\text{TiO}_2$  and Nd-doped  $\text{TiO}_2$  (Ti:Nd = 11:1) samples. The binding

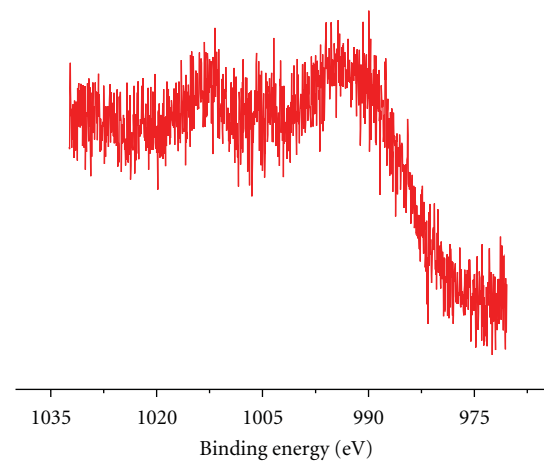


FIGURE 4: High-resolution XPS spectrum of Nd 3d for Nd-doped  $\text{TiO}_2$  with Ti:Nd = 11:1.

energy had 0.49 eV shift for  $\text{Ti } 2p_{3/2}$  and 0.65 eV for  $\text{Ti } 2p_{1/2}$ , indicating the presence of  $\text{Ti}^{4+}$  and  $\text{Ti}^{3+}$ . Besides, the graph of doped sample was fitted by three subpeaks with the binding energy of 460.05, 458.86, and 458.27 eV, which indicates the presence of  $\text{Ti}^{4+}$ , Nd-Ti, and  $\text{Ti}^{3+}$ , respectively. So, the complete incorporation of Nd into  $\text{TiO}_2$  lattice can be verified. The XPS spectra of the O 1s region of the pure  $\text{TiO}_2$  could be fitted into two subpeaks at 529.36 and 531.08 eV (Figure 6(a)), corresponding to the Ti-O bond in  $\text{TiO}_2$  and hydroxyl groups on the surface, respectively. However, the O 1s peak for Nd-doped  $\text{TiO}_2$  was located at 530.21 eV and could be fitted into three subpeaks at about 530.21, 531.34, and 532.84 eV (in Figure 6(b)), which can be ascribed to Ti-O, Nd-O, and hydroxyl group, respectively [26–28]. Therefore, three types of oxygen existed on the photocatalyst

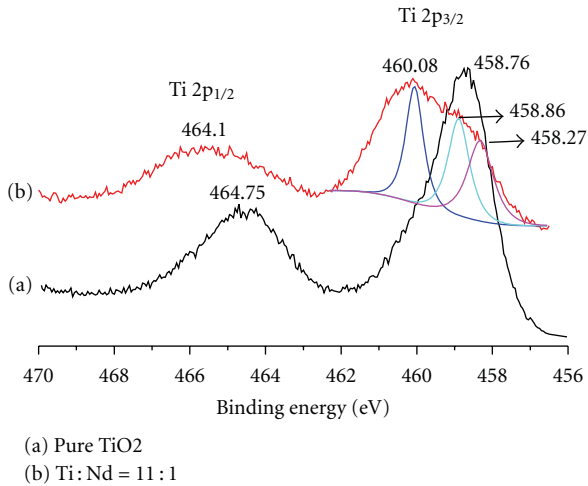


FIGURE 5: High-resolution XPS spectra of Ti 2p for pure TiO<sub>2</sub> (a) and Nd-doped TiO<sub>2</sub> with Ti:Nd = 11:1 (b).

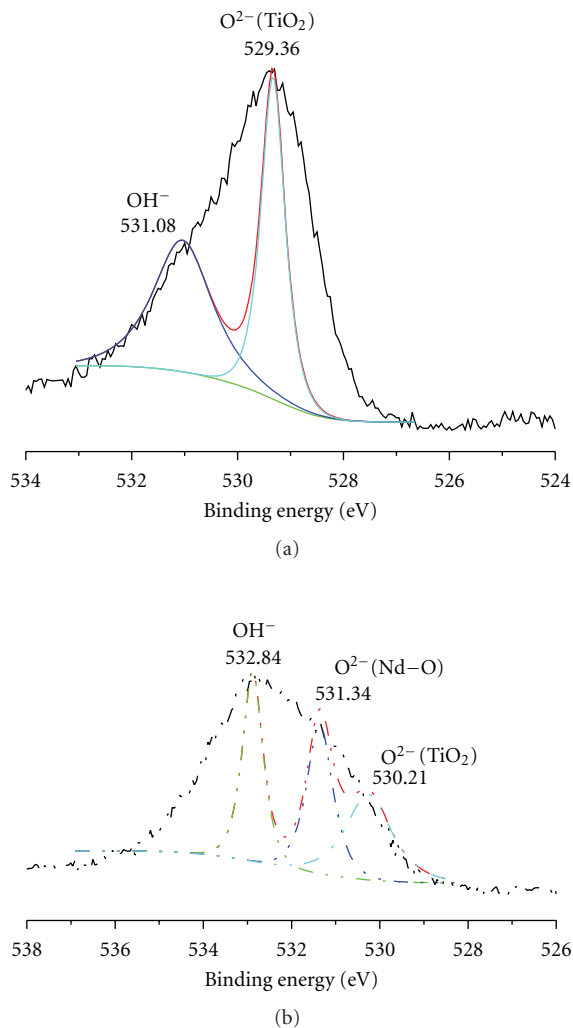


FIGURE 6: High-resolution XPS spectra of O 1s for pure TiO<sub>2</sub> (a) and Nd-doped TiO<sub>2</sub> with Ti:Nd = 11:1 (b).

surface, including Ti–O in TiO<sub>2</sub>, Nd–O, and hydroxyl group. These hydroxyl groups as hole trapped sites may inhibit the simple recombination of electron hole [29].

Surface textural characteristics of the samples pure TiO<sub>2</sub> and Nd-doped TiO<sub>2</sub> are derived from N<sub>2</sub> adsorption analysis. Specific surface area ( $S_{\text{BET}}$ ) by BET method, total pore volume calculated at  $P/P_0 = 0.99$ , and average pore diameter values are presented in Table 1. The adsorption isotherms (Figure 7) of the samples showed type IV behaviour with the typical hysteresis loop. This hysteresis is characteristic of mesoporous materials [30, 31]. The pore size distributions for the pure TiO<sub>2</sub> and Nd-doped samples are shown in Figure 8, which confirms the mesoporous nature of the samples. It can be seen in Table 1 that the doped sample had lower surface area and narrower average pore size distribution than the undoped one. This might be due to the slight increase of crystalline size for the doped titania mentioned in XRD pattern.

**3.2. Photocatalytic Activity of Prepared Samples.** The photocatalytic property of titania is known to depend on several factors like crystallinity, phase assemblage, and surface area [32]. The photocatalytic activity of neodymium-doped and undoped titania was studied through Rh-B degradation under visible light in comparison with commercial product P25. Figure 9 shows the variations of Rh-B concentration against irradiation time with the presence of photocatalysts. It can be seen that the concentration of Rh-B decreased gradually with the exposure time for the pure and doped TiO<sub>2</sub> samples. Without the presence of photocatalysts, almost no Rh-B could be degraded. The results illustrate that all of the prepared samples had the ability for Rh-B degradation under visible light even for pure TiO<sub>2</sub> and P25. Additionally, with the increase of Nd doping amount, the photocatalytic activity for the Nd-doped TiO<sub>2</sub> increased. However, when the amount of Nd in the doped TiO<sub>2</sub> was too much (Ti:Nd  $\geq$  6:1), the activity was even lower than that of pure TiO<sub>2</sub> and P25. So, there is an optional Nd doping amount, which is in accordance with the published studies [14, 33]. Nevertheless, the optional Nd doping amount is 0.5% [14] and 1 ~ 3 wt% [33] in the two papers. The amount calculated by raw reagents for the formation of Nd-doped TiO<sub>2</sub> samples was about 9%, which is much higher. In fact, there should not be so much Nd incorporated into TiO<sub>2</sub> in this case. The measurement of actual Nd amount in TiO<sub>2</sub> is in progress.

**3.3. Mechanism for Photocatalytic Activity Improvement by Nd Doping.** From Figure 9, we can see that even pure TiO<sub>2</sub> could degrade Rh-B under visible light. It is known that Rh-B can be excited by visible light and inject electrons to the conduction band of TiO<sub>2</sub>. So, the injected electrons react with O<sub>2</sub> molecules adsorbed on TiO<sub>2</sub> surface to yield  $\bullet\text{O}_2^-$  radical anion and subsequently HO $\bullet$  radical by protonation [34]. So, in this case, Rh-B can be degraded in even undoped TiO<sub>2</sub> and P25 systems although their photodegradation efficiency is not high.

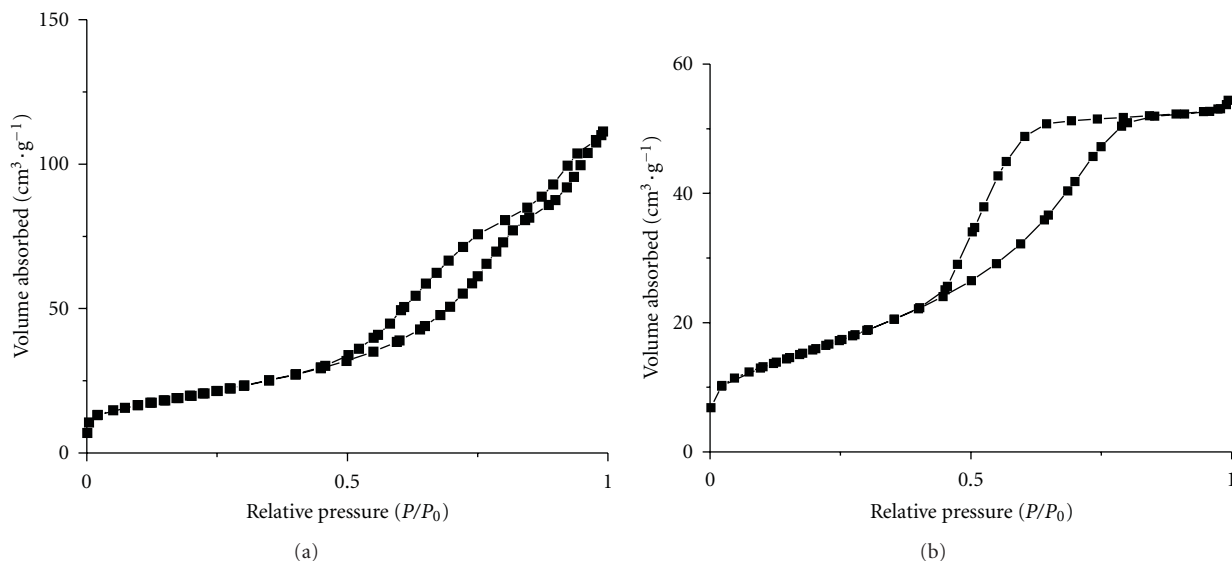


FIGURE 7: N<sub>2</sub> adsorption/desorption isotherms of pure TiO<sub>2</sub> (a) and Nd-doped TiO<sub>2</sub> with Ti: Nd = 11 : 1 (b).

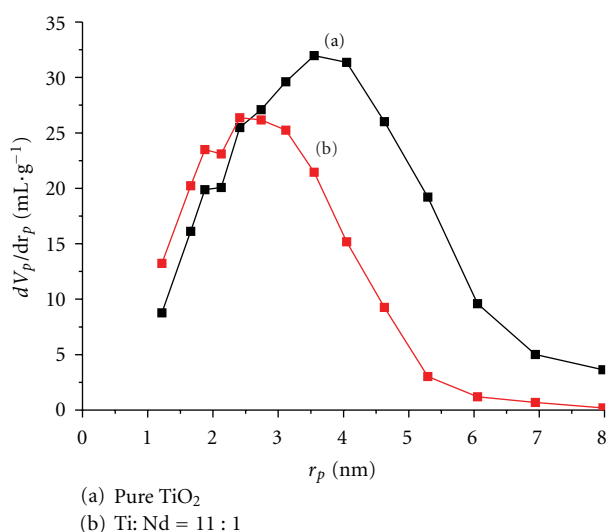


FIGURE 8: BJH pore size distribution curves for pure TiO<sub>2</sub> (a) and Nd-doped TiO<sub>2</sub> (Ti: Nd = 11 : 1) (b).

From Table 1 and Figure 7, we can see that the surface area of Nd-doped samples was lower than that of pure TiO<sub>2</sub> although all of them had mesoporous structure. So, based on dye and O<sub>2</sub> adsorption, there is no advantage for Nd doped samples compared with pure TiO<sub>2</sub>. As discussed in the XRD patterns and XPS spectra, there is Nd which may substitute titanium in the lattice and exist as the state of Nd<sup>3+</sup> although the ion radius of Nd<sup>3+</sup> is much larger than that of Ti<sup>4+</sup>. The doping energy level of Nd<sup>3+</sup>/Nd<sup>2+</sup> is -0.4 eV [35], which is more positive than the potential of conduction band of TiO<sub>2</sub> particles {E<sub>cb</sub> = -0.5 eV versus NHE (normal hydrogen electrode) at pH = 1} [36]. Therefore, after Nd doing, the electrons can be excited from valance band to the Nd<sup>3+</sup>/Nd<sup>2+</sup> doping energy level under

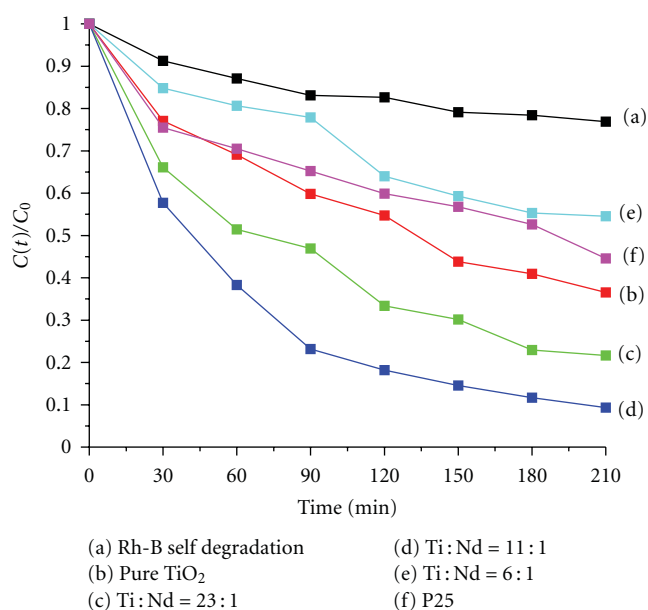


FIGURE 9: Photocatalytic degradation of Rh-B under visible light (solar simulator: 350 W Xenon lamp with a cutoff filter) with different conditions: (a) self degradation, (b) over pure TiO<sub>2</sub>, (c) over Nd-doped TiO<sub>2</sub> with Ti: Nd = 23 : 1, (d) over Nd-doped TiO<sub>2</sub> with Ti: Nd = 11 : 1, (e) over Nd-doped TiO<sub>2</sub> with Ti: Nd = 6 : 1, and (f) over P25.

visible light. The UV-Vis spectra verifies that the Nd doped TiO<sub>2</sub> had lower bandgap than TiO<sub>2</sub> and was responsive to visible light (Figure 3). Besides, the energy of Nd<sup>3+</sup>/Nd<sup>2+</sup> is below the conduction band of TiO<sub>2</sub>, so that it is easy for Nd<sup>3+</sup> to capture injected electron by Rh-B from the conduction band. The electrons on the Nd<sup>3+</sup>/Nd<sup>2+</sup> level can react with O<sub>2</sub> adsorbed on TiO<sub>2</sub> surface to yield •O<sub>2</sub><sup>-</sup> radical anion and subsequently HO• radical by protonation, just as the

electrons generated by Rh-B do. So, with the presence of part Nd in the lattice of  $\text{TiO}_2$ , there are more photogenerated electrons which participate in the formation of  $\cdot\text{O}_2^-$  radical anion and subsequently  $\text{HO}\cdot$  radical by protonation for dye degradation.

It can be seen from Figure 9 that the Nd-doped  $\text{TiO}_2$  with  $\text{Ti}:\text{Nd} = 6:1$  shows a negative effect on the photodegradation of Rh-B. In fact, metal ion dopant can act as a mediator of interfacial charge transfer or act as recombination center. So, there is an optimal value for dopant concentration [37]. Here, the doping energy level of  $\text{Nd}^{3+}/\text{Nd}^{2+}$  has three functions: firstly, it can capture electrons from the conduction band of  $\text{TiO}_2$  that injected from the dye, and thus the number of hydroxide radicals is reduced; secondly, electrons can be excited to the  $\text{Nd}^{3+}/\text{Nd}^{2+}$  energy level from the valence band of  $\text{TiO}_2$ , and then the holes leaving on the valence band can degrade dyes; thirdly,  $\text{Nd}^{3+}/\text{Nd}^{2+}$  energy level can be the recombination center if the dopant concentration is not proper. These three processes compete with each other, so it is critical to find an optimal dopant concentration. In our experiment, from the result of photocatalytic activity, we can deduce that Nd doping concentration of 4 ~ 9 at. %, resulting in the good photocatalytic performance of Nd-doped  $\text{TiO}_2$ .

From the discussed above, we know that Nd doping level exists between bandgap of  $\text{TiO}_2$  and is close to the conduction band, which corresponds to the calculation results [14]. So, with Nd-doped  $\text{TiO}_2$  as a photocatalyst irradiated under visible light, there are photogenerated holes and electrons which participate in the Rh-B degradation. It is well known that in liquid photocatalysis system, hole may oxidize organic pollutant directly or form hydroxide radical for degradation, and photogenerated electron can form  $\cdot\text{OH}$  through the reaction with adsorbed  $\cdot\text{O}_2^-$ . In order to explore which, photogenerated hole or electron, is mainly responsible for Rh-B degradation, some scavengers were used to investigate the specific reactive species that may play important roles in this process [18].  $\text{Na}_2\text{Cr}_2\text{O}_4$  was used as hole scavenger, KI as the scavenger for hole and  $\cdot\text{OH}$ , and Cr (VI) for electron. Figure 10 shows the photodegradation efficiencies of Rh-B over Nd-doped  $\text{TiO}_2$  ( $\text{Ti}:\text{Nd} = 11:1$ ) in the presence of the scavengers under visible light. It can be seen that when  $\text{Na}_2\text{Cr}_2\text{O}_4$  was used as diagnostic tool for suppressing the hole process, the photocatalytic degradation of Rh-B was inhibited but not down close to zero as shown in Figure 10. From this inhibited effect, it can be deduced that photogenerated holes played a role in the photodegradation of Rh-B under visible light. In the presence of KI as hole and  $\cdot\text{OH}$  scavenger, the removal efficiency of Rh-B was almost the same as that  $\text{Na}_2\text{Cr}_2\text{O}_4$ . It indicates that  $\cdot\text{OH}$  played a significant role in the system since the inhibition effect of  $\cdot\text{OH}$  can be regarded to be close to 100% after the deduction of hole effect. The addition of Cr (VI) as electron scavenger resulted in the degradation of only 6% of Rh-B after 90 min, which means that there was almost no activity for the photocatalyst with electron inhibition effect in the system. So, photogenerated electrons played a very important role in the degradation system. We know that the electrons resulted from Nd-doped  $\text{TiO}_2$  and excited dye have strong reductive ability and they can reduce the

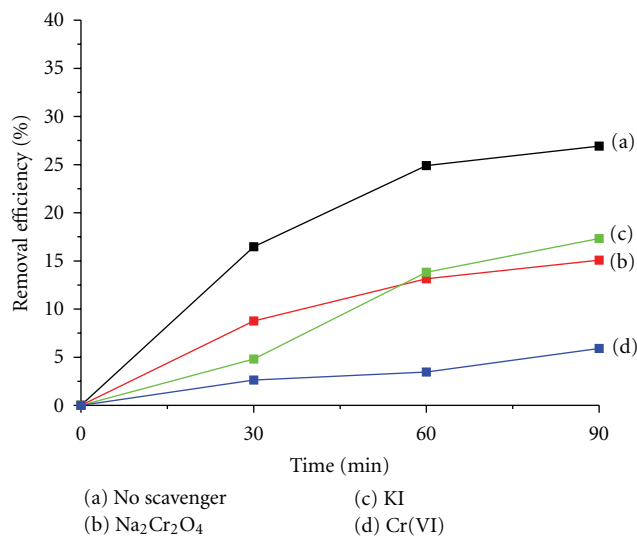


FIGURE 10: Photodegradation efficiencies of Rh-B ( $10\ \mu\text{M}$ ,  $100\ \text{mL}$ ) over  $0.1\ \text{g}$  of Nd-doped  $\text{TiO}_2$  with  $\text{Ti}:\text{Nd} = 11:1$  under visible light with the presence of different scavengers,  $5\ \text{mM}$  sodium oxalate and KI, and  $0.5\ \text{mM}$   $\text{K}_2\text{Cr}_2\text{O}_6$ .

adsorbed oxygen into  $\cdot\text{O}_2^-$  and then  $\cdot\text{OH}$  formation by protonation. These  $\cdot\text{OH}$  and  $\cdot\text{O}_2^-$  on the surface of the photocatalyst can degrade the adsorbed Rh-B [38]. From Figure 10, it can be concluded that  $\cdot\text{O}_2^-$  and  $\cdot\text{OH}$  are major reactive species for the photocatalytic degradation of Rh-B, and photogenerated electrons from Nd-doped  $\text{TiO}_2$  are responsible for the improvement of photocatalytic activity of the Nd-doped  $\text{TiO}_2$ .

In order to verify that  $\cdot\text{OH}$  is present in the photodegradation system, the changes of PL spectra of terephthalic acid solution with irradiation time were recorded and the data is shown in Figure 11. It can be seen that a gradual increase in PL intensity at about  $430\ \text{nm}$  was observed with the increase of irradiation time. However, no PL increase was observed in the absence of visible light or Nd-doped  $\text{TiO}_2$  sample. This suggests that the fluorescence is from the chemical reaction between terephthalic acid and  $\cdot\text{OH}$  formed via photogenerated holes and electrons. Usually, PL intensity is proportional to the amount of produced hydroxyl radical over the photocatalyst [38]. So, the amount of formed hydroxyl radical gradually increased for Rh-B degradation under visible light with the increase of time.

Moreover, since the radius of  $\text{Nd}^{3+}$  is much larger than that of  $\text{Ti}^{4+}$ , it will be difficult for all of Nd ions added to enter into  $\text{TiO}_2$  lattice. So, the presence of  $\text{Nd}^{3+}$  or Nd metal on nanoparticle surface may also promote the charge separation to improve photocatalytic activity of Nd-doped  $\text{TiO}_2$ , which has been described by many published papers [14, 39–43].

#### 4. Conclusion

In summary, a simple sol-gel method has been used for the preparation of Nd-doped titania nanoparticles with anatase and brookite phases. The prepared samples can

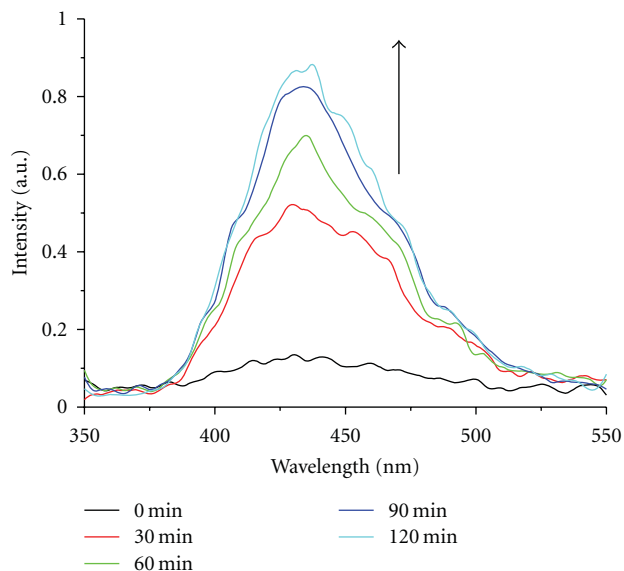


FIGURE 11: PL spectral changes with irradiation time over Nd-doped  $\text{TiO}_2$  with  $\text{Ti}:\text{Nd} = 11:1$  in terephthalic acid solution of  $5 \times 10^{-4}$  M.

achieve photocatalytic degradation of dye (Rh-B) under visible light, and Nd-doped  $\text{TiO}_2$  has better activity than pure  $\text{TiO}_2$  and P25. The enhanced activity is related to the change of crystalline structure of  $\text{TiO}_2$ . Partial Nd enters into  $\text{TiO}_2$  lattice for the formation of doping level, which makes  $\text{TiO}_2$  responsive to visible light. In Rh-B degradation system, hydroxide radicals as one of the reactive species are mainly produced by photogenerated electrons both from dye and Nd-doped  $\text{TiO}_2$  excitation and they are responsible for Rh-B degradation. The contribution from hole is not as pronounced as electron for the formation of hydroxide radicals. This study may shed light on the improvement of photocatalytic activity of  $\text{TiO}_2$  under solar light by using metal doping method.

## Acknowledgments

This work was financially supported by the National Natural Science Foundation of China (no. 20973070), the National Basic Research Program of China (no. 2009CB939704), the Key Project of the Ministry of Chinese Education (no. 109116), self-determined research funds of CCNU from the colleges' basic research, Natural Science Foundation of Jiangsu Province (no. BK2009724), and Industry R&D program in Zhenjiang City (no. GY2009003). The authors are also indebted to Professor Wen-Zhong Shen and Miss Dan-Hua Xu in Shanghai Jiaotong University for Raman spectrum measurements.

## References

- [1] Y. Xie, C. Yuan, and X. Li, "Photocatalytic degradation of X-3B dye by visible light using lanthanide ion modified titanium dioxide hydrosol system," *Colloids and Surfaces A*, vol. 252, no. 1, pp. 87–94, 2005.
- [2] Q. Xiang, J. Yu, W. Wang, and M. Jaroniec, "Nitrogen self-doped nanosized  $\text{TiO}_2$  sheets with exposed 001 facets for enhanced visible-light photocatalytic activity," *Chemical Communications*, vol. 47, no. 24, pp. 6906–6908, 2011.
- [3] Q. Xiang, J. Yu, and M. Jaroniec, "Nitrogen and sulfur codoped  $\text{TiO}_2$  nanosheets with exposed 001 facets: synthesis, characterization and visible-light photocatalytic activity," *Physical Chemistry Chemical Physics*, vol. 13, no. 11, pp. 4853–4861, 2011.
- [4] J. Yu, G. Dai, Q. Xiang, and M. Jaroniec, "Fabrication and enhanced visible-light photocatalytic activity of carbon self-doped  $\text{TiO}_2$  sheets with exposed 001 facets," *Journal of Materials Chemistry*, vol. 21, no. 4, pp. 1049–1057, 2011.
- [5] G. Shang, S. Yang, T. Xu, and H. Fu, "Mechanistic study of visible-Light-induced photodegradation of 4-chlorophenol by  $\text{TiO}_2-x\text{Nx}$  ( $0.021 < x < 0.049$ ) with low nitrogen concentration," *International Journal of Photoenergy*, vol. 2012, Article ID 759306, 9 pages, 2012.
- [6] N.-H. Lee, H.-J. Oh, S.-C. Jung, W.-J. Lee, D.-H. Kim, and S.-J. Kim, "Photocatalytic properties of nanotubular-shaped  $\text{TiO}_2$  powders with anatase phase obtained from titanate nanotube powder through various thermal treatments," *International Journal of Photoenergy*, vol. 2011, Article ID 327821, 7 pages, 2011.
- [7] F. Nerud, P. Baldrian, J. Gabriel, and D. Ogbeifun, "Decolorization of synthetic dyes by the Fenton reagent and the Cu/pyridine/ $\text{H}_2\text{O}_2$  system," *Chemosphere*, vol. 44, no. 5, pp. 957–961, 2001.
- [8] X. Chen, L. Liu, P. Y. Yu, and S. S. Mao, "Increasing solar absorption for photocatalysis with black hydrogenated titanium dioxide nanocrystals," *Science*, vol. 746, pp. 747–749, 2011.
- [9] M. Ksibi, S. B. Amor, S. Cherif, E. Elaloui, A. Houas, and M. Elaloui, "Photodegradation of lignin from black liquor using a UV/ $\text{TiO}_2$  system," *Journal of Photochemistry and Photobiology A*, vol. 154, no. 2-3, pp. 211–218, 2003.
- [10] J. Xie, D. Jiang, M. Chen et al., "Preparation and characterization of monodisperse Ce-doped  $\text{TiO}_2$  microspheres with visible light photocatalytic activity," *Colloids and Surfaces A*, vol. 372, no. 1–3, pp. 107–114, 2010.
- [11] X. Wu, P. Su, H. Liu, and L. Qi, "Photocatalytic degradation of Rhodamine B under visible light with Nd-doped titanium dioxide films," *Journal of Rare Earths*, vol. 27, no. 5, pp. 739–743, 2009.
- [12] S. Suárez, T. L. R. Hower, R. Portela, M. D. Hernández-Alonso, R. S. Freire, and B. Sánchez, "Behaviour of  $\text{TiO}_2$ -SiMgOx hybrid composites on the solar photocatalytic degradation of polluted air," *Applied Catalysis B*, vol. 101, no. 3-4, pp. 176–182, 2011.
- [13] H. Kisch and W. Macyk, "Visible-light photocatalysis by modified titania," *ChemPhysChem*, vol. 3, no. 5, pp. 399–400, 2002.
- [14] D. Zhao, T. Peng, J. Xiao, C. Yan, and X. Ke, "Preparation, characterization and photocatalytic performance of Nd<sup>3+</sup>-doped titania nanoparticles with mesostructure," *Materials Letters*, vol. 61, no. 1, pp. 105–110, 2007.
- [15] V. Štengl, S. Bakardjieva, and N. Murafa, "Preparation and photocatalytic activity of rare earth doped  $\text{TiO}_2$  nanoparticles," *Materials Chemistry and Physics*, vol. 114, no. 1, pp. 217–226, 2009.
- [16] A. L. Linsebigler, G. Lu, and J. T. Yates, "Photocatalysis on  $\text{TiO}_2$  surfaces: principles, mechanisms, and selected results," *Chemical Reviews*, vol. 95, no. 3, pp. 735–758, 1995.

- [17] Z. M. Wang, G. Yang, P. Biswas, W. Bresser, and P. Boolchand, "Processing of iron-doped titania powders in flame aerosol reactors," *Powder Technology*, vol. 114, no. 1–3, pp. 197–204, 2001.
- [18] L.-S. Zhang, K.-H. Wong, H.-Y. Yip et al., "Effective photocatalytic disinfection of *E. coli* K-12 using AgBr-Ag-Bi<sub>2</sub>WO<sub>6</sub> nanojunction system irradiated by visible light: the role of diffusing hydroxyl radicals," *Environmental Science and Technology*, vol. 44, no. 4, pp. 1392–1398, 2010.
- [19] K. V. Baiju, P. Periyat, W. Wunderlich, P. Krishna Pillai, P. Mukundan, and K. G. K. Warriar, "Enhanced photoactivity of neodymium doped mesoporous titania synthesized through aqueous sol-gel method," *Journal of Sol-Gel Science and Technology*, vol. 43, no. 3, pp. 283–290, 2007.
- [20] A. L. Castro, M. R. Nunes, M. D. Carvalho et al., "Doped titanium dioxide nanocrystalline powders with high photocatalytic activity," *Journal of Solid State Chemistry*, vol. 182, no. 7, pp. 1838–1845, 2009.
- [21] X. Su, J. Zhao, Y. Li et al., "Solution synthesis of Cu<sub>2</sub>O/TiO<sub>2</sub> core-shell nanocomposites," *Colloids and Surfaces A*, vol. 349, no. 1–3, pp. 151–155, 2009.
- [22] W. Xue, G. Zhang, X. Xu, X. Yang, C. Liu, and Y. Xu, "Preparation of titania nanotubes doped with cerium and their photocatalytic activity for glyphosate," *Chemical Engineering Journal*, vol. 167, no. 1, pp. 397–402, 2011.
- [23] H. Zhang and J. F. Banfield, "Understanding polymorphic phase transformation behavior during growth of nanocrystalline aggregates: insights from TiO<sub>2</sub>," *Journal of Physical Chemistry B*, vol. 104, no. 15, pp. 3481–3487, 2000.
- [24] Y. Yu, J. C. Yu, J. G. Yu et al., "Enhancement of photocatalytic activity of mesoporous TiO<sub>2</sub> by using carbon nanotubes," *Applied Catalysis A*, vol. 289, no. 2, pp. 186–196, 2005.
- [25] Y. Lv, L. Yu, H. Huang, H. Liu, and Y. Feng, "Preparation of F-doped titania nanoparticles with a highly thermally stable anatase phase by alcoholysis of TiCl<sub>4</sub>," *Applied Surface Science*, vol. 255, no. 23, pp. 9548–9552, 2009.
- [26] T. L. R. Hewer, E. C. C. Souza, T. S. Martins, E. N. S. Muccillo, and R. S. Freire, "Influence of neodymium ions on photocatalytic activity of TiO<sub>2</sub> synthesized by sol-gel and precipitation methods," *Journal of Molecular Catalysis A*, vol. 336, no. 1–2, pp. 58–63, 2011.
- [27] Y. H. Xu, C. Chen, X. L. Yang, X. Li, and B. F. Wang, "Preparation, characterization and photocatalytic activity of the neodymium-doped TiO<sub>2</sub> nanotubes," *Applied Surface Science*, vol. 255, no. 20, pp. 8624–8628, 2009.
- [28] U. I. Gaya and A. H. Abdullah, "Heterogeneous photocatalytic degradation of organic contaminants over titanium dioxide: a review of fundamentals, progress and problems," *Journal of Photochemistry and Photobiology C*, vol. 9, no. 1, pp. 1–12, 2008.
- [29] J. W. Shi, "Preparation of Fe(III) and Ho(III) co-doped TiO<sub>2</sub> films loaded on activated carbon fibers and their photocatalytic activities," *Chemical Engineering Journal*, vol. 151, no. 1–3, pp. 241–246, 2009.
- [30] W. Ho, J. C. Yu, J. Lin, J. Yu, and P. Li, "Preparation and photocatalytic behavior of MoS<sub>2</sub> and WS<sub>2</sub> nanocluster sensitized TiO<sub>2</sub>," *Langmuir*, vol. 20, no. 14, pp. 5865–5869, 2004.
- [31] S. J. Gregg and K. S. W. Sing, *Adsorption, Surface Area and Porosity*, Academic Press, London, UK, 2nd edition, 1982.
- [32] J. Xu, M. Chen, and D. Fu, "Study on highly visible light active Bi-doped TiO<sub>2</sub> composite hollow sphere," *Applied Surface Science*, vol. 257, no. 17, pp. 7381–7386, 2011.
- [33] S. Rengaraj, S. Venkataraj, J. W. Yeon, Y. Kim, X. Z. Li, and G. K. H. Pang, "Preparation, characterization and application of Nd-TiO<sub>2</sub> photocatalyst for the reduction of Cr(VI) under UV light illumination," *Applied Catalysis B*, vol. 77, no. 1–2, pp. 157–165, 2007.
- [34] T. Wu, G. Liu, J. Zhao, H. Hidaka, and N. Serpone, "Photoassisted degradation of dye pollutants. V. Self-photosensitized oxidative transformation of Rhodamine B under visible light irradiation in aqueous TiO<sub>2</sub> dispersions," *Journal of Physical Chemistry B*, vol. 102, no. 30, pp. 5845–5851, 1998.
- [35] Y. Xie, C. Yuan, and X. Li, "Photosensitized and photocatalyzed degradation of azo dye using Ln<sup>m+</sup>-TiO<sub>2</sub> sol in aqueous solution under visible light irradiation," *Materials Science and Engineering B*, vol. 117, no. 3, pp. 325–333, 2005.
- [36] C. Chen, X. Li, W. Ma, J. Zhao, H. Hidaka, and N. Serpone, "Effect of transition metal ions on the TiO<sub>2</sub>-assisted photodegradation of dyes under visible irradiation: a probe for the interfacial electron transfer process and reaction mechanism," *Journal of Physical Chemistry B*, vol. 106, no. 2, pp. 318–324, 2002.
- [37] Y. Cong, J. Zhang, F. Chen, M. Anpo, and D. He, "Preparation, photocatalytic activity, and mechanism of nano-TiO<sub>2</sub> Co-doped with nitrogen and iron (III)," *Journal of Physical Chemistry C*, vol. 111, no. 28, pp. 10618–10623, 2007.
- [38] J. Yu, Q. Xiang, and M. Zhou, "Preparation, characterization and visible-light-driven photocatalytic activity of Fe-doped titania nanorods and first-principles study for electronic structures," *Applied Catalysis B*, vol. 90, no. 3–4, pp. 595–602, 2009.
- [39] W. Choi, A. Termin, and M. R. Hoffmann, "The role of metal ion dopants in quantum-sized TiO<sub>2</sub>: correlation between photoreactivity and charge carrier recombination dynamics," *Journal of Physical Chemistry*, vol. 98, no. 51, pp. 13669–13679, 1994.
- [40] S. Rengaraj and X. Z. Li, "Enhanced photocatalytic reduction reaction over Bi<sup>3+</sup>-TiO<sub>2</sub> nanoparticles in presence of formic acid as a hole scavenger," *Chemosphere*, vol. 66, no. 5, pp. 930–938, 2007.
- [41] N. Serpone, "Is the band gap of pristine TiO<sub>2</sub> narrowed by anion- and cation-doping of titanium dioxide in second-generation photocatalysts?" *Journal of Physical Chemistry B*, vol. 110, no. 48, pp. 24287–24293, 2006.
- [42] J.-M. Herrmann, H. Tahiri, Y. Ait-Ichou, G. Lassaletta, A. R. González-Elipse, and A. Fernandez, "Characterization and photocatalytic activity in aqueous medium of TiO<sub>2</sub> and Ag-TiO<sub>2</sub> coatings on quartz," *Applied Catalysis B*, vol. 13, no. 3–4, pp. 219–228, 1997.
- [43] A. Sclafani and J.-M. Herrmann, "Influence of metallic silver and of platinum-silver bimetallic deposits on the photocatalytic activity of titania (anatase and rutile) in organic and aqueous media," *Journal of Photochemistry and Photobiology A*, vol. 113, no. 2, pp. 181–188, 1998.

## Research Article

# Photocatalytic Properties of Nitrogen-Doped $\text{Bi}_{12}\text{TiO}_{20}$ Synthesized by Urea Addition Sol-Gel Method

Jiyong Wei, Baibiao Huang, Peng Wang, Zeyan Wang, Xiaoyan Qin, Xiaoyang Zhang, Xiangyang Jing, Haixia Liu, and Jiaoxian Yu

State Key Laboratory of Crystal Materials, Institute of Crystal Materials, Shandong University, Jinan 250100, China

Correspondence should be addressed to Baibiao Huang, bbhuang@sdu.edu.cn

Received 25 July 2011; Revised 19 September 2011; Accepted 30 September 2011

Academic Editor: Jianguo Yu

Copyright © 2012 Jiyong Wei et al. This is an open access article distributed under the Creative Commons Attribution License, which permits unrestricted use, distribution, and reproduction in any medium, provided the original work is properly cited.

Undoped and nitrogen-doped  $\text{Bi}_{12}\text{TiO}_{20}$  materials were synthesized by urea addition sol-gel method. By adding urea, undoped, and N-doped gel-type precursors were synthesized by low-temperature dehydrolyzation. Nitrogen-doped and undoped nanocrystalline  $\text{Bi}_{12}\text{TiO}_{20}$  were prepared by annealing at  $600^\circ\text{C}$  for 30 minutes. From UV-Vis absorption and diffuse reflection spectrum, the absorbing band shifted from 420 to 500 nm by nitrogen doping. The bonds of Ti-N and N-O were identified by XPS spectra from the prepared materials, and the enhancement of visible light absorption was attributed to nitrogen's substitution of oxygen. Photocatalytic properties of prepared materials were characterized by the decomposition of Rhodamine B illuminated by whole spectra of 300 W Xe light. The photocatalyst  $\text{Bi}_{12}\text{TiO}_{20-y}\text{N}_y$  ( $y = 0.03$ ) with N/(N+O) mole ratio about 3% shows better performance than that of heavily doped  $\text{Bi}_{12}\text{TiO}_{20-z}\text{N}_z$  ( $z = 0.06$ ), undoped  $\text{Bi}_{12}\text{TiO}_{20}$ , and light-doped  $\text{Bi}_{12}\text{TiO}_{20-x}\text{N}_x$  ( $x = 0.01$ ) photocatalysts due to its better crystalline morphology.

## 1. Introduction

Environmental and energetic problems are great challenges for human beings now. The photosensitized electrolytic oxidation [1] and the electrochemical photolysis of water [2] on  $\text{TiO}_2$  electrode performed by Fujishima and Honda offered some solutions. In recent years,  $\text{TiO}_2$  and other photocatalysts have been extensively studied for environmental pollutant treatment [3] such as water disinfection [4].

However, wide bandgap semiconductor photocatalysts, such as  $\text{TiO}_2$ , can only absorb UV light, which only take 4% of the whole solar spectra owing to the wide bandgap. In order to expand the absorption spectra region of  $\text{TiO}_2$ , doping with nonmetallic atoms, such as nitrogen, fluorine and sulfur has been developed [5–18]. The conventional doping processes reported were commonly by the annealing of prepared  $\text{TiO}_2$  materials in  $\text{NH}_3$  or other dopant atmospheres [5–8]. Rengifo-Herrera et al. have reported N, S codoped commercial  $\text{TiO}_2$  powders [17] which were doped by the decomposition of thiourea as a nitrogen and sulfur source. Effects of calcination temperatures [19], morphologies [20], and composite [21] on photocatalytic activity were also studied.

Recently, photocatalysts containing ion units of  $(\text{Bi}_2\text{O}_2)^{2+}$ , such as  $\text{Bi}_2\text{WO}_6$  [22, 23] and bismuth titanate were extensively studied for the photocatalytic splitting of water and the photodegradation of organic pollutants. Bismuth titanate was a wide bandgap semiconductor with several crystal phases: ferroelectric perovskite phase ( $\text{Bi}_4\text{Ti}_3\text{O}_{12}$ ), dielectric pyrochlorite phase ( $\text{Bi}_2\text{Ti}_2\text{O}_7$ ), refractive sillenite phase ( $\text{Bi}_{12}\text{TiO}_{20}$ ), and so forth. Kudo and Hiji have studied bismuth titanate as potential photocatalyst [22]. Yao et al. [24–27] and other groups [28–36] explored nano crystalline materials of  $\text{Bi}_{12}\text{TiO}_{20}$  as visible light photocatalysts, and the as-prepared materials showed high photocatalytic activity for decomposing organic dyes under ultraviolet light irradiation. The further expansion of  $\text{Bi}_{12}\text{TiO}_{20}$  material's absorption to visible region is very important for the visible light responsive photocatalytic activity, because  $\text{Bi}_{12}\text{TiO}_{20}$  can only absorb light with wavelength below 420 nm (about 2.9 eV) [21–24]. Little work has been performed for nonmetallic (such as nitrogen and carbon) doping of bismuth titanate crystals, though the doping of  $\text{Bi}_{12}\text{TiO}_{20}$  nano- or single crystals with metal element [25, 26] and non-metallic element such as P for the influence of refractive optical properties has been studied [37].

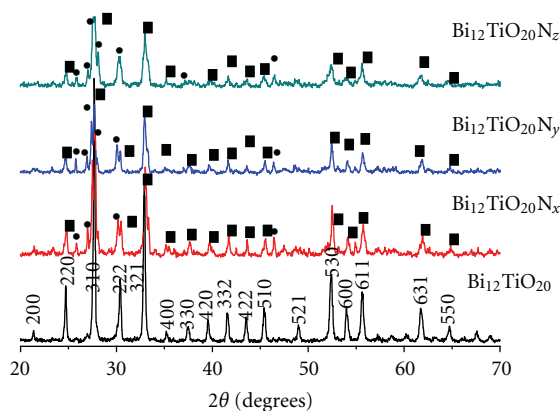


FIGURE 1: XRD spectrum of bismuth titanate:  $\text{Bi}_{12}\text{TiO}_{20}$ ,  $\text{Bi}_{12}\text{TiO}_{20-x}\text{N}_x$  ( $x = 0.01$ ),  $\text{Bi}_{12}\text{TiO}_{20-y}\text{N}_y$  ( $y = 0.03$ ), and  $\text{Bi}_{12}\text{TiO}_{20-z}\text{N}_z$  ( $z = 0.06$ ).

In this paper, nitrogen-doped bismuth titanate powders and films were prepared by sol-gel method and dip-coating method, respectively, the nitrogen dopant was introduced by the adding of urea in precursor solutions as additives, which is widely used as fertilizer. Urea can be dissolved in water and other polar solvents, and can release free  $\text{NH}_2^\bullet$  radicals as nitrogen sources during thermal decomposition. After preparation of urea included sol-gel precursors, high-temperature annealing was applied to undoped and doped  $\text{Bi}_{12}\text{TiO}_{20}$  precursors for crystallization and also for the in-place nitrogen doping by urea decomposing. The results of whole-spectra photocatalytic activities of nitrogen-doped and undoped  $\text{Bi}_{12}\text{TiO}_{20}$  were presented by the photodegradation of rhodamine b (RB) solutions.

## 2. Experimental Details

Undoped and nitrogen-doped  $\text{Bi}_{12}\text{TiO}_{20}$  nanocrystalline powders and films were prepared by sol-gel method and dip coating. Chemical agents of analytical grade were used in the experiments, such as acetic acid,  $\text{Bi}(\text{NO}_3)_3 \cdot 5\text{H}_2\text{O}$  and  $\text{Ti}(\text{OC}_4\text{H}_9)_4$ . Reagents were dissolved in ethylene glycol monomethyl ether solution while urea was used as nitrogen additive. Crystalline materials of undoped and nitrogen-doped  $\text{Bi}_{12}\text{TiO}_{20}$  were prepared by annealing of the sol-gel precursors at temperature of  $600^\circ\text{C}$  for about 30 minutes.

**2.1. Preparation of  $\text{Bi}_{12}\text{TiO}_{20}$  and Nitrogen-Doped  $\text{Bi}_{12}\text{TiO}_{20}$  Crystalline Materials.** The mole ratio of reagents  $\text{Bi}(\text{NO}_3)_3 \cdot 5\text{H}_2\text{O}$  and  $\text{Ti}(\text{OC}_4\text{H}_9)_4$  was 12:1 in the precursor solution for preparation of  $\text{Bi}_{12}\text{TiO}_{20}$  and  $\text{Bi}_{12}\text{TiO}_{20-x}\text{N}_x$  ( $x = 0.01$ ),  $\text{Bi}_{12}\text{TiO}_{20-y}\text{N}_y$  ( $y = 0.03$ ), and  $\text{Bi}_{12}\text{TiO}_{20-z}\text{N}_z$  ( $z = 0.06$ ) sol-gel precursors, with additional urea added for nitrogen-doped materials (molecule ratio of  $\text{NH}_2^\bullet : \text{Bi}^{3+}$  about 0:1, 1:1, 2:1, and 3:1 in sol-gel). The reagents were blended in acetic acid and ethylene glycol monomethyl ether solutions, and were dried by infrared light to get the gel.  $\text{Bi}_{12}\text{TiO}_{20}$  and  $\text{Bi}_{12}\text{TiO}_{20-x}\text{N}_x$  ( $x = 0.01$ ),  $\text{Bi}_{12}\text{TiO}_{20-y}\text{N}_y$  ( $y = 0.03$ ), and  $\text{Bi}_{12}\text{TiO}_{20-z}\text{N}_z$  ( $z = 0.06$ ) sillenite phase crystalline powders were obtained by annealing the gel precursors at  $600^\circ\text{C}$  for about 30 minutes.

**2.2. Preparation of  $\text{Bi}_{12}\text{TiO}_{20}$  Crystalline Films for UV-Vis Absorption Characterization.** Crystalline films of  $\text{Bi}_{12}\text{TiO}_{20}$ ,  $\text{Bi}_{12}\text{TiO}_{20-x}\text{N}_x$  ( $x = 0.01$ ),  $\text{Bi}_{12}\text{TiO}_{20-y}\text{N}_y$  ( $y = 0.03$ ), and  $\text{Bi}_{12}\text{TiO}_{20-z}\text{N}_z$  ( $z = 0.06$ ) were prepared by dipping glass chips into the prepared sol-gel precursor solutions, and then were dried by infrared light, and annealed at  $600^\circ\text{C}$  for 30 minutes in nitrogen atmosphere.

**2.3. Characterization Methods.** The crystal phases of prepared powders were identified by X-ray diffraction (XRD,  $\text{Cu K}\alpha$ , D/max-ra X-ray). Morphology of the doped and undoped  $\text{Bi}_{12}\text{TiO}_{20}$  nanocrystals was characterized by scanning electron microscopy (SEM, JEOL JSM6700F). The compositions and the electron bonding states of nitrogen-doped  $\text{Bi}_{12}\text{TiO}_{20}$  were characterized by X-ray photoelectron spectroscopy (XPS, ESCALAB 250 of Thermal Fisher Scientific). To study the red shift of absorption wavelength of nitrogen-doped materials, UV-Vis absorption spectra of  $\text{Bi}_{12}\text{TiO}_{20}$  crystalline films were performed by UV-Vis spectrophotometer (U-3500, 187 nm–3500 nm). The UV-Vis diffuse reflection spectra of doped and undoped  $\text{Bi}_{12}\text{TiO}_{20}$  powders were characterized by UV/Vis spectroscopy (UV-2550, Shimadzu). Photocatalytic activity of undoped and nitrogen-doped  $\text{Bi}_{12}\text{TiO}_{20}$  was characterized by the photodegradation of rhodamine b (RhB) solutions under the irradiation of 300 W Xe arc lamp (focused through a shutter window). The efficiency of the degradation processes was evaluated by monitoring the dye decolorization at the maximum absorption around 557 nm as a function of irradiation time in the separated RhB solution with a UV-vis spectrophotometer (UV-7502PC, Xinmao, Shanghai).

## 3. Results and Discussion

**3.1. X-Ray Characterization.** The crystal phases of synthesized doped and undoped nano crystalline materials were identified by X-ray diffraction. The XRD spectra of annealed  $\text{Bi}_{12}\text{TiO}_{20}$ ,  $\text{Bi}_{12}\text{TiO}_{20-x}\text{N}_x$  ( $x = 0.01$ ),  $\text{Bi}_{12}\text{TiO}_{20-y}\text{N}_y$  ( $y = 0.03$ ), and  $\text{Bi}_{12}\text{TiO}_{20-z}\text{N}_z$  ( $z = 0.06$ ) were shown in Figure 1. No phase transformation of  $\text{Bi}_{12}\text{TiO}_{20}$  structure (JCPDS no.78–1158) was observed by adding of urea as nitrogen

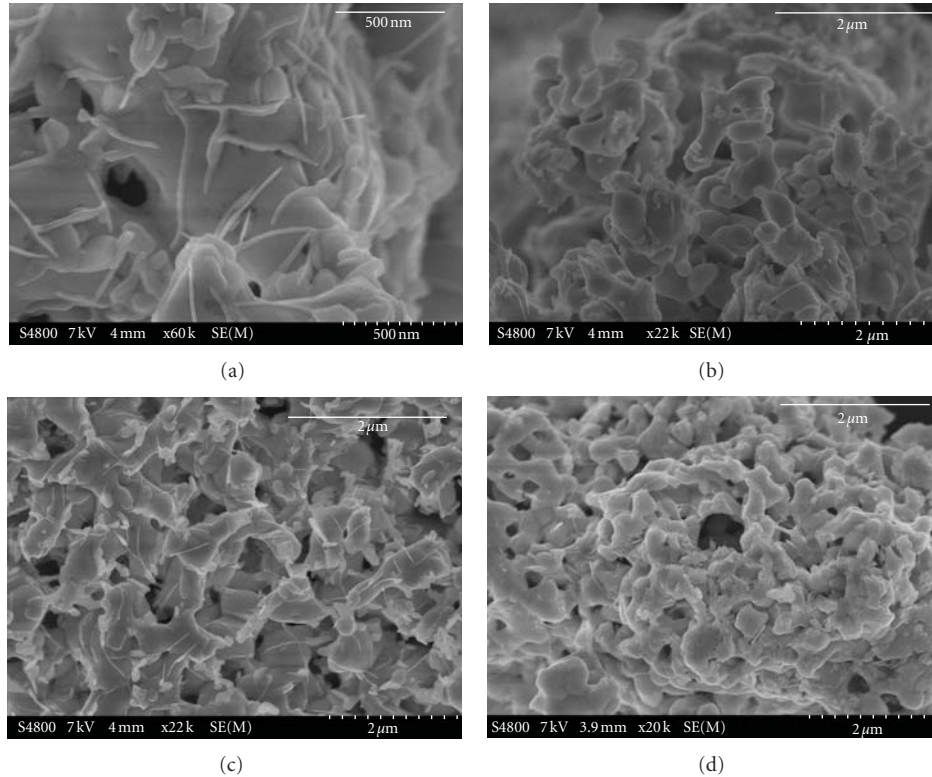


FIGURE 2: Morphologies of annealed undoped and nitrogen-doped  $\text{Bi}_{12}\text{TiO}_{20}$  micro- and nano crystals observed by SEM: (a)  $\text{Bi}_{12}\text{TiO}_{20}$ ; (b)  $\text{Bi}_{12}\text{TiO}_{20-x}\text{N}_x$  ( $x = 0.01$ ); (c)  $\text{Bi}_{12}\text{TiO}_{20-y}\text{N}_y$  ( $y = 0.03$ ); (d)  $\text{Bi}_{12}\text{TiO}_{20-z}\text{N}_z$  ( $z = 0.06$ ).

additive. The slight shift and broadening of XRD peaks showed the effect of nitrogen doping in  $\text{Bi}_{12}\text{TiO}_{20}$  structure materials. From Figure 1, the sharp diffraction peak and strong intensity of  $\text{Bi}_{12}\text{TiO}_{20}$  indicates good crystallinity; while after nitrogen doping, the diffraction peak intensity became weaker and the peaks broadened slightly. The (310) and (222) peak split into two peaks and shifted to lower angles with the increase of nitrogen dopant, which shows us there must be an increase for the interlamellar spacing of (310) and (222) crystal facets as nitrogen is doped in  $\text{Bi}_{12}\text{TiO}_{20}$ .

**3.2. Morphology of Nanocrystalline Bismuth Titanate Materials.** Morphologies of undoped and nitrogen-doped  $\text{Bi}_{12}\text{TiO}_{20}$  materials prepared by sol-gel synthesis and annealing were characterized by SEM as shown in Figure 2. The undoped  $\text{Bi}_{12}\text{TiO}_{20}$  microgel-like bulks dotted with nanoflakes were observed in Figure 2(a), with few holes due to the decomposition and elution of sol-gel precursor. With addition of urea in precursors, the decomposition eluted more gas and the microbulk became fractal bulks piled up as shown in Figures 2(b), 2(c), and 2(d); while with too much urea added, there are only fractal bulks and few nanoflakes, which may decrease the surface and refrain the photocatalytic performance of heavily nitrogen-doped  $\text{Bi}_{12}\text{TiO}_{20-z}\text{N}_z$  ( $z = 0.06$ ). The morphology of proper nitrogen-doped material is  $\text{Bi}_{12}\text{TiO}_{20-y}\text{N}_y$  ( $y = 0.03$ ), as shown in Figure 2(c), which is composed of separated nano bulks dotted with nanosheet-like crystals. The morphology of  $\text{Bi}_{12}\text{TiO}_{20-y}\text{N}_y$  ( $y = 0.03$ ) has more nano crystalline

facets and larger surface areas than other samples, which would show better photocatalytic performance than the other samples.

**3.3. Element Content and Doping of Nanocrystalline Bismuth Titanate Materials.** The chemical bonding states of as-prepared materials were characterized by XPS as shown in Figure 3. As shown in Figure 3(a), the XPS peaks of Bi4f, C 1s, N 1s, and Ti 2p were detected. The split of nitrogen 1s peak and carbon 1s peak shown in Figures 3(b) and 3(c) indicate the variety of bonding states. The split of N1s peaks in Figure 3(b) was assigned to N 1s peaks of N–O bond (401.6 eV) [38] and N–Ti bond (396.4 eV) [39, 40]. The N/(N+O) molar ratio calculated from the XPS peak is about 3%. The broadening and split of C 1s peak shown in Figure 3(c) were assigned to CO/ $\text{Bi}_2\text{O}_3$  (286.6 eV) and CO/ $\text{TiO}_2$  (288.5 eV) physical absorb circumstances [41]. So most carbon in the sample is absorbed CO, and the visible light absorption enhancement is attributed to the doping of nitrogen.

**3.4. UV-Vis Absorption Enhancement of Nitrogen-Doped Bismuth Titanate Nanocrystalline Films.** The UV-Vis absorption spectra of bismuth titanate nano crystalline films with different nitrogen doping ratios were characterized in Figure 4(a). The absorption spectra of undoped bismuth titanate were broadened successfully by urea-assisted sol-gel growth of nitrogen doping as shown in the UV-Vis absorption spectra of  $\text{Bi}_{12}\text{TiO}_{20}$  and  $\text{Bi}_{12}\text{TiO}_{20-x}\text{N}_x$  ( $x = 0.01$ )

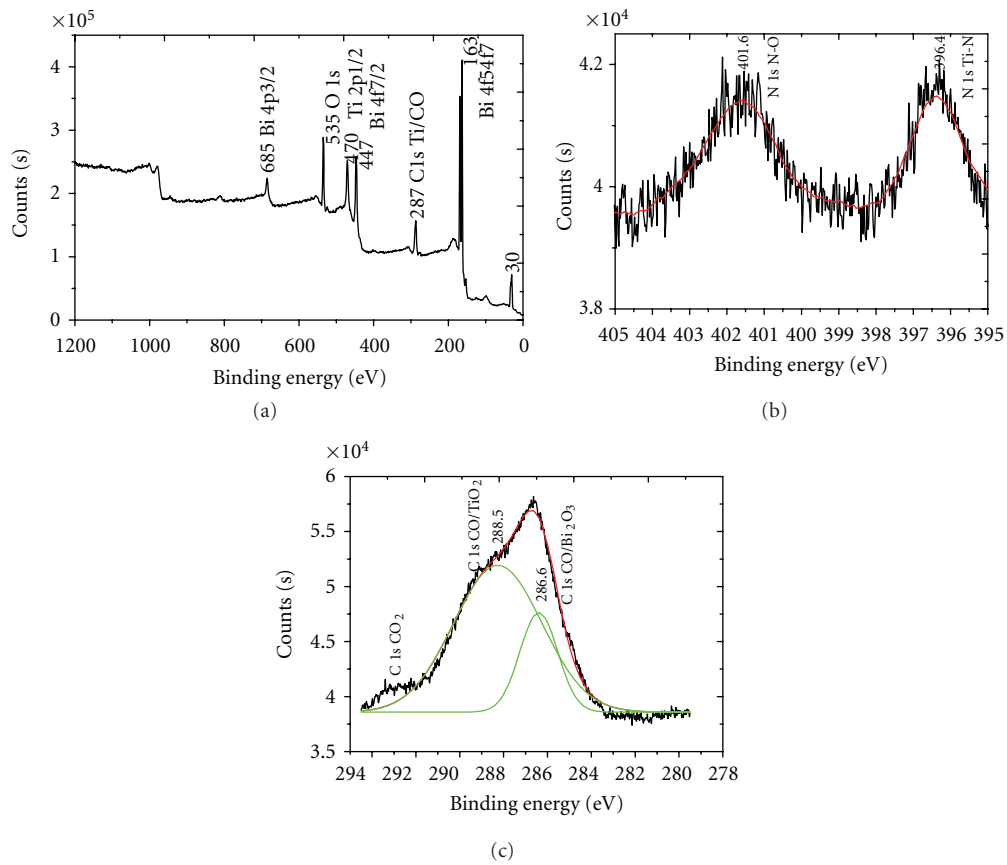


FIGURE 3: XPS absorption spectra of bismuth titanate  $\text{Bi}_{12}\text{TiO}_{20-y}\text{N}_y$  ( $y = 0.03$ ): (a) the whole spectrum of  $\text{Bi}_{12}\text{TiO}_{20-y}\text{N}_y$  ( $y = 0.03$ ); (b) spectrum of doped nitrogen; (c) spectrum of doped carbon.

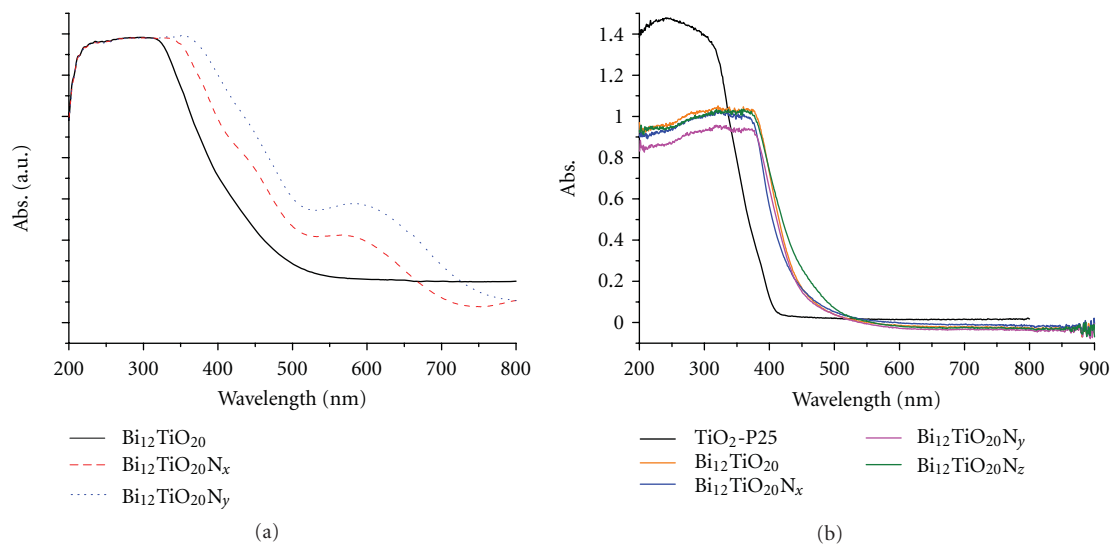
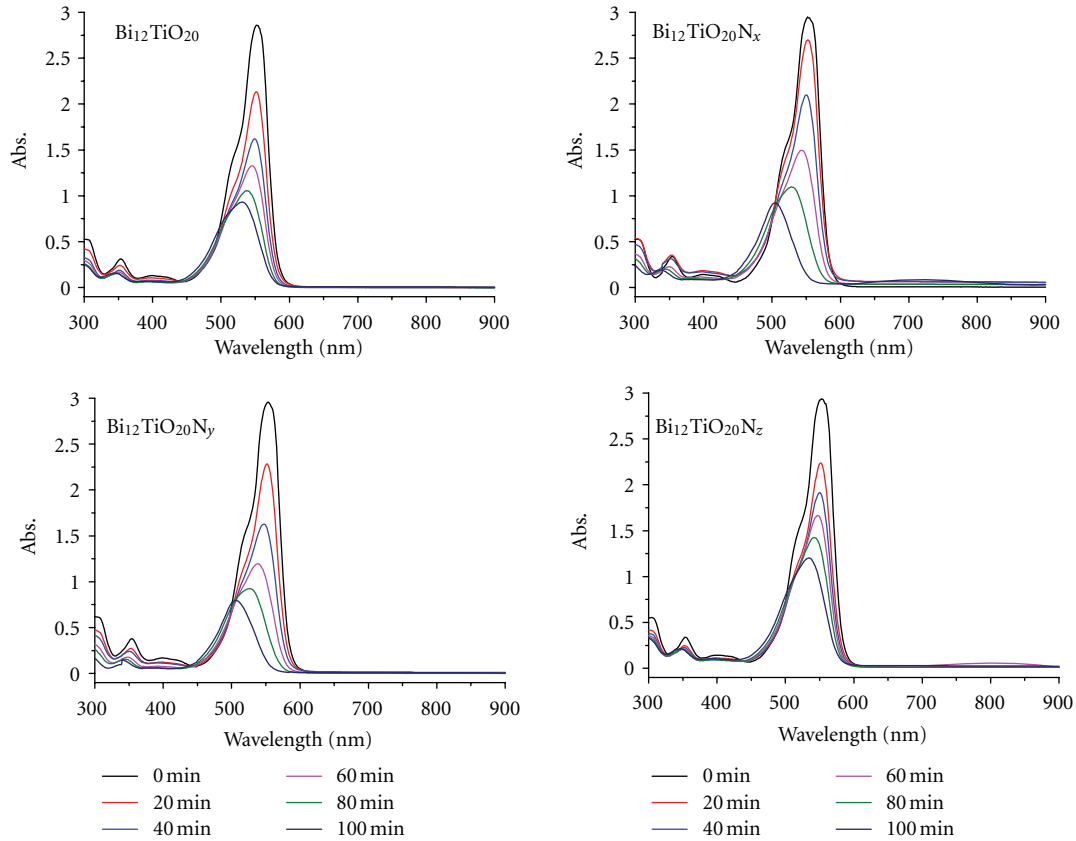
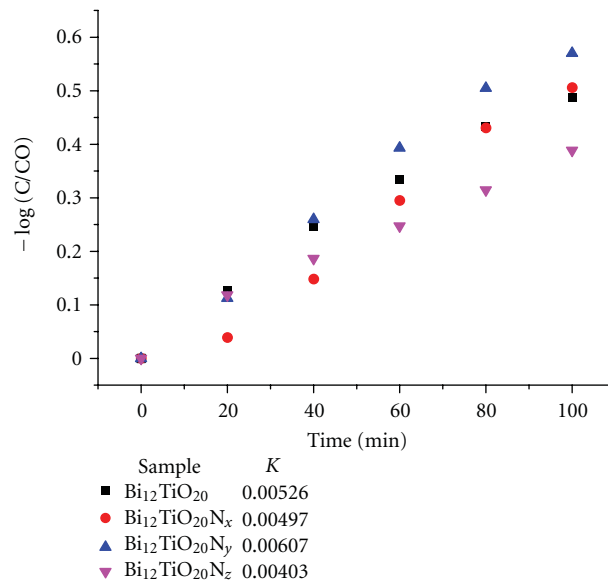


FIGURE 4: (a) Absorption spectra of films of bismuth titanate ( $\text{Bi}_{12}\text{TiO}_{20}$ ,  $\text{Bi}_{12}\text{TiO}_{20-x}\text{N}_x$  ( $x = 0.01$ ) and  $\text{Bi}_{12}\text{TiO}_{20-y}\text{N}_y$  ( $y = 0.03$ )) and (b) UV-Vis diffuse reflection spectra of powders  $\text{Bi}_{12}\text{TiO}_{20}$ ,  $\text{Bi}_{12}\text{TiO}_{20-x}\text{N}_x$  ( $x = 0.01$ ),  $\text{Bi}_{12}\text{TiO}_{20-y}\text{N}_y$  ( $y = 0.03$ ),  $\text{Bi}_{12}\text{TiO}_{20-z}\text{N}_z$  ( $z = 0.06$ ), and  $\text{TiO}_2\text{-P25}$ .



(a)



(b)

FIGURE 5: Photocatalytic decomposition of RhB by undoped and nitrogen-doped  $\text{Bi}_{12}\text{TiO}_{20}$  photocatalysts: (a) absorption spectra decay of RhB via time; (b) decomposition activity of samples.

and  $\text{Bi}_{12}\text{TiO}_{20-y}\text{N}_y$  ( $y = 0.03$ ) films by sol-gel deposition with and without nitrogen doping. The UV-Vis absorption spectra band edge of  $\text{Bi}_{12}\text{TiO}_{20}$  shifted from 400 nm to about 470 nm of nitrogen-doped  $\text{Bi}_{12}\text{TiO}_{20-y}\text{N}_y$  ( $y = 0.03$  with

$\text{NH}_2^*:\text{Bi}^{3+}$  about 1:1 solution, and  $\text{N}/(\text{N}+\text{O})$  mole ratios about 3%). The absorption spectra's broadening of nitrogen-doped  $\text{Bi}_{12}\text{TiO}_{20}$  was attributed to the doping of nitrogen's substitution of oxygen site that induced the narrowing of the

bandgap. There was an additional absorption peak at 580 nm wavelength that was attributed to the deep-level nitrogen dopant.

The UV-Vis diffuse reflection spectra of nitrogen-doped and undoped  $\text{Bi}_{12}\text{TiO}_{20}$  powders were characterized as shown in Figure 4(b), P25 was also used as a reference.  $\text{TiO}_2$ -P25 materials have intensive UV absorption and the absorption edge line at about 380 nm, while all  $\text{Bi}_{12}\text{TiO}_{20}$  of nitrogen-doped and undoped have less UV absorption but longer bandgap-related wavelength about 450 nm. The bandgap of nitrogen-doped  $\text{Bi}_{12}\text{TiO}_{20}$  versus undoped  $\text{Bi}_{12}\text{TiO}_{20}$  in DRS spectra varied about 20 nm, from 440 nm to 460 nm. The red shift of absorption edge wavelength of nitrogen-doped  $\text{Bi}_{12}\text{TiO}_{20}$  powders in DRS spectra is less than that in absorption spectra of nitrogen-doped  $\text{Bi}_{12}\text{TiO}_{20}$  films, which we attribute to the variation of N/(N+O) ratios from inner to the outer layer. As known, the absorption spectra of films show the absorption of whole bulk materials, while the DRS spectrum more attribute to materials' surfaces. While annealing, there may be more nitrogen dopant in inner part and more oxygen in surfaces, so the absorption spectra edge of whole film materials will show more red shift than the diffuse reflection spectra edge obtained only from powders' surface.

The absorption band edge of  $\text{Bi}_{12}\text{TiO}_{20}$  films and UV-Vis diffuse reflection band edge of  $\text{Bi}_{12}\text{TiO}_{20}$  powders were successfully expanded to visible light region of solar spectra by urea-assisted sol-gel method, which would greatly enhance the utilizing ratio of visible light region of solar spectra in photocatalysis and solar cell researches.

**3.5. Influence of Photocatalytic Capability of  $\text{Bi}_{12}\text{TiO}_{20}$  by Nitrogen Doping.** To study the relationship of photocatalytic property with nitrogen doping of bismuth titanate, photocatalysis of rhodamine b (RhB) by undoped and nitrogen-doped bismuth titanate was performed. The photocatalytic activity was characterized by the decomposition of 10 mg/L rhodamine b (RhB) solution, with 100 mg of photocatalyst added to 100 mL of rhodamine b (RhB) solution. The reaction system was irradiated by 300 W Xe lamps.

The photocatalytic ability of undoped  $\text{Bi}_{12}\text{TiO}_{20}$  materials had been studied by Yao et al. [24–26] and other groups [28, 29, 31, 33, 34]. Here we are concerned with relationship of photocatalytic ability of undoped and nitrogen-doped  $\text{Bi}_{12}\text{TiO}_{20}$  materials with different amount of urea added in precursors ( $\text{NH}_2^*:\text{Bi}^{3+}$  about 0:1, 1:1, 2:1, and 3:1). Different amount of urea added in precursor solution deduced to the different amount of nitrogen dopant in the  $\text{Bi}_{12}\text{TiO}_{20}$  photocatalysts. All samples were annealed at 600°C for 30 minutes.

As shown in Figure 5, the performance of catalyst  $\text{Bi}_{12}\text{TiO}_{20}$  and  $\text{Bi}_{12}\text{TiO}_{20-y}\text{N}_y$  ( $y = 0.03$ ) have better performance than other catalysts. The undoped and nitrogen-doped  $\text{Bi}_{12}\text{TiO}_{20-y}\text{N}_y$  ( $y = 0.03$ ) catalysts with N/(N+O) mole ratio about 0% and 3% were prepared by  $\text{NH}_2^*:\text{Bi}^{3+}$  about 0:1 and 2:1 in the precursor solutions, respectively.

The velocity constants of catalyst  $\text{Bi}_{12}\text{TiO}_{20}$  ( $k = 5.26 \times 10^{-3} \text{ min}^{-1}$ ) and catalyst  $\text{Bi}_{12}\text{TiO}_{20-y}\text{N}_y$  ( $y = 0.03$ ;  $k = 6.07 \times 10^{-3} \text{ min}^{-1}$ ) are about 1.5-times the velocity constant

of catalyst  $\text{Bi}_{12}\text{TiO}_{20-z}\text{N}_z$  ( $z = 0.06$ ;  $k = 4.03 \times 10^{-3} \text{ min}^{-1}$ ). So the nitrogen-doped  $\text{Bi}_{12}\text{TiO}_{20-y}\text{N}_y$  ( $y = 0.03$ ) photocatalyst with N/(N+O) mole ratio about 3% have better performance than undoped  $\text{Bi}_{12}\text{TiO}_{20}$ , light-doped  $\text{Bi}_{12}\text{TiO}_{20-x}\text{N}_x$  ( $x = 0.01$ ), and heavily doped  $\text{Bi}_{12}\text{TiO}_{20-z}\text{N}_z$  ( $z = 0.06$ ) photocatalysts.

The variation of whole spectra photocatalytic performance of undoped and nitrogen-doped  $\text{Bi}_{12}\text{TiO}_{20}$  was attribute to the morphologies as observed by SEM in Figure 2.  $\text{Bi}_{12}\text{TiO}_{20-y}\text{N}_y$  ( $y = 0.03$ ) have more crystalline nano crystal facets and larger surface areas than other samples, which lead to better photocatalytic performance than other samples. But a high level of nitrogen-doped (above 6% of N/(N+O)) would lead to the formation of more defects in nano crystals of prepared catalysts, and would influence the transportation of photogenerated electrons and holes. Though high level of nitrogen doping can effectively expand the visible light absorption, a high defects density would lead to poor photocatalytic activity.

## 4. Conclusions

In conclusion, by urea-assisted sol-gel method, undoped and nitrogen-doped  $\text{Bi}_{12}\text{TiO}_{20}$ ,  $\text{Bi}_{12}\text{TiO}_{20-x}\text{N}_x$  ( $x = 0.01$ ),  $\text{Bi}_{12}\text{TiO}_{20-y}\text{N}_y$  ( $y = 0.03$ ), and  $\text{Bi}_{12}\text{TiO}_{20-z}\text{N}_z$  ( $z = 0.06$ ) powders were prepared. After annealing, the morphologies of as-synthesized samples exhibit sheet-like morphologies. And by controlling the amount of urea added in the precursor solutions, photocatalyst with sheet-like morphologies with good crystalline facet and larger surface area can be synthesized.

The absorption spectra of nitrogen-doped  $\text{Bi}_{12}\text{TiO}_{20-x}\text{N}_x$  ( $x = 0.01$ ),  $\text{Bi}_{12}\text{TiO}_{20-y}\text{N}_y$  ( $y = 0.03$ ), and  $\text{Bi}_{12}\text{TiO}_{20-z}\text{N}_z$  ( $z = 0.06$ ) films were successfully expanded from about 400 nm of  $\text{Bi}_{12}\text{TiO}_{20}$  to about 500 nm, also from DRS spectra the band edge were successfully expanded from about 420 nm to about 460 nm, which would greatly enhance the utilization ratio of visible light in solar spectra. The expanded visible light can be attributed to the doping of nitrogen substituting of oxygen in  $\text{Bi}_{12}\text{TiO}_{20}$  crystal lattice. Photocatalytic performance of nitrogen-doped  $\text{Bi}_{12}\text{TiO}_{20-y}\text{N}_y$  ( $y = 0.03$ ) with N/(N+O) mole ratio about 3% is better photocatalytic activity than that of undoped, light-doped (below 1%), and heavily doped  $\text{Bi}_{12}\text{TiO}_{20-z}\text{N}_z$  ( $z = 0.06$ ) photocatalysts.

## Acknowledgments

This paper was financially supported by research grants from the National Basic Research Program of China (973 Program, no. 2007CB613302), and the National Science Foundation of China (nos. 20973102 and 51021062). The authors also express our thanks for the editor's patience.

## References

- [1] A. Fujishima, K. Honda, and S. Kikuchi, "Photosensitized electrolytic oxidation on semiconducting n-type  $\text{TiO}_2$  electrode," *Kogyo Kagaku Zasshi*, vol. 72, pp. 108–113, 1969.

- [2] A. Fujishima and K. Honda, "Electrochemical photolysis of water at a semiconductor electrode," *Nature*, vol. 238, no. 5358, pp. 37–38, 1972.
- [3] J. A. Byrne, P. A. Fernandez-Ibañez, P. S. M. Dunlop, D. M. A. Alrousan, and J. W. J. Hamilton, "Photocatalytic enhancement for solar disinfection of water: a review," *International Journal of Photoenergy*, vol. 2011, Article ID 764870, 12 pages, 2011.
- [4] J. Gamage and Z. Zhang, "Applications of photocatalytic disinfection," *International Journal of Photoenergy*, vol. 200, Article ID 764870, 11 pages, 2010.
- [5] R. Asahi, T. Morikawa, T. Ohwaki, K. Aoki, and Y. Taga, "Visible-light photocatalysis in nitrogen-doped titanium oxides," *Science*, vol. 293, no. 5528, pp. 269–271, 2001.
- [6] S. Sato, R. Asahi, T. Morikawa, T. Ohwaki, K. Aoki, and Y. Taga, "Photocatalysts sensitive to visible light—response," *Science*, vol. 295, no. 5555, pp. 626–627, 2002.
- [7] K. Nukumizu, J. Nunoshige, T. Takata et al., "TiN<sub>x</sub>O<sub>y</sub>F<sub>z</sub> as a stable photocatalyst for water oxidation in visible light (<570 nm)," *Chemistry Letters*, vol. 32, no. 2, pp. 196–197, 2003.
- [8] H. Liu and L. Gao, "(Sulfur, nitrogen)-codoped rutile-titanium dioxide as a visible-light-activated photocatalyst," *Journal of the American Ceramic Society*, vol. 87, no. 8, pp. 1582–1584, 2004.
- [9] H. Liu and L. Gao, "Codoped rutile TiO<sub>2</sub> as a new photocatalyst for visible light irradiation," *Chemistry Letters*, vol. 33, no. 6, pp. 730–731, 2004.
- [10] M. Mrowetz, W. Balcerski, A. J. Colussi, and M. R. Hoffmann, "Oxidative power of nitrogen-doped TiO<sub>2</sub> photocatalysts under visible illumination," *Journal of Physical Chemistry B*, vol. 108, no. 45, pp. 17269–17273, 2004.
- [11] Q. Zhang, J. Wang, S. Yin, T. Sato, and F. Saito, "Synthesis of a visible-light active TiO<sub>2</sub>-xS<sub>x</sub> photocatalyst by means of mechanochemical doping," *Journal of the American Ceramic Society*, vol. 87, no. 6, pp. 1161–1163, 2004.
- [12] T. Matsunaga and M. Inagaki, "Carbon-coated anatase for oxidation of methylene blue and NO," *Applied Catalysis B*, vol. 64, no. 1–2, pp. 9–12, 2006.
- [13] H. Yamashita, Y. Nishida, O. Chiyoda et al., "Design of efficient TTiO<sub>2</sub>/SiC photocatalysts from TiC-SiC nano particles for degradation of organic pollutants diluted in water," *Materials Science Forum*, vol. 510–511, pp. 9–12, 2006.
- [14] Y. Kesong, D. Ying, H. Baibiao, and H. Shenghao, "Theoretical study of N-doped TiO<sub>2</sub> rutile crystals," *Journal of Physical Chemistry B*, vol. 110, no. 47, pp. 24011–24014, 2006.
- [15] H. Yamashita, Y. Nishida, S. Yuan et al., "Design of TiO<sub>2</sub>-SiC photocatalyst using TiC-SiC nano-particles for degradation of 2-propanol diluted in water," *Catalysis Today*, vol. 120, no. 2, pp. 163–167, 2007.
- [16] K. Yang, Y. Dai, and B. Huang, "Study of the nitrogen concentration influence on N-doped TiO<sub>2</sub> anatase from first-principles calculations," *Journal of Physical Chemistry C*, vol. 111, no. 32, pp. 12086–12090, 2007.
- [17] J. A. Rengifo-Herrera, E. Mielczarski, J. Mielczarski, N. C. Castillo, J. Kiwi, and C. Pulgarin, "Escherichia coli inactivation by N, S co-doped commercial TiO<sub>2</sub> powders under UV and visible light," *Applied Catalysis B*, vol. 84, no. 3–4, pp. 448–456, 2008.
- [18] G. Shang, H. Fu, S. Yang, and T. Xu, "Mechanistic study of visible-light-induced photodegradation of 4-chlorophenol by TiO<sub>2-x</sub>N<sub>x</sub> (0.021 < x < 0.049) with low nitrogen concentration," *International Journal of Photoenergy*, vol. 2012, Article ID 759306, 9 pages, 2012.
- [19] L. Zhao, J. Ran, Z. Shu, G. Dai, P. Zhai, and S. Wang, "Effects of calcination temperatures on photocatalytic activity of ordered titanate nanoribbon/SnO<sub>2</sub> films fabricated during an EPD process," *International Journal of Photoenergy*, vol. 2012, Article ID 472958, 7 pages, 2012.
- [20] N.-H. Lee, H.-J. Oh, S.-C. Jung, W.-J. Lee, D.-H. Kim, and S.-J. Kim, "Photocatalytic properties of nanotubular-shaped TiO<sub>2</sub> powders with anatase phase obtained from titanate nanotube powder through various thermal treatments," *International Journal of Photoenergy*, vol. 2011, Article ID 327821, 7 pages, 2011.
- [21] M.-L. Chen and W.-C. Oh, "The improved photocatalytic properties of methylene blue for V<sub>2</sub>O<sub>3</sub>/CNT/TiO<sub>2</sub> composite under visible light," *International Journal of Photoenergy*, vol. 2010, Article ID 264831, 5 pages, 2010.
- [22] A. Kudo and S. Hiji, "H<sub>2</sub> or O<sub>2</sub> evolution from aqueous solutions on layered oxide photocatalysts consisting of Bi3+ with 6s<sup>2</sup> configuration and d<sup>0</sup> transition metal ions," *Chemistry Letters*, no. 10, pp. 1103–1104, 1999.
- [23] S. Yao, J. Wei, B. Huang et al., "Morphology modulated growth of bismuth tungsten oxide nanocrystals," *Journal of Solid State Chemistry*, vol. 182, no. 2, pp. 236–239, 2009.
- [24] W. F. Yao, H. Wang, X. H. Xu et al., "Photocatalytic property of bismuth titanate Bi<sub>12</sub>TiO<sub>20</sub> crystals," *Applied Catalysis A*, vol. 243, no. 1, pp. 185–190, 2003.
- [25] W. F. Yao, H. Wang, X. H. Xu et al., "Photocatalytic property of Zn-doped Bi<sub>12</sub>TiO<sub>20</sub>," *Journal of Materials Science Letters*, vol. 22, no. 14, pp. 989–992, 2003.
- [26] W. F. Yao, H. Wang, X. H. Xu et al., "Characterization and photocatalytic properties of Ba doped Bi<sub>12</sub>TiO<sub>20</sub>," *Journal of Molecular Catalysis A*, vol. 202, no. 1–2, pp. 305–311, 2003.
- [27] W. F. Yao, X. H. Xu, J. T. Zhou et al., "Photocatalytic property of sillenite Bi<sub>24</sub>AlO<sub>39</sub> crystals," *Journal of Molecular Catalysis A*, vol. 212, no. 1–2, pp. 323–328, 2004.
- [28] N. Thanabodeekij, E. Gulari, and S. Wongkasemjit, "Bi<sub>12</sub>TiO<sub>20</sub> synthesized directly from bismuth (III) nitrate pentahydrate and titanium glycolate and its activity," *Powder Technology*, vol. 160, no. 3, pp. 203–208, 2005.
- [29] X. H. Xu, W. F. Yao, Y. Zhang, A. Q. Zhou, Y. Hou, and M. Wang, "Photocatalytic properties of bismuth titanate compounds," *Acta Chimica Sinica*, vol. 63, no. 1, pp. 5–10, 2005.
- [30] T. Lin, Z. Pi, M. C. Gong, J. B. Zhong, J. L. Wang, and Y. Q. Chen, "Gas-phase photocatalytic oxidation of benzene over titanium dioxide loaded on Bi<sub>12</sub>TiO<sub>20</sub>," *Chinese Chemical Letters*, vol. 18, no. 2, pp. 241–243, 2007.
- [31] S. Xu, W. Shangguan, J. Yuan, J. Shi, and M. Chen, "Photocatalytic properties of bismuth titanate Bi<sub>12</sub>TiO<sub>20</sub> prepared by coprecipitation processing," *Materials Science and Engineering B*, vol. 137, no. 1–3, pp. 108–111, 2007.
- [32] S. Xu, W. Shangguan, J. Yuan, J. Shi, and M. Chen, "Preparations and photocatalytic degradation of methyl orange in water on magnetically separable Bi<sub>12</sub>TiO<sub>20</sub> supported on nickel ferrite," *Science and Technology of Advanced Materials*, vol. 8, no. 1–2, pp. 40–46, 2007.
- [33] J. Zhou, Z. Zou, A. K. Ray, and X. S. Zhao, "Preparation and characterization of polycrystalline bismuth titanate Bi<sub>12</sub>TiO<sub>20</sub> and its photocatalytic properties under visible light irradiation," *Industrial and Engineering Chemistry Research*, vol. 46, no. 3, pp. 745–749, 2007.
- [34] H. Zhang, M. Lü, S. Liu et al., "Preparation and photocatalytic properties of sillenite Bi<sub>12</sub>TiO<sub>20</sub> films," *Surface and Coatings Technology*, vol. 202, no. 20, pp. 4930–4934, 2008.

- [35] J. Hou, Y. Qu, D. Krsmanovic, C. Ducati, D. Eder, and R. V. Kumar, "Solution-phase synthesis of single-crystalline  $\text{Bi}_{12}\text{TiO}_{20}$  nanowires with photocatalytic properties," *Chemical Communications*, no. 26, pp. 3937–3939, 2009.
- [36] W. Wei, Y. Dai, and B. Huang, "First-principles characterization of Bi-based photocatalysts:  $\text{Bi}_{12}\text{TiO}_{20}$ ,  $\text{Bi}_2\text{Ti}_2\text{O}_7$ , and  $\text{Bi}_4\text{Ti}_3\text{O}_{12}$ ," *Journal of Physical Chemistry C*, vol. 113, no. 14, pp. 5658–5663, 2009.
- [37] V. Marinova, "Optical properties of  $\text{Bi}_{12}\text{TiO}_{20}$  doped with Al, P, Ag, Cu, Co and co-doped with Al + P single crystals," *Optical Materials*, vol. 15, no. 2, pp. 149–158, 2000.
- [38] Z. Shuxian, W. K. Hall, G. Ertl, and H. Knözinger, "X-Ray photoemission study of oxygen and nitric oxide adsorption on  $\text{MoS}_2$ ," *Journal of Catalysis*, vol. 100, no. 1, pp. 167–175, 1986.
- [39] S. Badrinarayanan, S. Sinha, and A. B. Mandale, "XPS studies of nitrogen ion implanted zirconium and titanium," *Journal of Electron Spectroscopy and Related Phenomena*, vol. 49, no. 3, pp. 303–309, 1989.
- [40] G. Soto, W. De La Cruz, and M. H. Fariás, "XPS, AES, and EELS characterization of nitrogen-containing thin films," *Journal of Electron Spectroscopy and Related Phenomena*, vol. 135, no. 1, pp. 27–39, 2004.
- [41] C. Ocal and S. Ferrer, "The strong metal-support interaction (SMSI) in Pt-TiO<sub>2</sub> model catalysts. A new CO adsorption state on Pt-Ti atoms," *The Journal of Chemical Physics*, vol. 84, no. 11, pp. 6474–6478, 1986.

## Research Article

# Preparation, Photocatalytic Activity, and Recovery of Magnetic Photocatalyst for Decomposition of Benzoic Acid

Te-Li Su,<sup>1</sup> Chyow-San Chiou,<sup>2</sup> and Hua-Wei Chen<sup>1</sup>

<sup>1</sup>Department of Cosmetic Application and Management, St. Mary's Medicine, Nursing and Management College, Yilan 266, Taiwan

<sup>2</sup>Department of Environmental Engineering, National I-Lan University, I-lan 26047, Taiwan

Correspondence should be addressed to Hua-Wei Chen, superlemi@smc.edu.tw

Received 15 May 2011; Revised 2 August 2011; Accepted 17 August 2011

Academic Editor: Jiaguo Yu

Copyright © 2012 Te-Li Su et al. This is an open access article distributed under the Creative Commons Attribution License, which permits unrestricted use, distribution, and reproduction in any medium, provided the original work is properly cited.

The purpose of this paper is to determine the experimental parameters of TiO<sub>2</sub> preparation for optimizing the removal rate of benzoic acid by magnetic photocatalytic oxidation process. Therefore, this paper intended to prepare a magnetic photocatalyst (TiO<sub>2</sub>/SiO<sub>2</sub>/Fe<sub>3</sub>O<sub>4</sub>) that can be recycled using an external magnetic field. Magnetic photocatalysts are characterized by X-ray diffraction (XRD), vibrating sample magnetometry (VSM), and Fourier transform infrared (FTIR) spectroscopy. The optimal the experimental parameters of TiO<sub>2</sub> preparation for the removal rate of photocatalysts were concluded as pH is 3, weight ratio of TiO<sub>2</sub>/SiO<sub>2</sub>(Fe<sub>3</sub>O<sub>4</sub>) is 1, and calcined temperature of TiO<sub>2</sub>/SiO<sub>2</sub>/Fe<sub>3</sub>O<sub>4</sub> is 350°C. Furthermore, the paramagnetic behaviors of the prepared TiO<sub>2</sub>/SiO<sub>2</sub>/Fe<sub>3</sub>O<sub>4</sub> gave rise to the magnetic photocatalyst, which could be separated more easily through the application of a magnetic field for reuse.

## 1. Introduction

Benzoic acid is one of the oldest chemical preservatives used in food, cosmetics, and drugs. Benzoic acid can also be detected in car exhaust gases, cigarettes, phytochemically degraded benzoic acid esters in fragrance ingredients, wastewater from wood production industries, foundry waste leachates, and ashes from municipal incinerators [1]. A common objective of AOPs [2–5] is to produce a large amount of radicals (especially OH), in order to oxidize organic matter. Semiconductor photocatalysis has become an increasingly promising technology in environmental remediation [6–8]. Various types of photocatalysts, titanium dioxide is now under intensive investigation for practical application in antimicrobial, deodorization, air and water purifications, and wastewater treatment due to its favorable physical/chemical properties, low cost, ease of availability, and high stability [9]. Typically, catalytic ozonation and photocatalytic oxidation are conducted in a suspension of submicrometer-sized particles [3, 4, 10] and, therefore, requires an additional separation step to remove the catalyst from treated water, which presents a major drawback in the application of UV/TiO<sub>2</sub> processing for treating wastewater.

One approach in overcoming this drawback has been the development of a magnetic photocatalyst that allows for easy catalyst removal by using an external magnet, simplifying the downstream recovery stage [11, 12]. Fe<sub>3</sub>O<sub>4</sub> has been generally used as a very important ferromagnetic material for wide application (pigment, recording materials, catalysis, magnetocaloric refrigeration, and drug-delivery carrier) due to its low cost, good hydrophilic and biocompatible properties. [4, 12–14]. However, a direct contact between magnetic iron oxide and TiO<sub>2</sub> photocatalyst usually gives rise to an unfavorable heterojunction, leading to an increase in electron-hole recombination and photodissolution [15]. Therefore, it is necessary to shield the magnetic iron oxide from direct contacts with titania by introducing a barrier layer. Silica is one of most commonly used support material in catalysis due to the stability, protection of core (iron oxide) and surface modification [15, 16]. Thus, this study investigates the reaction behavior of photocatalytic processes with magnetic photocatalyst (Fe<sub>3</sub>O<sub>4</sub> core and TiO<sub>2</sub>/SiO<sub>2</sub> shell) in treating wastewater to enhance the activity of the prepared magnetic photocatalyst and recover the photocatalyst.

There have been many parameters, such as pH, weight ratio, and calcined temperature, related to the Taguchi

method [17, 18] to removal rates. Efficiently determining the critical factors can improve the efficiency of the photocatalysts. The traditional trial-and-error method lacks proper overall planning of experimental parameters, thus, while it could acquire the most comprehensive experimental data, discussion and analysis of the correlation between experimental parameters was lacking. An experiment that tests all parameters takes an excessive amount of time and the photocatalysts conditions are difficult to control. This research has, therefore, applied the Taguchi method [19–22] to the removal rate of benzoic acid by a UV/magnetic photocatalyst process and the design of a series of experimental principles. The most influential parameters for removal rate of benzoic acid by UV/magnetic photocatalyst process were selected and matched with a customized experimental plan, in order that the experimental parameters of the photocatalysts could be analyzed, which was used to optimize the experimental parameters and improve the removal rate.

Therefore, in this paper, the Taguchi method was applied to determine the parameters for the optimal removal rate of benzoic acid by the UV/magnetic photocatalyst process. However, there are many experimental parameters and the process is complicated, the selection relies completely on experienced researchers, or by the trial and error method, in order to change the experimental parameters of the photocatalyst/UV process through multiple error attempts. This method is not only time consuming, increasing the trial time, but also simultaneously results in greater cost and difficulty in accumulating and passing on such experience.

## 2. Material and Methods

**2.1. Experimental Apparatus.** All experimental solutions were prepared with deionized water and reagent-grade chemicals. The photocatalytic activates under UV light illumination were evaluated by measuring the decomposition rate of benzoic acid. The batch cylindrical photoreactor was made of Pyrex glass with an effective volume of 1.5 liter and was water-jacketed to maintain the solution temperature, as illustrated in Figure 1. The UV light illumination was conducted using two black lamps (Sparkie BLB-S8W) of 8 W power with the maximum intensity at 365 nm. Photocatalytic decomposition of benzoic acid was assumed to be started when the prewarmed light source within the reactor was turned on. The aqueous solution containing benzoic acid was initially transferred to the column reactor, and the pH value of the solution was controlled by adding sodium hydroxide and/or perchlorates during the entire reaction time. Perchlorates and nitrates had very little effect of photocatalytic reaction, and sulfates or phosphates, even at millimolar concentrations, were found to be rapidly adsorbed by the catalyst and to reduce the rate of photocatalytic reaction by 20–70% [23]. Aliquots of the reaction solution were sampled at intermittent periods of reaction time. The samples were analyzed for concentrations of benzoic acid with a liquid chromatography equipped with a KANUER Smartline UV detector 2500, Alpha 10 Isocratic Pump, and SUPELCO 516 C-18 column.

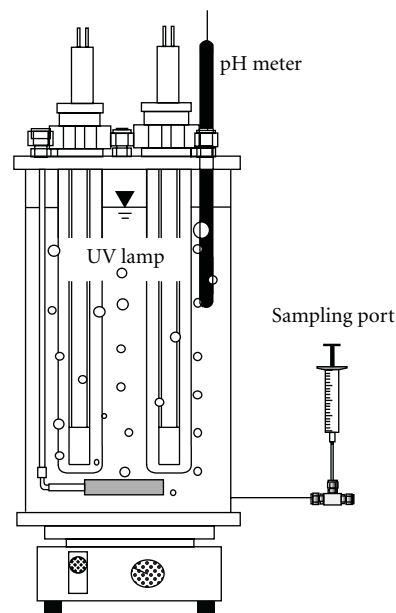


FIGURE 1: Experimental sketch of UV/TiO<sub>2</sub>/SiO<sub>2</sub>/Fe<sub>3</sub>O<sub>4</sub> system.

**2.2. Catalyst Preparation.** Magnetite (Fe<sub>3</sub>O<sub>4</sub>) was purchased from Sigma-Aldrich (St. Louis, Mo, USA) and used without any further purification. A total of 1.08 L of aqueous solution containing 20 g of Fe<sub>3</sub>O<sub>4</sub> particles was contained in a 2-L beaker at 90°C; the pH was maintained at 9.5 with 0.1 N NaOH, while being stirred by a mechanical stirrer. The appropriate amount of Degussa P-25 TiO<sub>2</sub> particles and Na<sub>2</sub>O·nSiO<sub>2</sub> was dispersed and dissolved, respectively, in 100 mL of deionized water; the aqueous solution was then mixed with the aqueous solution containing magnetite (Fe<sub>3</sub>O<sub>4</sub>) with a mechanical stirrer for 10 min. The magnetic photocatalysts (i.e., TiO<sub>2</sub>/SiO<sub>2</sub>/Fe<sub>3</sub>O<sub>4</sub>) were dried at 105°C after the pH value of the slurry solution was maintained at 8 with 5 N H<sub>2</sub>SO<sub>4</sub>. Finally, the TiO<sub>2</sub>/SiO<sub>2</sub>/Fe<sub>3</sub>O<sub>4</sub> was placed in an oven isothermally at 350°C, 550°C, and 750°C for 2 hours with nitrogen-pass, respectively.

**2.3. Instrumental Analysis.** The morphology and specific BET surface area of the TiO<sub>2</sub> were determined by a Rigaku RTP 300 X-ray diffractometer (XRD) and a Micromeritics ASAP 2000 analyzer, respectively. The functional groups of the synthesized magnetic photocatalysts (TiO<sub>2</sub>/SiO<sub>2</sub>/Fe<sub>3</sub>O<sub>4</sub>) were confirmed using an FTIR spectrometer (Spectrum 100, Perkin Elmer, USA). The magnetic behavior was analyzed using a vibrating sample magnetometer (VSM, Lake Shore 7407, Lake Shore, USA). The magnetic properties and functional groups of the photocatalysts were determined by a vibrating sample magnetometer (Lake Shore, 7407) and a Fourier Transform Infrared Spectrophotometer (Perkin Elmer, 1600), respectively. For experiments related to the photodecomposition of benzoic acid, the degradation of benzoic acid present in the reaction solution was analyzed by Spectra-Physics P1000 HPLC equipped with an UV detector.

**2.4. Taguchi Method.** Determining key factors is helpful for promoting experimental efficiency, and the traditional trial-and-error method lacked overall planning, which although it could provide large amounts of data, these were the least discussed and analyzed. In addition, such experiments are time consuming and waste production costs. Moreover, control of experimental conditions was not simple. In order to obtain higher photocatalytic performance of photocatalysts, the Taguchi method was adopted for experimental design. For this purpose, critical conditions were selected and applied in the experimental planning in order to determine the optimal experimental parameters promoting a photocatalytic performance of the photocatalysts.

By orthogonal array, useful statistical data and reliable effects of factors can be obtained in the least number of experiments. However, full factorial experiments require too many experimental repetitions, while fractional factorial experimental method is too complex. L9, which represents the nine experiments to be conducted, was selected in this research.

The basic purpose of parameter design is to determine a group of optimal experimental parameters. By the Taguchi method, quality characteristics and removal rate were transformed into an SN ratio, which is useful in the estimation of statistical efficiency quantity. Photocatalysts, able to yield higher removal rates, meet the requirements of this study. Therefore, it is the best to have large quality characteristics. The SN ratio of the larger-the-better is defined as

$$\eta = -10 \log \sum \frac{1}{n} \left( \frac{1}{y_i} \right)^2, \quad (1)$$

where  $y_i$  represents value of quality;  $n$  represents the total number of experiments.

Experiments for experimental planning design, according to an orthogonal array, can create the data required for the orthogonal array. Then, a response table can be established by transformation of the data from the orthogonal array experiments into SN ratios. The method selected for the transformation depends on the quality requested. Each average response,  $\bar{F}_i$  of  $F$ , can be calculated. Then, the value of main effect,  $\Delta F$  of each  $F$ , is calculated. A response table comprised of these data can be applied to analyze the effects of each factor. A larger  $\Delta F$  indicates a larger effect on quality characteristics; inversely, a less  $\Delta F$  indicates a lesser effect on quality characteristics. The calculation is as follows:

$$\bar{F}_i = \frac{1}{m} \sum_{j=1}^m y_{ij}, \quad (2)$$

$$\Delta F = \max\{\bar{F}_1, \bar{F}_2, \dots, \bar{F}_n\} - \min\{\bar{F}_1, \bar{F}_2, \dots, \bar{F}_n\},$$

where  $n$  represents level of factor;  $m$  represents the total number of level  $i$ ;  $y_i$  represents SN ratio of level  $i$ .

Confirmation experiments are to verify the reasonability of the constructed mathematical mode. Applying additional modes, using the level values of optimal factors, can predict the SN ratios under optimal conditions. The calculation is as follows:

$$\widehat{SN} = \bar{T} + \sum_{i=1}^n (F_i - \bar{T}), \quad (3)$$

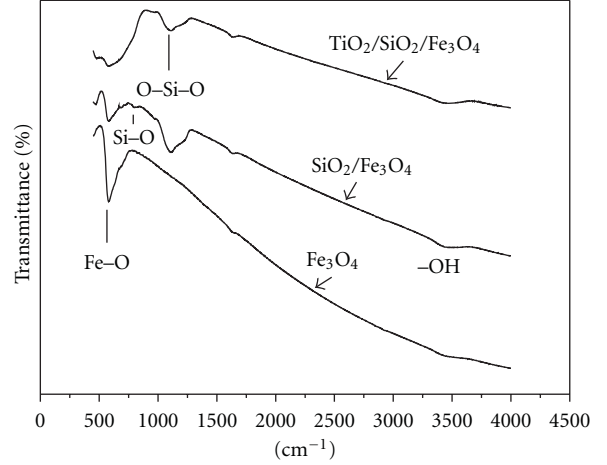


FIGURE 2: FTIR spectra of  $\text{Fe}_3\text{O}_4$ ,  $\text{SiO}_2/\text{Fe}_3\text{O}_4$ , and  $\text{TiO}_2/\text{SiO}_2/\text{Fe}_3\text{O}_4$ .

where  $\bar{T}$  represents average of all SN ratios;  $F_i$  represents SN ratio of experimental parameters.

To evaluate each observed value, its confidence interval must be calculated. The formula for calculating the confidence interval of the average of the expected values from confirmation experiments is as follows:

$$CI = \sqrt{F_{\alpha;1,\nu_2} \times MSE \times \left( \frac{1}{n_{\text{eff}}} + \frac{1}{r} \right)}, \quad (4)$$

where  $F_{\alpha;1,\nu_2}$  represents  $F$  value of the apparent level  $\alpha$ ;  $\alpha$  represents apparent level with confidence level  $1-\alpha$ ;  $\nu_2$  represents freedom of the error;  $MSE$  represents variance of error;  $n_{\text{eff}}$  represents the effective observed value;  $r$  represents the number of confirmation experiments,  $r \neq 0$ .

Finally, a CI of 95% is used to verify whether the predicted average value is acceptable or not, the verification equation is:

$$\widehat{SN} - CI \leq \mu \leq \widehat{SN} + CI. \quad (5)$$

### 3. Results and Discussion

**3.1. Surface Characteristics of Magnetic Photocatalyst.** The FTIR spectra of  $\text{Fe}_3\text{O}_4$ ,  $\text{SiO}_2/\text{Fe}_3\text{O}_4$ , and the prepared magnetic photocatalyst ( $\text{TiO}_2/\text{SiO}_2/\text{Fe}_3\text{O}_4$ ) are as shown in Figure 2. The result exhibits two basic characteristic peaks of  $\text{Fe}_3\text{O}_4$ ,  $\text{SiO}_2/\text{Fe}_3\text{O}_4$ , and  $\text{TiO}_2/\text{SiO}_2/\text{Fe}_3\text{O}_4$  at about  $3300 \text{ cm}^{-1}$  (O–H stretching) and  $550 \text{ cm}^{-1}$  (Fe–O vibration), which were attributed to the presence of FeOH in  $\text{Fe}_3\text{O}_4$  [24]. The peak at  $1100 \text{ cm}^{-1}$  was attributed to the Si–O–Si bond stretching of  $\text{SiO}_2/\text{Fe}_3\text{O}_4$  and  $\text{TiO}_2/\text{SiO}_2/\text{Fe}_3\text{O}_4$ . This result confirms that  $\text{SiO}_2$  was successfully coated on  $\text{Fe}_3\text{O}_4$ . Figures 3(a) and 3(b) showed the SEM micrographs of the  $\text{Fe}_2\text{O}_3/\text{SiO}_2$  and  $\text{Fe}_2\text{O}_3/\text{SiO}_2/\text{TiO}_2$ . SEM micrographs indicate that the particles on the coatings aggregated without significant difference.

The magnetic properties of the  $\text{SiO}_2/\text{Fe}_3\text{O}_4$  and  $\text{Fe}_3\text{O}_4$  cores were measured with a vibrating sample magnetometer

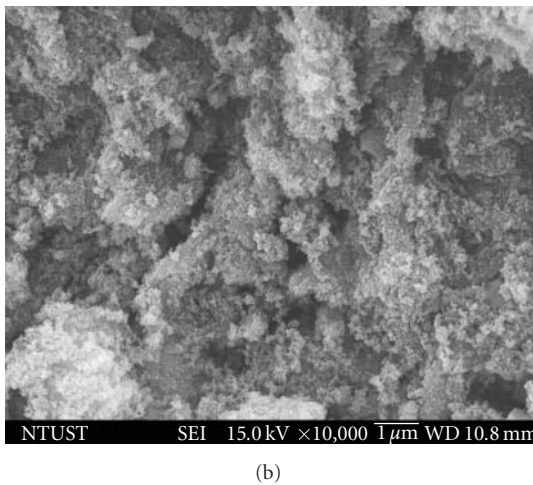
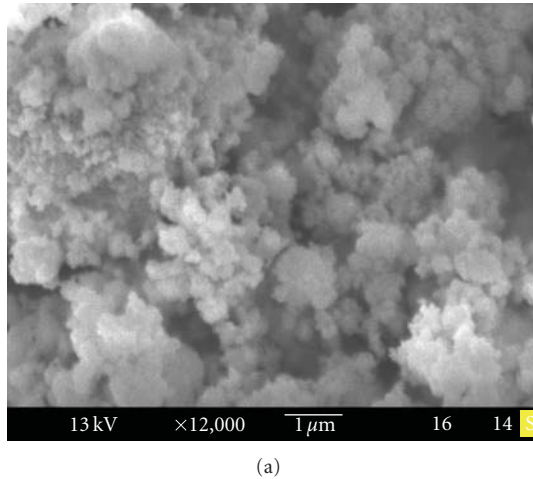


FIGURE 3: SEM images of (a)  $\text{Fe}_2\text{O}_3/\text{SiO}_2$  and (b)  $\text{Fe}_2\text{O}_3/\text{SiO}_2/\text{TiO}_2$ .

(VSM), as shown in Figure 4. The M-H plots showed the change in  $M_s$  of the particles after the incorporation of  $\text{SiO}_2$  and  $\text{TiO}_2$  shell. A decrease in  $M_s$  from 61.8 to 28.0  $\text{emu g}^{-1}$  was observed in  $\text{SiO}_2/\text{Fe}_3\text{O}_4$ . The decreased mass saturation magnetization was ascribed to the contribution of the nonmagnetic  $\text{SiO}_2$  and  $\text{TiO}_2$  shell to the total mass of particles. This observation is similar to those in reports where the attached gold shell was found to lower the saturation magnetization of magnetite particles [25]. The results indicated that the prepared samples exhibited paramagnetic behaviors at room temperature [11]. The paramagnetic behaviors of the prepared  $\text{TiO}_2/\text{SiO}_2/\text{Fe}_3\text{O}_4$  gave rise to the magnetic photocatalyst  $\text{TiO}_2/\text{SiO}_2/\text{Fe}_3\text{O}_4$ , which could be separated more easily through the application of a magnetic field.

According to the database of the Joint Committee on Powder Diffraction Standards (JCPDS), the XRD pattern of a standard  $\text{Fe}_3\text{O}_4$  crystal with a spinel structure has six characteristic peaks at  $2\theta = 30.1^\circ, 35.5^\circ, 43.1^\circ, 53.4^\circ, 57.0^\circ,$  and  $62.6^\circ$ , which are attributed to the (2 2 0), (3 1 1), (4 0 0), (4 2 2), (5 1 1), and (4 4 0) phases of  $\text{Fe}_3\text{O}_4$ , respectively, as shown in Figure 5. Based on the XRD spectra, the crystalline phases could be categorized into two primary components,

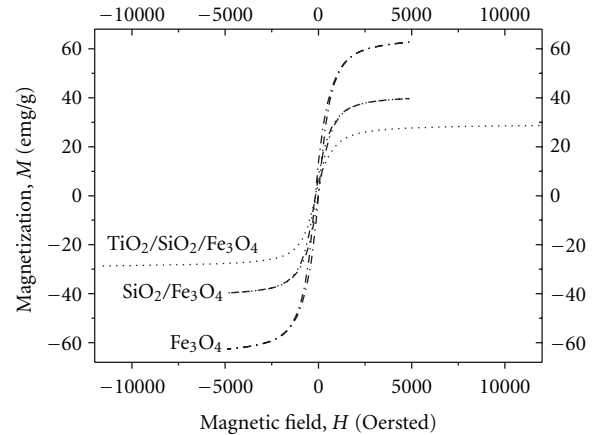


FIGURE 4: Magnetization versus applied magnetic field.

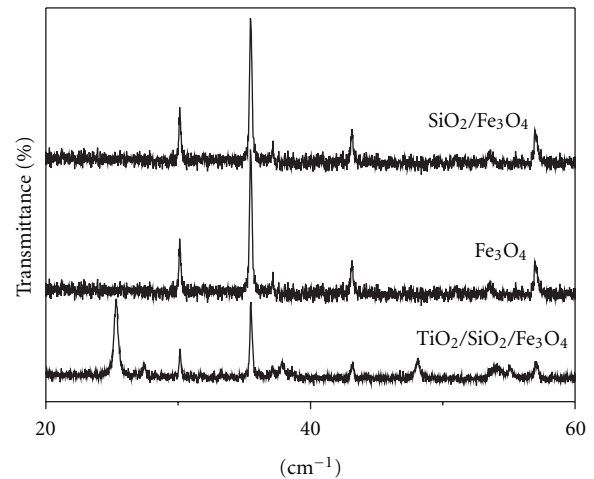


FIGURE 5: XRD spectra of the photocatalyst coatings.

an anatase (A) and a rutile (R) phase, and represented the intensity of the strongest anatase reflection of (101) plane at  $2\theta = 25.3^\circ \pm 0.1^\circ$ , anatase reflection of (200) plane at  $2\theta = 48.0^\circ \pm 0.1^\circ$ , and the intensity of the strongest rutile reflection of (110) plane at  $2\theta = 27.4^\circ \pm 0.1^\circ$ . Additionally, the anatase phase of  $\text{TiO}_2$  crystal is a tetragonal system in lattice geometry. The analysis results of the starting material  $\text{Fe}_3\text{O}_4$ , and  $\text{TiO}_2/\text{SiO}_2/\text{Fe}_3\text{O}_4$  fitted the pattern exhibited by standard magnetite. Therefore, it can be concluded that the magnetite, modified with  $\text{SiO}_2$ , also has a spinel structure, and that the modification does not cause a phase change in  $\text{Fe}_3\text{O}_4$ .

**3.2. Photocatalytic Decomposition of Benzoic Acid.** The photoactivity of  $\text{TiO}_2/\text{SiO}_2/\text{Fe}_3\text{O}_4$  was sensitively influenced by the temperatures of calcination, as shown in Table 1. The reaction rate constant of benzoic acid under UV light irradiation was decreased with the increased calcination temperature. The reasons described that the surface area of  $\text{SiO}_2/\text{TiO}_2/\text{Fe}_3\text{O}_4$  decreased as the calcinations temperature

TABLE 1: Effect of calcinations temperature on reaction rate constant and surface area.

Temperature (°C)	$k$ (min <sup>-1</sup> )	Surface area (m <sup>2</sup> g <sup>-1</sup> )	Recovery (%)
350	0.0059	32.75	93.7
550	0.0034	21.35	94.6
750	0.0005	9.29	96.4

raised from 350 to 750°C, in particular, the sample calcined at 750°C were almost completely inactive.

When the calcination temperature is over 700°C, the photocatalytic activity of thin films decreases, which is due to the formation of rutile and the sintering and growth of TiO<sub>2</sub> crystallites resulting in the decrease of surface area [26]. Furthermore, the paramagnetic behaviors of the magnetic photocatalyst TiO<sub>2</sub>/SiO<sub>2</sub>/Fe<sub>3</sub>O<sub>4</sub>, could be separated more easily by the application of a magnetic field. More than 90% of the magnetic photocatalyst with various temperatures of calcination was recovered and easily redispersed in aqueous solution for reuse.

The pH of the aqueous solution is one of the important environmental parameters significantly influencing the physicochemical properties of semiconductors, including the charge on the TiO<sub>2</sub> particle, the aggregation numbers of particles, and the positions of the conduction and valence bands [23]. The degradation of benzoic acid increased as pH value increased from 3 to 10. No adsorption was recorded at pH >6 as both catalyst and the substrate are negatively charged, since benzoic acid adsorption onto catalyst is not favored at neutral or alkaline conditions [27]. From experimental results [28], 0.1 mM of *o*-methylbenzoic acid could be completely decomposed in 2 h. The reaction was faster with lowering pH and was found to be apparent first-order following Langmuir-Hinshelwood model. Chen et al. [29] also obtained similar results, the reaction rate increased from acidic to a weak alkaline solution with TiO<sub>2</sub> photocatalyst. The surface of TiO<sub>2</sub> is negatively charged in solutions with pH greater than 6, because the point of zero charge of TiO<sub>2</sub> was determined to be about 6.0. The disassociated benzoic acid species also presented negative charge in solutions with pH greater than 4.2. Therefore, there is repulsion between a TiO<sub>2</sub> surface and benzoic acid.

**3.3. Taguchi Experimental Plan.** Before experiments were conducted, control factors and their levels must be first decided. Therefore, pH, weight ratio of TiO<sub>2</sub>/SiO<sub>2</sub>(Fe<sub>3</sub>O<sub>4</sub>), and calcined temperatures of TiO<sub>2</sub>/SiO<sub>2</sub>/Fe<sub>3</sub>O<sub>4</sub> were selected as control factors, and removal rate was chosen as the quality characteristic. Control factors and their levels are as shown in Table 2, in which the levels of the pH are set to a sliding level to reduce interactions; which are shown in Table 3. Because a higher removal rate is better, SN ratio was selected, as shown in (1).

According to Table 2, the selected control factors and their levels were applied in the L9 orthogonal array. Nine groups of experiments were conducted according to the L9 orthogonal array. Each group of experiments was repeated

TABLE 2: Factors and their levels for the experiments.

Factor	Level 1	Level 2	Level 3
A: pH <sup>a</sup>	A1	A2	A3
B: weight ratio of TiO <sub>2</sub> /SiO <sub>2</sub> (Fe <sub>3</sub> O <sub>4</sub> )	1	3	5
C: calcined temperatures of TiO <sub>2</sub> /SiO <sub>2</sub> /Fe <sub>3</sub> O <sub>4</sub>	350°C	550°C	750°C

<sup>a</sup>The numbers are explained in Table 2.

TABLE 3: pH levels.

Number <sup>a</sup>	Level 1	Level 2	Level 3
A1	3	5	7
A2	5	7	9
A3	7	9	10

three times, and the removal rate of each group was recorded, with twenty-seven data collected. These data were calculated according to (1) to yield SN ratios. The results are shown, as in Table 4. Next, SN ratios were computed according to (2) to yield the main effect of each control factor. A response table was drawn out, as indicated by Table 5. The optimal conditions determined were A1, B1, and C1; namely, pH is 3, weight ratio of TiO<sub>2</sub>/SiO<sub>2</sub>(Fe<sub>3</sub>O<sub>4</sub>) is 1, and calcined temperature of TiO<sub>2</sub>/SiO<sub>2</sub>/Fe<sub>3</sub>O<sub>4</sub> is 350°C. In addition, the effect of each parameter on the removal rate under different levels was therefore known. Factor C, calcined temperatures of TiO<sub>2</sub>/SiO<sub>2</sub>/Fe<sub>3</sub>O<sub>4</sub>, gave the greatest effect, and A, pH, provided the second greatest effect.

The surface area-decreased effect was similar to the conclusion of photocatalytic mineralization of phenol on TiO<sub>2</sub> P25, as reported by [30]. They suggested that the amount of the surface-adsorbed water and hydroxyl groups, which was oxidized to a hydroxyl radical (OH<sup>•</sup>), was decreased via thermal treatment. Due to the charge on the TiO<sub>2</sub> particle, the aggregation numbers of particles and disassociated species of contamination, and the optimal pH value of the aqueous solution were determined during the photocatalytic oxidation of contamination [29].

To further understand the effect of each factor on the removal rates of photocatalysts, the removal rates were analyzed by analysis of variance (ANOVA) [31], which was designed to determine the error of the variance in order to know what extent the effect of each factor has on photocatalysts. The result obtained would be useful in the evaluation of experimental errors, as shown in Table 5.

A larger F-ratio indicates that there is a larger factor effect. F-ratio is often larger than 2, indicating that there is a not small factor effect. An F-ratio larger than 4 indicates that there is a very large factor effect. From Table 6, the result shown in the analysis of variance indicates that removal rate is less affected by factor B. On the contrary, the F-ratios of factors C and A are larger than 4; therefore, they are significant factors.

The SN ratio of the optimal experimental parameters are calculated from removal rates, 55.3% (−5.15 dB) obtained from (3), (4), and (5), was confirmed by three experiments.

TABLE 4: The L9 experimental layout and experimental results.

Trial no.	Factor assignment			Average (%)	SN ratio (dB)
	A	B	C		
1	3	1	350°C	50.0	-6.02
2	5	3	550°C	33.0	-9.63
3	7	5	750°C	3.8	-28.40
4	5	1	550°C	24.2	-12.32
5	7	3	750°C	7.7	-22.27
6	9	5	350°C	23.8	-12.47
7	7	1	750°C	4.9	-26.20
8	9	3	350°C	10.8	-19.33
9	10	5	550°C	5.0	-26.02

TABLE 5: Average effect response for SN ratios.

	A	B	C
Level 1	-14.68	-14.85	-12.61
Level 2	-15.69	-17.08	-15.99
Level 3	-23.85	-22.30	-25.62
Effect	9.16	7.45	13.02
Rank	2	3	1

All SN ratios of removal rates fall in the 95% confidence interval,  $-24.0248 \leq \mu \leq 13.0008$  dB, which indicates that the experiment is reproducible and reliable.

Benzoic acid, present in an aqueous solution at pH 3, could be decomposed higher than 50% within approximately 120 min of the reaction time, as shown in Figure 6. The decomposition of benzoic acid by the UV/TiO<sub>2</sub>/SiO<sub>2</sub>/Fe<sub>3</sub>O<sub>4</sub> process was higher than that of the UV/TiO<sub>2</sub> (P25) process in this study. This could be explained by the addition of SiO<sub>2</sub> into photocatalysts retarding the crystallization of anatase phase. The addition of a second metal oxide, such as SiO<sub>2</sub>, ZrO<sub>2</sub>, and Al<sub>2</sub>O<sub>3</sub>, was also found to be an effective route to improve the thermal stability and UV photocatalytic activity of TiO<sub>2</sub> [32, 33]. Among them, SiO<sub>2</sub>-TiO<sub>2</sub> materials were most widely investigated in the photocatalysis field, as they exhibited higher photocatalytic activity than pure TiO<sub>2</sub>. Moreover, this SiO<sub>2</sub> layer inhibits the iron oxide core becoming a recombination center of electrons and holes. The transfer of photogenerated electrons and holes from TiO<sub>2</sub> to Fe<sub>3</sub>O<sub>4</sub> can be completely inhibited by introducing a wide bandgap SiO<sub>2</sub> layer as an electronic barrier [15, 16]. Furthermore, silica is also a good adsorbent towards organic molecules. The enhanced adsorption for RhB on silica adsorbent layer significantly increases the local concentration of RhB near the porous titania photoactive layer relative to the bulk solution [34].

#### 4. Conclusions

The optimal experimental parameters of TiO<sub>2</sub> preparation for the removal rate of photocatalysts were concluded as pH is 3, weight ratio of TiO<sub>2</sub>/SiO<sub>2</sub>(Fe<sub>3</sub>O<sub>4</sub>) is 1, and calcined temperatures of TiO<sub>2</sub>/SiO<sub>2</sub>/Fe<sub>3</sub>O<sub>4</sub> are 350°C. The SN ratios

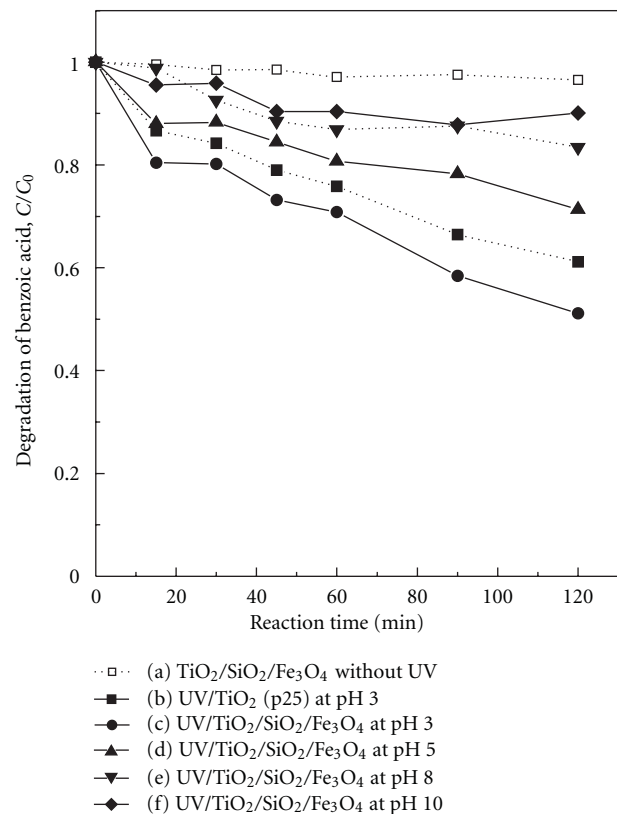


FIGURE 6: Degradation of benzoic acid by UV/magnetic photocatalyst process at solution temperature = 20°C, the initial concentration of benzoic acid = 10 mg L<sup>-1</sup>, TiO<sub>2</sub>/SiO<sub>2</sub>/Fe<sub>3</sub>O<sub>4</sub> = 0.5 g L<sup>-1</sup>.

in a confidence interval of 95%, as provided in the confirmation experiments, indicate the selected significant factor are reasonable, the results are reproducible, and in particular, the experiments are reliable. In addition, the result of analysis of variance indicates calcined temperature of TiO<sub>2</sub>/SiO<sub>2</sub>/Fe<sub>3</sub>O<sub>4</sub> is the most significant factor. The deviation contributed by Table 6 to error is less than 50%, which indicates that there were important factors in the experiments, rendering the results precise. This research provides a method suitable for optimizing other experimental parameters to promote experimental efficiency. Furthermore, the paramagnetic behaviors

TABLE 6: ANOVA of SN ratio for the removal rate of photocatalysts.

Source	Degree of freedom	Sum of squares	Variance	F-ratio	Pure sum of squares	Contribution (%)
A	2	151.61	75.81	6.57	128.54	23.98
B	2	87.75	43.87	3.80	64.67	12.06
C	2	273.67	136.83	11.86	250.59	46.74
Error	2	23.07	11.54		46.15	17.22
Total	8	536.10				100

of the magnetic photocatalyst  $\text{TiO}_2/\text{SiO}_2/\text{Fe}_3\text{O}_4$  could be separated more easily by the application of a magnetic field. More than 90% of the magnetic photocatalyst was recovered and easily redispersed in aqueous solution for reuse at various pH levels.

## Acknowledgment

This research was supported by the National Science Council, Taiwan, under Grant no. NSC 99-2622-E-562-002-CC3.

## References

- [1] A. Wibbertmann, J. Kielhorn, G. Koennecker, I. Mangelsdorf, and C. Melber, "Concise international chemical assessment document 26: benzoic acid and sodium benzoate," *Concise International Chemical Assessment Documents*, no. 26, pp. 1–48, 2000.
- [2] F. Chen, J. Zhao, and H. Hidaka, "Highly selective deethylation of Rhodamine B: adsorption and photooxidation pathways of the dye on the  $\text{TiO}_2/\text{SiO}_2$  composite photocatalyst," *International Journal of Photoenergy*, vol. 5, no. 4, pp. 209–217, 2003.
- [3] B. Y. Lee, S. W. Kim, S. C. Lee, H. H. Lee, and S. J. Choung, "Photocatalytic decomposition of gaseous formaldehyde using  $\text{TiO}_2$ ,  $\text{SiO}_2$ - $\text{TiO}_2$  and Pt- $\text{TiO}_2$ ," *International Journal of Photoenergy*, vol. 5, no. 1, pp. 21–25, 2003.
- [4] H. W. Chen, C. S. Chiou, and G. B. Hong, "Effect of magnetic catalysts on kinetic behavior of reactive black 5 decomposition by  $\text{O}_3/\text{H}_2\text{O}_2$  process," *Journal of Chemical Technology & Biotechnology*, vol. 86, no. 2, pp. 299–305, 2010.
- [5] J. Gamage and Z. Zhang, "Applications of photocatalytic disinfection," *International Journal of Photoenergy*, vol. 2010, Article ID 764870, 11 pages, 2010.
- [6] M.L. Chen and W. C. Oh, "The improved photocatalytic properties of methylene blue for  $\text{V}_2\text{O}_3/\text{CNT}/\text{TiO}_2$  composite under visible light," *International Journal of Photoenergy*, vol. 2010, Article ID 264831, 5 pages, 2010.
- [7] Q. Xiang, J. Yu, and M. Jaroniec, "Tunable photocatalytic selectivity of  $\text{TiO}_2$  films consisted of flower-like microspheres with exposed {001} facets," *Chemical Communications*, vol. 47, no. 15, pp. 4532–4534, 2011.
- [8] S. Liu, J. Yu, and M. Jaroniec, "Tunable photocatalytic selectivity of hollow  $\text{TiO}_2$  microspheres composed of anatase polyhedra with exposed {001} facets," *Journal of the American Chemical Society*, vol. 132, no. 34, pp. 11914–11916, 2010.
- [9] J. A. Byrne, P. A. Fernandez-Ibañez, P. S.M. Dunlop, D. M.A. Alrousan, and J. W.J. Hamilton, "Photocatalytic enhancement for solar disinfection of water: a review," *International Journal of Photoenergy*, vol. 2011, Article ID 798051, 12 pages, 2011.
- [10] J. Yu, X. Yu, B. Huang, X. Zhang, and Y. Dai, "Hydrothermal synthesis and visible-light photocatalytic activity of novel cage-like ferric oxide hollow spheres," *Crystal Growth and Design*, vol. 9, no. 3, pp. 1474–1480, 2009.
- [11] J. Xu, Y. Ao, D. Fu, and C. Yuan, "Low-temperature preparation of anatase titania-coated magnetite," *Journal of Physics and Chemistry of Solids*, vol. 69, no. 8, pp. 1980–1984, 2008.
- [12] S. Watson, J. Scott, D. Beydoun, and R. Amal, "Studies on the preparation of magnetic photocatalysts," *Journal of Nanoparticle Research*, vol. 7, no. 6, pp. 691–705, 2005.
- [13] H. Yang, X. Mao, Y. Guo et al., "Porous  $\alpha$ - $\text{Fe}_2\text{O}_3$  nanostructures with branched topology: growth, formation mechanism, and properties," *CrystEngComm*, vol. 12, no. 6, pp. 1842–1849, 2010.
- [14] S. Ni, X. Wang, G. Zhou et al., "Size controlled and morphology tuned fabrication of  $\text{Fe}_3\text{O}_4$  nanocrystals and their magnetic properties," *Journal of Alloys and Compounds*, vol. 505, no. 2, pp. 727–732, 2010.
- [15] D. Beydoun, R. Amal, G. K. C. Low, and S. McEvoy, "Novel photocatalyst: titania-coated magnetite. activity and photodissolution," *Journal of Physical Chemistry B*, vol. 104, no. 18, pp. 4387–4396, 2000.
- [16] X. Yu, S. Liu, and J. Yu, "Superparamagnetic  $\gamma$ - $\text{Fe}_2\text{O}_3/\text{SiO}_2/\text{TiO}_2$  composite microspheres with superior photocatalytic properties," *Applied Catalysis B*, vol. 104, no. 1-2, pp. 12–20, 2011.
- [17] G. Taguchi, *Introduction to Quality Engineering*, Asian Production Organization, Tokyo, Japan, 1986.
- [18] G. Taguchi, E. A. Elsayed, and T. C. Hsiang, *Quality Engineering in Production Systems*, McGraw-Hill, New York, NY, USA, 1989.
- [19] J. Zhou, D. Wu, and D. Guo, "Optimization of the production of thiocarbonylhydrazide using the Taguchi method," *Journal of Chemical Technology and Biotechnology*, vol. 85, no. 10, pp. 1402–1406, 2010.
- [20] T. L. Su, H. W. Chen, C. M. Ma, and C. F. Lu, "Improving the combed yarn qualities of OE rotor by using Grey-Taguchi method," *Fibres & Textiles in Eastern Europe*, vol. 85, no. 2, pp. 23–27, 2011.
- [21] S. Mavruz and R. T. Ogulata, "Taguchi approach for the optimisation of the bursting strength of knitted fabrics," *Fibres and Textiles in Eastern Europe*, vol. 79, no. 2, pp. 78–83, 2010.
- [22] A. B. Engin, Ö. Özdemir, M. Turan, and A. Z. Turan, "Color removal from textile dyebath effluents in a zeolite fixed bed reactor: determination of optimum process conditions using Taguchi method," *Journal of Hazardous Materials*, vol. 159, no. 2-3, pp. 348–353, 2008.
- [23] J. G. Yu, H. G. Yu, B. Cheng, X. J. Zhao, J. C. Yu, and W. K. Ho, "The effect of calcination temperature on the surface microstructure and photocatalytic activity of  $\text{TiO}_2$  thin films prepared by liquid phase deposition," *Journal of Physical Chemistry B*, vol. 107, no. 50, pp. 13871–13879, 2003.
- [24] K. Kabra, R. Chaudhary, and R. L. Sawhney, "Treatment of hazardous organic and inorganic compounds through

- aqueous-phase photocatalysis: a review," *Industrial and Engineering Chemistry Research*, vol. 43, no. 24, pp. 7683–7696, 2004.
- [25] N. T. S. Phan and C. W. Jones, "Highly accessible catalytic sites on recyclable organosilane-functionalized magnetic nanoparticles: an alternative to functionalized porous silica catalysts," *Journal of Molecular Catalysis A*, vol. 253, no. 1-2, pp. 123–131, 2006.
- [26] C. R. Vestal and Z. J. Zhang, "Atom transfer radical polymerization synthesis and magnetic characterization of  $\text{MnFe}_2\text{O}_4$ /polystyrene core/shell nanoparticles," *Journal of the American Chemical Society*, vol. 124, no. 48, pp. 14312–14313, 2002.
- [27] T. Velegraki and D. Mantzavinos, "Conversion of benzoic acid during  $\text{TiO}_2$ -mediated photocatalytic degradation in water," *Chemical Engineering Journal*, vol. 140, no. 1–3, pp. 15–21, 2008.
- [28] K. H. Wang, Y. H. Hsieh, C. H. Wu, and C. Y. Chang, "The pH and anion effects on the heterogeneous photocatalytic degradation of o-methylbenzoic acid in  $\text{TiO}_2$  aqueous suspension," *Chemosphere*, vol. 40, no. 4, pp. 389–394, 2000.
- [29] H. W. Chen, Y. Ku, and Y. L. Kuo, "Effect of Pt/ $\text{TiO}_2$  characteristics on temporal behavior of o-cresol decomposition by visible light-induced photocatalysis," *Water Research*, vol. 41, no. 10, pp. 2069–2078, 2007.
- [30] N. R. C. Fernandes MacHado and V. S. Santana, "Influence of thermal treatment on the structure and photocatalytic activity of  $\text{TiO}_2$  P25," *Catalysis Today*, vol. 107-108, pp. 595–601, 2005.
- [31] T. L. Su, H. W. Chen, and C. F. Lu, "Systematic optimization for the evaluation of the microinjection molding parameters of light guide plate with TOPSIS-based taguchi method," *Advances in Polymer Technology*, vol. 29, no. 1, pp. 54–63, 2010.
- [32] X. Z. Fu, L. A. Clark, Q. Yang, and M. A. Anderson, "Enhanced photocatalytic performance of titania-based binary metal oxides:  $\text{TiO}_2/\text{SiO}_2$  and  $\text{TiO}_2/\text{ZrO}_2$ ," *Environmental Science and Technology*, vol. 30, no. 2, pp. 647–653, 1996.
- [33] R. S. Sonawane, S. G. Hegde, and M. K. Dongare, "Preparation of titanium(IV) oxide thin film photocatalyst by sol-gel dip coating," *Materials Chemistry and Physics*, vol. 70, no. 3, pp. 744–750, 2002.
- [34] C. Anderson and A. J. Bard, "An improved photocatalyst of  $\text{TiO}_2/\text{SiO}_2$  prepared by a sol-gel synthesis," *Journal of Physical Chemistry*, vol. 99, no. 24, pp. 9882–9885, 1995.

## Research Article

# The Synthetic Effects of Iron with Sulfur and Fluorine on Photoabsorption and Photocatalytic Performance in Codoped TiO<sub>2</sub>

Xiaohua Li, Jibao Lu, Ying Dai, Meng Guo, and Baibiao Huang

*School of Physics, State Key Laboratory of Crystal Materials, Shandong University, Jinan 250100, China*

Correspondence should be addressed to Ying Dai, daiy60@sdu.edu.cn

Received 10 August 2011; Accepted 8 September 2011

Academic Editor: Jiaguo Yu

Copyright © 2012 Xiaohua Li et al. This is an open access article distributed under the Creative Commons Attribution License, which permits unrestricted use, distribution, and reproduction in any medium, provided the original work is properly cited.

The structural and electronic properties of iron-fluorine (Fe-F) and iron-sulfur (Fe-S) codoped anatase TiO<sub>2</sub> are investigated by first-principles based on density functional theory. Our results show that the formation energy of codoped system is lower than that of single-element doping, which indicates the synergic effect of codoping on the stability of the structure. Codopants introduced impurity gap states resulting in the electron transition energy reduction and thus the visible light absorption observed in the samples. It is concluded that Fe-S should be a better codoping pair because Fe-S codoping introduces extended impurity states resulting in stronger visible light absorption than that of Fe-F codoped compounds. This work gives understanding to the recent experiment and provides the evidence of choosing the more effective co-dopants in TiO<sub>2</sub>.

## 1. Introduction

Titanium dioxide has been extensively studied as a promising photocatalyst due to its cheap, stable, and nontoxic characteristics. However, the use of TiO<sub>2</sub> is limited by its wide band gap (~3.0 eV) which absorbs only ultraviolet light and accounts for just 5% of solar energy. Thus, modification of the electronic structure of TiO<sub>2</sub> to enable the visible light absorption is of great importance [1–3]. An efficient way is doping pure TiO<sub>2</sub> with metal [4–7] or nonmetal elements [8–12]. Metal elements diffused in the titanium lattice greatly enhance the visible light absorption because the impurity states introduced by the dopants lead to the visible light response of TiO<sub>2</sub>. However, localized states appearing in the band gap of the host semiconductor often result in the recombination of photogenerated carriers and consequently result in lower photocatalytic activity. A possible way to improve the photocatalytic performance of doped TiO<sub>2</sub> is to explore the cooperative effect by introducing more than one species of foreign elements to the host [13–16]. Appropriate choice of the codoping pair is the key factor. Recent experiment has reported that iron-sulfur (Fe-S) codoped

TiO<sub>2</sub> exhibits quite high photoactivity under visible light illumination and is stable for long-term applications [17]. It is proposed that the doped Fe<sup>3+</sup> ions can act as electron acceptor and efficiently prevent electron-hole recombination. In addition, Liu et al. [18] found that iron-fluorine (Fe-F) codoped TiO<sub>2</sub> displays excellent photocatalytic activity under visible light irradiation. In the experiment, they speculated that the as-prepared TiO<sub>2</sub> samples match the anatase type, with no trace of rutile or brookite impurity being observed, and they also demonstrated that F could substitute for O and Fe could substitute for Ti in Fe-F codoped anatase TiO<sub>2</sub>. Fluorine atom has one more valence electron than oxygen, and sulfur has the same outer-shell electron as oxygen atom; therefore, it is interesting to explore the origin of the high photocatalytic activity under visible light concerning these two kinds of codoped anatase TiO<sub>2</sub>.

We should have comprehensive knowledge of single-element-doped TiO<sub>2</sub> before exploiting the cooperative effects of the codoped systems. For Fe-doped TiO<sub>2</sub>, a number of studies have been reported experimentally and theoretically. Liu et al. [19] demonstrated that Fe-doped TiO<sub>2</sub> shows visible light responses and diminished recombination rates

of the photoexcited carriers. Fe at the 0.5 at.% level can significantly improve the photoactivity of TiO<sub>2</sub> for both oxidation and reduction reactions [20]. As for the F-doped TiO<sub>2</sub>, recent experimental studies suggested that F-doping neither causes any change in the adsorption edge nor affects the optical absorption of TiO<sub>2</sub> but is beneficial to the crystalline anatase phase [21–27]. Umebayashi et al. [28] suggested that S-doping causes the absorption edge of TiO<sub>2</sub> to be shifted into lower-energy region. The mixing of the S 3*p* states with VB increases the width of the VB itself and results in a decrease in the band gap due to S-doping [29].

In this work, we examine the microscopic electronic structures of Fe-S and Fe-F codoped anatase TiO<sub>2</sub> to explore the synthetic effects of the dopants by means of the first-principles density function theory (DFT) calculations. The defect formation energies are calculated to determine which configuration may be realized more easily in experiment. The codoping synergistic effect is specifically elucidated, and the corresponding related properties of Fe-S and Fe-F are compared to identify a better codoping pair. To obtain detailed insight, Fe, F, and S monodoped anatase TiO<sub>2</sub> structures are also studied systematically. Our theoretical calculations may provide a comprehensive explanation for experimentally observed visible-light photocatalytic activity in the metal and nonmetal codoped TiO<sub>2</sub> and may offer some helpful theoretical information for exploiting new effective photocatalysts.

## 2. Computational Method

We carry out the spin-polarized density functional calculations of Fe-S codoped, Fe-F codoped, and single-element-doped anatase TiO<sub>2</sub> using the Vienna ab initio simulation package (VASP) [30, 31]. The Perdew-Wang 91 of generalized gradient approximation (GGA) is implemented to describe the exchange correlation function. The projector-augmented wave (PAW) potential is used to represent the electron-ion interaction. The crystal lattice parameters are taken from previous calculations ( $a = 3.776$ ,  $c = 9.486$ ), which are in agreement with the experimental values ( $a = 3.785$ ,  $c = 9.514$ ) [32]. We use a  $2 \times 2 \times 1$  supercell containing 32 O atoms and 16 Ti atoms to model the bulk anatase TiO<sub>2</sub>. In the codoped calculation models, one oxygen atom is replaced by a S (or F) atom and titanium atom by iron. In the mono-doped TiO<sub>2</sub>, we have just one O atom substituted by S (or F). The Monkhorst-Pack k-point is set as  $4 \times 4 \times 4$  in the Brillouin zone of the supercell, and we choose the plane-wave cutoff energy of 400 eV. All the atoms are fully optimized until the force on each atom is less than 0.1 meV.

## 3. Results and Discussion

**3.1. Optimized Structure and Stability of Doped TiO<sub>2</sub>.** To investigate the relative stability of Fe-F and Fe-S codoped TiO<sub>2</sub>, we calculate the defect formation energies. For comparison, the energies of F, Fe, and S monodoped TiO<sub>2</sub> are also

studied. The formation energies  $E_f$  are calculated according to the following formulas:

$$\begin{aligned} E_f &= E_{\text{Fe-doped}} - E_{\text{pure}} - \mu_{\text{Fe}} + \mu_{\text{Ti}}, \\ E_f &= E_{\text{F(S)-doped}} - E_{\text{pure}} - \mu_{\text{F(S)}} + \mu_{\text{O}}, \end{aligned} \quad (1)$$

$$E_f = E_{\text{Fe/F(S)-codoped}} - E_{\text{pure}} - \mu_{\text{F(S)}} - \mu_{\text{Fe}} + \mu_{\text{O}} + \mu_{\text{Ti}},$$

in which  $E_{\text{Fe-doped}}$ ,  $E_{\text{F(S)-doped}}$ , and  $E_{\text{Fe/F(S)-codoped}}$  are total energies of Fe, F(or S) monodoped and Fe-F (or Fe-S) codoped TiO<sub>2</sub>, respectively.  $E_{\text{pure}}$  is the total energy of TiO<sub>2</sub> without dopants.  $\mu_{\text{Fe}}$ ,  $\mu_{\text{Ti}}$ ,  $\mu_{\text{F(S)}}$ , and  $\mu_{\text{O}}$  are the chemical potential of Fe, Ti, F(or S), and O, respectively. It is commonly known that if the doped systems have smaller formation energies, it means that they are in a relatively stable phase. It should be also mentioned that formation energy is in connection with crystal growth circumstance. We simulate the corresponding Ti-rich and O-rich conditions in our theoretical calculations. Under Ti-rich condition,  $\mu_{\text{Ti}}$  is gotten from bulk Ti and  $\mu_{\text{O}}$  is calculated according to the following formula:

$$2\mu_{\text{O}} + \mu_{\text{Ti}} = \mu_{\text{TiO}_2}. \quad (2)$$

Here  $\mu_{\text{TiO}_2}$  is energy of one formula unit of TiO<sub>2</sub>. Under O-rich,  $\mu_{\text{O}}$  can be obtained from the ground-state energy of the O<sub>2</sub> molecule ( $\mu_{\text{O}} = 1/2 \mu(\text{O}_2)$ ), while  $\mu_{\text{Ti}}$  is fixed by condition (2).

In codoped TiO<sub>2</sub> crystal lattice, dopants may substitute any host atoms however, not all of the configurations are stable. With the aim to find out the most stable configuration, different substitution sites according to the different distances between the two dopants are tested. Formation energy calculations imply that the structure with one Fe substituting for a Ti atom and simultaneously with one F (or S) at the first nearest neighboring (denoted as 1NN) O atom site is the most energetically favorable. We find that, in general, when the distances between the two dopants increase, the formation energies increase. This is probably because that the attraction forces between the anion and cation ions decrease when the two elements locate far from each other. Thus, it can be concluded that 1NN substitution is the most viable configuration in experimental process and then is chosen as our computational model hereafter (Figure 1).

The calculated formation energies of different-element-doped TiO<sub>2</sub> are summarized in Table 1, which suggests that (1) Fe mono-doped, Fe-F and Fe-S codoped TiO<sub>2</sub> are both energetically favorable under O-rich condition, but unfavorable under Ti-rich condition, (2) the formation of F mono-doped TiO<sub>2</sub> is thermodynamically favorable under both Ti-rich and O-rich conditions, but S monodoped TiO<sub>2</sub> is more stable under Ti-rich condition, which agrees with the former calculations [11], (3) the formation energy of Fe-F codoped TiO<sub>2</sub> is much lower than both Fe and F mono-doped TiO<sub>2</sub>. For Fe-S codoping under O-rich condition, the formation energy is smaller than S mono-doped but larger than Fe mono-doped TiO<sub>2</sub>. The lower formation energies of codoping systems indicate cooperative effects

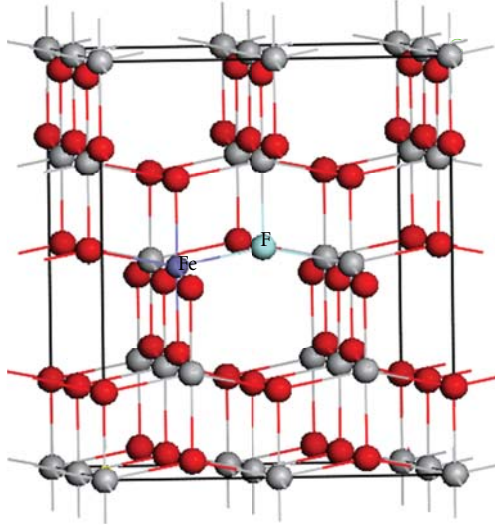


FIGURE 1: Structure of 48-atom anatase  $\text{TiO}_2$  codoped with F and Fe. The gray and red spheres represent Ti and O atoms, respectively.

TABLE 1: Formation energies  $E_f$  (eV) of single-element-doped and codoped  $\text{TiO}_2$  in different conditions.

	$E_f$ (eV)	
	Ti-rich	O-rich
Fe- $\text{TiO}_2$	5.51	-4.80
F- $\text{TiO}_2$	-4.97	0.18
S- $\text{TiO}_2$	-2.31	2.85
F-Fe- $\text{TiO}_2$	-0.19	-5.35
Fe-S- $\text{TiO}_2$	4.35	-0.80

of the different dopants and make the high photocatalytic semiconductor with higher dopants concentration more viable in experiment. Thus, we can conclude that codoped  $\text{TiO}_2$  samples have lower formation energies than mono-element-doped systems, which is due to the charge balance by incorporating both anion and cation ions. This effect is more obvious in Fe-F codoped  $\text{TiO}_2$  since the charge neutrality is well maintained relative to the undoped system, while the charge neutrality is not maintained so well for the Fe-S codoped  $\text{TiO}_2$ .

We further investigate the optimized structures of different-element-doped  $\text{TiO}_2$ . For Fe mono-doped  $\text{TiO}_2$ , the optimized O-Fe bond lengths (1.873 Å and 1.891 Å) are shorter than O-Ti bond lengths in pure  $\text{TiO}_2$  (1.930 Å and 1.973 Å). This is because that bond length is determined mainly by radius and electronegativity of bonded atoms. The electronegativity of iron (1.83) is stronger than that of titanium (1.54), and the ionic radius of iron (0.64 Å) is smaller than that of titanium (0.68 Å). In F mono-doped  $\text{TiO}_2$ , the distance between F and Ti (2.000 Å) is longer than O-Ti bond length (1.930 Å). This can be ascribed to the fact that electronegativity of F (3.98) is stronger than that of O (3.44) while the radius of  $\text{F}^-$  is a little bigger than that of  $\text{O}^{2-}$  (1.32). In S-doped  $\text{TiO}_2$ , the S-Ti bond lengths are 2.147 and 2.354 Å, which are much longer than the O-Ti

bond lengths in pure  $\text{TiO}_2$  due to the bigger atom radius of S. As for F-Fe codoped  $\text{TiO}_2$ , the optimized F-Fe bond length is 1.966 Å, 1.9% of distortion compared with that of the pure  $\text{TiO}_2$ , which is smaller than the distortions of both F-Ti and Fe-O bond length (3.6% and 2.8%, resp.). S-Fe bond length (1.979 Å) in Fe-S codoped  $\text{TiO}_2$  is longer than that of F-Fe (1.966 Å), which is due to the bigger atom radius of S than that of F. The distortion of optimized S-Fe bond length (2.5%) is smaller than that of both S-Ti and Fe-O bond length (11.2% and 2.8%, resp.) in S and Fe mono-doped  $\text{TiO}_2$ . The smaller distortion of codoped  $\text{TiO}_2$  is in connection with the smaller formation energy, and this should be ascribed to the synergetic effect of codoping.

**3.2. Electronic Structures.** To clarify how the dopants modify the electronic structure of  $\text{TiO}_2$ , we calculate the total density of states (DOS) and partial density of states (PDOS) of bulk  $\text{TiO}_2$  and doped  $\text{TiO}_2$  shown in Figure 2. For pure  $\text{TiO}_2$  (Figure 2(a)), the calculated band gap is 1.90 eV, which is consistent with the previous theoretical studies [33]. Although the theoretical band gap is smaller than the experimental value (3.2 eV) due to the well-known shortcoming of GGA, it is reasonable to analyze the relative variations of the electronic structure without considering the exact band gap value. We can see from Figure 2(a') that the top of the valence band (VBM) of pure  $\text{TiO}_2$  consists mainly of O 2p states, while the bottom of the conduction band (CBM) is dominated by Ti 3d states.

After substitution of fluorine for oxygen atom (Figure 2(b)), the Fermi level is pinned at the bottom of the conduction band which shows a donor character because of one more electron of F than that of host O. The PDOS (Figure 2(b')) shows that most of F 2p states are delocalized in the lower-energy range of VB and do not contribute to the band edge and may not lead to the absorption of visible light. Figure 2(c) shows that incorporation of iron into the lattice results in localized gap states. The Fermi level is pinned at the down-spin orbit of the gap states, which shows half-metallic character. Further projected density of states (PDOS) as shown in Figure 2(c') predicates that the minority- and majority-spin states within the gap are mainly attributed to Fe 3d. The impurity states induced above the VBM, below the CBM, and in the forbidden gap are beneficial to the visible light absorption. Figure 2(d) is the DOS of S-doped  $\text{TiO}_2$ , and the VBM has a little shift. From the calculated PDOS of Figure 2(d'), the valence band is composed mainly of O 2p, and the conduction band is mainly Ti 3d. The localized states are generated by S 3p about 0.7 eV above the VBM relative to the undoped one. The excitation from these occupied S 3p states to conduction band might lead to a decrease of the photon excitation energy and induce more significant red shift of absorption, which is consistent with experimental absorption spectra measurements. However, the localized gap states in the middle of the forbidden band in Fe-doped  $\text{TiO}_2$  provide recombination center of photogenerated electron-hole pair, which is detrimental to the photocatalytic activity. The improvement of photocatalytic activity originating from visible light absorption is weakened by the increase of

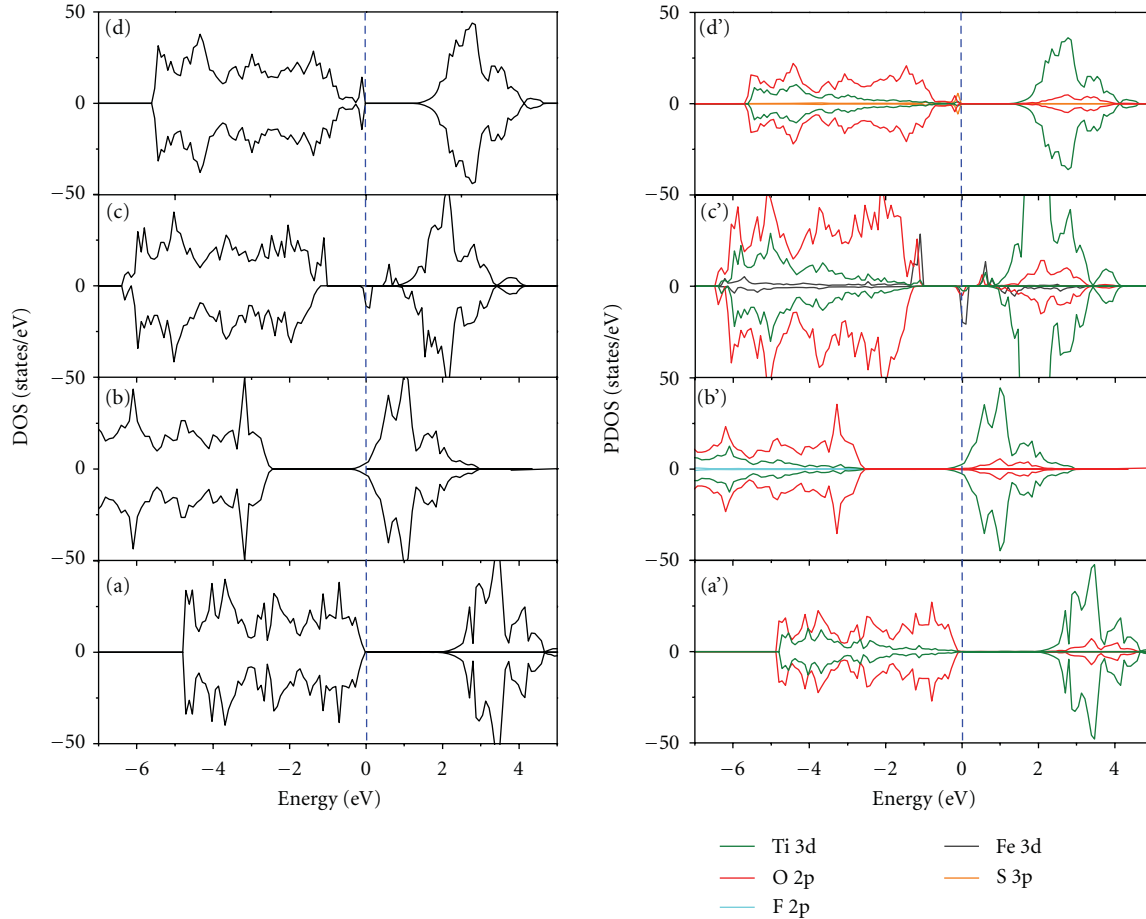


FIGURE 2: Total density of states (DOS) of (a) undoped anatase  $\text{TiO}_2$ , (b) F-doped  $\text{TiO}_2$ , (c) Fe-doped  $\text{TiO}_2$ , and (d) S-doped  $\text{TiO}_2$  and projected density of states (PDOS) of (a') pure  $\text{TiO}_2$ , (b') F-doped  $\text{TiO}_2$ , (c') Fe-doped  $\text{TiO}_2$ , and (d') S doped  $\text{TiO}_2$ . The dashed line represents the Fermi energy level.

recombination of the carriers and eventually limits the great enhancement of photocatalytic activity.

For Fe-F codoped  $\text{TiO}_2$  (Figure 3(a)), localized impurity states are introduced between VBM and CBM. The PDOS in Figure 3(a') demonstrates that three gap states mainly stem from Fe  $3d$  orbital. The energies needed for electrons excitation from two occupied up-spin states to the CBM are 1.6 and 0.9 eV, respectively, while the energy from down-spin state to CBM is 0.5 eV. Hence, the electron transition from these impurity energy levels to the conduction band would lead to an obvious reduction of absorption energy. Our results give a good explanation for the experimentally observed red shift of absorption edge of the Fe-F codoped anatase  $\text{TiO}_2$  [18]. However, as the Fe mono-doped structure, localized states introduced in the middle of the forbidden band can lead to the recombination of electro-hole pair and thus do harm to the photocatalytic activity. Therefore, even though codoping with Fe and F may promote the incorporation of dopants into the  $\text{TiO}_2$  host lattice, it will not have pronounced enhancement in the photocatalytic activity compared with Fe-doped  $\text{TiO}_2$ .

When Fe and S are introduced into  $\text{TiO}_2$  simultaneously, more obvious spin polarization can be observed in the band

edge compared with mono-doped  $\text{TiO}_2$  and localized gap states appear about 0.2 eV above the valence band with width of 0.4 eV and 0.2 eV below the conduction band with width of 0.6 eV (Figure 3(b)). The bandwidth decreases to 1.7 eV, 0.2 eV smaller than that of pure  $\text{TiO}_2$ , and the Fermi level is pinned in the gap states located below the conduction band due to the slight break of the charge neutrality by Fe-S codoping. Electron excitation from VBM to the gap states and CBM could lead to the visible light absorption as observed in experiment [17]. The PDOS shown in Figure 3(b') indicates that the gap states above the valence band are the mixing of Fe  $3d$ , O  $2p$ , and S  $3p$  orbitals while the states below the CBM are mainly hybridization of Fe  $3d$  and O  $2p$ . The formation energy reduction is found in both Fe-F and Fe-S codoped  $\text{TiO}_2$  which could enhance the solubility of dopants in the host lattice. Furthermore, the codoping of Fe and S produces extended states near the band edge and does not induce localized states in the center of the gap that often act as recombination centers. This electronic structure could enhance the visible light absorption and reduce the recombination of photogenerated electron-hole pairs. Moreover, the impurity states near the band edge are more extended than those of mono-doped and Fe-F-doped structures, which

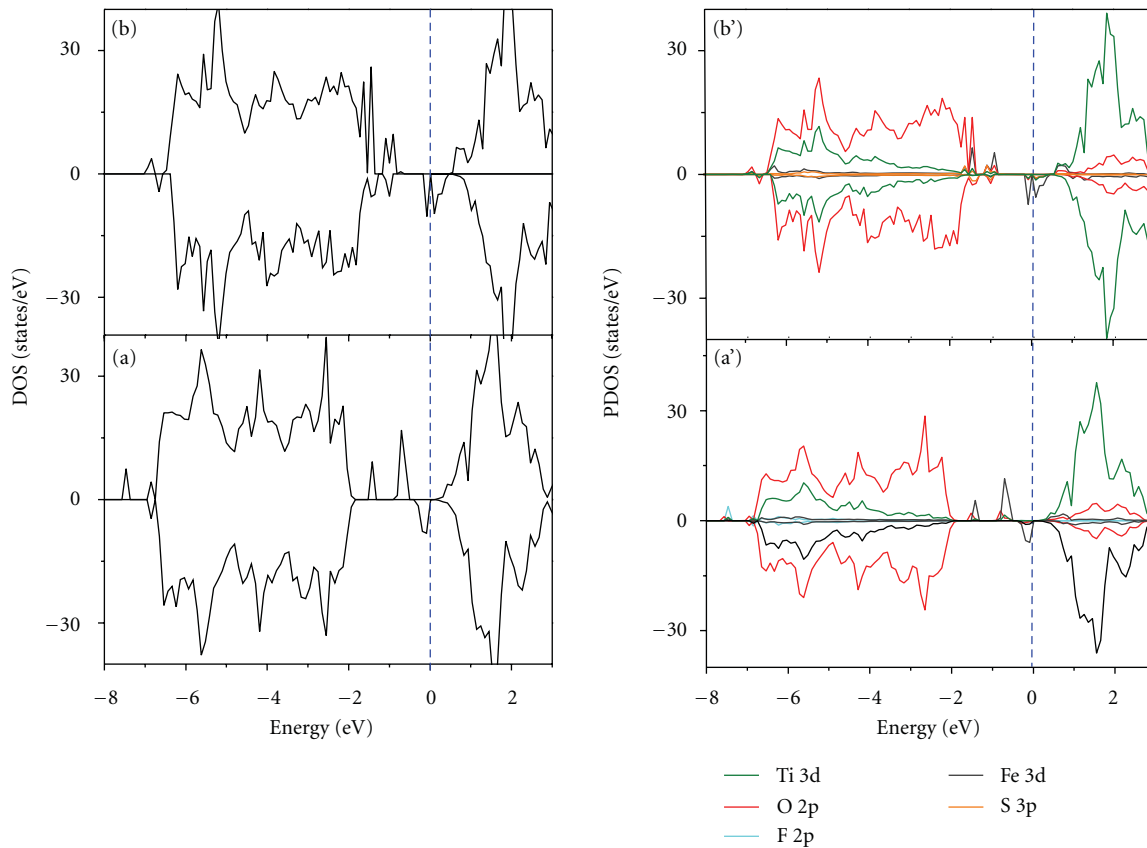


FIGURE 3: Total density of states (DOS) of (a) Fe-F codoped  $\text{TiO}_2$  and (b) Fe-S codoped  $\text{TiO}_2$  and projected density of states (PDOS) of (a') Fe-F codoped  $\text{TiO}_2$  and (b') Fe-S codoped  $\text{TiO}_2$ . The dashed line represents the Fermi energy level.

means that electron excitation between the valence band (conduction band) and impurity states can be more intense, and consequently the intensity of visible light absorption can be stronger. It should be mentioned that the mobility of the photo-carriers in the impurity states is lower than that in the valence band of pure  $\text{TiO}_2$ ; however, the impurity states near the band edge can also act as electron/hole traps, which reduces the recombination of photocarriers. Additionally, since the oxidation (reduction) power of photogenerated holes (electrons) in the gap states is reduced relative to that in the VB (CB) of pure  $\text{TiO}_2$ , one should accommodate a balance between the oxidation (reduction) power and visible light absorption of the photocatalysts.

Based on these analyses, we conclude that the Fe-S codoped  $\text{TiO}_2$  could possess the best photocatalytic activity under visible light irradiation among the Fe mono-doped and Fe-F, Fe-S codoped structures.

#### 4. Conclusions

We have examined the crystal structures and electronic and optical properties of Fe-F and Fe-S codoped anatase  $\text{TiO}_2$  based on DFT calculations. For comparison, Fe, S, and F single -doped  $\text{TiO}_2$  are also studied. Formation energy of the codoped system is much lower than that of the mono-element doping indicating the synergic effects of codopants

on the stability of the doped structure. The calculated results indicate that the codoped atoms introduce impurity energy levels in the band gap mainly composed of Fe  $3d$  states. Due to the less energy needed for an electron transition from the impurity energy levels to the conduction band bottom, codoped anatase  $\text{TiO}_2$  may show higher photocatalytic activity than the mono-doped one under visible light, which may account for the experimentally observed phenomenon. However, Fe-F codoping introduced localized gap states which may result in visible light absorption but decline the photocatalytic activity. Compared with Fe-F codoping, Fe-S codoped  $\text{TiO}_2$  produces gap states near the band edge that are extended and may greatly enhance the visible light absorption and reduce the carrier recombination. Consequently, the photocatalytic performance under visible light of Fe-S codoped  $\text{TiO}_2$  is better than that of Fe-F codoped one, and Fe-S should be a better codoping pair.

#### Acknowledgments

This work is supported by the National Basic Research Program of China (973 program, 2007CB613302), the National Science Foundation of China under Grant nos. 11174180 and 20973102, and the Natural Science Foundation of Shandong Province under Grant no. ZR2011AM009.

## References

- [1] J. Lu, Y. Dai, H. Jin, and B. Huang, "Effective increasing of optical absorption and energy conversion efficiency of anatase TiO<sub>2</sub> nanocrystals by hydrogenation," *Physical Chemistry Chemical Physics*, vol. 13, no. 40, pp. 18063–18068, 2011.
- [2] G. Shang, H. Fu, S. Yang, and T. Xu, "Mechanistic study of visible-light-induced photodegradation of 4-chlorophenol by TiO<sub>2</sub>-xNx (0.021 < x < 0.049) with low nitrogen concentration," *International Journal of Photoenergy*, vol. 2012, Article ID 759306, 9 pages, 2012.
- [3] J. A. Byrne, P. A. Fernandez-Ibañez, P. S. M. Dunlop, D. M. A. Alrousan, and J. W. J. Hamilton, "Photocatalytic enhancement for solar disinfection of water: a review," *International Journal of Photoenergy*, vol. 2011, Article ID 798051, 12 pages, 2011.
- [4] L. Jing, B. Xin, F. Yuan, L. Xue, B. Wang, and H. Fu, "Effects of surface oxygen vacancies on photophysical and photochemical processes of Zn-doped TiO<sub>2</sub> nanoparticles and their relationships," *Journal of Physical Chemistry B*, vol. 110, no. 36, pp. 17860–17865, 2006.
- [5] S. Zhu, L. M. Wang, X. T. Zu, and X. Xiang, "Optical and magnetic properties of Ni nanoparticles in rutile formed by Ni ion implantation," *Applied Physics Letters*, vol. 88, no. 4, Article ID 043107, pp. 1–3, 2006.
- [6] L. F. Fu, N. D. Browning, S. X. Zhang, S. B. Ogale, D. C. Kundaliya, and T. Venkatesan, "Defects in Co-doped and (Co, Nb)-doped TiO<sub>2</sub> ferromagnetic thin films," *Journal of Applied Physics*, vol. 100, no. 12, Article ID 123910, 2006.
- [7] A. di Paola, S. Ikeda, G. Marci, B. Ohtani, and L. Palmisano, "Transition metal doped TiO<sub>2</sub>: physical properties and photocatalytic behaviour," *International Journal of Photoenergy*, vol. 3, no. 4, pp. 171–176, 2001.
- [8] R. Asahi, T. Morikawa, T. Ohwaki, K. Aoki, and Y. Taga, "Visible-light photocatalysis in nitrogen-doped titanium oxides," *Science*, vol. 293, no. 5528, pp. 269–271, 2001.
- [9] C. di Valentin, G. Pacchioni, A. Selloni, S. Livraghi, and E. Giamello, "Characterization of paramagnetic species in N-doped TiO<sub>2</sub> powders by EPR spectroscopy and DFT calculations," *Journal of Physical Chemistry B*, vol. 109, no. 23, pp. 11414–11419, 2005.
- [10] T. Umabayashi, T. Yamaki, H. Itoh, and K. Asai, "Band gap narrowing of titanium dioxide by sulfur doping," *Applied Physics Letters*, vol. 81, no. 3, p. 454, 2002.
- [11] K. Yang, Y. Dai, B. Huang, and M. H. Whangbo, "Density functional characterization of the band edges, the band gap states, and the preferred doping sites of halogen-doped TiO<sub>2</sub>," *Chemistry of Materials*, vol. 20, no. 20, pp. 6528–6534, 2008.
- [12] V. K. Sharma, K. Winkelmann, Y. Krasnova, C. Lee, and M. Sohn, "Heterogeneous photocatalytic reduction of ferrate(VI) in UV-irradiated titania suspensions: role in enhancing destruction of nitrogen-containing pollutants," *International Journal of Photoenergy*, vol. 5, no. 3, pp. 183–190, 2003.
- [13] L. Jia, C. Wu, Y. Li et al., "Enhanced visible-light photocatalytic activity of anatase TiO<sub>2</sub> through N and S codoping," *Applied Physics Letters*, vol. 98, no. 21, Article ID 211903, 2011.
- [14] M. Xing, Y. Wu, J. Zhang, and F. Chen, "Effect of synergy on the visible light activity of B, N and Fe co-doped TiO<sub>2</sub> for the degradation of MO," *Nanoscale*, vol. 2, no. 7, pp. 1233–1239, 2010.
- [15] W. Wei, Y. Dai, M. Guo, L. Yu, and B. Huang, "Density functional characterization of the electronic structure and optical properties of N-doped, La-doped, and N/La-codoped SrTiO<sub>3</sub>," *Journal of Physical Chemistry C*, vol. 113, no. 33, pp. 15046–15050, 2009.
- [16] W. Wei, Y. Dai, M. Guo et al., "Codoping synergistic effects in N-doped SrTiO<sub>3</sub> for higher energy conversion efficiency," *Physical Chemistry Chemical Physics*, vol. 12, no. 27, pp. 7612–7619, 2010.
- [17] V. M. Menéndez-Flores, D. W. Bahnemann, and T. Ohno, "Visible light photocatalytic activities of S-doped TiO<sub>2</sub>-Fe<sup>3+</sup> in aqueous and gas phase," *Applied Catalysis B*, vol. 103, no. 1–2, pp. 99–108, 2011.
- [18] S. Liu, X. Sun, J. G. Li et al., "Fluorine- and iron-modified hierarchical anatase microsphere photocatalyst for water cleaning: facile wet chemical synthesis and wavelength-sensitive photocatalytic reactivity," *Langmuir*, vol. 26, no. 6, pp. 4546–4553, 2010.
- [19] Y. Liu, J. H. Wei, R. Xiong, C. X. Pan, and J. Shi, "Enhanced visible light photocatalytic properties of Fe-doped TiO<sub>2</sub> nanorod clusters and monodispersed nanoparticles," *Applied Surface Science*, vol. 257, no. 18, pp. 8121–8126, 2011.
- [20] W. Choi, A. Termin, and M. R. Hoffmann, "The role of metal ion dopants in quantum-sized TiO<sub>2</sub>: correlation between photoreactivity and charge carrier recombination dynamics," *Journal of Physical Chemistry*, vol. 98, no. 51, pp. 13669–13679, 1994.
- [21] D. Li, H. Haneda, S. Hishita, N. Ohashi, and N. K. Labhsetwar, "Fluorine-doped TiO<sub>2</sub> powders prepared by spray pyrolysis and their improved photocatalytic activity for decomposition of gas-phase acetaldehyde," *Journal of Fluorine Chemistry*, vol. 126, no. 1, pp. 69–77, 2005.
- [22] D. Li, H. Haneda, S. Hishita, and N. Ohashi, "Visible-light-driven N-F-codoped TiO<sub>2</sub> photocatalysts. 2. Optical characterization, photocatalysis, and potential application to air purification," *Chemistry of Materials*, vol. 17, no. 10, pp. 2596–2602, 2005.
- [23] A. Olasz, P. Mignon, F. Deproft, T. Veszprémi, and P. Geerlings, "Effect of the  $\pi - \pi$  stacking interaction on the acidity of phenol," *Chemical Physics Letters*, vol. 407, no. 4–6, pp. 504–509, 2005.
- [24] J. K. Zhou, L. Lv, J. Yu et al., "Synthesis of self-organized polycrystalline F-doped TiO<sub>2</sub> hollow microspheres and their photocatalytic activity under visible light," *Journal of Physical Chemistry C*, vol. 112, no. 14, pp. 5316–5321, 2008.
- [25] D. G. Huang, S. J. Liao, J. M. Liu, Z. Dang, and L. Petrik, "Preparation of visible-light responsive N-F-codoped TiO<sub>2</sub> photocatalyst by a sol-gel-solvothermal method," *Journal of Photochemistry and Photobiology A*, vol. 184, no. 3, pp. 282–288, 2006.
- [26] D. Huang, S. Liao, S. Quan et al., "Preparation of anatase F doped TiO<sub>2</sub> sol and its performance for photodegradation of formaldehyde," *Journal of Materials Science*, vol. 42, no. 19, pp. 8193–8202, 2007.
- [27] J. Tang, H. Quan, and J. Ye, "Photocatalytic properties and photoinduced hydrophilicity of surface-fluorinated TiO<sub>2</sub>," *Chemistry of Materials*, vol. 19, no. 1, pp. 116–122, 2007.
- [28] T. Umabayashi, T. Yamaki, H. Itoh, and K. Asai, "Band gap narrowing of titanium dioxide by sulfur doping," *Applied Physics Letters*, vol. 81, no. 3, p. 454, 2002.
- [29] T. Umabayashi, T. Yamaki, S. Yamamoto et al., "Sulfur-doping of rutile-titanium dioxide by ion implantation: photocurrent spectroscopy and first-principles band calculation studies," *Journal of Applied Physics*, vol. 93, no. 9, pp. 5156–5160, 2003.
- [30] G. Kresse and J. Furthmüller, "Efficient iterative schemes for ab initio total-energy calculations using a plane-wave basis set," *Physical Review B*, vol. 54, no. 16, pp. 11169–11186, 1996.
- [31] G. Kresse and J. Furthmüller, "Efficiency of ab-initio total energy calculations for metals and semiconductors using a

- plane-wave basis set,” *Computational Materials Science*, vol. 6, no. 1, pp. 15–50, 1996.
- [32] J. Zhu, Z. Deng, F. Chen et al., “Hydrothermal doping method for preparation of Cr<sup>3+</sup>-TiO<sub>2</sub> photocatalysts with concentration gradient distribution of Cr<sup>3+</sup>,” *Applied Catalysis B*, vol. 62, no. 3-4, pp. 329–335, 2006.
- [33] K. Yang, Y. Dai, and B. Huang, “Understanding photocatalytic activity of S- and P-doped TiO<sub>2</sub> under visible light from first-principles,” *Journal of Physical Chemistry C*, vol. 111, no. 51, pp. 18986–18994, 2007.

## Research Article

# Performance of Ag-TiO<sub>2</sub> Photocatalysts towards the Photocatalytic Disinfection of Water under Interior-Lighting and Solar-Simulated Light Irradiations

Camilo A. Castro, Adriana Jurado, Diana Sissa, and Sonia A. Giraldo

Centro de Investigaciones en Catálisis (CICAT), Universidad Industrial de Santander, Cra. 27 Calle 9, A.A. 678 Bucaramanga, Colombia

Correspondence should be addressed to Sonia A. Giraldo, [sgiraldo@uis.edu.co](mailto:sgiraldo@uis.edu.co)

Received 14 July 2011; Accepted 19 August 2011

Academic Editor: Jiaguo Yu

Copyright © 2012 Camilo A. Castro et al. This is an open access article distributed under the Creative Commons Attribution License, which permits unrestricted use, distribution, and reproduction in any medium, provided the original work is properly cited.

This paper reports the characterization and photoactivity of Ag-TiO<sub>2</sub> materials using different amounts of silver during the hydrothermal synthesis. Photocatalysts were characterized by means of TEM, XPS, XRD, DRS, and N<sub>2</sub> sorption isotherms to determine the textural properties. The photocatalyst's configuration was observed to be as anatase-brookite mixed phase particles with Ag partially oxidized aggregates on the TiO<sub>2</sub> surface, which increased visible light absorption of the material. Moreover, photoproduction of singlet oxygen was followed by EPR analysis under visible light irradiations following the formation of TEMPOL. Such photoproduction was totally decreased by using the singlet oxygen scavenger DABCO. Photocatalysts were tested towards the photocatalytic disinfection of water using a solar light simulator and an interior-light irradiation setup. Results evidenced an increase in the photooxidative effect of TiO<sub>2</sub>, while dark processes evidenced that part of the inactivation process is due to the Ag-TiO<sub>2</sub> surface bactericidal effect and possible lixiviated Ag<sup>+</sup>.

## 1. Introduction

The design of TiO<sub>2</sub>-based photoactive materials has been a major research topic during the last two decades [1–3]. TiO<sub>2</sub>, as a semiconductor, is activated under UV irradiation promoting charges that lead to the formation of reactive oxygen species when they interact with H<sub>2</sub>O and O<sub>2</sub> from the reaction media. Nowadays, recombination of the photogenerated charges [4, 5] and visible (vis) light response [4] are two drawbacks still to surpass in order to achieve efficient photocatalysts to be used under solar light or interior-lighting irradiations.

Water disinfection using TiO<sub>2</sub> had attracted research interest since the oxidative attack of photoproduced ROS may cause total inactivation of bacteria [6, 7] without generating harmful byproducts [8]. In order to increase its photooxidative effect, towards bacteria inactivation, TiO<sub>2</sub> has been modified with Ag, which increases vis light absorption [9–11] and has been proposed to decrease recombination [12], on TiO<sub>2</sub>

thin films [12] and powdered materials [13]. New insights have proposed electronic transitions arising from vis-excited Ag aggregates to the TiO<sub>2</sub> conduction band promoting its photobactericidal effect [14], as it has been observed on plasmonic photocatalysis [10]. Furthermore, Ag-containing antimicrobial devices are designed due to the well-known Ag bacteriostatic activity [15].

Ag-modified TiO<sub>2</sub> photocatalysts have been synthesized using the hydrothermal method since this is a relatively simple route to load TiO<sub>2</sub> nanoparticles with Ag [16, 17], with a wide range of optimum silver content from 0.1 to 6.5% wt correspondent to the major increase in photoactivity [11, 18, 19]. Ag has been proposed to be as aggregates located in crystals borders of TiO<sub>2</sub> particles [20, 21]. Since Ag<sup>+</sup> and Ti<sup>4+</sup> ionic radii are 1.16 [22] and 0.64 Å [23], respectively, it is not expected that Ag may be embedded into the TiO<sub>2</sub> structure.

The aim of this work is to present the performance of Ag-TiO<sub>2</sub> photocatalyst, obtained using the hydrothermal synthesis route, under different light irradiations setups such as

solar-simulated and interior-lighting lamps with different irradiation powers, towards the photocatalytic inactivation of *E. coli* in water. Moreover, materials were characterized using TEM, XPS, DRS, and N<sub>2</sub> adsorption-desorption isotherms in order to elucidate properties affecting the photoactivity. Results show an effective modification of TiO<sub>2</sub> with enhanced visible light absorption capacity as well as photoactivity.

## 2. Experimental

**2.1. Photocatalyst Synthesis.** Photocatalysts were hydrothermal synthesized as follows: 3.8 mL of titanium butoxide (99.9%, Fluka) was added dropwise to 19 mL of isopropanol (Suprasolv. grade reagent, Merck). Then, an adequate amount of AgNO<sub>3</sub> (Extra pure, Merck) was diluted in 2 mL of water (pH = 1.5) adjusted with HNO<sub>3</sub> (65%, Merck). Ag aqueous solution was added dropwise to the isopropoxide-isopropanol solution with an appropriate concentration to obtain Ag nominal weight percentages (% wt), of 0.5, 2, 4, and 8. Formed gel was steam-pressure-treated in autoclave during 3 h at 120°C and ~144 KPa. TiO<sub>2</sub> was obtained as described without addition of AgNO<sub>3</sub>. The obtained wet crystals were grounded in mortar, dried in oven at 60°C for 12 h, and kept in dark to avoid surface oxidation. Samples were labeled as Ag(x)-TiO<sub>2</sub>, x = Ag % wt.

**2.2. Photocatalyst Characterization.** Fresh Ag(x)-TiO<sub>2</sub> and TiO<sub>2</sub> samples were XPS-analyzed. To follow Ag states after a typical photocatalytic test a Ag(2)/TiO<sub>2</sub> suspension, without *E. coli*, was submitted 2 h to solar-simulated light irradiation, filtered and dried in oven at 60°C, and then XPS-analyzed. Analyses were carried out using an AXIS-NOVA photoelectron-spectrometer (Kratos-analytical, Manchester, UK) equipped with a monochromatic AlK $\alpha$  ( $h\nu = 1486.6$  eV) anode. Electrostatic-charge effect was overcompensated by means of the low-energy electron source working in combination with a magnetic immersion lens. C1s line at 284.8 eV was used as calibration reference. Spectra were decomposed using the CasaXPS program (Casa Software Ltd., UK) with a Gaussian/Lorentzian (70/30) product function after subtraction of a Shirley baseline. Assignment of Ag and Ti states was restricted using peak distances of 6 eV and 5.3 eV for Ag [12] and Ti [24], respectively.

X-ray diffraction (XRD) patterns were collected using a DMax-III B Rigaku system operated at room temperature, 40 kV and 80 mA with monochromatic Cu-K $\alpha$  radiation. The average crystallite size ( $d_{\text{XRD}}$ ) was calculated using the Scherrer equation applied to anatase peaks at  $2\theta = 25.2^\circ$  on samples' diffractograms. Al<sub>2</sub>O<sub>3</sub> corundum oxide was used to quantify crystalline phases for bare TiO<sub>2</sub> and the highest Ag loading in order to identify possible changes in phase composition and crystallinity due to Ag loading for modification.

Diffusive reflectance spectroscopy (DRS) was done using a UV-2401PC Shimadzu spectrophotometer with an ISR240A integrating sphere accessory. BaSO<sub>4</sub> was used as reference.

Transmission Electron Microscopy (TEM) analysis were performed in a Phillips HRTEM CM 300 (field emission gun, 120 kV) microscope.

Textural analyses of the photocatalysts were performed through N<sub>2</sub> adsorption-desorption isotherms obtained at 77 K in a Nova1200 equipment of Quantachrome. Before the analysis 0.15–0.2 g samples were degasified during 12 h at 373 K under 10<sup>-5</sup> mmHg vacuum. Specific surface area ( $S_{\text{BET}}$ ) and average pore diameter ( $d_p$ ) were obtained by means of BET and BJH methods, respectively.

Reactive scavenging of ROS by electron paramagnetic resonance spectroscopy (EPR) was done using 2 mL of 0.3 g/L Ag(2)-TiO<sub>2</sub> suspension and  $5 \times 10^{-2}$  mol/L of 2,2,6,6-tetramethyl-4-piperidinol (TMP-OH, 99%, Fluka), with spectral parameters:  $D_H = 1.58$  G,  $a_N = 16.9$  G, and  $g = 2.0066$ , and was prepared in ultrapure H<sub>2</sub>O, as well as, in D<sub>2</sub>O (99.9% atomic purity, Aldrich). 1,4-diazabicyclo [2,2,2] octane (DABCO, 99%, Fluka) was used as a singlet oxygen quencher [25]. Suspensions were kept in test tubes and ultrasound treated in a water bath with a frequency of 40 kHz for 1 min prior to illumination. 1 mL aliquot of the suspension was transferred into a 5 mL Pyrex beaker and exposed to illumination under constant magnetic stirring with a white light halogen spot source of 150 W from OSRAM reference Gx5.3 (93638) emitting vis. ~7  $\mu$ L aliquots of the illuminated suspensions were transferred into glass capillary tubes 0.7 mm ID and 0.87 mm OD, from VitroCom, NJ, USA. Tubes were sealed on both ends with Cha-Seal tube-sealing compound (Medex International, Inc., USA). To maximize sample volume in the active zone of the ESR cavity, assemblies of seven packed capillaries were positioned in a wider quartz capillary (standard ESR tube, 2.9 mm ID and 4 mm OD, Wilmad-LabGlass, Vineland, NJ, USA). Such setup resulted in ~65  $\mu$ L sample volume in the active zone of the ESR cavity, thus markedly improving sensitivity of measurements [26].

Experiments were performed using an ESR300 spectrometer (Bruker-BioSpin-GmbH) at room temperature, equipped with standard-rectangular mode TE<sub>102</sub> cavity. Routinely, for each experimental point five scan field-swept spectra were recorded with instrumental parameters: microwave frequency: 9.38 GHz, microwave power: 2.0 mW, sweep width: 120 G, modulation frequency: 100 kHz, modulation amplitude: 0.5 G, receiver gain:  $4 \times 10^{-4}$ , time constant: 20.48 ms, conversion time: 40.96 ms, and time per single scan: 41.9 s. Acquired EPR traces correspond to the second derivative of the sample's paramagnetic absorption.

**2.3. Photocatalytic Activity.** Photobactericidal activity was measured by sampling *E. coli* strain ATCC 11229 from Pyrex photoreactors with a 50 mL of a 0.1 g/L TiO<sub>2</sub> suspension. Before experiments, bacteria were inoculated into Luria Bertani growth media (1% wt, tryptone from Oxoid, 0.5% wt yeast extract from Oxoid, and 1% wt NaCl from Merck) and grown during 8 h at 37°C. During the stationary growth phase, bacteria were harvested by centrifugation at 5000 rpm for 10 min at 4°C. The obtained bacterial pellet was washed three times with saline solution (8 g/L NaCl, 0.8 g/L KCl in Milli-Q water, pH = 7 by addition of HCl or NaOH). A suitable cell concentration (10<sup>7</sup> colony forming units (CFU) per mL) was inoculated to reactors suspensions. Then, photocatalyst was added to each reactor. Suspensions were illuminated during 2 h, and samples (1 mL) were taken at

different time intervals. Serial dilutions were performed in saline solution and 10  $\mu\text{L}$  samples were inoculated 4 times in plate count agar (PCA, Merck). The number of colonies was counted after 24 h of incubation at 37°C.

*E. coli* +  $\text{TiO}_2$  suspensions were kept under magnetic stirring and illuminated under two different lamp setups: (1) 67lx of white light illumination, with 9.8  $\text{W}/\text{m}^2$  of irradiation, using a set of 5 natural sunshine light Phillips lamps (20 W), respectively, with emission between 360 and 700 nm or (2) 250 or 400  $\text{W}/\text{m}^2$  of solar-simulated light irradiation using a suntest system model CPS+ from ATLAS, with temperature and irradiation power control, and a Xenon lamp emitting light with wavelengths of 300 y 800 nm, and 5% of the irradiation corresponds to UV-A. The radiant flux was monitored with a Kipp & Zonen (CM3) power meter (Omni instruments Ltd., Dundee, UK) and a Hagner EC1 digital luxmeter.

Bacteria concentration was also followed in dark suspended and stirred Ag- $\text{TiO}_2$  and  $\text{TiO}_2$  suspensions to analyze possible induced dead by toxicity of the materials. Moreover, to analyze possible lixiviation of  $\text{Ag}^+$  ions an  $\text{Ag}(2)\text{TiO}_2$  suspension was stirred under darkness for 10 h and then filtered. Since *E. coli* is inactivated by  $\text{Ag}^+$  ions in solution it is possible then to determine if lixiviated Ag may decrease bacteria concentration [27]. Thus, *E. coli* was added to the filtered solution and bacteria concentration was determined by intervals of 2 h under darkness.

An additional determination of the *E. coli* concentration was made in order to analyze the time needed for effective disinfection. In this case a sample of each reactor with Ag- $\text{TiO}_2$  photocatalysts was taken after 1 h of irradiation and kept under darkness for 24 h. After this period the samples were submitted to plating and incubation as already described, and finally, colonies were counted on agar plates. The effective irradiation time (EDT) for inactivation was assigned to the sample with zero bacteria counting after 24 h under darkness and was labeled as  $\text{EDT}_{24}$ .

### 3. Results and Discussion

**3.1. Photocatalysts Features.** The optical response of the samples has been followed by means of the spectral response on DRS analyses. Figure 1 shows the DRS spectra of the  $\text{TiO}_2$ - and Ag-modified  $\text{TiO}_2$  samples.  $\text{TiO}_2$  spectrum consists of a wide absorption band below  $\sim 370$  nm ascribed to electron transitions from the valence band (VB), to the conduction band (CB) [28]. Moreover, an interesting light response was found for Ag-loaded samples. Increase in Ag concentration induces a shift in light absorption to the vis range for wavelengths up to 800 nm. DRS spectrum of the 0.5% Ag-loaded  $\text{TiO}_2$  sample did not show a significant increase in visible absorption capacity of the material, thus results are not presented. In addition, the 8% Ag-loaded sample shows a shoulder-like peak at  $\sim 460$  nm which has been proposed for  $\text{Ag}^0$  nanoparticles inducing vis light absorption [29]. Atoms, ions, and clusters of silver show characteristic absorption peaks with irradiation wavelengths from 190 nm 500 nm in DRS spectra. Bands at 190–230 nm ascribed to  $4d^{10}-4d^95s^1$

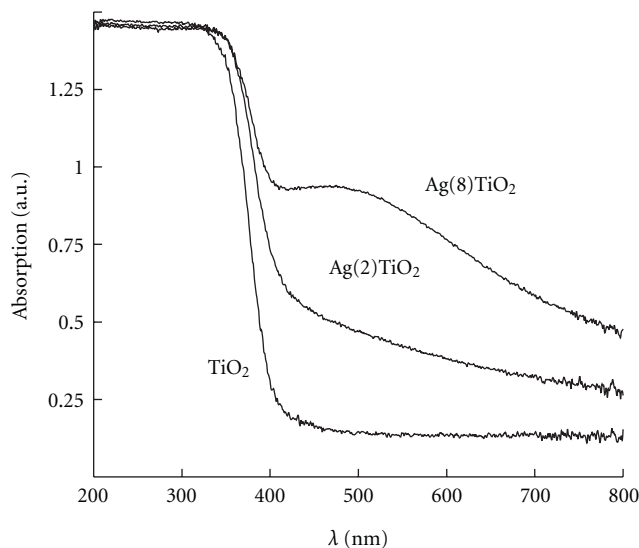


FIGURE 1: DRS spectra of the  $\text{TiO}_2$  and Ag- $\text{TiO}_2$  samples.

transitions in  $\text{Ag}^+$ , while those at 250–330 nm attributed to  $4d^{10}5s^1-4d^95s^15p^1$ ,  $4d^{10}5s^1-4d^95s^16p^1$ , or  $5s^1-p^1$  transitions in  $\text{Ag}^0$  [30], are overlapped by VB-to-CB transitions on  $\text{TiO}_2$  as previously observed. In addition,  $\text{Ag}_n^{\delta+}$  clusters (where  $n$  is in the range 2–13, and  $\delta = n - 1$ ) with  $n > 3$  present three absorption bands at 360, 460, and 500 nm [31]. Bands at 350–380 nm are attributed to Ag clusters of  $\sim 1$  nm size, while clusters of 10 nm size and crystallites absorb at 400–500 nm [30, 31].

Such shoulder-like peak has been observed for Ag nanoparticles inducing collective oscillations of the conduction band electrons with the incident light [32, 33]. This effect has also been observed for Au and Pt nanoparticles [34]. This electromagnetic resonance is known as a surface plasmon resonance effect which in this case may induce photoactivity of  $\text{TiO}_2$  under vis irradiation [35] as it will be discussed.

In contrast, a slight decrease in the slope of the absorption threshold is observed due to Ag loading of  $\text{TiO}_2$ . Such decrease is related to a decrease in the energy bandgap. Probably, the increase in N residues coming from the Ag salt precursor,  $\text{AgNO}_3$ , may lead to new intrabandgap states promoting electronic transitions of lower energy requirements between N and the  $\text{TiO}_2$  conduction band, thus leading to a decrease in the energy gap [36]. However, as we have stated, in a previous work,  $\text{NO}_3^-$  residues in Fe- $\text{TiO}_2$  samples, obtained by the hydrothermal route, do not promote photoactivity under vis light [4]. Therefore, DRS spectra observed in Figure 1 suggest that increased absorption due to Ag presence, with a peak at  $\sim 460$  nm, is possibly due to the localized surface plasmon resonance of Ag nanoparticles [37, 38].

Figure 2 shows the emission spectra of the chosen light setups. The Xenon and interior-lighting lamps have similar distribution spectra between 300 and 800 nm. Both lamps have low emissions under 400 nm in comparison to the emissions in the vis range (400–800 nm). This is supposed to activate  $\text{TiO}_2$  alone since its absorption threshold lies at 400 nm

as observed in Figure 1. However, the major part of both emission spectra suggests that vis irradiation predominates over UV irradiation thus giving the chance to activate surface Ag aggregates.

Figure 3 shows the X-ray diffractograms of samples. Anatase (A) is identified as the primary crystalline phase in both samples with peaks at  $2\theta$  of  $25.2^\circ$ ,  $37.9^\circ$ ,  $48.2^\circ$ ,  $55.0^\circ$ , and  $62.6^\circ$ . In addition, a slight peak at  $30.7^\circ$  assigned to brookite (B) is observed for all samples.  $\text{Al}_2\text{O}_3$  corundum (C) peaks are observed for  $\text{TiO}_2$  and  $\text{Ag}(8)\text{TiO}_2$  samples' diffractogram since this oxide was used in the quantification of the phase composition of these two samples, while Ag-related phases were not identified in any of the samples due to low concentrations. Ag loading did not cause significant changes in crystallinity since, as previously described,  $\text{Ag}^+$  ion radii is too large to replace  $\text{Ti}^{4+}$  ions in the  $\text{TiO}_2$  matrix. Furthermore, on quantitative XRD analysis it was determined that  $\text{TiO}_2$  sample is constituted of anatase, brookite, and amorphous in percentages of 38.4, 12.2, and 49.2%, respectively, while those for  $\text{Ag}(8)\text{TiO}_2$  are 39, 9.2, and 51.8%, respectively. As a consequence, since Ag does not change phase structure aggregates may be formed on crystal borders and on the surface of the photocatalyst, thus promoting vis light absorption as discussed in Figure 1.

Table 1 shows the calculated average crystallite size and some textural properties of the samples. A slight decrease in crystallite size was observed due to Ag loading probably due to obstruction to anatase crystallite growth by Ag aggregates located in crystal borders.  $\text{Fe}^{3+}$  modifications on  $\text{TiO}_2$ , using the same hydrothermal synthesis, promoted changes on the crystalline structure due to its similarity in sizes with  $\text{Ti}^{4+}$  ions, thus replacing Ti atoms and decreasing crystallite size [4]. Therefore, it is possible to suggest that during the synthesis Ag aggregates are deposited on the surface or grain boundaries.

TEM micrographs of the  $\text{TiO}_2$  and  $\text{Ag}(2)\text{TiO}_2$  samples are shown in Figure 4. As observed, the  $\text{TiO}_2$  sample is constituted of irregular particles with approximate sizes of 8–10 nm. The difference between  $d_{\text{XRD}}$  and the observed particle size in TEM analysis is due to agglomeration of crystallites. In addition, the  $\text{Ag}(2)\text{TiO}_2$  micrograph shows a similar size distribution to that of bare  $\text{TiO}_2$  as it was previously suggested in XRD analyses. Moreover, previously suggested Ag nanoparticles were not observed during the analysis probably due to low resolution of equipment.

Textural properties evidence mesoporous materials with high area. Ag loading caused a significant decrease in  $S_{\text{BET}}$  probably due to deposition of Ag aggregates on the  $\text{TiO}_2$  surface thus leading to pore obstruction [39]. Figure 5 shows type IV isotherms for  $\text{TiO}_2$  and  $\text{Ag}(2)\text{TiO}_2$  samples. Moreover, the sorption isotherm of the  $\text{TiO}_2$  sample demonstrated a hysteresis pattern between types H1 and H2, while that of the  $\text{Ag}(2)\text{TiO}_2$  sample shows a type H2 hysteresis loop. Type H1 loops are often assigned to agglomerates or compact or spherical particles with uniform size, while type H2 loops are attributed to pore size and shape distributions not well defined [40]. Therefore, it is possible to suggest that Ag modification distorted the distribution of pores of the mesoporous structure of  $\text{TiO}_2$  due to

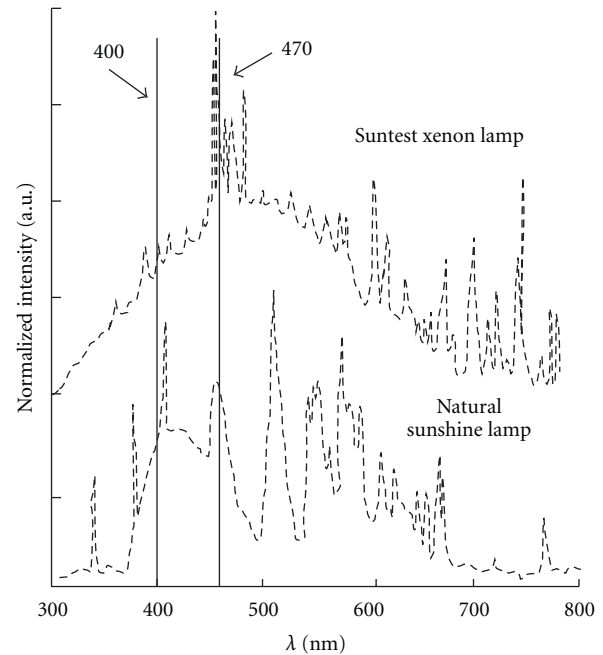


FIGURE 2: Emission spectra of the Xenon and natural sunshine lamps for interior lighting.

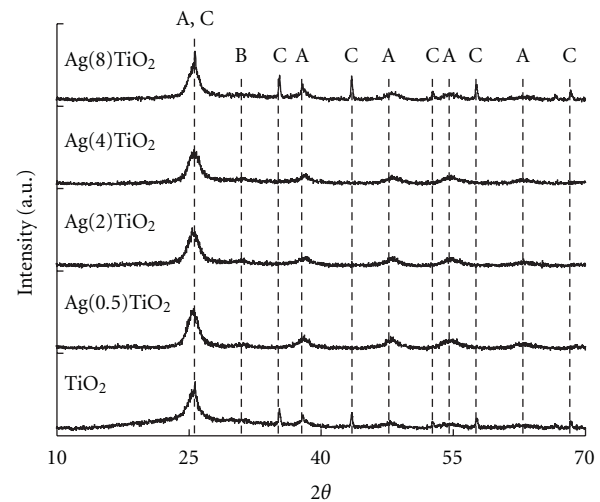


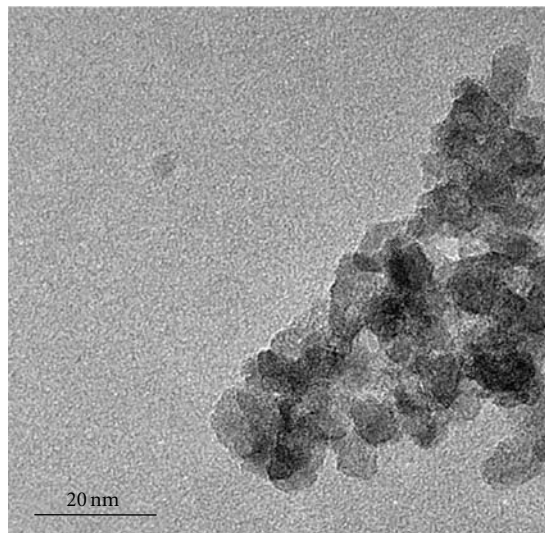
FIGURE 3: X-ray diffractograms of the  $\text{TiO}_2$  and  $\text{Ag-TiO}_2$  samples. A: Anatase, B: Brookite, C:  $\text{Al}_2\text{O}_3$  Corundum.

TABLE 1: Structural and textural properties of  $\text{TiO}_2$  and  $\text{Ag}(2)\text{TiO}_2$  samples.

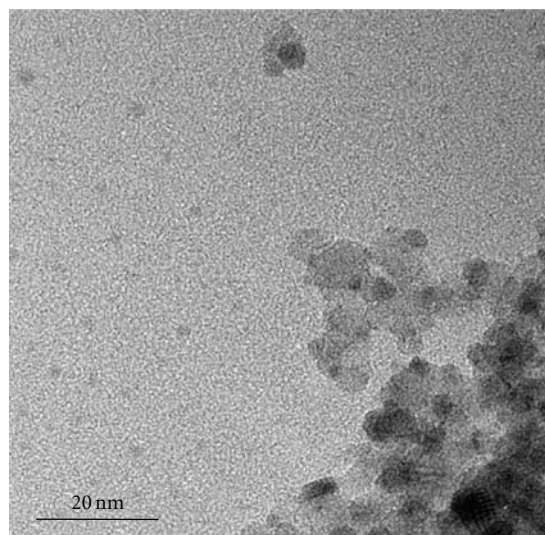
Sample	$d_{\text{XRD}}$ (Å)	$S_{\text{BET}}$ ( $\text{m}^2/\text{g}$ )	$d_p$ (Å)
$\text{TiO}_2$	4.42	370	22.9
$\text{Ag}(2)\text{TiO}_2$	3.18	234	19.7

$d_{\text{XRD}}$ : calculated crystallite size,  $S_{\text{BET}}$ : specific surface area,  $d_p$ : average pore size.

location of Ag aggregates on grain boundaries, as previously suggested.



(a)



(b)

FIGURE 4: TEM micrographs of the (a)  $\text{TiO}_2$  and (b)  $\text{Ag}(4)\text{TiO}_2$  samples. Index (b) is missed in the current phrase.

Figure 6 shows the Ti 2p and Ag 3d XPS spectra of the fresh and solar-simulated light irradiated  $\text{Ag}(2)\text{TiO}_2$  sample. The Ti 2p doublet of the fresh Ag-loaded sample is constituted by Ti 2p<sub>3/2</sub> and Ti 2p<sub>1/2</sub> peaks at 458.9 and 464.6 eV, respectively, indicating a predominant state of  $\text{Ti}^{4+}$  [41]. Moreover, the Ag 3d spectra of the fresh sample show Ag 3d<sub>5/2</sub> and Ag 3d<sub>3/2</sub> peaks at 368.4 and 374.4 eV, respectively. After peak deconvolution it is observed the presence of two different peaks for Ag3d<sub>5/2</sub>: one at 368.4 eV assigned to  $\text{Ag}^+$  [12, 42], while the peak at 368.7 eV is attributed to  $\text{Ag}^0$  [12, 43]. Thus, results suggest the coexistence of  $\text{Ag}_2\text{O}$  and  $\text{Ag}^0$  probably due to the oxidative action of isopropanol on  $\text{Ag}^+$  ions [44] during the synthesis process. Therefore, it is possible to suggest that Ag is deposited on the  $\text{TiO}_2$  surface as partially oxidized metallic aggregates. On the other side, the irradiated sample's XPS spectra evidences that the irradiation

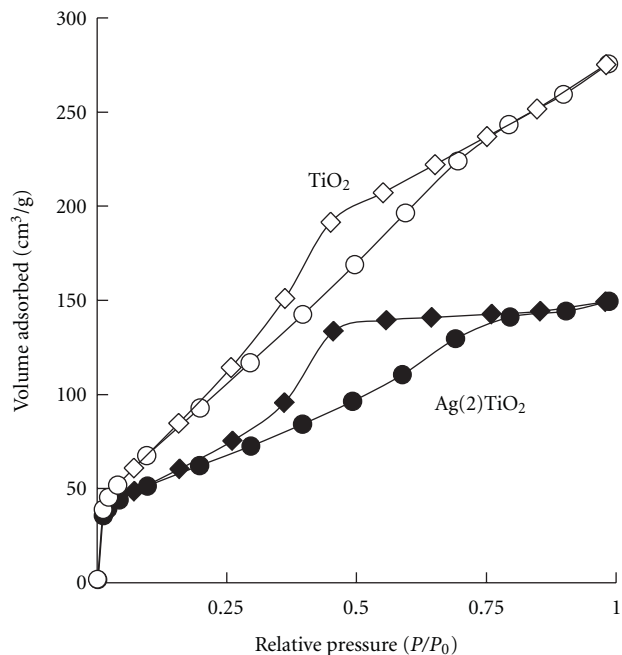


FIGURE 5:  $\text{N}_2$  (●, ○) adsorption, (◇, ◆) desorption isotherms of the  $\text{TiO}_2$  and  $\text{Ag}(2)\text{TiO}_2$  samples.

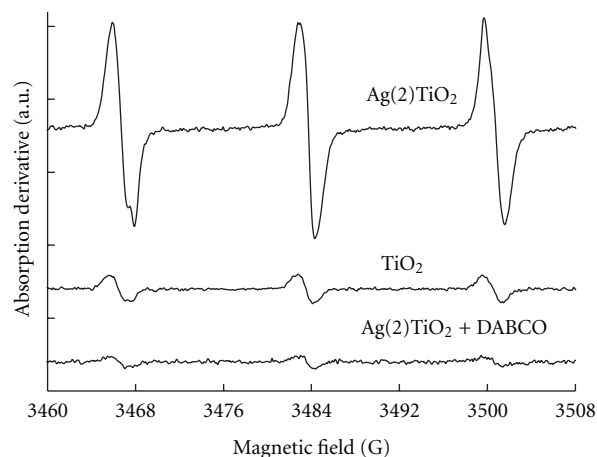


FIGURE 6: EPR spectra of  $\text{D}_2\text{O}$  suspensions of  $\text{Ag}(2)\text{TiO}_2$  and  $\text{TiO}_2$  with TMP-OH and DABCO after 80 min of visible light irradiation.

process shifts signals by  $\sim 1.1$  eV for the Ag 3d spectra, while that of Ti 2p is shifted by  $\sim 1$  eV. Ag peaks at 367.2 and 373.2 for Ag 3d<sub>5/2</sub> and Ag 3d<sub>3/2</sub> are assigned to  $\text{Ag}^{2+}$  species as suggested by Kaushik [45]. In addition, the Ti 2p shift indicates the formation of  $\text{Ti}^{3+}$  species on the  $\text{TiO}_2$  surface [46]. It has been observed that during irradiation of Ag- $\text{TiO}_2$  samples Ag is oxidized by action of photogenerated holes on the  $\text{TiO}_2$  VB [47], therefore it is possible to suggest that  $\text{Ti}^{4+}$  cations, in  $\text{TiO}_2$ , are reduced by released electrons during Ag oxidation.

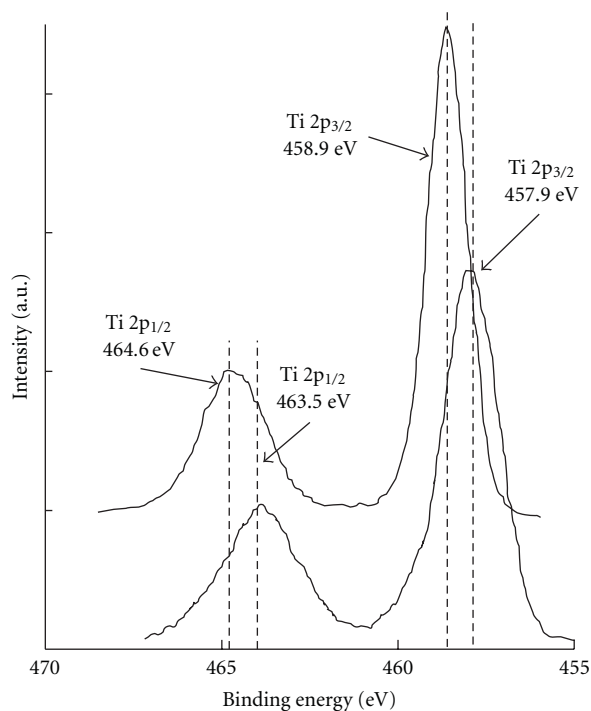
Moreover,  $\text{Ti}^{3+}$  is expected to be rapidly oxidized to  $\text{Ti}^{4+}$  by surrounding oxygen [48]. However, in this case the chosen synthesis route leads to formation of anatase-brookite mixed

phase oxide with ~50% of amorphous, as early discussed, including organic residues as we have observed in a previous work [4]. Such residues may protect surface oxidation of  $Ti^{3+}$  to  $Ti^{4+}$  thus allowing its detection in XPS analyses.

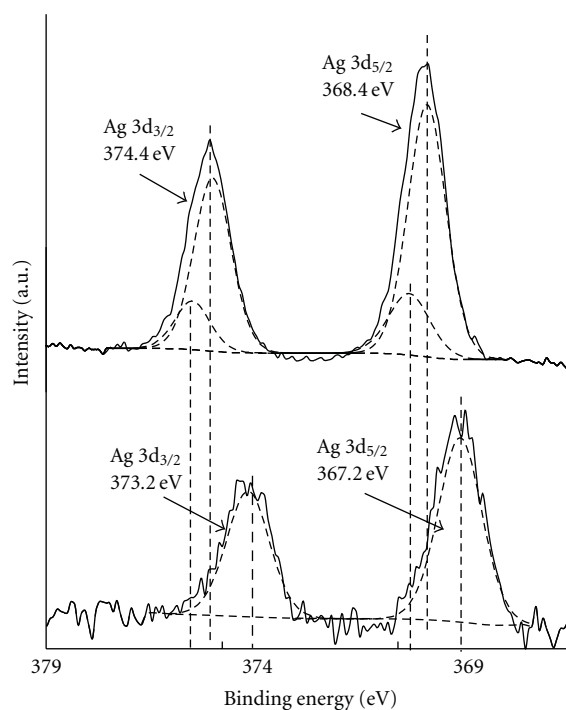
**3.2. Photocatalytic Production of ROS under Vis Irradiation.** Vis-irradiation-induced singlet oxygen ( $^1O_2$ ) formation was monitored by EPR. Figure 7 shows the signal obtained after 50 min of vis irradiation of  $TiO_2$  and  $Ag(2)TiO_2$  suspensions in presence of TMP-OH and DABCO.  $^1O_2$  formation was clearly evidenced for  $Ag(2)TiO_2$  with a characteristic 1 : 1 : 1 triplet signal of TEMPOL [49] as depicted in Figure 7. Moreover, the Ag-modified sample revealed an increase in TEMPOL signal thus evidencing a higher  $^1O_2$  photoproduction in comparison to  $TiO_2$ . Furthermore, the acquired signal of experiments in presence of DABCO revealed a total decrease in the intensity of TEMPOL signal. Since DABCO is a well-known  $^1O_2$  scavenger [50] it is possible to confirm its photocatalytic production by action of vis irradiation on  $Ag(2)TiO_2$  suspensions. Therefore, singlet oxygen is promoted by vis-excited Ag aggregates on the  $TiO_2$ 's surface, and thus it is possible to expect an increased photobactericidal activity of  $TiO_2$ .

**3.3. Photocatalytic Disinfection of Water and Postirradiation Events.** Figure 8(a) shows the bactericidal activity of  $TiO_2$  and Ag- $TiO_2$  samples in darkness. Results evidence zero toxicity of  $TiO_2$  while  $Ag(2)TiO_2$  and  $Ag(4)TiO_2$  samples totally decreased the *E. coli* population within 180 and 60 min of contact, respectively. Ag ionic species loaded on a substrate's surface have been observed to efficiently inactivate *E. coli* [41]. As a consequence, in our case  $Ag^+$  species are responsible of the bactericidal activity of the Ag- $TiO_2$  samples under darkness. Moreover, Figure 8(b) shows the evolution of *E. coli* added to a filtered solution of a 10 h dark-stirred  $Ag(2)TiO_2$  suspension. After 240 min of stirring the filtered solution and *E. coli*, it is observed that bacteria population is affected by the aqueous media. This suggests that  $Ag^+$  ions have been released from the photocatalyst's surface during the dark-stirring process, and after filtration may induce toxicity leading to bacteria death. Then, since the homogeneous bactericidal activity is observed after long times of lixiviation during stirring and the heterogeneous toxicity is observed after 180 min (Figure 8(a)), it seems probable that in-dark contact of the photocatalyst with *E. coli* the bactericidal activity is promoted by the toxicity of  $Ag^+$  ions on the photocatalyst surface, and of course, with time released ions play their bactericide role as observed in Figure 8(b). However, an additional heterogeneous photocatalytic effect has been observed to boost inactivation rates under different irradiation setups as discussed earlier.

On the other side, Figure 9 shows the photodisinfection tests results under 250 and 750  $W/m^2$  of solar-simulated light irradiation of Ag- $TiO_2$  samples and their correspondent EDT<sub>24</sub>. Figures 9(a) and 9(b) show the performance of  $TiO_2$ - and Ag-modified samples:  $Ag(2)TiO_2$  and  $Ag(4)TiO_2$ . The increase in Ag loading effectively enhanced the photodisinfecting effect of  $TiO_2$ . Moreover, the *E. coli* inactivation



(a)



(b)

FIGURE 7: XPS spectra of (a) the Ti 2p region of the  $TiO_2$  and  $Ag(2)TiO_2$  samples and (b) the Ag 3d region of the  $Ag(2)TiO_2$  (top) and solar-simulated light irradiated  $Ag(2)TiO_2$  (bottom) samples.

rates are boosted when increasing the irradiation power thus confirming the heterogeneity of the photocatalytic process as observed in Figure 9(b). Indeed, under 250  $W/m^2$  the  $Ag(2)TiO_2$  sample reaches total inactivation within 20 min,

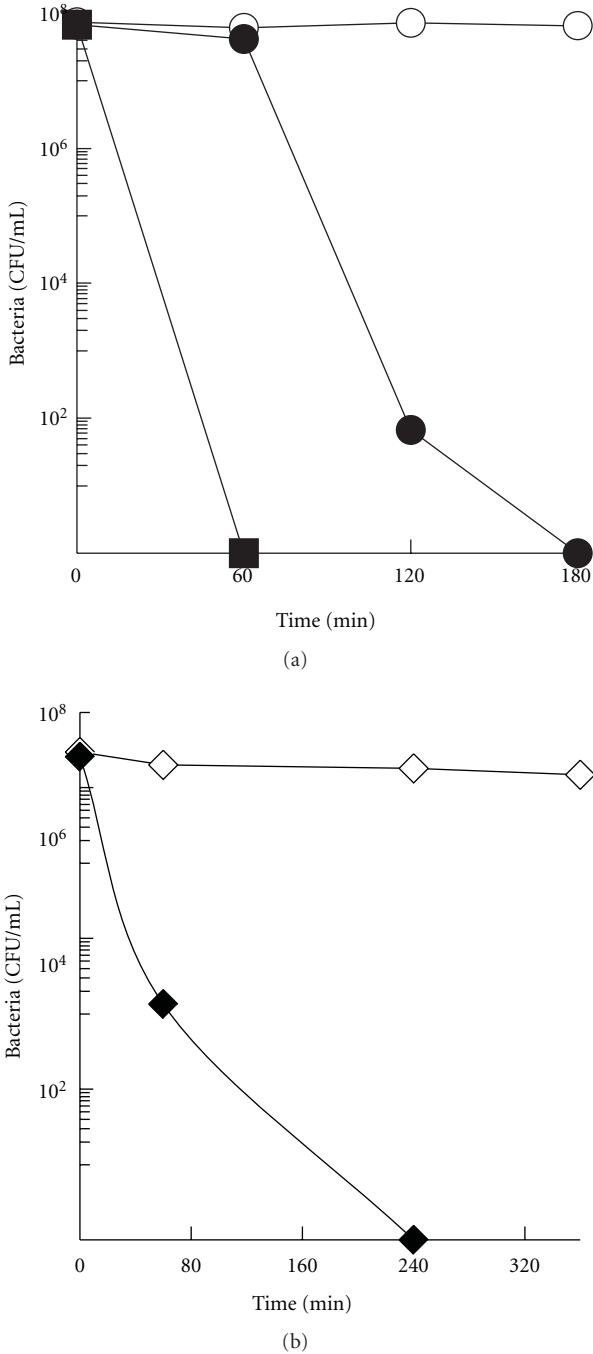


FIGURE 8: Dark events of *E. coli* with (a) (■) Ag(4)TiO<sub>2</sub>, (●) Ag(2)TiO<sub>2</sub>, and (○) TiO<sub>2</sub> samples and (b) filtered solutions of previously 10 h stirred suspensions of (◆) Ag(2)TiO<sub>2</sub>, and (◇) TiO<sub>2</sub>.

while the bactericidal effect reduced the population in 60 min (Figure 8). This effect is observed to increase under 400 W/m<sup>2</sup> of irradiation since the total inactivation, by the same sample, is reached after 10 min. Then, the photocatalytic effect decreases the inactivation time by 40 and 50 min, under 250 and 400 W/m<sup>2</sup>, respectively, indicating that the total bactericidal action is a sum of photoinduced processes and photocatalysts toxicity.

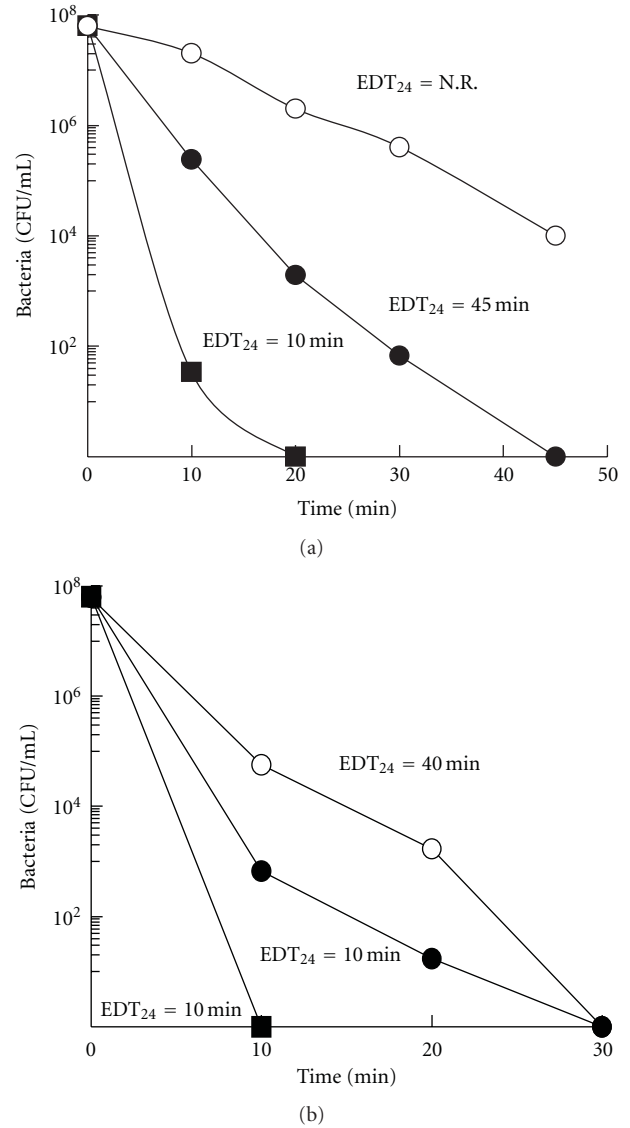


FIGURE 9: Photocatalytic water disinfection using: (■) Ag(4)TiO<sub>2</sub>, (●) Ag(2)TiO<sub>2</sub> and (○) TiO<sub>2</sub> samples, under (a) 250 and (b) 400 W/m<sup>2</sup> of solar-simulated light irradiation.

Furthermore, using irradiation of interior lighting lamps similar effects were observed. Such photocatalytic process can now be correlated to the photoproduction of ROS. As it was previously observed, the spectrum of the Xenon lamp has a ~50% of irradiance power correspondent to visible light, and even more, the excitation wavelength of the Ag nanoparticles on the TiO<sub>2</sub> surface is emitted by this source (~470 nm), thus singlet oxygen is produced. A vast majority of cell types, from prokaryotic to mammalian, undergo irreversible damage leading to cell death by exposure to singlet oxygen [51, 52], therefore in our case the *E. coli* inactivation is attributed to <sup>1</sup>O<sub>2</sub> photoproduction.

Moreover, samples of these experiments were kept in dark during 24 h and bacteria concentration was measured to determine the EDT<sub>24</sub>. It is observed that 10 min of solar-simulated light irradiation are required to achieve inactivation

without regrowth using the  $\text{Ag}(4)\text{TiO}_2$  sample, even if 10 min of irradiation do not lead to total inactivation as observed in Figure 9(a). On the other hand, the performance of  $\text{Ag}(2)\text{TiO}_2$  leads to an  $\text{EDT}_{24}$  of 45 min while that of  $\text{TiO}_2$  was not reached during the irradiation time. A similar effect was observed with  $400\text{ W/m}^2$  of irradiation as observed in Figure 9(b). However, in this case using  $\text{TiO}_2$  and  $\text{Ag}(2)\text{TiO}_2$  samples the correspondent  $\text{EDT}_{24}$  were 10 and 40 min, respectively, suggesting an increase in the effective oxidative action of the photocatalysts when increasing the irradiation power [53].

Furthermore, Figure 10 shows the results of the photocatalytic water disinfection using the  $\text{TiO}_2$  and  $\text{AgTiO}_2$  samples under irradiation of  $9.8\text{ W/m}^2$  of natural sunshine irradiation from interior-lighting lamps. Results evidence a fast decay of the *E. coli* concentration using the  $\text{Ag}(4)\text{TiO}_2$  sample, while  $\text{Ag}(2)\text{TiO}_2$  and  $\text{TiO}_2$  show lower performances. Such behavior was expected since the light irradiation setup, as previously discussed, has a wide peak of light irradiation at 470 nm which may effectively activate the photocatalyst surface as presented in Figure 2. Nevertheless, the  $\text{EDT}_{24}$  were diminished of course due to the decrease in light irradiation power.

It has been previously discussed that during the photocatalytic inactivation of *E. coli* it is necessary to achieve a sum of damages to achieve the complete inactivation of bacteria [54]. Moreover, Rincón and Pulgarín [53] have discussed that even achieving total inactivation during irradiation it is possible to observe regrowth of the bacteria population, after 24 h in dark, indicating that somehow the level of damage needed for absolute death has not been reached. Therefore, in our case we have observed that using Ag modified particles it is possible to achieve a true inactivation in short irradiation periods, as observed after dark periods of 24 h, even without reaching zero concentration of bacteria during irradiation. Such effect, as earlier discussed, is due to action of photoinduced and bactericidal processes.

Finally, to discuss photocatalyst stability it is possible to expect that losing active silver species on the photocatalyst's surface, during stirring, may lead to a less active surface photocatalysts, and therefore, studies focusing on improving Ag fixing and stability on  $\text{TiO}_2$  should be developed.

#### 4. Conclusions

$\text{Ag-TiO}_2$  photocatalysts, synthesized using the hydrothermal synthesis, lead to Ag aggregates on the  $\text{TiO}_2$  surface which increases the visible light response of  $\text{TiO}_2$ . In addition, such aggregates are partially oxidized particles that distorted the pore distribution of the samples. This photocatalyst configuration seems to promote photoactivity towards the photocatalytic disinfection of water under solar light and interior-light irradiations. Photoactivity was effectively correlated to the photoproduction of singlet oxygen under visible light irradiation as determined by EPR analyses using DABCO as a singlet oxygen quencher. Moreover, analysis of dark processes evidenced that part of the inactivation process

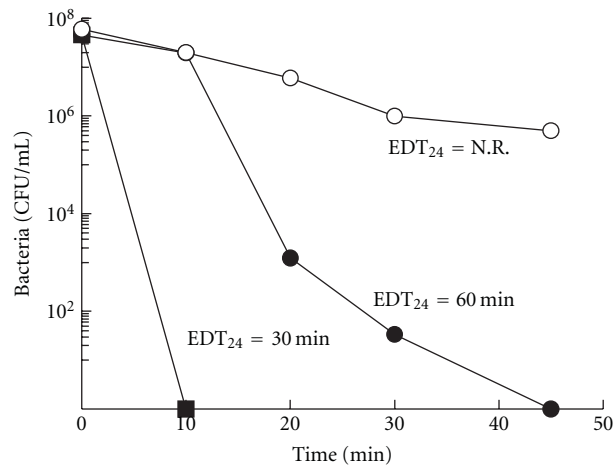


FIGURE 10: Photocatalytic water disinfection using (■)  $\text{Ag}(4)\text{TiO}_2$ , (●)  $\text{Ag}(2)\text{TiO}_2$ , and (○)  $\text{TiO}_2$  samples, under  $9.8\text{ W/m}^2$  of natural sunshine light irradiation of interior lighting.

is due to the bactericidal effect of silver in the surface and possible lixiviated  $\text{Ag}^+$  ions.

#### Acknowledgments

The authors express their gratitude to Professor Aristóbal Centeno, R.I.P, for his valuable life and academic advice. They still spread the research spirit he sowed on them. This work was financially supported by UIS through the project: Fijación de semiconductores sobre poliéster para obtención de textiles fotobactericidas, code: 5448. C. Castro thanks also A. Colciencias, Sena, and UIS for financial support to his finished Ph.D. studies. Special acknowledgments are to the Group of Electrochemical Engineering and the Laboratory of Complex Matter Physics, in the EPFL, Switzerland, for the XPS and EPR analyses.

#### References

- [1] J. A. Byrne, P. A. Fernandez-Ibañez, P. S.M. Dunlop, D. M.A. Alrousan, and J. W.J. Hamilton, "Photocatalytic enhancement for solar disinfection of water: a review," *International Journal of Photoenergy*, vol. 2011, Article ID 798051, 12 pages, 2011.
- [2] S.-J. Kim, N.-H. Lee, H.-J. Oh, S.-C. Jung, W.-J. Lee, and D.-H. Kim, "Photocatalytic properties of nanotubular-shaped  $\text{TiO}_2$  powders with anatase phase obtained from titanate nanotube powder through various thermal treatments," *International Journal of Photoenergy*, vol. 2011, Article ID 327821, 7 pages, 2011.
- [3] C. Wang and J. Yao, "Decolorization of methylene blue with  $\text{TiO}_2$  sol via UV irradiation photocatalytic degradation," *International Journal of Photoenergy*, vol. 2010, Article ID 643182, 6 pages, 2010.
- [4] C. A. Castro, A. Centeno, and S. A. Giraldo, "Iron promotion of the  $\text{TiO}_2$  photosensitization process towards the photocatalytic oxidation of azo dyes under solar-simulated light irradiation," *Materials Chemistry and Physics*, vol. 129, no. 3, pp. 1176–1183, 2011.

- [5] A. J. Frank, N. Kopidakis, and J. V. D. Lagemaat, "Electrons in nanostructured TiO<sub>2</sub> solar cells: transport, recombination and photovoltaic properties," *Coordination Chemistry Reviews*, vol. 248, no. 13-14, pp. 1165–1179, 2004.
- [6] C. A. Castro-López, A. Centeno, and S. A. Giraldo, "Fe-modified TiO<sub>2</sub> photocatalysts for the oxidative degradation of recalcitrant water contaminants," *Catalysis Today*, vol. 157, no. 1-4, pp. 119–124, 2010.
- [7] J. Gamage and Z. Zhang, "Applications of photocatalytic disinfection," *International Journal of Photoenergy*, vol. 2010, Article ID 764870, 11 pages, 2010.
- [8] A. G. Rincón, C. Pulgarin, N. Adler, and P. Peringer, "Interaction between *E. coli* inactivation and DBP-precursors-dihydroxybenzene isomers in the photocatalytic process of drinking-water disinfection with TiO<sub>2</sub>," *Journal of Photochemistry and Photobiology A*, vol. 139, no. 2-3, pp. 233–241, 2001.
- [9] M. K. Seery, R. George, P. Floris, and S. C. Pillai, "Silver doped titanium dioxide nanomaterials for enhanced visible light photocatalysis," *Journal of Photochemistry and Photobiology A*, vol. 189, no. 2-3, pp. 258–263, 2007.
- [10] K. Awazu, M. Fujimaki, C. Rockstuhl et al., "A plasmonic photocatalyst consisting of silver nanoparticles embedded in titanium dioxide," *Journal of the American Chemical Society*, vol. 130, no. 5, pp. 1676–1680, 2008.
- [11] B. Xin, L. Jing, Z. Ren, B. Wang, and H. Fu, "Effects of simultaneously doped and deposited Ag on the photocatalytic activity and surface states of TiO<sub>2</sub>," *Journal of Physical Chemistry B*, vol. 109, no. 7, pp. 2805–2809, 2005.
- [12] O. Akhavan and E. Ghaderi, "Self-accumulated Ag nanoparticles on mesoporous TiO<sub>2</sub> thin film with high bactericidal activities," *Surface and Coatings Technology*, vol. 204, no. 21-22, pp. 3676–3683, 2010.
- [13] Z. Xiong, J. Ma, W. J. Ng, T. D. Waite, and X. S. Zhao, "Silver-modified mesoporous TiO<sub>2</sub> photocatalyst for water purification," *Water Research*, vol. 45, no. 5, pp. 2095–2103, 2011.
- [14] W. Zhou, H. Liu, J. Wang, D. Liu, G. Du, and J. Cui, "Ag<sub>2</sub>O/TiO<sub>2</sub> nanobelts heterostructure with enhanced ultraviolet and visible photocatalytic activity," *ACS Applied Materials & Interfaces*, vol. 2, no. 8, pp. 2385–2392, 2010.
- [15] D. R. Monteiro, L. F. Gorup, A. S. Takamiya, A. C. Ruvollo-Filho, E. R. D. Camargo, and D. B. Barbosa, "The growing importance of materials that prevent microbial adhesion: antimicrobial effect of medical devices containing silver," *International Journal of Antimicrobial Agents*, vol. 34, no. 2, pp. 103–110, 2009.
- [16] Y. Lai, Y. Chen, H. Zhuang, and C. Lin, "A facile method for synthesis of Ag/TiO<sub>2</sub> nanostructures," *Materials Letters*, vol. 62, no. 21-22, pp. 3688–3690, 2008.
- [17] L. Miao, Y. Ina, S. Tanemura et al., "Fabrication and photochromic study of titanate nanotubes loaded with silver nanoparticles," *Surface Science*, vol. 601, no. 13, pp. 2792–2799, 2007.
- [18] A. Ziełńska, E. Kowalska, J. W. Sobczak et al., "Silver-doped TiO<sub>2</sub> prepared by microemulsion method: surface properties, bio- and photoactivity," *Separation and Purification Technology*, vol. 72, no. 3, pp. 309–318, 2010.
- [19] Y. Liu, C. Y. Liu, Q. H. Rong, and Z. Zhang, "Characteristics of the silver-doped TiO<sub>2</sub> nanoparticles," *Applied Surface Science*, vol. 220, no. 1–4, pp. 7–11, 2003.
- [20] J. Yu, J. Xiong, B. Cheng, and S. Liu, "Fabrication and characterization of Ag-TiO<sub>2</sub> multiphase nanocomposite thin films with enhanced photocatalytic activity," *Applied Catalysis B*, vol. 60, no. 3-4, pp. 211–221, 2005.
- [21] G. Oliveri, G. Ramis, G. Busca, and V. S. Escribano, "Thermal stability of vanadia-titania catalysts," *Journal of Materials Chemistry*, vol. 3, no. 12, pp. 1239–1249, 1993.
- [22] M. Kusakabe, Y. Ito, M. Arai, Y. Shirakawa, and S. Tamaki, "Ionic conductivity in silver-dissolved  $\alpha$ -CuI," *Solid State Ionics*, vol. 92, no. 1-2, pp. 135–138, 1996.
- [23] J. Maier, *Physical Chemistry of Ionic Materials: Ions and Electrons in Solids*, Wiley, London, UK, 2004.
- [24] M. C. Biesinger, L. W. M. Lau, A. R. Gerson, and R. S. C. Smart, "Resolving surface chemical states in XPS analysis of first row transition metals, oxides and hydroxides: Sc, Ti, V, Cu and Zn," *Applied Surface Science*, vol. 257, no. 3, pp. 887–898, 2010.
- [25] M. Styliadi, D. I. Kondarides, and X. E. Verykios, "Visible light-induced photocatalytic degradation of Acid Orange 7 in aqueous TiO<sub>2</sub> suspensions," *Applied Catalysis B*, vol. 47, no. 3, pp. 189–201, 2004.
- [26] Y. E. Nesmelov and D. D. Thomas, "Multibore sample cell increases EPR sensitivity for aqueous samples," *Journal of Magnetic Resonance*, vol. 178, no. 2, pp. 318–324, 2006.
- [27] Q. Chang, H. He, and Z. Ma, "Efficient disinfection of *Escherichia coli* in water by silver loaded alumina," *Journal of Inorganic Biochemistry*, vol. 102, no. 9, pp. 1736–1742, 2008.
- [28] H. Gerischer and A. Heller, "The role of oxygen in photooxidation of organic molecules on semiconductor particles," *Journal of Physical Chemistry*, vol. 95, no. 13, pp. 5261–5267, 1991.
- [29] Y. Tian and T. Tatsuma, "Plasmon-induced photoelectrochemistry at metal nanoparticles supported on nanoporous TiO<sub>2</sub>," *Chemical Communications*, vol. 10, no. 16, pp. 1810–1811, 2004.
- [30] M. Richter, A. Abramova, U. Bentrup, and R. Fricke, "Proof of reversible Ag<sup>+</sup>/Ag<sup>0</sup> redox transformation on mesoporous alumina by in situ UV-Vis spectroscopy," *Journal of Applied Spectroscopy*, vol. 71, no. 3, pp. 400–403, 2004.
- [31] G. A. Ozin, F. Hugues, S. M. Mattar, and D. F. McIntos, "Low nuclearity silver clusters in fajaussite-type zeolites: optical spectroscopy, photochemistry, and relationship to the photodimerization of alkanes," *Journal of Physical Chemistry*, vol. 87, no. 18, pp. 3445–3450, 1983.
- [32] B. Cheng, Y. Le, and J. Yu, "Preparation and enhanced photocatalytic activity of Ag@TiO<sub>2</sub> core-shell nanocomposite nanowires," *Journal of Hazardous Materials*, vol. 177, no. 1–3, pp. 971–977, 2010.
- [33] Q. Xiang, J. Yu, B. Cheng, and H. C. Ong, "Microwave-hydrothermal preparation and visible-light photoactivity of plasmonic photocatalyst Ag-TiO<sub>2</sub> nanocomposite hollow spheres," *Chemistry—An Asian Journal*, vol. 5, no. 6, pp. 1466–1474, 2010.
- [34] Z. Zheng, B. Huang, X. Qin, X. Zhang, Y. Dai, and M. -H. Whangbo, "Facile in situ synthesis of visible-light plasmonic photocatalysts M@TiO<sub>2</sub> (M = Au, Pt, Ag) and evaluation of their photocatalytic oxidation of benzene to phenol," *Journal of Materials Chemistry*, vol. 21, no. 25, pp. 9079–9087, 2011.
- [35] P. Wang, B. Huang, X. Qin et al., "Ag@AgCl: a highly efficient and stable photocatalyst active under visible light," *Angewandte Chemie*, vol. 47, no. 41, pp. 7931–7933, 2008.
- [36] B. Baruwati and R. S. Varma, "Synthesis of N-doped nano TiO<sub>2</sub> using guanidine nitrate: an excellent visible light photocatalyst," *Journal of Nanoscience and Nanotechnology*, vol. 11, no. 3, pp. 2036–2041, 2011.
- [37] R. Jin, Y. Cao, C. A. Mirkin, K. L. Kelly, G. C. Schatz, and J. G. Zheng, "Photoinduced conversion of silver nanospheres to nanoprisms," *Science*, vol. 294, no. 5548, pp. 1901–1903, 2001.

- [38] X. Wang, S. Li, H. Yu, and J. Yu, "In situ anion-exchange synthesis and photocatalytic activity of Ag 8W4O16/AgCl-nanoparticle core-shell nanorods," *Journal of Molecular Catalysis A*, vol. 334, no. 1-2, pp. 52–59, 2011.
- [39] W. Zhao, L. Feng, R. Yang, J. Zheng, and X. Li, "Synthesis, characterization, and photocatalytic properties of Ag modified hollow SiO<sub>2</sub>/TiO<sub>2</sub> hybrid microspheres," *Applied Catalysis B*, vol. 103, no. 1-2, pp. 181–189, 2011.
- [40] F. B. Li, X. Z. Li, C. H. Ao, S. C. Lee, and M. F. Hou, "Enhanced photocatalytic degradation of VOCs using Ln<sup>3+</sup>-TiO<sub>2</sub> catalysts for indoor air purification," *Chemosphere*, vol. 59, no. 6, pp. 787–800, 2005.
- [41] O. Akhavan, "Lasting antibacterial activities of Ag-TiO<sub>2</sub>/Ag/a-TiO<sub>2</sub> nanocomposite thin film photocatalysts under solar light irradiation," *Journal of Colloid and Interface Science*, vol. 336, no. 1, pp. 117–124, 2009.
- [42] M. Romand, M. Roubin, and J. P. Deloume, "ESCA studies of some copper and silver selenides," *Journal of Electron Spectroscopy and Related Phenomena*, vol. 13, no. 3, pp. 229–242, 1978.
- [43] B. Xin, Z. Ren, H. Hu et al., "Photocatalytic activity and interfacial carrier transfer of Ag-TiO<sub>2</sub> nanoparticle films," *Applied Surface Science*, vol. 252, no. 5, pp. 2050–2055, 2005.
- [44] Z. Y. Huang, G. Mills, and B. Hajek, "Spontaneous formation of silver particles in basic 2-propanol," *Journal of Physical Chemistry*, vol. 97, no. 44, pp. 11542–11550, 1993.
- [45] V. K. Kaushik, "XPS core level spectra and Auger parameters for some silver compounds," *Journal of Electron Spectroscopy and Related Phenomena*, vol. 56, no. 3, pp. 273–277, 1991.
- [46] F. Werfel and O. Brümmer, "Corundum structure oxides studied by XPS," *Physica Scripta*, vol. 28, no. 1, pp. 92–96, 1983.
- [47] A. Romanyuk and P. Oelhafen, "Formation and electronic structure of TiO<sub>2</sub>-Ag interface," *Solar Energy Materials and Solar Cells*, vol. 91, no. 12, pp. 1051–1054, 2007.
- [48] N. Sakai, R. Wang, A. Fujishima, T. Watanabe, and K. Hashimoto, "Effect of ultrasonic treatment on highly hydrophilic TiO<sub>2</sub> surfaces," *Langmuir*, vol. 14, no. 20, pp. 5918–5920, 1998.
- [49] R. Konaka, E. Kasahara, W. C. Dunlap, Y. Yamamoto, K. C. Chien, and M. Inoue, "Irradiation of titanium dioxide generates both singlet oxygen and superoxide anion," *Free Radical Biology and Medicine*, vol. 27, no. 3-4, pp. 294–300, 1999.
- [50] S. Kaur and V. Singh, "Visible light induced sonophotocatalytic degradation of Reactive Red dye 198 using dye sensitized TiO<sub>2</sub>," *Ultrasonics Sonochemistry*, vol. 14, no. 5, pp. 531–537, 2007.
- [51] T. A. Dahl, "Direct exposure of mammalian cells to pure exogenous singlet oxygen ( $\Delta_g\text{O}_2$ )," *Photochemistry and Photobiology*, vol. 57, no. 2, pp. 248–254, 1993.
- [52] Z. Cheng and Y. Li, "What is responsible for the initiating chemistry of iron-mediated lipid peroxidation: an update," *Chemical Reviews*, vol. 107, no. 3, pp. 748–766, 2007.
- [53] A. G. Rincón and C. Pulgarin, "Bactericidal action of illuminated TiO<sub>2</sub> on pure Escherichia coli and natural bacterial consortia: post-irradiation events in the dark and assessment of the effective disinfection time," *Applied Catalysis B*, vol. 49, no. 2, pp. 99–112, 2004.
- [54] J. Marugán, R. van Grieken, C. Sordo, and C. Cruz, "Kinetics of the photocatalytic disinfection of Escherichia coli suspensions," *Applied Catalysis B*, vol. 82, no. 1-2, pp. 27–36, 2008.

## Review Article

# Degrading Endocrine Disrupting Chemicals from Wastewater by TiO<sub>2</sub> Photocatalysis: A Review

**Jin-Chung Sin, Sze-Mun Lam, Abdul Rahman Mohamed, and Keat-Teong Lee**

*School of Chemical Engineering, Universiti Sains Malaysia, Engineering Campus, 14300 Nibong Tebal, Malaysia*

Correspondence should be addressed to Abdul Rahman Mohamed, chrahman@eng.usm.my

Received 13 June 2011; Revised 3 August 2011; Accepted 4 August 2011

Academic Editor: Jiaguo Yu

Copyright © 2012 Jin-Chung Sin et al. This is an open access article distributed under the Creative Commons Attribution License, which permits unrestricted use, distribution, and reproduction in any medium, provided the original work is properly cited.

Widespread concerns continue to be raised about the impacts of exposure to chemical compounds with endocrine disrupting activities. To date, the percolation of endocrine disrupting chemical (EDC) effluent into the aquatic system remains an intricate challenge abroad the nations. With the innovation of advanced oxidation processes (AOPs), there has been a consistent growing interest in this research field. Hence, the aim of this paper is to focus one such method within the AOPs, namely, heterogeneous photocatalysis and how it is used on the abatement of EDCs, phthalates, bisphenol A and chlorophenols in particular, using TiO<sub>2</sub>-based catalysts. Degradation mechanisms, pathways, and intermediate products of various EDCs for TiO<sub>2</sub> photocatalysis are described in detail. The effect of key operational parameters on TiO<sub>2</sub> photocatalytic degradation of various EDCs is then specifically covered. Finally, the future prospects together with the challenges for the TiO<sub>2</sub> photocatalysis on EDCs degradation are summarized and discussed.

## 1. Introduction

Disruption of the endocrine system in wildlife and humans by synthetic organic chemicals has recently received considerable attention worldwide due to the recognition of that the environment is contaminated with various endocrine disrupting chemicals (EDCs) that exert hormonal imbalance activity [1]. An endocrine disruptor is defined by the European Commission (1996) as an exogenous substance or a mixture that alters the function of the endocrine system and consequently causes adverse health effects in an organism or its progeny or (sub)populations [2]. The causative chemicals of endocrine disruption in wildlife populations are wide ranging and include a plethora of industrial chemicals such as polycyclic aromatic hydrocarbons (PAHs), brominated flame retardants, several pesticides, dioxins, parabens, bisphenol A, phthalates, organic solvents, and some heavy metals as well as the naturally occurring phytoestrogens [2–6].

EDCs can be classified according to the mode of their endocrine actions. The most commonly reported EDCs in the environment are estrogenic, antiestrogenic, antiandrogenic, androgenic, and thyroidal [8]. The EDCs may

function via modes of action such as mimicking endogenous hormones, antagonizing of hormone receptors, disrupting hormone secretion or metabolism, or disrupting natural hormone production pathways [9, 10]. Endocrine disruptors are also hypothesized to play a role in the pathogenesis of various disorders including male and female infertility, sexual underdevelopment, birth defects, endometriosis, and malignancies [2, 6, 11]. In fact, some EDCs have been shown to have multiple modes of action, which can lead to deleterious effects on the earth ecosystems [12]. Enormous examples of reproductive and developmental abnormalities have been reported over the years in a broad spectrum of wildlife including invertebrates, fish, amphibians, birds, and mammals [3, 5, 13], many of which are associated with EDCs exposure.

Enormous examples of endocrine disruption in wildlife involve animals that are living in or closely associated with the aquatic environment. This is perhaps not surprising considering that surface water acts as a sink for both natural and anthropogenic chemicals discharged into the environment [8, 14]. Sources by which EDCs contaminated the surface water are via sewage effluents from domestic and industrial facilities and industrial effluent discharges [15].

The quantity of chemicals within the aquatic environment together with the inherent susceptibility of aquatic life to the effects of EDCs, leads to significant impacts on the biota of aquatic ecosystems. In certain water bodies with large inputs of anthropogenic chemicals, aquatic life could be continually exposed to a huge range of EDCs at different concentrations. Concentration of EDCs in surface water has been reported in the ranges of  $\text{ng}\cdot\text{L}^{-1}$  for alkylphenols and bisphenols [16, 17]. Despite their low concentration present in the aquatic environment, the hormone-like chemicals have been listed as hazardous pollutants by both the US Environmental Protection Agency (USEPA) and the European Union (EU) due to the fact that even a trace amount of them is adequate to initiate estrogenic activity.

Various chemical, physical, and biological treatment processes are currently proposed for the removal of EDCs. However, conventional water and wastewater treatment plants using activated sludge and/or charcoal adsorption systems are ineffective and nondestructive for many EDCs including BPA and chlorophenols [19, 20]. In the recent years, an alternative to the conventional methods is “advanced oxidation processes” (AOPs) based on the in situ generation of non-selective and highly reactive species such as hydroxyl radicals ( $\cdot\text{OH}$ ), superoxide anion radicals ( $\text{O}_2^{\cdot-}$ ), and hydrogen peroxide ( $\text{H}_2\text{O}_2$ ) as initiators of the oxidative degradation. Among AOPs, heterogeneous photocatalysis using titanium dioxide ( $\text{TiO}_2$ ) has become the focus of intense interest, owing to its chemical and photostability, able to efficiently catalyze reactions and superior ability for the removing a large variety of organic and inorganic pollutants in aqueous media, even from the gaseous environment [21–24]. Since AOPs rely on the generation of highly reactive radicals to react with pollutants, there are many operational parameters such as light intensity and wavelength; initial substrate concentration, catalyst loading, solution pH, reaction temperature, and the presence of oxygen can affect the efficiency of these processes. Consequently, understanding the roles of various operational parameters is crucial from the perspective of efficient design and application of photocatalysis processes to ensure sustainable operation in wastewater treatment. This paper aims to address the fundamentals of heterogeneous photocatalytic degradation of common endocrine disruptors, namely, phthalates, bisphenol A and chlorophenols using  $\text{TiO}_2$ -based catalysts. This paper also describes the degradation pathways that EDCs undergo with some of the intermediates that are generated during their degradation. Moreover, the effect of key operational parameters on  $\text{TiO}_2$ -photocatalyzed degradation of EDCs is then presented. Finally, the future prospects together with the challenges for the  $\text{TiO}_2$  photocatalysis on EDCs degradation are summarized and discussed.

## 2. Overview of Industrial Endocrine Disruptors

Among numerous EDCs used in industrial processes, the three potential disruptors that have recently received scientific and public interest are phthalates, bisphenol A, and chlorophenols. The common feature of all is that they are

produced in huge quantities, and a substantial fraction is discharged into the environment.

**2.1. Phthalates.** Phthalates or phthalic acid esters (PAEs) have been widely used as plasticizers for polyvinyl chloride (PVC) resin, cellulose film coating, styrene, adhesives, cosmetics, pulp and paper manufacturing [15, 25–28]. Other important usages of PAEs are in plumbing, nonionic surfactants, pesticide formulations, construction materials, and vinyl upholstery, to impart flexibility and softness to plastics [29]. About 60 different phthalates are produced worldwide and consumed for diverse purposes. During product manufacturing and wasteland filling, many phthalates-based chemicals are easily transported to the environment, in which they are bonded noncovalently to allow the required degree of flexibility. The PAEs such as dimethyl phthalate (DMP) and diethyl phthalate (DEP) are among the most frequently identified in diverse environmental samples including surface marine waters, freshwaters, and sediments [30, 31]. In Malaysia, studies focusing on concentrations of PAEs in highly industrialized Klang Valley have found varying concentrations of PAEs ranging from 0.1 to  $64.3\ \mu\text{g}\cdot\text{L}^{-1}$  in the river water and 0.49 to  $15.0\ \mu\text{g}\cdot\text{L}^{-1}$  in sediments [32]. The estrogenic activity of eight PAEs such as dibutyl phthalate (DBP), butylbenzyl phthalate (BBP), dihexyl phthalate (DHP), diisooheptyl phthalate, di-*n*-octyl phthalate, diiso-nonyl phthalate, and diisodecyl phthalate was discovered by Zacharewski et al. [33]. Further studies in fish have shown that both BBP and DEP induced vitellogenin (VTG) at an exposure to low concentration in the range of  $\mu\text{g}\cdot\text{L}^{-1}$  via the water [34, 35]. Numerous in vivo screens and tests have demonstrated that PAEs mediated their effects through binding to the estrogen receptor [33, 36]. In addition to these estrogenic effects, some PAEs are also considered to be toxic to microorganisms, aquatic life, and human beings [37]. Recent studies have indicated that phthalate metabolites such as monoethyl phthalate (MEP), mono-(2-ethylhexyl) phthalate (MEHP), mono-*n*-butyl phthalate (MBP), and monobenzyl phthalate (MBzP) can induce DNA damage in human sperm [38, 39].

**2.2. Bisphenol A.** Bisphenol A (BPA) was first discovered as an estrogen in the mid of 1930s, when it was used as an estrogen for clinical use [8]. Then, in the 1950s, BPA was used to react with carbonyl dichloride to produce polycarbonate polymer and subsequently to synthesize epoxy resins, which are now used widely including as lacquer preservatives in the lining of food cans, in automotive parts, and in compact discs [1]. In addition, BPA is consumed as a resin in dental fillings, as powder paints, as additives in thermal paper, as a developer in dyes, optical lenses, and for encapsulation of electrical and electronic parts. BPA is currently produced at a rate about 2.5 million ton/yr worldwide with a significantly increasing trend [40, 41]. Due to its large-scale production and extensive applications, BPA has become an integral part of wastewater streams. The contaminant may also be transferred from different sources to food via (i) food processing by contact with resins, plastics, lacquers, gaskets,

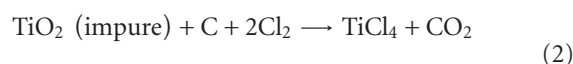
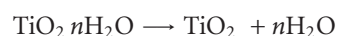
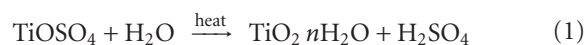
and containers and (ii) migration from packaging and bottling materials. One of the first reports of the estrogenic activity of migrating BPA from polycarbonate flasks during autoclaving was documented in 1993 [42]. BPA has also been shown to be estrogenic via *in vivo* screenings [43, 44]. *In vivo* effects in rat, a low-dose effect of BPA was observed [45]. Whereas, *in vivo* studies in fish, a concentration of  $16 \mu\text{g}\cdot\text{L}^{-1}$  BPA in the water can affect the progression of spermatogenesis [46]. Furthermore, BPA has also been found to have the paradoxical effect to block the beneficial effects of estradiol on neuronal synapse formation and the potential to disrupt thyroid hormone action [47–49]. More extensive reviews on endocrine effects of BPA can be found in the literatures [50–52].

**2.3. Chlorophenols.** Of all the nineteen chlorophenols, only seven of these compounds include monochlorophenols, 2,4-dichlorophenol, 2,4,6-trichlorophenol, 2,4,5-trichlorophenol, 2,3,4,5-tetrachlorophenol, 2,3,4,6-tetrachlorophenol, and pentachlorophenol have been used by the industry [54]. 2,4-dichlorophenol (DCP) and pentachlorophenol (PCP), in particular, have been shown to have endocrine disrupting effects [55, 56]. In general, compound with a higher substituted chlorine atom appears to be rather more resistant to biodegradation—the half life in water can reach 3.5 months in aerobic waters for PCP and some years in organic sediments [57]. The occurrence of these compounds in drinking water can cause objectionable taste and odour at concentration below  $10 \mu\text{g}\cdot\text{L}^{-1}$  and affecting adversely the environment [54, 58, 59]. Due to broad-spectrum antimicrobial properties, these compounds have been used in wood preservation, disinfectants, leather, paints, agricultural seeds (for nonfood uses), and pulp and paper manufacturing. In addition, they have been widely employed in many industrial processes as synthesis intermediates in the production of pesticides, herbicides, fungicides, insecticides, pharmaceuticals, and dyes. The presence of DCP and PCP have reported to induce VTG synthesis in fish at concentrations of  $1.0 \text{ mg}\cdot\text{L}^{-1}$  for 21-day exposure and  $200 \mu\text{g}\cdot\text{L}^{-1}$  for 28-day exposure, respectively, [60, 61]. PCP has also been demonstrated to affect pituitary function and the release of gonadotrophins in fish at concentration of  $750 \mu\text{g}\cdot\text{mL}^{-1}$  for 48-h exposure [62]. As for many other EDCs, longevity of exposure affects both the threshold and the magnitude of the response; PCP and DCP have shown bioconcentration factor values of  $(4.9 \pm 2.8) \times 10^3$  and  $(3.4 \pm 3.0) \times 10^2$ , respectively, at their low concentrations around  $\mu\text{g}\cdot\text{L}^{-1}$  [63].

### 3. Degradation of EDCs in Wastewater by $\text{TiO}_2$ Photocatalytic Reactions

**3.1. Titanium Dioxide Photocatalyst.** Titanium dioxide ( $\text{TiO}_2$ ), also known as titanium (IV) oxide or titania, is the naturally occurring oxide of titanium. In nature,  $\text{TiO}_2$  exists in three different polymorphs that are rutile, anatase, brookite.  $\text{TiO}_2$  is typically extracted from minerals

such as ilmenite, leucosene ores, or rutile beach sand and commercially produced using sulphate route—the ground slag or ilmenite is digested with strong sulphuric acid to produce titanium oxysulphate and iron sulphate. The titanium oxysulphate is then subjected to selective thermal hydrolysis to produce hydrated  $\text{TiO}_2$ . This is further washed and calcined to produce  $\text{TiO}_2$  (1) and chlorine route—rutile is converted to titanium tetrachloride by chlorination in the presence of petroleum coke. The titanium tetrachloride is then condensed to a liquid and reacted with hot oxygen to form  $\text{TiO}_2$  (2) [65, 66]:



In general,  $\text{TiO}_2$  structures of rutile, anatase, and brookite can be described in terms of ( $\text{TiO}_6$ ) octahedral. These three crystal structures differ from one another by the distortion of each octahedral and by the assembly patterns of the octahedral chains. Anatase is built up from octahedrals which are mainly connected by their vertices. Octahedral structures in rutile are mostly connected by the edges. Both vertical and edge connections are found in the octahedral structure of brookite [7, 67]. Even though both anatase and rutile are the same tetragonal system, anatase has longer vertical axis of the crystals than rutile. Meanwhile, brookite has an orthorhombic crystalline system (Figure 1). Among these crystal structures, only anatase and rutile are photocatalytically active. Moreover, rutile is the thermodynamically most stable phase of  $\text{TiO}_2$ . It is by about 1.2 to 2.8  $\text{kcal}\cdot\text{mol}^{-1}$  more stable than anatase with temperature ranges from 700 to 1000°C. Based on optical absorption spectra, 3.2 eV is the band gap energy of anatase and in rutile 3.0 eV is its energy, implying the rutile has an aggressive excitation of solar radiation [67, 68]. Calcinated  $\text{TiO}_2$ , especially in the rutile form, is very stable and insoluble in water; it is also insoluble or partly soluble in concentrated and hot acids.

According to historical documents,  $\text{TiO}_2$  was first discovered in the form of black sand in 1791 on the beaches of Cornwall, England, by William Gregor, who recognized the presence of a new element in ilmenite. The potential use of  $\text{TiO}_2$  was not established until earlier in the last century, when the Norwegian chemists, Jebsen and Farup, worked on  $\text{TiO}_2$  extraction from ilmenite. They revealed that the extracted  $\text{TiO}_2$  has a very high refractive index and thus, enabled its potential as a pigment. Independently of Jebsen and Farup, Rossi and Barton in the United States have also started with the extraction of  $\text{TiO}_2$  from minerals of ilmenite, titaniferous iron ores, and rutile their researches eventually led to the establishment of production site at Niagara Falls towards the end of the First World War. Until the turn of the 1930s, gradually growing of uncoated

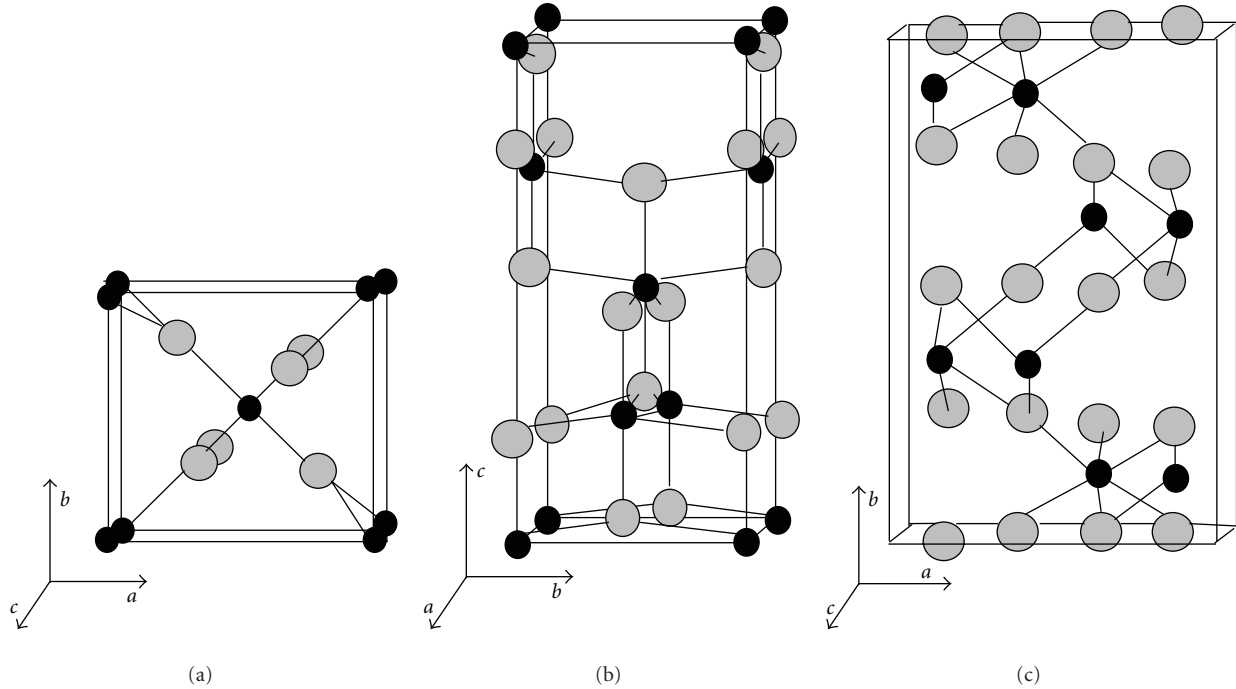


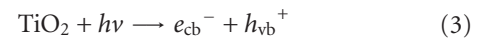
FIGURE 1: Crystal structures of rutile (a), anatase (b), and brookite (c) [7].

anatase and rutile pigments manufacturing activities have been evidenced, driving to the full scale of  $\text{TiO}_2$  production [65].

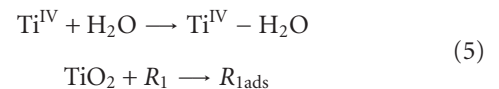
The revolution of  $\text{TiO}_2$  was started when Fujishima and Honda [71] discovered the possibility of water splitting by photochemical cell having an inert cathode and rutile  $\text{TiO}_2$  anode in 1972. This event marked the beginning of a new era in heterogeneous photocatalysis. As a consequence, the application of  $\text{TiO}_2$  photocatalysis extended to environmental frontiers. Frank and Bard [72] for the first time reported the possibilities of using  $\text{TiO}_2$  to degrade cyanide in aqueous medium under solar irradiation. Subsequent reports of photocatalytic reduction of  $\text{CO}_2$  by Inoue et al. [73] attracted more interest in  $\text{TiO}_2$  photocatalysis. In addition to environmental remediation,  $\text{TiO}_2$  is also an inorganic chemical widely used in paints, plastics, inks, paper, personal care products, and electronic components. These widespread applications of  $\text{TiO}_2$  are attributed to the stability of its chemical structure, biocompatibility, physical, optical, and electrical properties [74].

**3.2. Mechanism of  $\text{TiO}_2$  Photocatalysis.** Heterogeneous photocatalysis is an increase in the rate of a thermodynamically allowed ( $\Delta G < 0$ ) reaction in the presence of photocatalyst with the increase originating from the creation of some new reaction pathways involving photogenerated species and a decrease of the activation energy [67]. Generally, there are five essential key steps in the heterogeneous photocatalysis on the surface of  $\text{TiO}_2$ , namely, the (1) photoexcitation, (2) diffusion, (3) trapping, (4) recombination, and (5) oxidation [75–80].

**3.2.1. Photoexcitation.** Upon irradiation of  $\text{TiO}_2$  with light energy equivalent to or greater than its band gap energy, the electron is excited from the valence band (vb) to the conduction band (cb). Figure 2 illustrates the mechanism of electron-hole pair generation when the  $\text{TiO}_2$  particle is irradiated with sufficient light energy ( $h\nu$ ). The photoexcitation leaves behind a positive hole in the valence band and, therefore, creating the electron-hole pair:



**3.2.2. Diffusion.** In this step, water molecules ( $\text{H}_2\text{O}$ ) and organic pollutant (R) are diffused to the interface of  $\text{TiO}_2$  surface, forming spatial bonding with the  $\text{TiO}_2$  solid:



**3.2.3. Trapping.** Water molecules and hydroxyl ions ( $\text{OH}^-$ ) are available as electron donors and react with the photo-generated holes to form highly reactive and strong oxidizing hydroxyl radicals ( $\cdot\text{OH}$ ). On the contrary, oxygen molecules ( $\text{O}_2$ ) are efficient electron acceptors. Through the reduction of  $\text{O}_2$  with photogenerated electron, reactive superoxide radical anions ( $\text{O}_2^{\cdot-}$ ) are produced. This reaction would

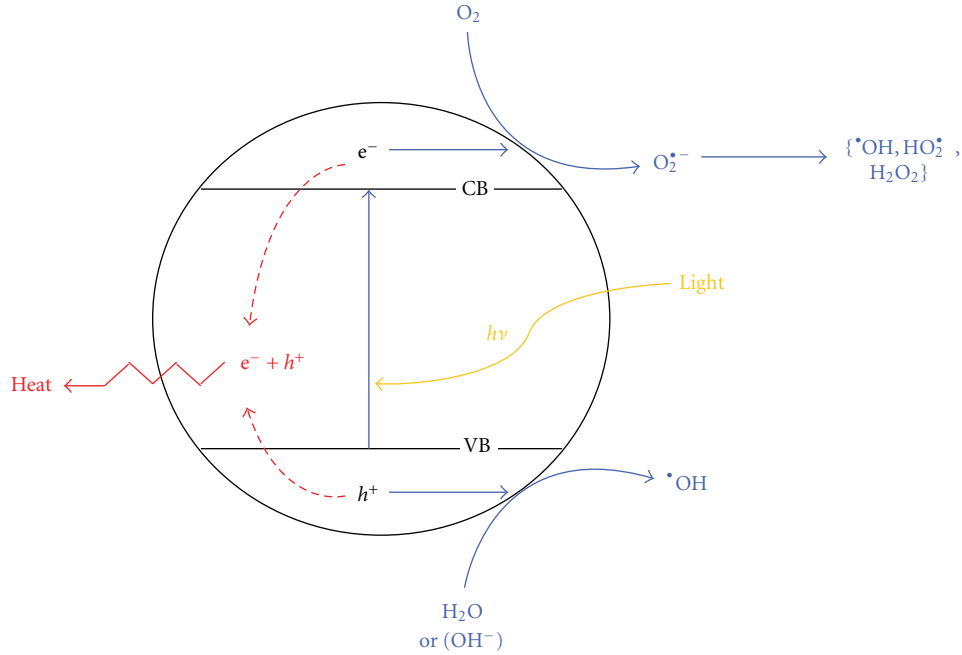
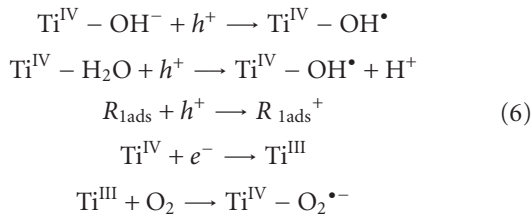


FIGURE 2: Schematic diagram illustrating the mechanism of photocatalysis on TiO<sub>2</sub> particles.

provide an additional pathway capable of totally mineralizing of the EDCs molecules:

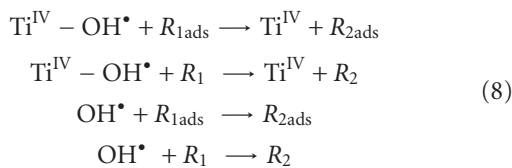


**3.2.4. Recombination.** In competition with charge transfer to diffused organic pollutants, there is the opportunity that both electron-hole pair recombination and trapped carrier recombination happen. These recombinations can occur either in the volume of the TiO<sub>2</sub> or on the surface of TiO<sub>2</sub>, liberating input energy as heat:

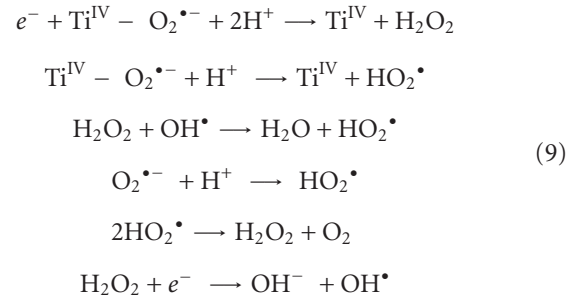


**3.2.5. Oxidation.** The resulted •OH radicals in the reacting system can initiate radical reactions, subsequently oxidizing the organic pollutants. Other radicals such as hydroperoxyl radicals (HO<sub>2</sub><sup>•</sup>) and hydrogen peroxide (H<sub>2</sub>O<sub>2</sub>) are also generated and involved in the reactions to degrade EDCs in water as follows.

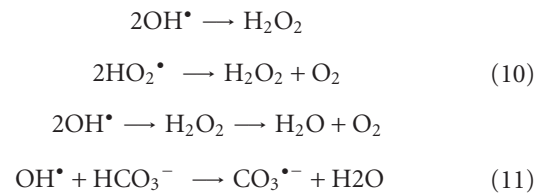
(i) Reaction with radical attack on organic pollutants:



(ii) Other reactions with radical:



(iii) Nonproductive radical reactions:



The primary photoreactions (3) to (11) reveal the indispensable role of charge carriers (electron-hole pair) in the TiO<sub>2</sub> photocatalysis. Essentially, •OH, HO<sub>2</sub><sup>•</sup>, and O<sub>2</sub><sup>•-</sup> radicals as well as photogenerated hole (h<sup>+</sup>) are highly reactive intermediates that will attack repeatedly in the reacting system and ultimately lead to complete mineralization of the EDCs. The mediation of radical oxidative species in the photocatalytic reaction has been evidenced by electron paramagnetic resonance spectroscopy (EPR) using spin trap such as 5,5-dimethylpyrroline-N-oxide (DMPO). This process led to the formation of a stable free radical whose EPR spectra was the characteristic of the trapped

$\cdot\text{OH}$  radical [81]. Another analysis of the  $\cdot\text{OH}$  radical formation on photocatalyst surface in solution has been performed through simple terephthalic acid-fluorescence (TA-FL) technique. Using this technique, the intensity of the peak attributed to 2-hydroxyterephthalic acid was known to be proportional to the amount of  $\cdot\text{OH}$  radicals formed [82, 83]. More recently, the  $\cdot\text{OH}$  radical produced on various photocatalysts has also been quantitatively investigated by Xiang et al. [84] via photoluminescence (PL) technique using coumarin (COU) as a probe molecule. Furthermore, electron spin resonance (ESR) has been used to study the radical oxidative species detection in solutions. This technique allowed to monitor the presence of  $\cdot\text{OH}$ ,  $\text{HO}_2\cdot$ , and  $\text{O}_2^{\cdot-}$  radicals in photocatalytic systems [18, 85–87].

#### 4. Degradation Pathways of Various EDCs

Photocatalytic degradation reactions of organic pollutants usually take more than one elementary step to complete. An intermediate is the reaction product of each of these steps which eventually forms the final product in the last step. The desired final products for a complete photocatalytic degradation reaction are  $\text{CO}_2$  and  $\text{H}_2\text{O}$ . Identification of these reaction intermediates would provide a further insight into the mechanism involved in the photocatalytic degradation process and will help to get a total picture of the degradation pathway. On this facet, the photocatalytic degradation schemes for some phthalates, bisphenol A, and chlorophenols suggested by researchers are given as below. For one thing, as to different types of organic pollutants, the degradation pathways are different. For another, as to a certain organic pollutant, the degradation pathway will be possibly different if different catalysts or different experiment conditions are applied.

##### 4.1. Phthalates

**4.1.1. Dimethyl Phthalate.** Ding et al. [18] studied the photocatalytic degradation pathway of dimethyl phthalate (DMP) using  $\text{TiO}_2$ -pillared montmorillonite as catalyst under UV irradiation. The photocatalytic degradation pathway of DMP is presented in Figure 3. By GC-MS analysis, a total of twelve products were detected from the photocatalytic degradation of DMP. In the first pathway,  $\cdot\text{OH}$  radicals added to the aromatic ring of the DMP and yielded hydroxylated DMP. With the further degradation of the intermediate, 2,3-dihydroxymethyl benzoate, 2,4-dihydroxymethyl benzoate and 2,6-dihydroxymethyl benzoate were observed. These three intermediates were reported to form by attack of another  $\cdot\text{OH}$  radical on different positions in the benzene ring and removal of an ester group from hydroxylated DMP at the same position. Moreover, these three intermediates were also formed by the double attack of  $\cdot\text{OH}$  radicals on the benzene ring of methyl benzoate. By ring-rupturing reactions, these aromatic intermediates were presumably further oxidized into aliphatic intermediates, such as 2,3-butanediol, 1,2-propanediol, and 1,2-glycol, and finally mineralized into  $\text{CO}_2$  and  $\text{H}_2\text{O}$ . In the second pathway, a carbonyl group

of DMP was excited after the photon absorption, and then cleavage of one C-C bond connecting the  $\text{COOCH}_3$  group to the aromatic ring occurred; in succession, methyl benzoate was generated. Subsequently with further single  $\beta$ -cleavage of the ester group, removal of a  $\cdot\text{CH}_3$  radical occurred, and benzoic acid with a carbonic acid ( $\text{COOH}$ ) structure was formed. The benzene ring of benzoic acid was demonstrated to attack by  $\cdot\text{CH}_3$  or  $\cdot\text{OH}$  radicals alternatively generated 2,3-dimethyl-benzoic acid and 2-hydroxybenzoic acid, respectively. The resulting intermediate of 2,3-dimethyl-benzoic acid further decomposed completely into  $\text{CO}_2$  and  $\text{H}_2\text{O}$ , while 2-hydroxybenzoic acid followed by a ring-cleaving process to give rise to 2-hydroxy-3-methylbutyric acid, which oxidized also into  $\text{CO}_2$  and  $\text{H}_2\text{O}$  at last.

**4.1.2. 1,2-Diethyl Phthalate.** Muneer et al. [53] identified the intermediates and degradation pathway of 1,2-diethyl phthalate (DEP) in aqueous suspensions of  $\text{TiO}_2$  through GC-MS analysis. A proposed degradation pathway of DEP is shown in Figure 4. The GC-MS analysis of DEP at 195-min irradiated mixture showed the formation of three photoproducts  $\text{C}_{12}\text{H}_{16}\text{O}_5$ ,  $\text{C}_8\text{H}_4\text{O}_3$ , and  $\text{C}_{10}\text{H}_{10}\text{O}_4$  appearing at reaction times of 15.4, 16.8, and 26.8 min, respectively.

**4.1.3. Dibutyl Phthalate.** Xu et al. [64] investigated the photocatalytic degradation of dibutyl phthalate (DBP) catalyzed by polyoxotungstate/ $\text{TiO}_2$  nanocomposites under simulated solar irradiation. The photocatalytic degradation intermediates and pathway are shown in Figure 5. Their findings revealed that DBP ( $\text{C}_{16}\text{H}_{22}\text{O}_4$ ) was attacked by  $\cdot\text{OH}$  radicals at aromatic ring and aliphatic chain to produce three different hydroxylated intermediate isomers of  $\text{C}_{16}\text{H}_{22}\text{O}_5$  ((a), (b), and (c)). Under the oxidation of  $\cdot\text{OH}$  radicals, isomers (a) and (b) lost butoxy groups to produce different isomers of  $\text{C}_8\text{H}_6\text{O}_5$  ((e) and (f), resp.). Meanwhile, isomer (c) was converted to aldehyde of  $\text{C}_{16}\text{H}_{20}\text{O}_5$  (g).  $\text{C}_{12}\text{H}_{14}\text{O}_4$  (d) was formed by the cleavage of the alkyl-oxygen bond of DBP. Decarboxylation from intermediates (d) to (f) resulted in  $\text{C}_{11}\text{H}_{14}\text{O}_2$  (h) and  $\text{C}_7\text{H}_6\text{O}_2$  (i). In addition, cleavage of alkyl-oxygen bond in  $\text{C}_{11}\text{H}_{14}\text{O}_2$  (h) also generated  $\text{C}_7\text{H}_6\text{O}_2$  (i). With a further decarboxylation from  $\text{C}_7\text{H}_6\text{O}_2$  (i), dihydroxybenzene and; quinone, were stated to form. Quinone was further oxidized, and thereby ring-opening reaction happened, leading to a series of aliphatic acids including butanedioic acid, formic acid, and acetic acid. Additionally, when  $\cdot\text{OH}$  radicals attacked directly two carbon atoms in  $\alpha$ -position of DBP, both of the positions were broken into a long chain structure of  $\text{C}_{11}\text{H}_{16}\text{O}_2$  (j). In the end, all the intermediates were mineralized to  $\text{CO}_2$  and  $\text{H}_2\text{O}$ .

**4.1.4. n-Butyl Benzyl Phthalate.** Xu et al. [69] examined the photocatalytic degradation of n-butyl benzyl phthalate (BBP) using  $\text{TiO}_2$  as catalyst under UV light irradiation. With the identification of intermediates, a proposed pathway of the photocatalytic degradation of BBP is presented in Figure 6. The results in their investigation showed that monobutyl phthalate, monobenzyl phthalate, and phthalic acid were the main intermediates of BBP degradation. The

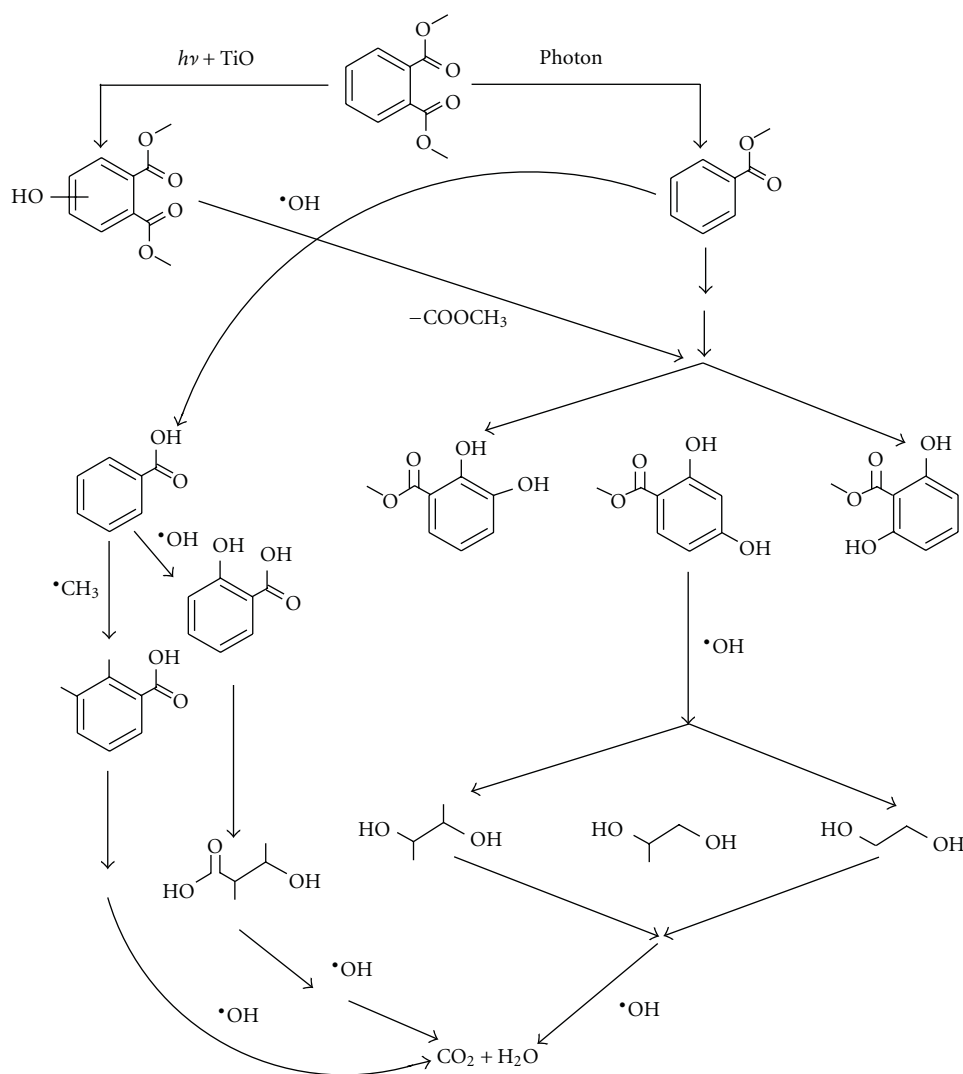


FIGURE 3: Photocatalytic degradation scheme for DMP [18].

formation of these three intermediates involved the electron transfer reactions and reactions with  $\cdot\text{OH}$  radicals. The BBP upon the transfer of an electron was reported to form a radical anion, which was further attacked by  $\cdot\text{OH}$  radicals forming the anionic species. By the loss of a butanol or benzyl alcohol, the species were converted to monobutyl phthalate and monobenzyl phthalate. Under the actions of electrons and then  $\cdot\text{OH}$  radicals, both monobutyl phthalate and monobenzyl phthalate were converted to phthalic acid.

**4.1.5. Di(2-ethylhexyl)phthalate.** Chung and Chen [70] studied the degradation of di(2-ethylhexyl)phthalate (DEHP) by  $\text{TiO}_2$  photocatalysis. The possible degradation pathway of DEHP is demonstrated in Figure 7. In their photocatalytic degradation process,  $\cdot\text{OH}$  and  $\cdot\text{H}$  radicals initially attacked the aliphatic chain of DEHP and yielded the intermediates such as benzoic acid, phthalic acid, 2-(butoxycarbonyl)benzoic acid, mono (2-ethylhexyl)phthalate, octyl 4-hydroxybenzoate, and 2-[(octyloxy)carbonyl]benzoic acid. With a further attack from the reactive

radicals, the aromatic opened products were formed and finally mineralized to final products of  $\text{CO}_2$  and  $\text{H}_2\text{O}$ .

**4.2. Bisphenol A.** Tao et al. [88] tested the photocatalytic degradation of bisphenol A (BPA) using  $\text{TiO}_2$ -loaded mesoporous MCM-41 under UV irradiation ( $\lambda = 365.0\text{--}366.3\text{ nm}$ ). Through the GC-MS analysis, the photocatalytic degradation intermediates and the pathway of bisphenol A are shown in Figure 8. Their results noticed that 4-(1-hydroxy-1-methyl-ethyl)-phenol (HMEP) and phenol were initially produced via the photocleavage of phenyl groups by  $\cdot\text{OH}$  radicals attack. 4-vinyl phenol was then generated by dehydration from HMEP and subsequently oxidized to 4-hydroxyacetophenone. Additionally, 2-methyl-2,3-dihydrobenzofuran was reported to be produced from phenol. These single aromatic intermediates were further oxidized through ring rupturing reactions into aliphatic intermediates containing  $\text{C}_4\text{H}_{10}\text{O}$ ,  $\text{C}_5\text{H}_{10}\text{O}$ , and  $\text{C}_6\text{H}_{14}\text{O}_2$ , which were mineralized into  $\text{CO}_2$  and  $\text{H}_2\text{O}$  ultimately.

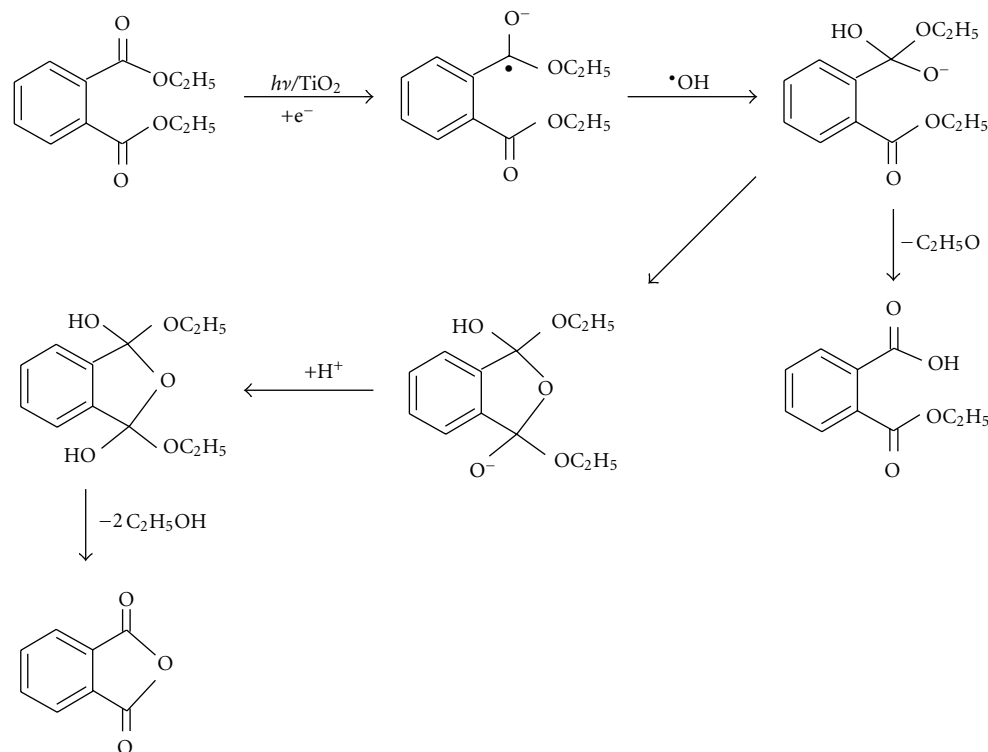


FIGURE 4: Photocatalytic degradation scheme for DEP [53].

### 4.3. Chlorophenols

**4.3.1. 2,4-Dichlorophenol.** Zang et al. [89] investigated the photocatalytic degradation of 2,4-dichlorophenol (DCP) catalyzed by  $\text{TiO}_2$  suspensions. The proposed photocatalytic degradation pathway of DCP is presented in Figure 9. Their study noted that DCP was firstly converted to chlorohydroquinone, which was converted to chlorobenzoquinone and hydroxybenzoquinone. Then, hydroxybenzoquinone was reported to convert into acidic intermediates. Subsequently, the formed acidic intermediates were oxidized to final products of  $\text{CO}_2$  and  $\text{H}_2\text{O}$ .

**4.3.2. Pentachlorophenol.** Jung et al. [90] studied the photocatalytic degradation of pentachlorophenol (PCP) using  $\text{TiO}_2$  thin films coated on stainless steel cloth. The photocatalytic degradation pathway of PCP is shown in Figure 10. In the primary photocatalytic degradation process,  $\cdot\text{OH}$  radicals attacked the PCP and yielded intermediates such as tetrachlorocatechol, tetrachlorohydroquinone, and tetrachlororesorcinol. With the further degradation of the intermediates, 1,2,4,5-tetrachloro-*p*-benzoquinone, 1-hydro-2,4,5-trichloro-*p*-benzoquinone, and hydroxyhydroquinone were formed. Eventually, an oxidative aromatic ring-opening reaction happened and rendered the formation of short-chain carboxylic acids, such as tartaric, oxalic, malic, hydroxymalonic, and glycolic, followed by oxidation to  $\text{CO}_2$ .

## 5. Operating Parameters in Photocatalytic Processes

The rate and efficiency of a photocatalytic reaction depends on a number of operating parameters that govern the degradation of EDCs in wastewater such as light intensity and wavelength, initial substrate concentration, catalyst loading, solution pH, reaction temperature, and dissolved oxygen.

**5.1. Effect of Light Intensity and Wavelength.** Light irradiation plays a significantly important role in all of photocatalytic reactions and generates the photons required for the electron transfer from the valence band to the conduction band of a semiconductor photocatalyst. The energy of a photon is related to its wavelength, and the overall energy input to the photocatalytic process is dependent on the light intensity. Therefore, the effects of both intensity and wavelength have been studied in numerous investigations for various organic pollutants including phthalates, bisphenol A, and chlorophenols. It has been reported that at low light intensity (catalyst dependent, surface reaction limited) the rate was linearly proportional to the light intensity, while at medium-high intensity, the rate became proportional to the square root of the light intensity, and, at higher light intensity, the rate was independent of the light intensity [91–93]. This variation is likely due to the recombination of photogenerated electron-hole pairs under different irradiation intensities. Huang and

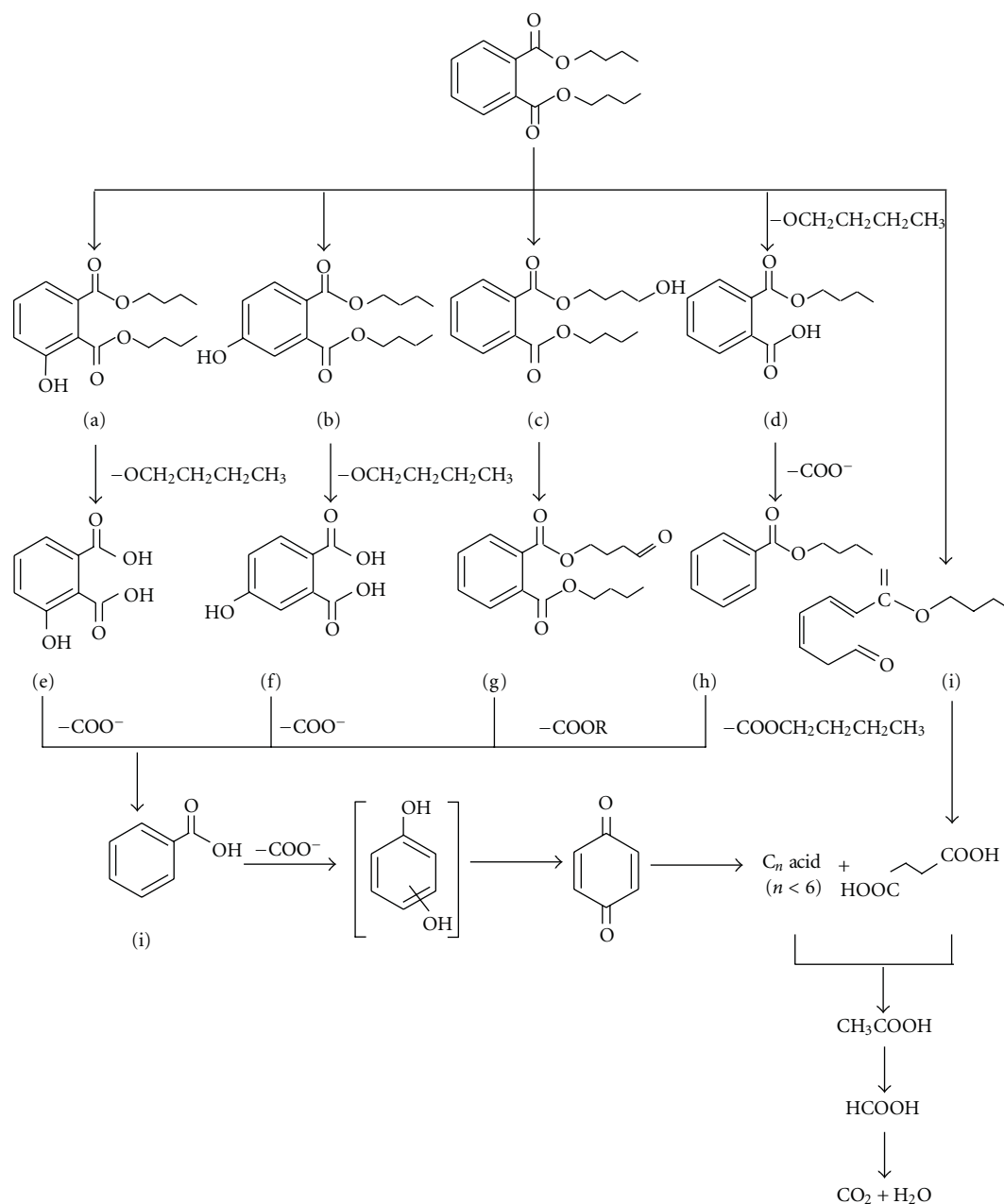


FIGURE 5: Photocatalytic degradation scheme for DBP [64].

Chen [94] examined the effect of light intensity on the photocatalytic degradation of diethyl phthalate (DEP) using TiO<sub>2</sub> as catalyst. The degradation efficiency of DEP was observed to increase linearly with UV radiation intensity up to  $2.50 \times 10^{-6}$  Einstein·l<sup>-1</sup>·s<sup>-1</sup> and then only smaller changes when the light intensity increased from  $2.50 \times 10^{-6}$  to  $4.00 \times 10^{-6}$  Einstein·l<sup>-1</sup>·s<sup>-1</sup>. Their study explained that, at lower UV intensity, the photocatalytic degradation was limited. As the UV intensity increased, more •OH radicals were formed, thus, resulted in the increase of DEP degradation. Above certain UV intensity, the reaction rate went from first order of pollutant concentration to one-half order. Bayarri et al. [95] compared the degradation and mineralization

efficiencies of 2,4-dichlorophenol (DCP) using lamps of UV-A and UV-ABC over TiO<sub>2</sub>. The degradation and mineralization efficiencies using UV-ABC were reported to be more efficient than using UV-A. This improvement was related to the combined use of photolysis, photocatalysis, and synergistic effects due to associated photolysis and photocatalysis. Chan et al. [96] tested the effect of UV intensity on the photocatalytic degradation of di(2-ethylhexyl)phthalate (DEHP), and the TiO<sub>2</sub> degradation efficiency increased rapidly from 0 to about 40% with increasing of light intensity from 0 to  $8.4 \text{ W} \cdot \text{m}^{-2}$ . After that, the increase in degradation efficiency gradually slowed and reached a maximum of about 72% at  $33.6 \text{ W} \cdot \text{m}^{-2}$ . The influence of

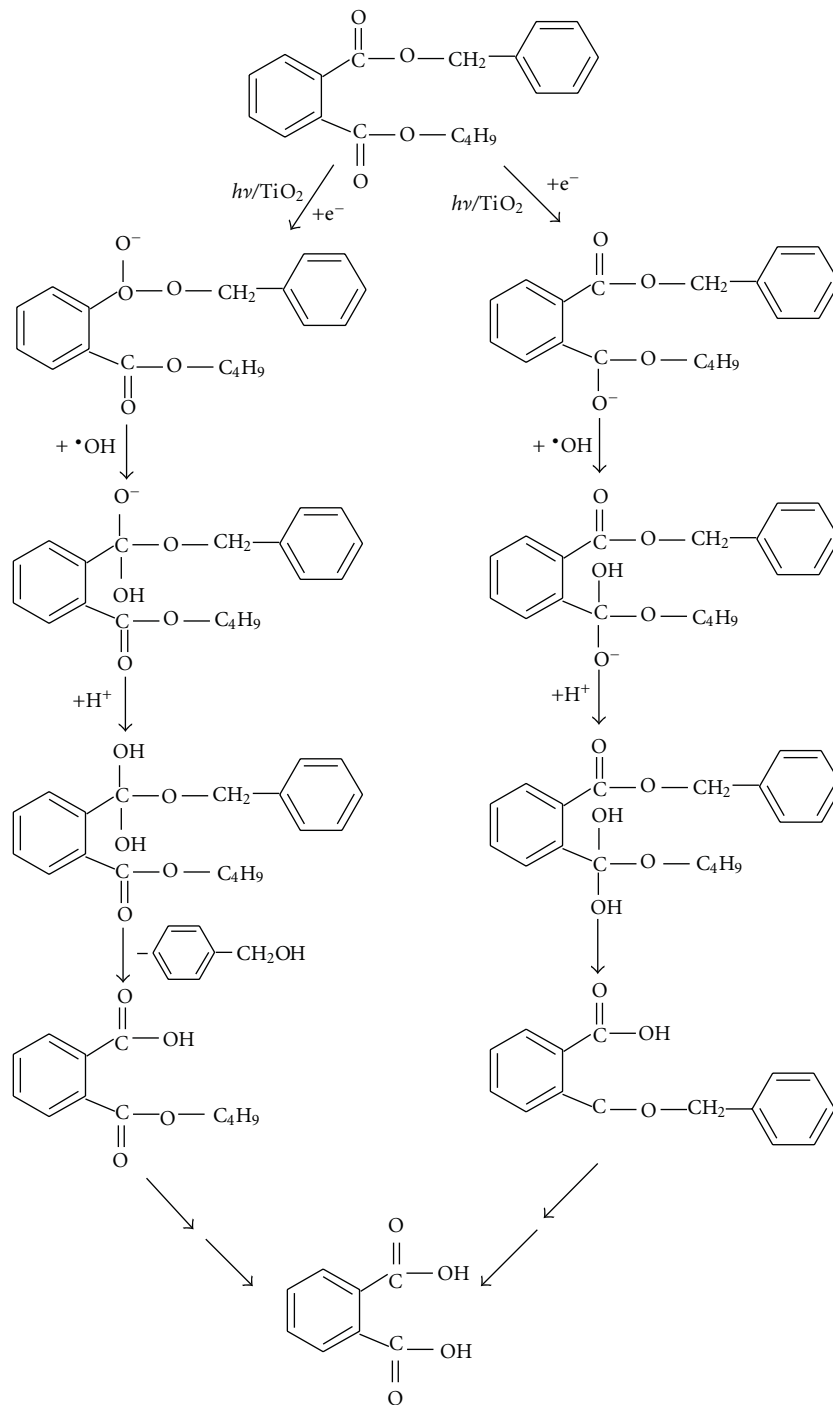


FIGURE 6: Photocatalytic degradation scheme for BBP [69].

light intensity on the photocatalytic degradation of bisphenol A has also been studied over TiO<sub>2</sub> suspension [97]. The degradation efficiency was reported to increase rapidly in the light intensity up to 0.35 mW·cm<sup>-2</sup>, and then the efficiency increased gradually. Lee et al. [98] investigated the effect of light intensity on the photocatalytic degradation of bisphenol A over immobilized TiO<sub>2</sub> by turning on different number of UV lamps ( $\lambda = 365$  nm). The results in their work indicated that the degradation rate constant increased from

0.27 to 0.77 h<sup>-1</sup> as the number of the UV lamps increased from 1 to 6. They went further to measure the photon rate of UV lamp and found that the rates were 2.8, 10.1 and 18.3  $\mu\text{E}\cdot\text{s}^{-1}$ ; respectively, as 1, 3, and 6 UV lamps were used in the reactor. The enhanced degradation rate was related to the increase of photon rate. Using TiO<sub>2</sub> as catalyst, Minero et al. [99] examined the effect of solar irradiation intensity on the photocatalytic degradation of pentachlorophenol (PCP). Their findings revealed that the PCP degradation and

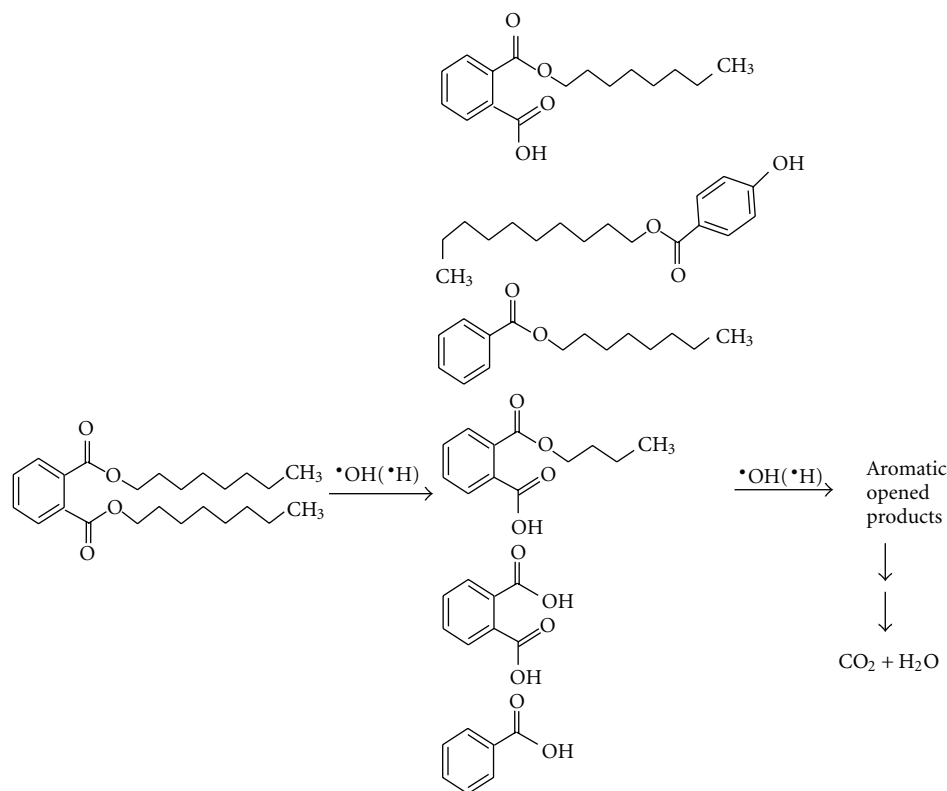


FIGURE 7: Photocatalytic degradation scheme for DEHP [70].

TOC disappearance rates increased linearly with increasing the solar light intensity. The effects of light intensity and wavelength on the photocatalytic activity of immobilized  $\text{TiO}_2$  have also been investigated on the degradation of bisphenol A (BPA) [100]. In their work, three different light sources: germicidal lamp ( $\lambda = 254 \text{ nm}$ ), blacklight lamp ( $\lambda = 360 \text{ nm}$ ), and vita-lite lamp (visible region) were used to study the effect of light wavelength. The used of both UV lamps was shown to have higher efficiency for the degradation of BPA. The degradation rate constants were reported to be  $0.00111 \text{ min}^{-1}$  and  $0.0067 \text{ min}^{-1}$  for germicidal lamp and black-light lamp, respectively, compared to  $0.0012 \text{ min}^{-1}$  for vita-lite lamp. This effect was ascribed to the insufficient energy of visible lamp to induce the photocatalytic degradation of BPA. On the other hand, the degradation of BPA was accelerated using the germicidal lamp at different light intensities. The degradation rate constant was noticed to increase from  $0.0111$  to  $0.0268 \text{ min}^{-1}$  as the light intensity increased from  $2$  to  $6 \text{ W}\cdot\text{L}^{-1}$ . Liao and Wang [101] also observed an enhancement of dimethyl phthalate (DMP) degradation with increasing the UV light intensity. The enhanced degradation efficiency was attributed to the higher light intensity provided more light energy for the breaking of chemical bonds of DMP, and the reactions between the light and the  $\text{TiO}_2$  catalyst improved the generation of  $\bullet\text{OH}$  radicals in the solution.

**5.2. Effect of Initial Substrate Concentration.** Due to the fact that, as the concentration of model pollutant increases, more

and more molecules of the organic compound get adsorbed on the surface of the photocatalyst, the initial substrate concentration can influence the extent of reaction rate at the surface of the photocatalyst. Table 1 summarizes a variety of EDCs studied under various initial concentrations. Kuvuran et al. [102] examined the effect of initial concentration on the photocatalytic degradation of 2,4-dichlorophenol (DCP) using UV/ $\text{TiO}_2$ . Increase in the DCP concentration from  $0.1$  to  $0.5 \text{ mM}$  decreased the degradation rate constant,  $k_{\text{obs}}$ , from  $0.0259$  to  $0.0061 \text{ min}^{-1}$ . Tsai et al. [20] found that the degradation efficiency of bisphenol A (BPA) was strongly dependent on the initial substrate concentration. The degradation efficiency of BPA over  $\text{TiO}_2$  suspension decreased gradually, ranging from  $100\%$  to  $97\%$  as the initial substrate concentration increased from  $1$  to  $20 \text{ mg}\cdot\text{L}^{-1}$ . Nevertheless, the BPA concentration increased from  $20$  to  $50 \text{ mg}\cdot\text{L}^{-1}$ ; the degradation efficiency showed a significant decreasing trend, ranging from  $97\%$  to  $67\%$ . Jung et al. [90] investigated the effect of initial concentration in the range of  $2.5$  to  $10 \text{ mg}\cdot\text{L}^{-1}$  on the photocatalytic degradation of pentachlorophenol (PCP) using  $\text{TiO}_2$  thin films coated on stainless steel cloth. Maximum PCP degradation was observed at  $2.5 \text{ mg}\cdot\text{L}^{-1}$ . Chung and Chen [70] conducted the  $\text{TiO}_2$  photocatalytic experiment at different di(2-ethylhexyl)phthalate (DEHP) concentrations ranged from  $25$  to  $300 \text{ }\mu\text{g}\cdot\text{L}^{-1}$ . Their results showed that the degradation efficiency decreased with the increased concentration of DEHP. This was attributed to the rise of internal optical density, which caused the solution became impermeable to UV light. Thiruvengkatachari et al.

TABLE 1: Effect of initial substrate concentration on the photocatalytic degradation of various EDCs.

Organic pollutant	Light source	Photocatalyst	Tested initial concentration (mg·L <sup>-1</sup> )	Optimum initial concentration (mg·L <sup>-1</sup> )	Reference
Di- <i>n</i> -butyl phthalate	UV	TiO <sub>2</sub> /glass beads	2.5–12.5	2.5	Chiou et al. [105]
2,4-Dichlorophenol	UV	Ti-GAC	15.3–33.2	15.3	Gu et al. [106]
Bisphenol A	Solar	TiO <sub>2</sub> /Ti	0.15–0.60	0.30	Daskalaki et al. [107]
Bisphenol A	Solar	TiO <sub>2</sub> -P25/Ti	0.15–0.60	0.15	Daskalaki et al. [107]
Bisphenol A	UV	Zr/TiO <sub>2</sub>	15–60	15	Gao et al. [108]
<i>n</i> -Butyl benzyl phthalate	UV	TiO <sub>2</sub>	0.5–2.5	0.5	Xu et al. [69]
2,4-Dichlorophenol	Visible	TiO <sub>2</sub> /porphyrin	10–100	10	Chang et al. [109]
Bisphenol A	UV	TiO <sub>2</sub>	5–20	5	Wang et al. [110]
Pentachlorophenol	UV	TiO <sub>2</sub> /SS	2.5–10	2.5	Jung et al. [90]
Bisphenol A	UV	TiO <sub>2</sub> /PF	10–50	10	Wang et al. [104]
Di(2-ethylhexyl)phthalate	UV	TiO <sub>2</sub>	0.025–0.3	0.025	Chung and Chen [70]
Dimethyl phthalate	UV	TiO <sub>2</sub>	5–80	5	Liao and Wang [101]

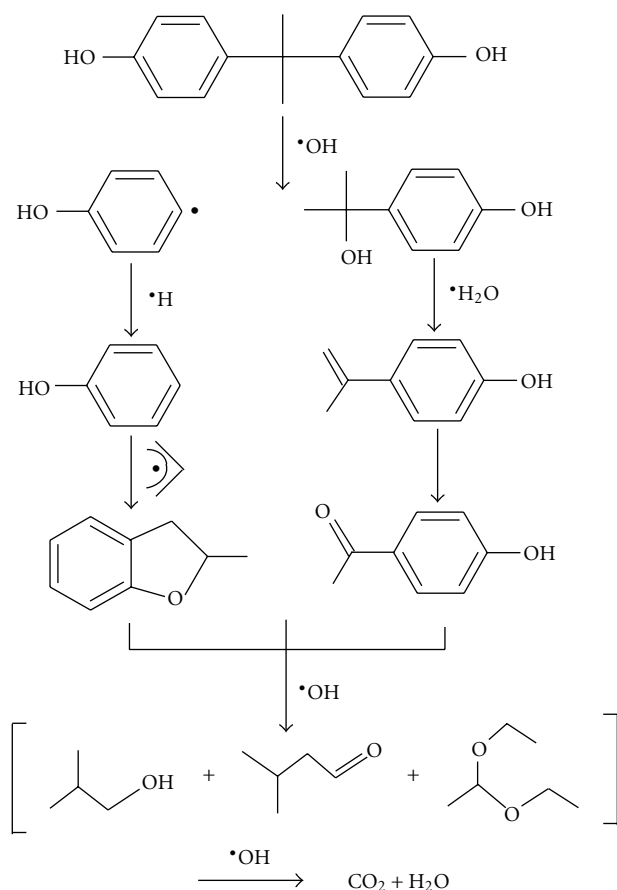


FIGURE 8: Photocatalytic degradation scheme for BPA [88].

[103] investigated the effect of initial concentration on the photocatalytic degradation of bisphenol A (BPA) in the presence of TiO<sub>2</sub>. After 10 h of UV irradiation, degradation efficiencies of 78%, 55%, and 30% were obtained for initial BPA concentration of 10, 50 and, 100 mg·L<sup>-1</sup>, respectively.

The effect of initial concentration on the bisphenol (BPA) degradation has also been investigated by employing immobilized TiO<sub>2</sub> as catalyst [104]. Under the conditions tested, the highest BPA degradation rate was achieved when the BPA initial concentration was 10 mg·L<sup>-1</sup>. The BPA degradation rate after 10 h of reaction time decreased when the initial BPA concentration increased from 10 to 50 mg·L<sup>-1</sup>. At higher initial concentration, the accumulation of BPA molecules in the inner layer spacing on the TiO<sub>2</sub> surface resulted in the adsorption competition for active sites between BPA molecules, which thereby decreased the amount of reactive •OH radicals attacking BPA molecules. This led to a decrease in BPA degradation.

Using TiO<sub>2</sub>/glass beads, Chiou et al. [105] studied the effect of initial concentration on the photocatalytic degradation of di-*n*-butyl phthalate (DBP) under UV light irradiation ( $\lambda = 365$  nm). The degradation efficiency was found to decrease as the initial DBP concentration increased. The degradation process followed a pseudo-first-order reaction. The observed rate constant was shown to vary from 0.0188 to 0.0130 min<sup>-1</sup> as the DBP concentration increased from 2.5 to 12.5 mg·L<sup>-1</sup>. Muneer et al. [53] studied the effect of substrate concentration (0.1–1.0 mM) on the photocatalytic degradation of 1,2-diethyl phthalate (DEP) using Degussa P25 and Hombikat UV 100. The photonic efficiencies for both employed photocatalysts increased as the initial concentration of DEP increased up to 0.25 mM and then decreased. In the presence of Zr/TiO<sub>2</sub>, Gao et al. [108] considered the influence of initial concentration on the photocatalytic degradation of bisphenol A (BPA) over the concentration ranged from 15 to 60 mg·L<sup>-1</sup>. The degradation rates were high at lower concentration range and then decreased with increasing the BPA's initial concentration. The degradation was observed to fit well with the pseudo-first-order kinetic model. Tatti et al. [111] studied the effect of initial concentration on the photocatalytic mineralization of 2,4-dichlorophenol and pentachlorophenol over immobilized TiO<sub>2</sub>. In their study, both chlorinated

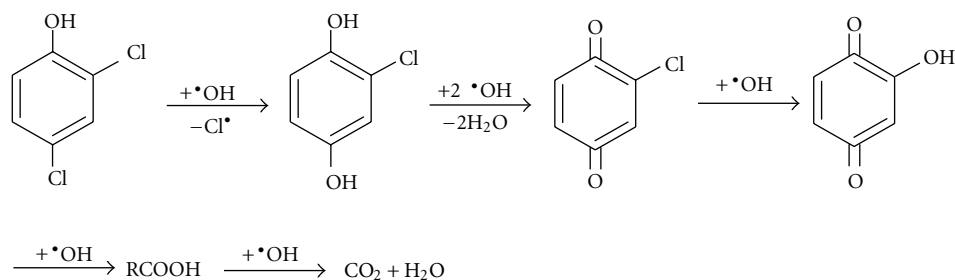


FIGURE 9: Photocatalytic degradation scheme for DCP [89].

phenol concentrations were varied in the range of  $9.9 \times 10^{-4}$  to  $3.8 \times 10^{-5}$  M. The degradation rates of the chlorinated phenols were observed to decrease linearly with the increase in the initial concentration. Using  $\text{TiO}_2$  supported on GAC, Gu et al. [106] reported that the degradation efficiency of 2,4-dichlorophenol (DCP) decreased from 100% to 70.2% with initial concentration increasing from 15.3 to  $33.2 \text{ mg} \cdot \text{L}^{-1}$ . This was ascribed to that increase of the DCP concentration can decrease the path length of photons entering the reaction solution, resulting in weak photons absorption on the surface of supported  $\text{TiO}_2$ . Thus, the DCP degradation decreased. As shown in many literature reports, the initial substrate concentration dependence of the degradation rate of organic pollutant can be realized by the fact that the photocatalytic reaction occurs on  $\text{TiO}_2$  particles as well as in solution. On the surface of  $\text{TiO}_2$  particles, the reaction occurs between the  $\cdot\text{OH}$  radicals generated at the active  $\text{OH}^-$  sites and organic molecules from the solution. When the initial substrate concentration is high, the number of these available active sites is reduced by organic molecules because of their competitive adsorption onto  $\text{TiO}_2$  surface. Since the intensity of light and the irradiation time are constant, the  $\cdot\text{OH}$  radicals formed on the surface of  $\text{TiO}_2$  remained practically the same. Thus, the active  $\cdot\text{OH}$  radicals attacking the organic pollutants decreased due to the lower ratio of the  $\cdot\text{OH}/\text{organic pollutant}$ . In addition, a significant amount of light may also be absorbed by the organic molecules rather than the  $\text{TiO}_2$  at a higher initial substrate concentration. This condition can be ascribed to the increase in the initial concentration, led to less photons reached to the  $\text{TiO}_2$  surface, and resulted in a slower production of  $\cdot\text{OH}$  radicals. Consequently, the degradation rate is decreased, since fewer  $\cdot\text{OH}$  radicals are available to degrade more organic molecules. Furthermore, the formation of intermediates during the photocatalytic reaction of target pollutant also affected the reaction rate. The generated intermediates may compete with the organic molecules for the limited adsorption and active sites on  $\text{TiO}_2$  surface. According to several authors [112–116], this competition could be more marked in the presence of a high concentration level of reaction intermediates produced by the degradation of higher initial substrate concentration.

**5.3. Effect of Catalyst Loading.** It is well documented that the rate and efficiency of photocatalytic degradation would increase with catalyst loading. The increase in the efficiency seems to be due to the effective surface area of catalyst

and the absorption of light. At lower catalyst loading, the absorption of light controlled the photocatalytic process due to the limited catalyst surface area. However, as the catalyst loading increased, an increase in the active surface area of  $\text{TiO}_2$  is obtained. The enlarged amount of photons absorbed and the amount of organic pollutants adsorbed on the  $\text{TiO}_2$  surface improved the photocatalytic degradation. When the  $\text{TiO}_2$  loading is overloaded nevertheless, owing to an increase in the particles aggregation, the surface that absorbed the photons is not increasing in a geometrical ratio [104]. In addition, the number of active sites on the  $\text{TiO}_2$  surface also decreased because of the decrease in light penetration due to light-scattering effect with an increase of the turbidity of the suspension and leading to the shrinking of the effective photoactivated volume of suspension. The integration of these two reasons resulted in a reduced performance of photocatalytic activity rather than the linearly increased with the overloaded catalyst. Hence, many researchers have verified that there was an optimum amount of catalyst loading in the photocatalysis studies [74, 92, 117–119]. Table 2 lists the effect of catalyst loading on the photocatalytic degradation of various EDCs in numerous studies. Kuo and Lin [120] studied the effect of catalyst concentration ( $0.5\text{--}3.0 \text{ g} \cdot \text{L}^{-1}$ ) on the photocatalytic degradation of bisphenol A (BPA) irradiated using UV lamp. Their results showed that the photocatalytic degradation rate of BPA increased linearly with  $\text{TiO}_2$  concentration up to  $2 \text{ g} \cdot \text{L}^{-1}$  and then decreased due to the reduction of UV light penetration. Chan et al. [96] observed that the degradation efficiency of di(2-ethylhexyl)phthalate (DEHP) increased gradually from 8.64% to 69.87% as the concentration of  $\text{TiO}_2$  increased from 0 to  $150 \text{ mg} \cdot \text{L}^{-1}$ . However, further increase in the catalyst concentration from 150 to  $400 \text{ mg} \cdot \text{L}^{-1}$  resulted in a decrease in the degradation efficiency from 69.87% to 55.87%. Xu et al. [69] examined the effect of  $\text{TiO}_2$  dosage ( $0\text{--}5 \text{ g} \cdot \text{L}^{-1}$ ) on the photocatalytic degradation of *n*-butyl benzyl phthalate (BBP) over  $\text{TiO}_2$  suspension. After 2 h of UV irradiation, the highest degradation efficiency of BBP was achieved at the concentration of  $2 \text{ g} \cdot \text{L}^{-1}$ .

Chung and Chen [70] carried out a series of experiments to assess the optimum  $\text{TiO}_2$  catalyst loading by varying the amount of catalyst from 0 to  $500 \mu\text{g} \cdot \text{L}^{-1}$  in the di(2-ethylhexyl)phthalate (DEHP) solution. As the amount of  $\text{TiO}_2$  increased, the total surface area for the photocatalytic reaction was also reported to be increased. Therefore, the DEHP degradation was improved. Further increase in the

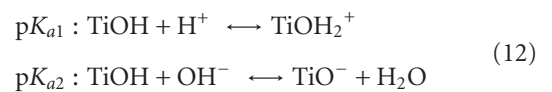
TABLE 2: Effect of catalyst loading on the photocatalytic degradation of various EDCs.

Organic pollutant	Light source	Photocatalyst	Tested catalyst concentration ( $\text{g}\cdot\text{L}^{-1}$ )	Optimum catalyst concentration ( $\text{g}\cdot\text{L}^{-1}$ )	Reference
Di(2-ethylhexyl)phthalate	UV	TiO <sub>2</sub>	0–0.0005	0.0001	Chung and Chen [70]
Bisphenol A	Solar	TiO <sub>2</sub>	0–20.0	10.0	Kaneco et al. [97]
Bisphenol A	UV	TiO <sub>2</sub>	0–3.0	0.5	Tsai et al. [20]
2,4-Dichlorophenol	UV	Ti-GAC	5.0–9.0	9.0	Gu et al. [106]
1,2-Diethyl phthalate	UV	TiO <sub>2</sub>	0–5.0	1.0	Muneer et al. [53]
Pentachlorophenol	UV	TiO <sub>2</sub> /SS	0–20.4	10.1	Jung et al. [90]
<i>n</i> -Butyl benzyl phthalate	UV	TiO <sub>2</sub>	0–5.0	2.0	Xu et al. [69]
Bisphenol A	UV	Ti-MCM-41	0–0.2	0.1	Tao et al. [88]
2,4-Dichlorophenol	UV	TiO <sub>2</sub>	0–2.0	0.5	Bayarri et al. [121]
Dibutyl phthalate	UV	TiO <sub>2</sub>	0.001–0.005	0.005	Bajt et al. [122]
Diethyl phthalate	UV	TiO <sub>2</sub>	0.04–0.4	0.2	Huang and Chen [94]

amount of catalyst showed a negative effect. Under the conditions investigated, the maximum degradation was noticed at  $100 \mu\text{g}\cdot\text{L}^{-1}$  of TiO<sub>2</sub>. The decrease in degradation above  $100 \mu\text{g}\cdot\text{L}^{-1}$  was ascribed to the saturation of the catalyst surface area and scattering of light. Kaneco et al. [123] indicated that the degradation of di-*n*-butyl phthalate (DBP) (0–30 mg) increased with catalyst amount up to 5 mg. Then, the degradation efficiency decreased slightly and became nearly constant when the TiO<sub>2</sub> was higher than 10 mg. An increase in the amount of catalyst provided greater number of active sites available for DBP adsorption, however, the simultaneous increase in the light scattering and agglomeration of free catalyst particles hindered the degradation of DBP. Consistent trend of results has also been observed on the solar photocatalytic degradation of bisphenol A (BPA) using TiO<sub>2</sub> as a catalyst [97]. The degradation efficiency was found to increase with increasing catalyst content up to a level of 500 mg, and, thereafter, the efficiency was nearly constant. The photocatalytic degradation of  $2.5 \text{ mg}\cdot\text{L}^{-1}$  pentachlorophenol (PCP) for different concentrations of TiO<sub>2</sub> thin film coated on the surface of stainless steel cloth has also been investigated [90]. The results showed that the PCP degradation followed the order of  $2\% \text{ (w}\cdot\text{w}^{-1}) \text{ TiO}_2 \geq 1\% \text{ TiO}_2 > 0.5\% \text{ TiO}_2 > 0.1\% \text{ TiO}_2$ . Since the change of catalyst concentration from 1% to 2%  $\text{w}\cdot\text{w}^{-1}$  did not have much effect on the PCP degradation efficiency, they suggested that 1%  $\text{w}\cdot\text{w}^{-1}$  TiO<sub>2</sub> was the optimal catalyst concentration for the photocatalytic degradation of PCP. Using the TiO<sub>2</sub> loaded on MCM-41, Tao et al. [88] studied the effect of catalyst loading ranging from 0 to 0.2 g on the photocatalytic degradation of bisphenol A (BPA). Their findings demonstrated that the BPA degradation efficiency increased as the catalyst loading increased from 0 to 0.1 g. Nevertheless, further increase in catalyst loading showed an adverse effect due to interception of the light by the suspension and aggregation of catalyst particles. In the presence of TiO<sub>2</sub> supported on GAC, Gu et al. [106] investigated the effect of catalyst loading in the range of 5.0 to  $9.0 \text{ g}\cdot\text{L}^{-1}$  on the photocatalytic degradation of 2,4-dichlorophenol (DCP). The increase of the catalyst dosage was observed to have a faster degradation of DCP,

and the degradation efficiency was increased from 50% with  $5.0 \text{ g}\cdot\text{L}^{-1}$  Ti-GAC to 100% with  $9.0 \text{ g}\cdot\text{L}^{-1}$  Ti-GAC. The increase of Ti-GAC dosage was reported to enhance the interactions between catalytic components and UV, leading to an increase of  $\cdot\text{OH}$  radicals formation. This led to an increase in its degradation. Giménez et al. [124] tested the effect of catalyst concentration ( $0\text{--}2 \text{ g}\cdot\text{L}^{-1}$ ) on the solar photocatalytic degradation of 2,4-dichlorophenol (2,4-DCP) in the CPC modules and the flat reactors. The observed optimum catalyst concentrations were  $0.5 \text{ g}\cdot\text{L}^{-1}$  and  $0.2 \text{ g}\cdot\text{L}^{-1}$  for the CPC modules and the flat reactor, respectively, on the degradation of 2,4-DCP. Further increase in the catalyst concentration in both reactors decreased the degradation rate. This suggests that the different designs of reactor (such as larger exposure area, more UV lamp, or faster agitation) might affect the optimal catalyst loading. In any given application, the optimum catalyst loading has to be determined in order to avoid an ineffective excess of catalyst and to ensure total absorption of efficient photons.

**5.4. Effect of Solution pH.** The pH of an aqueous solution significantly affects all metal oxide semiconductors including the surface charge on the semiconductor particles and the size of the aggregates formed [115, 125]. Due to amphoteric behaviour of TiO<sub>2</sub> particle suspended in aqueous solution, the effect of solution pH on degradation rate depends on the acid-base properties of the semiconductor surface and can be explained on the basis of zero-point charge. The principal amphoteric surface functionality is the “titanol” surface group, TiOH. Hydroxyl groups on the TiO<sub>2</sub> surface can undergo the following acid-base equilibrium [78, 126, 127]:



where  $K_a$  is the acidity constant. The  $\text{p}K_a$  values for Degussa P-25 TiO<sub>2</sub> have been estimated as 4.5 for  $\text{p}K_{a1}$  and 8 for  $\text{p}K_{a2}$ , which resulted in a pH of zero-point charge ( $\text{pH}_{\text{zpc}} = 0.5(\text{p}K_{a1} + \text{p}K_{a2})$ ) of 6.25 [128–130]. Accordingly, TiO<sub>2</sub> surface is protonated becoming positively charged as  $\text{TiOH}_2^+$

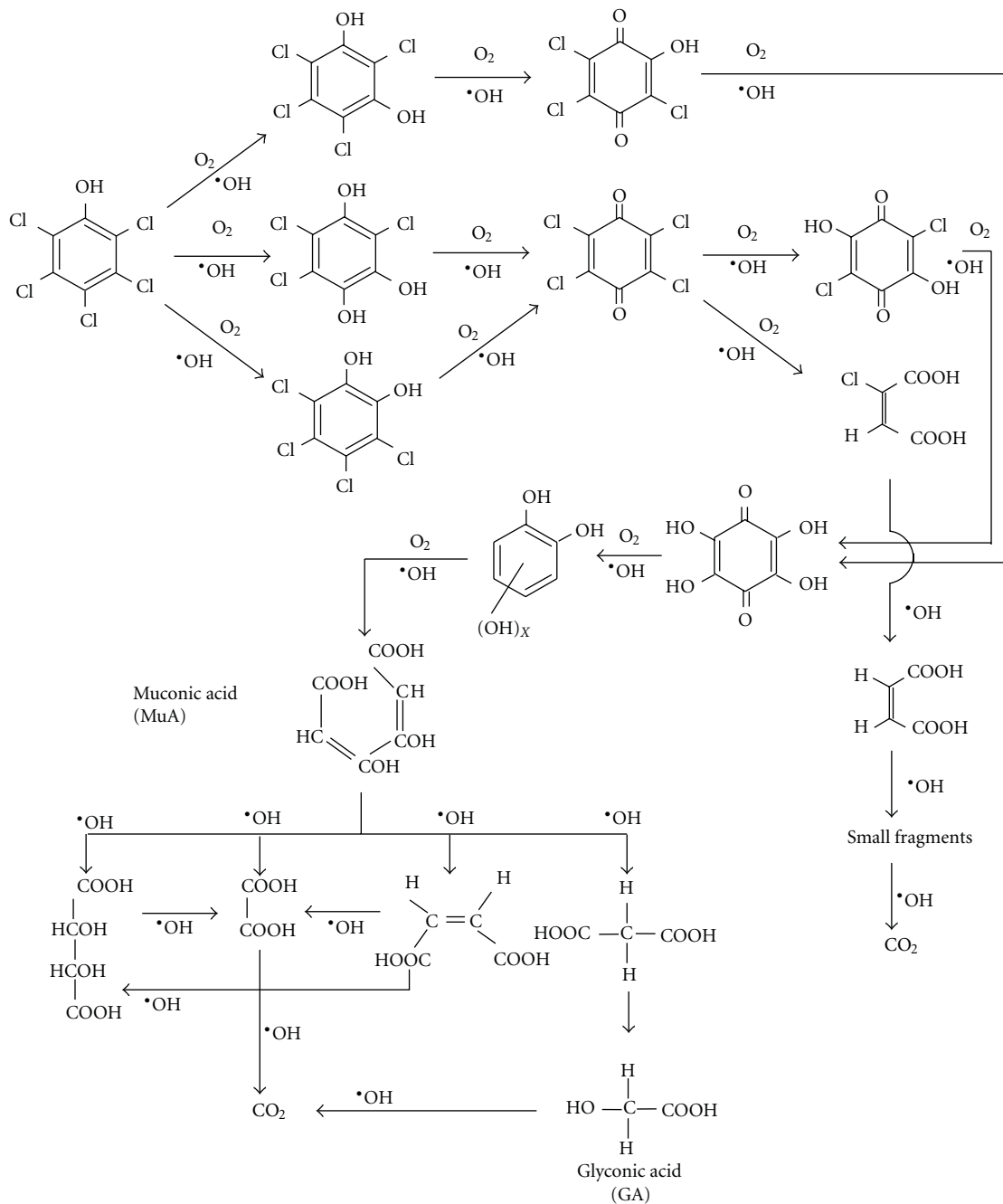


FIGURE 10: Photocatalytic degradation scheme for PCP [90].

below pH 6.25, and, above this pH, catalyst surface is predominantly negatively charged by adsorbed  $\text{OH}^-$  ions present as  $\text{TiO}^-$ . In addition, the pH of the solution can affect the formation of  $\cdot\text{OH}$  radicals by the reaction between  $\text{OH}^-$  ions and positive holes. The positive holes are favoured as major oxidation species at low pH, whereas  $\cdot\text{OH}$  radicals are favoured as principal oxidizing species responsible for the degradation process at neutral or high pH levels [92]. It was stated that, in alkaline medium, excess of  $\text{OH}^-$  ions on the  $\text{TiO}_2$  surface as well as in the reaction solution facilitated the formation of  $\cdot\text{OH}$  radicals, and, thus, the efficiency of the

process is logically enhanced. Wastewaters usually contain a mixture of large complex organic pollutants which may not be neutral. These organic pollutants present in wastewater differ greatly in several parameters, particularly in their speciation behaviour, solubility in water, and hydrophobicity. While some organic pollutants are uncharged at common pH conditions typical of natural water or wastewater, others exhibit a wide variation in speciation (or charge) and physicochemical properties. At pH below its  $\text{pK}_a$  value, an organic pollutant is primarily in its molecular form. Above this  $\text{pK}_a$  value, an organic pollutant tends to undergo

deprotonation becoming negatively charge. These characteristics can significantly affect selective adsorption and photocatalytic degradation of charged pollutants by altering the surface charge of  $\text{TiO}_2$  when a variation of solution pH takes place [131, 132]. Table 3 presents the solution pH influence on the photocatalytic degradation of various EDCs.

Liao and Wang [101] studied the effect of pH in the range of 3 to 11 on the photocatalytic degradation of dimethyl phthalate (DMP) over  $\text{TiO}_2$  under UV light irradiation. The efficiency of DMP degradation in acidic solution at pH 5 was found to be higher than the alkaline solution. The enhanced degradation efficiency in acidic medium was due to more  $\text{H}^+$  ions in the solution; more conduction band electron could migrate to the surface of the catalyst and reacted with  $\text{O}_2$  to generate more  $\cdot\text{OH}$  radicals. Lin et al. [141] reported on the influence of pH on the photocatalytic degradation of pentachlorophenol (PCP) using metal-modified  $\text{TiO}_2$  over the pH range of 3 to 11. Their results showed that the degradation of PCP enhanced in an acidic medium, and the maximum degradation rate was achieved in the solution at pH 3. At pH 3, the degradation rate of 1.0 wt% metal-modified  $\text{TiO}_2$  was shown in the order of  $\text{Au/TiO}_2 > \text{Ag/TiO}_2 > \text{Pt/TiO}_2 > \text{Cu/TiO}_2$ . In acidic solution, the positive surface charge of  $\text{TiO}_2$  strongly attracted the negatively charged PCP since its  $\text{p}K_a$  value was 4.74, resulting in an increase of PCP degradation. The variation of bisphenol A (BPA) degradation efficiency under different pH values has been investigated [98]. Under the conditions tested, the photocatalytic degradation of BPA using immobilized  $\text{TiO}_2$  was done more rapidly in acidic solution than in alkaline solution. After 6 hr of irradiation, the degradation rate constants were reported to be  $0.54 \text{ h}^{-1}$ ,  $0.16 \text{ h}^{-1}$ , and  $0.01 \text{ h}^{-1}$  at pH 3, 7, and 10, respectively. Kuo and Lin [120] studied the influence of solution pH on the photocatalytic degradation of bisphenol A (BPA). Their results showed that the BPA degradation rate followed the order of  $\text{pH } 4 > \text{pH } 7 > \text{pH } 10$  in the UV/ $\text{TiO}_2$  system. Since the  $\text{p}K_a$  value of BPA is 9.6–10.2, the coulombic repulsion between negatively charged  $\text{TiO}_2$  surfaces and BPA molecules resulted in weak adsorption of BPA onto the surface of  $\text{TiO}_2$  at high pH. The photocatalytic degradation of BPA over UV/ $\text{TiO}_2$  was reported to obey the pseudo-first-order kinetics. Using the nitrogen-doped  $\text{TiO}_2$ , Subagio et al. [137] studied the effect of pH on the photocatalytic degradation of bisphenol A (BPA) irradiated under blue LED lights ( $\lambda = 465 \text{ nm}$ ). The results in their work showed that the BPA degradation rate increased from  $0.507 \text{ h}^{-1}$  to  $1.342 \text{ h}^{-1}$  with increasing the pH value from 3 to 10. It is important to note that the photocatalytic degradation of some organic pollutants is more efficient in alkaline solution [137] and others at about neutral pH [69]. It has earlier been reported that in alkaline solution, there is a higher concentration of  $\text{OH}^-$  ions, which can lead to the photogeneration of much of the reactive  $\cdot\text{OH}$  radicals and, thus, increasing the rate of BPA degradation. In the presence of porphyrin/ $\text{TiO}_2$  and visible light irradiation, Chang et al. [109] also noticed that the degradation of 2,4-dichlorophenol (2,4-DCP) was most favoured at a higher pH (10.0) but went on at a slower and inefficient rate at pH 4.0. The pH variations influence (3.4–11.2) on the photocatalytic

degradation of diethyl phthalate (DEP) has also been studied using  $\text{PW}_{12}/\text{TiO}_2$  composite [64]. Under the stimulated sunlight irradiation, the degradation efficiency was shown to be greater at higher pH due to more efficient generation of  $\cdot\text{OH}$  radicals on the catalyst surface with an increase of  $\text{OH}^-$  ion concentration. Daskalaki et al. [107] tested the effect of initial solution pH on the photocatalytic degradation of bisphenol A (BPA) using both TIP film ( $\text{TiO}_2$  prepared by sol-gel method) and P-25 film immobilized on Ti support. After 180 min of solar irradiation, the BPA degradation efficiencies were 42%, 86%, 90%, and 62% for TIP film and 70%, 84%, 95%, and 90% for P-25 film at initial pH values of 3, 6, 8, and 10, respectively. The increased photocatalytic performance recorded at pH 8 was due to the fact that favourable formation of  $\cdot\text{OH}$  radicals at alkaline conditions. At pH above 8, BPA was reported in the forms of  $\text{BPA}^-$  and  $\text{BPA}^{2-}$ , and, thus, repulsion will eventually occur with negatively charged  $\text{TiO}_2$ . On the contrary, Xu et al. [69] observed that the degradation efficiency of *n*-butyl benzyl phthalate (BBP) using  $\text{TiO}_2$  under neutral pH was beneficial and had higher degradation efficiency than that in the alkaline medium. At pH 7.0, the surface of  $\text{TiO}_2$  at isoelectric point can adsorb the largest amount of BBP molecules. At higher pH (10.0), negative charges predominated on the surface of  $\text{TiO}_2$  particles, which restrained the BBP degradation. Hanna et al. [135] studied the effect of pH on the photocatalytic degradation of pentachlorophenol (PCP) in water and in  $2 \text{ mmol} \cdot \text{l}^{-1}$  cyclodextrin solution. The degradation rates were found to be higher at pH 7 than that obtained at pH 11. Wang and Lim [133] investigated the effect of initial pH on the photocatalytic degradation of bisphenol A (BPA) catalyzed by C-N doped  $\text{TiO}_2$ . The order of degradation rates was shown to be  $\text{pH } 7 > \text{pH } 9 \approx \text{pH } 5 > \text{pH } 3 > \text{pH } 11$ . The enhanced degradation efficiency at pH 7 was due to the  $\cdot\text{OH}$  radicals easier to generate by oxidizing more  $\text{OH}^-$  ions available on  $\text{TiO}_2$  surface. At higher pH, BPA was deprotonated into bisphenolate anions ( $\text{p}K_a$  of BPA = 9.6–10.2). Thus, degradation of BPA was inhibited as BPA possessed similar charge to  $\text{TiO}_2$ , which resulted in mutual repulsion. In summary, different organic pollutants have different activities in photocatalytic reaction. Some are degraded effectively at lower pH, while others degraded effectively at higher pH. All these may be attributed to the type of catalyst used and the nature of the organic pollutant to be degraded. Therefore, appropriate pH control strategies should be implemented for an efficient photocatalytic water treatment process.

**5.5. Effect of Reaction Temperature.** A number of studies have been indicated on the dependence of the photocatalytic reaction rate of degradation of organic pollutants on the reaction temperature. Such dependency could be realized when operating the photocatalytic process under natural sunlight, where the reaction temperature of stream may increase as the solar irradiation contains a considerable infrared (IR) factor [75]. Generally, as the photocatalytic process proceeds on the surface of the  $\text{TiO}_2$ , higher reaction temperatures would promote collision frequency between the organic pollutants and the catalyst, leading to higher reaction rates.

TABLE 3: Effect of solution pH on the photocatalytic degradation of various EDCs.

Organic pollutant	Light source	Photocatalyst	Range of solution pH	Optimum solution pH	Reference
Dimethyl phthalate	UV	TiO <sub>2</sub>	3.0–11.0	5.0	Liao and Wang [101]
Bisphenol A	Visible	C-N/TiO <sub>2</sub>	3.0–11.0	7.0	Wang and Lim [133]
2,4-Dichlorophenol	UV	TiO <sub>2</sub>	3.5–10.6	10.6	Trillas et al. [134]
Bisphenol A	UV	TiO <sub>2</sub>	4.0–10.0	4.0	Kuo and Lin [120]
Diethyl phthalate	Solar	PW <sub>12</sub> /TiO <sub>2</sub>	3.4–11.2	11.2	Xu et al. [64]
Pentachlorophenol	UV	TiO <sub>2</sub>	7.0–11.0	7.0	Hanna et al. [135]
2,4-Dichlorophenol	UV	Porphyrin/TiO <sub>2</sub>	4.0–10.0	10.0	Chang et al. [109]
<i>n</i> -Butyl benzyl phthalate	UV	TiO <sub>2</sub>	3.0–11.0	7.0	Xu et al. [69]
Bisphenol A	Solar	N/TiO <sub>2</sub> /AC	3.0–11.0	3.0	Yap et al. [136]
Bisphenol A	Visible	N/TiO <sub>2</sub>	3.0–10.0	10.0	Subagio et al. [137]
1,2-Diethyl phthalate	UV	TiO <sub>2</sub>	3.0–9.0	6.0	Muneer et al. [53]
Bisphenol A	Solar	TiO <sub>2</sub> /Ti	3.0–10.0	8.0	Daskalaki et al. [107]
Bisphenol A	Visible	TiO <sub>2</sub>	4.0 – 10.0	4.0	Kuo et al. [138]
2,4-dichlorophenol	UV	Fe <sup>o</sup> /TiO <sub>2</sub> /ACF	2.0–10.0	6.0	Liu et al. [139]
Bisphenol A	UV	Zr/TiO <sub>2</sub>	2.0–11.0	9.0	Gao et al. [108]
Di(2-ethylhexyl)phthalate	UV	TiO <sub>2</sub>	2.0–12.0	12.0	Chan et al. [140]

Nevertheless, several researchers have reported that, while an increase in photocatalytic reaction temperature may enhance the reaction rate of organic pollutants, reaction temperature would also lower the adsorption of organic pollutants and could reduce the oxygen concentration in the solution [142, 143]. This is consistent with Arrhenius equation, where the rate constant  $k$  is linearly proportional to the exponential  $(-1/T)$ :

$$k = A \exp\left(-\frac{E_a}{RT}\right), \quad (13)$$

where  $A$ ,  $E_a$ ,  $T$ , and  $R$  are the frequency factors, activation energy, temperature (K), and universal gas constant, respectively. In addition, as the irradiation energy simply serves to overcome the energy barrier for the process that it is often found the apparent activation energy is very small (a few  $\text{Kj}\cdot\text{mol}^{-1}$ ) [144]. Hence, the photocatalytic process does not appear to be particularly temperature sensitive. Chung and Chen [70] found that, the efficiency of photocatalytic degradation of di(2-ethylhexyl)phthalate (DEHP) increased gradually as the temperature increased from 20 to 40°C but was insignificant. The effect of temperature on the solar photocatalytic degradation of bisphenol A (BPA) using TiO<sub>2</sub> has been investigated in the range of 10 to 70°C [97]. Although the degradation efficiency of BPA increased steadily as the temperature increased, the appreciable change was not observed within their temperature range studied. Similar trend of results has also been observed for the photocatalytic degradation of dibutyl phthalate (DBP) using TiO<sub>2</sub> suspension [123]. The increase of degradation efficiency was reported to be insignificant in the temperature range of 10 to 40°C. In the photocatalytic degradation of bisphenol A (BPA) using immobilized TiO<sub>2</sub>, the effect of temperature was studied in the range of 21.2 to 30.5°C [104]. Their finding revealed that the temperature has a limited influence

on BPA degradation rate. The observed activation energy was relatively low and estimated to be  $0.814 \text{ Kj}\cdot\text{mol}^{-1}$ ; thus, no heating requirement was reported on the BPA photocatalytic system. Tsai et al. [20] examined the effect of temperature ranging from 10 to 70°C on the degradation efficiency of bisphenol A (BPA) under UV irradiation. Their results showed that the temperature played a less important role on the TiO<sub>2</sub> photocatalytic reaction system although the appreciable change in the enhancement of degradation efficiency was observed in the range of 10 to 25°C. In sum, the optimum temperature is generally in the medium temperature range ( $20^\circ\text{C} \leq \theta \leq 80^\circ\text{C}$ ). This absence of heating is attractive for photocatalytic reactions carried out in aqueous media and in particular for photocatalytic water purification [145].

**5.6. Effect of Dissolved Oxygen.** Oxygen dissolved in solution is typically employed as an effective electron scavenger in most heterogeneous photocatalyzed reactions. The O<sub>2</sub> can be reduced to the O<sub>2</sub><sup>•-</sup> anions, which prevents the photogenerated conduction band electron from recombination or being further reacted to form H<sub>2</sub>O<sub>2</sub> and •OH radicals. Due to its electrophilic property, dissolved O<sub>2</sub> plays an indispensable role in the TiO<sub>2</sub> photocatalytic reaction [67]. Basically, the O<sub>2</sub> does not affect the adsorption on the TiO<sub>2</sub> catalyst surface since reduction reaction occurs at a different location from where oxidation takes place. The concentration of oxygen also influences the reaction rate, but it seems that the difference between using air ( $p_{\text{O}_2} = 0.21 \text{ bar}$ ) or pure O<sub>2</sub> ( $p_{\text{O}_2} = 1 \text{ bar}$ ) is not very drastic. It has been stated that the rate of reaction was independent of O<sub>2</sub> concentrations below air saturation levels, suggesting also that the mass transfer of O<sub>2</sub> to the close vicinity of the catalyst surface could be rate-controlling step [143]. According to Henry's law, it is assumed that the concentration of O<sub>2</sub> adsorbed

on  $\text{TiO}_2$  from the liquid phase is proportional to the gas phase  $p_{\text{O}_2}$ . In this equilibrium law, it is also necessary to account for the decrease in  $\text{O}_2$  solubility with increasing the reaction temperature. Apart from its electron scavenging role, the dissolved  $\text{O}_2$  is also suggested to induce the cleavage mechanism for aromatic rings in organic pollutants that are present in the water matrices [67].

Zang et al. [89] studied the effect of dissolved  $\text{O}_2$  on the photocatalytic degradation of 2,4-dichlorophenol (DCP) catalyzed by  $\text{TiO}_2$  suspensions. Their results showed that the DCP degradation under air saturation was better than that in the absence of air. Precisely, after the photocatalytic system was saturated with air, a thirtyfold increase in DCP mineralization rate was observed. Such an increase in mineralization rate was explained by the formation of additional  $\cdot\text{OH}$  radicals via reactions of  $\text{O}_2$  with  $e^-$  and  $\text{H}^+$ . Yuan et al. [146] compared the efficiency of  $\text{TiO}_2/\text{UV}$  system on the photocatalytic degradation of dimethyl phthalate (DMP) using different gases. The experiment results performed in aqueous DMP with an  $\text{N}_2$  gas flow showed that the degradation efficiency was very limited, while addition of  $\text{O}_2$  as an electron acceptor with a concentration about  $35 \text{ mg}\cdot\text{L}^{-1}$  substantially increased the DMP degradation. Gu et al. [106] investigated the effect of  $\text{O}_2$  flow rate in the range of 4 to  $8 \text{ L}\cdot\text{min}^{-1}$  on the photocatalytic degradation of 2,4-dichlorophenol (DCP) using  $\text{TiO}_2$  supported on GAC. Their findings revealed that the photocatalytic activity of Ti-GAC increased rapidly and obtained a maximum degradation efficiency of 82.5% at  $6 \text{ L}\cdot\text{min}^{-1}$  as the  $\text{O}_2$  flow rate increased from 4 to  $6 \text{ L}\cdot\text{min}^{-1}$ . Further increase in the  $\text{O}_2$  flow rate from 6 to  $8 \text{ L}\cdot\text{min}^{-1}$  decreased the photocatalytic activity slightly to 79%. The increased photocatalytic degradation efficiency was attributed to the coefficient of enhanced mass transfer and  $\cdot\text{OH}$  radicals generation. The decrease in photocatalytic degradation efficiency at  $8 \text{ L}\cdot\text{min}^{-1}$  ascribed to high bubbling rate can provide a bubble cloud to impede the interactions between UV and catalytic activity center. Chin et al. [147] reported on the effect of aeration rate ( $0.2\text{--}4.0 \text{ L}\cdot\text{min}^{-1}$ ) to provide good mixing and a desirable level of dissolved  $\text{O}_2$  on the photocatalytic degradation of bisphenol A (BPA). Under the conditions tested, an optimum of  $0.5 \text{ L}\cdot\text{min}^{-1}$  was observed on the BPA degradation using  $\text{TiO}_2$  as catalyst. The effect of different gases on photocatalytic degradation of bisphenol A (BPA) in the presence of  $\text{TiO}_2$  and  $\beta$ -cyclodextrin has also been examined by purging air and  $\text{N}_2$  gas [110]. Compared to the case where there was no additional of electron acceptor (by purging  $\text{N}_2$  in BPA solution), the efficiency of BPA degradation increased significantly with the addition of air during the 60-min reaction time. This was related to electron-hole pairs which can easily recombine in the absence of  $\text{O}_2$ .

## 6. Conclusions and Future Prospects

The paper revealed the fact that the increasing consumption of EDCs worldwide has raised significant public concern due to their effects that exerted hormonal imbalance activity even in trace concentrations in water bodies. Sources of EDCs, phthalates, bisphenol A, and chlorophenols in particular, and

their effects on the environment, have been discussed. The photocatalysis using  $\text{TiO}_2$ , based catalysts has been shown to be efficient for the degradation and mineralization of various EDCs in wastewater in the presence of UV, visible, or solar light and oxygen. By the detailed illumination for the degradation pathways and intermediate products of these EDCs, this paper can provide theoretic evidences for seeking new and high efficiency of photocatalytic reactions for EDCs. The findings also suggested that various operational parameters such as light intensity and wavelength, initial substrate concentration, catalyst loading, solution pH, reaction temperature, and the presence of oxygen can influence considerably the photocatalytic degradation rate and efficiency of EDCs. Optimization of the operational parameters is of paramount importance from the design and the operational points of view when selecting a sustainable and competent technique for the wastewater treatment processes. The application of this technique under multicomponents of EDCs using the optimization of process parameters needs further attention as the pollutants in the real-world wastewater are in the form of mixture. Additionally, most of the photocatalysis studies concentrated only on the degradation rate, and efficiency of target EDCs disregarding the toxicity and estrogenic potency of the degradation intermediates. This aspect should not be overlooked while reporting any future work. A demonstrated ability to use  $\text{TiO}_2$ -based catalysts at a pilot scale for photocatalytic degradation of EDCs would certainly benefit the environment. Although this paper is nonexhaustive in the scope of photocatalytic degradation of EDCs, it does, however, address the fundamental principles and application in this area.

## Acknowledgments

This study is supported under Research Universiti (RU) Grants (nos. 854001 and 814004) from Universiti Sains Malaysia. The authors gratefully acknowledge the financial support from the Malaysia Government through the MyPhD scheme.

## References

- [1] I. Gültekin and N. H. Ince, "Synthetic endocrine disruptors in the environment and water remediation by advanced oxidation processes," *Journal of Environmental Management*, vol. 85, no. 4, pp. 816–832, 2007.
- [2] M. M. Brouwers, H. Besselink, R. W. Bretveld et al., "Estrogenic and androgenic activities in total plasma measured with reporter-gene bioassays: relevant exposure measures for endocrine disruptors in epidemiologic studies?" *Environment International*, 2011.
- [3] C. Porte, G. Janer, L. C. Lorusso et al., "Endocrine disruptors in marine organisms: approaches and perspectives," *Comparative Biochemistry and Physiology Part C*, vol. 143, no. 3, pp. 303–315, 2006.
- [4] N. Diano, V. Grano, L. Fraconte et al., "Non-isothermal bioreactors in enzymatic remediation of waters polluted by endocrine disruptors: BPA as a model of pollutant," *Applied Catalysis B*, vol. 69, no. 3–4, pp. 252–261, 2007.

- [5] S. Esplugas, D. M. Bila, L. G. T. Krause, and M. Dezotti, "Ozonation and advanced oxidation technologies to remove endocrine disrupting chemicals (EDCs) and pharmaceuticals and personal care products (PPCPs) in water effluents," *Journal of Hazardous Materials*, vol. 149, no. 3, pp. 631–642, 2007.
- [6] F. A. Caliman and M. Gavrilescu, "Pharmaceuticals, personal care products and endocrine disrupting agents in the environment—a review," *Clean—Soil, Air, Water*, vol. 37, no. 4-5, pp. 277–303, 2009.
- [7] R. Janisch, P. Gopal, and N. A. Spaldin, "Transition metal-doped TiO<sub>2</sub> and ZnO—present status of the field," *Journal of Physics Condensed Matter*, vol. 17, no. 27, pp. R657–R689, 2005.
- [8] C. H. Walker, *Organic Pollutant: An Ecotoxicological Perspective*, Taylor and Francis, Boca Raton, Fla, USA, 2nd edition, 2009.
- [9] O. Shen, G. Du, H. Sun et al., "Comparison of in vitro hormone activities of selected phthalates using reporter gene assays," *Toxicology Letters*, vol. 191, no. 1, pp. 9–14, 2009.
- [10] M. Plotan, C. T. Elliott, M. L. Scippo et al., "The application of reporter gene assays for the detection of endocrine disruptors in sport supplements," *Analytica Chimica Acta*, vol. 700, no. 1-2, pp. 34–40, 2011.
- [11] J. K. Hess-Wilson and K. E. Knudsen, "Endocrine disrupting compounds and prostate cancer," *Cancer Letters*, vol. 241, no. 1, pp. 1–12, 2006.
- [12] F. Eertmans, W. Dhooze, S. Stuyvaert, and F. Comhaire, "Endocrine disruptors: effects on male fertility and screening tools for their assessment," *Toxicology in Vitro*, vol. 17, no. 5-6, pp. 515–524, 2003.
- [13] M. K. Skinner, M. Manikkam, and C. Guerrero-Bosagna, "Epigenetic transgenerational actions of endocrine disruptors," *Reproductive Toxicology*, vol. 31, no. 3, pp. 337–343, 2011.
- [14] J. P. Sumpter, "Environmental control of fish reproduction: a different perspective," *Fish Physiology and Biochemistry*, vol. 17, no. 1-6, pp. 25–31, 1997.
- [15] O. O. Olujimi, O. S. Fatoki, J. P. Odendaal, and J. O. Okonkwo, "Endocrine disrupting chemicals (phenol and phthalates) in the South African environment: a need for more monitoring," *Water SA*, vol. 36, no. 5, pp. 671–682, 2010.
- [16] H. S. Chang, K. H. Choo, B. Lee, and S. J. Choi, "The methods of identification, analysis, and removal of endocrine disrupting compounds (EDCs) in water," *Journal of Hazardous Materials*, vol. 172, no. 1, pp. 1–12, 2009.
- [17] J. L. Zhao, G. G. Ying, F. Chen et al., "Estrogenic activity profiles and risks in surface waters and sediments of the Pearl River system in South China assessed by chemical analysis and in vitro bioassay," *Journal of Environmental Monitoring*, vol. 13, no. 4, pp. 813–821, 2011.
- [18] X. Ding, T. An, L. Guiying et al., "Photocatalytic degradation of dimethyl phthalate ester using novel hydrophobic TiO<sub>2</sub> pillared montmorillonite photocatalyst," *Research on Chemical Intermediates*, vol. 34, no. 1, pp. 67–83, 2008.
- [19] N. Venkatchalam, M. Palanichamy, B. Arabindoo, and V. Murugesan, "Enhanced photocatalytic degradation of 4-chlorophenol by Zr<sup>4+</sup> doped nano TiO<sub>2</sub>," *Journal of Molecular Catalysis A*, vol. 266, no. 1-2, pp. 158–165, 2007.
- [20] W. T. Tsai, M. K. Lee, T. Y. Su, and Y. M. Chang, "Photodegradation of bisphenol-A in a batch TiO<sub>2</sub> suspension reactor," *Journal of Hazardous Materials*, vol. 168, no. 1, pp. 269–275, 2009.
- [21] J. G. Yu, H. G. Yu, B. Cheng, X. J. Zhao, J. C. Yu, and W. K. Ho, "The effect of calcination temperature on the surface microstructure and photocatalytic activity of TiO<sub>2</sub> thin films prepared by liquid phase deposition," *Journal of Physical Chemistry B*, vol. 107, no. 50, pp. 13871–13879, 2003.
- [22] J. Yu, L. Zhang, B. Cheng, and Y. Su, "Hydrothermal preparation and photocatalytic activity of hierarchically sponge-like macro-/mesoporous Titania," *Journal of Physical Chemistry C*, vol. 111, no. 28, pp. 10582–10589, 2007.
- [23] S. Liu, J. Yu, and M. Jaroniec, "Tunable photocatalytic selectivity of hollow TiO<sub>2</sub> microspheres composed of anatase polyhedra with exposed 001 facets," *Journal of the American Chemical Society*, vol. 132, no. 34, pp. 11914–11916, 2010.
- [24] N. H. Lee, H. J. Oh, S. C. Jung, W. J. Lee, D. H. Kim, and S. J. Kim, "Photocatalytic properties of nanotubular-shaped TiO<sub>2</sub> powders with anatase phase obtained from titanate nanotube powder through various thermal treatments," *International Journal of Photoenergy*, vol. 2011, Article ID 327821, 7 pages, 2011.
- [25] P. Patnaik, *A Comprehensive Guide to the Hazardous Properties of Chemical Substances*, Wiley Interscience, New Jersey, NJ, USA, 3rd edition, 2007.
- [26] N. Adhoum and L. Monser, "Removal of phthalate on modified activated carbon: application to the treatment of industrial wastewater," *Separation and Purification Technology*, vol. 38, no. 3, pp. 233–239, 2004.
- [27] S. Venkata Mohan, S. Shailaja, M. Rama Krishna, and P. N. Sarma, "Adsorptive removal of phthalate ester (Di-ethyl phthalate) from aqueous phase by activated carbon: a kinetic study," *Journal of Hazardous Materials*, vol. 146, no. 1-2, pp. 278–282, 2007.
- [28] M. H. Wu, N. Liu, G. Xu et al., "Kinetics and mechanisms studies on dimethyl phthalate degradation in aqueous solutions by pulse radiolysis and electron beam radiolysis," *Radiation Physics and Chemistry*, vol. 80, no. 3, pp. 420–425, 2011.
- [29] C. R. Fang, J. Yao, Y. G. Zheng et al., "Dibutyl phthalate degradation by *Enterobacter sp.* T5 isolated from municipal solid waste in landfill bioreactor," *International Biodeterioration and Biodegradation*, vol. 64, no. 6, pp. 442–446, 2010.
- [30] Y. Jing, L. S. Li, Q. Y. Zhang, P. Lu, P. H. Liu, and X. H. Lü, "Photocatalytic ozonation of dimethyl phthalate with TiO<sub>2</sub> prepared by a hydrothermal method," *Journal of Hazardous Materials*, vol. 189, no. 1-2, pp. 40–47, 2011.
- [31] F. Zeng, W. Liu, H. Jiang, H. Q. Yu, R. J. Zeng, and Q. Guo, "Separation of phthalate esters from bio-oil derived from rice husk by a basification-acidification process and column chromatography," *Bioresource Technology*, vol. 102, no. 2, pp. 1982–1987, 2011.
- [32] G. H. Tan, "Residue levels of phthalate esters in water and sediment samples from the Klang River basin," *Bulletin of Environmental Contamination and Toxicology*, vol. 54, no. 2, pp. 171–176, 1995.
- [33] T. R. Zacharewski, M. D. Meek, J. H. Clemons, Z. F. Wu, M. R. Fielden, and J. B. Matthews, "Examination of the *in vitro* and *in vivo* estrogenic activities of eight commercial phthalate esters," *Toxicological Sciences*, vol. 46, no. 2, pp. 282–293, 1998.
- [34] J. E. Harries, T. Runnalls, E. Hill et al., "Development of a reproductive performance test for endocrine disrupting chemicals using pair-breeding fathead minnows (*Pimephales promelas*)," *Environmental Science & Technology*, vol. 34, no. 14, pp. 3003–3011, 2000.

- [35] A. V. Barse, T. Chakrabarti, T. K. Ghosh, A. K. Pal, and S. B. Jadhao, "Endocrine disruption and metabolic changes following exposure of *Cyprinus carpio* to diethyl phthalate," *Pesticide Biochemistry and Physiology*, vol. 88, no. 1, pp. 36–42, 2007.
- [36] H. R. Andersen, A. M. Andersson, S. F. Arnold et al., "Comparison of short-term estrogenicity tests for identification of hormone-disrupting chemicals," *Environmental Health Perspectives*, vol. 107, no. 1, pp. 89–108, 1999.
- [37] O. Bajt, G. Mailhot, and M. Bolte, "Degradation of dibutyl phthalate by homogeneous photocatalysis with Fe(III) in aqueous solution," *Applied Catalysis B*, vol. 33, no. 3, pp. 239–248, 2001.
- [38] S. M. Duty, N. P. Singh, M. J. Silva et al., "The relationship between environmental exposures to phthalates and DNA damage in human sperm using the neutral comet assay," *Environmental Health Perspectives*, vol. 111, no. 9, pp. 1164–1169, 2003.
- [39] R. Hauser, J. D. Meeker, N. P. Singh et al., "DNA damage in human sperm is related to urinary levels of phthalate monoester and oxidative metabolites," *Human Reproduction*, vol. 22, no. 3, pp. 688–695, 2007.
- [40] C. A. Staples, K. Woodburn, N. Caspers, A. T. Hall, and G. M. Klecka, "A weight of evidence approach to the aquatic hazard assessment of bisphenol A," *Human and Ecological Risk Assessment*, vol. 8, no. 5, pp. 1083–1105, 2002.
- [41] A. Latorre, S. Lacorte, and D. Barceló, "Presence of nonylphenol, octylphenol and bisphenol a in two aquifers close to agricultural, industrial and urban areas," *Chromatographia*, vol. 57, no. 1-2, pp. 111–116, 2003.
- [42] A. V. Krishnan, P. Stathis, S. F. Permuth, L. Tokes, and D. Feldman, "Bisphenol-A: an estrogenic substance is released from polycarbonate flasks during autoclaving," *Endocrinology*, vol. 132, no. 6, pp. 2279–2286, 1993.
- [43] J. A. Brotons, M. F. Olea-Serrano, M. Villalobos, V. Pedraza, and N. Olea, "Xenoestrogens released from lacquer coatings in food cans," *Environmental Health Perspectives*, vol. 103, no. 6, pp. 608–612, 1995.
- [44] S. C. Laws, S. A. Carey, J. M. Ferrell, G. J. Bodman, and R. L. Cooper, "Estrogenic activity of octylphenol, nonylphenol, bisphenol A and methoxychlor in rats," *Toxicological Sciences*, vol. 54, no. 1, pp. 154–167, 2000.
- [45] K. Kobayashi, M. Miyagawa, R. S. Wang, M. Suda, S. Sekiguchi, and T. Honma, "Effects of in utero and lactational exposure to bisphenol A on thyroid status in F1 rat offspring," *Industrial Health*, vol. 43, no. 4, pp. 685–690, 2005.
- [46] P. Sohoni and J. P. Sumpter, "Several environmental oestrogens are also anti-androgens," *Journal of Endocrinology*, vol. 158, no. 3, pp. 327–339, 1998.
- [47] N. J. MacLusky, T. Hajszan, and C. Leranthe, "The environmental estrogen bisphenol A inhibits estradiol-induced hippocampal synaptogenesis," *Environmental Health Perspectives*, vol. 113, no. 6, pp. 675–679, 2005.
- [48] R. T. Zoeller, R. Bansal, and C. Parris, "Bisphenol-A, an environmental contaminant that acts as a thyroid hormone receptor antagonist in vitro, increases serum thyroxine, and alters RC3/neurogranin expression in the developing rat brain," *Endocrinology*, vol. 146, no. 2, pp. 607–612, 2005.
- [49] D. P. Mohapatra, S. K. Brar, R. D. Tyagi, and R. Y. Surampalli, "Physico-chemical pre-treatment and biotransformation of wastewater and wastewater Sludge—fate of bisphenol A," *Chemosphere*, vol. 78, no. 8, pp. 923–941, 2010.
- [50] R. M. Bergeron, T. B. Thompson, L. S. Leonard, L. Pluta, and K. W. Gaido, "Estrogenicity of bisphenol A in a human endometrial carcinoma cell line," *Molecular and Cellular Endocrinology*, vol. 150, no. 1-2, pp. 179–187, 1999.
- [51] M. V. Maffini, B. S. Rubin, C. Sonnenschein, and A. M. Soto, "Endocrine disruptors and reproductive health: the case of bisphenol-A," *Molecular and Cellular Endocrinology*, vol. 254–255, pp. 179–186, 2006.
- [52] L. N. Vandenberg, M. V. Maffini, C. Sonnenschein, B. S. Rubin, and A. M. Soto, "Bisphenol-a and the great divide: a review of controversies in the field of endocrine disruption," *Endocrine Reviews*, vol. 30, no. 1, pp. 75–95, 2009.
- [53] M. Muneer, J. Theurich, and D. Bahnemann, "Titanium dioxide mediated photocatalytic degradation of 1,2-diethyl phthalate," *Journal of Photochemistry and Photobiology A*, vol. 143, no. 2-3, pp. 213–219, 2001.
- [54] M. Czaplicka, "Sources and transformations of chlorophenols in the natural environment," *Science of the Total Environment*, vol. 322, no. 1-3, pp. 21–39, 2004.
- [55] M. Auriol, Y. Filali-Meknassi, R. D. Tyagi, C. D. Adams, and R. Y. Surampalli, "Endocrine disrupting compounds removal from wastewater, a new challenge," *Process Biochemistry*, vol. 41, no. 3, pp. 525–539, 2006.
- [56] V. Belgiorno, L. Rizzo, D. Fatta et al., "Review on endocrine disrupting-emerging compounds in urban wastewater: occurrence and removal by photocatalysis and ultrasonic irradiation for wastewater reuse," *Desalination*, vol. 215, no. 1-3, pp. 166–176, 2007.
- [57] K. Abe and K. Tanaka, "Fe<sup>3+</sup> and UV-enhanced ozonation of chlorophenolic compounds in aqueous medium," *Chemosphere*, vol. 35, no. 12, pp. 2837–2847, 1997.
- [58] W. F. Young, H. Horth, R. Crane, T. Ogden, and M. Arnott, "Taste and odour threshold concentrations of potential potable water contaminants," *Water Research*, vol. 30, no. 2, pp. 331–340, 1996.
- [59] M. Pera-Titus, V. García-Molina, M. A. Baños, J. Giménez, and S. Esplugas, "Degradation of chlorophenols by means of advanced oxidation processes: a general review," *Applied Catalysis B*, vol. 47, no. 4, pp. 219–256, 2004.
- [60] J. Zha, Z. Wang, and D. Schlenk, "Effects of pentachlorophenol on the reproduction of Japanese medaka (*Oryzias latipes*)," *Chemico-Biological Interactions*, vol. 161, no. 1, pp. 26–36, 2006.
- [61] X. Zhang, J. Zha, W. Li, L. Yang, and Z. Wang, "Effects of 2,4-dichlorophenol on the expression of vitellogenin and estrogen receptor genes and physiology impairments in chinese rare minnow (*Gobiocypris rarus*)," *Environmental Toxicology*, vol. 23, no. 6, pp. 694–701, 2008.
- [62] W. C. Dorsey and P. B. Tchounwou, "Pentachlorophenol-induced cytotoxic, mitogenic, and endocrine-disrupting activities in channel catfish, *Ictalurus punctatus*," *International Journal of Environmental Research and Public Health*, vol. 1, no. 2, pp. 90–99, 2004.
- [63] T. Kondo, H. Yamamoto, N. Tatarazako et al., "Bioconcentration factor of relatively low concentrations of chlorophenols in Japanese medaka," *Chemosphere*, vol. 61, no. 9, pp. 1299–1304, 2005.
- [64] L. Xu, X. Yang, Y. Guo et al., "Simulated sunlight photodegradation of aqueous phthalate esters catalyzed by the polyoxotungstate/titania nanocomposite," *Journal of Hazardous Materials*, vol. 178, no. 1-3, pp. 1070–1077, 2010.
- [65] E. Reck and M. Richards, "TiO<sub>2</sub> manufacture and life cycle analysis," *Pigment & Resin Technology*, vol. 28, no. 3, pp. 149–157, 1999.

- [66] K. K. Sahu, T. C. Alex, D. Mishra, and A. Agrawal, "An overview on the production of pigment grade titania from titania-rich slag," *Waste Management & Research*, vol. 24, no. 1, pp. 74–79, 2006.
- [67] O. Carp, C. L. Huisman, and A. Reller, "Photoinduced reactivity of titanium dioxide," *Progress in Solid State Chemistry*, vol. 32, no. 1-2, pp. 33–177, 2004.
- [68] Z. Chen, W. Li, W. Zeng et al., "Microwave hydrothermal synthesis of nanocrystalline rutile," *Materials Letters*, vol. 62, no. 28, pp. 4343–4344, 2008.
- [69] X. R. Xu, S. X. Li, X. Y. Li et al., "Degradation of n-butyl benzyl phthalate using TiO<sub>2</sub>/UV," *Journal of Hazardous Materials*, vol. 164, no. 2-3, pp. 527–532, 2009.
- [70] Y. C. Chung and C. Y. Chen, "Degradation of Di-(2-ethylhexyl) phthalate (DEHP) by TiO<sub>2</sub> photocatalysis," *Water, Air, & Soil Pollution*, vol. 200, no. 1-4, pp. 191–198, 2009.
- [71] A. Fujishima and K. Honda, "Electrochemical photolysis of water at a semiconductor electrode," *Nature*, vol. 238, no. 5358, pp. 37–38, 1972.
- [72] S. N. Frank and A. J. Bard, "Heterogeneous photocatalytic oxidation of cyanide ion in aqueous solutions at TiO<sub>2</sub> powder," *Journal of the American Chemical Society*, vol. 99, no. 1, pp. 303–304, 1977.
- [73] T. Inoue, A. Fujishima, S. Konishi, and K. Honda, "Photoelectrocatalytic reduction of carbon dioxide in aqueous suspensions of semiconductor powders," *Nature*, vol. 277, no. 5698, pp. 637–638, 1979.
- [74] U. G. Akpan and B. H. Hameed, "Parameters affecting the photocatalytic degradation of dyes using TiO<sub>2</sub>-based photocatalysts: a review," *Journal of Hazardous Materials*, vol. 170, no. 2-3, pp. 520–529, 2009.
- [75] D. S. Bhatkhande, V. G. Pangarkar, and A. A. C. M. Beenackers, "Photocatalytic degradation for environmental applications—a review," *Journal of Chemical Technology and Biotechnology*, vol. 77, no. 1, pp. 102–116, 2001.
- [76] U. I. Gaya and A. H. Abdullah, "Heterogeneous photocatalytic degradation of organic contaminants over titanium dioxide: a review of fundamentals, progress and problems," *Journal of Photochemistry and Photobiology C*, vol. 9, no. 1, pp. 1–12, 2008.
- [77] H. Choi, S. R. Al-Abed, D. D. Dionysiou, E. Stathatos, and P. Lianos, "Chapter 8 TiO<sub>2</sub>-based advanced oxidation nanotechnologies for water purification and reuse," *Sustainability Science and Engineering*, vol. 2, no. C, pp. 229–254, 2010.
- [78] M. N. Chong, B. Jin, C. W. K. Chow, and C. Saint, "Recent developments in photocatalytic water treatment technology: a review," *Water Research*, vol. 44, no. 10, pp. 2997–3027, 2010.
- [79] K. Y. Foo and B. H. Hameed, "Decontamination of textile wastewater via TiO<sub>2</sub>/activated carbon composite materials," *Advances in Colloid and Interface Science*, vol. 159, no. 2, pp. 130–143, 2010.
- [80] J. A. Byrne, P. A. Fernandez-Ibañez, P. S. M. Dunlop, D. M. A. Alrousan, and J. W. J. Hamilton, "Photocatalytic enhancement for solar disinfection of water: a review," *International Journal of Photoenergy*, vol. 2011, Article ID 798051, 12 pages, 2011.
- [81] S. M. Chang, P. H. Lo, and C. T. Chang, "Photocatalytic behavior of TOPO-capped TiO<sub>2</sub> nanocrystals for degradation of endocrine disrupting chemicals," *Applied Catalysis B*, vol. 91, no. 3-4, pp. 619–627, 2009.
- [82] Q. Xiao, Z. Si, J. Zhang, C. Xiao, and X. Tan, "Photoinduced hydroxyl radical and photocatalytic activity of samarium-doped TiO<sub>2</sub> nanocrystalline," *Journal of Hazardous Materials*, vol. 150, no. 1, pp. 62–67, 2008.
- [83] Y. Li, J. Wang, S. Peng, G. Lu, and S. Li, "Photocatalytic hydrogen generation in the presence of glucose over ZnS-coated ZnIn<sub>2</sub>S<sub>4</sub> under visible light irradiation," *International Journal of Hydrogen Energy*, vol. 35, no. 13, pp. 7116–7126, 2010.
- [84] Q. J. Xiang, J. G. Yu, and P. K. Wong, "Quantitative characterization of hydroxyl radicals produced by various photocatalysts," *Journal of Colloid and Interface Science*, vol. 357, no. 1, pp. 163–167, 2011.
- [85] G. Liu, J. Zhao, and H. Hidaka, "ESR spin-trapping detection of radical intermediates in the TiO<sub>2</sub>-assisted photo-oxidation of sulforhodamine B under visible irradiation," *Journal of Photochemistry and Photobiology A*, vol. 133, no. 1-2, pp. 83–88, 2000.
- [86] H. Fu, L. Zhang, S. Zhang, Y. Zhu, and J. Zhao, "Electron spin resonance spin-trapping detection of radical intermediates in N-doped TiO<sub>2</sub>-assisted photodegradation of 4-chlorophenol," *Journal of Physical Chemistry B*, vol. 110, no. 7, pp. 3061–3065, 2006.
- [87] G. F. Shang, H. B. Fu, S. G. Yang, and T. G. Xu, "Mechanistic study of visible-light-induced photodegradation of 4-chlorophenol by TiO<sub>2-x</sub>N<sub>x</sub> with low nitrogen concentration," *International Journal of Photoenergy*, vol. 2012, Article ID 759306, 9 pages, 2012.
- [88] H. Tao, S. Hao, F. Chang et al., "Photodegradation of bisphenol A by titania nanoparticles in mesoporous MCM-41," *Water, Air, & Soil Pollution*, vol. 214, no. 1-4, pp. 491–498, 2011.
- [89] L. Zang, C. Y. Liu, and X. M. Ren, "Photochemistry of semiconductor particles. Part 4. Effects of surface condition on the photodegradation of 2,4-dichlorophenol catalysed by TiO<sub>2</sub> suspensions," *Journal of the Chemical Society, Faraday Transactions*, vol. 91, no. 5, pp. 917–923, 1995.
- [90] O. J. Jung, S. H. Kim, and K. H. Cheong, "Photocatalytic degradation of pentachlorophenol (PCP) using TiO<sub>2</sub> thin films prepared by CVD," *Environmental Engineering Research*, vol. 6, no. 4, pp. 199–210, 2001.
- [91] D. F. Ollis, E. Pelizzetti, and N. Serpone, "Photocatalyzed destruction of water contaminants," *Environmental Science & Technology*, vol. 25, no. 9, pp. 1522–1529, 1991.
- [92] I. K. Konstantinou and T. A. Albanis, "TiO<sub>2</sub>-assisted photocatalytic degradation of azo dyes in aqueous solution: kinetic and mechanistic investigations: a review," *Applied Catalysis B*, vol. 49, no. 1, pp. 1–14, 2004.
- [93] K. Mehrotra, G. S. Yablonsky, and A. K. Ray, "Macro kinetic studies for photocatalytic degradation of benzoic acid in immobilized systems," *Chemosphere*, vol. 60, no. 10, pp. 1427–1436, 2005.
- [94] W. B. Huang and C. Y. Chen, "Photocatalytic degradation of diethyl phthalate (DEP) in water using TiO<sub>2</sub>," *Water, Air, & Soil Pollution*, vol. 207, no. 1-4, pp. 349–355, 2010.
- [95] B. Bayarri, M. N. Abellán, J. Giménez, and S. Esplugas, "Study of the wavelength effect in the photolysis and heterogeneous photocatalysis," *Catalysis Today*, vol. 129, no. 1-2, pp. 231–239, 2007.
- [96] H. W. Chan, C. M. Chan, P. O. Ang, and P. K. Wong, "Integrated biosorption and photocatalytic oxidation treatment of di(2-ethylhexyl)phthalate," *Journal of Applied Phycology*, vol. 19, no. 6, pp. 745–753, 2007.

- [97] S. Kaneco, M. A. Rahman, T. Suzuki, H. Katsumata, and K. Ohta, "Optimization of solar photocatalytic degradation conditions of bisphenol A in water using titanium dioxide," *Journal of Photochemistry and Photobiology A*, vol. 163, no. 3, pp. 419–424, 2004.
- [98] J. M. Lee, M. S. Kim, and B. W. Kim, "Photodegradation of bisphenol-A with TiO<sub>2</sub> immobilized on the glass tubes including the UV light lamps," *Water Research*, vol. 38, no. 16, pp. 3605–3613, 2004.
- [99] C. Minero, E. Pelizzetti, S. Malato, and J. Blanco, "Large solar plant photocatalytic water decontamination: effect of operational parameters," *Solar Energy*, vol. 56, no. 5, pp. 421–428, 1996.
- [100] H. J. Son, C. W. Jung, and S. H. Kim, "Removal of bisphenol-a using rotating photocatalytic oxidation drum reactor (RPODR)," *Environmental Engineering Research*, vol. 13, no. 4, pp. 197–202, 2008.
- [101] W. Liao and P. Wang, "Microwave-assisted photocatalytic degradation of dimethyl phthalate using a microwave discharged electrodeless lamp," *Journal of the Brazilian Chemical Society*, vol. 20, no. 5, pp. 866–872, 2009.
- [102] E. Kusvuran, A. Samil, O. M. Atanur, and O. Erbatur, "Photocatalytic degradation kinetics of di- and tri-substituted phenolic compounds in aqueous solution by TiO<sub>2</sub>/UV," *Applied Catalysis B*, vol. 58, no. 3-4, pp. 211–216, 2005.
- [103] R. Thiruvengkatachari, T. O. Kwon, and I. S. Moon, "Application of slurry type photocatalytic oxidation-submerged hollow fiber microfiltration hybrid system for the degradation of bisphenol A (BPA)," *Separation Science and Technology*, vol. 40, no. 14, pp. 2871–2888, 2005.
- [104] R. Wang, D. Ren, S. Xia, Y. Zhang, and J. Zhao, "Photocatalytic degradation of Bisphenol A (BPA) using immobilized TiO<sub>2</sub> and UV illumination in a horizontal circulating bed photocatalytic reactor (HCBPR)," *Journal of Hazardous Materials*, vol. 169, no. 1-3, pp. 926–932, 2009.
- [105] C. S. Chiou, J. L. Shie, C. Y. Chang, C. C. Liu, and C. T. Chang, "Degradation of di-n-butyl phthalate using photoreactor packed with TiO<sub>2</sub> immobilized on glass beads," *Journal of Hazardous Materials*, vol. 137, no. 2, pp. 1123–1129, 2006.
- [106] L. Gu, Z. X. Chen, C. Sun, B. Wei, and X. Yu, "Photocatalytic degradation of 2,4-dichlorophenol using granular activated carbon supported TiO<sub>2</sub>," *Desalination*, vol. 263, no. 1–3, pp. 107–112, 2010.
- [107] V. M. Daskalaki, Z. Frontistis, D. Mantzavinos, and A. Katsaounis, "Solar light-induced degradation of bisphenol-A with TiO<sub>2</sub> immobilized on Ti," *Catalysis Today*, vol. 161, no. 1, pp. 110–114, 2011.
- [108] B. Gao, T. M. Lim, D. P. Subagio, and T. T. Lim, "Zr-doped TiO<sub>2</sub> for enhanced photocatalytic degradation of bisphenol A," *Applied Catalysis A*, vol. 375, no. 1, pp. 107–115, 2010.
- [109] M. Y. Chang, Y. H. Hsieh, T. C. Cheng, K. S. Yao, M. C. Wei, and C. Y. Chang, "Photocatalytic degradation of 2,4-dichlorophenol wastewater using porphyrin/TiO<sub>2</sub> complexes activated by visible light," *Thin Solid Films*, vol. 517, no. 14, pp. 3888–3891, 2009.
- [110] G. Wang, F. Wu, X. Zhang, M. Luo, and N. Deng, "Enhanced TiO<sub>2</sub> photocatalytic degradation of bisphenol A by  $\beta$ -cyclodextrin in suspended solutions," *Journal of Photochemistry and Photobiology A*, vol. 179, no. 1-2, pp. 49–56, 2006.
- [111] L. Tatti, D. Niego, F. Rota et al., "Mathematical modelling of pilot-plant photomineralization of chlorophenols in aqueous solution, by photocatalytic membranes immobilizing titanium dioxide," *Chemosphere*, vol. 34, no. 1, pp. 41–49, 1997.
- [112] C. M. So, M. Y. Cheng, J. C. Yu, and P. K. Wong, "Degradation of azo dye Procion Red MX-5B by photocatalytic oxidation," *Chemosphere*, vol. 46, no. 6, pp. 905–912, 2002.
- [113] M. Sleiman, D. Vildoza, C. Ferronato, and J. M. Chovelon, "Photocatalytic degradation of azo dye Metanil Yellow: optimization and kinetic modeling using a chemometric approach," *Applied Catalysis B*, vol. 77, no. 1-2, pp. 1–11, 2007.
- [114] R. A. Damodar and T. Swaminathan, "Performance evaluation of a continuous flow immobilized rotating tube photocatalytic reactor (IRTPR) immobilized with TiO<sub>2</sub> catalyst for azo dye degradation," *Chemical Engineering Journal*, vol. 144, no. 1, pp. 59–66, 2008.
- [115] S. M. Lam, J. C. Sin, and A. R. Mohamed, "Parameter effect on photocatalytic degradation of phenol using TiO<sub>2</sub>-P25/activated carbon (AC)," *Korean Journal of Chemical Engineering*, vol. 27, no. 4, pp. 1109–1116, 2010.
- [116] J. C. Sin, S. M. Lam, and A. R. Mohamed, "Optimizing photocatalytic degradation of phenol by TiO<sub>2</sub>/GAC using response surface methodology," *Korean Journal of Chemical Engineering*, vol. 28, no. 1, pp. 84–92, 2011.
- [117] M. L. Chin, A. R. Mohamed, and S. Bhatia, "Performance of photocatalytic reactors using immobilized TiO<sub>2</sub> film for the degradation of phenol and methylene blue dye present in water stream," *Chemosphere*, vol. 57, no. 7, pp. 547–554, 2004.
- [118] S. Merabet, A. Bouzaza, and D. Wolbert, "Photocatalytic degradation of indole in a circulating upflow reactor by UV/TiO<sub>2</sub> process-Influence of some operating parameters," *Journal of Hazardous Materials*, vol. 166, no. 2-3, pp. 1244–1249, 2009.
- [119] J. Yao and C. X. Wang, "Decolorization of methylene blue with TiO<sub>2</sub> sol via UV irradiation photocatalytic degradation," *International Journal of Photoenergy*, vol. 2010, Article ID 643182, 2010.
- [120] C. Y. Kuo and H. Y. Lin, "Photocatalytic activity of TiO<sub>2</sub> prepared by adding polyethyleneglycol," *Reaction Kinetics and Catalysis Letters*, vol. 96, no. 1, pp. 147–155, 2009.
- [121] B. Bayarri, J. Giménez, D. Curcó, and S. Esplugas, "Photocatalytic degradation of 2,4-dichlorophenol by TiO<sub>2</sub>/UV: kinetics, actinometries and models," *Catalysis Today*, vol. 101, no. 3-4, pp. 227–236, 2005.
- [122] O. Bajt, J. Zita, P. Novotná, J. Krýsa, and J. Jirkovský, "Photocatalytic degradation of dibutyl phthalate: effect of catalyst immobilization," *Journal of Solar Energy Engineering*, vol. 130, no. 4, pp. 0410051–0410055, 2008.
- [123] S. Kaneco, H. Katsumata, T. Suzuki, and K. Ohta, "Titanium dioxide mediated photocatalytic degradation of dibutyl phthalate in aqueous solution-kinetics, mineralization and reaction mechanism," *Chemical Engineering Journal*, vol. 125, no. 1, pp. 59–66, 2006.
- [124] J. Giménez, D. Curcó, and M. A. Queral, "Photocatalytic treatment of phenol and 2,4-dichlorophenol in a solar plant in the way to scaling-up," *Catalysis Today*, vol. 54, no. 2-3, pp. 229–243, 1999.
- [125] N. Modirshahla, A. Hassani, M. A. Behnajady, and R. Rahbarfam, "Effect of operational parameters on decolorization of Acid Yellow 23 from wastewater by UV irradiation using ZnO and ZnO/SnO<sub>2</sub> photocatalysts," *Desalination*, vol. 271, no. 1–3, pp. 187–192, 2011.
- [126] A. Neren Ökte and Ö. Yilmaz, "Photodecolorization of methyl orange by yttrium incorporated TiO<sub>2</sub> supported ZSM-5," *Applied Catalysis B*, vol. 85, no. 1-2, pp. 92–102, 2008.

- [127] Y. Li, C. Ren, S. Peng, G. Lu, and S. Li, "Effect of preparation method of colloidal platinum on performance of 12-tungstosilicate for photocatalytic hydrogen generation," *Journal of Molecular Catalysis A*, vol. 246, no. 1-2, pp. 212–217, 2006.
- [128] C. Kormann, D. W. Bahnemann, and M. R. Hoffmann, "Photolysis of chloroform and other organic molecules in aqueous titanium dioxide suspensions," *Environmental Science & Technology*, vol. 25, no. 3, pp. 494–500, 1991.
- [129] Y. Li, G. Lu, and S. Li, "Photocatalytic hydrogen generation and decomposition of oxalic acid over platinumized TiO<sub>2</sub>," *Applied Catalysis A*, vol. 214, no. 2, pp. 179–185, 2001.
- [130] Y. X. Li, F. He, S. Q. Peng, D. Gao, G. X. Lu, and S. B. Li, "Effects of electrolyte NaCl on photocatalytic hydrogen evolution in the presence of electron donors over Pt/TiO<sub>2</sub>," *Journal of Molecular Catalysis A*, vol. 341, no. 1-2, pp. 71–76, 2011.
- [131] C. H. Chiou, C. Y. Wu, and R. S. Juang, "Influence of operating parameters on photocatalytic degradation of phenol in UV/TiO<sub>2</sub> process," *Chemical Engineering Journal*, vol. 139, no. 2, pp. 322–329, 2008.
- [132] Q. J. Xiang, J. G. Yu, and M. Jaroniec, "Tunable photocatalytic selectivity of TiO<sub>2</sub> films consisted of flower-like microspheres with exposed 001 facets," *Chemical Communications*, vol. 47, no. 15, pp. 4532–4534, 2011.
- [133] X. Wang and T. T. Lim, "Solvothermal synthesis of C-N codoped TiO<sub>2</sub> and photocatalytic evaluation for bisphenol A degradation using a visible-light irradiated LED photoreactor," *Applied Catalysis B*, vol. 100, no. 1-2, pp. 355–364, 2010.
- [134] M. Trillas, J. Peral, and X. Domènech, "Photocatalyzed degradation of phenol, 2,4-dichlorophenol, phenoxyacetic acid and 2,4-dichlorophenoxyacetic acid over supported TiO<sub>2</sub> in a flow system," *Journal of Chemical Technology and Biotechnology*, vol. 67, no. 3, pp. 237–242, 1996.
- [135] K. Hanna, C. De Brauer, P. Germain, J. M. Chovelon, and C. Ferronato, "Degradation of pentachlorophenol in cyclodextrin extraction effluent using a photocatalytic process," *Science of the Total Environment*, vol. 332, no. 1-3, pp. 51–60, 2004.
- [136] P. S. Yap, T. T. Lim, M. Lim, and M. Srinivasan, "Synthesis and characterization of nitrogen-doped TiO<sub>2</sub>/AC composite for the adsorption-photocatalytic degradation of aqueous bisphenol-A using solar light," *Catalysis Today*, vol. 151, no. 1-2, pp. 8–13, 2010.
- [137] D. P. Subagio, M. Srinivasan, M. Lim, and T. T. Lim, "Photocatalytic degradation of bisphenol-A by nitrogen-doped TiO<sub>2</sub> hollow sphere in a vis-LED photoreactor," *Applied Catalysis B*, vol. 95, no. 3-4, pp. 414–422, 2010.
- [138] C. Y. Kuo, C. H. Wu, and H. Y. Lin, "Photocatalytic degradation of bisphenol A in a visible light/TiO<sub>2</sub> system," *Desalination*, vol. 256, no. 1-3, pp. 37–42, 2010.
- [139] L. Liu, F. Chen, and F. Yang, "Stable photocatalytic activity of immobilized Fe<sup>0</sup>/TiO<sub>2</sub>/ACF on composite membrane in degradation of 2,4-dichlorophenol," *Separation and Purification Technology*, vol. 70, no. 2, pp. 173–178, 2009.
- [140] C. M. Chan, K. H. Wong, W. K. Chung, T. S. Chow, and P. K. Wong, "Photocatalytic degradation of di(2-ethylhexyl)phthalate adsorbed by chitin A," *Water Science & Technology*, vol. 56, no. 7, pp. 125–134, 2007.
- [141] Y. J. Lin, S. L. Tseng, W. J. Huang, and W. J. Wu, "Enhanced photocatalysis of pentachlorophenol by metal-modified titanium (IV) oxide," *Journal of Environmental Science and Health Part B*, vol. 41, no. 7, pp. 1143–1158, 2006.
- [142] R. Thiruvengkatahari, T. O. Kwon, and S. Moon, "A total solution for simultaneous organic degradation and particle separation using photocatalytic oxidation and submerged microfiltration membrane hybrid process," *Korean Journal of Chemical Engineering*, vol. 22, no. 6, pp. 938–944, 2005.
- [143] S. Malato, P. Fernández-Ibáñez, M. I. Maldonado, J. Blanco, and W. Gernjak, "Decontamination and disinfection of water by solar photocatalysis: recent overview and trends," *Catalysis Today*, vol. 147, no. 1, pp. 1–59, 2009.
- [144] K. Rajeshwar, "Photoelectrochemistry and the environment," *Journal of Applied Electrochemistry*, vol. 25, no. 12, pp. 1067–1082, 1995.
- [145] J. M. Herrmann, "Heterogeneous photocatalysis: fundamentals and applications to the removal of various types of aqueous pollutants," *Catalysis Today*, vol. 53, no. 1, pp. 115–129, 1999.
- [146] B. L. Yuan, X. Z. Li, and N. Graham, "Reaction pathways of dimethyl phthalate degradation in TiO<sub>2</sub>-UV-O<sub>2</sub> and TiO<sub>2</sub>-UV-Fe(VI) systems," *Chemosphere*, vol. 72, no. 2, pp. 197–204, 2008.
- [147] S. S. Chin, T. M. Lim, K. Chiang, and A. G. Fane, "Hybrid low-pressure submerged membrane photoreactor for the removal of bisphenol A," *Desalination*, vol. 202, no. 1-3, pp. 253–261, 2007.

## Research Article

# Highly Selective Deethylation of Rhodamine B on TiO<sub>2</sub> Prepared in Supercritical Fluids

Yuzun Fan,<sup>1</sup> Guoping Chen,<sup>1</sup> Dongmei Li,<sup>1</sup> Yanhong Luo,<sup>1</sup> Nina Lock,<sup>2</sup>  
Anca Paduraru Jensen,<sup>3</sup> Aref Mamakhel,<sup>3</sup> Jianli Mi,<sup>2</sup> Steen B. Iversen,<sup>3</sup>  
Qingbo Meng,<sup>1</sup> and Bo B. Iversen<sup>2</sup>

<sup>1</sup> Beijing National Laboratory for Condensed Matter Physics, Institute of Physics, Chinese Academy of Sciences, Beijing 100190, China

<sup>2</sup> Center for Materials Crystallography, Department of Chemistry and Interdisciplinary Nanoscience Center, Aarhus University, 8000 Aarhus, Denmark

<sup>3</sup> SCF Technologies A/S, Smedeholm 13B, 2730 Herlev, Denmark

Correspondence should be addressed to Qingbo Meng, qbmeng@iphy.ac.cn and Bo B. Iversen, bo@chem.au.dk

Received 15 June 2011; Accepted 1 July 2011

Academic Editor: Jiaguo Yu

Copyright © 2012 Yuzun Fan et al. This is an open access article distributed under the Creative Commons Attribution License, which permits unrestricted use, distribution, and reproduction in any medium, provided the original work is properly cited.

Pure phase anatase TiO<sub>2</sub> nanoparticles with sizes of 5–8 nm and varying crystallinity were synthesized in supercritical isopropanol/water using a continuous flow reactor. Their photodegradation of rhodamine B (RhB) was evaluated under visible light irradiation. The as-prepared TiO<sub>2</sub> nanoparticles show much higher photodegradation efficiencies than commercial Degussa P25 TiO<sub>2</sub>. Moreover, the photodegradation of RhB on the as-prepared TiO<sub>2</sub> follows a different process from that on P25 TiO<sub>2</sub>, quicker N-deethylation and slower cleavage of conjugated chromophore structure. Based on PXRD, TEM, and BET measurements, these two photodegradation properties have been explained by the physicochemical properties of TiO<sub>2</sub>.

## 1. Introduction

Titanium dioxide (TiO<sub>2</sub>) has been extensively studied for degrading organic pollutants due to its high photocatalytic activity, chemical inertness, non-photocorrosion, nontoxicity, and low cost [1–7]. However, it only responds to ultraviolet light which accounts for about 4% of the solar spectrum. Photosensitization of TiO<sub>2</sub> by dyes has been used to utilize the visible light efficiently [8, 9]. The dye molecules absorb photons to be excited from ground state to excited state. Then the electrons are injected into the conduction band of TiO<sub>2</sub> while the dye molecules turn into its cationic radical. The electrons are scavenged by the molecular oxygen absorbed on the surface of TiO<sub>2</sub> to yield a series of active oxygen species which degrade the dye. Choosing proper organic pollutants to photosensitize TiO<sub>2</sub>, two objectives can be achieved: (1) utilization of TiO<sub>2</sub> under visible light irradiation and (2) degradation of organic pollutants.

It is well known that photocatalytic reactions usually take place on the surface of the catalyst, hence the surface

properties of TiO<sub>2</sub> are important in determining the photocatalytic activity. These properties include morphology [10, 11], particle size [12], crystal structure [13–15], crystallinity [16], pH value of the particle suspension [3], and adsorption of potential pollutants [17, 18]. Tuning the surface properties of TiO<sub>2</sub> photocatalysts through the preparation method is a primary way to enhance its activity [19, 20]. Recently, supercritical fluids have been used as reaction media for synthesis of nanomaterials [21–25]. Supercritical fluids exhibit physicochemical properties which are between those of liquids and gasses. Furthermore, the solubility can be effectively manipulated by small continuous changes in pressure and temperature around the critical point. The use of supercritical fluids as solvents gives significantly lower particle sizes in the nanometer range. This is believed to be due to the fact that instantaneous crystal nucleation and crystallization are faster than crystal growth. Furthermore, the method is fast and environmentally friendly, as the precursors are typically solutions of simple metal salts in water or alcohols. The short synthesis time enables synthesis under

continuous flow as an alternative to conventional batch reactions giving less operational downtime. The supercritical fluid technique may be a new way for preparation of highly active photocatalysts.

Most supercritical fluid studies of TiO<sub>2</sub> nanoparticles have focused on their physical characterization [21–23]. In this paper, we have synthesized nanocrystalline anatase TiO<sub>2</sub> in supercritical isopropanol/water. Attention was focused on evaluating their photodegradation of rhodamine B (RhB) under visible light irradiation. The results indicate that the photodegradation efficiencies of our synthesized TiO<sub>2</sub> are significantly higher than that of the standard photocatalyst P25 TiO<sub>2</sub>. The photodegradation pathways for RhB, namely, cleavage of the conjugated chromophore structure and N-deethylation, were also investigated.

## 2. Experimental

**2.1. Supercritical Synthesis of TiO<sub>2</sub>.** Degussa P25 TiO<sub>2</sub>, which is a mixture of anatase and rutile in the weight ratio 8:2, was used as purchased. A series of TiO<sub>2</sub> samples, herein referred to as the 102 series, was prepared in a continuous flow supercritical process similar to that described in [22], but with a proprietary mixing zone design, that promotes an extremely fast and efficient mixing. The TiO<sub>2</sub> samples were synthesized using a first fluid with a flow rate of 24 mL/min of 0.25 M Titanium TetraIsoPropoxide (TTIP) in isopropanol and a second fluid (48 mL/min flow rate) comprising water adjusted to pH 11.2 using NH<sub>4</sub>OH. The two fluid streams were pressurized to 300 bars. The reaction temperature in the mixing zone was controlled by heating fluid number two to the temperature required to obtain a specific temperature in the mixing zone. Fluid one was in all cases preheated to 100°C. The reactions were quenched immediately after the mixing zone. The TiO<sub>2</sub> samples 102-1 and 102-2 were synthesized in a two step procedure. First, a particle suspension was produced at one temperature, and subsequently this particle suspension was recirculated to the mixing zone as fluid and heated to a second temperature by mixing with fluid two in the same flow ratio. Thus, the TiO<sub>2</sub> samples 102-1 and 102-2 were first synthesized at 180°C and 280°C, respectively, in the mixing zone and recirculated through the system at 320°C. Sample 102-3 was synthesized directly at a mixing zone temperature of 270°C without recirculation. The residence time in the mixing chamber was from 12 s at 180°C to 9.5 s at 320°C. The residence time decreases with increasing the temperature due to the density decrease with increasing the temperature. Hence, the total reaction time is of the order 20 s for the two-step procedure (102-1, 102-2) and approximately 10 s for the directly synthesized sample 102-3. The main motivation for recirculating the nanoparticles in the reactor is to achieve a high crystallinity without substantially decreasing the surface area due to crystal growth. In the first synthesis it is expected that the particles primarily consist of a crystalline core with an amorphous shell. Upon reheating further crystallization will first take place from the outside of the particles, since this region is heated first. The produced suspensions were

processed to dry powders in a rotary evaporator. The powder was redispersed to a 30 wt% suspension of particles in ethanol using a Netzsch nanomill with 60 micron ZrO<sub>2</sub> particles as milling media.

**2.2. Characterization.** Powder X-ray diffraction (PXRD) data were collected on an STOE diffractometer in transmission geometry using Cu K $\alpha_1$  radiation. Transmission electron microscopy (TEM) images were recorded on a Philips CM20 electron microscope equipped with a LaB<sub>6</sub> filament at 200 kV. Diffuse reflection spectra were measured on a UV-visible spectrophotometer (UV-2550, Shimadzu). The Brunauer-Emmett-Teller (BET) specific surface area was determined by nitrogen adsorption-desorption isotherm measurements at 77 K (ASAP 2020, Micromeritics).

**2.3. Photodegradation Performance.** The photodegradation efficiencies of the samples were determined based on the degradation of RhB under visible light irradiation. The light source was a 500 W halogen lamp (Institute of Electric Light Source, Beijing) which was fixed inside a cylindrical pyrex vessel and cooled by a circulating water jacket (pyrex). A long-pass glass filter was used to cut off the light with wavelengths below 420 nm before the sample was irradiated. The radial flux was measured with a radiant power/energy meter (70260, Oriel); the average light intensity was 100 mW·cm<sup>-2</sup>. For a typical photodegradation test, a reaction solution was prepared from 25 mg of the nanocrystalline TiO<sub>2</sub> sample and 50 mL of 2 × 10<sup>-5</sup> M RhB aqueous solution. The pH value of the reaction solutions was controlled at about 5.2. The solutions were magnetically stirred in the dark for 30 minutes to ensure the establishment of an adsorption/desorption equilibrium of RhB on the TiO<sub>2</sub> surfaces. At certain time intervals during the irradiation, 3 mL of the turbid reaction solution was centrifuged to remove the TiO<sub>2</sub> catalyst. The concentration of RhB was determined by measuring the absorbance of the resulting clear solution with a UV-visible spectrophotometer (UV-2550, Shimadzu).

## 3. Results and Discussion

The TiO<sub>2</sub> samples were characterized by PXRD (Figure 1). The diffraction pattern of the 102 series samples can be indexed as the anatase phase of TiO<sub>2</sub>, whereas additional diffraction peaks corresponding to the rutile phase of TiO<sub>2</sub> are observed for P25 TiO<sub>2</sub>. The peaks of the 102 series samples are broader than those of P25 TiO<sub>2</sub>, indicating the samples prepared in supercritical fluids consist of smaller crystallites.

The 102 series powders were mixed with CaF<sub>2</sub>, and PXRD data were collected and Rietveld refined allowing determination of the particle size and crystallinity (i.e., determination of the fraction of crystalline material in the sample). Two parameters were used to describe the profile of each phase with a Thompson-Cox-Hastings pseudo-Voigt function. The Gaussian *W* parameter and the Lorentzian size parameter *Y* were used for the description of the TiO<sub>2</sub> peak shapes, while the CaF<sub>2</sub> peak shapes were described using

TABLE 1: Summary of physicochemical properties of TiO<sub>2</sub>.

Sample <sup>a</sup>	Crystallite size (nm)	BET (m <sup>2</sup> /g)	Dye adsorp. (%)	Dye degradation (%) <sup>b</sup>	Crystallinity (%)
102-1	7.8	239	9.3	76.9	55
102-2	7.5	229	5.4	65.0	58
102-3	5.0	346	19.7	95.8	50
P25	21	52	2.5	20.6	73(anatase)/18(rutile)

<sup>a</sup>The nanoparticles were used for RhB degradation with an initial dye concentration of  $2 \times 10^{-5}$  M and a catalyst concentration of 0.5 g/L.

<sup>b</sup>The dye degradation was obtained after visible irradiation for 60 min.

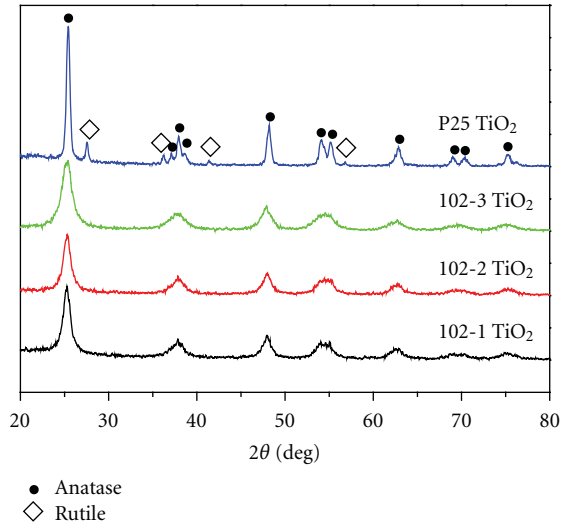


FIGURE 1: PXRD patterns of the TiO<sub>2</sub> nanoparticles.

$W$  and the Lorentzian strain parameter  $X$  [24, 26]. As an example the refinement of 102-1 TiO<sub>2</sub>/CaF<sub>2</sub> is shown in Figure 2. The fit of the peak at 53° is rather poor and may point to some degree of anisotropy of the particles, which is not described by this Rietveld model. However, previous TEM studies have shown that a spherical model is generally a good approach to describe nanocrystalline TiO<sub>2</sub> synthesized in supercritical fluids [21].

The full width at half maximum (FWHM) of the (101) TiO<sub>2</sub> peak was calculated from the profile parameters, and the instrumental broadening, determined from PXRD data collected on a silicon standard, was subtracted. The crystallite sizes,  $d$ , are determined from the FWHM of the (101) peak using the Scherrer equation:  $d = 0.9\lambda/(\beta \cos \theta)$ , where  $\lambda$  (0.154056 nm) is the X-ray wavelength,  $\theta$  is the angle of Bragg diffraction, and  $\beta$  is the difference between the FWHM and the instrumental broadening. The results are shown in Table 1. The crystallite size decreases as P25 > 102-2~102-1 > 102-3. A TEM image of the 102-3 sample is shown in Figure 3. There is a good agreement between the sizes determined from the PXRD data and TEM.

The phase fractions of crystalline TiO<sub>2</sub> and CaF<sub>2</sub> were determined by Rietveld refinement. Based on these, the crystallinity of the TiO<sub>2</sub> samples were determined (see Table 1).

Figure 4 presents the UV-visible diffuse reflection spectra of TiO<sub>2</sub>. The absorption band edges of the 102 series samples

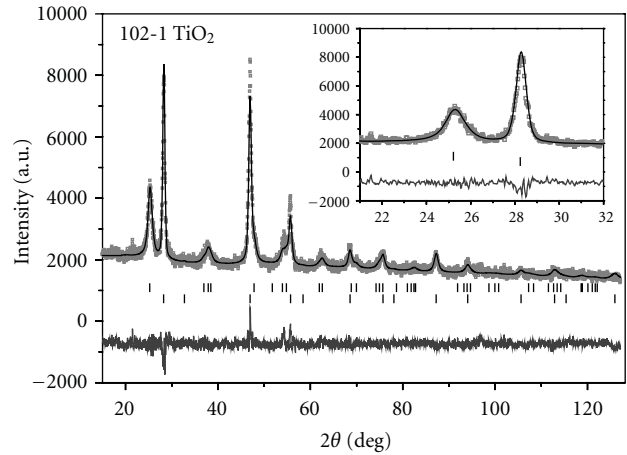


FIGURE 2: Rietveld refinement of a 102-1 TiO<sub>2</sub>/CaF<sub>2</sub> mixture. The vertical lines indicate Bragg positions for anatase (top) and CaF<sub>2</sub> (bottom), respectively. The inset shows an enlargement of the angular region 21–32°, in which the peak at 25.5° is the TiO<sub>2</sub> (101) peak. The  $R_f$  factors are 7.0% and 6.5%, respectively, for the TiO<sub>2</sub> and CaF<sub>2</sub> phases.

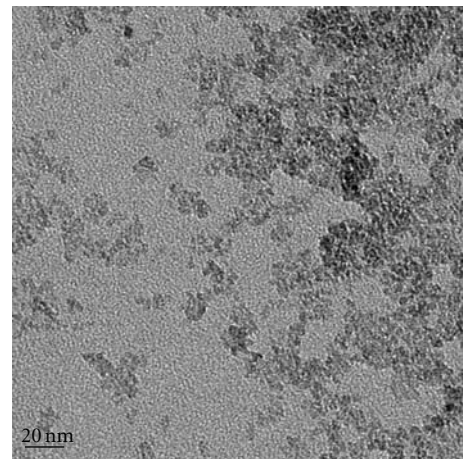


FIGURE 3: TEM image of the 102-3 TiO<sub>2</sub> sample.

of TiO<sub>2</sub> are blue shifted compared with that of P25 TiO<sub>2</sub>. This can be explained by the sample composition, as anatase has a larger bandgap (3.2 eV) than rutile (3.0 eV). The 102 series of TiO<sub>2</sub> consists of pure anatase, while P25 TiO<sub>2</sub> is a mixture of anatase and rutile. For the 102 series of TiO<sub>2</sub>, due to the quantum size effect, the order of the hypsochromic shifts of the absorption band edge is 102-3 > 102-1 ~ 102-2.

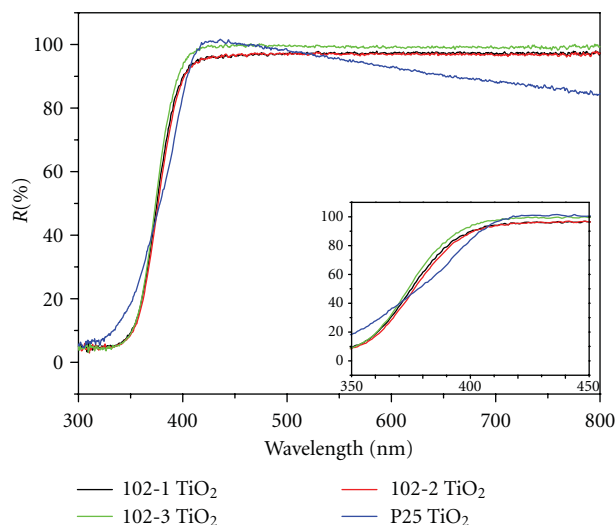


FIGURE 4: UV-visible diffuse reflection spectra of TiO<sub>2</sub>. The inset shows an enlarged UV-Visible diffuse reflection spectra between 350 and 450 nm.

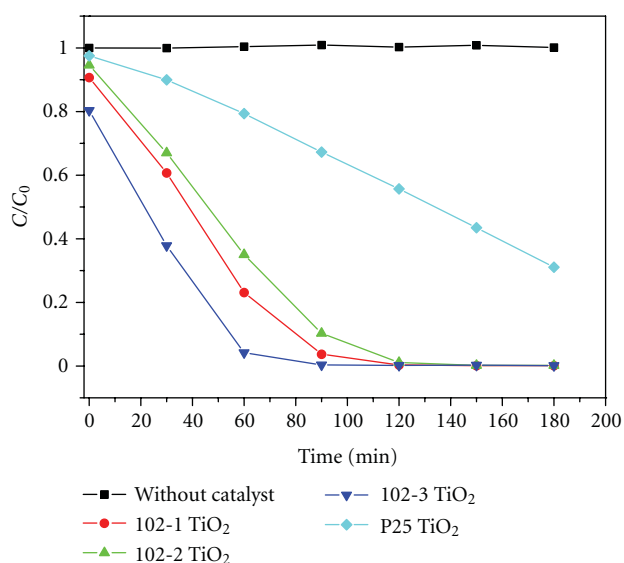


FIGURE 5: RhB concentration changes during the photodegradation of RhB.  $C_0$  is the initial RhB concentration before adsorption to the TiO<sub>2</sub> surfaces, and  $C$  is the temporal concentration of RhB after equilibrium adsorption.

Due to the overlap between the energy distribution function of the excited RhB and the conduction band of TiO<sub>2</sub> [3, 27], TiO<sub>2</sub> can be photosensitized by RhB dye to utilize the visible light efficiently. Figure 5 shows the photodegradation of RhB by TiO<sub>2</sub> samples under visible light irradiation. As can be seen RhB is very stable in aqueous solution without presence of a photocatalyst. The decrease in the RhB concentration ( $C/C_0 < 1$ ) before irradiation at  $t = 0$  min reflects the extent of dye adsorbed onto the TiO<sub>2</sub> photocatalyst. The amounts of adsorbed dye on the 102-1, 102-2, and 102-3 TiO<sub>2</sub> are 9.3%, 5.4%, and 19.7%, respectively, which is much greater than that on the P25 TiO<sub>2</sub> (2.5%). The degradation rates of the 102 series of

TiO<sub>2</sub> are correspondingly much greater than that of the P25 TiO<sub>2</sub>. After visible light irradiation for 60 min, the percentage of the degraded dye for the 102-1, 102-2, 102-3, and P25 TiO<sub>2</sub> are 76.9%, 65.0%, 95.8%, and 20.6%, respectively. These results could be well explained by the specific surface area since the photodegradation reaction takes place on the surface of the photocatalyst. The BET surface areas of the TiO<sub>2</sub> samples were determined to be 239 m<sup>2</sup>/g for 102-1 TiO<sub>2</sub>, 229 m<sup>2</sup>/g for 102-2 TiO<sub>2</sub>, 346 m<sup>2</sup>/g for 102-3 TiO<sub>2</sub>, and 52 m<sup>2</sup>/g for P25 TiO<sub>2</sub>. The specific surface area of the 102 series of TiO<sub>2</sub> is obviously larger than that of P25 TiO<sub>2</sub>, which is attributed to the relatively small crystallite sizes of the 102 TiO<sub>2</sub> samples. This accounts for the enhanced photodegradation activity of the 102 series. As summed up in Table 1 the 102 TiO<sub>2</sub> samples have smaller crystallite sizes, larger specific surface areas, and higher dye adsorption than P25. This leads to better photodegradation efficiencies. It is interesting to note that the data indicate that crystallite size and dye adsorption efficiency are the primary factors determining the photodegradation efficiency. Thus, the smallest nanoparticles, 102-3 (~5 nm), clearly outperform the larger 102-1 and 102-2 nanoparticles (~7-8 nm).

During the photodegradation of RhB a clear difference in the spectral change between the P25 TiO<sub>2</sub> and 102 series of TiO<sub>2</sub> is observed. Thus, there are clear differences in the extent of blue-shift in the major absorption band of RhB (Figure 6(a)). Basically, there are two photodegradation pathways for RhB: (1) cleavage of the whole conjugated chromophore structure and (2) N-deethylation [18, 28, 29]. Following the first pathway the main peak position remains constant while the peak intensity decreases. During the second pathway, which has the N-deethylation, the main peak position gradually blue shifts according to the following absorption maxima: RhB, 554 nm; N,N,N'-Triethyl-rhodamine, 539 nm; N,N'-Diethyl-rhodamine, 522 nm; N-Ethyl-rhodamine, 510 nm; Rhodamine, 498 nm [30]. In most cases the two degradation pathways coexist and compete.

For the P25 TiO<sub>2</sub> dispersion the major absorption band decreases gradually with little blue shift (Figure 6(b)), indicating that the cleavage of the whole conjugated chromophore structure is the main pathway. In contrast, for the 102 series of TiO<sub>2</sub>, exemplified by 102-3 TiO<sub>2</sub>, the major absorption band shifts from 554 to 498 nm within 90 min irradiation and upon further irradiation rhodamine undergoes a slower decomposition (Figure 6(c)), indicating N-deethylation as the main pathway. The cleavage of the conjugated chromophore structure can be estimated by the peak intensity. From the molar extinction coefficient  $\epsilon_{\max}$  (RhB,  $11.5 \times 10^4 \text{ M}^{-1} \cdot \text{cm}^{-1}$ ; rhodamine,  $8.4 \times 10^4 \text{ M}^{-1} \cdot \text{cm}^{-1}$ ), rhodamine should have a peak intensity at 498 nm of ca. 70% of the RhB intensity at 554 nm assuming the conjugated ring structure is not destroyed [31]. For the 102-3 TiO<sub>2</sub> dispersion, after full N-deethylation (90 min irradiation), about 11.7% of the conjugated chromophore structure is destroyed, and about 33% is destroyed after 180 min irradiation, which indicates initially quick N-deethylation and slow cleavage of the conjugated chromophore structure. For the P25 TiO<sub>2</sub> dispersion, about 68.9% is destroyed within

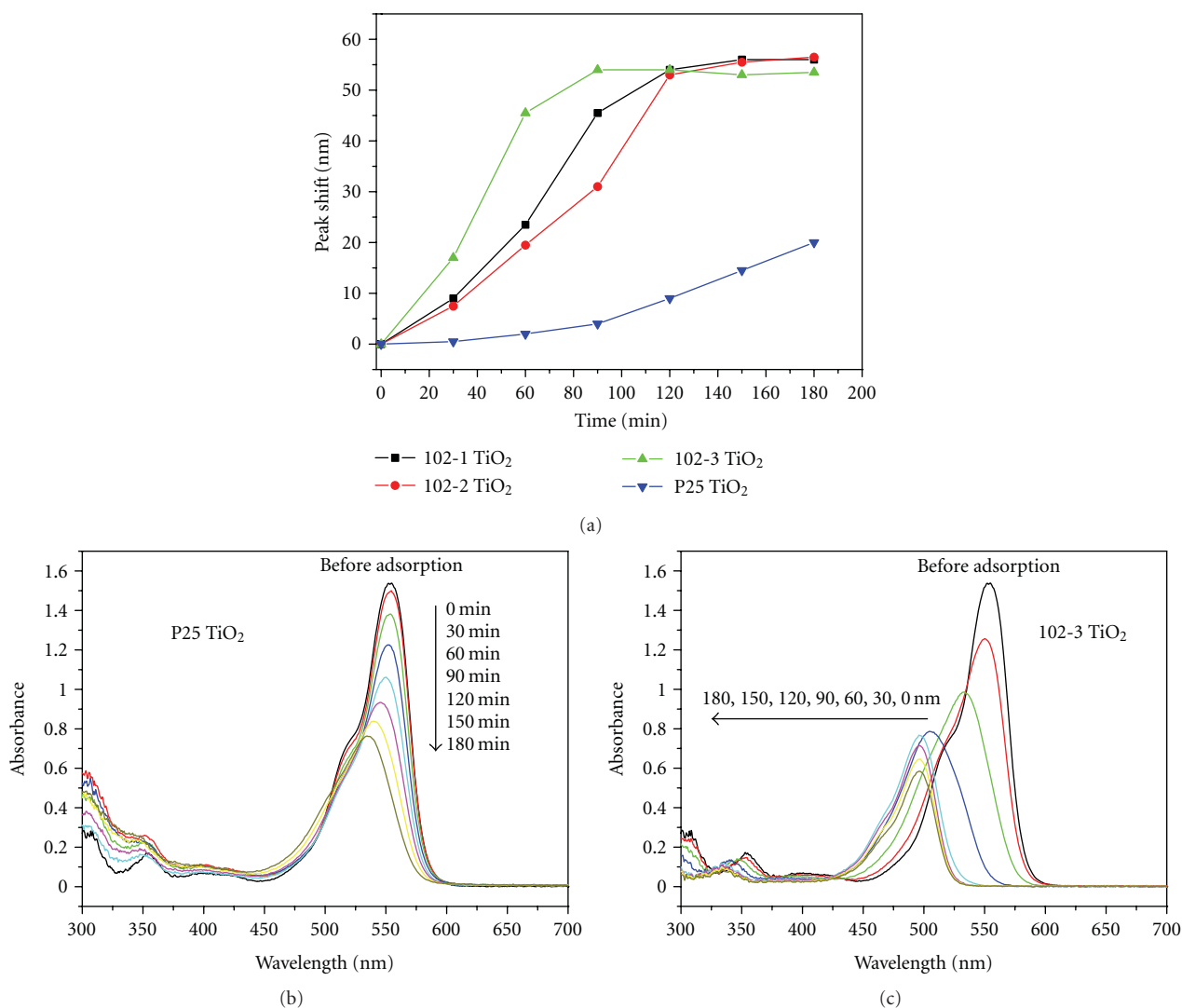


FIGURE 6: (a) Hypsochromic shifts of the major absorption band of RhB with irradiation time. (b) Gradual spectral changes of RhB in aqueous P25 TiO<sub>2</sub> dispersion under visible light irradiation. (c) Gradual spectral changes of RhB in aqueous 102-3 TiO<sub>2</sub> dispersion under visible light irradiation.

180 min irradiation, which means slow N-deethylation and relatively fast cleavage of conjugated chromophore structure. The difference in the degradation process of RhB between the P25 TiO<sub>2</sub> and 102 series of TiO<sub>2</sub> may be due to their different crystallinity. Lower crystallinity leads to quicker N-deethylation and slower cleavage of conjugated chromophore structure (102 series of TiO<sub>2</sub>), while higher crystallinity leads to slower N-deethylation and quicker cleavage of conjugated chromophore structure (P25 TiO<sub>2</sub>).

#### 4. Conclusions

TiO<sub>2</sub> nanoparticles synthesized in supercritical isopropanol/water have smaller crystallite sizes, larger specific surface area, and higher dye adsorption efficiency than commercial P25 TiO<sub>2</sub>. This leads to higher photodegradation efficiencies in degradation of rhodamine B than for P25 TiO<sub>2</sub>. Interestingly, rhodamine B undergoes quicker N-deethylation

and slower cleavage of conjugated chromophore structure on the 102 series of TiO<sub>2</sub> than on P25 TiO<sub>2</sub>. The absolute crystallinity of the nanoparticles seems to affect the photodegradation process to a large extent: the lower crystallinity, the quicker N-deethylation, and slower cleavage of conjugated chromophore structure.

#### Acknowledgments

This work was financially supported by the National Natural Science Foundation of China (Grant no. 20725311, 20873178, 21073231, and 51072221), the Ministry of Science and Technology of China (863 Project, no. 2009AA033101), Foundation of the Chinese Academy of Sciences (no. KJCX2-YW-W27, KGCX2-YW-386-1, KGCX2-YW-363), and the Danish Strategic Research Council and the Danish National Research Foundation.

## References

- [1] A. Fujishima, X. Zhang, and D. A. Tryk, "TiO<sub>2</sub> photocatalysis and related surface phenomena," *Surface Science Reports*, vol. 63, no. 12, pp. 515–582, 2008.
- [2] M. R. Hoffmann, S. T. Martin, W. Choi, and D. W. Bahnemann, "Environmental applications of semiconductor photocatalysis," *Chemical Reviews*, vol. 95, no. 1, pp. 69–96, 1995.
- [3] C. Chen, W. Ma, and J. Zhao, "Semiconductor-mediated photodegradation of pollutants under visible-light irradiation," *Chemical Society Reviews*, vol. 39, no. 11, pp. 4206–4219, 2010.
- [4] J.-M. Herrmann, "Heterogeneous photocatalysis: state of the art and present applications," *Topics in Catalysis*, vol. 34, no. 1-4, pp. 49–65, 2005.
- [5] F. Han, V. S. R. Kambala, M. Srinivasan, D. Rajarathnam, and R. Naidu, "Tailored titanium dioxide photocatalysts for the degradation of organic dyes in wastewater treatment: a review," *Applied Catalysis A*, vol. 359, no. 1-2, pp. 25–40, 2009.
- [6] J. A. Byrne, P. A. Fernandez-Ibañez, P. S. M. Dunlop, D. M. A. Alrousan, and J. W. J. Hamilton, "Photocatalytic enhancement for solar disinfection of water: a review," *International Journal of Photoenergy*, vol. 2011, Article ID 798051, 12 pages, 2011.
- [7] J. Gamage and Z. S. Zhang, "Applications of photocatalytic disinfection," *International Journal of Photoenergy*, vol. 2010, Article ID 764870, 11 pages, 2010.
- [8] J. Zhao, T. Wu, K. Wu, K. Oikawa, H. Hidaka, and N. Serpone, "Photoassisted degradation of dye pollutants. 3. Degradation of the cationic dye rhodamine B in aqueous anionic surfactant/TiO<sub>2</sub> dispersions under visible light irradiation: evidence for the need of substrate adsorption on TiO<sub>2</sub> particles," *Environmental Science and Technology*, vol. 32, no. 16, pp. 2394–2400, 1998.
- [9] B. O'Regan and M. Grätzel, "A low-cost, high-efficiency solar cell based on dye-sensitized colloidal TiO<sub>2</sub> films," *Nature*, vol. 353, no. 6346, pp. 737–740, 1991.
- [10] N. H. Lee, H. J. Oh, S. C. Jung, W. J. Lee, D. H. Kim, and S. J. Kim, "Photocatalytic properties of nanotubular-shaped TiO<sub>2</sub> powders with anatase phase obtained from titanate nanotube powder through various thermal treatments," *International Journal of Photoenergy*, vol. 2011, Article ID 327821, 7 pages, 2011.
- [11] M. L. Chen and W. C. Oh, "The improved photocatalytic properties of methylene blue for V<sub>2</sub>O<sub>3</sub>/CNT/TiO<sub>2</sub> composite under visible light," *International Journal of Photoenergy*, vol. 2010, Article ID 264831, 5 pages, 2010.
- [12] H. D. Jang, S. K. Kim, and S. J. Kim, "Effect of particle size and phase composition of titanium dioxide nanoparticles on the photocatalytic properties," *Journal of Nanoparticle Research*, vol. 3, no. 2-3, pp. 141–147, 2001.
- [13] J. Zhang, Q. Xu, Z. Feng, M. Li, and C. Li, "Importance of the relationship between surface phases and photocatalytic activity of TiO<sub>2</sub>," *Angewandte Chemie International Edition*, vol. 47, no. 9, pp. 1766–1769, 2008.
- [14] Y. Wang, L. Zhang, K. Deng, X. Chen, and Z. Zou, "Low temperature synthesis and photocatalytic activity of rutile TiO<sub>2</sub> nanorod superstructures," *Journal of Physical Chemistry C*, vol. 111, no. 6, pp. 2709–2714, 2007.
- [15] Z. Ding, G. Q. Lu, and P. F. Greenfield, "Role of the crystallite phase of TiO<sub>2</sub> in heterogeneous photocatalysis for phenol oxidation in water," *Journal of Physical Chemistry B*, vol. 104, no. 19, pp. 4815–4820, 2000.
- [16] M. E. Simonsen, H. Jensen, Z. Li, and E. G. Søgaard, "Surface properties and photocatalytic activity of nanocrystalline titania films," *Journal of Photochemistry and Photobiology A*, vol. 200, no. 2-3, pp. 192–200, 2008.
- [17] F. Chen, J. Zhao, and H. Hidaka, "Highly selective deethylation of Rhodamine B: adsorption and photooxidation pathways of the dye on the TiO<sub>2</sub>/SiO<sub>2</sub> composite photocatalyst," *International Journal of Photoenergy*, vol. 5, no. 4, pp. 209–217, 2003.
- [18] Q. Wang, C. Chen, D. Zhao, W. Ma, and J. Zhao, "Change of adsorption modes of dyes on fluorinated TiO<sub>2</sub> and its effect on photocatalytic degradation of dyes under visible irradiation," *Langmuir*, vol. 24, no. 14, pp. 7338–7345, 2008.
- [19] Q. J. Xiang, J. G. Yu, and M. Jaroniec, "Tunable photocatalytic selectivity of TiO<sub>2</sub> films consisted of flower-like microspheres with exposed 001 facets," *Chemical Communications*, vol. 47, no. 15, pp. 4532–4534, 2011.
- [20] S. Liu, J. Yu, and M. Jaroniec, "Tunable photocatalytic selectivity of hollow TiO<sub>2</sub> microspheres composed of anatase polyhedra with exposed 001 facets," *Journal of the American Chemical Society*, vol. 132, no. 34, pp. 11914–11916, 2010.
- [21] P. Hald, J. Becker, M. Bremholm et al., "Supercritical propanol-water synthesis and comprehensive size characterisation of highly crystalline anatase TiO<sub>2</sub> nanoparticles," *Journal of Solid State Chemistry*, vol. 179, no. 8, pp. 2674–2680, 2006.
- [22] L. L. Toft, D. F. Aarup, M. Bremholm, P. Hald, and B. B. Iversen, "Comparison of T-piece and concentric mixing systems for continuous flow synthesis of anatase nanoparticles in supercritical isopropanol/water," *Journal of Solid State Chemistry*, vol. 182, no. 3, pp. 491–495, 2009.
- [23] H. Jensen, K. D. Joensen, S. B. Iversen, and E. G. Søgaard, "Low temperature synthesis of metal oxides by a supercritical seed enhanced crystallization (SSEC) process," *Industrial and Engineering Chemistry Research*, vol. 45, no. 10, pp. 3348–3353, 2006.
- [24] N. Lock, P. Hald, M. Christensen, H. Birkedal, and B. B. Iversen, "Continuous flow supercritical water synthesis and crystallographic characterization of anisotropic boehmite nanoparticles," *Journal of Applied Crystallography*, vol. 43, no. 4, pp. 858–866, 2010.
- [25] J. Becker, P. Hald, M. Bremholm et al., "Critical size of crystalline ZrO<sub>2</sub> nanoparticles synthesized in near- and supercritical water and supercritical isopropyl alcohol," *ACS Nano*, vol. 2, no. 5, pp. 1058–1068, 2008.
- [26] H. Jensen, K. D. Joensen, J. E. Jørgensen, J. S. Pedersen, and E. G. Søgaard, "Characterization of nanosized partly crystalline photocatalysts," *Journal of Nanoparticle Research*, vol. 6, no. 5, pp. 519–526, 2004.
- [27] T. Takizawa, T. Watanabe, and K. Honda, "Photocatalysis through excitation of adsorbates. 2. A comparative study of rhodamine B and methylene blue on cadmium sulfide," *Journal of Physical Chemistry*, vol. 82, no. 12, pp. 1391–1396, 1978.
- [28] H. Park and W. Choi, "Photocatalytic reactivities of nafion-coated TiO<sub>2</sub> for the degradation of charged organic compounds under UV or visible light," *Journal of Physical Chemistry B*, vol. 109, no. 23, pp. 11667–11674, 2005.
- [29] K. Yu, S. Yang, H. He, C. Sun, C. Gu, and Y. Ju, "Visible light-driven photocatalytic degradation of rhodamine B over NaBiO<sub>3</sub>: pathways and mechanism," *Journal of Physical Chemistry A*, vol. 113, no. 37, pp. 10024–10032, 2009.
- [30] T. Watanabe, T. Takizawa, and K. Honda, "Photocatalysis through excitation of adsorbates. 1. Highly efficient

N-deethylation of rhodamine B adsorbed to CdS," *Journal of Physical Chemistry*, vol. 81, no. 19, pp. 1845–1851, 1977.

- [31] T. Wu, G. Liu, J. Zhao, H. Hidaka, and N. Serpone, "Photoassisted degradation of dye pollutants. V. Self-photosensitized oxidative transformation of Rhodamine B under visible light irradiation in aqueous TiO<sub>2</sub> dispersions," *Journal of Physical Chemistry B*, vol. 102, no. 30, pp. 5845–5851, 1998.

## Research Article

# Effects of Calcination Temperatures on Photocatalytic Activity of Ordered Titanate Nanoribbon/SnO<sub>2</sub> Films Fabricated during an EPD Process

Li Zhao,<sup>1,2</sup> Jingrun Ran,<sup>1</sup> Zhan Shu,<sup>1</sup> Guotian Dai,<sup>2</sup> Pengcheng Zhai,<sup>1</sup> and Shimin Wang<sup>2</sup>

<sup>1</sup>State Key Laboratory of Advanced Technology for Materials Synthesis and Processing, Wuhan University of Technology, Luoshi Road 122#, Wuhan 430070, China

<sup>2</sup>Ministry of Education Key Laboratory for the Green Preparation and Application of Functional Materials, Hubei University, Wuhan 430062, China

Correspondence should be addressed to Shimin Wang, shiminwang@126.com

Received 13 May 2011; Accepted 15 June 2011

Academic Editor: Jiaguo Yu

Copyright © 2012 Li Zhao et al. This is an open access article distributed under the Creative Commons Attribution License, which permits unrestricted use, distribution, and reproduction in any medium, provided the original work is properly cited.

Ordered titanate nanoribbon (TNR)/SnO<sub>2</sub> films were fabricated by electrophoretic deposition (EPD) process using hydrothermally prepared titanate nanoribbon as a precursor. The formation mechanism of ordered TNR film on the fluorine-doped SnO<sub>2</sub> coated (FTO) glass was investigated by scanning electron microscopy (SEM). The effects of calcination temperatures on the phase structure and photocatalytic activity of ordered TNR/SnO<sub>2</sub> films were investigated and discussed. The X-ray diffraction (XRD) results indicate that the phase transformation of titanate to anatase occurs at 400°C and with increasing calcination temperature, the crystallization of anatase increases. At 600°C, the nanoribbon morphology still hold and the TiO<sub>2</sub>/SnO<sub>2</sub> film exhibits the highest photocatalytic activity due to the good crystallization, unique morphology, and efficient photogenerated charge carriers separation and transfer at the interface of TiO<sub>2</sub> and SnO<sub>2</sub>.

## 1. Introduction

A large number of investigations have focused on the semiconductor photocatalyst for its applications in solar energy conversion and environmental purification since Fujishima and Honda discovered the photocatalytic splitting of water on the TiO<sub>2</sub> electrodes in 1972 [1–9]. Among various oxide semiconductor photocatalysts, titania is a very important photocatalyst for its strong oxidizing power, nontoxicity, and long-term photostability [10–13]. However, TiO<sub>2</sub> acting as a photocatalyst has an inherent and significant shortcoming: the fast recombination of the photogenerated charge carriers (hole-electron pairs). Thus, it is of great importance to reduce the recombination of photogenerated charge carriers in TiO<sub>2</sub> to enhance its photocatalytic activity for practical and commercial use. Coupling TiO<sub>2</sub> with other semiconductors can provide a beneficial solution for this drawback [14–20]. For example, Tada et al. [14, 16, 17] and our previous work [19] conducted a systematic research on the SnO<sub>2</sub> as a cou-

pled semiconductor and confirmed that the photogenerated electrons in the TiO<sub>2</sub>/SnO<sub>2</sub> system can accumulate on the SnO<sub>2</sub> and photogenerated holes can accumulate on the TiO<sub>2</sub> because of the formation of heterojunction at the TiO<sub>2</sub>/SnO<sub>2</sub> interface, which can result in lower recombination rate of photogenerated charge carriers and higher quantum efficiency and thus better photocatalytic activity. Moreover, conventional powder photocatalysts have serious drawbacks such as the need for posttreatment separation in a slurry system and their easy aggregation, resulting in the low photocatalytic activity [14]. Therefore, the development of two-dimensional (2D) film photocatalysts with efficient electron-hole utilization and favorable recycling characteristics is a challenge for practical applications [21].

Various approaches, such as vacuum evaporation, sputtering, chemical vapor deposition, and sol-gel methods, have been contributed to the fabrication of 2D thin film. However, these approaches have some disadvantages for industry applications. Vacuum evaporation, sputtering, and chemical

vapor deposition methods require special apparatuses for deposition of films, and sol-gel method needs coating repeatedly in order to get thick films. Recently, a versatile and facile method, electrophoretic deposition (EPD) method, was successfully utilized to fabricate thin film materials [19, 20]. The EPD method exhibits many advantages, such as higher deposition rate, reproducibility, and efficient control over thickness and morphology of the films through tuning the applied current or potential. Moreover, the EPD method can be used to deposit films on different shaped and sized substrates, which can be extended to a large scale and commercial applications.

Our recent work indicates that titanate nanotube films could be obtained by the EPD method [20]. However, there is no report on the preparation of ordered titanate nanoribbon/SnO<sub>2</sub> films for photocatalytic application. Herein, we present a facile and effective approach for the preparation of ordered titanate nanoribbons/SnO<sub>2</sub> films by the EPD process using hydrothermally prepared titanate nanoribbon as a precursor. The formation mechanism of ordered titanate nanoribbons films during the EPD process was investigated by SEM results. Moreover, the effects of calcination temperatures on the phase structure and photocatalytic activity of ordered TNR/SnO<sub>2</sub> were investigated and discussed.

## 2. Experimental

**2.1. Preparation of Titanate Nanoribbon.** Titanate nanoribbon was synthesized by a hydrothermal method using commercial TiO<sub>2</sub> powder (P25, Degussa, Germany) as a starting material according to our previous reported method [22]. In a typical preparation, 1.5 g P25 was mixed with 140 mL of 10 M NaOH solution followed by hydrothermal treatment of the mixture at 200°C in a 200 mL Teflon-lined autoclave for 48 h. After hydrothermal reaction, the precipitate was separated by filtration and washed with a 0.1 M HCl solution and distilled water until the pH value of the rinsing solution reached ca. 6.5, approaching the pH value of the distilled water. The washed sample was dried in a vacuum oven at 60°C for 8 h.

**2.2. Preparation of Ordered TNR/SnO<sub>2</sub> Films.** The ordered TNR films were deposited on FTO glass (Sheet resistance 14–20 ohm/sq) using an EPD method. The electrolyte solution was obtained by adding 1.5 g titanate nanoribbons powder to 200 mL mixed solution of 60 mL ethanol and 140 mL distilled water and then ultrasonicated for 20 min. The pH value of the electrolyte was adjusted to about 9.0 by addition of tetra-methyl-ammonium hydroxide for controlling the surface charge of TNR. The isoelectric point of TNR was reported to be about 5.5 [23, 24]. Therefore, TNR in the pH 9 electrolyte solution had a negatively surface charge density and would be attracted to positive electrode. During the EPD, the cleaned FTO glass was kept at a positive potential while pure silver foil was used as the counter electrode. The linear distance between the two electrodes was about 4 cm. The applied voltage was 15 V. The coated substrates were rinsed with distilled water, dried in air, and calcined at 300, 400, 500, and 600°C in air for 2 h, respectively.

**2.3. Characterization.** X-ray diffraction (XRD) patterns were obtained on a D/MAX-RB X-ray diffractometer (Rigaku, Japan) using Cu K $\alpha$  irradiation at a scan rate of 0.05° 2 $\theta$  s<sup>-1</sup> and were used to determine the identity of any phase present. The accelerating voltage and the applied current were 15 kV and 20 mA, respectively. Transmission electron microscopy (TEM) and high-resolution transmission electron microscopy (HRTEM) analyses were conducted with an H-600 STEM/EDX PV9100 microscope, using 200 kV accelerating voltage. Morphology observation was performed on a JSM-6700F field emission scanning electron microscope (FESEM, JEOL, Japan).

**2.4. Measurement of Photocatalytic Activity.** Rhodamine B (RhB), one of the N-containing dyes, which are resistant to biodegradation and direct photolysis, is a popular probe molecule in the heterogeneous photocatalysis reaction. It is often used as a tracer dye within water to determine the rate and direction of flow and transport. Rhodamine dyes fluoresce and can thus be detected easily and inexpensively with instruments called fluorometers. Rhodamine dyes are used extensively in biotechnology applications such as fluorescence microscopy, flow cytometry, and fluorescence correlation spectroscopy. In USA, RhB is suspected to be carcinogenic, and thus products containing it must contain a warning on its label. Therefore, we chose it as a model pollutant compound to evaluate the photocatalytic activity of the as-prepared calcined TNR/SnO<sub>2</sub> films [25]. Photocatalytic activity of the calcined TNR/SnO<sub>2</sub> films was evaluated and compared by the photocatalytic decolorization of RhB aqueous solution at ambient temperature, as reported in the previous studies [25, 26]. The calcined TNR/SnO<sub>2</sub> films were settled in a 20 mL RhB aqueous solution with a concentration of 1.0  $\times$  10<sup>-5</sup> mol L<sup>-1</sup> in a dish with a diameter of 9.0 cm. A 15 W 365 nm UV lamp (Cole-Parmer Instrument Co.) was used as a light source. The absorbance of RhB at 554 nm was measured by a UV-Vis spectrophotometer (UV2550, Shimadzu, Japan). According to the Lambert-Beer Law [27, 28], the absorbance ( $A$ ) of RhB is proportional to its concentration ( $c$ ), which generally followed the following equation:

$$A = \epsilon bc, \quad (1)$$

where  $\epsilon$  is the molar absorption coefficient and  $b$  is the thickness of the absorption cell. In our experiment, all the testing parameters were kept constant, so the  $\epsilon$  and  $b$  can be considered as a constant. Therefore, the changes of the concentration ( $c$ ) of RhB aqueous solution can be determined by a UV-Vis spectrophotometer. As for the RhB aqueous solution with low concentration, its photocatalytic decolorization is a pseudo-first-order reaction and its kinetics may be expressed as follows [29]:

$$\ln\left(\frac{A_0}{A_t}\right) = kt, \quad (2)$$

where  $k$  is the apparent rate constant and  $A_0$  and  $A_t$  are the initial and reaction absorbance of RhB aqueous solution, respectively.

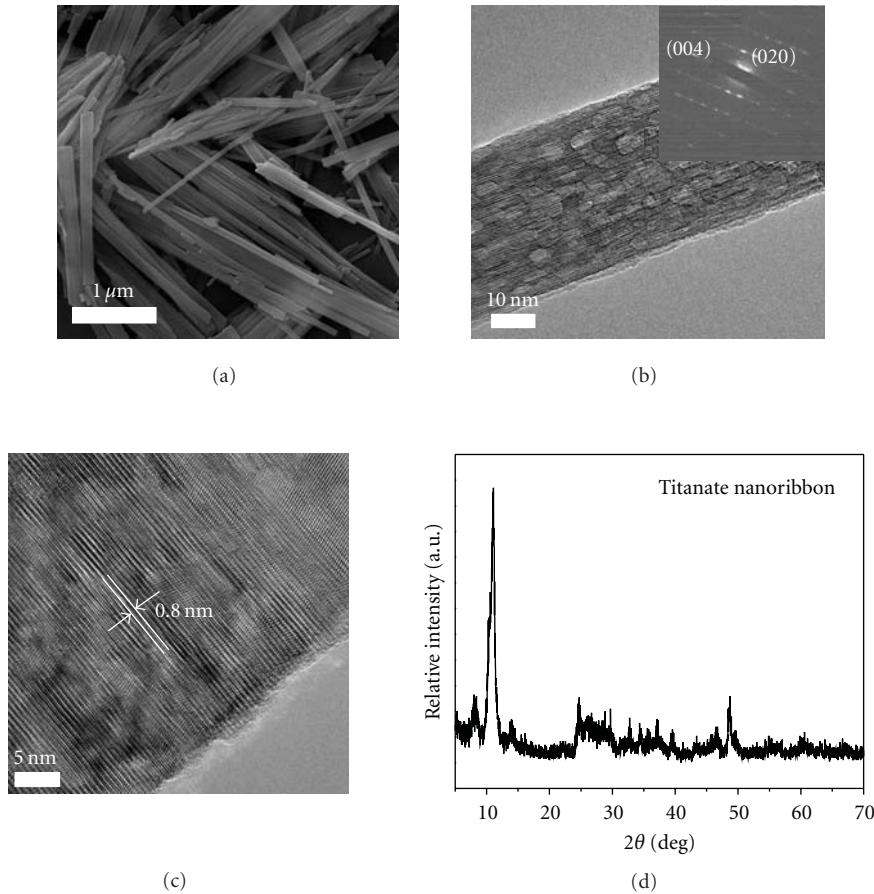


FIGURE 1: SEM image (a), TEM image (b), SAED pattern (inset in b), HRTEM image (c), and XRD pattern (d) of the as-prepared titanate nanoribbon.

### 3. Results And Discussion

#### 3.1. Morphology and Phase Structure of the As-Prepared TNR.

Figure 1(a) shows the SEM image of well-dispersed TNR with a length range from several micrometers to several tens of micrometers and a width of 30–300 nm. As shown in Figure 1(b), a typical image of belt-like structure was obtained, indicating a high aspect ratio (the width to the thickness) of 3–15 for the as-prepared TNR, similar to the previous reported work [30]. Moreover, the XRD pattern of as-prepared TNR (Figure 1(d)) exhibited a feature similar to that of alkali or hydrogen titanates such as  $\text{H}_2\text{Ti}_3\text{O}_7$  [31],  $\text{Na}_x\text{H}_{2-x}\text{Ti}_3\text{O}_7$  [32], or  $\text{Na}_y\text{H}_{2-y}\text{Ti}_n\text{O}_{2n+1} \cdot x\text{H}_2\text{O}$  [33] due to a similar structure of layered titanate family. TEM and HRTEM were further used to observe the morphology and microstructures of the as-prepared TNR. Figures 1(b) and 1(c) exhibit the TEM and HRTEM images of TNR, respectively. As shown in Figures 1(b) and 1(c), an obvious layered structure in the titanate nanoribbon could be observed, and the layer spacing was about 0.8 nm, corresponding to the diffraction peak located at ca.  $11^\circ$  in Figure 1(b). Moreover, the selected area electron diffraction (SAED) pattern (inset in Figure 1(b)) also reveals that the titanate nanoribbon is

single crystalline in structure according to the features of the diffraction pattern.

#### 3.2. Formation Mechanism of the Ordered TNR Film Deposited on FTO Glass.

The formation mechanism of ordered TNR film is investigated by SEM. As shown in Figure 2(a), before deposition (0 min), FTO glass exhibits relatively rough surfaces, and the  $\text{SnO}_2$  grains with size of 50–150 nm can be clearly observed. The clear grain boundary indicates that  $\text{SnO}_2$  is well crystallized. After deposition for 1 min, a large amount of TNRs are randomly deposited on FTO glass (Figure 2(b)). As the deposition time increases, more TNRs are further deposited on the surface of substrate. Interestingly, as the deposition time increased to 3 min, ordered TNR film is obtained (Figure 2(c)). However, why the early formed TNR film appears disorder structure or morphology? This is ascribed to the fact that FTO film contains different sized grains, and thus its surface is not smooth. After deposition for certain time, the surface roughness of FTO film decreases, the electric field near the surface becomes uniform, especially, the negative charged TNRs repel each other, and their strong Brownian motion causes restructure and rearrange of deposited TNR [25].

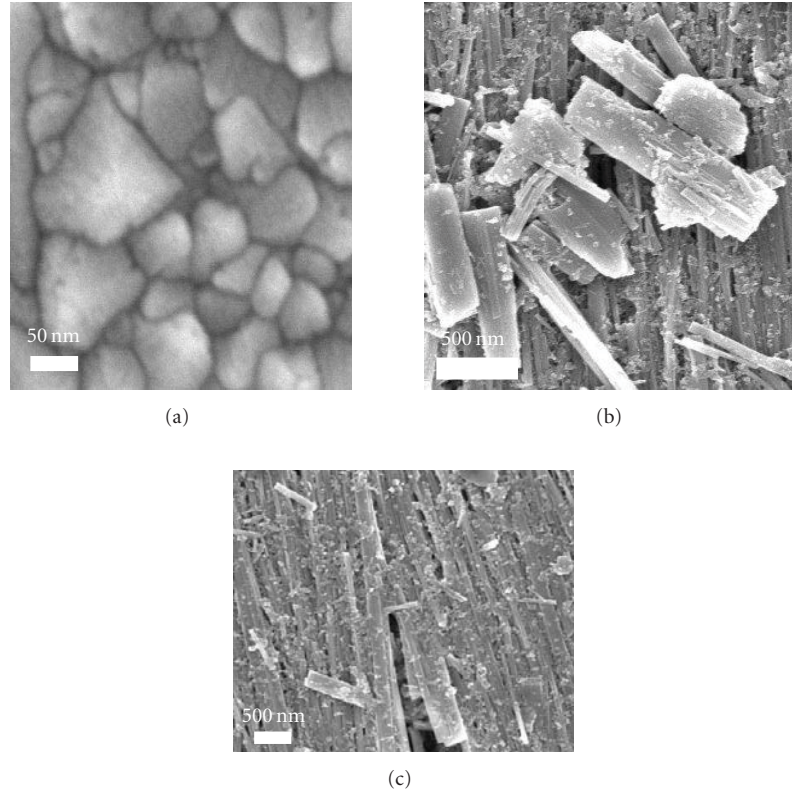


FIGURE 2: SEM images of FTO glass (a) and TNR films deposited for (b) 1 min and (c) 3 min.

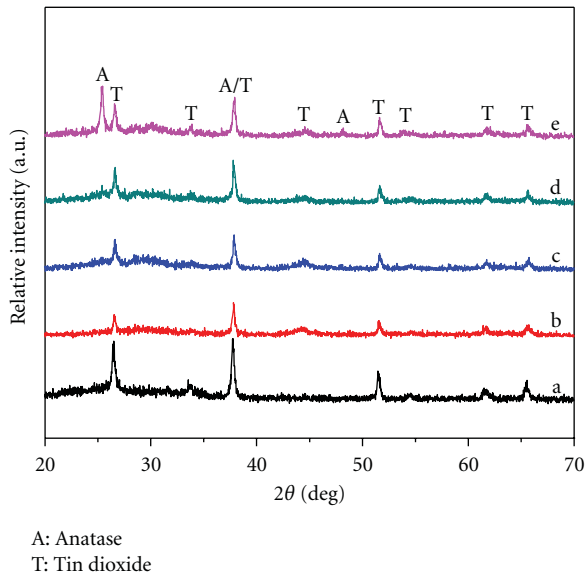


FIGURE 3: XRD patterns of (a) the substrate and the TNR/SnO<sub>2</sub> films calcined at (b) 300, (c) 400, (d) 500, and (e) 600°C.

Therefore, it is not surprising that ordered TNR film can be easily obtained due to the synergistic effects of the above factors [34].

**3.3. Phase Structure and Morphology of the Calcined TNR/SnO<sub>2</sub> Film.** XRD was used to identify and determine the phase structures of the calcined TNR/SnO<sub>2</sub> film. Figure 3 shows the XRD patterns of the FTO substrate and the TNR/SnO<sub>2</sub> film calcined at various temperatures. As shown in Figure 3(a), for pure FTO substrate, strong and sharp diffraction peaks can be observed, and all peaks are indexed to SnO<sub>2</sub> (space group:  $P4_2/mnm$  (136);  $a = 4.750 \text{ \AA}$ ,  $c = 3.198 \text{ \AA}$ , JCPDS no. 46-1088). Figures 3(b)–3(e) show the XRD patterns of the TNR/SnO<sub>2</sub> film calcined at 300 to 600°C. At 300°C, it can be seen that only SnO<sub>2</sub> phase is identified in the calcined TNR/SnO<sub>2</sub> film and no other diffraction peaks are observed, indicating the amorphous states of TNR film. However, as the calcination temperature increases to 400°C, a small peak at  $2\theta = 25.5^\circ$  appears, indicating the formation of anatase phase (space group:  $I4_1/amd$  (141);  $a = 3.785 \text{ \AA}$ ,  $c = 9.514 \text{ \AA}$ , JCPDS no. 21-1272). With further increase in calcination temperature from 400 to 600°C, the peak intensities of anatase increase, implying the enhancement of crystallization of the anatase phase and the growth of crystallites.

Further observation on the morphology and microstructure of the calcined TNR/SnO<sub>2</sub> film was performed with SEM. Figures 4(a) and 4(b) show the surface and cross section SEM images of the TNR/SnO<sub>2</sub> film calcined at 600°C for 2 hours. As shown in Figure 4(a), the calcined TNR still exhibits relatively uniform and ordered structure. The nanoribbons are densely packed and deposited almost

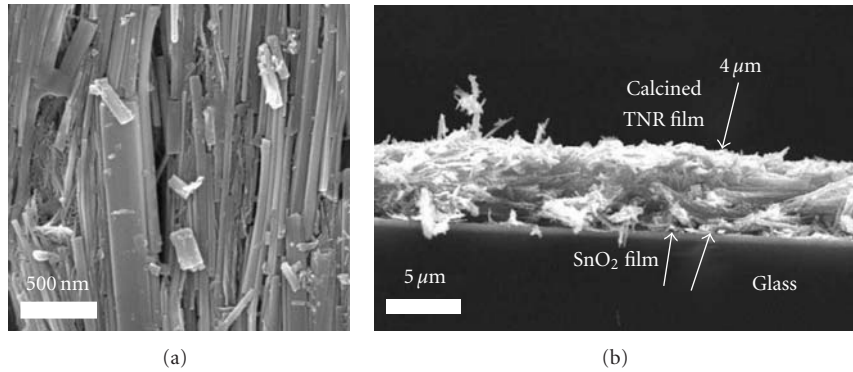


FIGURE 4: Surface (a) and cross section (b) SEM images of TNR/SnO<sub>2</sub> film calcined at 600°C for 2 h.

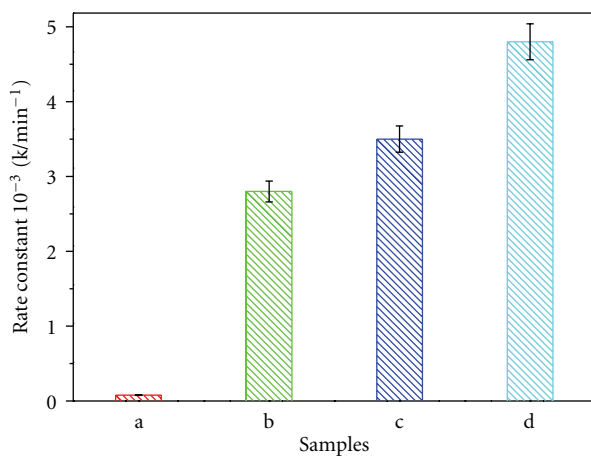


FIGURE 5: The apparent rate constant ( $k$ ) of TNR/SnO<sub>2</sub> films calcined for 2 h at (a) 300, (b) 400, (c) 500, and (d) 600°C.

along the same direction, which are parallel to the substrate, and the thickness of calcined TNR film is about 4  $\mu\text{m}$  (Figure 4(b)). Moreover, Figure 4(b) shows that the SnO<sub>2</sub> film exhibits a thickness of about 500 nm. This SEM observation confirms the intimate contact between TiO<sub>2</sub> film and SnO<sub>2</sub> film, which could facilitate the interfacial transfer of photogenerated electrons and holes.

**3.4. Photocatalytic Activity of Calcined TNR/SnO<sub>2</sub> Films.** The photocatalytic activity of the TNR/SnO<sub>2</sub> film calcined at various temperatures was evaluated by photocatalytic decolorization of RhB aqueous solution at room temperature under UV irradiation. However, under dark conditions without light illumination, the concentration of RhB almost does not change for every measurement in the presence of calcined TNR/SnO<sub>2</sub> film. Illumination in the absence of calcined TNR/SnO<sub>2</sub> film does not result in the photocatalytic decolorization of RhB. Therefore, the presence of both UV illumination and calcined TNR/SnO<sub>2</sub> film is necessary for the efficient degradation. Figure 5 shows the apparent rate constants ( $k$ ) of TNR/SnO<sub>2</sub> film calcinated at various temperatures. It can be seen that the calcination temperature has a great effect on the photocatalytic activity of the

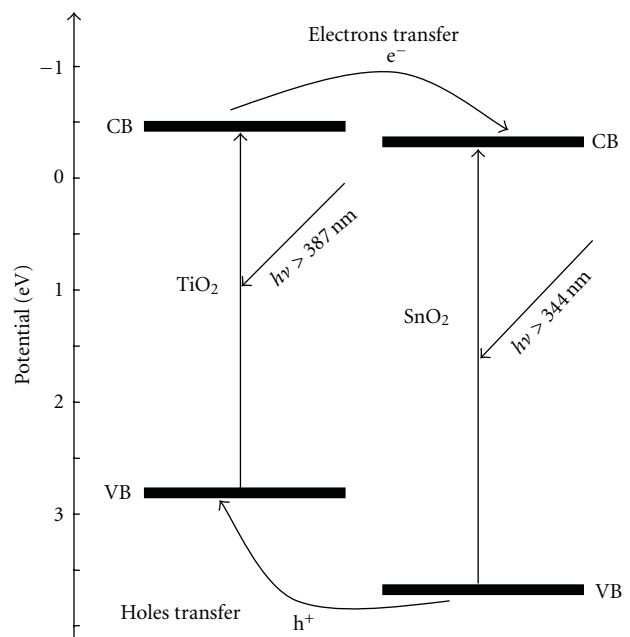


FIGURE 6: Schematic diagram of the charge-transfer process in the TiO<sub>2</sub>/SnO<sub>2</sub> films.

TNR/SnO<sub>2</sub> films. The TNR/SnO<sub>2</sub> films calcined at 300°C show weak photocatalytic activity probably due to absence or low crystallization of anatase phase in the calcined TNR film. However, when the calcination temperature increases to 400°C, the calcined TNR/SnO<sub>2</sub> film shows a decent photocatalytic activity, and the corresponding  $k$  value reaches  $2.8 \times 10^{-3}$  K/min. This can be attributed to the formation of anatase phase and the bilayer structures of TiO<sub>2</sub>/SnO<sub>2</sub> films in favor of separation of photogenerated charge carrier [14, 16–18, 35–37]. Figure 6 show the charge separation and transfer mechanism of TiO<sub>2</sub>/SnO<sub>2</sub> films. Both TiO<sub>2</sub> and SnO<sub>2</sub> are  $n$ -type semiconductors with bandgap energies greater than 3.0 eV and strongly absorb UV light. Upon bandgap excitation, charge carriers (electron-hole pairs) are generated in each semiconductor film. The conduction band (CB) edges of anatase TiO<sub>2</sub> and SnO<sub>2</sub> are located

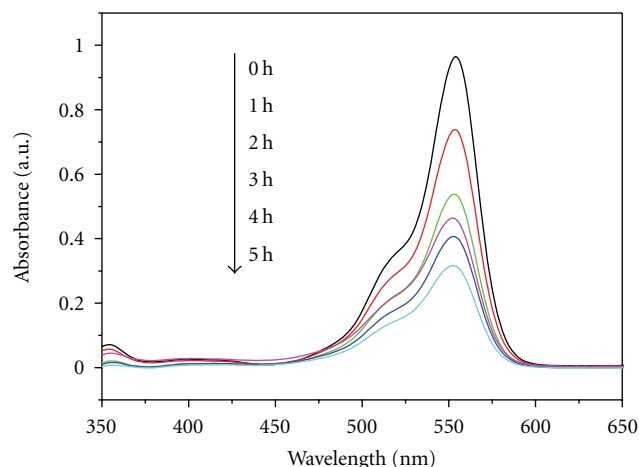


FIGURE 7: Absorption changes of RhB aqueous solution at room temperature in the presence of the TNR/SnO<sub>2</sub> film calcined at 600°C under UV irradiation.

at  $-0.34$  and  $+0.07$  V versus normal hydrogen electrode (NHE) at pH 7, respectively. The valence band (VB) edge of SnO<sub>2</sub> ( $+3.67$  V) is more positive than that of anatase TiO<sub>2</sub> ( $+2.87$  V) [36, 37]. In terms of the energetics, electrons flow into the SnO<sub>2</sub> layer, while holes oppositely diffuse into the TiO<sub>2</sub> layer. Consequently, more holes reach the TiO<sub>2</sub> surface to cause oxidation reaction, whereas electrons are probably consumed for reduction of O<sub>2</sub> at the edge of the SnO<sub>2</sub> film. Therefore, the interfacial electrons transfer from TiO<sub>2</sub> to SnO<sub>2</sub> can explain the high photocatalytic activity of the TiO<sub>2</sub>/SnO<sub>2</sub> films. That is to say, a better charge separation in the composite film is enhanced by a fast electron-transfer process from the conduction band of TiO<sub>2</sub> to that of SnO<sub>2</sub>. Levy et al. [38] and Zhou et al. [19] also reported the same results that photoelectrons and holes transferred toward the reverse direction on the interface of TiO<sub>2</sub>/SnO<sub>2</sub>, resulting in a good photocatalytic activity.

As the temperature further increases, the photocatalytic activity of the calcined TNR/SnO<sub>2</sub> films increased obviously due to the enhancement of crystallization of anatase (Figure 3). At 600°C, the highest photocatalytic activity is observed, and the  $k$  value is about  $4.8 \times 10^{-3}$  K/min, which can be ascribed to good crystallization and the fast photogenerated charge carriers separation and transfer at the interface of the calcined TNR/SnO<sub>2</sub> films.

Figure 7 shows the change of absorption spectra of RhB aqueous solution during photocatalytic decolorization using the TNR/SnO<sub>2</sub> films calcined at 600°C as the photocatalyst. It can be seen that the intensity of absorption peak gradually decreases with increasing UV irradiation time. After UV irradiation for ca. 300 min, the intensity of absorption peak of RhB aqueous solution is very weak, and it becomes colorless, indicating that the calcined TNR films can completely decolorize RhB aqueous solution under UV irradiation. Therefore, the ordered TNR/SnO<sub>2</sub> films prepared by the EPD method could be useful for environmental protection such as air purification, water disinfection, and hazardous waste remediation due to their cheap preparation process, controllable structure, strong adhesion, and good photocatalytic activity.

## 4. Conclusions

We have successfully fabricated ordered TNR/SnO<sub>2</sub> via an EPD method using hydrothermally prepared TNR as a precursor. The formation mechanism of ordered TNR film on FTO glass substrate was investigated by SEM. The calcination temperature has a great effect on the phase structure and photocatalytic activity of TNR/SnO<sub>2</sub> films. When the calcination temperature increases to 600°C, the highest photocatalytic activity was obtained on the calcined TNR/SnO<sub>2</sub> film due to the formation of well-crystallized anatase phase, the unique morphology, and the fast charge carrier separation and transfer at the interface of TiO<sub>2</sub> and SnO<sub>2</sub>. This ordered TNR/SnO<sub>2</sub> should also have many potential applications in photocatalysis, catalysis, solar cell, and so on.

## Acknowledgments

This work was partially supported by China Postdoctoral Science Foundation funded Project (20100471164). This work was also financially supported by the Hubei Province Key Laboratory of Macromolecular Material, Educational Commission of Hubei Province of China (Q20091007), and Natural Science Foundation of Hubei Province of China (2009CDB351).

## References

- [1] A. Fujishima and K. Honda, "Electrochemical photolysis of water at a semiconductor electrode," *Nature*, vol. 238, no. 5358, pp. 37–38, 1972.
- [2] M. R. Hoffmann, S. T. Martin, W. Choi, and D. W. Bahnemann, "Environmental applications of semiconductor photocatalysis," *Chemical Reviews*, vol. 95, no. 1, pp. 69–96, 1995.
- [3] J. G. Yu and J. R. Ran, "Facile preparation and enhanced photocatalytic H<sub>2</sub>-production activity of Cu(OH)<sub>2</sub> cluster modified TiO<sub>2</sub>," *Energy & Environmental Science*, vol. 4, no. 4, pp. 1364–1371, 2011.
- [4] J. G. Yu, J. F. Xiong, B. Cheng, and S. W. Liu, "Fabrication and characterization of Ag-TiO<sub>2</sub> multiphase nanocomposite thin films with enhanced photocatalytic activity," *Applied Catalysis B*, vol. 60, no. 3–4, pp. 211–221, 2005.
- [5] F. B. Li, X. Z. Li, and M. F. Hou, "Photocatalytic degradation of 2-mercaptobenzothiazole in aqueous La<sup>3+</sup>-TiO<sub>2</sub> suspension for odor control," *Applied Catalysis B*, vol. 48, no. 3, pp. 185–194, 2004.
- [6] J. G. Yu, T. T. Ma, and S. W. Liu, "Enhanced photocatalytic activity of mesoporous TiO<sub>2</sub> aggregates by embedding carbon nanotubes as electron-transfer channel," *Physical Chemistry Chemical Physics*, vol. 13, no. 8, pp. 3491–3501, 2011.
- [7] A. L. Linsebigler, G. Lu, and J. T. Yates, "Photocatalysis on TiO<sub>2</sub> surfaces: principles, mechanisms, and selected results," *Chemical Reviews*, vol. 95, no. 3, pp. 735–758, 1995.
- [8] P. V. Kamat, R. Huehn, and R. Nicolaescu, "A "sense and shoot" approach for photocatalytic degradation of organic contaminants in water," *Journal of Physical Chemistry B*, vol. 106, no. 4, pp. 788–794, 2002.
- [9] J. G. Yu, G. P. Dai, and B. Cheng, "Effect of crystallization methods on morphology and photocatalytic activity of anodized TiO<sub>2</sub> nanotube array films," *The Journal of Physical Chemistry C*, vol. 114, no. 45, pp. 19378–19385, 2010.
- [10] M. Ni, M. K. H. Leung, D. Y. C. Leung, and K. Sumathy, "A review and recent developments in photocatalytic

- water-splitting using  $\text{TiO}_2$  for hydrogen production,” *Renewable and Sustainable Energy Reviews*, vol. 11, no. 3, pp. 401–425, 2007.
- [11] Y. X. Li, G. X. Lu, and S. B. Li, “Photocatalytic transformation of rhodamine B and its effect on hydrogen evolution over  $\text{Pt}/\text{TiO}_2$  in the presence of electron donors,” *Journal of Photochemistry and Photobiology A*, vol. 152, no. 1–3, pp. 219–228, 2002.
- [12] J. G. Yu, Y. R. Su, and B. Cheng, “Template-free fabrication and enhanced photocatalytic activity of hierarchical macro-/mesoporous titania,” *Advanced Functional Materials*, vol. 17, no. 12, pp. 1984–1990, 2007.
- [13] A. A. Nada, M. H. Barakat, H. A. Hamed, N. R. Mohamed, and T. N. Veziroglu, “Studies on the photocatalytic hydrogen production using suspended modified  $\text{TiO}_2$  photocatalysts,” *International Journal of Hydrogen Energy*, vol. 30, no. 7, pp. 687–691, 2005.
- [14] H. Tada, A. Hattori, Y. Tokihisa, K. Imai, N. Tohge, and S. Ito, “A patterned- $\text{TiO}_2/\text{SnO}_2$  bilayer type photocatalyst,” *Journal of Physical Chemistry B*, vol. 104, no. 19, pp. 4585–4587, 2000.
- [15] Z. Liu, D. D. Sun, P. Guo, and J. O. Leckie, “An efficient bicomponent  $\text{TiO}_2/\text{SnO}_2$  nanofiber photocatalyst fabricated by electrospinning with a side-by-side dual spinneret method,” *Nano Letters*, vol. 7, no. 4, pp. 1081–1085, 2007.
- [16] T. Kawahara, Y. Konishi, H. Tada, N. Tohge, and S. Ito, “Patterned  $\text{TiO}_2/\text{SnO}_2$  bilayer type photocatalyst. 2. Efficient dehydrogenation of methanol,” *Langmuir*, vol. 17, no. 23, pp. 7442–7445, 2001.
- [17] H. Tada, Y. Konishi, A. Kokubu, and S. Ito, “Patterned  $\text{TiO}_2/\text{SnO}_2$  bilayer type photocatalyst. 3. Preferential deposition of Pt particles on the  $\text{SnO}_2$  underlayer and its effect on photocatalytic activity,” *Langmuir*, vol. 20, no. 9, pp. 3816–3819, 2004.
- [18] Y. Cao, X. Zhang, W. Yang et al., “A bicomponent  $\text{TiO}_2/\text{SnO}_2$  particulate film for photocatalysis,” *Chemistry of Materials*, vol. 12, no. 11, pp. 3445–3448, 2000.
- [19] M. H. Zhou, J. G. Yu, S. W. Liu, P. C. Zhai, and L. Jiang, “Effects of calcination temperatures on photocatalytic activity of  $\text{SnO}_2/\text{TiO}_2$  composite films prepared by an EPD method,” *Journal of Hazardous Materials*, vol. 154, no. 1–3, pp. 1141–1148, 2008.
- [20] J. G. Yu and M. H. Zhou, “Effects of calcination temperature on microstructures and photocatalytic activity of titanate nanotube films prepared by an EPD method,” *Nanotechnology*, vol. 19, no. 4, Article ID 045606, 2008.
- [21] J. G. Yu, X. J. Zhao, and Q. N. Zhao, “Effect of surface structure on photocatalytic activity of  $\text{TiO}_2$  thin films prepared by sol-gel method,” *Thin Solid Films*, vol. 379, no. 1–2, pp. 7–14, 2000.
- [22] H. G. Yu, J. G. Yu, B. Cheng, and M. H. Zhou, “Effects of hydrothermal post-treatment on microstructures and morphology of titanate nanoribbons,” *Journal of Solid State Chemistry*, vol. 179, no. 2, pp. 349–354, 2006.
- [23] H. Tokudome and M. Miyauchi, “Electrochromism of titanate-based nanotubes,” *Angewandte Chemie*, vol. 44, no. 13, pp. 1974–1977, 2005.
- [24] H. Tokudome and M. Miyauchi, “Titanate nanotube thin films via alternate layer deposition,” *Chemical Communications*, vol. 10, no. 8, pp. 958–959, 2004.
- [25] J. G. Yu and L. F. Qi, “Template-free fabrication of hierarchically flower-like tungsten trioxide assemblies with enhanced visible-light-driven photocatalytic activity,” *Journal of Hazardous Materials*, vol. 169, no. 1–3, pp. 221–227, 2009.
- [26] J. G. Yu, Q. J. Xiang, J. R. Ran, and S. Mann, “One-step hydrothermal fabrication and photocatalytic activity of surface-fluorinated  $\text{TiO}_2$  hollow microspheres and tabular anatase single micro-crystals with high-energy facets,” *CrytEngComm*, vol. 12, no. 3, pp. 872–879, 2010.
- [27] H. Kumazawa, M. Inoue, and T. Kasuya, “Photocatalytic degradation of volatile and nonvolatile organic compounds on titanium dioxide particles using fluidized beds,” *Industrial and Engineering Chemistry Research*, vol. 42, no. 14, pp. 3237–3244, 2003.
- [28] D. Hornero-Mendez and M. I. Minguez-Mosquera, “Rapid spectrophotometric determination of red and yellow isochromic carotenoid fractions in paprika and red pepper oleoresins,” *Journal of Agricultural and Food Chemistry*, vol. 49, no. 8, pp. 3584–3588, 2001.
- [29] J. G. Yu, H. G. Yu, B. Cheng, X. J. Zhao, J. C. Yu, and W. K. Ho, “The effect of calcination temperature on the surface microstructure and photocatalytic activity of  $\text{TiO}_2$  thin films prepared by liquid phase deposition,” *The Journal of Physical Chemistry B*, vol. 107, no. 50, pp. 13871–13879, 2003.
- [30] J. Yu, J. C. Yu, W. Ho, L. Wu, and X. Wang, “A simple and general method for the synthesis of multicomponent  $\text{Na}_2\text{V}_6\text{O}_{16} \cdot 3\text{H}_2\text{O}$  single-crystal nanobelts,” *Journal of the American Chemical Society*, vol. 126, no. 11, pp. 3422–3423, 2004.
- [31] Q. Chen, W. Z. Zhou, G. H. Du, and L. M. Peng, “Trititanate nanotubes made via a single alkali treatment,” *Advanced Materials*, vol. 14, no. 17, pp. 1208–1211, 2002.
- [32] X. M. Sun and Y. D. Li, “Synthesis and characterization of ion-exchangeable titanate nanotubes,” *Chemistry*, vol. 9, no. 10, pp. 2229–2238, 2003.
- [33] J. Canales and P. G. Bruce, “ $\text{TiO}_2$ -B nanowires,” *Angewandte Chemie*, vol. 43, no. 17, pp. 2286–2288, 2004.
- [34] L. Zhao, J. G. Yu, J. J. Fan, P. C. Zhai, and S. M. Wang, “Dye-sensitized solar cells based on ordered titanate nanotube films fabricated by electrophoretic deposition method,” *Electrochemistry Communications*, vol. 11, no. 10, pp. 2052–2055, 2009.
- [35] K. Vinodgopal and P. V. Kamat, “Enhanced rates of photocatalytic degradation of an azo dye using  $\text{SnO}_2/\text{TiO}_2$  coupled semiconductor thin films,” *Environmental Science and Technology*, vol. 29, no. 3, pp. 841–845, 1995.
- [36] J. Shang, W. Yao, Y. Zhu, and N. Wu, “Structure and photocatalytic performances of glass/ $\text{SnO}_2/\text{TiO}_2$  interface composite film,” *Applied Catalysis A*, vol. 257, no. 1, pp. 25–32, 2004.
- [37] A. Hattori, Y. Tokihisa, H. Tada, and S. Ito, “Acceleration of oxidations and retardation of reductions in photocatalysis of a  $\text{TiO}_2/\text{SnO}_2$  bilayer-type catalyst,” *Journal of the Electrochemical Society*, vol. 147, no. 6, pp. 2279–2283, 2000.
- [38] B. Levy, W. Liu, and S. Gilbert, “Directed photocurrents in nanostructured  $\text{TiO}_2/\text{SnO}_2$  heterojunction diodes,” *Journal of Physical Chemistry B*, vol. 101, no. 10, pp. 1810–1816, 1997.

## Research Article

# Mechanistic Study of Visible-Light-Induced Photodegradation of 4-Chlorophenol by $\text{TiO}_{2-x}\text{N}_x$ with Low Nitrogen Concentration

Guangfeng Shang,<sup>1</sup> Hongbo Fu,<sup>1</sup> Shaogui Yang,<sup>2</sup> and Tongguang Xu<sup>3</sup>

<sup>1</sup>Department of Environmental Science and Engineering, Fudan University, Shanghai 200433, China

<sup>2</sup>State Key Laboratory of Pollution Control and Resource Reuse, School of the Environment, Nanjing University, Nanjing 210046, China

<sup>3</sup>Department of Chemistry, Tsinghua University, Beijing 100084, China

Correspondence should be addressed to Hongbo Fu, fuhb@fudan.edu.cn

Received 7 April 2011; Accepted 3 May 2011

Academic Editor: Jiaguo Yu

Copyright © 2012 Guangfeng Shang et al. This is an open access article distributed under the Creative Commons Attribution License, which permits unrestricted use, distribution, and reproduction in any medium, provided the original work is properly cited.

$\text{TiO}_{2-x}\text{N}_x$  powders with low N-doping concentrations ( $0.021 < x < 0.049$ ) were prepared by annealing commercial  $\text{TiO}_2$  (P-25) under an  $\text{NH}_3$  flow at  $550^\circ\text{C}$ . Regardless of UV or visible case, the photoactivities of the samples decreased as  $x$  increased, and  $\text{TiO}_{1.979}\text{N}_{0.021}$  showed the highest activity for the 4-chlorophenol (4-CP) decomposition under the visible-light irradiation. The visible-light response for N-doped  $\text{TiO}_2$  could arise from an N-induced midgap level, formed above the valence band (O 2p). Electron spin resonance (ESR) measurements and the radical scavenger technologies gave the combined evidence that the active species ( $\bullet\text{OH}$  and  $\text{O}_2\bullet^-$ ) are responsible for the photodecomposition of 4-CP over  $\text{TiO}_{2-x}\text{N}_x$  under the visible irradiation. A possible photocatalytic mechanism was discussed in detail.

## 1. Introduction

Semiconductor photocatalysis has been the focus of numerous investigations because of its application for the destruction of chemical contaminants and water splitting [1–5]. Among all the materials,  $\text{TiO}_2$  remains the most promising owing to its superior photoreactivity, high corrosion resistance, and nonhazardous nature. Even so, the poor solar efficiency (maximum 5%) has hindered the commercialization of this technology [6–8]. Various approaches have been attempted to enhance the visible-light utilization of  $\text{TiO}_2$ . A classical example is the doping of  $\text{TiO}_2$  with transition-metal elements [9, 10]. However, the doped materials have been shown to suffer from thermal instability, and the metal centers act as electron traps, which reduces the photocatalytic efficiency. Dye sensitization in photochemical systems has also been explored extensively [11, 12]. Dyes possessing carboxylate or hydroxyl functions, in particular, interact with the surface of  $\text{TiO}_2$  particles, thereby providing the path for electron-transfer from the excited dye adsorbate to the semiconductor. Unfortunately, this technology cannot

be practically used for detoxification of waste water since the photosensitizers may be gradually photodegraded and become less effective.

Recently, the band gap of  $\text{TiO}_2$  has been narrowed successfully by doping with nonmetal cations, by replacing lattice oxygen with B, C, N, or S dopants [13–16]. It is widely recognized that anionic nonmetal dopants may be more appropriate for the extension of photocatalytic activity into the visible-light region, because the related impurity states are supposed to be close to the valence band maximum [17]. Furthermore, the position of the conduction band minimum, which must be kept at the level of the  $\text{H}_2/\text{H}_2\text{O}$  potential, when  $\text{TiO}_2$  is used for the photoelectrolysis of water into hydrogen and oxygen, is not affected [17].

Among all the nonmetal cations, substitutional N-doping was found to be particularly effective in decreasing the band gap of  $\text{TiO}_2$  through the mixing of N and O 2p states. The presence of nitrogen doping extends the optical absorption of  $\text{TiO}_2$  to the visible-light spectrum and enhances the visible-light-driven photocatalysis [18–24]. Generally, N-doped  $\text{TiO}_2$  samples have been produced by

different preparative procedures: (i) treating TiO<sub>2</sub> powder with NH<sub>3</sub> gas at high temperature (>500°C) followed by partial reoxidation in air [15, 17]; (ii) via “nitridation” of TiO<sub>2</sub> colloidal nanoparticles with alkylammonium salts at room temperature [18]; (iii) hydrolysis of NH<sub>x</sub>/TiO<sub>2</sub> mixtures to gain powder samples [20]; (iv) to produce carbon-substituted N-doped sample by a flame pyrolysis at high temperature [25]. The various N-doped TiO<sub>2</sub> catalysts have been applied to bleach methylene blue [18], split water [23], and oxidatively degrade 2-propanol [26], 4-CP [19], acetone vapors [27], and for the photokilling of harmful pathogens as well as peroxidation of the cell membrane of biomolecules [20]. Indeed, the visible-light-induced photocatalysis of the N-doped TiO<sub>2</sub> is effective.

However, it is quite debatable as to the origin of the visible-light responses for N-doped TiO<sub>2</sub> to date. On the basis of a theoretical analysis, Han et al. [15] suggested that visible-light responses for N-doped TiO<sub>2</sub> arose from band narrowing by mixing of N 2p and O 2p orbitals. Irie et al. [26] insisted that visible light sensitivity of N-doped TiO<sub>2</sub> was due to an isolated N 2p state rather than the narrowing of the band gap. Further, Lindgren et al. [28] reported that N 2p was situated close to the valence band maximum by using the photoelectrochemical measurements and that the conduction band edge remained unchanged by N-doping. Ihara et al. [27] argued that the oxygen vacancies were contributed to the Vis activity and the doped N atoms only enhance the stabilization of these oxygen vacancies.

Another question relates to the photodegradation mechanism involved in the N-doped TiO<sub>2</sub> photocatalysis. It has been reported that a variety of organic compounds are mineralized into CO<sub>2</sub> and inorganic species on N-doped TiO<sub>2</sub> under visible-light illumination [18, 19, 26]. However, it still remains conjectural whether the certain product comes from a direct reaction with photogenerated holes or via reactions with surface intermediates of the water photooxidation reaction. It is thus quite difficult to get definite conclusions on the reaction mechanism. An examination of the formation of active oxygen species can provide useful information about the fate of the valence hole and the conduction electrons, and lead to a greater understanding of the visible-induced photocatalysis by N-doped TiO<sub>2</sub> in general.

In the previous work, we have already observed the photocatalytic process mediated by N-doped TiO<sub>2</sub> using an ESR technique [29]. In this report, to further observe the mechanism of this photocatalytic system, N-doped TiO<sub>2</sub> powders were firstly prepared by annealing the commercial P-25 (TiO<sub>2</sub>) in NH<sub>3</sub> flow at 550°C. The samples were characterized by X-ray photoelectron spectroscopy (XPS), X-ray diffraction (XRD), and UV-Vis diffused reflection spectrum (DRS). 4-CP decomposition was used as a probe reaction to evaluate the photocatalytic activities of these powders under UV and Vis irradiation. The formation of active oxygen species was detected by spin-trap electron spin resonance (ESR) techniques and the radical scavenger technologies to provide an overall understanding of the reaction mechanisms.

## 2. Experimental Section

**2.1. Materials.** Commercial P-25 (Degussa, 50 m<sup>2</sup> g<sup>-1</sup>, 75% rutile, and 25% anatase) was treated in a flow reactor system in an N<sub>2</sub> gas atmosphere (1 atm) at 550°C. For doping, the N<sub>2</sub> flow was replaced by NH<sub>3</sub> for 5~25 min after the target temperature had been reached. Subsequently, the crystals were kept in flowing N<sub>2</sub> for 1 h at 550°C and then cooled in flowing N<sub>2</sub>. For comparison, undoped P-25 was also annealed under N<sub>2</sub> flow at 550°C for 25 min as a reference sample.

The spin trap 5, 5-dimethyl-1-pyrroline-N-oxide (DMPO) was kindly supplied. Stock solutions of DMPO in deaerated water were prepared under argon and stored in the dark bottles at -20°C. All chemicals were reagent grade and used without further purification. Deionized and doubly distilled water were used throughout this study.

**2.2. Characterization.** XPS analysis was obtained using a PHI 5300 ESCA instrument with an Al K $\alpha$  X-ray source at a power of 250 W. The pass energy of the analyzer was set at 35.75 eV and the base pressure of the analysis chamber was <3  $\times$  10<sup>-9</sup> Torr. The binding energy scale was calibrated with respect to the C 1s peak of hydrocarbon contamination fixed at 285.0 eV. According to Irie et al. [26], the peak at 396 eV is derived from Ti-N bonds. Therefore, the  $x$  values (nitrogen concentrations) in TiO<sub>2-x</sub>N<sub>x</sub> were estimated by comparing to the product of the 396 eV peak area multiplied by the nitrogen sensitivity factor to the product of the 531 eV peak area (O 1s, Ti-O bonds) multiplied by the oxygen sensitive factor. XRD patterns of the powders were recorded by a Bruker D8 Advance X-ray diffractometer by using Cu K $\alpha$  radiation and a 2 $\theta$  scan rate of 2° min<sup>-1</sup>. UV-Vis DRS was obtained by using a Hitachi U-3010 spectrometer.

**2.3. Photoreactor and Light Source.** The photocatalytic activities were evaluated by the decomposition of 4-CP when irradiated with UV ( $\lambda = 254$  nm) and Vis light ( $\lambda > 420$  nm). UV light was obtained by a 12 W Hg lamp (Institute of Electric Light Source, Beijing) and the average light intensity was 150  $\mu$ W.cm<sup>-2</sup>. In the case of Vis light irradiation, a 500 W xenon lamp (Institute of Electric Light Source, Beijing) was focused through a window, as a 420 nm cutoff filter was placed onto the window face of the cell to ensure the desired irradiation light. The average light intensity was 30 mW.cm<sup>-2</sup>. The irradiation area was approximately 40 cm<sup>2</sup>. The radiant flux was measured with a power meter from the Institute of Electric Light Source (Beijing, China).

**2.4. Procedures and Analyses.** Aqueous suspensions of 4-CP (usually 100 mL, 10 mg L<sup>-1</sup>) and 0.1 g of the catalysts were placed in a vessel. Prior to irradiation, the suspensions were magnetically stirred in the dark for ca. 30 min to ensure the establishment of an adsorption/desorption equilibrium. The suspensions were kept under constant air-equilibrated conditions before and during the irradiation. At given time intervals, 3 mL aliquots were sampled and centrifugated to remove the particles. The filtrates were analyzed by recording variations in the absorption band (224 nm) in the UV-Vis

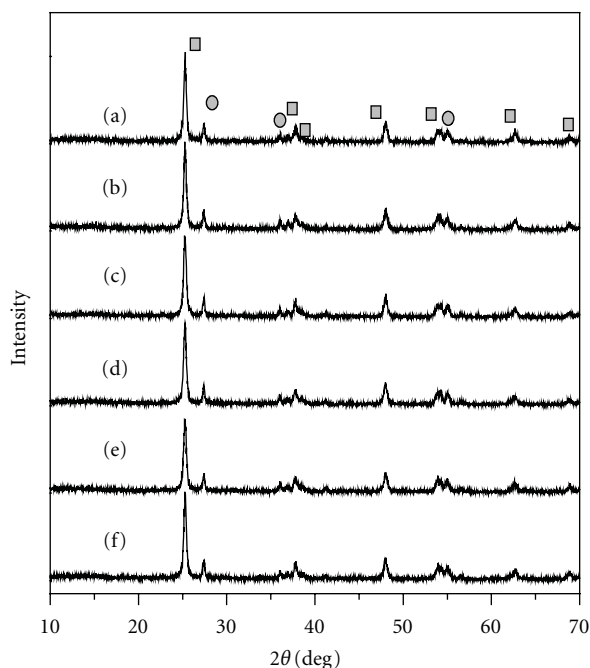


FIGURE 1: XRD patterns of the N-doped  $\text{TiO}_2$  samples annealed under  $\text{NH}_3$  flow for different time; (a) 0 min, (b) 5 min, (c) 10 min, (d) 15 min, (e) 20 min, (f) 25 min; the anatase ( $\square$ ) and the rutile ( $\circ$ ).

spectra of 4-CP using a Hitachi U-3010 spectroscopy. The intermediate products in the filtered sample were determined by a Hewlett-Packard HPLC equipped with an UV detector adjusted to 270 nm and the ODS-2 spherisorb column (125 mm length, 4 mm internal diameter, and  $5\ \mu\text{m}$  particle diameters). The mobile phase was a mixture of 50 : 50 (v/v) of  $\text{CH}_3\text{OH}$  to deionized water with a flow rate of  $1.0\ \text{mL min}^{-1}$ .

**2.5. ESR Measurements.** ESR signals of radicals spin-trapped by DMPO were recorded at ambient temperature on a Bruker ESR 300 E spectrometer: the irradiation source was a Quanta-Ray Nd:YAG pulsed laser system ( $\lambda = 355\ \text{nm}$  or  $532\ \text{nm}$ , 10 Hz). The settings for the ESR spectrometer were: center field, 3486.70 G; sweep width, 100 G; microwave frequency, 9.82 GHz; modulation frequency, 100 kHz; power, 5.05 mW. To minimize experimental errors, the same quartz capillary tube was used for all ESR measurements.

### 3. Results and Discussion

**3.1. Sample Characterization.** XRD patterns of the as-prepared samples are shown in Figure 1. Degussa P-25 nanopowder sample, though dominantly of the anatase form, also contains some notable contribution from the rutile structure (ratio approximately 3 : 1) [18]. Replacing an O atom with an N atom in  $\text{TiO}_2$  does not result in significant structural changes, although the N atom has a larger ion radius (0.171 nm) than that of the O atom (0.132 nm) [24]. Ti-N bond length, 1.964 Å, is only slightly longer than that of Ti-O, 1.942 Å. Therefore, the structural modifications due

to the N doping are relatively minor [30]. This could also be understood that the concentration of the doped N atom (given later) might be low to cause a shift.

Global XPS profiles for the as-prepared samples are shown in Figure 2(a). According to XPS spectra, the samples contain only Ti, O, and N atoms. And binding energies for O 1s, Ti 2s, Ti 2p, and C 1s are 533.2, 576.3, 473.5, and 285.0 eV, respectively. Figure 2(b) shows the N 1s spectra of the as-prepared samples. A new peak at 396 eV was observed, which is generally considered as evidence for the presence of Ti-N bonds, suggesting that the oxygen sites were substituted by nitrogen atoms [26]. In contrast,  $\text{N}_2$  gas annealed samples did not display a peak at 396 eV. The peak at 400 eV could be ascribed to N atoms from adventitious  $\text{N}_2$ ,  $\text{NH}_3$ , or N-containing organic compounds adsorbed on the surface [18]. The estimated  $x$  values from the XPS spectra were 0.021, 0.029, 0.035, 0.041, and 0.049 for the samples prepared at  $\text{NH}_3$  flow for 5, 10, 15, 20, and 25 min, respectively.

Various forms of N-doped  $\text{TiO}_2$ , including powders, films, and nanoparticles, have been investigated by XPS [17–19, 31–33]. In most cases, a peak at 396–397 eV was detected and attributed to substitutional nitrogen doping given the proximity to the typical binding energy of 397 eV in Ti-N [31]. However, in a few recent papers, this feature was found to be completely absent while the peaks at higher binding energies (399–404 eV) were observed [19, 32]. In some other cases, both features have been observed [17, 24, 33]. Since the peaks for nitrites and nitrates fall at a very high binding energy (407–408 eV), nitrogen species in doped  $\text{TiO}_2$  are expected to be in a lower oxidation state [33].

**3.2. Photoabsorbance Properties and Band Structures.** Figure 3 shows UV-Vis DRS of  $\text{TiO}_{2-x}\text{N}_x$  and  $\text{TiO}_2$ . Noticeable shifts of the absorption shoulders into the Vis-light region were observed for  $\text{TiO}_{2-x}\text{N}_x$ . This absorption shoulder at 400–550 nm is related to the presence of nitrogen since it increases with nitrogen content. Additionally, the absorption edge of new band well agrees with the reported value for the N-doped  $\text{TiO}_2$  system [19, 24]. These samples, after they have been doped, are pale-yellow in color, and the colors were darker gradually as  $x$  increased whereas the undoped sample is white. The color of the N doping samples are partially due to the bulk reduction of the crystal, because the thermal decomposition of  $\text{NH}_3$  on the  $\text{TiO}_2$  surface results in the evolution of molecular hydrogen, which reduces the crystal electronically [17]. In addition, the presence of the Vis absorption band indicates that nitrogen penetrates into the single crystal and effectively changes the electronic structure of  $\text{TiO}_2$  [17, 26].  $\text{TiO}_2$  is an indirect gap semiconductor, and the band gaps of the  $\text{TiO}_{2-x}\text{N}_x$  and  $\text{TiO}_2$  can be estimated from tangent lines in the plots of the square root of the Kubelka-Munk functions against the photon energy [26], as shown in the insert of Figure 3. The tangent lines, which are extrapolated to  $\alpha^{1/2} = 0$ , indicate the band gaps of  $\text{TiO}_{2-x}\text{N}_x$  and  $\text{TiO}_2$  are  $E_g = 2.95\ \text{eV}$ .

In the present study, the electronic structure of N-doped  $\text{TiO}_2$  was newly investigated by DFT calculations. We optimized the lattice parameters and atomic positions of  $\text{TiO}_2$  by minimizing the total energy of anatase structure.

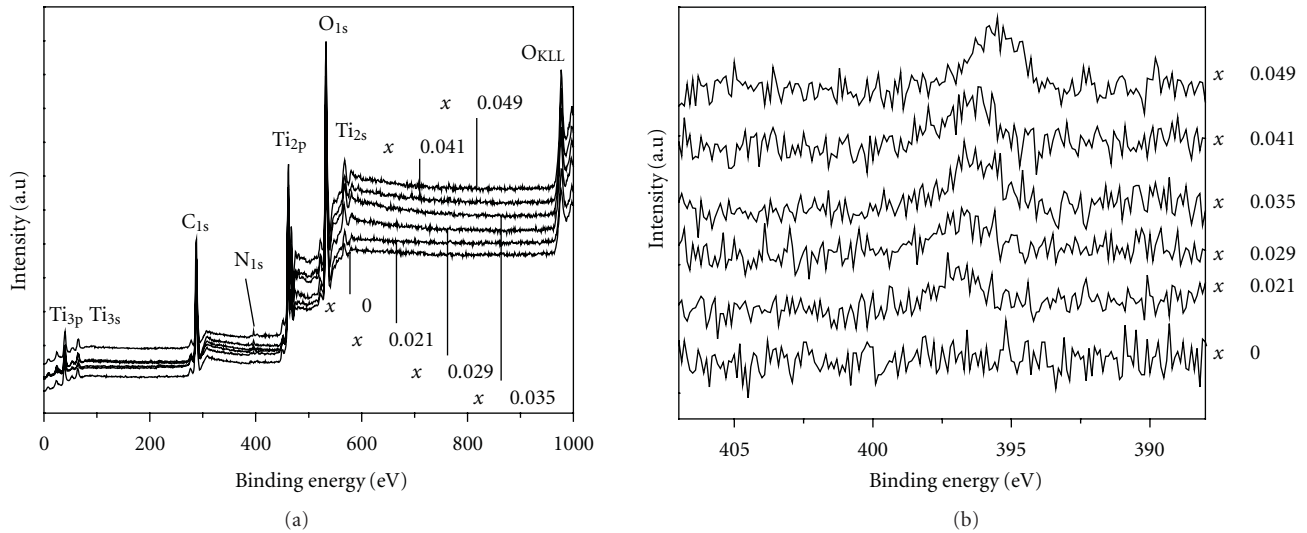


FIGURE 2: Global XPS of  $\text{TiO}_2-x\text{Nx}$  (a), and the N 1s peak of  $\text{TiO}_2-x\text{Nx}$  around the 400 eV regions (b).

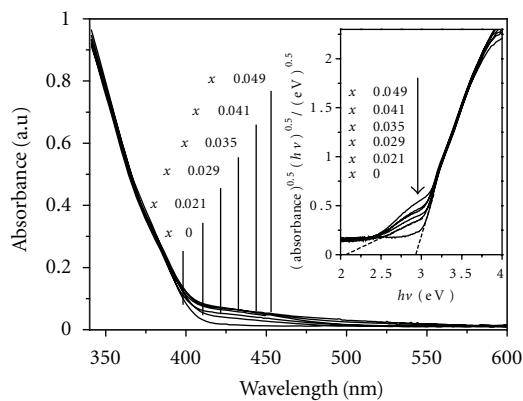


FIGURE 3: UV-Vis DR spectra of  $\text{TiO}_2-x\text{Nx}$ .

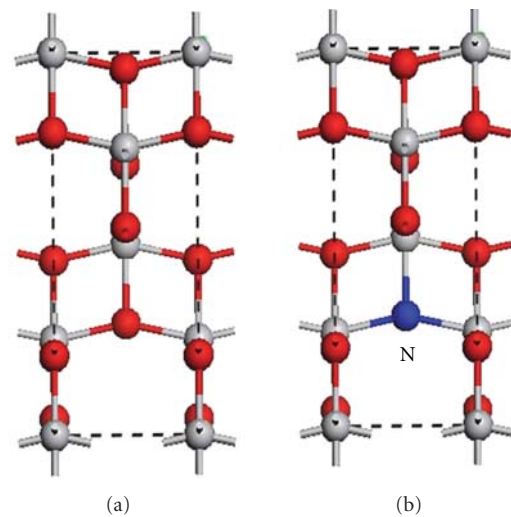


FIGURE 4: Unit cells of  $\text{TiO}_2$  (anatase) (a) and N-doped  $\text{TiO}_2$  (b). The red, gray, and blue spheres represent the O, Ti, and N ions, respectively.

The atomic positions of N-doped  $\text{TiO}_2$  were optimized based on the theoretical lattice constants of  $\text{TiO}_2$  without imposing any symmetry. N doping was modeled by replacing 1 oxygen atoms in the 20-atom anatase supercell, as shown in Figure 4. The resulting stoichiometry is  $\text{TiO}_{2-x}\text{N}_x$  with  $x = 0.149$ . The DOS results of  $\text{TiO}_2$  were shown in Figure 5(a). The occupied bands of  $\text{TiO}_2$  were classified into four bands. The lower-energy side in the occupied bands consisted of solely Ti 4s (1~2#). The middle part of the occupied bands consisted of Ti 3p orbitals (3~8#) and O 2s orbitals (9~16#), respectively. The higher-energy side, that is, corresponded to the valence band (VB), consists of O 2p orbitals (13~24#). The bottom of conduction band (CB) was formed by the Ti 3d orbitals, with a small contribution of the O 2p (25~34#); the top of CB was formed by the Ti 3d orbitals (35~36#). Thus, the highest occupied and lowest unoccupied molecular orbital levels were composed of the O 2p and Ti 3d orbitals, respectively. The band gap of  $\text{TiO}_2$  was estimated to be 2.27 eV. Generally, the band gap calculated

by DFT is smaller than that obtained experimentally, which is frequently pointed out as a common feature of DFT calculations [34]. The DOS result of N-doped  $\text{TiO}_2$  were shown in Figure 5(b). One can see that the VB of N-doped  $\text{TiO}_2$  is composed of the hybrid orbitals of O 2p and N 2p. The calculated band gap of  $\text{TiO}_2$  was narrowed by 0.41 eV due to the N doping. Asahi et al. calculated by the band structure of  $\text{TiO}_{2-x}\text{N}_x$ , where  $x = 0.25$  and 0.12, that is, when 12.5 and 6% of the oxygen sites were substituted by nitrogen, and reported that mixing the N 2p and O 2p states narrowed the band gap. The present DOS calculation is in agreement with their conclusion. However, it keenly contradicts with the UV-Vis spectra of N-doped  $\text{TiO}_2$  (Figure 3), which showed N-doping did not narrow the band gap of  $\text{TiO}_2$  [15].

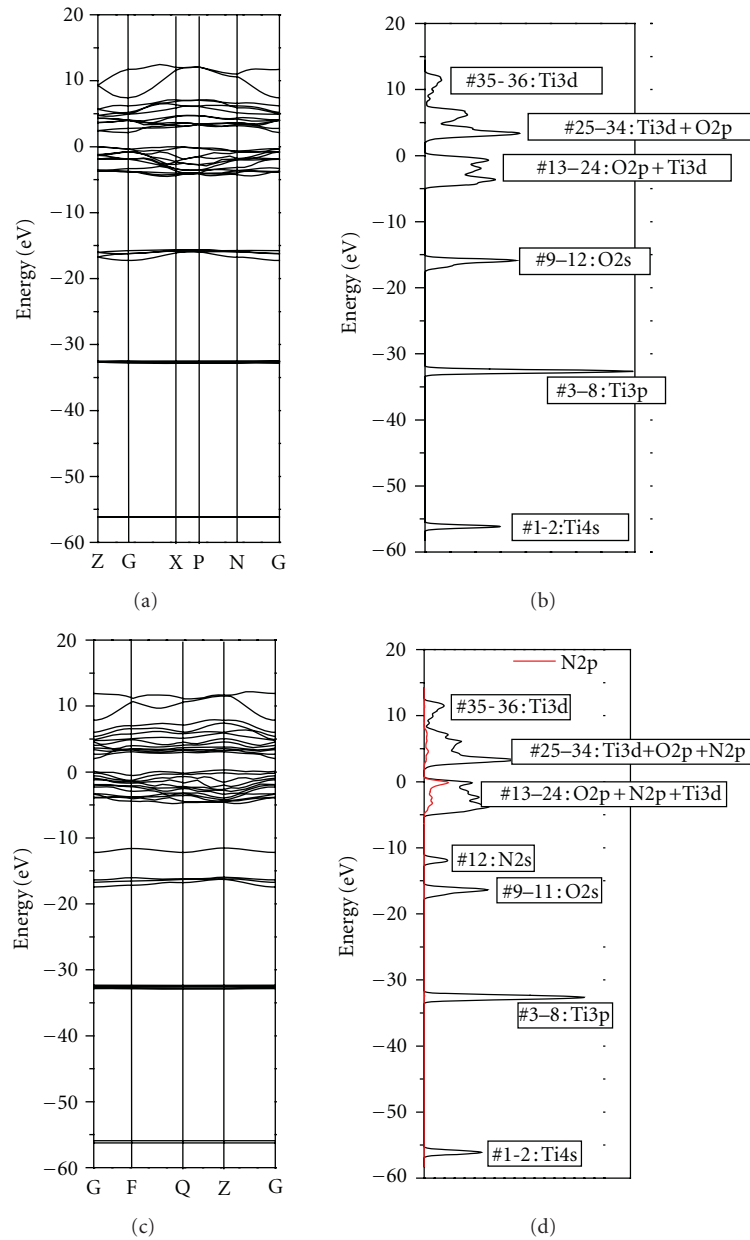


FIGURE 5: Total DOS: (a)  $\text{TiO}_2$  (anatase), (b) N-doped  $\text{TiO}_2$ .

The procedure of including more N atoms in the same supercell is more accurate than using smaller unit cell as it allows a direct comparison of the various levels of doping on the band structure of the material. Valentin et al. [30] calculated the band gap of  $\text{TiO}_{2-x}\text{N}_x$  with  $0.031 < x < 0.094$  by modeling the 96-atom supercell replaced by 1, 2, or 3 nitrogen atoms. Their analysis of the electronic energy levels showed that N doping did not cause the shift of the position of both top and bottom of the O 2p valence band, as well as of the conduction band, with respect to the undoped material. This is in contrast with the conclusion of Asahi et al. [15]. Therefore, the N doping amount could be a vital factor [26]. It is plausible that the band structure of  $\text{TiO}_{2-x}\text{N}_x$  with the

lower values of  $x < 0.05$  should differ from the higher values of  $x > 0.12$ .

**3.3. Photocatalytic Activity.** To explore the photocatalytic activities of the as-prepared samples, the degradation of 4-CP was investigated in both UV and Vis irradiation. 4-CP does not absorb in the Vis region, and therefore the presence of indirect semiconductor photocatalysis can be excluded [19].

Figure 6(a) shows the changes of 4-CP concentration as a function of time in the presence of  $\text{TiO}_{2-x}\text{N}_x$  powders under UV irradiation. The undoped  $\text{TiO}_2$  exhibited the highest activity for 4-CP decomposition. 59% loss of 4-CP in concentration was observed in the presence of P-25

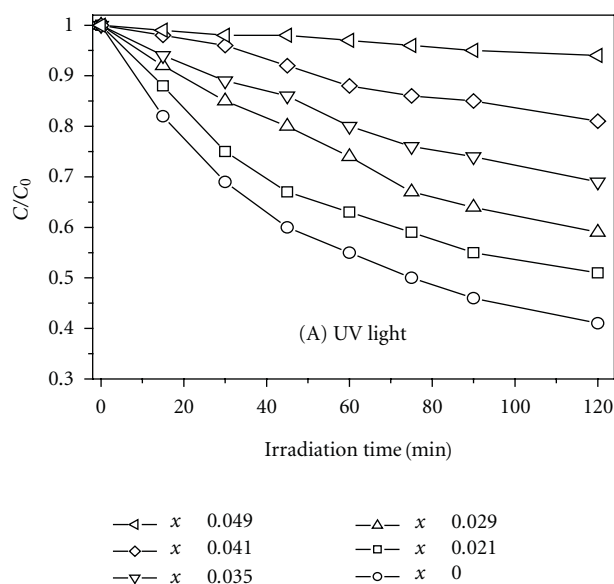


FIGURE 6: Photodecomposition of 4-CP by  $\text{TiO}_{2-x}\text{N}_x$  under UV light (a) and Vis light (b).

for 120-minute irradiation. The photocatalytic activity of  $\text{TiO}_{2-x}\text{N}_x$  greatly depended on the concentration of N doping. It is obvious that the photocatalytic activity of  $\text{TiO}_{2-x}\text{N}_x$  decreased as  $x$  value increase. 19, 31, 41, and 49% 4-CP were photodegraded in the presence of the sample  $x = 0.041, 0.035, 0.029,$  and  $0.021$  for 120 min, respectively. Almost no degradation occurred in the case of the sample  $x = 0.049$ . It is important to keep or improve UV photoactivity of  $\text{TiO}_2$  when it is functionalized for Vis-light-driven catalysis because the most desired solar light source contains about 5% UV and the efficiency of light utilization for a  $\text{TiO}_2$ -based photocatalyst is much higher for UV than for Vis light [24]. In the present work, the N doping plays a passive role on the UV activity of  $\text{TiO}_2$ .

Similar experiments were conducted under Vis-light irradiation, as shown in Figure 6(b). Irradiating the undoped  $\text{TiO}_2$  ( $x = 0$ ) with Vis light did not generate the decrease of 4-CP in concentration, as  $\text{TiO}_2$  is not Vis-light sensitive. The degradation of 4-CP, however, was observed from all the doped samples, suggesting that N-doping for  $\text{TiO}_2$  is an effective and feasible approach for achieving Vis-light-driven photocatalysis. As the  $x$  value increased, the photoactivity of the sample decreased, which is similar with the case of UV irradiation.

Many factors, for example, surface area, crystallinity, surface hydroxyl density, and oxygen vacancies, affect the activity of a photocatalyst. The activity of a photocatalyst is a combined effect of many factors [24]. In our case, the N-doping concentration dominated these factors because other preparation conditions were identical. Therefore, it is easy to understand that the N-doping concentration in the catalyst could be responsible for the difference of the photoactivity. Irrespective of UV or Vis case, the photoactivities of the N-doped samples decrease with the increase of the N-doping

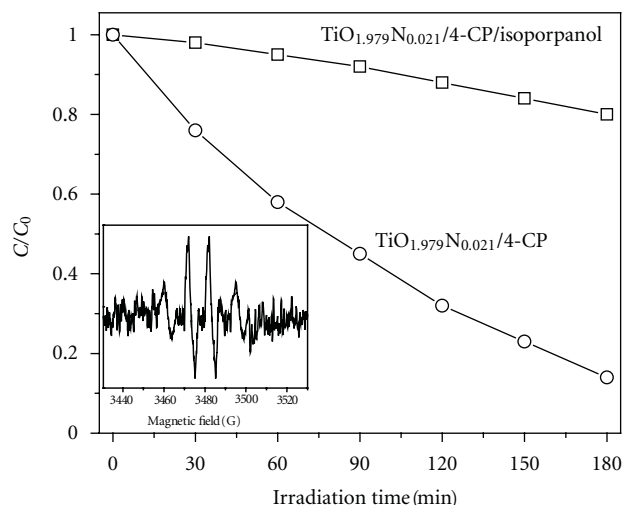


FIGURE 7: Normalized concentration profiles showing 4-CP degradation kinetics upon addition of isopropanol under visible irradiation. Inset: DMPO spin-trapping ESR spectrum under visible irradiation in 4-CP/ $\text{TiO}_{1.979}\text{N}_{0.021}$  aqueous solution. Catalyst loading,  $0.5 \text{ g L}^{-1}$ ; 4-CP,  $10 \text{ mg L}^{-1}$ ; isopropanol,  $1 \times 10^{-5} \text{ M}$ ; the DMPO concentration,  $1.6 \times 10^{-2} \text{ M}$ .

concentration. This is ascribed to the double-faced behaviors of the doped N atoms. The UV-Vis spectra in Figure 3 indicated that the N-doping improved the Vis absorption and increased the number of photons taking part in the photocatalytic reaction. Undoubtedly, this could enhance the photocatalytic activity. On the other hand, they also act as a recombination center of photogenerated charge carriers, and thus deteriorate photocatalysis [26]. The passive role of the N-doped atoms as a recombination center is primary. This was inferred from our results showing a much higher photocatalytic activity is corresponding to the lower  $x$  value.

**3.4. Formation of Radicals.** To probe the nature of the reactive oxygen species generated during the irradiation of the present system, the photodegradation of 4-CP by  $\text{TiO}_{1.979}\text{N}_{0.021}$  in the presence of isopropanol under visible irradiation was performed. The results are shown in Figure 7. It was found that addition of isopropanol, a known scavenger of  $\bullet\text{OH}$  radicals, prohibited greatly the degradation of 4-CP, indicated that the free  $\bullet\text{OH}$  radicals were involved in this photoreaction system. The direct evidence of the reactive oxygen species possibly involved in the photodegradation process was examined by EPR technique (DMPO), as shown in the inset of Figure 7. No ESR signals were observed either when 4-CP was absent or when the reaction was performed in the dark in the presence of the catalysts. Under Vis irradiation the characteristic quartet peaks of DMPO- $\bullet\text{OH}$  adduct with 1 : 2 : 2 : 1 in the intensity were observed after a 80-second irradiation, which are consistent with the similar spectra reported by others for the  $\bullet\text{OH}$  adduct [35].

Although the formation of the superoxide radical anion was expected owing to the scavenging of the electrons by  $\text{O}_2$ , because the N doping did not affect the conduction band of  $\text{TiO}_2$  [17], the spin-adduct DMPO- $\bullet\text{OOH}/\text{O}_2\bullet^-$  was not

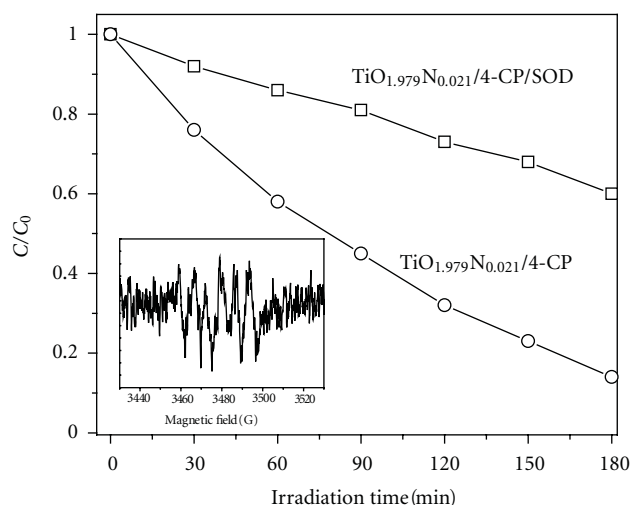


FIGURE 8: Normalized concentration profiles showing 4-CP degradation kinetics upon addition of SOD under Vis irradiation. Inset: DMPO spin-trapping ESR spectra under Vis irradiation in 4-CP/TiO<sub>1.979</sub>N<sub>0.021</sub> ethanol solutions. Catalyst loading, 0.5 g L<sup>-1</sup>; 4-CP, 10 mg L<sup>-1</sup>; SOD, 10000 units; the DMPO concentration, 1.6 × 10<sup>-2</sup> M.

detected in the aqueous system. It is well documented that the superoxide radical anions are produced first and remain stable in an organic solvent medium (at least in methanol) [36]. When the fraction of H<sub>2</sub>O is increased, such as occurs in a CH<sub>3</sub>OH/H<sub>2</sub>O mixed solvent system, the superoxide radical anion tends to be unstable, especially in H<sub>2</sub>O alone. It is probably because the facile disproportionation reaction of superoxide in water precludes the slow reactions between •OOH/O<sub>2</sub>•<sup>-</sup> and DMPO ( $k = 10$  and  $6.6 \times 10^3 \text{ M}^{-1} \text{ s}^{-1}$ , resp.) [37]. Consequently, we recorded the ESR spectra of the DMPO-•OOH/O<sub>2</sub>•<sup>-</sup> spin adducts in methanolic media, and the results were as shown in the inset of Figure 8. The six characteristic peaks of •OOH/O<sub>2</sub>•<sup>-</sup> adducts were observed under Vis irradiation, and the signal intensity increased slightly with irradiation time. No such signals were observed in the dark; that is, generation of O<sub>2</sub>•<sup>-</sup> anions in the N-doped TiO<sub>2</sub> system inherently implicates irradiation. The effect of superoxide dismutase (SOD) on the 4-CP degradation rate was also observed. The results are shown in Figure 8. The presence of SOD (ca. 10000 units), which catalyzes the dismutation of O<sub>2</sub>•<sup>-</sup>, led to a marked suppression of 4-CP photodegradation. This was in good agreement with the ESR measurement. Kinetics studies by ESR measurements and the radical scavenger techniques clarify that the degradation of visible-light-induced degradation of 4-CP over N-doped TiO<sub>2</sub> is derived mainly by the radical reaction, which is similar to that of TiO<sub>2</sub> under UV light irradiation.

**3.5. Proposed Degradation Pathway.** During the photocatalytic degradation, the aromatic intermediates were detected by HPLC. The three intermediates generated during the 4-CP degradation are hydroquinone (HQ), hydroxyhydroquinone (HHQ), and benzoquinone (BQ). Figure 9 illustrates the profiles of the intermediated products during

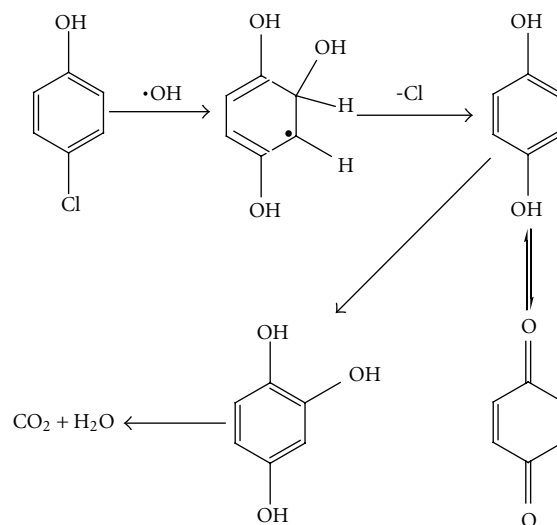


FIGURE 9: Reaction pathway for the photocatalytic degradation of 4-CP in the presence of TiO<sub>1.979</sub>N<sub>0.021</sub> under visible irradiation.

the 4-CP degradation using N-doped TiO<sub>2</sub> under Vis-light irradiation.

The initial step is the formation of electron hole pairs on the surface of the catalysts when irradiated by the visible light. The photoinduced electrons at the catalyst surface are scavenged by the ubiquitously present molecular oxygen to yield first O<sub>2</sub><sup>-</sup>, whence on protonation yields the HO<sub>2</sub> radicals, and to further produce OH whereas the generated holes can react with hydrated surface of the catalyst, resulting in the formation of surface-bound OH directly. Thus the activated oxygen species, OH, O<sub>2</sub><sup>-</sup>, and HO<sub>2</sub> radicals were involved in this photochemical process. However, it is believable that surface-bound and solvated OH radicals are a main oxidant to attack 4-CP. 4-CP is first oxidized into HQ, and then HQ is further oxidized into HHQ and the opening of the ring, and finally the complete mineralization to H<sub>2</sub>O and CO<sub>2</sub>.

## 4. Conclusions

TiO<sub>2-x</sub>N<sub>x</sub> (0.021 < x < 0.049) has prepared by annealing under an NH<sub>3</sub> flow at 550°C. XRD and XPS confirmed that the so-prepared samples had nitrogen substituted at some of the oxygen sites in TiO<sub>2</sub>. The Ndoping did not cause the red shift of the absorbed edge of TiO<sub>2</sub> and revealed that the new absorption shoulder at 400~475 nm, suggesting that an isolated narrow band formed above the valence band could be responsible for the Vis light response of the oxynitride powders. The samples showed the photoactivities for the decomposition of 4-CP under both UV and Vis irradiation. When irradiating with UV or Vis light, the activity of the sample decreased with the increase of the N-doping concentration. ESR measurements gave the clear experimental evidence that the active species, such as •OH and O<sub>2</sub>•<sup>-</sup>, generated and participate in the photodegradation of 4-CP over the N-doped TiO<sub>2</sub> catalyst.

## Acknowledgments

Financial support was provided by National Natural Science Foundation of China (no. 40975074,20747002) and the Pujiang Talent Program of Shanghai, Doctor project for young teachers of Ministry of Education (20070246028), the Key Laboratory of Industrial Ecology and Environmental Engineering, China Ministry of Education, State Key Laboratory of Pollution Control and Resource Reuse (PCRRF10014).

## References

- [1] J. Gamage and Z. S. Zhang, "Applications of photocatalytic disinfection," *International Journal of Photoenergy*, vol. 2010, no. 2010, pp. 764870–764881, 2010.
- [2] J. Yu, L. Qi, and M. Jaroniec, "Hydrogen production by photocatalytic water splitting over Pt/TiO<sub>2</sub> nanosheets with exposed {001} facets," *Journal of Physical Chemistry C*, vol. 114, no. 30, pp. 13118–13125, 2010.
- [3] J. Yu, Y. Hai, and B. Cheng, "Enhanced photocatalytic H<sub>2</sub>-production activity of TiO<sub>2</sub> by Ni(OH)<sub>2</sub> cluster modification," *Journal of Physical Chemistry C*, vol. 115, no. 11, pp. 4953–4958, 2010.
- [4] J. Anthony, P. A. Fernandez-Ibañez, P. S. M. Dunlop, D. M. A. Alrousan, and J. W. J. Hamilton, "Photocatalytic enhancement for solar disinfection of water: a review," *International Journal of Photoenergy*, vol. 2011, no. 2011, pp. 1–12, 2011.
- [5] M. L. Chen and W. C. Oh, "The improved photocatalytic properties of methylene blue for V<sub>2</sub>O<sub>5</sub>/CNT/TiO<sub>2</sub> composite under visible light," *International Journal of Photoenergy*, vol. 2010, pp. 264831–264836, 2010.
- [6] B. Naik, K.M. Parida, and C. S. Gopinath, "Facile synthesis of N- and S-incorporated nanocrystalline TiO<sub>2</sub> and direct solar-light-driven photocatalytic activity," *Journal of Physical Chemistry C*, vol. 114, pp. 19473–19482, 2010.
- [7] W. Choi and S. Kim, "Kinetics and mechanisms of photocatalytic degradation of (CH<sub>3</sub>)<sub>n</sub>NH<sub>4-n</sub><sup>+</sup> (0 ≤ n ≤ 4) in TiO<sub>2</sub> suspension: the role of OH radicals," *Environmental Science and Technology*, vol. 36, no. 9, pp. 2019–2025, 2002.
- [8] W. Ho, J. Yu, J. Lin, and P. Li, "Preparation and photocatalytic behavior of MoS<sub>2</sub> and WS<sub>2</sub> nanocluster sensitized TiO<sub>2</sub>," *Langmuir*, vol. 20, no. 14, pp. 5865–5869, 2004.
- [9] A. Di Paola, S. Ikeda, G. Marci, B. Ohtani, and L. Palmisano, "Transition metal doped TiO<sub>2</sub>: physical properties and photocatalytic behaviour," *International Journal of Photoenergy*, vol. 3, no. 4, pp. 171–176, 2001.
- [10] X. Z. Li and F. B. Li, "Study of Au/Au<sup>3+</sup>-TiO<sub>2</sub> photocatalysts toward visible photooxidation for water and wastewater treatment," *Environmental Science and Technology*, vol. 35, no. 11, pp. 2381–2387, 2001.
- [11] E. Bae and W. Choi, "Highly enhanced photoreductive degradation of perchlorinated compounds on dye-sensitized metal/TiO<sub>2</sub> under visible light," *Environmental Science and Technology*, vol. 37, no. 1, pp. 147–152, 2003.
- [12] J. J. He, A. Hagfeldt, S. E. Lindquist et al., "Phthalocyanine-sensitized nanostructured TiO<sub>2</sub> electrodes prepared by a novel anchoring method," *Langmuir*, vol. 17, no. 9, pp. 2743–2747, 2001.
- [13] W. Zhao, W. Ma, C. Chen, J. Zhao, and Z. Shuai, "Efficient degradation of toxic organic pollutants with Ni<sub>2</sub>O<sub>3</sub>/TiO<sub>2-x</sub>B<sub>x</sub> under visible irradiation," *Journal of the American Chemical Society*, vol. 126, no. 15, pp. 4782–4783, 2004.
- [14] S. Khan, M. Al-Shahry, and W. B. Ingler, "Efficient photochemical water splitting by a chemically modified n-TiO<sub>2</sub>," *Science*, vol. 297, no. 5590, pp. 2243–2245, 2002.
- [15] K. S. Han, D.K. Lee, and J. W. Lee, "Nature of N 2p, Ti 3d, O 2p hybridization of N-doped TiO<sub>2</sub> nanotubes and superior photovoltaic performance through selective atomic N doping," *Chemistry*, vol. 17, no. 9, pp. 2579–2582, 2011.
- [16] S. Liu, J. Yu, and W. Wang, "Effects of annealing on the microstructures and photoactivity of fluorinated N-doped TiO<sub>2</sub>," *Physical Chemistry Chemical Physics*, vol. 12, no. 38, pp. 12308–12315, 2010.
- [17] O. Diwald, T. L. Thompson, T. Zubkov, G. Goralski, S. D. Walck, and J. T. Yates, "Photochemical activity of nitrogen-doped rutile TiO<sub>2</sub>(110) in visible light," *Journal of Physical Chemistry B*, vol. 108, no. 19, pp. 6004–6008, 2004.
- [18] Q. Xiang, J. Yu, and M. Jaroniec, "Nitrogen and sulfur co-doped TiO<sub>2</sub> nanosheets with exposed {001} facets: synthesis, characterization and visible-light photocatalytic activity," *Physical Chemistry Chemical Physics*, vol. 13, no. 11, pp. 4853–4861, 2010.
- [19] S. Sakthivel, M. Janczarek, and H. Kisch, "Visible light activity and photoelectrochemical properties of nitrogen-doped TiO<sub>2</sub>," *Journal of Physical Chemistry B*, vol. 108, no. 50, pp. 19384–19387, 2004.
- [20] R. Bacsá, J. Kiwi, T. Ohno, P. Albers, and V. Nadtochenko, "Preparation, testing and characterization of doped TiO<sub>2</sub> active in the peroxidation of biomolecules under visible light," *Journal of Physical Chemistry B*, vol. 109, no. 12, pp. 5994–6003, 2005.
- [21] X. Hong, Z. Wang, W. Cai et al., "Visible-light-activated nanoparticle photocatalyst of iodine-doped titanium dioxide," *Chemistry of Materials*, vol. 17, no. 6, pp. 1548–1552, 2005.
- [22] C. Burda, Y. Lou, X. Chen, A. C. S. Samia, J. Stout, and J. L. Gole, "Enhanced nitrogen doping in TiO<sub>2</sub> nanoparticles," *Nano Letters*, vol. 3, no. 8, pp. 1049–1051, 2003.
- [23] G. R. Torres, T. Lindgren, J. Lu, C. G. Granqvist, and S. E. Lindquist, "Photoelectrochemical study of nitrogen-doped titanium dioxide for water oxidation," *Journal of Physical Chemistry B*, vol. 108, no. 19, pp. 5995–6003, 2004.
- [24] D. Li, H. Haneda, S. Hishita, and N. Ohashi, "Visible-light-driven N-F-codoped TiO<sub>2</sub> photocatalysts. 1. Synthesis by spray pyrolysis and surface characterization," *Chemistry of Materials*, vol. 17, no. 10, pp. 2588–2595, 2005.
- [25] S. U. M. Khan, M. Al-Shahry, and W. B. Ingler Jr., "Efficient photochemical water splitting by a chemically modified n-TiO<sub>2</sub>," *Science*, vol. 297, no. 5590, pp. 2243–2245, 2002.
- [26] H. Irie, Y. Watanabe, and K. Hashimoto, "Nitrogen-concentration dependence on photocatalytic activity of TiO<sub>2-x</sub>N<sub>x</sub> powders," *Journal of Physical Chemistry B*, vol. 107, no. 23, pp. 5483–5486, 2003.
- [27] T. Ihara, M. Miyoshi, Y. Iriyama, O. Matsumoto, and S. Sugihara, "Visible-light-active titanium oxide photocatalyst realized by an oxygen-deficient structure and by nitrogen doping," *Applied Catalysis B*, vol. 42, no. 4, pp. 403–409, 2003.
- [28] T. Lindgren, J. M. Mwabora, E. Avandaño et al., "Photoelectrochemical and optical properties of nitrogen doped titanium dioxide films prepared by reactive DC magnetron sputtering," *Journal of Physical Chemistry B*, vol. 107, no. 24, pp. 5709–5716, 2003.
- [29] H. Fu, L. Zhang, S. Zhang, Y. Zhu, and J. Zhao, "Electron spin resonance spin-trapping detection of radical intermediates in N-doped TiO<sub>2</sub>-assisted photodegradation of 4-chlorophenol," *Journal of Physical Chemistry B*, vol. 110, no. 7, pp. 3061–3065, 2006.

- [30] C. D. Valentin, G. Pacchioni, and A. Selloni, "Origin of the different photoactivity of N-doped anatase and rutile TiO<sub>2</sub>," *Physical Review B*, vol. 70, no. 8, pp. 1–4, 2004.
- [31] O. Diwald, T. L. Thompson, E. G. Goralski, S. D. Walck, and J. T. Yates Jr., "The effect of nitrogen ion implantation on the photoactivity of TiO<sub>2</sub> rutile single crystals," *Journal of Physical Chemistry B*, vol. 108, no. 1, pp. 52–57, 2004.
- [32] X. Chen and C. Burda, "Photoelectron spectroscopic investigation of nitrogen-doped titania nanoparticles," *Journal of Physical Chemistry B*, vol. 108, no. 40, pp. 15446–15449, 2004.
- [33] C. D. Valentin, G. Pacchioni, A. Selloni, S. Livraghi, and E. Giamello, "Characterization of paramagnetic species in N-doped TiO<sub>2</sub> powders by EPR spectroscopy and DFT calculations," *Journal of Physical Chemistry B*, vol. 109, no. 23, pp. 11414–11419, 2005.
- [34] R.M. Dreizler and E. K. Gross, *Density Functional Theory: An Approach to the Quantum Many-Body Problem*, Springer, Berlin, Germany, 1990.
- [35] Y. Huang, J. Li, W. Ma, M. Cheng, and J. Zhao, "Efficient H<sub>2</sub>O<sub>2</sub> oxidation of organic pollutants catalyzed by supported iron sulfophenylporphyrin under visible light irradiation," *Journal of Physical Chemistry B*, vol. 108, no. 22, pp. 7263–7270, 2004.
- [36] C. Chen, W. Zhao, P. Lei, J. Zhao, and N. Serpone, "Photosensitized degradation of dyes in polyoxometalate solutions versus TiO<sub>2</sub> dispersions under visible-light Irradiation: mechanistic implications," *Chemistry*, vol. 10, no. 8, pp. 1956–1965, 2004.
- [37] G. Liu, X. Li, and J. Zhao, "Photooxidation pathway of sulforhodamine-B. Dependence on the adsorption mode on TiO<sub>2</sub> exposed to visible light radiation," *Environmental Science and Technology*, vol. 34, no. 18, pp. 3982–3990, 2000.